Wind and Seismic Effects

PROCEEDINGS OF THE 17th JOINT
PANEL MEETING OF THE U.S.-JAPAN
COOPERATIVE PROGRAM IN WIND AND SEISMIC EFFECTS

Noel J. Raufaste, EDITOR

Center for Building Technology
National Engineering Laboratory
National Bureau of Standards
Gaithersburg, MD 20899

U.S. DEPARTMENT OF COMMERCE, Malcolm Baldrige, Secretary
NATIONAL BUREAU OF STANDARDS, Ernest Ambler, Director

Issued May 1986

PREFACE

The U.S.-Japan Cooperative Program in Natural Resources (UJNR) was established in 1964 for the exchange of technical information and experience mutually beneficial to the economics and welfare of both countries. The Panel on Wind and Seismic Effects held its first joint meeting in 1969 in Tokyo, Japan. The joint meeting has been held annually ever since, alternating in Japan the odd numbered years and the U.S. in the even numbered years.

The Seventeenth Joint Meeting was held in Tsukuba, Japan May 21-24, 1985. Under five themes, forty-seven technical papers were presented for discussion. Ten Panel task committees held their meetings during this period.

These proceedings include the program of the Seventeenth Joint Meeting, the Panel resolutions, and the technical papers. Acknowledgement is extended to those U.S. Panel members who helped edit for clarity the technical papers.

Preparation of the proceedings was partially supported by funds from the U.S. Federal Agencies providing members to the U.S. Panel.

Noel J. Raufaste, Secretary
U.S. Panel on Wind and
Seismic Effects

SI CONVERSION UNITS

In view of the present accepted practice for wind and seismic technolog, common units of measurements were used through this publication. In recognition of the position of the United States as a signatory to the General Conference on Weights and Measures, which gave official status to the International System of Units (SI) in 1960, the table below is presented to facilitate conversion to SI Units. Readers interested in making further use of the coherent system of SI units are referred to NBS SP 330, 1977 Edition, The International System of Units; and ASTM Standard for Metric Practice.

TABLE OF CONVERSION FACTORS TO SI UNITS

	Customary Units	International (SI) Unit	Conversion Approximate
Length	inch (in)	meter (m)[a]	1 in = 0.0254 m*
	foot (ft)	meter (m)	1 ft = 0.3048 m*
Force	pound (lbf)	newton (N)	1 lbf = 4.48 N
	kilogram (kgf)	newton (N)	1 kgf = 9.807 N
Pressure or Stress	pound per square	newton/per square	
	inch (psi)	meter	1 psi = 6895 N/m^2
	kip per square	newton per square	
	inch (ksi)	meter	1 ksi = $6895 \times 10^3 N/m^2$
Energy	inch·pound (in-lbf)	joule (J)	1 in·lbf = 0.1130 J
	foot·pound (ft-lbf)	joule (J)	1 ft·lbf = 1.3558 J
Torque or Bending Moment	pound·inch	newton-meter (N·m)	1 lbf·in = 0.1130 N·m
	pound·foot (lbf-ft)	newton-meter (N·m)	1 lbf·ft = 1.3558 N·m
Weight	pound (lb)	kilogram (kg)	1 lb = 0.4536 kg
Unit Weight	pound per cubic foot (pcf)	kilogram per cubic meter (kg/m^3)	1 pcf = 16.018 kg/m^3
Velocity	foot per second (ft/sec)	meter per second (m/s)	1ft/s = 0.3048 m/s
Acceleration	foot per second square (ft/s^2)	meter per second square (m/s^2)	1 ft/s^2 = 0.3048 m/s^2

[a] Meter may be subdivided. A centimeter (cm) is 1/100 m and a millimeter (mm) is 1/1000 m.

* Exactly

ABSTRACT

The Seventeenth Joint Meeting of the U.S.-Japan Panel on Wind and Seismic Effects was held in Tsukuba, Japan from May 21 through 24, 1985. This publication, the proceedings of the Joint Meeting, includes the program, list of members, formal resolutions, and technical papers.

Papers were presented under five themes:

Theme I - WIND ENGINEERING
Theme II - EARTHQUAKE ENGINEERING
Theme III - STORM SURGE AND TSUNAMIS
Theme IV - U.S.-JAPAN COOPERATIVE RESEARCH PROGRAM
Theme V - REPORTS ON THE NIHONKAI-CHUBU EARTHQUAKE AND THE NAGANOKEN-SEIBU EARTHQUAKE

Subjects covered in the papers presented include:

(1) characteristics of strong winds;
(2) wind loads on structures and design criteria;
(3) earthquake ground motions;
(4) soil liquefaction studies and methods to improve liquefaction resistance;
(5) seismic loads on structures and design criteria;
(6) stress analyses of pipelines during earthquakes;
(7) full-scale seismic experiments;
(8) earthquake hazard reduction program;
(9) use of the microcomputer for earthquake studies;
(10) quantitative evaluation of damages caused by winds and earthquakes; and,
(11) tsunami research projects.

KEYWORDS: Accelerograph; codes; design criteria; disaster; earthquakes; earthquake hazards; geotechnical engineering; ground failures; liquefaction; pipeline; seismicity; solids; standards; structural engineering; structural response; tsunami; wind loads; and winds.

CONTENTS

CONTENTS

CONTENTS

CONTENTS

SCHEDULE OF THE 17th JOINT MEETING

May 19 (Sun)	U.S. members arrive at Narita; other U.S. members who attended Task Committee D join in Tsukuba
20 (Mon)	Visit Tsukuba EXPO '85
21 (Tue)	Opening Session Technical Sessions Reception (Hosted by the Engineer General of the Ministry Of Construction)
22 (Wed)	Technical Sessions Task Committees
23 (Thu)	Technical Sessions Task Committees
24 (Fri)	Technical Sessions Reports of Task Committees Adoption of Final Resolution Closing Session
25 (Sat)	Tsukuba-Tokyo
26 (Sun)	Tokyo-Matsumoto-Kamikochi, Nagano Pref.
27 (Mon)	Kamikochi--(Kisofukushima
29 (Wed)	Kisofukushima-- Nakatsugawa I.C.-- Nagoya-- Kobe
30 (Thu)	Kobe-- Naruto (Honshu-Shikoku Bridges)-- Kobe (Port Island, Harbor)
31 (Fri)	Kobe-- Kyoto
June 1 (Sat)	Kyoto-- Tokyo
2 (Sun)	U.S. members leave Japan

PROGRAM OF THE SEVENTEENTH JOINT MEETING

Tuesday - May 21

Opening Session 10:30 - 12:00

Call to order by Dr. Nobuyuki Narita, Secretary-General, Japan Panel

Remarks by: Tetsuo Kutsukake, G. H. Hlfrich, Hirofumi Satake, Masateru Tominaga, and R. N. Wright

Technical Session 13:00 - 17:20

Session 1: Theme I - WIND ENGINEERING Chairman: M. Tominaga

13:00-13:20 Interpretation of Section Model Aeroelastic Results in the case of Cable-Stayed Bridges
R. H. Scanlan (A. M. Abdel-Ghaffar)

13:20-13:40 Characteristics of Aerodynamic Forces on Bridge Decks in Smooth Flow and in Turbulent Flow
N. Narita, H. Tada, K. Yokoyama and H. Sato

13:40-14:00 Field Measurements on the Deer Isle-Sedgwick Suspension Bridge
H. R. Bosch (H. S. Lew)

14:00-14:20 Discussion

Session 2: Theme I - WIND ENGINEERING Chairman: M. Tominaga

14:20-14:40 Wind Tunnel Modeling for Flow Around Buildings
T. Murota, T. Okuma and H. Okada

14:40-15:00 Automatic Detection of Gust Fronts with a Single Doppler Radar
H. Ueda, Dusan S. Zrnic and H. Takahashi

15:00-15:20 Discussion

15:20-15:40 Break

Session 3: Theme IV - U.S.-JAPAN COOPERATIVE RESEARCH PROGRAM
Chairman: M. Tominaga

15:40-16:00 Recommended U.S.-Japan Joint Research on Seismic Behavior of Buried Pipelines and Telecommunications Systems
M. Shinozuka

16:00-16:20 Experimental Investigation on Hysteretic Behavior of Reinforced Concrete Bridge Pier Columns
T. Iwasaki, K. Kawashima, R. Hagiwara, K. Hasegawa, T. Koyama and T. Yoshida

16:20-16:40 Re-Evaluation of Liquefaction Resistance Curves
R. M. Chung, H. B. Seed, A. G. Franklin and J. A. Farrar

16:40-17:00 In-situ Test for Assessing the Liquefaction Potential Using Vibratory Cone Penetrometer
Y. Sasaki, Y. Koga, Y. Itoh, T. Shimazu and M. Kondoh

17:00-17:20 Discussion

18:30- Reception

Wednesday - May 22

Technical Session 9:00 - 12:20

Session 4: Theme IV - U.S.-JAPAN COOPERATIVE RESEARCH PROGRAM
Chairman: R. N. Wright

9:00-9:20 U.S.-Japan Joint Earthquake Research Program Involving Large-Scale Experiments on Masonry Structures -- Japanese Side Research Plan --
S. Okamoso, Y. Yamazaki, A. Baba, M. Teshigawara and H. Hiraishi

9:20-9:40 Inelastic Seismic Tests on a Full-Scale Six-story Eccentric-K Braced Steel Building
-- U.S./Japan Cooperative Earthquake Research Program --
H. Yamanouchi, M. Midorikawa, I. Nishiyama and M. Hirosawa

9:40-10:00 A Summary Report of the U.S.-Japan Workshop on Evaluation of Structural Performance
R. N. White and G. R. Fuller

10:00-10:20 Discussion

10:20-10:40 Break

Session 5: Theme II: EARTHQUAKE ENGINEERING Chairman: R. N. Wright

10:40-11:00 Earthquake Hazard Reduction Program of the Department of State
P. E. Gurvin

11:00-11:20 Strong Motion Instrumentation in Bureau of Reclamation Program
R. B. MacDonald and A. Viksne

11:20-11:40 Array Observationof Strong-Motion Earthquake in Fuchu Area
S. Kinoshita, K. Ohtani and T. Mikoshiba

11:40-12:00 Implications of Recent Advances in Instrumentation for Strong-Motion Studies
R. D. Borcherdt

12:00-12:20 Discussion

12:20-13:20 Lunch

Technical Session 13:20 - 14:00

Session 6: Theme II - EARTHQUAKE ENGINEERING Chairman: R. N. Wright

13:20-13:40 Dynamic Behaviours of a Rockfill Dam During Earthquakes
N. Matsumoto, N. Yasuka and M. Shiga

13:40-14:00 Vibration Test of Richard B. Russell Concrete Dam After Reservoir Impoundment
R.J. Smith

14:00-14:20 Discussion

14:20-14:30 Break

14:30-17:00 Task Committee Meetings
B: Large-Scale Testing Programs
C: Repair and Retrofit of Existing Structures
E: Land Use Program for Controlling Natural Hazard Effects
H: Soil Behavior and Stability During Earthquakes
I: Storm Surge and Tsunamis

18:00- Reception

Thursday - May 23

Technical Session 9:00 - 12:40

Session 7: Theme II - EARTHQUAKE ENGINEERING Chairman: M. Tominaga

9:00-9:20 Earthquake Resistant Bridge Design in California
J. H. Gates

9:20-9:40 Seismic Analysis, Instrumentation and Dynamic Testing of Cable-Supported Bridges
A. M. Abdel-Ghaffar

9:40-10:00 Earthquake Resistant Design of Building Foundation
--Introduction and Commentary on "Design Guide for the Building Foundation Against Seismic Force"--
Y. Sugimura

10:00-10:20 Shear Resistance of Unreinforced Hollow Concrete Block Masonry Walls
K. Woodward and F. Rankin

10:20-10:40 Discussion

10:40-11:00 Break

Session 8: Theme II - EARTHQUAKE ENGINEERING Chairman: M. Tominaga

11:00-11:20 An Experimental Study on Sliding Rigid Body in Water During Earthquake
T. Uwabe, N. Higaki and S. Noda

11:20-11:40 A Rapid Seismic Analysis Procedure for Anchored Sheet Pile Bulkheads
T. K. Lew

11:40-12:00 Design of Piles for Slopes
H. Tada, K. Ohshima, Y. Sato and R. Abo

12:00-12:20 Dynamic Stresses and Displacements in a Buried Tunnel
S. K. Datta, K. C. Wong and A. H. Shah

12:20-12:40 Discussion

12:40-13:40 Lunch

Technical Session 13:40 - 14:00

Session 9 Chairman: M. Tominaga

13:40-14:00 A Short Slide Presentation on Survey of the Recent Chilean Earthquake
J. H. Gates

14:00-14:20 A Short Slide Presentation on Survey of the Recent Chilean Earthquake
H. Tsuchida

14:20-14:30 Break

Task Committee Meetings 14:30 - 17:20

A: Strong-Motion Instrumentation Arrays and Data
D: Evaluation of Performance of Structures
F: Disaster Prevention Methods for Lifeline Systems
G: Wind Characteristics and Structural Response
J: Wind and Earthquake Engineering for Transportation Systems

Friday - May 24

Technical Session 9:00 - 12:20

Session 10: Theme III - STORM SURGE AND TSUNAMIS Chairman: R. N. Wright

9:00-9:20 Damages of Coastal and River structures Caused by the Nihonkai-chubu Earthquake Tsunami
T. Uda and A. Omata

9:20-9:40 Progress in Developing Tsunami Data Base
J. F. Lander and P. A. Lockridge

9:40-10:00 Tsunamis in the Japan Sea with Numerical Calculation
Y. Tsuji and H. Takahashi

10:00-10:20 Discussion

10:20-10:40 Break

Session II: Theme V - REPORTS ON THE NIHONKAI-CHUBU EARTHQUAKE AND THE NAGANOKEN-SEIBU EARTHQUAKE Chairman: R. N. Wright

10:40-11:00 Study on Economical Losses Caused by Change of Cargo Flow at Port of Akita Due to the Nihonkai-chubu Earthquake, 1983
A. Yonezawa and H. Tsuchida

11:00-11:20 Landslides and Damages Due to the Naganoken-seibu Earthquake of September 14,1984
M. Tominaga, Y. Sasaki, K. Senoo, H. Yoshimatsu, E. Taniguchi, M. Nakano, N. Obinata, Y Hars and T. Kuwabara

11:20-11:40 Geomorphogical Characteristics and Factors of the Large-Scale Landslide and Detritus Flow on the South Slope of Ontake Volcano Caused by the Naganoken-seibu Earthquake, 1984
M. Nagaoka, Y. Hoshino, Y. Takei, S. Ichikawa and H. Saito

11:40-12:00 Seismological Studies on the Naganoken-seibu Earthquake, 1984, based on JMA Seismic Network
M. Takeo, N. Mikami and M. Ichikawa

12:00-12:20 Discussion

Reports of Task Committees 13:20 - 15:00 Chairman: M. Tominaga

- A: Strong-Motion Instrumentation Arrays and Date
- B: Large-Scale Testing Programs
- C: Repair and Retrofit of Existing Structures
- D: Evaluation of Performance of Structures
- E: Land Use Program for Controlling Natural Hazard Effects
- F: Disaster Prevention Methods for Lifeline Systems
- G: Wind Characteristics and Structural Response
- H: Soil Behavior and Stability During Earthquakes
- I: Storm Surge and Tsunamis
- J: Wind and Earthquake Engineering for Transportation Systems

15:00-15:10 Break

15:10-15:40 Adoption of Final Resolution Chairman: M. Tominaga

15:40- Break

16:00-16:20 Closing Session
Closure by Dr. Nobuyuki Narita

OPENING SESSION

Tuesday - May 21, 1985 (10:30-12:00)

Conference Hall (8th Floor), Public Works Research Institute

Call to order by Dr. Nobuyuki Narita, Secretary-General, Japan Panel
Assistant Director-General, Public Works Research Institute

Remarks by Mr. G. H. Helfrich, Counselor for Scientific and Technological Affairs, Embassy of the United States of America

Remarks by Mr. Hirofumi Satake, Director, International Affairs Division Promotion Bureau, Science and Technology Agency

Remarks by Dr. Masateru Tominaga, Chairman, Japan Panel, Director-General Public Works Research Institute, Ministry of Construction

Remarks by Dr. Richard N. Wright, Chairman, U. S. Panel, Director, Center for Building Technology, NEL, National Bureau of Standards, Department of Commerce

Introduction of Japan Panel Members by Japanese Chairman and U.S. Panel Members by U. S. Chairman

Election of Conference Chairman

Adoption of Agenda

Adjourn

Group Photograph

U.S. PANEL MEMBERS-WIND AND SEISMIC EFFECTS
1985

Dr. Richard N. Wright, Chairman
Director, Center for Building Technology
National Bureau of Standards
Gaithersburg, MD 20899
(301) 921-3377

Dr. H. S. Lew, Secretariat
Leader, Construction Safety Group
Structures Division
Center for Building Technology
National Bureau of Standards
Gaithersburg, MD 20899
(301) 921-2647

Dr. S. T. Algermissen
Office of Earthquake Studies
Branch of Earthquake Tactonics, USGS
Denver Federal Center
Stop 978, Box 25046
Denver, CO 80225
(303) 236-1611

Dr. Celso S. Barrientos
Supervisory Physical Scientist
NOAA/NESDIS
3300 Whitehaven Street, NW
Washington, DC 20235
(202) 634-7379

Dr. Eddie N. Bernard
Director, Pacific Marine
Environmental Laboratory
7600 San Point Way, NE
Seattle, WA 98115
(206) 526-6239 FTS 292-6800

Dr. Roger D. Borcherdt
Chief, Branch of Engineering
Seismology and Geology
Office of Earthquake Studies, USGS
345 Middlefield Road
Menlo Park, CA 94025
(415) 323-8111 X2755

Dr. A. Gerald Brady
Physical Scientist
Office of Earthquake Studies
U.S. Geological Survey
345 Middlefield Road
Menlo Park, CA 94025
(415) 323-8111

Dr. John J. Burns, Jr.
Head, Structures Section
Office of Research
U.S. Nuclear Regulatory
Commission
Washington, DC 20555
(301) 443-7860

Dr. James Choromokos, Jr.
Director
Research and Development
Department of the Army
DAEN-RDZ-A
Washington, DC 20314
(202) 272-0254

Dr. Charles G. Culver
Chief, Structures Division
National Bureau of Standards
Gaithersburg, MD 20899
(301) 921-2196

Dr. A. G. Franklin
Chief, Earthquake Engineering
and Geophysics Division
Geotechnical Laboratory
U.S. Army Engineer Waterways
Experiment Station
Vicksburg, MS 39180
(601) 634-2658

Mr. G. Robert Fuller
Chief, Standards Branch
Manufactured Housing Construction
Standards Division, Room 9156
Housing and Urban Development
Washington, DC 20411
(202) 755-6920

Mr. James H. Gates
Office of Structures Design
Department of Transportation
1120 N Street
Sacramento, CA 95814
(916) 445-3810

Dr. Riley M. Chung
Leader, Geotechnical Engineering
Group, Structures Division
National Bureau of Standards
Gaithersburg, MD 20899
(301) 921-2647

Dr. Michael P. Gaus
Section Head of Critical Engineering
Division of Emerging and Critical
Engineering Systems
National Science Foundation
1800 G Street, NW
Washington, DC 20550
(202) 357-9500

Mr. Peter E. Gurvin
A/FBO, SA-6
Department of State
Washington, DC 20620
(202) 235-3689

Dr. Walter W. Hays
Deputy for Research Application
U.S. Geological Survey
Office of Earthquake Survey
905 National Center
Reston, VA 22043
FTS 928-6472 or (703) 860-6471

Dr. William B. Joyner
Geophysicist
Office of Earthquake Studies
Branch of Ground Motion and
Faulting, USGS
342 Middlefield Road
Menlo Park, CA 94025
(415) 323-8111

Mr. Richard W. Kramer
Civil Engineer
Technical Review Staff, D-3210
Bureau of Reclamation
P. O. Box 25007
Denver, CO 80225
FTS 776-8539 or (303) 236-8539

Mr. Richard Krimm
Office of Natural and
Technological Hazards
Federal Emergency Management Agency
Washington, DC 20472
(202) 646-2871

Mr. Paul K. Krumpe
Office of Foreign Disaster Assistance
Agency for International Development
Department of State
Washington, DC 20523
(202) 632-5916

Mr. James F. Lander
Deputy Director
National Geophysical Data Center
NOAA/NESDIS
325 Broadway
Boulder, CO 80303
FTS 320-6215 or (303) 497-6215

Dr. E. V. Leyendecker
Leader, Earthquake Hazards Reduction
Group, Structures Division
Center for Building Technology
National Bureau of Standards
Gaithersburg, MD 20899
(301)921-3471

Mr. Robert MacDonald
Geologic Service Branch
Code D
1630 Bureau of Reclamation
Building 67, Denver Federal Center
Denver, CO 80225
FTS 786-4195 or (303) 236-8428

Dr. Richard D. McConnell
Office of Construction
Veterans Administration
811 Vermont Avenue, NW
Washington, DC 20420
(202) 389-3103

Dr. Francis G. McLean
Chief, Division of Research and
Laboratory Services, D-1500
Bureau of Reclamation
P. O. Box 25007
Denver, CO 80225
FTS 776-5981 or (303) 234-3303

Dr. Richard D. Marshall
Structural Engineering Group
Structures Division
Center for Building Technology
National Bureau of Standards
Gaithersburg, MD 20899
(301) 921-2170

Mr. John F. Meehan
Principal Structural Engineer
Research Director
Structural Safety Section
Office of the State Architect
Department of General Services
Sacramento, CA 95805
(916) 445-8730

Dr. John B. Scalzi
Program Director, Systems
Engineering for Large Structures
National Science Foundation
1800 G Street, NW, Room 1130
Washington, DC 20550
(202) 357-7710

Mr. Joseph T. Schaefer
Chief, Techniques Development Unit
National Severe Storm Forecast Center
National Weather service, NOAA
601 E. 12th Street
Room 1728 Federal Building
Kansas City, MO 64106
(816) 374-3367

Dr. Charles Scheffey
Science Advisor, Offices of Research,
Development and Technology
Federal Highway Administration
6300 Georgetown Pike
McLean, VA 22101
(703) 285-2054

Mr. Robert J. Smith
Department of the Army
Office of the Chief of Engineers
DAEN-CWE-DS
Washington, DC 20314
(202) 272-0219

Dr. Lawrence A. Soltis
Supervisory Research Engineer
Engineering design Criteria
Forest Products Laboratory
Forest Service, Dept. of Agriculture
Madison, WI 53705
(608) 264-5910

Mr. K. Thirumalai
Earthquake Hazards Mitigation Section
National Science Foundation
1800 G Street, NW, Room 1130
Washington, DC 20550
(202) 357-9500

Mr. Stanley K. Takahashi
Structures Division
Naval Civil Engineering Laboratory
Port Huemene, CA 93043
(805) 982-4684

Alternates

Mr. Michael Changery
National Climatic Center
Federal Building
Asheville, NC 28787
(704) 258-2850 ext. 217

Mr. Roger Kenneally
Structures Section
Office of Research
U.S. Nuclear Regulatory Commission
Washington, DC 20555
(301) 443-7860

Mr. Robert R.Ledzian
Senior Staff Assistant for
Research, WO-220
Bureau of Reclamation
Department of the Interior
18th at C Streets, NW
Washington, DC 20240
(202) 343-6703

Mr. Ronald J. Morony
Program Manager
Building Technology Research Staff
Department of Housing and Urban
Development
Washington, DC 20410
(202) 755-0640

JAPANESE PANEL MEMBERS - WIND AND SEISMIC EFFECTS
1985

Dr. Masateru Tominaga, Chairman
Director-General
Public Works Research Institute
Ministry of Construction
Asahi 1-banchi, Toyosato-machi, Tsukuba-gun
Ibaraki-ken 305
0298-64-2211

Dr. Nobuyuki Narita, Secretary-General
Assistant Director-General
Public Works Research Institute
Ministry of Construction
Asahi 1-banchi, Toyosato-machi, Tsukuba-gun
Ibaraki-ken 305
0298-64-2211

Mr. Tsunekazu Fukui, Deputy Secretary-General
Director, Planning and Research
Administration Department
Public Works Research Institute
Ministry of Construction
Asahi 1-banchi, Toyosato-machi, Tsukuba-gun
Ibaraki-ken 305
0298-64-2211

Dr. Yoshimi Goda
Deputy Director-General
Port and Harbour Research Institute
Ministry of Transport
3-1-1, Nagase, Yokosuka-shi,
Kanagawa-ken 239
0468-41-5410

Dr. Sadaiku Hattori
Director, International Institute of
Seismology and Earthquake Engineering
Building Research Institute
Ministry of Construction
Tatehara 1-banchi, Oh-ho-machi, Tsukuba-gun
Ibaraki-ken 305
0298-64-2151

Dr. Masaya Hirosawa
Director, Research Planning
and Information Department
Building Research Institute
Tatehara 1-banchi, Oh-ho-machi, Tsukuba-gun
Ibaraki-ken 305

Dr. Masaji Ichikawa
Head, Seismology and Volcanology Division
Meteorological Agency (JMA)
1-1, Nagamine, Yatabe-machi, Tsukuba-gun
Ibaraki-ken 305
0298-51-7111

Dr. Yuji Ishiyama
Head, Building Engineering Division
International Institute of Seismology
and Earthquake Engineering (I.E.S.E.E.)
Building Research Institute
Ministry of Construction
Tatehara 1-banchi,Oh-ho-machi,Tsukuba-gun
Ibaraki-ken 305
0298-64-2151

Dr. Toshio Iwasaki
Director, Earthquake Disaster Prevention
Department
Public Works Research Institute
Ministry of Construction
Asahi 1-banchi,Toyosato-machi,Tsukuba-gun
Ibaraka-ken 305
0298-64-2211

Dr. Kazuhiko Kawashima
Head, Earthquake Engineering Division
Earthquake Disaster Prevention Department
Public Works Research Institute
Ministry of Construction
Asahi 1-banchi,Toyosato-machi,Tsukuba-gun
Ibaraki-ken 305
0298-64-2211

Mr. Yasuyuki Koga
Head, Soil Dynamics Division
Construction Method and Equipment Dept.
Public Works Research Institute
Ministry of Construction
Asahi 1-banchi,Toyosato-machi,Tsukuba-gun
Ibaraki-ken 305

Dr. Keizo Masamura
Head, Typhoon Research Division
Meteorological Research Institute (MRI)
Japan Meteorological Agency (JMA)
1-1, Nagamine, Yatabe-machi, Tsukuba-gun
Ibaraki-ken 305
0298-51-7111

Dr. Norihisa Matsumoto
Head, Fill Type Dam Division
Dam Department
Public Works Research Institute
Ministry of Construction
Asahi 1-banchi,Toyosato-machi,Tsukuba-gun
Ibaraki-ken 305
0298-64-2211

Mr. Tatsuo Murota
Head, Building Aerodynamics Division
Structural Engineering Department
Building Research Institute
Ministry of Construction
Tatehara 1-banchi, Oh-ho-machi, Tsukuba-gun
Ibarai-ken 305
0298-64-2151

Mr. Masatoshi Nagaoka
Head, Geographical Research Office
Geographical Research Institute
Ministry of Construction
Kitazato 1-banchi, Yatabe-machi, Tsukuba-gun
Ibaraki-ken 305

Dr. Keikichi Naito
Head, Meteorological Satellite Division
Meteorological Research Institute (MRI)
Japan Meteorological Agency (JMA)
1-1, Nagamine, Yatabe-machi, Tsukuba-gun
Ibaraki-ken 305
0298-51-7111

Dr. Setsuo Noda
Chief, Earthquake Resistant Structures
Laboratory, Structure Division
Port and Harbour Research Institute
Ministry of Transport
3-1-1, Nagase, Yokosuka-shi, Kanagawa-ken 239
0468-41-5410

Mr. Kazuya Ohshima
Head, Foundation Engineering Division
Structure and Bridge Department
Public Works Research Institute
Ministry of Construction
Asahi 1-banchi, Toyosato-machi, Tsukuba-gun
Ibaraki-ken 305
0298-64-2211

Mr. Keiichi Ohtani
Chief, Earthquake Engineering Laboratory
Second Research Division
National Research Center for
Disaster Prevention
Science and Technology Agency
3-1, Tennodai, Sakura-mura, Niihari-gun
Ibaraki-ken 305
0298-51-1611

Mr. Shin Okamoto
Diroctor, Production Department
Building Reseach Institute
Ministry of Construction
Tatehara 1-banchi, Oh-ho-machi, Tsukuba-gun
Ibaraki-ken 305
0298-64-2151

Dr. Yasushi Sasaki
Head, Ground Vibration Division
Earthquake Disaster Prevention Department
Public Works Research Institute
Ministry of Construction
Asahi 1-banchi,Toyosato-machi,Tsukuba-gun
Ibaraki-ken 305
0298-64-2211

Mr. Hiroshi Shinohara
Head, Bridge Division
Structure and Bridge Department
Public Works Research Institute
Ministry of Construction
Asahi 1-banchi,Toyosato-machi,Tsukuba-gun
Ibaraki-ken 305
0298-64-2211

Dr. Yoshihiro Sugimura
Head, Foundation Engineering Division
Structure Engineering Department
Building Research Institute
Ministry f Construction
Tatehara 1-banchi,Oh-ho machi,Tsukuba-gun
Ibaraki-ken 305
0298-64-2151

Dr. Hirohiko Tada
Director, Structure and Bridge Department
Public Works Research Institute
Ministry of Construction
Asahi 1-banchi,Toyosato-machi,Tsukuba-gun
Ibaraki-ken 305
0298-64-2211

Dr. Hiroshi Takahashi
Director-General
National Research Center for Disaster
Prevention,Science and Technology Agency
3-1, Tennodai, Sakura-mura, Niihara-gun
Ibaraki-ken 305
0298-51-1611

Dr. Haime Tsuchida
Director, Structure Division
Port and Harbour Research Institute
Ministry of Transport
3-1-1,Nagase,Yokosuka-shi,Kanagawa-ken 239

Dr. Takaaki Uda
Head, Coastal Engineering Division
River Department
Public Works Research Institute
Ministry of Construction
Asahi 1-banchi,Toyosato-machi,Tsukuba-gun
Ibaraki-ken 305
0298-64-2211

Mr. Koichi Yokoyama, Secretary
Head, Structure Division, Structure and
Bridge Dept., Public Works Research Institute,
Ministry of Construction, Asahi 1-banchi,
Toyosato-machi, Tsukuba-gun, Ibaraki-ken 305

MEMBERS OF TASK COMMITTEES

	Task Committee	U.S. Side	Japanese Side
A.	Strong-Motion Instrumentation Arrays and Data	* A.G. Brady W.B. Joyner J.F. Lander F.G. McLean	* Hajime Tsuchida Sadaiku Hattori Masaji Ichikawa Yuji Ishiyama Keiichi Ohtani Yasushi Sasaki
B.	Large-Scale Testing Programs	* E.V. Leyendecker H.S. Lew J.B. Scalzi C.F. Scheffey	* Keiichi Ohtani Yuji Ishiyama Yasuyuki Koga Setsuo Noda Shin Okamoto Koichi Yokoyama
C.	Repair and Retrofit of Existing Structures	* J.B. Scalzi P.E. Gurvin H.S. Lew R.D. McConnell C.F. Scheffey	* Masaya Hirosawa Yuji Ishiyama Toshio Iwasaki Shin Okamoto Hirohiko Tada
D.	Evaluation of Performance of Structures	* G.R. Fuller R.D. McConnell J.F. Meehan J.B. Scalzi S.K. Takahashi	* Shin Okamoto Yuji Ishiyama Kazuya Ohshima Hirohiko Tada
E.	Land Use Program for Controlling Natural Hazard Effects	* S.T. Algermissen A.G. Brady G.R. Fuller R.D. Marshall	* Kazuhiko Kawashima Sadaiku Hattori Toshio Iwasaki Masatoshi Nagaoka Yoshihiro Sugimura
F.	Disaster Prevention Methods for Lifeline Systems	* K. Thirumalai E.V. Leyendecker J.B. Scalzi S.K. Takahashi	* Toshio Iwasaki Kazuhiko Kawashima Tatsuo Murota Setsuo Noda Keiichi Ohtani Yasushi Sasaki
G.	Wind Characteristics and Structural Response	* R.D. Marshall C.S. Barrientos M.P. Gaus S.K. Takashashi C.F. Scheffey	* Keikichi Naito Keizo Masamura Tatsuo Murota Nobuyuki Narita Koichi Yokoyama
H.	Soil Behavior and Stability During Earthquakes	* A.G. Franklin R. Chung F.G. McLean R.J. Smith	* Yasushi Sasaki Yasuyuki Norihisa Matsumoto Kazuya Ohshima Yoshihiro Sugimura Hajime Tsuchida
I.	Storm Surge and Tsunamis	* C.S. Barrientos E.N. Bernard M.P. Gaus J.F. Lander	* Yoshimi Goda Keizo Masamura Masaji Ichikawa Hiroshi Takahashi Takaaki Uda
J.	Wind and Earthquake Engineering for Transportation Systems	* C.F. Scheffey A.G. Franklin H.S. Lew E.V. Leyendecker	* Hirohiko Tada Toshio Iwasaki Kazuhiko Kawashima Nobuyuki Narita Kazuya Ohshima Hiroshi Shinohara Yasushi Sasaki

* Chairman

U.S. PARTICIPANTS
AT THE
SEVENTEENTH JOINT MEETING
1985

Dr. Richard N. Wright, Chairman
Director
Center for Building Technology
National Bureau of Standards
Gaithersburg, Maryland 20899
(301)921-3377

Dr. H. S. Lew, Secretariat
Leader, Construction Safety Group
Structures Division
Center for Building Technology
National Bureau of Standards
Gaithersburg, Maryland 20899
(301) 921-2647

Dr. Roger D. Borcherdt
Chief, Branch of Engineering
Seismology and Geology
Office of Earthquake Studies, USGS
345 Middlefield Road
Menlo Park, CA 94025
(415) 323-8111 Ext. 2755

Dr. A. G. Franklin
Chief, Earthquake Engineering and
Geophysics Division
Geotechnical Laboratory
U.S. Army Engineer Waterways
Experiment Station
Vicksbrug, MS 39180
(601) 634-2658

Mr. G. Robert Fuller
Chief, Standards Branch
Manufactured Housing Construction
Standards Division
Department of Housing and Urban
Development, Room 9156
Washington, DC 20410
(202) 755-6920

Mr. James H. Gates

Office of Structures Design
Department of Transportation
State of California
1120 N Street
Sacramento, CA 95814
(916) 445-3810

Dr. Michael P. Gaus
Section Head of Critical Engineering
Division of Emerging and Critical
Engineering Systems
National Science Foundation
1800 G Street, NW
Washington, DC 20550
(202) 357-9500

Mr. Peter E. Gurvin
A/FBO, SA-6
Department of State
Washington, DC 20520
(202) 235-3689

Mr. James F. Lander
Deputy Director, National Geophysical
Data Center, NOAA/NESDIS
325 Broadway
Boulder, CO 80303
FTS 776-5981 (303) 234-3303

Mr. Robert MacDonald
Geologic Service Branch
Code D-1630
Bureau of Reclamation
Building 67, Denver Federal Center
Denver, CO 80225
FTS 776-4195 (303) 236-4195

Mr. Robert J. Smith
Department of the Army
Office of the Chief of Engineers
DAEN-CWE-DS
Washington, DC 20314
(202) 272-0219

Mr. Stanley K. Takahashi
Structures Division
Civil Engineering Laboratory
Naval Construction Battalion Center
Port Huemene, CA 93043
(805) 982-4684

TEMPORARY MEMBERS

Dr. A. M. Abdel-Ghaffar, Associate
Professor, Princeton University

Dr. M. Shinozuka, Prof., Columbia Univ.

Dr. R. N. White, Prof., Cornell Univ.

RESOLUTIONS OF THE SEVENTEENTH JOINT MEETING
U.S.-JAPAN PANEL ON WIND AND SEISMIC EFFECTS (UJNR)

Public Works Research Institute
Tsukuba Science City, Japan

May 21-24, 1985

The following resolutions are hereby adopted:

1. The Seventeenth Joint Panel Meeting provided an extremely valuable exchange of technical information which was beneficial to both countries. In view of the importance of cooperative programs on the subject of wind and seismic effects, the continuation of Joint Panel Meetings is considered essential.

2. The following activities have been carried out since the Sixteenth Joint Meeting:

   a. Several technical documents, including strong motion records, research reports, post-earthquake damage records, and workshop proceedings were exchanged.

   b. Several workshops were held to develop joint research activities and methodologies for wind and seismic disaster mitigation.

   c. A joint post-earthquake investigation of damage due to the 1984 Naganoken-Seibu Earthquake was conducted.

   These activities are considered by the Panel to be essential in carrying out its objectives. Similar activities should be encouraged and supported by each side.

3. The Panel recognizes the accomplishments of the U.S.-Japan Cooperative Program on Large Scale Testing. The Panel endorses the Implementing Arrangement for the Coordinated Research Program on LargeScale Testing of Masonry Structures and establishment of a Joint Technical Coordinating Committee on Masonry Research (JTCCMAR).

4. The Panel endorses the following workshops proposed by the Task Committees:

   a. In-situ Testing Methods for Evaluation of Soil Liquefaction Potential-----Task Committee (H), (August, 17-20, 1985).

   b. Second U.S.-Japan Bridge Workshop-----Task Committee (J), (August 19-22, 1985)

   c. Repair and Retrofit of Existing Structures-----Task Committee (C), (August, 1986 or May, 1987)

   d. Evaluation of Structural Performance of Buildings-----Task Committee (D), (May, 1986).

e. Lifeline Earthquake Engineering-----Task Committee (F), (May, 1986).

f. Computational and Experimental Methods in Tsunami and Storm Surge -----Task Committee (I).

Dates and locations are to be determined by the chairmen of each Task Committee with concurrence by chairmen of the Joint Panel. Results of each workshop shall be presented at subsequent Joint Panel Meeting.

5. The Panel recognizes the importance of continued exchange of personnel, technical information, research data and recorded data on significant earthquakes and strong winds, and use of available facilities in both countries. Thus, these activities should be strengthened and expanded. To facilitate the exchange of personnel, the Panel will continue to assist such exchanges by providing official Panel sponsorship and channels of communication for proper arrangements to be made by each side.

6. The Panel recommends that for future Joint Panel Meetings, priority attention be given to following items:

   a. Coordination and liaison between Task Committees. Task Committee Chairmen should furnish copies of appropriate Task Committee correspondence to the Secretariat of both sides for proper dissemination.

   b. Increased emphasis on wind engineering research and damage investigations.

   c. Task Committee meetings should give attention to development of research needs, priorities, and recommendations for future joint research programs.

7. Recognizing that wind and seismic disaster mitigation plans benefit disaster-prone countries worldwide, that many developing countries suffer from natural disasters such as extreme winds, storm surge, earthquakes and tsunamis, and that both the U.S. and Japan have been involved in international technical cooperation programs, the Panel will continue efforts to develop and coordinate projects which provide aid and training to developing countries and maintain the exchange of technical information.

8. The Eighteenth Joint Meeting of the UJNR Panel on Wind and Seismic Effects will be in May 1986 at Washington, D.C. (USA). Specific dates, program and itinerary will be proposed by the U.S. Panel with concurrence by the Japanese Panel.

Theme I

WIND ENGINEERING

INTERPRETATION OF SECTION MODEL AEROELASTIC RESULTS IN THE CASE OF CABLE-STAYED BRIDGES

By

Robert H. Scanlan*

ABSTRACT

The paper focuses on the aeroelastic wind tunnel sectional model of a bridge deck and close interpretation of its relation to the prototype and to other models. The inadequacy of such model for cable-stayed bridges, where vibration modes are more complex than for the older suspension bridges, is apparent. The deserved popularity of the section model rests, however, on the important insights that can be gained from it notwithstanding. The most important of these is the information that leads to aerodynamically favorable modifications of sectional form. Furthermore, an effort is made, in this paper, to distinguish categorically between mechanical-dynamic and purely aerodynamic effects. Finally, the theory which is outlined and applied to a cable-stayed bridge design offers means for a systematic, mode-by-mode investigation of bridge vulnerability to wind-induced instability. In addition, the central role of torsional motion in driving an instability is underlined, and its aerodynamic interaction with vertical and sway effects are delineated. In conclusion, the paper emphasizes the expanded use of the flutter derivatives, particularly those related to damping, as the most fundamental analog results obtainable from section model test.

KEY WORDS: Aerodynamic Damping, Aeroelasticity, Cable-Stayed Bridge, Flutter, Mechanical Damping, Mode Shapes, Section Model, Stability (Aerodynamic), Wind-Tunnel (Tests), Wind Velocity (Critical)

1. INTRODUCTION

The wind tunnel has long been employed to investigate the potential effect of wind on long, flexible bridges. The most common, and economical, device used in this endeavor, has been the elastically sprung deck section model, but the problem recurs as to what extent such a model represents the dynamics of the prototype bridge. The correct answer to this is that such a model cannot ever truly represent the action of the full bridge. This is more particularly apparent for cable-stayed bridges, where vibration modes are more complex than for the older suspension types. The deserved popularity of the section model rests, however, on the important insights that can be gained from it notwithstanding. The most important of these is the information that leads to aerodynamically favorable modifications of sectional form. Yet, in the process of investigation, certain dynamical misunderstandings have continued to arise, notable in failing to distinguish categorically between mechanical-dynamic and purely aerodynamic effects. It proves to be especially effective to identify the latter alone through use of the section model.

It has been assumed, for example, that endowing the dynamic model with the lowest bending and torsion frequencies (to scale) of the full bridge provides the model with enough freedoms and conservatism so that its eventual response amplitudes and possible instabilities mimic the critical ones of the prototype. It has further been argued that the model must possess not simply the mass and mass moment of inertia of the chosen representative deck section, but those corresponding to what that section effectively manifests when moving in certain particular "lowest" modes of the prototype. For example, a strong argument has been made [1] for locating and using, for the model, the correct effective rotation point of the representative

*Professor, Department of Civil Engineering, Princeton University, Princeton, NJ 08544

deck section when it is participating in the expected full-bridge torsional instability mode.

It is the purpose of the present paper to enter into a more fundamental discussion of this and related issues. This will be concerned with the two aspects: dynamics and aerodynamics.

2. BEAM EXAMPLE

It can easily be demonstrated that a dynamic load that acts over only a limited portion of a given beam nonetheless excites all complete vibration modes of that beam. To extrapolate from this example to bridges, an aerodynamic action confined to the bridge deck alone (or portion thereof) will excite all full-bridge modes. This is a consequence of the dynamics alone and is independent of any special character that the aerodynamics may exhibit. Nevertheless, it is a matter of experience with full-bridge models, and with a documented case like the Tacoma Narrows incident, that flutter -- when it does occur -- takes place preponderantly in a single mode that closely resembles an eigenmode of the structure. What circumstances are effective in "choosing" this mode? It is probable that it is the mode susceptible of absorbing the most destabilizing energy from the wind. It is also a mode in which most of the energy is concentrated in the bridge deck. Some light is shed on this question by bridge flutter aerodynamics.

2.1 Bridge Deck Unsteady Aerodynamics

A number of wind velocity observations [2,3,4], together with recent experience of the author and A. Abdel-Ghaffar on the Golden Gate Bridge (to be reported elsewhere), have indicated that conditions of very low turbulence (2 to 3%) often occur in the wind approaching at bridge height over water fetches. This argues for testing bridge models under laminar approach flow as a conservative design measure. Thus, while the buffeting of models is an important study, it may be considered separately. The present remarks are therefore first confined to bridge stability under laminar approach flow.

Let a bridge deck section at spanwise deck station x be considered that has three degrees of freedom, based at its local c.g., namely h (vertical), α (twist about c.g.), and p (lateral sway in the alongwind direction); see Fig. 1. If the section undergoes sinusoidal motion in the freedoms noted at circular frequency ω, let $K = B\omega/U$ be a dimensionless frequency, where B is deck width, U is lateral approach velocity of the wind. Under these conditions, the respective motion-dependent lift, drag, and moment (per unit span) on the section are given [5,6] is air of density ρ, by

$$L = \frac{1}{2}\rho U^2 B\left[K H_1^*(K)\frac{\dot{h}}{U} + K H_2^*(K)\frac{B\dot{\alpha}}{U} + K^2 H_3^*(K)\alpha\right] \quad (1)$$

$$D = \frac{1}{2}\rho U^2 B\left[K P_1^*(K)\frac{\dot{p}}{U} + K P_2^*(K)\frac{B\dot{\alpha}}{U} + K^2 P_3^*(K)\alpha\right] \quad (2)$$

$$M = \frac{1}{2}\rho U^2 B^2\left[K A_1^*(K)\frac{\dot{h}}{U} + K A_2^*(K)\frac{B\dot{\alpha}}{U} + K^2 A_3^*(K)\alpha\right] \quad (3)$$

where $H_i^*(K)$, $P_i^*(K)$, $A_i^*(K)$ are experimentally determined dimensionless "flutter" coefficients that characterize the self-excited aerodynamics of the bridge deck geometric form.

2.2 Full Bridge Modal Dynamics

The full bridge responds in (dimensionless) vibration modes $\bar{\phi}_i(x,y,z)$ that have x,y,z displacement components at each point of the entire structure. If the bridge is modeled as a set of discrete point masses m_r, then the total kinetic energy of the system is, summing over all masses:

$$T = \frac{1}{2}\sum_r m_r(\dot{u}_r^2 + \dot{v}_r^2 + \dot{w}_r^2) \quad (4)$$

where (u_r, v_r, w_r) are the displacement components of mass m_r.

Any motion $\bar{u}(x,y,z,t)$ of the structure may be expressed as a sum of modal responses

$$\bar{u}(x,y,z,t) = \sum_i \xi_i(t)\,\bar{\phi}_i(x,y,z)B \quad (5)$$

Use of this form permits writing the alternative form for T:

$$T = \frac{1}{2}\sum_i I_i \dot{\xi}_i^2 \quad (6)$$

where the generalized inertias I_i are defined by

$$I_i = B^2 \int\int\int_{\text{entire bridge}} m(x,y,z)\,\bar{\phi}_i\cdot\bar{\phi}_i\,dx\,dy\,dz \quad (7)$$

$m(x,y,z)$ being the continuously distributed mass per unit volume. In practice, this integral is usually evaluated in discrete terms. The equations of motion of the system become

$$I_i[\ddot{\xi}_i + 2\zeta_i\omega_i\dot{\xi}_i + \omega_i^2\xi_i] = Q_i(t) \tag{8}$$

where ξ_i are uncoupled from each other, and ζ_i and ω_i, respectively, represent the damping ratio and the natural circular frequency of the i^{th} mode.

For convenience in developing the form of the generalized force Q_i, let the motion of the deck section at x be described by the following, where $h_i(x)$, $p_i(x)$, $\alpha_i(x)$ are the (dimensionless) components (those portions of the total bridge mode $\bar{\phi}_i(x,y,z)$ that represent deck motions only) of $\bar{\phi}_i(x,y,z)$ at deck section x respectively in the vertical, lateral, and twist degrees of freedom:

$$h(x,t) = \sum_i \xi_i(t)\, h_i(x)B \tag{9}$$

$$p(x,t) = \sum_i \xi_i(t)\, p_i(x)B \tag{10}$$

$$\alpha(x,t) = \sum_i \xi_i(t)\, \alpha_i(x) \tag{11}$$

Then, for any single mode i, the value of $Q_i(t)$ will be developed from the following expressions for motion-related lift, drag, and moment, respectively, appropriate to that mode:

$$L_i = \frac{1}{2}\rho U^2 B\left[K_i H_1^*(K_i)\frac{\dot{\xi}_i h_i(x)B}{U} + K_i H_2^*(K_i)\frac{B\dot{\xi}_i\alpha_i(x)}{U} + K_i^2 H_3^*(K_i)\,\xi_i\alpha_i(x)\right] \tag{12}$$

$$D_i = \frac{1}{2}\rho U^2 B\left[K_i P_1^*(K_i)\frac{\dot{\xi}_i p_i(x)B}{U} + K_i P_2^*(K_i)\frac{B\dot{\xi}_i\alpha_i(x)}{U} + K_i^2 P_3^*(K_i)\,\xi_i\alpha_i(x)\right] \tag{13}$$

$$M_i = \frac{1}{2}\rho U^2 B^2\left[K_i A_1^*(K_i)\frac{\dot{\xi}_i h_i(x)B}{U} + K_i A_2^*(K_i)\frac{B\dot{\xi}_i\alpha_i(x)}{U} + K_i^2 A_3^*(K_i)\,\xi_i\alpha_i(x)\right] \tag{14}$$

where $K_i = B\omega_i/U$ and total lift, drag, and moment are $\sum_i L_i$, $\sum_i D_i$, $\sum_i M_i$, respectively.

The increments in h, p, and α for a virtual displacement $\delta\xi_i$ are, respectively,

$$\delta h = h_i(x)B\,\delta\xi_i \tag{15}$$

$$\delta p = p_i(x)B\,\delta\xi_i \tag{16}$$

$$\delta\alpha = \alpha_i(x)\,\delta\xi_i \tag{17}$$

so that the net generalized aerodynamic force in mode i is (neglecting intermodal cross-couplings):

$$Q_i(t) = \int_{\text{span}} [L_i(x,t)\, h_i(x)B + D_i(x,t)\, p_i(x)B + M_i(x,t)\alpha_i(x)]dx \tag{18}$$

$$\frac{Q_i(t)}{\frac{1}{2}\rho U^2 B^2} = K_i H_1^*(K_i)\frac{\dot{\xi}_i B}{U}G_{h_ih_i} + K_i H_2^*(K_i)\frac{B\dot{\xi}_i}{U}G_{h_i\alpha_i} + K_i^2 H_3^*(K_i)\xi_i G_{h_i\alpha_i} + K_i P_1^*(K_i)\frac{\dot{\xi}_i B}{U}G_{p_ip_i} + K_i P_2^*(K_i)\frac{B\dot{\xi}_i}{U}G_{p_i\alpha_i} + K_i^2 P_3^*(K_i)\xi_i\, G_{p_i\alpha_i} + K_i A_1^*(K_i)\frac{\dot{\xi}_i B}{U}G_{h_i\alpha_i} + K_i A_2^*(K_i)\frac{\dot{\xi}_i B}{U}G_{\alpha_i\alpha_i} + K_i^2 A_3^*(K_i)\xi_i\, G_{\alpha_i\alpha_i} \tag{19}$$

where the following definitions have been employed:

$$\text{(a)}\quad G_{h_ih_i} = \int_{\text{span}} h_i^2(x)dx$$

$$\text{(b)}\quad G_{h_i\alpha_i} = \int_{\text{span}} h_i(x)\,\alpha_i(x)dx$$

$$\text{(c)}\quad G_{p_ip_i} = \int_{\text{span}} p_i^2(x)dx$$

$$\text{(d)}\quad G_{p_i\alpha_i} = \int_{\text{span}} p_i(x)\,\alpha_i(x)dx$$

$$\text{(e)}\quad G_{\alpha_i\alpha_i} = \int_{\text{span}} \alpha_i^2(x)dx \tag{20}$$

The equation of motion for the i^{th} mode can be rewritten

$$I_i[\ddot{\xi}_i + 2\tilde{\zeta}_i\tilde{\omega}_i\dot{\xi}_i + \tilde{\omega}_i^2\xi_i] = 0 \qquad (21)$$

where the net effective damping ratio $\tilde{\zeta}_i$ and frequency $\tilde{\omega}_i$ are given by the expressions

$$\tilde{\zeta}_i = \frac{\omega_i}{\tilde{\omega}_i}\left\{\zeta_i - \frac{\rho B^4}{4\,I_i}\left[H_1^*(K_i)G_{h_ih_i} + H_2^*(K_i)G_{h_i\alpha_i} + P_1^*(K_i)G_{p_ip_i} + P_2^*(K_i)G_{p_i\alpha_i} + A_1^*(K_i)G_{h_i\alpha_i} + A_2^*(K_i)G_{\alpha_i\alpha_i}\right]\right\} \qquad (22)$$

$$\frac{\tilde{\omega}_i^2}{\omega_i^2} = 1 - \frac{\rho B^4}{2\,I_i}\left[H_3^*(K_i)G_{h_i\alpha_i} + P_3^*(K_i)G_{p_i\alpha_i} + A_3^*(K_i)G_{\alpha_i\alpha_i}\right] \qquad (23)$$

Note that $\tilde{\omega}_i \simeq \omega_i$. However, this is not of great importance to the present discussion, since the shift in K-value from mechanical eigen frequency to aerodynamically influenced characteristic frequency is small. On the other hand, the shift in value of ζ_i to $\tilde{\zeta}_i$ as given by Eq. (22), is of considerable importance to the condition of flutter stability.

If aerodynamic cross-coupling terms associated with H_2^*, A_1^*, P_2^*, are provisionally neglected as small, and $\tilde{\omega}_i \simeq \omega_i$, the result for $\tilde{\zeta}_i$ becomes

$$\tilde{\zeta}_i = \zeta_i - \frac{\rho B^4}{4\,I_i}\left[\left[H_1^*(K_i)G_{h_ih_i} + P_1^*(K_i)G_{p_ip_i} + A_2^*(K_i)G_{\alpha_i\alpha_i}\right]\right]. \qquad (24)$$

Since most flutter depends upon effective torsional damping, the role of $\tilde{\zeta}_i$ will be especially important.

2.3 Single-Mode Bridge Flutter

Equation (24) emphasizes the principal aerodynamic damping mechanisms that function in any given mode of the bridge. The present paper focuses in fact, on aerodynamic damping.

Bridge flutter is almost invariably a damping-related phenomenon. The classical frequency- and mode-coalescence associated with high-speed, flat-plate flutter occurs seldom, if ever, in bridge flutter. The latter is invariably a bluff-body instability associated with separated flow, and it is usually driven -- even when torsion and vertical motion are in fact coupled -- by a separately unstable torsional self-excitation mechanism [7]. Such a flutter mechanism is radically different from classical, stiffness-coupled flutter. Bridge structures tend to be both strong and massive relative to wind forces; they are thus little deformed away from their natural vibration modes by wind effects. On the other hand, wind damping forces -- i.e., forces linked to the velocities of structural deflection -- can become comparable in magnitude to mechanical damping forces. Therein lies the apparent "paradox" that was once such a mystery in cases like the Tacoma one.

In any single mode, $\tilde{\zeta}_i = 0$ signifies instability. Hence the flutter velocity U_{cr} for that mode is such that $K_i = K_{cr} = B\omega_i/U_{cr}$ and, from Eq. (24)

$$H_1^*(K_{cr})G_{h_ih_i} + P_1^*(K_{cr})G_{p_ip_i} + A_2^*(K_{cr})G_{\alpha_i\alpha_i} \simeq \frac{4\,\zeta_i I_i}{\rho B^4} \qquad (25)$$

defines the flutter condition.

In the study of the stability of a given bridge cross-section, the flutter coefficients H_1^*, P_1^*, A_2^* are first experimentally obtained as functions of K. For the particular mode i, the parameters I_i, $G_{h_ih_i}$, $G_{p_ip_i}$, and $G_{\alpha_i\alpha_i}$ are calculated. The left hand side of expression (25) is then evaluated for a series of K values. If one such value exceeds the right-hand side of (25), the critical flutter velocity for that mode is exceeded. The process permits systematic evaluation of the stability of each of the bridge modes successively, the one providing the lowest value of U_{cr} being considered the most critical. This procedure offers a physical rationale for the selection of the correct flutter mode of the bridge.

The case of modern cable-stayed bridge designs presents new circumstances. In these structural

configurations, the 3D bridge eigenmodes are typically seen to contain, along the deck span, simultaneous contributions to bending, torsion, and lateral sway. It is then no longer possible to categorize a given eigenmode simply as pure bending or pure torsion; it will simultaneously contain elements of all possible motions. A major conclusion from this fact is that, in the general case, a simple section model is incapable of accomplishing a fully correct one-to-one analog simulation of the prototype. The model may continue to serve, however, as the analog test bed for extracting the aeroelastic coefficients.

The choice of prototype mode most "eligible" to be the eventual flutter mode should not depend merely on the visual or judgmental selection of one mode, from among many, that appears to be "mostly bending" or "mostly torsion". Such a choice requires the guidance offered by theory, using measured dimensionless aerodynamic coefficients. These latter permit the complete separation of the aerodynamic side of the problem from the dynamic side, whether model or prototype.

2.4 Example: Modal Properties of Cable-Stayed Bridge

The first 20 modes of a cable-stayed bridge design [8] were made available to the author. The first 13 modes of this set are sketched in Figs. 1 through 13. The deck, approximately uniform throughout the span, had a mass of 434.4 slugs/ft and a mass moment of inertia per unit span of 259,100 slugs ft^2/ft about its c.g. Modes 3 (largely deck bending) and 13 (largely deck torsion) were selected on a judgmental basis to be modeled via a rigid, spring-supported deck section model for wind tunnel study. Full-bridge generalized inertias I_i, calculated for each mode i, were normalized at unit value. Similar inertias, calculated over the deck only, were also calculated. Further, the values of certain modal integrals $G_{\alpha_i\alpha_i}$, $G_{h_ih_i}$, and $G_{p_ip_i}$, in consistent units,* were additionally calculated. The results for the first 13 modes are presented in Table 1. (B = 100 ft. = 1200 in. for the bridge deck.) Included in Table 1 for later reference are a set of reduced velocities U/NB, based on a high-wind velocity U = 160 mph.

A first remark about the results of Table 1 is that, while a number (8) of modes exhibit about 90% or more of their generalized inertia as being due to deck action, certain other modes are notably low in deck contribution, for example, modes 6 and 7. In fact, these two modes are strong in torsion (see Figs. 6 and 7) and might even have been selected on a purely intuitive basis as candidates for section model torsional simulation. It is clear for such modes that application of the method of Ref. [1] would lead to serious underestimation of the modal inertia. Instead, mode 13, with the highest value of the $G_{\alpha_i\alpha_i}$ parameter, was chosen for this modeling. Mode 3 was chosen for model simulation in the bending degree of freedom, although two other modes (9 and 12) have slightly higher values of the $G_{h_ih_i}$ parameter.

It is particularly worth noting that, in mode 13:

$$\frac{I_i \text{ (deck only)}}{G_{\alpha_i\alpha_i}} = \frac{0.955}{0.3640}\times 10^5$$

$$= 262{,}363 \text{ mugs in}^2/\text{in}$$

$$= 262{,}363 \text{ slugs ft}^2/\text{ft}$$

and, in mode 3:

$$\frac{I_i \text{ (deck only)}}{B^2\, G_{h_ih_i}} = \frac{0.935}{0.3031}$$

$$= 3.0848 \text{ mugs in}^2/\text{in}^3$$

$$= 3.0848 \text{ mugs/in}$$

$$= 444.2 \text{ slugs/ft}$$

These two calculated values are good approxima-

*In the computer program used, modes were normalized on the basis that $I_i = 1$ for all modes. Input mass units used were "mugs" (1 mug weighs 386.4 lb); input length units used were inches. Thus, nominal units for I_i can be assessed as mug in^2; nominal units for $G_{\alpha_i\alpha_i}$, $G_{h_ih_i}$, $G_{p_ip_i}$ are inches; the modes α_i, h_i, p_i are considered dimensionless.

tions, respectively, to the deck inertia values (259,100 slugs ft^2/ft and 434.4 slugs/ft) of the type given at the introduction of this example. It is of further interest to note that similar calculations hold for all modes that exhibit strong character in any one of the freedoms: bending, sway, or twist. In Table 1, the largest modal integral value in each mode is underlined. In one case (mode 11), two modal integrals are of comparable magnitude. In particular, modes 1, 3, 4, 5, 9, 10, 12 are distinct enough in either bending or sway to yield calculations of deck mass that are of the same order as that given by mode 3.

The above facts emphasize that, particularly for cable-stayed bridges, problems can exist in the selection of appropriate prototype modes that are to be simulated in the section model. One possibility for such selection might be to choose, among all modes considered, the one for which the value of $G_{\alpha_i\alpha_i}$, $G_{p_ip_i}$, $G_{h_ih_i}$ was the largest (i.e., the largest among the underlined values of Table 1). However, while these integrals offer a quantitative indication that the mode is "mostly bending" or "mostly torsion", etc., they also directly influence the degree of participation of aerodynamic damping mechanisms. These effects are not as easy to judge intuitively and require a sound theory.

This situation is characterized by the form of Eq. (25), wherein aerodynamic damping derivative terms are multiplied respectively by the modal integrals given in Table 1. The aerodynamic damping terms H_1^* and P_1^* are usually negative, effectively enhancing stability. The coefficient usually most likely to become positive, or destabilizing, is A_2^*. We examine therefore in the present bridge case, the effect of typical values of H_1^*, P_1^* and A_2^* upon the stability of various modes. The following convenient formulas for H_1^*, P_1^* and A_2^* will be employed:

$$H_1^* = -1.25\left(\frac{U}{NB}\right) \tag{26}$$

$$P_1^* = -0.064\left(\frac{U}{NB}\right) \tag{27}$$

$$A_2^* = +0.004\left(\frac{U}{NB}\right)\left[\left(\frac{U}{NB}\right)^2 - 4\right] \tag{28}$$

where $U/NB = 2\pi/K$, N is the modal frequency in Hz. These formulas are chosen to correspond to fairly typical experimental values of these coefficients. It is noted, however, that the formula given for A_2^* describes a particularly severe case, or one with greater than average instability tendencies. This is introduced intentionally to illustrate the influence of such tendencies in torsion and to perceive, in particular, how they may participate in the full criterion, Eq. (25), for instability.

By Eq. (28), $A_2^* \geq 0$ for $(U/NB) \geq 2$. The method of procedure used here is to fix the maximum expected cross-wind velocity at 160 mph. Thus $U/NB = 2.35/N$. This value is listed for each mode in the last column of Table 1. With this value and the formulas given for H_1^*, P_1^*, A_2^*, the value of the left-hand side of Eq. (25) is calculated.

Note first that, taking $\zeta_i = 0.01$, $I_i = 1$, $\rho = 0.002378$ slugs/ft^3 $= (12)^{-4} \times 0.002378$ mugs/in^3, and $B = 100$ ft $= 1200$ in, yields the criterion

$$\frac{4\,\zeta_i I_i}{\rho B^4} = \frac{4(0.01)1\times 12^4}{0.002378\ 12^4\times 10^8}$$

$$= 1.6821\times 10^{-7}\ \text{(inches)}.$$

All modes of Table 1, except one, result in calculations that do not meet the criterion for flutter. However, the flutter criterion is exceeded at 160 mph for mode 13, which yields:

$$\left[H_1^*\, G_{h_ih_i}\right]_{i=13} = (-1.25)(3.25)(0.1375)\times 10^{-12}$$

$$= -0.5586\times 10^{-12}$$

$$\left[P_1^*\, G_{p_ip_i}\right]_{i=13} = (-0.064)(3.25)(-.2006)\times 10^{-8}$$

$$= -0.04172\times 10^{-8}$$

$$\left[A_2^* G_{\alpha_i \alpha_i}\right]_{i=13} =$$

$$0.004(3.25)\ [(3.25)^2 - 4][0.3640] \times 10^{-5}$$

$$= + 3.10540 \times 10^{-7}$$

$$\text{sum} = 3.1012 \times 10^{-7}$$

Since $3.1012 \times 10^{-7} > 1.6821 \times 10^{-7}$ flutter is possible in this mode at 160 mph.

Another interesting mode is mode 1, which is unstable in torsion but simultaneously damped via the sway action. For this mode,

$$\left[H_1^* G_{h_i h_i}\right]_{i=1} = (-1.25)(13.72)(0.1414) \times 10^{-11}$$

$$= -2.4250 \times 10^{-11}$$

$$\left[P_1^* G_{p_i p_i}\right]_{i=1} = (-0.064)(13.72)(0.2242) \times 10^{-6}$$

$$= -1.9687 \times 10^{-7}$$

$$\left[A_2^* G_{\alpha_i \alpha_i}\right]_{i=1} =$$

$$0.004(13.72)[(13.72)^2 - 4](0.1816) \times 10^{-7}$$

$$= 1.8362 \times 10^{-7}$$

$$\text{sum} = -1.3278 \times 10^{-8} < 1.6821 \times 10^{-7}$$

In this example, the proclivity for flutter in torsion (which alone exceeds the criterion) is annulled by the damping effect of sway. This illustrates how an effect (sway) usually neglected may aid stability. It also illustrates how near to flutter vulnerability a low mode may come if it exhibits appreciable torsion.

In general, given the data and procedures of the present example, all modes of a bridge may be systematically examined in the manner illustrated based upon experimental knowledge of the coefficients H_1^*, P_1^*, A_2^*.

3. SUMMARY AND CONCLUSIONS

The paper focuses on the aeroelastic wind tunnel sectional model of a bridge deck and close interpretation of its relation to the prototype and to other models. The viewpoint is particularly espoused that bridge dynamics and unsteady aerodynamics may usefully be divorced, conceptually, from one another and reunited via theory. It is particularly useful to have in hand, as separate data, the flutter aerodynamic damping coefficients.

When the theory outlined is applied to a cable-stayed bridge design, it points out needed refinements of interpretation regarding wind tunnel test results for this newer type of configuration, particularly in view of the greater modal complexities observed. The method offers means for a systematic, mode-by-mode investigation of bridge vulnerability to wind-induced instability.

The central role of torsional motion in driving an instability is underlined, and its aerodynamic interactions with vertical and sway effects are delineated. The paper emphasizes the expanded use of the flutter derivatives -- particularly those related to damping -- as the most fundamental analog results obtainable from section model test.

4. REFERENCES

1. Irwin, H. P. A. H.: "Centre of Rotation for Torsional Vibration of Bridges," Jnl. Indus. Aerodynamics, 4 (1979), pp. 123-132.
2. Scanlan, R. H.: "On the State of Stability Considerations for Suspended-Span Bridges under Wind," Practical Experiences with Flow-Induced Vibration, Univ. Karlsruhe, Germany, 1979, Paper F1.
3. Teunissen, H. W.: "Validation of Boundary-Layer Simulation: Some Comparisons between Model and Full-Scale Flows," Wind Tunnel Modeling for Engineering Applications, Cambridge Univ. Press, U.K., pp. 217-235.
4. Shiotani, H. and Ari, H.: "Lateral Structures of Gusts in High Winds," Proceedings, Third Intl. Conf. on Wind Effects on Bldgs. and Structures, Saikon Co., Ltd., Tokyo, 1971, p. 535-543.
5. Scanlan, R. H. and Tomko, J. J.: "Airfoil and Bridge Deck Flutter Derivatives," Jnl. Eng. Mech. Div., ASCE, Vol. 97, No. EM6, Dec. 1971, pp. 1717-1737.

6. Scanlan, R. H.: "The Action of Flexible Bridges Under Wind," Parts I and II, Jnl. Sound and Vibration (1978), Vol. 60(2), pp. 187-199 and 201-211.

7. Nakamura, Y., and Yoshimura, T.: "Binary Flutter of Suspension Bridge Deck Sections," Jnl Eng. Mech. Div., ASCE, Vol. 102, EM4, Aug. 1976, pp. 685-700.

8. Christopher, B. and Stroch, S., Private Communication, Greiner Engineering Sciences, Inc., Tampa, Florida, February 1985.

TABLE 1

Mode Number	Freq. (Hz)	I_i (deck only)	$G_{\alpha_i\alpha_i}$	$G_{h_ih_i}$ inches	$G_{p_ip_i}$ inches	Description of form	V/NB @ 160 mph = 2.35/N
1	0.171	0.992	0.1816 E-07	0.1414 E-11	0.2242 E-06	lateral	13.72
2	0.188	0.781	0.3354 E-11	0.0896 E-07	0.4358 E-10	vertical	12.48
*3	0.270	0.935	0.3193 E-13	0.2105 E-06	0.2064 E-12	vertical	8.69
4	0.349	0.890	0.3614 E-12	0.2010 E-06	0.1662 E-11	vertical	6.72
5	0.389	0.894	0.4876 E-07	0.1685 E-11	0.1975 E-06	lateral	6.03
6	0.516	0.050	0.7846 E-07	0.3021 E-13	0.0739 E-07	torsion	4.57
7	0.522	0.062	0.9214 E-07	0.3644 E-13	0.0795 E-07	torsion	4.50
8	0.552	0.694	0.5313 E-07	0.0729 E-09	0.1317 E-06	lateral	4.25
9	0.555	0.947	0.1778 E-10	0.2133 E-06	0.4478 E-10	vertical	4.23
10	0.645	0.975	0.5484 E-14	0.2201 E-06	0.3812 E-13	vertical	3.64
11	0.696	0.653	0.1239 E-06	0.4637 E-12	0.1130 E-06	tors.-lat.	3.37
12	0.714	0.988	0.2264 E-11	0.2238 E-06	0.1817 E-12	vertical	3.29
*13	0.721	0.955	0.3640 E-05	0.1375 E-12	0.2006 E-08	torsion	3.25

*Selected to be simulated via wind tunnel sectional model

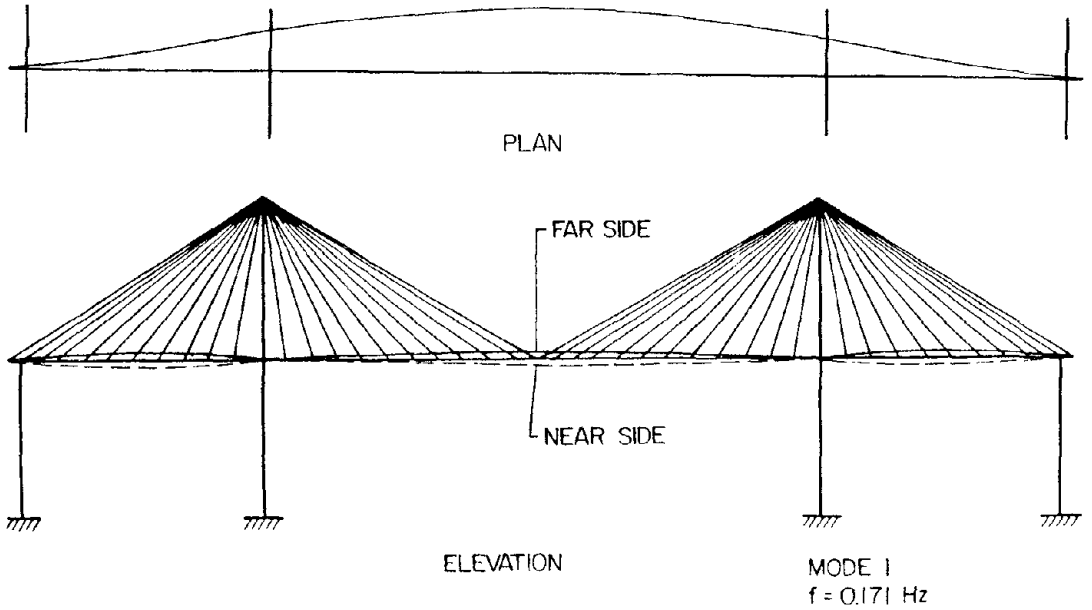

Figure 1

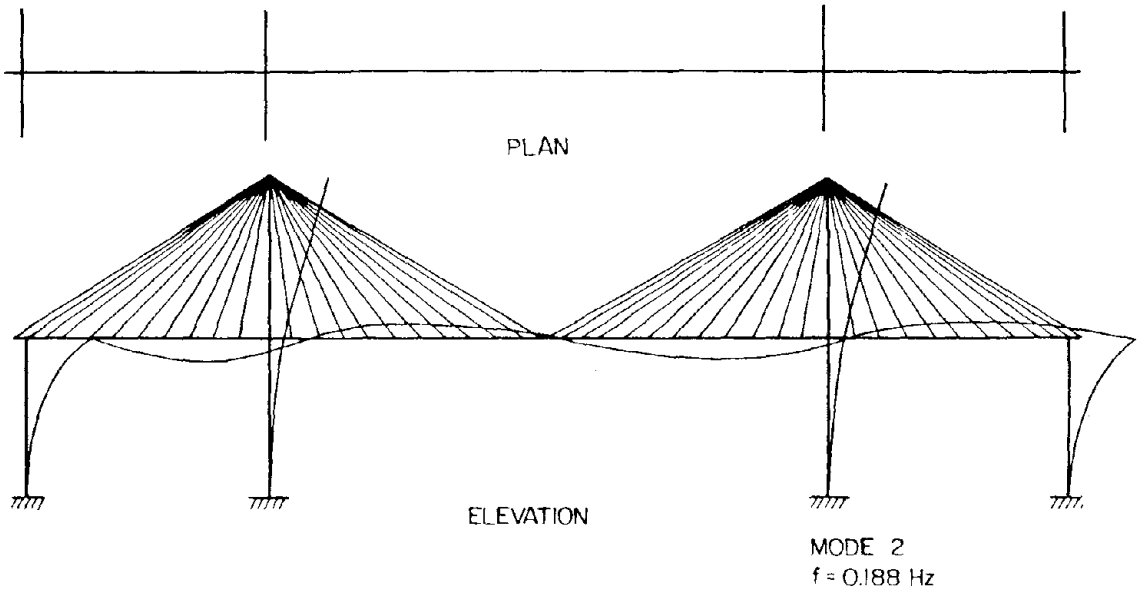

Figure 2

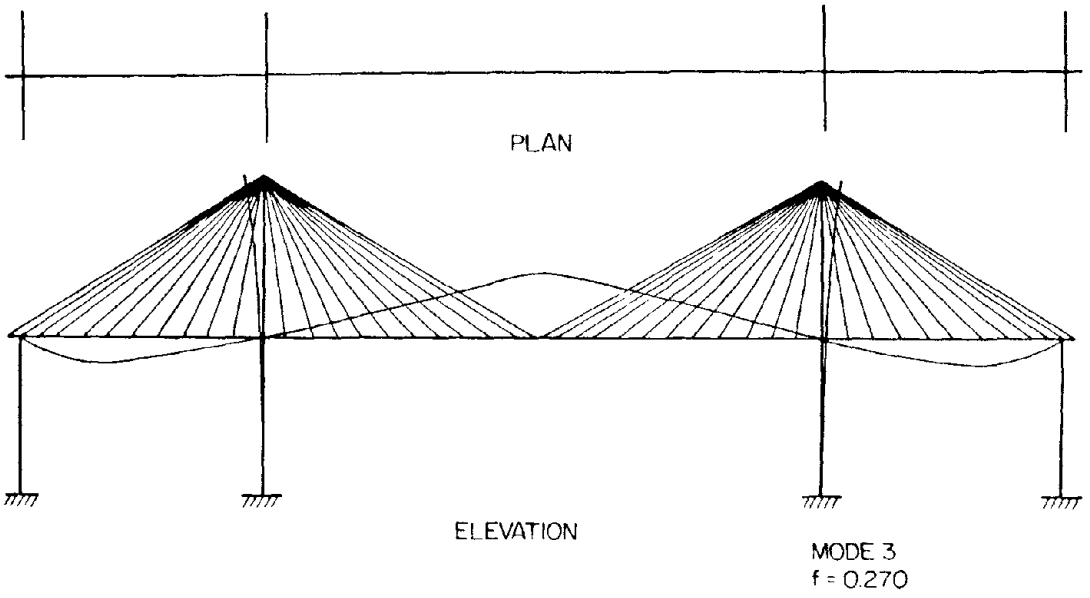

Figure 3

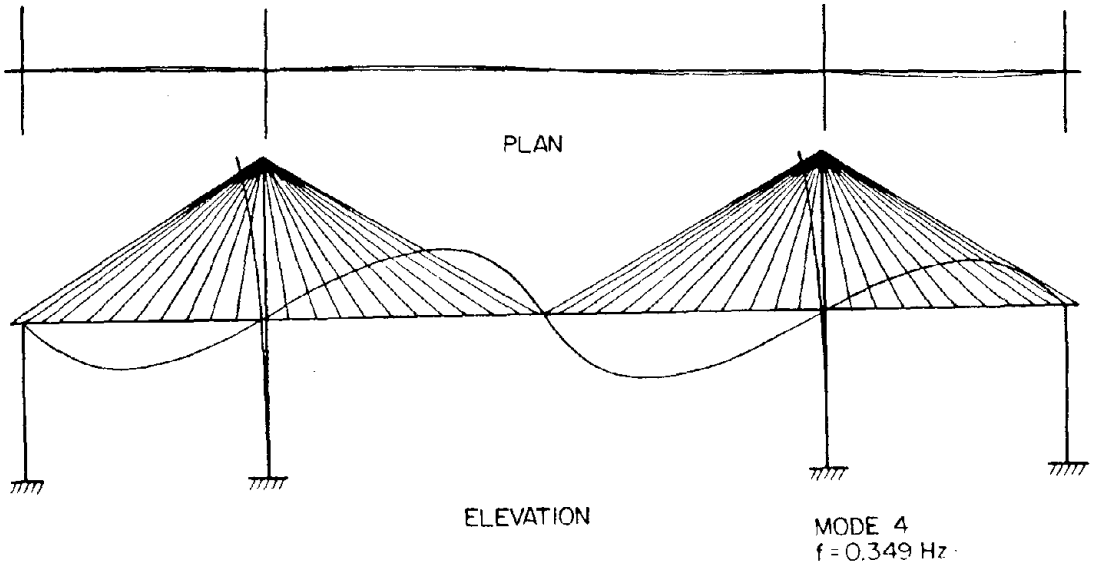

Figure 4

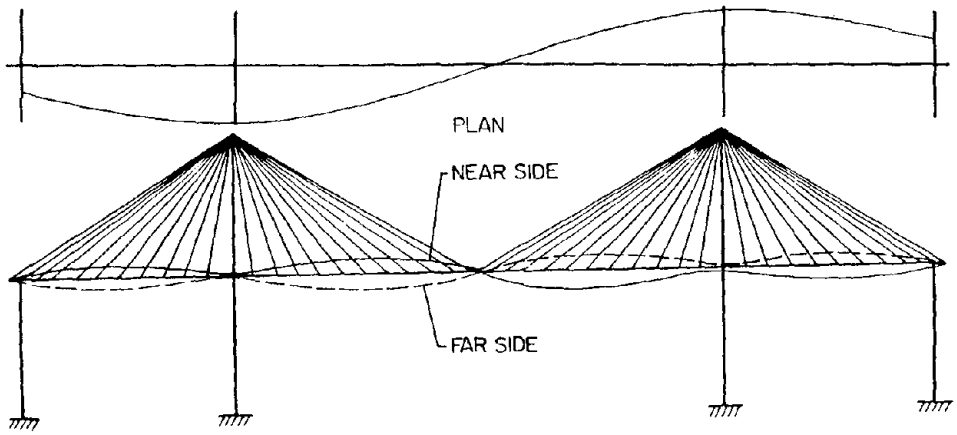

Figure 5

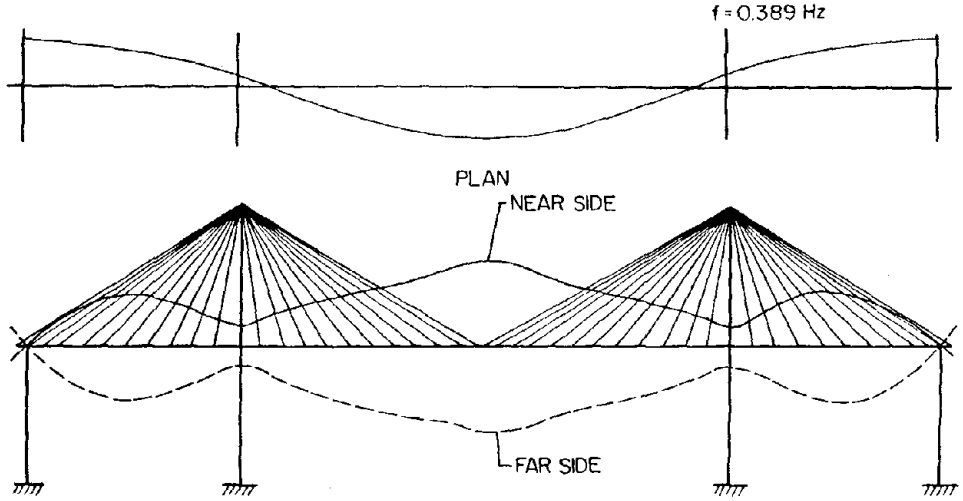

Figure 6

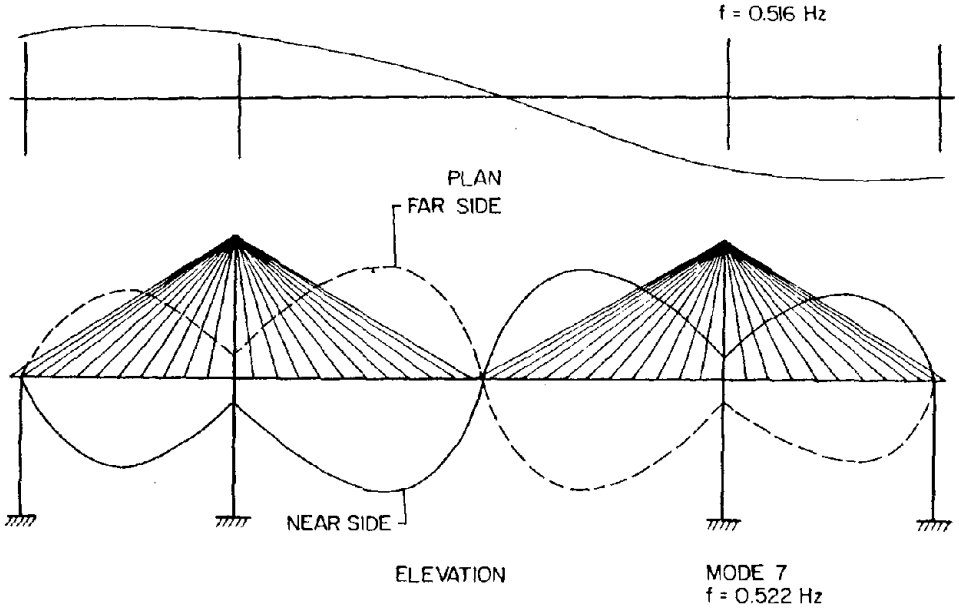

Figure 7

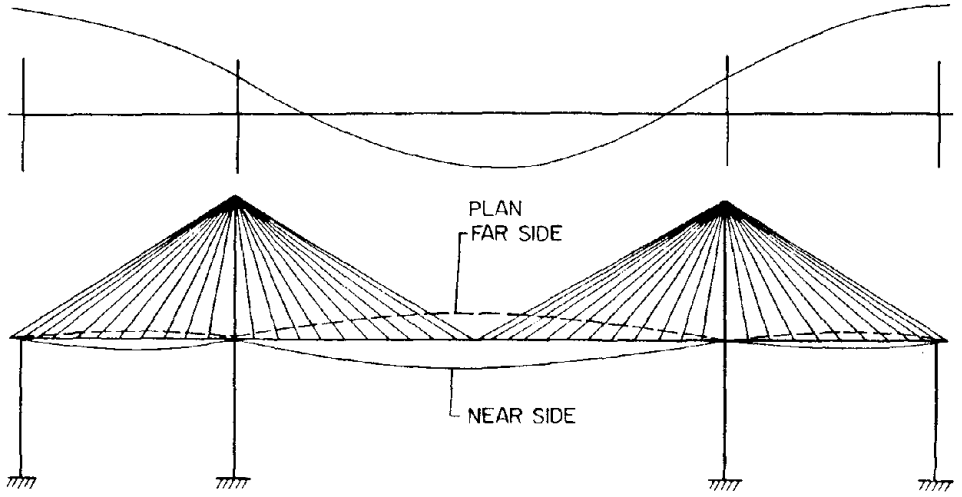

Figure 8

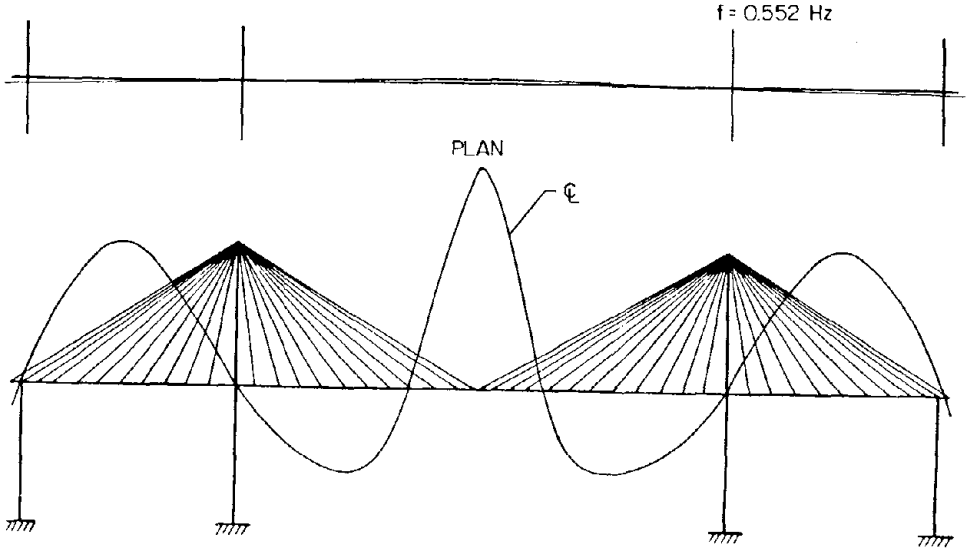

Figure 9

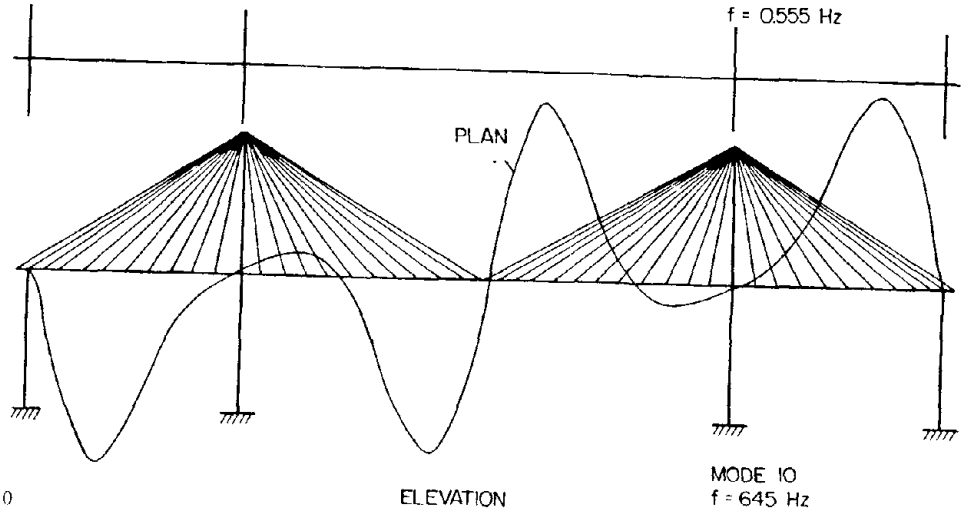

Figure 10

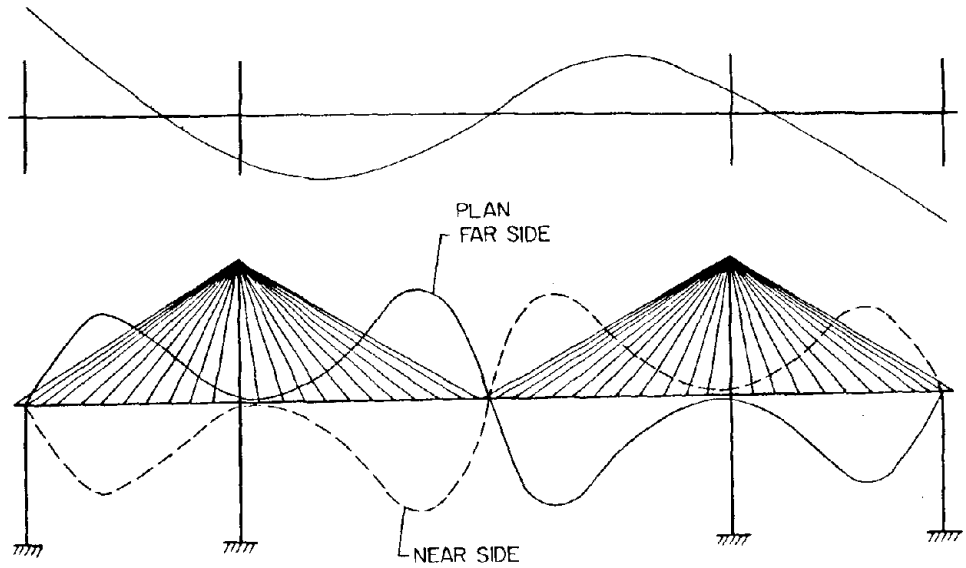

Figure 11

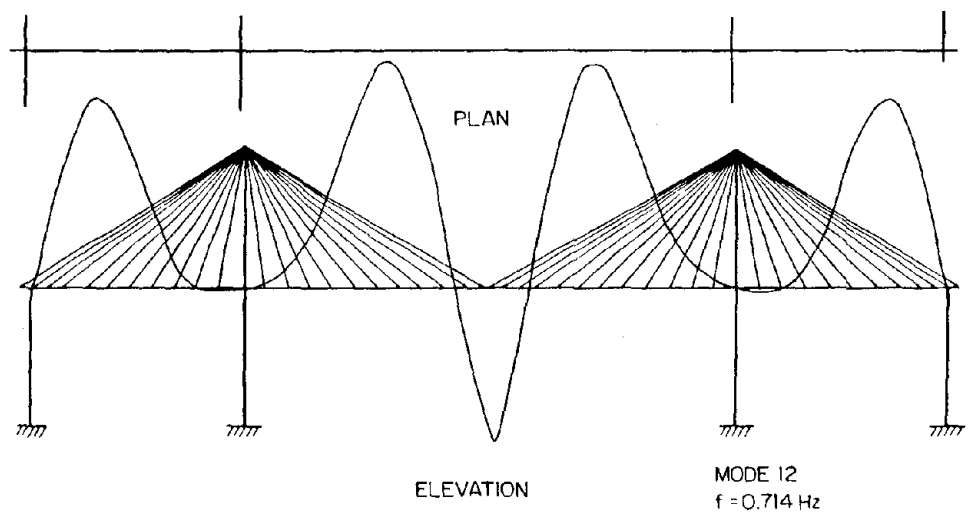

Figure 12

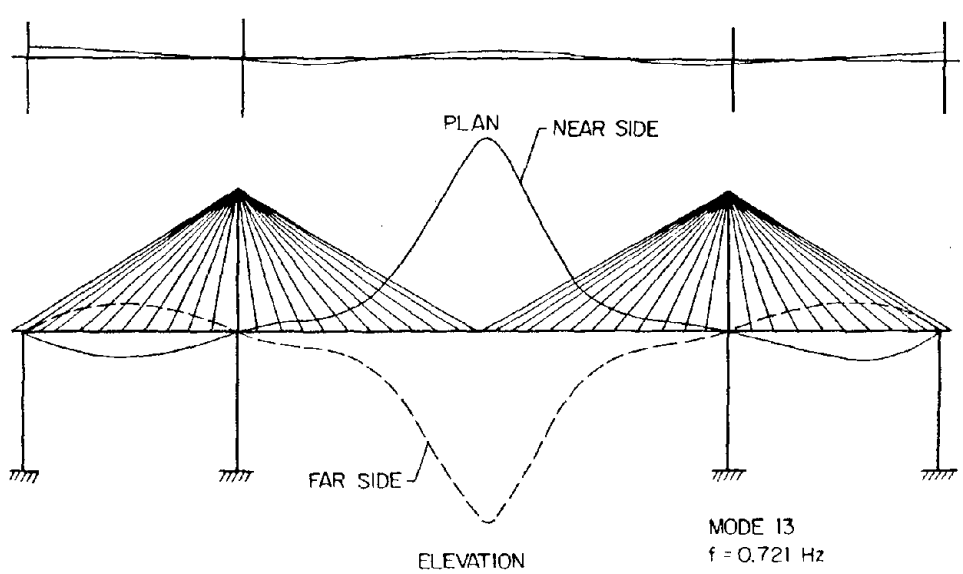

Figure 13

CHARACTERISTICS OF AERODYNAMIC FORCES ON BRIDGE DECKS IN SMOOTH FLOW AND IN TURBULENT FLOW

by

Nobuyuki Narita[1], Hirohiko Tada[2], Koichi Yokoyama[3] and Hiroshi Sato[4]

ABSTRACT

The wind-resistance of long-span bridges in Japan has been mostly investigated and proved through the wind tunnel tests in smooth flow. Natural wind, however, is turbulent flow, whose wind speeds vary with time and space. Recent studies have shown that the characteristics of aerodynamic forces on bridge decks in turbulent flow are different from those in smooth flow. Therefore, the effects of turbulence on wind-induced vibrations of bridges should be investigated in order to establish the rational wind-resistant design method.

In this paper are described the characteristics of fluctuating lift forces, which cause vertical bending vibrations in bridge decks. The fluctuating lift forces acting on some typical bridge decks were measured both in smooth and turbulent flow, and the effects of turbulence and cross-sectional shape of decks on the fluctuating lift forces were clarified.

KEY WORDS: Aerodynamic (forces), Bending (vertical vibration), Bridge (decks), Damping (aerodynamic), Lift (forces), Smooth (flow), Suspension Bridges, Turbulent (flow), Vibration (wind-induced) Wind Tunnel (testing).

[1]Dr. of Eng., Asst. Director General, Public Works Research Institute, Ministry of Construction, Japan.

[2]Dr. of Eng., Director, Structure and Bridge Department, Public Works Research Institute, Japan.

[3]Head, Structure Division, Structure and Bridge Department, Public Works Research Institute, Japan.

[4]Research Engineer, Structure Division, Public Works Research Institute, Japan.

1. INTRODUCTION

The wind-resistance of long-span bridges in Japan has been mostly investigated and proved through the wind tunnel tests in smooth flow. The wind-induced vibrations of long-span bridges are classified into self-excited vibrations (vibrations caused by the fluctuating aerodynamic forces which are generated by the vibrations of the structure itself and which promote the vibrations) and forced vibrations (vibrations caused by the fluctuating aerodynamic forces which are generated by vortices behind the structure or by approaching turbulence).

Buffeting, the forced vibrations caused by approaching turbulence, cannot be observed in the smooth flow, and it has been shown in recent studies[1,2,3] that the characteristics of aerodynamic forces on bridge decks in turbulent flow are different from those in smooth flow. Therefore, the effects of turbulence on wind-induced vibrations of bridges should be investigated in order to establish the rational wind-resistant design method.

From these points of view, the characteristics of fluctuating lift forces, which cause vertical bending vibrations to bridge decks, were investigated. The fluctuating lift forces acting on some typical bridge decks were measured both in smooth and turbulent flow.

2. CHARACTERISTICS OF TURBULENCE USED IN EXPERIMENT

The experiments were made in the Low Speed Wind Tunnel-B of Public Works Research Institute, whose specification is shown in Table 1. The turbulence was generated by a coarse grid whose mesh size is 0.25m and whose bar size is 0.05m. The position

and the shape of the grid are shown in Figs. 1 and 2, respectively. The mean wind speeds of the turbulent flow were uniformly distributed along the y-axis (x-axis is along the main flow direction, and y-axis is horizontal and perpendicular to x-axis, and z-axis is vertical). The characteristics of the turbulent flow are as follows.

	Fluctuating Wind Speed	
	u:x-comp.	w:z-comp.
Intensity of Turbulence	I_u=6.2%	I_w=5.0%
Scale of Turbulence:		
y-direction	L_x^u=0.09m	L_x^w=0.04m
z-direction	L_y^u=0.04m	L_y^w=0.04m

The Power Spectral Density Functions of u and w (S_{uu} and S_{ww}, respectively) at the position where the lift forces were measured, were compared with those of natural wind. In the comparison, frequency f was reduced by deck width B and mean wind speed U. S_{uu} and S_{ww} were reduced by J^2 and f. They are shown in Figs. 3 and 4. In the figures, the value of one box girder bridge was applied to B (18.25m for real bridge and 0.30m for model). S_{uu} and S_{ww} of natural wind were estimated from the data of ESDU.[4] According to ESDU, S_{uu} and S_{ww} of natural wind depend on the height and the roughness length of the terrain surface (z_0). In the figures, the height was assumed to be 50m and z_0 was changed from 10^{-4}m to 1m. The relations between z_0 and terrain description are as follows.

z_0=1m: center of large towns,
$z_0=10^{-1}$m: outskirts of town or farmland
$z_0=10^{-2}$m: fairly level grass plains
$z_0=10^{-4}$m: calm open sea

The turbulence intensity of u generated by the grid corresponds to that of the calm open sea. The scale ratio (the ratio of the scale of turbulence to the bridge deck width) is about 1/30 of natural wind. The intensity of w corresponds to that of fairly level grass plains, and the scale ratio is about 1/10 of natural wind.

2.1 Relations Between The Wind-Induced Vertical Bending Vibrations and the Fluctuating Lift Forces

Wind-induced vibrations of vertical bending mode of long-span bridges can be estimated using the following equation of motion.

$$M_i[\ddot{q}_i + 2\zeta_i\omega_i\dot{q}_i + \omega_i^2 q_i] = P_i \qquad (1)$$

where $M_i = \int_0^l m(x)\Phi_i^2(x)dx$, M_i; generalized mass of i^{th} mode, m; mass per unit length, l; bridge length, x; axis along the bridge length, Φ_i; i^{th} mode shape, $h(x,t) = \Sigma q_i(t)\Phi_i(x)$, h; displacement of vertical bending vibration, t; time, q_i; i^{th} generalized coordinate, ζ_i; structural damping ratio of i^{th} mode, ω_i; natural circular frequency of i^{th} mode, $(\cdot) = d(\ )/dt$.

P_i on the right hand side of Eq. (1) means i^{th} generalized force due to the fluctuating lift force. In general, the fluctuating lift force is the summation of self-excited component P_{Si} and forced component P_{Ei}.

$$P_i = P_{Si} + P_{Ei} \qquad (2)$$

where, $P_{Si} = \int_0^l p_S\Phi_i(x)dx$, $P_{Ei} = \int_0^l p_E\Phi_i(x)dx$, p_S; self-excited component of fluctuating lift force per unit length, p_E; forced component of fluctuating lift force per unit length.

The self-excited component can be expressed as follows.

$$p_S = (1/2)\rho U^2 B[C_{LH}^R(h/B) + C_{LH}^I(\dot{h}/U)] \qquad (3)$$

where ρ; air density, U; mean wind speed, B; bridge deck width, C_{LH}^R; coefficient of the self-excited lift force in phase with the vibrational displacement. C_{LH}^I; coefficient of the self-excited lift force in phase with the vibrational velocity.

P_{Si} can be written as follows, using the orthogonality condition of mode shapes.

$$P_{Si} = q_i[\int_0^l (1/2)\rho U^2 C_{LH}^R \Phi_i^2 dx] + \dot{q}_i[\int_0^l (1/2)\rho UBC_{LH}^I \Phi_i^2 dx] \qquad (4)$$

Substituting Eq. (2) into Eq. (1) and moving P_{Si} to the left hand side, then the following equation is obtained

$$M_i[\ddot{q}_i + 2(\zeta_i + \zeta_{ai})\omega_i\dot{q}_i + \omega_{ai}^2 q_i] = P_{Ei} \qquad (5)$$

where, $\zeta_{ai} = -[\int_0^1 (1/2)\rho UBC_{LH}^I \Phi_i^2 dx]/(2M_i\omega_i)$, ζ_{ai}; aerodynamic damping ratio of i^{th} mode, $\omega_{ai}^2 = \omega_i^2 - [\int_0^1 (1/2)\rho U^2 C_{LH}^R \Phi_i^2 dx]/M_i$, ω_{ai}; apparent circular frequency of i^{th} mode in wind.

As is shown in Eq. (5), both self-excited component (which results in ζ_{ai} and ω_{ai}) and forced component P_{Ei} act on bridge decks. When $\zeta_i + \zeta_{ai} \leqq 0$, that is when the summation of structural damping and aerodynamic one is 0 or negative, then the aerodynamic instability will take place even if P_{Ei} is 0. The wind-induced vibrations caused by this mechanism is called self-excited vibrations. Galloping is the divergent self-excited vibration of vertical bending mode. The characteristics of galloping can be predicted if the characteristics of self-excited component of fluctuating lift forces or the aerodynamic damping are clarified.

Vibrations will also take place due to the forced component of lift forces even if the summation of structural damping and aerodynamic one is positive. Buffeting is the forced vibration due to approaching turbulence. The magnitude of the forced vibration depends on the forced component and aerodynamic damping. It increases with the magnitude of the forced component, and it decreases as the summation of structural damping and aerodynamic one increases.

2.2 Measurement Method of Fluctuating Lift Forces

The fluctuating lift forces were measured using the dynamic balance[5] developed at the Structure Division of PWRI. Sectional models of bridge decks were kept at rest or shaken in heaving mode with an amplitude of B/100. The measurement was made both in smooth laminar flow and in turbulent flow whose characteristics are described in Chapter 2. Before the measurement of the lift forces on oscillating models, inertia forces are balanced out by adjusting the mass and the position of dummy weights to measure the lift forces only. Shaking frequencies were swept from 0.1Hz to 5.0 Hz, and the models were shaken more than 100 cycles at every frequency. The vibrational displacement of the models were measured by optical displacement meter at the same time as the lift force.

The coefficients of self-excited lift force C_{LH}^R and C_{LH}^I or logarithmic aerodynamic damping δ_a can be calculated from the frequency response function between vibrational displacement and lift forces. For linear system with input x and output y, the frequency response function $H_{yx}(f)$ can be obtained from Power Spectral Density Function (PSDF) S_{xx} and Cross Spectral Density Function (CSDF) S_{yx} as follows.[6]

$$H_{yx}(f) = S_{yx}(f)/S_{XX}(f) \tag{6}$$

The fluctuating lift forces L acting on the vibrating model whose length is l can be written as

$$L = (1/2)\rho U^2 Bl[C_{LH}^R(h/B) + C_{LH}^I(\dot{h}/U)] + \int_0^l p_E dx \tag{7}$$

If the independence between the vibrational displacement h and the forced component of the lift forces p_E is assumed, the C.S.D.F. of L and h, S_{Lh} is

$$S_{Lh} = (1/2)\rho U^2 Bl(C_{LH}^R/B + i2\pi f C_{LH}^I/U)S_{hh} \tag{8}$$

Therefore, C_{LH}^R and C_{LH}^I can be calculated from the frequency response function of L and h. H_{Lh}, as follows.

$$C_{LH}^R(f_r) = \text{Real}\ (H_{Lh})/((1/2)\rho U^2 l) \tag{9}$$

$$C_{LH}^I(f_r) = \text{Im}(H_{Lh})/[((1/2)\rho U^2 l)\cdot(2\pi f_r)] \tag{10}$$

where $f_r = (fB)/U$. Real; real part, Im; imaginary part. Aerodynamic damping depends on C_{LH}^R, C_{LH}^I and mode shape in general. When the effect of C_{LH}^R is negligible and the mode shape is uniform, it can be calculated as

$$\sigma\cdot\delta_a = -\text{Im}(H_{Lh})/[(8\pi f_r^2)((1/2)\rho U^2 l)] \tag{11}$$

where, σ; reduced mass $(=m/(\rho B^2))$.

The self-excited component of fluctuating lift forces was transformed into $\sigma\cdot\delta_a$ in this paper. On the other hand, the forced component L acting on the model at rest was reduced to C_L by dynamic pressure $(1/2)\rho U^2$, model width B and model length l. Then its standard deviation $\tilde{C}_L$ and P.S.D.F. S_{CLCL} were calculated.

3. EXPERIMENTAL RESULTS

From Fig. 5 to Fig. 12, shown are cross-sectional shapes of the bridge decks tested, the product of reduced mass and aerodynamic damping $\sigma \cdot \delta_a$, and P.S.D.F. of the coefficient of the forced component S_{CLCL}. The standard deviation of C_L, $\tilde{C}_L$ are also shown in the figures.

$\sigma \cdot \delta_a$ were measured in a range of relatively small f_r, that is relatively high wind speeds. $\sigma \cdot \delta_a$ of the relatively thick bridge decks (model A to D) becomes negative at small f_r in smooth flow. It corresponds to the onset of self-excited vibrations of vertical bending mode, what is called galloping. In turbulent flow, however, the f_r at which $\sigma \cdot \delta_a$ turns negative becomes much smaller (model B), or $\sigma \cdot \delta_a$ remains positive even at the smallest f_r in the measurement range (model A, C, D). It suggests that the possibility of galloping is much smaller in turbulent flow than in smooth flow.

On the other hand, $\sigma \cdot \delta_a$ of the relatively thin bridge decks (model E to G) and $\sigma \cdot \delta_a$ of the stiffening truss (model H) are positive both in smooth and turbulent flow. It suggests that no galloping will take place for these bridge decks. The effect of turbulence on $\sigma \cdot \delta_a$ is negligible in case of very thin bridge decks (model G) and stiffening truss (model H).

S_{CLCL} and $\tilde{C}_L$ were measured both in smooth and turbulent flow for model B. It is found that $\tilde{C}_L$ in turbulent flow becomes about 3 times as large as $\tilde{C}_L$ in smooth flow, and that the f_r where large power is concentrated becomes smaller in turbulent flow. For other models, measurements were made only in turbulent flow. It is found that $\tilde{C}_L$ decreases as bridge deck becomes thinner.

4. CONCLUSIONS

The fluctuating lift forces acting on some typical bridge decks were measured in both smooth flow and in turbulent flow generated by the coarse grid. The following characteristics were clarified.

1. Negative aerodynamic damping acts on the relatively thick bridge decks in high wind speeds of smooth flow, that is, self-excited vibrations of vertical bending mode, galloping, may occur. In turbulent flow, however, aerodynamic damping remains positive up to higher wind speed, and the possibility of galloping becomes smaller.
2. Turbulence hardly changes the characteristics of aerodynamic damping in strong winds in case of very flat bridge decks and stiffening trusses. The aerodynamic damping is positive and may increase the apparent damping.
3. The forced component of the fluctuating lift forces acting on the relatively thick bridge decks becomes much larger in turbulent flow than in smooth flow.
4. The forced component of the fluctuating lift forces in turbulent flow decreases as bridge deck becomes thinner.

5. REFERENCES

1. A. G. Davenport, N. Isymov and T. Miyata: The experimental determination of the response of suspension bridge to turbulent wind. Prod. 3rd Int. Conf. on Wind Effects on Bldgs. and Sts., Tokyo, 1971.
2. W. H. Melbourne: West Gate Bridge wind tunnel tests. Aug. 1973.
3. H. P. A. H. Irwin and G. D. Schuyler: Experiments on a full aeroelastic model of Lions Gate Bridge in smooth and turbulent flow. Laboratory Technical Report, National Research Council Canada, Oct. 1977.
4. ESDU: Engineering Science Data. Wind Engineering, Volume 1, Wind and turbulence data. Engineering Science Data Unit Ltd., 1982.
5. T. Okubo, N. Narita and K. Yokoyama: Some approaches for improving wind stability of cable-stayed girder bridges. Proc. 4th Int. Conf. on Wind Effects on Bldgs. and Sts., Heathrow, 1975.
6. J. S. Bendat and A. G. Piersol: Random Data, Wiley-Interscience, 1971.

Table 1. The Specification of the Low Speed Wind Tunnel B

Type	Göttingen Type	
Dimension	Test Section	
	Width	1,000 mm
	Height	2,000 mm
	Length	3,000 mm
	Contraction Cone	
	Inlet	3,000 mm × 5,000 mm
	Outlet	1,000 mm × 2,000 mm
	Contraction Ratio	7.50 : 1.00
	Total Path	55,000 mm
Blower	Type	Axial with Fixed Blades
	Diameter	1,500 mm
	Total Pressure	40.0 mm Aq
	Total Wind Volume	70.0 m^3/sec
	Maximum Rotation	1,250.0 rpm
	Maximum Power	50.0 KW
Flow	Maximum Wind Speed	30.0 m/sec
	Turbulence Intensity	less than 0.5%

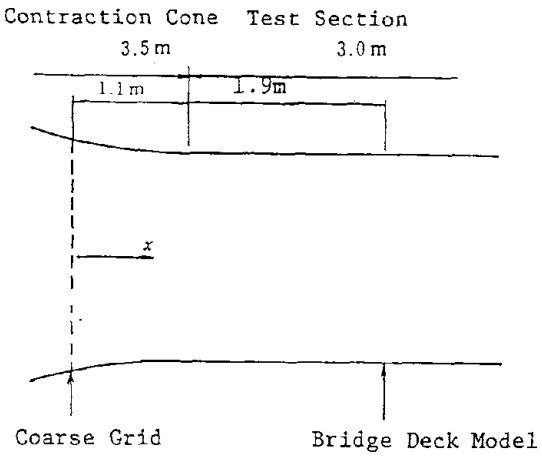

Fig.1. Position of the Coarse Grid

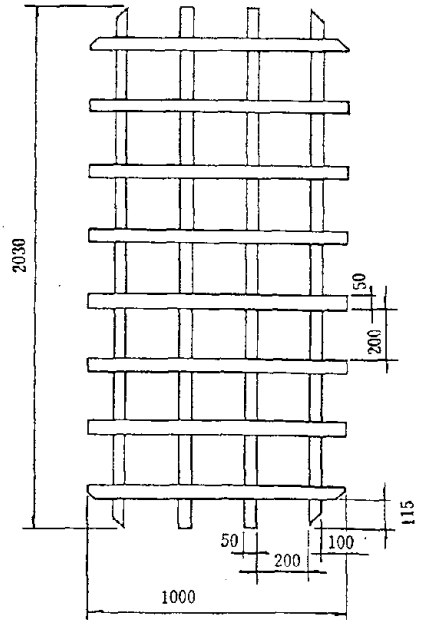

Fig.2. Coarse Grid

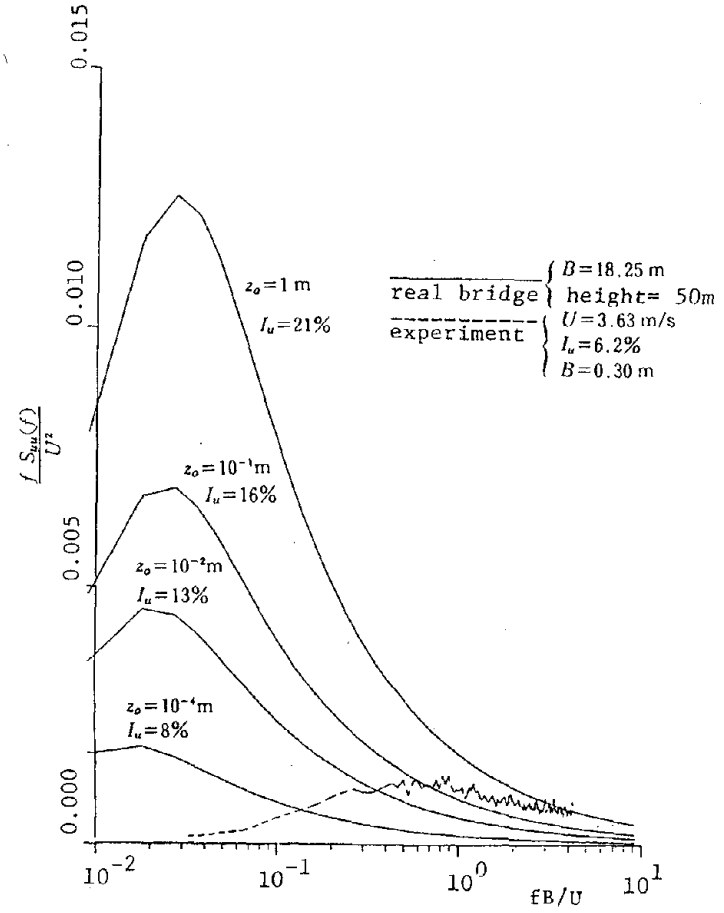

Fig.3 P.S.D.F. of u

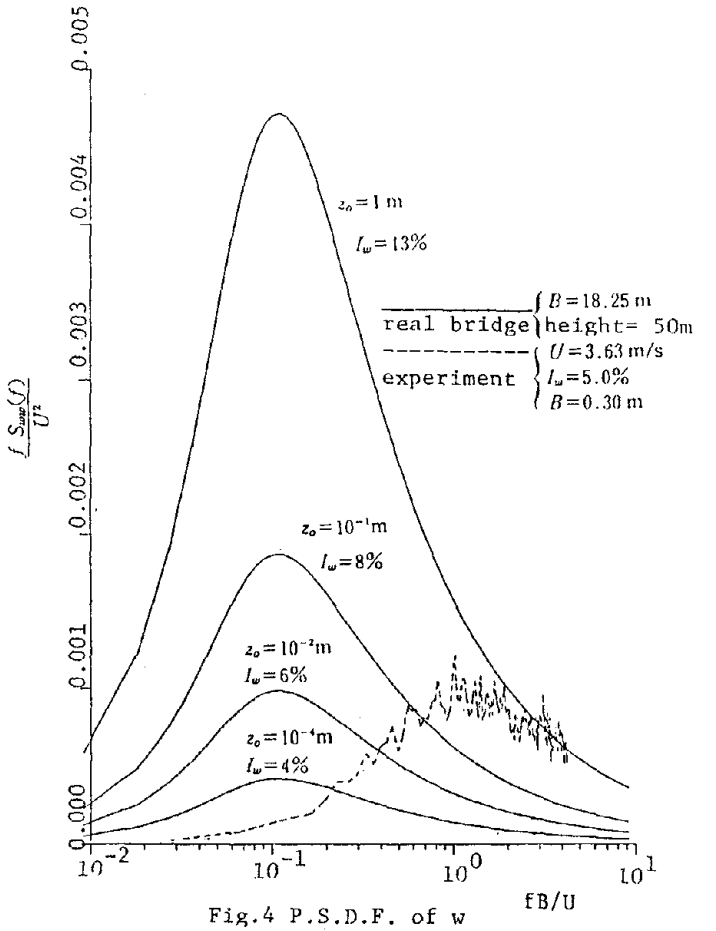

Fig.4 P.S.D.F. of w

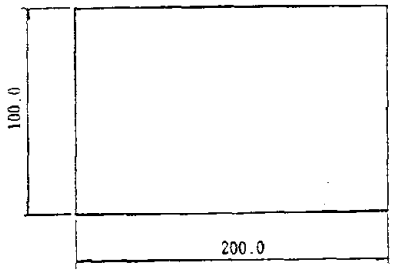

B/H=2.0

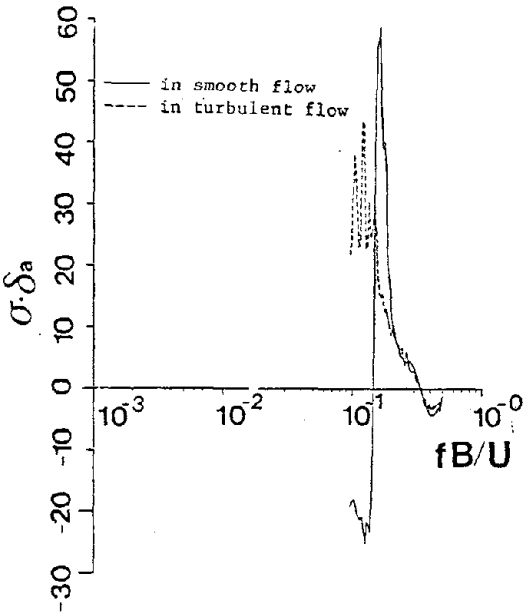

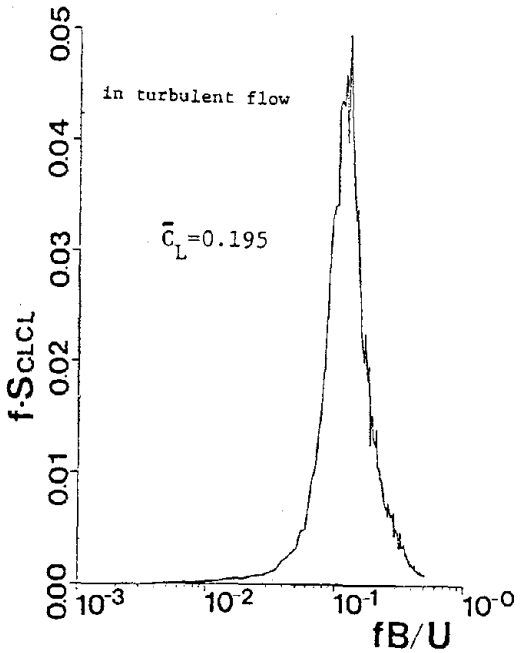

Fig.5. Model A

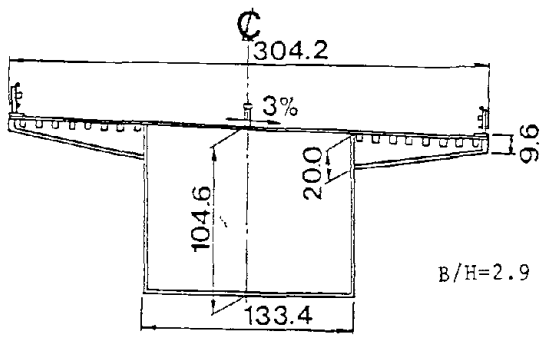

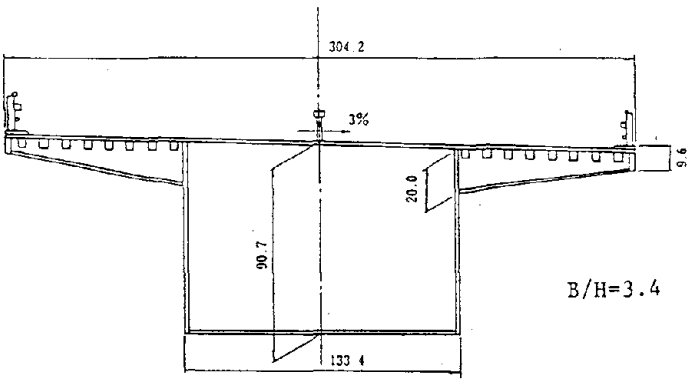

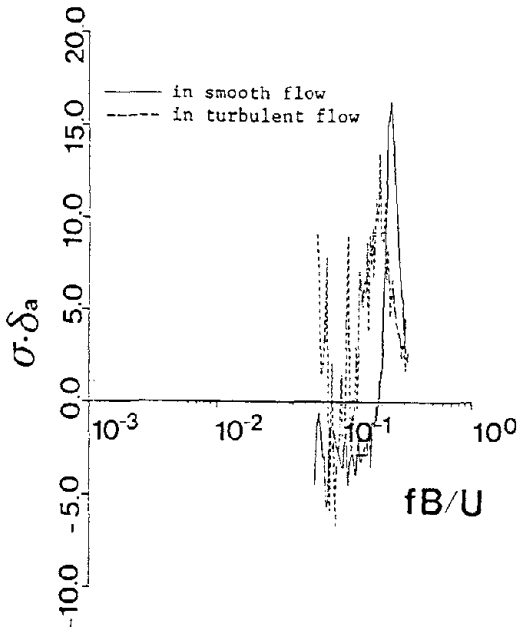

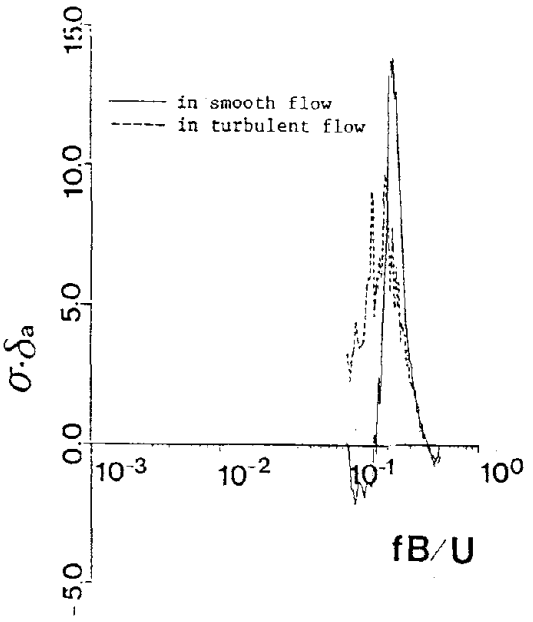

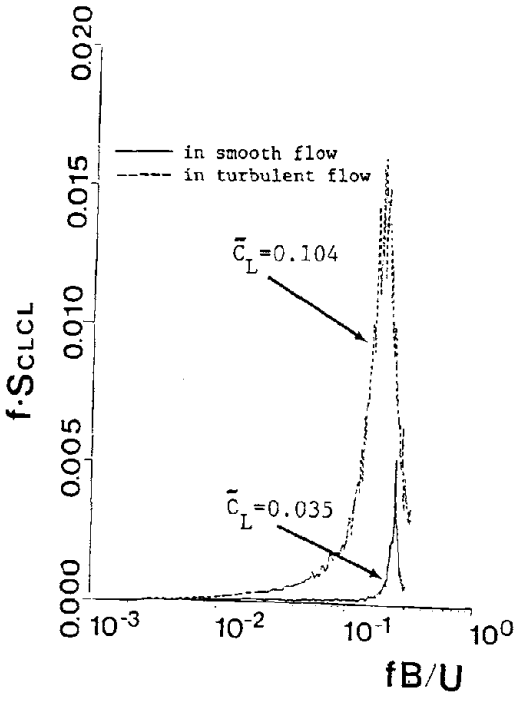

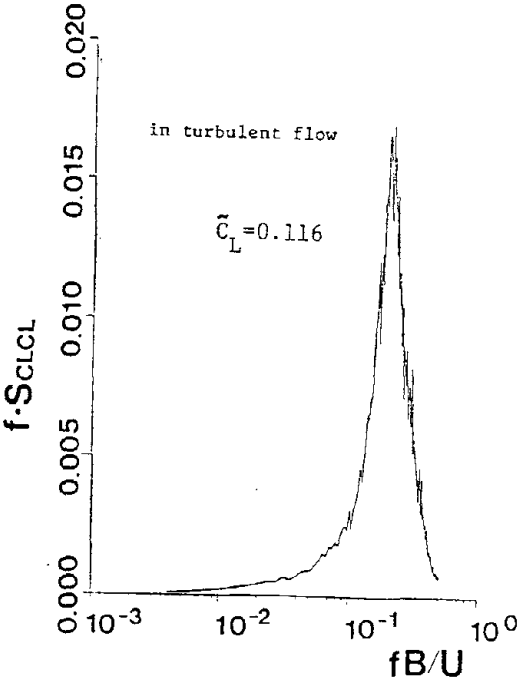

Fig.6. Model B

Fig.7. Model C

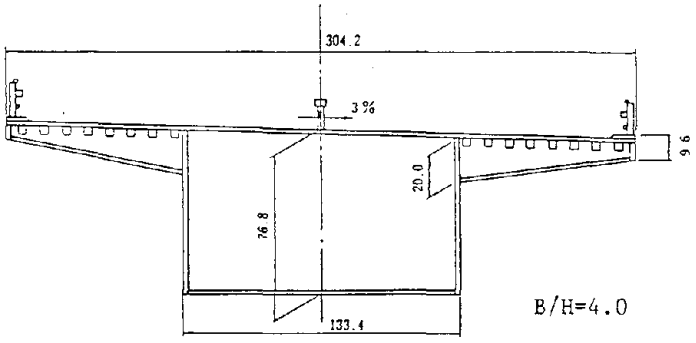

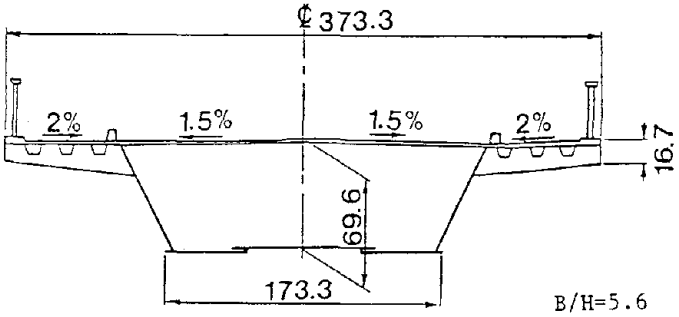

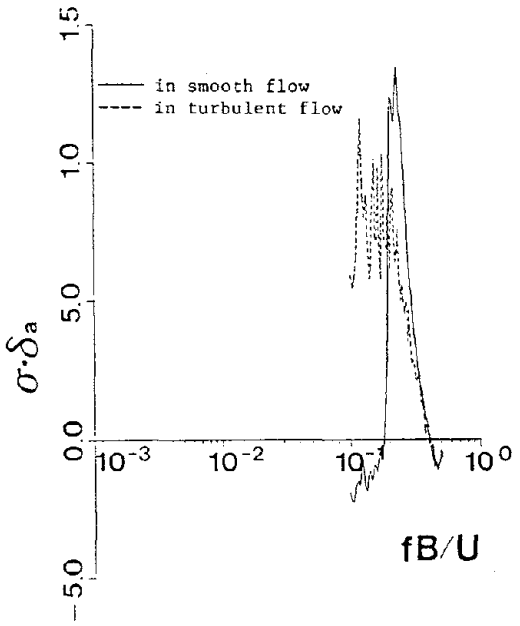

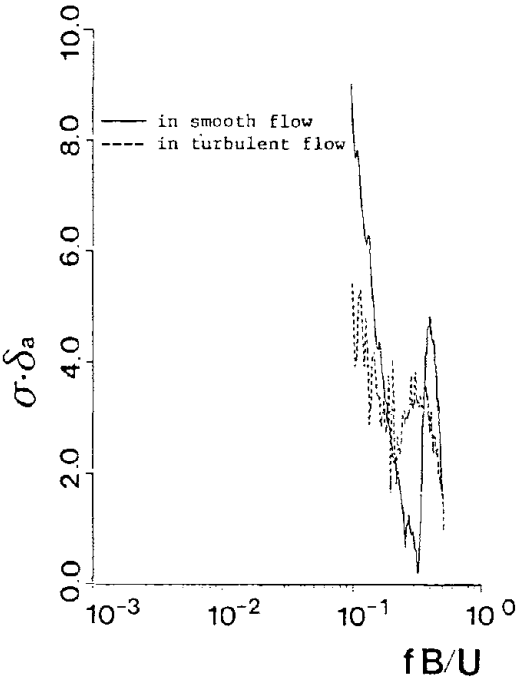

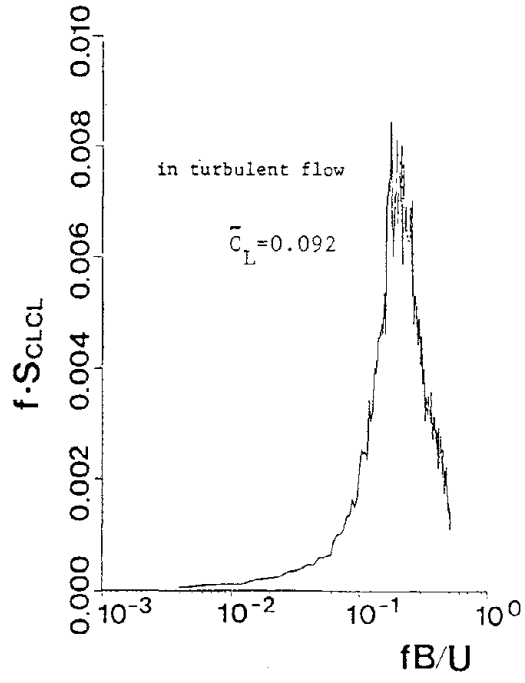

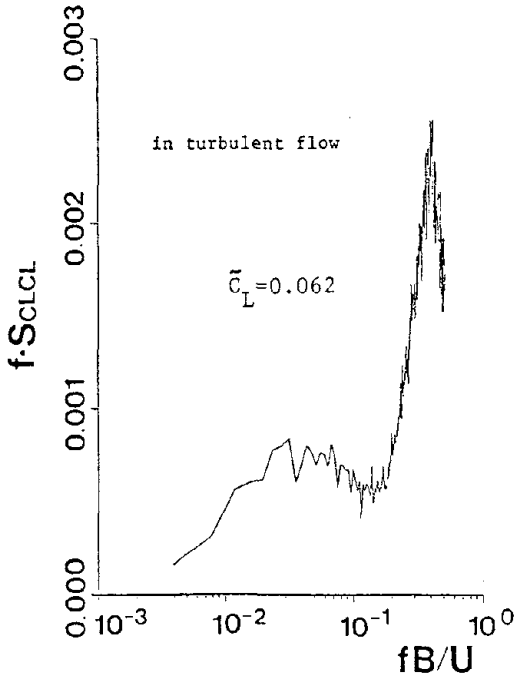

Fig.8. Model D

Fig.9. Model E

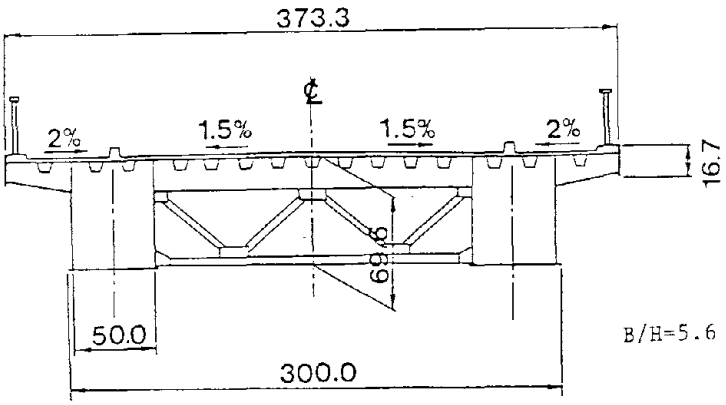

B/H=5.6

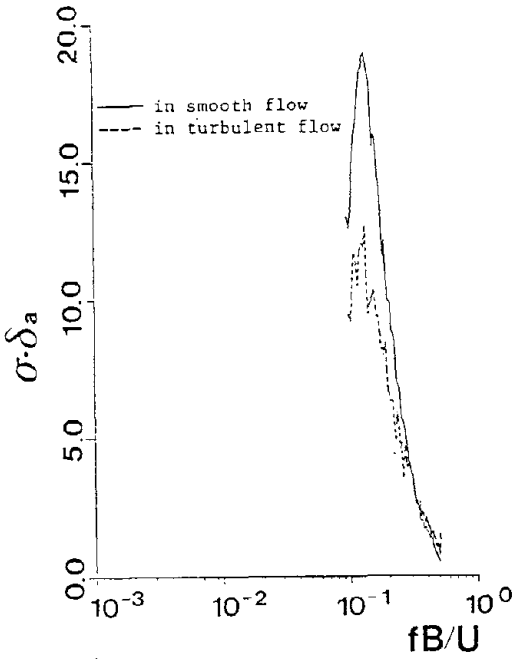

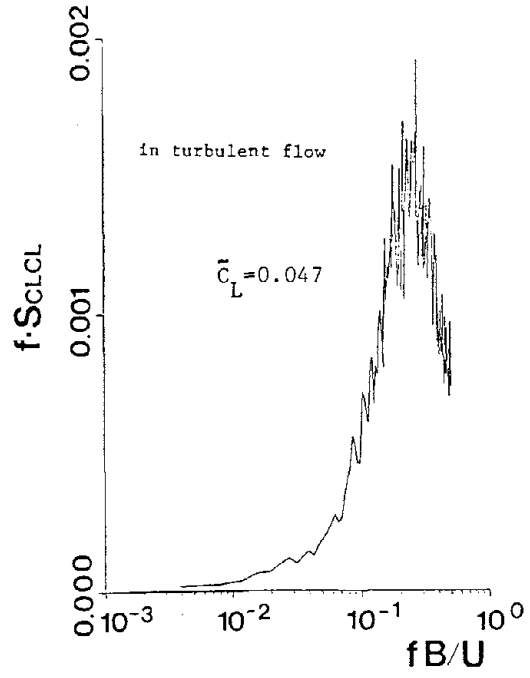

Fig.10. Model F

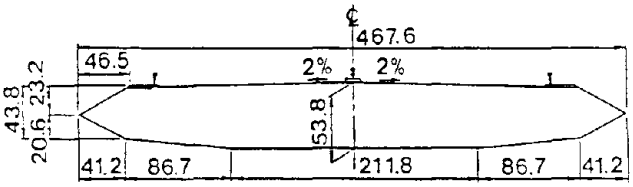

B/H=8.7

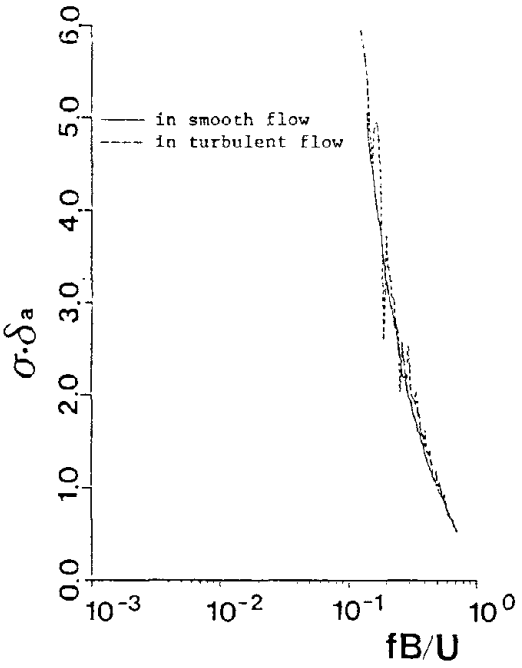

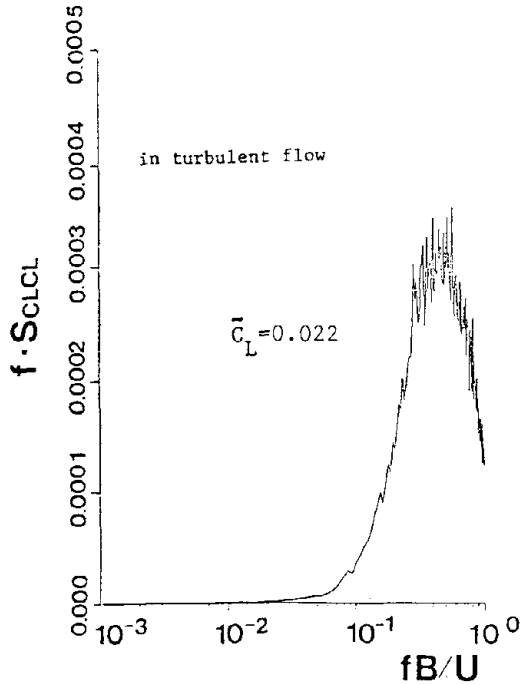

Fig.11. Model G

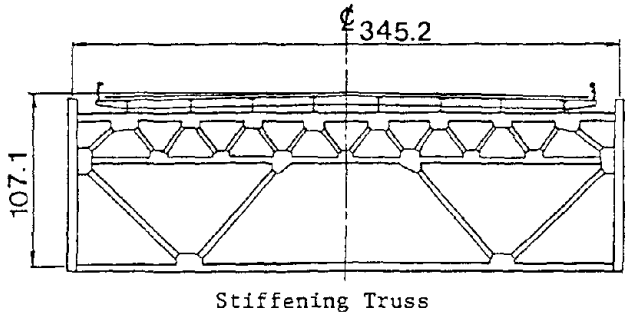

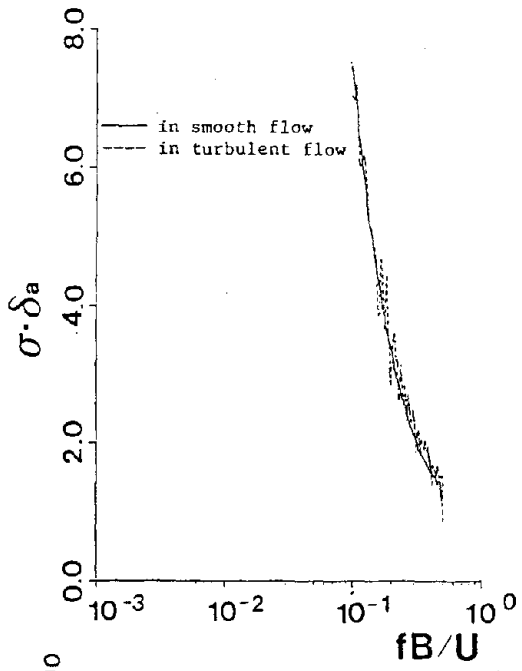

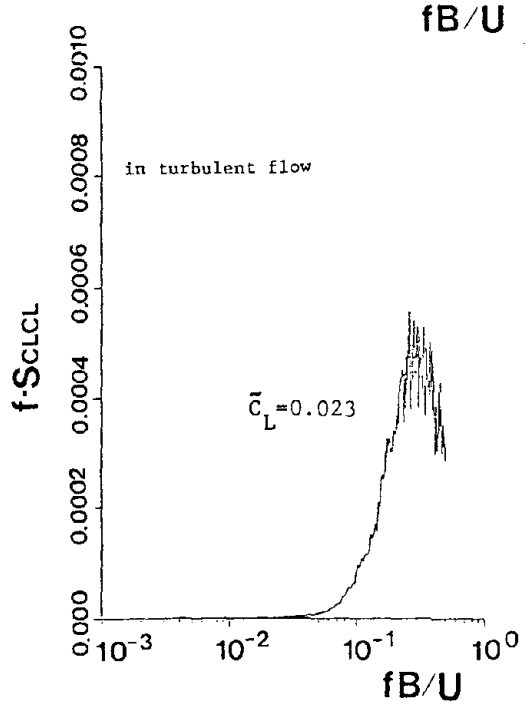

Fig.12. Model H

"Field Measurements on the
Deer Isle-Sedgwick Suspension Bridge"

by

Harold R. Bosch*

ABSTRACT

This paper first provides a general introduction to Federal Highway Administration's Wind Engineering Research Program which deals, in part, with full-scale measurement of wind characteristics and bridge response to wind loadings. It then focuses on a current program of field testing that is being conducted in cooperation with the Maine Department of Transportation on the Deer Isle-Sedgwick Suspension Bridge. Details of the bridge structure, bridge site, and instrumentation system are presented. Data analysis is discussed and samples of the results are provided. Comments are made regarding future work and plans.

Keywords

Suspension bridge, full-scale measurements, wind characteristics, bridge vibration, wind turbulence, aerodynamic stability

1. INTRODUCTION

During the past 15 years, the Federal Highway Administration (FHWA) has sponsored as well as conducted many research studies addressing the question of wind and earthquake loadings on highway structures. As part of Federally Coordinated Project 5A, "Bridge Loading and Design Criteria," the research has covered such areas as design procedures, computer modeling, field instrumentation systems, wind tunnel testing, shake table testing, retrofitting, and full-scale field testing [1].

With the objective of obtaining a better characterization of the wind environment in the vicinity of highway structures, bridges in particular, and a clearer understanding of the structure's response to the wind loadings, major effort within Task 1 of FCP Project 5A has been and is being directed toward development of automated bridge instrumentation systems and evaluation of data collected by such systems. Information collected traditionally consists of wind parameters such as velocity components, direction, turbulence intensity, turbulence scale, turbulence spectrum, and associated bridge response parameters such as displacements, accelerations, strains, damping, and frequencies.

The FHWA installed its first field wind instrumentation system on the Newport, Rhode Island Suspension Bridge in cooperation with the Rhode Island Turnpike and Toll Bridge Authority. Sensors were located on outrigger booms and positioned symmetrically along the main span. While in operation, the system successfully recorded the passage of Hurricane Doria and analysis of this data is documented in several research reports [2]. The instrumentation was then relocated to Sitka, Alaska where it was modified to incorporate improvements and installed on the Sitka Harbor

*Research Structural Engineer,
Federal Highway Administration,
6300 Georgetown Pike, McLean,
Virginia 22101, U.S.A.

Cable-Stayed Bridge. In a 5 year cooperative effort with the Alaska Highway Department, data was collected on the Nation's first vehicular cable-stayed bridge. Vortex excitation of the free-standing pylon towers, response of the deck, and wind characteristics at the site have been evaluated and are reported in various papers and reports [2, 3]. Following the Sitka investigation, the wind instrumentation system was installed on the Perrine Memorial Bridge in Twin Falls, Idaho to study wind induced vibration of the bridge columns. This bridge structure, spanning the Snake River Canyon, consists of a four-lane deck on plate girders supported by slender, unbraced columns atop a steel arch. Column motion was measured before and after installation of special damping devices [4]. The instrumentation system was next moved to the Pasco-Kennewick Intercity Bridge in the State of Washington. This structure is the first concrete cable-stayed bridge in the United States. Wind characteristics at this inland site and bridge response measurements have been documented in a recent report and several papers [5]. In 1981, the FHWA instrumentation system was completely refurbished and several new types of sensors were added to upgrade and expand its capability [6]. The system was then installed on the Deer Isle-Sedgwick Suspension Bridge in State of Maine. Through a cooperative arrangement with the Maine Department of Transportation (MEDOT), FHWA is investigating the aerodynamic stability of the Deer Isle Bridge in order to provide recommendations regarding bridge rehabilitation. This study is currently underway and will be described in more detail in what follows.

2. DEER ISLE-SEDGWICK SUSPENSION BRIDGE

The Deer Isle-Sedgwick Bridge, illustrated in Figure 1, is a conventional suspension structure located near Penobscot Bay on the coast of Maine. Built in 1938, the bridge spans Eggemoggen Reach and consists of a girder-stiffened deck similar in cross section to the original Tacoma Narrows Bridge. The main span is 1080 ft (329m) in length with side spans of 484 ft (148m) and approach spans of 130 ft (40m) for a total bridge length of 2308 ft (704m). As shown in Figure 2, the structure is symmetrical with two towers and the roadway has a 6.5% grade to provide vertical navigational clearance of 85 ft (26m) at midspan. The 2-lane deck consists of a 4.5 in (11cm) concrete slab having a width of 20 ft (6m). Stiffening girders are 6.5 ft (2m) deep and spaced 23.5 ft (7m) apart. Figure 3 provides additional deck and tower details.

2.1 Bridge Site

The bridge site is situated in Hancock County approximately 55 miles (88 km) east of Augusta and 35 miles (56 km) south of Bangor. This location is noted on the map of Maine which has been included as Figure 4. The bridge carries State Route 15 over Eggemoggen Reach and connects Sedgwick on the mainland with Deer Isle and Stonington on the Islands. The longitudinal axis of the structure lies on a NE-SW orientation with the mainland being at the north end of the bridge and Little Deer Isle at the south end. The countryside to the north consists of heavily forested, rolling hills varying in elevation to a few hundred feet. To the south and east are many forested, low-lying islands, Deer Isle being the largest, with the Atlantic Ocean beyond. To the west there is Penobscot Bay with a small mountain range beyond.

3. INSTRUMENTATION - SENSORS

A large array of instruments has been installed on the Deer Isle Bridge to monitor the wind environment and structural response to wind loadings. The positions of sensors on the bridge are indicated in Figure 5. Mean wind

speed and direction are measured by two skyvane sensors mounted on the top and bottom of the north bridge tower. The upper skyvane is 18 ft (5.5m) above the tower top while the lower one is located approximately 30 ft (10m) above the water. Air temperature is measured by three thermistor probes installed at the top and bottom of the same tower and at the instrument house north of the bridge. Six tri-axis anemometers are used to monitor wind turbulence quantities (speed, direction, intensity, scale) at the elevation of the bridge span. These anemometers are mounted on 12 ft (3m) outriggers cantilevered from the east side of the superstructure and spaced in a logarithmic array. Each anemometer set is aligned with the bridge so that the "U" component is normal to the longitudinal bridge axis (facing southeast), "V" component is parallel to the bridge axis (facing northeast), and "W" component points upward. The tri-axis anemometers employed are dynamic instruments which are capable of tracking velocity fluctuations in the frequency range of interest.

Bridge deck response is monitored by six pairs of single-axis, servo accelerometers installed along the north side span and main span. Accelerometer stations on the side span are located at midspan and the quarter point nearest the north tower. For the main span, stations are located at midspan, both quarter points, and the eighth point nearest the north tower. At each station, an accelerometer mounted inside a weathertight enclosure is clamped to the bottom flange of each stiffening girder. The axis of each accelerometer is oriented to point upward to measure vertical motion. The pair of accelerometers at each station define the vertical displacement and rotation of the span at that point. The whole array of stations are used to determine mode shape and frequency for the structure.

To examine tower motion, three accelerometers are used at the top cross girder of the north tower. Two of these are mounted at the top of each tower leg with their axes oriented to point northeast. This defines bending and twisting of the tower top. The third is pointed southeast to indicate tower sway.

3.1 Instrumentation - Data Recorder

Data recording equipment as well as lab test equipment, parts, and supplies are housed in a small instrument house located just off the north end of the bridge. This building is outfitted with heat, air conditioning, telephone, security system, and motor-generator (for conditioning incoming power). Analog signals from all sensors located on the bridge are routed to this instrument house via multi-conductor, shielded cable installed on the west side of the bridge. Approximately 20,000 ft (6096m) of cable was required to instrument the Deer Isle Bridge. To insulate the instrumentation from lightning strikes, protection devices were installed in each accelerometer enclosure and at the input panel in the instrument house.

The analog signals from the bridge sensors are passed through signal conditioning and amplified to provide maximum resolution in the recording system. Anemometer gains were adjusted to accommodate wind velocities up to 100 mph (161 Km/H) and accelerometer gains adjusted to handle .25g. Amplified signals from the deck anemometers and all accelerometers are low-pass filtered at 10 Hz to avoid aliasing of the data. All signals are then routed to the data recorder.

The recorder is an automated data acquisition system (DAS) equipped with dual 9-track digital tape drives providing enough capacity for 8

hours of recording [6]. Figure 6 illustrates the data path and control logic employed by the data acquisition system. The DAS continuously scans up to 60 channels of analog input at a rate of 20 Hz. Data recording does not begin until either wind velocities or bridge accelerations exceed preset levels for a selected period of time. Once initiated, recording continues until signals drop below these threshold values. This mode enables unattended operation and optimizes use of available data storage capacity. While recording, the system continuously scans all channels, converts the analog signals to digital data, and stores this data on magnetic tape for later processing. When one tape fills, the recorder automatically switches to the other drive and continues without loss of data. Wind speed and direction measured by the two tower anemometers are also recorded on strip-chart recorders. This recording is continuous and documents the day-to-day wind conditions at the site regardless of whether or not the DAS is active.

3.2 Data Reduction and Analysis

After wind and bridge response data has been recorded on digital tape, the tapes are forwarded to Turner-Fairbank Highway Research Center (TFHRC) for preprocessing and evaluation. This data reduction is accomplished by FHWA staff using various microcomputers. Data tapes are first scanned for errors. Raw data is converted to engineering units using sensor calibrations obtained in the field and channel statistics such as minimum, maximum, mean, and standard deviation are compiled for 10/20-minute blocks of data. A typical 10-minute summary is provided in Table 1. This information is used to evaluate system performance and to identify events which warrant detailed study. Mean wind speed and direction obtained from the skyvane sensors on the tower are displayed in polar form and evaluated to detect any trends in the recorded data. Figure 7 is a polar plot of wind activity at the top of the north bridge tower. This graph represents an accumulation of recorded data and is up dated each time new information is obtained. Hourly means are obtained from the continuous chart recordings and plotted in time-history fashion for each month. As demonstrated in Figure 8, this technique is a useful means of compressing large volumes of data and enables identification of significant storm events.

Detailed data analysis is being performed for FHWA by a research contractor. As events of interest are identified during the preprocessing, copies are made and forwarded to the contractor for detailed analysis. The data processing sequence is illustrated in Figure 9. This analysis is accomplished in three stages. In the initial stage, raw data is converted to engineering units and summarized using program TAPSUM much the same as was done during preprocessing by FHWA. The intermediate stage prepares anemometer data from selected events for detailed analysis by applying response corrections and rotating the data into the desired coordinate system. This is accomplished using program MASTER. The final stage of data processing involves spectral analysis of the time series data. In ANAL2, time series data is first prepared for analysis by point averaging, detrending, and tapering. Next, fast Fourier transform techniques are employed to process data from 1, 2, or 3 channels simultaneously. This analysis provides statistics on all the data as well as power spectral densities and auto correlations for the individual series. In addition, co-spectral and quadrature spectral densities,

coherence, squared coherence, phase difference, and lagged cross-correlations are available for each pair of series.

Bridge displacements are extracted from acceleration time histories using a sophisticated double integration program called DAISMA [7]. Figure 10 is an example of a measured acceleration record and the computed displacement time history. Bridge mode shapes are determined using a semi-automated process which examines spectral amplitude data searching for pronounced peaks. Figure 11 is a spectral plot of deck acceleration at accelerometer 9 with 7 peaks identified. Similar results for all accelerometers are listed in Table 2. Bending modes are derived using the average signal from the accelerometer pair at each bridge station. The difference between signals from each pair is used to develop torsional modes. Bending modes which have been identified so far are illustrated in Figure 12.

Wind spectra obtained for each selected event are compared with three theoretical models. Typical spectral comparisons for the "U" and "W" wind components are shown in Figures 13 and 14, respectively. In addition, turbulence intensity and scale are computed for comparison with existing meteorological data. Typical values obtained from two wind events are included in Table 3.

4. FUTURE WORK

All data collected to date has been pre-processed and summarized; however, only a small portion has received detailed analysis and evaluation. Therefore, analysis will continue. Attention will be focused on determining the full range of bridge displacements, developing torsional mode shapes, extracting structural damping values, identifying vortex shedding parameters (including Strouhal number) and evaluating the along-span coherence of turbulence.

The existing data set provides extensive wind coverage from the west, some from the east, and very little from the north or south. Wind velocities are generally in the 20-50 mph (32-80 Km/H) range. So far, no major bridge motions or vortex induced response have been identified. More information is needed regarding severe storms containing high wind velocities or strong turbulence as well as weak fronts containing mild, steady winds. Better directional coverage is also desirable. To accomplish this, a newer and more flexible data acquisition system with remote communications capability was installed at the instrument house in the fall of 1984 and data acquisition is continuing.

5. REFERENCES

(1) O'Fallon, J., "FCP Annual Progress Report - Year Ending September 30, 1984," Project 5A, FHWA, September 1984

(2) Gerhardt, C. L., et al, "Selected Wind and Bridge Motion Data Recorded at Long-Span Bridge Sites, " Report No. FHWA-RD-76-180, FHWA, August 1976

(3) Nelson, D., et al, "Wind and Bridge Motion Data Recorded at the Cable-Stayed Bridge, Sitka, Alaska, " Report No. FHWA-RD-78-57, FHWA, May 1977

(4) Cheng, D., "Aerodynamic Stability of Long Columns With Elastic End Constraints," Report No. FHWA?RD-81/133, FHWA, February 1982

References (continued)

(5) Bampton, M., et al, "Pasco-Kennewick Cable-Stayed Bridge Wind and Motion Data," Report No. FHWA/RD-82/067, FHWA, February 1983

(6) Strope, L., "FHWA Data Acquisition System, " Unpublished Report, FHWA, January 1982

(7) Miklofsky, H., "Digitization and Integration of Strong Motion Accelerographs, Report No. FHWA-RD-77-92, FHWA, August 1977

TABLE 1. Tape Summary - 10 Minute Data Block

DEER ISLE - SEDGWICK BRIDGE

Tape Number: 119 Block Size: 1925 Channels: 60
Start Record: 4801 End Record: 5200

Day: 290 Time: 18:33:30 Pwr: 0
Day: 290 Time: 18:43:43 Pwr: 0

CHANNEL	MINIMUM	MAXIMUM	MEAN	STD DEV
0	-0.0326	0.0131	-0.0021	0.0045
1	-0.0268	0.0096	-0.0008	0.0037
2	-0.0233	0.0117	-0.0054	0.0038
3	-0.0114	0.0095	-0.0007	0.0034
4	-0.0114	0.0114	-0.0003	0.0032
5	-0.0110	0.0073	-0.0003	0.0030
6	-0.0106	0.0106	-0.0001	0.0034
7	-0.0112	0.0130	-0.0006	0.0036
8	-0.0129	0.0129	-0.0008	0.0034
9	-0.0141	0.0121	-0.0008	0.0038
10	-0.0113	0.0094	-0.0009	0.0037
11	-0.0165	0.0110	-0.0002	0.0035
12	-0.0113	0.0094	0.0018	0.0029
13	-0.0038	0.0152	0.0081	0.0029
14	0.0011	0.0118	0.0078	0.0016
15	0.0000	0.0000	0.0000	0.0000
16	0.0000	0.0000	0.0000	0.0000
17	0.0000	0.0000	0.0000	0.0000
18	0.0000	0.0000	0.0000	0.0000
19	0.0000	0.0000	0.0000	0.0000
20	-21.5469	0.7695	-11.5911	5.3622
21	-5.7268	10.7377	1.4961	2.1137
22	-8.8629	10.5970	-2.0139	3.2206
23	-25.6511	3.0178	-12.8086	6.2303
24	-8.4861	10.8005	1.3423	2.3343
25	-9.8163	12.7035	-2.5282	3.5603
26	-24.6868	2.3144	-13.6838	5.6273
27	-4.6756	8.5720	1.3423	1.9319
28	-9.0240	12.2850	-1.9814	3.2273
29	-26.7996	0.7657	-13.4075	5.7328
30	-5.6221	7.7304	1.2650	2.1762
31	-10.7949	11.5659	-3.7344	3.0344
32	-24.8110	7.7534	-10.5602	6.3790
33	-7.2088	9.3714	1.5625	2.2305
34	-10.2116	10.9823	-2.4041	3.6457
35	-23.0859	5.3867	-11.2640	5.9269
36	-7.2427	12.3125	1.0122	3.6451
37	-11.3280	13.8240	-2.4072	3.5438
38	0.0000	0.0000	0.0000	0.0000
39	0.0000	0.0000	0.0000	0.0000
40	0.0000	0.0000	0.0000	0.0000
41	0.0000	0.0000	0.0000	0.0000
42	0.0000	0.0000	0.0000	0.0000
43	-5.0781	-5.0781	-5.0781	0.0001
44	5.0781	5.1563	5.1355	0.0345
45	0.0000	0.0000	0.0000	0.0000
46	0.0000	0.0000	0.0000	0.0000
47	0.0000	0.0000	0.0000	0.0000
48	0.0000	0.0000	0.0000	0.0000
49	0.0000	0.0000	0.0000	0.0000
50	17.1875	25.0000	21.0977	1.6296
51	253.7500	386.8750	271.1813	4.4200
52	67.5000	77.5000	72.0375	1.8911
53	47.5000	50.0000	47.9500	0.9617
54	50.0000	50.0000	50.0000	0.0000
55	-1.7969	-1.7969	-1.7969	0.0000
56	18.7500	28.1250	23.5859	1.7707
57	196.8750	219.3750	208.8000	3.8015
58	0.0000	0.0000	0.0000	0.0000
59	0.0000	0.0000	0.0000	0.0000

TABLE 2. Spectral Amplitudes - Deck Acceleration

TABLE 40 - ACCELEROMETERS REFERENCED TO ACCELEROMETER 8 -- TABLE OF AMPLITUDES

band	frequency	accel 1	accel 2	accel 3	accel 4	accel 5	accel 6	accel 7	accel 8	accel 9	accel 10	accel 11	accel 12	accel 13	accel 14	accel 15
VARIANCE =>		0.000277	0.000234	0.000417	0.000378	0.000260	0.000242	0.000188	0.000229	0.000325	0.000325	0.000204	0.000201	0.000002	0.000002	0.000002
1	9.94784	0	0	0	0	0	0	0	0	0	0	0	0	0	0	0
2	9.07254	0.049556	-0.04537	0	0	0	0	0	0	0	0	0	0	0	0	0
3	8.27425	0	0	0	0	0	0	0	0	0	0	0	0	0	0	0
4	7.54621	0	0	0	-0.01617	0	0	0	0	0	0	0.042929	0.042102	0	0	0
5	6.88222	0	0	0	0	0	0	0	0	0	0	0	0	0	0	-1.20177
6	6.27866	-0.08307	-0.06432	0	0	0	0	0	0	0	0	0	0	-0.98854	0	0
7	5.72438	0	0	0	0	0	0	0	0	0.031116	0.031116	0	0	0	0	0
8	5.2207	0	0	-0.27710	-0.07744	0.111763	-0.09936	0	0.046334	0	0	0	0	0	0	0
9	4.6134	0	0	0	0	0	0	-0.07763	0	-0.02897	-0.02897	0.093995	-0.07547	0	0	0
10	4.34239	0	0	0	0	0	0	0	0	0	0	0	0	0	0	0
11	6.96031	0	0.349635	-0.18511	0.138356	0	0	0	0	0	0	0	0	0	0	0
12	3.61184	-0.31824	0	0	0	-0.13729	0	0	0	-0.05102	-0.05102	0	0	0	0	0
13	3.29404	0	0	0	0	0	-0.17991	0.119957	0.120212	0	0	-0.14323	-0.14924	0.370077	0.303215	-0.52802
14	3.0042	0	0	0	0	0	0	0	0	0	0	0	0	0	0	0
15	2.73986	0	0	0	0	0	0	0	0	0	0	0	0	0	0	0
16	2.49078	0	0	-0.19929	0.248074	-0.09751	-0.10057	0	0	0	0	0	0	-0.42110	0	-0.37186
17	2.2692	0	0	0	0	0	0	0	0	0	0	0	0	0	0	0
18	2.0784	-0.24435	-0.27924	0.059032	0	0	0	0	0	0	0	0	0	0	0	0
19	1.89552	0	0	0	0	0	0	0	0	0.108172	0.108172	0	0	0	-0.19712	0
20	1.72874	0	0	0	0	-0.12029	-0.07338	0.283783	0.275347	0	0	-0.21213	-0.30288	0	0	0
21	1.57663	0	0	0	0	0	0	0	0	0	0	0	0	0	0	0
22	1.4379	0.085830	0	5.558478	5.487038	0	0	0	0	0	0	0	0	0	0.499961	0
23	1.31138	0	0	0	0	0	0	0	0.337305	0.367365	-0.73223	-0.73223	0.335793	0	0.291323	0	0.246498
24	1.19597	0	0	0	0	0	0	0	0	0	0	0	0	0	0	0	0
25	1.09076	0	0	0	0	2.3942	2.166553	0	0	0	0	0	0	0	0	0	0
26	0.99478	0	0	0	0	0	0	0	0	0	0	0	0	0	0	0	0
27	0.90725	0	1.064544	0	0.317226	0	0	0	1.499881	0	0	1.300167	1.418314	0	-3.44955	0.172498
28	0.82743	0	0	0	0	0	0	0	0	0	0	0	0	0	0	0	0
29	0.75462	0	0	0	0	0	0	0.920562	0	0	0	0	0	0	0	0	0
30	0.68822	-2.17816	-2.25422	-0.55150	-0.62990	0	0	0	0.835872	-1.97208	-1.97208	0	0.814751	0.693853	0.606495	0.930250
31	0.62767	0	0	0	0	0	0	0	0	0	0	0	0	0	0	0	0
32	0.57244	0	0	0	0	0	0	0	0	0	0	0	0	0	0	0	0
33	0.52207	-0.94077	-0.91274	0	0	0	0	0	0	0	0	0	0	0.941281	0	0.952794
34	0.47613	0	0	-0.23416	-0.24484	0.398616	0.386744	1.530088	1.38761	0	0	-1.50154	-1.4962	0	0	0
35	0.43424	0	0	0	0	0	0	0	0	0	0	0	0	0	0	0
36	0.39603	0	0	0	0	0	0	0	0	0	0	0	0	0	0	0
37	0.36118	0	0	0	0	0	0	0	0	0	0	0	0	0	0	0
38	0.3294	0	0	0	0	0	0	0	0	0	0	0	0	0	0	0
39	0.30042	0	0	0	0	0	0	0	0	0	0	0	0	0	0	0
40	0.27399	-0.13495	-0.11991	-0.03231	-0.03596	0.057960	0.059173	0.380941	0.352899	1.130804	1.130804	0.398917	0.404177	0.255882	-0.00530	0.287724
41	0.24988	0	0	0	0	0	0	0	0	0	0	0	0	0	0	0
42	0.22789	0	0	0	0	0	0	0	0	0	0	0	0	0	0	0
43	0.20784	0	0	0	0	0	0	0	0	0	0	0	0	0	0	0
44	0.18955	0	0	0	0	0	0	0	0	0	0	0	0	0	0	0
45	0.17287	0	0	0	0	0	0	0	0	0	0	0	0	0	0	0
46	0.15766	0	0	0	0	0	0	0	0	0	0	0	0	0	0	0
47	0.14379	0	0	0	0	0	0	0	0	0	0	0	0	0	0	0
48	0.13114	0	0	0	0	0	0	0	0	0	0	0	0	0	0	0
49	0.1196	0	0	0	0	0	0	0	0	0	0	0	0	0	0	0
50	0.10908	0	0	0	0	0	0	0	0	0	0	0	0	0	0	0
51	0.09948	0	0	0	0	0	0	0	0	0	0	0	0	0	0	0
52	0.09073	0	0	0	0	0	0	0	0	0	0	0	0	0	0	0
53	0.08274	0	0	0	0	0	0	0	0	0	0	0	0	0	0	0
54	0.07545	0	0	0	0	0	0	0	0	0	0	0	0	0	0	0
55	0.06882	0	0	0	0	0	0	0	0	0	0	0	0	0	0	0
distance=>		242	242	363	363	619	619	754	754	1024	1024	1294	1294	484	484	484

TABLE 3. Turbulence Properties for Selected Events

TURBULENCE INTENSITIES AND LENGTH SCALES

TAPE #	ANEMOMETER	COMPONENT	RECORDS	TURBULENCE INTENSITY	LENGTH SCALE (M)
15	4	U	1-1024	0.4260	16.0
15	5	U	1-1024	0.4631	18.0
15	6	U	1-1024	0.4649	22.0
15	1	U	1-1024	0.3998	23.0
15	5	U	1-1024	0.4631	18.0
15	2	U	1-1024	0.1925	14.0
40	4	U	5-1029		
40	5	U	5-1029	0.1132	674.0
40	6	U	5-1029	0.1040	534.0
40	1	U	5-1029	0.1147	451.0
40	5	U	5-1029	0.1132	674.0
40	2	U	5-1029	0.1131	452.0
40	4	W	5-1029	0.0503	74.0
40	5	W	5-1029	0.0582	92.0
40	6	W	5-1029	0.0542	66.0
40	1	W	5-1029	0.0498	85.0
40	5	W	5-1029	0.0582	92.0
40	2	W	5-1029	0.0622	134.0

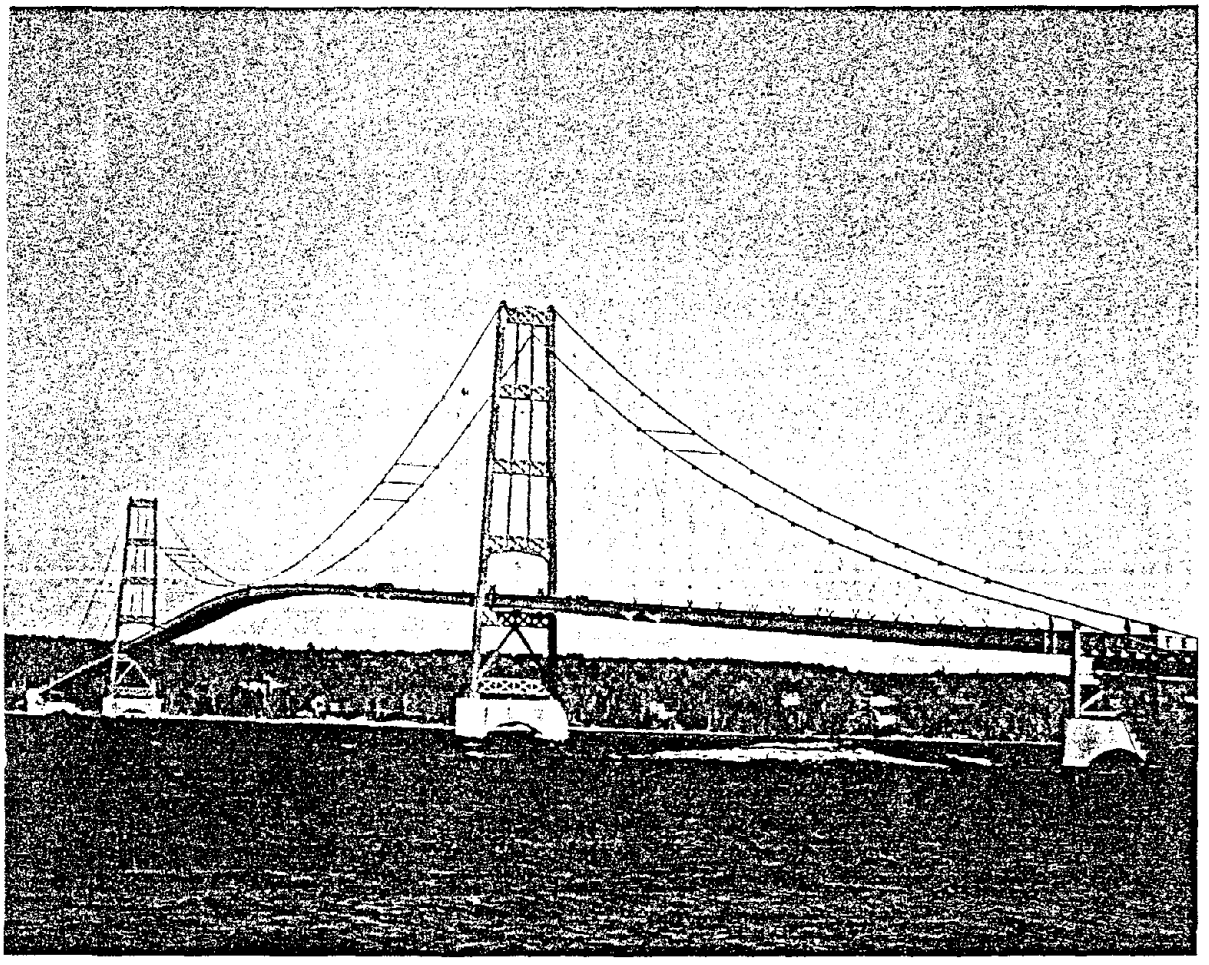

FIGURE 1. Deer Isle-Sedgwick Suspension Bridge

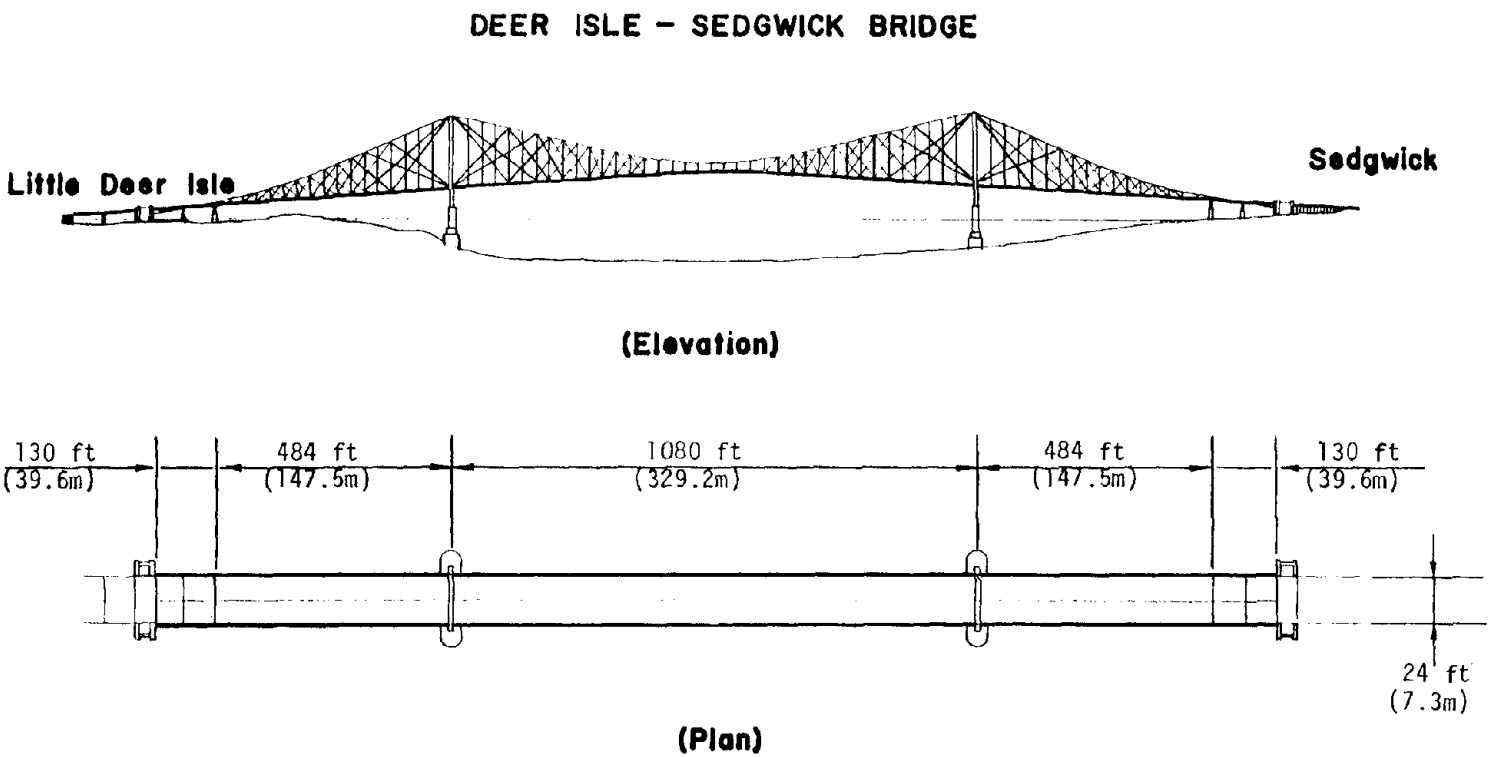

FIGURE 2. Bridge Plan and Elevation Views

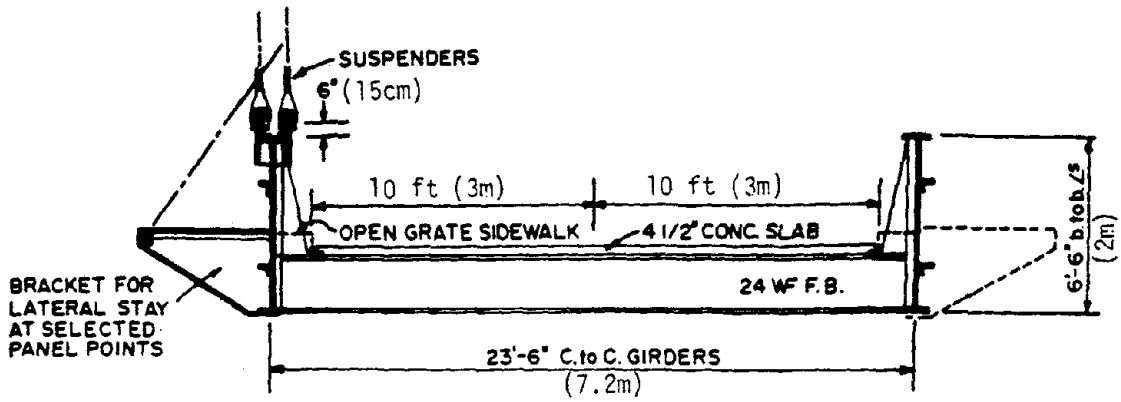

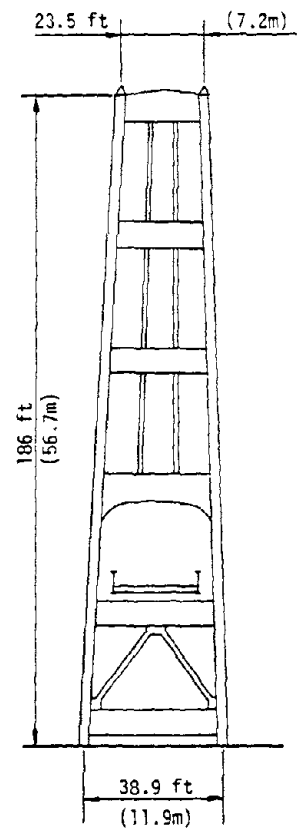

FIGURE 3. Bridge and Tower Cross Section

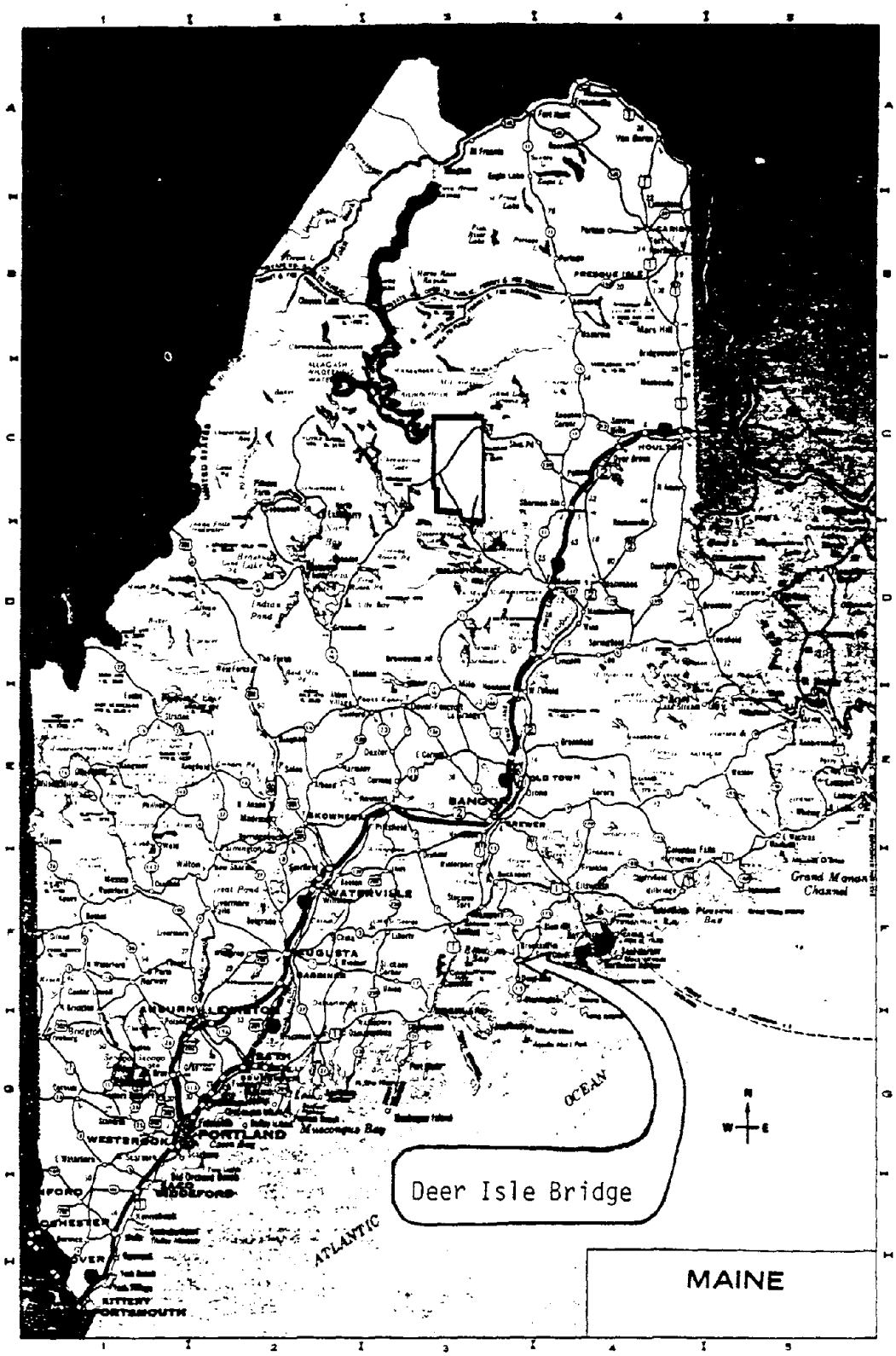

FIGURE 4. Site Location Map

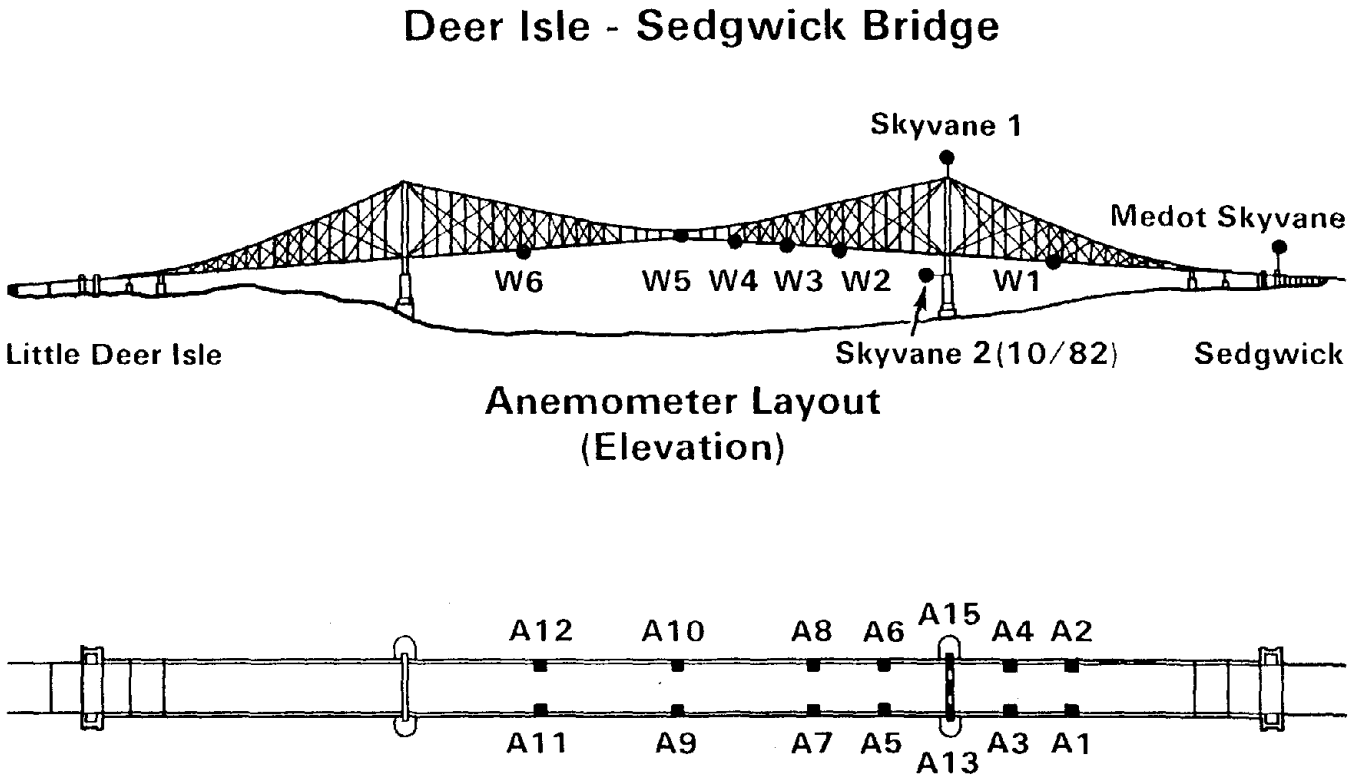

FIGURE 5. FHWA Instrumentation Layout

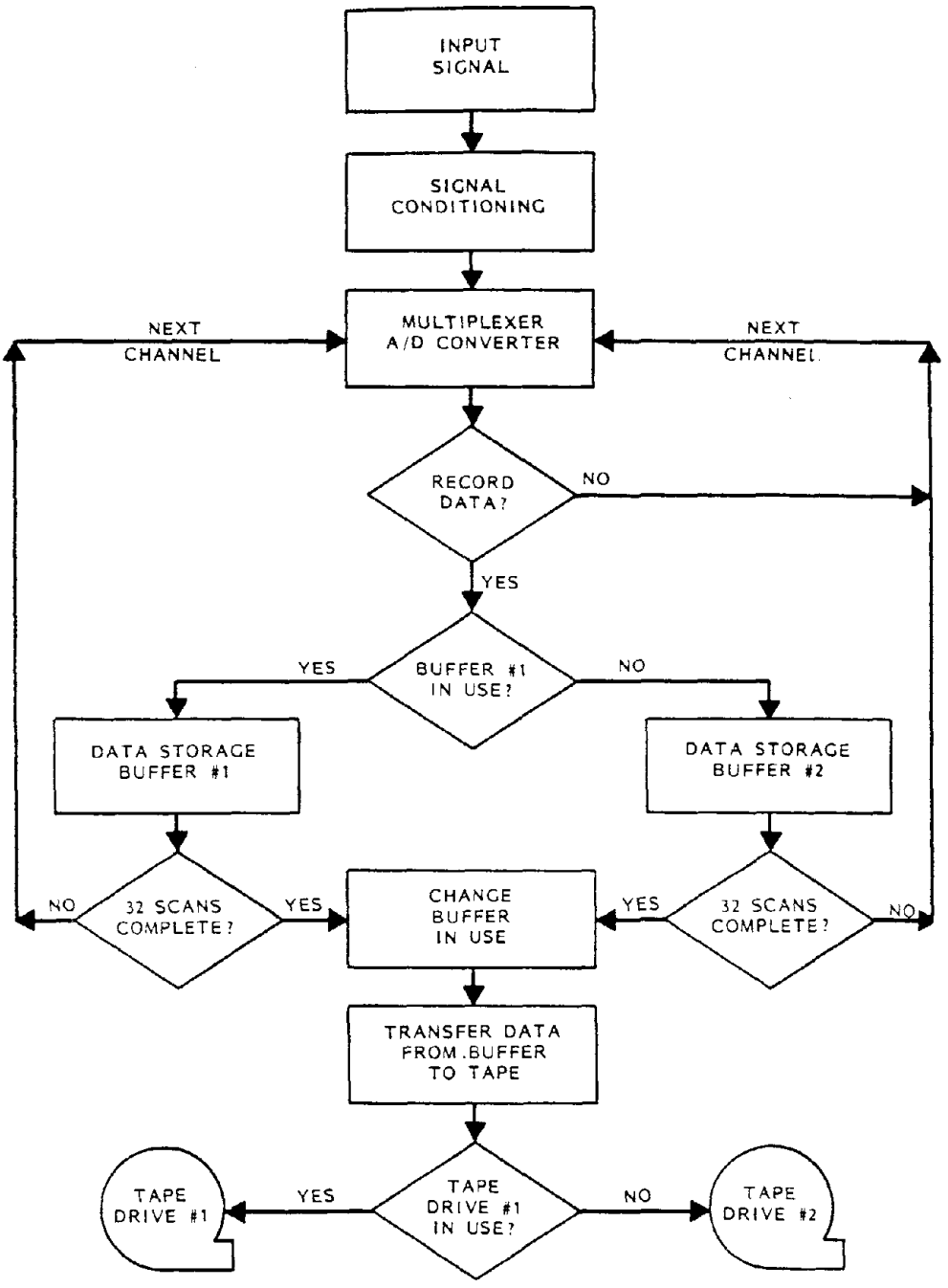

FIGURE 6. DATA ACQUISITION SYSTEM SCHEMATIC

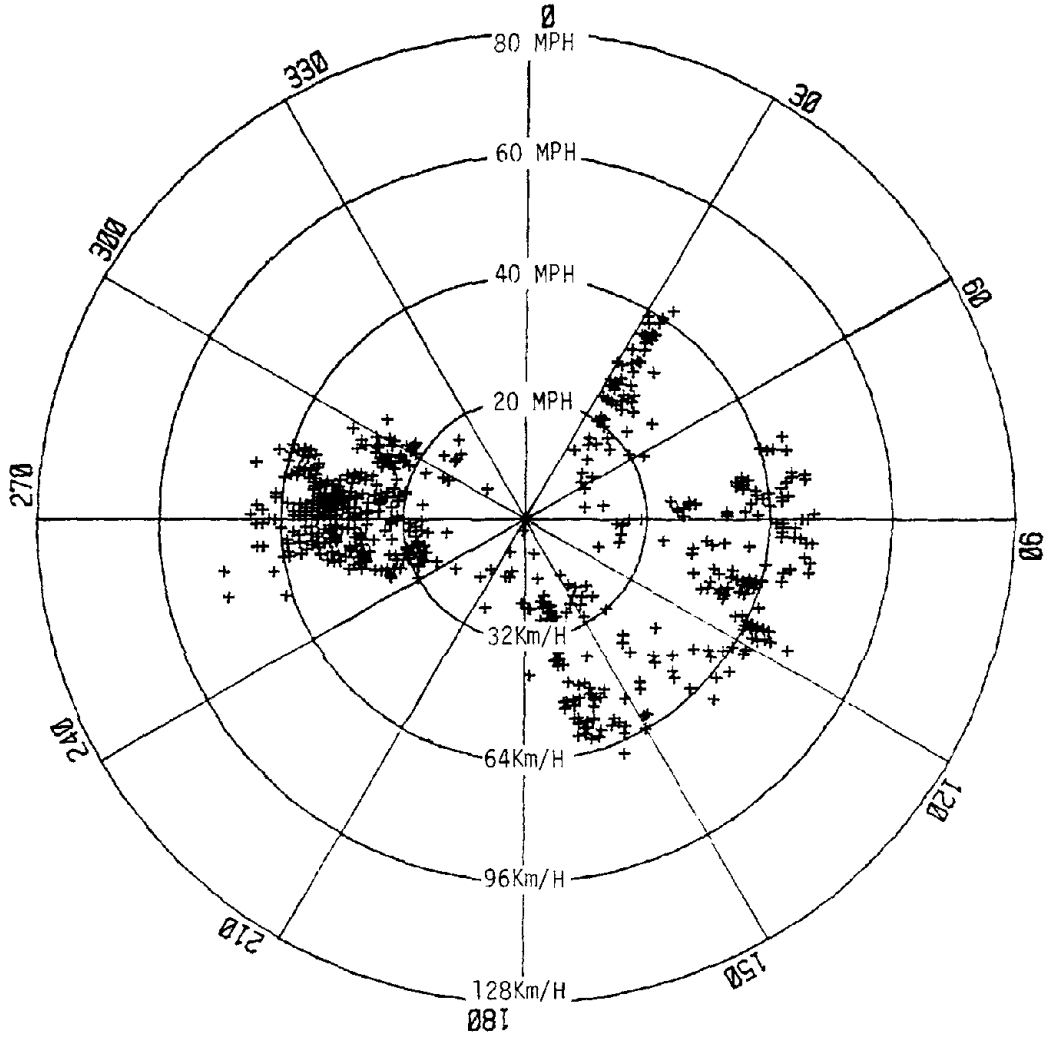

WIND ANGLE VS. RESULTANT WIND VELOCITY

TOP OF NORTH TOWER

FIGURE 7. Polar Plot of Recorded Wind Events

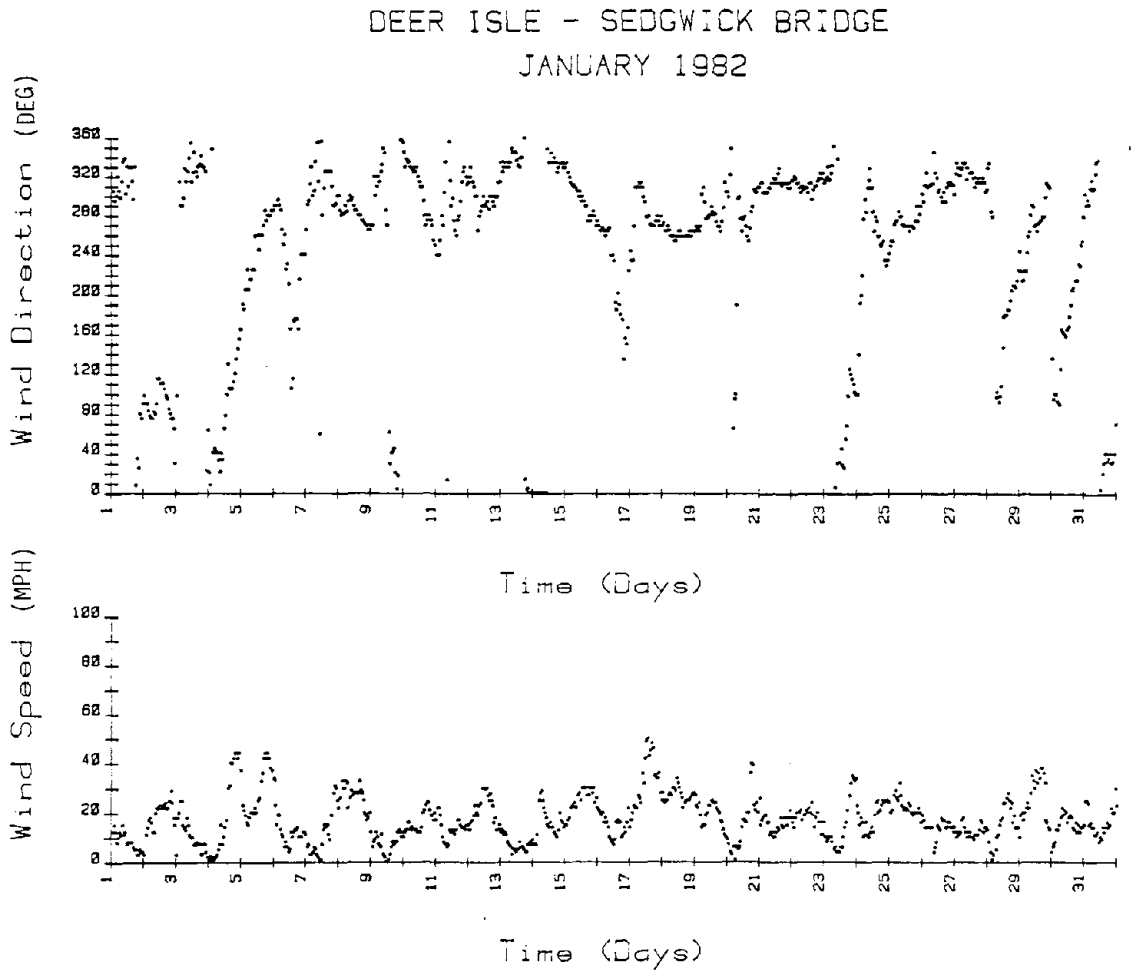

Figure 8. Monthly Summary of Wind Activity

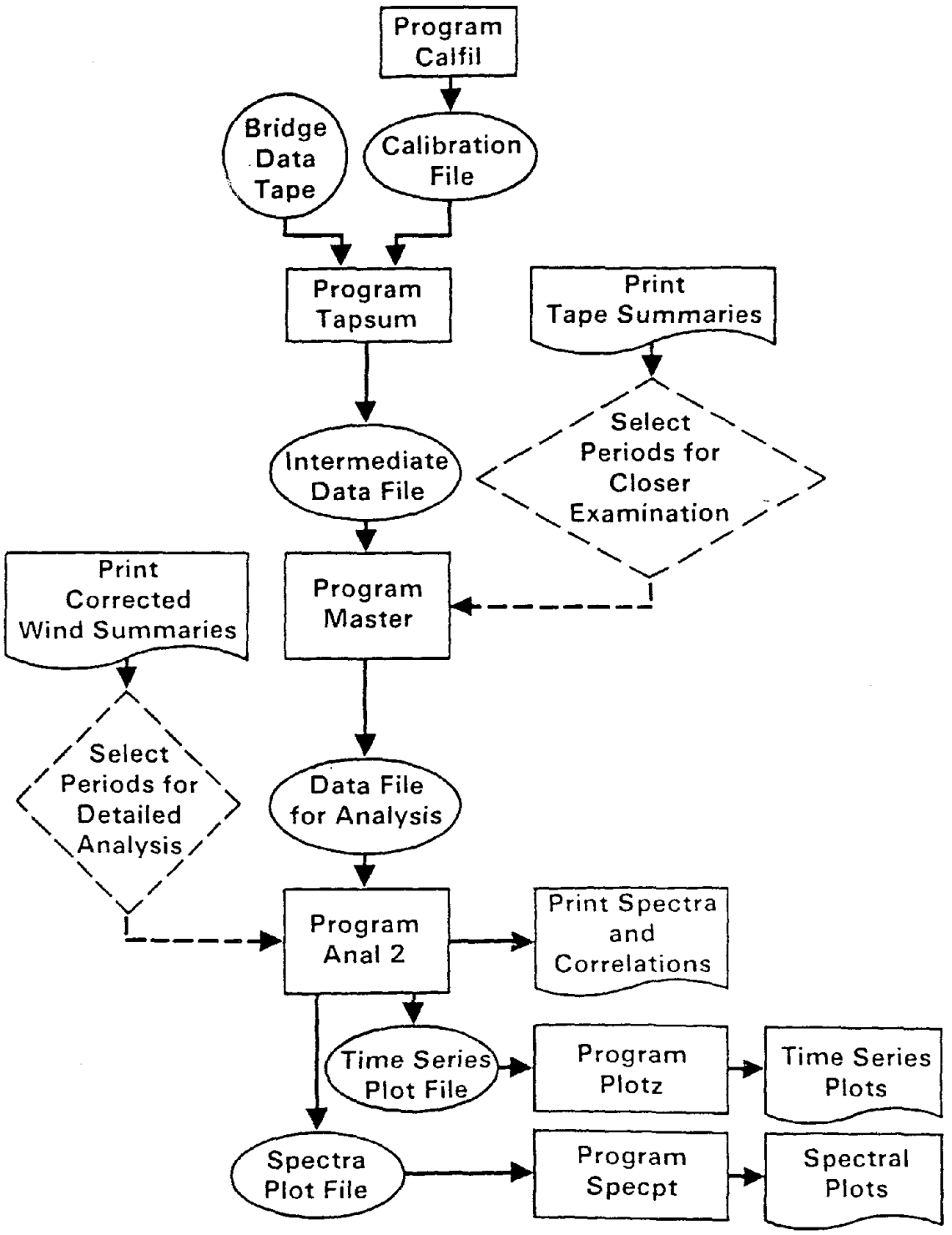

FIGURE 9. Data Processing Sequence

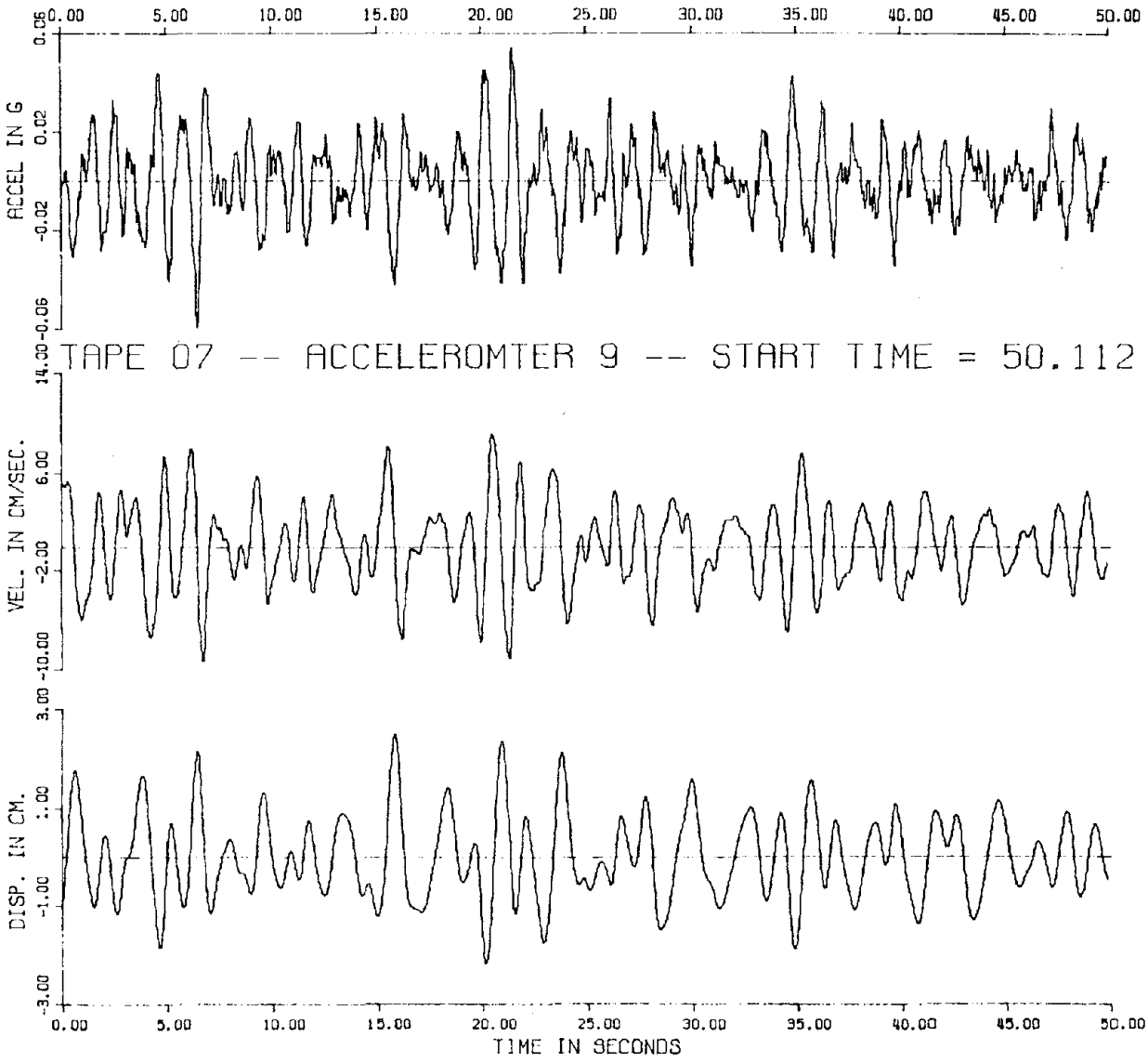

FIGURE 10. Double Integration Input and Output

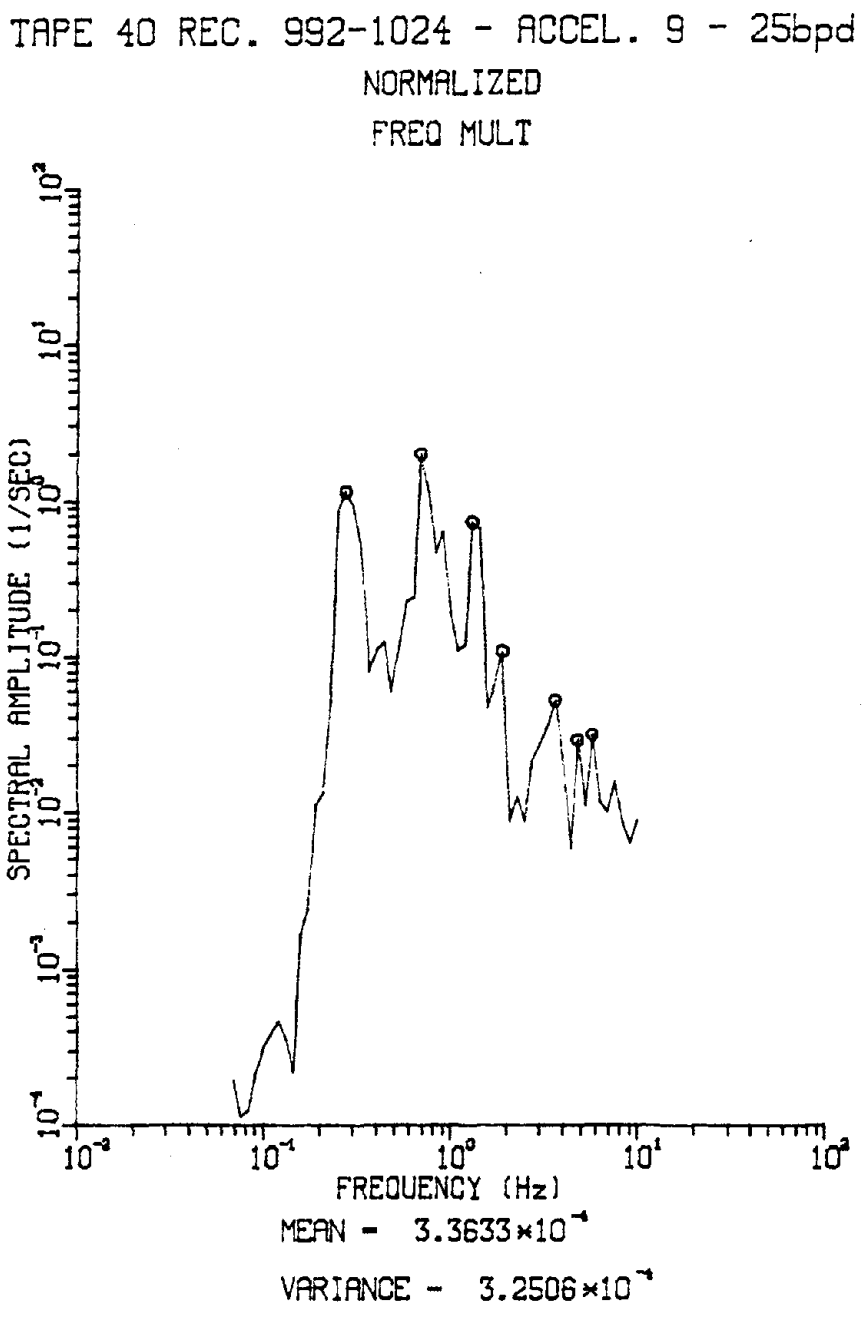

FIGURE 11. Accelerometer Spectral Amplitude

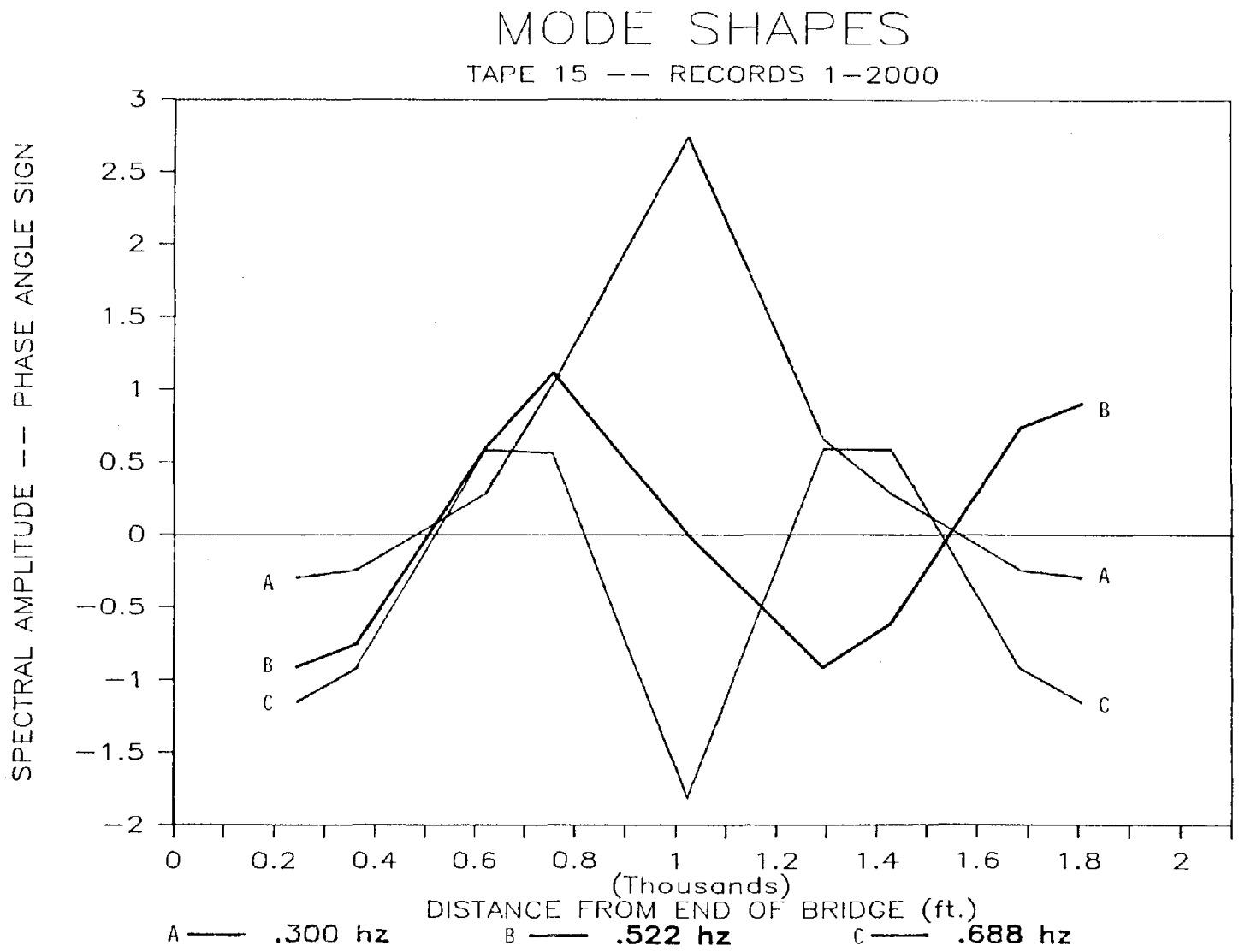

FIGURE 12. Mode Shapes - Vertical Bending

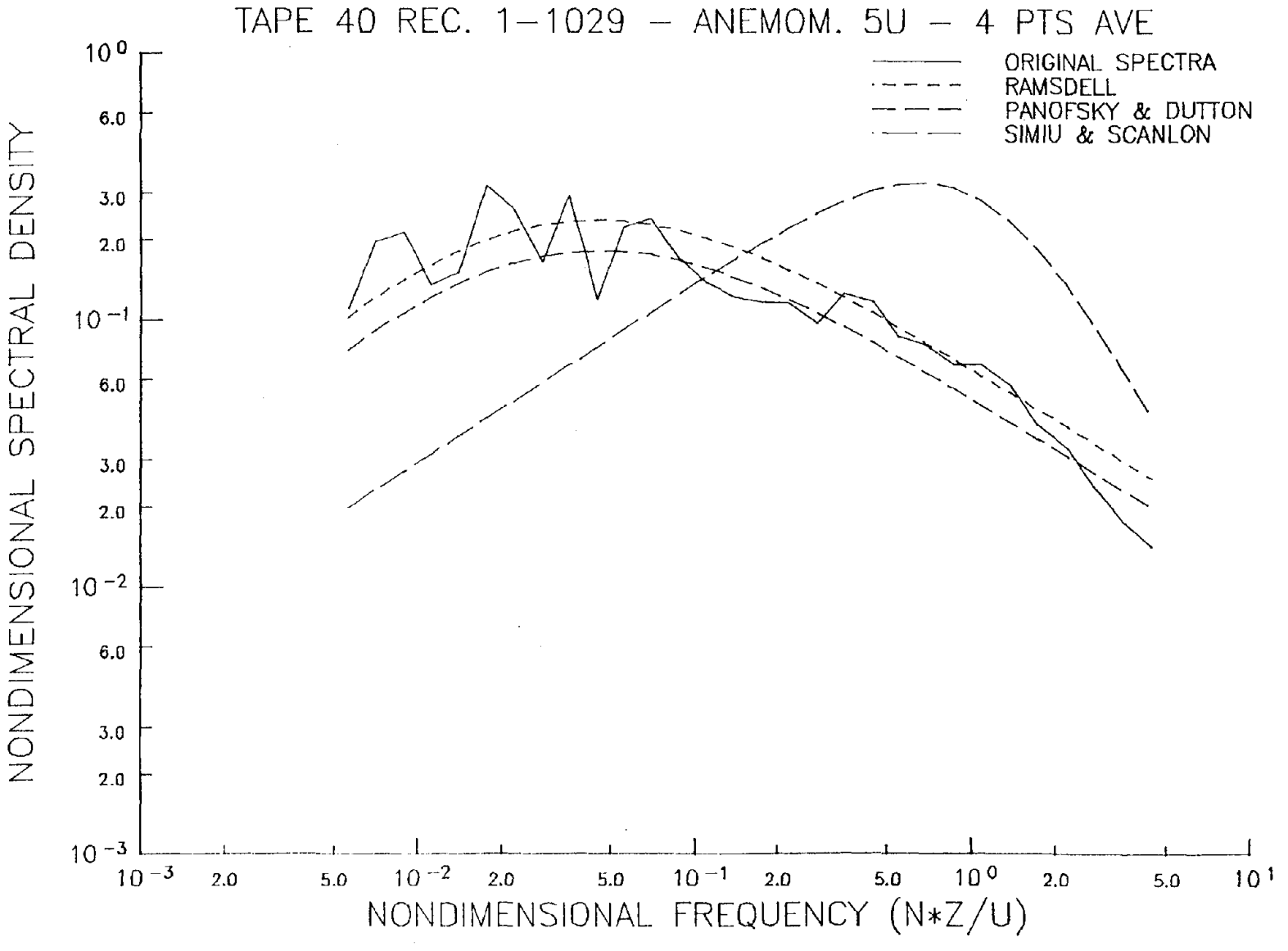

FIGURE 13. Wind Spectral Density - U Component

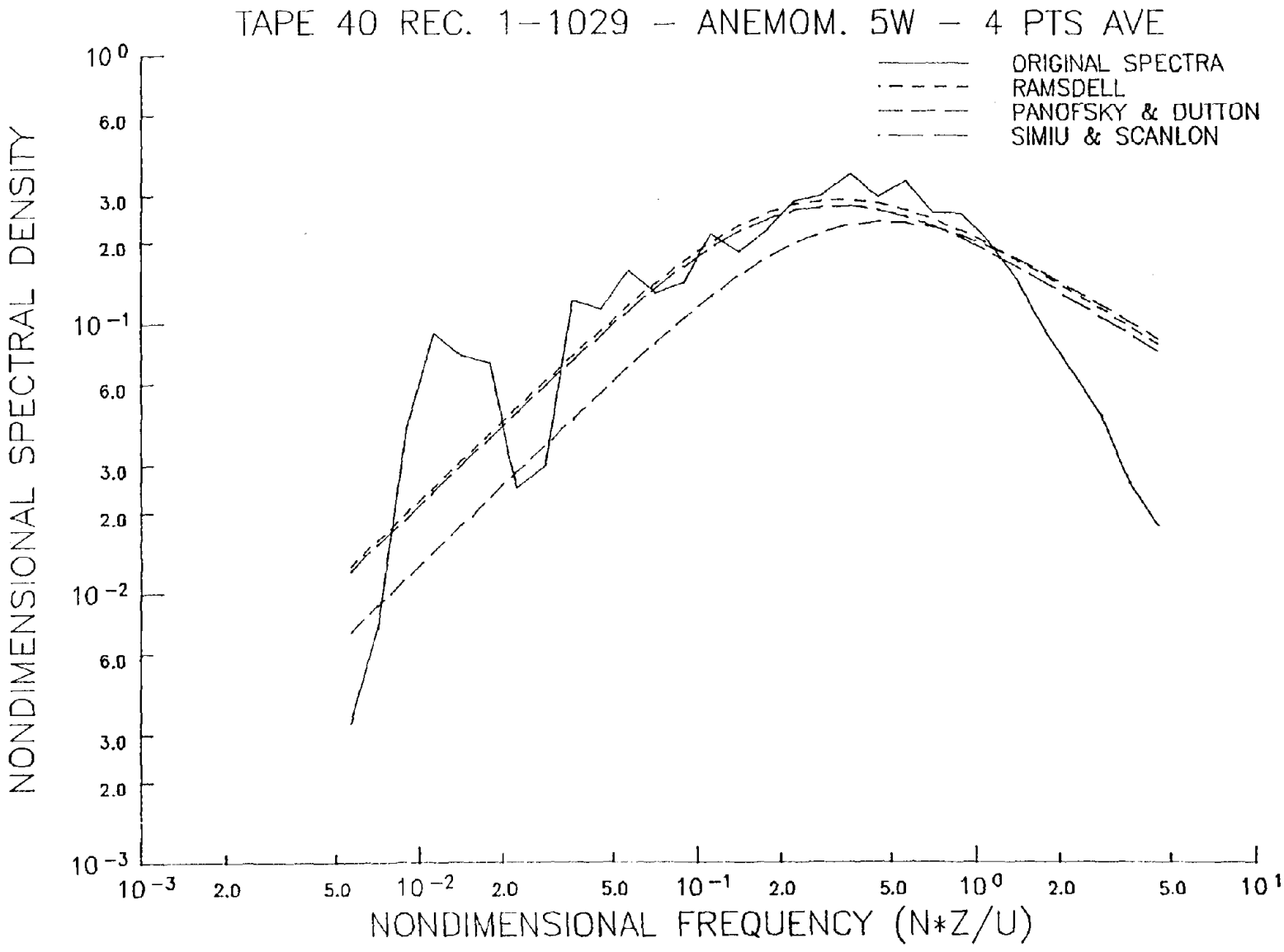

FIGURE 14. Wind Spectral Density - W Component

WIND TUNNEL MODELING FOR FLOW AROUND BUILDINGS

BY

Tatsuo MUROTO[1], Hisashi OKADA[2], Takeshi OHKUMA[3]

ABSTRACT

In Japan since 1965, the wind flow around tall buildings has caused many disputes between residents who live near tall buildings and building owners. In these disputes, detailed and accurate wind speed distribution data are requested from the concerned parties.

Those data are usually obtained by wind tunnel tests, using at hundredth scale, scale-models set in a turbulent boundary layer. Similarity parameters chosen are:

a. average wind speed profile;
b. turbulence intensity profile of wind.

Taking into account that the geometrical similitude of scale models can not be satisfied perfectly and that wind profiles in a specific area can not always be known with sufficient accuracy, we must conclude that the accuracy of conventional wind tunnel test data is not clear quantitatively.

To solve this problem, the Building Research Institute and the Building Center of Japan conducted cooperative research from 1981 to 1984. Twenty-three research groups in Table 1 participated in this project.

1. INTRODUCTION

1.1 Similarity Parameters Selected

In this research, the following parameters were selected and their effects on similarity were in vestigated by wind tunnel tests.

A. Geometric similitude of wind tunnel model
(1) modeling of exterior surface of buildings
(2) modeling of trees on ground surface
(3) modeling of built-up areas surface around tall buildings
B. Flow similarity parameters (Fig. 1)
(1) R/H
(2) α
(3) $\sigma\mu$ /U

1.2 Field Observation Data

Three cases of field observation data shown in Table 2 were selected as similarity criteria. Since the wind speed distribution around tall buildings change remarkably according to the atmospheric stability condition, field observation data used for comparison were limited to those observed in neutral atmospheric conditions or in high wind conditions.

1.3 Wind Tunnel Tests

Five wind tunnel models were made for tests. They are scale models of Shinjuku, Tsukishima and Ichikawa area corresponding to field observations stated above. Scale models were as follows:

Sinjuku	1/500, 1/1000
Tsukishima	1/200, 1/500
Ichikawa	1/300

These wind tunnel models were tested in thirteen different wind tunnels.

2. TEST RESULTS

2.1 Modeling of Exterior Surface of Buildings

A 14 story apartment house located in the center of Tsukishima area has floors projected 1.5m from an exterior wall horizontally at each level. These projected floors were modeled in four types. Corresponding to the difference in modeling, wind speed distribution near ground changed slightly

[1] Head, Aerodynamic Sec., Structural Engineering Division, Building Research Institute
[2] Senior Research Officer, ditto
[3] Professor, Faculty of Engineering, Kanagawa University

at points near windward corners of the center building.

2.2 Modeling Of Trees

Field observation wind data in Tsukishima area were subjected to the influence of roadside trees. Six types of model trees were included in a Tsukishima model. Wind speeds along the street were measured for each type. Test results lead to the conclusion; similarity of wind speed shapes and solidity ratios of model trees have poor agreement with prototypes.

2.3 Modeling of Built-up Area Around Tall Buildings

Effects of R/H (Fig. 1) on the wind speed distribution in wind tunnel model center were investigated for Shinjuku, Tsukishima and Ichikawa model. The following conclusions were obtained.

(1) After the wind passed the leading edge of a wind tunnel model, wind velocity profile of approaching flow begins to break at its lower parts and new boundary layer (inner boundary) begins to develop in the place.

(2) Thickness of inner boundary layer increases with the distance x from the leading edge at the rate of 0.05x.

(3) At the area located in the leeward side of the leading edge of wind tunnel models by 10h (for Shinjuku model, h is the average height of building models) or 25h (for Ichikawa model), wind speed distribution near ground surface is not subject to the effect of change in approaching flow profile. In such areas, wind speed distributions agree very well with those in field observations.

(4) In wide open areas or around buildings projecting higher than inner boundary layer, wind speed distribution does not agree with those in field observation. In order to get good similarity in those areas, buildings in the windward city area must be modeled more widely than 10h or 25h.

2.4 Wind Velocity Profile

When we observed wind speeds U and U_h simultaneously at a point i near the ground and reference point respectively, we call the ratio U/U_h as "wind speed ratio" at point i. When the wind velocity profile of approaching flow is expressed by an exponential function with exponent 1/n, it is noted as wind speed ratio, $R_{1/n}$.

Fig. 3 shows the correlation between $R_{1/3}$, $R_{1/6}$ and $R_{1/4}$ obtained in Tsukishima model for R/H of 3 and reference height of 600mm (300mm in full scale). Presenting the relation between $R_{1/n}$ and $R_{1/4}$ as

$$R_{1/n} = A_{1/n} \cdot R_{1/4} \qquad (1)$$

Coefficient A becomes larger than 1 for n larger than 4 and becomes smaller than 1 for n smaller than 4. This means that the wind speed ratio decreases with the increasing exponent of wind speed profile.

On the other hand, the coefficient A changes its value when the reference height changes as shown in Fig. 4. This figure also shows that if the reference point is set at height between 30 to 70m, the value of A will not change so largely. This suggests that setting the reference point at this height, we will obtain the same wind speed distribution independent of the wind velocity profile of approaching flow. This is seen clearly in Fig. 5, which shows correlations of wind speed ratios for reference height of 58.1m.

Fig. 6 shows wind velocity profiles at some points in Tsukishima and Ichikawa model. In this figure, each of wind velocity profiles looks similar at height from 30 to 70m. This agrees with the height range stated above.

In the case of Shinjuku model, different features were observed. Figs. 7 and 8 show ratios r_s/r at points LOC. 10, 17, 7 and 8 (r_s: wind velocity ratio for exponent of approaching flow $\alpha = 1/4$, reference point: top of a high rise building). ⊙ in the figure corresponds to field observation data. LOC.10 and 17 in Fig. 7 located on the windward side of high rise buildings and LOC. 7 and 8 located on the leeward. According to the figures, wind speed ratios at the windward points do not

change so largely for α of 1/4 to 1/3 but for α less than 1/4 it increases with decreasing α. At the leeward points, on the other hand, wind speed ratios are nearly equal to field observation value and do not change for all α. This suggests that the wind speed ratio at points leeward of high rise buildings is independent of approaching flow profiles. This is also known from Fig. 9 showing wind velocity profiles at some point leeward of high rise buildings.

We can derive the following inference from these facts:

The windward area of high rise buildings is covered by the inner boundary layer developed by windward buildings and the corresponding wind speed distribution is realized there. If the reference point is set outside of the inner boundary layer, wind speed ratio observed at a point depends on the wind speed profile of approaching wind. This is the same phenomenon observed in cases of Tsukishima and Ichikawa models. For the leeward side of high rise buildings, wind speed distributions are strongly influenced by wakes induced by high rise buildings rather than by both inner boundary layer and the approaching flow.

With regard to the effect of wind velocity profiles of approaching flow on the similarity of wind tunnel tests, we obtain the following conclusions:

(1) When all the points including reference point are involved in the inner boundary layer, the wind speed ratios observed are not influenced by the wind speed profile of approaching flow.

(2) When the reference point is located outside of inner boundary layer, wind speed ratios for points near the ground depend on the wind speed profile of approaching flow. Therefore, when wind tunnel models do not have sufficient area around tall buildings, the wind speed profile of approaching flow must be made as similar as possible to the real condition.

(3) Wind speed ratios in the leeward area of high rise buildings are influenced mainly by the wake of high rise buildings rather than by inner boundary layer and approaching flow.

2.5 Boundary Layer Thickness

The effect of boundary layer thickness on similarity is small when the modeling area is sufficiently large to develop the thick inner boundary layer. Therefore, for smaller modeling area (R/H=3$\sim$8), the influence of boundary layer thickness is observed.

Fig. 10 shows the correlation of wind speed ratios for boundary layer thickness δ of 70, 100, and 180m in Tsukishima model. These values correspond to δ /H of 1.75, 2.5, and 4.5. From this figure no special effect of boundary layer thickness is observed.

Fig. 11 shows that wind speed profiles at a point leeward of the high rise buildings change largely when δ /H changes 0.8 to 2.5.

3. CONCLUSIONS

The following are conclusions from the work presented in this report:

(1) To expect good similiarity, wind tunnel models must involve sufficiently wide area around the tall buildings undergoing testing.

(2) The area of modeling must be enough for the inner boundary layer developed from the leading edge to involve the tall building concerned and the surrounding buildings.

(3) The minimum distance of modeling area (distance from an observation point to the leading edge) was 10 and 25 times the averaging building height in Shinjuku and Ichikawa area, respectively.

(4) When the modeling area is small, the wind profile must be made as similar to the real condition as possible.

Wind speed ratios obtained in wind tunnel tests conducted under experimental conditions shown in Table 3 and field observation data are compared in Figs. 12 to 14 for reference. In these figs. ● and ○ correspond to the average wind speed ratio for wind tunnel tests and field observation

respectively, and the length of bars extending up and downward from the circle correspond to the standard deviation of wind speed ratios. These figures show the following:

(1) Shinjuku (Fig. 12)

Wind speed ratios for wind tunnel tests are larger than field data at several points but wind speed distribution patterns are in good agreement.

(2) Tsukishima (Fig. 13)

The difference in wind tunnel tests and field observation is large at point A for wind direction N and point E for wind direction SW and SSW, but at the other points both are in good agreement. A is a special point influenced by trees and E is a point very near to the corner of the apartment house.

(3) Ichikawa (Fig. 14)

Wind tunnel test results are in good agreement with field observation data. Larger differences are seen in case of S and SSW winds. This is due to the unsimilarity of separation flow at the building corner.

Table 1 List of Research Groups participated

Institution	Member	Symbol
Osaka City University	Eiji Kimoto	N
Ohbayashi-Gumi Ltd., Technical Research Institute	Akihisa Kawaguchi	A
Kajima Corporation, Kajima Institute of Construction Technology	Hayatoshi Sanada	B
Wind Engineering Institute	Masaaki Yoshida	O
Kanagawa University	Takeshi Ohkuma Hisao Marukawa	C
Kanazawa Institute of Technology	Takeo Matsumoto	P
Kyoto University, Diseaster Prevention Research Institute	Junji Katsura Yoshihito Taniike	Q
Kumagaya-Gumi Co., Ltd., Institution of Technology	Hiroki Kashiwagi Kazutami Kohashi	S
Building Research Institute, Ministry of Construction	Hisashi Okada Tatsuo Murota	D
Shimizu Construction Co. ,Ltd., The Research Laboratory	Kunio Fujii	E
Central Glass Co., Ltd.	Tomohisa Ishikawa	T
Taisei Corporation, Technical Research Institute	Yutaka Asami	U
Takenaka Koumuten Co., Ltd., Technical Research Laboratory	Yoshiteru Iwasa Yoshihiro Mataki	F
Tokyu Construction Co., Ltd., Technological Research Institute	Nobuo Kato	G
Tokyo Institute of Polytechnic	Nobuyuki Kobayashi Yukio Tamura	H
Institute of Industrial Science, University of Tokyo	Shuuzo Murakami	I
Tokyo Denki University	Hiromitsu Kawai	J
Toda Construction Co., Ltd.	Kyouichi Higaki	V
Nippon Sheet Glass Co., Ltd.	Saburou Kawabata	K
College of Industrial Technology, Nihon University	Eizou Maruta	L
Hazama-Gumi Co., Ltd.	Shuuichi Takakura	W
Fujita Corporation, Technical Research Laboratory	Yasuyuki Utsumi Youichi Shimada	M
Mitsui Construction Co., Ltd.	Kazuo Tsukamoto	X

Table 2 Description of Field Observations at Three Areas

Item	Name of areas		
	Shinjuku	Tsukishima	Ichikawa
Address	Nishishinjuku Shinjuku-ku, Tokyo	1-Tsukishima Chuoh-ku,Tokyo	Gyoutoku Ichikawa-city,Chiba
Observation points are located	in and around a city area involved 100-200m high buildings	along streets with trees around 14story apartment house	in a small open park next to 7story apartment house
SUrrounding area	city area involves middle and low rise buildings	city area involves middle and low rise buildings	city area involves middle and low rise buildings
Reference point	tops of 2 high rise buildings, of 237m and 187m high	top of the apartment house of 58.1m high	top of a two story school building, 2km apart from the observation field. 16.7m above ground
Observation points: number height	10 2-9m	17 1.5-8m	12 5m
Anemometer reference point other points	vane type 3-cup type	urtra sonic type urtra sonic and 3-cup type	vane type 3-cup type
Period of observation	1977.7-1978.1 1979.12-1980.11	1978.9-1979.8	1976.10-1977.9

Table 3 Wind Tunnel Test Condition

Parameter	Shinjuku	Tsukishima	Ichikawa
Modeling of trees	no	Type A	no
Extent of modeling of region roundabout R R/H	 1200m 6	 200m 5	 320m 16
Approaching flow δ δ/H α	 220m 1.1 1/3	 140m 3.5 1/4	 270m 14.3 1/4
Reference Point location height	top of a building 187m	top of a building 58.1m	center of turn table 16.7m
Model scale	1/500	1/200	1/300

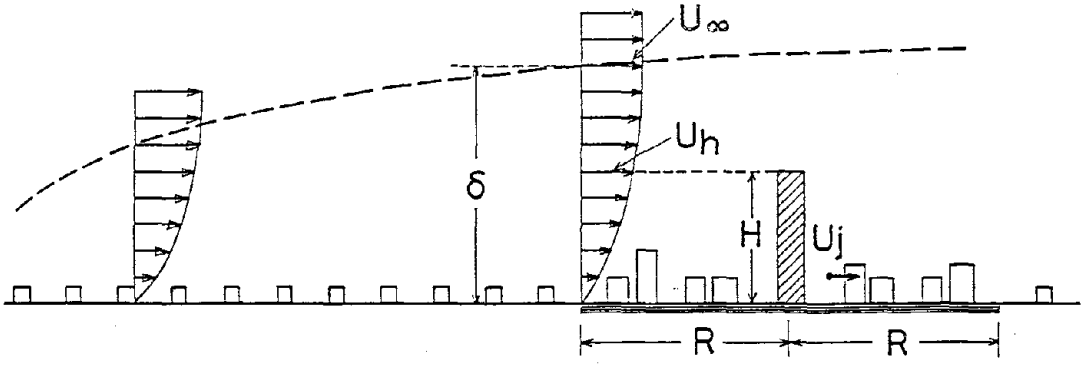

Fig.1 Schematic Description of Boudary Layer Wind Tunnel Tests

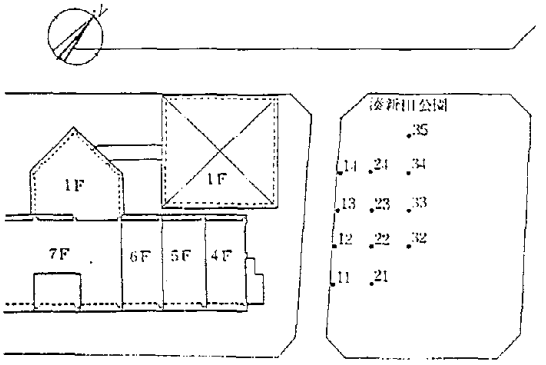

Fig.2 Layout of Observation Points

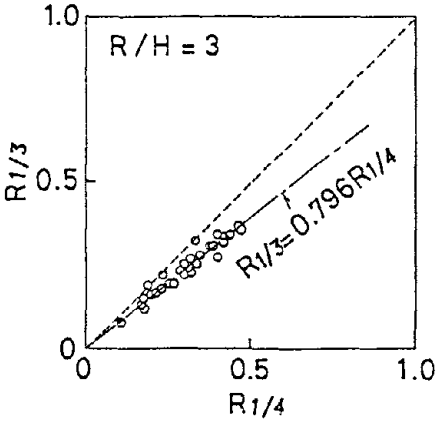

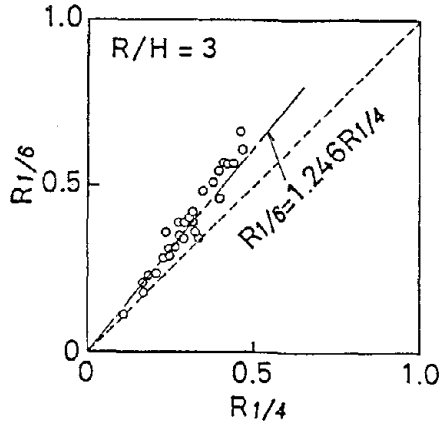

Fig.3 Correlation between $R_{1/n}$'s refered to Wind Speed at the Gradient Height

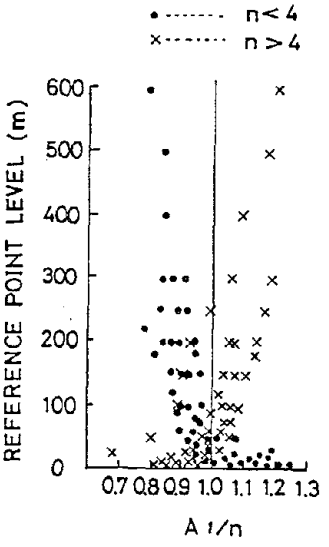

Fig.4 Relation between $A_{1/n}$ and Reference Point Level

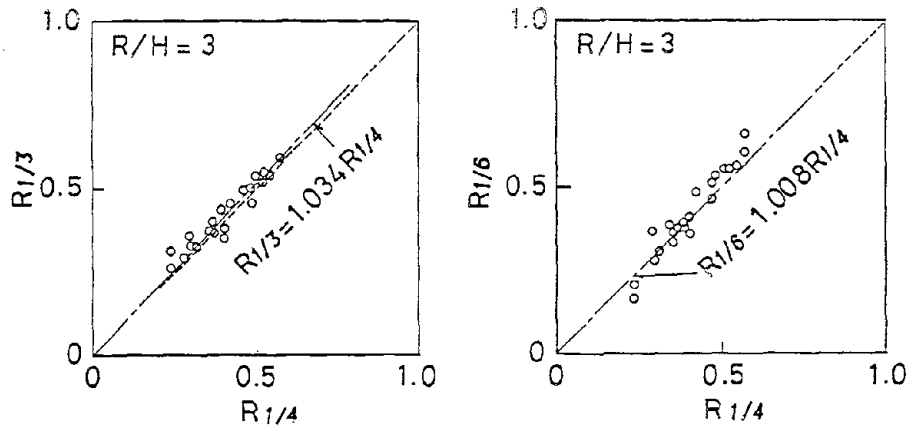

Fig.5 Correlation between $R_{1/n}$'s refered to Wind Speed at Buiding Height

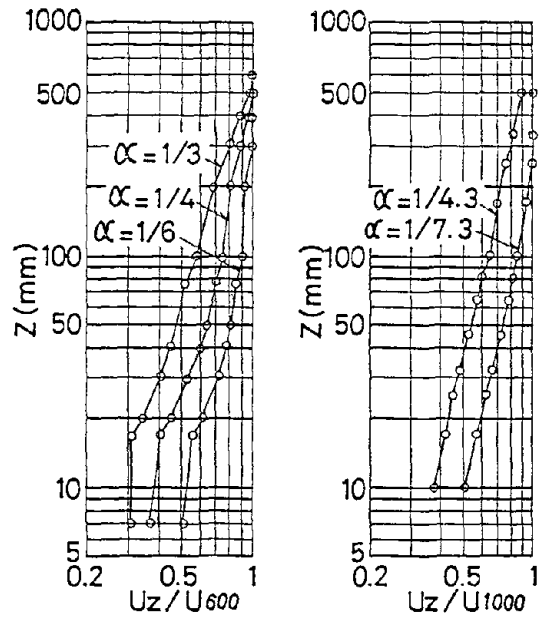

Fig.6 Wind Velocity Profile

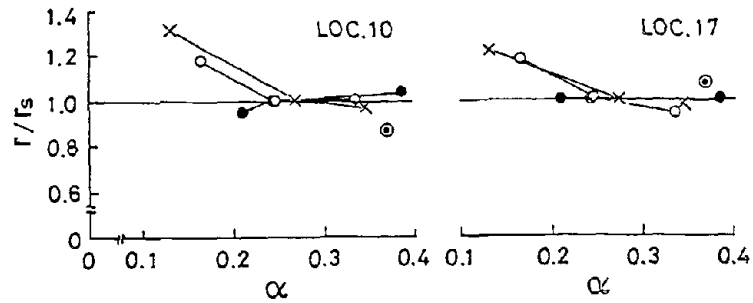

Fig.7 Effect of α on Wind Speed Ratio on the Windward of High-rize Buildings

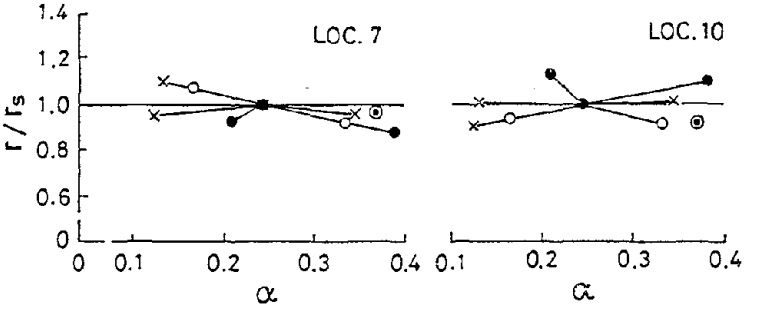

Fig.8 Effect of α on Wind Speed Ratio on the Leeward of High-rize Buildings

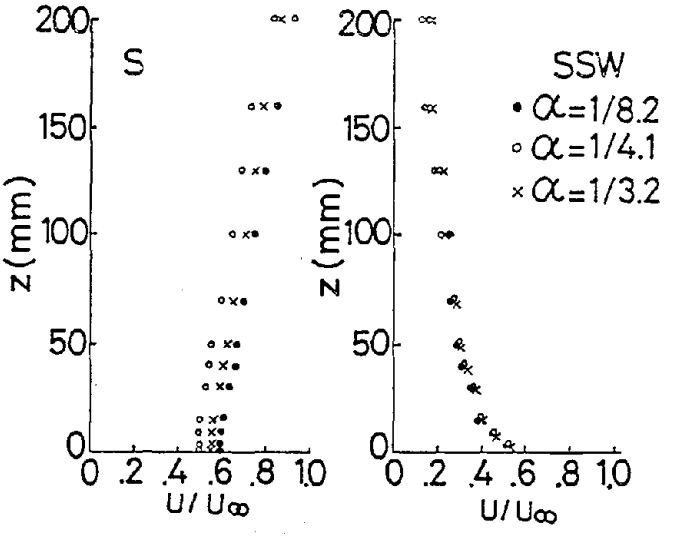

Fig.9 Wind Profile on the Leeward of High-rize Buildings (Shinjuku)

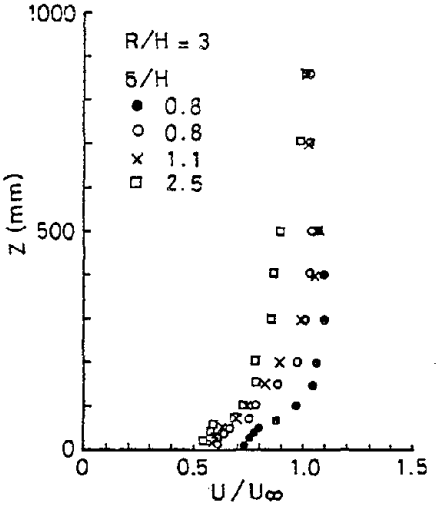

Fig.11 Effect of Boudary Layer Thickness on Wind Profile (Shinjuku)

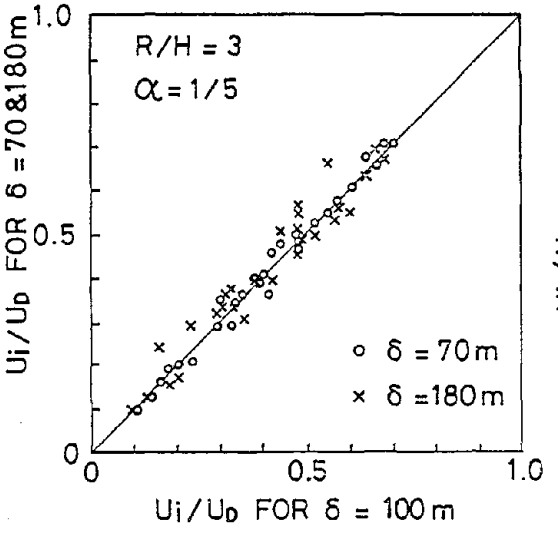

Fig.10 Effect of Boudary Layer Thickness on Wind Speed Ratio (Tsukishima)

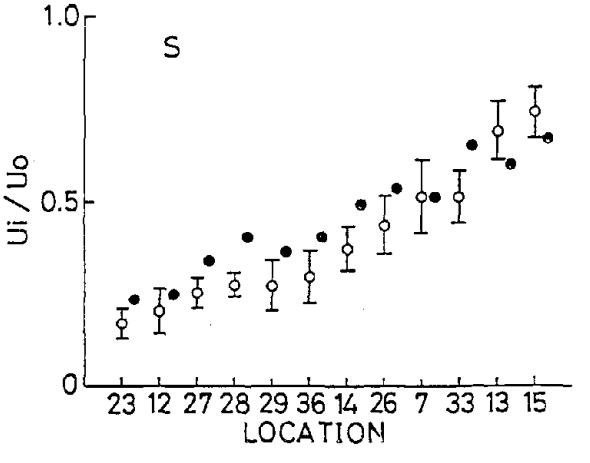

Fig.12 Wind Tunnel Test Results compared with Field Observation Data (Shinjuku)

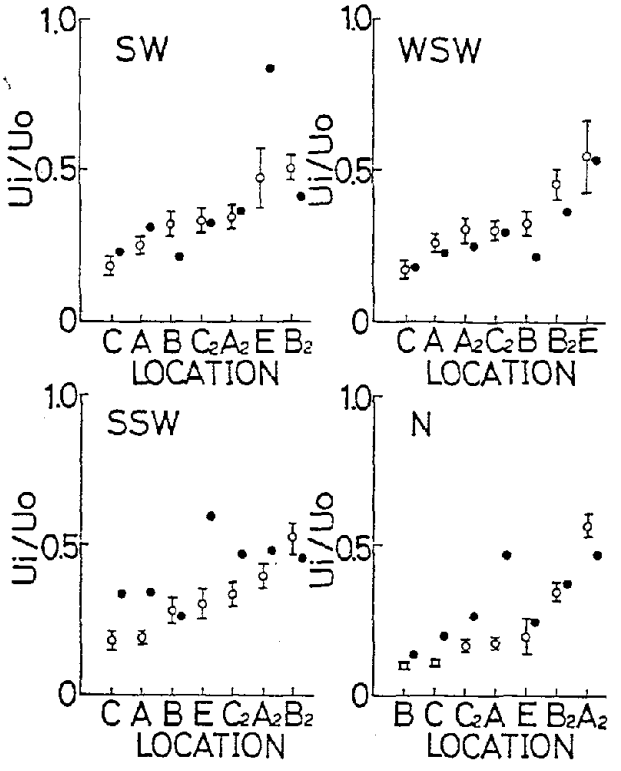

Fig.13 Wind Tunnel Test Results compared with Field Observation Data (Tsukishima)

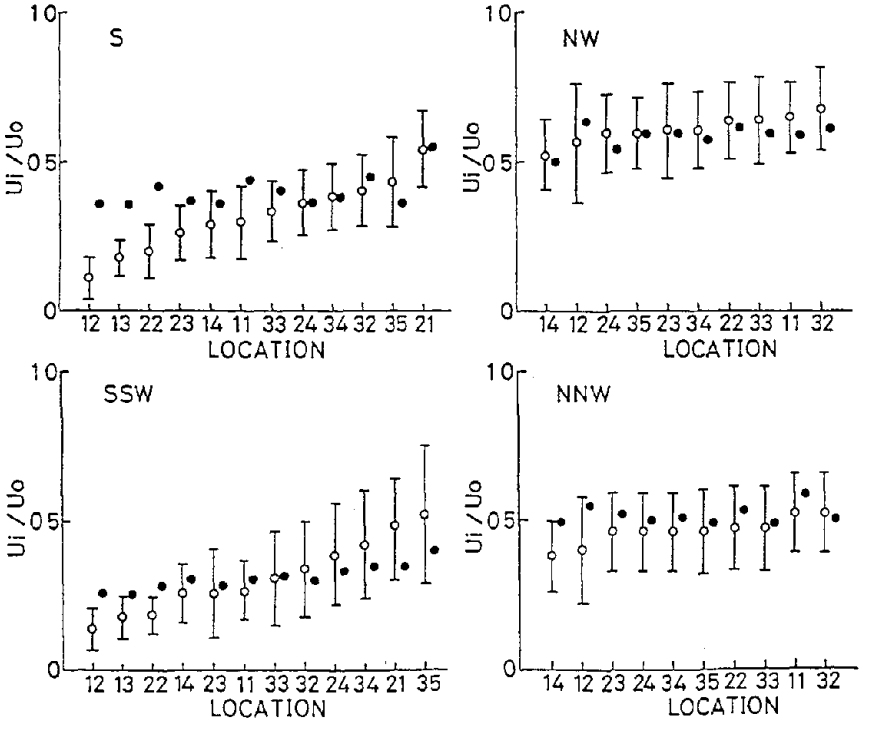

Fig.14 Wind Tunnel Test Results compared with Field Observation Data (Ichikawa)

AUTOMATIC DETECTION OF GUST FRONTS WITH A SINGLE DOPPLER RADAR

by

Hiroshi Uyeda[1], Dusan S. Zrnic'[2] and Hiroshi Takahashi[1]

Abstract

A procedure is developed that detects and tracks gust fronts automatically. It does not rely on a single method but requires simultaneous operation of two related algorithms. The convergence algorithm measures radial convergence and hence only gusts propagating along radials can be readily detected. The mesocyclone-shear algorithm measures azimuthal shear and is suitable for detecting gusts parallel with radials as well as low-level vortices. Long shear lines that these algorithms detect are classified as gusts whereas symmetric shear features are rejected if their shear and flux or "momentum" are insignificant; otherwise they are classified as low-level vortices. To locate gusts we use second order polynomials in the range-azimuth plane. It is shown that predicted gust locations from simple linear projections of the least square fitted curves agree very well with actual gust locations.

KEY WORDS: Algorithm; Convergence; Doppler (spectral moments); Gust (wind engineering); Least Square (fitting); Momentum; Shear; Vortex.

1. INTRODUCTION

Early displays of Doppler spectral moments demonstrated that many hazardous weather features produce characteristic signatures that human observers can readily interpret (Wood and Brown, 1983). Among the most dramatic signatures are those of mesocyclonic circulations (Sirmans and Doviak, 1973); tornado vortex signatures (Brown et al, 1978); divergence signatures (Lemon and Burgess, 1980; Zrnic' and Gal-Chen, 1983; Doviak and Zrnic', 1984; Wilson et al., 1984); and shear lines associated with gust fronts (Zrnic' and Lee, 1983).

Although recognition of these signatures by trained human observers is not complicated, there are strong reasons to develop automated techniques that would help or in some cases even replace the human operator. When several patterns need to be examined, quantified, and remembered for correlations in space or time, the machines become superior. Furthermore, a machine's performance is consistent regardless of the environmental conditions and is not subject to the boredom and fatigue that affect humans.

With procurement plans for Next Generation Weather Radar (NEXRAD) well under way in the United States of America, a need exists to provide as much assistance as possible to interpretation of radar displays. So far, several algorithms have been developed and tested to serve that purpose (NEXRAD Algorithms Report, 1983). This paper concerns algorithms that detect and track gust fronts; major part of it is condensed from a report (Uyeda and Zrnic', 1984) prepared for the Federal Aviation Administration and the National Weather Service. Further details on case studies are described in Uyeda and Zrnic' (1985).

2. GUST FRONT CHARACTERISTICS FROM DOPPLER RADAR MEASUREMENTS

A gust front is associated with a thunderstorm downdraft. Gust fronts and thunderstorm downdrafts are hazardous to aircraft because of a sudden change in the horizontal wind component (Fig. 1). The convergence occurs about the frontal discontinuity because fluids with two different velocities are moving toward each other. The cool outflow air is flowing underneath

[1]National Research Center for Disaster Prevention, Science and Technology Agency, Japan.

[2]National Severe Storms Laboratory, Environmental Research Laboratories, National Oceanic and Atmospheric Administration, Japan.

the warm moist inflow. Ahead of the outflow the environmental air has a strong velocity component toward the front.

An intense front propagating forward or away from the radar produces at low levels a very well defined line of convergent radial velocities (Zrnic' and Lee, 1983). The frontal position is also detectable from the Doppler spectrum widths, which are large at the front, behind it, and sometimes even ahead of it. Alas, the reflectivity field offers almost no clue to the precise position of the front and none whatever about the turbulence ahead.

Frontal characteristics have been documented for several fronts (Zrnic' and Lee, 1983), and a detailed discussion of their dynamics in the lower 400 m can be found in the report by Goff (1975). On the basis of their observations and our previous experience with the divergence algorithm (Zrnic' and Gal-Chen, 1983), we decided to attempt detection of the convergence line in the Doppler velocity field. We have applied the principles from the divergence algorithm to detect convergence lines instead.

For most orientations of the gust front except when it is parallel to a radial, a Doppler radar would detect convergence as a decrease in the velocities along a radial. Our algorithm capitalizes on this simple fact. However, fronts parallel to radials do not produce radial convergence signatures. To detect such fronts the mesocyclone-shear detection algorithm (Hennington and Burgess, 1981) must be used.

3. PATTERN RECOGNITION ALGORITHM DETECTION OF RADIAL CONVERGENCE

Our gust front pattern recognition algorithm is modeled after the mesocyclone and divergence algorithms (Zrnic' et al., 1984; Zrnic' and Gal-Chen, .1983). Therefore only a brief description is given here.

The algorithm starts by searching along a radial for runs of decreasing velocities, which characterize radial convergence. This search is done by comparing consecutive velocities. When a run terminates, a pattern vector is formed; its six components are beginning velocity v_b, ending velocity v_e, beginning range r_b, ending range r_e, azimuth, and maximum gradient g_m defined by

$$g_m = \max\left(\frac{v_{n-4} - v_{n+4}}{r_{n+4} - r_{n-4}}\right) \tag{1}$$

where v_n is a smoothed (i.e., nine-point average) velocity corresponding to a range r_n between beginning and ending ranges of a pattern vector. We estimate this gradient from data spaced nine points apart because the spacing further smooths the gradient over the same (matched) length as the one used for averaging the velocities.

Before the pattern vector is saved for further processing, its gradient defined as

$$g = \frac{v_b - v_e}{r_e - r_b} \tag{2}$$

and "flux"

$$f = (v_b - v_e)(r_e - r_b) \tag{3}$$

are checked against a set of thresholds. If the vector fails low gradient L_g or low "flux" L_f thresholds, it is discarded; otherwise, a check against high thresholds is made. If the vector passes either high "flux" H_f or high gradient H_g thresholds, it is saved for later sorting. We caution the reader that the term "flux" used here is a carry-over from the divergence algorithm. All the thresholds and their values used in the present study are summarized in Table 1.

After the completion of a scan, all saved pattern vectors are sorted into features according to their proximity. Two vectors belong to the same feature if the range and azimuth centers r_{ci}, az_i satisfy

$$\left(|r_{ci} - r_{cj}| < l_r\right) \quad \text{and} \quad \left(|az_i - az_j| < l_a\right) \tag{4}$$

where l_r is a threshold for radial distance and l_a for azimuthal distance. Features with very

few pattern vectors are immediately discarded; the remaining features are further processed.

Features with azimuthal length L, larger by a factor of 2 from average width W, are classified as fronts (F). Features with smaller azimuthal lengths are classified as shear lines (S). We have often observed that pattern vectors representing secondary surges are classified in the same feature as the primary gust front. This is because pattern vectors are statistical and out distance criterion is liberal. Therefore pattern vectors in a feature that lie on the same radial (i.e., have the same azimuths) are separated. So if the gust front is approaching the radar, all pattern vectors along common radials with centers farthest from the radar are taken out of the feature and classified as belonging to a secondary surge. Our dealiasing consisted of checking the continuity of radial velocities. We compared a nine-point running average with the first non-averaged value outside the nine points and made corrections whenever the difference between the two exceeded the unambiguous value v_a (Nyquist velocity).

3.1 Construction of Pattern Vectors

The method by which pattern vectors are obtained in the gust front algorithm is somewhat different from that used in the mesocyclone algorithm. Namely, a nine-point running average of the velocities along a radial is first performed so that the effective range resolution is 1.35 km. This equals the minimum width of a 2-dBZ gust contour (Zrnic' and Lee, 1983). Averaging reduces the fluctuations due to estimation errors and turbulence. But even with this smoothing, we observed that deviations of velocities about a linear fit in range were enough to break up what seems to be a single, continuous pattern vector.

We contrast these results with those of mesocyclone algorithm where comparisons of adjacent velocities are sufficient to yield valid pattern vectors. For equal shear the percent deviation of incremental velocity (due to noise) with respect to the mean between two adjacent range locations is considerably larger than the corresponding percent deviation between two adjacent azimuths.

For these reasons we have added a seven-point look ahead capability to our vector construction routine. The procedure looks at seven adjacent (in range) velocities and selects the maximum of the minima, which is less than or equal to the current velocity. Thus, the algorithm leaps from a maximum location to next maximum point and connects the segments until there is an increase (over more than seven consecutive points) of velocities with range.

Next we show a typical example of Doppler spectral moments along a radial that is cutting through a gust front (Fig. 2). An increase in reflectivity is evident in Fig. 2 where the radial is perpendicular to the front. When the radial is tangent to the front, no clear signatures are obtainable from the spectral moments along a radial (a figure of this is not shown). Otherwise the smoothed mean velocities clearly exhibit a region of large gradient, which is included in pattern vectors whose beginning and ending is indicated in Fig. 2. It is apparent in this figure that the location of maximum gradient is a better indicator of the front's position than the midpoint of the pattern vector.

3.2 Gradient and "Flux Thresholds

Because our detection algorithm relies heavily on kinematic properties of gust fronts (i.e., gradient and "flux"), we state here some statistical data concerning these quantities that influenced the choices in Table 1. We had examined the gradient versus "flux" data for several gust fronts in order to obtain the detection region in the gradient - "flux" plane. This region is also described by the thresholds in Table 1.

From several examples it became evident that detection is not very sensitive to small variation of thresholds about the chosen values. Since the detection algorithm sorts pattern vectors according to proximity with rather conservative distances (Table 1), we note that a loss of several vectors does not affect detection. Similarly, false vectors are extremely unlikely to form elongated

features and thus are rejected by the sorting routine.

3.3 Detection of Azimuthal Shear

It is possible to detect fronts that are tangent to radials if the mesocyclone algorithm (Zrnic' et al., 1984) is used. This is because the converging winds on either side of the line are not perpendicular to the line; the environmental flow usually has a component along the gust; behind the gust the flow has a cyclonic curvature so that a cyclonic shear is seen in the mean velocity display. Anticyclonic shear may also characterize the transition between the environment and the outflow, especially if the wind shear vector progresses counterclockwise with height.

We decided to adapt the mesocyclone-shear algorithm (Hennington and Burgess, 1981) so that it can detect azimuthal shear near the ground. Because cyclonic shear is prevalent and because of time constraints, we made modifications to detect only cyclonic shear. The main changes needed for low-level shear are the thresholds listed in Table 2. These were obtained after several trials with a limited number of data.

3.4 Tracking of Gust Fronts

Once the gust front feature has been identified, there are several options for displaying and tracking it. In order to display the front at sites remote from the main computer, it is desirable to characterize the front's shape with a small number of parameters. We have found that with a convergence algorithm a least-squares fitted curve,

$$r = A\theta^2 + B\theta + C \qquad (5)$$

can be used very effectively both to display the front and to extrapolate its position into the future. In (5) θ's are azimuths of pattern vectors and r's can be either the average value $(r_b + r_e)/2$, of the pattern vector range or the range to the maximum gradient of a pattern vector. In order to track the front, its range center and azimuth center at two consecutive times t_1, t_2 are needed. Then, assuming that the front's propagation velocity equals the velocity at which the center is moving, the front's position can be projected for later times. This is done by advecting the curve (5) at a time t_2 with the estimated propagation velocity.

For azimuthal shear lines detected by the mesocyclone-shear algorithm, it is natural to regress θ on r because θ has a quadratic dependence (arc) on r. So we use

$$\theta = Ar^2 + Br + C \qquad (6)$$

where the data pairs (θ_i, r_i) are the centers of pattern vectors.

4. CASE STUDIES

We examined the performance of our algorithm on five different cases: April 13, 1981, May 29, 1980, April 26, 1984, May 9, 1981 and April 10, 1981. The data were obtained by the Doppler radar (λ = 10cm) of the National Severe Storms Laboratory at Norman, Oklahoma. In this section, three of them are explained precisely. As ground truth we use the positions of the gust as indicated by the velocity discontinuities on color displays and on contour plots. We also show examples of tracking and outputs such as feature area, "flux", and gradient as a function of range.

4.1 April 13, 1981

A very intense front developed in a squall line that passed by some surface stations and over Cimarron on this day (see Fig. 10 in Zrnic' and Lee (1983)). We applied the algorithm to seven scans and chose three consecutive scans at 1.2° in elevation to illustrate detection and tracking. We superposed the gust front position on the velocity contours to obtain Fig. 3. There the deduced front's shape follows quite well the $-10\ m \cdot s^{-1}$ velocity contour and is at the locations that one would subjectively determine from the color display. Note that the arc stops at 40 km to the west of radar and about 30 km to the north. From the color display we inferred that the front extends beyond these ranges, but because it becomes tangential to the radial, it cannot be detected with radial convergence measurements.

These gusts exhibit height continuity as seen in Fig. 4, where the secondary surges (2 and 3) are found at four elevation angles and the primary surge is present at all five elevations examined. The continuity should extend through two to three lowest elevations for practical use of the detection method. In order to establish track the front must be detected at least in two consecutive scans at the same elevation.

Three consecutive positions of the front are shown in Fig. 5. We used the locations of maximum gradients to trace the front and perform the fitting curve. Finding maximum gradients requires an additional pass through the velocity data contained between r_b and r_c of a pattern vector. The forecast position of the front (Fig. 5) is in reasonable agreement with the actual position; maximum displacements between the two are less than 4 km. To improve further the forecast positions would require intervals shorter than 5-7 min between scans. The values of average gradient, average "flux", average of maximum gradients, and area depend on the development stage of the front. The area (here 280-430 km^2) tends to increase closer to the radar if elevation is constant because more pattern vectors that would otherwise fall below the beam can be detected. Average gradients between 1.5 and 2 $m \cdot s^{-1} \cdot km^{-1}$, maximum gradient larger than 5 $m \cdot s^{-1} \cdot km^{-1}$, and fluxes between 100 and 400 $m \cdot s^{-1} \cdot km$ are typically encountered in strong gusts; this is illustrated in Table 3.

Because the frontal discontinuity on this day extended also along a radial, we ran the modified mesocyclone shear algorithm to see how it would detect and connect the azimuthal shear to the radial convergence. Results for the three scans are extremely promising (Fig. 6). Gust positions estimated from convergence and from azimuthal shear join smoothly and even overlap a bit.

4.2 May 29, 1980

We chose this gust (Fig. 7) for two reasons: (1) it was moving away from the radar, and we wanted to see how the algorithm would perform in such a situation. (2) It had a "line echo wave pattern" with a cyclonic couplet. This front is also discussed by Zrnic' and Lee (1983), who show the three moments on their Fig. 7. The gust front algorithm has no provision for circulation detection, but in an operational setup several algorithms that detect and track hazardous weather features must be used concurrently. Thus, a composite of hazards needs to be presented to operators for further interpretation and warnings. Therefore, we also subjected these data to the mesocyclone algorithm (Zrnic' et al, 1984).

As expected, the gust front algorithm detected the southern and northern portions of the wave but failed to connect the two. The azimuthal limits of the radar antenna were such that the southern portion of the line was not covered during the first two scans and that is why the front from 140° to 180° was detected only in the third scan (Fig. 7). The northern part of the line tracks as well as in the previous examples, with the standard error between the fitted curves and the data below 1 km. From the position of the center at three consecutive elevations we deduce that the southern portion of the gust had a slope of about 7.5°, which is quite close to the slope of 8.5° that Zrnic' and Lee (1982) show in a cross section of another gust on their Fig. 6. We have found (Uyeda and Zrnic', 1984) that the area, average "flux", average gradient, average of maximum gradient, and rms errors are also consistent with the previous two examples (Table 3).

The mesocyclone algorithm detected mesocyclonic shear (M) between the two lines (Fig. 7). It estimated the azimuthal extent (diameter) to be 2.3 km and the radial 2.4 km, which enables us to draw the core with the small circle.

4.3 April 26, 1984

Because the winds of this front were very turbulent (Uyeda and Zrnic', 1984) and disrupted flights from and to the Will Rogers Airport in Oklahoma City, we included this case in our tests. A TWA flight 163 encountered severe turbulence on

approach and had to be diverted to Tulsa.

A meteorological feature prominent on the velocity display was a long (80 km) convergence boundary (gust front). Strong southerly winds ahead of the gust front apparently identified a low-level jet associated with the storm system. Winds were gusting up to 25 $m \cdot s^{-1}$ at the surface and gusting higher than 35 $m \cdot s^{-1}$ at the topmost level (444 m) of the KTVY instrumented tower. Doppler velocities confirm that strong flow extended to the aircraft altitude (2 km and beyond).

Doppler spectrum width display showed large widths at the frontal discontinuity as well as ahead of the tower. This was confirmed by high variability in the recorded tower winds, which change by as much as 14 $m \cdot s^{-1}$ in 10 s.

The frontal outflow was rather shallow (<1 km) and the discontinuity could be seen clearly only at 0.5° in elevation (about 0.3 km height at a range of 40 km). At the next elevation, 1.5°, it was not visible. The shape of the primary front depicted by a five-point running average of maximum gradient location in Fig. 8 reproduces very well the pattern seen on color displays (Uyeda and Zrnic', 1984). The forecast position agrees with the actual location of the front even though the forecast center and the actual center are displaced by about 10 km. Their displacement is along the frontal discontinuity and thus does not affect the front's position in range but only influences its azimuthal extent. Tabulated parameters are generally consistent with previous cases. The rms error is on the high side because the front is long and has kinks; therefore, a second-order polynomial is not a best model for its shape.

5. SUMMARY AND CONCLUSIONS

The procedure we have developed to detect and track gust fronts automatically does not rely on a single method but requires simultaneous operation of several related algorithms. These algorithms process one or two radials of Doppler velocity data in real time. We have not incorporated in our programs the simultaneous operations but have separately tested the various subsets of a general low level (less than 3 km above ground) hazard detection algorithm. The flow chart in Fig. 9 depicts the low level hazard algorithm as we envision it. In order to discriminate between gust fronts and short convergence lines, a convergence algorithm developed in this report is used. Calculations commensurate with radial update rates are required on one radial at a time for constructing pattern vectors that are later (at the end of a scan) sorted into features. Our convergence algorithm measures the radial convergence, and hence only gusts propagating along radials can be readily detected. For detecting gusts that are aligned along radials, we have employed the mesocyclone-shear algorithm, which requires storage and operation on two consecutive radials of velocity data. The long shear lines that this algorithm detects are classified as gusts whereas symmetric shear features are rejected if their shears and momentum are insignificant or are classified as low-level vortices that are known to accompany wavelike gusts. Shears of intermediate length (10 to 20 km) may be classified as spurious.

Downdraft and tornado vertex signatures (TVS) represent low level hazards that can be detected with the same basic technique of building pattern vectors, and that is why they are included in the flow chart (Fig. 9) even though they have not been developed yet. Other low-level hazards such as turbulence and hail require spectrum width and reflectivity data as well as different algorithms for identification; that is why they are not included in the chart.

After sorting of pattern vectors, the resulting features are classified and tracked. It appears that convergence lines (i.e., lines obtained from the convergence algorithm) shorter than 10-20 km can be discarded. Distinguishing by length and symmetry between hazardous and spurious features is not unique with the mesocyclone-shear algorithm because mesocyclones are symmetric and of small extent as are spurious shear lines. Therefore, checking the length and continuity in time may

be a most effective means to eliminate spurious shears.

Overall detection of gust fronts from measurements of radial velocity gradients and azimuthal shear is feasible. The results exceeded our expectations; there was no undetected front among the test cases. However, spurious shear and false alarms due to overlaid echoes were inevitably present. These can be significantly reduced by checking their length as well as time-height continuity.

Here, we discuss the applicability of developed algorithms and algorithms shown in Fig. 9 to observations of Japanese weather phenomena. The heavy rainfall associated with Baiu and Typhoon along the seacoast of the Pacific Ocean and the heavy snowfall and snowstorm along the seacoast of the Japan Sea are severe weather phenomena in Japan. For detection and forecast of them, observation of wind field is essential.

When we apply a Doppler radar for low-altitude weather observation in mountainous Japan, we have to think about proper radar wavelength. A 3 cm radar would not be sufficient for the observation of heavy rainfalls and snowfalls because of attenuation. A 10 cm radar would not be practical for low altitude observation in Japan because of ground clutter, however it is very powerful for the observation of large area. A 5 cm Doppler radar would be appropriate for the observation of Japanese severe weather.

For understanding of weather effects to building, it would be very useful to observe low altitude wind field by a Doppler radar. It would also be necessary to examine wind shear distribution and spectrum width distribution by a Doppler radar for the understanding of wind effects.

6. ACKNOWLEDGEMENTS

We appreciate the help of Yosefa Gal-Chen during the initial stages of algorithm development. Don Burgess provided us with the information concerning the weather situation on April 26, 1984, when TWA flight 163 encountered turbulence. This work was supported by the Joint System Program Office (National Weather Service) and by the Federal Aviation Administration Grant No. DTFA01-8-Y-10524. One of the Authors (Hiroshi Uyeda) was supported by the Science and Technology Agency, Japan and Cooperative Institute for Mesoscale Meteorological Studies for his stay at the National Severe Storms Laboratory.

7. REFERENCES

Brown, R. A., L. R. Lemon, and D. W. Burgess, 1978: "Tornado detection by Doppler radar," Mon. Wea. Rev., 106, 29-38.

Doviak, R. J., and D. S. Zrnic', 1984: Doppler Radar and Weather Observations. Academic Press, New York, NY.

Goff, R. D. 1975: "Thunderstorm outflow kinematics and dynamics," NOAA Tech. Memo ERL-NSSL-75. Available from National Technical Information Service, Operations Div., Springfield, VA 22151.

Hennington, L., and D. W. Burgess, 1981: "Automatic recognition of mesocyclones from single Doppler radar data," Preprints, 20th Radar Meteorology Conference. American Meteorological Society, Boston, pp. 704-706.

Lemon, L. R., R. J. Donaldson, Jr., D. W. Burgess, and R. A. Brown, 1977: "Doppler radar application to severe thunderstorm study and potential real-time warning," Bulletin, Am. Meteor. Soc., 58, 1187-1193.

_____, and D. W. Burgess, 1980: "Magnitude and implications of high speed outflow at severe storm summits." 19th Conference on Radar Meteorology, American Meteorological Society, Miami, Florida, pp. 364-368.

NEXRAD (Next Generation Weather Radar) Algorithm Report, 1983: Prepared by the NEXRAD Joint System Program Office, Gramax Building, Room 900, 8060 13th, Silver Spring, MD 20910.

Sirmans, D., and R. J. Doviak, 1973: "Pulsed-Doppler velocity isotach display of storm winds in real time," J. Appl. Meteor., 12, 694-697.

Uyeda, H., and D. S. Zrnic', 1984: "Automatic detection of gust fronts." Report prepared for the Federal Aviation Administration and the Joint System Program Office. National Severe Storms Laboratory, 1313 Halley Circle, Norman, OK 73069.

Uyeda, H., and D. S. Zrnic', 1985: "Automatic detection of gust fronts." J. Atmospheric and Oceanic Technology. (To be published.)

Wilson, J. W., R. D. Roberts, D. Kessinger, and J. McCarthy, 1984: "Microburst wind structure and evaluation of Doppler radar for airport wind shear detection," J. of Clim. and Appl. Meteor., 23, 898-915.

Wood, V. T., and R. A. Brown, 1983: "Single Doppler velocity signatures: An atlas of

patterns in clear air/widespread precipitation and convective storms," NOAA Tech. Memo. ERL NSSL-95. Available from National Technical Information Service, Operations Div., Springfield, VA 22151.

Zrnic', D. S., and J. T. Lee, 1982: "Pulsed Doppler radar detects weather hazards to aviation," J. Aircraft, 19, 183-190.

Zrnic', D. S., and Y. Gal-Chen, 1983: "Divergence measurement in storm tops," Report for the Joint Systems Program Office. National Severe Storms Laboratory, 1313 Halley Circle, Norman, OK 73069.

Zrnic', D. S. and J. T. Lee, 1983: "Investigation of the detectability and lifetime of gust fronts and other weather hazards to aviation," FAA Report No. DOT/FAA/PM-83/33.

Zrnic', D. S., D. W. Burgess, and L. D. Hennington, 1984: "Automatic detection of mesocyclonic shear," accepted by the J. Tech.

TABLE 1

Thresholds for Detecting Radial Convergence Lines

THRESHOLD	NUMERICAL VALUE
High Gradient	$H_g = 0.65\ m \cdot s^{-1} \cdot km^{-1}$
Low Gradient	$L_g = 0.50\ m \cdot s^{-1} \cdot km^{-1}$
High "Flux"	$H_f = 100\ m \cdot s^{-1} \cdot km$
Low "Flux"	$L_f = 30\ m \cdot s^{-1} \cdot km$
Max. azimuthal separation between vectors	$l_a = 4°$
Max. range separation between vectors	$l_r = 4.0$ km
Reflectivity Threshold	-15 dBZ
Height Threshold	2 km (and below)

TABLE 2

Thresholds for Detecting Azimuthal Shear Lines

	THRESHOLD	NUMERICAL VALUES
L_s	Low shear	$1.5\ m \cdot s^{-1} \cdot km^{-1}$
H_s	High shear	$2.0\ m \cdot s^{-1} \cdot km^{-1}$
L_m	Low momentum	$25\ m \cdot s^{-1} \cdot km$
H_m	High momentum	$50\ m \cdot s^{-1} \cdot km$
M	Minimum number of vectors allowed in a feature	10
l_a	Maximum distance between the azimuthal centers of two vectors for classification in the same feature	3.3°
l_r	Maximum radial distance between two vectors	4 km
z_t	Reflectivity threshold	-15 dBZ

TABLE 3

Minimum, Average, and Maximum Value of Gust Front Parameters

DATE	Range of Center (km) min,avr,max	Length (km) min,avr,max	Area (km^2) min, avr, max	Avr. Grad. ($ms^{-1} \cdot km^{-1}$) min, avr, max	Avr of Max. Grad. ($ms^{-1} \cdot km^{-1}$) min, avr, max	Avr. "Flux" ($ms^{-1} \cdot km$) min, avr, max	RMS Error (km) min, avr, max
April 13, 1981	25, 28, 39	12, 30, 44	280, 340, 430	1.3, 1.6, 1.9	5.3, 5.9, 6.5	83, 255, 365	0.8, 1.3, 1.5
May 9, 1981	47, 68, 83	13, 48, 63	100, 430, 760	1.4, 1.7, 2.1	4.6, 5.2, 6.4	79, 231, 321	0.8, 2.1, 3.3
May 29, 1981	24, 34, 48	12, 25, 33	200, 317, 480	1.5, 2.0, 3.0	8.4, 9.1, 9.9	108, 335, 438	0.2, 0.6, 1.0
April 10, 1981*	52, 55, 57	70, 73, 79	- - -	4.6, 5.0, 5.5	- - -	66, 63, 68	1.2, 1.5, 2.2
April 26, 1984	41, 45, 49	77, 85, 91	840, 965, 1075	2.5, 2.6, 2.6	9.0, 9.4, 9.7	351, 383, 437	1.6, 2.0, 2.6

*This front was detected with the mesocyclone-shear algorithm; the rest were detected with the convergence algorithm

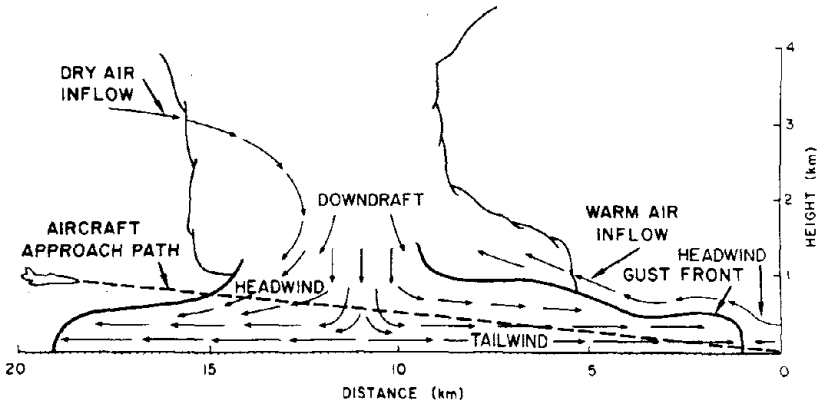

Figure 1. Schematic of a thunderstorm downdraft and associated gust front on the approach path to an airport. Note the sudden change in the horizontal wind component at the distance of about 11 km. In particular cases and at particular stages in the life of a storm, the horizontal scale of the disturbance may be substantially smaller or larger. (From Zrnic and Lee (1983))

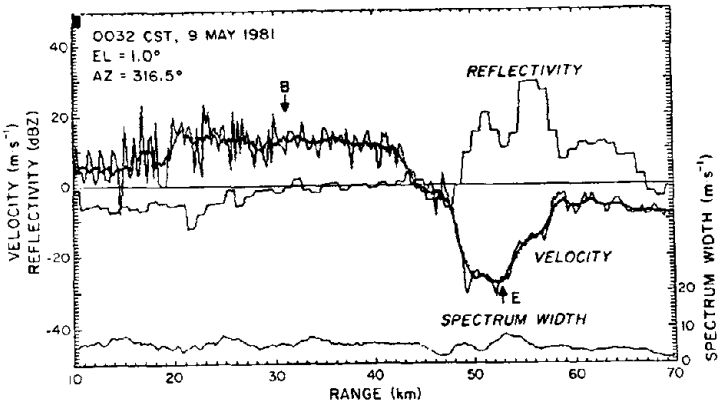

Figure 2. Profiles of equivalent reflectivity factor, mean velocity and Doppler spectrum width along radials for a gust of May 9, 1981. Both raw and nine-point averaged mean velocities are shown. The spectrum width is a nine-point running average. The beginning, B, and ending, E, of the pattern vectors are indicated.

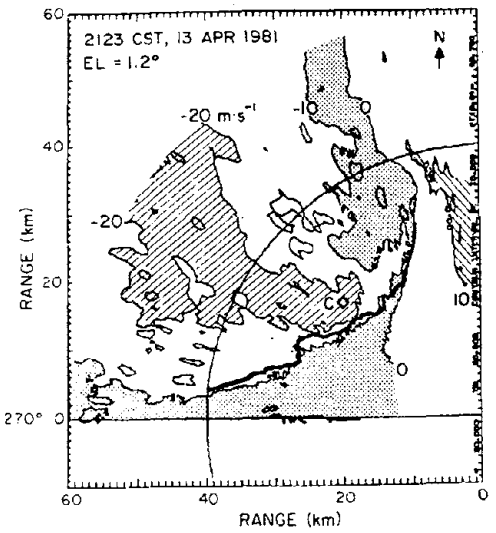

Figure 3. Contours of mean Doppler velocities for the gust front of April 13, 1981. The contour interval is 10 $m \cdot s^{-1}$. Objectively determined location of the front (thick line) is superposed. The square next to C is at the center (r_c, az_c) of the front.

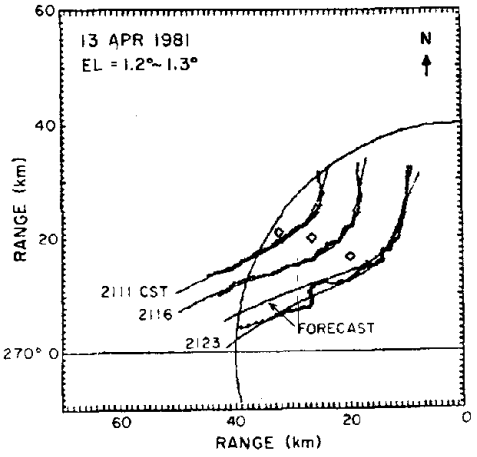

Figure 5. Three consecutive positions of the front (April 13, 1981). The smooth curves are least squares fits to the data, and the forecast position is indicated. The range mark is at 40 km from the radar. Centers of the pattern vectors were used to trace the gust. squares indicate the centers of these three front lines.

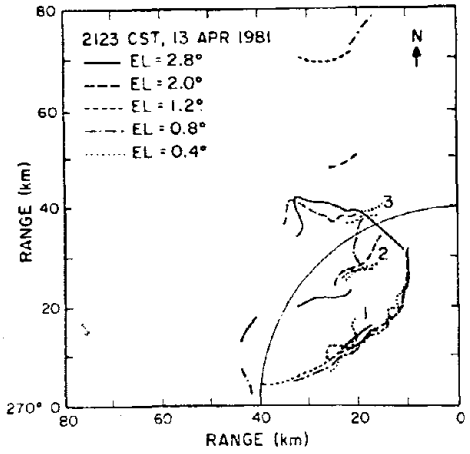

Figure 4. Detected gust lines in one volume scan of April 13, 1981.

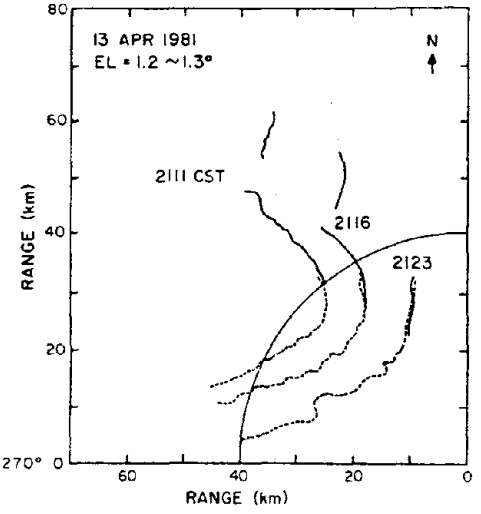

Figure 6. Detected gust fronts. Dashed line is a five-point running average of maximum gradient locations (from convergence algorithm) and the solid line is a five-point running average of pattern vector centers (from mesocyclone-shear algorithm).

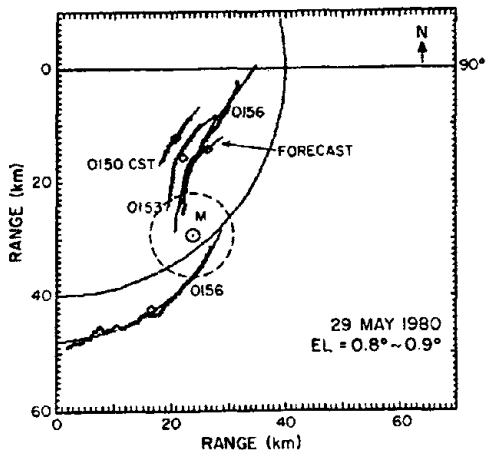

Figure 7. Three consecutive positions of the front on May 29, 1980. The smooth curves are least squares fits to the data, and the forecast position is indicated. The range mark is at 40 km from the radar. The small circle indicates the core of a mesocyclonic vortex, and the dashed circle has a diameter three times larger than the core.

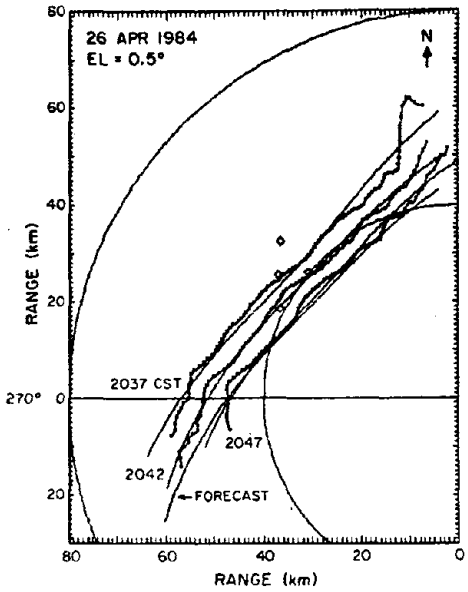

Figure 8. Three consecutive positions of the front for April 26, 1984. Five-point running average, least squares fitted curves, and a forecast position are shown. Square indicates the center of each curve.

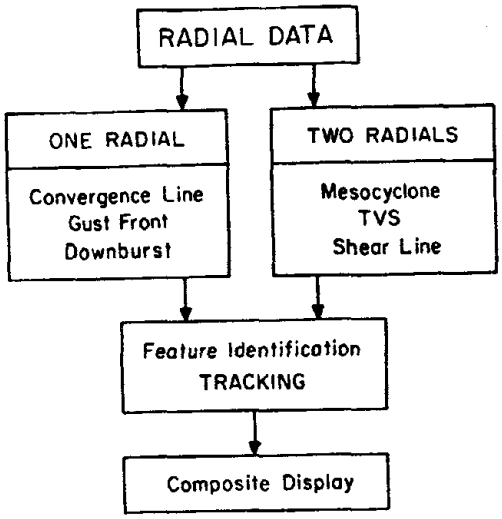

Figure 9. Algorithm for detecting weather hazards near the ground.

Theme II

EARTHQUAKE ENGINEERING

EARTHQUAKE HAZARD REDUCTION PROGRAM OF THE DEPARTMENT OF STATE

BY

PETER E. GURVIN

ABSTRACT

The Department of State owns or leases a large inventory of buildings throughout the world some of which are located in areas of high seismic risk. The Department has initiated a seismic hazard reduction program to upgrade the seismic resistance of our buildings through either replacement or retrofit. The seismic design requirements for our major buildings may have been over-taken by a greater design condition that relates to the terrorist threat!

1. INTRODUCTION

The Office of Foreign Buildings Operations of the Department of State was created by the Foreign Service Buildings Act of 1926 and is responsible for the design, construction, acquisition, and maintenance of our diplomatic and consular facilities overseas.

Perhaps the most significant aspect of the Department's facility posture is the sheer magnitude of these aspects. They total nearly 10,000 buildings covering 46 million square feet in 256 cities in the world. These facilities are worth 3 billion dollars. The percentage mix of our buildings are 23 percent U.S. Government owned and 77 percent short term lease.

A typical post consists of three office buildings, five "other" community and support facilities, and 30 residential buildings ranging from the Ambassador's residence to 25 individual homes.

2. HISTORICAL EARTHQUAKE DAMAGE

It may be of interest to review the past historical performance of the Department of State's buildings during past earthquakes. Many thousands of people lost their lives in these devastating earthquakes.

The following is a summarization of performance of the Embassies and Consulates as far as known:

DATE	LOCATION	MAGNITUDE	COMMENT
9-1-1923	Tokyo	M=7.2	Embassy buildings destroyed by fire See Appendix A
3-1-1931	Managua	M=	American Legation destroyed
7-29-1967	Caracas	M=6.5	Non-structural damage to Embassy
12-23-1972	Managua	M=6.2	Embassy damaged beyond repair
2-4-1976	Guatemala City	M=7.5	Non-structural damage
3-4-1977	Bucharest	M=7.2	Non-structural damage
6-20-1978	Thessaloniki	M=6.5	Non-structural damage
3-3-1984	Santiago	M=7.4	Non-structural damage

1) Chief, Civil Structural Engineering, Office of Foreign Buildings, Department of State, Washington, DC

3. DEPARTMENT OF STATE SEISMIC DESIGN CRITERIA

The National Earthquake Hazards Reduction Program, developed in accordance with the National Earthquake Hazards Reduction Act of 1977 (PL95-124), stated that this program "should proceed on the basis of a balanced strategy reflecting relative seismic risk and mitigation of highest hazards on a priority basis". "A Federal example in construction: the Federal Government should set a strong example in the construction of its own facilities and develop guidelines and standards for Federally assisted or licensed facilities."

This Federal Law was primarily directed towards internal U.S. Government Agencies. However, the Department of State believed that to the maximum extent possible the intent of the program should be incorporated into the management of the State Department's design and construction program outside of the U.S.

First of all, I would like to give you some insight into how our design program for major office and staff housing is accomplished. All major designs, with a few exceptions, are accomplished by U.S. design firms. Our basic structural design guidance, including earthquake design, refers to the current Uniform Building Code. Almost 99 percent of our buildings are of reinforced concrete so the American Concrete Institute Standards also form a fundamental reference for design.

An exception to the above is the recently completed U.S. Embassy housing project at Mitsui Compound in Tokyo which was structurally designed by the Japanese firm of Kirmura Structural Engineers. In addition to U.S. design standards, the construction plans and specifications have to take into consideration the country where the facilities are to be built and therefore relate to available materials, level of construction expertize, and also the construction norms of the country.

4. EARTHQUAKE HAZARD REDUCTION PROGRAM

The initial stumbling block for overseas building designs for FBO was to obtain a proper zoning according to the zones used in the Uniform Building Code as used in the U.S. based on zones 0 through 4. In order to obtain an idea or gross zoning for the world, FBO contracted with the soil consulting engineering firms of Woodward-Clyde (1) and Dames/Moore (2) to zone all Foreign Service Posts according to the 1976 Uniform Building Code format. This global zoning has proved to be very useful to obtain a first-cut on the seismic design requirement for new design of buildings for various cities worldwide. More in-depth seismic zoning would be accomplished on a case by case basis depending on the size of the project. Secondly, this global zoning provided a basis for preliminary recommendations for action toward reduction of the earthquake risk of existing buildings in FBO's inventory.

The preliminary seismic-exposure estimates as given by Dames/Moore and Wooward-Clyde are summarized in the Appendix B. These estimates place approximately 15 percent of the cities with Foreign Service Posts in zones higher than zone 3 and over 40 percent in zones higher than 2. In general, the zoning appears to be conservative. As an example, let's look at the zone recommendation for Lisbon which was given as zone 4. Karnik (3) indicates that damage evaluated at MMI IX (Modified Mercalli Intensity) has been observed in the region which provides some support toward a rating of 4. Sozen (4) noted that in a study of comparative seismicity as given in Figure 1 (5), the seismicity of Portugal is only a fraction of that of California. Seismic zone 4 is assigned to areas within seismic zone 3, depending on the proximity to certain major fault systems. Seismic zone 3 is assigned to areas where major damage corresponding to MM Intensity VII or higher can occur.

FBO recently completed a new Chancery in Lisbon. At the beginning of the design we took a more in depth look at the seismic estimate for Lisbon. This study (6) based on the seismicity of the region and evaluation of local faults resulted in the recommendation to use zone 3. FBO has made some other site specific studies which also resulted in a lowering of the zone estimates as given in the Appendix.

It should be noted that further specific site studies are useful only if their is a real payback for the reduction in zoning. The reduction in a zone from 4 to 3 may have a nominal effect on the overall cost of the building, and the design could be carried out for the initial assessment. In any event the preliminary assessment reports have proved useful in the structural design of new buildings.

The second purpose of the seismic zoning report was to obtain a basis for development of a list indicating which buildings at our 256 Posts should be investigated on a priority basis. The steps in the preliminary process were defined as follows:

Step 1 Relative Seismic Exposure
Step 2 Occupancy
Step 3 Vintage and Location
Step 4 Classification According to Building Material
Step 5 Preliminary Structural Evaluation

In our hazard reduction program it was decided to concentrate on the high occupancy buildings, which would be the Chanceries and office annexes. Since 1982, our office has received about $85,000 per year for preliminary structural

As a result of these evaluations, our office has used the outcome to prioritize seismic strengthening or make recommendations for total replacement of buildings. Currently, new Embassy Office building designs are about to begin or are under design for these locations of high seismicity; Caracas, Damascus, Dhaka, La Paz, Nicosia, Osaka-Kobe, Ottawa, Rangoon, and Santiago. While $85,000 is not a large sum the seismic reduction program has provided valuable input for justification by management for new projects where existing buildings have proved to be totally deficient.

5. CURRENT CAPITAL PROGRAM IMPACT

As a prologue to our prior discussion on seismic hazard reduction program, the Beruit bombing of July 1983, the Kuwait Chancery bombing of September 1983, and the Beruit Chancery Annex bombing of September 1984 have changed our structural design guidance for new office buildings and also the size of our building program. 87 persons lost their lives in these terrorist attacks and of course, many more were severly injured. Among other design initiatives being implemented as a result of the terrorist threat are that all new office buildings are designed for Uniform Building Code Zone 3 earthquake design regardless ofthe location. Blast loading is a different loading condition than earthquake loading but ductility in structural design is important to both situations.

Our building program has dramatically been enlarged, Congress authorized 13 new office buildings this year at a cost of $170 million, mainly in the Middle East. In addition, a special Panel on Security for the Secretary of State has been recently quoted in the Washington Post newspaper as recommending that the Department replace over 140 Embassies at a cost of 3.3 billion dollars.

In conclusion, the earthquake threat as a governing design parameter may have been overtaken by the terrorist threat with regard to State Department facilities.

1. "Seismic Exposure Assessment", report prepared for Department of State, Office of Foreign Building Operations by Woodward-Clyde Consultants, San Francisco, California. June 1979.

2. "Seismic Exposure Assessment", report prepared for Department of State, Office of Foreign Building Operations by Dames and Moore, Cranford, New Jersey. June 1979.

3. "Seismicity of the European Area", V. Karnik, D. Reidel Publishing Co., Dordrecht, Holland. 1969 (two volumes).

4. "Review of Seismic - Exposure Estimates for Foreign Service Costs and a Preliminary Plan for Identification of Hazardous Buildings", report prepared for the Department of State, Office of Foreign Building Operations, by Mete A. Sozen, University of Illinois. August 1979.

5. "Structural Safety", V. Ferry Borges and M. Castanheta, Laboratoria Nacional de Engenharia Civil, Second Edition, Lisbon, Portugal. March 1971 pp. 235-239.

6. "Seismic Considerations for New U.S. Embassy, Lisbon", report prepared by Woodward-Clyde Consultants, New York, NY. November 1979.

APPENDIX A

Tokyo

Historical Sketch of the Embassy Property

The present Diplomatic and Consular buildings of the United States replace wooden buildings that were used by the United States Legation and Embassy from 1889 until they were destroyed by earthquake and fire on September 1, 1923. There were three houses on what is now the lower compound, which was all that the United States held at the time of the disaster. One was a two storied frame building in which the Ambassador had his residence. To it was attached the chancery which occupied a wing extending towards the Reinanzaka hill road. The archives were housed in a brick vault in the chancery. This vault withstood the fire. The main entrance at that time was by a gate on the north side near the Reinanzaka road. There was a gravel roadway to the house which stood on an oval, and a flower bed. At the eastern end of the oval was a bungalow usually occupied by the Counselor. In the southeastern part of the property was a house built by Mr. R. S. Miller for his own use when he was Japanese Secretary - a grade now specially provided for. This was a two-story structure and was approached from the street by a separate driveway which ran ran behind the Counselor's house. The property sloped down this driveway to the street and near the gate of the back driveway was a sort of stable and storehouse.

The property was formerly a graveyard. It was purchased about 1888 by Baron Okura, the merchant, founder of Okura Gumi, who erected the main building on the understanding that it would be used by the American Minister (as he then was) as an office and residence. The bungalow was erected subsequently. In 1889 the Japanese Government purchased the property from Baron Okura and leased it formally to the American Legation. It was the property of the Japanese Government until 1896, when the United States purchased the buildings and took the land on perpetual lease. The consideration was $16,000. It was later discovered that a small piece of land at the northern corner of the Reinanzaka hill road had not been included in the perpetual leasehold. As perpetual leaseholds were no longer permissible after 1899, this property has been held as an ordinary lease. The Consulate General was moved to Tokyo from Yokohama after the earthquake of 1923.

The old buildings were painted white and the property was separated from the street on the north by a low wall surmounted by a hedge. The garden was well kept. A large wisteria vine was trained over the arbor at the back of the Ambassador's house where there was a covered porch. There were trees and bushes, the latter mostly flowering, and the grounds had a distinctly pleasing appearance.

The "upper compound" at the top of the hill where the Ambassador's house now stands belonged to the Imperial Household and was commonly known as the "Ito Property" from the fact that the first Prince Ito lived there when he was connected with the Imperial Household. There was a brick house on the lot which was destroyed in the earthquake. The Imperial Household sold the property to the United States in 1925.

APPENDIX B

SEISMIC EXPOSURE EVALUATION TABLES

A.1 SCOPE: This listing is a preliminary evaluation of seismic exposure of foreign service posts throughout the world where the U. S. Department of State has the responsibility for owned and/or leased buildings. In this listing, seismic exposure is defined as the estimated level and likelihood of seismic effects of earthquakes in the area expressed in terms of seismic zones as defined in the Uniform Building Code of 1979.

A.2 BASIS OF EVALUATION: This evaluation is based on available information on the regional tectonic condition and an assessment of the historical seismic activity in the area of each location. Where the available information was incomplete, it was supplemented by the judgement of experts in geology, seismology, and earthquake engineering based on their work on research and projects in the respective regions. An indication of the confidence in the assessment exposure is included in the classification of sites into zones. The evaluation also included identification of the latest local earthquake code and a listing of relevant seismic activity.

A.3 SUMMARY: A summary of the results of the seismic exposure evaluation is given in the table following this section.

COUNTRY	CITY	ZONE	DEGREE OF CONFIDENCE
AFGHANISTAN	Kabul	4	M
CHILE	Santiago	4	L-M
CHINA	Peking	4	M
CHINA	Tihwa	4	M
COLOMBIA	Bogota	4	M
ECUADOR	Quito	4	M-H
EL SALVADOR	San Salvador	4	M
GREECE	Thessaloniki	4	L
GUATEMALA	Guatemala	4	H
ICELAND	Reckjavik	4	M-H
INDONESIA	Bandung	4	L
INDONESIA	Jakarta	4	L
INDONESIA	Surabaya	4	L
IRAN	Tabriz	4	H
JAPAN	Okinawa, Naha	4	M-H
JAPAN	Osake-Kobe	4	M-H
JAPAN	Tokyo	4	H
JAPAN	Yokohama	4	H
NEPAL	Kathmandu	4	M-H
NICARAGUA	Managua	4	H
PERU	Lima	4	M
PHILIPPINES	Cebu	4	M
PHILIPPINES	Manila	4	M
PORTUGAL	Ponta Delgado	4	M
SICILY	Palermo	4	M-H
TIAWAN	Taipei	4	M-H
TURKEY	Istanbul	4	M
TURKEY	Izmir	4	M
CANADA	Quebec	3+	M-H
COLUMBIA	Buenaventure	3+	L-M
COLUMBIA	Cali	3+	L-M
JAMAICA	Kingston	3+	M-H
NEW ZEALAND	Wellington	3+	M-H
PAKISTAN	Islamabad	3+	M
PERU	Piura	3+	L-M
VENEZUELA	Caracas	3+	H
ALBANIA	Tirana	3	H
ALGERIA	Algiers	3	L-M
ALGERIA	Oran	3	L-M
ANTILLES	Curacao	3	M
BANGLADESH	Dacca	3	L
BOLIVIA	Lapaz	3	L-M
BULGARIA	Sofia	3	M
BURMA	Mandalay	3	L
BURMA	Rangoon	3	L

COUNTRY	CITY	ZONE	DEGREE OF CONFIDENCE
BURUNDI	Bulumbura	3	L
CANADA	Vancouver	3	M-H
CHINA	Mukden	3	L-M
COLUMBIA	Medellin	3	L-M
COSTA RICA	San Jose	3	L
CYPRUS	Nicosia	3	M
DOMINICAN REPUBLIC	Santo Domingo	3	M
ECUADOR	Guayaquil	3	M
ETHIOPIA	Asmara	3	L
FIJI	Suva	3	L-M
FRANCE	Marseille	3	L-M
FRANCE	Nice	3	L-M
FRENCH WEST INDIES	Martinique	3	M
GREECE	Athens	3	L-M
HAITI	Port au Prince	3	M
HONDURAS	Tegucigalpa	3	M
INDIA	Bombay	3	L-M
INDIA	New Delhi	3	M
INDONESIA	Medan	3	L
IRAN	Isfahan	3	H
IRAN	Shiraz	3	M-H
IRAN	Tehran	3	M-H
ISRAEL	Haifa	3	M
ISRAEL	Jerusalem	3	M
ISRAEL	Tel Aviv	3	M
ITALY	Florence	3	M
JAPAN	Fukuoka	3	M-H
JAPAN	Sapporo	3	M
JORDAN	Amman	3	M
LEBANON	Beirut	3	M
MALAWI	Blantyre	3	L
MALAWI	Lilongwe	3	L
MALAWI	Zomba	3	L
MALTA	Valletta	3	L
MEXICO	Guadalajara	3	M
MEXICO	Mexico City	3	M
MEXICO	Tijuana	3	M-H
MOROCCO	Tangier	3	M
NEW ZEALAND	Auckland	3	M-H
PANAMA	Colon	3	M
PANAMA	Panama	3	M
PAPAU NEW GUINEA	Port Moresby	3	L
PHILIPPINES	Baguio	3	M
PORTUGAL	Lisbon	3	M
PORTUGAL	Opporto	3	L
RUMANIA	Bucharest	3	M
RWANDA	Kigali	3	L
SAIPAN	Saipan	3	L
SOUTH AFRICA	Capetown	3	M-H
SOUTHERN RHODESIA	Salisbury	3	L

COUNTRY	CITY	ZONE	DEGREE OF CONFIDENCE
SYRIA	Aleppo	3	L-M
SYRIA	Damascus	3	L-M
TERR. OF AFARS AND ISSAS		3	L
TRINIDAD	Port-of-Spain	3	M
TUNISIA	Tunis	3	L-M
TURKEY	Adana	3	L-M
YUGOSLAVIA	Zagreb	3	M
ZAIRE	Bukavu	3	L
AUSTRIA	Vienna	2+	M
CANADA	Montreal	2+	H
CHINA	Tsingtao	2+	M
CZECHOSLOVAKIA	Bratislava	2+	L-M
FRANCE	Strasbourg	2+	M
GERMANY	Stuttgart	2+	M
GHANA	Accra	2+	L
HUNGARY	Budapest	2+	M
IRAQ	Baghdad	2+	L-M
ITALY	Genoa	2+	L-M
ITALY	Naples	2+	L-M
ITALY	Trieste	2+	L-M
PAKISTAN	Peshawar	2+	M
YUGOSLAVIA	Belgrade	2+	M
ADEN	Aden	2	L
BARBADOS	Bridgetown	2	M
BELGIUM	Brussels	2	M
CANADA	Halifax	2	M-H
CANADA	Ottawa	2	H
CANADA	St. Johns	2	M-H
CHINA	Canton	2	L-M
CHINA	Nanking	2	L-M
CHINA	Shanghai	2	L-M
CUBA	Santiago de Cuba	2	M
ENGLAND	London	2	L
EGYPT	Alexandria	2	L-M
EGYPT	Cairo	2	M
EGYPT	Port Said	2	L
ETHIOPIA	Addis Ababa	2	L
FINLAND	Helsinki	2	M-H
FRANCE	Bordeaux	2	M
GERMANY	Bonn	2	M
GERMANY	Frankfurt	2	L-M
HONG KONG	Hong Kong	2	L
INDIA	Calcutta	2	M
ITALY	Milan	2	L-M
ITALY	Rome	2	L-M
ITALY	Turin	2	L-M
KENYA	Nairobi	2	L
LIBYA	Tripoli	2	L
MEXICO	Ciudad Juarez	2	M

COUNTRY	CITY	ZONE	DEGREE OF CONFIDENCE
MEXICO	Hermosillo	2	M
MOROCCO	Casablanca	2	M
MOROCCO	Rabat	2	M
NORWAY	Oslo	2	L
PAKISTAN	Karachi	2	M
PAKISTAN	Lahore	2	M
POLAND	Krakow	2	L-M
SAUDI ARABIA	Jeddah	2	M
SOUTH AFRICA	Johannesburg	2	L
SOUTH AFRICA	Pretoria	2	L
SPAIN	Barcelona	2	L-M
SPAIN	Bilbao	2	L-M
SPAIN	Seville	2	L-M
SWEDEN	Goteborg	2	M-H
SWITZERLAND	Bern	2	M
SWITZERLAND	Zurich	2	M
TURKEY	Ankara	2	M-H
UGANDA	Kampala	2	L
VENEZUELA	Maracaibo	2	M-H
YEMEN	Sanaa	2	M
ZAIRE	Lubumbashi	2	L
ZAMBIA	Lusaka	2	L
AUSTRIA	Salzburg	1+	M
DENMARK	Copenhagen	1+	L-M
MEXICO	Mazatlan	1+	M
AUSTRALIA	Canberra	1	M
AUSTRALIA	Melbourne	1	M
AUSTRALIA	Perth	1	M
AUSTRALIA	Sydney	1	M
BELGIUM	Antwerp	1	M
BOLIVIA	Santa Cruz	1	L-M
CANADA	Calgary	1	M
CANADA	Toronto	1	M-H
CANADA	Winnipeg	1	M-H
COLUMBIA	Barranquilla	1	L-M
CUBA	Havana	1	M
CZECHOSLOVAKIA	Prague	1	L-M
ENGLAND	Edinburgh(Scotland)	1	L
ENGLAND	Hamilton(Scotland)	1	L
ENGLAND	Liverpool	1	M
FRANCE	Lyon	1	M
GERMANY	Dusseldorf	1	M
GERMANY	Munich	1	M
IRAQ	Basra	1	L-M
KUWAIT	Kuwait	1	L-M
LAOS	Vientiane	1	L
LESOTHO	Maseru	1	L
LIBERIA	Monrovia	1	L
LUXEMBOURG	Luxembourg	1	M
MALAYSIA	Kuala Lumpur	1	L

COUNTRY	CITY	ZONE	DEGREE OF CONFIDENCE
MOZAMBIQUE	Maputo	1	L
OMAN	Muscat	1	L-M
POLAND	Poznan	1	M
POLAND	Warsaw	1	M
SINGAPORE	Singapore	1	L
SOUTH AFRICA	Durban	1	L
SOUTH AFRICA	Natal	1	L
SWAZILAND	Mbabane	1	L
SWEDEN	Stockholm	1	H
SWITZERLAND	Geneva	1	M
TANZANIA	Dar es Salaam	1	L
TANZANIA	Zanzibar	1	L
THAILAND	Chiang Mai	1	L
TOGO	Lome	1	L
U.A.E.	Abu Dhabi	1	L
ANGOLA	Luanda	0	M
ARGENTINA	Buenos Aires	0	M
AUSTRALIA	Brisbane	0	M
BAHAMAS	Nassau	0	L
BAHRAIN	Manama	0	L
BELIZE	Belize City	0	L
BERMUDA	Hamilton	0	L
BOTSWANA	Gaberone	0	L
BRAZIL	Belem	0	L
BRAZIL	Belo Horizonte	0	L
BRAZIL	Brazilla	0	L
BRAZIL	Manaus	0	L
BRAZIL	Porto Allegre	0	L
BRAZIL	Recife	0	L
BRAZIL	Rio de Janeiro	0	L
BRAZIL	Salvador	0	L
BRAZIL	Sao Paulo	0	L
CAMAROON	Yaounde	0	L
CENTRAL A.R.	Bangui	0	L
CHAD	Ndjamena	0	L
CONGO	Brazzaville	0	L
COTONOU	Benin	0	L
EQUATORIAL GUINEA	Malabo	0	L
FRANCE	Paris	0	M
GABON	Libreville	0	L
GAMBIA	Banjul	0	L
GERMANY	Berlin	0	M
GERMANY	Bremen	0	M
GERMANY	Hamburg	0	M
GUINEA	Conakry	0	L
GUINEA	Bissau	0	L
GUYANA	Georgetown	0	L
INDIA	Madras	0	L
IRELAND	Belfast	0	L

COUNTRY	CITY	ZONE	DEGREE OF CONFIDENCE
IRELAND	Dublin	0	L
IVORY COAST	Abidjan	0	L
KOREA	Seoul	0	M
MALAGASY REPUBLIC	Tananarive	0	L
MALI	Bamako	0	L
MAURITANIA	Nouakchott	0	L
MAURITIUS	Port Louis	0	L
MEXICO	Matamoros	0	M
MEXICO	Merida	0	L
MEXICO	Monterrey	0	M
MEXICO	Nuevo Laredo	0	M
NETHERLANDS	Amsterdam	0	L-M
NETHERLANDS	The Hague	0	L-M
NETHERLANDS	Rotterdam	0	L-M
NIGER	Niamey	0	L
NIGERIA	Ibadan	0	L
NIGERIA	Kaduna	0	L
NIGERIA	Lagos	0	L
PARAGUAY	Asuncion	0	M
QUATAR	Doha	0	L
SAUDI ARABIA	Dhahran	0	L
SAUDI ARABIA	Riyadh	0	L
SENEGAL	Dakar	0	L
SEYCHELLES	Victoria	0	L
SIERRA LEONE	Freetown	0	L
SOMALI REPUBLIC	Magadiscio	0	L
SPAIN	Madrid	0	M
SRI LANKA	Colombo	0	L
SURINAM	Paramaribo	0	L
THAILAND	Bangkok	0	L
THAILAND	Songkhla	0	L
THAILAND	Udorn	0	L
U.A.E.	Dubai	0	L
UPPER VOLTA	Ouagadougou	0	L
URUGUAY	Montevideo	0	L
USSR	Kiev	0	L
USSR	Leningrad	0	L
USSR	Moscow	0	L
VIETNAM	Saigon	0	L
ZAIRE	Kinshasa	0	L

TABLE 1

STEPS IN THE PRELIMINARY RANKING PROCESS

STEP 1: RELATIVE SEISMIC EXPOSURE
Eliminates buildings in Zones 2 and below

STEP 2: OCCUPANCY
Eliminate buildings which are seldom occupied and which do not house essential equipment

STEP 3: VINTAGE AND LOCATION
For each location, rank buildings according to date of construction

STEP 4: CLASSIFICATION ACCORDING TO BUILDING MATERIAL

STEP 5: PRELIMINARY STRUCTURAL EVALUATION

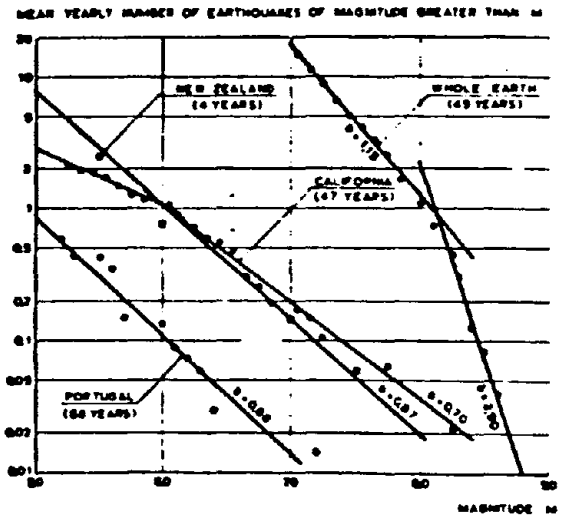

Fig. 1. Mean Yearly Number of Earthquakes of Magnitudes Greater Than M in Portugal, California, and New Zealand

LIST OF SLIDES SHOWN WITH PRESENTATION OF PAPER

Slide 1 - FBO INTRODUCTION
Slide 2 - FBO FACILITIES, SCALE OF MAGNITUDE
Slide 3 - FBO SQUARE FOOTAGE BREAKDOWN OF FACILITIES
Slide 4 - TYPICAL FOREIGN SERVICE POST
Slide 5 - 1931 MANAGUA CHANCERY
Slide 6 - 1967 CARACUS CHANCERY
Slide 7 - 1972 MANAGUA CHANCERY
Slide 8 - 1972 MANAGUA CHANCERY
Slide 9 - 1976 GUATEMALA CITY CHANCERY
Slide 10 - 1976 GUATEMALA CITY CHANCERY
Slide 11 - 1976 GUATEMALA CITY RESIDENCE
Slide 12 - 1976 GUATEMALA CITY RESIDENCE
Slide 13 - 1977 BUCHAREST CHANCERY
Slide 14 - 1977 BUCHAREST CHANCERY
Slide 15 - 1978 THESSALONIKI CONSULATE
Slide 16 - 1978 THESSALONIKI CONSULATE
Slide 17 - 1984 SANTIAGO CHANCERY
Slide 18 - 1984 SANTIAGO CHANCERY
Slide 19 - TOKYO MITSUI HOUSING COMPOUND
Slide 20 - DAR ES SALEM CHANCERY
Slide 21 - DAR ES SALEM CHANCERY
Slide 22 - 1983 BERUIT CHANCERY
Slide 23 - 1983 BERUIT CHANCERY FLOOR PLAN
Slide 24 - 1983 BERUIT CHANCERY COLUMN DAMAGE
Slide 25 - 1983 KUWAIT CHANCERY ANNEX
Slide 26 - 1983 KUWAIT CHANCERY ANNEX
Slide 27 - 1984 BERUIT CHANCERY ANNEX
Slide 28 - 1984 BERUIT CHANCERY ANNEX
Slide 29 - SCHEMATIC, PRESSURE ON BUILDING
Slide 30 - SCHEMATIC, BLAST IMPACT ON FRAME

STRONG MOTION INSTRUMENTATION IN BUREAU OF RECLAMATION PROGRAMS

Robert Mac Donald and Andy Viksne
Bureau of Reclamation

ABSTRACT

The Bureau (Bureau of Reclamation) deployed its first strong motion earthquake instrument array in 1937; however, in the intervening years until the 1971 San Fernando earthquake, only a few additional sites were instrumented. The near-failure of the Lower San Fernando Dam (Lower Van Norman Reservoir) gave new impetus to the installation of strong motion instruments in Bureau dams and related structures and 31 sites are now instrumented. Bureau considerations in the selection of sites to be instrumented and the deployment of strong motion instruments at the various sites are discussed. These considerations have evolved to meet the data requirements for response analyses, and generally conform to typical state-of-the-art practices dealing with strong motion instrumentation of water resource structures.

Keywords: Earthquake; Instrument Array; Strong-motion

1. INTRODUCTION

In 1937, Hoover Dam, located in an area that is considered relatively aseismic, except for occasionally intense but low levels of seismicity, became the first Bureau dam to have strong motion earthquake instruments installed. Until 1970, strong motion instruments were installed at only four other sites in Montana, California, Utah, and Arizona. From 1970, and especially since the near-failure of Lower San Fernando Dam during the 1971 San Fernando earthquake, the Bureau has accelerated its strong motion program and added 26 installations with an additional 12 sites planned for the near future (figure 1). These installations represent only a fraction of the nearly 300 storage dams constructed and operated by the Bureau. As the Bureau network of strong motion instrument sites expands, reevaluation for optimum deployments regarding the many site and instrumentation characteristics are constantly underway. The following paragraphs discuss Bureau guidelines for instrumentation and deployment.

2. SITE SELECTION CONSIDERATIONS

Bureau dams are located throughout the 17 westernmost states of the contiguous United States. Strong motion earthquake instrument deployment at selected dams and other water-resource related structures is taking place and will continue for many years to come. Discussions of site selection factors for strong motion instruments and the distribution of such instruments in the United States have been made by Viksne (1979) and Hudson (1984). The present goal of the Bureau strong motion program is to continue deploying instruments considering the following factors:

(1) Seismic zoning and proximity to faults capable of causing earthquakes

(2) Dimensions of the dam and reservoir

(3) Foundation materials

(4) Method of construction/type of dam

(5) New versus existing dams

(6) Water-resource lifeline features of special interest

The most important factor controlling the Bureau instrumentaton program is the location within prioritized seismic zones. The Bureau uses the Uniform Building Code (1982) Seismic Zone Map as the basic guideline for this purpose

influence strong motion instrument siting priorities. Foundations that contain unconsolidated silts or fine-grained sands and are, therefore, potentially liquefiable are important considerations. Hydraulic fill structures are vulnerable to failures under strong ground motion (Seed, et al, 1977) and may be prioritized for instrumention over earth embankments emplaced with modern compaction methods. Jackson Lake Dam in northwest Wyoming represents a hydraulically emplaced embankment on a potentially liquefiable foundation in seismic zone 3 and very close to Teton fault, considered capable of causing a magnitude 7.5 earthquake. Jackson Lake Dam is not only instrumented, but plans are underway for a more earthquake-resistant structural modification of the dam.

3. DEPLOYMENT AT STRUCTURES

The deployment of strong motion instrumentation (generally referred to as "instrument(s)" in the following paragraphs) in dams requires special site-specific evaluations and consideration of dynamic analysis results (Bolt and Hudson, 1975; Negmatullaev, et al, 1978; Viksne, 1979; Fedock, 1982, 1984; Maley and Etheredge, 1984; Chugh, 1985) when installations are planned. Fedock (1982, 1984) subdivides a hypothetical instrument array into three categories, free-field, input, and response motion instrumentation.

3.1 Free Field Instruments-An ideal free-field strong motion installation will obtain ground motion records that are unaffected by nearby man-made structures, by any enclosure for the instruments, or by unusual topographic sitings. Under these criteria, the installation of ideal free-field instruments may be an elusive goal. The Bureau has located free-field instruments near a number of structure sites, and at some of these sites, free-field is the only type of installation. Fedock (1984) recommends free-field instruments near both abutments and at the toe of an "ideal" dam; such instrumentation to be placed at a distance beyond any significant influence of the dam to the recorded ground motion. For structural analyses purposes, the Bureau does not require free-field installations if an array that includes input and response motion (see below) instrumentation is in place. Some of the Bureau installations are free-field simply because of access or siting limitations around the dams, especially downstream. There are a large number of dams in the United States with nearby "free-field" instruments, for example in California (figure 4). More study is required to determine the extent of the influence of large structures, such as dams and their concomitant reservoir loads and ground water effects, on earthquake strong motion to be certain of structure-independent free-field sites.

3.2 Input Motion Instruments - Input motion instruments may involve surface or subsurface emplacements, or both. For surface arrays at dams, the Bureau locates the input motion components of the strong motion array at the downstream toe and on the abutments as close to the dam as possible. Most of these instruments are placed in prefabricated housings on concrete pads firmly secured to the underlying foundation rock or surficial material. Instruments at the toe are located as close to the maximum section as possible. A field review of a few typical dams selected at random will demonstrate that exterior siting conditions are difficult at the toes of most dams due to backwater from downstream reservoirs, tailwater from power plants, spillways, stilling basins, plunge pools, outlet works, or other features not amenable for instrumentation sites. Similar conditions can exist at the dam/abutment contact area where topographic and access considerations frequently allow little room for satisfactory instrument sites. In the abutment areas, an ideal installation in a spatially restricted area would be a small chamber in the natural material where maintenance problems could be minimized. Interior or subsurface input motion emplacements

(figures 1 through 4). There is no doubt that such zoning is very broad and that there are "zones within zones" that must be considered in the Bureau's sequential deployment of strong motion instruments. Within zones 3 and 4, the zones of highest instrumentation priority, dam locations may vary greatly in respect to proximity of faults capable of causing earthquakes and earthquake magnitude and recurrence exposure levels. Within seismic zone 4 in California, for example, the USGS (Geological Survey), CDMG (California Division of Mines and Geology) and the University of Southern California have located arrays of strong motion instruments where historical seismicity indicates strong motion events will occur in the relatively near future (Rojahn and Borcherdt, 1983; Maley and Etheredge, 1984). An example of a subzone of seismic zone 3 where the Bureau considers significant seismicity possible during the lifetime of its dams is in east-central California, where Boca, Stampede and Prosser Creek Dams are located. Both Boca and Stampede Dams have been instrumented for a number of years and the instrumentation of nearby Prosser Creek Dam is planned (figure 2).

The basic program with regard to seismic zoning calls for the installation of strong motion instruments on all existing storage dams in seismic zone 4 and on most of the significant storage dams in seismic zone 3. Two of the Bureau's large pumping plants, Dos Amigos and Pleasant Valley, in seismic zone 3 have strong motion instruments and instrumentation is planned for two additional pumping plants, Pacheco and Coyote, now under construction and located in seismic zone 4. These two additional pumping plants are of special interest because of their lifeline functions and proximity to the major, active Calaveras and San Andreas faults. The Santa Clara pipeline, which crosses the Calaveras fault between the Pacheco and Coyote pumping plants, will also be instrumented. The Yuma desalization plant, which now has a nearby free field strong motion installation, will be instrumented upon completion of construction in the near future.

Newer dams, outside of seismic zones 3 and 4, have been or are planned for strong motion instrumentation because of engineering concerns for a complete suite of dam instrumentation, including strong motion. This concern may occasionally transcend seismic zone boundary and seismic exposure considerations. Bureau strong motion instrumentation planning does, however, take into account site-specific detailed seismotectonic studies throughout the Western United States that are done by the Bureau, other agencies, and private industry. These studies are extending our knowledge of causative earthquake structures such that existing seismic zoning, in terms of magnitude and seismic recurrence to be expected, will require modifications and refinements. The Bureau, therefore, views seismic zone maps as state-of-the-art guidelines which can be modified by engineering judgement. Strong motion instrumentation, as related to water resource structures throughout the Western United States, is concentrated in seismic zones 3 and 4, but still widely distributed throughout seismic zone 2 (figures 3 and 4).

Early in the Bureau's strong motion program, large dams and reservoirs had high priority for strong motion instrumentation because of size and not because of seismic zoning. Therefore, Hoover, Hungry Horse, Bradbury, Flaming Gorge, and Glen Canyon Dams had strong motion instruments installed as a construction-related activity from 1937 to 1960. Only one of these dams, Bradbury, located in southern California, is in seismic zone 3 or 4.

The present Bureau practice is to consider seismic zoning as the predominant siting factor, but size, foundation materials and method of construction are other parameters which may

consist of borehole instrumentation in the foundation of earth dams and installations in selected galleries of concrete dams. Drainage and grouting galleries, when excavated in earth dam foundations, can be utilized as input motion sites for strong motion instruments.

Many Bureau dams are built on deep deposits of unconsolidated surficial materials in the bottoms of valleys and canyons. If such deposits represent the typical foundation conditions at the base of a dam, then input motion is best represented from instrumentation located on the surficial materials as close to the base of the dam as feasible, and not, for example, on any bedrock that might be outcropping in the area. However, at some sites, both bedrock and surficial deposits may be instrumented.

3.3 Response Motion Instrumentation-The Bureau ideally installs one or two response instruments on the crest of both earth and concrete dams. The primary location is where maximum deformation during strong motions is expected. This primary location is, based on past analyses, usually at the maximum section. Many Bureau dams are asymmetrical because of differences in abutment slopes, stream channels not in the center of the valley, or other topographic features often related to geologic structures. The maximum section, therefore, may be far from the actual center of the dam crest. Other locations may be selected such as about one-third of the crest length from an abutment and/or on the downstream of the face of the dam. These locations are basically for backup and special applications. Additional strong motion instrument locations throughout concrete or embankment dams may be desired for dynamic analyses after earthquakes.

If a dynamic analysis of a structure has been done prior to strong motion instrument deployment, the response instrument locations would be specified based on the analysis. Specific locations would be where lower safety factors and higher loads are expected. These locations would be site specific for each structure and for earth dams depend upon: (1) zoning geometry of the dam, (2) types of materials used in the zones; and (3) the nature of the foundation.

Figure 5, showing a plan and section of Sugar Pine Dam in California, is an example of a relatively large instrument array. There are four downhole accelerometer units in Sugar Pine Dam. One is located on bedrock for input motion and the others in the dam in zones 1 and 3A for response motion.

For embankment dams, instruments are installed on or in selected embankment material zones through the use of surface sites or boreholes. Access is important in such selections. The galleries in many concrete dams usually allow a choice of internal locations. Ideally, the response and input strong motion instrumentation will be located in the same crosssection normal to the longitudinal axis of the dam and thus provide the basis for analyses that compares calculated with actual response of the dam to earthquake loadings.

3.4 Payback Records-Payback records, meaning the Bureau received good strong motion records from its investment in instrumentation, were obtained at Pleasant Valley Pumping Plant, one of two Bureau pumping plants currently having strong motion instruments. The Pleasant Valley Pumping Plant had a maximum input (at the base) acceleration of 0.33g recorded during the May 2, 1983 Coalinga earthquake (figure 6). Minimum instrument placement at these pumping plants require instruments to be located at the ground surface or near the foundation/structure contact and at the top of the steel superstructure to obtain data for an adequate response analysis (figure 7).

In comparing the pumping plant foundation strong motion records with those of the switchyard (figure 6 and 8), it is seen that the switchyard or "free-field" instrument recorded peak horizontal accelerations slightly over 50 percent larger than those of the foundation in both the main magnitude M_L = 6.5 earthquake of May 2, 1983 and the M_L = 5.1 aftershock of May 9, 1983. The epicentral and hypocentral distances were 9 km and 14 km, respectively, for the May 2 earthquake and 10 km and 16.4 km, respectively, for the May 9 aftershock. The topographic effects on ground motion are emphasized in this case. The input motion peak acceleration is lower than the "free-field" motion because the input motion instrument is at the base of the pumping plant in a deep excavation in piedmont alluvial fan deposits, whereas the switchyard "free-field" instrument is located near the top of the cut slope of the pumping plant excavation (figure 7). As previously discussed under "free-field instruments", the pumping plant mass could have had some influence on the ground motion and could have dampened it during both the May 2 earthquake and the May 9 aftershock.

The two response motion instruments located on the first floor and on a steel beam just beneath the roof of the pumping plant experienced instrument malfunction and false triggering due to crane operation vibrations before the main earthquake shock and no records were obtained. The film was replaced and accelerations from some of the aftershocks were recorded. In the aftershock of May 9, 1983 the basement instrument recorded a maximum horizontal acceleration of 0.14g while the roof instrument recorded 0.24g. Since, during the main shock, a horizontal acceleration of 0.33g was recorded in the basement, a proportional extrapolation would indicate that a horizontal acceleration of over 0.5g could have occurred during the main earthquake in the superstructure of the plant. False triggering at the Pleasant Valley Pumping Plant has been eliminated by making the basement instrument the primary starter and interconnecting it to the other instruments in the plant. An option to eliminate false triggering would have been to reset the threshold acceleration of the first floor and "roof" instruments at a higher level than 0.01 g, at which (presently) all Bureau accelerographs are set.

In California, the Pacheco and Coyote pumping plants, as well as the Santa Clara pipeline, will be situated much closer to the active San Andreas and Calavaras faults than the Dos Amigos and Pleasant Valley pumping plants, which already have strong motion instruments. The Santa Clara pipeline, located between the Pacheco and Coyote pumping plants, will cross the Calaveras fault. Instruments that will alert the pipeline operations center of predetermined levels of strong ground motion (probably 0.25g) at the pipeline-fault crossing are planned, such instrumentation to utilize a typical electromagnetic trigger to actuate a warning device and to give an alert. This instrumentation will also automatically cause a shut off of water flows in the Santa Clara pipeline until onsite inspections can be performed after triggering-level earthquakes. Similar electromagnetic triggers are used as switches in nuclear power plants (Rihn and Beckmann, 1979). Seismic alarm devices (prototypes) using vertical accelerometers as accelerograph triggers and used to actuate warning horns and lights, have been designed and are in use by the Corps of Engineers for water resource related life-line structures (R. Ballard, personal communication). These Corps of Engineers seismic alarm devices are installed at seven sites in California.

4. TYPES OF STRONG MOTION INSTRUMENTS DEPLOYED BY THE BUREAU AND SOME INSTALLATION CONDITIONS

Except for a few older model RFT-250 and RFT-350 accelerographs, the Bureau utilizes SMA-1

accelerographs on all surface installations. Models FBA-3 and FBA-13 accelerometers are utilized in boreholes. All borehole accelerometers are installed in conjunction with CRA-1 recorders. Manufacturer's specifications and other papers (Pauly, 1984) discuss details of these instruments.

All of the self-contained accelerographs are three-component, optical mechanical units which produce analog records. A component system is used for several borehole systems, wherein accelerometers and a starting device are placed in the borehole, and are hard-wired to a centralized recording unit at some remote location. The self-contained and borehole systems photo-optically record the data. The systems remain in a standby condition until ground motions (0.01g or more) are detected by the seismic trigger which then actuates a recording lamp and a film (70 mm) drive motor contained in every system.

As mentioned earlier, most of the surface instruments are located in prefabricated housings and bolted onto concrete pads. The pads are usually designed so that they have a natural frequency (30-32 H_Z), which is higher than the frequency of the accelerometers (20 H_Z range) and considerably higher than seismic frequencies of interest (Bureau of Reclamation, 1985). Instruments placed in the interior of dams, such as those in the galleries of a concrete dam or, less frequently, in drainage or grouting galleries under embankment dams, may be bolted to the floor of the gallery or gallery alcoves. The three component accelerographs contain three accelerometers in orthogonal arrangement with the horizontal units both parallel and perpendicular to the longitudinal axis of the dam (tangentially and perpendicularly if an arch dam).

Downhole accelerometers originally were installed in boreholes and then grouted into place. In order to deal with instrument malfunction, current practice is to attach a stress cable to the instrument and to backfill around the triaxial downhole units with pea gravel. In this way an option of washing the instrument free of the gravel pack and then removing the instrument from the hole is retained. Borehole strong motion instruments have been successfully installed and removed by the Bureau using a gravel pack and cable during installation.

5. OPERATION AND MAINTENANCE CONSIDERATIONS

Optical-mechanical, self-contained accelerographs which record on 70 mm photographic film are the most widely used strong motion type worldwide due to their low cost, high reliability, simple operation, and straight forward maintenance/repair procedures (Pauly, 1984). They are preferred over both analog and digital tape and solid state recording methods; however, improvements in these alternate types continue to be made. After triggering, up to 25 cumulative minutes of motions equal or stronger than 0.01g can be stored (recording continues for 10 seconds after motions drop below 0.01g level).

Several calibration tests, both laboratory and field, must be conducted before the instruments are installed. Instrument sensitivity, or the deflection of the seismograph trace under 1.0g loading, is generally performed by the manufacturer under laboratory conditions before the equipment is brought to the field. Calibration tests for damping and natural frequency are easily performed in the field. These calibration tests are recorded at the beginning and end of each roll of film.

Two timing traces are continuously recorded with the earthquake ground motions. One of these traces is always a square wave pulse produced internally. The second trace may be another square wave pulse, a binary time code controlled by an accurate oscillator and set according to an external clock, or, more commonly, a WWVB Bureau of Standards radio signal time code. The timing is necessary so that each motion event can be clearly identified for correlation with events on other records.

Most of the maintenance of Bureau strong motion instruments is carried out through a cooperative effort between the Bureau and the USGS. Typically, a technician checks the instrument installation every six months and removes the exposed portion of the film if the instrument has been triggered. If a significant earthquake occurs in the vicinity of an instrumented dam, an additional check is made for strong motion records. If strong motion has been recorded, the analog record is routinely digitized, corrected for film distortion, variable film speed, and instrument response, and the record filtered to remove long period noise.

The maintenance of the Bureau's strong motion arrays is complicated by the diversity of the sites, such as extremes in elevation and climate. Both heat and cold have to be dealt with; the addition of sun roofs and improved air circulation by venting has lessened heat problems, while electric heating and insulated shelters have dealt with extremely cold conditions. Drainage is an important aspect of surface instrument sites, and poor drainage has temporarily caused operational problems and shutdowns. In attempts to locate instrument housings out of the way of access roads and work areas, the housings have been located close to cut slopes. Sloughing material and minor slides have both threatened and caused damage to housings at these sites. Small concrete revetments now protect several housings.

6. DISCUSSION - STRONG MOTION INSTRUMENTATION IN BUREAU PROGRAMS

The safety of its dams and continued research into design, construction, and maintenance of water resource features are primary concerns of the Bureau's mission. The relationship of the installation of strong motion instruments with structural safety is not quite direct. For Bureau purposes, strong motion instruments are primarily research tools for understanding structural response to earthquakes.

In order for an instrument array to have any payback, it is necessary for the structure in question to be subjected to strong earthquake motions. The closer those motions are to damaging motions, the more knowledge is to be gained.

Strong motion records of seismic events wherein significant shaking occurred in dams are very few. Those records that are applicable to dams of modern construction are even fewer. Thus, available strong motion data, in relation to dam design, are small in quantity and poorly applicable. Nevertheless, existing strong motion data are valued for the confidence they produce when applying, in design considerations, parameters judged to be adequate dynamic loadings.

The preceding discussion has presented a perspective of strong motion instrumentation in Bureau programs. This is useful in further discussion that follows involving strong motion issues such as utilization of data, cost-effective equipment, optimum deployment, function completion and additional research needed.

6.1 Utilization of Data - The primary value of strong motion data to water resource structure design engineers is that the accrued data can be used to check that actual response of structures to earthquakes are within design

limits and that the actual response conforms to assumed response. This was accomplished successfully at Pleasant Valley Pumping Plant. For example, structural periods determined by a dynamic analysis of a finite element model conformed to structure periods (response motion) recorded during the 1983 Coalinga earthquake at the Pumping Plant.

6.2 Cost - Effective Equipment - The use of relatively low cost and reliable optical-mechanical self-contained accelerograph is planned for all surface sites. Digital recording accelerographs will continue to be considered as alternatives, especially as technical modifications are constantly being made in improving efficiency, reliability, and sensitivity of the digital system.

There has been a less then desirable operating reliability of the borehole units. Even though the Bureau's installation plan for "sanding in" these borehole instruments with pea gravel and an attached stress cable is satisfactory for retrieval and replacement, the deployment of borehole instruments is presently being reevaluated.

6.3 Optimum Deployment-The general requirements for a strong motion instrument array at a damsite have been previously discussed. When dealing with the site-specific aspects of instrumenting a dam, however, detailed consideration of constraining factors in surface and subsurface deployment are necessary. These considerations may be as simple as maintenance access or may require a detailed study of an embankment dam's material and zoning, available gallery locations in concrete dams, or a knowledge of traffic patterns and operational activities with their subsequent limitation of sites.

Optimum deployment will be achieved when analysis requirements have been satisfied by the most efficient and dependable instrumentation siting pattern. The initial cost of the equipment, the cost of the site preparation, which is relatively high if borehole instruments are utilized, and maintenance costs must be reasonable.

Optimum deployment regarding instrument locations relative to dams and other related structures requires considerable study of each site. The effect of topography on ground motion is not well understood; this aspect of strong motion is considered in more detail under the discussion of additional research needs which follows.

6.4 Function Completion-In most Bureau studies and investigation programs the following question has to be answered: "When has this investigation program collected enough data to be satisfactory for the purpose intended?" All too often time and funding factors make the decision. Refined investigations after basic data are gathered frequently belong in the "level of diminishing returns" and in Bureau design the lack of such refinements can often be relegated to an area synonymous with "engineering risk."

Strong motion instrumentation in the Bureau is subject to the same scrutiny as any other program in the name of economy and "payback", and with the advent of significant ground motion and subsequent records at a site, the function completion of that strong motion instrumentation should be considered. In this context, the 1983 actuation of the Pleasant Valley Pumping Plant array by strong motion raises an issue regarding the value to the Bureau of continuing deployment at this location. The following facts are pertinent: (1) The ground motion and subsequent loadings on the pumping

plant are probably the maximum that can be expected. Even though the earthquake main shock was of moderate magnitude, the epicentral distance was only 9 km from the pumping plant, (2) Another similar earthquake is not expected within the lifetime of the pumping plant (the return period for similar or greater earthquakes on the causative fault structure is estimated at 350 years [Geological Survey, 1984]), (3) Analyses have indicated an acceptable structural response and no structural damage resulted.

6.5 Research Needs-Much research is currently underway in the study of earthquake strong motion; however, three research areas stand out as being particularly applicable to optimal array deployment at dams. The first area involves the site topography, especially the effect of the proximity of valley slopes or canyon walls on ground motion. The shape and height of valley slopes are probably factors. Davis and West, 1973, Chang, 1980, and Chang, 1985, discuss topographic effects on strong ground motion from empirical observations. The second area involves the effects on strong ground motion of surficial deposits (soils), especially, under large water resource structures. The third area involves the effects of dams and reservoirs on strong ground motion. Long-term, detailed, empirical studies are visualized as necessary to gather adequate data for analyses.

7. REFERENCES

[1] Ballard, R.F., Jr., Earthquake Engineering and Geophysics Division, Waterways Experiment Station, Corps of Engineers, Vicksburg, Mississippi, personal communication, April 1985.

[2] Borcherdt, R.D., "The Coalinga Earthquake Sequence Commencing May 2, 1983," Geological Survey Open-File Report 83-511, 1983.

[3] Bolt, B.A. and Hudson, D.E., Seismic Instrumentation of Dams," Journal of the Geotechnical Engineering Division, ASCE, November 1975.

[4] Bureau of Reclamation, "Bureau of Reclamation Strong Motion Instrumentation Site Characteristics," Department of the Interior, Denver, Colorado, 1985.

[5] Chang, F.K., "The Effects of Elevation and Site Conditions on Ground Motion of the San Fernando, California, Earthquake, 9 February 1971," Proceedings of the Seventh World Conference on Earthquake Engineering, Volume II, Istanbul, Turkey, September 1980.

[6] Chang, F.K., "Analysis of Strong-motion Data from the Mount Borah, Idaho, Earthquake of 28 October 1983," Miscellaneous Paper GL-85-12, U.S. Army Engineer Waterways Experiment Station, Corps of Engineers, Vicksburg, Mississippi, May 1985.

[7] Chugh, A.K., "Dynamic Response Analysis of Embankment Dams," International Journal for Numerical and Analytical Methods in Geomechanics, 1985.

[8] Davis, L.L. and L.R. West, "Observed Effects of Topography on Ground Motion," Bulletin of the Seismological Society of America, Volume 63, No. 1, pp. 283-298, February 1973.

[9] Fedock, J.J., "Strong-Motion Instrumentation of Earth Dams," Geological Survey Open-File Report 82-469, 1982.

[10] Fedock, J.J., "Strong-Motion Instrumentation of Earth Dams," Proceedings of the Eight World Conference on Earthquake Engineering, Volume VII, San Francisco, California, July 1984.

[11] Hudson, D.E., "Strong Motion Accelerograph Systems - Problems and Prospects," Proceedings of the Eighth World Conference on Earthquake Engineering," Volume II, San Francisco, California, July 1984.

[12] Kuribayashi, E., H. Tsuchida and M. Watabe, "Maintenance of the Strong-Motion Accelerograph and the Data Processing of the Records," Proceedings of the Seventh Joint UJNR Panel Conference, Tokyo, Japan, May 1975.

[13] Maley, R.P., "The United States Strong-Motion Network: Field Operations," Proceedings of the Seventh Joint UJNR Panel Conference, Tokyo, Japan, May 1975.

[14] Maley, R.P., and E.C. Etheredge, "The Development of Ground and Structural Response Strong-Motion Instrumentation Arrays in the United States," Proceedings of the Eighth World Conference on Earthquake Engineering, Volume II, San Francisco, California, July 1984.

[15] Negmattulaev, S. Kh., G.S. Seleznyov, D.W. Simpson and C. Rojahn, "Engineering and Seismological Observations at Dams," Proceedings of the Second International Conference on Microzonation, Volume II, San Francisco, California, 1978.

[16] Pauly, S.E., "Strong Motion Accelerograph Selection," Proceedings of the Eighth World Conference on Earthquake Engineering, Volume II, San Francisco, California, 1984.

[17] Rihn, W.J. and W.J. Beckmann, "Electromagnetic Starters for Strong Motion," Kinemetrics Application Note No. 15, Pasadena, California, August 1979.

[18] Rojahn, C. and R.D. Borcherdt, "On the status of In Situ Strong Ground Motion and Structural Response Investigations," Proceedings of the Fourteenth Joint UJNR Conference, pp. 617-654, 1983.

[19] Seed, H.B., F.I. Makdisi and P. DeAlba, "The Performance of Earth Dams During Earthquakes," Report No. UCB/EERC-77/20, Earthquake Engineering Research Center, College of Engineering, University of California, Berkeley, California.

[20] Uniform Building Code, Seismic Zone Map of the United States, 1982.

[21] Viksne, A., "Bureau of Reclamation Strong Motion Instrumentation Program," Proceedings of the Third National Congress on Pressure Vessels and Piping, San Francisco, California, June 1979.

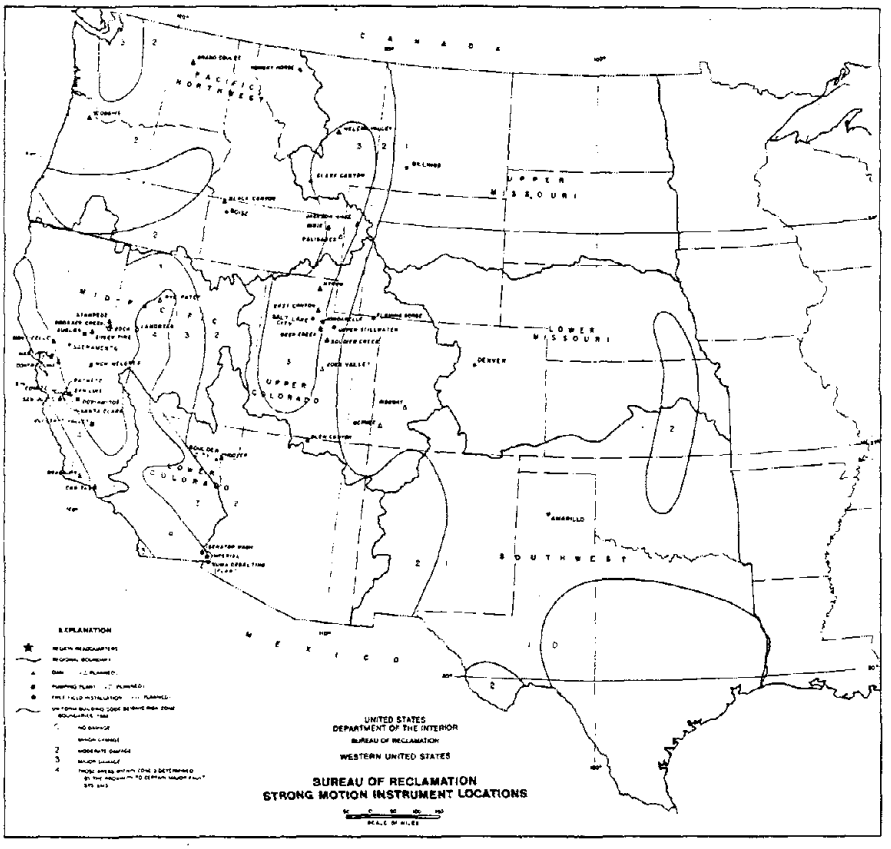

Fig. 1 Distribution of Bureau of Reclamation strong motion installations.

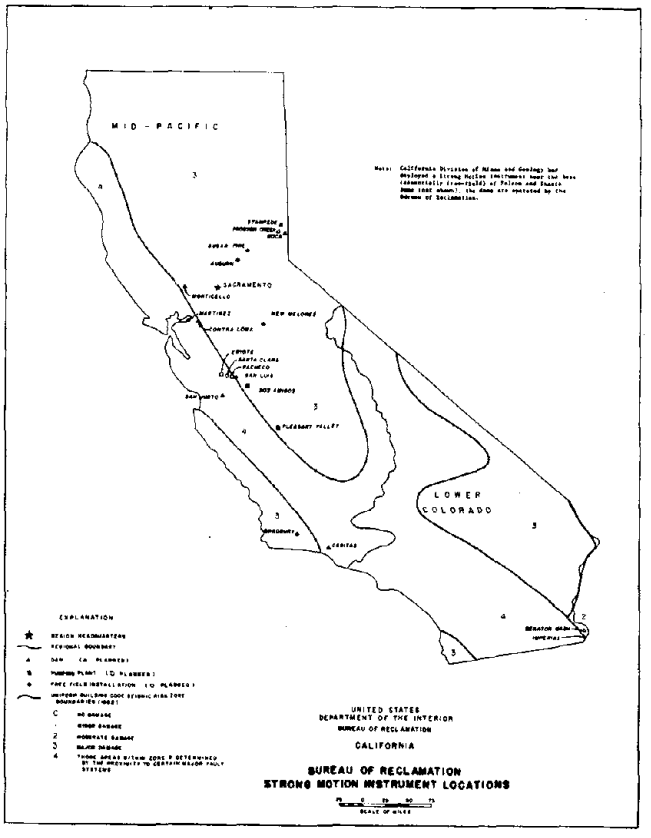

Fig. 2 Distribution of Bureau of Reclamation strong motion installations in California.

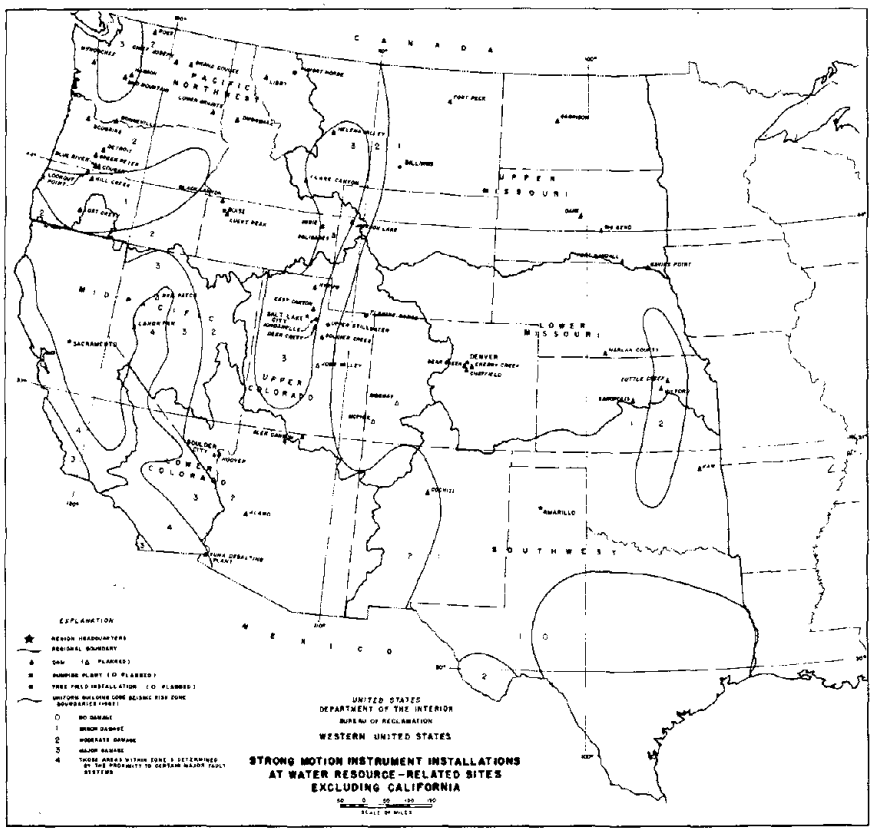

Fig. 3 Distribution of strong motion installations at water resource features throughout the western United States — excluding California.

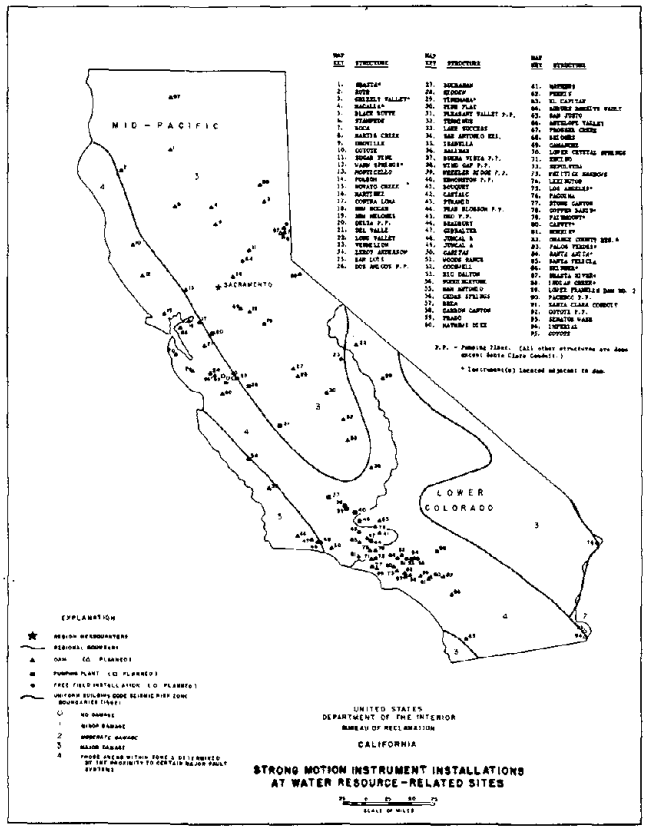

Fig. 4 Distribution of strong motion installations at water resource features throughout California.

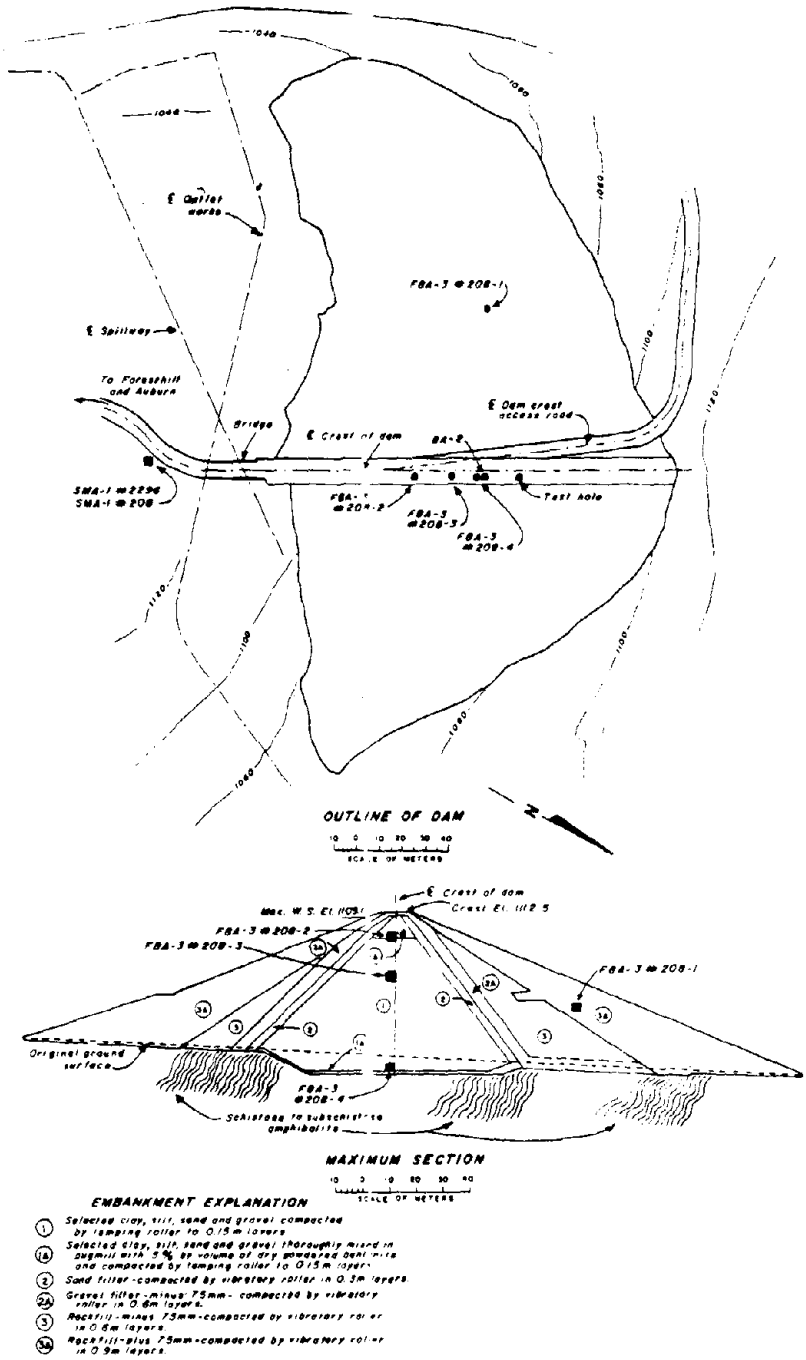

Fig. 5 Plan and section of Sugar Pine Dam showing strong motion instrument locations.

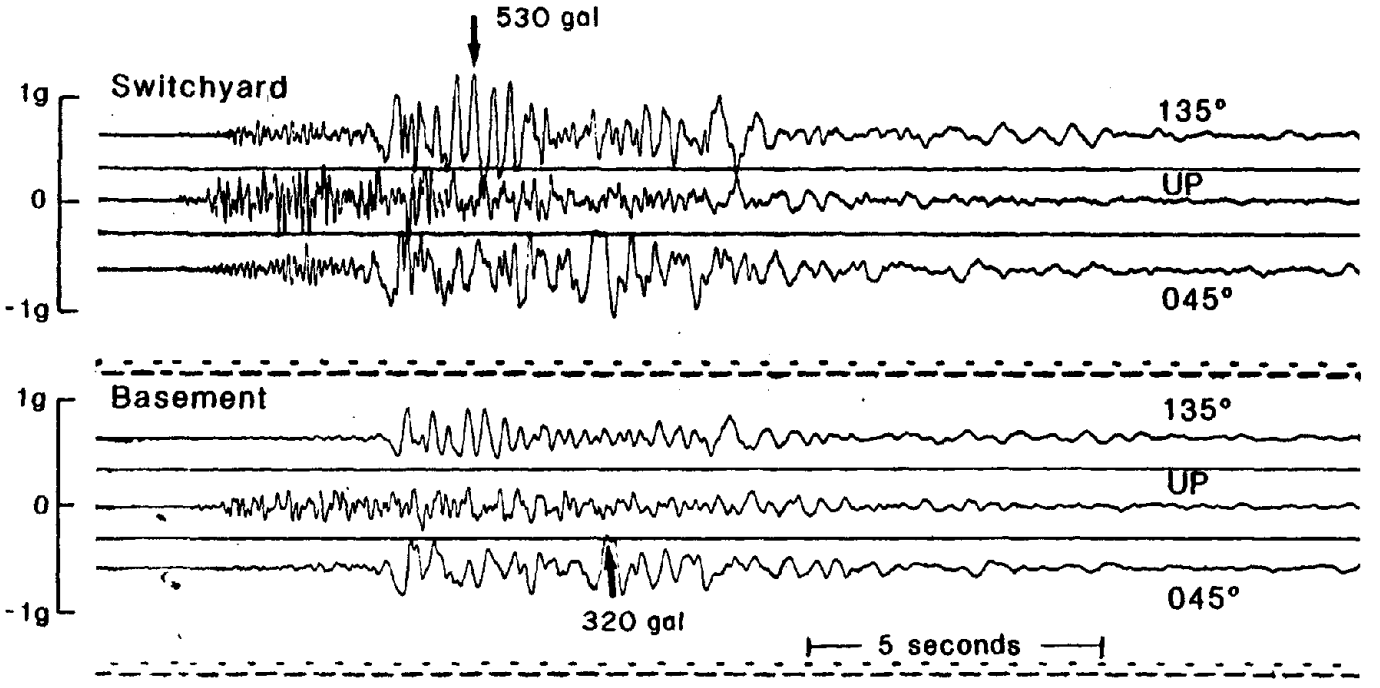

Fig. 6 Strong motion records from Pleasant Valley Pumping Plant during main shock of Coalinga Earthquake, May 2, 1983 (after Borcherdt, 1983).

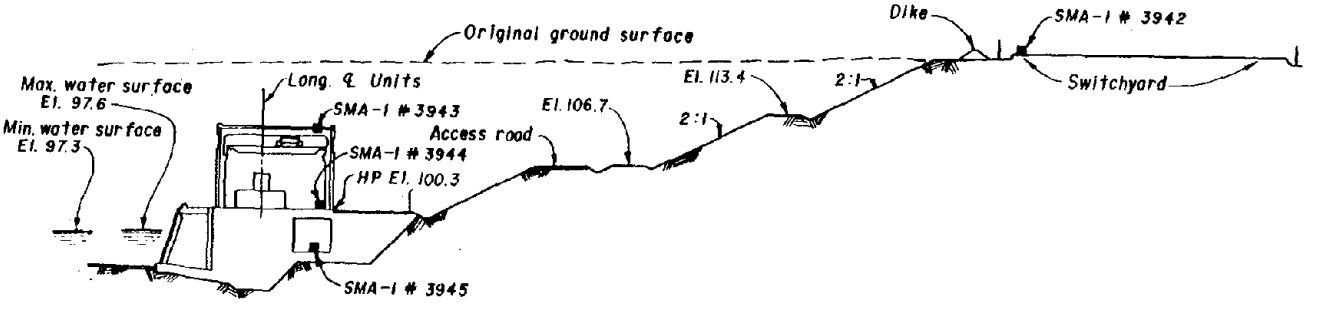

Fig. 7 Section through Pleasant Valley Pumping Plant showing location of strong motion instruments.

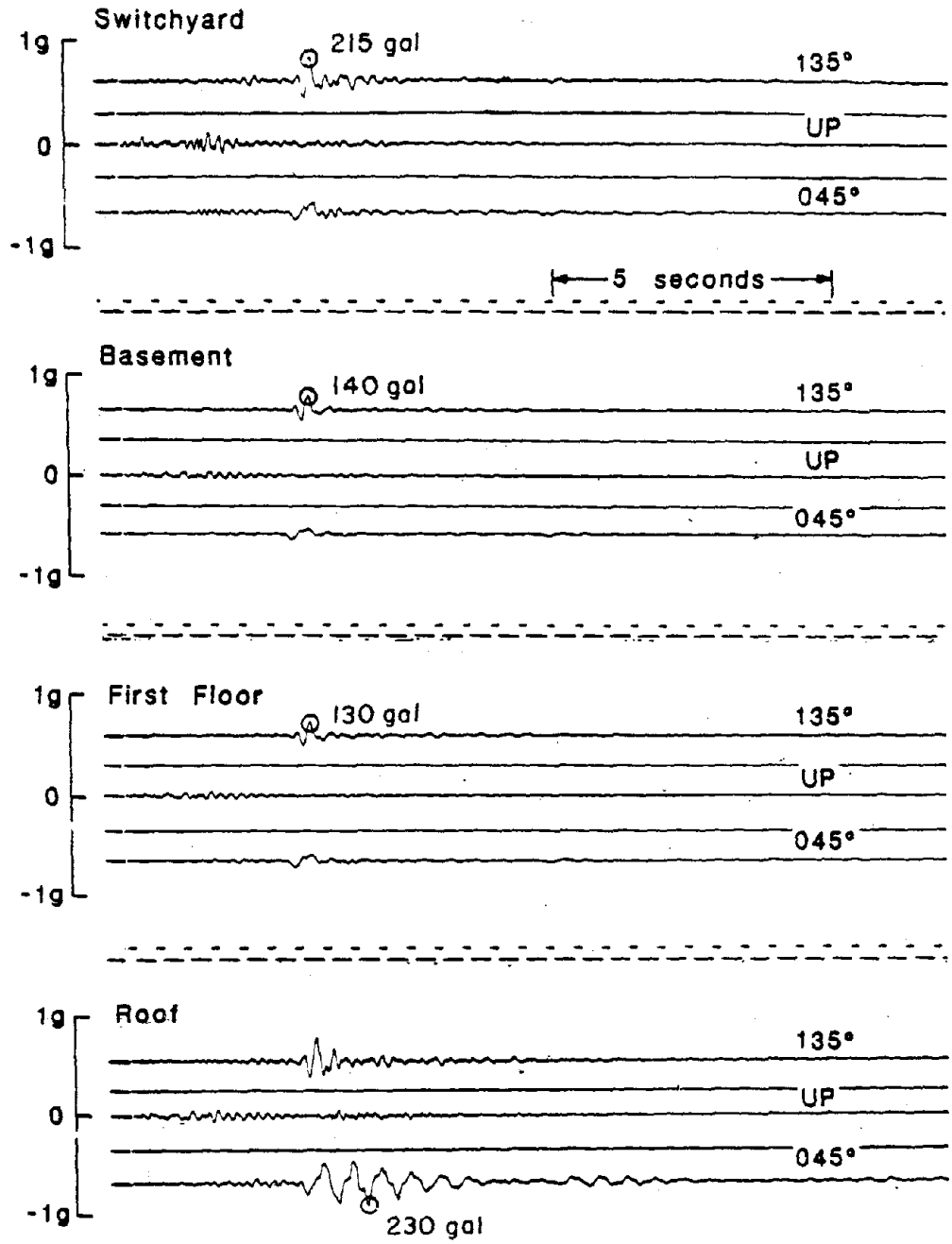

Fig. 8 Strong motion records from Pleasant Valley Pumping Plant array during Coalinga Earthquake aftershock of May 9, 1983 (after Borcherdt, 1983)

ARRAY OBSERVATION OF STRONG-MOTION EARTHQUAKES IN THE FUCHU AREA

BY

Keiichi OHTANI, Shigeo KINOSHITA,

Tadashi MIKOSHIBA

ABSTRACT

In order to investigate the earthquake response of thick sedimentary layers in the Tokyo metropolitan area, the National Research Center for Disaster Prevention has been performing strong-motion observations. For that purpose, two types of the observational systems arrays at the Fuchu area, i.e., the vertical array by four triaxial accelerometers and the horizontal array by five velocity-meters, have been established.

In this report, we will introduce the outline of the observational study at the Fuchu area located in the west of Tokyo, the velocity-type strong-motion seismograph, and the observed examples of seismic waves propagating in the thick sedimentary layers.

Keywords: Earthquake; Strong-motion

1. INTRODUCTION

In the Tokyo metropolitan area, the sedimentary layers of several kilometers in thickness on the Pre-Tertiary basement, are among the most important factors of earthquake disasters. Therefore, several studies have been performed to estimate the velocity structures of the thick sedimentary layers and base layer, to observe the strong-motion waves on and in such layers, and to simulate the observed waves theoretically. The National Research Center for Disaster Prevention (NRCDP) has proceeded with the observational study of strong-motion earthquakes in the metropolitan area.

In this report we will introduce an observational study at the Fuchu area located west of Tokyo. The purpose of observation at the above-mentioned area is to investigate the earthquake response of the thick sedimentary layers. The seismic waves within the period of 7 to 10 seconds are predominant because of the modulation effects by the thick sedimentary layers. In such period ranges, the velocity waves are emphasized as compared with the acceleration waves. Also, the velocity-type strong-motion seismographs are now accurate enough for practical usage. Therefore, the velocity-type strong-motion seismograph array has been constructed at the Fuchu area.

2. ARRAY OBSERVATION OF STRONG-MOTION EARTHQUAKES

2.1 OUTLINE OF OBSERVATION

The observational sites are located at the Fuchu area in the west of Tokyo (see Figure 1). This array consists of the center site FCH (Fuchu crustal activity observatory) and five satellite sites: ING, KFC, TMA, HFC, AND CHF. A triaxial velocity-type seismograph is installed at all sites.

At site FCH, three boreholes were drilled with depths of 200 m, 500 m, and 2,750 m, respectively. The bottom of the deepest borehole of 2,750 m is 750 m below the upper boundary of the Pre-Tertiary basement. A triaxial force-balanced type accelerometer is installed at

the bottom of each well. The same accelerometer is also installed on the surface ground at the site. Each seismometer is connected to a digital event recorder. The seismic signals are digitized as 12-bit words at 50 samples per second. Each recorder has digital delay memory which stores the seismic signals for 10 seconds, and a common time base. The crystal clock of each instrument is corrected every day by radio. By January 1983, all instruments were in place.

The actual extent of velocity structure variations is already known in some measure, from borehole information (velocity loggings) from site FCH and the results of seismic prospecting by using the explosions. Table 1 is the result of estimated velocity structures of shear-wave from site FCH. The sedimentary layers over the Pre-Tertiary basement have a thickness of about 2 kilometers. In this array area, the Pre-Tertiary basement is dipping from the west to the east. Based upon the results shown in Table 1, shear waves with the period of from 7 to 10 seconds are predominant at site FCH. But, the basement is dipping from the west to the east in this area so that the above-mentioned predominant shear waves have different characteristics, as compared with the response characteristics of SH-waves propagating in horizontally layered models.

2.2 Velocity-Type Strong-Motion Seismograph

We have used a new velocity-type strong-motion seismograph in this array observation. This seismograph is installed on the ground surface at each site.

In this section, we mention simply the content of the new velocity-type seismograph. The fundamentals of this seismometer are shown in Fig. 2. Voltages $e_s(t)$ is generated across the terminals of a signal coil that is fixed to the mass m and is moved through a magnetic field with velocity $\dot{x}(t)$. The motion $x(t)$ of a pendulum is relative to the seismometer frame. The voltage $e_s(t)$ is proportional to this relative velocity $\dot{x}(t)$ between mass and magnet. The constant of proportionality is the generator constant G_s.

The induced voltage $e_s(t)$ is fed into a servo-amplifier with a gain of A_1 so that the output voltage of amplifier is $e_v(t) = A_1 e_s(t)$. By the voltage $e_v(t)$, feedback current $i_f(t)$ flows through the feedback circuit as follows:

$$i_f(t) = A_1 G_s \dot{x}(t)/z_t \qquad (1)$$

where z_t is impedance of the feedback circuit. The current $i_f(t)$ produces the restoring force $G_f i_f(t)$ acting on the mass. G_f is the motor constant of the feedback coil.

It follows that the equation of the pendulum's motion is

$$\ddot{x}(t) + \omega_0^2 x(t) = -\ddot{y}(t) - G_f i_f(t)/m \qquad (2)$$

where $y(t)$ is ground displacement and ω_0 is natural angular frequency.

When the spring constant is k, ω_0 is natural angular frequency.

When the spring constant is k, w_o equals to $\sqrt{k/m}$. From equation (1), equation (2) has a following solution for h>>1:

$$\dot{x}(t) = -\frac{1}{2h_{w_o}}\dot{y}(t) \qquad (3)$$

where

$$h = \frac{A_1 G_s G_f}{2 m_{w_o} z_t} \qquad (4)$$

The feedback current is fed into a current amplifier with the gain of A_2. For $A_2 \gg 1$, the output current of the amplifier is represented as follows:

$$i_o(t) \fallingdotseq -\frac{1}{C R_f}\int i_f(t)\,dt, \qquad (5)$$

where R_f is output impedance of the amplifier. With a load resistance R_0, the final output voltage $e_0(t)$ is following results from equations (1), (2), (3), and (5):

$$e_o(t) = \frac{R_o i_o(t)}{\frac{m R_o}{G_f C R_f}}\dot{y}(t). \qquad (6)$$

The voltage $e_0(t)$ is in proportion to ground velocity. The absolute value of seismometer sensitivity is determined by mass m, load resistance $R_0/C\ R_f$ and motor constant G_f. Amplifiers and signal detector do not influence the accuracy of measurement.

The actual seismometer used in practical seismometery has specifications shown in Table 2. Fig. 3 shows the overall frequency characteristics. In our seismometry, the sensitivity of the seismograph is 50 mV/kine. Photo 1 shows the velocity-meter and the recorder.

3. EXAMPLES OF OBSERVED WAVES

Fig. 4 is an illustration of recorded waveforms across the whole array. This record demonstrates clearly the process in which a direct shear wave is modulated by the thick sedimentary layers.

The record was obtained during the earthquake which had origin at the Eastern Yamanashi Prefecture. It is a well known fact that earthquakes whose origins are located in the Eastern Yamanashi Prefecture are convenient for investigation of the effects of wave propagation in the thick sedimentary layers of the metropolitan area. This fact is based on the total reflection of seismic waves at the upper boundary of basement.

The earthquake of Feburary 14, 1984 (M=5.2) which produced the NS-component record shown in Fig. 4, is regarded as an aftershock of an earthquake of August 8, 1983 (M=6.0). The N-S component is almost identical to SH-component. The wave train shown in Fig. 4 has five parts: P-wave and its coda, direct S-wave (S_0), two total reflected pulses of S_0 (S_1 and S_2), later large amplitude wave packets, and final coda wave. The waves S_0, S_1, S_2 and later packets appear to be necessary to explain the shear wave modulated by the sedimentary layers.

The pulses corresponding to S_0, S_1, and S_2 in the wave trains recorded by velocity-meters installed on the ground surface are clearly seen in the records by bore-hole observation. Two pulses S_1 and S_2 are phase modulated waves of S_0, propagating between the surface of the basement and the ground surface, a kind of multiple reflection. Phase velocities of S_0, S_1, and S_2 in Fig. 4 are 3.9 km/s, 2.1 km/s

and 1.7 km/s, respectively. These values show that these pulses are propagating in down-dip direction.

The SH-waves with predominant periods of about 8 seconds will be modulated to equal the pulses S_0, S_1, and S_2. To observe this, the bandpass filtering with the central frequency 0.125 Hz and the damping factor 0.2 is applied to the transverse component records obtained at the site TMA. Fig. 5 shows these results and also those of two records obtained during the earthquakes of the Western Nagano Prefecture. Fig. 5, then, shows that when the magnitude of an earthquake is large, the seismic wave with a period of about 8 seconds develops, and that the wave shapes with a period of about 8 seconds are almost equal, independent of the magnitude of earthquake.

This fact is explained by making use of Hilbert transform. An example of model wave, which is obtained by considering the dipping structure of basement, is also shown in the same figure.

4. CONCLUDING REMARKS

This report is an introduction of the Fuchu array observation progression by NRCDP. We explained the outline of observation and the examples of seismic waves propagating the thick sedimentary layers.

Quantitative study is underway now, and will be reported at a later date.

5. ACKNOWLEDGMENTS

The present work would not have been possible without the aid of the members of the second research division of NRCDP. In particular, the authors would like to thank Dr. H. Takahashi, Mr. M. Takahashi, Mr. H. Suzuki, and Mr. K. Itoh.

6. REFERENCE

Yamamizu, F., Takahashi, H., Goto, N., and Ohta, Y., 1981, Shear wave velocites in deep soil deposits, *Zisin*, v. 34, p. 465-479 (in Japanese).

Table 1. Velocity structure of the S-waves at the site FCH. (after Yamamizu, *et al.*, 1981)

No.	Thickness (m)	Velocity (km/s)	Density (t/m^3)
1	4	140	1.7
2	12	350	1.8
3	6	420	1.8
4	22	360	1.8
5	6	530	1.8
6	6	600	1.9
7	20	440	1.8
8	14	460	1.9
9	115	540	2.0
10	856	780	2.0
11	963	1190	2.2
12	726	2530	2.5
13		2530	2.5

Table 2. Specifications of seismometer

(1)	Mass (m)	43 gram
(2)	Natural frequency (f_0)	1.43 Hz
(3)	Generator constant (G_s)	2.5 volt/kine
(4)	Motor constant (G_f)	2.86×10^6 dyne/A
(5)	Amplifiers	
	Voltage gain of A_1	54 dB
	Current gain of A_2	> 90 dB
(6)	Load constants	
	C	1 μF
	R_f	1 MΩ
	R_t	0.1 - 1kΩ

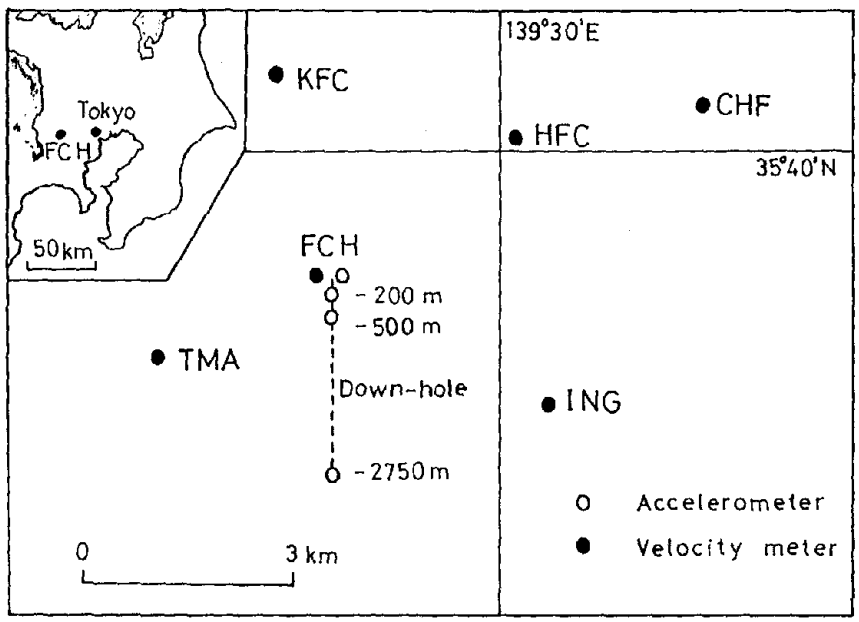

Fig. 1 Layout of seismographs at the Fuchu area.

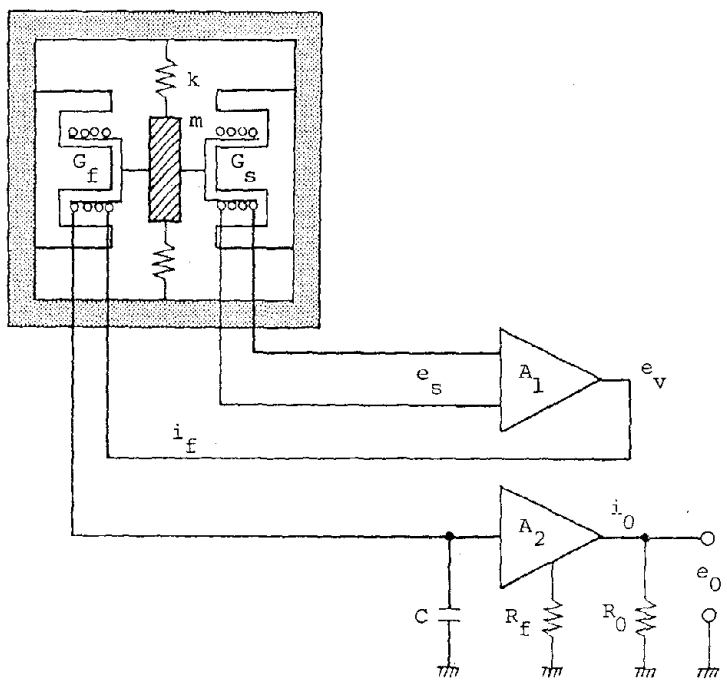

Fig. 2 Fundamentals of velocity type seismometer.

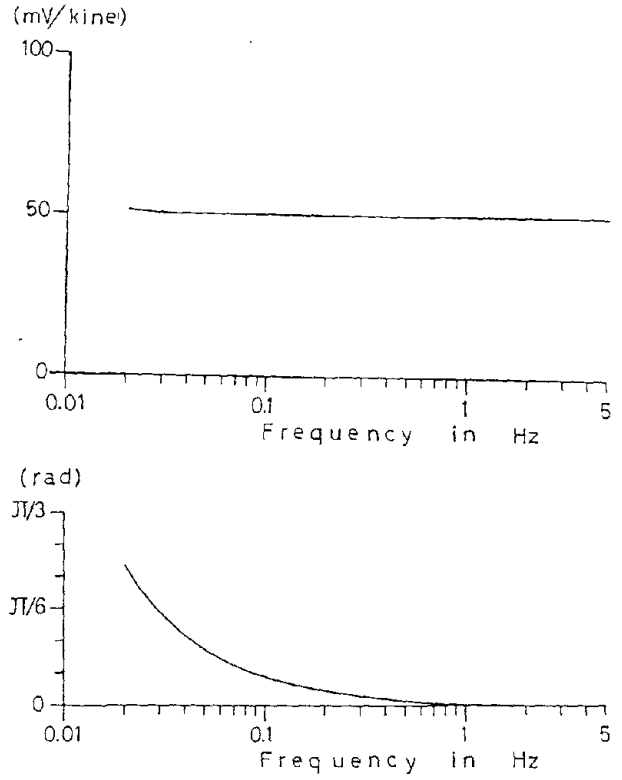

Fig. 3 Frequency characteristics of seismograph.

Photo 1 The velocity-meter and the recorder.

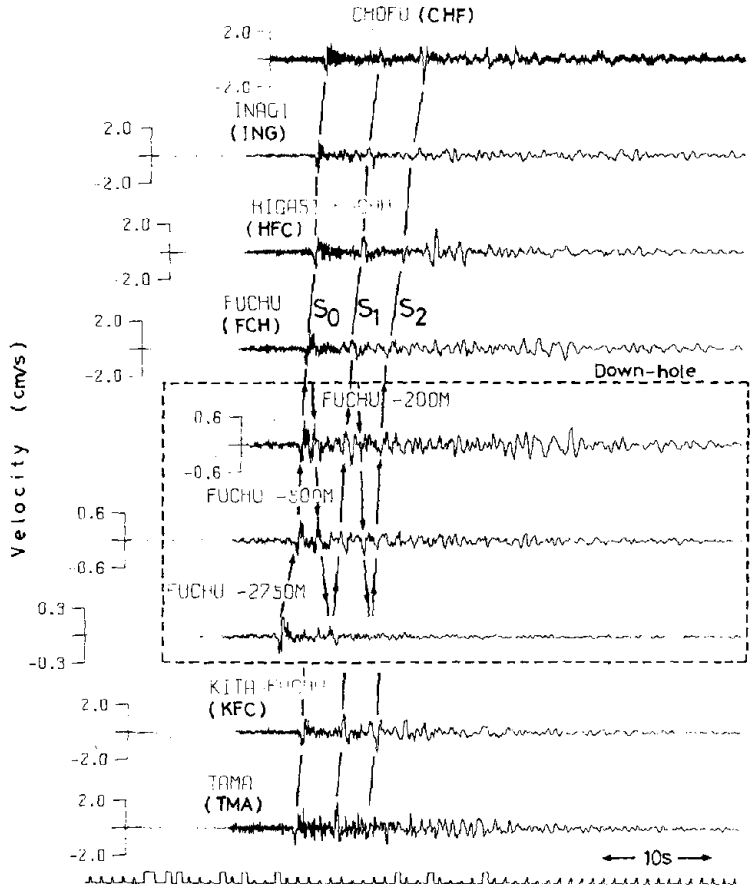

Fig. 4 Velocity waves obtained by array observation shown in Fig. 1.

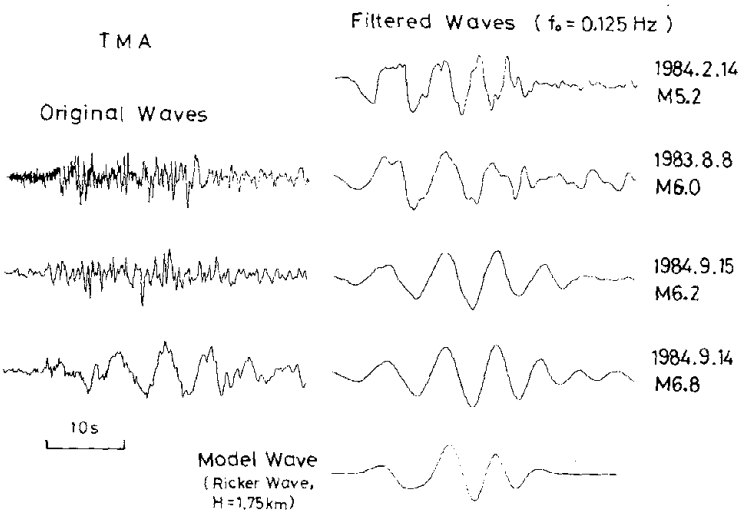

Fig. 5 Velocity waves and its filtered waves observed at the site TMA.

IMPLICATIONS OF RECENT ADVANCES IN INSTRUMENTATION FOR STRONG-MOTION STUDIES

BY

R. D. Borcherdt

ABSTRACT

Studies in seismology and engineering within the last decade have emphasized the importance of available strong-motion data sets recorded near moderate eartyhquakes and the need to record improved data sets near large earthquakes in the future. Recent advances in instrumentation permit strong-motion signals to be recorded over broader bandwidths, with wider dynamic range and signal resolution, and greater data accessibility via computer. These improvements in data quality suggest that seismic displacements calculated from accelerometer recordings can be inferred to longer periods, more stable estimates of seismic source parameters (e.g., moment, corner frequency, seismic source dimension) can be developed, effects of crust and local site structure on seismic wave propagation (e.g., wave conversion, f_{max}, Q^{-1}, and scattering) can be determined more accurately, and non-linear structural response, including high-frequency (50-100Hz) signals associated with failure of structural components, can be better resolved. A general microcomputer controlled data acquisition system (GEOS) has been developed by the U.S. Geological Survey and deployed to acquire improved-quality strong-motion data sets. Data sets acquired with the GEOS illustrate the significance of broad frequency bandwidth and wide dynamic range for future strong-motion studies.

Keywords: General Earthquake Observation System (GEOS), Strong-Motion, Instrumentation, Microcomputer, Data Acquisition, Earthquake Engineering, Engineering Seismology

1. INTRODUCTION

Recent advances in technology offer new opportunities for improving the quality and computer accessibility of strong-motion data. Improved hardware components permit greater frequency bandwidth, wider dynamic range, and less power consumption. Microcomputers allow software control of various hardware components, efficient and reliable execution of system tasks, increased flexibility in system design, and increased digital processing capabilities. Modern storage media extend data capacity and provide compatible format for mini-computer systems, which when deployed in the field permit extensive pre-processing of large volumes of data during field experiments.

This paper describes a General Earthquake Observation System (GEOS) developed to incorporate recent advances in technology. Implications of these advances for strong-motion studies, especially bandwidth and signal resolution, are discussed in the contest of date recently recorded on the GEOS.

2. A BROAD BAND MICRO-COMPUTER-BASED DATA ACQUISITION SYSTEM

The portable digital data acquisition system was developed by the U.S. Geological Survey for use in a wide variety of both passive and active seismic experiments (3). Versatility in system application was achieved by isolationof the appropriate system functions on hardware modules controlled by a central microcomputer via a general computer bus. CMOS hardware components were utilized to reduce quiescent power consumption to less than 2 watts for use of the system as either a portable recorder in remote locations or in an observatory setting with inexpensive backup power sources. The GEOS, together with two sets of three-component sensors (force balance accelerometer and velocity transducer) and ferrite WWVB antenna, is shown in Figure 1.

The hardware modules comprising the system are shown in Figure 2.

The signal conditioning module for the GEOS is configured with six input channels, selectable under software control, to permit acquisition of seismic signals ranging in amplitude from a few nanometers of seismic background noise to 2g in acceleration for ground motions near large events. The analog-to-digital conversion module is equipped with a 16 bit CMOS analog-to-digital converter which affords 96 dB of linear dynamic range or signal resolution; this, together with two sets of sensors, implies an effective system dynamic range of about 180 dB. A data buffer with direct memory access capabilities allows for maximum throughput rates of 1200 sps. With sampling rates selectable under software control as any integral quotient of 1200, broad and variable system bandwidth ranging from (10^{-5} - 5×10^{2} Hz) is achieved for use of recorders with a wide variety of sensor types.

Modern high density (1600 - 6400 bpi) compact tape cartridges offer large data storage capacities (1.25 - 33 Mbyte) in ANSI standard format, to facilitate data accessibility via mini-computer systems. Read capabilities of cartridge tape recorders is utilized to allow recording parameters and system operational software to be changed automatically. Read capability also allows systems equipped with modems to transmit data via telecommunications to a central data processing laboratory. Microcomputer control of time standard provides capability to synchronize internal clock to internal receivers (such as WWVB and satellite), external master clock, or conventional digital clocks. Convenient system set-up and flexibility to modify the system in the field for a wide variety of applications is achieved using a 32-character alphanumeric display under control of the micro-computer.

Flexibility to modify the system to incorporate future improvements in technology is achieved by using a ringed software architecture and modular hardware components. Incorporation of new hardware modules is accomplished in a straightforward manner by replacing appropriate module and corresponding segments of controlling software. The flexibility afforded by micro-computer technology to modify the system for specialized applications and to incorporate changes in technology allows seismic signals, detectable by a wide variety of sensors to be recorded over a broad band of frequencies with high resolution.

2.1 Implications of Broad Bandwidth and High Signal Resolution for Strong-Motion Studies

The system response designed for strong-motion applications of the GEOS (Figure 3) was intended to allow large amplitude near source signals of 1-10 Hz as detected by a forced-balance accelerometer (FBA) to be recorded on scale, while at the same time permitting much smaller amplitude high-frequency signals (30-100 Hz) as might be detected on FBA's or velocity transducers to be recorded with high signal resolution. The design system response together with that for two types of sensors frequently used for aftershock studies in the near source region of large earthquakes is shown in Figure 3. With digitization rates and anti-aliasing filters, selectable under software control, the design system response allows signals ranging from essentially DC to 500 Hz to be recorded at high resolution without aliasing. Gain settings, selectable under software control, allow two sets of three-component data, ranging in amplitude over 180 dB, to be recorded simultaneously.

To date, the most extensive application of the GEOS has been the acquisition of near-source aftershock data following earthquakes near Mammoth Lakes, California (M 5.2), Coalinga, California (M 6.5), Newcombe, New York (M 5.2), Borah Peak, Idaho (M_s 7.3), and Santiago, Chile (M 7.8). Several thousand events, recorded and analyzed during these

studies, have provided an opportunity to test and develop many of the design features under field conditions. The several hundred aftershocks recorded at ten GEOS stations in the epicentral region of the mainshock (M 6.5) near Coalinga, California provided on-scale three-component recordings of ground motion for essentially all events ranging in magnitude from less than 1 to 5.1 with the events greater than M 3.5 providing recordings with signal resolution greater than 40 dB. Detailed descriptions of the Coalinga data sets are provided by Borcherdt [2,3]. Examples of data from these studies illustrate the significance of broad bandwidth and high signal resolution for studies of seismic source and wave propagation characteristics.

The largest aftershock of the Coalinga sequence (M 5.1, 5/9/83), was recorded at a distance of about 14 km on a standard strong-motion recorder (SMA-1) and a GEOS with sensors for the two recorders, separated by a distance of about 25 m (Figure 4). The SMA time histories were digitzed at 600 sps, filtered to prevent aliasing, and decimated to 200 sps. The GEOS time histories were recorded at 200 sps with high-cut anti-aliasing filters corners set at 50 Hz. As sensors with similar responses were used to record at each location, comparison of time histories and acceleration spectra illustrate improvements in data quality permitted by improvements in recording instrumentation. Utilization of a data buffer or pre-event memory, allows the initial P wave onset to be recorded as well as background/instrument noise levels. This information, if routinely recorded on strong motion recorders, could augment studies of seismicity and crustal structure as well as studies of differential ground motion as recorded on closely spaced instruments. Comparison of the acceleration spectra shows that the spectra inferred from the two recorders are approximately the same for the frequency band 0.8-25 Hz, but that increased amplitude resolution and frequency bandwidth allow seismic signals as high as the corner on the anti-aliasing filter (50 Hz) to be resolved on the GEOS recording.

The velocity time history and displacement spectra inferred by McGarr *et al.* (1984) for a recording obtained at another GEOS station of the M 5.1 Coalinga aftershock is shown in Figure 5. The inferred displacement spectra with a Nyquist frequency of 100 Hz, shows discernible seismic displacements ranging over more than 7 orders of magnitude. The increase of signal resolution and bandwidth illustrated in Figures 4 and 5 provides a basis for inferring seismic displacement fields to longer periods, a basis for more stable estimates of seismic source parameters such as moment and corner frequency, and an improved basis to estimate effects of seismic wave propagation such as intrinsic absorption, f_{max}, and effects of local site conditions. The improved capability to resolve high frequency strong motions implies improved estimates of non-linear structural behavior, as well as high frequency signals associated with structural failure.

Capability to resolve seismic frequencies as high as 300 Hz can be useful for near-source studies in high Q environments. An example of such data collected in New Brunswick, Canada by E. Cranswick (pers. commun.) is shown in Figure 6. The velocity time history, recorded with high resolution at 1200 sps, was utilized to infer the displacement time history by removing the base line, using the average of the first 512 points, and straighforward integration. The resulting displacement spectra suggests seismic radiation as high as 200-250 Hz and emphasizes the significance of both bandwidth and dynamic range in defining the nature of near-source seismic radiation fields.

The ability to resolve periods of strong motion longer than about 20 seconds have been limited by capabilities of the sensor, sensor coupling to the Earth, and dynamic range of

available recorders. Recent advances in technology to measure Earth strain over 7 decades in frequency [6] up to frequencies of 5-10 Hz, may also prove useful in documenting the nature of long period seismic radiation near the source of a great earthquake. For example, the Sacks-Evertson strainmeter [9] is sensitive to strain signals over about 9 orders of magnitude in amplitude and periods ranging from months to 0.1 sec. Utilization of this sensor together with appropriate band-pass filtering and a recorder with wide dynamic range would allow examination of possible long period, near-source signals not discernable using conventional recorders and accelerometers. As an example, Figure 7 shows the Earth strain as detected at a depth of 200 m near San Juan Bautista, California on a Sacks-Evertson dilatometer and recorded on the GEOS. The upper time history shows the Earth tidal strains at 0.1 sps for a 28-hour interval and the seismic energy radiated by a nuclear detonation at a distance of about 400 km. The lower trace shows strain variations radiated by the nuclear explosion plotted at an expanded scale and at the sampling rate of 50 sps used to record the data.

The broad bandwidth and wide dynamic range of both the sensor and the recorder allow the short period strain variations of 0.5-20 seconds radiated by the nuclear explosion to be resolved as well as the large amplitude tidal variations of 12 and 24 hour periods. Such signal detection capabilities offer new opportunities for detection of near-source long-period variations as might occur in the epicentral region of great earthquakes.

3. ACKNOWLEDGEMENTS

This effort is the result of dedicated contributions by a number of poeple to develop and produce the GEOS (listed in alphabetical order): J. Fletcher, G. Jensen, G. Maxwell (software design and development), J. VanSchaack, and R. Warrick. E. Cranswick, C. Mueller, and G. Sembera played key roles in acquiring the data sets for the aftershock sequences. M. Johnston has supervised the successful deployment of numerous Sacks-Evertson dilatometers throughout the State of California, making the dilatometer data set discussed herein possible. Data for Figures 3, 5, 7, and 8 were prepared by R. Warrick, C. Mueller, E. Cranswick, and M. Johnston, respectively. Manuscript reviews by W. Joyner and G. Brady are appreciated.

5. REFERENCES

[1] Aki, K. and P.G. Richards (1980). *Quantitative Seismology Theory and Methods*, vol. 1, W. H. Freeman and Co., San Francisco, Calif., 557 pp.

[2] Borcherdt, R.D., C. Mueller, and L. Wennerberg (1983). Effects of local geological conditions in the vicinity of Coalinga, California *in* Workshop on Site-Specific Effects of Soil and Rock on Ground Motion and Implications for Earthquake-Resistant Design, July 26-28, 1983, ed. by Walter Hays, *U.S. Geol. Surv. Open-File Rept. 83-845*.

[3] Borcherdt, R.D., E. Cranswick, G. Maxwell, C. Mueller, R. McClearn, G. Sembera, and L. Wennerberg (1984). Digital strong-motion data recorded by U.S. Geological Survey near Coalinga, California, in Coalinga, California, earthquake of May 2, 1983, reconnaissance report, *Earthquake Eng. Res. Inst. Rpt. 84-03*, 89-98.

[4] Borcherdt, R.D., J.B. Fletcher, E.G. Jensen, G. L. Maxwell, J. R. VanSchaack, R.E. Warrick, E. Cranswick, M.J.S. Johnston, and R. McClearn, A general earthquake observation system, submitted, *Bull. Seismol. Soc. Am.*

[5] Cranswick, E., R. Wetmiller, and J. Boatwright (1985). High-frequency observations and source parameters of small aftershocks recorded at hard

rock sites, *Bull. Seismol. Soc. Am.* (in press).

[6] Johnston, M.J.S. and R.D. Borcherdt (1984). Earth strain in the period range 0.1 to 10,000 seconds at six borehole sites within the San Andreas fault system in California, *EOS, Trans., Am. Geophys. Un.*, **65**, p. 1015, Fall Mtg., San Francisco, CA.

[7] McGarr, A., C. Mueller, J. B. Fletcher, and M. Andrews (1985). Ground motion parameters of the 1983 Coalinga, California earthquakes: implications for crustal strength, *U.S. Geol. Surv. Open-File Rpt. 84-639*, (in press).

[8] Mueller, C.S., and Cranswick, E. (1985). Source parameters from locally-recorded aftershocks of the January 9, 1982, Miramichi earthquake, *Bull. Seismol. Soc. Am.*, (in press).

[9] Sacks, I.S., S. Sugehiro, D.W. Evertson, and Y. Yamaguchi (1971). Sacks-Evertson strainmeter, its installation in Japan and some preliminary results concerning strain steps, *Pap. Met. Geophys.*, Tokyo, 22, 195-208.

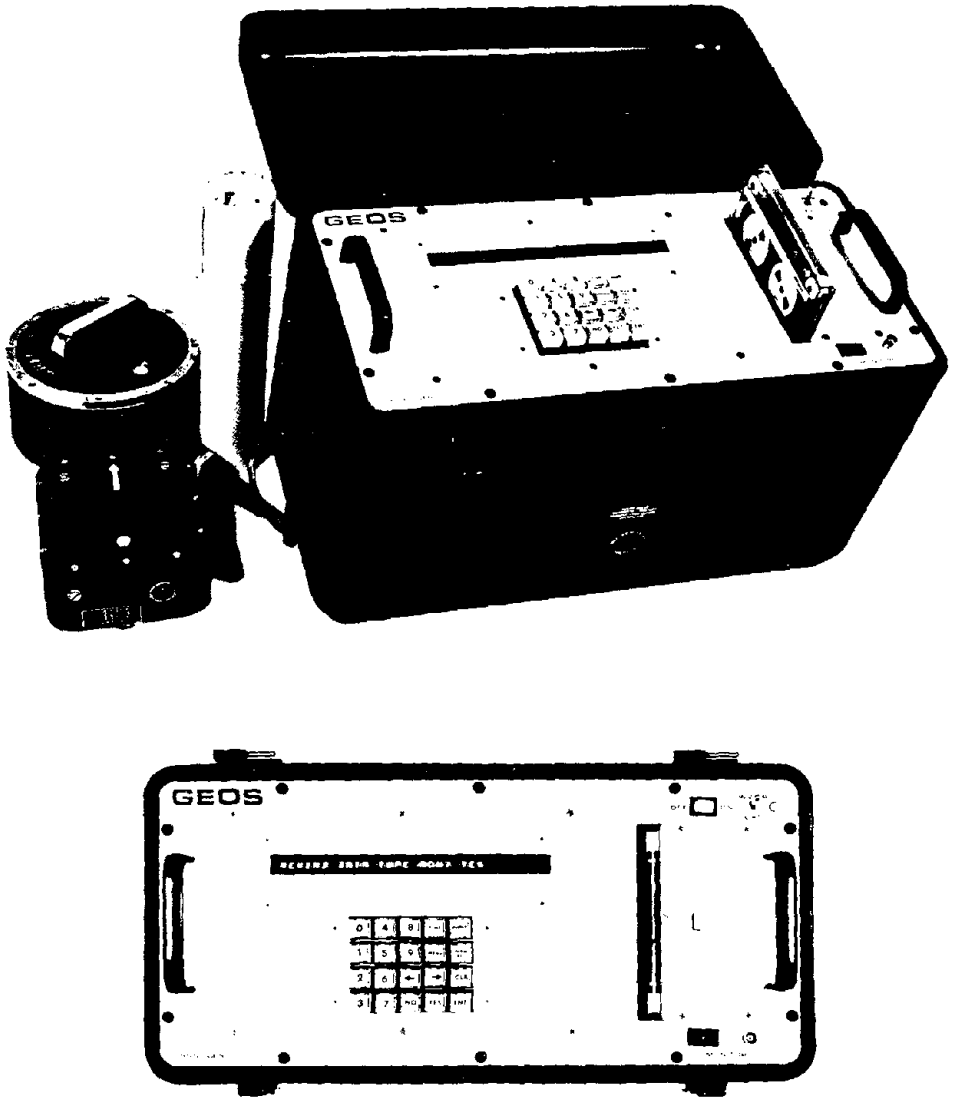

Figure 1. Side and front-panel view of the General Earthquake Observation System (GEOS), together with a WWVB radio antenna and two sets of three-component sensors commonly used to provide more than 180 dB of linear dynamic range. System operation for routine applications requires only initiation of power. Full capability to reconfigure system in the field is facilitated by simple operator response to English-language prompts via keyboard.

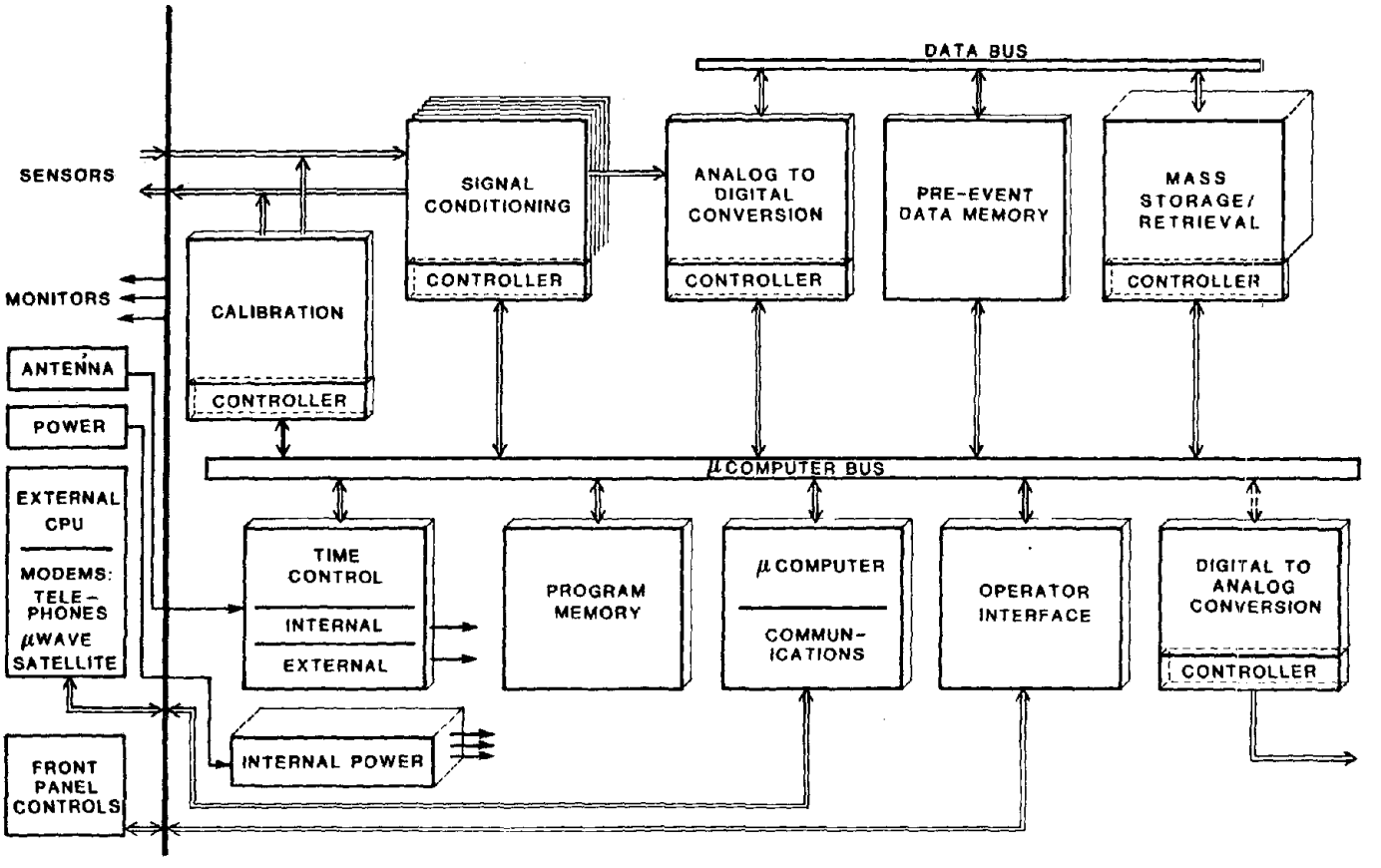

Figure 2. General system configuration for the GEOS, showing required system functions isolated on separate hardware modules. Central CPU control of each module via general computer bus permits full capability to configure system for most field applications and facilitates incorporation of improvements in technology.

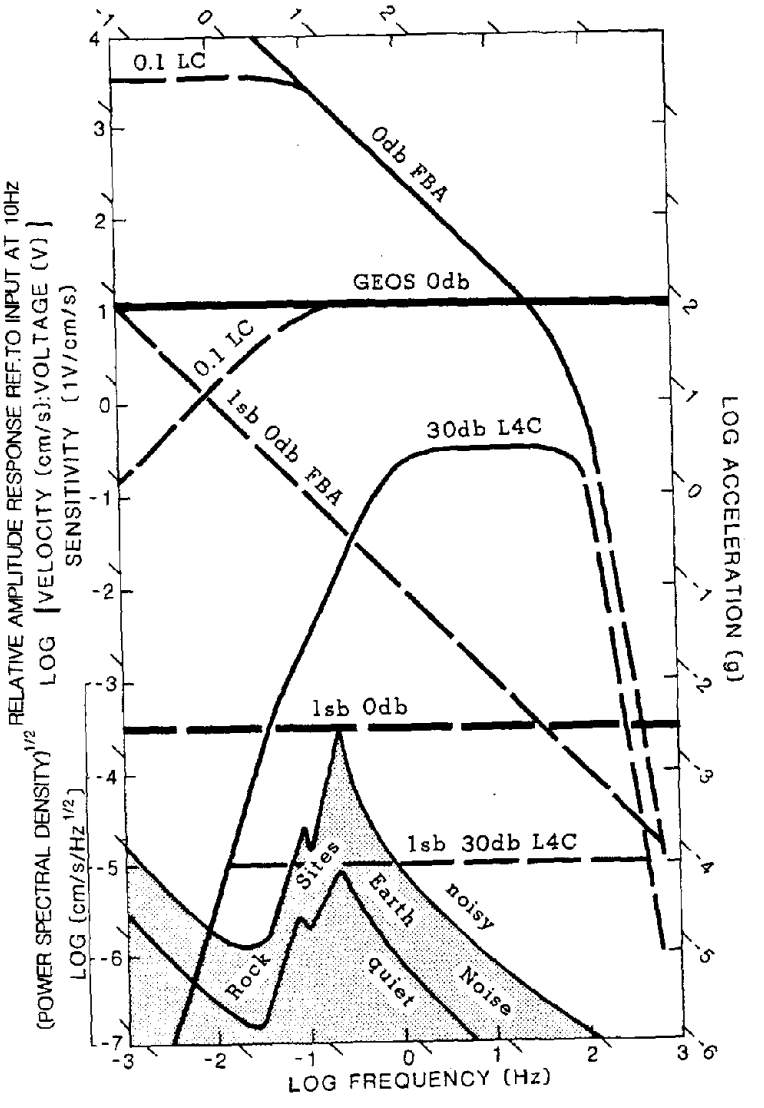

Figure 3. Relative amplitude response of the GEOS recorder, GEOS with L4-C velocity transducer and force balanced accelerometer (FBA) and square root of power spectral density for Earth noise [1]. Amplitude responses were determined for recorder with constant input voltage of 10 V, for recorder with L4-C 10 cm/sec or 10 V with sensitivity of 1 V/cm/sec at 10 Hz, and for recorder with FBA with constant input acceleration of 2g. Two sets of sensors operating simultaneously and linear dynamic range of 96 dB for Earth gain setting allow system to record 10 Hz signals with amplitudes ranging from 2 nm in displacement to 2 g in acceleration on scale without operator intervention.

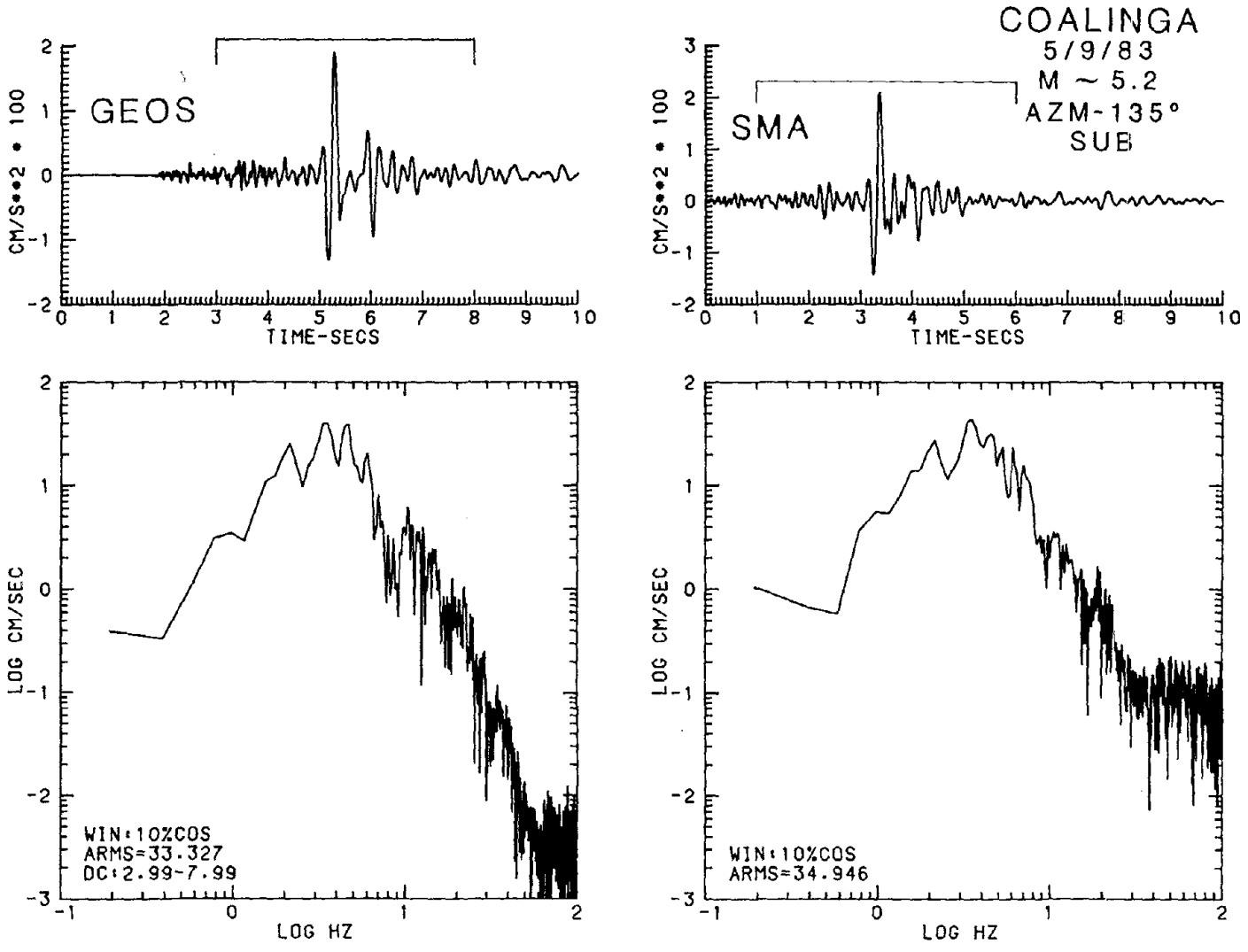

Figure 4. Strong ground motions and spectra recorded on GEOS and SMA-1 units separated by a distance of about 25 m for 135° horizontal component of motion generated by a magnitude 5.1 aftershock near Coalinga. The time histories and spectra obtained on the two instruments are similar between 0.8 and 25 Hz. Seismic energy is discernible in the SMA-1 spectrum as high as 25 Hz, and in the GEOS spectrum as high as 50 Hz.

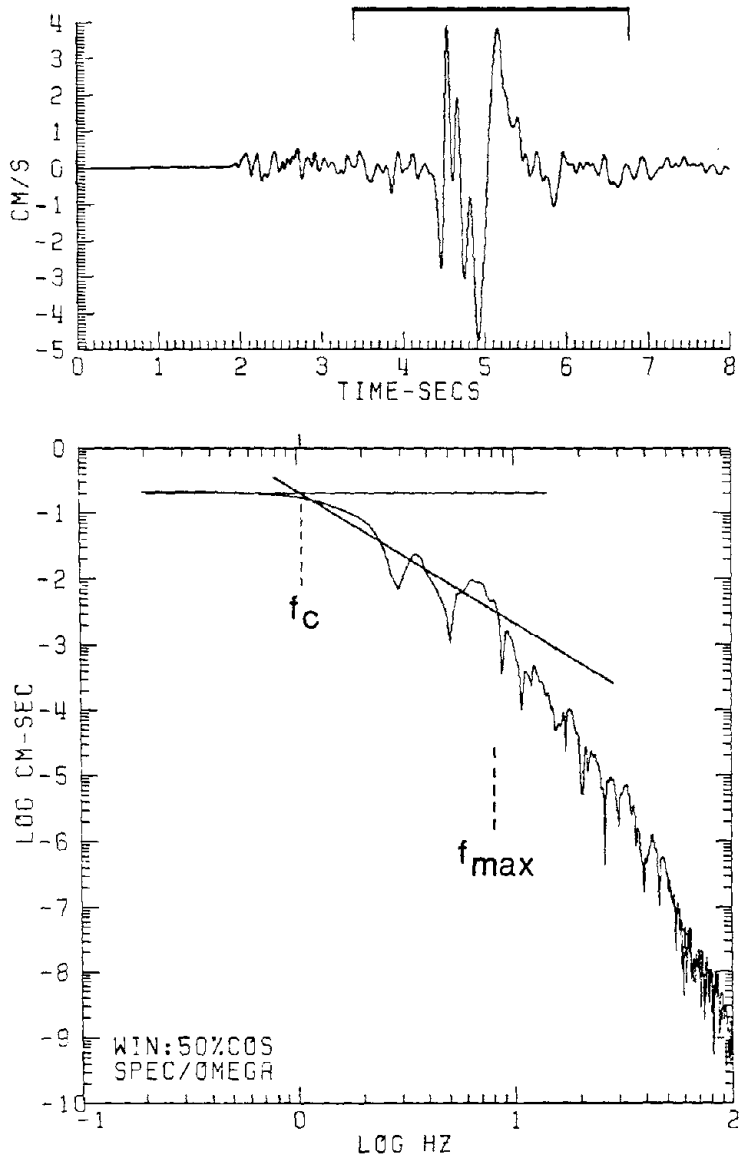

Figure 5. Time history of ground velocity and displacement spectra calculated by McGarr *et al.* [7] from a recording of a M 5.1 aftershock near Coalinga, California. The time history was inferred from a GEOS recording of ground motion as detected by a forced balance accelerometer at a distance of about 12 km from the hypocenter. The seismic displacement field is discernible over 7 orders of magnitude in amplitude and up to frequencies as high as 60-80 Hz.

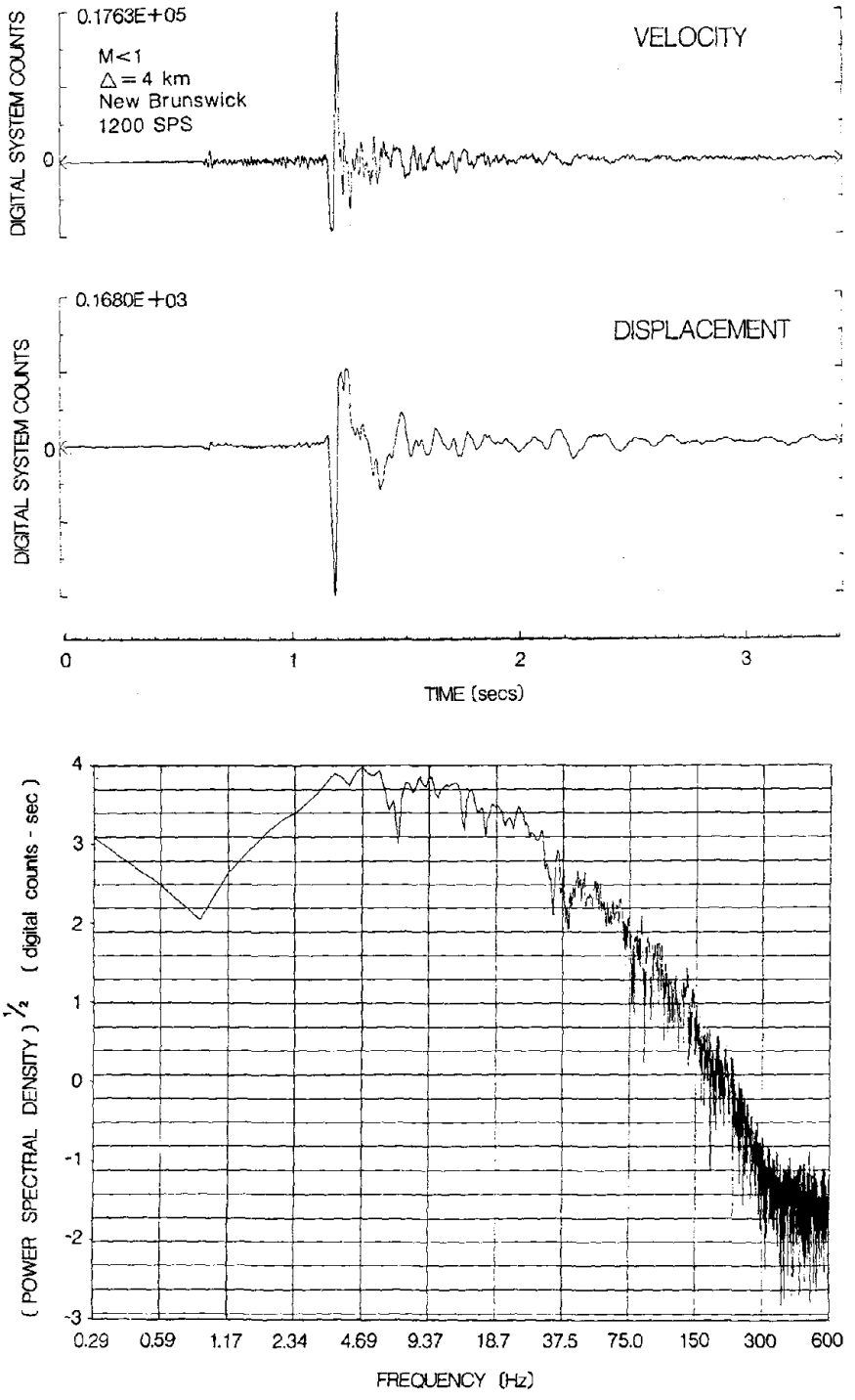

Figure 6. Horizontal ground velocity, inferred displacement (integration, only dc removed), and displacement spectra determined from GEOS recording of a small earthquake (M < 1, Δ = 4 km) near Miramichi, New Brunswick. The computer displacement spectra, with a Nyquist frequency of 600 Hz, shows a dynamic range of 102 dB and detectable seismic frequencies as high as 300 Hz.

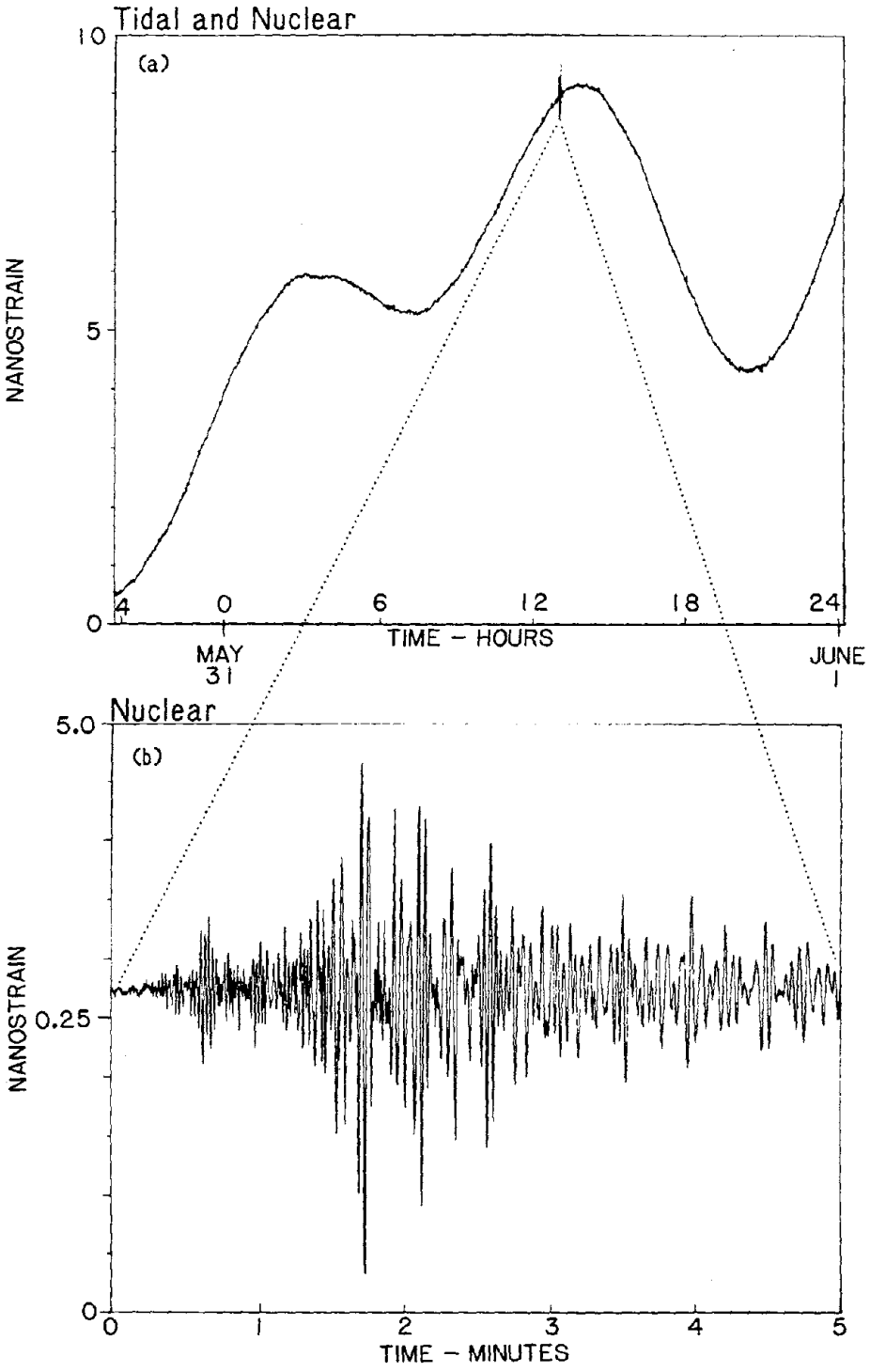

Figure 7. Variations in Earth strain detected by Sacks-Evertson dilatometer and recorded on a GEOS unit at a site near San Juan Bautista, California. Upper plot shows tidal strains at 0.1 sps for a 28-hour interval, and strains associated with detonation of a nuclear device in Nevada at a distance of 400 km. Lower figure shows strain variations recorded from nuclear explosion, plotted at an expanded scale and at 50 sps used to record the data.

DYNAMIC BEHAVIOR OF A ROCKFILL DAM DURING EARTHQUAKES

Norihisa Matsumoto
Nario Yasuda
Minori Shiga

Public Works Research Institute
Ministry of Construction

ABSTRACT

The Dam Department of PWRI, Ministry of Construction, has been continuing to measure the earthquake motions at Miho Dam, which is a rockfill dam with central impervious core, and has conducted geophysical investigations to obtain dynamic deformation properties of the dam body. One of the authors presented the dynamic analysis of the dam by using the recorded accelerograms, at the 13th[1] and 15th[2] Joint Meeting of UJNR (both at Tsukuba). At that time, however, we had not yet obtained laboratory test data on dynamic shear moduli and damping ratios for the materials of Miho Dam, and hence we used the material properties of a similar rockfill dam. This time, we conducted large-scale cyclic triaxial testing for rockfill materials borrowed from the quarry site of Miho Dam, and succeeded in obtaining the dynamic shear moduli (or moduli of rigidity) and damping ratios for the strain range of 10^{-5} to 10^{-3}. In this paper, we describe the results of response analysis computed by using the obtained laboratory material properties and recorded base accelerograms as an input.

Key Words: Earthquake Engineering, Rockfill Dams, Dynamic Analysis, Dynamic Behavior.

1. INTRODUCTION

Miho Dam is a 95.0-m-high rockfill dam with a central earth core; its maximum section is shown in Figure 1. The impervious zone of the dam is thin and most of the dam is composed of rockfill materials. The rockfill consists of three zones, i.e. smaller, intermediate,and larger rocks. Figure 2 shows the grain size distribution of each zone. Since the fifty percent grain size of the smaller rock zone is about 5.00 mm, all zones are pervious, having permeability coefficients larger than 1.0×10^{-3} cm/sec, which indicates that the rock zones have free drainage ability. Core materials of the impervious zone are well graded soils with gravels which were produced at the stockpile by blending weathered rock with scoriaceous tephra. The core zone was placed in layers of 20 cm thickness and compacted by 12 passes of a sheepsfoot roller. The filter zone was compacted in layers of 40 cm thickness by 12 passes of a 32 ton bulldozer. The rock zone was compacted in layers of 100 cm thickness by 4 passes of vibratory roller. The void ratio, specific gravity and density of each zone are listed in Table 1. Each zone is compacted to high density as shown in Table 1.

The rock forming the foundation of Miho Dam is andesitic pyroclastics resulting from submarine volcanic activity of the early Neogene, partly intruded by pyroxene andesite dyke. The bed rock is well indurated hard rock with a P-wave velocity of 4.0 to 4.5 km/sec.

2. LARGE SCALE CYCLIC TRIAXIAL TESTS

Cyclic triaxial tests were conducted on the rockfill materials of Miho Dam. The main features of performance are shown in Table 2,

and Figure 3 illustrates the equipment. The displacement transducer and load cell are placed inside the triaxial cell to exclude mechanical errors caused by friction from measured values. The two separated sensors, each of which is a disk-shaped coil, are used as a displacement transducer. Since the capacity of this displacement device is limited to 5 mm, the position of the target is adjusted by shifting it to conform to the axial displacement during consolidation. The gradation of the materials tested is shown in Figure 4, and is almost identical with the gradation of the smaller rock, as shown in Figure 2. The diameter of the specimen is 30 cm, and the height is 60 cm. The materials are in an air-dried condition, with a water content of 0.3 percent. The specimens were at first uniformly consolidated with a confining pressure of 1.0 kgf/cm^2, and then cyclic deviatoric axial stress σ_{ad} of 0.2 Hz was applied to the axial stress σ_a, after the volumetric change rate was confirmed as negligibly small, i.e. less than 0.05 percent a minute. The twelfth stress-strain loop of the cyclic loading was used for obtaining dynamic deformation properties at each stress level. The deviatoric stress was increased gradually at the same confining pressure, and the specimen was subjected to next confining pressure when the strain reached around 1×10^{-3}.

The four levels of confining pressures were taken for a specimen as 1, 2, 3 and 4 kgf/cm^2.

The shear modulus G was computed as follows:

$$E_d = \sigma_{ad}/\varepsilon_{ad}$$

$$G = E_d/2(1+\nu) \qquad (1)$$

$$\gamma = (1+\nu) \cdot E_d$$

The damping ratio h was obtained as follows (see Figure 5):

$$h = 1/2\pi \cdot \Delta W/W \qquad (2)$$

Here the value 0.35[2] of Poisson's ratio was used for Equation (1), because this value has been obtained independent of the depth from the results of geophysical investigation in Miho Dam.

Figure 6 shows the relation of shear modulus to shear strain. The shear modulus becomes larger with increasing confining pressure. The data points are rather scattered in the strain range smaller than 5×10^{-6} because of the inadequate performance of the pickups. The shear moduli obtained from the geophysical investigation are also plotted in Figure 6. Comparing the shear moduli obtained from laboratory tests with the field geophysical investigation, the laboratory testing gives us a little bit higher shear modulus than field testing at a given depth. However, the difference is so small that it can be considered that the two testing methods give us similar results. Here, we assumed that the confining pressure in the laboratory tests represents the stress in the dam at the depth of Z, through the following relations.

Mean principal stress σ'_m can be expressed by the following equation by assuming the plain strain deformation in the dam axis direction.

$$\sigma'_m = 1/3\ (1+\nu) \cdot (1+K)\sigma'_1$$

where $K = \sigma'_3/\sigma'_1$ = principal stress ratio

The observed earth pressure in Miho Dam gives us:

$$\sigma'_1 = 0.9 \cdot \sigma_v \qquad (3)$$

where σ_v = overburden load

Therefore, σ'_m will be related to depth Z as

$$\sigma'_m = 0.9/3\ (1+\nu)\ .\ (1+K)\gamma\ .\ Z$$

γ = weight of unit volume (t/m^3)
Z = depth(m) from the dam surface

In Equation (3), the values of ν, K and γ for Miho Dam are respectively, 0.5, 0.35 and 2.31.

Figure 7 shows the normalized shear moduli obtained by divding by G_o, a shear modulus corresponding to very small strain. The relation between normalized shear modulus and shear strain in Figure 7 is almost the same for four different confining pressures.

Figure 8 illustrates the relationship between damping ratio and shear strain. The effects of confining pressures on damping ratio are not obvious in this coarse granular materials, differing from the case of fine clean sand such as Toyoura standard sand.

3. RECORDED EARTHQUAKE MOTIONS

Miho Dam was instrumented with two strong motion accelerometers at the crest and downstream toe of the dam as in Figure 1. Since the accelerometer at the toe was placed on the bedrock, the accelerograms recorded by this accelerometer were used as an input motion in the dynamic response analysis.

Miho Dam was subjected to considerable earthquake shaking at three times, although it suffered no damage from the shaking [3,4]. The main features of each event are listed in Table 3, and the epicenters are shown in Figure 9. The recorded accelerograms were digitized at 0.01 second intervals and were replotted in Figure 10. The peak acceleration and predominant frequencies are shown in Table 4.

4. DYNAMIC RESPONSE ANALYSIS

The two-dimensional dynamic response analysis was performed by using the results of laboratory cyclic triaxial tests and the field geophysical investigation, and recorded earthquake motions. The computed response was to be compared to the recorded response. QUAD-4 was used in the computation.

The initial shear modulus in the dam was given according to the overburden depth based on the results of geophysical investigation shown in Figure 11. Figure 12, in which two curves were obtained from cyclic triaxial tests, was used for the G to γ relation.

The damping of the material itself was evaluated by the hysteretic damping of the cyclic triaxial testing, and another dissipation damping at the boundary between dam and foundation was added to this hysteretic damping. After Kanai[5], the dissipation damping between two layers is given by the following equation, when the excitation frequency is the resonant one.

$$h = \frac{1}{\pi} \ln \left| \frac{1+\alpha}{1-\alpha} \right| \qquad (4)$$

where

$$\alpha = \sqrt{\frac{\rho' G'}{\rho G}} = \frac{\rho' V's}{\rho Vs}$$

α = impedance ratio
ρ' = density of upper layer (kgf/cm^3)
G' = shear modulus of upper layer (kgf/cm^2)
ρ = density of lower layer (kgf/cm^3)
G = shear modulus of lower layer (kgf/cm^2)

In Miho Dam, the S-wave velocity of the dam and foundation are 0.5 km/sec and 2.0 km/sec, respectively; and the density of the dam and foundation are 2.3 kgf/cm^3 and 2.5 kgf/cm^3, respectively. Therefore, the impedance ratio α is 0.23, and h becomes about 15 percent. As

the dissipation damping at the boundary is not taken into account in the computer program, this 15 percent damping was added to the internal hysteretic damping.

The finite element discretization of the dam is illustrated in Figure 13.

Figure 14 shows the frequency response function of the dam crest to the foundation after the final iteration. The first and second natural frequency of the analytical model are 1.8 to 1.9 Hz, and about 3.3 Hz, respectively. The first natural frequency of the model is coincident with the measured data.

Figure 15 shows the response acceleration of the dam crest. In the case of the East Izu Peninsula Off Earthquake, the peak value of acceleration is 70 gal in computation and 66 gal in measurement, so there is good coincidence in peak acceleration, and an average level of amplitude during the main motion from 7 sec to 12 sec. On the other hand, in the case of the East Yamanashi Prefecture Earthquake, the peak value from the computation is 34 gal, while the measured value is 87 gal, and in the case of the West Kanagawa Prefecture Earthquake, the computed value of 187 gal is smaller than the measured value of 253 gal. The foundation motions of the East Yamanashi Prefecture and West Kanagawa Prefecture Earthquakes contain much high frequency components, because these two events occurred within ten and several km from the dam site. The computation procedure might not be appropriate for evaluating high frequency input motion. In the case of the East Izu Peninsula Off Earthquake, the input motion did not contain much high frequency components, and hence the computation gave us a good coincidence. However, the high frequency components during the initial part of the motion in the measured accelerogram do not exist in the computation results.

5. CONCLUSIONS

1. Due to the improvements of the large-scale cyclic triaxial test apparatus, the shear modulus and damping ratio of rockfill materials were obtained for the strain range of 5×10^{-6} to 1×10^{-3}.
2. The shear modulus resulted from laboratory testing was a little bit larger than that from the field geophysical investigation.
3. There was a good coincidence between measured and computed response in the case of the East Izu Peninsula Off event by using the QUAD-4 computation program. However, much consideration should be given in the case of high frequency input motion in the use of this program.

6. REFERENCES

1) N. Matsumoto, S. Kondo, "Observed behavior and analysis of rockfill dam during earthquake," 13th UJNR, 1981.
2) N. Matsumoto, M. Toyoda, M. Shiga, "Distribution of the dynamic shear modulus in a prototype rockfill dam," 15th UJNR, 1983.
3) N. Matsumoto, S. Kondo, H. Katahira and M. Shiga, "Earthquake motions at rock foundations of dam sites," Technical memorandum No. 1789, P.W.R.I., 1982 (in Japanese).
4) N. Matsumoto, N. Yasuda, M. Shiga, "Characteristics of earthquake accelerograms recorded at damsites," Large Dam, No. 108, June, 1984 (in Japanese).
5) Katsutada Sezawa, Kiyoshi Kanai, "Damping in Seismic Vibrations of a Surface Layer due to an Obliquely Incident Disturbance,' Earthquake Research Institute, Sep., 1936 No. 14.

6) Y. Sawada, T. Takahashi, A. Sakurai, and H. Yajima, "Material Property Distribution and Dynamic Characteristics of Rockfill Dams -- A consideration based on elastic wave --," Central Research Institute of Electric Power, Report No. 377008, 1977 (in Japanese).

Table 1 Void Ratio, Specific Gravity and Density for Each Zone

Zone	Void Ratio	Specific Gravity	Dry Density (t/m^3)	Saturated Density (t/m^3)
Core	0.42	2.86	2.01	2.31
Filter	0.25	2.88	2.30	2.50
Rock	0.26	2.92	2.31	2.52

Table 2 Main Features of Performance

Specimen size	ϕ30cm x h60cm
Control system	Electro-Hydraulic-Servo
Wave form	Sinusoidal, triangular, and earthquake waves
Axial loading	Maximum loading capacity compression - 20 tf
	Maximum loading capacity extension - 10 tf
	Frequency range 0.2 - 10 Hz
Confining pressure	Max. 15 kgf/cm^2
	Frequency range 0.2 - 5 Hz

Table 3 Generals of Earthquakes

	Date	Magnitude	Depth(km)	Epicentral Distance(km)
East Izu Peninsula Off	'80,6,29	6.7	10	56
East Yamanashi Prefecture	'81,4,14	4.5	20	13
West Kanagawa Prefecture	'83,8,8	5.8	30	14

Table 4 Maximum Acceleration and Predominant Frequencies

	Component	Max. Acceleration	Predominant Frequencies
East Izu Peninsula Off	F. Up/Downstream	30.9 (gal)	3.0, 4.0, 6.6, 7.9
	F. Axis	33.0	2.2, 3.0, 4.1, 8.3
	F. Vertical	12.0	0.8, 2.2, 4.3, 6.8
	D. Up/Downstream	66.4	2.0, 3.2, 3.8
	D. Axis	81.1	1.6, 2.7, 3.1, 5.8
	D. Vertical	37.6	2.4, 3.2, 3.9, 7.0
East Yamanashi Prefecture	F. Up/Downstream	32.0	6.9, 8.5, 9.6
	F. Axis	38.0	1.2, 3.1, 3.5, 6.8, 8.8
	F. Vertical	11.0	1.2, 2.0, 4.9, 6.8
	D. Up/Downstream	87.5	2.7, 3.4, 5.3, 6.8
	D. Axis	104.1	2.9, 4.0, 5.2, 7.5
	D. Vertical	73.0	3.3, 7.4, 8.5, 9.9
West Kanagawa Prefecture	F. Up/Downstream	149.0	1.0, 2.6, 6.5, 7.5, 9.0
	F. Axis	91.4	1.3, 2.3, 6.0, 8.0
	F. Vertical	53.6	3.3, 4.7, 5.9, 6.3, 11.3
	D. Up/Downstream	253.7	1.8, 2.6, 5.3, 6.2, 6.9, 8.3
	D. Axis	206.4	1.7, 2.3, 5.0, 6.2
	D. Vertical	165.8	2.8, 6.2, 6.8, 8.3

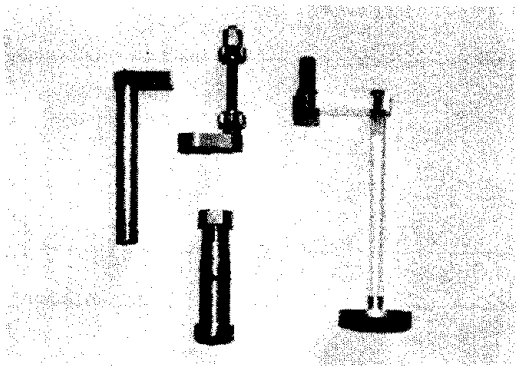

Photo 1 Target for Displacement Sensor

Photo 2 Target and Displacement Sensor

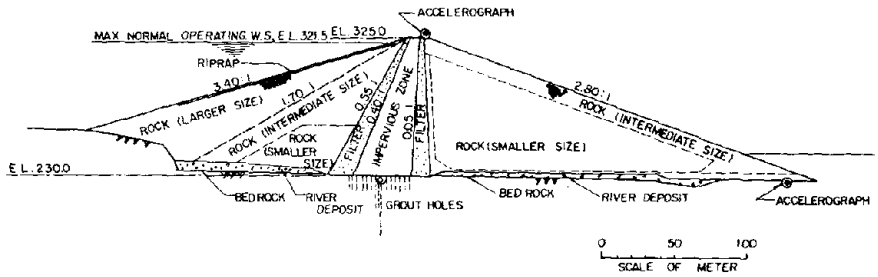

Fig. 1 Standard Cross Section

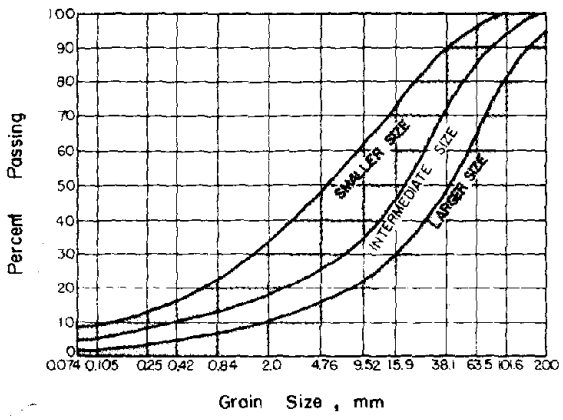

Fig. 2 Grain Size Distribution

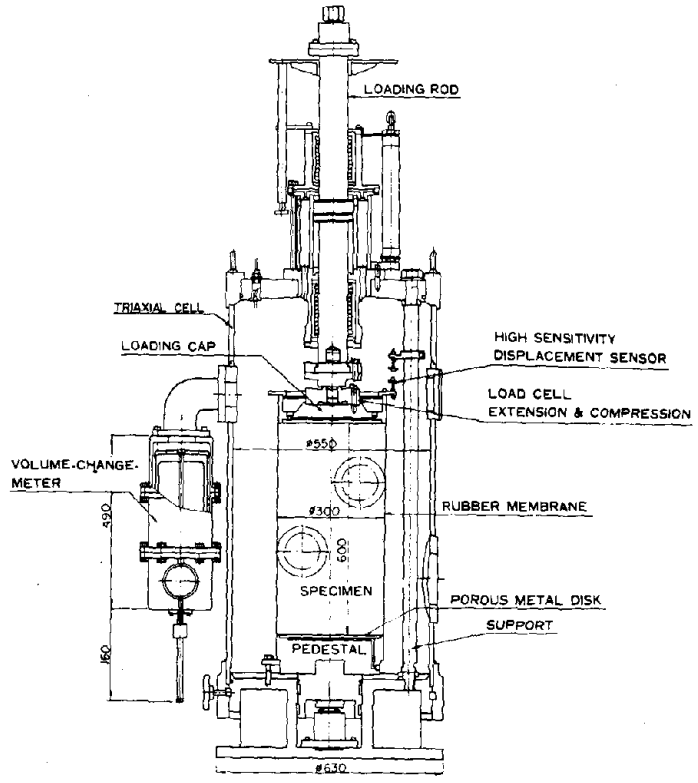

Fig. 3 Cyclic Triaxial Testing Apparatus

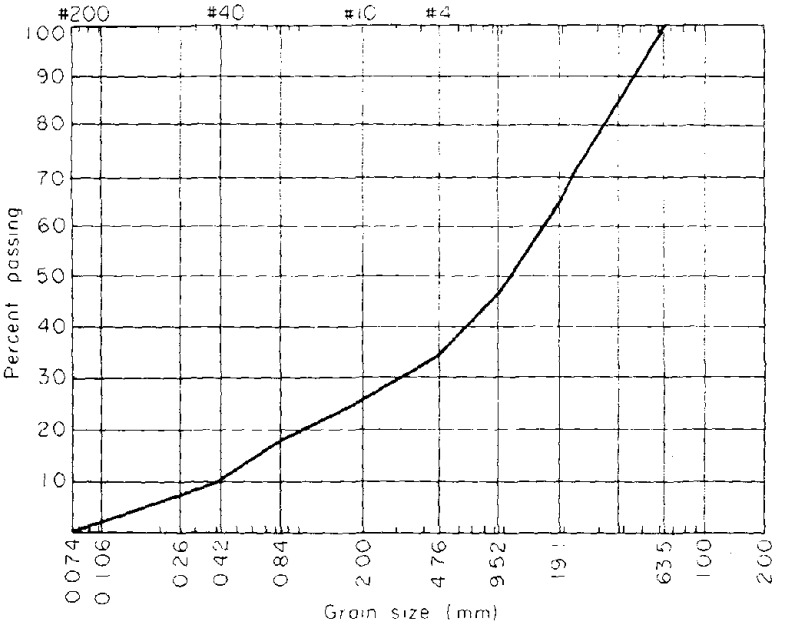

Fig. 4 Grain Size Distribution of Specimen

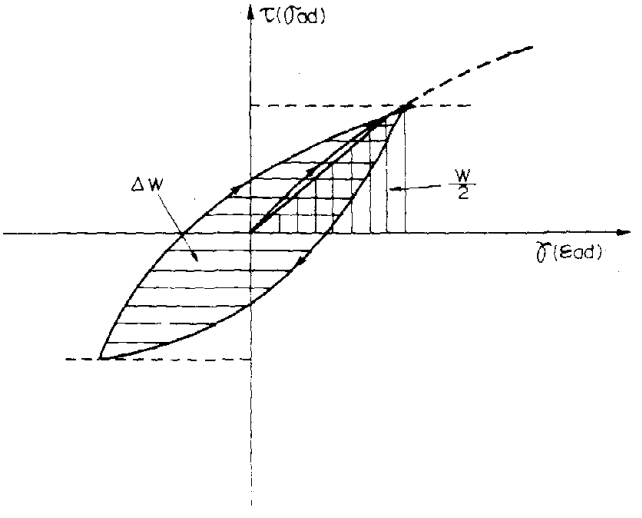

Fig. 5 Stress ∿ Strain

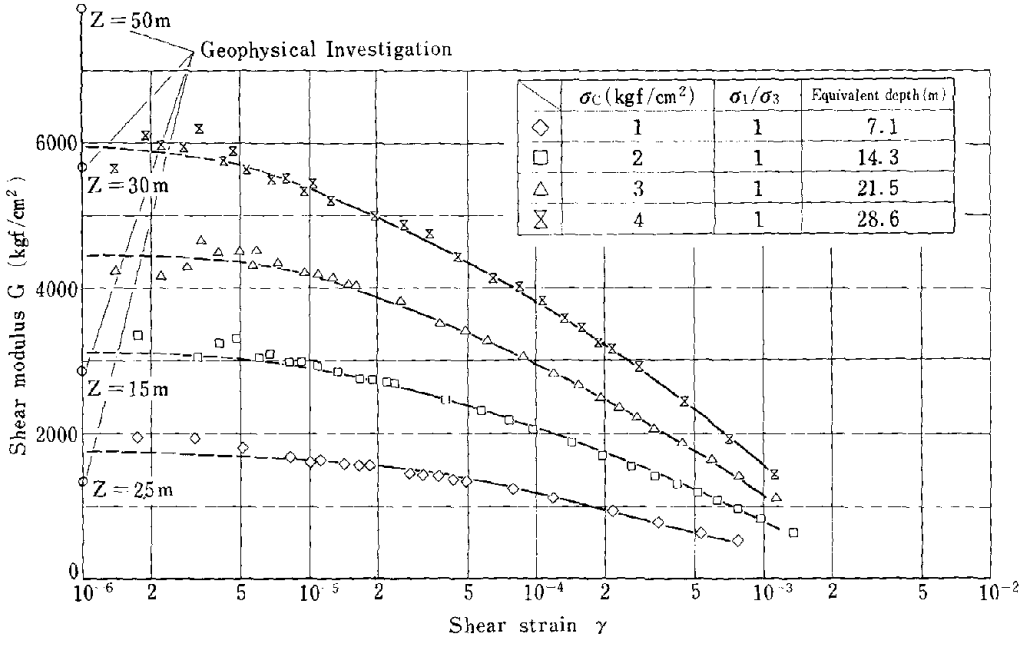

Fig. 6 Shear Modulus (G) ∿ Shear Strain

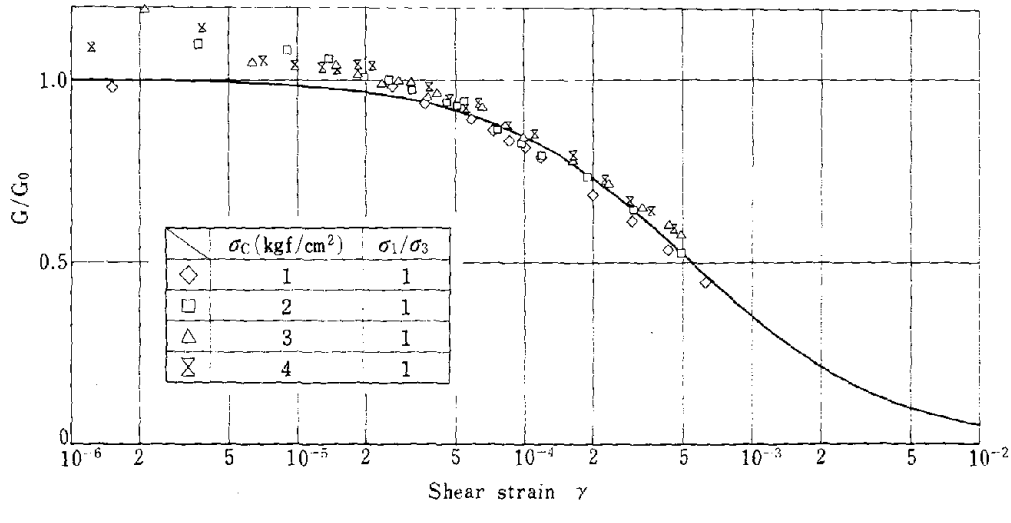

Fig. 7 G/G_0 ∿ Shear Strain

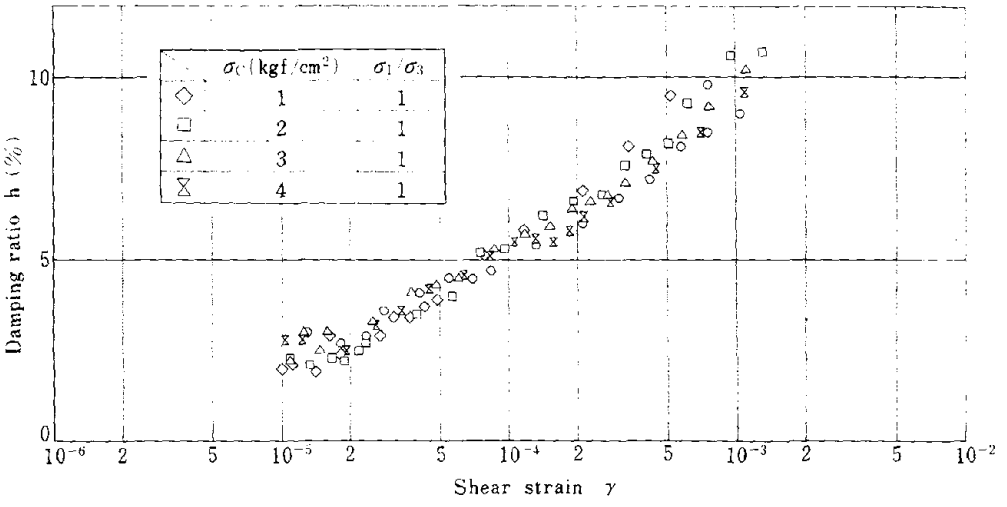

Fig. 8 Damping Ratio ∿ Shear Strain

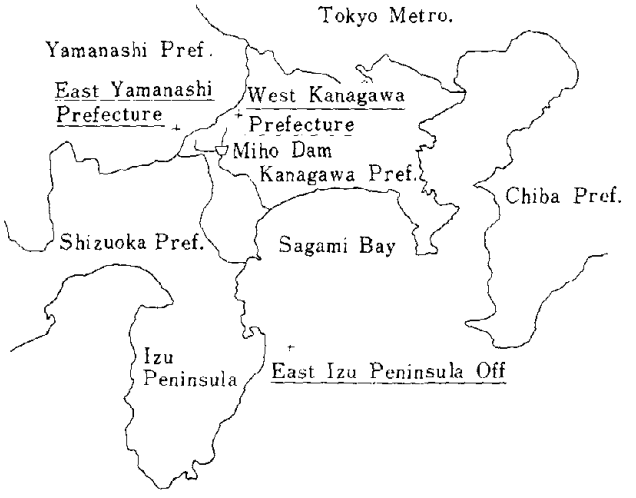

Fig. 9 Geographical Locations of Epicenters

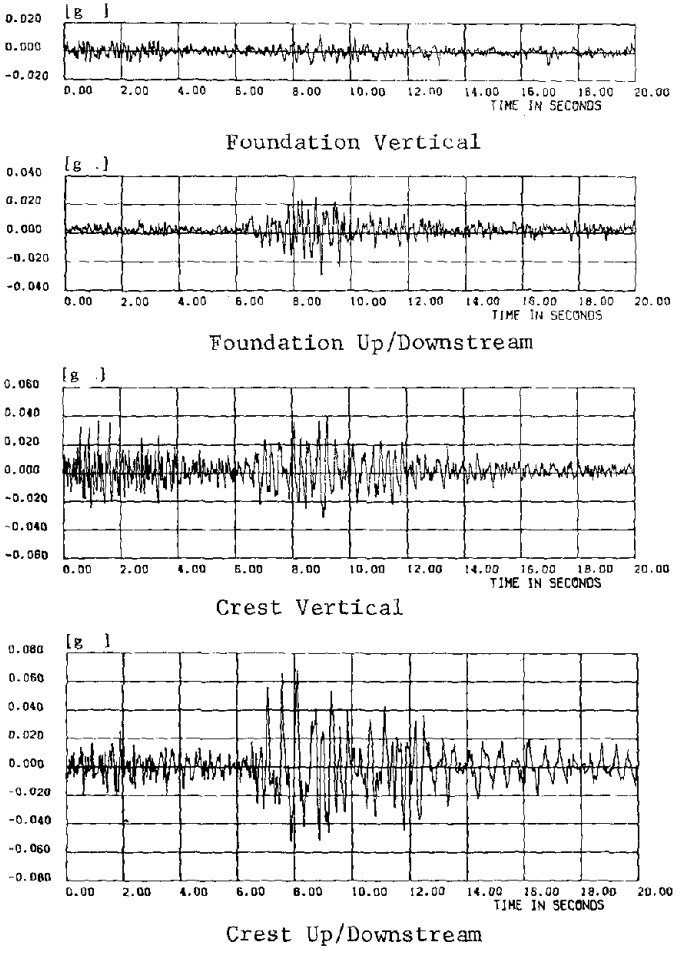

Fig. 10(a) Observed Earthquake (East Izu Peninsula Off)

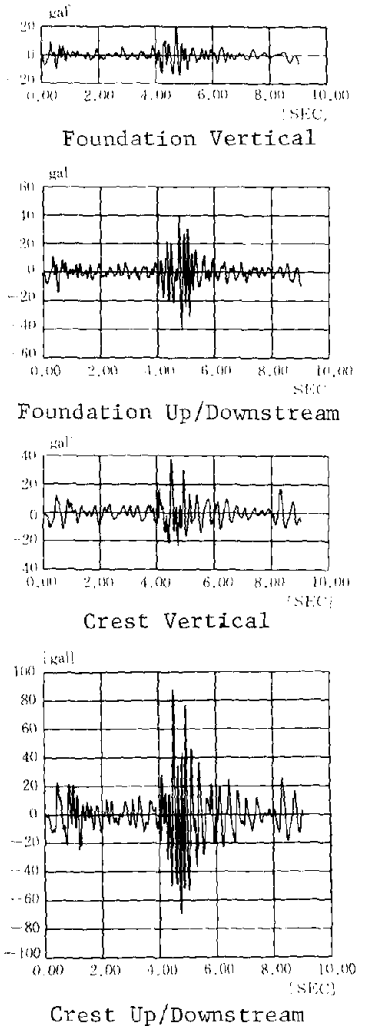

Fig. 10(b) Observed Earthquake (East Yamanashi Prefecture)

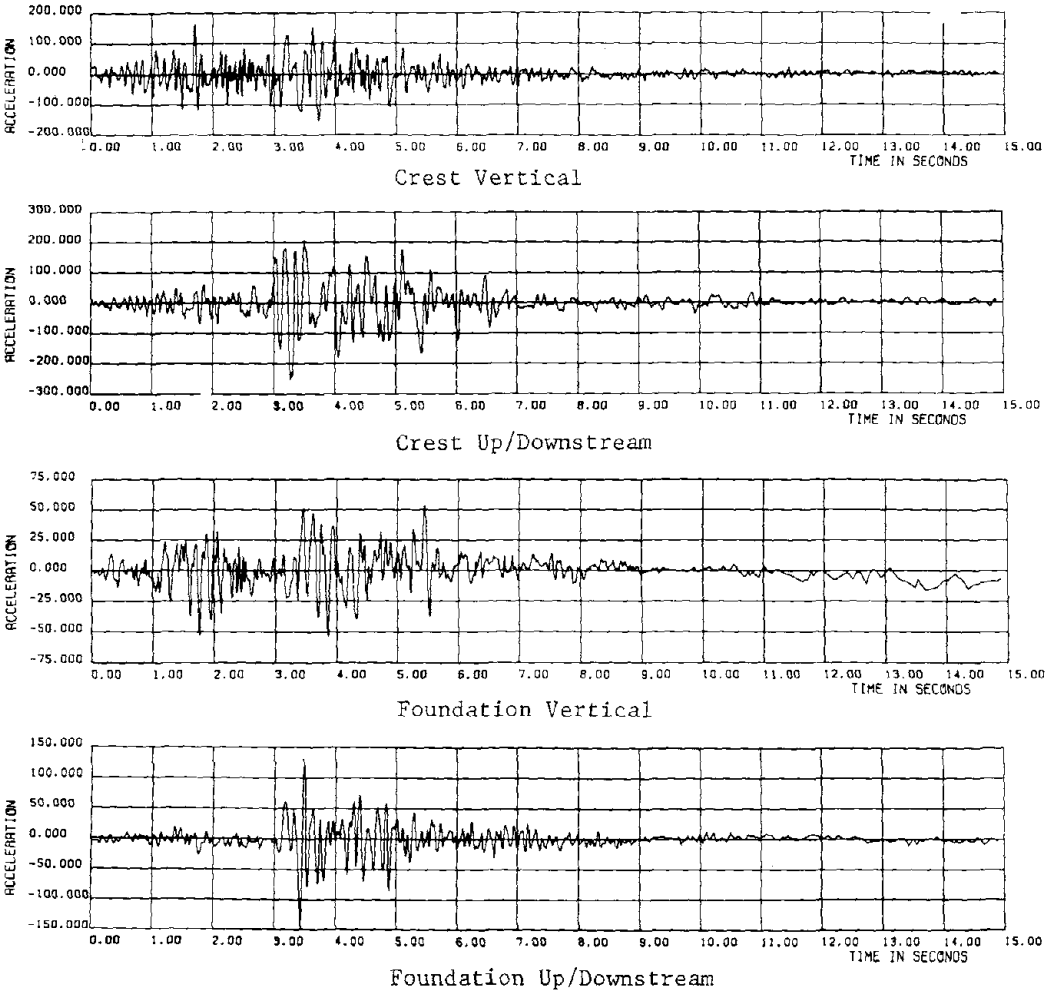

Fig. 10(c) Observed Earthquake (West Kanagawa Prefecture)

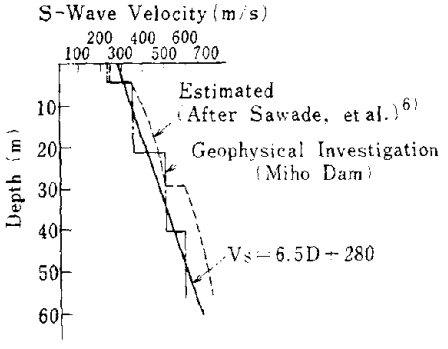

Fig. 11 Determination of Initial Shear Modulus (S-Wave Velocity)

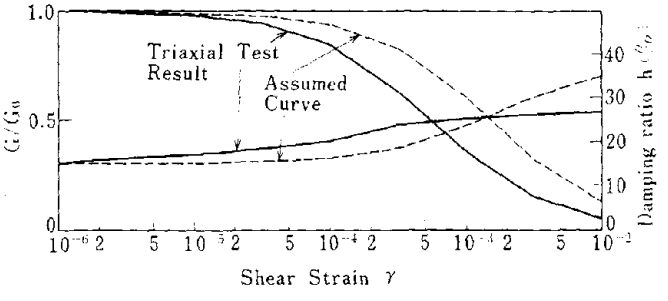

Fig. 12 Strain Dependency of Shear Modulus and Damping Ratio for Computation

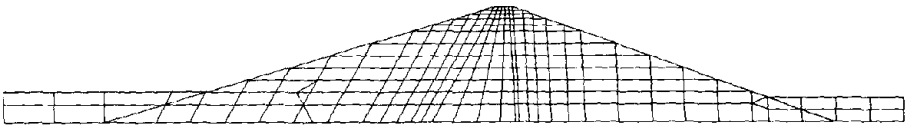

Fig. 13 F.E.M. Discritization for Computation

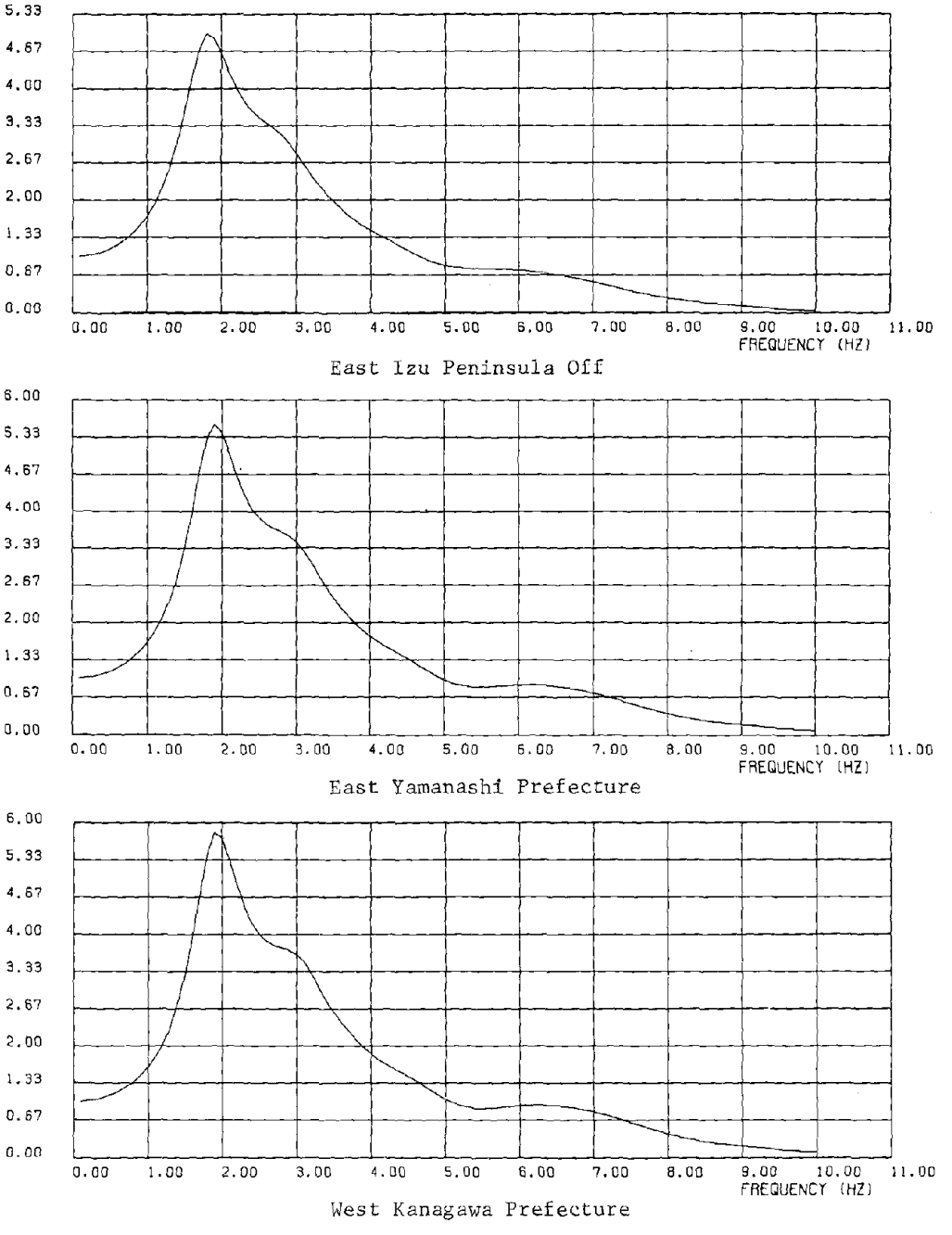

Fig. 14 Calculated Frequency Response Function at Crest

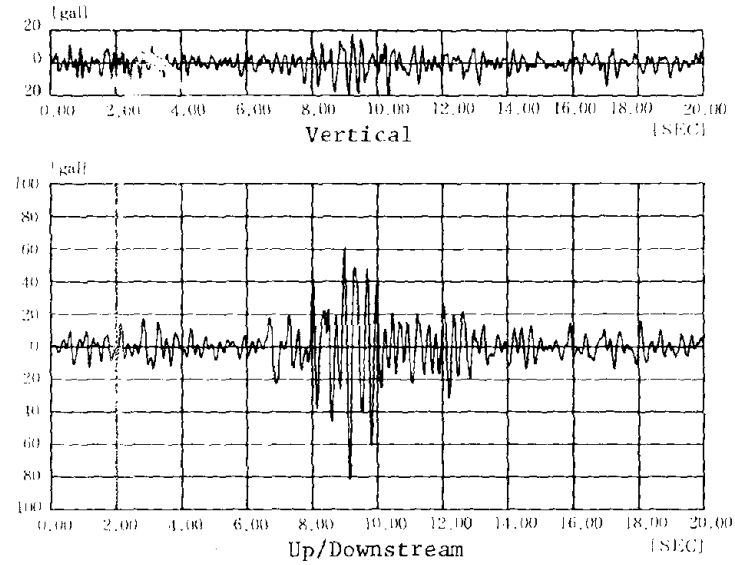

Fig. 15(a) Calculated Response Acceleration at Crest (East Izu Peninsula Off)

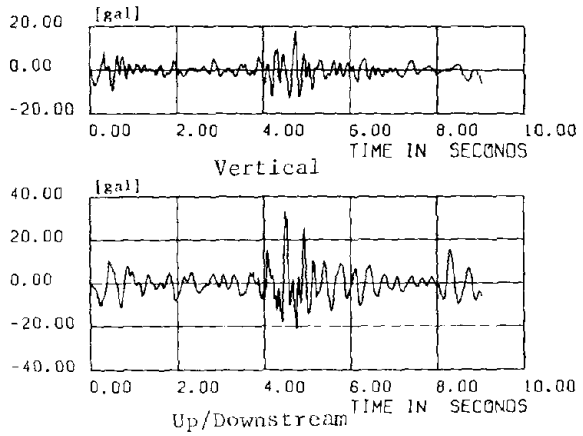

Fig. 15(b) Calculated Response Acceleration at Crest (East Yamanashi Prefecture)

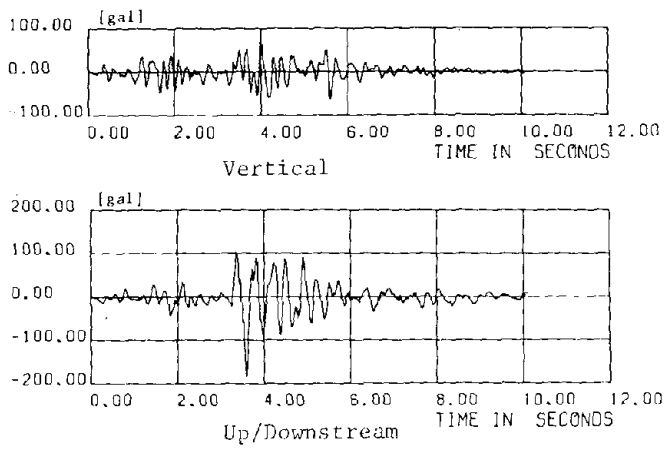

Fig. 15(c) Calculated Response Acceleration at Creast (West Kanagawa Prefecture)

VIBRATION TEST OF RICHARD B. RUSSELL CONCRETE DAM AFTER RESERVOIR IMPOUNDMENT

BY

R. J. SMITH

ABSTRACT

A second forced vibration test of Richard B. Russell Dam was conducted after a reservoir was impounded. The dynamic properties of a concrete gravity dam with hydrodynamic interaction were experimentally measured. Richard B. Russell Dam has recently been built by the Corps of Engineers approximately 170 miles (272 kilometers) from the mouth of the Savannah River between the States of Georgia and South Carolina. The crest of the concrete gravity part of the dam is 1884 feet long (574 meters) and is composed of 13 nonoverflow, 8 intake, and 11 spillway monoliths, the tallest of which is approximately 200 feet high (61 meters). The average reservoir height was 174 (52 meters)feet during the tests.

The structure was excited at three locations by a crest mounted 17,000 pound (7711 kilograms) inertial mass which was driven by an electrohydraulic servo-controlled actuator. The force input to the dam was computed as the product of the measured acceleration and the 17,000-pound (7711 kilograms) mass. Servo accelerometers with sensitivities ranging from 0.25 to 5.0 volts per g measured the horizontal accelerations of all 32 monoliths and the distributions of horizontal acceleration with elevation in the three drive point monoliths. Dynamic pressures were measured during two tests at the upstream face of the tallest nonoverflow monolith. Piezoelectric pressure transducers with a charge sensitivity of approximately 150 pico-coulombs per psi measured the dynamic pressures.

The results reveal the dynamic characteristics of the complex structure with hydrodynamic interaction. The natural frequencies, mode shapes, and damping ratios were determined. Results were compared with the previous test of the structure without the reservoir impounded. Relative joint motion was observed above a low response threshold.

Key Words: Forced Vibration Test; Frequencies; Mode Shapes; Damping Ratios; Transfer Functions; Accelerations

1. INTRODUCTION

In order to develop better design procedures for concrete dams subjected to earthquake forces, an understanding of the significant parameters that influence the dynamic properties of such structures is necessary. Assumptions regarding geometry, boundary conditions, and interaction with the foundation and reservoir can significantly affect earthquake response calculations. The vibration tests provide the means for determining the dynamic properties of the Richard B. Russell concrete dam and evaluating the various parameters that influence these properties.

The concrete dam includes a spillway section, a non-overflow section, and an intake section. The crest of the concrete gravity part of the dam is 1884 feet long (574 meters) and is composed of 13 non-overflow, 8 intake and 11 spillway monoliths, the tallest of which is approximately 200 feet (61 meters) high.

Forced vibration tests were made on the Richard B. Russell Dam before and after impoundment of the reservoir to determine the natural frequencies, mode shapes, modal damping ratios, and relative joint movements. The first low-level forced vibration test was conducted in January and February 1982 which seized a rare opportunity to experimentally measure the dynamic properties of a concrete gravity dam without hydrodynamic interaction. Another forced vibration test was performed in June and July 1984 after impoundment of the reservoir. This provides an experimental measure of the prototype hydrodynamic interaction and a comparison of the changes of the dynamic properties. The validity of 2-D and 3-D finite element analyses were checked against the experimentally measured dynamic properties.

The dynamic properties of the dam will also be used to provide a record of the dam's structural condition as built. In the event an earthquake should damage the dam in the future, the test data will be useful in determining the significance of the damage.

2. EXPERIMENTAL EQUIPMENT

Richard B. Russell Dam was excited by a 17,000-lb (7,711-kg.) inertial mass which was welded to a steel plate which was epoxied to the mass concrete of the dam. The force input to the dam was computed as the product of the measured acceleration and the 17,000-lb. mass.

Accelerometers were used to measure the horizontal accelerations of the concrete dam. Most of these accelerometers have a sensitivity of approximately 5 volts per g. A few of the close-in measurements were taken using 0.25 vol' per g accelerometers. The accelerometers have a

Office Chief of Engineers
Washington, D. C.

frequency response range from zero to 500 Hz. Analog signals were recorded on a tape and later digitized on a structural dynamics analyzer.

Peizoelectric pressure transducers were used to measure the hydrodynamic pressures. The transducers were mounted in special waterproof canisters bolted to the dam face by divers.

3. VIBRATION TESTS

The dam was excited at three different monoliths by the crest-mounted inertial mass. The force input was in an upstream-downstream direction. The three exciter locations were at monolith 7, a nonoverflow monolith with the mass mounted on the crest at elevation 494 feet (150 meters); monolith 16, a monolith between intake and spillway with the mass mounted in a recess at elevation 483 feet (147 meters); and monolith 22, a spillway monolith with the mass mounted on the crest at elevation 494.

Ideally it would be desirable to excite the dam at one location and mount enough transducers at all points of interest to measure the response of the structure. This was not possible because of the limited number of accelerometers available. The first set of crest and cantilever tests were performed starting with the 17,000-lb. inertial mass located on the crest of monolith 7. The first array of accelerometers was placed along the crest at the center of monoliths 1 to 16 to monitor the horizontal upstream-downstream motion. The 17,000-lb. mass was then moved to monolith 16 and the accelerometers were placed along the crest at the center of monoliths 7 to 22. So the accelerometer locations overlap on the crest of monoliths 7 to 16. The inertial mass was next moved to monolith 22 and the accelerometers were placed along the crest at the center of monoliths 16 to 32, so the accelerometer locations overlap on the crest of monoliths 16 to 22.

The accelerometers were placed at different elevations on both the upstream and downstream faces of monolith 7 to measure the horizontal cantilever motions. The accelerometers were placed at different elevations in the access shaft of monoliths 16 and 22.

Relative joint motion was measured at three locations and consisted of two accelerometers closely spaced on each side of the monolith joint being monitored. The measurements were made at non-overflow monolith joint 15-16 and intake crest joints 13-14 and 14 and 15.

All the tests were 1/2 decade/minute sine sweeps for 20 Hz to 2 Hz. This rate was found to be slow enough for a required quasi-steady state condition to provide enough data in a given time interval for adequate digital time resolution. Each test lasted about 5 minutes; but there were many hours of preparation required to conduct a test for a given array. The electrical signals output from the accelerometers and the vibrator were recorded as analog signals on a 32-track tape recorder.

4. DATA REDUCTION AND EXPERIMENTAL RESULTS

To conduct a modal analysis (obtaining the natural frequencies, damping ratios, and mode shapes) the recorded data were played back into a structural dynamic analyzer to digitize the analog signals. The force input and one of the response-accelerometers output formed an input/output (I/O) pair to compute a frequency response (transfer) function and coherence function. Typical frequency response (FRF) and coherence functions are shown in Figures I and II respectively. The coherence function is used to reveal the existence of any signals which may be contaminating the transfer function measurements. Modal parameters are identified in the analyzer by mathematically matching (curve fitting) an analytical form of a transfer function to measured data.

Hydrodynamic pressures were measured at monolith 7 with the exciter positioned on monolith 7. The piezoelectric transducers were placed at six elevations on the upstream face. The hydrodynamic pressures were successfully recorded during the low level vibration test in the frequency range of 2 to 25 hertz. To date the data has not been reduced. This will be included in the final report.

Ambient vibrations were present during the test. The main cause of these vibrations was water flowing over the spillway and through the low level sluices. The ambient vibrations were recorded and will be accounted for as the spectral density functions are prepared.

Work on the modal analysis is still underway. Preliminary results indicate a shift in three natural frequencies as shown in Table 1. Also shown are the frequencies arrived at by three dimensional finite element analysis of the dam without the reservoir. This analysis is discussed in detail in the attached Appendix A. The forced vibration test results were obtained by using a peak-picking method on the imaginary part of the frequency response function. The preliminary results also indicate no significant change in the damping ratios from values obtained in the first forced vibration test.

5. DISCUSSION OF RESULTS

Figure III shows the mode shapes in plan view of the crest of the dam for monoliths 8 to 21.

Figures IV, V, and VI show the comparative results of the dam crest mode shapes for both forced vibration tests and the 3-D finite element analysis. Changes in the maximum response location of the dam and a shift in frequencies occurs when there is a reservoir impoundment.

6. CONCLUSIONS

Since gathered data are still being reduced, only preliminary conclusions can be reached at this time. The final report for this study will include a complete analysis of the prototype tests results and a three-dimensional finite element analysis comparison including hydrodynamic interaction effects. To date we can conclude that:

a) Added water mass caused a decrease in the frequencies evaluated thus far.

b) The abutment on the Georgia side of the dam was not complete at the time the first test was made. The added mass of the additional soil caused a slight increase in the stiffness of the structure at the Georgia-side abutment.

c) The powerhouse is located at the downstream toe of the structure. It was not completed at the time of the first test but was at the time of the second test. This affected the rigid body modes the greatest.

d) The 3-D finite element analysis estimated frequencies higher than those measured experimentally. This is reasonable since the FE models are an approximation of the dam using a discrete number of degrees of freedom.

e) The best mode shape correlation was between the results from the experiment and the 3-D FE flexible foundation model for the dam with no reservoir.

SUMMARY OF FREQUENCIES

(ALL IN HERTZ)

MODE NO.	PROTOTYPE TESTS 1ST	PROTOTYPE TESTS 2ND	3-D FE ANALYSES FIXED BASE	3-D FE ANALYSES FLEXIBLE BASE
1	5.9	4.0	7.3	6.9
2	6.8	5.3	8.2	7.7
3	7.6	6.6	9.7	9.1

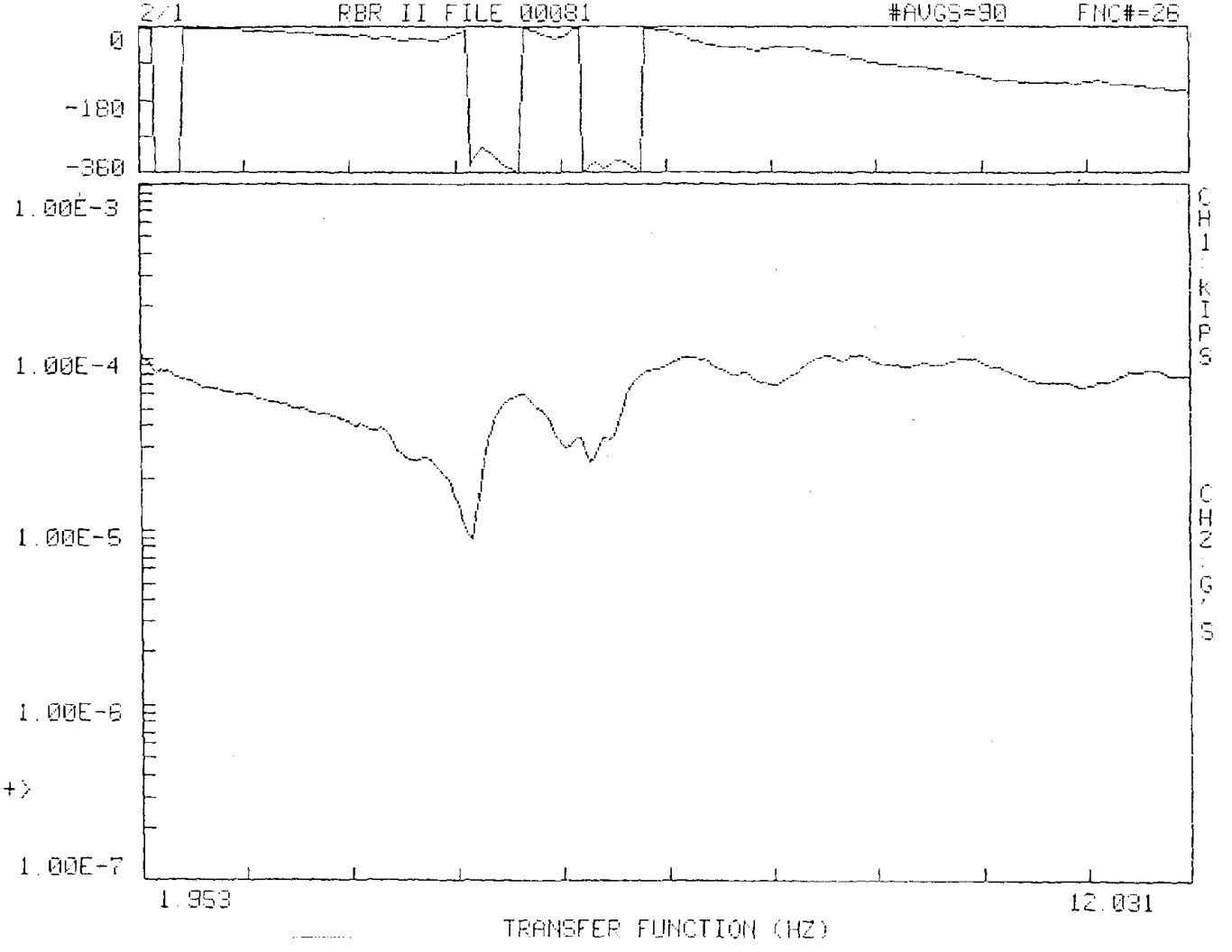

FIG. 1 EL 495, INPUT MONOLITH 16, OUTPUT MONOLITH 13-

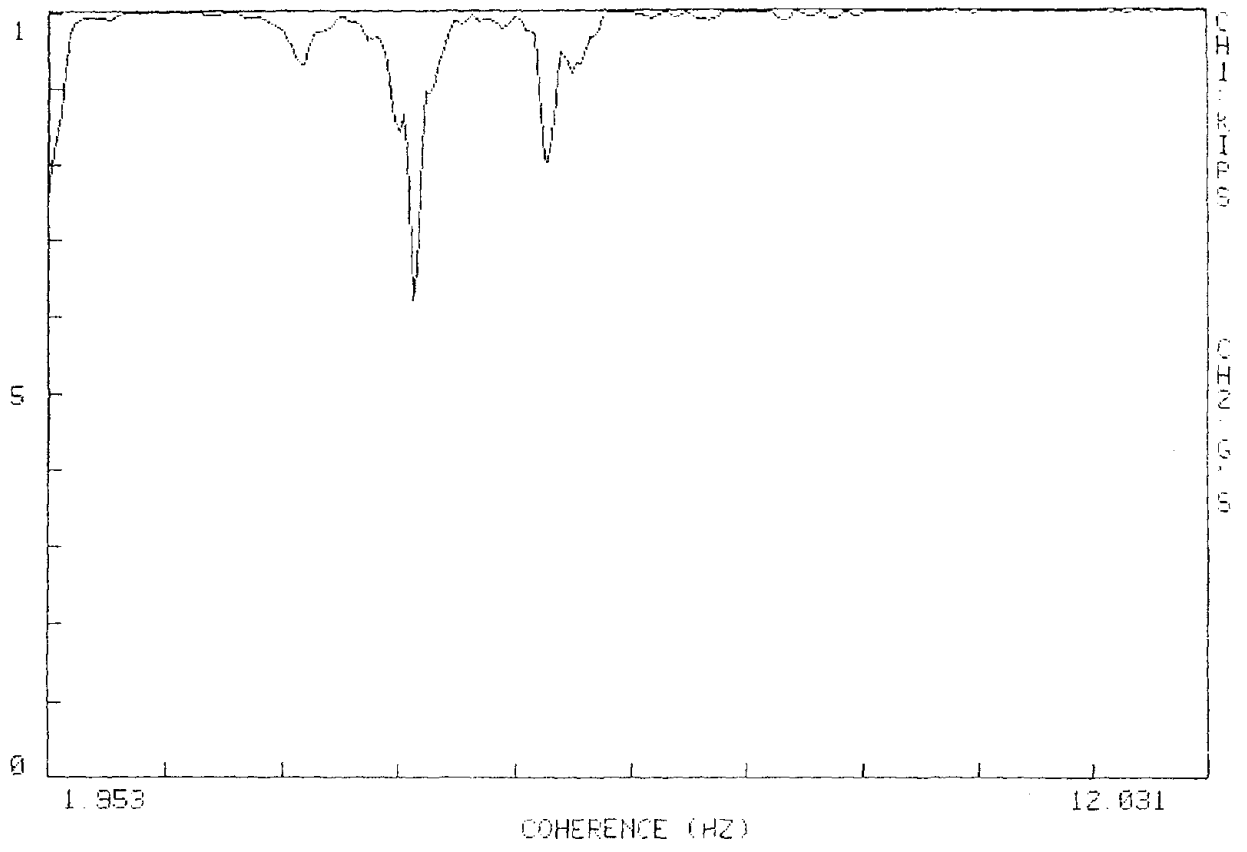

FIG. 2 EL 495, INPUT MONOLITH 16, OUTPUT MONOLITH 13 -

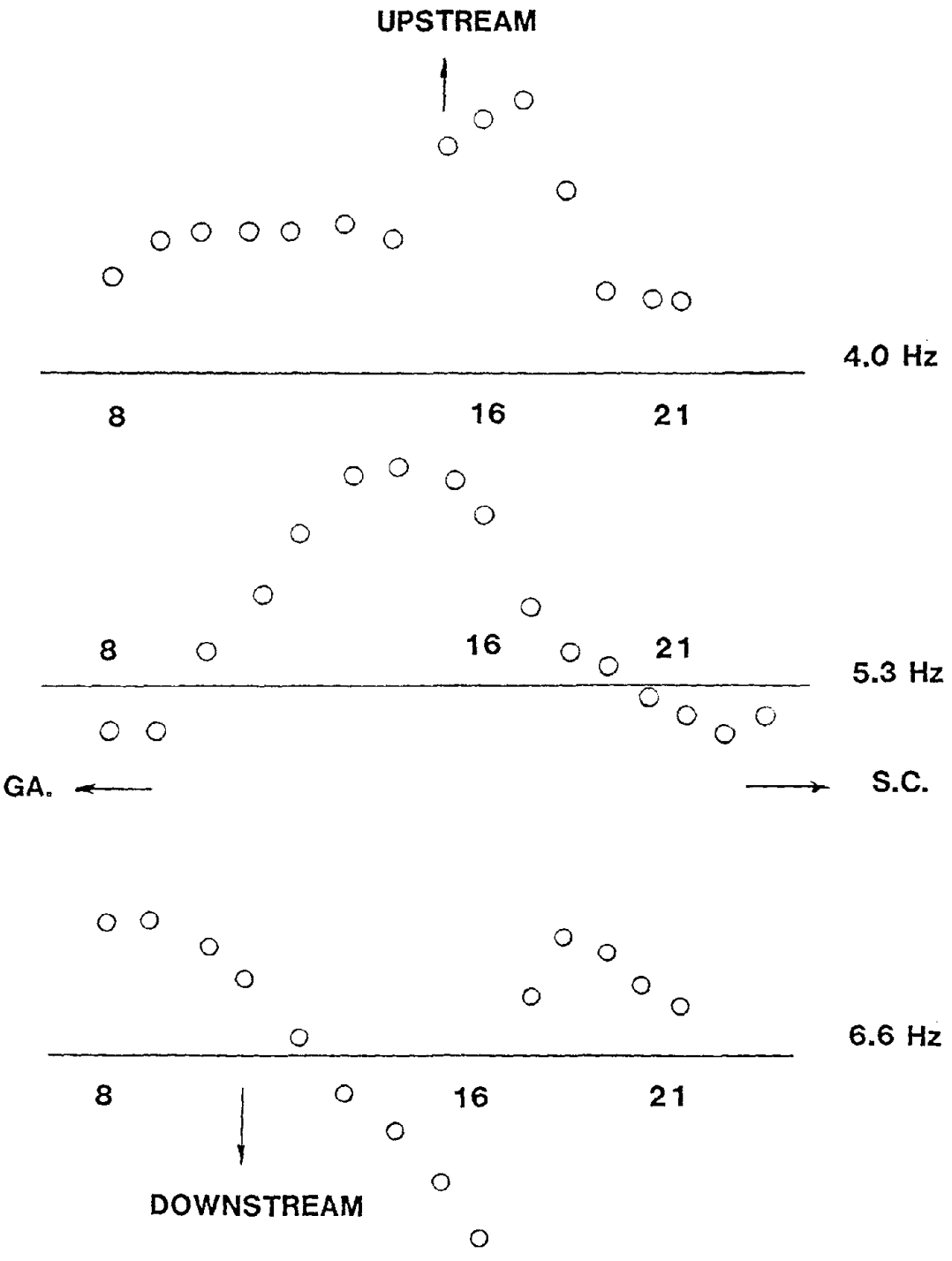

CREST PLAN VIEW OF MODE
SHAPES FROM MONOLITHS 8-21

FIG. 3

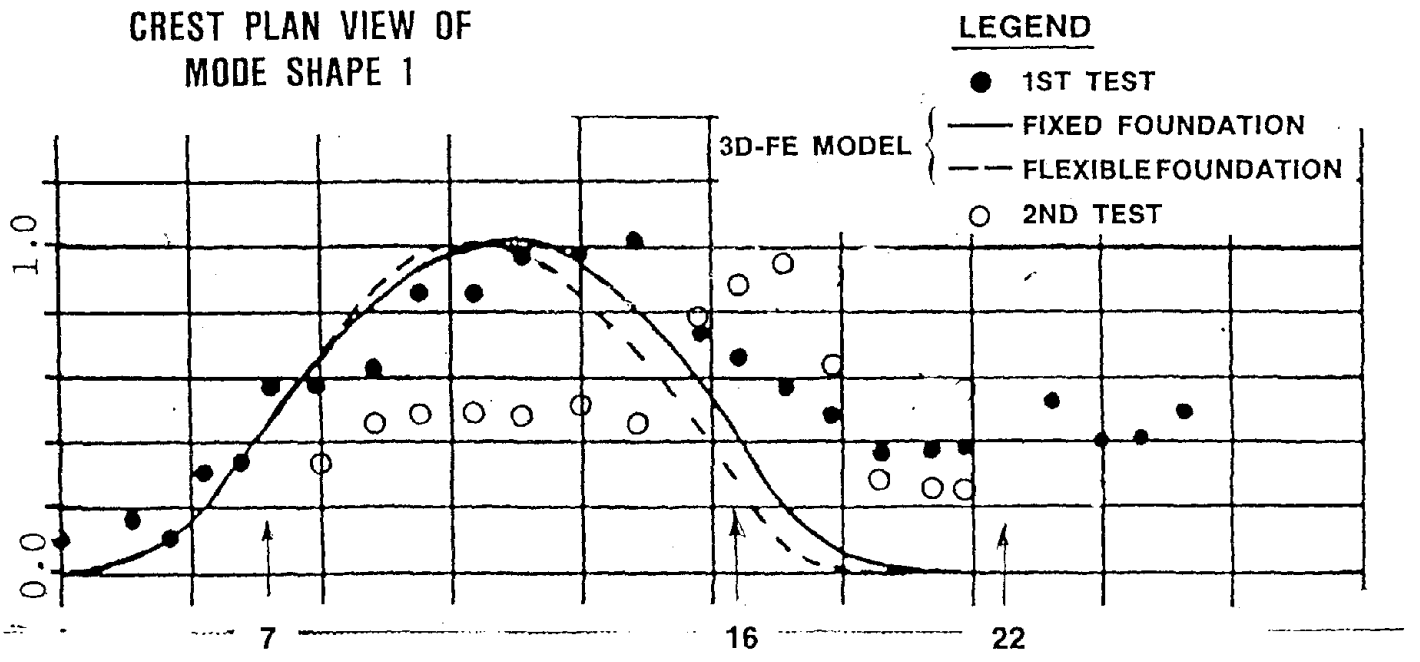
CREST PLAN VIEW OF
MODE SHAPE 1
LEGEND
1ST TEST
3D-FE MODEL
FIXED FOUNDATION
FLEXIBLE FOUNDATION
2ND TEST
1.0
0.0
7
16
22

FIG. 4

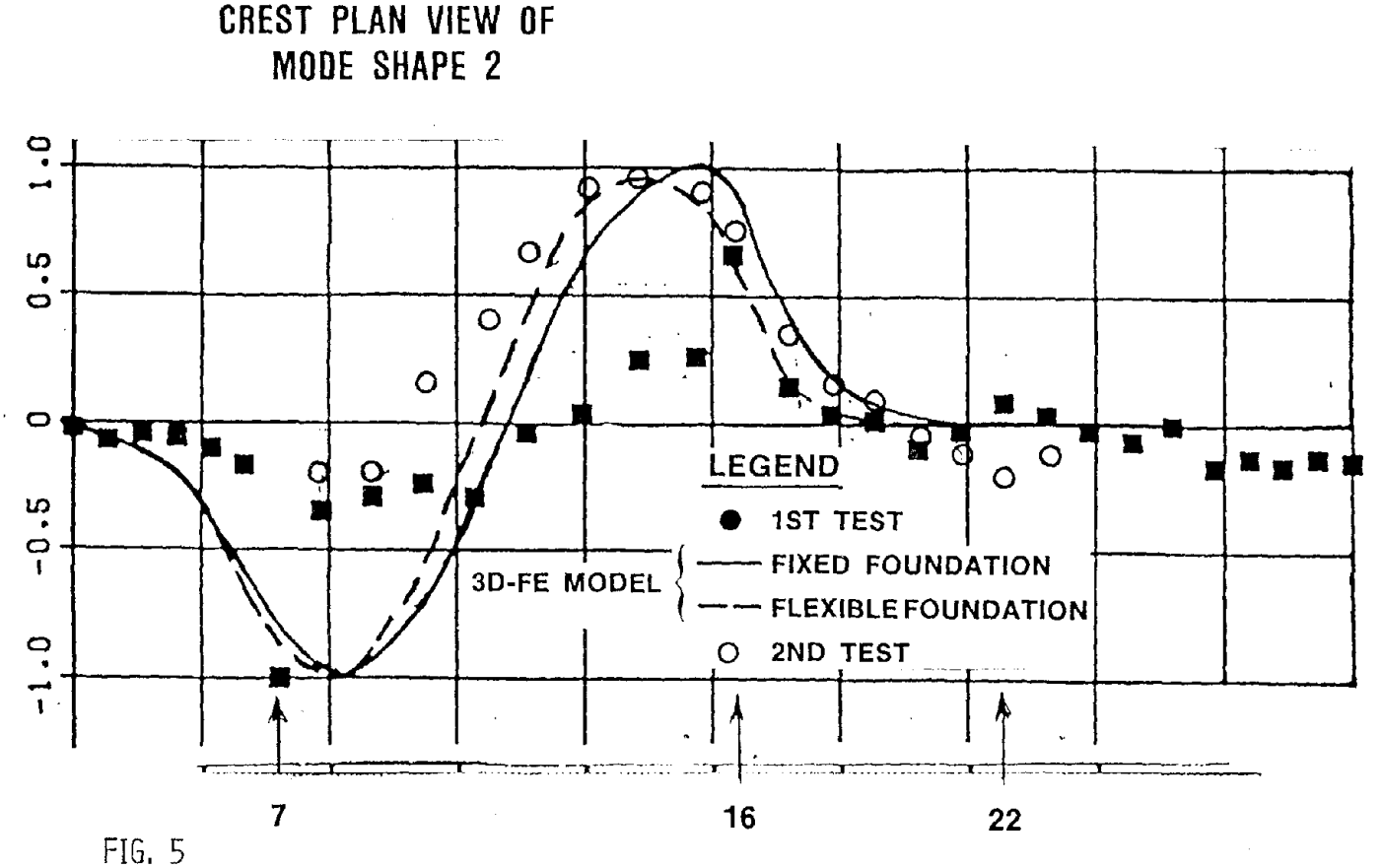
CREST PLAN VIEW OF
MODE SHAPE 2
1.0
0.5
0
-0.5
-1.0
LEGEND
1ST TEST
3D-FE MODEL
FIXED FOUNDATION
FLEXIBLE FOUNDATION
2ND TEST
7
16
22

FIG. 5

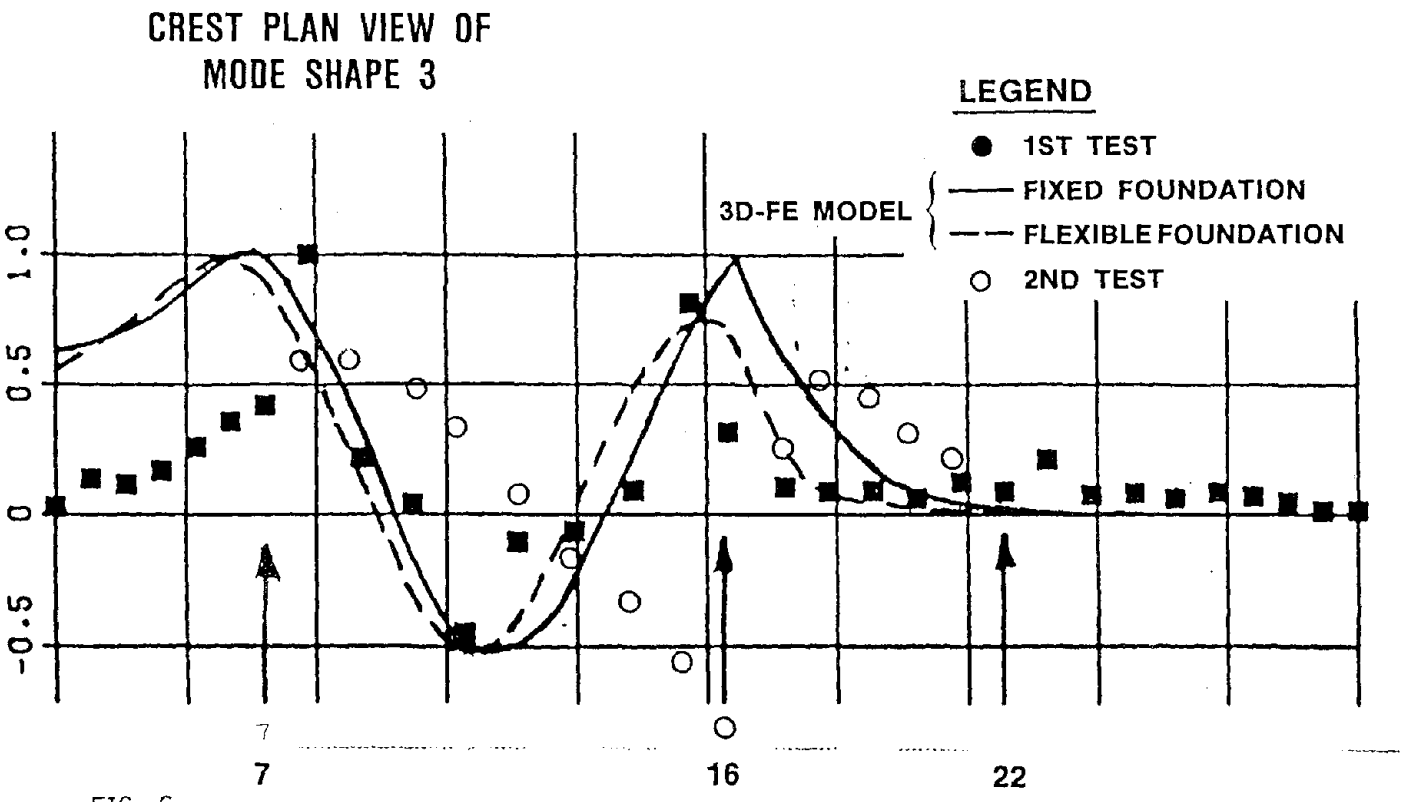
CREST PLAN VIEW OF
MODE SHAPE 3
LEGEND
1ST TEST
3D-FE MODEL
FIXED FOUNDATION
FLEXIBLE FOUNDATION
2ND TEST
1.0
0.5
0
-0.5
7
16
22

FIG. 6

APPENDIX A

LINEAR FINITE ELEMENT COMPARISON WITH EXPERIMENTAL MODAL ANALYSIS FOR A CONCRETE GRAVITY DAM

Vincent P. Chiarito
Research Structural Engineer
U. S. Army Engineer Waterways Experiment Station
P. O. Box 631
Vicksburg, Mississippi 39180

ABSTRACT

Three-dimensional finite element (FE) analyses of a concrete gravity dam were conducted to determine the dam's natural frequencies and mode shapes. The results of the linear elastic FE analyses were compared to the dynamic properties computed from experimental results. Two models for the foundation were used. The first model used a fixed base for the foundation (or a rigid foundation) and the second used vertical and horizontal spring elements. The springs were used only to qualitatively model the effect of dam-foundation interaction. A modal assurance criterion was used to evaluate the correlation between mode shapes computed from the FE dynamic analyses and experimental results.

INTRODUCTION

The results of linear elastic three-dimensional (3-D) dynamic finite element (FE) analyses of the Richard B. Russell Dam with an empty reservoir were compared to the experimental results of the first prototype vibration test.(1) This comparison provides one basis for assessing the accuracy of linear elastic FE models for predicting dynamic properties of concrete gravity dams. A subspace iteration method was used to solve for the undamped natural frequencies and mode shapes in the FE analyses.

The dam was modelled with its in situ boundary conditions present at the time of the vibration test.(1) Two FE models bounded assumptions for the stiffness of the foundation: (1)fixed foundation-completely rigid and (2) flexible foundation-modelled with vertical and horizontal springs. No attempt was made in this paper to completely determine the effects of dam-foundation interaction during earthquakes.

The crest length of the concrete dam is 1,884 feet (574 meters) and is composed of 13 nonoverflow, 8 intake, and 11 spillway monoliths. The tallest monolith is approximately 200 feet (61 meters) high.(1) Two-dimensional (2-D) and 3-D parameter studies were conducted to obtain appropriate FE grid sizes for each of the three differently shaped monoliths. A compatible grid was found for all of the monoliths , thus making possible the generation of the nodal and element data with the computer. Figures 1 through 3 show typical sections of the monoliths and the resulting 3-D grids of each monolith. In Figure 4 the resulting 3-D FE grid of the Richard B. Russell Dam is shown. The 3-D FE model is composed of 3-D solid brick, beam, and plate elements. The comparison between the analytical (FE) and the experimental mode shapes was evaluated using a modal assurance criterion.(2)

FINITE ELEMENT MODEL

The grid for the FE model was developed by conducting 2-D and 3-D modal analyses of each isolated monolith. For each monolith uniform 2-D grids were constructed and the FE modal analysis results were compared to those resulting from the grids shown in Figures 1, 2, and 3. The parameter studies involved using dynamic material properties determined by previous tests on standard 6- by 12-in. (152- by 305-mm.) concrete cylinders. (3) Favorable results were obtained when the 2-D and 3-D modal analyses using the uniform grids were compared to analyses using the grid for the entire 3-D FE model .

Three element types were used to model the dam.(4) Variable-number-nodes (8 to 21 nodes) thick shell and 3-D elements were used to model the mass concrete of the nonoverflow , intake , and spillway monoliths. Beam elements were used to model the roadways connecting the

concrete piers of the spillway monoliths at the crest elevation. Plate elements were used to model the concrete spillway piers. Figure 2b shows the penstock tube openins modelled as elements with a smaller stiffness than the mass concrete's stiffness through the width of the intake monoliths. Figure 3b shows the locations of the beam and plate elements for a 3-D FE grid of two spillway monoliths. Once the compatible grid was found for the interfacing sections among the three monoliths, the nodal point and the element data were generated with a computer.

The boundary conditions for the fixed base model were such that all nodes along the base had all degrees of freedom deleted. The nodes at the two dam-abutment sections , except at the base, had degrees of freedom defined in the plane of each section.(3) Vertical and horizontal springs were attached to the previously fixed nodes of the base. The spring constant was computed from available results for the dynamic elastic modulus of the foundation.(5) The springs allowed motion only in the vertical plane perpendicular to the longitudinal axis of the dam. The degrees of freedom at the dam-abutment interfaces were still allowed in the plane of those two sections of the dam. A total of 5,190 and 5,606 degrees of freedom were used for the fixed base and the flexible base FE models, respectively.

RESULTS

The 3-D shapes shown in Figure 5 are the first five normal modes of the dam's vibration assuming a rigid foundation model. At 8.1 Hz the major response is associated with the sidesway of the roadway and concrete spillway pier system. The other mode shapes show that the major responses of the dam are associated with bending of the dam perpendicular to the longitudinal axis of the dam. Mode no. 5 at 10.3 Hz is the shape computed by the FE analysis but not measured experimentally. This was suspected due to the possibility of the exciter locations existing at nodes of that mode shape during the vibration test.(1) The fixity of the dam abutment interfaces was not modelled so the crest of the dam at the ends is free.

Comparisons of the mode shapes are shown in Figure 6. The solid symbols represent the normalized mode shape vectors of the experimental results. The solid and dotted lines respectively represent the normalized mode shapes for the flexible and fixed foundation models. Table 1 summarizes the results of the comparisons in Figure 6. In Figure 6a the comparison of the results from the three estimates of mode no. 1 is favorable. Modelling the foundation flexibility improved the correlation between mode shapes as computed by the modal assurance criterion value.(2) The frequencies estimated by the FE models are higher than frequencies measured experimentally. This is reasonable since the FE models are an approximation of the dam using a discrete number of degrees of freedom. The FE model in this case is stiffer than the actual dam. For a qualitative comparison the mode shapes all seem to have the largest amplitude in the same general location on the crest of the dam. The modal assurance criterion does indicate quantitatively how good the comparison is among modes.

CONCLUSIONS

A 3-D linear FE analysis has been compared with previous experimental estimates of the modal parameters of a concrete gravity dam. Using available dynamic material properties of the dam concrete and the foundation, a 3-D FE model was successfully developed to estimate the linear elastic modal properties of the dam. The modal assurance criterion was computed for mode shape comparisons between the experimental and the FE results. The values computed using the modal assurance criterion ranged from 0.29 to 0.72. Quantitative comparisons indicate that a reasonable 3-D FE model was developed from available material properties for computing the dam's first natural mode of vibration. A mode shape that was not measured experimentally was computed by the 3-D FE analyses. The modal assurance criterion was useful for evaluating the correlation among the mode shapes. The best mode shape correlation was between the results from the experiment and the 3-D FE flexible foundation model.

ACKNOWLEDGEMENTS

The results presented herein, unless otherwise noted, were obtained from research conducted under the Structural Engineering Research Program of the U. S. Army Engineer Waterways Experiment Station. Permission was granted by the Office, Chief of Engineers to publish this information.

REFERENCES

(1) Chiarito, Vincent P., and Mlakar, Paul F. "Modal Test of a Concrete Gravity Dam," Proceedings of the 2nd International Modal Analysis Conference, Volume 1, pp. 142-148, 1984.

(2) Allemang, R. J., and Brown, D. L. "A Correlation Coefficient for Modal Vector Analysis," Proceedings of the 1st International Modal Analysis Conference, pp. 110-116, 1982.

(3) Chiarito, Vincent P., and Mlakar, Paul F. "Vibration Test of Richard B. Russell Concrete Dam Before Reservoir Impoundment," TR-SL-83-2, May, 1983.

(4) Bathe, K. J., Wilson, E. L., and Peterson, F. E. "SAPIV: A Structural Analysis Program for Static and Dynamic Response of Linear Systems," University of California, Earthquake Engineering Research Center, Richmond, California, 1973.

(5) Chiarito, Vincent P., Wang, Xianru, and Chen, Yangyou, "Linear Elastic, Three-Dimensional Finite Element Modal Analysis of Richard B. Russell Concrete Dam Before Reservoir Impoundment," Technical Report SL-85-nn, U. S. Army Engineer Waterways Experiment Station, Vicksburg, Ms., 1985.

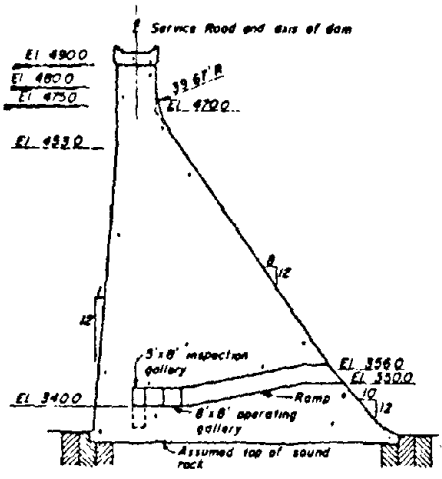

TYPICAL NONOVERFLOW

FIGURE 1 a. View of typical nonoverflow section.

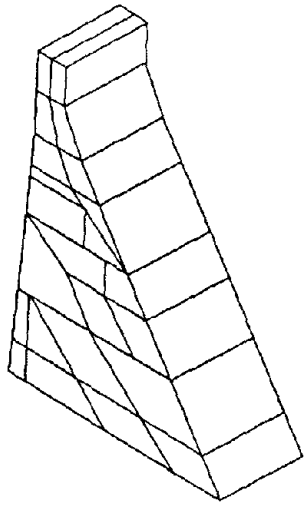

b. View of typical 3-D FE grid of one nonoverflow monolith.

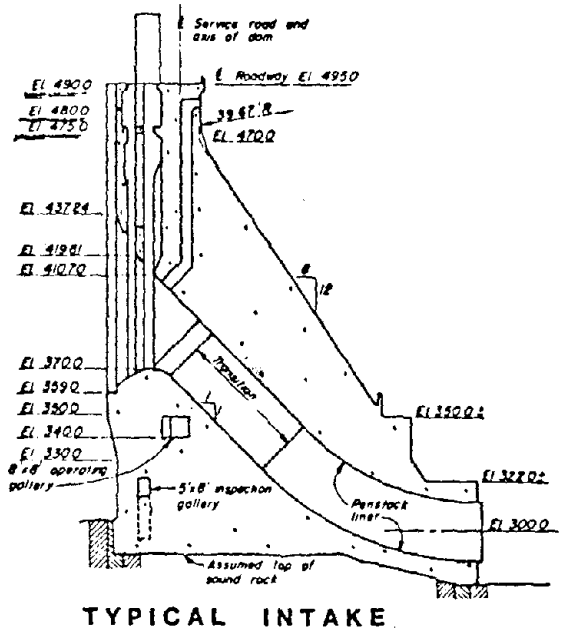

TYPICAL INTAKE

FIGURE 2 a. View of typical intake section.

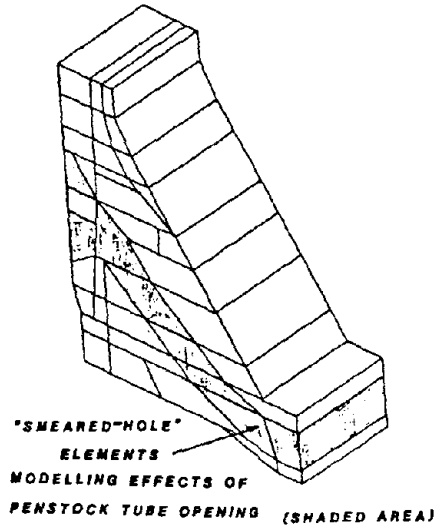

b. View of typical 3-d FE grid of one intake monolith.

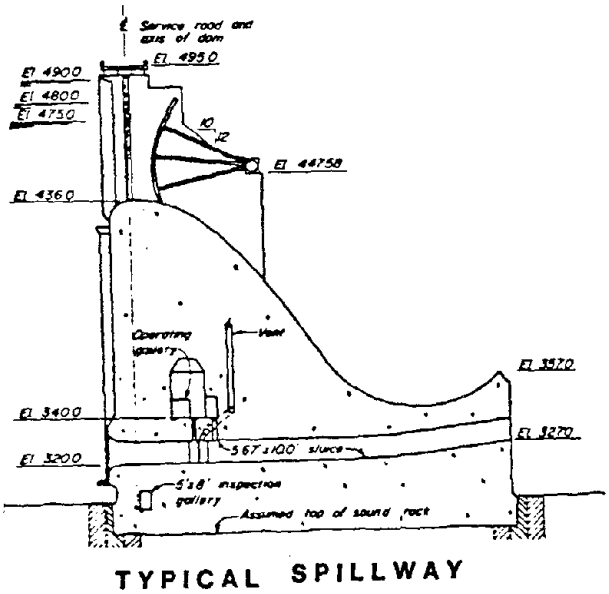

FIGURE 3 a. View of typical spillway section.

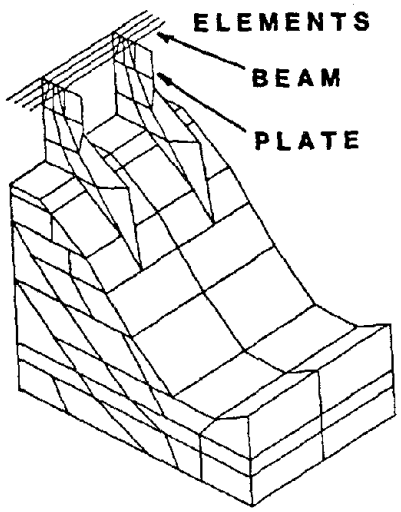

b. View of typical 3-D FE grid of one spillway monolith.

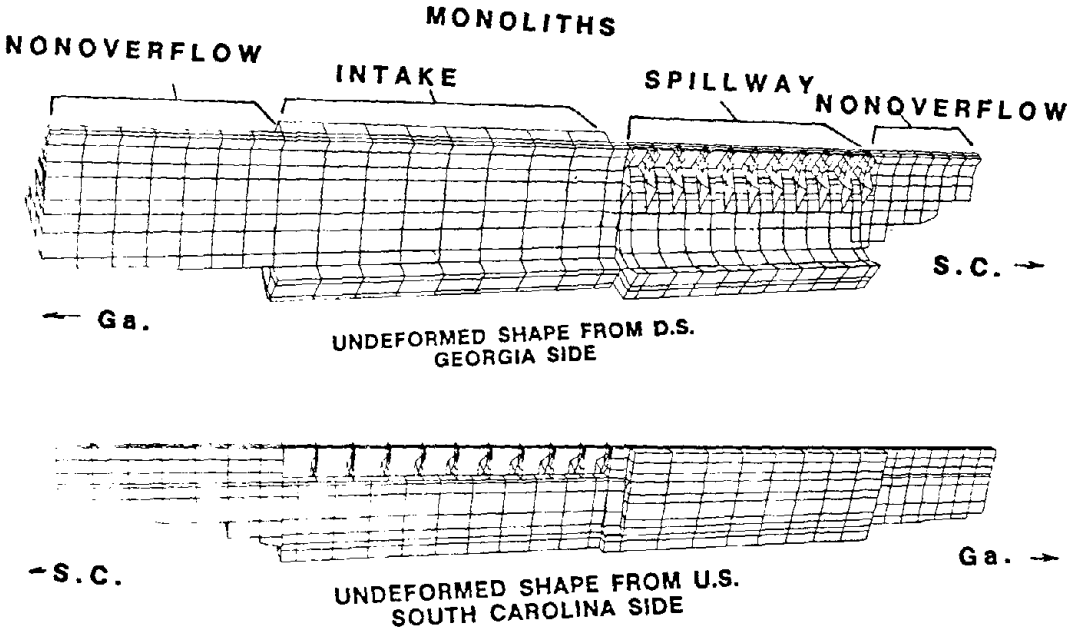

FIGURE 4. View of 3-D FE grid of entire dam from downstream (D.S.) Georgia (Ga.) and upstream (U.S.) South Carolina (S.C.) sides.

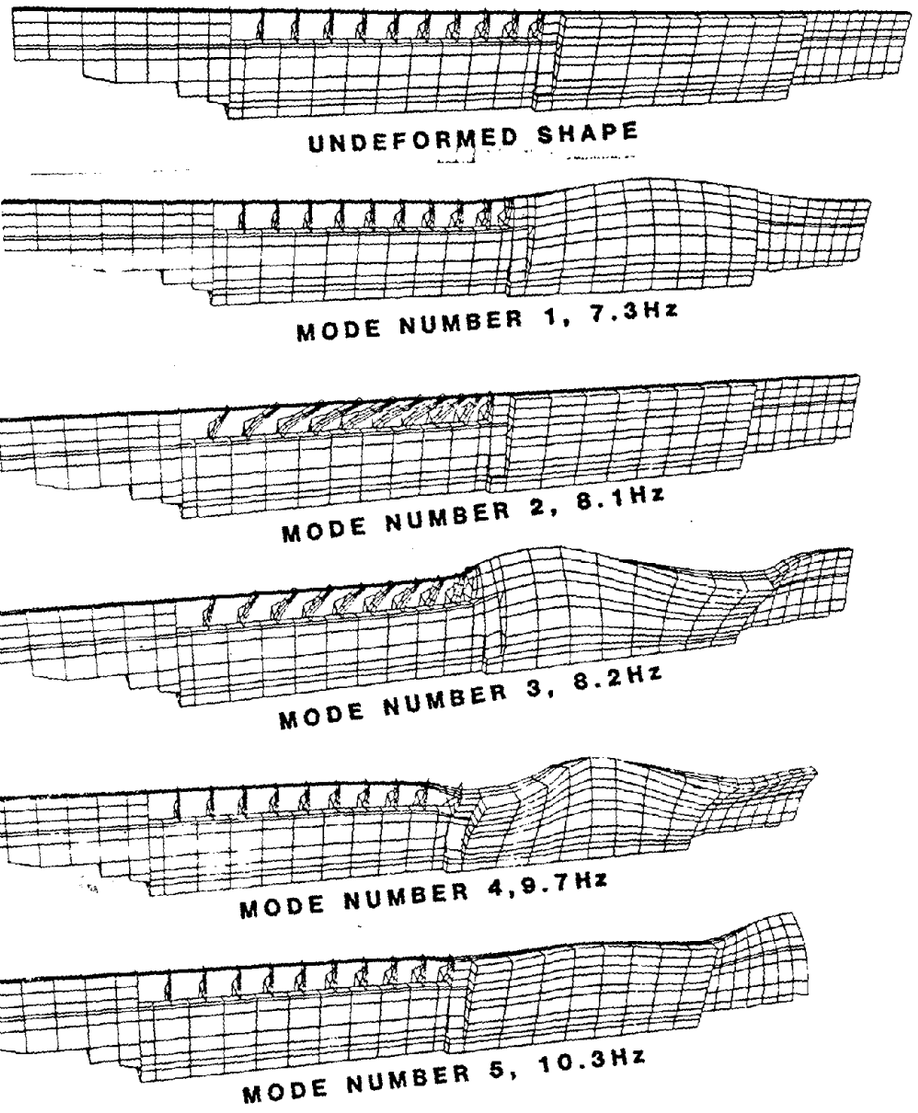

FIGURE 5. View of 3-D mode shapes computed by the FE model for the fixed base model.

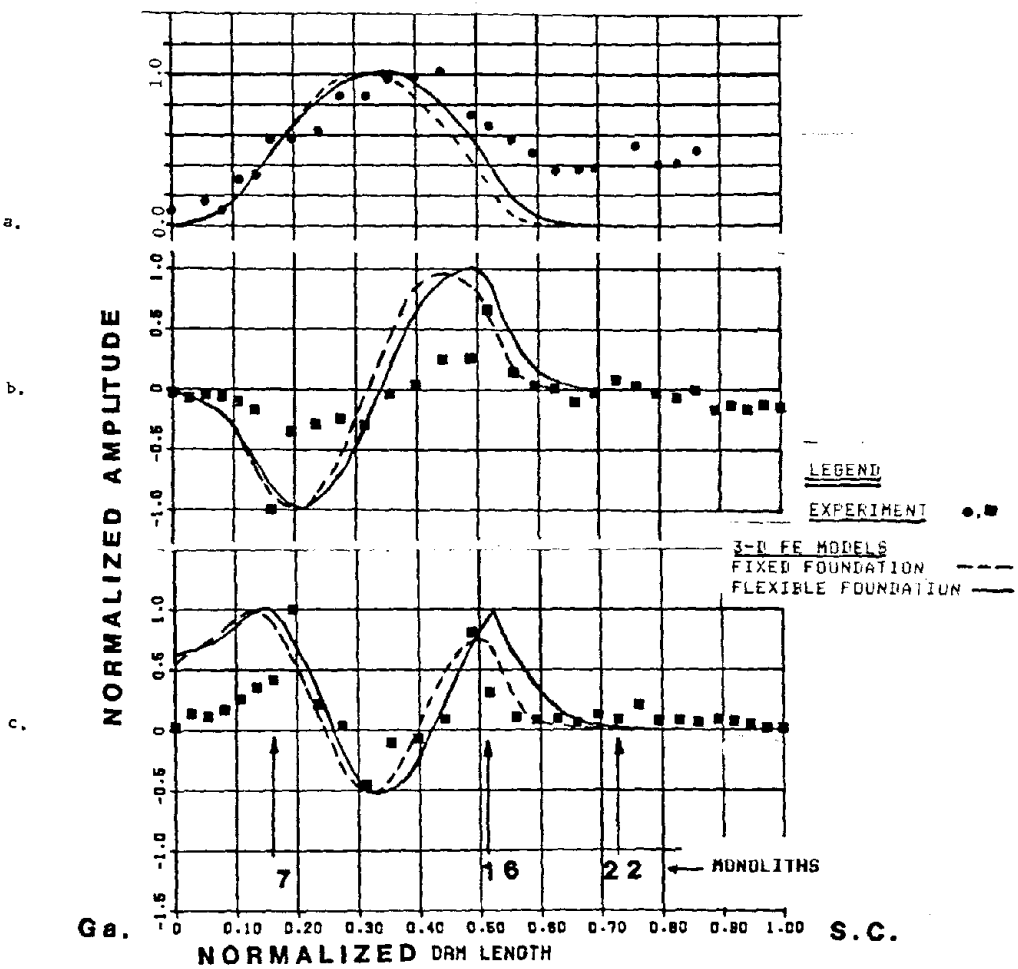

FIGURE 6. Plan view of normalized mode shapes at the crest.

TABLE 1. Summary of mode shape comparisons.

REFER TO FIGURE 6 PART	PROTOTYPE VIBRATION TEST (3)		3-D FE DYNAMIC ANALYSES					
			FIXED BASE			FLEXIBLE BASE		
	MODE NUMBER	FREQUENCY (Hz.)	MODE NUMBER	FREQUENCY (Hz.)	MACN *	MODE NUMBER	FREQUENCY (Hz.)	MACN *
a	1	5.9	1	7.3	0.67	1	6.9	0.72
b	2	6.8	2	8.2	0.29	2	7.7	0.33
c	3	7.6	3	9.7	0.54	4	9.1	0.69

*CORRELATION VALUE COMPUTED BY MODAL ASSURANCE CRITERION(2)

EARTHQUAKE RESISTANT BRIDGE DESIGN IN CALIFORNIA

by
James H. Gates (1)

ABSTRACT

The current seismic design criteria for bridges in California at CALTRANS is discussed. A second criteria which now being used in the United States outside of California, which was developed by the Applied Technology Council, is also discussed This second criteria was recently adopted by the American Association of State Highway and Transportation Officials (AASHTO), as a national guideline specification. The procedure used in California for the preparation of site-specific response spectra is also discussed. Other recent developments discussed include the application of interactive computer programs to column and foundation design, current column and footing details, the current status of the California seismic retrofit program for bridges and information on results from the the instrumentation of California bridges for strong-motions.

1. INTRODUCTION

This paper is an extension and update of the previous paper presented at the UJNR in 1983 (11).

The current seismic design criteria for bridges in California is based on work at CALTRANS after the 1971 San Fernando earthquake (9,10,17). Later efforts by the Applied Technology Council (16), resulted in a second criteria which now being used in the United States outside of California. This second criteria was recently adopted by the American Association of State Highway and Transportation Officials (AASHTO), as a national guideline specification (13). Although there are differences between these two criteria, the underlying philosophy of each are identical. Both utilize elastic force level spectra with a post-analysis reduction for ductility. The design force in a particular member is thus dependent on the seismicity, site conditions and the post-yield characteristics of the member itself. Both criteria permit the development of special site-specific elastic spectra.

This paper will describe the procedure used in California for the preparation of site-specific response spectra Other recent developments discussed include the application of interactive computer programs to column and foundation design, current column and footing details, the current status of the California seismic retrofit program for bridges and further information on results from the the instrumentation of California bridges for strong-motions.

2. DEVELOPMENT OF SITE-SPECIFIC RESPONSE SPECTRA

The CALTRANS seismic criteria (3), permits the development of special design response spectra for specific sites. The spectrum is a 5% damped elastic acceleration spectrum which describes the maximum expected response at the surface of the site. This spectrum is referred to as an 'ARS' spectrum; where AR is the acceleration spectrum in rock-like material at the site and S is the soil amplification factor (9,10,17).

The use of site-specific spectra is usually limited to large projects in high seismic regions. For example: The Route 105 Freeway, (or Century Freeway), to be located in Los Angeles will extend eastward from the Los Angeles International Airport approximately 18 miles (29 km). The estimated cost of this project is about $1.5 billion (US), including approximately $450 million (US) for over 200 structures. The project is expected to be completed in late 1992.

A series of site-specific response spectra were developed by CALTRANS TRANSLAB (6), for use in the design of the structures along the 18 mile (29 km) length of the project.

An extensive geotechnical investigation was performed, evaluating the materials along the length of the project (12). The surficial deposits along the length of the project were then characterized into three regions (6):

1. Recent dune deposits at the westerly end of the project.

2. Upper-Pleistocene terrace deposits in the middle portion of the project.

3. Recent alluvial deposits at the easterly portion of the project.

Eleven active faults were considered in the evaluation of the seismicity of the project area. One of these faults, the Newport-Inglewood, crosses the proposed freeway alignment in a NW-SE direction.

A tabulation of the active faults considered showing the distances to the project area and assumed magnitudes and durations are shown in Table 1.

Sensitivity studies were conducted to determine the effect of the distant faults on the motions at the project site and It was concluded that

(1) Structural Mechanics Engineer California Department of Transportation (CALTRANS)
Division of Structures, Office of Structures Design

the motions from the nearby Newport-Inglewood fault represented a conservative envelope of the response spectra for the range of rock motions at the site.

The field investigation for the ground response analysis consisted of thirteen, 6 inch (152 mm) holes drilled to depths of 200 to 350 feet (61 to 107 m), (6). In addition to densities and standard penetration tests, shear wave velocity profiles as deep as 350 feet (107 m) were determined using the procedure developed and documented by Beeston and McEvilly in 1977 (1). This procedure determines the velocity of a surface generated shear wave which is propagated downward to a geophone located in the bore hole. Several soil and shear velocity profiles were averaged to obtain a series of composite profiles for a series of six zones along the length of project. These zones are shown in Table 2. Boring logs for structures along the project length were reviewed to assure that computed spectra would be representative of ground motions for the sites within the zone.

Bedrock motions within the six zones were established by considering the closest distance from the causative fault to the zone and the maximum credible magnitude (See Table 1). The characteristics of the bedrock motions used for each zone were computed based on work by Seed et al. (22,23).

Two earthquake time histories were utilized to describe the bedrock motions; a deconvoluted 1940 El Centro rock motion by Seed and an artificial rock motion generated by Romstad (20).

Surface motions were computed by propagating both of these rock motions to the surface of a one-dimensional soil column.

The computer program, SHAKE (21) was used for this analysis.

The computation of the surface (or ARS) spectra was performed using a procedure similar to that used to develop the CALTRANS standard ARS curves (3,17). Recent investigators (2,14) have described this procedure as capable of obtaining a reasonable approximation of the motions at a site. The procedure is as follows:

1. Analyze a representative soil column for the bedrock motion using the SHAKE program (21).

2. Compute the 5% damped elastic response spectra for both the applied rock motion and the computed surface motion.

3. Compute the soil amplification curve (S curve) by dividing the surface spectrum by the rock spectrum.

4. Compute the surface ARS spectrum by multiplying the CALTRANS normalized rock spectra, R (17), by the peak rock acceleration at the site, A, and the computed soil amplification, S.

All soil columns were analyzed using a depth to rock-like material of 300 feet (92 m). This depth was selected after performing a series of sensitivity studies which evaluated the effects of depth variations to 600 feet (183 m) (6).

Smooth envelope spectra were prepared for each of the six zones. A comparison plot of the ARS curves developed for the project is shown in Fig. 1.

3. COLUMN AND FOOTING DESIGN

Recent criteria for the seismic resistant design of bridges (3,13) requires that any connections which are expected to undergo plastic deformation be able to develop the plastic moment and resultant shear as a limiting value. In California, this means that the plastic forces usually become the limiting design values to be used in the design of the connections. This load case when evaluated alone, tends to simplify the design of the connection.

In reality however, this requirement adds another level of complexity to the design process and the design engineer must now consider plastic loads in addition to evaluating loads at the factored and service level.

At CALTRANS the design of the column member is highly automated. An interactive computer program, YIELD, (7) is used to evaluate the column member for factored, service and plastic loads and determine vertical, shear and confinement reinforcement.

The current CALTRANS design specification (3), requires the extension of the confining spiral reinforcement into the adjacent cap or footing. The details for a typical single column/footing and column/cap connection are shown in Fig. 2. Shear and confinement reinforcement consists of continuous closely spaced spirals (usually #6 or 19 mm bars). These spirals are spliced by welding or 80 diameter lap splices with 135 degree, 10 inch (254 mm) hooks at ends. This will assure that the spiral will remain effective when the column is subjected to large excursions into the ductile range. Rectangular columns are reinforced for shear and confinement by using a series of interlocking spirals spaced not greater than 0.75 times the spiral diameter.

The design of the footing is also automated at CALTRANS using the program, FOOT, (8). Footings are evaluated for factored, service and plastic loads from the column. Plastic moments are applied at 15 degree intervals to consider the effect of plastic action in any direction.

Top footing reinforcement is designed for all imposed loads including uplift on piles and the weight of footing and overburden.

Allowable soil stresses or pile loads vary depending on the class of loading:

Allowable soil stresses or Pile Loads In Terms of Ultimate (3)

Material	Loading	Foundation Allowable (Times) Ultimate	
Soil	Service	0.33	Soil Stress
Soil	Factored	0.50	Soil Stress
Soil	Seismic & Plastic	1.00	Soil Stress
Pile	Service	0.50	Pile Load
Pile	Factored	0.75	Pile Load
Pile	Seismic & Plastic	1.00	Pile Load

4. PILE SHAFT FOUNDATIONS

Drilled pile shaft foundations are being used at an increasing number of locations on California bridge projects. The drilled shaft foundation is generally cheaper than other foundation types and permits the location of columns in tight locations with a minimum of disturbance to existing facilities. The use of this foundation is generally limited to areas where soil conditions permit economical excavation for the shaft and where ground water is not encountered. The presence of ground water does not prohibit the use of the drilled shaft, however the cost becomes considerably higher in this case.

It is more expensive to maintain the shaft walls underwater (usually thru the use of bentonite slurry) and underwater concrete placement is required. Vertical load tests by CALTRANS on carefully installed slurry seal piles have shown that the resulting pile is equal in strength to a normal dry constructed shaft (15).

Drilled shaft dimensions vary from 6 to 8 feet (1.8 to 2.4 m) in diameter and 30 to 60 feet (9 to 18 m) into the ground.

Construction of the foundation consists of drilling of the shaft excavation, installation of the reinforcement cage and placement of the concrete.

Column reinforcement is continuous but may be spliced by welding or approved connectors, however staggered lap splices are permitted for #11 (36 mm) bars or smaller in columns over 34 feet (10 m) high. Lap splices are not permitted near areas where plastic hinges are expected to form. Fig. 3 shows the reinforcement details for a typical 7 foot (2.1 m) diameter drilled shaft and column.

The design problems involved with the use of the pile shaft are slightly different from those of ordinary pile and spread footing foundations. The pile shaft has a softer lateral stiffness and therefore requires more refined foundation data at an earlier stage in the design process. This softer lateral stiffness must also be considered in the design and analysis of the superstructure as well as the substructure components.

5. COLUMN/PILE SHAFT DESIGN PROCEDURE

1. Determine an equivalent column length. The equivalent length of a column/shaft member is defined as that length of column plus pile shaft which when fixed at the bottom will produce the same deflections at the top of the column for a given load as the actual column plus shaft surrounded by soil.

2. Analyze the bridge with the equivalent column lengths and determine column loads to be used in programs YIELD(7) and PILE(8). The superstructure may be designed at this time.

3. Design the TOP of column reinforcement for all load groups I thru VII using the YIELD program(7) and the equivalent column lengths.

4. Using the PILE program(19,24) determine the maximum moments in the pile shaft for the components of group loads I thru VII. Detailed soil data from Engineering Geology is required for use of the PILE program(19,24).

5. Using the YIELD program(7), determine the amount of vertical reinforcement required to resist the maximum moment in the pile shaft. The plastic moment capacity of the column and shaft is also determined at this time.

6. Using the PILE program(19,24), analyze the pile shaft for the plastic condition. The plastic moment, the associated axial load, and the assumed plastic shear are applied at the top of the column. The program is then run interactively by incrementing the shear until a plastic hinge forms in the pile shaft.

   The shear reinforcement is then designed for the lesser of the shears resulting from seismic plastic hinging or group loads I to VI and unreduced elastic group load VII.

7. Perform a final check of the overall stability of the pile shaft using the PILE program (19,24). The pile shaft is considered stable when a substantial decrease in pile

shaft length does not result in excessive deflection. The amount of reserve shaft length is an indication of the factor of safety against overturning. A stability ratio greater than 1.0 is mandatory. A good rule of thumb is; the greater the uncertainty of the soil, then the greater the stability ratio. A stability ratio below 1.5 is not recommended without extremely reliable soil data.

6. THE CALIFORNIA SEISMIC RETROFIT PROGRAM

The California Department of Transportation has, since 1971 been involved in the retrofit of existing highway bridges.

The California retrofit program began almost immediately after the 1971 San Fernando Earthquake.

The California Department of Transportation identified about 1247 bridges (out of about 13,000) which are primarily deficient in seat width. These unrestrained joints represented the prime focus of the Departments retrofit program. The average retrofit project consists of the addition of steel restrainer cables at expansion joints. To date 1070 of the 1247 bridges have been retrofit at a cost of $40.5 million. The $54 million project, which started in 1971, is expected to be completed in 1985.

7. STRONG MOTION INSTRUMENTATION

The California Department of Conservation, Division of Mines and Geology has been involved in the development of data on the characteristics of earthquake generated strong motions for about twelve years. A legislative statute brought the Division's Strong Motion Instrumentation Program into being on January 1, 1972. This statute gave the Division the role of procuring and installing strong motion instruments on representative structures (including bridges) and in various geologic environments throughout the state. The Statute has since been expanded (January 1, 1977), to mandate the instrument maintenance and record processing. The Division has been collecting data and archiving records since September 1976.

Funding for the California Strong Motion Instrumentation Program comes from a tax on building permits and currently amounts to about $1,000,000 annually.

Current instrumentation consists of approximately 316 ground response stations, 71 building stations, 22 dam stations, 4 bridge stations and 1 tunnel station.

A catalog of strong motion records recovered by the Strong Motion Instrumentation Program thru 1983 (4,5), is available. Four California bridges are currently instrumented under the program:

Meloland Road Overcrossing (El Centro area)

Route 154/101 Separation (Hollister area)

Painter Street Overcrossing (Eureka area)

Yincent Thomas Suspension Bridge (Los Angeles area)

The Painter Street Overcrossing, (Bridge Number 4-236) is a two span cast-in-place prestressed box girder bridge on a two column monolithic bent over Route 101 in the town of Rio Del (near Eureka) in northern California. The bridge is located on a 39 degree skew. The bridge is instrumented to record 20 channels of data collected on two CRA recording systems (18).

Strong shaking has been recorded at this bridge from three separate earthquakes:

EARTHQUAKES RECORDED AT PAINTER STREET OVERCROSSING (18)

Earthquake	Date, Time (GMT)	Mag (ML)	Epicentral Distance	Maximum Accel.
Trinidad-Offshore	8 Nov 1980, 10:27	6.9	72 mi	0.34g
Rio Dell	16 Dec 1982, 06:53	4.4	15 mi	0.60g
Cape Mendocino-Offshore	24 Aug 1983, 13:36	5.5	61 mi	0.27g

Magnetic tape No. RIODEL8083 with 18 files of data including uncorrected and corrected acceleration data and response and Fourier Amplitude spectra are available for reproduction and handling costs. A Preliminary report describing the strong motion data recorded at the Rio Dell Overpass (18) is also available, (a final report of this data is in preparation).

Send to:

California Division of Mines and Geology
Office of Strong Motion Studies
2811 'O' Street
Sacramento, CA 95816
USA

8. FUTURE NEEDS AND DEVELOPMENTS

Criteria

Some effort should be directed toward a unified worldwide seismic criteria for bridges. Efforts in the United States, Japan and New Zealand are going in somewhat different directions and if the criteria were closer, then resultant research would be more capable of cooperative efforts.

Columns and Footings

There is an increasing need improved analysis methods and criteria which considers the effects of both vertical accelerations and the variations of vertical loads on columns during large seismic events.

Standard details with proven seismic resistance, especially for columns about 3 to 6 foot, (0.9 to 1.8 m) diameter should be developed with connection and footing details of proven toughness.
These members could be used in moderate seismic regions with little design effort and they would provide excellent seismic resistance.

The largest unknown in current design criteria is the non-linear effects of both the soils and the plastic hinging in columns. These effects should be more explicitly addressed in the criteria rather than built in implicitly.

Research and Testing

Full-scale testing continues to be the only way to definitely answer questions about the ability of bridge components to bridge to withstand large excursions into the plastic region.

Cooperative research projects should be developed to test full sized, prototype structures to destruction. The magnitude of such an effort is so large that cooperative projects can spread the costs among a number of sponsors.

Better definition of the ground motions and force levels close to faults continues to be needed. Current motions are justifiably conservative and until proven otherwise will be exaggerated in order to be safe.

Procedures for defining and designing for the out-of-phase displacements over the length of a bridge needs to be developed. The overall significance of these displacements on the total seismic forces in the system is unknown.

9. REFERENCES

1. Beeston, H.E., and McEvilly, T.E., "Shear Wave Velocities From Down-Hole Measurements", Earthquake Engineering and Structural Mechanics, Vol 5, 1977, pp. 181-190.

2. Bell, J.M. and Hoffman, R.A., "Design Earthquake Motions Based on Geologic Evidence.", Proceedings of the ASCE Geotechnical Engineering Division Specialty Conference, Earthquake Engineering and Soil Dynamics, Pasadena, CA, June 19-21, 1978, Vol 1, pp 231-271.

3. "Bridge Design Specifications Manual", Standard Specifications for Highway Bridges Adopted by the American Association of State Highway and Transportation Officials, Twelfth Edition, 1977, With Interim Revisions Thru 1982, Washington, D.C., With Revisions by the California Department of Transportation, Office of Structures Design, Sacramento, CA, July, 1984.

4. "Catalog of Strong Motion Accelerograph Records Recovered by Office of Strong Motion Studies before January 1, 1982", California Division of Mines and Geology, Special Report 154, 1982.

5. "Catalog of Strong Motion Accelerograph Records Recovered by Office of Strong Motion Studies during 1982", California Division of Mines and Geology, Special Report 154 - Supplement A, 1983.

6. "Century Freeway Ground Response Study", by the Office of the Transportation Laboratory, California Department of Transportation,Sacramento, CA, August, 1983.

7. "Column Design by Yield Surface 'YIELD'", Instructions to Users by the California Department of Transportation Office of Structures Design, Bridge Computer Manual, Chapter 5-3, July, 1983.

8. "Footing Analysis/Design Program 'FOOT'", Instructions to Users by the California Department of Transportation Office of Structures Design, Bridge Computer Manual, Chapter 8-2, July, 1983.

9. Gates, James H., "California's Seismic Design Criteria for Bridges", Journal of the Structural Division, ASCE, Vol 102, No. ST12, December, 1976, pp. 2301-2313.

10. Gates, James H., "Factors Considered in the Development of the California Seismic Design Criteria for Bridges", Proceedings of a Workshop on Earthquake Resistance of Highway Bridges held on January 29-31, 1979. Applied Technology Council, Palo Alto, CA, 1979, pp 141-162.

11. Gates, James H., "Seismic Resistant Bridge Design in California", UJNR, Proceedings of the 15th Joint Meeting of the U.S.-Japan Panel on Wind and Seismic Effects, Tsukuba, Japan, May, 1983, Paper No. 2-19.

12. "Geotechnical Report for the Route 1/105 El Segundo-Norwalk Transportation Corridor", A Report by the District 7 Materials Section, California Department of Transportation, Los Angeles, CA April, 1974.

13. "Guide Specifications for Seismic Design of Highway Bridges 1983", Highway Subcommittee on Bridges and Structures 1982. American Association of State Highway and Transportation Officials, Washington, D.C.

14. Hays, Walter W., "Procedures for Estimating Ground Motions.", United States Department of the Interior, Geological Survey, Professional Paper 1114, Washington, DC, 1980.

15. "Load Test - 48 inch Diameter Pile, Constructed by Slurry Displacement Method, Guadalupe River Viaduct, Bridge No. 37-308 R/L, 04-Scl-87-5.8", California Department of Transportation Division of Structures, by R.C. Wilhelms, Engineering Geology Branch, May 5, 1975.

16. Mayes, Ronald L. and Sharpe, Roland L., "Seismic Design Guidelines for Highway Bridges.", Applied Technology Council, Palo Alto, CA and The Federal Highway Administration, Office of Research and Development, Washington, DC, Report No. FHWA/RD-81/081, October, 1981.

17. "Memos to Designers", 15-10, Earthquake Design (Commentary), California Department of Transportation, Office of Structures Design, Sacramento, CA, July, 1984.

18. "Processed Strong-Motion Data from the Painter Street Overpass -- Preliminary Report -- Plots to Accompany Tape RIODEL8083", California Division of Mines and Geology, Sacramento, CA.

19. Reese, Lymon C. and Sullivan, W. Randall, "Documentation of Computer Program COM624", Geotechnical Engineering Center, Bureau of Engineering Research, The University of Texas, Austin, Texas, Aug., 1980.

20. Romstad, K.M., Bruce, J., and Hutchinson, J.R., "Site Dependent Earthquake Motions", Journal of the Geotechnical Engineering Division, ASCE, Vol 104, No. GT11, November, 1978, pp 1389-1400.

21. Schnabel, P.B., Lysmer, J., and Seed, H.B., "SHAKE: A Computer Program for Earthquake Response Analysis of Horizontally Layered Sites." Report EERC 72-12, Earthquake Engineering Research Center, University of California, Berkeley, CA, 1972.

22. Seed, H.B., and Schnabel, P.B., "Accelerations in Rock from Earthquakes in the Western United States." Report EERC 72-2, Earthquake Engineering Research Center, University of California, Berkeley, CA, 1972.

23. Seed, H.B., Idriss, I.M., and Kiefer, F.W., "Characteristics of Rock Motions During Earthquakes." Report EERC 68-5, Earthquake Engineering Research Center, University of California, Berkeley, CA, 1968.

24. "Shaft Pile Analysis", Instructions to Users by the California Department of Transportation Office of Structures Design, Bridge Computer Manual, Chapter 8-1, July, 1983.

Table 1. -- Active Faults and Associated Magnitudes (6,12)

Fault	Distance to Proj. Limits Mi. (km)	Maximum Historic Magnitude (Richter)	Maximum Credible Mag. (Richter)	Maximum Credible Duration (sec)
Cucamonga	24-40 (39-64)	---	6.6	18
Malibu-Santa Monica	8-18 (13-29)	5.2	7.5	30
Newport-Inglewood	3-12 (5-19)	6.3	6.5	24+
Palos Verdes	8-14 (13-23)	---	7.2	24+
Raymond Hill	12-14 (19-23)	---	7.5	30
San Andreas	37-44 (60-71)	8.3	8.3	40+
San Fernando	23 (37)	6.4	6.6	18
Santa Susanna	26 (42)	---	6.7	18+
Sierra Madre	18-24 (29-39)	---	6.6	18
Simi-Northridge	22 (35)	---	7.5	30
Whittier-Elsinore	8-14 (13-23)	---	7.6	30

Table 2 -- Zones covered by ARS Spectra (6)

Curve No.	General Description	Coverage Mi.	(km)
1	Airport Viaduct	0.9	1.4
2	San Diego Frwy. (Rte 405) Interchange	3.9	6.3
3	Harbor Frwy. (Rte 11) Interchange	4.3	6.9
4	Alameda Viaduct	3.0	4.8
5	Long Beach Frwy. (Rte 7) Interchange	3.6	5.8
6	San Gabriel R. Frwy. (Rte 605) Interchange	2.5	4.0

Figure 1 Final ARS Curves

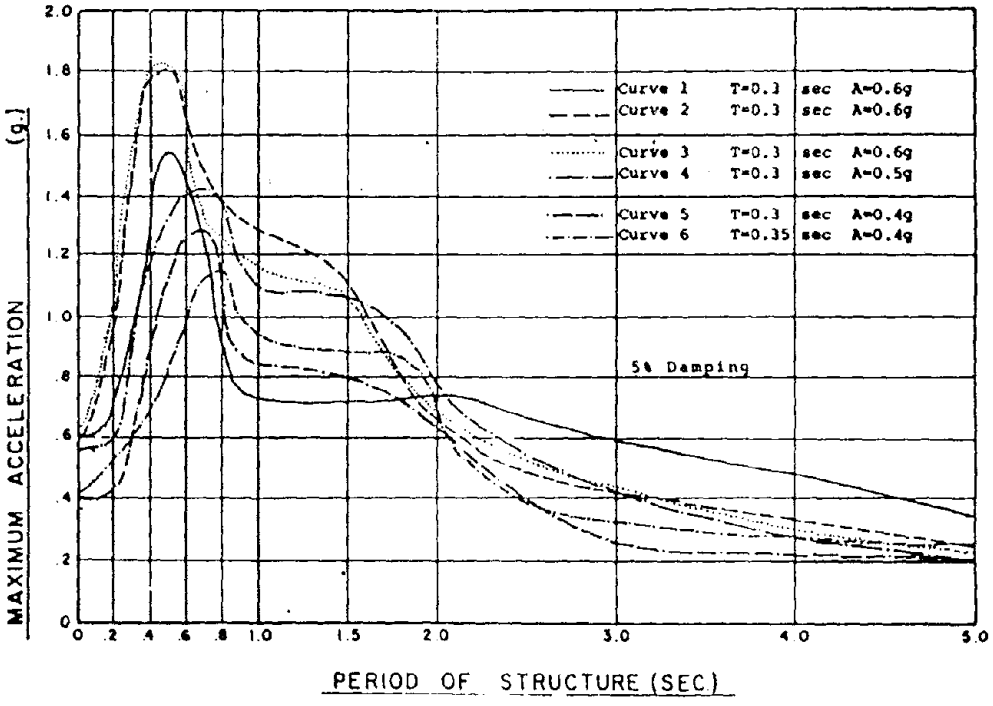

Figure 2 Typical Single Column Bent on Footing

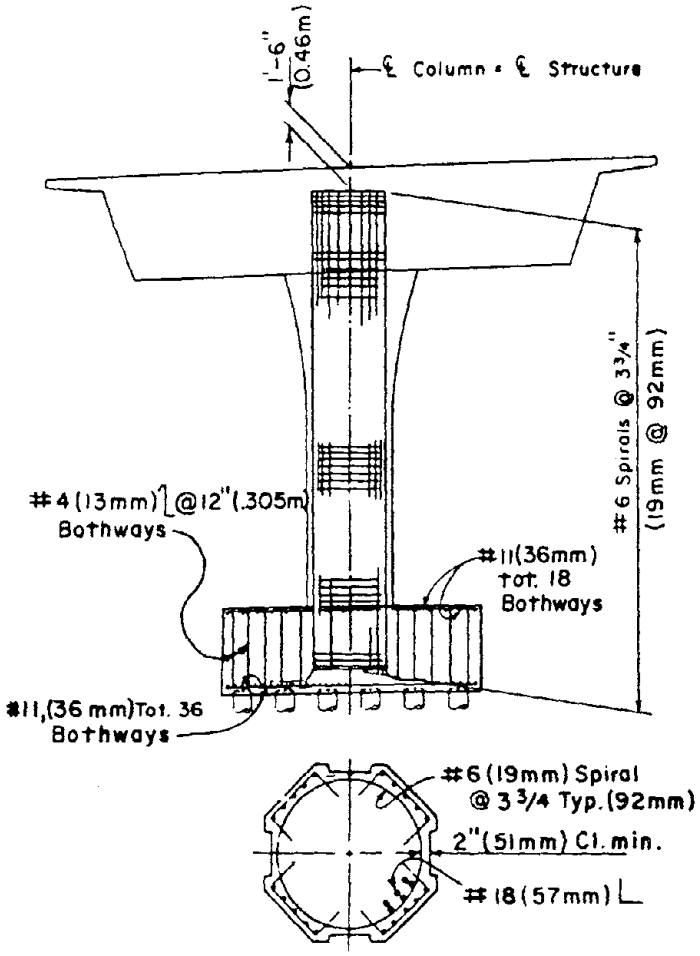

Figure 3 Typical Single Column Bent With Shaft Foundation

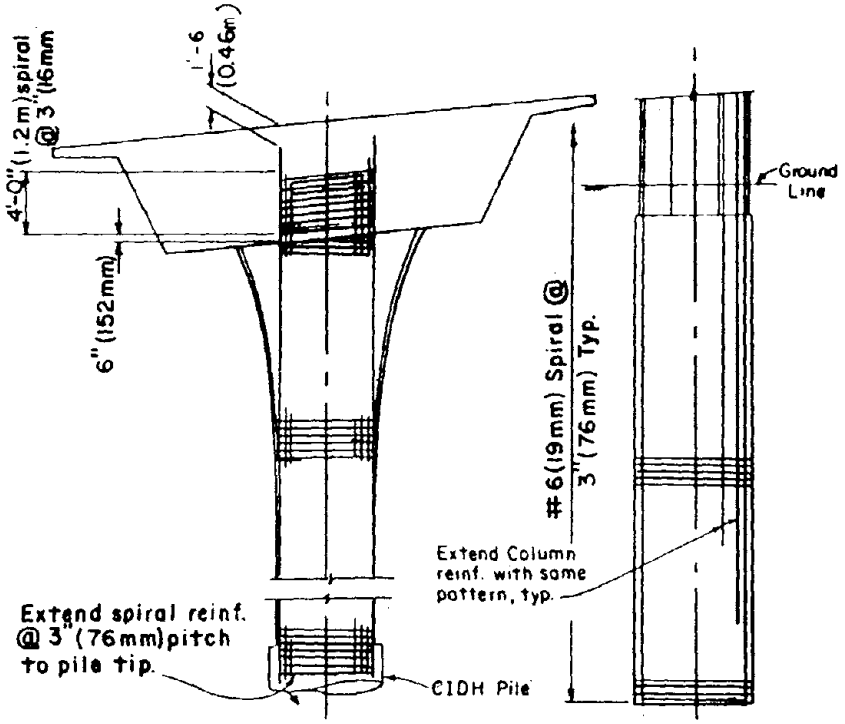

SEISMIC ANALYSIS, INSTRUMENTATION AND DYNAMIC TESTING OF CABLE-SUPPORTED BRIDGES

BY

Ahmed M. Abdel-Ghaffar*

ABSTRACT

This overview paper summarizes two phases of extensive research that was concerned with: (1) full-scale ambient vibration measurements of suspension bridges, and (2) the earthquake response analysis of long-span cable-supported bridges when subjected to multiple-support seismic excitations. In the first phase extensive experimental investigations were conducted on the Golden Gate Bridge to determine its dynamic characteristics. Comparison with previously computed mode shapes and frequencies showed good agreement with the experimental results. Based on a comprehensive earthquake-response analysis of cable-supported bridges relevant observations and conclusions were made. In addition, the paper sheds some light on the recommendations regarding permanent strong-motion instrumentation of these long-span bridges.

KEY WORDS: Ambient Vibration, Cable-Stayed Bridges, Damping, Dynamic Testing (Full-Scale), Earthquake (Response), Measurements, Mode Shapes, Multiple-Support Excitations, Natural Frequencies, Suspension Bridges.

1. INTRODUCTION

Devastating earthquakes will unquestionably occur in the future in the seismically active zones in our planet. Uncertainty exists only as to the scale of the damage and when and where such earthquakes will occur. The economic and human costs of major earthquakes are predominantly associated with the behavior of structures and the lifelines that supply and connect them. In both urban and suburban areas, the consequences of severed lifelines (e.g., bridges, water lines, ..., etc.), in addition to collapsing structures can be devastating.

*Associate Professor, Dept. of Civil Engineering, Princeton University, Princeton, NJ 08544

In general, there are significant deficiencies in our present understanding of how reliably to design, construct, analyze, and retrofit earthquake-resistant structures. It is believed that these deficiencies stem from a lack of reliable data on the behavior of full-scale structures subjected not only to forces from earthquakes but to ambient forces from environmental factors such as wind, traffic, microtremors and functional activities. There is no doubt that proper strong-motion instrumentation of major structures in anticipation of the occurrence of earthquakes, and the dynamic full-scale testing of structures will provide the most valuable information for a rapid and cost-effective improvement in the seismic-resistance of structures.

Earthquakes in the United States and other parts of the world have consistently demonstrated that bridges are vulnerable to damage by earthquakes. And there is a strong need for continued evaluation of the seismic design, performance, and retrofitting of bridges as well as for the dissemination of research developments and pertinent practical experience among researchers, design engineers and government representatives confronted with the earthquake hazard.

Long-span bridges, such as suspension and cable-stayed bridges represent a very important component in lifeline-transportation structures. The relatively flexible and extended-in-plane configuration of such structures makes them susceptible to a unique class of vibration problems. Earthquake damage to such long-span bridges interrupts their primary function -- the safe and economical movement of people and materials. The damage is

even more serious when an earthquake causes a large number of casualties and hampers the general ability of people to respond to the emergency. Thus, significant efforts should be made to ensure that these essential long-span structures will continue to function after an earthquake and be structurally serviceable after a strong earthquake.

This overview paper summarizes two phases of extensive research that was concerned with: (1) full-scale ambient vibration measurements of the Golden Gate Suspension Bridge (San Francisco, CA), and (2) the earthquake-response characteristics of long-span cable-supported bridges (such as suspension and cable-stayed bridges) when subjected to multiple-support seismic excitations. In addition, the paper sheds some light on the recommendations regarding permanent strong motion instrumentation of these long-span bridges.

1.1 Full-Scale Ambient Vibration Measurements

Performing tests on full-scale structures is the only sure way of assessing the reliability of the various assumptions employed in formulating mathematical or finite-element models of structures. It is also a very reliable way of determining the parameters of major interest in structural dynamic, wind, and earthquake engineering problems. Furthermore, ambient-vibration data can provide valuable information pertaining to the optimal locations for strong-motion instrumentation.

1.1.1 Ambient Vibration Measurements of the Gate Bridge

Extensive experimental investigations [1] were conducted on the Golden Gate Bridge to determine, using ambient vibration data, the mode shapes, the associated frequencies, and the damping of the bridge vibration. The ambient vibration tests involved the simultaneous measurement of vertical, lateral, and longitudinal vibrations of the suspended span and the measurement of longitudinal and lateral vibration of the main tower. Measurements were made at selected points on different cross sections of the stiffening structure and the tower. A total of 91 modal frequencies and mode shapes of the suspended span and a total of 46 modal frequencies and modes of vibration of the tower are determined. Finally, comparison with previously computed mode shapes and frequencies shows good agreement with the experimental results.

1.1.2 Description of the Bridge

The Golden Gate Bridge (Figs. 1, 2, 3) which lies across the entrance to San Francisco Bay and joins the northern and southern peninsulas was completed in 1937. The main span is 4200 ft, and side spans are 1125 ft long each and are suspended from the main cables. The width of the roadway is 90 ft, and provides six traffic lanes and two sidewalks. The towers (Fig. 3) are made up of two shafts that are connected by horizontal struts in the panels that comprise the upper 500 ft of each tower. The towers are anchored to massive concrete piers which are founded on rock. The two cables are 36.5 inches in diameter.

1.1.3 Description of the Instrumentation

Figure 4 summarizes the instrumentation used in the tests, the measuring procedures, the data processing, and the experimental set-up of the ambient vibration tests. More details of the description of the instrumentation can be found in Ref. 1. The following is a brief summary of the instrumentation:

1. Motion-Sensing Transducers: bridge response was measured at various locations using Kinemetrics' Model FBA-I and FBA-II Force-Balance Accelerometers.
2. Signal Conditioning: signals from the accelerometers were amplified and filtered using three Kinemetrics' Model SC-1 four-channel Signal Conditioners.
3. Recording: the amplified and filtered data were recorded simultaneously on a Honeywell Model 5600E 14-channel FM tape recorder.
4. Spectrum Analyzer: A Hewlett-Packard 3582A dual channel Spectrum Analyzer was used in the field to observe the frequency content of the data.
5. Electronic Analog-Digital Converter: the recorded analog signals were digitized using the Kinemetrics DDS-1103 electronic analog-digital converter.

1.1.4 Center and Side Span Measurements

The vertical, longitudinal, and lateral motion of the center and side spans on half of the bridge were measured using 12 channels of accelerometers. During each testing session, six accelerometers were mounted at one of the stations (1-18) indicated in Fig. 1. The positions and orientations of these six accelerometers were located at the cross section indicated by R (Station 8 in Fig. 2), where they remained throughout the tests on both spans. Summing the outputs of accelerometers C and E (Fig. 2) gives the purely vertical motion while subtracting their outputs gives the torsional motion. Similarly, summing the outputs of accelerometers A and B gives the purely lateral motion while subtracting their outputs provides information on the torsional motion. Figure 5 shows a type of Fourier amplitude spectra of the recorded motion.

1.1.5 Tower Pier Measurements

The longitudinal and lateral motions of the south tower were measured using 9 channels of accelerometers. The reference station was chosen to be at the roadway level (Station 5 of Fig. 3). Purely longitudinal vibration was obtained by summing the outputs of accelerometers A and C (Fig. 3) while torsional motion was obtained by subtracting their outputs.

1.1.6 Natural Frequencies, Modes of Vibrations, and Damping

The procedure for determining mode shapes was to divide the spectral amplitude of the response at a given station by the spectral amplitude of the simultaneously recorded response at the reference station. In this way, an amplitude proportional to the mode shape amplitude at that station is obtained for a given frequency of vibration. Repeating this procedure for every station, the mode shapes are determined. The phase of the response was compared to that of the reference instrument to determine the signs of the modal displacements. The measured mode shapes and natural periods are compared to those obtained by theoretical analyses [1,2]; Figs. 6 and 7, respectively, show some of these comparative results for the suspended spans and tower; certain similarities and differences between the measurements and the computations are apparent, but in general there is an excellent agreement between the measured and computed mode shapes and their associated natural periods.

1.2 Earthquake Response of Long-Span Cable-Supported Bridges

Significant improvement in the earthquake resistance of long-span bridges requires additional information and understanding in three primary areas:

1. Improved knowledge of the forces and deformations generated by strong ground shaking, particularly those induced by multiple-support seismic excitations; the relatively flexible and extended-in-plane configuration of such structures makes them susceptible to a unique class of vibration problems.
2. empirical data on the behavior of structural components and on the interaction of structures with foundation-soil systems, when subjected to propagating strong-ground motions, and
3. development and verification of mathematical models that can be used to calculate the response of these structures to seismic forces ranging from low-amplitude vibrations to damage initiation and ultimately to collapse.

Obviously, the best sources of data and information on the above-mentioned areas, for improved earthquake engineering of existing long-span bridges, are heavily instrumented structures that experience natural earthquakes. The need for such information has been extensively noted in the technical recommendations and in the proceedings of numerous meetings dealing with the problems of earthquake hazards including those sponsored by the National Academy of Sciences and the National Science Foundation [6,7,8]; the economic return on capital invested in full-scale dynamic testing and strong-motion instrumentation is thought, by the research community, to be high.

The accuracy of calculated earthquake-response characteristics for long-span bridge structures depends upon a sound knowledge of the expected

ground motions at different supporting sites. Earthquake ground motions in the three orthogonal directions of a long-span bridge may be transmitted to the superstructure through the tower bases (piers) and the abutments or anchorages, as illustrated by Fig. 8. The bridge may be long with respect to the wave-lengths of motion in the frequency range of importance to its earthquake response. Because of this fact, different portions of the bridge can be subjected to significantly different excitations, a problem not normally important for buildings. The essential feature of this problem is that the motion at the supporting points a given distance apart on the surface of the ground may receive long period earthquake motions that are nearly equal, but experience short period motions that are dissimilar and uncorrelated. In general the correlation of the motion at these points is extremely complicated, particularly in the case of a long-span bridge, with different foundation conditions, subjected to seismic waves with different angles of incidence and different travel paths. In that case, marked differences in amplitude as well as phase could occur over distance of the order of a few wave-lengths of the motion.

Based on a comprehensive earthquake-response analsis [2] of both suspension and cable-stayed bridges, the following relevant observations and conclusions merit mentioning:

1. Both theoretical dynamic analyses [6] and full-scale ambient vibration tests of suspension bridges have indicated that modes of vibration of the structure can be separated into two groups. In one group, the displacements of the stiffening structures and cables are predominant, and in the other group, the displacements of the towers are predominant. Furthermore, the vibrations of the suspended structure can be distinctly categorized into vertical, torsional, and lateral vibrations; that is, one occurs mainly independently of the other. It was then possible in such cases, to view the truly 3-D modes of the bridge as being "essentially bending" or "essentially torsion" without appreciable error. On the other hand, for modern cable-stayed bridges the 3-D bridge mode shapes are typically seen to contain, along the deck span, simultaneous contributions to bending, torsion, and lateral sway. Thus in that case, it is then no longer possible to categorize a given eigenmode simply to pure bending or pure torsion; it will simultaneously contain elements of all possible motions. This distinct difference should have an impact on the approach to the earthquake-response analysis.
2. Multiple-support seismic response of the cable-supported bridges requires that the total displacements (or response quantities) may be decomposed into quasi- (or pseudo-) static displacements and relative (or vibrational) displacements. For such highly statically indeterminate structural systems quasi-static displacements are those resulting from the static application of support displacements. Figure 9 shows the quasi-static function associated with the vertical displacement of the four supports of a suspension bridge, while Fig. 11 shows the vibrational and total displacement response of a cable-stayed bridge tower (the bridge was treated as a 3-D structure and ground motion inputs were taken from existing ground motion records recorded at time-synchronized close-spaced stations from the 1979 El Centro earthquake).
3. It was found that a relatively large number of modes, closely-spaced in the frequency domain, participate in the earthquake response of a long-span bridge (see Figs. 10 and 12). Uniform ground motion for such a long-span structure is not a good assumption since it results in nonconservative responses. The vibrational stresses induced in the cable-suspended structure under multiple-support seismic excitation are significant live loads and may come close to or exceed design yield stresses. Furthermore, it was found that the P-Δ effects of the tower response have significant role in the design values of the base bending-moment.
4. In the analysis of longitudinal tower-pier vibration, the effect of the soil flexibility underlying and surrounding the pier upon the

mode shapes and natural frequencies as well as the response displacements, stresses, and shear forces is very important (Fig. 13). Thus the estimation of soil properties underlying the foundation is essential in design. The response stresses in the tower-pier system under earthquake excitation are significant but are still below their yield values.

5. Finally, it should be emphasized that assurance of the aerodynamic stability of a suspension bridge does not in any way imply the safety of these structures during earthquake loading. Both the inputs and the responses, as well as the possible modes of failure, are different for the two kinds of excitation. A multiple-support analysis methodology is essential in the earthquake resistant design of such a long-span structure. More details on this phase of research can be found in Ref.[2].

2. INSTRUMENTATION AND FUTURE RESEARCH NEEDS

The ambient vibration studies of both the Vincent-Thomas Bridge [3] and the Golden Gate Bridge [1] will be of great value in the development of a set of recommendations regarding a comprehensive strong-motion instrumentation system for the national long-span cable-supported bridges, in general, and the Californian three suspension bridges, in particular. These latter bridges are: (1) San Francisco-Oakland Bay Bridge: which has the most urgent instrumentation priority; as a prerequisite to proper permanent instrumentation both comprehensive ambient vibration survey and an extensive earthquake-response analysis of the bridge should be conducted, (2) Golden Gate Bridge: which needs a back-up earthquake-engineering system to complement and support the currently proposed space-technology system, and (3) the Vincent-Thomas Bridge: which needs upgrading of its current strong-motion instrumentation system (of Fig. 14).

The practical experience gained from these ambient vibration studies should be utilized to test more important U.S. long-span bridges, such as suspension and cable-stayed bridges, particularly in the Midwest and Eastern U.S. (where there are seismically active zones that are subject to frequent, small-to-moderate earthquakes). In addition, more research is needed to acquire more understanding of the earthquake problem of long-span cable-supported bridges.

In conclusion, full-scale, small-amplitude dynamic testing is essential in working toward the above-mentioned goals because the data generated -- consisting essentially of a definition of the natural vibration characteristics of the structure under study, and the interaction of these with the immediate environment -- would be useful (1) in confirming the reliability of analytical and numerical models and, (2) in identifying the optimal locations for strong-motion instrumentation to yield the utmost structural-response information. The data may also provide the basis for research on fundamental problems related to earthquake engineering.

3. ACKNOWLEDGMENTS

The authors are grateful to the people of the Golden Gate Bridge, Highway and Transportation District. This research is supported by Grants (CEE81-13567, CEE-8017736, and CEE-8342559) from The National Science Foundation and the Department of Transportation.

4. REFERENCES

1. Abdel-Ghaffar, A. M., Scanlan, R. H. and Diehl, J., "Analysis of the Dynamic Characteristics of the Golden Gate Bridge by Ambient Vibration Measurements," Civil Engineering Dept. Report SM-85-1, Princeton University, Princeton, NJ February 1985.

2. Rubin, L. I., Abdel-Ghaffar, A. M. and Scanlan, R. H., "Earthquake Response of Long-Span Suspension Bridges," Civil Engineering Dept. Report SM-83-4, Princeton University, Princeton, NJ, June 1983.

3. Abdel-Ghaffar, A. M. and Housner, G. W., "Ambient Vibration Tests of Suspension Bridge," Journal of the Engineering Mechanics Division, Proceedings of the American Society of Civil Engineers, Vol. 104, No. EM5, October 1978, pp. 983-999.

4. Rojahn, C., Ragsdale, J., and Cooper, J., "Strong-Motion Instrumentation Scheme for the

Vincent-Thomas Suspension Bridge," Nov. 1980, Open-file USGS, Engineering Branch.

5. Abdel-Ghaffar, Ahmed M., "Dynamic Analysis of Suspension Bridge Structures," Earthquake Engineering Research Laboratory, EERL 76-01, California Institute of Technology, May 1976, Pasadena, CA.

6. National Research Council, Earthquake Engineering Facilities and Instrumentation, National Academy Press, Washington, DC, 1984, 33 pp.

7. Committee on Earthquake Engineering Research (1982), Earthquake Engineering Research--1982, National Academy Press, Washington, DC.

8. Earthquake Engineering Research Institute (1984), Experimental Research Needs for Improving Earthquake-Resistant Design of Buildings: Overview and Recommendations, Report No. 84-02 Earthquake Engineering Research Institute, Berkeley, CA.

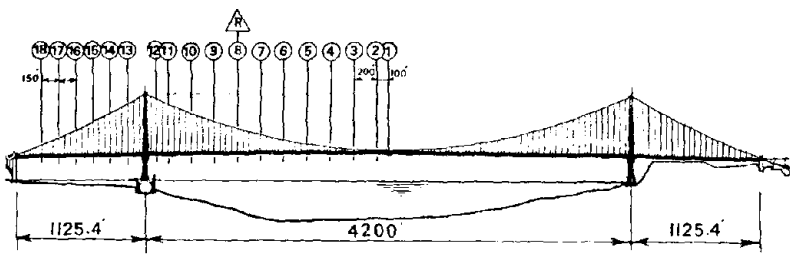

Fig. 1 Measurement stations along the suspended structure.

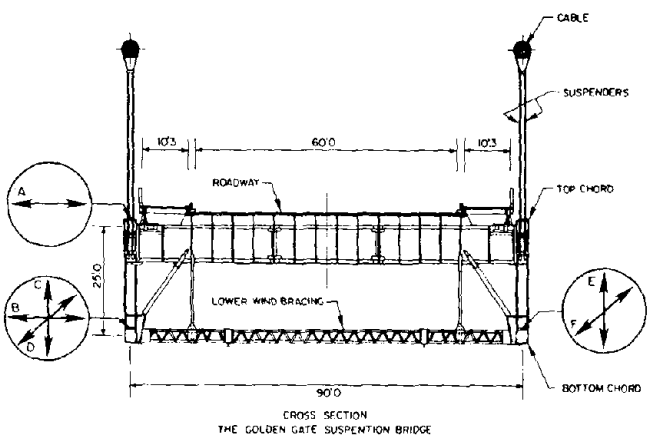

Fig. 2 Positions and orientation of the six accelerometers at a typical cross-section of the suspended structure.

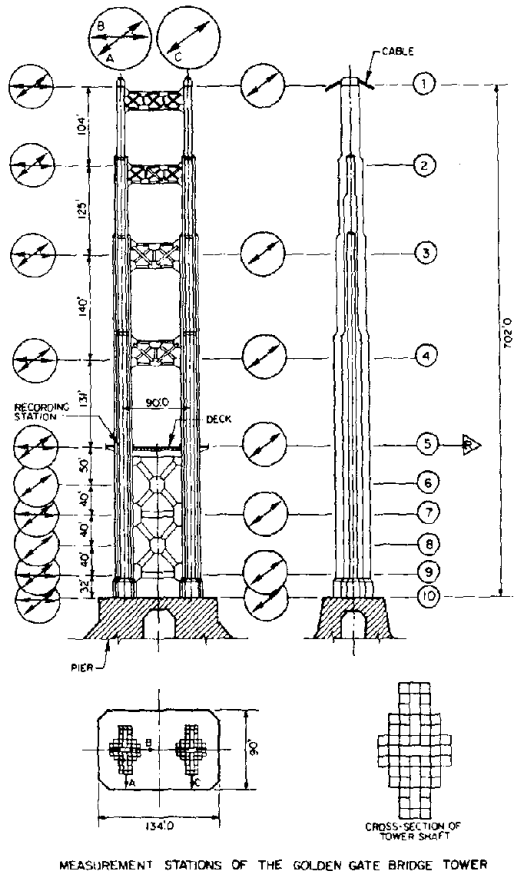

Fig. 3 Measurement stations of the Golden Gate tower.

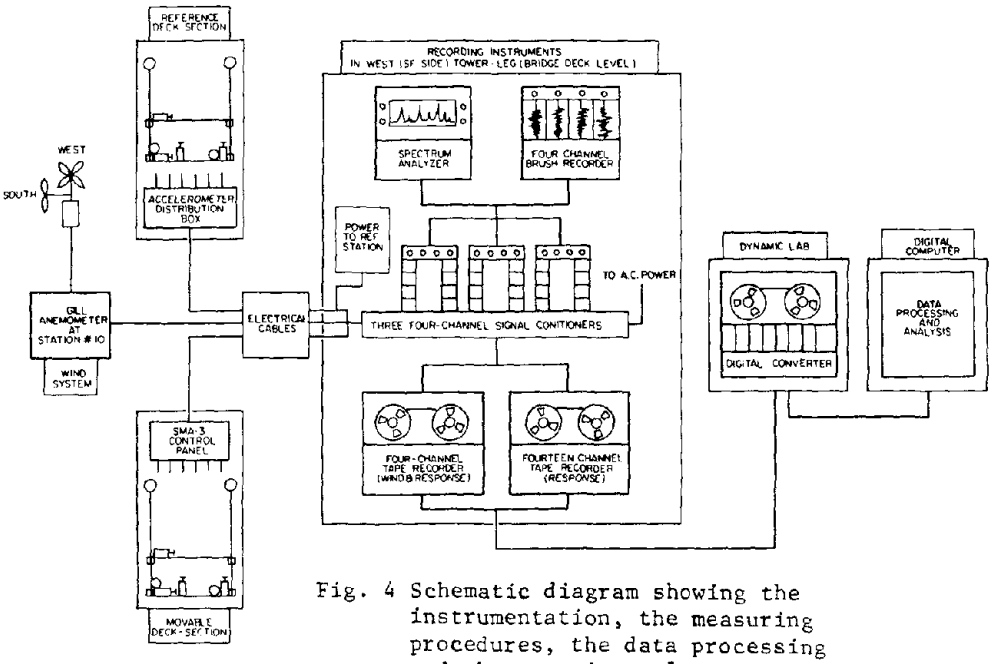

Fig. 4 Schematic diagram showing the instrumentation, the measuring procedures, the data processing and the experimental set-up of the ambient vibration tests.

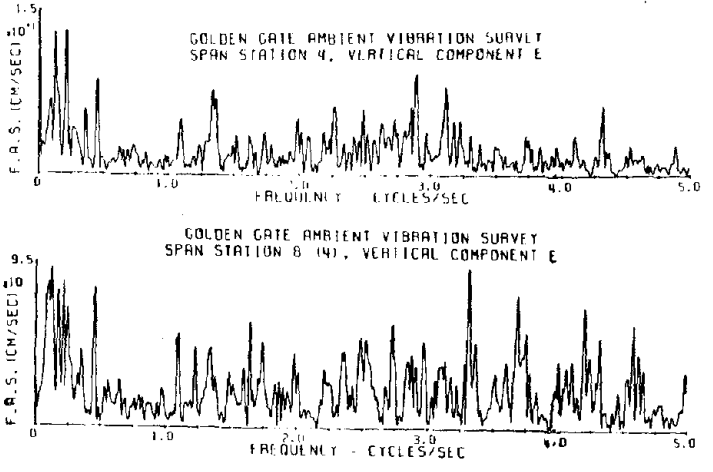

Fig. 5 Fourier amplitude spectra of the recorded acceleration on Station 4 of the span and the corresponding reference

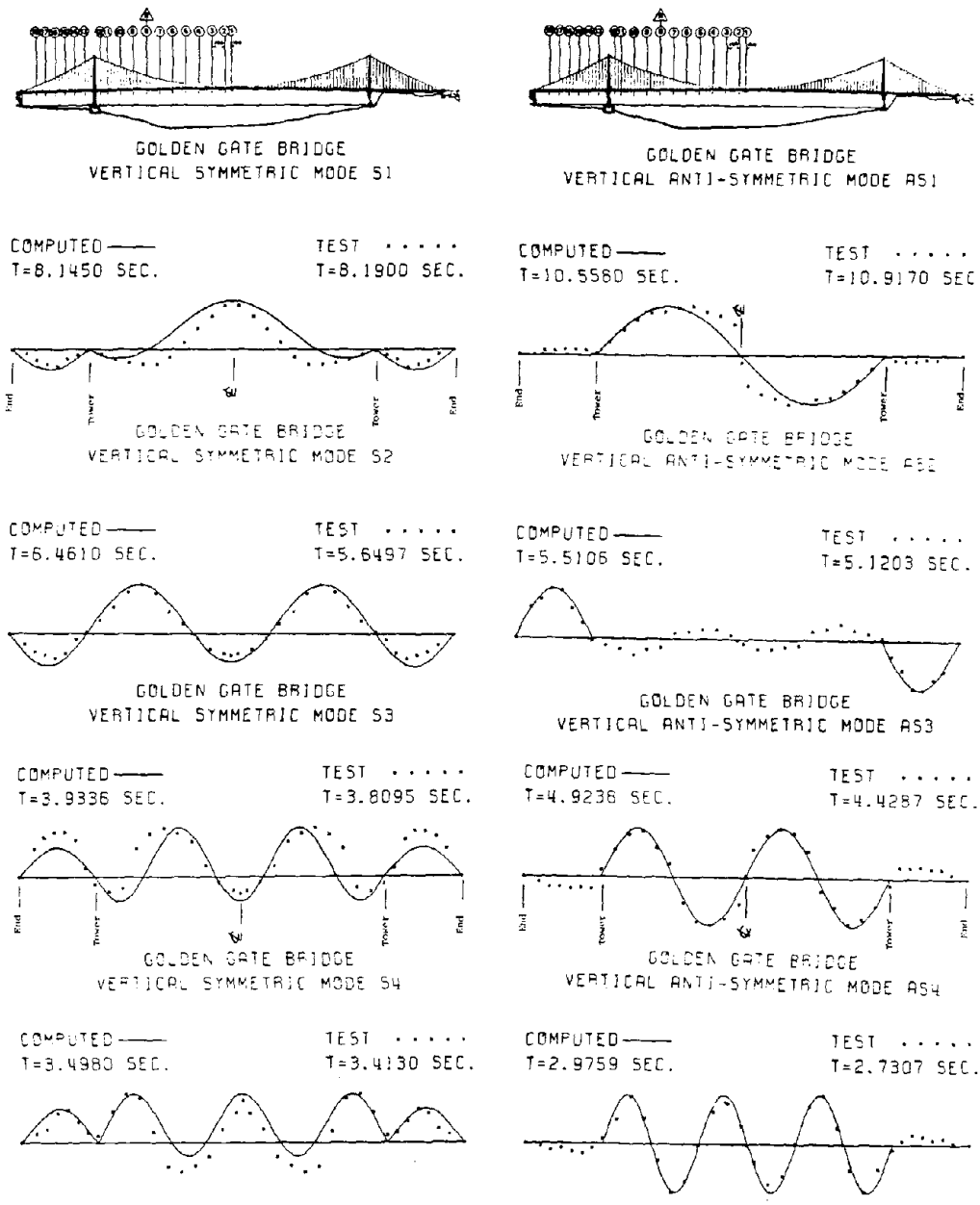

Fig. 6 Comparison between computed and measured first four natural periods and mode shapes of symmetric and antisymmetric vertical vibration of the stiffening structure of the Golden Gate Bridge.

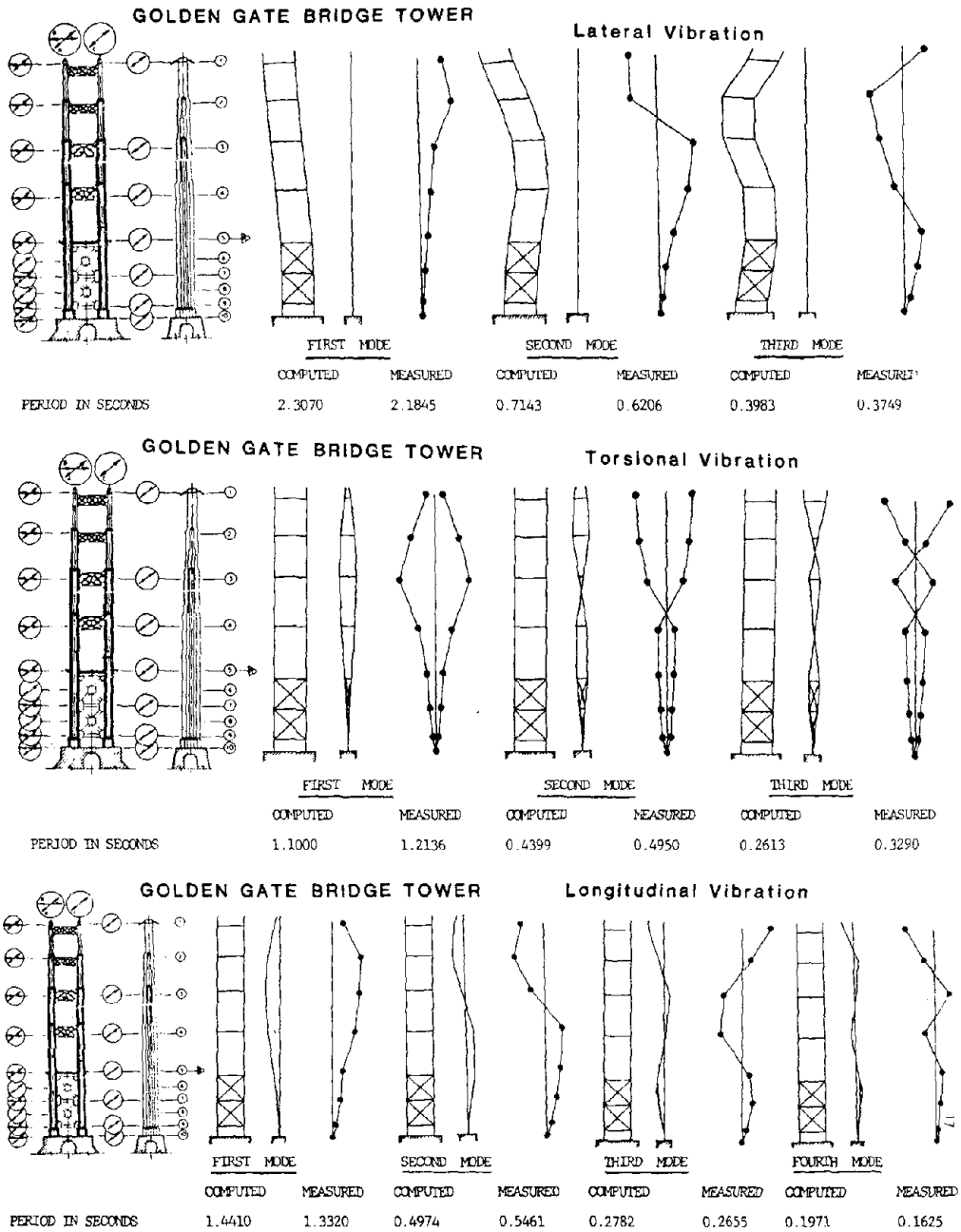

Fig. 7 Comparison between computed and measured natural periods and mode shapes of vibration of the Golden Bridge tower.

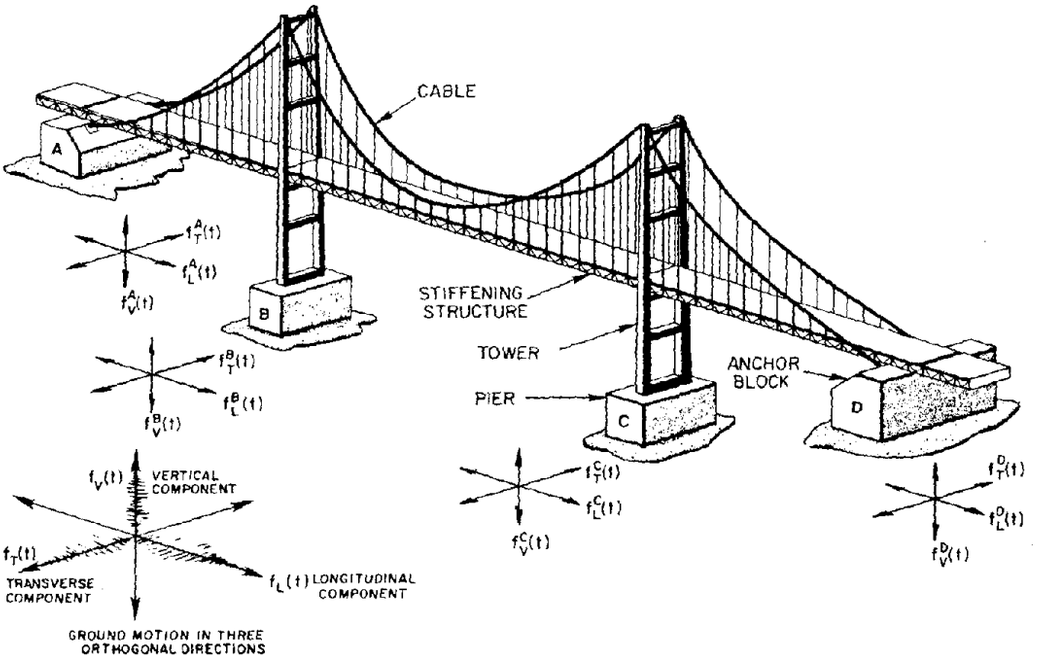

(a) SUSPENSION BRIDGE

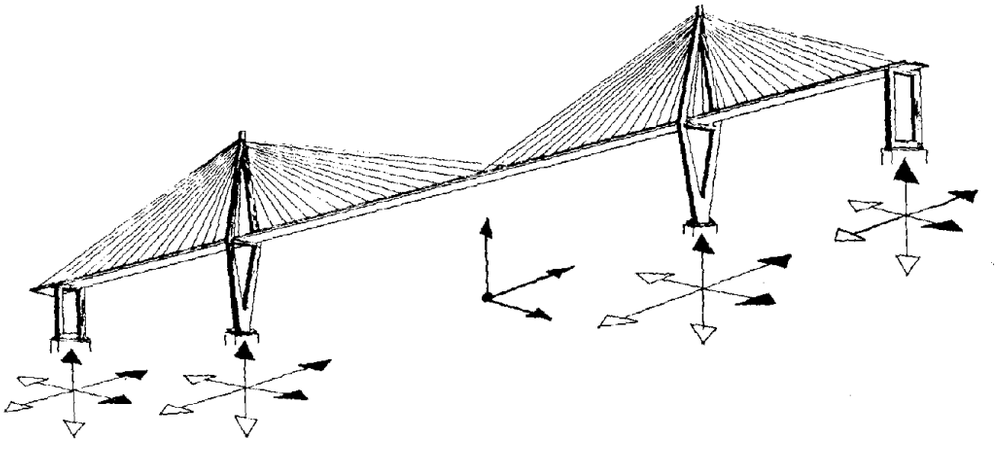

(b) CABLE-STAYED BRIDGE

Fig. 8 Typical three-dimensional cable-supported bridges subjected to multiple seismic input motions at their supporting points.

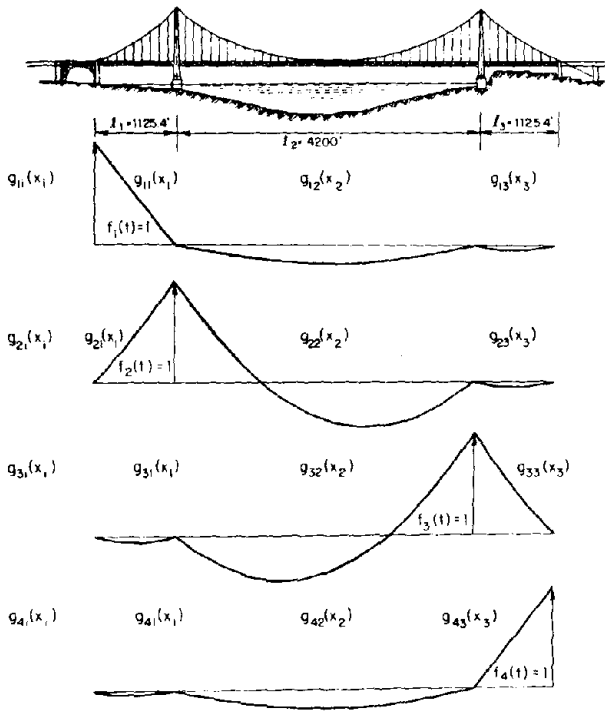

Fig. 9 Quasi-static functions of the vertical displacements at the four supporting points.

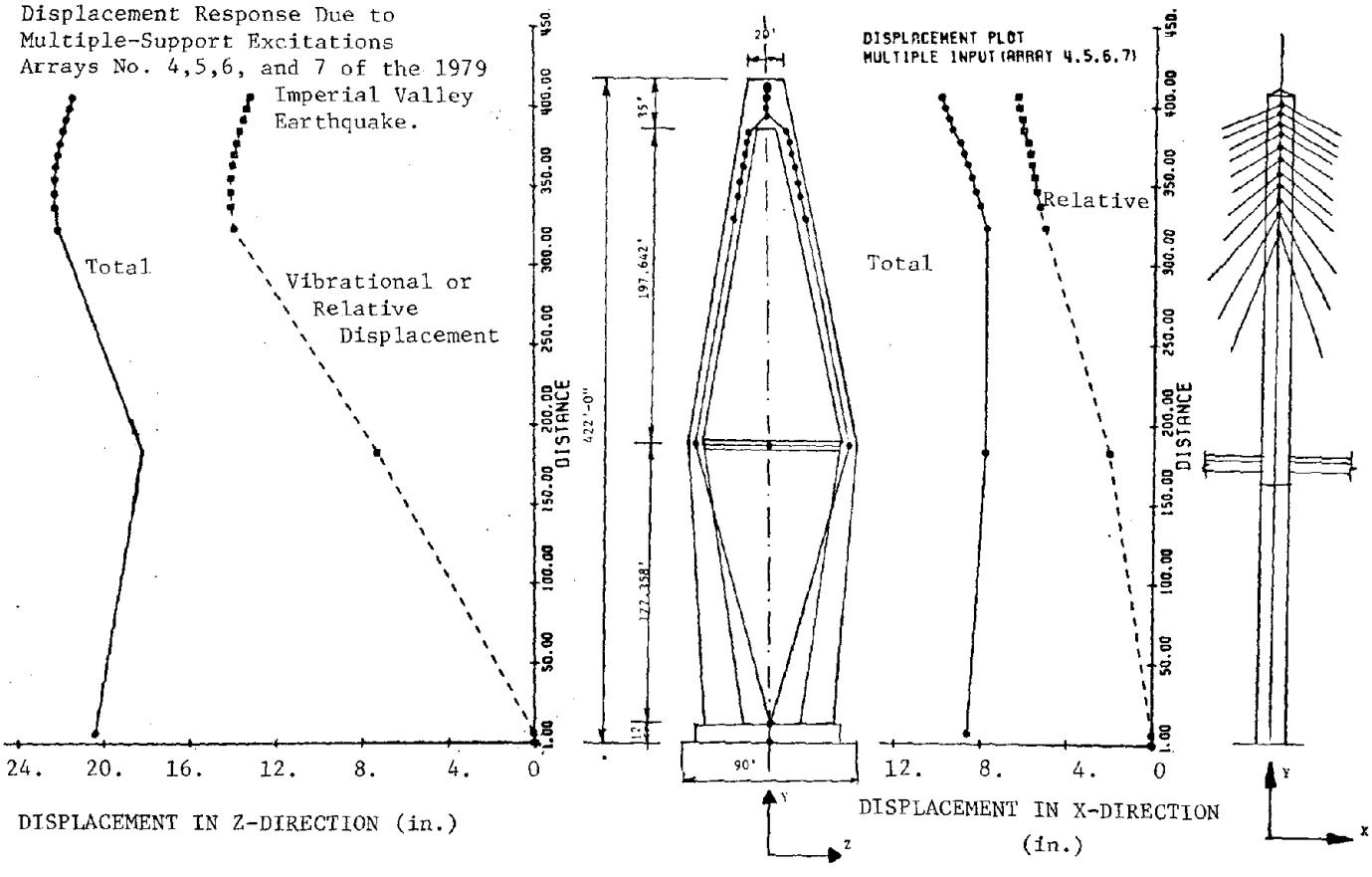

Fig. 11 Vibrational (relative) and total displacement response of tower of a cable-stayed bridge due to multiple-support seismic excitations.

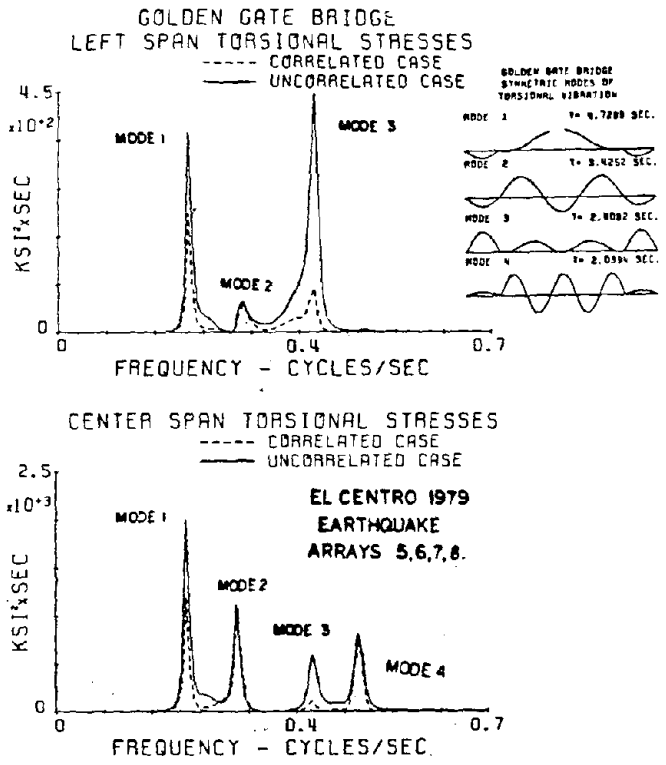

Fig. 10 Autospectra of midspan (side and center spans) torsional stress response due to multiple-support seismic excitations.

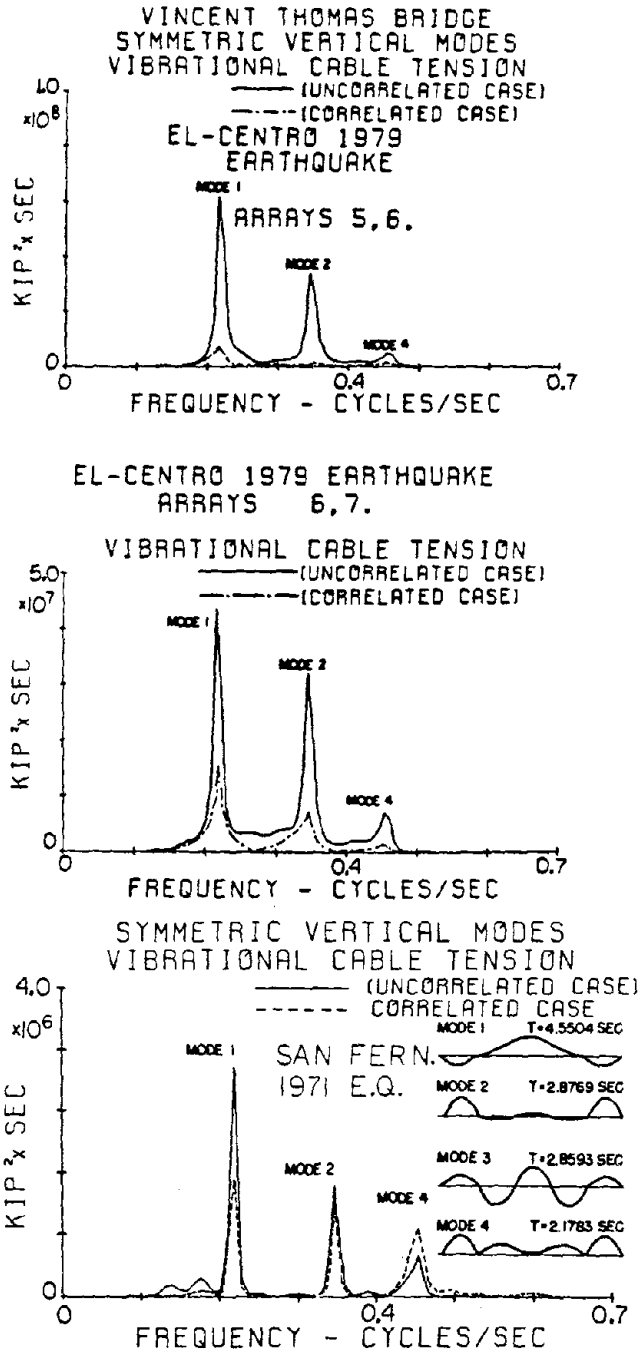

Fig. 12 Autospectra of vibrational cable-tension response due to different earthquake inputs.

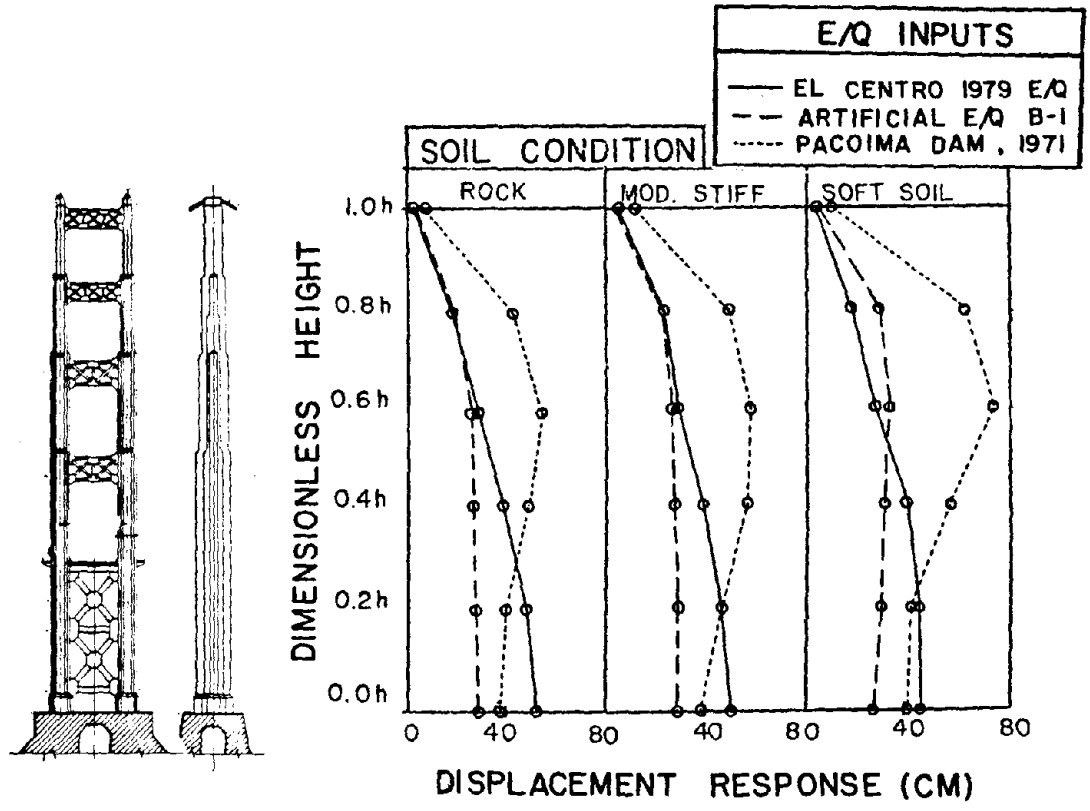

Fig. 13 Displacement response of a suspension bridge tower.

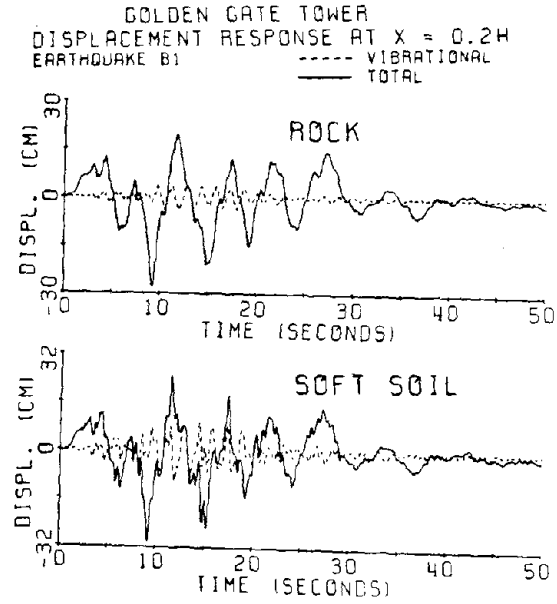

SAN PEDRO-TERMINAL ISLAND SUSPENSION BRIDGE

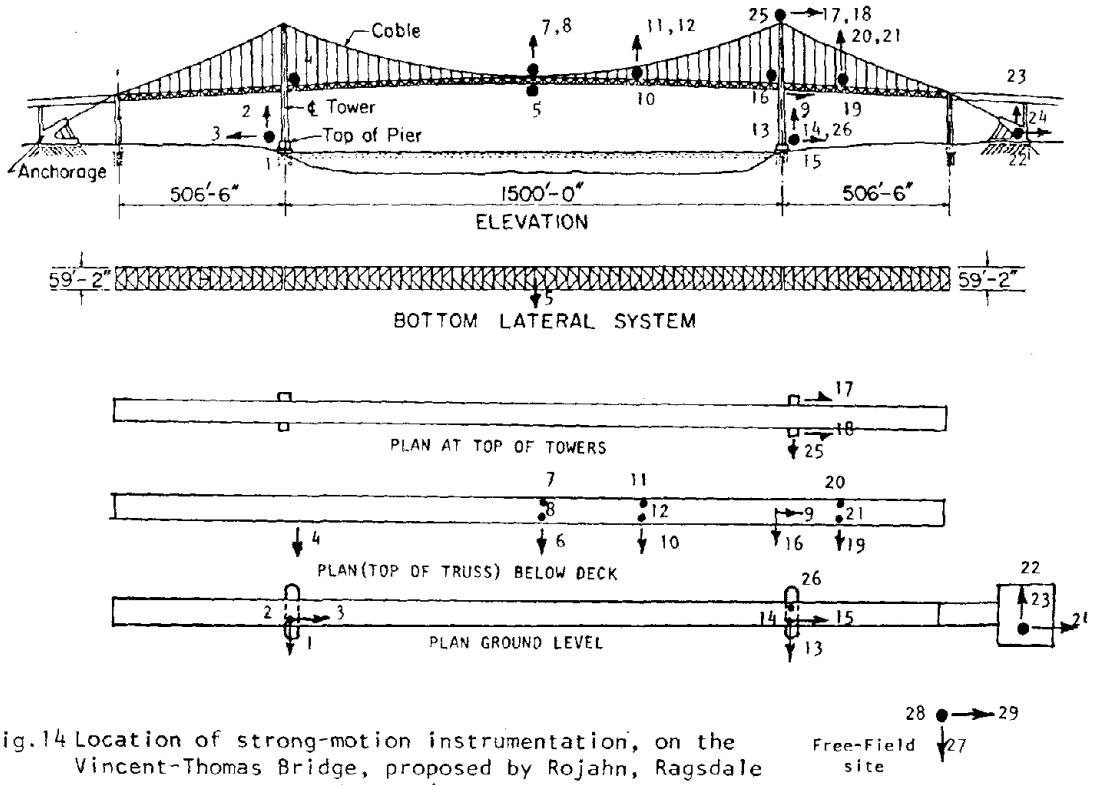

Fig.14 Location of strong-motion instrumentation, on the Vincent-Thomas Bridge, proposed by Rojahn, Ragsdale and Cooper in 1980 (Ref. 4).

EARTHQUAKE RESISTANT DESIGN OF BUILDING FOUNDATION

- Introduction and Commentary on "DESIGN GUIDE FOR THE BUILDING FOUNDATION AGAINST SEISMIC FORCE" -

by

Yoshihiro SUGIMURA*

ABSTRACT

Some important points and bases of the "Design Guide for the Building Foundation against Seismic Force" enacted in September 1984 are introduced in this report. As historical background, two events gave impetus to establish the Guide. The first was the enactment of the New Earthquake Resistance Standard for buildings in 1981, and the second was the experience of damage to concrete piles due to the Off-Miyagi prefecture earthquake in 1978.

The Guide is composed of eight chapters. In Chapter 1, basic policies are described to provide structural safety of building foundations that is equal to or greater than that of the superstructure in allowable capacity design. Chapter 2 prescribes the setting of design external forces to be applied to building foundations. For pile foundations, the reduction of horizontal forces on piles due to effects of the embedded portion is also described.

The design of spread foundations is introduced in Chapter 3, and design of pile foundations in Chapter 4, respectively. Since more problems involve pile foundations than spread foundations, more pages are given to pile foundations, i.e., bearing capacity, pull-out resistance, horizontal resistance and combined stresses of piles.

Allowable stresses for various pile materials are summarized in Chapter 5. In Chapters 6 to 8, precautions for design of pile head joints, design of underground walls, and cutting methods for pile heads are described.

KEY WORDS: Earthquake Resistant Design; Foundations; Design Guide; Earthquake Engineering; Pile Foundation; Spread Foundations.

1. INTRODUCTION

Since the enactment of the New Earthquake Resistance Standard for the Enforcement Ordinance of the Uniform Building Code in Japan, revised in June 1981, the preparation of a building foundation guide conforming to the Standard had been strongly requested. Under such circumstances, the Ministry of Construction held several meetings with the Building Foundation Review Sub-Committee (chairman: Professor Ohsaki, University of Tokyo, at that time) of the Building Engineering Examination Committee, and the "Proposed Design Guide for the Building Foundation against Seismic Force" was formulated in March 1982. The contents of this Guide had been investigated by many organizations involved in the design of foundations and was revised and enacted from September 1984 as the official design guide, i.e., "Design Guide for the Building Foundation against Seismic Force". Some important points and bases of the concepts of the Guide are introduced with some commentaries in this report.

* Head of Geotechnical Engineering Division, Structural Engineering Department, Building Research Institute, Ministry of Construction

2. HISTORICAL BACKGROUND OF THE GUIDE

The historical background of the Guide is summarized in Table 1. From the latter half of the 1950's into the 1960's, the Japan Industrial Standard (JIS) provided production methods for precast concrete (RC) piles, steel pipe (SP) piles and prestressed concrete (PC) piles, successively. This fact shows the structural properties of piles to be changing gradually from the preceding primitive condition to the higher strength condition in these two decades.

On the other hand, two important earthquakes occurred in the 1960's, i.e., the Niigata earthquake in 1964 and the Off-Tokachi earthquake in 1968. Although some examples of damage to piles were found due to these two earthquakes, the more conspicuous damage was overturning or collapse of buildings due to liquefaction in the Niigata earthquake or due to landslide in the Off-Tokachi earthquake. In particular, liquefaction phenomena in sand deposits in Niigata city gave a shock to researchers and engineers in soil mechanics and foundation engineering, so that, since then research works have been continued mainly for liquefaction phenomena.

In the first half of the 1970's, two kinds of regulation were revised and executed. The first is the Notice No. 111 of the Ministry of Construction in 1971, and the second is the Building Foundation Design Standard of the Architectural Institute of Japan (AIJ) in 1974. These are mainly prescribing bearing capacity of spread foundations and pile foundations against permanent load. Of course, effects of liquefaction and precautions are included in these regulations, but aseismic design of foundations is not always described systematically.

From the middle of the 1970's, research works preparing for a new aseismic design of buildings by considering dynamic effects were started, based on the experience of the past earthquake damage, earthquake observation results and so on. These research works were mainly concerned with superstructures, but there was awareness of the significance of establishing new systematic design methods for building foundations as well as superstructures.

After the earthquakes in the Izu peninsula area accompanied by damage due to landslides and faults in 1974 and in 1978, the Off-Miyagi prefecture earthquake occurred in 1978. This earthquake made, as it were, an epoch to the aseismicity of building foundations, because some examples were found in Sendai city of piles supporting buildings being severely damaged without any effects of change of ground condition, such as liquefaction, landslide, or fault. Furthermore, the important point is that the piles that were heavily damaged were prestressed high strength concrete (PHC) piles which had been developed recently to be of higher strength than other types of concrete piles. This experience of damage gave impetus to establishing an aseismic design method for building foundations, and the activity of the Building Foundation Review Sub-Committee was started in 1979.

In 1981, the New Earthquake Resistance Standard was enacted, and the Proposed Design Guide was exhibited in 1982 as the outcome of the activity of the Building Foundation Review Sub-Committee. The Japan Industrial Standard also prescribed the production method for PHC piles in 1982, based on the experience of damage due to the Off-Miyagi prefecture earthquake. After that, damage to piles of similar type was found in subsequent earthquakes, i.e., the Off-Urakawa earthquake in 1982 and the Nihonkai Chubu earthquake in 1983, which showed the necessity of enforcement of the Guide widely as soon as possible. Finally, the contents of the Guide were revised on the basis of various opinions from

many organizations, and enacted from 1984 as the official design guide.

3. CONFIGURATION AND ENGINEERING POSITION OF THE GUIDE

The configuration of the Guide is as illustrated in Fig. 1. The features of the contents of the Guide are as follows:

1) As basic policies, the Guide is to be applied to building foundations in allowable capacity design against seismic force, and its purpose is to provide structural safety equal to or higher than that of the superstructure. The Guide also emphasizes that possibility of collapse of the ground such as liquefaction, landslide or settlement, as those examples shown in Photo 1 to Photo 6, should be separately investigated and countermeasures taken in advance of the application of the Guide in order to maintain the safety of building sites.

2) Design external forces acting on building foundations are established, and the influence of combined external forces of both horizontal and vertical forces is emphasized. Also, the effects of decrease in horizontal force due to embedment in the case of pile foundations are clearly described.

3) Since pile foundations involve more problems than spread foundations, most of the description of the design calculation method is for pile foundations. In addition to investigating bearing capacity and pull-out force, the calculation formulae for elastic combined stresses in pile sections are introduced.

4) The allowable stress for the pile material has been determined for each kind of stress in the pile section to be calculated, and also provisions are made with emphasis upon the relation to ultimate capacity design and the relation to empirical concerns such as workability.

5) Precautions for design of pile head joints, for execution of work for handling pile heads, and for design of underground walls are indicated.

Though it was originally intended to arrange systematically the present findings on earthquake resistance of foundations in the Guide, it has been not possible to organize a complete system. The subject matter of the Guide includes items which are still in research work and thus cannot be applied, items which are still not clarified and cannot be applied, and items which are still unsolved but adopted in the Guide because of the necessity in the administration and enforcement. Thus, the Guide is in a position to function as a tentative index until a better design guide is prepared in the future.

4. DESIGN EXTERNAL FORCES TO FOUNDATION DURING EARTHQUAKE

The design external forces on the foundation during an earthquake are outlined in Fig. 2. The horizontal force is equal to the value of the shearing force at the lowest floor (including basement) prescribed in the New Earthquake Resistance Standard plus the horizontal force at the foundation (usually determined by the seismic coefficient method). The vertical force is equal to the value of permanent axial force plus or minus the axial force due to overturning moment. The design load is, therefore, considered as an inertia force of the superstructure. In the case of a pile foundation, the horizontal force may be reduced by the value of α (but α shall not be more than 0.7) given by Eq. (1)

because of the effects of embedment such as a basement.

$$\alpha = 1 - 0.2 \frac{\sqrt{H}}{\sqrt[4]{D_f}} \quad (1)$$

where,

α : participation ratio of horizontal force of embedment

H : height of the portion above the ground surface (m)

D_f : depth of embedment (m)

The relations of Eq. (1) are shown in Fig. 3 for the case of D_f larger than 2 m. The basis of these relations is as follows. If the equilibrium of the horizontal forces on the embedded portion is assumed to be as shown in Fig. 4, then the following equations are obtained:

$$Q_b = Q_w + Q_f + Q_p \quad (2)$$

$$\alpha = \frac{Q_w + Q_f}{Q_b} \quad (3)$$

Each resisting element is indicated in Table 2. The passive resistance at the front surface (one side only) is assumed to be an elastic spring. The frictional resistance at side surfaces (both sides) is assumed to be of bilinear type that reaches the maximum value when the displacement is 1 cm. The unit frictional force is used as 80% of the normal value because both sides do not act effectively depending on the direction of the seismic force. Frictional resistance at the base surface is neglected here because of the possibility that an opening will occur between the base of foundation and the soil surface due to settlement of the ground.

Under the conditions described above, numerical analyses were performed for the examples shown in Fig. 5, and the results are shown in Fig. 6, in form of the participation ratio for horizontal force of each resisting element. It is recognized that the participation ratios of piles are similar for any types of ground. The participation ratios of the embedded portion, i.e., sum of passive resistance and frictional resistance, are also similar for any types of ground, even though each resistance element itself varies depending on the ground conditions.

Similar analytical studies were made by Kishida et al. (1979) and Kotohda et al. (1980). The participation ratios of the embedded portion studied by Kishida et al. (1979) are slightly larger than the results shown in Fig. 6, but the results obtained by Kotohda et al. (1980) are very close to those shown in Fig. 6.

The participation ratio for piles has characteristics as follows. If there is any embedment of even one story basement, the participation ratio suddenly decreases to the range of 0.8 to 0.6. But this ratio does not decrease in proportion to the number of stories of basement. If the number of stories above the ground increases, the participation ratio also increases but not in the proportion to the number of stories. And then, if the increasing and decreasing tendency of the participation ratio of pile is expressed in the form of functions, the participation ratio will approximately become proportional to the square root of the above-ground height H and inversely proportional to the one-fourth power of D_f, the depth of embedment. Equation (1) was derived based on the facts mentioned above. Figure 6 can be redrawn as shown in Fig. 7 and thus Eq. (1) indicates the average relation from the results of the trial calculations.

If the depth of embedment is small, the passive reaction and friction resistance of the ground cannot be predicted sufficiently well, so that the range of D_f less than 2 m is omitted in

Fig. 3. The Guide recommends the application of Eq. (1) only for the case of D_f larger than or equal to 2 m.

With respect to the seismic force on building foundations and the participation ratios of the embedded portion and piles, as described above, there still remain many factors to be further studied and investigated. For example, the behavior of the foundation during an earthquake is definitely affected by the effects of the ground such as dynamic earth pressure during an earthquake. Thus, it seems to be not adequate to evaluate the design force merely with respect to the inertia force of the superstructure, or the relation of Fig. 6 seems to be insufficient since the behavior of the foundation is also affected by the plan shape as well as the depth of embedment. It should be noted, therefore, that the relation of Eq. (1) may be possibly improved or revised depending on the progress of future studies.

4.1 Design of Spread Foundations

For spread foundations, bearing capacity of the ground and slip-out of the foundation should be investigated (see Fig. 8). The bearing capacity should be examined as the short-time allowable unit bearing capacity, since the duration of action of external forces during an earthquake is very short. If there is possibility of liquefaction, it should be separately investigated and the necessary countermeasures should be taken as stated previously. For spread foundations, the influence of inclined loads as combined external forces must be taken into account and, in certain cases, an increase of about 10 to 20% in contact pressure may occur.

With respect to uplift of foundation, the Guide does not specifically prohibit occurrence of any uplift in the calculations, but foundations must be designed by taking full precautions for distribution and shape of the contact pressure and the rigidity of the foundation beam. Also, no special provisions are set forth for the ratio of the area of the uplifted portion to the total bottom surface area, because uplift rarely occurs or is normally considered to be very small under the conditions of design external forces. Thus, uplift is not prohibited but is desired to be extremely small.

4.2 Design of Pile Foundations

Items to be investigated for pile foundations are summarized in Fig. 9. For the vertical direction, it is required to examine the short-time allowable bearing capacity and the short-time allowable pull-out resistance of the pile. The former should conform to Notice No. 111 of the Ministry of Construction and the latter to Article 27 of the Building Foundation Design Standard of the Architectural Institute of Japan. That is to say, if design capacity is not determined based on loading test results, the following equations must be satisfied for each case.

For bearing capacity per pile,

$$R_a = \frac{2}{3} \{\alpha \bar{N} A_p + \left(\frac{\bar{N}_s}{5} L_s + \frac{\bar{q}_u}{2} L_c \right) \psi\} \quad (4)$$

where,

R_a : short-time allowable bearing capacity (t/pile) (weight of pile should be reduced in case of cast-in-place concrete pile)

α : coefficient of point resistance (30 for driven pile, 20 for embedded pile, and 15 for cast-in-place concrete pile)

$\bar{N}$: average value of Standard Penetration Test (SPT) blow count around the pile tip (range of 1B in lower part and 4B in upper part from

pile tip should be considered in the case of driven piles; B = diameter of pile)

A_p : section area of pile tip (m^2)

$\bar{N}_s$: average value of SPT blow count in sandy soil layer

L_s : total thickness of sandy soil layer (m)

$\bar{q}_u$: average value of unconfined compression strength in clayey soil layer (t/m^2)

L_c : total thickness of sandy soil layer (m)

ψ : perimeter of pile cross section (m)

For pull-out resistance per pile as a single pile,

$$ {}_tR_a = \frac{2}{3} \cdot \int_o^L \psi \tau dz + W_p \qquad (5) $$

where,

${}_tR_a$: short-time allowable pull-out resistance (t/pile)

L : length of pile (m)

ψ : perimeter of pile cross section (m)

τ : pull-out resistance per unit area (t/m^2)

for clay : $\tau = \frac{q_u}{4}$

for sand : $\tau = \frac{N}{5}$ (driven pile)

$\tau = \frac{N}{10}$ (embedded pile and cast-in-place concrete pile)

q_u : unconfined compression strength (t/m^2) (values of not more than 20 are applied for driven piles and values not more than 10 for embedded piles and cast-in-place concrete piles)

N : SPT blow count (values of not more than 50 are applied for driven piles and values not more than 25 for embedded piles and cast-in-place concrete piles)

W_p : weight of pile (t)

For pull-out resistance per pile as a pile group,

$$ {}_tR_a = \frac{1}{n} \left(AW + \frac{2}{3} \int_o^L \psi_g S \, dz \right) \qquad (6) $$

where,

${}_tR_a$: Short-time allowable pull-out resistance (t/pile)

n : number of piles

A : section area of polygon made by connecting the outside of the pile group (m^2)

W : weight of pile and soil per unit area at the bottom of pile group (t/m^2)

L : pile length (m)

ψ_g : distance around the polygon made by connecting the outside of the pile group (m)

S : shear strength of soil (t/m^2)

It should be noted that the details of the method of determination of soil constants set forth in the Guide may be slightly different from those of the Standard of the Architectural Institute of Japan.

For the horizontal direction, necessary parameters such as displacement and bending moment at the pile head should be calculated by the theory of bending of a beam on an elastic foundation under the conditions of fixing ratio of the pile head as shown by the following equations:

$$y_o = \frac{Q_p}{4EI\beta^3} R_{y_o} \tag{7}$$

$$M_o = \frac{Q_p}{2\beta} R_{M_o} \tag{8}$$

$$M_{max} = \frac{Q_p}{2\beta} R_{M_{max}} \tag{9}$$

$$z_m = \frac{1}{\beta} R_{z_m} \tag{10}$$

where,

$$\beta = \sqrt[4]{\frac{k_h B}{4EI}} \tag{11}$$

$$R_{y_o} = 2 - \alpha_r \tag{12}$$

$$R_{M_o} = \alpha_r \tag{13}$$

$$R_{M_{max}} = \exp\left[- \tan^{-1} \left(\frac{1}{1 - \alpha_r}\right) \right] \Big/ \sqrt{(1 - \alpha_r)^2 + 1} \tag{14}$$

$$R_{z_m} = \tan^{-1}\left[\frac{1}{1 - \alpha_r} \right] \tag{15}$$

where,

y_o : displacement at pile head (cm)

M_o : bending moment at pile head (kg.cm)

M_{max} : maximum bending moment in the ground (kg.cm)

z_m : depth of the position where M_{max} occurs (cm)

Q_p : horizontal force at pile head (kg)

B : diameter of pile (cm)

EI : flexural rigidity of pile ($kg.cm^2$)

k_h : coefficient of subgrade reaction (kg/cm^3)

α_r : fixing ratio at pile head (1 for fixed condition, 0 for pinned condition)

With respect to the pile length L (cm), the condition of $\beta L \geq 3$ must be satisfied. If it is not satisfied, the pile must be separately investigated as a short pile.

It is recommended that intermediate values of the fixing ratio α_r be determined by experimental results between 1 and 0, which correspond to a completely fixed condition and completely pinned condition, respectively. However, if experiments are not performed, a fixed pile head condition is adopted as a rule to make calculations on the safe side, based on the examples of damage due to the Off-Miyagi prefecture earthquake in 1978 reported by Sugimura (1981), some of which are shown in Photo 7 to Photo 12. Various types of damage are recognized in these photos, i.e., complete crushing, direct shear or inclined shear cracks, tensile breaking of PC bars, and buckling at the near part of the pile head. Photo 13 to Photo 16 show other types of earthquake damage of the pile head joint, foundation slab, pile cap, and foundation beam. Hair cracks are often found at the pile head as shown in Photo 17 and Photo 18, which were not caused by an earthquake but by the construction work of cutting the pile head. All of these examples show the importance of details of the pile head joint and its degree of fixing in earthquake resistant design of pile foundations.

However, as design philosophy of the Guide, it is not intended to encourage the complete fixing of the pile head. Instead, it is rather intended to recommend calculations on the basis of fixed condition unless the design is based on special studies or experiments on pile head joints. For the detail of joints, it is natural that there will be a design method which takes

account of some degree of freedom of pile head, and there should be room left for judgement by the designers. Therefore, further progress in research and study of pile head joints including the concept of not connecting the pile head to the foundation slab is especially desirable.

No special allowable values for horizontal displacement are set forth in the Guide. By reason that the allowable horizontal displacement is primarily determined by the intended use of a building, it is desirable to determine the displacement individually as required. Nevertheless, if any rough idea is needed, about 3 cm may be recommended as the value corresponding to Eq. (7). Of course, a smaller allowable value should be established for a building containing precision machines and thus requiring smaller displacement.

The Guide indicates some other comments, i.e., that there is a possibility of projection of the pile head due to settlement of the ground, that larger stress in the pile may occur at much deeper locations, compared with the stress distribution derived from the calculation, and that a different calculating method may be required for a section which varies considerably with depth. The Guide also shows the results of comparison and review of many studies made on coefficients of horizontal subgrade reaction. The most desirable method is, of course, to determine the coefficient of horizontal subgrade reaction by horizontal loading test of piles. If such experiments cannot be performed, the following equation is recommended to be used as well as the Road Bridge Standard Regulation in Japan.

$$k_h = 0.8E_o B^{-3/4} \qquad (16)$$

where,

k_h : coefficient of horizontal subgrade reaction (kg/cm^3)

E_o : elastic modulus of soil (kg/cm^2)

B : diameter of pile (cm)

For determination of the elastic modulus of the soil, there are three methods, i.e., direct measurement by pressuremeter in the borehole, by unconfined or triaxial compression test, or for sandy soil deposits only, the empirical relation $E_o = 7N$ where N is the SPT blow count.

The above review of pile foundations deals mainly with properties of the ground, and now it becomes necessary to investigate the stress condition of the pile material itself. The outline of the investigation is indicated in Fig. 10 and Table 3. Basically, it is required to calculate the combined normal stress and shearing stress based on axial force and bending moment by applying the theory of elasticity. Some noteworthy features are as follows:

1) While the concrete at the tension side of bending is ignored for cast-in-place concrete piles and precast concrete piles, as in the case of columns of the superstructure, the total section is considered to be effective for precast-prestressed concrete piles, i.e., prestressed concrete piles and prestressed high strength concrete piles.

2) Effective prestress is used as existing stress in the equations for calculating stress in the pile section.

3) For shearing force, the value of the mean stress multiplied by shape factor is basically used, by calculations based on oblique tensile stress are applied for precast-prestressed concrete piles. Furthermore it is recommended that the value of shearing force be increased by 50%, i.e., $Q_D = 1.50Q_p$ is used as the design shear force for all types of concrete piles, in order to avoid brittle failure.

4) About 1 mm of thickness as allowance against corrosion is provided outside for steel pipe piles, based on the results of corrosion tests for steel material in various types of ground during the last ten years by Ohsaki (1981).

4.3 Allowable Stress of Pile Material

Allowable stresses for various kinds of pile materials are listed in Table 4. The range of ultimate compression strength of concrete, and the representative design values usually used in each case of concrete piles in Japan are as follows:

1) In the case of cast-in-place concrete piles, concrete is usually designed with ultimate compression strength in the range of 180-270 kg/cm^2, and the design value most frequently used is 210 kg/cm^2 or 240 kg/cm^2.

2) As for the kinds of precast concrete, the Japan Industrial Standard (JIS) prescribes that the ultimate compression strength of concrete must not be less than 400 kg/cm^2, 500 kg/cm^2 and 800 kg/cm^2 for precast concrete (RC) piles, prestressed concrete (PC) piles and prestressed high strength concrete (PHC) piles, respectively. Thus, these values are usually selected as design strengths. But the real strength in most cases lies in the ranges of 400-500 kg/cm^2 (RC piles), 500-600 kg/cm^2 (PC piles) and 800-900 kg/cm^2 (PHC piles).

It should be noted that the long-time allowable compressive stress in concrete for precast-prestressed concrete piles is different from that conventionally set forth in the customary formula in the Foundation Structure Design Standard of Architectural Institute of Japan, as shown by the following equations

$$\sigma_a = \frac{F_c - 0.6\sigma_e}{4.5} \qquad \text{(A.I.J.)} \qquad (17)$$

$$\sigma_a = \frac{F_c}{4} \qquad \text{(this Guide)} \qquad (18)$$

where,

F_c : compressive strength of concrete (kg/cm^2)

σ_a : long-time allowable compressive stress in concrete (kg/cm^2)

σ_e : effective prestress (kg/cm^2)

The main reason for changing the function from Eq. (17) to Eq. (18) is as follows: The effective prestress is to be adopted in the equations for calculating stress of the pile section as existing stress, as mentioned before, and is considered to be independent of the setting of the allowable stress in the concrete. The allowable bending-tensile stress is also specified because the whole section is considered to be effective against bending. Therefore, under conditions where the bending stress is mixed in, the stress of the pile section should be investigated with the allowable compressive stress for the compression side and with the allowable bending-tensile stress for the tension side.

The process of determining the short-time allowable bending-tensile stress as a function of effective prestress is as follows: The ultimate axial force-bending moment interaction curve of the pile material can be determined by bending failure theory of reinforced concrete, as shown in Fig. 11. The relation of axial force-bending moment interaction to the allowable stresses is determined by elastic stress superposition theory; as shown, for instance, by the triangle shape in Fig. 11. Then, the value of the short-time allowable bending-tensile stress is set so as to satisfy the following relation.

$$\frac{LA_f}{LA_a} \geq 1.75 \qquad (19)$$

LA_f is the extension line connecting the state of long-time axial force (point L) to the state of load condition under the design external force (point A_e); i.e., a change of bending moment and axial force from point L to point A_e occurs due to the design force in the case of the pull-out state. The extension is made under the assumption that the fluctuation in axial force and in bending moment will not depend on the magnitude of the seismic force. Therefore, Eq. (19) indicates an allowance ratio up to failure, and corresponds to the securing of a ratio greater than 1.75. Since the ratio LB_f/LB_a of the compression side, determined by the short-time allowable compression stress, is always larger than 1.75 for this kind of pile, the relation shown in Eq. (19) need be specified only for the pull-out side.

The allowable bending-tensile stress of concrete established by the method stated above can be approximately expressed by the functions of the amount of effective prestress as shown in Table 4.

Figure 12 shows the axial force-bending moment interaction relation of the failure state and the short-time allowable stress for each class of prestress, i.e., 40 kg/cm^2 for class A, 80 kg/cm^2 for class B and 100 kg/cm^2 for class C. If the axial force fluctuation ratio to the long-time axial force exceeds 1 (tensile force occurs in pile), it becomes very difficult to satisfy the conditions of Eq. (19), particularly for the case of a small amount of prestress. To avoid this kind of situation, it is recommended that the pile be used within the shaded range illustrated in Fig. 12.

Allowable shearing stresses in concrete are shown in Fig. 13 for the case of the long-time state. Some piles conform to the standards for columns and beams of the superstructure, while other conform to the method for calculating oblique tensile stress. The upper limits have been specified in order to avoid excessive differences. But, as for shearing characteristics, there still remain problems such as insufficient experimental data and extrapolation of results obtained for columns and beams with ordinary strength concrete to piles with high strength concrete.

Actually, the amount of reinforcing against shear force is extremely small and the difference between piles and columns as structural members is great. Photo 19 and photo 20 show the test results of PHC piles recently performed in the Building Research Institute, the purpose of which was to reproduce earthquake damage and to investigate bending-shear properties of PHC piles. Cyclic loads in both directions were applied to the approximately central part of the pile supported by a fixed end (footing) and another pinned end. As the final state, shear failure of the pile occurred within such a range that the stress condition of the pile did not reach the maximum bending strength. According to this test result, the values of allowable shearing stress presented here may not be always required or sufficient. For shearing characteristics of piles, therefore, it is highly desirable to accumulate sufficient data similar to the test results mentioned above.

The allowable stress for steel pipe piles may be as same as that conventionally used, but the thickness allowance against corrosion should be handled from a different viewpoint. According to the results of observations by Ohsaki (1981) for the last ten years, the average annual amount of corrosion is found to be about 0.02 mm. Thus, about 1 mm is appropriate as the total thickness of corrosion for 50 years, from

been revised to 1 mm.

4.4 Design of Underground Walls

If horizontal force is reduced on the basis of effects of embedment in the case of a pile foundation, the reduced portion of the force must be supported by underground walls. If this force is defined by αQ, then αQ is supported by the passive resistance component Q_w of the front surface and frictional resistance component Q_f of side surfaces. As seen in Fig. 6, participation ratios corresponding to these components will vary considerably depending on the properties of the ground, depth of embedment, plan of the building, horizontal displacement of the underground walls, and so on. In particular, it is necessary to assign a small participation ratio to the frictional resistance because it has more indeterminate factors than the passive resistance. Therefore, the participation ratios of about 3/4 and about 1/4 are recommended for Q_w and Q_f, respectively.

The force corresponding to the passive resistance is to be added to the ordinary design external force for the underground wall (generally, earth pressure at rest) in the form of a uniform distribution with depth. According to the results of measurements of earth pressure during an earthquake at the basement of a building in Yokohama City, reported by Ikuta et al. (1979), the seismic increment of earth pressure has a constant distribution with depth, or a distribution pattern almost equal to an inverse triangle shape, as shown in Fig. 14.

5. ADDITIONAL COMMENT

Points and bases of "Design Guide for the Building Foundation against Seismic Force" are summarized above. Although the Guide was the findings available to date, there still remain many unknown factors and items to be examined in the future with respect to earthquake resistance of building foundations. The author hopes that the Guide will be a starting point for breaking the present situation where there has been no appropriate design guide, and will function as a seed which may develop further studies in this field.

6. ACKNOWLEDGEMENT

The author wishes to express his gratitude to the members of the Building Foundation Review Sub-Committee listed below, for discussions about the Guide. The author also wishes to thank the members listed below of the Working Group established under the Sub-Committee and managed by himself, for preparing and amending the draft of the Guide.

Members of the Building Foundation Review Sub-Committee (as of March 1982)

Chairman: Dr. Yorihiko Ohsaki (University of Tokyo)

Members: Dr. Akira Enami (Nihon University)
Dr. Hideaki Kishida (Tokyo Institute of Technology)
Dr. Osamu Sakaguchi (Building Research Institute)
Mr. Yoshihiro Maekawa (Save Energy Organization for Residence and Building)
Dr. Makoto Watabe (Building Research Institute)

Expert Members: Mr. Masaaki Endo (Takenaka Komuten Company)
the late Dr. Yasunori Koizumi (Tokyo Metropolitan University)
Prof. Kikuo Kotohda (Waseda University)
Mr. Katsumi Yano (Nikken Sekkei Limited)

Members of the Working Group of the Sub-Committee (as of March 1982)

Members: Dr. Hiroshi Oh-oka (Building Research Institute)
Mr. Norimichi Ohki (Takenaka Technical Research Laboratory)
Dr. Shin Okamoto (Building Research Institute)
Dr. Tetsuo Kubo (Building Research Institute)
Mr. Fumio Chatani (Ohbayashigumi Technical Research Laboratory)
Dr. Shoich Nakai (Shimizu Construction Company)
Mr. Tsuneyoshi Hagiwara (Kajima Institute of Construction Technology)
Mr. Jyoji Yamashita (Taisei Corporation)
Dr. Manabu Yoshimura (Building Research Institute)

References

Ikuta, Y., Maruoka, M., Minota, T. and Naganou, M. (1979). "Record of Lateral Pressure Taken During Earthquake," Soils and Foundations, Vol 19, No. 4, pp. 85-92.

Kishida, H., Yamato, S. and Nakai, S. (1979). "Horizontal Resistance of Pile by Considering Embedment of Foundation" (in Japanese), Kenchiku Gijutsu, No. 329, pp. 147-163.

Kotohda, K., Kazama, S. and Muroki, M. (1980). "Research on Horizontal Resistance of Basement-pile System, Part 1" (in Japanese), Proceedings of 15th Annual Meeting of Japanese Society of Soil Mechanics and Foundation Engineering, pp. 1009-1012.

Ohsaki, Y. (1981). "Corrosion of Steel Piles Driven in Soil Deposits," Research Report 81-04, Department of Architecture, University of Tokyo.

Sugimura, Y. (1981). "Earthquake Damage and Design Method of Piles," Proceedings of 10th International Conference on Soil Mechanics and Foundation Engineering, Stockholm, Vol 2, pp. 865-868.

Table 1 Historical Background of the Guide

Earthquake and main damage		Japan Industrial Standard	Administrative activity
		Precast concrete pile (1955)	
Niigata (1964)	Liquefaction Pile damage	Steel pipe pile (1963)	
Off-Tokachi (1968)	Landslide Pile damage	Prestressed concrete pile (1968)	
			Notice No.111 of the Ministry of Construction (1971)
Off-Izu peninsula (1974)	Landslide Fault		Building Foundation Design Standard of AIJ (1974)
Izu-Ohshima kinkai (1978)	Landslide Fault		
Off-Miyagi pref. (1978)	Pile damage Landslide		Building Foundation Review Sub-Committee (1979)
			New Earthquake Resistance Standard (1981)
Off-Urakawa (1982)	Pile damage	Prestressed high strength concrete pile (1982)	Proposed Design Guide (1982)
Nihonkai chubu (1983)	Liquefaction Pile damage		Design Guide (1984)

Table 2 Condition of Resisting Element at Embedment

Passive resistance at front surface Q_w	Friction resistance at side surfaces Q_f	Horizontal resistance of pile Q_p
$Q_w = K_w A_w y_w$ $= \frac{\pi E A_w y_w}{2L(1-\mu^2)} \times \left[m \log_e \frac{1+\sqrt{m^2+1}}{m} + \log_e (m+\sqrt{m^2+1})\right]^{-1}$ A_w : Area of front surface of embedment y_w : Amount of displacement E : Modulus of deformation of soil Sand : $E = 7.7(N+26)(kg/cm^2)$ Clay : $E = 105\ q_u(kg/cm^2)$ N : Mean N value q_u : Unconfined compression strength L : Short side of front surface of embedment μ : Poisson's ratio m : Long side to short side ratio of front surface of embedment Value of maximum passive earth pressure Qw_{max} should be as follows: Sand : $Qw_{max} = k_p \gamma z$, $k_p = (1+\sin\phi)/(1-\sin\phi)$ Clay : $Qw_{max} = q_u + \gamma z$ ϕ : Internal angle of friction γ : Unit weight of soil z : Depth	$Q_f = 2A_f f y_f$ $(y_f \leq 1\ cm)$ $Q_f = 2A_f f$ $(y_f > 1\ cm)$ A_f : Area of side surface of embedment y_f : Amount of displacement f : To be 80% of the maximum unit friction force of side surface Sand : $f = 0.8 \times N/50(kg/cm^2)$ Clay : $f = 0.8 \times q_u/2(kg/cm^2)$ N : N-value q_u : Unconfined compression strength 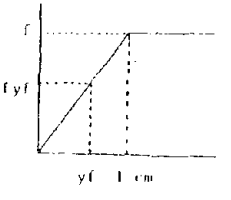	Within the range of $Q_w < Qw_{max}$ $Q_p = \frac{Q_B}{1+\frac{\beta A_w (2f+k_h y)}{n k_h \beta}}$ $(y_w \leq 1\ cm)$ $Q_p = \frac{QB - 2fA_w}{1+\frac{\beta A_w K_w}{n k_h \beta}}$ $(y_w > 1\ cm)$ However, the horizontal resistance was derived after calculating the displacement of fixed pile head: $y_p = \frac{\beta Q_p}{n k_h \beta}$, $\beta = \sqrt[4]{\frac{k_h \beta}{4EI}}$ and by solving under the condition of $y_w = y_f = y_p$, $A_w = A_f$ where, n : Numbers of piles β : Diameter of pile k_h: Coefficient of horizontal subgrade reaction EI: Flexural rigidity of pile

Table 3 Method of determination of Stresses in pile material

Kind of pile	Axial force-bending moment	Shear
Cast-in-place concrete pile	In accordance with the review for columns of superstructure (concrete at tensile side is ignored.)	$\frac{4Q_p}{3A} \leqq f_s$
Precast concrete pile		$2\frac{Q_p}{A} \leqq f_s$
Precast-prestressed concrete pile	$-f_b \leqq \frac{N}{A_e} + \sigma_e + \frac{M}{I_e} y \leqq f_c$	$\frac{Q_p S_o}{2tI} \leqq \frac{1}{2}\sqrt{(\sigma_g + 2\sigma_d)^2 - \sigma_g^2}$ $\sigma_g = \sigma_e + \frac{N}{A_e}$
Steel pipe pile	$-f_b \leqq \frac{N}{A} + \frac{M}{I} y \leqq f_c$	$2\frac{Q_p}{A} \leqq f_s$

N: Axial force (positive for compression and negative for tension); M: Bending moment; Q_p: Shearing force; t: Thickness of wall of pile; A: Cross sectional area; A_e: Equivalent cross sectional area of concrete; I: moment of inertia of pile; I_e: Equivalent geometrical moment of inertia of concrete; S_o: moment of area of pile; y: Radius of pile (positive at bending compression side, negative at bending tension side); σ_e: Effective prestress; σ_d: Allowable oblique tensile stress; f_b: Allowable tensile stress or allowable bending tensile stress; f_c: Allowable compressive stress or allowable bending compressive stress; f_s: Allowable shearing stress

Table 4 Allowable Stresses for Various Kinds of Pile Materials

Concrete

Kind of pile		Long-time			Short-time			Remarks
		Compression	Shear	Bond	Compression	Shear	Bond	
Cast-in-place concrete pile	In Water	$\frac{F_c}{4.5}$ and 60	$\frac{F_c}{45}$ and $\frac{1}{1.5}(5+\frac{F_c}{100})$	$\frac{F_c}{15}$ and $\frac{1}{1.5}(13.5+\frac{F_c}{25})$	Two timed that of long-time	1.5 times that of long-time		F_c : Ultimate compression strength of concrete σ_e : Effective prestress
	Not in water	$\frac{F_c}{4}$ and 70	$\frac{F_c}{40}$ and $\frac{3}{4}(5+\frac{F_c}{100})$	$\frac{3F_c}{40}$ and $\frac{3}{4}(13.5+\frac{F_c}{25})$				
Precast concrete pile		$\frac{F_c}{4}$	$\frac{3}{4}(5+\frac{F_c}{100})$	$\frac{3}{4}(13.5+\frac{F_c}{25})$				
Kind of pile		Compression	Bending tensile	Oblique tensile stress	Compression	Bending-tensile	Oblique tensile stress	
Prestressed concrete pile		$\frac{F_c}{4}$ and 150	$\frac{\sigma_e}{4}$ and 20	$\frac{0.07F_c}{4}$ and 9	Two times that of long-time	1.5 times that of long-time		
Prestressed high strength concrete pile		$\frac{F_c}{4}$ and 225	$\frac{\sigma_e}{4}$ and 25	$\frac{0.07F_c}{4}$ and 12				

Kind of pile	Compression	Tension	Bending	Shear	Compression	Tension	Bending	Shear	Remarks
Steel pipe pile	$\frac{F^*}{1.5}$	$\frac{F}{1.5}$	$\frac{F^*}{1.5}$	$\frac{F}{1.5\sqrt{3}}$	1.5 times that of long-time				F : Yield tension strength of steel F*: Refer to the note shown below

Steel reinforcing bar (deformed bar)

Kind of material	Compression	Tension		Compression	Tension	Remarks
		Other than shear reinforcement	Shear reinforcement		Shear reinfocement and others	
Less than 28 mm	$\frac{F}{1.5}$ and 2200	$\frac{F}{1.5}$ and 2200	$\frac{F}{1.5}$ and 2000	1.5 times that of long-time and 3000		F : Yield tension strength of reinforcing steel bars
Over 28 mm	$\frac{F}{1.5}$ and 2000	$\frac{F}{1.5}$ and 2000	$\frac{F}{1.5}$ and 2000			

Steel materials for prestressed concrete

During initial tensioning	$0.70f_1$ or $0.80f_2$, whichever smaller, f_1 : Standard tensile strength, f_2 : Standard yield strength

$F^*/F = 0.8 + 2.5\ t/r (0.01 \leqq t/r \leqq 0.08)$

$F^*/F = 1.0\ (t/r \geqq 0.08)$

r : Radius of pile

t : Thickness excluding the thickness allownce against corrosion

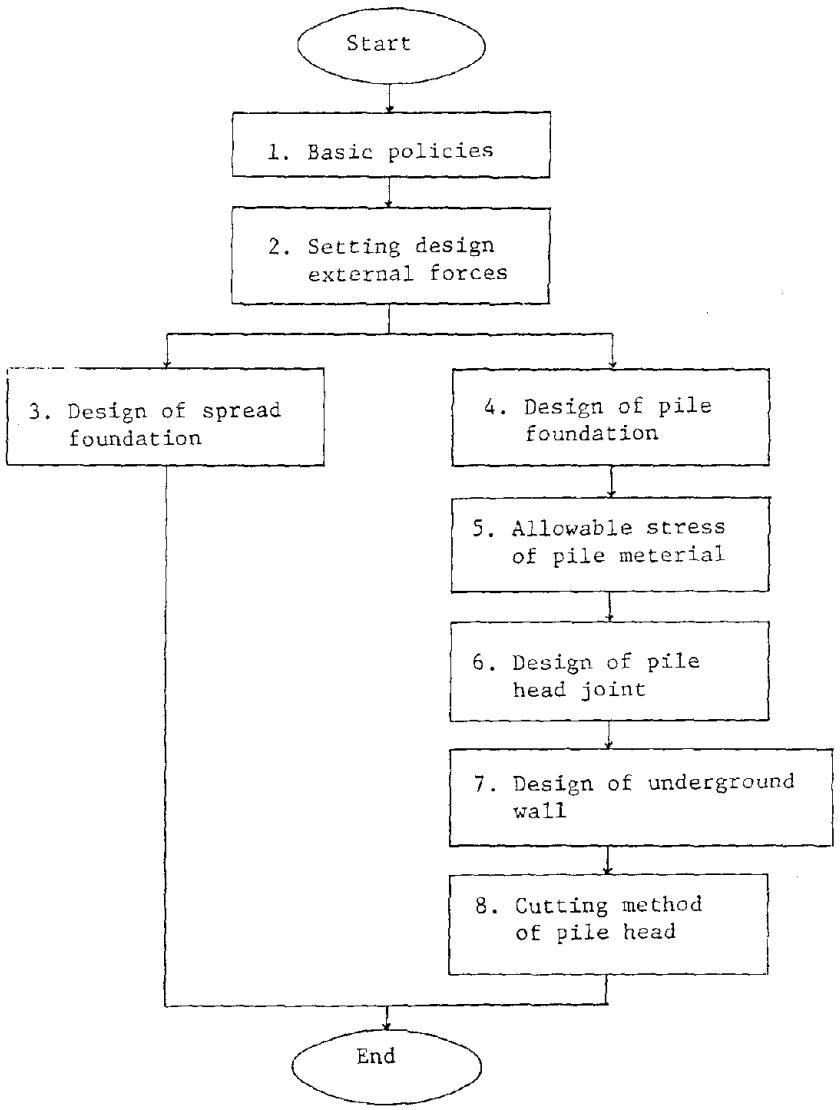

Fig. 1 Contents of the Guide

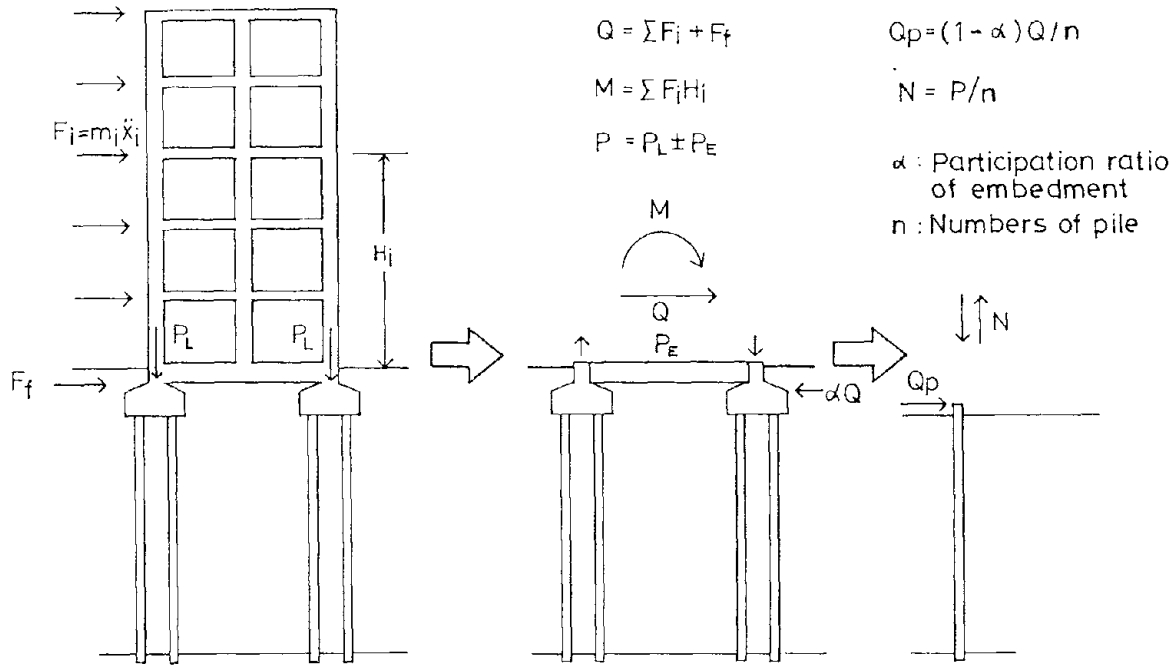

Fig. 2 Design External Forces during Earthquake

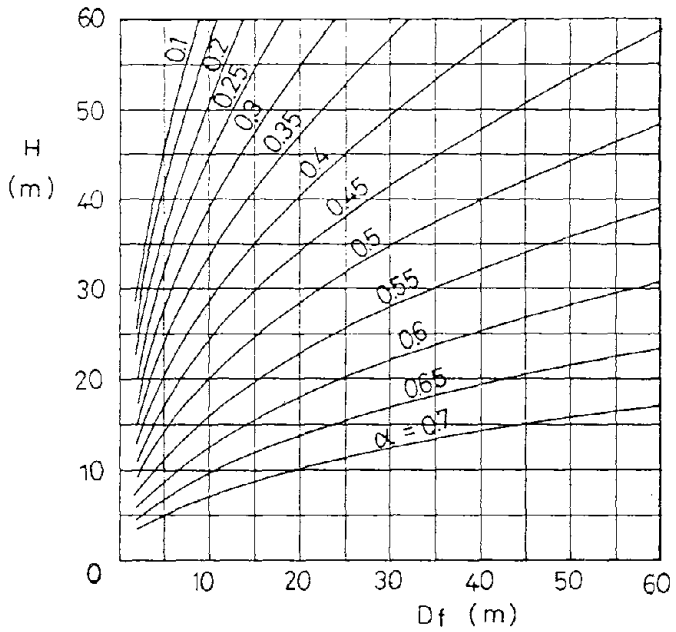

Fig. 3 Values of Horizontal Force Reduction Ratio α

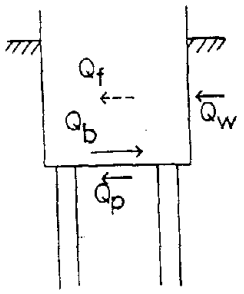

Q_b : Acting external force

Q_w : Passive resistance at the front surface

Q_f : Frictional resistance at the side surfaces

Q_p : Horizontal resistance of pile

Fig. 4 Equilibrium of Force at the Embedded Portion

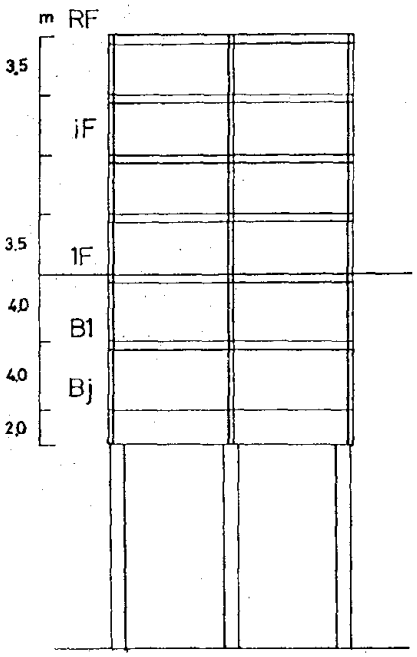

Numbers of story : 3, 6, 10

Basement stories : 1 to 4

Ground condition :

Sand : N = 10, 20

Clay : q_u = 0.5, 1 kg/cm^2

Pile : Steel pipe pile

ϕ = 609.6

t = 12.7

P_a = 116 t/pile

Fig. 5 Combination of the Exercises for Trial Calculation (Building with a square plan)

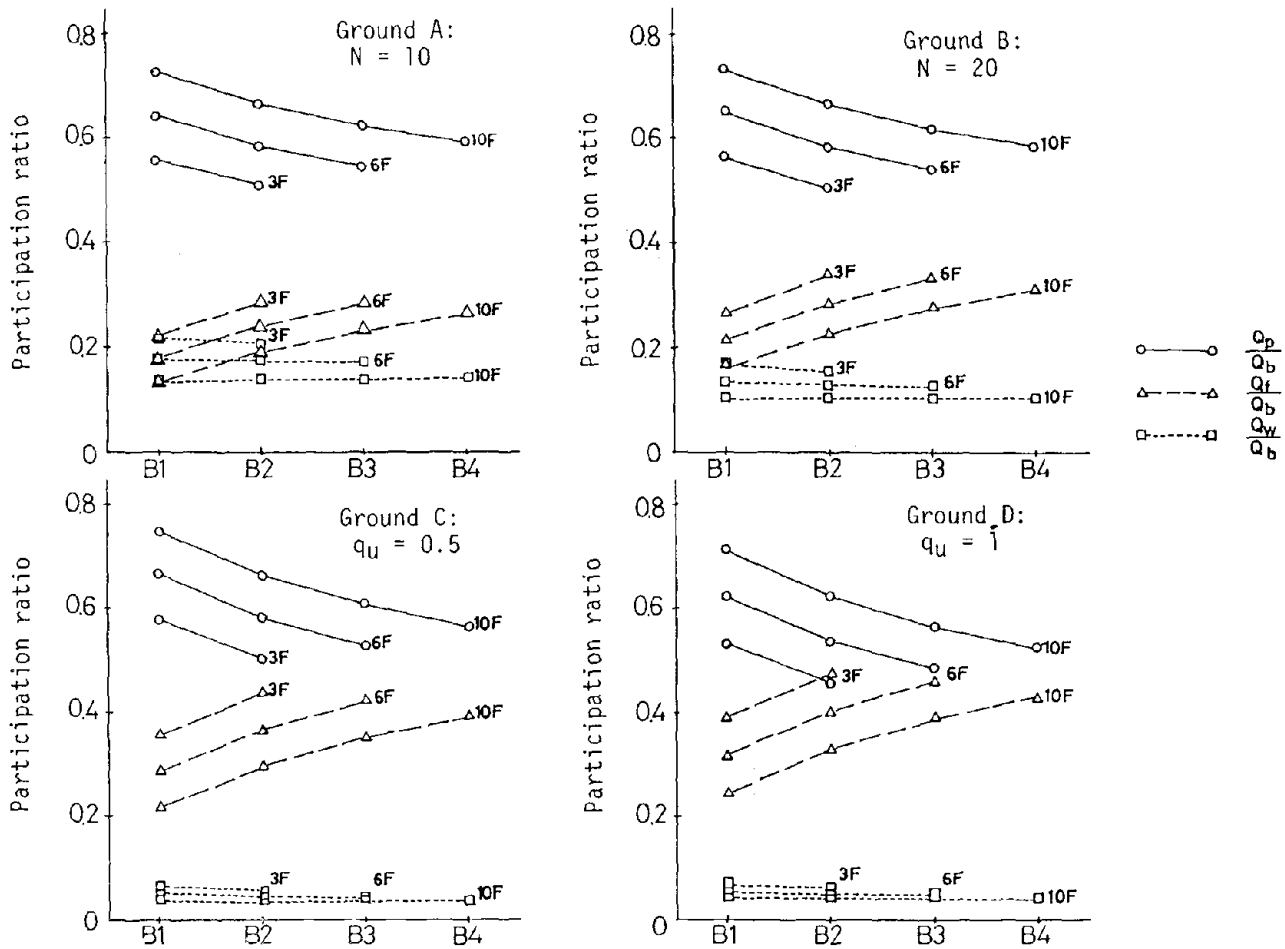

Fig. 6 Horizontal Force Participation Ratios of Resisting Elements Obtained from the Numerical Analysis

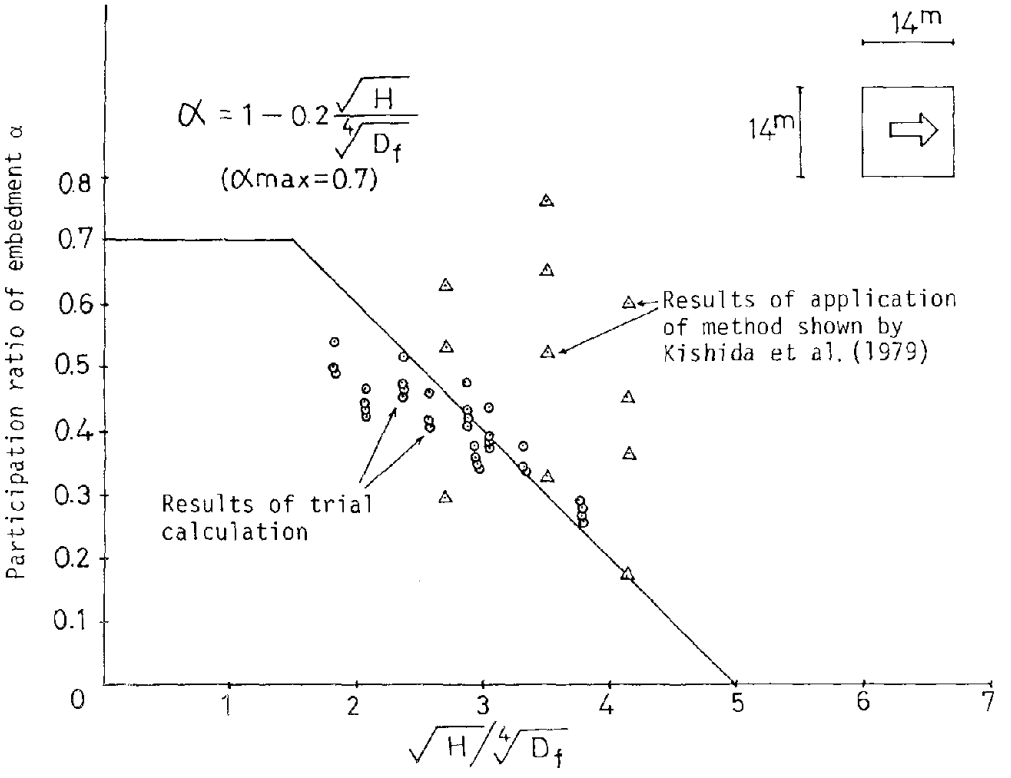

Fig. 7 Relation between Eq. (1) and the Results of the Trial Calculations

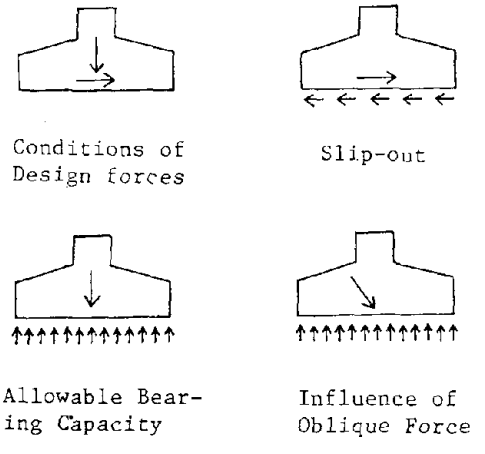

Fig. 8 Design of Spread Foundation

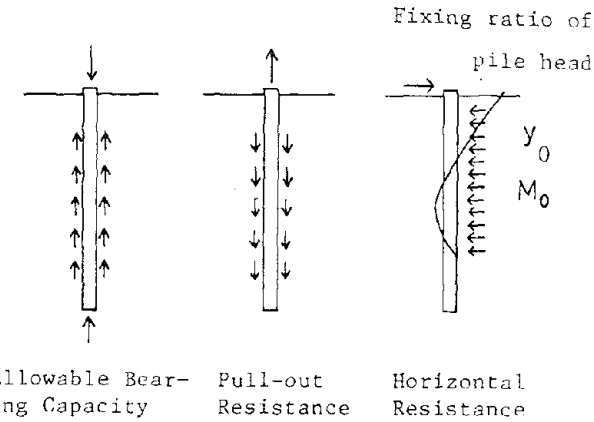

Fig. 9 Design of Pile Foundation

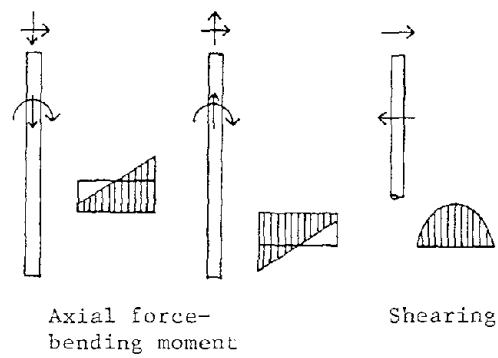

Fig. 10 Investigation on the Stress of Pile Material

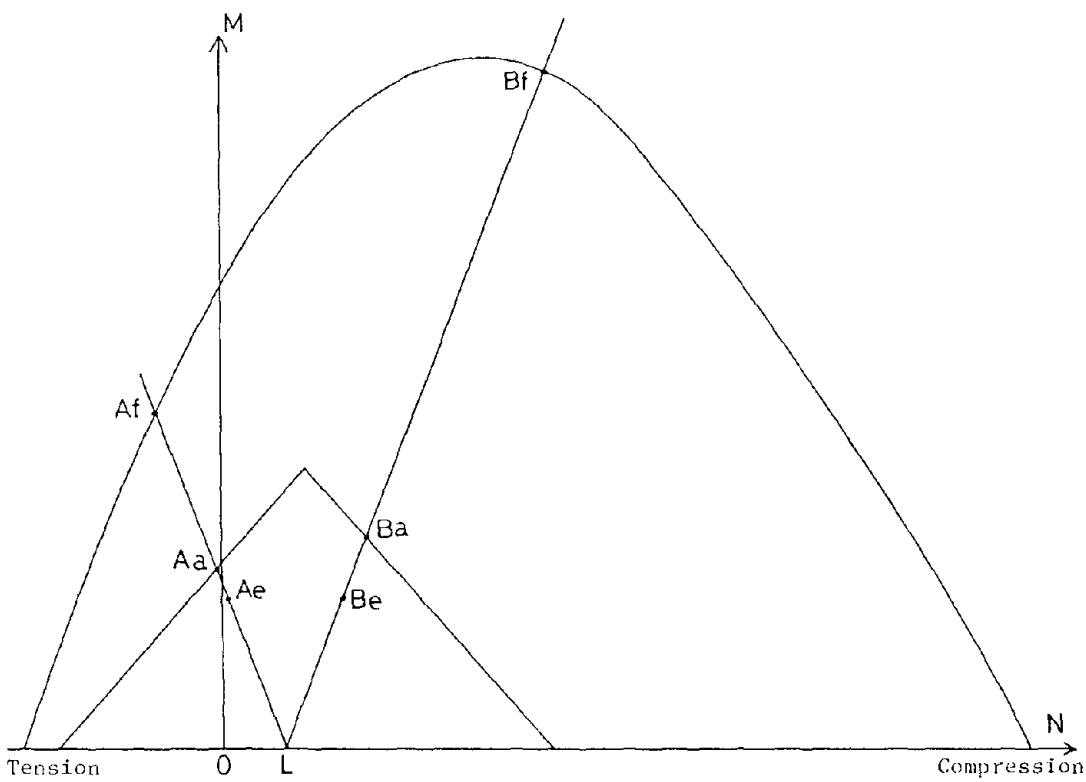

Fig. 11 Method of Finding the Allowable Stress

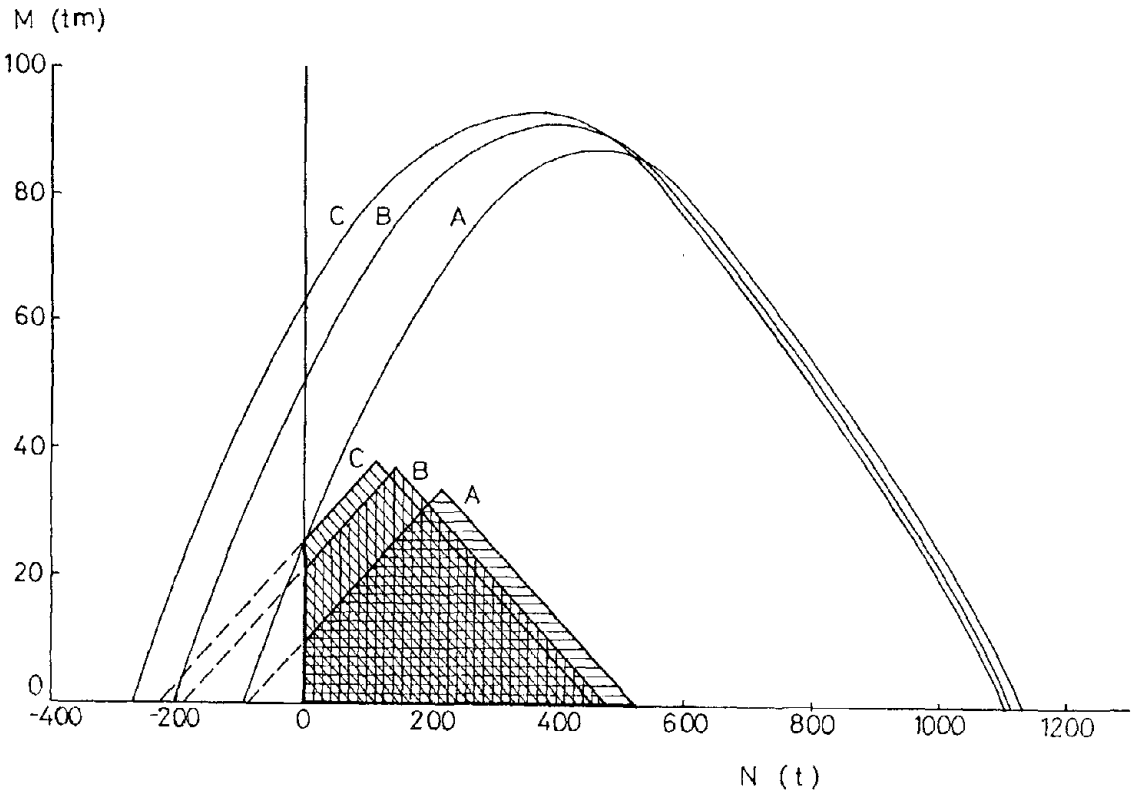

Fig. 12 Recommended Range of Use in the Allowable Capacity Design

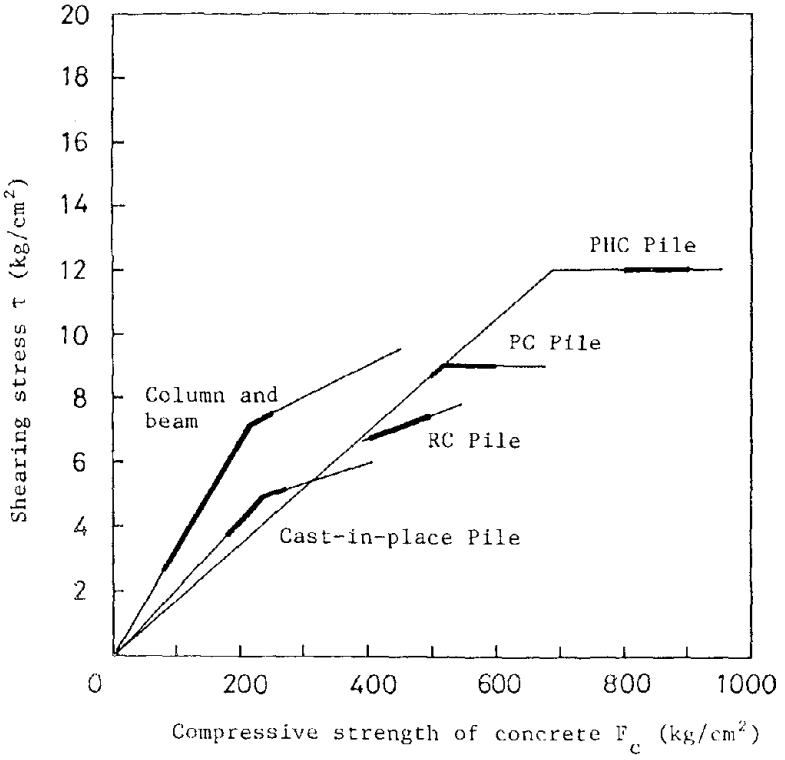

Fig. 13 Comparison of Allowable Shearing Stresses in various Kinds of Pile (Long-time)

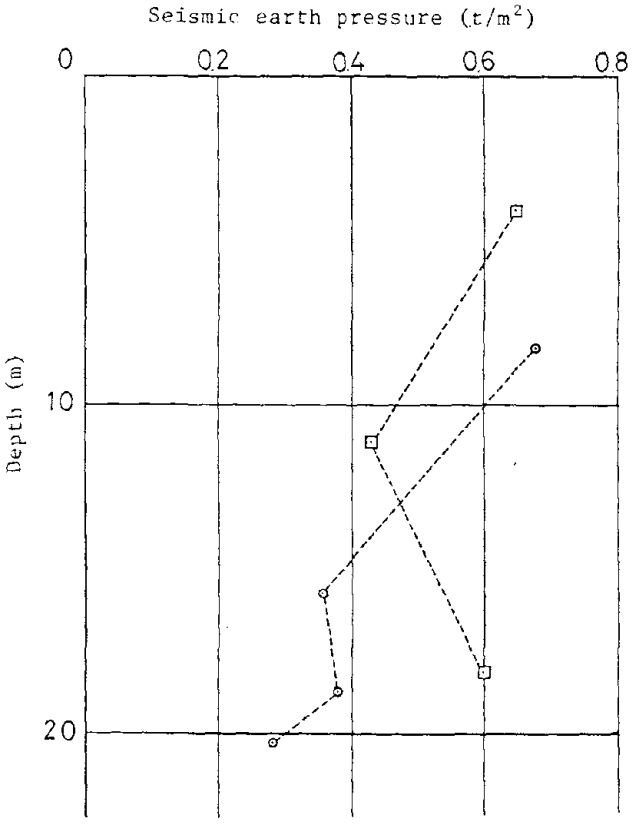

Fig. 14 Results of Measurement of Seismic Earth Pressure [after Ikuta et al. (1979)]

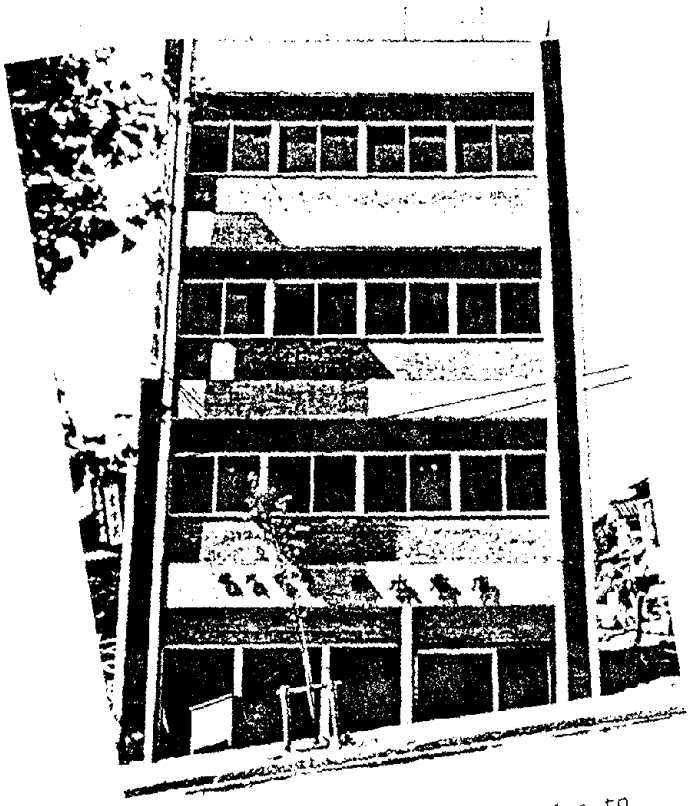

Photo 1 Overturning of Building due to Liquefaction (Niigata earthquake 1964)

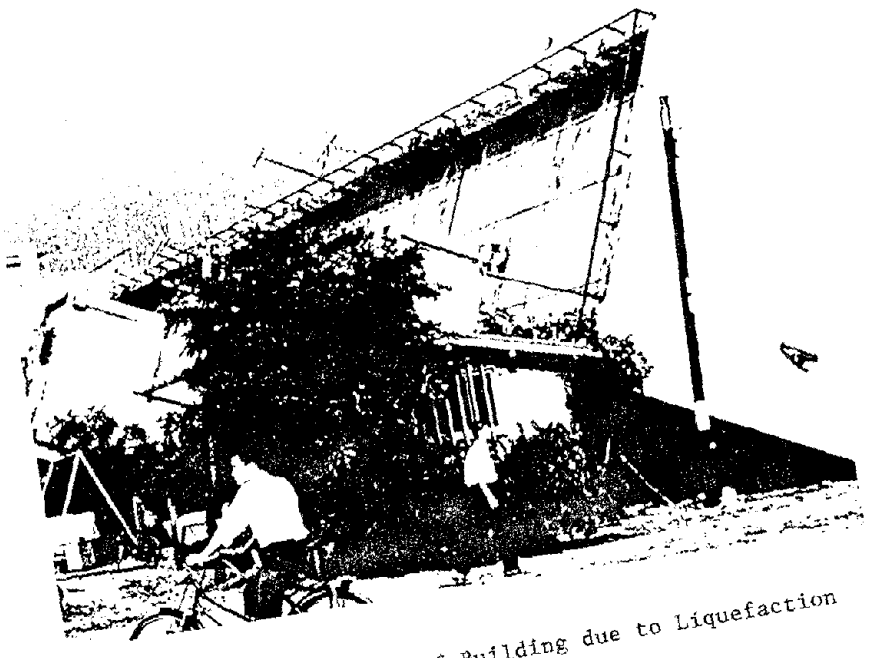

Photo 2 Overturning of Building due to Liquefaction (Niigata earthquake 1964)

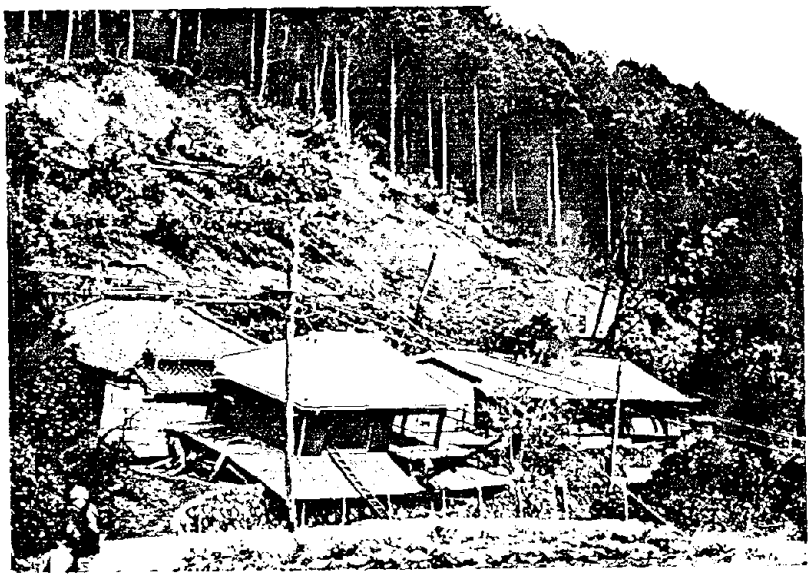

Photo 3 Landslide of the Hill at the Back of Houses (Izu-Ohshima kinkai earthquake 1978)

Photo 4 Detail of Damage of Photo 3 (Izu-Ohshima kinkai earthquake 1978)

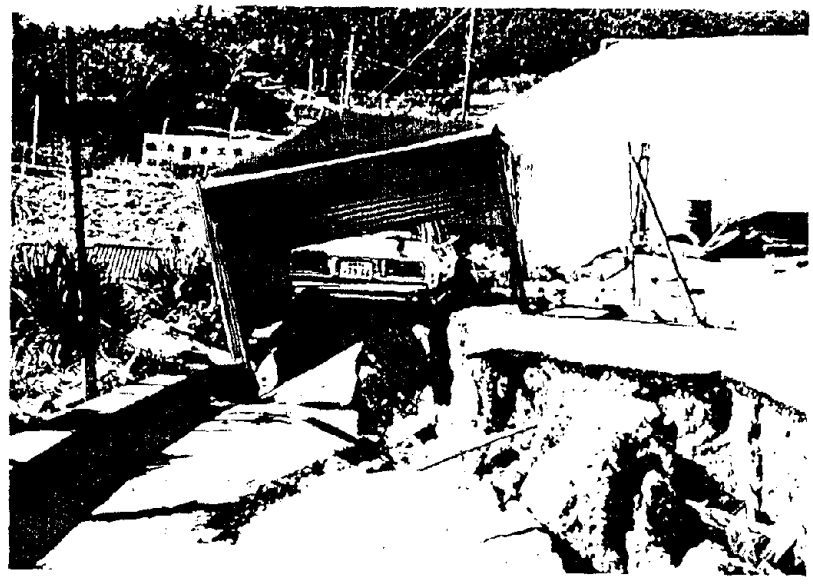

Photo 5 Collapse of Fill Ground (Izu-Ohshima kinkai earthquake 1978)

Photo 6 Damage due to Seismic Fault (Izu-Ohshima kinkai earthquake 1978)

Photo 7 Crush of PHC Pile (Off-Miyagi prefecture earthquake 1978)

Photo 8 Buckling of PC Bars (Off-Miyagi prefecture earthquake 1978)

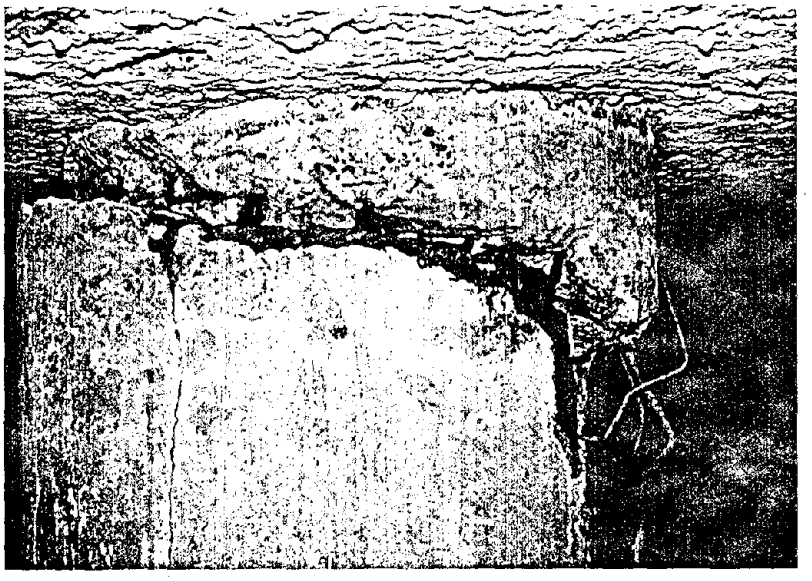

Photo 9 Shear Failure of PHC Pile (Off-Miyagi prefecture earthquake 1978)

Photo 10 Shear Failure of PHC Pile (Off-Miyagi prefecture earthquake 1978)

Photo 11 Tensile Breaking of PC Bars (Off-Miyagi prefecture earthquake 1978)

Photo 12 Damage of PC Piles (Off-Miyagi prefecture earthquake 1978)

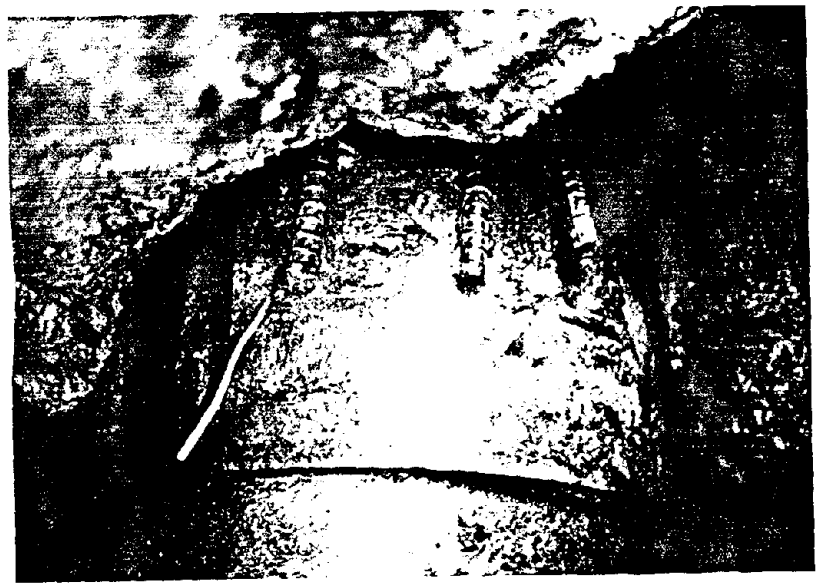

Photo 13 Damage of Joint between Steel Pipe Piles and Foundation Slab (Off-Urakawa earthquake 1982)

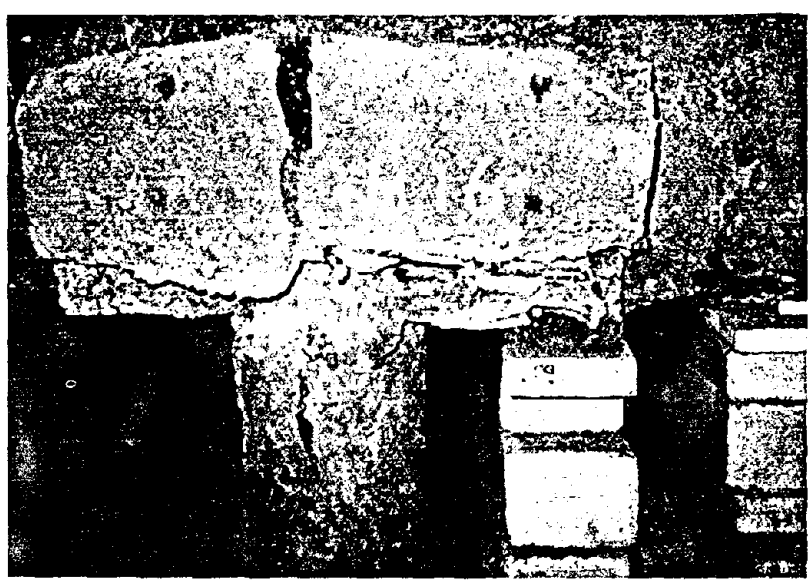

Photo 14 Failure of Pile Cap (Off-Miyagi prefecture earthquake 1978)

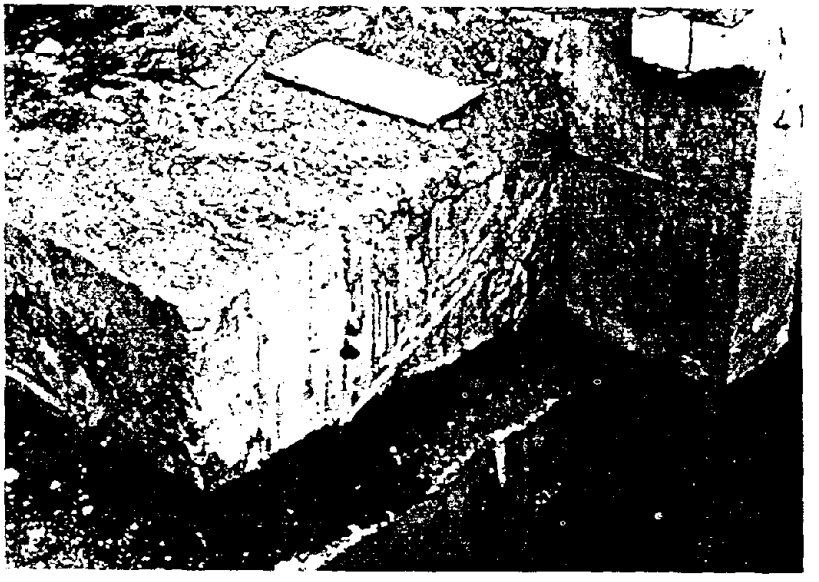

Photo 15 Cracks of Foundation Slab (Off-Tokachi earthquake 1968)

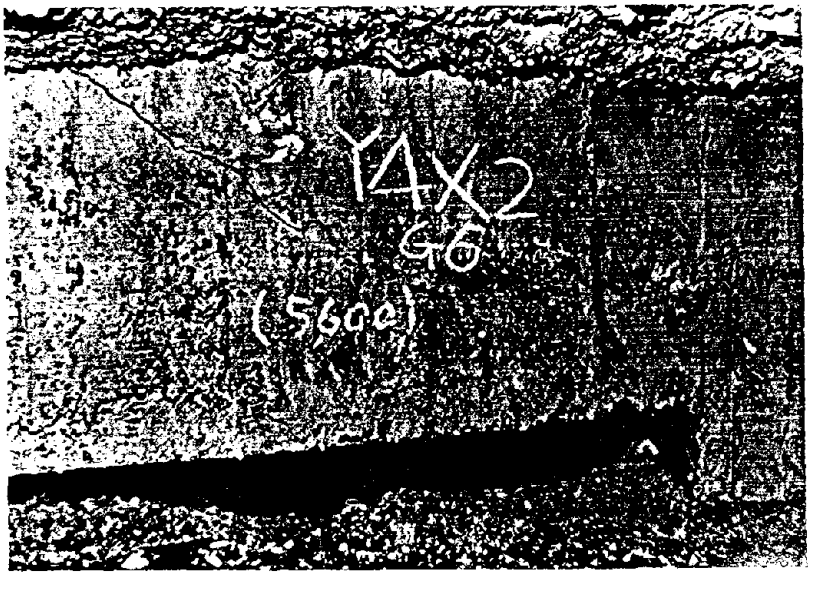

Photo 16 Cracks of Foundation Beam (Off-Tokachi earthquake 1968)

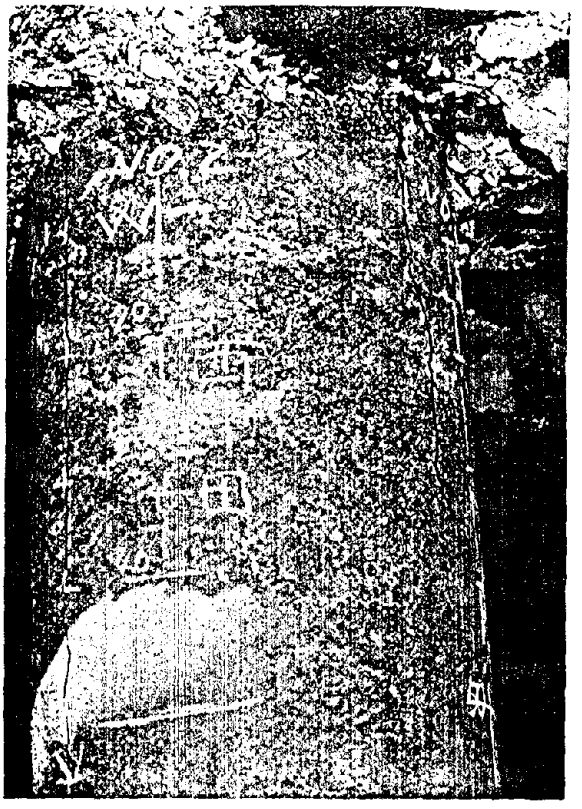

Photo 17 Hair Cracks due to Cutting Work of Pile Head (PHC Pile)

Photo 18 Hair Cracks due to Cutting Work of Pile Head (PHC Pile)

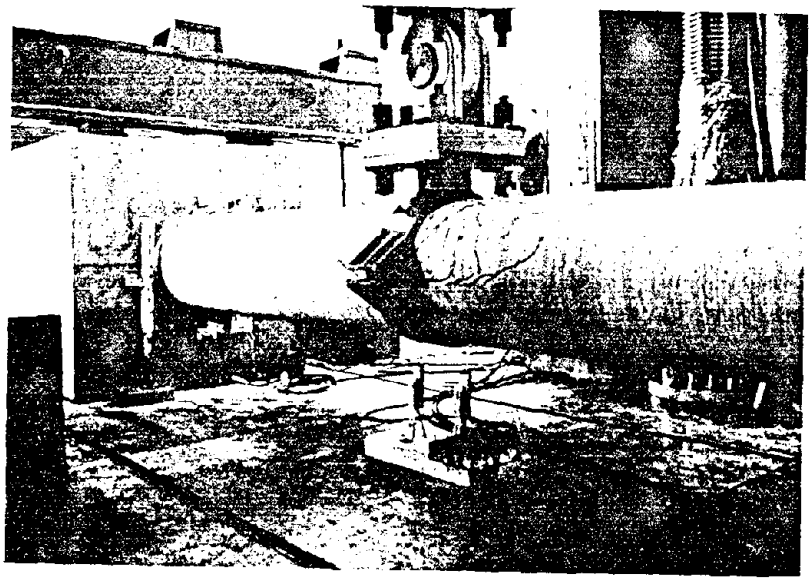

Photo 19 Bending-Shear test of Prestressed High Strength Concrete Pile

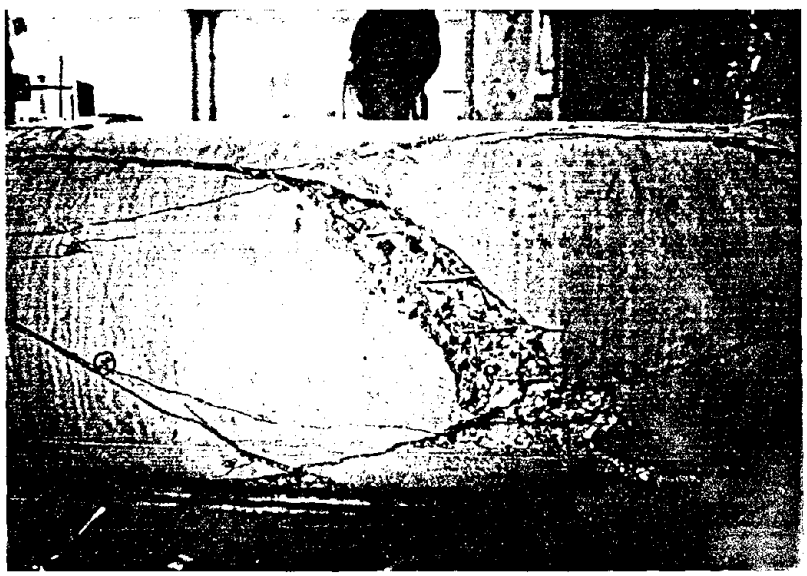

Photo 20 An Example of Shear Failure as the Final State

SHEAR RESISTANCE OF UNREINFORCED HOLLOW CONCRETE BLOCK MASONRY WALLS

BY

Kyle Woodward and Frank Rankin

National Bureau of Standards

Gaithersburg, Maryland 20899

ABSTRACT

An experimental investigation is described which has as its primary focus the determination of the shear resistance exhibited by unreinforced, ungrouted, hollow concrete block masonry walls. Thirty-two wall panel tests are reported. The parameters in the investigation include the amount of applied vertical compressive stress, wall aspect-ratio, block strength, and mortar type. All of the wall panels have heights and thicknesses of 64 in. and 8 in., respectively. Four different wall lengths are used to vary the aspect ratio: 48 in., 64 in., 80 in., and 96 in. The vertical compressive stress varies from approximately 100 psi to 500 psi based on the wall net cross-sectional area. The block have gross area unit strengths of either 1800 psi or 1300 psi, while the mortar is proportioned as either a Type S or a Type N. The wall panels are tested in the NBS Tri-directional Test Facility which imposes well defined boundary conditions at the top and bottom of the walls. The resulting data presented in this paper include the lateral load (shear) versus wall displacement relationships, crack pattern maps, and wall strains along their diagonals. One of the principal findings of the investigation is that the relationship between increasing amounts of applied vertical compressive stress and the resulting increased shear resistance is significant and nearly linear. The other major observation is that there exists a critical diagonal tension strain, independent of the varied parameters, which defines the onset of wall diagonal tension cracking.

1. INTRODUCTION

The Center for Building Technology of the National Bureau of Standards is currently undertaking a program of experimental research on the shear resistance and behavior of shear-dominated masonry walls. The parameters under study are applied vertical (axial) compressive stress, wall aspect ratio (length-to-height), block and mortar type, horizontal and vertical reinforcement, out-of-plane loadings, and loading history. This paper reviews the test program on ungrouted, unreinforced hollow concrete block masonry walls. Supplemental information on the research may be found in references 1, 2, and 3.

The investigation reported herein involved tests on thirty-two wall panels whose nominal dimensions are 8 in. thick, 64 in. high, and either 48 in., 64 in., 80 in., or 96 in. long. The walls are subjected to a vertical compressive stress in combination with in-plane lateral displacement. In addition to the variation of aspect ratio, the vertical compressive stress, block strength, and mortar type are also varied in this series of tests. The resulting data include in-plane lateral load resistance, wall displacement, and strains measured at discrete locations on the wall faces.

This paper presents a brief description of the materials properties, wall panel details and fabrication, test setup, and instrumentation. The data include load-displacement relationships, crack pattern maps, and wall diagonal strain measurements.

2. WALL PANEL DETAILS AND TEST SETUP

2.1 Materials

All materials used in constructing the wall panels and companion prisms are commercially avail-

able and are representative of those commonly used in building construction. The concrete masonry units are two-core hollow block and have nominal dimensions of 8 in. x 8 in. x 16 in. The block labeled as high strength have a gross area of 119.2 sq. in., a net solid area of 61.5 sq. in., and a gross area compressive strength of 1813 psi based on the average of six unit tests. The block labeled as low strength have a gross area of 119.8 sq. in., a net solid area of 60.4 sq. in., and a gross area compressive strength of 1304 psi based on the average of nine unit tests. The mortar is either Type S proportioned with 1 part by volume of portland cement, 3/8 part by volume of lime, and 4 parts by volume of sand or Type N proportioned with 1 part by volume of portland cement, 1 part by volume of lime, and 5 parts by volume of sand.

2.2 Details and Fabrication

A typical wall panel is shown in Fig. 1. The wall panels are constructed in running bond with a 50 percent overlap of block in alternate wall courses. The panels are fabricated and cured in a controlled environment laboratory from materials stored in the same environment for at least 30 days. The wall panels are built using face-shell bedding except for the two end cross-webs. The joints are struck flush, but not tooled. Mortar cubes and prisms are also built and later tested as companion specimens to the wall panels. The mortar cubes are 2 in. x 2 in. x 2 in. and the prisms are made by stack bonding three stretcher units.

The details of each wall panel are listed in Table 1. The wall panel identifier is a two-part mnemonic with the two parts separated by a hyphen. That part of the identifier preceding the hyphen is descriptive and has the form mABn. The m term denotes the wall length in inches, while the n term specifies the approximate vertical compressive stress applied to the wall. The stress is based on the net cross-sectional area of the wall and is expressed in units of psi. The A term indicates the block strength with A being replaced by either H for the high strength block or L for the low strength block. Similarly, the B term denotes the mortar strength (type) using H for high strength (Type S) and L for low strength (Type N). The terms high and low strength are used only in a relative sense and do not imply an absolute measure. That part of the identifier following the hyphen is a construction code and provides for unique identification of each wall.

2.3 Test Setup

The test setup (Fig. 2) is the NBS Tri-directional Test Facility (NBS/TTF), a permanent loading apparatus designed to test building components using three-dimensional loading histories. The NBS/TTF is a computer-controlled loading apparatus which applies forces/displacements in all six degrees of freedom at one end of a test specimen. The other end of the specimen is fixed. The six degrees of freedom are the translations and rotations in and about three orthogonal axes. The application of such actions is accomplished by seven closed-loop, servo-controlled hydraulic actuators which receive their instructions by means of computer-generated commands. A simplified sketch of the test method for applying in-plane displacement to a wall panel is shown in Fig. 3.

2.4 Instrumentation

In the interest of brevity, only that instrumentation which provides data used in this paper is described. The loads imposed on the wall panels are measured by load transducers incorporated in the hydraulic actuators. The readings from these devices are adjusted to account for geometry changes and the combined effects of all of the hydraulic actuators. The wall panel displacement (in-plane) is measured by displacement transducers mounted horizontally between the top course of the wall and an external fixed reference (Fig. 4). The diagonal strain referenced in future discussion is computed from the displacement measured by a displacement transducer mounted diagonally on the wall panel (Fig. 4). All of the instrumentation

is connected to a computer-based, analog-to-digital converter having a sample rate of 50,000 samples per second.

3. TEST RESULTS

3.1 General Behavior

In general, the primary form of distress exhibited by the wall panels was a diagonal-tension type of failure as illustrated by the typical crack patterns in Fig. 5. However, there were exceptions. Flexural distress in the form of horizontal flexural tension cracks in the mortar bed joints occurred if the applied vertical compressive stress was insufficient to suppress this failure mode. It should be noted that even the walls exhibiting flexural distress, did, in fact, suffer a local diagonal-tension distress in a corner block and when the vertical compressive stress was increased, the primary mode of distress changed to a general diagonal-tension failure. In all of the walls tested, the final failure of the wall was the result of crushing in the high flexural compression zone of the wall. The term final failure denotes an inability to sustain the applied vertical compression load in combination with the imposed lateral displacement.

While the cracking pattern was relatively insensitive to the parameters studied in the test program, it appeared that the orientation of the cracking was influenced by both the level of vertical compressive stress and the wall aspect ratio. The tendency of the diagonal cracking to follow the mortar joints, or to pass through the units, was affected by vertical compressive stress, block strength, and mortar strength. Walls built with the low strength mortar exhibited a pronounced tendency to exhibit mortar joint cracking while the walls built with the high strength mortar exhibited much more cracking through the block. Increased vertical compressive stress increased the likelihood of block cracking, especially for the high strength block and mortar combinations.

The 48 in., 64 in., and 80 in. walls tended to form a consistent corner-to-corner diagonal crack pattern which essentially separated the wall into two triangular segments. The shear transfer between the two segments took place along the diagonal crack by shear friction. The 96 in. long wall, by contrast, did not form the corner-to-corner crack. The crack pattern which formed (Fig. 6) did not separate the wall into triangular segments but, instead, included a horizontal crack in the high flexural compression region of the wall. The combination of favorable crack orientation (horizontal) and high normal compressive stress permitted a much more efficient shear friction mechanism to form than was possible in the shorter walls. In fact, 96 in. walls were able to resist more lateral load through the shear friction mechanism than from the diagonal-tension mechanism, thus first cracking was not coincident with the maximum lateral load resistance.

3.2 Shear Stress-Displacement Relationships

The shear stress versus wall displacement curves for all of the tests are shown in various combinations in Figures 7 through 9. Shear stress is computed by dividing the measured in-plane lateral load by the net cross-sectional area of the wall. There appears to be a common form to the curves regardless of the variation in parameters. The effect of the applied vertical compressive stress is much more pronounced on the maximum stress achieved than on the initial stiffness of the wall. This observation excludes the gross differences in the stress-displacement relationship for the walls having flexural distress prior to diagonal-tension distress. As the applied vertical compressive is increased, the shear stress, or conversely the wall displacement, at which the curve exhibits nonlinearity also increases. Thus, higher applied vertical compressive stress has a negligible impact on the absolute wall displacement at which the wall reaches its maximum resistance. Therefore, the displacement which causes diagonal cracking is relatively

independent of vertical stress, but the maximum resistance and initial stiffness are increased by vertical compressive stresses.

The effect of the block and mortar strengths on the initial stiffness of the walls is interactive. The walls made with high strength block tend to exhibit significant differences in stiffness when the low strength mortar data are compared with the high strength mortar data (Fig. 7). Similarly, though not shown in the figures, differences are pronounced when the stiffness of walls made with high strength mortar, but low and high strength block are compared. However, comparison of the data from walls with low strength block and low strength mortar versus walls with low strength block and high strength mortar (Fig. 8) show no discernible differences in stiffness. This lack of apparent effect is also true for the comparison of high strength block-low strength mortar and low strength block-low strength mortar (not shown in figure). The overall behavior tends to suggest that the stiffness of the wall is strongly related to its probable final crack path (mortar joint or through block) and ultimately its weakest material component.

The aspect ratio of the walls has a strong influence on the maximum shear resistance, but the data do not indicate a similar influence on the stiffness of the walls (Fig. 9). The actual effect may exist, but may not be discernible within the scatter of the test data.

3.3 Maximum Shear Stress Resistance

The maximum shear stresses computed from the maximum measured lateral loads along with the other pertinent data are listed in Table 2 for all the wall panels. The maximum shear stresses for the 48 in., 64 in., and 96 in. long wall panels are plotted versus the applied vertical compressive stress in Fig. 10. Clearly, there is an increase in maximum shear resistance with increased vertical compressive stress. The nature of the relationship between the shear stress and the vertical stress is affected by the wall aspect ratio and the combination of material strengths. Figure 10 illustrates the significant effect of aspect ratio, but the effect becomes pronounced only for the higher levels of vertical stress. Larger aspect ratios produce higher values of maximum shear resistance. The impace of material strengths on the maximum shear stress-applied vertical stress relationship is also shown in Fig. 10. The most advantageous combination in terms of maximum resistance is, not surprisingly, high strength block and mortar. The lease advantageous is the low strength block and mortar, but as with aspect ratio, the effect of material strength becomes significant only for the higher levels of applied vertical compressive stress.

The lines plotted in Fig. 11 are best-fit approximations developed using regression analyses of the data. The particular data used in developing each line are identified by the line labels. Generally, the approximations are linear with the exceptions of the line 64LH which is quadratic. The label 64XX is the line including all of the data for the 64 in. long walls. The shaded region is bounded by ordinates 2e above and below the 64XX line. The symbol e denotes the standard error of estimate of the regression analysis. The curves exhibit a definite tendency to converge at lower levels of vertical compressive stress and diverge at higher vertical compressive stresses. The equation of the line 64XX is

$$v = 70.8 + 0.313a$$

where v is the maximum shear stress and a is the applied vertical compressive stress both in units of psi. The value of e is 17.4 psi and the correlation coefficient is 0.91. The vertical lines on the plot in Fig. 11 denote the range of vertical stresses for which data is actually available. The regression lines extending beyond these limits are extrapolations to show possible trends.

3.4 Diagonal Strain

The general mode of distress exhibited by the

test specimens is diagonal cracking, indicative of a diagonal tension failure. It is reasonable to expect that the diagonal tension strain should provide a reasonable predictor of the onset of wall distress. The relationships between shear stress and the diagonal wall strain computed from measured displacements are shown in Fig. 12 for all of the 64 in. long wall tests. With certain exceptions, the curves in Fig. 12 suggest the existance of a common diagonal tension strain, in the range of 100-150 microstrain, at the onset of diagonal cracking. Diagonal cracking is indicated in the relationships by the sudden large increase in diagonal tension strain (displacement) with little or no increase in load resistance. The exceptions are wall tests having high vertical compressive stresses. The commonality of the threshold diagonal strain suggest a material criterion which defines the onset of diagonal cracking independent of strength and vertical compressive stress.

4. CONCLUSIONS

The following conclusions are based on the experimental test data obtained in the investigation described in this paper.

- A nearly linear relationship existed between increased amounts of vertical compression and the resulting maximum in-plane shear resistance of the wall panels when other parameters are held constant.

- The lateral displacement coincident with the attainment of diagonal cracking was not significantly influenced by the amount of vertical compression applied to the wall panel, or the wall aspect ratio, or the material strenghts.

- Tensile strain across the wall panel diagonal was the critical determinant of diagonal cracking and there appeared to exist a threshold strain of about 150 microstrain above which diagonal cracking occurred.

- The maximum shear resistance was affected by aspect ratio and material strengths for higher levels of applied vertical compressive stress, generally being higher for larger aspect ratio and increased material strengths.

REFERENCES

1. Woodward, Kyle and Rankin, Frank, "Influence of Vertical Compressive Stress on Shear Resistance of Concrete Block Masonry Walls," Report No. NBSIR 84-2929, National Bureau of Standards Gaithersburg, MD, October 1984, 61 pp.

2. Woodward, Kyle and Rankin, Frank, "Influence of Aspect Ratio on Shear Resistance of Concrete Block Masonry Walls," Report No. NBSIR 84-2993, National Bureau of Standards, Gaithersburg, MD, January 1985, 64 pp.

3. Woodward, Kyle and Rankin, Frank, "Influence of Block and Mortar Strength on Shear Resistance of Concrete Block Masonry Walls," Report in preparation, National Bureau of Standards, Gaithersburg, MD.

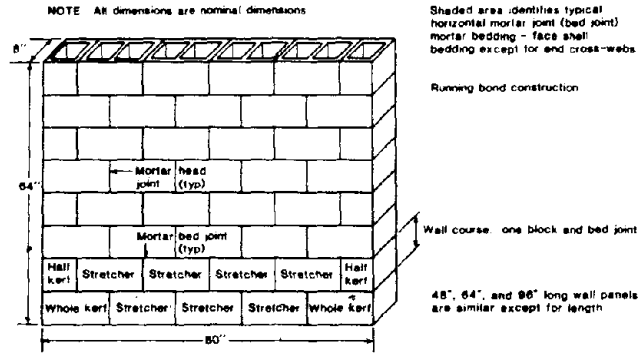

Figure 1. Typical wall panel.

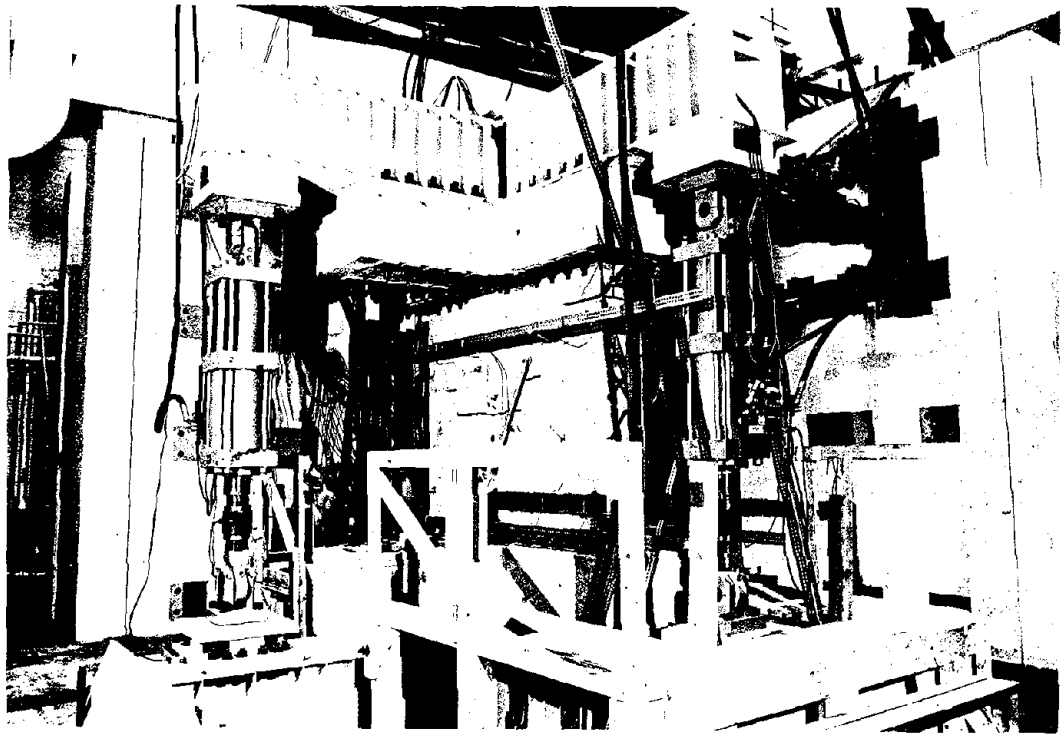

Figure 2. Test setup (NBS/TIF).

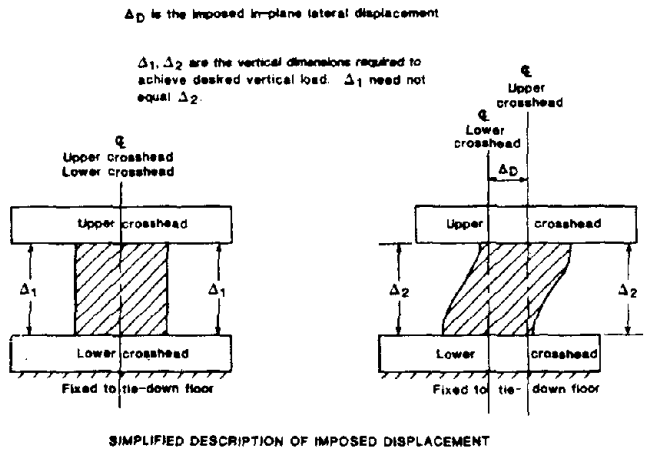

Figure 3. Test method.

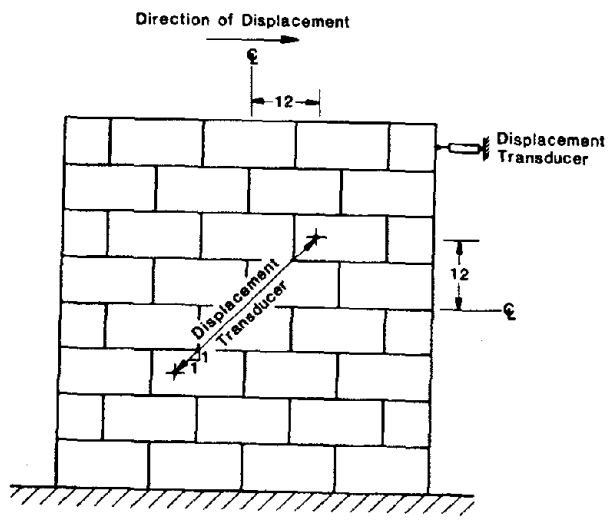

Figure 4. Instrumentation.

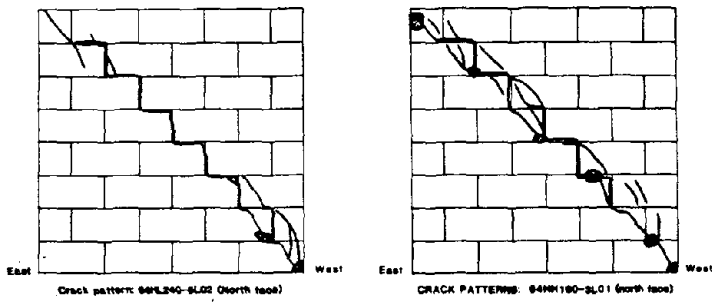

Figure 5. Typical crack patterns.

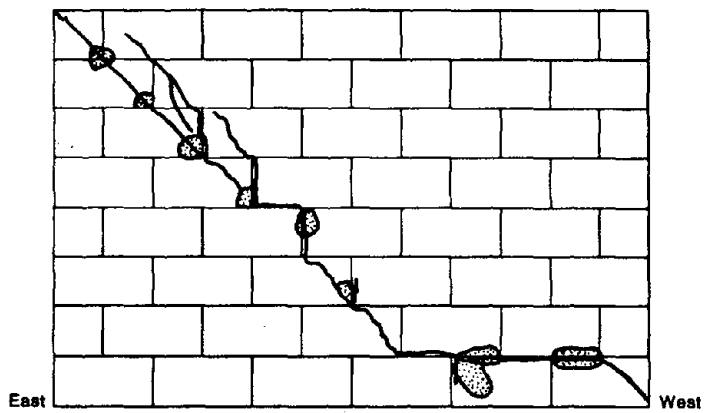

Figure 6. Crack pattern for 96 in. wall.

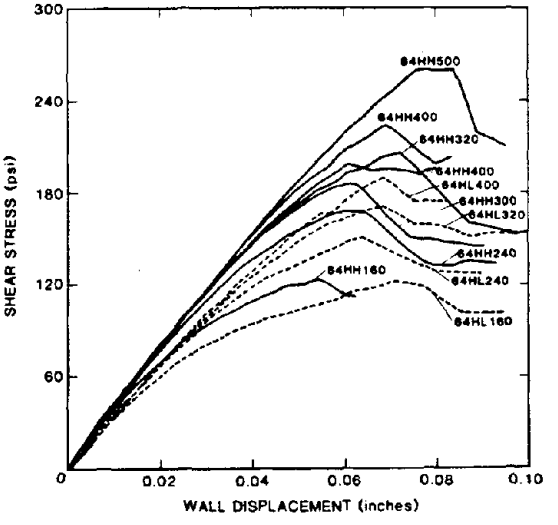

Figure 7. Effect of a block strength-mortar type combination on stress-displacement relationship.

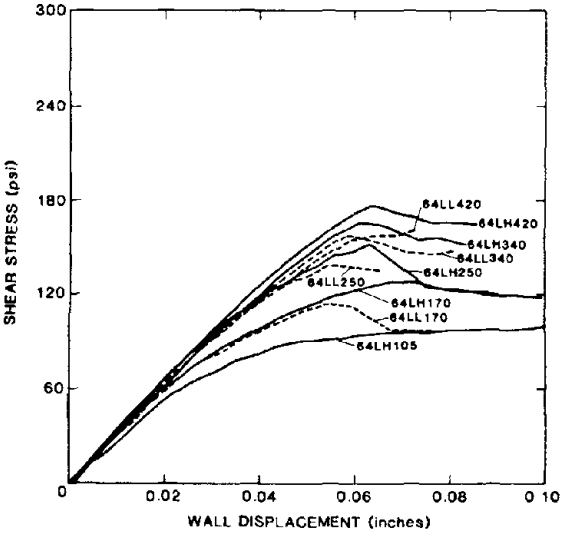

Figure 8. Effect of a block strength-mortar type combination on stress-displacement relationship.

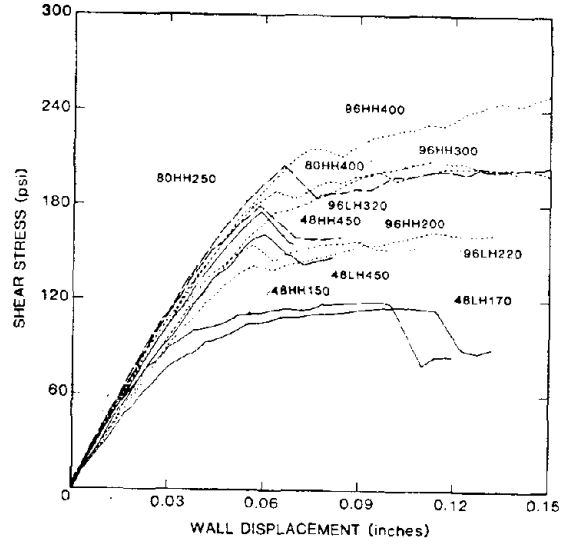

Figure 9. Effect of aspect-ratio on stress-displacement relationship.

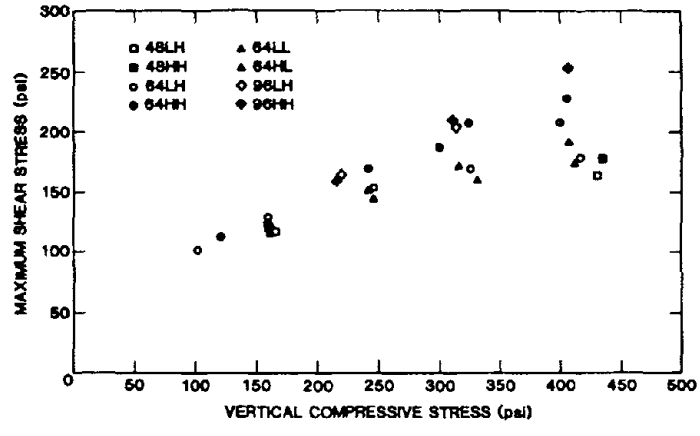

Figure 10. Maximum shear stress versus applied vertical stress.

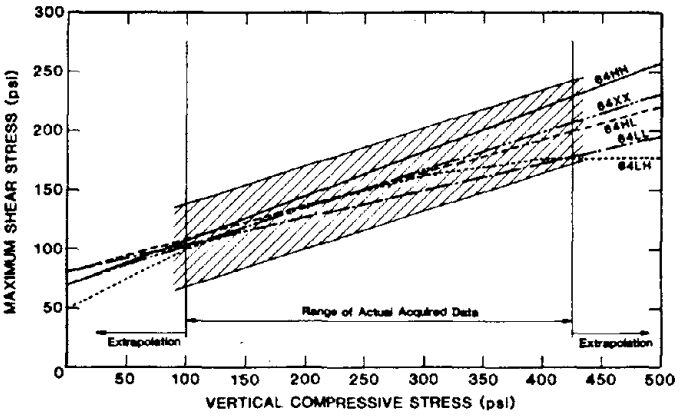

Figure 11. Regression analysis of data.

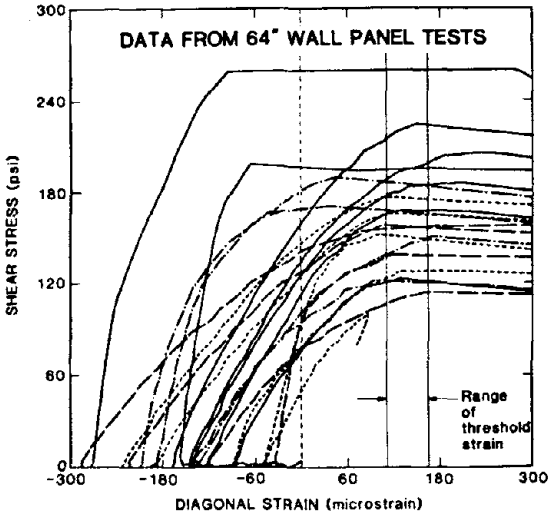

Figure 12. Stress versus diagonal wall stress.

Table 1. Wall Panel Details

Wall Panel Identifier	Mortar Cube 28 Day Compressive Strength (psi)	Prism Bedding	Prism Compressive Strength (psi)
64HH120-2L04	2437	Face Shell	1839
64HH160-3L01	1825	Face Shell	1820
64HH240-3L04	2237	Face Shell	2132
64HH300-2L05	2160	Face Shell	1870
64HH320-3L03	2095	Face Shell	2091
64HH400-3L02	2139	Full Area	2810
64HH400-2L03	2232	Face Shell	2074
64HH500-2L06	2191	Face Shell	2005
48HH150-3L06	1847	Full Area	2661
48HH450-3L05	2055	Full Area	2645
80HH250-3L07	1994	Face Shell	1867
80HH400-4L01	3254	Face Shell	2050
96HH200-4L03	3076	Face Shell	1917
96HH300-4L02	2746	Full Area	2615
96HH400-4L04	2425	Full Area	2783
64HL160-5L01	1826	Face Shell	2049
64HL240-5L02	1809	—	—
64HL320-5L03	1761	—	—
64HL400-5L04	1490	Face Shell	1923
64LL170-6L07	1987	Face Shell	1522
64LL250-6L06	1841	Full Area	1955
64LL340-6L08	1591	Full Area	1983
64LL420-6L09	1505	Face Shell	1443
64LH105-6L01	2646	Face Shell	1630
64LH170-6L02	2657	Full Area	2033
64LH250-6L03	2772	Face Shell	1522
64LH340-6L04	3127	Full Area	2133
64LH420-6L05	3110	—	—
48LH170-6L10	2985	Face Shell	1447
48LH450-6L11	2892	Full Area	2094
96LH220-6L12	2700	Face Shell	1537
96LH320-6L13	2810	Full Area	2025

Note: The mortar cube stress is based on an area of 4 sq. in. The values listed are the average of at least three cube tests. Mortar cubes are removed from the molds after 24 hours and air cured in the laboratory environment until tested.

The prism stress is based on the unit net solid area. The values listed are the average of at least three prism tests.

Table 2. Wall Panel Maximum Shear Stresses

Wall Panel Identifier	Wall Net Cross-Sectional Area (sq. in.)	Applied Vertical Compressive Stress (psi)	Maximum Shear Stress Resistance (psi)
64HH120-2L04	246.0	122	113
64HH160-3L01	246.0	162	123
64HH240-3L04	246.0	243	167
64HH300-2L05	246.0	305	186
64HH320-3L03	246.0	325	206
64HH400-3L02	246.0	406	205
64HH400-2L03	246.0	406	227
64HH500-2L06	246.0	507	260
48HH150-3L06	184.5	163	117
48HH450-3L05	184.5	434	175
80HH250-3L07	307.5	228	178
80HH400-4L01	307.5	390	202
96HH200-4L03	369.0	217	157
96HH300-4L02	369.0	312	208
96HH400-4L04	369.0	407	251
64HL160-5L01	246.0	163	122
64HL240-5L02	246.0	243	151
64HL320-5L03	246.0	316	171
64HL400-5L04	246.0	407	190
64LL170-6L07	241.6	162	115
64LL250-6L06	241.6	246	144
64LL340-6L08	241.6	332	158
64LL420-6L09	241.6	413	174
64LH105-6L01	241.6	103	101
64LH170-6L02	241.6	161	128
64LH250-6L03	241.6	248	152
64LH340-6L04	241.6	327	166
64LH420-6L05	241.6	418	177
48LH170-6L10	181.2	165	116
48LH450-6L11	181.2	430	162
96LH220-6L12	362.4	220	163
96LH320-6L13	362.4	315	203

AN EXPERIMENTAL STUDY ON SLIDING RIGID BODY IN WATER DURING EARTHQUAKE

BY

Tatsuo UWABE,* Norihiro HIGAKI** and Setsuo NODA***

ABSTRACT

Shaking table tests of model blocks were conducted to study sliding behavior of a rigid body in water during earthquakes. Accelerations and hydrodynamic pressures on the model block decreased at the onset of sliding and remained the same during sliding. Static and dynamic coefficients of friction obtained from vibration tests, with intertia/forces from added mass corresponding to hydrodynamic pressures on the model block, were almost the same values as those measured by Euler's method. A method to estimate displacements of the sliding block during earthquakes was presented. Calculated displacements based on horizontal and vertical base accelerations showed relatively good agreement to the measured values.

Keywords: Damage Deformation; Earthquakes

1. INTRODUCTION

1.1 General

Many studies for earthquake disaster prevention have been done in the Tokai area where a large earthquake is predicted to occur in the near future. This investigation of seismic stability of port and coastal facilities evaluates whether each facility will be damaged by the Tokai earthquake or not by means of the evaluation method reported by Tsuchida et al.[1] In order to take effective countermeasures for earthquake disaster prevention, it is necessary to know how each facility is damaged; that is, to know the damage deformation characteristics. One of the structures whose damage deformation values are desired to be evaluated is a gravity type structure. A principal earthquake damage to a gravity type structure is a sliding failure. Thus, it is necessary to develop the method to evaluate a permanent sliding displacement of gravity type structures.

As use of the ocean space expands, a scale of offshore structures becomes large with the increase of the walter depth at the construction site. A large composite type breakwater which consists of a rubble mound and concrete caissons is planed for construction at mouth of Kamaishi bay in 60 m water depth. During earthquakes the hydrodynamic pressures increase with the water depth. It is necessary that the width of the caisson be large to prevent it from sliding. In the design of the usual breakwater, the sliding stability of the caisson et al is not discussed because the ground motions do not occurr in one direction but turn and because the duration of the earthquake is not long. And in a foreign design standard of the offshore structures the slide and overturn stability are not analyzed. Judging from the above description it is considered that the gravity type structures may be designed without the sliding stability analysis. But in case of the important large structures it is necessary to know an allowable sliding displacement during earthquakes in the design because there are many earthquakes in Japan. A calculation method of sliding displacement during earthquakes is desired to be discussed in full detail. It is also necessary to investigate the effect of the waters on sliding gravity type

*Chief and **former member of Earthquake Disaster Prevention Laboratory, and ***Chief, Earthquake Resistant Structures Laboratory, Structures Division, Port & Harbour Research Institute

structures in the waters.

In his 1965 Rankine Lecture, Newmark 2) described simple concepts for computing the displacement of a sliding mass in an embankment subjected to earthquake accelerations. Franklin and Chang 3) reported the calculation results of Newmark method for 169 strong motion earthquake records. Richards and Elms 4) presented a new method for designing gravity retaining walls considering allowable sliding displacements. Sim and Berrill 5) studied shaking table tests of a model gravity retaining wall to verify the Richards and Elms design method. In addition to these there are a study of Makdisi and Seed 6) and a study of Nadim and Whitman 7). In Japan Fujino, Sasaki and Hakuno 8) reported the slip of a friction controlled mass on a horizontal foundation excited by earthquakes. Toki, Sato and Miura 9) reported a separation and a sliding between soils and structures during strong ground motions using a joint element.

In the studies mentioned above values of static and dynamic coefficients of friction, the relation between them were not discussed in detail, and the validity of the calculation methods for sliding displacement during earthquakes was not checked, except the study of Sim and Berrill. The sliding of gravity type structures in water during earthquakes was not analyzed in past studies. Therefore, this paper is concerned with these points. Accordingly, presented are the sliding behavior of model blocks in the water, static and dynamic coefficients of friction, and validation of the calculation method used for sliding displacement. Simple rigid body models were examined as the first step of sliding analysis for gravity type structures. Shaking table tests of rigid body models, made of mortar, on an acrylic sheet, or on an inclined mortar board, with or without water, were examined.

2. RIGID BODY MODEL DESCRIPTION

Four kinds of rigid body models were used in this study, models identified by A, B1, B2, C, and D. Models B1 and B2 are similar, but Table 1 shows the unit weight (rounded to one decimal), the dimension, the weight (the weight that includes pickups is also shown) and the kind of test. Model A is a low model to clearly illustrate the sliding behavior. Model D is also low and was used for preparatory tests to select a proper accelerometer. Model C is heavier than the others.

3. STATIC COEFFICIENT OF FRICTION TESTS

3.1 Slide Test Setup

The test setup, as shown in Fig. 1, is used to measure static coefficients of friction. A pulling load is applied by using a container of lead shot as shown on the left side of Fig. 1. A strain-gauge type load cell, whose rated capacity is 50kgf (490N), was used to measure the pulling load. An inductive-type displacement transducer, whose amplitude limit is 25mm, was used to measure displacement. The contact surface between the model and the acrylic sheet is either dry or wet. The water was put to 1 cm from the acrylic sheet surface for the wet contact surface. A full infiltration of the water between the model and the acrylic sheet was confirmed before the test. The tests of the wet surface were matched with the shaking table tests of rigid body models in the water described after.

3.2 Test Results

Table 2 shows the test results. According to Table 2, the average static coefficients of friction for the model B1 is 0.52 (a standard deviation is 0.02). As the static coefficient of friction for the model B1 with the wet surface, at an average of 4 times of tests were 0.52, it is considered that there is no change of the static coefficients of friction in surface conditions.

4. EULER'S TEST FOR STATIC AND DYNAMIC COEFFICIENT OF FRICTION

4.1 Euler's Test

The well-known Euler's test gives static and dy-

namic coefficients of friction from a sliding mass on a slope. The coefficients of friction for a mass on a slope, μ_s static and μ_d dynamic are as follows 10).

$$\mu_s = \tan \theta_s$$

$$\mu_d = \tan \theta_s - \frac{2 \cdot S}{g \cdot t_s^2 \cdot \cos \theta_s}$$

where,

θ_s: Angle of inclination to start sliding
S: Distance of sliding down (m)
t_s: Time to slide distance of S (s)
g: Acceleration of gravity

Fig. 2 shows the Euler's test setup. The inclined board was pushed up by a oil jack to make a rigid body model start sliding. Two kinds of tests, the rigid body model B2 on the acrylic sheet (No. 1) and the rigid body model B1 on the mortar board (No. 2) were examined.

The angle of inclination was obtained from measuring the sliding direction of acceleration of gravity by an accelerometer on the inclined board. The time for the rigid body model to slide certain distance was measured as follows. An instance to start sliding was detected by the displacement transducer on top of the inclined board shown in Fig. 2. The instant the model comes to the end of sliding its distance was recorded by a displacement transducer at the lower part of the inclined board shown in Fig. 2. The time to slide a distance was calculated from records of the two displacement transducers and a recorder.

4.2 Test Results

Test results are shown in Tables 3 and 4. Table 3 shows test results of Model B2 on the acrylic sheet, and Table 4 shows those of the Model B1 on the mortar board. According to Table 3, the average static coefficients of friction obtained from Euler's tests is smaller than the average value measured in Section 2. As shown in Table 4, the static coefficients of friction on the mortar board are larger than those on the acrylic sheet.

As shown in Tables 3 and 4, the dynamic coefficient of friction is smaller than the static one. A dynamic to static ratio is about 0.7 on the acrylic sheet and about 0.8 on the mortar board. The difference between dynamic and static coefficients of friction for the acrylic sheet are larger than that for the mortar board.

5. SHAKING TABLE TESTS OF SLIDING RIGID BODY MODEL IN WATER

5.1 Model and Instrument Description

Table 5 shows accelerometers used in this test. A waterproof inductive-type displacement transducer whose amplitude limit is $\pm$10mm was used to measure the sliding displacement of the rigid body model. The accelerometers and the displacement transducers were fixed by an adhesive. A strain-gauge (rated capacity of 0.5 kgf/cm^2 (49 KPa) and pressure gauges were used to measure the hydrodynamic pressure on the model. The pressure gauges were embedded in the rigid body model. Figs. 3, 4 and 5 show models and pickups. Models used for these tests were A, B2 and D. Model D was used for preparatory tests to select a proper accelerometer. The models were put on the acrylic sheet or on the mortar board fixed on the shaking table. The water depth in tests of models in the water was 25 cm.

5.2 Shaking Table and Type of Excitation

The shaking table of the Port and Harbour Research Institute, Ministry of Transport was used. A glass-sided rectangular box on the shaking table is 5m long, 1.5m wide, and 1.5m high. As a duration time of an excitation was short, and as it was considered that the distance between the model and the wall in exciting directions is long enough, a wave absorber was not placed in front of the wall in exciting directions.

Types of excitation are a periodic 10-sine-wave

and an earthquake wave. The 10-sine-wave means a periodic excitation of 10-wave with a certain frequency and a uniform amplitude. The frequency of 10-sine-wave excitation was selected from 5, 7, 10, 20 and 30 Hz. The amplitude of the 10-sine-wave was given to be strong enough to cause model sliding. The wave used for the earthquake excitation is a strong-motion earthquake record (S-1210, E-W component) obtained on the rock at Ofunato port in 1978-Miyakiken-oki earthquake. The duration time of the record was not modified, and the amplitude was scaled to cause model sliding.

5.3 Selection of Accelerometer Used in Tests

An accelerometer used in tests was selected from small and water-proof instruments with a proper rated capacity and frequency characteristics. The important point in the selection was the frequency characteristics of the accelerometer. A flat response range of the frequency was uncertain to measure the accurate acceleration waveform of sliding model. Then a preparatory test to select a proper accelerometer was conducted for the 5 kinds of accelerometers whose frequency range is different as shown in Table 5.

The accelerations of 5 kinds of accelerometers on the model D shown in Fig. 3 were compared by a periodic excitation test. Fig. 6 shows a test result. Solid lines shown in Fig. 6 are the waveforms of a accelerometer A3 whose upper limit of a frequency range is highest; dotted lines are those of other accelerometers. According to Fig. 6 waveforms of accelerometer A2 and A5 are different from that of the accelerometer A3, and waveforms of accelerometer A1 and A5 are similar to that of A3.

As mentioned above there was no difference in the acceleration waveform of the accelerometer whose upper limit of frequency range is more than 150Hz. Therefore, it was decided that the accelerometer A1 whose frequency range is from 0 to 150Hz was used for this study. The accelerometers shown in Figs. 4 and 5 are all A1. As the rate of error is probably high in small acelerations measured by this accelerometer whose rated capacity is $\pm$ 10 G (9800 Gal.), attention was given measuring small accelerations.

6. RESULTS OF SHAKING TABLE TESTS

6.1 Slide of Rigid Body Model During Vibration

Fig. 7 shows test results of model A on the acrylic sheet by 10-sine-wave excitation with a frequency of 10Hz. Horizontal accelerations at each measuring point, displacement and vertical accelerations are shown in order in Fig. 7. According to the acceleration waveforms of model A an amplitude of model accelerations decreased instantaneously at the moment to cause a sliding displacement and remained the same level during sliding. The reason why accelerations of the model decrease is a change of coefficient of friction from static to dynamic. A complete discussion is described below. A high frequency component of about 100Hz was observed in vertical acceleration shown in Fig. 7. It was observed that vertical accelerations show a tendency of an increase in the amplitude with an increase of the frequency of input sine waves. Though the acceleration waveforms of models on set of the first sliding are mentioned above, the acceleration waveforms on set of the second sliding was not the same as the first one.

Fig. 8 shows the test results of model B2 in the water on the acrylic sheet by 10-sine-wave excitation with a frequency of 5Hz. In Fig. 8 hydrodynamic pressures on the rigid body model are also shown. These waveforms show the same tendency in waveforms of horizontal accelerations.

6.2 Hydrodynamic Pressure on Rigid Body Model

Waveforms of hydrodynamic pressures on the rigid body model are shown in Fig. 8. Fig. 9 shows the maximum amplitude of hydrodynamic pressures in right half and maximum accelerations in left half versus the water depth. The dotted line shows the calculated values of Westergaard's formula

with a seismic coefficient that is equal to a ratio of the maximum acceleration at the middle height (AH4) to acceleration of gravity. This calculated value is similar to the observed values. Though it is considered that the wall in exciting directions have an effect on the observed hydrodynamic pressures, this effect seems to be small because of the long distance between wall and the model that is nine times longer than the water depth.

The amplitude of hydrodynamic pressures decreased instantaneously at the moment of sliding and remained at the same level during sliding as did the accelerations. Then hydrodynamic pressures on set of sliding were compared with those during sliding. Fig. 10 shows ratios of hydrodynamic pressures during sliding to those at the instant of sliding. According to Fig. 10 the decreasing rates are from 20 to 30% and are almost the same at each height.

6.3 Coefficient of Friction Obtained from Shaking Table Tests

A concept of static and dynamic coefficients of friction for a rigid body model during vibration is described at first before discussions of coefficients of friction obtained from shaking table tests. Fig. 11 shows a slide of a rigid body subjected by a periodic loading without a vertical motion. As shown in Fig. 11 the rigid body starts sliding by an inertia force that is equal to a static friction force, and continues sliding under a dynamic friction force that is smaller than static one until a relative velocity becomes zero. Though it was considered that coefficients of friction decrease continuously from static to dynamic values with increase of a relative velocity and approach a certain value (10), it is accumed in this report that the coefficients of friction decrease discontinuously from static to dynamic value and remain dynamic values during sliding. As described before the model accelerations decreased instantaneously at the moment to cause a sliding displacement and remained at the same levels during sliding. As described before the model acceleration decreased instantaneously at the moment to cause a sliding displacement and remained at the same levels during sliding. Therefore the above assumption is likely valid to calculate a sliding displacement. The calculation method of a sliding displacement is discussed in the next section.

Coefficients of friction based on the above assumption were obtained from shaking table tests. The test results of model A which shows a sliding behavior clearly were first discussed. As shown in Fig. 7 the amplitude of model accelerations reached a maximum at the moment to cause a sliding displacement, and it was considered that the model started sliding at this instant. Then the static coefficients of friction were calculated from the maximum horizontal accelerations and the vertical accelerations. The horizontal accelerations of the model remained at almost the same levels after sliding started. It is assumed that dynamic coefficients of friction hold constant during sliding; the dynamic coefficient of friction were calculated from the average of horizontal accelerations during sliding. This dynamic coefficient of friction is called the "average dynamic coefficients of friction" in this report. Fig. 12 shows static and average dynamic coefficient of friction of a model on the acrylic sheet or on the mortar board. According to Fig. 12 the ratio of dynamic to static coefficient of friction is about 70% on the acrylic sheet and about 90% on the mortar board.

Secondly, test results of the model B2 with the water depth of 25 cm and without the water described. In calculations of coefficients of friction of a model the added mass of which inertia force corresponds to twice the hydrodynamic pressure on a side wall of the model was considered. As the acceleration of the model top was about 20% larger than that of the model bottom in some cases the average of accelerations at each level were used to calculate coefficients of friction. The

method to calculate static and dynamic coefficient of friction for model B2 is similar to that of model A. In calculations of dynamic coefficient of friction with the water the reduced hydrodynamic pressures during sliding were used.

Fig. 13 shows static coefficients of friction for model B2 with and without the water versus input maximum accelerations. Static coefficients of friction for model B2 with the water are a little smaller than those without the water. It was guessed that one reason to cause this difference was the characteristics of the pressure gauge and the accelerometer (an accelerometer whose rated capacity is ±10G (9800 Gal) was used in case of small input accelerations from restriction of the frequency characteristics). Both coefficients of friction obtained from slide tests in Section 3 and Euler's tests shown in Fig. 13 are likely the same as those without the water. In view of the results described, it was concluded that the sliding behavior of a rigid body in the water was able to be discussed in consideration of the added mass that is twice the hydrodynamic pressures on a side wall of a rigid body divided by acceleration of gravity.

Fig. 14 shows static and dynamic coefficient of friction obtained from shaking table tests. In Fig. 14 the results of Euler's tests are also shown. The ratios of dynamic to static coefficient of friction for Euler's tests were slightly small compared with those of shaking table tests.

7. DISPLACEMENT COMPUTING METHOD OF SLIDING RIGID BODY DURING EARTHQUAKES

7.1 Concepts for Displacement Computing Method of Sliding Rigid Body

In this report the displacement of a sliding rigid body during earthquakes was computed from the concepts shown in Fig. 11. In Fig. 11 A(t) is the input acceleration, μ_s and μ_d are the static and dynamic coefficient of friction and g is acceleration of gravity. A rigid body starts sliding when the input acceleration A(t) is equal to $\mu_s \cdot g$. As the acceleration of the rigid body becomes $\mu_d \cdot g$ during sliding, the difference between the input acceleration and the rigid body acceleration results. It was assumed that the coefficients of friction decrease discontinuously from static to dynamic value and remains a dynamic value during sliding. As the input acceleration decreases and turns to another direction during sliding, the rigid body does not continue sliding to one direction but moves in one united foundation when the relative velocity is equal to zero. This difference of accelerations between the foundation and the rigid body during sliding gives a relative permanent displacement. The permanent displacement is obtained from the integral of the relative velocity that is the integral of the difference of accelerations between the foundation and the rigid body during sliding. In this report the sliding displacement of the rigid body were calculated by this method.

In this case without the vertical motion shown in Fig. 11 the rigid body returns to the initial place after one period of sine excitation. But the rigid body does not always return to the initial place with a certain vertical motion. As the permanent residual displacement to one side was observed in some cases of shaking table tests, the effect of a vertical acceleration should be considered. Therefore the vertical accelerations were also used for the displacement computation of the sliding rigid body in this report.

7.2 Comparison of Observed and Calculated Results

The relative displacements of a sliding rigid body were calculated under the following.

i) The input motions are horizontal and vertical accelerations (AH1, AV1).
ii) Coefficients of friction obtained in Chapter 6 were used.
iii) The first sliding of 10-sine-wave excitation was discussed.
iv) The effect of the water on a sliding

rigid body was evaluated by the added mass that is twice the hydrodynamic pressures on a side wall of a rigid body divided by acceleration of gravity.

Table 6 shows the computed results. The time histories of computed and observed sliding displacement are shown in Fig. 15 for the model B2 on the acrylic sheet and in Fig. 16 for the model A on the acrylic sheet.

Though there were two computed displacements which were 3 and 0.5 times respectively than observed ones, other computed displacements were almost the same as observed displacements. Therefore it was concluded that the displacement computing method presented here was valid for the the sliding rigid body that does not show a large response. The displacement computing method of a sliding rigid body that shows large response will be discussed in the future.

Coefficient of friction used in the calculations were estimated from shaking table tests. It is troublesome that shaking table tests are always conducted to obtain coefficient of friction. Then Euler's test is useful to obtain coefficients of friction.

8. CONCLUSION

Shaking table tests of rigid body models and computed displacement of a sliding rigid body report were discussed. Results, conclusions follow:

(1) According to the shaking table tests, the amplitude of acceleration decreases instantaneously at the start of displacement and remains at the same level during sliding (see Fig. 7). Therefore it may be assumed that the coefficient of friction charges from the static to the dynamic value and remains a dynamic value during sliding.

(2) Static and dynamic coefficients of friction based on the above assumption were obtained from the acceleration waveforms of a rigid body model. Both values are nearly the same as those of Euler's tests (see Fig. 14).

(3) Coefficients of friction obtained in consideration of the added mass that is twice the hydrodynamic pressure on a side wall of a rigid body divided by accleration of gravity were nearly the same as those of a rigid body model without the water (see Fig. 13). Therefore, it may be concluded that the added mass that is twice the hydrodynamic pressure on a side wall of a rigid body divided by acceleration of gravity can be used to calculate the sliding displacement of a rigid body during earthquakes.

(4) The hydrodynamic pressure on the rigid body model decreased instantaneously at the moment of displacement and remained at the same level during sliding (see Fig. 8). The waveform of the hydrodynamic pressure was similar to that of acceleration.

(5) The displacement computing method considerating paragraphs (1) to (4) revealed the same observed results. Therefore it is concluded that this displacement computing method of a sliding rigid body that does not show a large response is valid (see Table 6, Fig. 15 and Fig. 16).

9. ACKNOWLEDGEMENT

The authors wish to thank Dr. Hajime Tsuchida, Director of Structures Division, Port and Harbour Research Institute, Ministry of Transport for many helpful discussions.

10. REFERENCES

1) Tsuchida, H., Inatomi, T., Noda, S., Uwabe, T., Yagyu, T. and Murata, T.: Method of evaluation for Seismic Stability of Port and Coastal Facilities, Technical Note of the Port and Harbour Research Institute, No. 336, June 1980

2) Newmark, N.M.: Effects of Earthquakes on Dams and Embankments, Geotechnique, Vol. 15, No. 2, Jan. 1965

3) Franklin, A.G. and Chang, F.K.: Permanent Displacements of Earth Embankments by Newmark Sliding Block Analysis, Miscellaneous Paper S-71-17, U.S. Army Engineer Waterways Experiment Station, Nov. 1977

4) Richard, R., Jr. and Elms, D.G.: Seismic Behavior of Gravity Retaining Walls, Proc. of ASCE, Vol. 105, No. GT4, pp. 449-464, Apr. 1979

5) Sim, L.C. and Berrill, J.B.: Shaking Table Tests on A Model Retaining Wall, Proc. S. Pacific Reg. Conf. Earthquake Engineering, Wellington, May 1979

6) Madkisi, F.I. and Seed, H.B. Simplified Produre for Estimating Dam and Embankment Earthquake-induced Deformations, Proc. of ASCE, Vol. 104, No. GT7, pp. 849-867, July 1978

7) Nadim, F. and Whitman, R.V.: Seismically Induced Movement of Retaining Walls, Proc. of ASCE, Vol. 109, No. GT7, July 1983

8) Fujino, Y., Sasaki, Y. and Hakuno, M.: Slip of a Friction-controlled Mass Excited by Earthquake Motions, Bull. Earthq. Res. Inst., Vol. 53, 1978

9) Toki, K., Sato, T. and Miura, F.: Separation and Sliding Between Soil and Structure During Strong Ground Motion, Proc. of JSCE, No. 302, 1980

10) Soda, N.: Friction Story, Iwanami Shinsho, 1980

Table 1 Rigid body model

Model	Unit weight (gf/cm^3)	HeightxWidth xLength (cm)	Weight(kgf)		Kind of test		
			No pickups	Include pickups	Tensile test	Euler's test	Sliding test
A	1.6	5 x 23 x 30	5.5	5.9			o
B1	1.6	28 x 23 x 30	30.7	31.9	o	o	
B2	1.6	28 x 23 x 30	31.3	32.5		o	o
C	2.1	28 x 23 x 30	40.4	41.6	o		
D	2.1	10 x 23 x 30	14.3	14.9			o

Table 2 Results of slide test

Model	Test No.	Static coef. of friction		
		Observed Value	Average	Standard Deviation
B1	1	0.47	0.52	0.03
	2	0.50		
	3	0.49		
	4	0.50		
	5	0.53		
	6	0.53		
	7	0.54		
	8	0.55		
	9	0.54		
C	1	0.62	0.63	0.02
	2	0.63		
	3	0.63		
	4	0.59		
	5	0.64		
	6	0.65		
	7	0.64		
	8	0.62		
	9	0.61		
	10	0.67		

Table 3 Results of Euler's test (No.1)

Model B2 on acrylic sheet, Sliding distance 150 cm

No.	Angle of sliding board (Degree)	Time elapsed (s)	Velocity (m/s)	Coef. of friction	
				Static	Dynamic
1	29.0	1.57	0.96	0.55	0.41
2	29.9	1.43	1.05	0.58	0.40
3	29.6	1.62	0.93	0.57	0.44
4	30.1	1.31	1.15	0.58	0.37
5	29.6	1.48	1.01	0.57	0.41
6	27.8	2.20	0.68	0.53	0.46
7	33.1	1.17	1.28	0.65	0.39
8	29.8	1.48	1.01	0.57	0.41
9	29.9	1.51	0.99	0.58	0.42
10	29.9	1.47	1.02	0.58	0.41
11	29.8	1.49	1.01	0.57	0.41
12	30.9	1.35	1.11	0.60	0.40
13	31.0	1.44	1.04	0.60	0.43
			Average	0.58	0.41
			Standard deviation	0.03	0.02

Table 4 Results of Euler's test (No.2)

Model B1 on mortar board, Sliding distance 146 cm

No.	Angle of sliding board (Degree)	Time elapsed (s)	Velocity (m/s)	Coef. of friction Static	Coef. of friction Dynamic
1	36.9	1.50	0.97	0.75	0.58
2	32.2	1.71	0.85	0.63	0.51
3	32.8	2.01	0.73	0.65	0.56
4	35.6	1.47	0.99	0.71	0.54
5	29.8	1.84	0.79	0.57	0.47
6	32.9	1.42	1.03	0.66	0.47
			Average	0.66	0.52
			Standard deviation	0.06	0.04

Table 5 Accelerometer

Symbol	Type	Amplitude limit	Size(mm)	Weight (gf)	Frequency range(Hz)	
A1	Strain-gauge	±10G	18x18x24	40	0-150	Water-proof
A2	Semi-conductor element	± 5G	3.7x3.7x9	2	0- 80	
A3	Servo	± 2G	46x46x109	530	0-370	
A4	Strain-gauge	±10G	16x16x16	17	0-350	
A5	Strain-gauge	±10G	18x18x24	40	0- 60	Water-proof

Table 6 Calculated and observed relative displacement

Case	No.	Model	Water depth (cm)	Input wave	Input max. acc. (Gal)	Coef. of friction for calculation Static	Coef. of friction for calculation Dynamic	Relative displacement(mm) Observed D1	Observed D2	Calculated
1	9	A*	0	Sine wave 10 Hz	842	0.73	0.55		0.22	0.73
1	12	〃	〃	Sine wave 20 Hz	740	0.76	0.55	0.05	0.07	0.08
1	22	〃	〃	Earthq. wave	682	0.59	0.52	0.26	0.26	0.29
5	8	〃	〃	Sine wave 7 Hz	690	0.68	0.53	0.40	0.41	0.26
5	4	〃	〃	Sine wave 10 Hz	726	0.69	0.57	0.18	0.27	0.30
3	34	B2	〃	Sine wave 5 Hz	573	0.57	0.49	0.46	0.45	0.36
4	6	〃	25	Sine wave 5 Hz	130	0.45	0.34	0.15	0.15	0.08
6	3	A**	0	Sine wave 10 Hz	631	0.65	0.61	0.04	0.03	0.02
6	12	〃	〃	Sine wave 20 Hz	650	0.61	0.56	0.02	0.01	0.02

A*,B2 : on acrylic sheet, A**: on mortar board

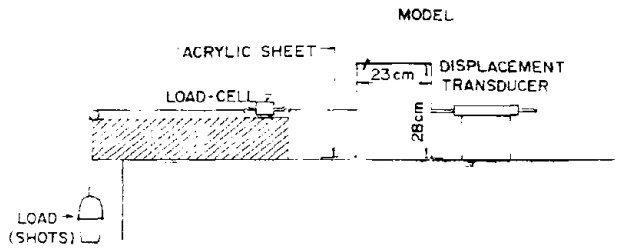

Fig.1 Slide test setup

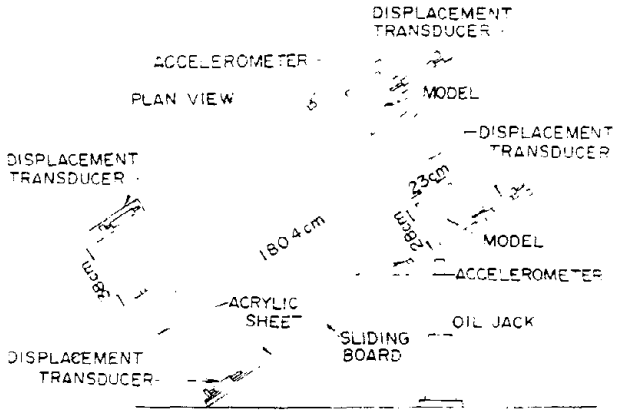

Fig.2 Euler's test setup

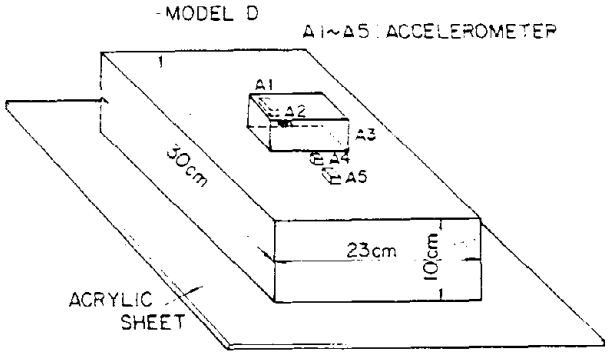

Fig.3 Model D and pickups

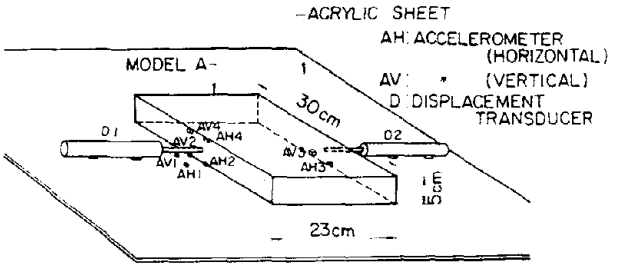

Fig.4 Model A and pickups

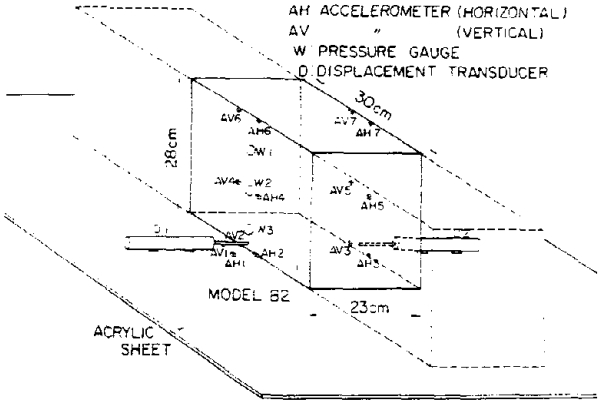

Fig.5 Model B2 and pickups

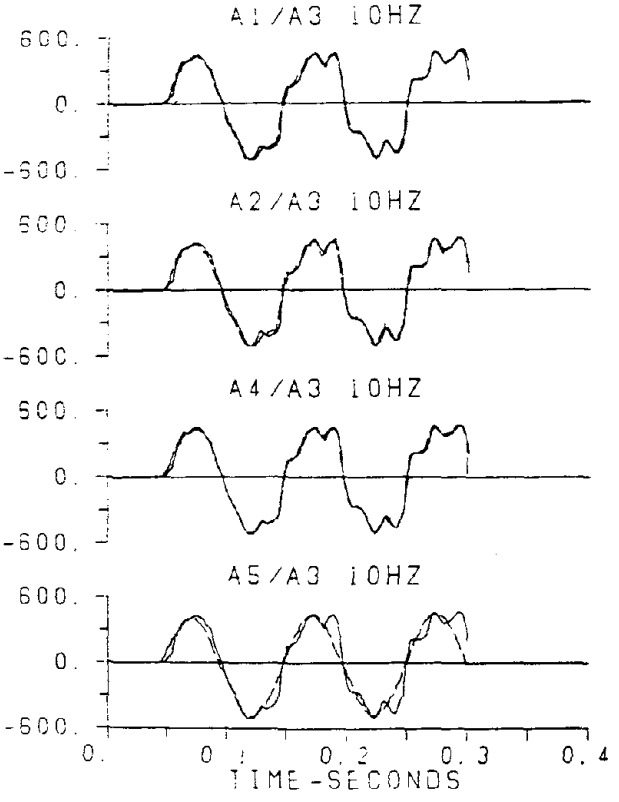

Fig.6 Observed waveforms of accelerometers

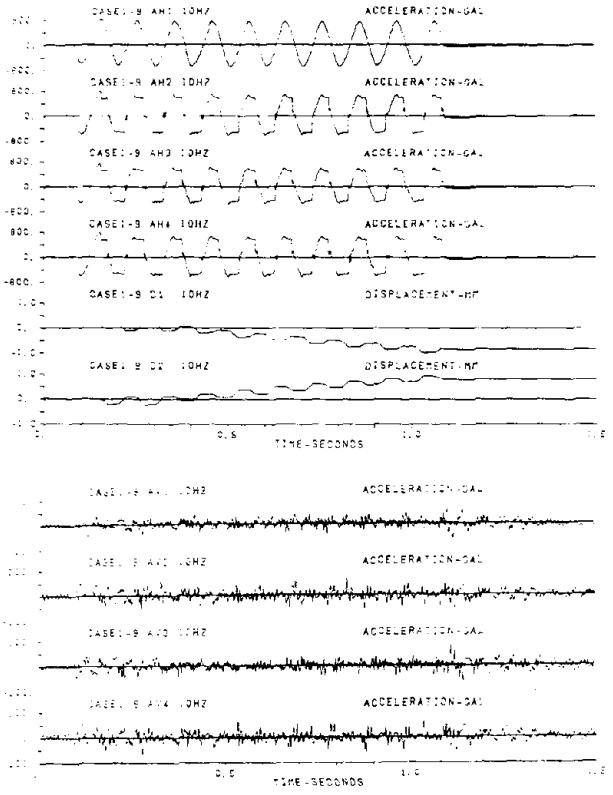

Fig.7 Results of sliding test (Model A)

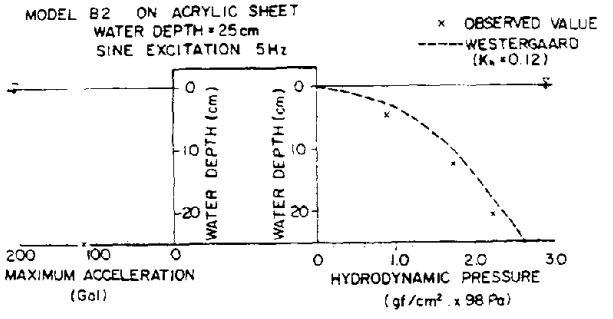

Fig.9 Hydrodynamic pressures on model B2

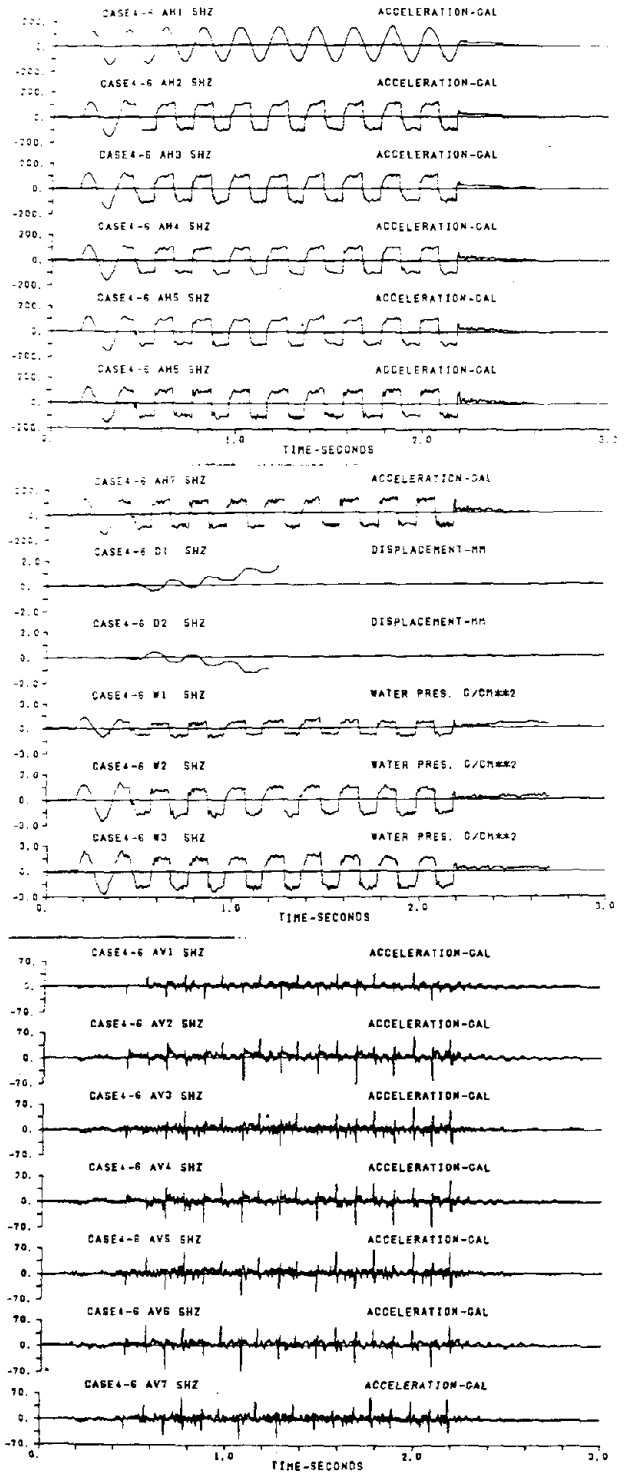

Fig.8 Results of sliding test (Model B2)

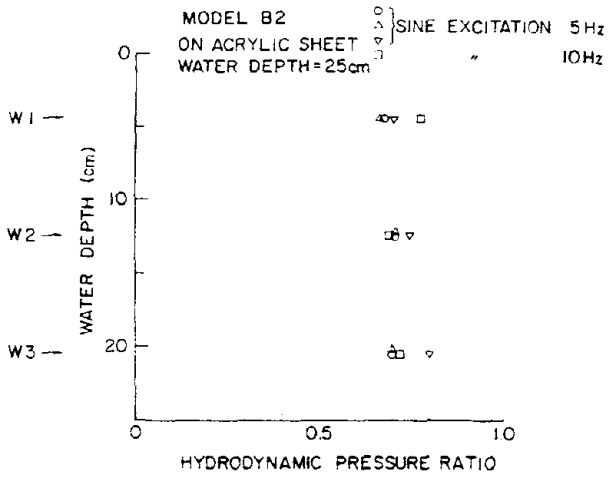

Fig.10 Ratio of hydrodynamic pressure after sliding to that before sliding

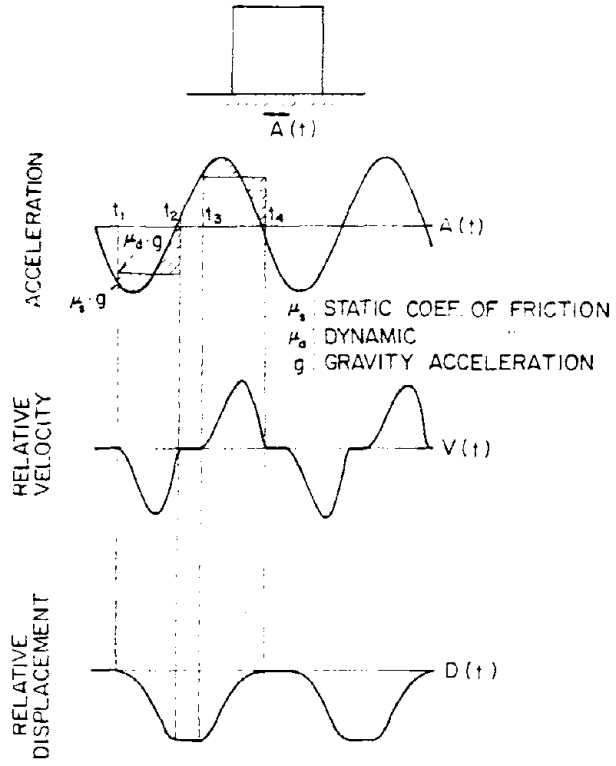

Fig.11 Sliding block under horizontal sine excitation

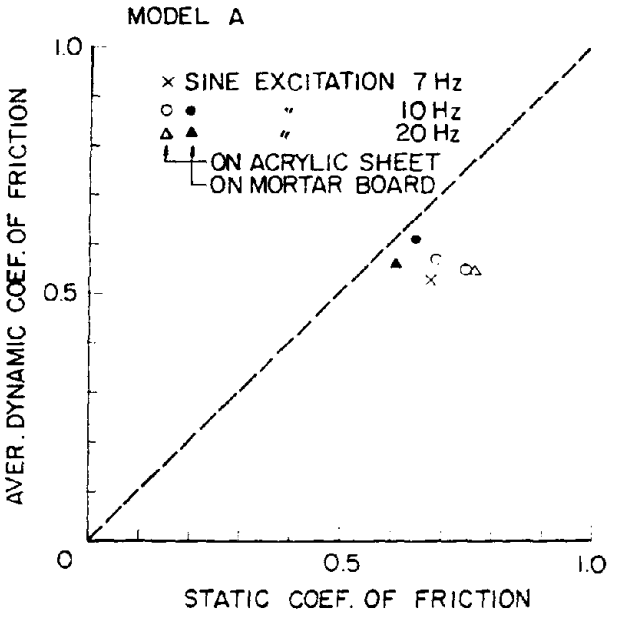

Fig.12 Static and dynamic coef. of friction
(Model A)

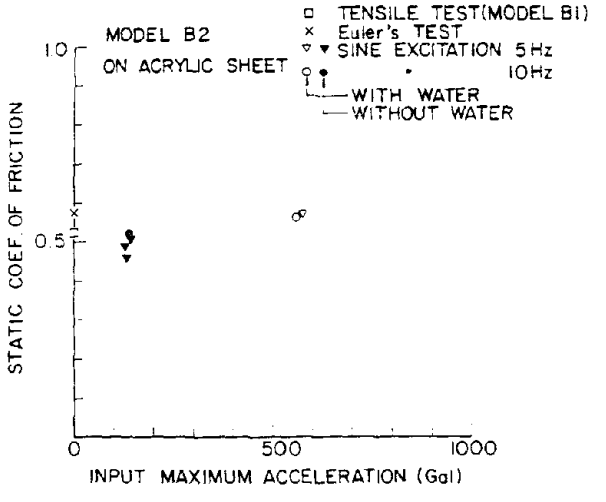

Fig.13 Static coef. of friction
(Model B2 with and without water)

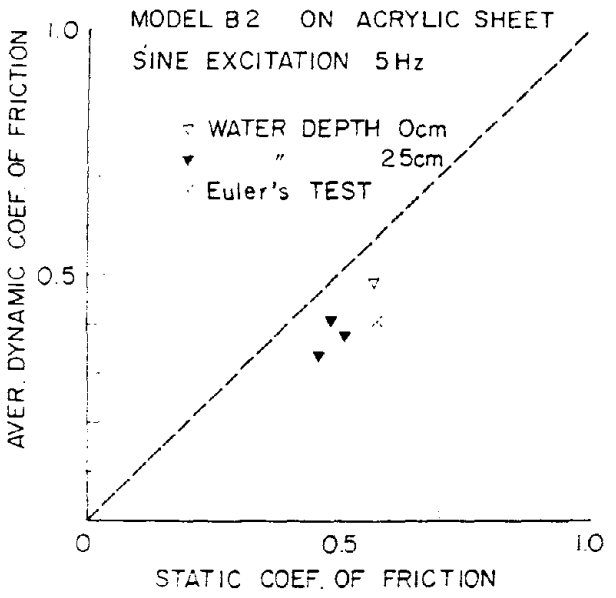

Fig.14 Static and dynamic coef. of friction (Model B2)

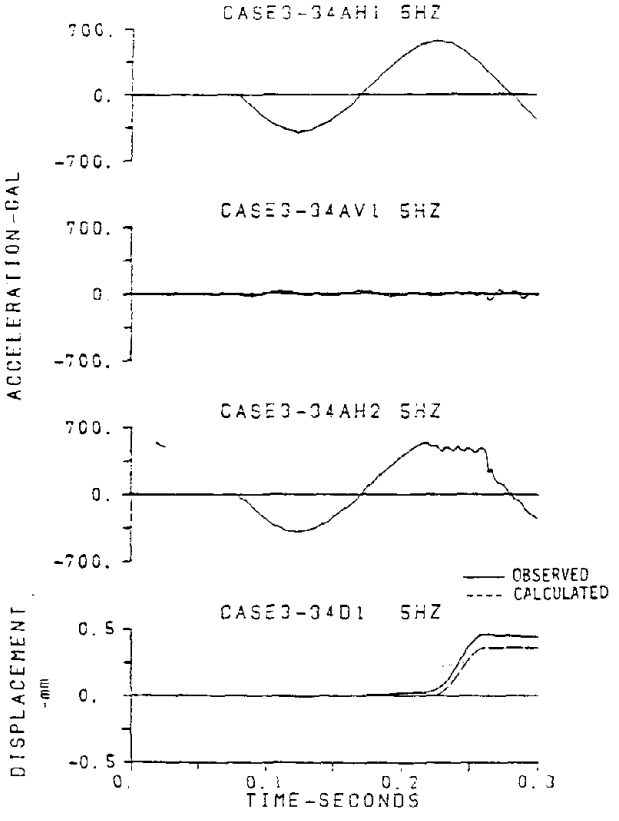

Fig.15 Calculated and observed relative displacement (Model B2)

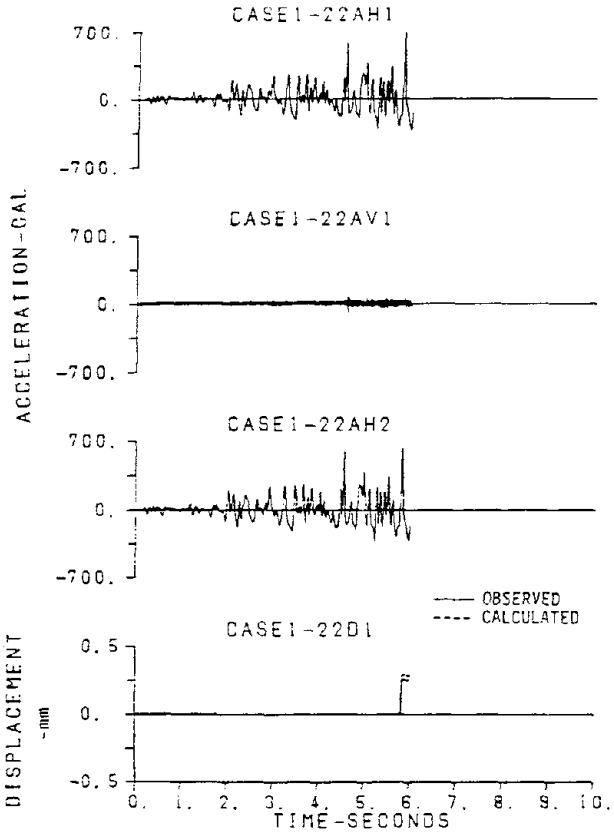

Fig.16 Calculated and observed relative displacement (Model A)

A RAPID SEISMIC ANALYSIS PROCEDURE FOR ANCHORED SHEET PILE BULKHEADS

BY

T. K. Lew*

ABSTRACT

Typical failures modes of steel sheet pile bulkheads in past major earthquakes are presented to provide insight into the failure mechanisms involved. Because they have a significant influence on the response of the bulkhead, the lateral active and passive earth pressures and residual water pressure acting on the bulkhead under earthquake conditions are given. Soil considered include cohesionless soils, soils with cohesion and angle of internal friction such as silty sand, and cohesive soil such as clay and silt. A rapid seismic analysis procedure is presented for anchored steel sheet pile bulkheads. In the procedure, the adequacy of the depth of penetration of the sheet piles, the sheet pile section in bending, tie rod section and connections, tie rod anchorage are evaluated. Concepts for strengthening inadequate bulkheads are given. In addition, guidelines are given for the seismic analysis of steel sheet pile bulkheads with relieving platform.

Keywords: Seismic analysis, Bulkheads, Earth pressure, Failure modes, Tie rod anchorage, Cohesive soil, Cohesionless soil

1. INTRODUCTION

The Navy's port and harbor facilities play an important role in the U.S. military system. Cargoes of military material and personnel are loaded, unloaded, shipped, and stored at such facilities. In addition, these facilities provide berthing for the repair and maintenance of the Navy's ships that support this function. The interruption of this vital function could reduce the effectiveness of the U.S. military in responding to the nation's interest around the world.

Many of the Navy's port and harbor facilities are located in regions with relatively high seismicity. Experience from past major earthquakes indicates that these facilities are susceptible to severe damage from earthquake ground motions at the site. Although damage to port and harbor facilities generally does not involve the risk of many human lives, such damage can definitely interrupt the ability or reduce the effectiveness of a Naval activity on performing its intended function. In past major earthquakes, damage to port and harbor facilities includes [1, 2]:

- Settlement of filled land
- Settlement or collapse of breakwaters
- Sliding, tilting, or collapse of quaywalls
- Tilting, bulging at the face of the revetment, sliding, and collapse of sheet pile bulkheads
- Buckling of pier piles
- Collapse of pier sheds

Many of the older Navy port and harbor structures located in relatively high seismicity regions were designed and constructed with little or no seismic provisions as was common with the prevalent engineering practice during their design. Consequently, many of these older waterfront facilities may be susceptible to damage from major earthquake motions at the site. There is a need for relatively rapid analysis procedures to evaluate the Navy's existing waterfront structures. Those structures found to be inadequate are then analyzed in detail to determine the degree of strengthening required.

As a part of an ongoing investigation of the earthquake safety of Naval facilities, the Naval Civil Engineering Laboratory (NCEL) has developed a rapid seismic analysis procedure for gravity quaywalls [3].

This investigation was authorized by the Naval Facilities Engineering Command (NAVFAC) under Project Order N0002584WR1052W of 19 Oct 1983.

1.1 Objective

The primary objective of this investigation is to develop a relatively rapid seismic analysis procedure for anchored steel sheet pile bulkheads. The secondary objective is to provide concepts for strengthening those bulkheads found to be seismically inadequate.

*Naval Civil Engineering Laboratory, Port Hueneme, CA 93043

1.2 Approach

Typical failure modes of steel sheet pile bulkheads in past major earthquakes are presented to provide insight into the failure mechanisms involved. Because they have a significant influence on the response of the bulkhead, the lateral active and passive earth pressures and residual water pressure acting on the bulkhead under earthquake conditions are given. Soils considered include cohesionless soils, soils with cohesion and angle of internal friction ϕ such as silty sand, and cohesive soils such as clay and silt. Earth pressure coefficients for cohesionless soils are obtained from the Mononobe-Okabe [4,5] equations. A procedure is presented for the rapid seismic analysis of anchored steel sheet pile bulkheads. In the procedure, the adequacy of the depth of penetration of the sheet piles, the sheet pile section in bending, tie rod section and connections, and tie rod anchorage are evaluated. The earthquake stability of the bulkhead as a gravity wall is evaluated. Where appropriate, stability against circular slip is examined. Finally, concepts for strengthening bulkheads that are found to be seismically inadequate are presented.

1.3 Scope

The analysis procedure presented is for steel sheet pile bulkheads embedded in medium to dense cohesionless, c-ϕ, and stiff cohesive soils. For relatively stiff sheet piles, such as those fabricated from precast concrete, the analysis procedure presented is not valid and the free-earth support method [6] with moment reduction using Rowe's curves [7] is recommended. However, the procedure presented for computing the active and passive earth pressures and residual water pressure is valid. Furthermore, the procedure implicitly assumes that the cohesionless soil encountered does not lose more than 15% of its static strength under earthquake ground shaking and large pore pressure buildup is not a problem, i.e., soil liquefaction is not a problem. The surface of the ground adjacent to the bulkhead is assumed to be horizontal, which is commonly the case.

2. TYPICAL FAILURE MODES IN PAST EARTHQUAKES

In this section, the typical failure modes of sheet pile bulkheads and their causes under ordinary loading conditions are presented. Then, typical failure modes of sheet pile bulkheads in past major Japanese earthquakes and their probable causes are given to provide insight into the mechanisms involved.

Before discussing the typical failure modes of sheet pile bulkheads under ordinary loading conditions, it is instructive to examine the behavior of anchored bulkheads under load. The bulkhead sheet piling is loaded horizontally on the backface by the active earth pressure and the residual water pressure. The sheet piling acts as a beam supported by the tie rod near the top and by the soil below the dredge line in front. Both of these supp rts are not rigid and move and deform under load. The bottom support of the sheet piling is derived from the passive pressure developed in the soil*.

Rotation about the base of a rigid retaining wall from the at-rest condition is required to develop active and passive pressures in a cohesionless soil. The active (minimum) earth pressure is developed by rotating the wall away from the soil. By contrast, passive (maximum) earth pressure is developed by rotating the wall into the soil. For a given cohesionless soil, the rotation required to develop the active pressure is smaller than that required to develop the passive earth pressure. This relationship holds even if a safety factor (SF) of 2.0 is used for the passive earth pressure (resistance). For example, using the experimental results given in Figure 1 of Reference 8, the following wall rotations are tabulated:

Condition	Wall Rotation (rad)	
	Dense Sand	Loose Sand
Active	0.0005	0.002
Passive (SF = 2.0)	0.012	0.007

*For clarity, the contribution of the horizontal bearing capacity of the soil is neglected.

The wall rotations for the passive case above correspond to the maximum pressure divided by a safety factor of 2. Thus, the rotation of the bulkhead head about the toe in dense sand required to develop the passive resistance is 24 times that required to develop the active pressure. The corresponding rotation required to develop the passive resistance in loose sand is 3.5 times that required to develop the active pressure.

Generally, a rotation about the toe of the sheet piling of the order of 1 degree (0.01 rad) can be expected for bulkheads in loose or dense sand even under ordinary loading conditions.

By contrast, the lateral displacement at the top of the bulkhead is controlled by the lateral stiffness of the tie rod anchorage system, i.e., the axial stiffness of the tie rod, the axial and/or bending stiffness of the anchor, and the stiffnesses of the soil supporting the tie rod anchorage. The stiffnesses of the tie rod and anchor are determined by the design stresses of the materials used. Although they do contribute to the overall stiffness of the tie rod anchorage system, their effect on the overall stiffness of the system is relatively small. The lateral stiffness of the tie rod anchor system is controlled primarily by the stiffness of the soil supporting the anchor. In the case of concrete wall or vertical pile or sheet pile anchors, the anchorage system stiffness is controlled by the compressibility of the soil in front of the anchor. For the A-frame pile anchor, the lateral stiffness of the anchor system is controlled primarily by the shear stiffness of the soil along its contact surfaces with the piles and the compressibility of the soil at the tip of the compression pile.

The combined active earth pressure and residual water pressure distribution on the inside face of the bulkhead is generally trapezoidal in shape with the pressure increasing toward the bottom of the sheet piling. Based on the principles of static equilibrium, the percentage of the horizontal load supported by the tie rod is smaller than that supported by the soil in front of the bulkhead below the dredge line. As mentioned earlier, both the top and bottom supports of the sheet piling are not rigid. The tie rod support moves outward due to the removal of tie rod sag, the stretching of the tie rod, and movement of the tie rod anchor required to develop resistance under load. The anchorage moves due to the deformation of the supporting soil. The tie rod/anchorage system is generally not stiff enough to prevent the sheet piling from moving outward at that level. The soil below the dredgeline in front of the bulkhead also deforms to develop the needed resistance under load.

In the great majority of cases the failure modes of sheet pile bulkheads under ordinary loading conditions [6, 9] are:

- Excessive tilting of the bulkhead
- Lateral translation of the bulkhead and fill as a whole

Essentially all the bulkhead failures under ordinary loading conditions are due to one or two causes [6]:

- The designer has estimated the earth pressure and earth resistance on the basis of the "angle of repose" concept, and
- he has failed to notice the source of weakness in the ground below the toe of the sheet piles.

Except for loose dust-dry sand, there is no relationship between the angle of repose and the angle of internal friction. Nonetheless, several bulkheads have been constructed in which soft clay was assigned an angle of internal friction of 11 degrees based on the approximate slope of one in five commonly observed on front of a sheet of hydraulic fill. All these bulkheads have failed [6].

In some cases, excessive tilting of the bulkhead was due to the shifting of the tie rod anchorage

resulting from the placement of a heavy surcharge immediately behind the anchorage. This problem can be avoided by placing the surcharge far away from the anchorage or supporting the surcharge by vertical piles. In other cases, excessive tilting of the bulkhead was caused by failure of the tie rod anchorage resulting from the inadequate compaction of the backfill material in front of the anchorage.

Some sheet pile bulkheads driven into sand underlain by a soft clay stratum have failed because of an outward movement of the bulkhead and fill as a whole [6]. Although the bulkhead and anchorage designs were satisfactory, the designer had failed to consider the subsoil stratum that laterally supports the portion of the sheet piles below the dredge line. It would be difficult to prevent such a translation. In such situations, driving the sheet piles through the soft stratum and installation of the A-frame type of tie rod anchorage is indicated. Alternatively, a relieving platform supported on piles with point bearing below the soft stratum may be used.

If the submerged natural earth in front of the bulkhead slopes downward, the slope can fail along a sliding surface below the tie rod anchorage and toe of the sheet piles. Several bulkhead failures of this type have occurred on the Wangpoo River at Shanghai, China. Most of these failures occurred within 2 hours after low tide following spring tide [6]. This type of failure also suggests the importance of considering draw down of the water level from tsunami in the seismic analysis of bulkheads.

The majority of the earthquake damage data for steel sheet pile bulkheads comes from Japan [2,10-12]. Typical failure modes of steel sheet pile bulkheads observed in past major Japanese earthquakes are as follows:

- Sheet piles tilting toward the water with the revetment face bulging out
- Settlement of the ground behind the sheet piling
- Cracking of the concrete apron
- Fracturing of the tie rod
- Tie rod anchoring plates or walls shifted forward with the ground surface behind the plates or walls caved in
- Parapet wall tilting and collapsing

For bulkheads with a relieving platform, the platform is shifted toward the sea. If the platform has a tie rod anchorage, the anchorage is also damaged with the tie rod fracturing or the anchor plate being pulled forward.

The tie rod anchor is the most critical element of an anchored bulkhead. The anchor pull from the bulkhead sheet piles are transferred through the tie rods to the tie rod anchorage. In turn, the tie rod anchorage transfers the anchor pull to the soil laterally supporting the anchorage. A large number of tie rods have been fractured and anchor plates have slid out in major Japanese earthquakes [1]. Once the tie rod has fractured or the anchor has slid out sufficiently to reduce the tie rod tension to a small fraction of its former value, the anchored bulkhead behaves like a cantilever retaining wall and tilts excessively.

However, it is not practical nor economical to design and construct a cantilever sheet pile bulkhead for heights greater than 15 feet above the dredge line. Maintaining the alignment for such a bulkhead is a problem under ordinary conditions even for heights less than 15 feet. The alignment problem will be acerbated by the earthquake loading. Anchored bulkheads are designed for heights as high as 50 feet. Thus, special attention should be given to the safety of the tie rods and their connections and precaution should be taken to prevent the tie rod anchorage from sliding excessively due to passive type soil failure.

It is hypothesized that the outward tilting and bulging of the revetment face observed in past

earthquakes was caused by the failure of the tie rod/anchorage system, i.e., the tie rods, their connections, and the tie rod anchorage. The fracturing of the tie rods and their connections can occur suddenly, leading to excessive tilting of the bulkhead and bulging of the revetment face.

The tilting and bulging of the bulkhead is expected to be a gradual process. This is because the active and passive failure of the soil surrounding the sheet piling and tie rod anchorage is progressively gradual. The active and passive failure surfaces in the soil do not form instantaneously nor does sliding along these planes take place instantaneously once they have formed. Sliding along the failure planes occurs as a series of outward increments [3]. The anchor pull is equal to the sum of the active earth pressure and residual water pressure that act over the height of the sheet piling minus the passive pressure exerted by the soil in front of the sheet piling below the dredge line. Each outward displacement increment of the sheet piling occurs when the anchor pull plus the active pressure acting on the back of the tie rod anchorage, induced by the inward earthquake ground acceleration pulse, exceeds the passive resistance of the soil in front of the anchorage. By contrast, an outward directed earthquake ground acceleration pulse will not cause the bulkhead to tilt and bulge inward because such a movement requires forces that are about ten times larger than that required to produce the outward displacement. However, inward tilting of the bulkhead can occur in a soft soil site as a result of sliding instability due to circular slip of the bulkhead and fill as a whole.

In some cases, the tie rod anchorage failed because it is located too close to the bulkhead. The resistance of the tie rod anchorage is reduced if it is located near the active soil failure zone. The resistance of the tie rod anchorage is nil when it is located entirely within the active failure zone. Furthermore, the active soil failure zone spreads away from the bulkhead with increasing earthquake ground acceleration. That is, the angle that the active failure plane makes with the horizontal plane decreases with increasing earthquake ground acceleration. Similarly, the angle that the passive failure plane makes with the horizontal plane decreases with increasing ground acceleration. For the concrete wall anchorage to be fully effective, the active failure plane drawn from the intersection of the sheet piling with the dredge line and the passive failure plane drawn tangent to the bottom of the tie rod anchor wall or plate should intersect at or above the ground surface (see Figure 2).

Even when the tie rod anchorage remains intact during a major earthquake, some tilting and bulging of the revetment face from the earthquake ground motions can still be expected due to the rotation about the toe of the sheet piling and displacement of the tie rod anchorage required to develop the passive resistance of the supporting soil. Sheet pile bulkheads in Japan have experienced outward tilting of between 5 to 10 degrees without collapse. While asthetically undesirable, rotations of such magnitude are not expected to have a serious effect on the function of the bulkhead. However, utility lines connected to the bulkhead must be designed to accommodate the relative displacements associated with such rotations and remain functional.

Settlement of the ground immediately behind the sheet piling and the tie rod anchorage, and the cracking of the concrete apron is generally caused by the outward and downward movement of the active soil wedge (Figure 2) by sliding along the failure surface. Granted, a portion of this localized settlement may be caused by the uneven consolidation of the soil during the earthquake ground shaking. Uneven settlement of the soil from earthquake ground shaking can only be avoided by selecting sites that are not

susceptable to such effects and carefully controlling the compaction of the backfill soil.

Parapet attached to the top of the bulkhead sheet piles will tilt with the piles. If the connections of the parapet to the sheet piles are inadequate, the parapet can collapse into the water during a severe earthquake.

For sheet pile bulkheads with relieving platform, the shifting of the platform toward the sea is caused by the earthquake induced inertia forces on the platform and the fill and surcharge that it supports and the inadequate lateral stiffness and resistance provided by vertical piles supporting the platform. The inertia force on the platform can be decreased by reducing the total weight (mass) of the platform. Lateral stiffness and resistance required by the platform are best provided by the installation of batter pile under the platform. A tie rod/deadman anchorage is not effective for a relieving platform supported on vertical piles because such an anchorage generally cannot accommodate the large outward movement of the platform and supporting piles without fracturing the tie rod and/or shifting the anchorage.

The yielding or fracturing of the sheet pile sections of the bulkhead due to bending in past major earthquakes is rare. The observed yielding of the sheet pile section in bending is associated with excessive tilting. The localized yielding occurred at only one section along the length of the sheet piling. Furthermore, the observed yielding did not lead to the collapse of the bulkhead. Fracturing of the sheet pile section has occurred at welded splices due to excessive residual stresses from welding. Thus, care must be taken during field welding to reduce the resulting residual stresses. The rare occurrence of yielding or fracturing of the sheet pile section by bending suggests that the Japanese design procedure used to determine the bending moments in the sheet piling is adequate.

3. LATERAL EARTH PRESSURES AND RESIDUAL WATER PRESSURES

In this section, the active and passive lateral earth pressures recommended for the rapid seismic analysis of sheet pile bulkheads are presented. To facilitate calculations, equations for computing the pressures at the top and bottom of each soil layer, the resultant force acting on each layer, and its location with respect to the top of each layer are given. The angles that the active and passive failure planes make with the horizontal plane are presented to aid in the determination of the required location of the tie rod anchorage relative to the bulkhead. Procedure for computing the resulting horizontal force on the bulkhead from line and point loads on the ground surface in the vicinty of the bulkhead is given. Finally, a procedure for computing the residual water pressure acting on the bulkhead is presented.

3.1 Lateral Earth Pressures

For cohesionless soils, the active (K_A) and passive (K_P) earth pressure coefficients are obtained from computer generated curves based on the Mononobe-Okabe [4,5] equations for a vertical wall with a wall friction angle (δ) to angle of internal friction (ϕ) ratio, delta/phi of 0.5 (Figures 3 and 4). The angles that the active (Z_A) and passive (Z_P) failure planes of the soil make with the horizontal plane (see Figure 2) are also obtained from the computer generated curves, based on the Mononobe-Okabe equations, given in Figures 5 and 6. The validity of the Mononobe-Okabe equations for computing the lateral earth pressures on bulkheads under simulated seismic excitation has been verified by a number of laboratory experiments [13-18]. However, it should be noted that all the experiments were performed on dry sand instead of saturated sand commonly encountered in sheet pile bulkhead construction.

In Reference 3, a parametric study was performed on the effects that the earthquake acceleration coefficient, k, the soil angle of internal friction, ϕ, and the wall friction angle to

angle of internal friction ratio, δ/ϕ, have on the active and passive pressure coefficients (K_A and K_p) and the angles that the active and passive failure planes of the soil make with the horizontal plane (Z_A and Z_p). The following are the trends observed from the results of the study pertinent to the behavior of anchored sheet pile bulkheads.

The active lateral earth pressure coefficient K_A:

- Increases with the earthquake acceleration coefficient, k
- Decreases with increasing soil angle of internal friction, ϕ
- Decreases somewhat as the wall friction angle to soil angle of internal friction ratio δ/ϕ increases

The passive lateral earth pressure coefficient, K_P:

- Decreases with increasing earthquake acceleration coefficient, k
- Increases with increasing soil angle of internal friction, ϕ
- Increases with the absolute value of the wall friction angle to soil angle of internal ratio, δ/ϕ

The angle that the failure plane of the active soil wedge makes with the horizontal plane, Z_A:

- Decreases with increasing earthquake acceleration coefficient, k
- Increases with the soil angle of internal friction, ϕ
- Decreases slightly as the ratio of wall friction angle to soil angle at internal friction (δ/ϕ) increases

The angle that the failure plane of the passive soil wedge makes with the horizontal plane Z_p:

- Decreases with increasing earthquake acceleration coefficient, k
- Increases or decreases with increasing soil angle of internal friction, ϕ, depending on the range of earthquake acceleration coefficient.
- Decreases as the ratio of the wall friction angle to soil angle of internal friction (δ/ϕ) increases

Of the observed trends, the increase in active earth pressure coefficient and the decrease in passive earth pressure coefficient with earthquake acceleration coefficient have the greatest effect on the seismic response of sheet pile bulkheads.

According to Figure 3, the K_A value for a soil with ϕ (phi) = 35 degrees increases from 0.25 to 0.38 (about 52%) when the earthquake acceleration coefficient increases from 0 to 0.20. Because the lateral earth pressure on the bulkhead increases with K_A, the bulkhead must be able to accommodate this increase and remain functional. According to Figure 4, the K_p value for a soil with ϕ = 35 degrees decreases from 7.3 to 6.1 (about 16%) for the same increase in earthquake acceleration coefficient. Because the sheet pile bulkhead generally depends on the passive resistance of the soil below the dredge line and of the soil in front of the tie rod anchor to prevent outward translation and rotation about the toe of the sheet piling, its resistance to outward displacement would be reduced under earthquake ground shaking.

The observed increase in K_A and decrease in K_P values with increasing earthquake acceleration coefficient suggest that the tie rod pull will also increase with the earthquake acceleration coefficient. This is because the tie rod pull is generally determined from the difference between active and passive pressures acting over the height of the sheet piling. On the other hand, the capacity of a concrete wall or short sheet pile tie rod anchor is equal to the difference between the passive pressure acting in front and the active pressure acting on the back of the anchor. Thus, the capacity of a tie rod anchor decreases with increasing earthquake acceleration coefficient while the anchor pull it resists increases.

Futhermore, K_A decreases with an increase in ϕ and δ/ϕ ratio. The opposite is true for K_P. Whenever there is an uncertainty in the backfill

angle of internal friction ϕ, the smaller ϕ value should be used to determine the seismic adequacy of the bulkhead. K_A only decreases slightly with increasing δ/ϕ ratio. By contrast, K_p increases significantly with the δ/ϕ ratio. Although experimental data indicate that a $\delta/\Phi = 2/3$ can be obtained under favorable conditions, $\delta/\phi = 0.5$ was selected for the analysis procedure to provide static K_p values that closely match values recommended by Terzaghi [6].

The observed decreases of the angles Z_A and Z_P with increasing earthquake acceleration coefficient can shift the deadman anchor from the fully passive zone (to the right of the passive failure plane in Figure 2) to the intermediate zone between the active and passive failure planes where the lateral resistance of the anchor may be reduced.

In this study, a sand is considered as silty if it has more than 5% by weight that passes the number 200 mesh.

For soils with cohesion (c) and internal friction angle (ϕ), c-ϕ soils, such as silty sand, the active and passive pressures are computed approximately by substituting the K_A and K_P values from Figures 3 and 4 into the Rankine equations for active and passive pressures. The Z_A and Z_P angles are assumed to be the same as those for cohesionless soils with the same angle of internal friction.

For cohesive soils, the active earth pressure is assumed to be a function of (1 + k), where k is the earthquake acceleration coefficient. By contrast, the passive earth pressure is assumed to be a function of (1 - k). The cohesion, c, is assumed to be unaffected by the earthquake acceleration coefficient. Approximate equations for Z_A and Z_P were developed for $k \leq 0.2$.

Whenever possible, it is best to determine the needed soil properties from laboratory testing of representative samples. When such data are not available, the data presented in Table 1 can be used.

Reliance should not be placed on the passive resistance provided by soil backfill unless its placement is well controlled and thoroughly compacted. Backfill soils for bulkheads are usually deposited under water and their structures are likely to be loose.

3.1.1 Active Pressure-Soil in the field generally consists of different layers and the earth pressures are computed at the top and bottom of each layer (Figure 7). The computation for each pressure component is carried out from the uppermost layer downward. In cases where the ground water table is located in a soil layer, the layer is separated into two artificial layers, one above the water table and one below the water table. Computations are carried out for a unit width of bulkhead.

3.1.2 Cohesionless Soils

$$p_{A_{ti}} = K_{A_i}\left(q + \bar{p}_{Z_{ti}}\right) \quad (1)$$

$$p_{A_{bi}} = K_{A_i}\left(q + \bar{p}_{Z_{ti}} + \gamma_i h_i\right) \quad (2)$$

where: $p_{A_{ti}}$ = active earth pressure at top of layer i; lb/ft^2

$p_{A_{bi}}$ = active earth pressure at bottom of layer i; lb/ft^2

K_{A_i} = active earth pressure coefficient for layer i (See Figure 3)

q = surcharge; lb/ft^2

$\bar{p}_{Z_{ti}}$ = effective vertical soil pressure at the top of soil layer i; lb/ft^2. This is equal to the sum of the effective vertical soil pressures from the soil layers above. Use the dry unit weight, γ, for soil layers above the water table and the submerged unit weight, γ'; for soil layers below the water table; lb/ft^2

γ_i = dry unit weight of the soil in layer i, if it is located above the water table. If it is below the water table, use the submerged unit weight γ'; lb/ft^3

h_i = thickness of soil layer i; ft

c-ϕ Soils.

$$p_{A_{ti}} = K_{A_i}\left(q + \bar{p}_{Z_{ti}}\right) - 2c_i\sqrt{K_{A_i}} \quad (lb/ft^2) \tag{3}$$

where: c_i = cohesion of soil layer i; lb/ft^2

$$p_{A_{bi}} = K_{A_i}\left(q + \bar{p}_{Z_{ti}} + \gamma_i h_i\right) - 2c_i\sqrt{K_{A_i}} \quad (lb/ft^2) \tag{4}$$

Cohesive Soils.

$$p_{A_{ti}} = \left(q + \bar{p}_{Z_{ti}}\right)(1 + k) - 2c_i \quad (lb/ft^2) \tag{5}$$

or

$$p_{A_{ti}} = 0.5\left(q + \bar{p}_{Z_{ti}}\right)(1 + k) \quad (lb/ft^2) \tag{6}$$

where: k = earthquake acceleration coefficient

Use the larger value from Equations 5 and 6.

$$p_{A_{bi}} = \left(q + \bar{p}_{Z_{ti}} + \gamma_i h_i\right)(1 + k) - 2c_i \quad (lb/ft^2) \tag{7}$$

or

$$p_{A_{bi}} = 0.5\left(q + \bar{p}_{Z} + \gamma_i h_i\right)(1 + k) \ (lb/ft^2) \tag{8}$$

Use the larger value from Equations 7 and 8.

3.1.3 Passive Pressure

Neglect the effect of the surcharge on the passive resistance.

Cohesionless Soils.

$$p_{P_{ti}} = K_{P_i}\bar{p}_{Z_{ti}} \quad (lb/ft^2) \tag{9}$$

$$p_{P_{bi}} = K_{P_i}\left(\bar{p}_{Z_{ti}} + \gamma_i h_i\right) \quad (lb/ft^2) \tag{10}$$

where: $p_{P_{ti}}$ = passive earth pressure at top of soil layer i; lb/ft^2

$p_{P_{bi}}$ = passive earth pressure at bottom of soil layer i; lb/ft^2

K_{P_i} = passive earth pressure for soil layer i (See Figure 4)

C-ϕ Soils.

$$p_{P_{ti}} = K_{P_i}\bar{p}_{Z_{ti}} + 2c_i\sqrt{K_{P_i}} \quad (lb/ft^2) \tag{11}$$

$$p_{P_{bi}} = K_{P_i}\left(\bar{p}_{Z_{ti}} + \gamma_i h_i\right) + 2c_i\sqrt{K_{P_i}} \quad (lb/ft^2) \tag{12}$$

Cohesive Soils.

$$p_{P_{ti}} = \bar{p}_{Z_{ti}}(1 - k) + 2c_i \quad (lb/ft^2) \tag{13}$$

$$p_{P_{bi}} = \left(\bar{p}_{Z_{ti}} + \gamma_i h_i\right)(1 - k) + 2c_i \quad (lb/ft^2) \tag{14}$$

3.1.4 Resultant Force & Location

Results from laboratory experiments on model retaining walls or anchored sheet pile bulkheads subjected to simulated earthquake excitation [13-18] indicate that the distribution of the seismic component of the earth pressure is approximately parabolic. Consequently, the location of the seismic resultant force is located at a height above the base higher than one-third times the height of the wall considered. However, the location of the resultant force above the base increases with the rigidity of the structure. It is located at about H/3 above the base for a very flexible structure and at about 2H/3 above the base for a very rigid structure, where H is the height of the wall or bulkhead. For simplicity and convenience, both the static and seismic lateral earth pressure distributions are assumed to be triangular and increase linearly with depth in this study. Accordingly, the resulting pressure distribution for each soil layer will be triangular or trapezoidal.

For ease of computation, artificial layers are sometimes created within a given soil layer and the force resultants and their locations are then computed for the newly created layers.

For a triangular pressure distribution, the resultant lateral force of soil layer i is

$$P_i = \frac{1}{2} p_{bi} h_i \tag{15}$$

and located at

$$\bar{h}_i = \frac{2}{3} h_i \tag{16}$$

below the top of the layer.

For a trapezoidal pressure distribution, the resultant lateral force of soil layer i is

$$P_i = \frac{1}{2}(p_{ti} + p_{bi}) h_i \tag{17}$$

and located at

$$h_i = \frac{h_i(p_{ti} + 2p_{bi})}{3(p_{ti} + p_{bi})} \tag{18}$$

below the top of the layer.

where: p_{ti} = lateral earth pressure at top of soil layer i; lb/ft^2

p_{bi} = lateral earth pressure at bottom of soil layer i; lb/ft^2

h_i = thickness of soil layer i; ft

3.2 Angles that the Active and Passive Soil Failure Planes Make with the Horizontal Plane

3.2.1 Cohesionless and c-ϕ Soils. Determine Z_A and Z_p from Figures 5 and 6, respectively. To check the required location of the deadman anchor relative to the bulkhead for full effectiveness, plot the active soil failure plane angles, Z_A, starting with the layers that contain the intersection of the bulkhead sheet piles with the dredge line (see Figure 2) and work upward. Then, plot the passive soil failure plane Z_p, starting with the soil layer that contains the bottom of the anchor. Draw the Z_p line for that layer so that it is tangent to the bottom of the anchor.

3.2.2 Cohesive Soils. Determine Z_A and Z_p from Equations 19 and 20 given below. These approximate equations were developed by the writer for earthquake acceleration coefficients, k, of less than or equal to 0.2 using the computer generated curves from the Mononobe-Okabe equations. They are not valid for earthquake accelerations coefficient k greater than 0.2.

$$Z_A = 45° - 1.4 \tan^{-1} k \quad (19)$$

$$Z_p = 45° - 0.66 \tan^{-1} k \quad (20)$$

3.3 Line and Point Loads

Heavy line and point loads near the bulkhead are best supported by vertical piles to minimize their effect on the bulkhead. For line loads and point loads not supported by vertical piles, use the procedure given in Figure 8 to compute the equivalent horizontal force and its location on the bulkhead. The curves given in the figure were developed by Terzaghi [6] on the assumption of an unyielding wall and are approximately double those values from elastic equations. A sheet pile bulkhead is generally flexible and yields (displaces) under load, reducing the loading exerted by the line or point loads. Because of the conservatism built into the curves, no attempt was made to modify the curves for seismic effects.

3.4 Residual Water Pressure

Unless more accurate information is available, assume the residual water level, h_u, to be two-thirds of the tidal range above the low water level (LWL) (see Figure 7). Under earthquake excitation, the pore water in the soil is assumed to move with the surrounding soil. Hence,

$$p_{RW_t} = 0 \quad (lb/ft^2) \quad (21)$$

$$p_{RW_b} = (1 + k)\, \gamma_w\, h_u \quad (lb/ft^2) \quad (22)$$

where: P_{RW_t} = residual water pressure at the top of the ground water table; lb/ft^2

P_{RW_b} = residual water pressure at the LWL; lb/ft^2

γ_w = unit weight of seawater = 64 lb/ft^3

h_u = height of the residual water level above the LWL; ft

k = earthquake acceleration coefficient

4. PROCEDURE FOR ANCHORED SHEET PILE BULKHEADS

In this section, a rapid seismic analysis procedure developed for the analysis of anchored sheet pile bulkheads is presented. The analysis procedure includes the following major steps:

- Determination of the loads acting on the sheet piling
- Determine the adequacy of the depth of penetration of the sheet piling
- Determine the maximum bending stress in the sheet piling
- Determine the adequacy of the tie rod and tie rod connections.
- Determine the adequacy of the tie rod anchorage
- Check for other potential modes of failure that have not been considered previously that can have a significant effect on the behavior of the bulkhead considered, such as circular slip for sheet piling embedded in soft soil sites.

After an examination of the various design and analysis procedures for anchored sheet pile bulkheads in the literature [1,2,6,8,9,19-22], the procedure given in Chapter 5 of Reference 19 for sheet pile type quaywalls was selected for adaptation in this study. The procedure was

selected because of its simplicity. Furthermore, the adequacy of the procedure has been verified by surveys of postearthquake damage to sheet pile bulkheads designed or analyzed by the procedure [1,11,12].

4.1 Loading

The loading on the anchored sheet pile bulkhead included the active earth pressure, the residual water pressure, and the passive earth pressure (Figure 7). In addition, the loading should include the earthquake-induced inertia force on the concrete parapet if appropriate. This outward directed force is equal to the mass of the parapet per unit width of bulkhead times the earthquake acceleration coefficient, k. Berthing forces on the bulkhead is neglected in the analysis because the probability of the maximum berthing force acting simultaneously with the earthquake-induced forces is very remote.

The procedure for computing the lateral earth pressures and residual water pressure acting on the sheet pile bulkhead for cohesionless, c-ϕ, and cohesive soils were given previously in the section on "Lateral Earth Pressures and Residual Water Pressure."

Currently, there are no established seismic coefficients for the pseudo-static analysis of anchored sheet pile bulkheads in the United States. It is suggested that the seismic acceleration coefficients given in Table 2 be used tentatively for the rapid analysis procedure until more precise data becom available.

4.2 Depth of Penetration

The steel sheet piles are driven to a sufficient depth below the dredge line to limit the outward movement of the sheet piles under load to a sufficiently small value.

The required depth of penetration is determined by taking the summation of moments about the tie rod setting point of the forces due to the active earth pressure and residual water pressure and the passive pressure (Figure 7). This can be expressed by the following generalized equation:

$$SF = \frac{\Sigma M_{resisting}}{\Sigma M_{driving}} \geq 1.2 \qquad (23)$$

where: $M_{resisting}$ = resisting moment about the tie rod setting point from the passive earth pressure and the active earth pressure above the tie rod level

$M_{driving}$ = driving moment about the tie rod setting point from the active earth pressure and residual water pressure

NOTE: Include the moment contribution from line or point load to $M_{driving}$ or $M_{resisting}$. A line or point load contributes to $M_{driving}$ if the resulting lateral force acts on the sheet piling below the tie rod setting point. Otherwise, it contributes to $M_{resisting}$.

In normal design, the required depth of penetration for the sheet piling is computed from an equation similar to Equation 23. Then, the actual depth of penetration is determined by increasing the computed depth by a percentage of the computed value to account for uncertainties in the soil properties from boring samples (typically spaced at 100-foot intervals) and potential scouring at the dredge line. In the U.S., the computed required depth of penetration is commonly increased by 20%. By contrast, the Japanese authorities [9] specify a 20% increase above the computed depth for cohesionless soils and a 50% increase above the computed depth for cohesive soils. In determining the seismic adequacy of an existing bulkhead, use the computed depth of penetration whenever possible. Otherwise, use 83.3% (1/1.2) or some appropriate fraction of the actual depth of penetration.

For a site consisting of different soil layers, it is convenient to compute the resultant active and passive forces acting on each soil layer and their location relative to the tie rod setting

point before computing $M_{driving}$ and $M_{resisting}$ in Equation 23.

4.3 Bending Stress

In the determination of the maximum bending moment in the sheet piling, the sheet piling is assumed to be a virtual simply supported (SS) beam with supports at the tie rod level and at the dredge line (Figure 9). The beam is loaded by the active earth pressure and the residual water pressure upward from the dredge line. If appropriate, include the outward earthquake-induced inertia force acting on the concrete parapet and lateral forces acting on the sheet piling from a point or line loads.

The above SS beam assumption and loading condition is valid for relatively flexible sheet piles embedded in medium to dense cohesionless soil and stiff cohesive soil sites. For sites where the compact material below the dredge line is located below a layer of soft material, assume the lower support of the virtual beam to be located at the bottom of the soft layer. For special situations such as relatively stiff steel sheet piling embedded in a soft soil site or the toe of the sheet piling embedded in rock, the free-earth or other appropriate methods should be used in determining the maximum bending moment [8].

Evaluation of the adequacy of the sheet piles in bending consists of the following steps:

1. Compute the reactions on the virtual beam shown in Figure 9 by summing moments about the top and bottom beam supports according to the principles of statics. Check the answers by taking a summation of the horizontal forces. Remember to include other appropriate forces mentioned earlier but not shown in Figure 9. Neglect any loading on the beam below the dredge line.

2. Determine the location of the maximum bending moment by locating the point of zero shear on the sheet piling below the tie rod setting point. The soil layer in which the maximum moment occurs is located by summing algebraically the horizontal forces acting on the virtual beam sequentially from the top. The maximum bending moment is located in the soil layer below the tie rod where the net shear force on the virtual beam becomes zero. The location of the maximum bending moment within that layer is obtained by summing all the horizontal forces from the top of the bulkhead to the top of the soil layer and adding the force within the layer expressed as an unknown, x, distance from the top of the layer and setting the resulting equation to zero and solving for x.

3. Determine the maximum bending moment corresponding to location x on the virtual beam.

4. Determime the maximum bending stress in the sheet piling (f_{bs}) and compare it against the permissible value.

$$f_{bs} = \frac{M_{max\ s}}{S_s} \leq 1.2\ F_y \qquad (24)$$

where: $M_{max\ s}$ = maximum bending moment in the sheet piling; in-lb

S_s = sections modulus of the sheet piling per foot of bulkhead; $in.^3$

F_y = minimum specified static yield strength of the sheet piling material; lb/in^2

The maximum stress of $1.2\ F_y$ under seismic loading was considered acceptable because the maximum moment is located in a section below the low water level (LWL) where corrosion is not a problem. The yield strength of steel increases by about 10% above the static value under rapid load with a rise time between 0.01 second and 0.1 second such as those from a major earthquake [24,25]. The actual yield strength of steel is generally about 20% higher than the minimum specified static value. Furthermore, a maximum bending stress of $1.2\ F_y$ corresponds to a ductility factor* of about 1.2 which is considered acceptable functionally. As mentioned earlier,

*Ductility factor = maximum displacement/displacement at yield.

yielding of bulkheads in bending in past major earthquakes has been rare.

4.4 Tie Rod and Tie Rod Connection Stresses

Once the tie rod and/or its connections have failed, an anchored sheet pile bulkhead behaves as a cantilevered retaining wall and tilts outward excessively. The tie rod may be subjected to secondary bending stress from the uneven settlement of the surrounding soil as a result of earthquake ground shaking. Moreover, the tie rod and its connections are generally located near the tidal zone where corrosion is most severe. Thus, it would be desirable to assign a higher safety factor to the tie rod and its connections to ensure that they will not fail under earthquake loading.

To remain functional, the tie rod and its connections must be able to transmit the static and earthquake induced forces without fracturing. Accordingly, the maximum stresses in the tie rod and its connections are limited to less than or equal to $0.6\ F_y$, where F_y is the static yield strength of the material considered. No attempt will be made to cover the various configurations of the tie rod connections. Equations for computing the maximum axial stress in the tie rod and the maximum bending stress in the wale are as follows.

4.5 Tie Rod Stress

1. Determine the maximum tension acting on the tie rod, T, from

$$T = A_p\ d/\cos\theta \quad \text{(lb)} \qquad (25)$$

where: A_p = reaction of the tie rod setting point from the determination of the maximum bending moment in the sheet piling (Figure 9); lb/ft

d = tie rod spacing; ft

θ = angle that the tie rod makes with the horizontal plane; degree

2. Determine the maximum axial stress in the tie rod, f_{at}, from

$$f_{at} = \frac{T}{A_{net}} \leq 0.6\ F_y \quad \text{(psi)} \qquad (26)$$

where: A_{net} = net area of tie rod; $in.^2$

F_y = static yield strength of tie rod material; psi

4.6 Wale Stress

1. Determine the maximum bending moment in the wale, $M_{max\ w}$, from

$$M_{max\ w} = \frac{T\ d}{10} \quad \text{(ft-lb)} \qquad (27)$$

2. Determine the maximum bending stress in the wale, f_{bw}:

$$f_{bw} = \frac{M_{max\ w}}{S_w}\ (12\ in./ft) \leq 0.6\ F_y\ (psi) \qquad (28)$$

where: S_w = section modulus of wale; $in.^3$

F_y = static yield strength of wale material; psi

4.7 Tie Rod Anchorage

The tie rod cannot carry out its intended function if its anchorage is located too close to the bulkhead where the capacity of the anchorage is reduced. As mentioned earlier in the section on "Lateral Earth Pressures and Residual Water Pressure," the active soil failure zone (wedge) spreads away from the bulkhead and the passive soil failure zone spreads toward the bulkhead with increasing earthquake acceleration coefficient. This, in effect, reduces the distance between the anchorage and the bulkhead. In addition, the tie rod anchorage must provide adequate resistance against lateral displacement if the bulkhead is to remain functional. This requirement is satisfied indirectly by providing the tie rod anchorage with a specified safety factor against ultimate soil failure.

4.8 Location

4.8.1 Concrete Wall Anchorage. To be fully effective, the position of the concrete wall anchorage should be located such that the active failure plane drawn from the intersection of the sheet piling with the dredge line and the passive failure plane drawn tangent to the lower edge of the concrete wall anchorage does not intersect below the ground surface as shown in

Figure 2. If the active and passive failure planes intersect below the ground surface, the effective height of the wall anchorage is equal to the actual height, h_A, minus the height of the top of the wall anchorage above the intersection of the two planes (Figure 10). The effective height is used for computing the lateral resistance of the anchor.

4.8.2Vertical Pile Anchorage. To be fully effective, the position of the vertical pile anchorage should be located such that the passive failure plane drawn from a point $l_{ml}/3$ below the tie rod setting point at the anchorage and the active failure plane drawn from the intersection of the bulkhead sheet piling with the dredge line intersects at or above the plane containing the tie rod as shown in Figure 11a. Here, l_{ml} is the depth from the tie rod setting point at the anchorage to the point where the bending moment in the vertical pile first becomes zero. The pile head is assumed to be free and the virtual ground surface is assumed to be located at the tie rod setting point of the anchorage. A detailed discussion of the analysis of pile behavior and capacities under lateral loads is beyond the scope of this study. Readers unfamiliar with the subject can refer to References 26 to 30. For readers familiar with the subject, materials needed for pile analysis are given in Reference 8.

When the active and passive failure planes of the soil intersect below the horizontal surface containing the tie rod, assume the ground surface to be located at the same level as the intersection of the two planes in the determination of the response and capacity of the vertical pile anchorage.

4.8.3Sheet Pile Anchorage. When the sheet pile anchorage can be considered as a long pile, it should be located relative to the bulkhead as for vertical pile anchorage for full effectiveness. A sheet pile is considered long if its length, L, to relative stiffness factor, T, ratio $L/T \geq 5$, where $T = (EI/f)^{1/5}$, E = modulus of pile material, I = moment of inertia of pile, and f = coefficient of variation of subgrade reaction of the supporting soil [8]. When the sheet pile anchorage cannot be considered as long piles, the portion of the sheet pile anchorage below a distance of $l_{ml}/2$ should be neglected in the analysis. Here, l_{ml} has the same meaning as for vertical pile anchorage.

4.8.4A-Frame Pile Anchorage. To be fully effective, the position of the A-frame piles should be located behind the active failure plane drawn from the intersection of the bulkhead sheet piling with the dredge line, Figure 11b. Otherwise, neglect the soil support for the portion of the A-frame piles above the active failure plane in the analysis.

4.9 Resistance

4.9.1Concrete Wall Anchorage. Determine the safety factor of the concrete wall anchorage against sliding under the action of the active and passive pressures and inertia force (Figure 12) using the equation:

$$SF = \frac{E_P}{A_P + E_A + I_w} \geq 2.0 \qquad (29)$$

where: A_p = anchor pull; lb

E_A = active force; lb

E_p = passive force; lb

I_w = wall inertia force; lb

$= k \times W_w$

k = earthquake acceleration coefficient

W_w = weight of wall anchor; lb

The procedure for determining the earth pressures acting on the concrete wall anchorage is the same as that for the bulkhead sheet piles, except that the residual water pressure on each side of the wall anchorage cancel each other.

Evaluate the adequacy of the concrete wall in bending in the horizontal and vertical direc-

tions by assuming that the earth pressure is distributed approximately uniformly and that the anchorage is a continuous beam in the horizontal direction and a cantilever beam in the vertical direction.

$$M_H = \frac{T\ d}{12} \tag{30}$$

$$M_V = \frac{T\ h_A}{8\ d} \tag{31}$$

where: M_H = maximum horizontal bending moment; ft-lb

M_V = maximum vertical bending moment; ft-lb/ft

T = tie rod tension; lb

d = tie rod spacing; ft

h_A = height of concrete wall anchorage; ft

The concrete wall anchorage should have a safety factor of equal to or greater than 1.5 against ultimate failure in flexure with a strength reduction factor of $\phi = 1.0$ for flexure. (Readers unfamiliar with the design and analysis of reinforced concrete structures can refer to Reference 31.)

4.9.2Vertical Pile Anchorage. Vertical pile anchorage should be analyzed as vertical piles subjected to an external load from the tie rod tension, T [8]. Whenever possible, the ultimate lateral resistance of the vertical piles should be determined from field tests. A safety factor (SF) of ≥ 2.0 should be provided against the ultimate soil failure. If concrete piles are used, they should have a SF of ≥ 1.5 against ultimate failure in flexure with a strength reduction factor $\phi = 1.0$. If steel sheet piles are used, the maximum bending stress should be limited to $\leq 1.2\ F_y$, where F_y = minimum specified static yield strength.

4.9.3Sheet Pile Anchorage. When the length of sheet pile below the tie rod setting point is long enough to be considered as a long pile ($L/T \geq 5$), the sheet pile should be analyzed as a vertical pile anchorage.

When the sheet pile cannot be considered as a long pile, it should be analyzed as a concrete wall anchorage with the assumption that the sheet pile terminates (not effective) at a point $l_{m1}/2$ below the tie rod setting point at the anchorage (Figure 13). Here l_{m1} is the distance between the tie rod setting and the first point where the bending moment is equal to zero in the sheet pile when the sheet pile anchorage is considered as a free-headed long pile with the tie rod setting point as the virtual ground surface.

4.10A-Frame PileAnchorageA-frame pile anchorage should be analyzed as batter piles subjected to the external loading from the tie rod tension [8]. Whenever possible, the utlimate capacity of the piles should be determined from field tests. The piles should be provided with the following safety factor against ultimate failure of the soil:

Loading Type	Safety Factor
Compression	
Bearing	1.5
Friction	2.0
Tension	2.5

For A-frame piles located behind the active soil failure plane (Figure 11b), the piles are primarily subjected to axial stresses. The soil strengths generally control the pile design. However, the axial strengths of the pile and its connections should have a safety factor of equal to or greater than 2.0 against ultimate failure to ensure that the anchorage remains functional under the earthquake loading. Where appropriate, the bending strengths of the A-frame piles should be considered. The recommended safety factors for concrete and steel piles in flexure were given earlier.

4.11 Other Considerations

Besides failing by excessive outward tilting due to failure of the tie rod anchorage system, an anchored sheet pile bulkhead may fail by sliding instability of the soil and bulkhead as a whole due to lateral movement of the soil that pro-

vides support to the buried portion of the bulkhead sheet piling.

Circular Slip in Soft Soil Sites. Sheet pile bulkheads embedded in soft clay soil sites should be evaluated for sliding instability against circular slip. A safety factor of equal to or greater than 1.2 against circular slip is adequate. An example of the analysis procedure presented in the previous sections including a procedure for performing circular slip analysis is given in Reference 32.

Slide Along Soft Stratum Beneath the Toe of Sheet Piling. Sheet piles embedded in sites where the relatively compact soil beneath the dredge line is underlain by a shallow layer of soft material beneath the toe of the sheet piles should be checked for sliding instability along the bottom of the soft layer. The bulkhead is analyzed as a virtual gravity type wall whose lower edge is defined by the bottom of the soft soil layer and right boundary defined by the right-most extent of tie rod anchorage and whose left boundary is defined by the bulkhead sheet piles (Figure 14). Potential outward sliding of the wall is driven by earthquake inertia force induced on the mass bounded by the virtual wall boundaries and the active earth pressure and residual water pressure acting on the right boundary of the virtual wall. This potential movement is resisted by the frictional and cohesive forces along the bottom of the virtual wall and the passive earth pressure exerted by the soil on front of the virtual wall below the dredge line. A safety factor, resisting force divided by driving force, of equal to or greater than 1.2 is adequate.

If tsunami draw down is a potential hazard at the bulkhead site, the increase in hydrostatic pressure on the bulkhead from the tsunami draw down should be considered in the seismic evaluation of the bulkhead.

5. CONCEPTS FOR STRENGTHENING INADEQUATE BULKHEADS

In this section, concepts for strengthening sheet pile bulkheads that are found to be seismically inadequate by the analysis procedure are presented. Theoretically, concepts for strengthening inadequate sheet pile bulkheads are only limited by the imagination of the engineer and his experience. However, the strengthening concepts that are practical for a particular bulkhead at a particular site are controlled by the soils at the site, configuration of the utility lines in the vicinity of the bulkhead, and economics.

Depth of Penetration

It is not practical to increase the depth of penetration of the sheet piles for those existing bulkheads found to have inadequate depth of penetration. The only thing that can be done is to increase the passive resistance of the soil below the dredge line in front of the sheet piling and/or to reduce the active earth pressure acting on the back of the sheet piling by chemical or cement grout injection of the soil. Chemical or cement grouting, whose effectiveness is generally limited to granular soil sites, are very expensive and may only be justifiable in cases where the lead time for the construction of a new bulkhead is a problem.

Bending Capacity of Sheet Piles

Theoretically, steel cover plates can be welded by divers at the critical section of the sheet piles found to be inadequate. However, this generally cannot be justified economically. Fortunately, yielding of the steel sheet pile due to bending has occurred only rarely in past major earthquakes. Yielding of the sheet piles from excessive bending during earthquakes is expected to be gradual and not catastrophic.

Tie Rod/Anchorage

New tie rods can be installed at above or between the existing tie rods if the existing tie rods are found to be inadequate. New wales will be needed if the new tie rods are to be installed at a level above the existing ones. The capacity of the tie rod anchorage will generally be found to be inadequate for those bulkheads

with inadequate tie rods. Existing concrete wall anchors can be strengthened by driving short sheet piles in front of the concrete anchorage and pouring new concrete between the two to make the old concrete wall and new steel sheet piles act compositely together as a unit. This technique was proposed by Casagrande [33] for improving the anchorage of an existing bulkhead at Cleveland, Ohio. Alternatively, the new tie rods can be anchored to new tie rod anchorage constructed behind the existing one. The location of the new anchorage will most probably be determined by the location of the existing utility lines in the vicinity of the old anchorage and the location of the active and passive failure planes in the soil.

6. ACKNOWLEDGMENT

The continual support by Mr. J. Tyrrell (NAVFAC Code 04BA) is appreciated.

7. REFERENCES

1. S. Okamoto. Introduction to earthquake engineering. New York, N.Y., John Wiley and Sons, 1973.

2. S.D. Werner and S.J. Hung. Seismic response of port and harbor facility, Agbabian Associates, Report no. R-8122-5395. El Segundo, Calif., Oct 1982. (National Science Foundation Grant no. CEE-8012337)

3. Naval Civil Engineering Laboratory. Technical Memorandum M-51-83-11: A rapid seismic analysis procedure for gravity quaywalls, by T.K. Lew. Port Hueneme, Calif., Aug 1983.

4. N. Mononobe. "Earthquake-proof construction of masonry dams," in Proceedings of the World Engineering Conference, vol 9, 1929, p 275.

5. S. Okabe. "General theory of earth pressure," Journal, Japanese Society of Civil Engineers, vol 12, 1926, p 1.

6. K. Terzaghi. "Anchored bulkheads," Transactions of the American Society of Civil Engineers, vol 119, 1954, pp 1243-1280.

7. P. Rowe. "Anchored sheet pile walls," in Proceedings of the Institute of Civil Engineers, London, vol 1, Pt 1, Jan 1952, pp 27-70.

8. Naval Facilities Engineering Command. NAVFAC Design Manual 7.2: Foundations and earth structures, Alexandria, Va., May 1982.

9. James R. Ayers and R.C. Stokes. "The design of flexible bulkheads," American Society of Civil Engineers, paper no. 2676, vol 119, 1954, pp 373-383.

10. R. Amano, et al. "A seismic design of quay walls in Japan," in Proceedings of the First World Conference on Earthquake Engineering, Berkely, Calif., Jun 1956, paper 32-1.

11. Japanese Port and Harbour Research Institute. "The damage to port structures by the 1978 Miyagi-Ken-Oki earthquake," by H. Tsuchida, et al., Technical Note no. 325, 1979.

12. Japanese Port and Harbor Research Institute. "Damage to harbour structures by the 1968 Tokachi-Oki earthquake, the investigation of the Tsunami caused by the 1968 Tokachi-Oki earthquake," 1968. (in Japanese)

13. N. Mononobe and H. Matsuo. "On the determination of earth pressures during earthquakes," in Proceedings of the World Engineering Conference, vol 9, 1929, p 176.

14. L.S. Jacobsen (1939). Described in Appendix D of "The Kentucky Project" Technical Report no. 13, Tennessee Valley Authority, 1951.

15. H. Matsuo. "Experimental study on the distribution of earth pressure acting on a vertical wall during earthquakes," Journal, Japanese Society of Civil Engineers, vol 27, no. 2, 1941.

16. Y. Ishii, H. Arai, and H. Tsuchida. "Lateral earth pressure in an earthquake," in Proceedings of the Second World Conference on Earthquake Engineering, vol I, Jul 11-18, 1960. Tokyo, Japan.

17. H. Matsuo and S. Ohara. "Lateral earthquake pressure and stability of quay walls during earthquakes," in Proceedings of the Second World Conference on Earthquake Engineering, vol II, Jul 11-18, 1960. Tokyo, Japan.

18. S. Kurata, H. Arai, and T. Yokoi. "On earthquake resistance of anchored sheet pile bulkheads," in Proceedings of the Third World

Conference on Earthquake Engineering, 1960. New Zealand.

19. The Overseas Coastal Area Development Institute of Japan. Technical standards for port and harbour facilities in Japan, Tokyo, Japan, 1980.

20. U.S. Army Waterways Experiment Station. Instruction Report K-81-2: User's Guide: Computer program for design and analysis of sheet pile walls by classical methods (CSHTWAL). Report I, Computation process, by William P. Dawkins, Vicksburg, Miss., Feb 1981.

21. Department of the Army, Office of the Chief of Engineers. Draft EM 1110-2-2906: Engineering and design of pile structures and foundations, Washington, D.C., Nov 1970.

22. Naval Facilities Engineering Command. NAVFAC Design Manual (DM) 25.4: Seawalls, bulkheads, and quaywalls, Alexandria, Va., Jul 1981.

23. Naval Facilities Engineering Command. NAVFAC P-355: Seismic design for buildings, Alexandria, Va, Feb 1982.

24. U.S. Air Force Weapons Laboratory, Air Force Systems Command. AFWL-TR-74-102: The Air Force manual for design and analysis of hardened structures, by R.E. Crawford, C.J. Higgins and E.M. Bultmann. Kirtland Air Force Base, N.M., Oct 1974.

25. Naval Civil Engineering Laboratory. Technical Report R642: Dynamic tests on selected structural steel by W.L. Cowell, Port Hueneme, Calif., Sep 1969. (AD 695375)

26. W.C. Teng. Foundation design. Prentice-Hall International, 1962.

27. A.W. Skempton. "The bearing capacities of clays," in Proceedings of the Building Research Congress, London, 1951.

28. M.F. Tomlinson. "The adhesion of piles driven in clay soils," in Proceedings of the Fourth International Conference on Soil Mechanics and Foundation Engineering, London, 1957.

29. Canadian Geotechnical Society. Canadian Foundation engineering manual, Canadian Geotechnical Society, 1978.

30. L.C. Reese and H. Matlock. "Non-dimensional solutions for laterally loaded piles with soil modulus assumed proportional to depth," in Proceedings of the Eighth Texas Conference on Soil Mechanics and Foundation Engineering, Austin, Tex., American Society of Civil Engineers, 1956.

31. C.K. Wang and C.G. Salmon. Reinforced concrete design. Harper and Row, New York, 1979.

32. Naval Civil Engineering Laboratory. Technical Memorandum M51-85-01: A Rapid Seismic Analysis Procedure for Anchored Sheetpile Bulkheads, by T.K. Lew, Port Hueneme, CA., March, 1985.

33. Leo Casagrande. "Comments on conventional design of retaining structures," American Society of Civil Engineers Journal of the Soil Mechanics and Foundations Division. Feb 1973, SM2, pp 181-198.

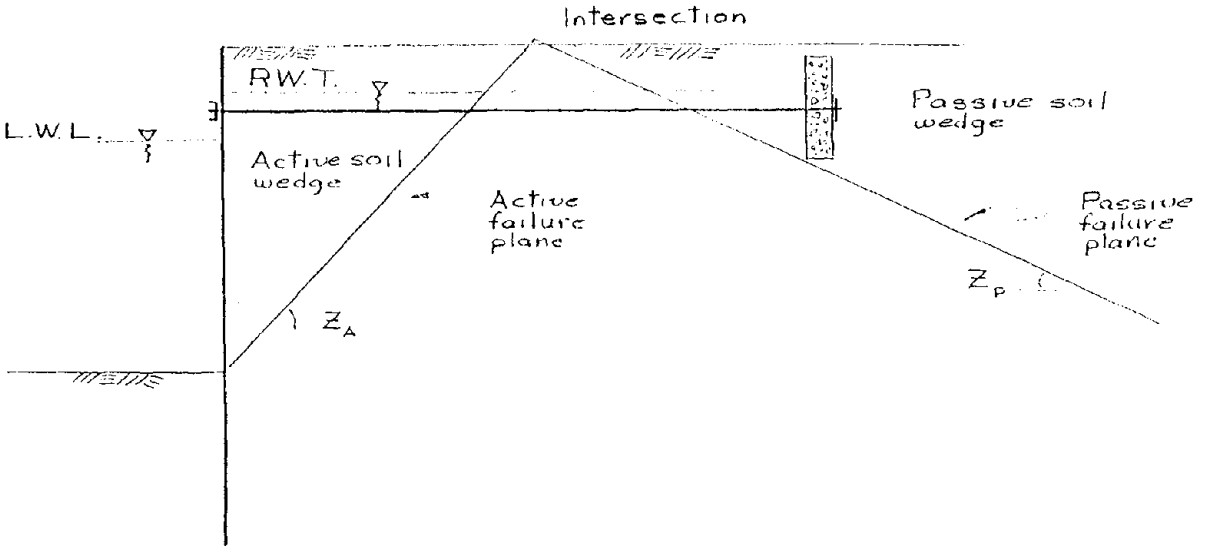

Figure 2. Location of the tie rod anchorage relative to active and passive failure planes in order to be fully effective.

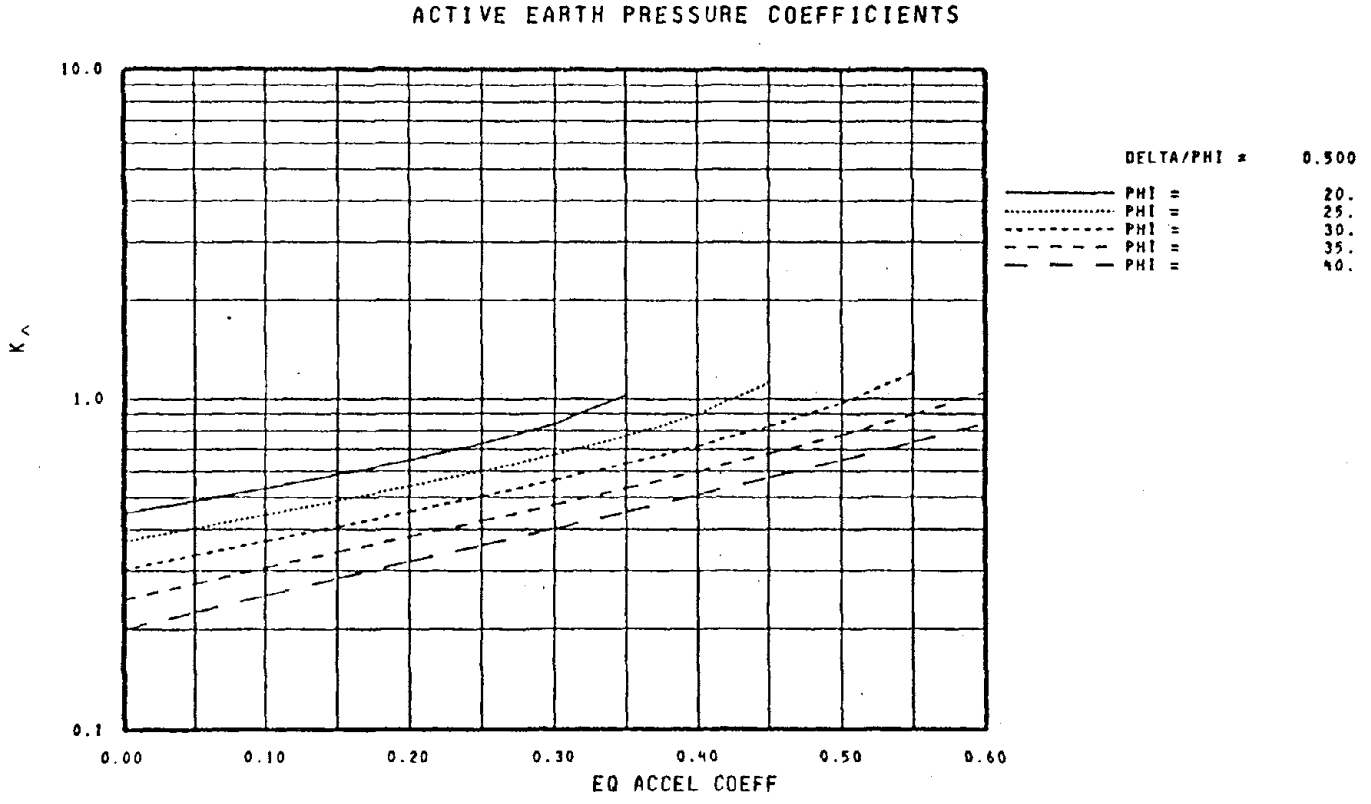

Figure 3. Active lateral earth pressure coefficient (K_A) versus earthquake acceleration coefficient (k) for DELTA/PHI = 0.500 (from Reference 3).

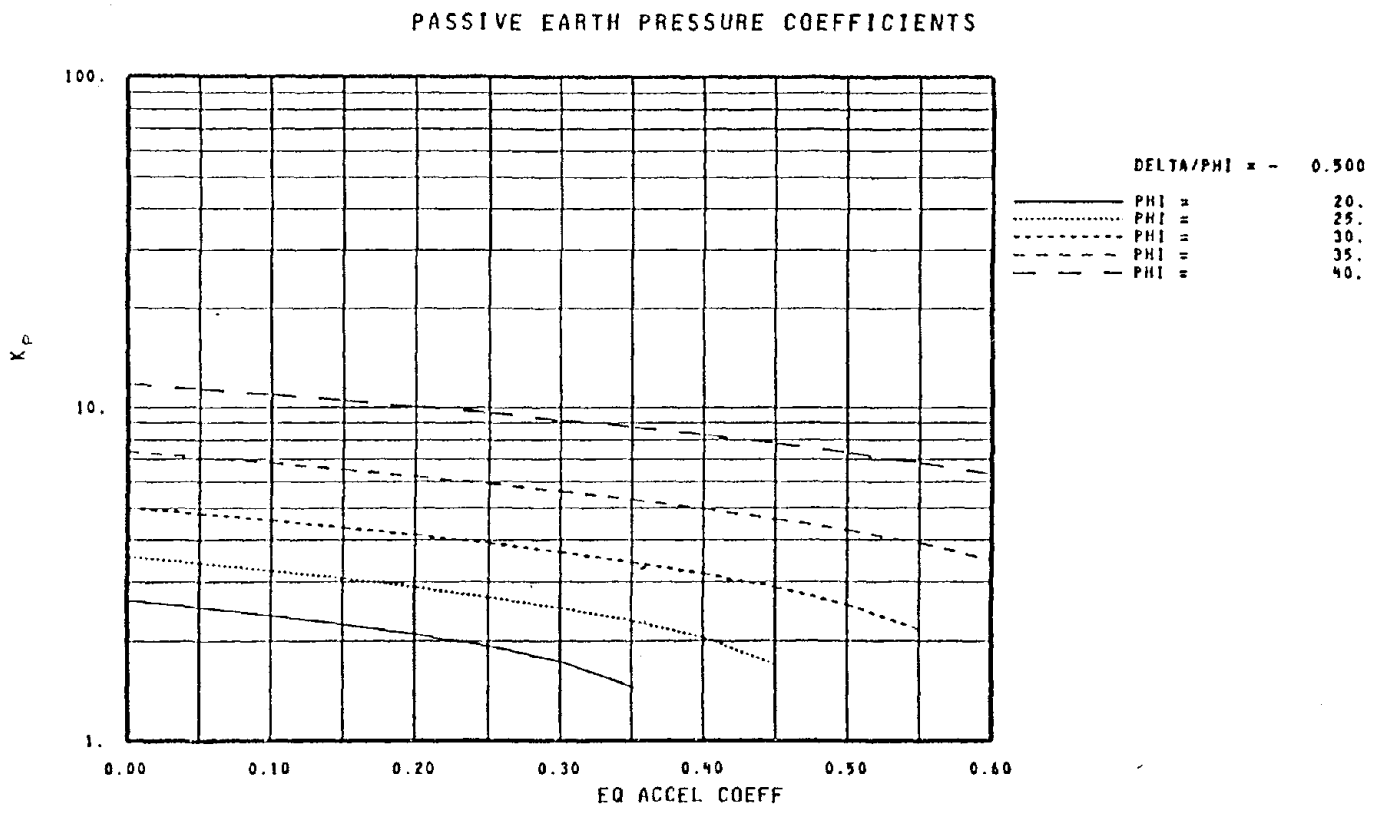

Figure 4. Passive lateral earth pressure coefficient (K_p) versus earthquake acceleration coefficient (k) for DELTA/PHI = 0.500 (from Reference 3).

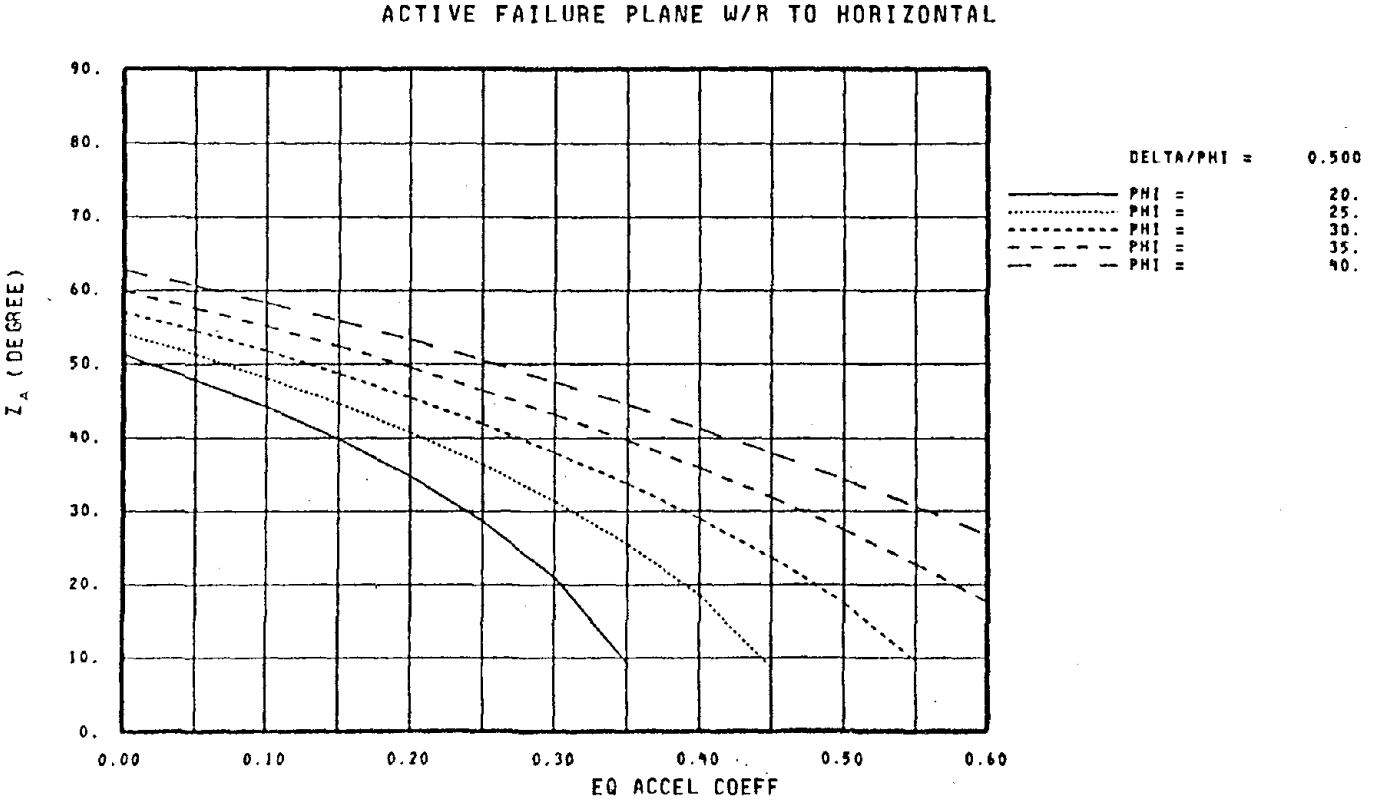

Figure 5. Active soil failure plane angle (Z_A) versus earthquake acceleration coefficient (k) for DELTA/PHI = 0.500 (from Reference 3).

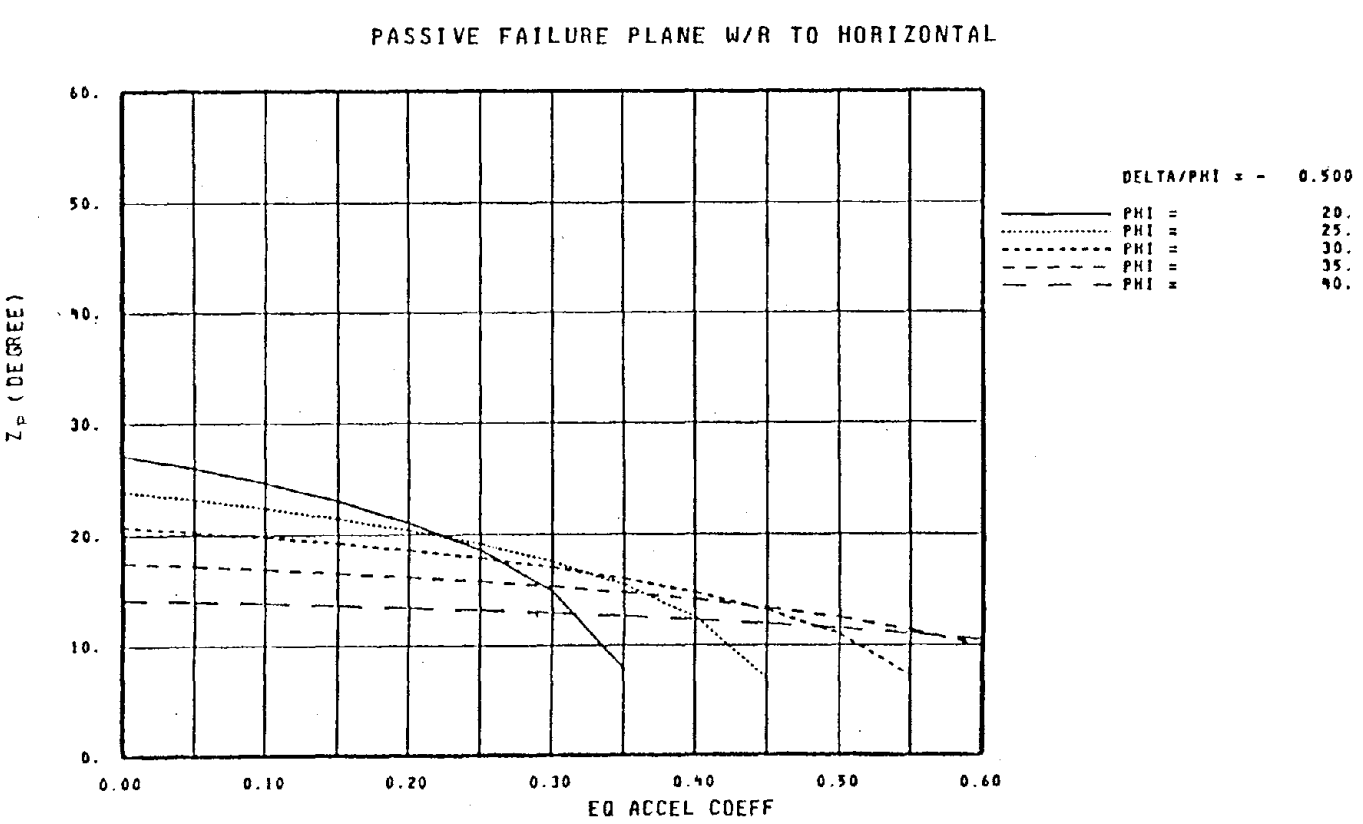

Figure 6. Passive soil failure plane angle (Z_p) versus earthquake acceleration coefficient (k) for DELTA/PHI = 0.500 (from Reference 3).

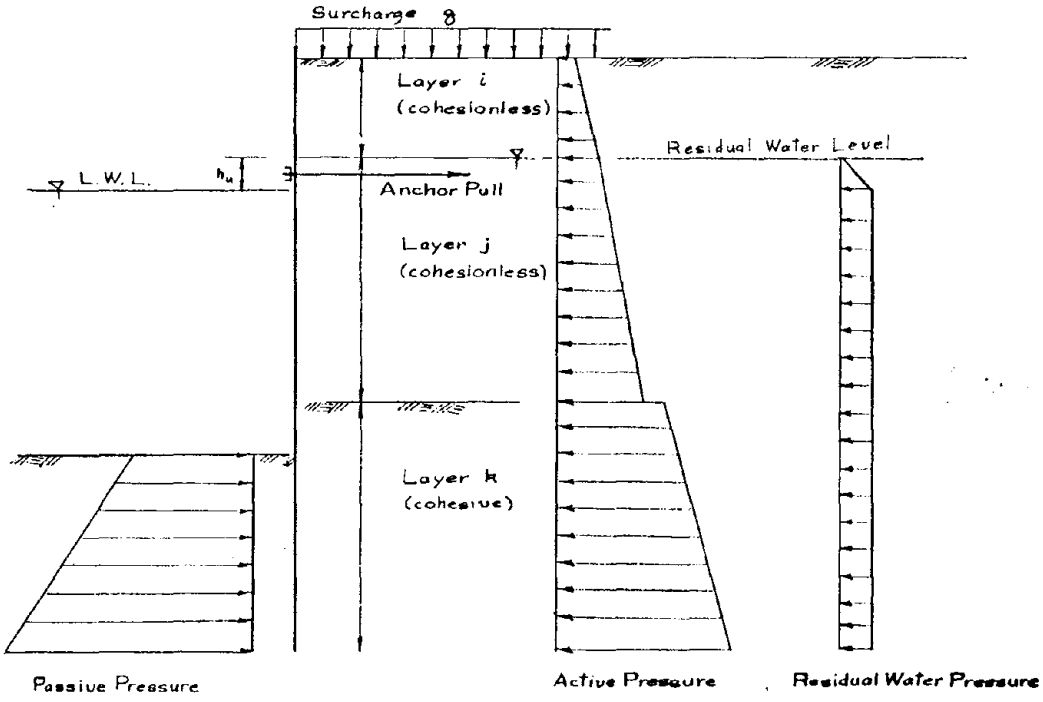

Figure 7. Lateral earth pressures and residual water pressure acting on anchored sheet pile bulkhead.

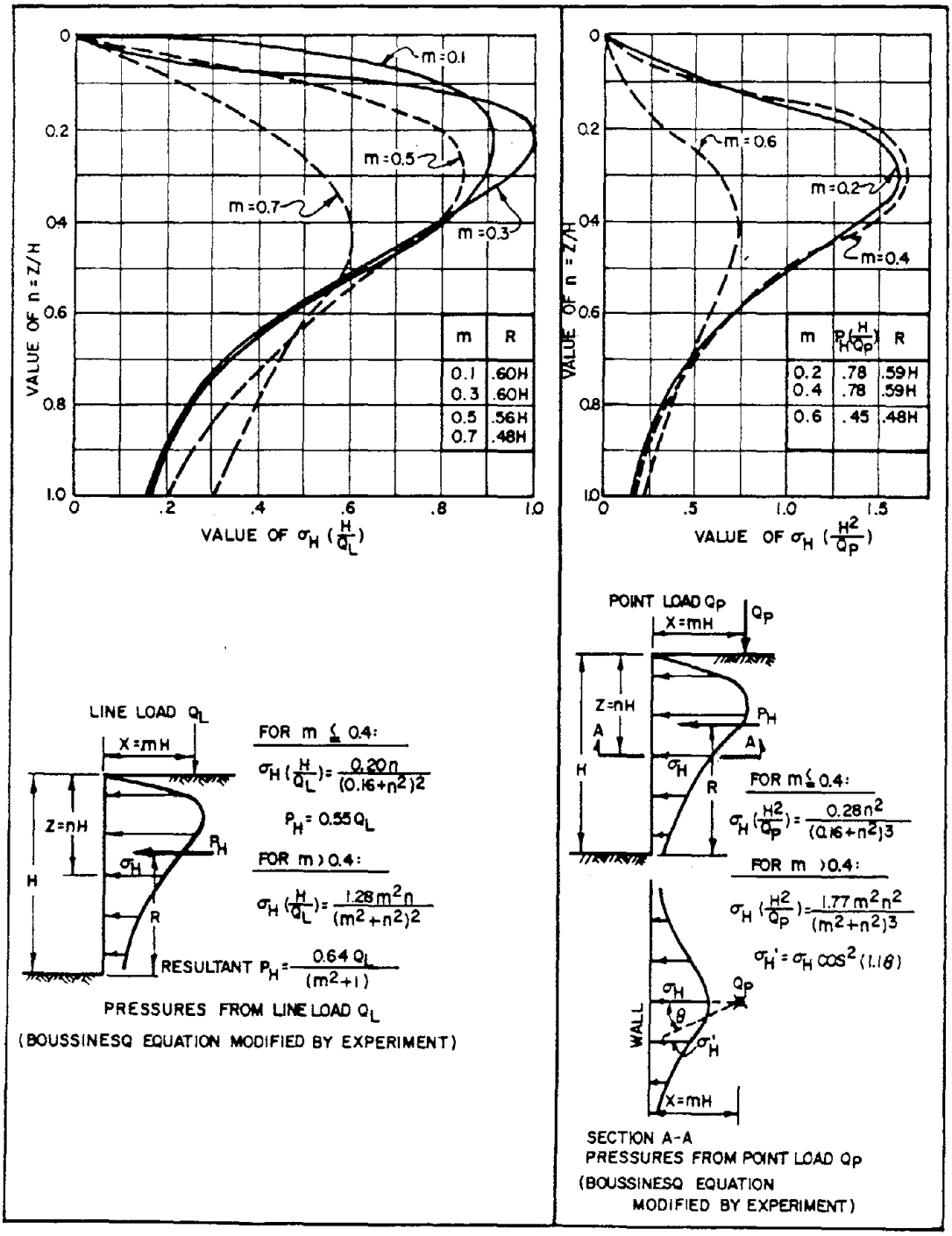

Figure 8. Horizontal pressures on rigid wall from surface load (from Reference 8).

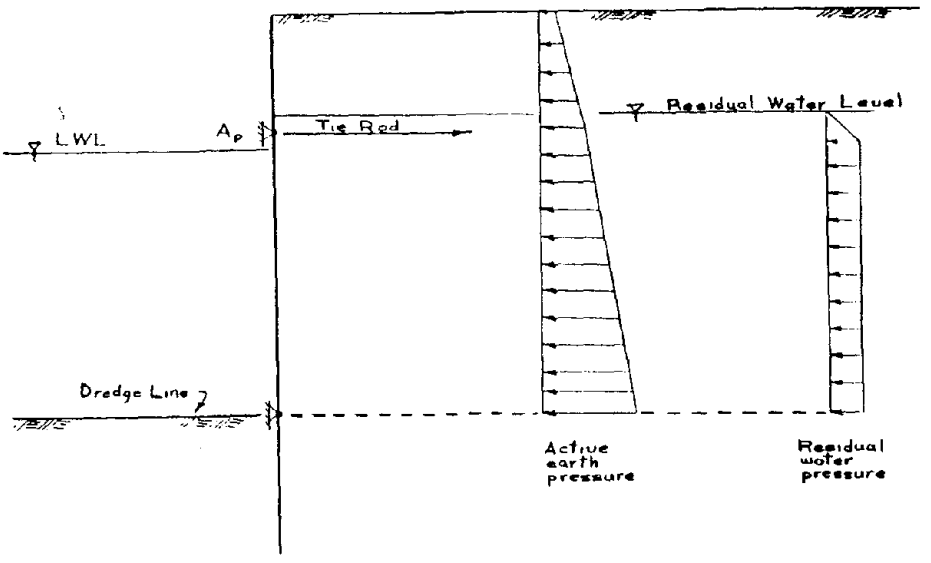

Figure 9. Virtual beam used for determining the bending moment in the sheet piling.

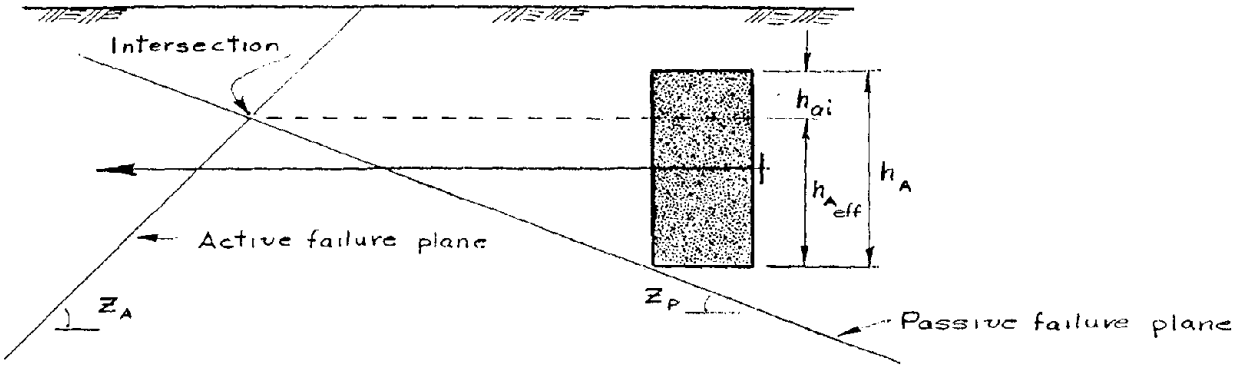

Effective height of anchorage

$$h_{A_{eff}} = h_A - h_{ai}$$

where h_{ai} = height of wall anchorage above the intersection of active and passive failure planes

h_A = actual height of wall anchorage

Figure 10. Effective height of wall anchorage when the intersection of the active and passive soil failure planes is below the ground surface.

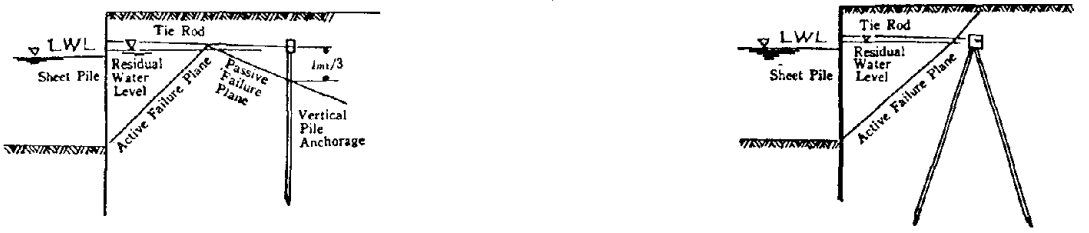

a. Vertical pile anchorage

b. A-frame pile anchorage

Figure 11. Location of pile anchorage relative to bulkhead for full effectiveness (after Reference 19).

where

A_P	=	anchor pull	(lb)
E_A	=	active force	(lb)
E_P	=	passive force	(lb)
I_w	=	wall inertia force	(lb)
	=	$k \times W_w$	
k	=	earthquake acceleration cofficient	
W_w	=	weight of wall anchorage	(lb)

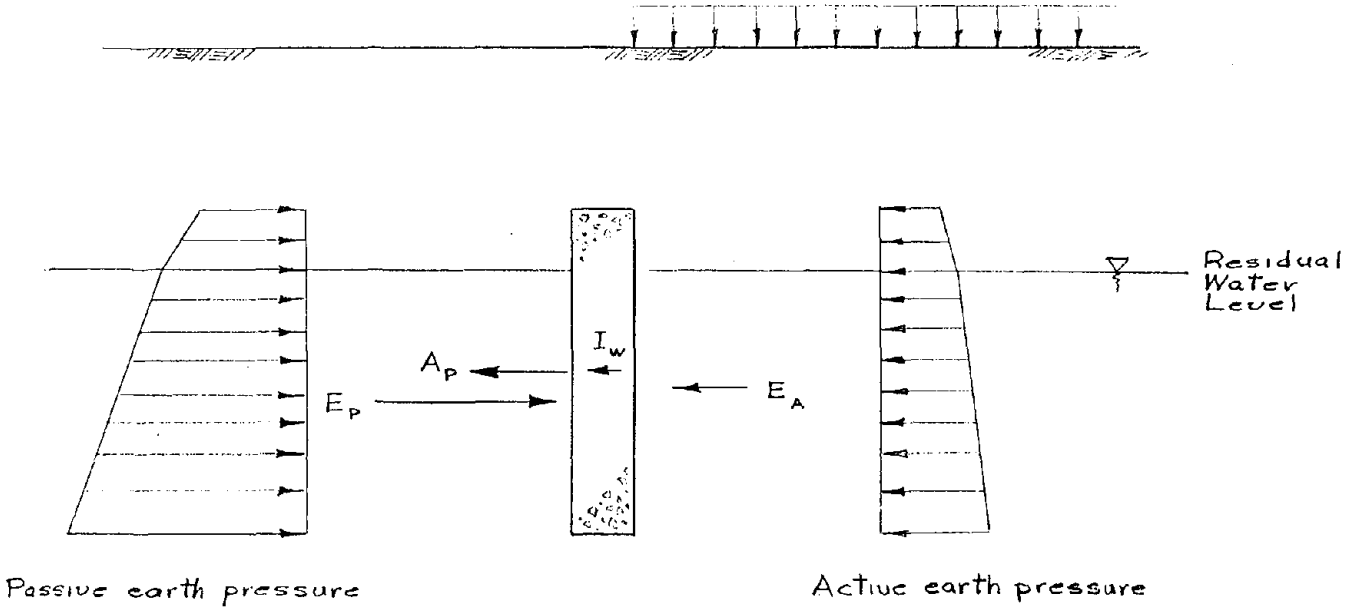

Figure 12. External forces acting on wall anchorage for tie rod.

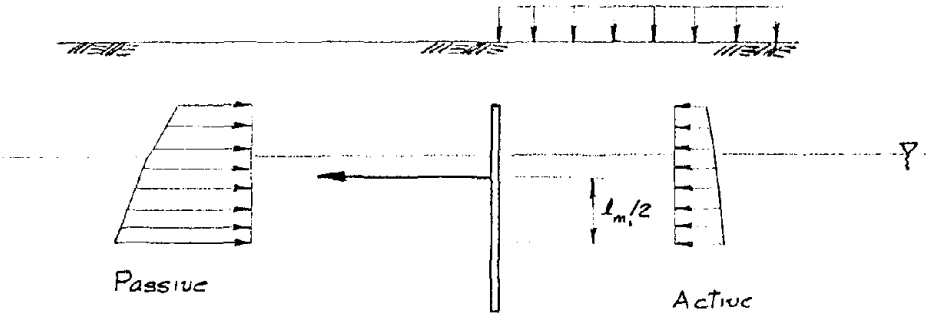

Figure 13. Virtual earth pressure acting on short sheet pile anchorage for tie rod.

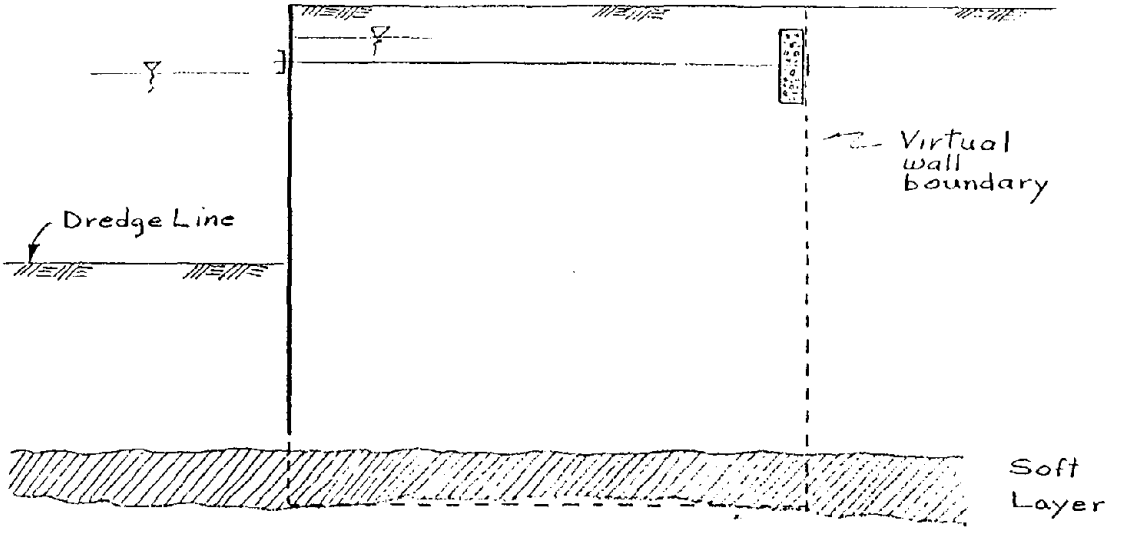

Figure 14. Anchored sheet pile bulkhead analyzed as virtual gravity type wall.

DESIGN OF PILES FOR SLOPES

Hirohiko Tada[I], Kazuya Oshima[II], Yukio Sato[III]
and Ryoichi Abo[III]

ABSTRACT

Generally there is no problem with the vertical bearing capacity of piles provided on mountains and other slopes if they are driven into a satisfactory bearing layer, but their horizontal bearing capacity in the direction of the slope for the force of inertia in an earthquake, for example, is much smaller than in level ground. Moreover, there is no established way of determining this horizontal bearing capacity and in fact, no definite method of calculation is shown even in the Specifications for Highway Bridges (1).

The Foundation Engineering Division, Public Works Research Institute, has investigated the realities of sinso (deep bed method) pile design and execution and conducted model tests to see the effects of the ground slope on the behavior of piles upon which horizontal force works and establish a method to design them. Of these, the results of the model test with sandy ground has already been reported (2). This time, we will report on the results of our fact-finding survey for design and execution and of our model test with soil cement ground.

According to the fact-finding survey, the commonly used design values for sinso piles are 2-4 m for pile diameter, 10-20 m for pile length and about 5 for the pile length/pile diameter. From the design classification, this places them in the category of limited-length piles intermediate between caissons and long piles.

In the model test, meanwhile, we have confirmed that it is logical for the horizontal resistance of piles on sloping ground to be determined by a calculating method taking the plasticization of the ground into consideration and that the method to find the coefficient of ground reaction (k-value) and plastic resistance used for this calculation is basically the same with soil cement ground as it is with sandy ground.

Key Words: Earthquake Engineering, Foundations, Pile Foundations, Lateral Loads.

1. INTRODUCTION

Recently, with the progress of road improvement, road structure foundations have come to be more frequently constructed on mountain slopes. Sinso piles are commonly used for these foundations provided in sloping ground for reasons concerning the execution of work, such as the relative freedom from the fear of ground loosening by pit excavation, and the saving of the trouble of bringing and installing heavy equipment. Sinso piling involves digging shafts into the ground while sheathing with corrugated sheets or liner plates and forming cast-in-place reinforced concrete piles in the shafts.

When a horizontal force works on an ordinary long pile, the ground is gradually destroyed from the surface and its displacement progresses with the increase of load and, generally, no definite yield point exists. Therefore, the horizontal bearing capacity of

I) D. Eng.; Director of Structure and Bridge Department, Public Works Research Institute, Ministry of Construction.
II) Head of Foundation Engineering Division, Structure and Bridge Department.
III) Member of Foundation Engineering Division.

the pile is set so that the pile-head displacement cannot exceed the prescribed level.

In the case of a highway bridge foundation, this prescribed displacement is normally so small as to prevent large statically indeterminate stress on the superstructure, and to give necessary rigidity to the substructure itself. Here, since the ground can practically be regarded as an elastic body, the stress, displacement and ground reaction in different parts of the pile can be determined by the theory of beams on an elastic bed.

However, in the case of sinso piles (limited-length piles) on sloping ground, it is considered necessary to check not only the pile-head displacement but also the pile stability with respect to horizontal forces because the horizontal bearing power of the ground in the direction of the slope is small. It is also deemed necessary to use a somewhat large design pile-head displacement by determining ground reaction in the consideration of the ground plasticization because, in this case, the use of small design pile-head displacement is sometimes very uneconomical, as it is with ordinary piles.

However, all has not yet been thoroughly elucidated on matters such as the effect of the ground slope on the behavior of piles on which a horizontal force works and so the Foundation Engineering Division, Public Works Research Institute, is conducting experiments and research to clarify these issues and to establish a method for the design of sinso piles for sloping ground (3).

2. REALITIES OF DESIGN AND CONSTRUCTION OF SINSO PILES

A survey was made on sinso piles constructed during fiscal 1982 by the Ministry of Construction's construction offices throughout Japan, the Hokkaido Development Bureau, and the Okinawa General Bureau. The cases covered include various types of superstructure, in ratios as indicated in Fig. 2.1 in terms of the number of places of executed work (total: 38) and in Fig. 2.2 in terms of the number of sinso piles used (total: 230). These superstructures were mostly for bridges.

We shall see hereunder about the bridge foundations. The inclination angle of the ground was as indicated in Fig. 2.3 and about 3/4 represented sloping ground. A considerable number of the foundations were constructed on steep slopes of more than 40°.

The per-substructure number of piles used was as indicated in Fig. 2.4. About half of them represented single-pile cases and about 1/3 double-pile cases. The work was designed so that the number of piles could be minimized by using large piles.

Pile diameter D, pile length ℓ, and pile length ratio ℓ/D are shown in Figs. 2.5 - 2.7.

The pile diameter was 2-4 m in more than 90% of the cases while the pile length was 10-20 m in more than 70%. The ℓ/D was commonly about 5 and, in about 90% of the cases, ranged from 3 to 9. From the design classification, most piles belonged in the category of limited-length piles -- intermediate between caissons and long piles.

If horizontal resistance is expected in the design, then the gap developing between the strutting material and the natural ground must be carefully backfilled. The backfill material used was cement mortar with the amount of cement and the flow value as shown in Figs. 2.8 and 2.9. For backfilling mortar, importance is attached not so much to strength as to the capacity to fill the gap.

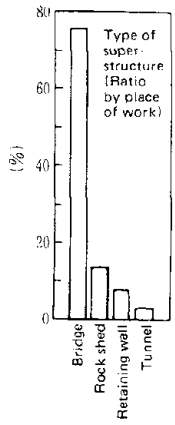

Fig. 2.1

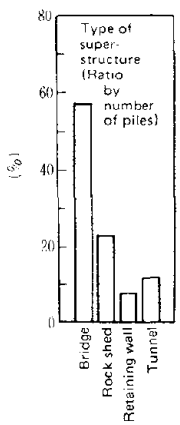

Fig. 2.2

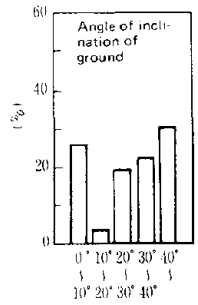

Fig. 2.3

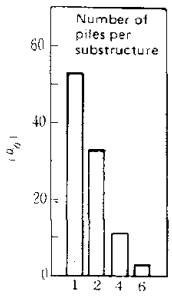

Fig. 2.4

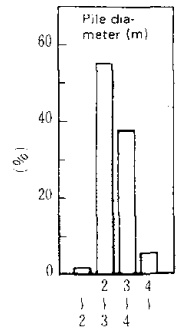

Fig. 2.5

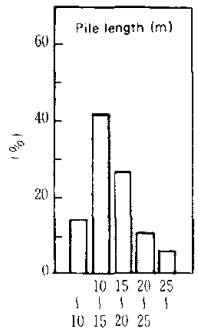

Fig. 2.6

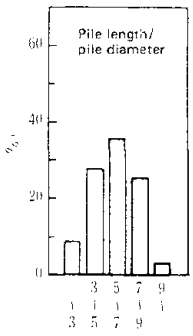

Fig. 2.7

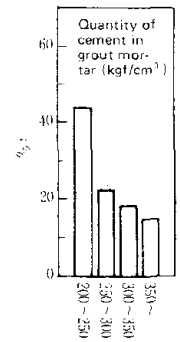

Fig. 2.8

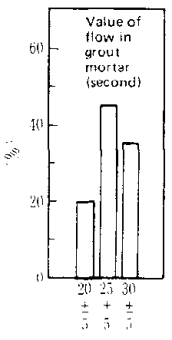

Fig. 2.9

Fig. 2. Characteristics of cases surveyed

3. MODEL TEST

3.1 Purpose of Test

Fig. 3.1 shows one of the ordinary models used to calculate the behavior shown by sinso piles on sloping ground when a horizontal force works on them. The ground constants used for this model are the lateral k-value k_H, vertical k-value k_V, bottom rotation spring constant K_R, bottom shearing spring constant K_S and the plastic resistance of ground q. However, the primary purpose of the test was to clarify K_H and q which are presumed to profoundly affect the horizontal bearing capacity of piles.

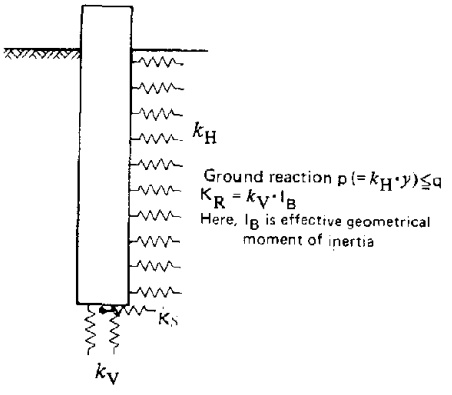

Fig. 3.1 Model of Pile

3.2 Test Conditions

When making a model test, it is necessary to satisfy the condition of similarity between the prototype and the model.

The factors to be considered when studying the law of similarity concerning the horizontal bearing capacity of piles would probably include horizontal load P (kgf), flexural rigidity of pile E_pI (kgf·cm^2), modulus of deformation of ground E_o (kgf/cm^2), k-value k (kgf/cm^3), pile length ℓ (cm), pile diameter D (cm), unit weight of ground γ (kgf/cm^3), shearing resistance angle of ground ϕ, and cohesion of ground c(kgf/cm^2).

Since the dimensional matrix rank of these nine factors is 2, the physical quantity ratio between the model and the prototype (scale factor) can be freely selected for only two factors. Scale factors for the other factors may be set so that seven independent non-dimensional quantities $\pi_1 - \pi_7$ can be equal between the model and the prototype.

From the results of the fact-finding survey, it is considered appropriate to use 1/20 as the scale factor for the length and the diameter of sinso piles in general, providing that their length and diameter are 10 m and 2 m, respectively. Also, if the scale factor of γ is 1, the scale factor of other factors can be set as indicated in Table 3.1.

Table 3.1 Scale Factor of Factors

Non-dimensional quantity	Factor	Scale factor
	ℓ	1/10
	γ	1
$\pi_1 = \ell/D$	D	1/10
$\pi_2 = P/\gamma\ell^3$	P	$1/10^3$
$\pi_3 = E_pI/\gamma\ell^5$	E_pI	$1/10^5$
$\pi_4 = E_o/\gamma\ell$	E_o	1/10
$\pi_5 = k/\ell$	k	1
$\pi_6 = \phi$	ϕ	1
$\pi_7 = c/\gamma\ell$	c	1/10
$\pi_8 = \beta\ell$	$\beta\ell$	1

Selecting soft-rock ground as the object ground for the prototype, the physical quantities of prototypes and models of pile and ground can be set as in Table 3.2, which also lists the values of non-dimensional quantities $\beta \cdot \ell$ obtained by dimensionally analyzing the governing equation based on the assumption that piles are beams on an elastic bed. Here, β is called the characteristic value of the piles and $\beta = \sqrt[4]{(k \cdot D)/(4 \cdot E_p \cdot I)}$.

The model ground, from the target value of E_o, corresponds to loose sandy ground but was

Table 3.2 Physical Quantities of Ground and Piles

Physical quantity	Prototype	Model
E_0 (kgf/cm^2)	1500	150
k (kgf/cm^3)	10	10
γ (kgf/cm^3)	1.7	1.7
ϕ	40°	40°
c (kgf/cm^2)	3	0.3
ℓ (cm)	1000	100
D (cm)	200	20
$E_p \cdot I$ (kgf·cm^2)	2.12×10^{13}	2.12×10^{8}
$\beta \cdot \ell$	2.2	2.2

prepared, using lean-mix soil cement, to provide ground approximating soft rock and liable to fragile destruction.

From the target value of E_pI, a vinyl chloride pipe is suitable for use as a model pile. However, a steel pipe pile was used instead, for the purposes of approximating the prototype $\beta \cdot \ell$, the main factor governing the behavior of the limited-length pile for horizontal force, so as to not cause yielding of the pile body prior to the destruction of the soil cement ground, and also to improve precision in the model manufacture and stress measurement.

3.3 Test Method

In the test, a model pile was installed in the ground prepared in a test soil tank, as in the case of sandy ground, and a horizontal force was exerted against the pile head, using a hydraulic jack and a wire rope (see Fig. 3.2)

Loading was made by the 4-cycle formula using load control with 1/16 of the design maximum load as the load stage. The load, the displacement on the pile head and the ground surface, and the bending strain in the pile body were measured by, respectively, load cell, displacement gauge and strain gauge.

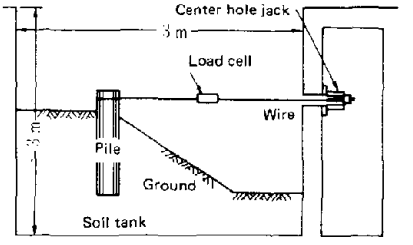

Fig. 3.2 Equipment of Experiment

Cracks developed on the ground surface in the loading process were noted and underground sliding surfaces were examined by digging the ground after loading.

The test cases are shown in Table 3.3. In all test cases, data for model piles were: outside diameter 21.6 cm, pipe thickness 0.4 cm, and setting length 100 cm.

Table 3.3 Test Cases

Type of ground	Angle of inclination of ground (deg.)
Sand (S)	0, 10, 20, 30, 40
Soil cement (R1 - R6) C/S = 1, 2, 3, 4, 6%	0, 20, 30, 40

Note) Figure for R represents C/S (%).

3.4 Test Results

3.4.1 Ground Constants

Unconfined compression tests were conducted using compacted samples of the soil cement used to produce the model ground, or samples cut out of the model ground and shaped after the loading process.

There were considerable variations in the test results but it is deemed that the unconfined compression strength qu and E_o of the model

ground prepared were generally within the range in Table 3.4, according to the ratio c/S of the soil cement.

Table 3.4 Physical Constants of Test Ground

Type of ground c/S (%)	qu (kgf/cm^2)	E_o (kgf/cm^2)	c (kgf/cm^2)	ϕ (deg.)
1	0.8	400	0.19	40
2	5.7	1850	1.33	40
3	1.6	950	0.37	40
4	4.3	1300	1.00	40
6	10.9	3150	2.54	40

Note) c was calculated from qu by the following expression on the assumption that $\phi = 40°$.

$$c = \frac{1 - \sin\phi}{2 \cdot \cos\phi} \cdot qu$$

3.4.2 Horizontal Bearing Capacity

In the test, loading was continued until either the ground in front of the pile was destroyed or the stress of the pile body approached the yield point. It was deemed that the horizontal force reached its ultimate when, in the load vs. pile-head displacement curves thus obtained, load decreased or almost ceased to increase as displacement increased.

Test cases where ultimate horizontal bearing capacity was obtained are as indicated in Fig. 3.3.

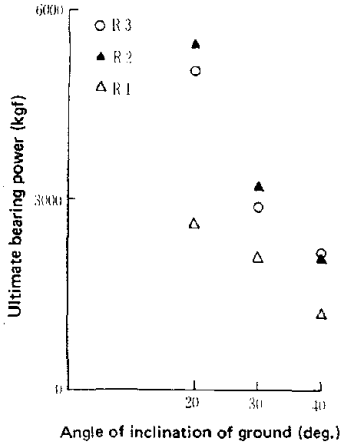

Fig. 3.3 Horizontal Bearing Capacity vs. Angle of Inclination

The ultimate horizontal bearing capacity tended to decrease with the increase of the inclination angle of the ground. This is a sign that it is necessary for sinso piles in sloped ground to be checked for stability of horizontal force.

3.4.3 Inversely Calculated k-Value

Assuming the piles to be beams on an elastic bed, the fundamental equation for their stress and displacement can be shown by Equation (3.1).

$$\frac{d^4y}{dx^4} + \frac{1}{E_pI} kDy = 0 \qquad (3.1)$$

where

y = Horizontal displacement of pile (cm)

x = depth in direction of pile axis from ground surface (cm)

The stress and displacement of the limited-length pile can be obtained by solving Equation (3.1) under the boundary conditions at the pile head and the pile tip.

From the measured values of horizontal force and pile-head displacement, the k-value, assumed to be constant with depth, can be obtained by the solution of Equation (3.1). An example of the relation between the inversely calculated k-value and the pile displacement at the ground-surface (D, R6) is shown in Fig. 3.4.

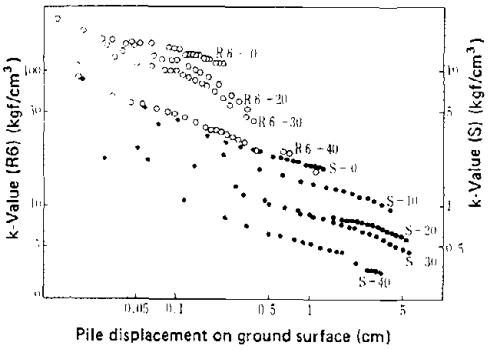

Fig. 3.4 Relation Between Inversely Calculated k-Value and Pile Displacement

In this example, the k-value decreases with the increase of pile displacement. Other cases are omitted for reasons of space but are much the same as this example. In Equation (3.2), showing the decrease of this k-value, n is generally within the range of 0.1 to 0.6 and indicates the nonlinearity of the k-value based on the inelastic behavior of the ground.

$$k = k_o \, (y/y_o)^{-n} \qquad (3.2)$$

where

k = k-value at time when pile displacement is y cm (kgf/cm^3)

k_o = k-value at time when pile displacement is y_o cm (kgf/cm^3)

The relation between the inversely calculated k-value and the inclination angle of the ground is shown in Fig. 3.5. This k-value is the value

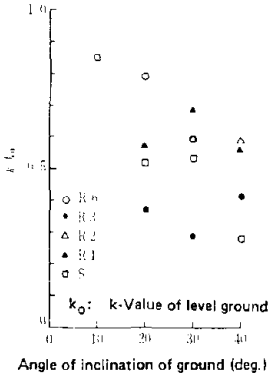

Fig. 3.5 Inversely calculated k-value vs. Angle of Inclination

at the time when the pile displacement is 0.2 cm. In the case of soil cement ground, ground strength varies widely, but there is the general tendency that the k-value deceases with the increase of the inclination angle of the ground.

3.4.4 Distribution of Ground Reaction and Distribution of k-Value

The bending moment in the pile section can be obtained from the measured value of bending strain in the pile body by Equation (3.3).

$$M = \varepsilon \frac{E_p r}{I} \qquad (3.3)$$

where

M = Bending moment (kgf·cm)

ε = Bending strain

E_p = Young's modulus of pile (kgf/cm^2)

r = Distance from neutral axis to point of measurement (cm)

I = Geometrical moment of inertia of pile (cm^4)

Assuming piles to beams on an elastic bed, the relation of pile displacement and ground reaction with the bending moment can be shown by Equation (3.4).

$$E_p I \frac{d^2y}{dx^2} = -M$$

$$E_p I \frac{d^4y}{dx^4} = -p \qquad (3.4)$$

where p = Ground reaction (kgf/cm^2)

If M is approximated by a polynomial in x by the method of least squares, from the distribution of M at different points of measurement, the distribution of p can be obtained by Equation (3.4). Also, the distribution of k-value can be obtained by Equation (3.5) from the distributions of y and p.

$$k = p/y \qquad (3.5)$$

Examples of the distribution of ground reaction and the distribution of k-value (S-0, 30, R6-0,

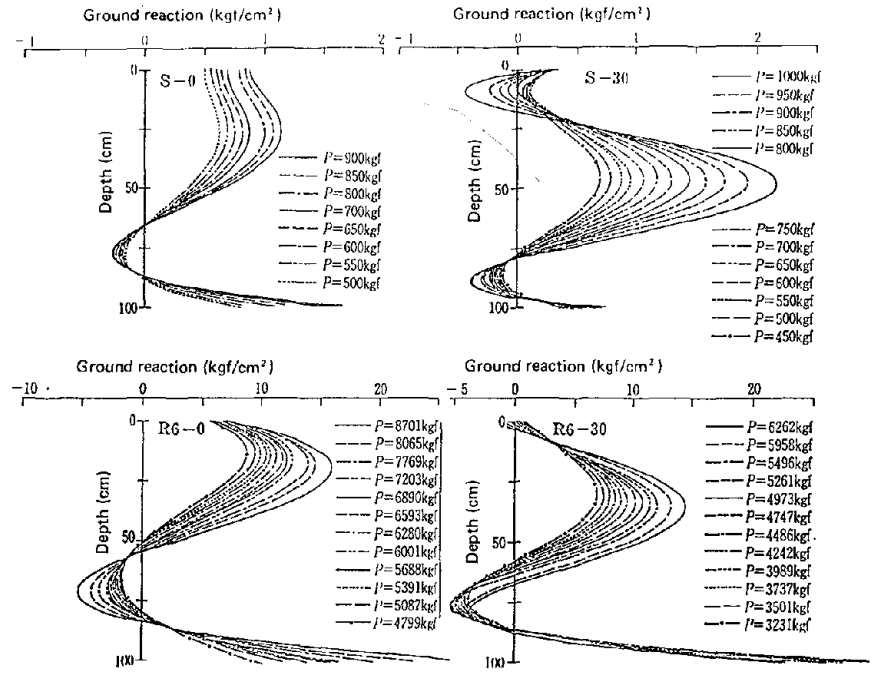

Fig. 3.6 Distribution of Ground Reaction (No. 1)

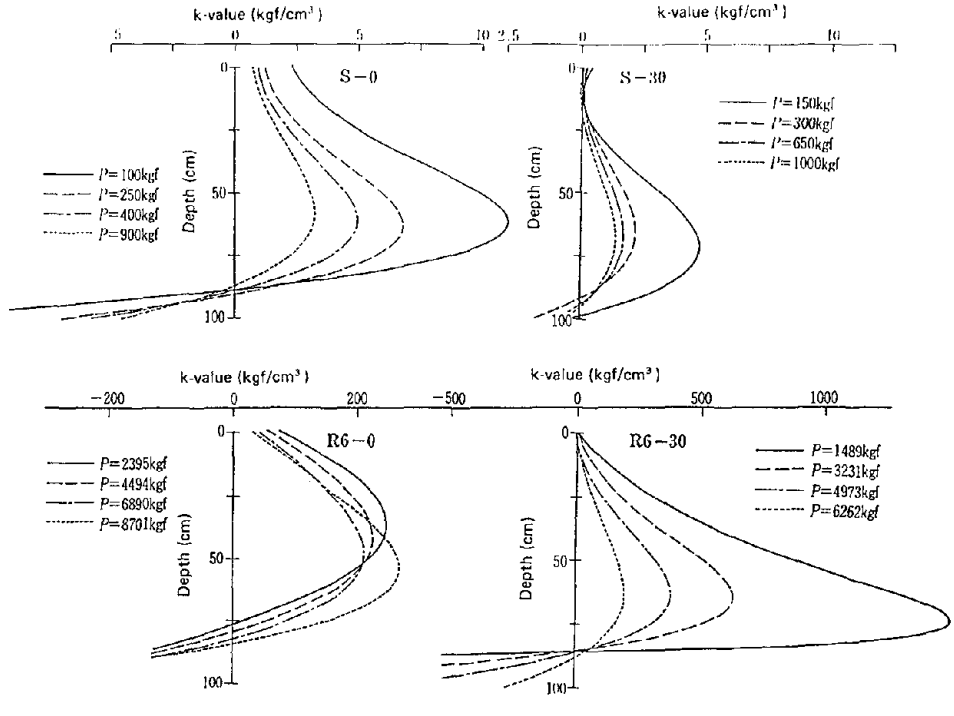

Fig. 3.7 Distribution of k-Values

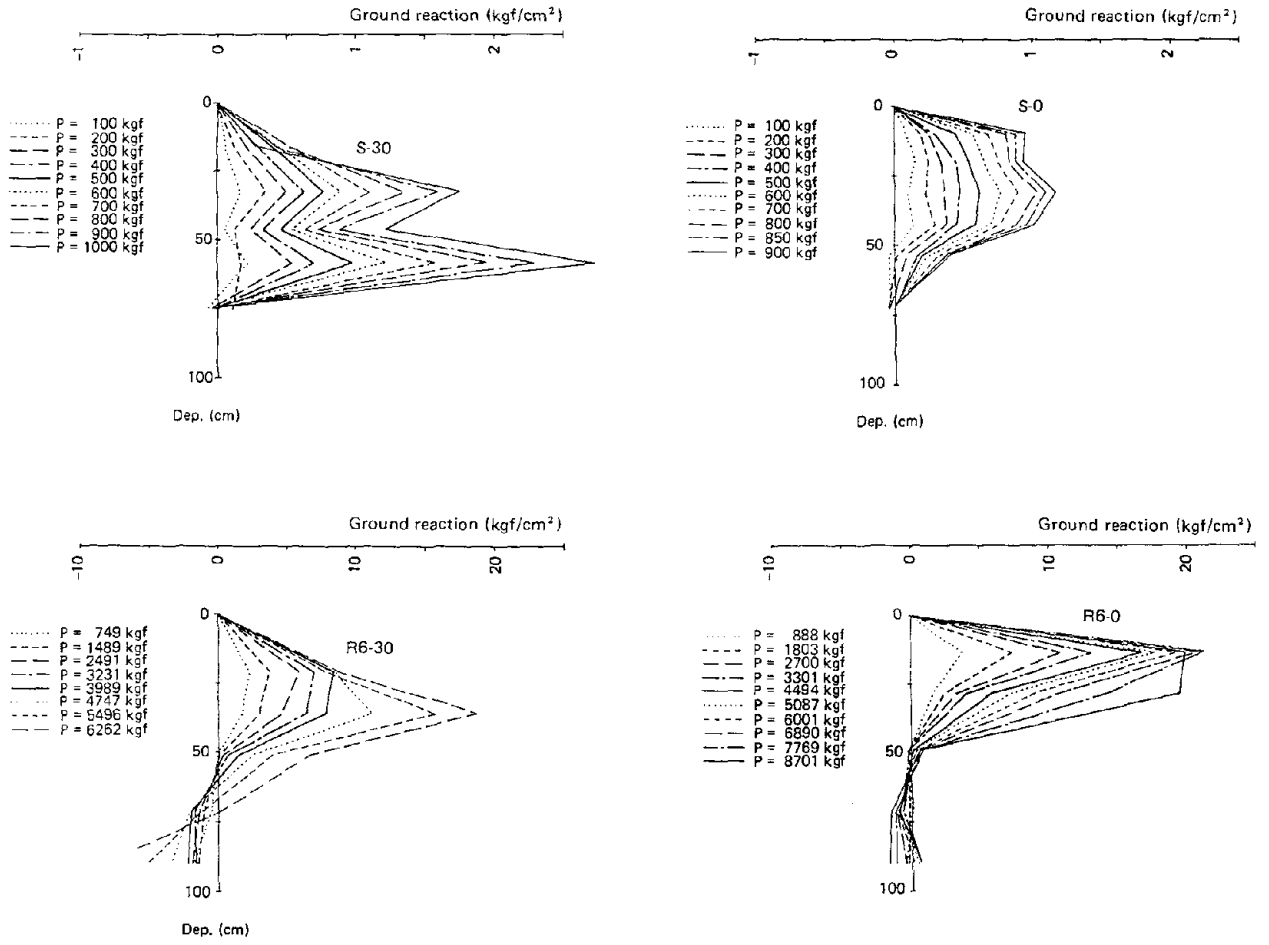

Fig. 3.8 Distribution of Ground Reaction (No. 2)

30) are shown in Fig. 3.6 and Fig. 3.7. These are the results of approximation of M by the 6th-degree polynomial in x. Mention of the other cases is omitted for reason of space.

The center of rotation of the pile (the point at which the ground reaction is 0) is deeper in sloping ground than in level ground and its depth increases with increase of the load. This indicates that the relative rigidity of the pile increases due to the decrease of the k-value by the slope of the ground in front of the pile, the decrease of the k-value by non-linearity, and the apparent decrease of the k-value by the plasticization of the ground in front of the pile near the ground surface; and the pile has assumed a behavior close to that of a caisson.

The position at which the maximum ground reaction of the maximum k-value occurs is deeper in sloping ground than in level ground. This indicates that the k-value is generally small near the ground surface and increases with depth because the ground is unrestrained on its surface. However, in the case of sloping ground, the k-value decreases further because the ground in front of the pile is limited in its horizontal direction near the ground surface.

The ground reaction near the ground surface tends to decrease with the increase of load in the case of sloping ground. This seems to indicate that the ground is plasticized from the ground surface to a certain depth and ground reaction for this extent does not increase with the increase of load. This is more manifest in Fig. 3.8 which shows the distribution of the ground reaction obtained by geometrically differentiating measured values of bending.

3.4.5 Inversely Calculated k-Value (Trapezoidal Distribution)

The distribution of the k-value becomes greater with the increase of depth, as seen in 3.4.4. But here, let us simplify it and assume it to be a trapezoidal distribution, as shown in Fig. 3.9. Since, in this case, ℓ_K in the fundamental equation (3.1) for the stress and displacement of the pile is a function of x, the solution cannot be easily obtained. However, if each k-value at n-points of equal division of the pile are given, it is possible to solve this numerically by the method of redundant reaction.

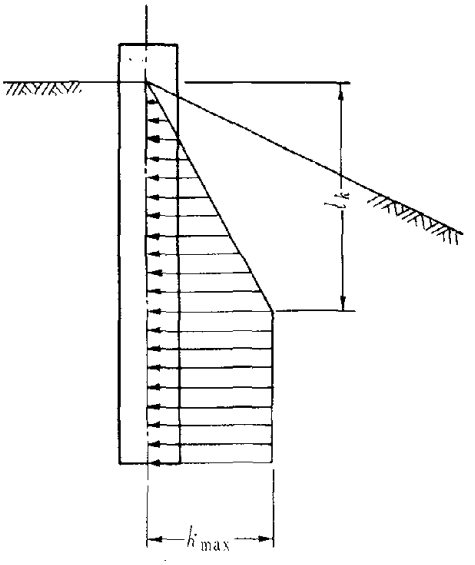

Fig. 3.9 Distribution Shape of k-Values

First, k_{max} is obtained inversely from the measured values of the horizontal force and pile-head displacement for the cases with 0, 20, 40 and 60 cm as values of ℓ_K in Fig. 3.9. Out of the different cases of ℓ_K and k_{max} obtained, the case where the calculated value of the bending moment distribution of the pile agrees well with its measured value is used for the inversely calculated k-value (distribution).

An example of the relation between the calculated value and measured value of bending

moment in the pile thus obtained is shown in Fig. 3.10. It shows ℓ_K of the inversely calculated k-value to be larger in sloping ground than in level ground. The values in agreement with the experimental value for R6, for instance, are in the vicinity of ℓ_K = 60 cm in sloping ground (30°), compared with the vicinity of only ℓ_K = 20 cm for level ground. This is similar to the tendency in the position of occurrence of maximum k-value in the k-value distribution in 3.4.4.

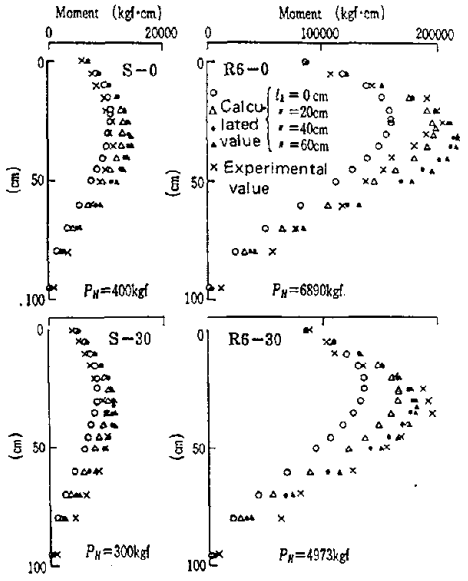

Fig. 3.10 Comparison of Pile Bearing Moment Distribution

4. DESIGN POLICY FOR SINSO PILES ON SLOPED GROUND

4.1 Design Constants

What was known about constants from the model test is consolidated below.

1. The inversely calculated k-value decreases with increase of the inclination angle of the ground.
2. The k-value is small near the ground surface and increases with depth.
3. With the increase of load, the ground is plasticized from the surface to a certain depth.

We shall discuss more about the quantitative evaluation of design constants hereunder.

Let us first see about the k-value distribution. Assuming that the k-value distribution is trapezoidal, as indicated in Fig. 3.9, it is possible to have a numerical solution from load vs. pile-head displacement, as described in 3.4.5. The ratio between the inversely calculated k-value in 3.4.3 and k_{max} obtained from the load vs. pile-head displacement falls with the increase of ℓ_K/D, as indicated in Fig. 4.1. From both Fig. 4.1 and Fig. 3.5, it

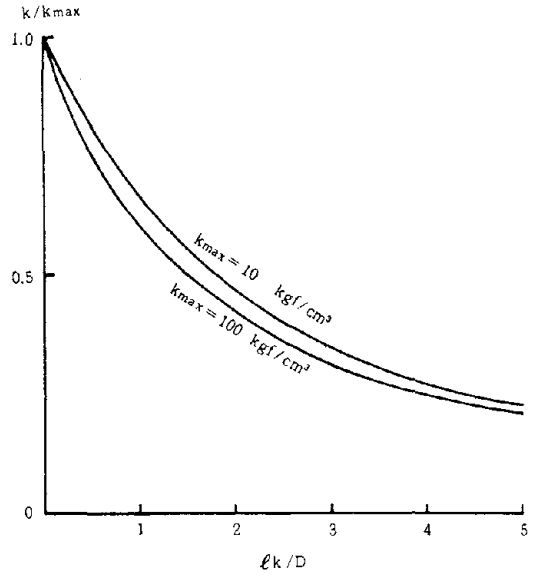

Fig. 4.1 Ratio of Inversely Calculated k-Value and k_{max}

is probably reasonable for ℓ_K to be obtained by Equation (4.1) according to the inclination angle of the ground, Θ.

$$\ell_K/D = \alpha \cdot \Theta \qquad (4.1)$$

where

α = Coefficient of k-value decrease by slope of ground. Believed to be approximately $\alpha = 0.05 - 0.1$.

Θ = Angle of inclination of ground (deg.)

Let us next see about the plastic resistance of the ground. For cases where the ground surface is sloping and the ground is highly cohesive, as it is with soft-rock ground, it seems to be advisable to obtain the plastic resistance by Coulomb's theory of earth pressure, where the equilibrium of forces of the soil body held between the pile and the sliding surface (soil wedge) is considered. Here, let us consider the equilibrium of force indicated in Fig. 4.2, assuming the sliding surface to be plane and

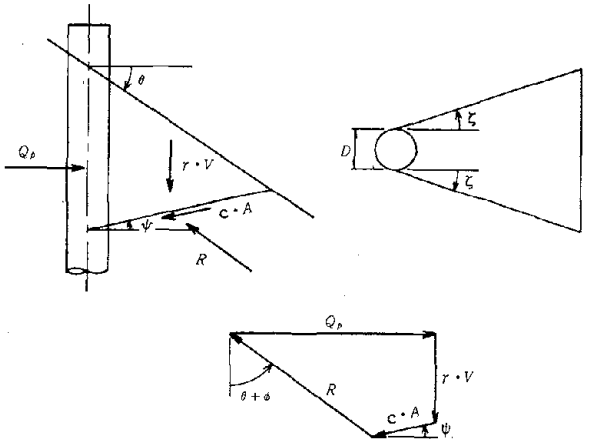

Fig. 4.2 Equilibrium of Forces of Soil Wedge

ignoring resistance on the sides of the soil wedge and friction between the pile and the ground. In this case, plastic resistance Q_p can be obtained by Equation (4.2) providing that the angle of the sliding surface Ψ is the angle at which Q_p is minimal.

$$Q_p = \frac{\gamma \cdot V + c \cdot A \cdot \sin \Psi}{\cos (\Psi + \phi)} \cdot \sin (\Psi + \phi) + c \cdot A \cdot \cos \Psi$$

$$V = \left(\frac{D}{2} + \frac{\cos \theta \cdot \tan \zeta}{\sin (\theta + \Psi)} \cdot \frac{z}{3}\right) \cdot \frac{\cos \theta \cdot \cos \Psi}{\sin (\theta + \Psi)} \cdot z^2 \qquad (4.2)$$

$$A = \left(D + \frac{\cos \theta \cdot \tan \zeta}{\sin (\theta + \Psi)} \cdot z\right) \cdot \frac{\cos \theta}{\sin (\theta + \Psi)} \cdot z$$

where

Q_p = Plastic resistance of ground (kgf)

V = Volume of soil wedge (cm^3)

A = Bottom area of soil wedge (cm^2)

Ψ = Angle formed by sliding surface with horizontal plane

ζ = Spread angle of sliding surface

z = Depth from ground surface to sliding surface (cm)

Fig. 4.3 shows the plastic resistance of ground obtained by Equation (4.2) from the physical constant of the model ground, using $\phi = 40°$ and $c = 1.27$ kgf/cm^2. Since the plastic resistance of ground in Fig. 4.3 is quite close to the ground reaction distribution in Fig. 3.8, it seems to be reasonable for plastic resistance of the ground to be obtained by expression (4.2).

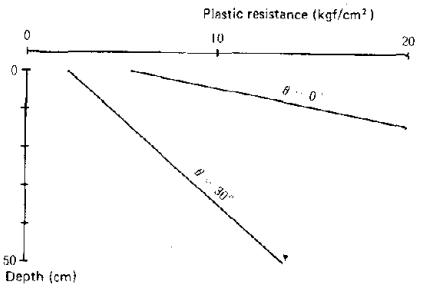

Fig. 4.3 Calculated Value of Plastic Resistance of Ground

Here, the cohesion of the model ground is estimated at 1/2 in consideration of such factors as the variation of ground. Considering also the great impact of the value of c on Q_p calculated by expression (4.2), the ground cohesion must be estimated carefully.

4.2 Design Method

Basically, the elasto-plastic ground reaction method must be used for soft-rock ground, too,

to design sinso piles on sloping ground. For analysis, "the Pile and Caisson Calculating Program Taking the Ground Plasticization into Consideration," (4) prepared by the Foundation Engineering Division, Public Works Research Institute, is used.

The characteristics of this program are as follows:

1. It assumes the use of a limited-length elastic body as a pile.
2. It assumes the use of a completely elastic body as ground. In other words, the relation between ground reaction force and displacement is bilinear.
3. The pile and the ground are subdivided in the depth direction. Therefore, the pile data and ground constants can be changed with depth. Also, a ground constant can be changed rectilinearly even within each of the layers obtained by subdividing.
4. The calculating method used combines the characteristic matrix method and the method of redundant reaction.

Fig. 4.4 compares the experimental values of horizontal force vs. pile-head displacement in soft-rock ground and the values calculated by this program. The values by elasto-plastic calculation agree well with the experimental values. This indicates that if design constants are properly obtained, the behavior of piles on sloping ground can be satisfactorily analyzed by this program.

5. CONCLUSIONS

It has been confirmed that the behavior of piles on sloping ground can be elucidated by a model test and analyzed well by elasto-plastic calculation.

In the future, we are planning to continue analytic studies on the quantitative evaluation of

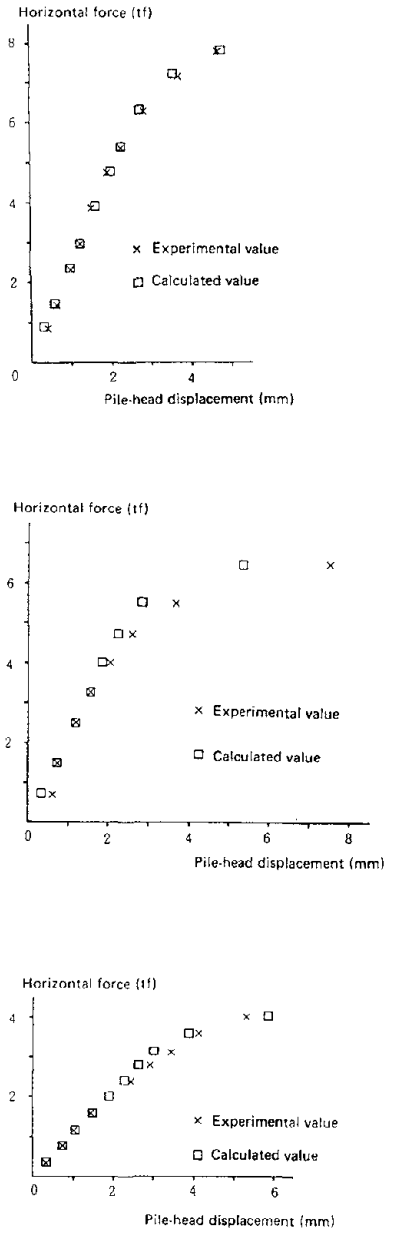

Fig. 4.4 Comparison of Horizontal Force vs. Pile-head Displacement

design constants and the applicability of elasto-plastic calculation in accordance with the results of real-pile tests, and establish a method to design piles for sloping ground.

6. BIBLIOGRAPHY

(1) Japan Road Association: Specifications for Highway Bridges, IV: Substructure, 1980.

(2) Misato Murakami, Kazuya Oshima, Yukio Sato and Ryoichi Abo: Experiments and Research on Lateral Resistance of Piles in Slopes, Sixteenth Joint Meeting, U.S.-Japan Panel on Wind and Seismic Effects, 1984.

(3) Hideya Asanuma et al.: A Study on Pile Foundations in Slopes, Public Works Research Institute Technical Memorandum No. 1949, February 1983.

(4) Yukitake Shioi et al.: Estimation Scheme for Inversely Calculated k-Values in Large Diameter Piles, Public Works Research Institute Technical Memorandum No. 1817, September 1981.

DYNAMIC STRESSES AND DISPLACEMENTS IN A BURIED TUNNEL

S. K. Datta
K. C. Wong
Department of Mechanical Engineering
University of Colorado, Boulder, CO 80309

A. H. Shah
Department of Civil Engineering
University of Manitoba, Winnipeg, Canada R3T 2N2

ABSTRACT

Dynamic three-dimensional response of a tunnel of noncircular shape in an infinite elastic medium has been studied in this paper. Also studied is the two-dimensional (plane strain) response of a tunnel buried in a semi-infinite elastic medium. In both cases it is found that significant dynamic amplification of stresses and displacements occurs in a tunnel embedded in a soft ground when the wavelength is long. In addition, in the latter case the peak values are significantly influenced by the depth of embedment.

1. INTRODUCTION

Dynamic three-dimensional response of a tunnel embedded in an elastic medium is a subject of interest for proper earthquake resistant design. Although this subject has received some attention, no careful analysis is available that takes into account the interaction of the tunnel with its surrounding ground. Our recent studies [1-14] of seismic response of pipelines have shown the importance of the interaction effects. Here we solve by a combined finite element method and eigenfunction expansions the full three dimensional equations of motion of the tunnel and the surrounding infinite ground. The problem gets considerably more complex when the tunnel is embedded in a semi-infinite medium. For the sake of simplifying the computations we then consider the two-dimensional (plane strain) case and show that the depth of embedment plays an important role in determining the dynamic amplification.

2. GOVERNING EQUATIONS AND SOLUTION

It is assumed that the tunnel is infinite in length and is perfectly bonded with the surrounding ground, which is assumed to be linearly elastic, isotropic and homogeneous. Assuming harmonic time dependence, the displacement $u(x,y,z)e^{-i\omega t}$ satisfies the equation

$$\mu^{\alpha}\nabla^2 \underset{\sim}{u} + (\lambda^{\alpha} + \mu^{\alpha})\, \underset{\sim}{\nabla}\, \underset{\sim}{\nabla} \cdot u = -\rho^{\alpha}\omega^2 \underset{\sim}{u} \qquad (1)$$

where λ, μ are Lame constants and ρ the density of the material. Superscript α takes the values I or II depending on whether the point is in the surrounding ground or in the tunnel wall. Note that the region inside the tunnel is empty. Thus the boundary conditions are

$$\tau_{ij}^{II} n_j = 0 \qquad \text{on } S_1 \qquad (2)$$

$$\left.\begin{aligned} \underset{\sim}{u}^{I} &= \underset{\sim}{u}^{II} \\ \tau_{ij}^{I} n_j &= \tau_{ij}^{II} n_j \end{aligned}\right\} \text{ on } S_2 \qquad (3)$$

S_1 and S_2 are the inner and outer surfaces of the tunnel, τ_{ij} is the stress tensor and n is the unit normal vector to S_1 or S_2. The geometry of a tunnel of general cross section is shown in Fig. 1a and the end view of the tunnel considered here is shown in Fig. 1b.

We will consider seismic waves propagating along the length of the tunnel with speed $c = \omega/\epsilon$, where $\lambda(=2\pi/\epsilon)$ is its wavelength. Then it can be shown that the general solution to (1) is given by

$$\underset{\sim}{u} = \underset{\sim}{\nabla}\,\phi + \underset{\sim}{\nabla} \wedge (\psi\, \underset{\sim}{e}_z) + \frac{1}{k_2}\, \underset{\sim}{\nabla} \wedge \underset{\sim}{\nabla} \wedge (\chi\, \underset{\sim}{e}_z) \qquad (4)$$

with

$$\begin{aligned} \phi &= f(x,y)\, e^{i(\varepsilon z-\omega t)} \\ \psi &= g_3(x,y)\, e^{i(\varepsilon z-\omega t)} \\ \chi &= g_1(x,y)\, e^{i(\varepsilon z-\omega t)} \\ k_2 &= \omega/c_2 \end{aligned} \tag{5}$$

Here c_2 is the shear wave speed in the material. The equations satisfied by f, g_1, and g_3 are

$$\nabla^2 f + (k_1^2 - \varepsilon^2) f = 0 \tag{6}$$

$$\nabla^2 \begin{pmatrix} g_1 \\ g_3 \end{pmatrix} + (k_2^2 - \varepsilon^2) \begin{pmatrix} g_1 \\ g_3 \end{pmatrix} = 0 \tag{7}$$

where

$$\nabla^2 \equiv \frac{\delta^2}{\delta x^2} + \frac{\delta^2}{\delta y^2}$$

and $k_1 = \omega/c_1$, c_1 being the longitudinal wave speed in the material.

If the cross section of the tunnel is circular, then Eqs. (6) and (7) can be solved by separation of variables in terms of Bessel functions for each circumferential mode number n. However, for noncircular cross sections this is not useful. But the eigenfunction solution in polar coordinates can be used outside a circle of radius R_B (Fig. 1b) that surrounds the tunnel. The solution in the interior of this circle (B) is obtained by a finite element method and matched with the exterior solution on B by using a variational principle. This is an extension to three dimensions of the method used for two dimensions in [5, 10, 15].

In the exterior region R_1 the solutions f, g_1, and g_3 are

$$f = \sum_{n=-\infty}^{\infty} C_n K_n(\gamma r)\, e^{in\theta} \tag{8}$$

$$g_1 = \sum_{n=-\infty}^{\infty} C_{1n} K_n(\delta r)\, e^{in\theta} \tag{9}$$

$$g_3 = \sum_{n=-\infty}^{\infty} C_{3n} K_n(\gamma r)\, e^{in\theta} \tag{10}$$

where K_n is the modified Bessel function of the second kind and

$$\gamma = \sqrt{\varepsilon^2 - k_1^2}\ , \quad \delta = \sqrt{\varepsilon^2 - k_2^2}.$$

The displacements and stresses in R_1 can be obtained by substituting Eqs. (8) to (10) in (5) and (4) and using the stress - strain relations. Details of these expressions can be found in [16].

The interior region R_2 (including the tunnel) is divided into finite elements having N_1 interior nodes and N_B boundary nodes on B. The displacement field within each element is expressed in terms of the shape functions N_j and the nodal displacements q_j^e

$$\left\{ u^e \right\} = [N] \left\{ q_j^e \right\} \tag{11}$$

where the superscript stands for an element and the subscript j for the jth node of the element. The strain within an element is given by a 6x1 matrix as

$$\left\{ \varepsilon^e \right\} = [L][N] \left\{ q_j^e \right\} = [B] \left\{ q_j^e \right\} \tag{12}$$

where [L] is an operator matrix given by

$$[L] = \begin{bmatrix} \partial/\partial x & 0 & 0 \\ 0 & \partial/\partial y & 0 \\ 0 & 0 & i\varepsilon \\ 0 & i\varepsilon & \partial/\partial y \\ i\varepsilon & 0 & \partial/\partial x \\ \partial/\partial x & \partial/\partial y & 0 \end{bmatrix} \tag{13}$$

Note that in writing (12) and (13) it has been assumed that the displacement of the jth node is

$$\underset{\sim}{q}_j^e \; e^{i\varepsilon z}$$

and the shape functions are independent of z.

The energy functional F can be written as

$$F = \underset{\sim}{q}_{x_I}^{*T} \; S_{II} \; \underset{\sim}{q}_{x_I} + \underset{\sim}{q}_{x_I}^{*T} \; S_{IB} \; \underset{\sim}{q}_{x_B} + \underset{\sim}{q}_{x_B}^{*} \; S_{BI} \; \underset{\sim}{q}_{x_I} + \underset{\sim}{q}_{x_B}^{*T} \; S_{BB} \; \underset{\sim}{q}_{x_B} \tag{14}$$

in which $\underset{\sim}{q}_{x_I} = \underset{\sim}{q}_{x_I}^{II}$ and $\underset{\sim}{q}_{x_B} = \underset{\sim}{q}_{x_B}^{II}$. The superscripts * and T designate complex conjugate and transpose, respectively. The elemental impedance matrices are defined as

$$[S^e] = \iint_{R_e} \{[B^*]^T[D][B] - \rho_e \omega^2 \, [N]^T[N]\} \, dxdy \tag{15}$$

for an isotropic material [D] is given by

$$[D] = \begin{bmatrix} D_1 & D_2 & D_2 & 0 & 0 & 0 \\ D_2 & D_1 & D_2 & 0 & 0 & 0 \\ D_2 & D_2 & D_1 & 0 & 0 & 0 \\ 0 & 0 & 0 & D_3 & 0 & 0 \\ 0 & 0 & 0 & 0 & D_3 & 0 \\ 0 & 0 & 0 & 0 & 0 & D_3 \end{bmatrix} \tag{16}$$

where

$$D_1 = \lambda_e + 2\mu_e, \; D_2 = \lambda_e, \; D_3 = \mu_e.$$

The continuity of the displacement on B implies that

$$\underset{\sim}{q}_{x_B}^{II} = \underset{\sim}{q}_{x_B}^{(s)} + \underset{\sim}{q}_{x_B}^{(i)} \tag{17}$$

where $\underset{\sim}{q}_{x_B}^{(s)}$ is found from (4) by using (5) and (8) and $\underset{\sim}{q}_{x_B}$ is the incident seismic disturbance assumed to have originated outside B. Substituting (17) in (15) and taking variation, we obtain

$$\begin{bmatrix} S_{II} & S_{IB}G_{xy} \\ G_{xy}^{*T}S_{BI} & G_{xy}^{*T}S_{BB}G_{xy} \end{bmatrix} \begin{Bmatrix} \underset{\sim}{q}_{x_I} \\ \underset{\sim}{a} \end{Bmatrix} = \begin{Bmatrix} - S_{IB} & \underset{\sim}{q}_{x_B}^{(i)} \\ - G_{xy}^{*T} \; S_{BB} & \underset{\sim}{q}_{x_B}^{(i)} + \underset{\sim}{p}_B^{(1)} \end{Bmatrix} \tag{18}$$

Here $\underset{\sim}{p}_B^{(1)}$ is the interaction force acting at the nodes on B on the material in R_2 due to that in R_1. Matrix $[G_{xy}]$ is defined by the equation

$$\{ \underset{\sim}{q}_{x_B}^{(s)} \} = [G_{xy}] \; \{\underset{\sim}{a}\} \tag{19}$$

$$\{\underset{\sim}{a}\} = \left\{ c_1 \; c_{11} \; c_{31} \; \cdots \; c_{N_B} \; c_{1N_B} \; c_{3N_B} \right\}^T$$

Note that in writing (18) the series appearing in Eqs. (8) to (10) have been summed from

$n = -\frac{1}{2} N_B + 1$ to $\frac{1}{2} N_B$ and we have written

$c_i = c_{-\frac{1}{2} N_B + i}$, $c_{1i} = c_{1, -\frac{1}{2} N_B + i}$,

$c_{3i} = c_{3, -\frac{1}{2} N_B + i}$ $(i = 1, \ldots, N)$. Consistent with (19) it can be shown that, by using the principle of virtual work,

$$\left\{ p_{\underset{\sim}{B}}^{(1)} \right\} = [R] \{\underset{\sim}{a}\} + \left\{ p_B^{(i)} \right\} \tag{20}$$

where $[R]$ and $\{p_{\underset{\sim}{B}}^{(i)}\}$ are approximated by

$$[R] = R_B \ \Delta\theta \ [G_{r\theta}^{*}]^T [F_{r\theta}], \tag{21}$$

$$\{p_{\underset{\sim}{B}}^{(i)}\} = R_B \ \Delta\theta \ [G_{r\theta}^{*}] \{\sigma_{\underset{\sim}{r}_B}^{(i)}\}. \tag{22}$$

In writing (21) and (22) it has been assumed that the circle B is divided into N equidistant points. The expressions for $[G_{r\theta}]$ and $[F_{r\theta}]$ can be found in [16].

Substituting (20) in (18) and transferring all the terms contained in $\{a\}$ to the left-hand side, we get the following equation to solve for $\{q_{x_I}\}$ and $\{a\}$ simultaneously.

$$\begin{bmatrix} S_{II} & S_{IB}G_{xy} \\ G_{xy}^{*T}S_{BI} & G_{xy}^{*T}S_{BB}G_{xy} - R \end{bmatrix} \begin{Bmatrix} \underset{\sim}{q}_{x_I} \\ \underset{\sim}{a} \end{Bmatrix} = \begin{Bmatrix} -S_{IB} \ \underset{\sim}{q}_{x_b}^{(i)} \\ -G_{xy}^{*T}S_{BB} \ \underset{\sim}{q}_{x_B}^{(i)} + \underset{\sim}{p}_B^{(i)} \end{Bmatrix} \tag{23}$$

Once the interior nodal displacements $\{\underset{\sim}{q}_{x_I}\}$ are known they can be used in (12) to calculate the strains, which in turn can be used to calculate the stresses. The numerical results thus obtained are discussed in the next section.

In the above derivation it was assumed that the surrounding ground was infinite in extent. If the ground is semi-infinite and the tunnel is buried in it at a depth H (Fig. 2), then the representations (8) to (10) have to be modified to include the free surface effects. This causes considerable algebraic complications. The analysis is somewhat simplified if it is assumed that the waves are moving perpendicular to the length of the tunnel and there is no displacement along the length. This corresponds to setting $\varepsilon = 0$ in Eqs. (5) to (7) and $\chi = 0$ in Eq. (4). The corresponding solution has recently been discussed in [10] and some of the numerical results presented there for this case are discussed in the following section.

3. NUMERICAL RESULTS AND DISCUSSION

Numerical results are first presented for the case of a tunnel embedded in an infinite medium. It is assumed that the tunnel is excited by plane P, SV and SH waves propagating in the yz-plane. The potentials ϕ, χ, and ψ (Eq. 4) for these three incident waves are given by:

(1) P wave

$$\phi^{(i)} = e^{i(\varepsilon z+\gamma_1 y)-i\omega t}, \quad \psi^{(i)} = \chi^{(i)} = 0.$$

(2) SV wave

$$\chi^{(i)} = \frac{k_2}{i\delta_1} e^{i(\varepsilon z+\delta_1 y)-i\omega t}, \quad \phi^{(i)} = \psi^{(i)} = 0.$$

(3) SH wave

$$\psi^{(i)} = \frac{k_2}{i\delta_1} e^{i(\varepsilon z+\delta_1 y)-i\omega t}, \quad \phi^{(i)} = \chi^{(i)} = 0.$$

Note that if θ_0 is the angle made by the incident wave propagation direction with the y-axis then $\varepsilon = k_1 \sin\theta_0$ for the P wave and $\varepsilon = k_2 \sin\theta_0$ for the S wave. Thus $\gamma_1 = k\cos\theta_0$ and $\delta_1 = k_2\cos\theta_0$.

The material making up the tunnel is assumed to be concrete with the properties

$\rho \equiv$ mass density = 2.24 kg/m^3

$E \equiv$ Young's modulus = 1.6×10^7 kN/m^2

$\sigma \equiv$ Poisson's ratio = 0.2

Two types of ground materials were considered. The properties are given in table 1.

Different incidence angles were considered. For each angle of incidence axial and hoop stresses were computed at the outer surface of the tunnel wall and were normalized with respect to the maximum stress associated with the incident wave. In Figs. 3 and 4 maximum normalized axial

and hoop stresses for incident P wave are shown against the incident angles. Here case I refers to tunnel in soft soil and case II that in rock. It is seen that in case I the hoop stress is nearly constant and is always greater than the axial stress. In case II, however, the hoop stress decreases rapidly with increasing θ_0 and becomes less than the axial stress when the wave is moving nearly along the axis of the tunnel. Also, larger stresses are induced in case I than in case II. Fig. 5 shows the comparison of the hoop stresses in cases I and II at two different frequencies. Here the incidence angle is 5°. Fig. 6 shows the corresponding results for θ_0 = 85°.

We then show in Figs. 7 and 8 the maximum axial and hoop stresses for incident SV wave. It is found that much larger axial stresses are induced in case I than case II. Also axial stresses are much larger than the hoop stresses in case I, whereas they are nearly the same in case II. Figs. 9 and 10 show the results for SH wave. Here it is found that maximum hoop stress decreases with increasing θ_0 both in case I and case II. On the other hand, axial stress increases with θ_0 in case I but decreases in case II.

Comparison of the results for the three types of incident waves shows that when the waves are moving nearly along the axis, maximum stress is induced by a P wave. At an intermediate angle, however, SV wave induced the largest axial stresses. At nearly vertical incidence, it is the SH wave that causes the largest hoop stress.

In the next set of figures we show the hoop stresses induced in a tunnel embedded in a semi-infinite elastic medium. As mentioned before, we considered now the plane strain case (ε=0). Plane P, SV, and Rayleigh wave incidences were considered. The material properties of the tunnel and the ground were the same as described before. Figs. 11 and 12 show the results for a plane P wave moving at an angle of 40° with the negative y-axis. It is seen that the hoop stresses increase with frequency at small depths, but increase initially with frequency and then decrease for large depths. It is also seen that larger stresses occur at smaller depths. For comparison purposes the results for SV wave for tunnels in rock and soft soil are shown in Fig. 13. Much larger stresses are found to occur in case I than in case II. Also, the variation of stresses along the circumference is significantly different in the two cases. This was found to be true for the P wave also. Variation of hoop stresses in a tunnel with the changes in the angle of incidence of SV wave is shown in Fig. 14. Large variations are found to occur with different angles of incidence and these are more pronounced in case II than in case I. For P wave it was found that in case II results were not too sensitive to changes in the angle of incidence. Finally, Fig. 15 shows the variation of hoop stress with frequency for an incident Rayleigh wave moving along the positive x-axis. This figure is to be contrasted with Fig. 12, where incident P wave is considered. Very large stress concentrations are caused by Rayleigh waves near the corners of the base of the tunnel, more so on the shadow side than on the illuminated side. This was found also for SV waves (Fig. 14).

4. CONCLUSION

In this paper we have presented a combined finite element and eigenfunction expansion technique to solve the problem of seismic response of a noncircular shaped tunnel. Three-dimensional dynamic response analysis of the tunnel in an infinite medium shows that large hoop stresses develop in the tunnel wall when the surrounding ground is soft. In fact, these are always larger than the axial stresses for incident P waves. It is also found that the SV waves induce the largest axial stresses in the wall when the surrounding ground is soft. The

effect of depth of embedment of the tunnel in a half-space is found to be quite significant. For the sake of simplifying our calculations we have considered only the plane strain problem in this case.

This study suggests that future research should take into account the effect of layering in a half-space on the dynamic three-dimensional response of buried tunnels. It appears that the presence of soft layers overlying hard substrate may significantly influence the response.

5. ACKNOWLEDGMENTS

The work reported here was supported in part by a grant (CEE 81-20536) from the National Science Foundation under the Earthquake Hazards Mitigation Program. Partial support was received also from the Natural Science and the Engineering Research Council of Canada by grant A-7988.

6. REFERENCES

1. S. K. Datta, A. H. Shah, and T. Chakraborty, "Dynamic Response of Pipelines to Moving Loads," in Earthquake Behavior and Safety of Oil and Gas Storage Facilities, Buried Pipelines, and Equipment, ed. T. Ariman, PVP-Vol. 77, ASME, New York, 1983, pp. 246-253.

2. S. K. Datta, A. H. Shah, and K. C. Wong, "Dynamic Amplification of Stresses and Displacements Induced in a Buried Pipe in a Semi-infinite Medium," CUMER 83-3, Department of Mechanical Engineering, University of Colorado, Boulder.

3. S. K. Datta, T. Chakraborty, and A. H. Shah, "Dynamic Response of Pipelines to Moving Loads," Earthquake Engineering and Structural Dynamics, 12 (1984), pp. 59-72.

4. S. K. Datta, T. Chakraborty, and A. H. Shah, "Dynamic Response of Pipelines to Moving Loads," Proceedings of the Eighth World Conference on Earthquake Engineering, July 21-28, San Francisco, CA, Vol. VII, pp. 295-302

5. S. K. Datta, A. H. Shah, and K. C. Wong, "Dynamic Stresses and Displacements in Buried Pipe," ASCE Journal of Engineering Mechanics, 110 (1984), pp. 1451-1466.

6. K. C. Wong, A. H. Shah, S. K. Datta, and P. M. O'Leary, "Dynamic Amplification of Displacements and Stresses around Buried Pipelines and Tunnels," in Earthquake Source Modeling, Ground Motion, and Structural Response, ed. S. K. Datta, AMD-Vol. 10, PVP-Vol. 80, The American Society of Mechanical Engineers, New York, 1984, pp. 147-161.

7. K. C. Wong, A. H. Shah, and S. K. Datta, "Dynamic Amplification of Stresses and Displacements Induced in a Buried Tunnel," CUMER 84-1, January 1984, Department of Mechanical Engineering, University of Colorado, Boulder.

8. P. M. O'Leary and S. K. Datta, "Dynamic Response of Buried Pipeline at Low Frequencies," Journal of Pressure Vessel Technology, Transactions of ASME, 107 (1985), pp. 44-50.

9. S. K. Datta, P. M. O'Leary, and A. H. Shah, "Dynamic Response of Buried Pipelines to Incident Longitudinal and Shear Waves," CUMER 84-3, January 1984, Department of Mechanical Engineering, University of Colorado, Boulder. (Also to appear in Journal of Applied Mechanics.)

10. K. C. Wong, A. H. Shah, and S. K. Datta, "Dynamics Stresses and Displacements in a Buried Tunnel," ASCE Journal of Engineering Mechanics, 111, (1985), pp. 218-234.

11. P. M. O'Leary and S. K. Datta, "Dynamics of Buried Pipelines," to appear in the Advances in Underground Pipeline Engineering, ASCE, 1985.

12. P. M. O'Leary and S. K. Datta, "Dynamics of Buried Pipelines," to appear in the International Journal of Soil Dynamics and Earthquake Engineering, 1985.

13. K. C. Wong, A. H. Shah, and S. K. Datta, "Dynamics of Underground Pipelines and Tunnels," to be presented at the 1985 PVP Summer Conference, New Orleans, LA, June 23-27, 1985. Also to appear in the Proceedings.

14. S. K. Datta, A. H. Shah, and P. M. O'Leary, "Seismic Response Analysis of Embedded Pipelines," to be presented at the 2nd International Conference on Soil Dynamics and Earthquake Engineering, June 28-July 3, 1985. Also to appear in the Proceedings.

15. S. K. Datta, K. C. Wong, and A. H. Shah, "Dynamic Stresses and Displacements around Cylindrical Cavities of Arbitrary Shape," Journal of Applied Mechanics, Transactions of ASME, 51 (1984), pp. 798-803.

16. K. F. Chow, Three Dimensional Motion of a Tunnel Buried in an Infinite Medium, M.S. Thesis, Department of Civil Engineering, University of Manitoba, Winnipeg, Canada.

TABLE 1

Material Properties of Soft Soil and Rock

Material Properties	Case I Soft Soil	II Rock
ρ kg/m^3	$2.665 * 10^3$	$2.665 * 10^3$
E N/m^2	$6.9 * 10^8$	$7.567 * 10^9$
σ	0.45	0.25

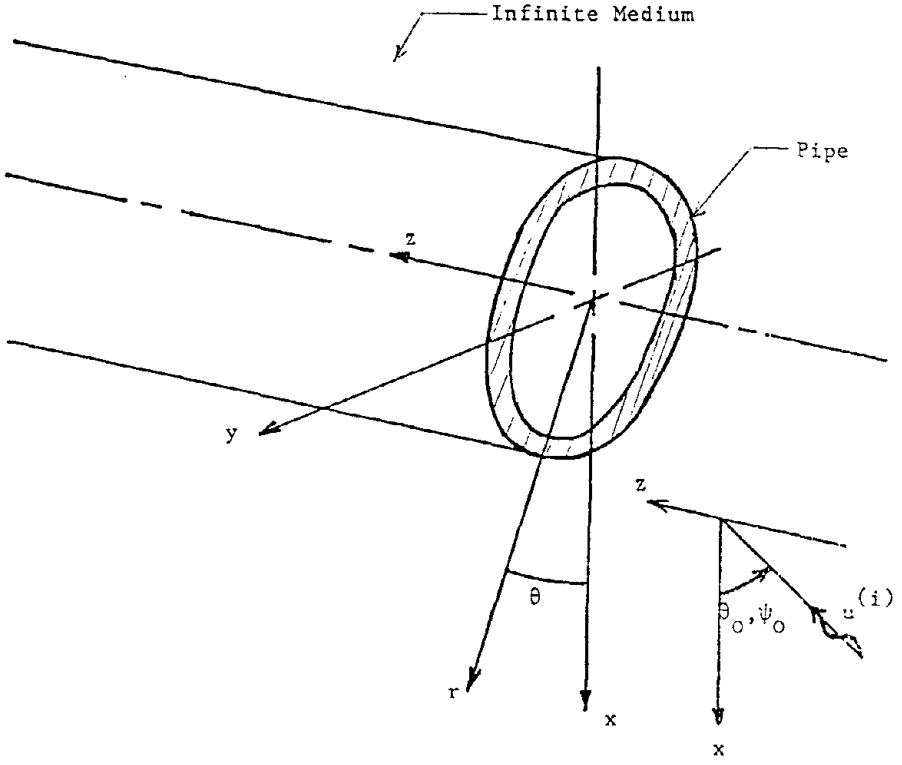

Fig. 1a Geometry of the Pipe or Tunnel

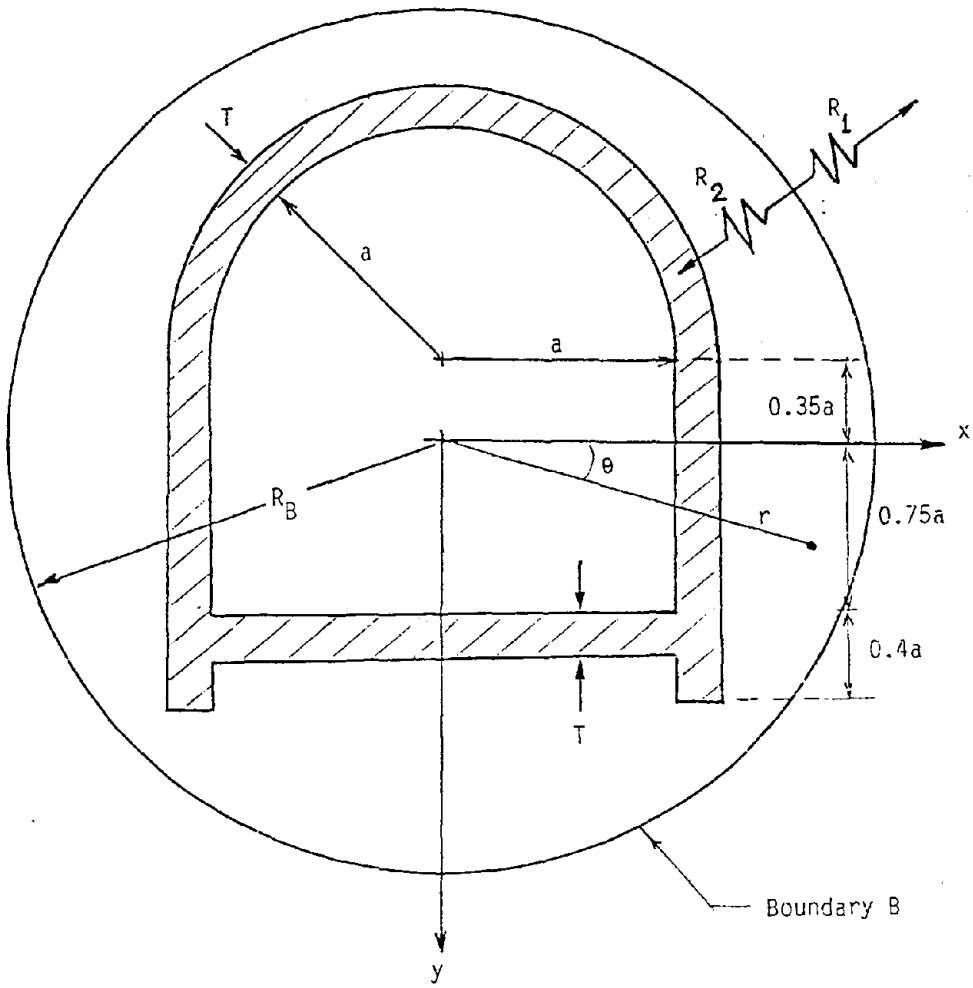

Fig. 1b Geometry of Tunnel (End View)

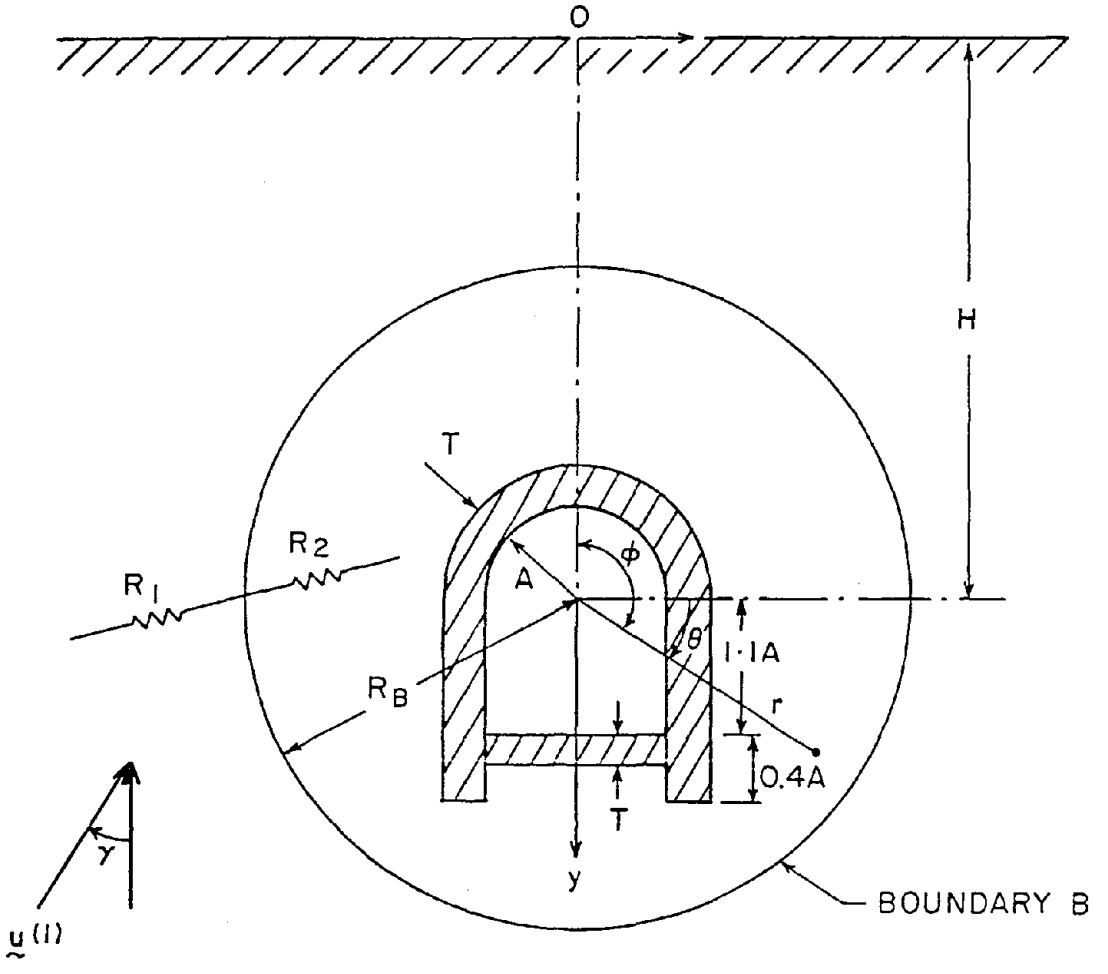

Fig. 2 Tunnel in a Half-space

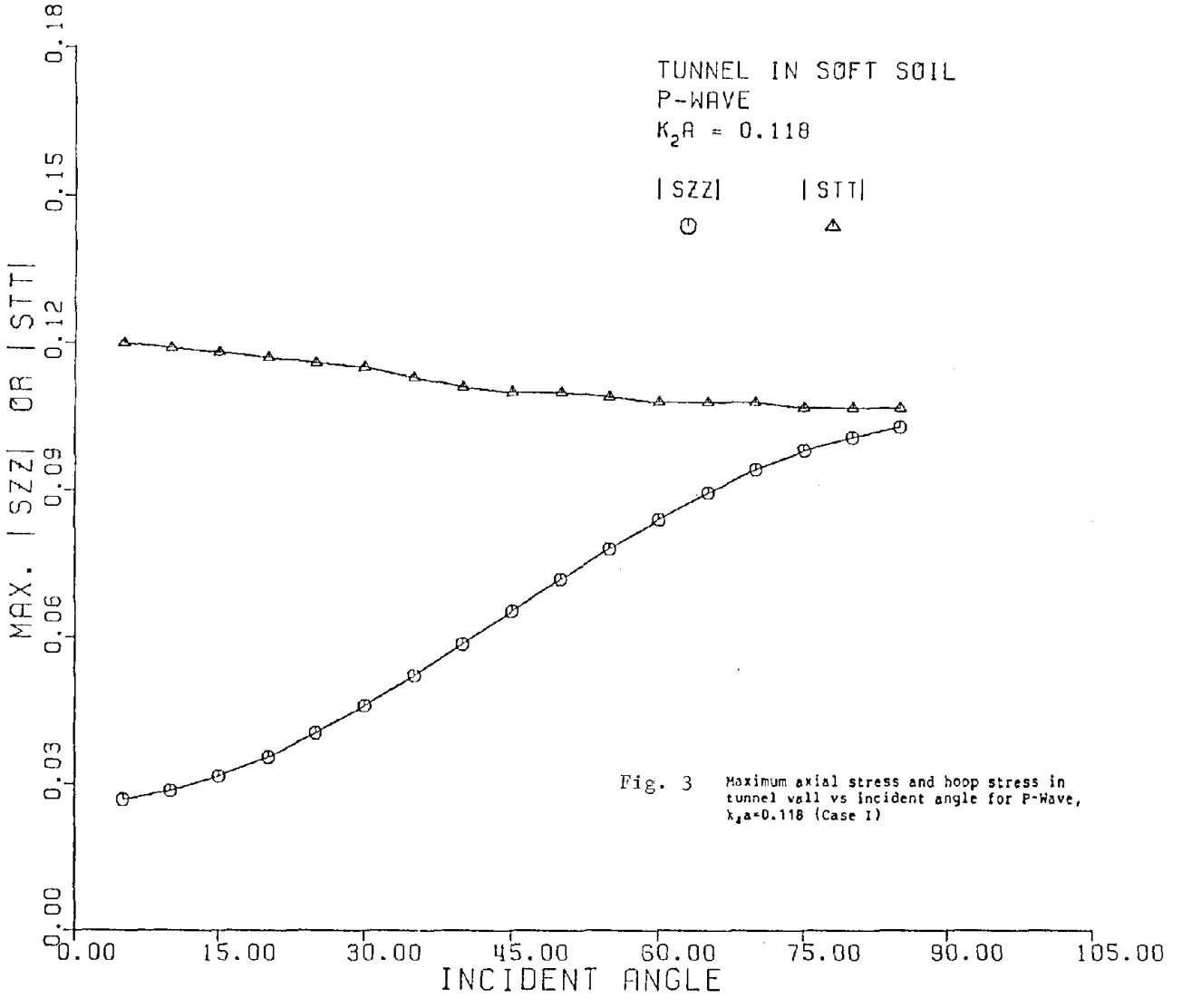

Fig. 3 Maximum axial stress and hoop stress in tunnel wall vs incident angle for P-Wave, k_2a=0.118 (Case I)

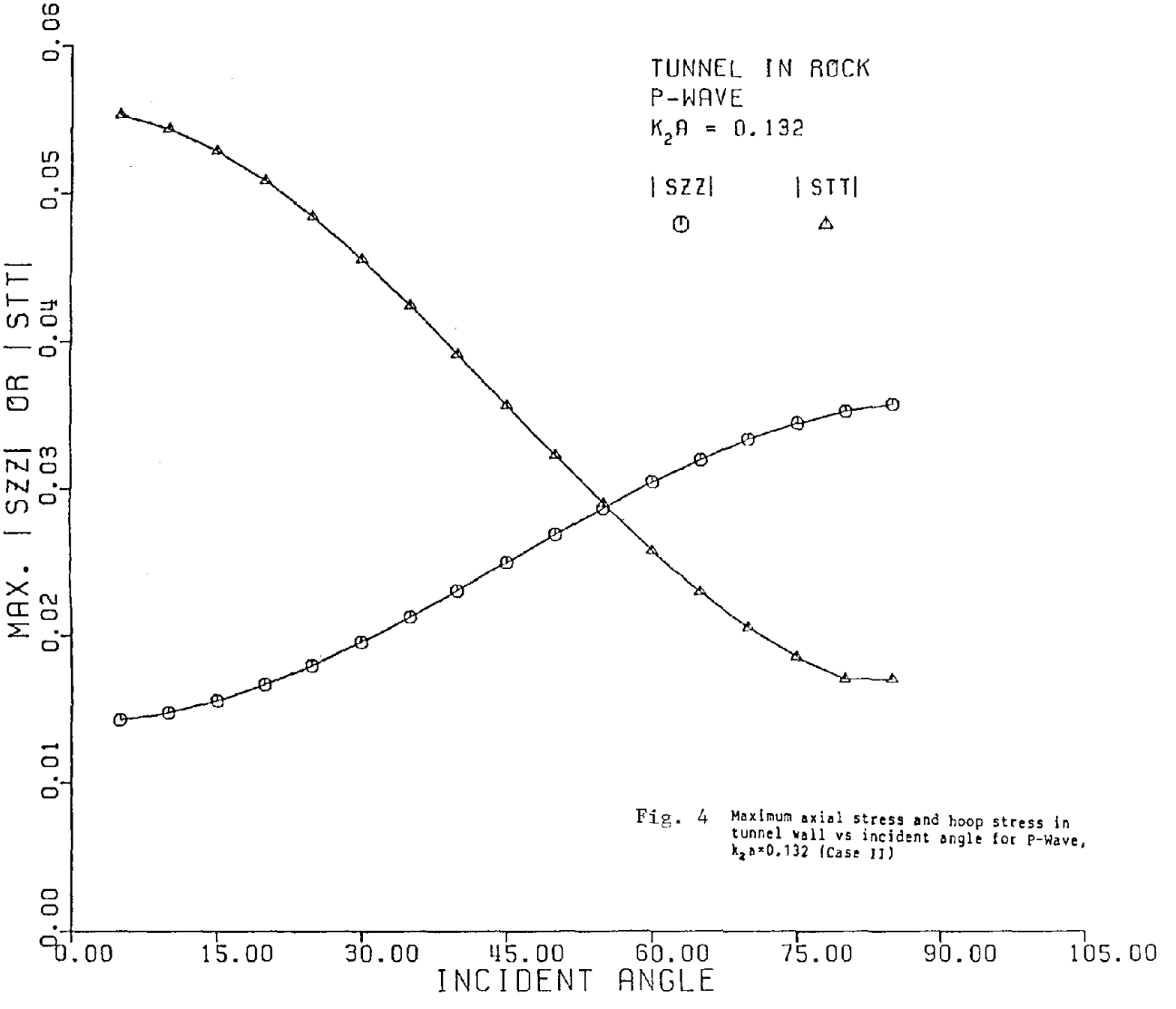

Fig. 4 Maximum axial stress and hoop stress in tunnel wall vs incident angle for P-Wave, k_2a=0.132 (Case II)

P-WAVE (5 DEG.)
STT (CONCRETE)

TUNNEL IN ROCK			TUNNEL IN SOFT SOIL		
$\frac{\omega A}{2\pi}$ (M/SEC)		NF	$\frac{\omega A}{2\pi}$ (M/SEC)		NF
89.50	+	0.277	89.50	○	3.530
134.33	×	0.623	134.33	△	7.930

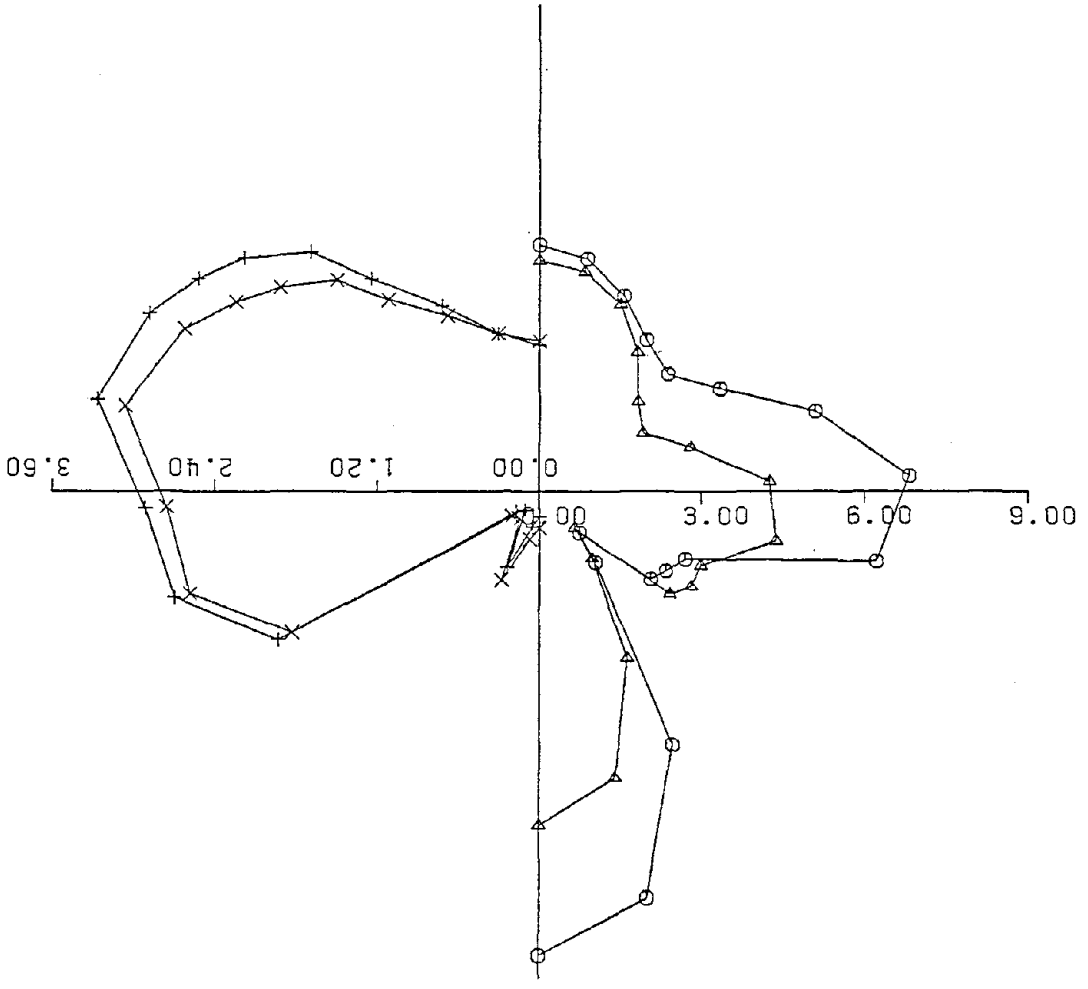

Fig. 5 Comparison between Case I and Case II for normalized hoop stress in tunnel wall for P-Wave, incident angle = 5°

P-WAVE (85 DEG.)
STT (CONCRETE)

TUNNEL IN ROCK			TUNNEL IN SOFT SOIL		
$\frac{\omega a}{2\pi}$ (M/SEC)		NF	$\frac{\omega a}{2\pi}$ (M/SEC)		NF
89.50	+	0.094	89.50	○	2.910
134.33	×	0.212	134.33	△	6.540

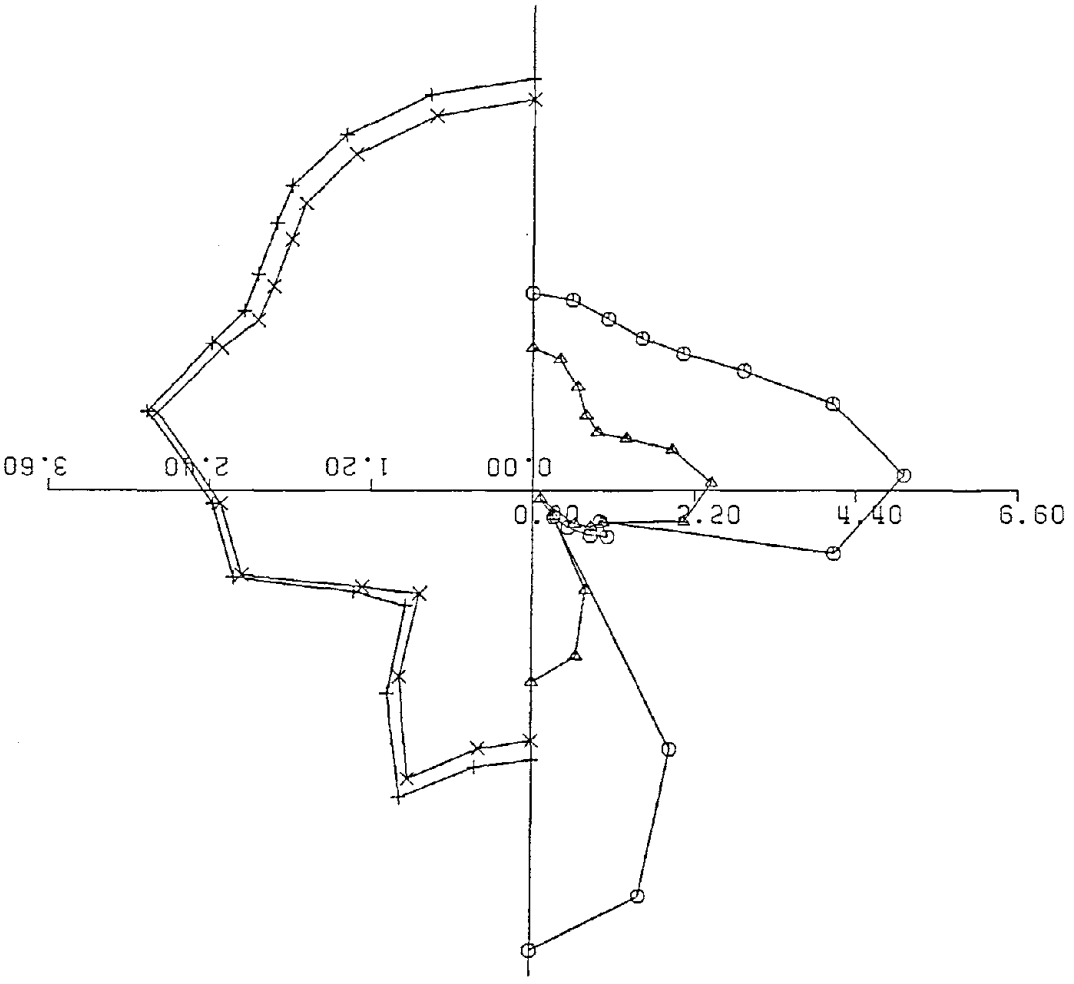

Fig. 6 Comparison between Case I and Case II for normalized hoop stress in tunnel wall for P-Wave, incident angle = 85°

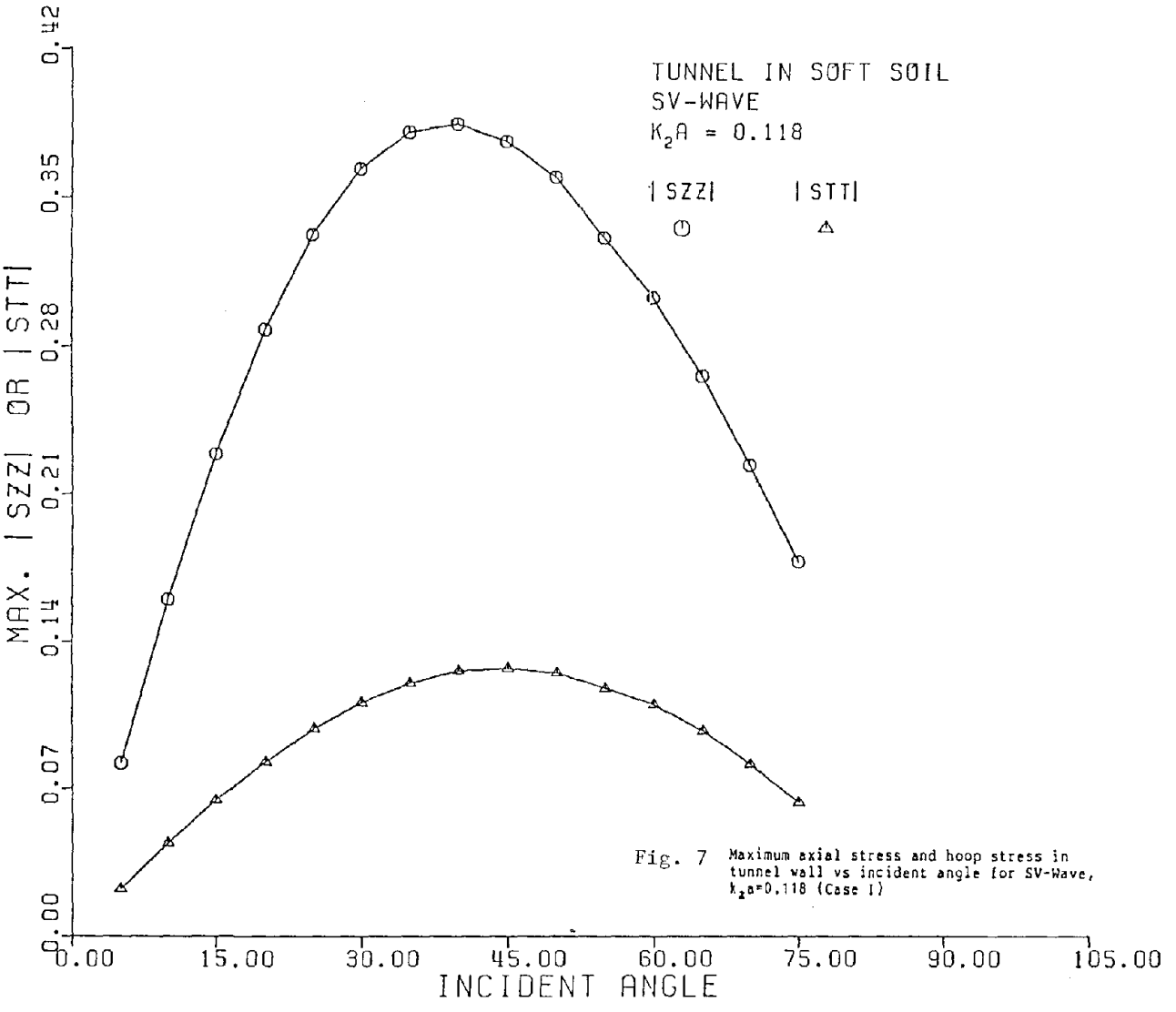

Fig. 7 Maximum axial stress and hoop stress in tunnel wall vs incident angle for SV-Wave, k_2a=0.118 (Case I)

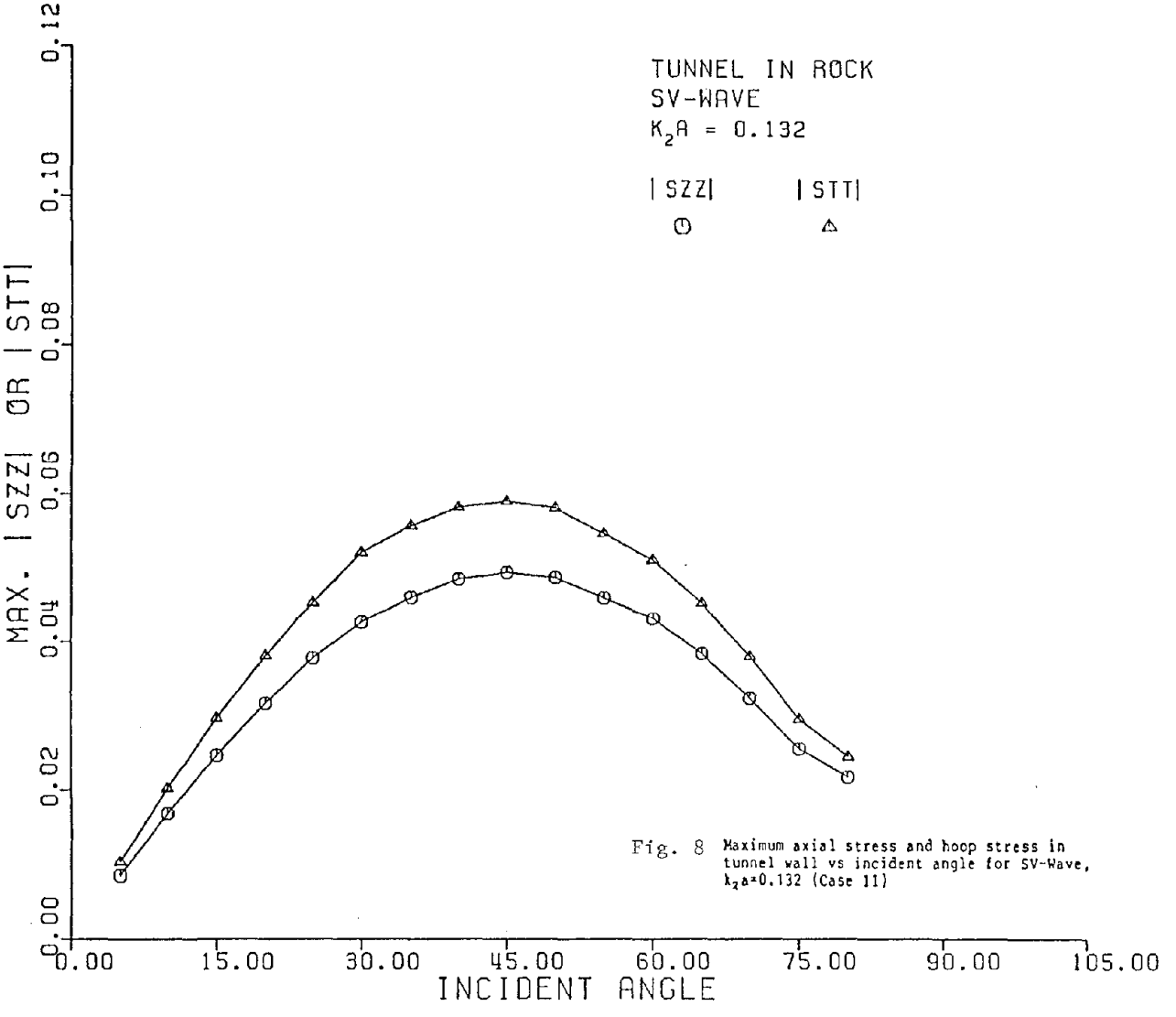

Fig. 8 Maximum axial stress and hoop stress in tunnel wall vs incident angle for SV-Wave, k_2a=0.132 (Case 11)

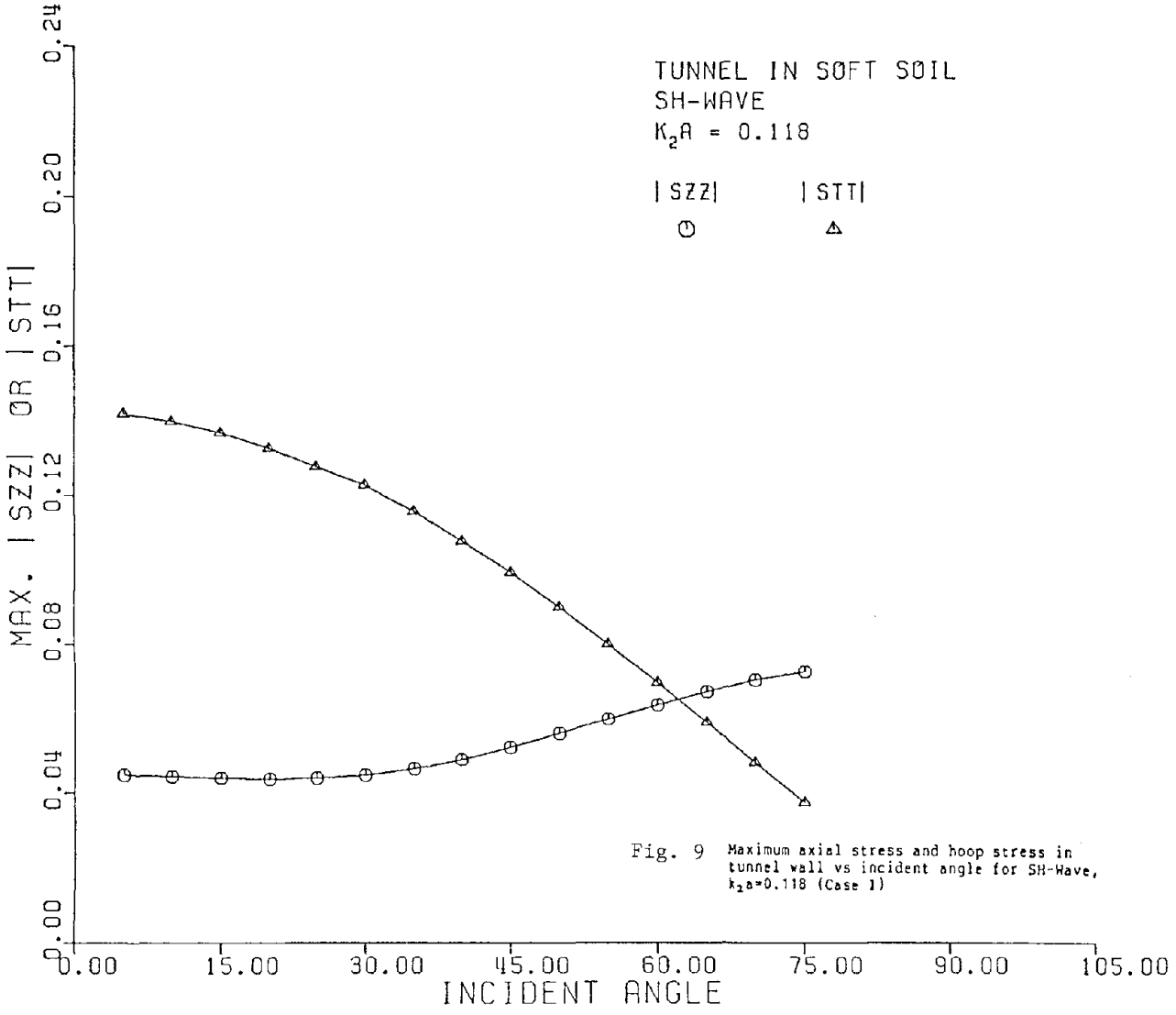

Fig. 9 Maximum axial stress and hoop stress in tunnel wall vs incident angle for SH-Wave, k_2a=0.118 (Case I)

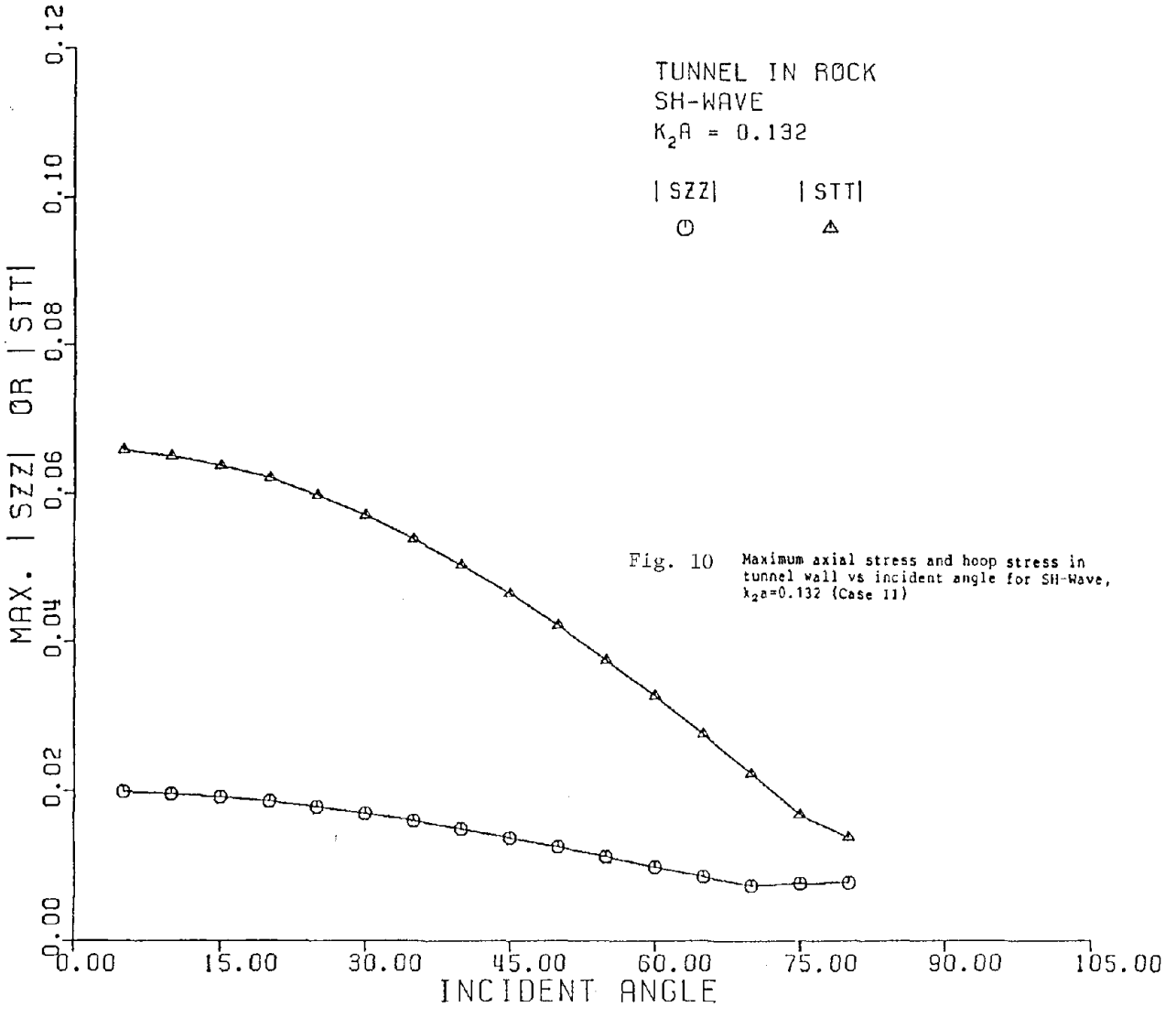

Fig. 10 Maximum axial stress and hoop stress in tunnel wall vs incident angle for SH-Wave, k_2a=0.132 (Case 11)

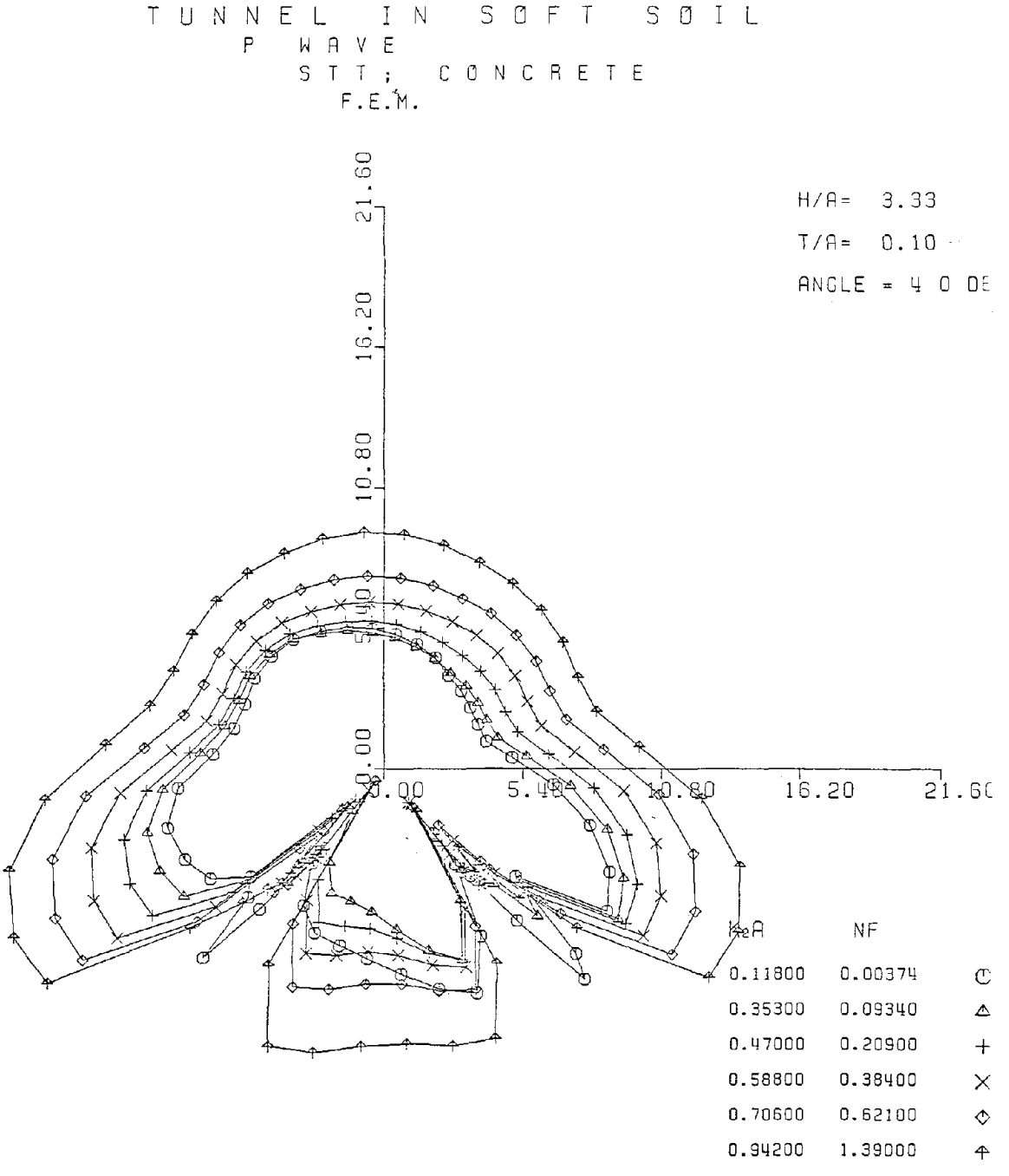

Fig. 11 Hoop Stress in a Tunnel in a Half-space Due to Incident P Wave. Depth Ratio = 3.33

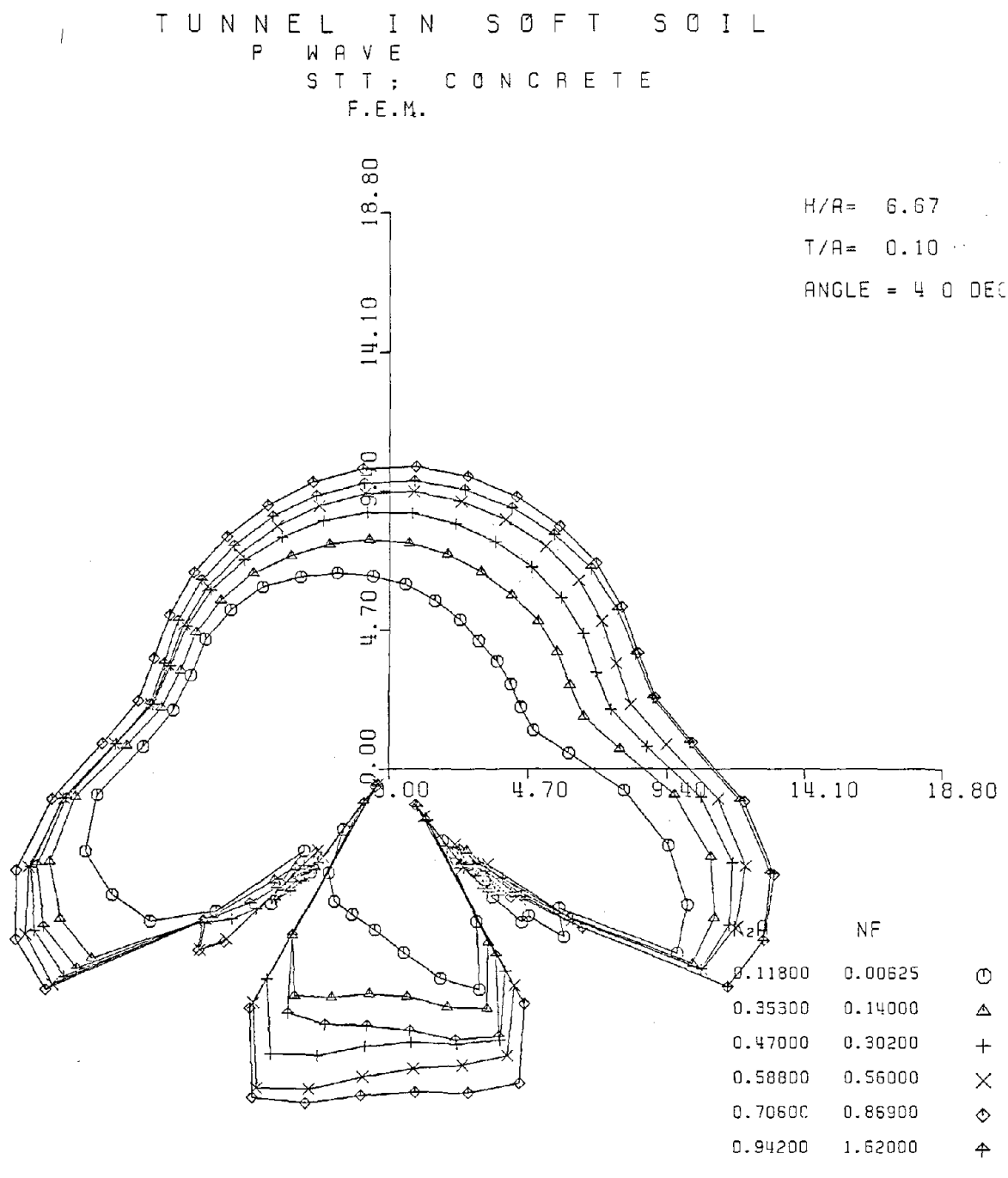

Fig. 12 Hoop Stress in a Tunnel in a Half-space due to Incident P Wave. Depth Ratio = 6.67

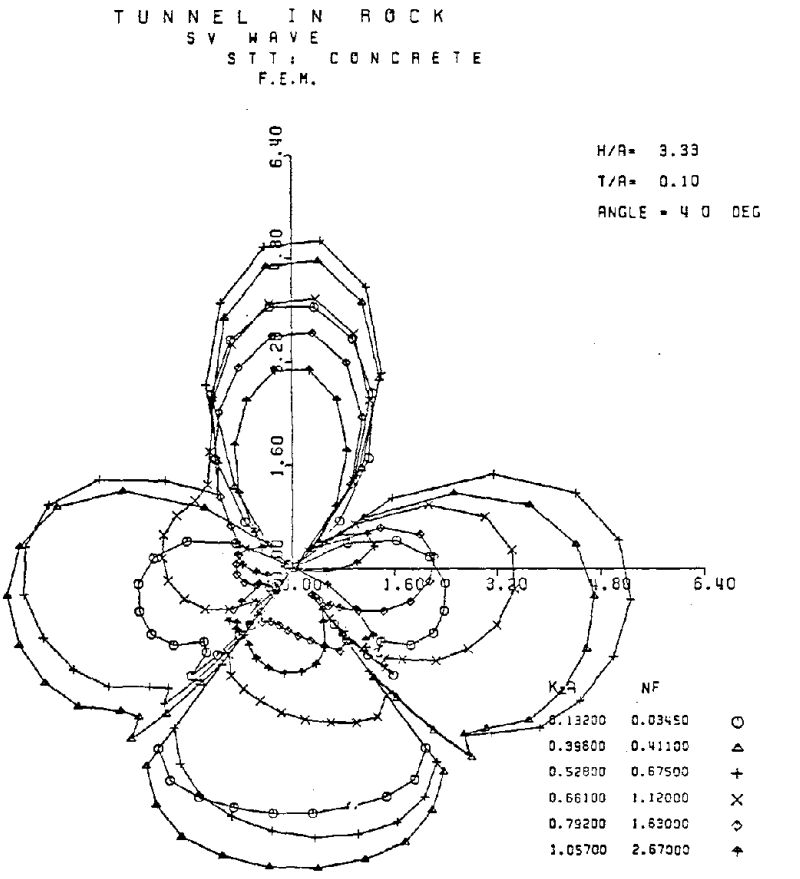

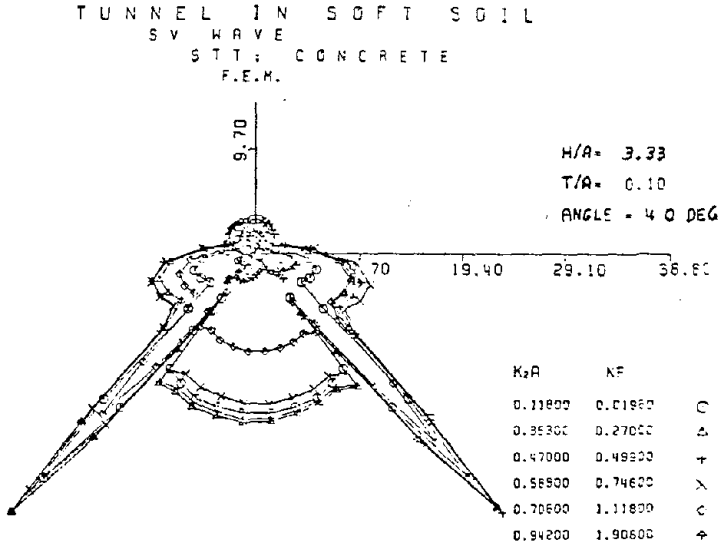

Fig. 13 Hoop Stress in a Tunnel Embedded in Rock and Soft Soil due to Incident SV Wave.

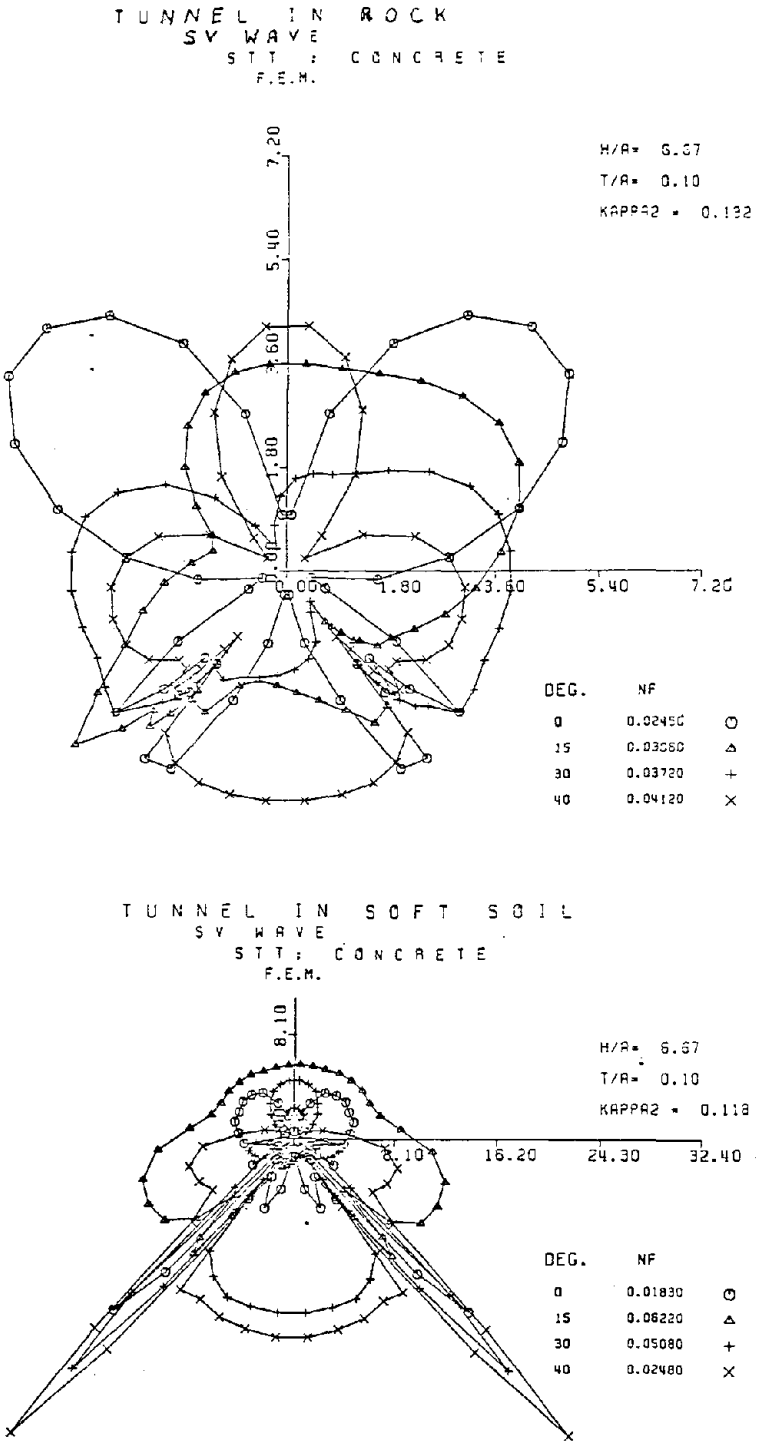

Fig. 14 Hoop Stress in a Tunnel Embedded in Rock and Soft Soil due to SV Wave Incident at Different Angles.

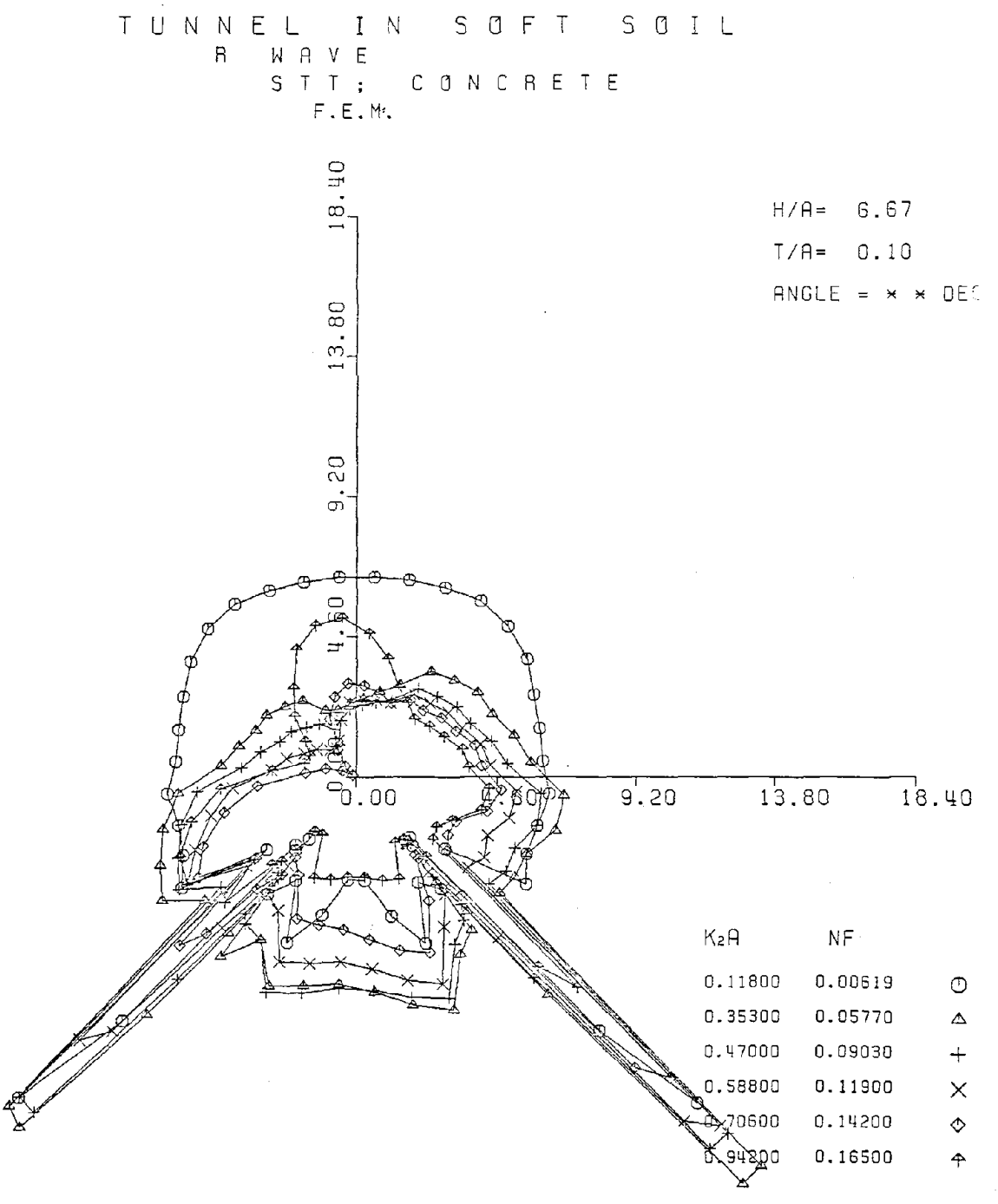

Fig. 15 Hoop Stress in a Tunnel due to Rayleigh Wave Propagating From Left to Right.

Theme III

STORM SURGE AND TSUNAMIS

DAMAGES TO COASTAL AND RIVER STRUCTURES CAUSED BY THE NIHONKAI-CHUBU EARTHQUAKE TSUNAMI

Takaaki Uda, Public Works Research Institute
Atsushi Omata, Public Works Research Institute

Abstract

The 1983 Nihonkai-Chubu Earthquake Tsunami damaged many coastal structures and river administration facilities. These were investigated by using photographs taken right after the tsunami. The dominant types of damage were scouring around the structure, collapsing of the structure, and scattering of the blocks of detached breakwater or wave dissipation breakwater. Damage patterns are classified with respect to the kind of structure and estimated external force. Finally, all instances of damages are counted. In total, 63 coastal structures and 12 river administration facilities were damaged.

1. INTRODUCTION

The Nihonkai-Chubu Earthquake Tsunami which occurred at noon on May 26, 1983, caused devastation along the Japan Sea Coasts. The author reported on the tsunami inundation and the general view of damages due to the tsunami in the previous paper[1]. Many coastal structures and river administration facilities were damaged by the tsunami. In order to consider countermeasures to future tsunamis, it is important to classify the damages to the structures. In this study, photographs illustrating the characteristics of the damage are presented and a pattern classification is done.

The northern coast of Akita Prefecture, as shown in Figure 1, is selected for the study area as extensive tsunami damage was reported there. The damage to coastal structures and river administration facilities are investigated in detail. Typical examples of the damaged structures are the cases of the stair-type revetments in Noshiro Port and Kotohama Coast, the detached breakwaters of the Hachimori Coast and wave dissipation breakwaters of the Minehama Coast.

The circumstances of the damage occurring to the river administration facilities on the Mizusawa, the Hanawa, the Tako and the Yoneshiro Rivers in northern part, and the Shibikawa River in southern part of region are investigated. Most of these rivers are located in the northern part as one group and the rest in the south. No rivers enter the sea between the Yoneshiro River and Kotohama Coast as shown in Figure 1 and sand dunes extend along the coastline. There is a sea cliff between Kotohama Coast and Oga Peninsula. This cliff is interrupted at some locations along the coast by small streams emptying into the sea producing a lowland around the mouth. The Shibikawa River is one of the rivers having such a characteristic. In the following sections, damage to structures due to the tsunami are shown by some photographs and a pattern classification of damages is made.

2. DAMAGES TO COASTAL STRUCTURES

In this section damage to coastal structures due to the tsunami are discussed. The kinds of structures damaged are coastal revetments, detached breakwaters and wave dissipation breakwaters only. Some characteristic cases will be discussed, since it is impossible to investigate all of the cases of damages to the structures.

An example of a damaged coastal revetment is the stair-type revetment in Noshiro Port. The coast is located north from the Yoneshiro River. Figure 2 shows the damage to the stair-type revetment. At the end joint of the revetment a depression occurred and a large crack was formed between the stair part of the revetment and the top. The foundation of the top of the revetment was scoured by the tsunami. The cause of the damage is considered to be due to both the earthquake and the tsunami, judging from the form of the damage to the revetment.

A second example is the damage to the stair-type revetment on the in Kotohama Coast. Figure 3 shows the situation behind the revetment. The top of the revetment, which is made of concrete 20 cm thick, collapsed. A small drainpipe existed at this site.

The return flow of the tsunami that overflowed the top of the revetment concentrated on the pipe. Therefore, it is believed that the earth around the drainpipe was washed away, forming a cavity, and allowing the top of the revetment to collapse.

One characteristic damage due to the 1983 Nihonkai-Chubu Earthquake Tsunami was the scattering of concrete blocks. The damage is revealed in photographs. A general view of these has already been given in the previous paper[1]. Figure 4 was taken from the shore near the detached breakwater along the Hachimori Coast right after the first onset of the tsunami. The seabed beyond the detached breakwater is visible since the tsunami has retreated offshore. The blocks are scattered around the detached breakwater. Figure 5 shows the detail of the scattering of the blocks, including many 8-ton blocks scattered toward the shore.

Next, an example of damage to wave dissipation breakwaters is shown. Wave dissipation breakwaters differ from detached breakwaters on the position of construction relative to the shoreline. A detached breakwater is built off the initial shoreline. On the other hand a wave dissipation breakwater is built on the beach inland from the shoreline. Figure 6 shows the scattering of blocks of wave dissipation breakwater at the Minehama Coast. Concrete blocks weighing 4 tons were scattered deep into the protection forests. The forests were damaged, but they were effective in preventing concrete blocks or floating debris from being transported deep into the land. The return flow frequently concentrated on a narrow zone along the sand dunes. In such a region the sand dunes were eroded due to the return flow of the tsunami as shown in the figure. Figure 7 shows the same kind of situation of scattering of blocks on the Minehama Coast.

Regarding the scattering of blocks, it is thought that the buoyancy effect caused by the rise of sea water level and the high velocity of the tsunami front have important roles, though the exact nature is not known. The tsunami propagated on the gently sloping bottom as shown in Figure 1, and then in the form of a bore with short period oscillations[2]. This must effectively increase the impulsive force exerted on structures.

2.1 Damage to River Structures

Damages to the river administration facilities in five rivers in Akita Prefecture are shown. The locations of these five rivers are depicted in Figure 1. In what follows, damage in each river is investigated in detail by using photographs.

In the Mizusawa River the river revetment which was located 300 m from the river mouth was broken for a distance of 148 m. The revetment collapsed and extensive scouring occurred behind the revetment. The foot protections in front of the revetment were carried away. Figures 8 and 9 show the characteristics of the damages. These photographs were taken from the downstream and upstream ends of the revetment, respectively. The earth behind the revetment was washed away. The downstream side of the revetment has fallen down and the upstream side was scoured severely due to the tsunami overflowing the revetment. The cause of the breakdown of the revetment is as follows. First, the tsunami caused scouring behind the revetment and the stability of the structure was decreased. Next, it was collapsed by the return flow of the tsunami.

In the Hanawa River the revetment which was located 250 m from the river mouth was broken for a distance of 202 m. Damages due to the collapsing of the slope protection and the scouring of the embankment are noted. Figures 10 and 11 show the damage to the embankment. Figure 10 was taken from the downstream side of the damaged embankment. The embankment was broken severely at the location adjacent to the river mouth. Figure 11 shows the details of the damaged revetment of combined blocks. The combined blocks were gathered together. Because the body of the dike was made of earth, it was broken easily and the embankment was scoured.

The Tako River meanders in the counterclockwise direction near the river mouth. The dike of the meandering part of the river was reinforced with a revetment. The revetment facing to the sea was severely broken. Figure 12 was taken from the river mouth looking in the upstream direction. The river dike was eroded at two locations: right and left from the center of Figure 12. The embankment shown near the center of Figure 12 was severely damaged

and a bridge crossing the river was carried away. The slope protection of the embankment was also broken. Figure 13 shows the details of damage to the embankment at the downstream side. The blocks were scattered, and the top of the embankment was eroded severely. Figure 14 shows the damage at the upstream site. A large scouring hole was formed behind the dike. The hole formed by scouring was 55 m long, 18 m wide and 2.5 m deep at maximum. Figure 15 shows the scouring of the abutment shown in the lefthand side of Figure 14. The ground under the abutment was scoured to a depth of about 0.7 m.

In the Yoneshiro River the river revetment was broken due to the vibration of the earthquake and to the tsunami at a location about 600 m upstream from the river mouth. Figure 16 shows the damage to the revetment. The low-water concrete revetment was moved forward and scouring occurred at the top of the revetment although the exact cause is not known. The surmised events are as follows: first, the revetment was partially destroyed by the earthquake, and then the scouring and the subsidence occurred due to the tsunami attack after the earthquake. Near the same location as shown in Figure 17, a high-water revetment of combined concrete was carried away. This may have been due to the tsunami current.

Finally, the damage to the revetment in the Shibikawa River is discussed. The Shibikawa River is located south of the other four rivers as is shown in Figure 1. Sea cliffs stand around the river mouth and a low land is confined near the river mouth. The tsunami strongly invaded into the river mouth from the north and a paddy field was destroyed by the flow over the river revetment. The revetment which extended along the river was extensively broken. The damage to the revetment was severe on the lefthand side of the river. Figure 18 was taken from the right embankment and shows the damage to the revetment on the lefthand side of the river. The main cause of the damage may be due to the return flow of the tsunami, since the revetment collapsed and the fill under the revetment was carried away.

2.2 Pattern Classification of Damage

In the previous sections, the types of damage to coastal structures and river administration facilities were disclosed by using photographs taken right after the tsunami. Here the pattern of the damage and the estimated external force will be discussed. In order to generalize the result of the classification, some patterns of damage which were not observed in the present tsunami will be included.

First, the patterns of damage to coastal dikes and revetments are expressed in Table 1. Damage to structures that was caused mainly by the return flow of the tsunami consist of scouring of the toe, forward inclining or falling down of the revetment and damage to the parapet. Damage to structures due to tsunami run-up include the falling of the upper structure of the coastal dike and damage to the parapet. These were frequently found when reinforced concrete was not used between the body and the upper structure, and when there existed a weak point in the structure.

There are other kinds of damage caused by both the vibration of the earthquake and by the tsunami. The damage to the stair-type revetment occurring at Noshiro Port is an example of these kinds of damage.

Regarding detached breakwaters and wave dissipation breakwaters, a dominant feature of the damage was the scattering of the constituent blocks. This must be one of the characteristics of the present tsunami. In addition, the subsidence of the blocks was frequently found. Table 2 sums up these types of damage. Though it was found that a large number of the blocks had subsided, there was a problem in counting the number. This is because it was not always known whether the cause was due to the tsunami when the subsidence of the blocks was noted or due to wind waves sometime before the tsunami attack.

Patterns of damage to river administration facilities are summed up in Table 3. The kinds of damaged structures include the body of the embankment, the revetment and the foot protection. Slope failure caused by the vibration of the earthquake which occurred near the river mouth was included in the damages to the body of the embankment. In addition, scouring of the slope and the breakdown of the dike were found. Regarding the types of damage to the revetment, breakdown of the slope of the low-water revetment, scouring behind the revetment, forward inclining or falling of the revetment and collapsing of the slope protection were found. The causes are

thought to be as follows: regarding the inclining or falling down of the revetment, scouring behind the revetment is caused by the overflow or the return flow of the tsunami decreasing the stability of the structure. Then the structure collapsed due to the current of the tsunami. The slope protection made of combined blocks was lost when the blocks were carried away by the current of the tsunami.

Finally, Table 4 counts up the number of instances of damage with the classification of the damage pattern. In the table each case was counted as one when two kinds of damages occurred at the same location. The total number of instances of damage to coastal structures and river administration facilities are 63 and 12, respectively.

3. SUMMARY

In this paper the damage to coastal structures and river administration facilities due to the 1983 Nihonkai-Chubu Earthquake Tsunami were investigated by using photographs taken right after the tsunami. Next, the damage patterns were classified with respect to the kind of structures and estimated external force. As a result, tables showing the pattern classification of damages were obtained regarding coastal dike, revetment, detached breakwater, wave dissipation breakwater and river administration facilities. Finally, all of the cases were counted. It is found that the number of instances of damage to coastal structures and river administration facilities are 63 and 12, respectively.

4. REFERENCES

1) Uda, T., Inundation damages due to the 1983 Nihonkai-Chubu Earthquake Tsunami, The 16th Joint Meeting U.S.-Japan Panel on Wind and Seismic Effects, pp. 739-752, 1984.

2) Shuto, N., Behavior of the 1983 Nihonkai-Chubu Earthquake Tsunami in the northern part of Akita Prefecture, 31 Japanese Conf. on Coastal Eng., pp. 247-251, 1984 (in Japanese).

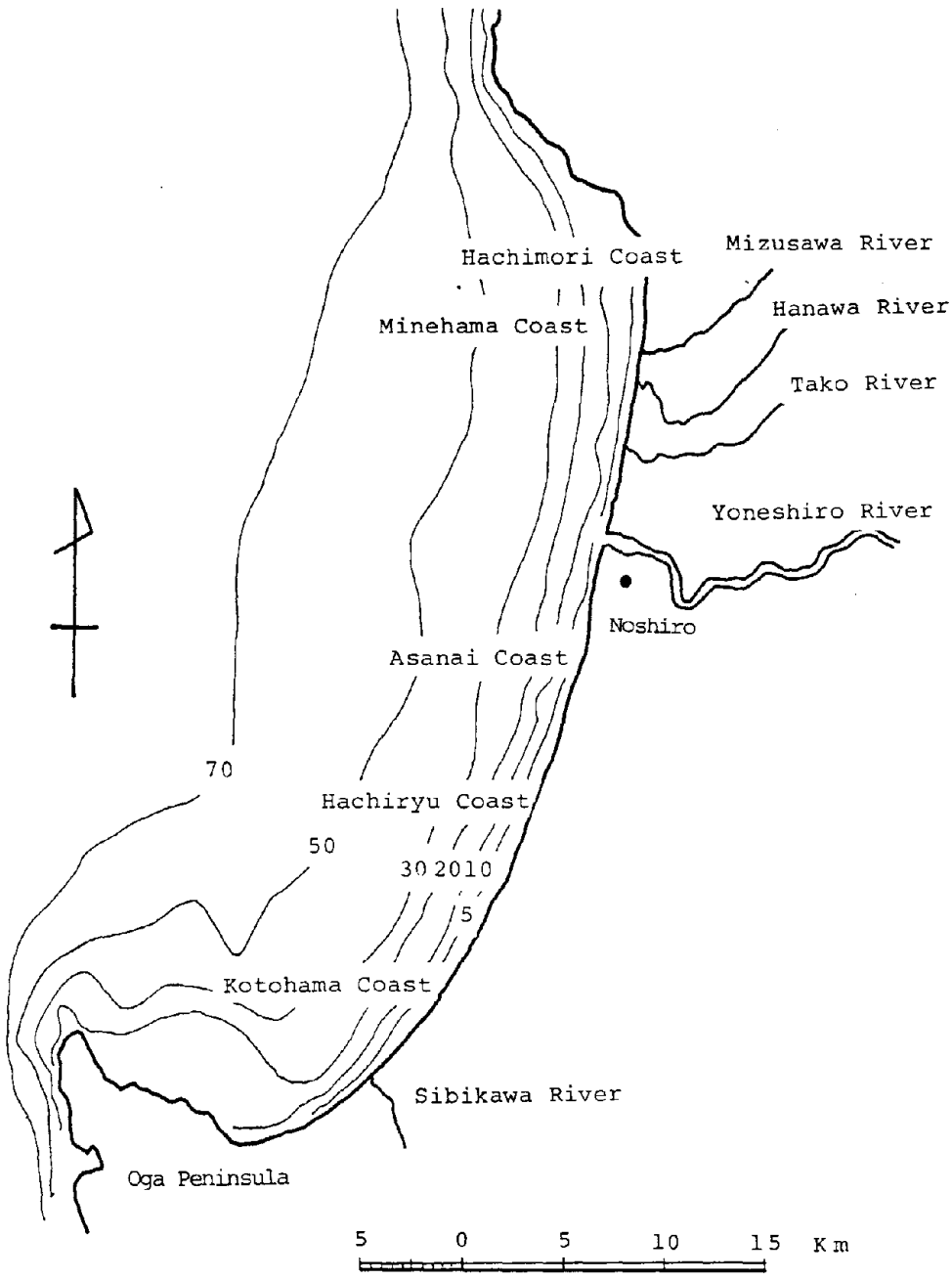

Fig. 1 Location map of coasts and rivers in Akita Prefecture

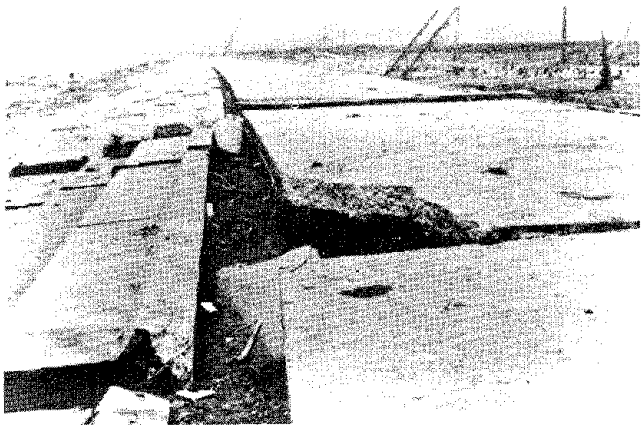

Fig. 2 Damaged stair-type revetment of Ochiai Coast in Noshiro Port

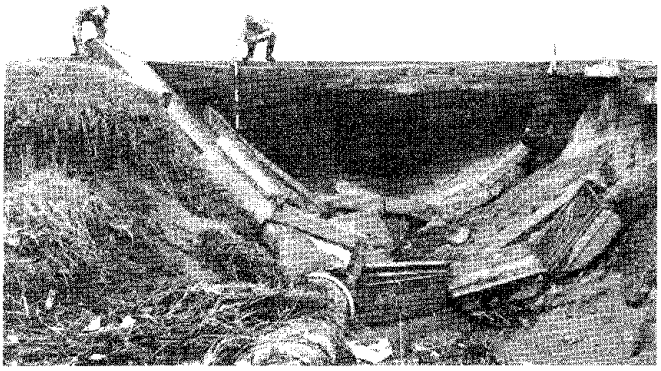

Fig. 3 Damage behind the stair-type revetment in Kotohama Coast

Fig. 4 Retreated sea water after the first attack of tsunami in Hachimori Coast

Fig. 5 Scattering of concrete blocks of detached breakwater in Hachimori Coast

Fig. 6 Scattering of concrete blocks of wave dissipation breakwater in Minehama Coast (1)

Fig. 7 Scattering of concrete blocks of wave dissipation breakwater in Minehama Coast (2)

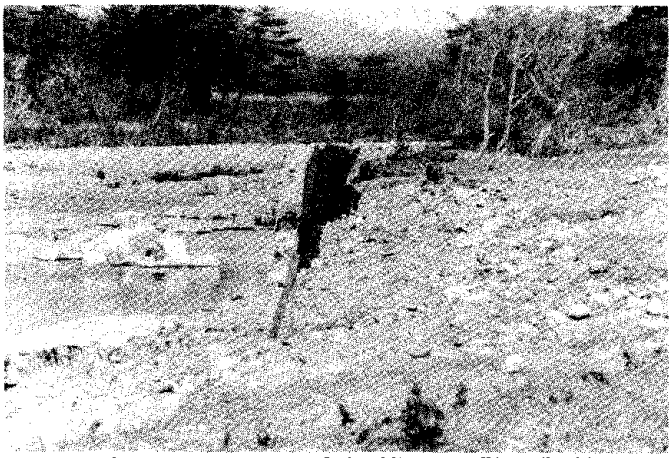

Fig. 8 Damaged revetment of the Mizusawa River (looking upstream)

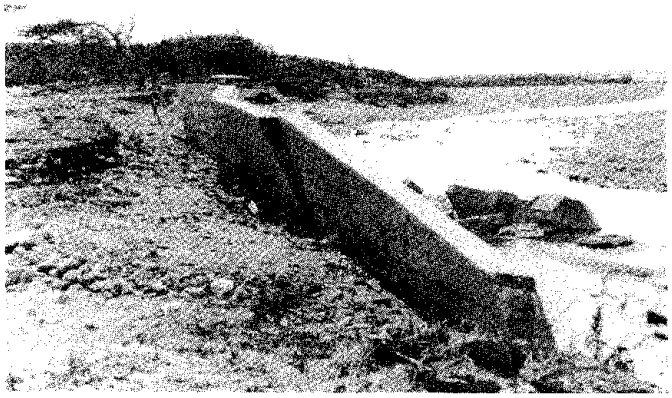

Fig. 9 Damaged revetment of the Mizusawa River (looking downstream)

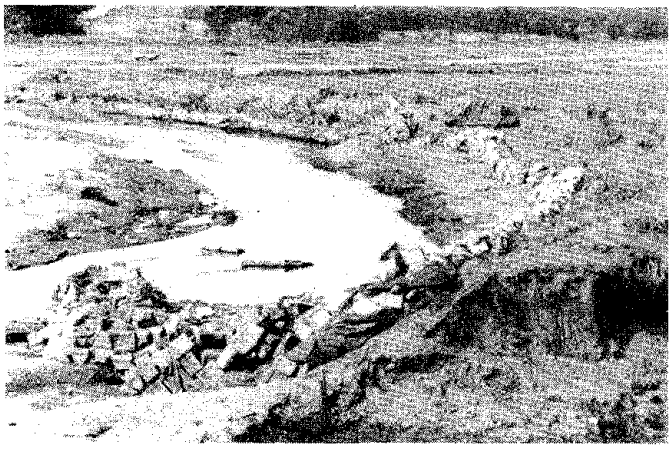

Fig. 10 Damaged embankment of the Hanawa River

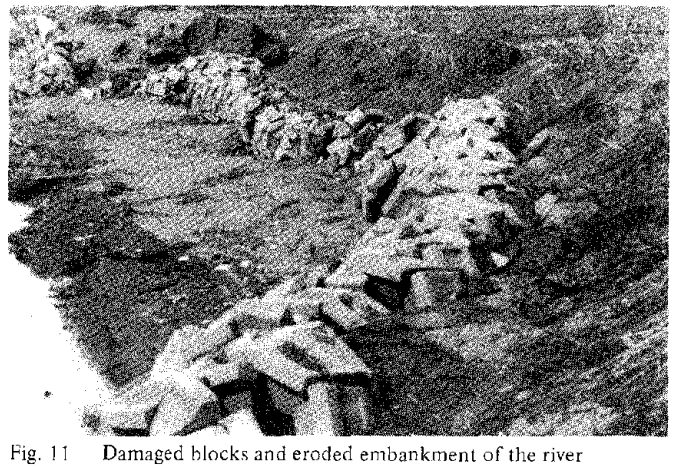

Fig. 11 Damaged blocks and eroded embankment of the river

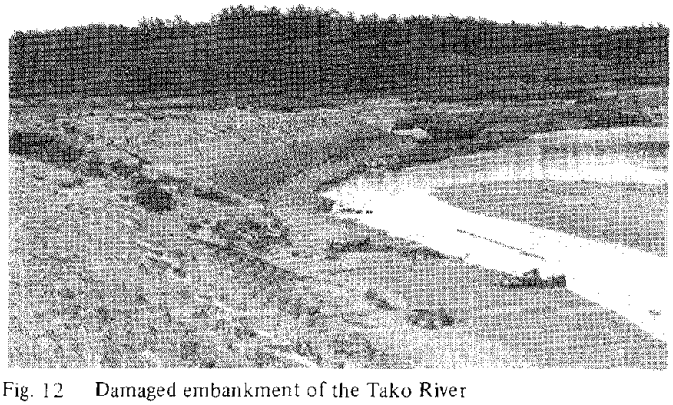

Fig. 12 Damaged embankment of the Tako River

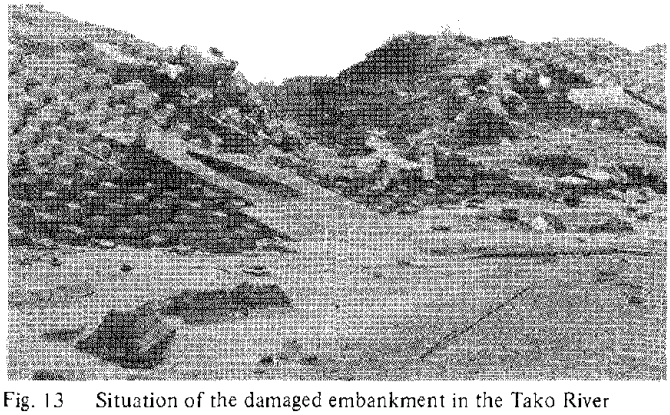

Fig. 13 Situation of the damaged embankment in the Tako River

Fig. 14 Scouring behind the dike of the Tako River

Fig. 15 Scouring under the abutment

Fig. 16 Damaged revetment of the Yoneshiro River

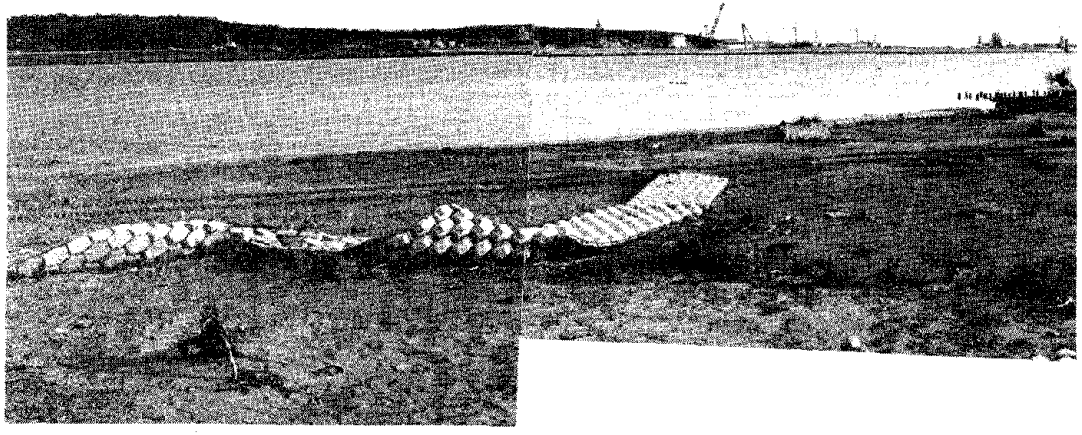

Fig. 17 Combined blocks carried away by tsunami

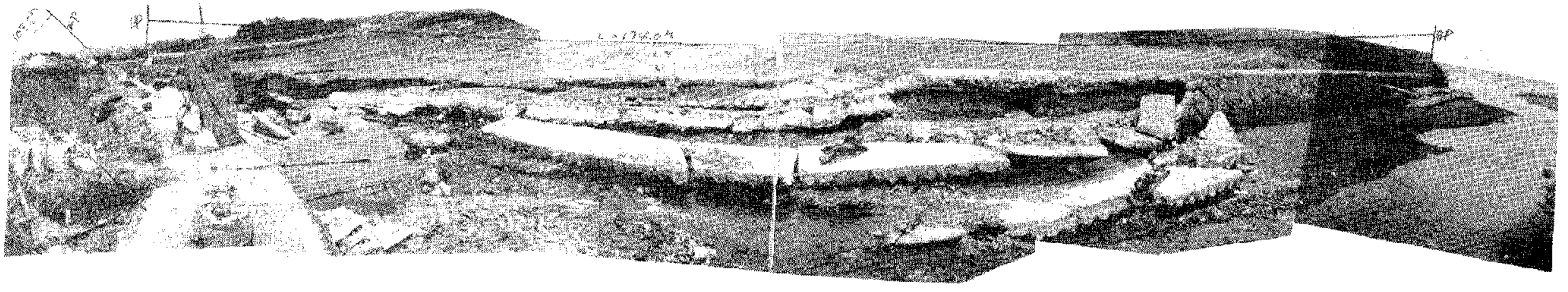

Fig. 18 Damaged revetment of the Shibikawa River

Table 1 Pattern classification of damages of coastal dike and revetment

Ex. force	Pattern of damage
Tsunami (reteat)	Scouring of the toe 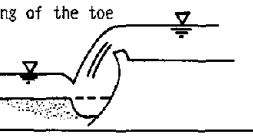
	Forward inclining of the revetment 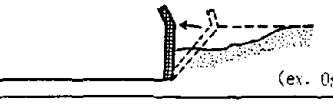 (ex. Oga Coast)
	Falling down (forward)  (ex. Kodomari F.P.)
	Damage of the parapet 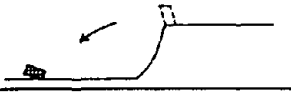
Tsunami (run-up)	Falling of upper structures of the coastal dike (backward) (ex. Iwanate F.P.) 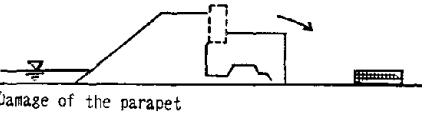
	Damage of the parapet 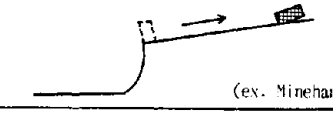 (ex. Minehama Coast)
Earthquake & Tsunami	Damage of the stair-type revetment 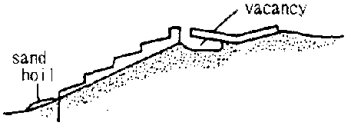 (ex. Noshiro port)

F.P. Fishery Port

Table 2 Pattern classification of damages of detached breakwater and wave dissipation breakwater

Scattering of the blocks	Subsidence of the blocks
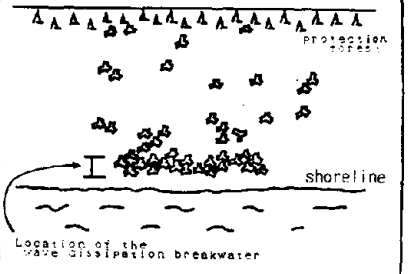 Blocks of the wave dissipation breakwater were carried landward and scattered by tsunami	Breakwater (Foot protection) 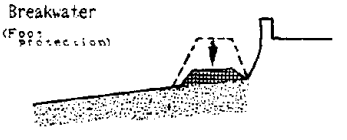 Wave-dissipation breakwater  Detatched breakwater 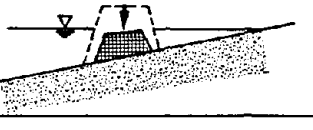

Table 3 Pattern classification of damages of river administration facilities

Facility	Pattern of damage
Body of the embankment	Slope collapsing 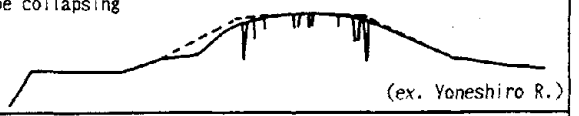 (ex. Yoneshiro R.)
	Scouring of the crown & backslope  (ex. Yoneshiro R.)
	Breaking 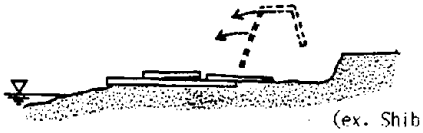 (ex. Shibikawa R.)
Revetment	Breakdown of the slope of the low-water revetment 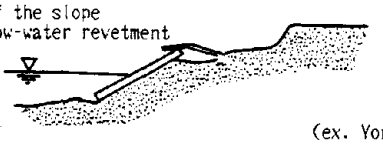 (ex. Yoneshiro R.)
	Scouring behind the revetment 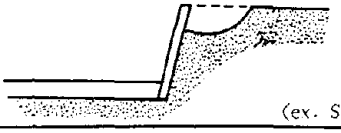 (ex. Shibikawa R.)
	Forward inclining  (ex. Mizusawa R.)
	Falling 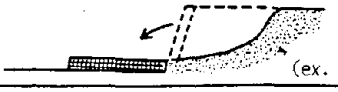 (ex. Mizusawa R.)
	Collapsing of slope protection  (ex. Hanawa R.)
Foot protection	Scattering of the concrete blocks 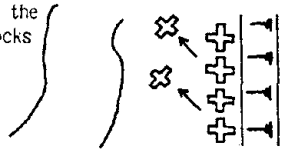 (ex. Mizusawa R.)

R. River

Table 4 Summary of pattern classification

	Ex. force*	Facility	Pattern of damage	Number
Shore protection facilities	Tsunami (reteat)	Revetment and Embankment	Scouring of the toe	3
			Forward inclining of the revetment	2
			Falling down (forward)	3
			Damage of the parapet	1
	Tsunami (run-up)		Falling of upper structures of the coastal dike (backward)	2
			Damage of the parapet	1
	Earthquake & Tsunami		Damage of the stair-type revetment	2
	Tsunami	Breakwater (Foot protection)	Scattering of the blocks	5
			Subsidence of the blocks	14
		Wave dissipation breakwater	Scattering of the blocks	6
			Subsidence of the blocks	1
		Detatched breakwater	Scattering of the blocks	17
			Subsidence of the blocks	6
River administration facilities	Tsunami	Body of the embankment	Slope collapsing	1
			Scouring of the crown & backslope	1
			Breaking	3
		Revetment	Breakdown of the slope of the low-water revetment	1
			Scouring behind the revetment	1
			Forward inclining	1
			Falling	1
			Collapsing of slope protection	2
		Foot protection	Scattering of the concrete blocks	1

* Estimated external force causing the damage

PROGRESS IN DEVELOPING TSUNAMI DATA BASE

by James F. Lander and Patricia A. Lockridge
National Geophysical Data Center, NOAA
Boulder, CO

ABSTRACT

In support of the Tsunami Hazard Reduction Using System Technology (THRUST) demonstration project for Chile, the National Geophysical Data Center (NGDC) has published a multi-colored map of Tsunamis in the Pacific Basin (1900-1983) (approximately 110 x 150 cm). NGDC is also preparing a compilation of information about Chilean tsunamis including occurrences, local and distant effects, marigraphic data, tide station locations and characteristics, photographs and a selected bibliography for joint publication with the Chilean Hydrographic Institute later this year.

Substantial progress has been made in producing a digital data base of tsunami occurrences, including reported wave heights, effects and references. For example, this file can be used to produce lists or maps of destructive tsunamis, tsunamis which produced waves and/or damage beyond the source region, tsunamis caused by or associated with volcanic eruptions, tsunamis effecting certain regions from both local or remote sources, and tsunamis producing runup heights of a specified level or higher. It can be used for a variety of statistical purposes. This paper illustrates some of these.

The file will be completed for the Pacific Basin and extended to include tsunamis in the Mediterranean and Caribbean Seas, and Atlantic Ocean. Information on source dimensions as inferred from earthquake aftershocks and information on focal mechanism will also be added to the file over the next several years.

Key Words: Tsunamis, Seismic Sea Waves, Natural Hazards, Pacific Basin, Chile, Japan, Hawaii

1. INTRODUCTION

As part of an AID-sponsored project to develop a comprehensive program to mitigate tsunami devastation in developing countries, the National Geophysical Data Center agreed to produce an educational map depicting the history of occurrence of tsunamis in the Pacific and to develop a data base of available data to support the program in its demonstration project for Chile. For convenience, a digital data base on the occurrence and effects of tsunamis in the Pacific was developed from available sources (1, 2, 4, 5, 6, 7). The map, "Tsunamis of the Pacific Basin, 1900-1983" has been published and a compilation of data and information on tsunamis which have affected Chile is being readied for publication with the Chilean Hydrographic Institute later this year. The digital data base has proved to be a valuable resource in itself and considerable progress has been made to extend its coverage in time and areas included and of details of effects. There are, of course, limitations on the completeness and types of data available from around the Pacific and from earlier times. Earthquake recording devices and recorders were few and primitive until well into the 20th Century.

Also, much of the area has only a short historical record. The rapid development of much of the Pacific coastal regions makes it essential to determine the risks from tsunamis and develop counter measures against them.

2. DIGITAL TSUNAMI DATA BASE

The current file consists of data drawn essentially from published references for all events except the smaller tsunamis (less than 1.5 meters wave heights or undamaging) prior to 1900 (1, 2, 4, 5, 6, 7, 8, 9, 10). The file contains information on date, location, effects, reference to original source, and a validity code. Where available, it will have information on wave height, earthquake magnitude, and tsunami magnitude and intensity. The validity code ranges from 4 (certain) to 0 (no tsunami). A validity code is necessary as it is not always clear from accounts whether the observed wave activity was due to a meteorological source (storm surge) or a

tectonic source such as an earthquake. Also, some tsunamis are listed under an erroneous date in some catalogs due to misconversion from the several calendar systems in use over the historical period. These are left in the file with intensity 0 to prevent their being re-entered in the file.

Entries for some areas such as Hawaii and Chile have been completed for all known events. The file is being actively expanded to complete the entries from available sources, add new sources including, in particular, the Japanese history and other areas such as the Atlantic Ocean and the Mediterranean and Caribbean Seas.

Table 1 illustrates the present contents.

2.1 Examples From Digital Data

The following examples have been drawn from the file to illustrate some types of questions which can be addressed. The file is still incomplete so changes in detail may be expected. The principal conclusions, however, should be valid. Also, other researchers using other methods may have previously published results similar to these illustrations of the uses of the file.

Much of the interest in tsunamis focuses on their capability to cause damage. Table 2 lists 94 destructive tsunamis in the last 100 years, for an average of approximately one per year. Figure 1 shows the location of these events. Most lie along the western margin of the Pacific. Figure 2 shows a map of boundaries defined for tsunami source regions in this report.

Most damaging tsunami effects are limited to the generating region. Of the 94 damaging tsunamis in the last 100 years, only 9 (10 percent) caused damage beyond their source region. These are shown on Figure 3. At least in the last 100 years all such tsunamis have originated in Japan, Kuril-Kamchatka, Aleutian Islands and South America. Table 3 lists these events, exclusive of the Sea of Japan events. Note that in almost every instance Hawaii receives the largest waves outside of the source region.

Figure 4 summarizes the frequency of occurrence of tsunamis by region. The diagonal represents the total number of damaging tsunamis originating in an area. The columns represent the damage caused in each region by tsunamis originating in a region.

Regions 0, 1, 2, 3, 4 and 8 have not generated tsunamis destructive beyond their region in the last 100 years while region 9, South America, has generated tsunamis destructive to five other regions. The rows show the history of destructive tsunamis in a region. Hawaii, for example, has generated only three locally damaging tsunamis but has experienced damage from nine more tsunamis generated remotely. Every source region for remotely damaging tsunamis has generated tsunamis damaging to Hawaii.

Figure 5 shows a similar diagram for fatalities. Japan, while not a notable producer of destructive tsunamis (13 in the last 100 years), has by far the most fatalities. Even excluding the 1896 Sanriku tsunami, it has had over 9,000 fatalities. It is noteworthy that 99 percent of the approximately 50,000 fatalities are due to locally generated tsunamis. Meaningful damage values are rarely available but the ratio of damage from regionally generated tsunamis versus damage from tsunamis from remote sources is probably between 90 percent (frequency of occurrence of damaging tsunamis ratio) and 99 percent (number of fatalities ratio). Except for Hawai which has most of the fatalities from remote source tsunamis and a far greater risk from these tsunamis than from local tsunamis, all other regions have a far greater risk from local and regional tsunamis. It seems clear that improved preparedness and warnings for local tsunamis have the greatest potential for saving lives but it remains necessary to have accurate warning for remote sourced tsunamis for which hours to nearly a day's warning times are possible.

The frequency of occurrence of damaging tsunamis decreases rapidly with the lower earthquake magnitude. Figure 6 shows that two-thirds of the damaging tsunamis are associated with earthquakes of magnitude 7.5 or greater. Still, for local tsunami warning purposes, earthquakes as small as magnitude 6 or less may need to be considered. About 1600 people have been killed this century by tsunamis from these smaller earthquakes, three times more than those killed from remote sourced tsunamis. Table 4 lists these lower magnitude destructive tsunamis. This understates the risk since magnitudes are not always reported nor are damages always cataloged for

smaller events, particularly in the first half of this century.

The file can be used to locate the tsunamis which have effected an area. Figure 7 shows the location of tsunamis effecting Hawaii. Hawaii is at risk from all sources of tsunamis capable of producing destructive tsunamis beyond the source region and, in fact, probably the wave heights observed there could be used to predict wave heights elsewhere around the Pacific.

The file is being used to determine the historical effects of tsunamis originating in one region have on another region. Japanese tsunamis, again exclusive of the Sea of Japan earthquakes, are shown to have caused damage only once (1933, Hawaii). The file can also be used to identify the threat that remote sourced tsunamis pose for a region. Chile, for example, has experienced eight tsunamis from remote sources in the last 100 years but only the 1964 Alaskan tsunami caused damage and that was minor.

Tsunamis caused by volcanic sources may not be fully included in hazard warnings. The file contains information on over 50 volcanic tsunamis in the Pacific in the last 100 years. Over 100 fatalities from this source are listed.

The above examples illustrate some of the questions which the digital file can treat. While caution must be used in applying the historical record to future events and the deficiencies of the data must be remembered, the information has potential for improving the local and Pacific tsunami warning system.

3. REFERENCES

1. Iida, K., D. Cox and G. Pararas-Carayannis, "Preliminary Catalog of Tsunamis Occurring in the Pacific Ocean," Hawaiian Institute of Geophysics, University of Hawaii, 1967.

2. Cox, Doak C., Kumizi Iida, S. L. Solov'ev, and George Pararas-Carayannis, "Pacific Tsunami Historic File," National Oceanic and Atmospheric Administration, Boulder, Colorado, unpublished manuscript.

3. Solov'ev, S. L., and Ch. N. Go, "Map of the Source Regions and Heights of Tsunamis in the Pacific Oceans," Moscow, 1977 (Russian legends).

4. Solov'ev, S. L., and Ch. N. Go, "A Catalogue of Tsunamis of the Eastern Shore of the Pacific Ocean," Nauka Publishing House, Moscow, 1977.

5. Solov'ev, S. L., and Ch. N. Go, "A Catalogue of Tsunamis of the Western Shore of the Pacific Ocean," Nauka Publishing House, Moscow, 1974.

6. ITIC Newsletter, International Tsunami Information Center, Honolulu, Hawaii, published quarterly 1968-1976.

7. Tsunami Newsletter, International Tsunami Information Center, Honolulu, Hawaii, 1977-1983.

8. Cox, Doak C. and George Pararas-Carayannis with revisions by Jeffrey P. Calebaugh, "Catalog of Tsunamis in Alaska," SE Report-1 - National Oceanic and Atmospheric Administration, World Data Center-A, Boulder, Colorado, 1976.

9. Pararas-Carayannis, George with revisions by Jeffrey P. Calebaugh, "Catalog of Tsunamis in Hawaii," SE Report-4, National Oceanic and Atmospheric Administration, World Data Center-A, Boulder, Colorado, 1977.

10. United States Earthquakes, U.S. Department of the Interior, Geological Survey and U.S. Department of Commerce, National Oceanic and Atmospheric Administration, annual volumes, 1944-1980.

11. Lockridge, P. A., R. H. Smith, "Tsunamis in the Pacific Basin," National Geophysical Data Center, National Oceanic and Atmospheric Administration, Boulder, Colorado, 1984.

12. Bernard, Eddie N., James F. Lander, Gerald T. Hebenstreit, "Feasibility Study on Mitigating Tsunami Hazards in the Pacific," NOAA Technical Memorandum ERL PMEL-37, December 1982.

13. Lander, James F., "Data Services Supporting the THRUST Project," United States-Japan Panel on Wind and Seismic Effects, 16th Joint Meeting, May 15-18, 1984.

TABLE 1

TSUNAMI DATA FILE CONTENTS

	NR. OF EVENTS (validities 2-4)	NR. OF EVENTS REPORTING WAVE HEIGHTS	NR. OF LOCATIONS REPORTING WAVE HEIGHTS	NR. OF EVENTS REPORTING DEATHS OR DESTRUCTION	NR. OF LOCATIONS REPORTING DEATHS OR DESTRUCTION
CURRENT FILE*	789	268	1825	259	644
CHILE ONLY	250	82	295	34	126
20TH CENTURY ONLY	407	170	1453	87	255

* DOES NOT YET INCLUDE MINOR TSUNAMIS BEFORE 1900

EXCEPT FOR CHILE AND HAWAII.

TABLE 2

DESTRUCTIVE TSUNAMIS OF LAST 100 YEARS SORTED BY REGION WITH DAMAGE CODE AND NUMBER OF DEATHS, 1885-1984

DATE	LAT.	LONG.	E.MAG	RUNUP	SOURCE	VALID.	CAUSE	DAMAGE	DEATHS
REGION 0	3 TOTAL; 1 CONSIDERABLE DAMAGE; 35 DEATHS								
1903 11 29				10.0	HAWAII	4		C	
1951 08 21	19.5	-156.0 12	6.90	3.6	HAWAII	4	T	C	33
1975 11 29	19.4	-155.1 05	7.20	8.0	HAWAII	4	T	B	2
REGION 1	3 TOTAL; 1 CONSIDERABLE DAMAGE; 10 DEATHS								
1917 06 25	-15.6	-173.0 SH	8.30	12.0	SAMOA ISLANDS	4	T	B	
1947 03 26	-38.8	178.6 SH	7.00	4.6	N. NEW ZEALAND	3	T	C	
1953 09 14	-18.6	178.6 60	6.80	2.0	FIJI ISLANDS	4	T&L	C	C
REGION 2	15 TOTAL; 6 CONSIDERABLE DAMAGE; 3 EXTENSIVE DAMAGE; 407 DEATHS								
1895 03 06	-8.5	150.0	7.5		W. SOLOMON SEA	4	T	A	26
1906 09 15	-7.0	149.0 SH	8.00	1.5	W. SOLOMON SEA	4	T	B	
1919 05 07	-6.0	153.0	7.75	2.5	BISMARCK SEA, NEW GUINEA	4	T	B	C
1926 09 17	-11.6	160.0 50	7.00	2.0	SOLOMON ISLANDS	4	T	B	
1930 12 24	- 1.3	144.3	5.75	2.5	MELANESIA	4	T	A	5
1931 10 04	-10.6	161.8 SH	7.90	9.0	SOLOMON ISLANDS	4	T	A	50
1938 05 13	- 6.0	147.7 SH	7.50		BISMARCK SEA, NEW GUINEA	3	T	C	
1939 04 30	-10.6	158.6 50	8.00	10.5	SOLOMON ISLANDS	3	T	C	12
1951 02 22	- 3.6	142.6		3.5	BISMARCK SEA, NEW GUINEA	2	T	C	
1970 11 01	-4.9	145.5 20	7.00	3.0	BISMARCK SEA, NEW GUINEA	4	T	C	3
1971 07 14	- 5.5	153.9 47	8.00	3.0	BISMARCK SEA, NEW GUINEA	4	T	C	1
1971 07 26	- 4.9	153.2 48	8.00	3.5	BISMARCK SEA, NEW GUINEA	4	T	B	
1974 02 01+	- 7.4	155.6 40	7.00	4.0	SOLOMON ISLANDS	4	T	C	
1975 07 21	- 6.6	154.9 50	6.70	2.0	SOLOMON ISLANDS	4	T	B	200
1979 09 12	- 1.7	135.9 05	8.10	2.0	W. IRIAN, INDONESIA	2	T	B	100
REGION 3	18 TOTAL; 6 CONSIDERABLE DAMAGE; 6 EXTENSIVE DAMAGE; 5,378 DEATHS								
1885 04 30	-2.5	127.5	7.2		CERAM	3	T&V	C	C
1889 09 06	3.1	125.6	8.0		N. MOLUCCA IS., INDONESIA	4	T&V	B	C
1899 09 30	-3.5	128.5	7.8		BANDA SEA, INDONESIA	4	T&V	A	3,620
1907 01 04	1.5	97.0	7.50	2.8	SW. SUMATRA	4	T	A	400
1907 03 30	3.0	122.0	7.25	4.0	CELEBES SEA, INDONESIA	2	T	A	
1918 08 15	5.6	123.0 SH	8.30	7.0	CELEBES SEA, INDONESIA	4	T	B	B
1921 05 14	0.0	118.1	6.25		MAKASSAR STRAIT, INDONESIA	2	T	B	
1927 12 01	- 0.5	119.5	6.00	15.0	CELEBES SEA, INDONESIA	2	T	C	14
1928 08 04	-8.3	121.5	----	10.0	FLORES SEA, INDONESIA	4	V	B	128
1938 05 20	- 0.7	120.3	7.50	2.8	N. MOLUCCA ISLANDS, INDONESIA	4	T	C	17
1939 12 22	0.0	123.0150	8.60		N. MOLUCCA ISLANDS, INDONESIA	3	T	C	
1965 01 24	- 2.4	126.0 6	7.60	4.0	CERAM ISLAND, INDONESIA	4	T	B	71
1967 04 11	- 3.3	119.4 33	5.50	3.0	MAKASSAR STRAIT, INDONESIA	3	T	C	13
1967 04 12	5.5	97.3 58	7.50	2.0	MALAY PENINSULA	3	T	C	
1968 08 14	0.2	119.8 23	6.10	10.0	BANDA SEA	4	T	A	200
1969 02 23	-3.1	118.8 33	6.88		MAKASSAR STRAIT, INDONESIA	4	T	A	600
*1977 08 19	-11.0	118.4 SH	8.00	30.0	SUNDA ISLANDS	4	T	B	100
1979 07 18	- 8.5	123.5		10.0	LOMBLEN ISLAND, INDONESIA	2	T&L	A	187
REGION 4	7 TOTAL; 5 CONSIDERABLE DAMAGE; 5,059 DEATHS								
1897 09 21	6.8	122.5	8.5		SULU SEA, PHILIPPINES	4	T	B	13
1933 12 25	12.8	124.0	----	1.4	E. SAMAR ISLAND, PHILIPPINES	2	V	B	9
1934 02 14	17.6	119.0 SH	7.60	1.0	W. LUZON ISLAND, PHILIPPINES	4	T	B	
1948 01 25	10.6	122.0 SH	8.20	2.0	SULU SEA, PHILIPPINES	4	T		20
1949 12 29	18.0	121.0 SH	7.20	2.0	E. LUZON ISLAND, PHILIPPINES	3	T	C	16
1975 10 31	13.0	126.2 33	7.40		PHILIPPINE TRENCH	4	T	B	1
1976 08 16	6.3	124.0 SH	8.00	4.9	MORO GULF, PHILIPPINES	2	T	B	5,000
REGION 5	13 TOTAL; 3 CONSIDERABLE DAMAGE; 7 EXTENSIVE DAMAGE; 36,500 DEATHS								
*1896 06 15	39.6	144.2	7.6		SANRIKU, JAPAN	4	T	A	27,122
1911 06 15	29.0	129.0	8.90	2.0	RYUKYU TRENCH	4	T	B	6
1914 01 12	31.0	130.4	6.20	3.0	SEIKAIDO, JAPAN	4	T	C	35

DATE	LAT.	LONG.	E.MAG	RUNUP	SOURCE	VALID.	CAUSE	DAMAGE	DEATHS
1923 09 01	35.3	139.5 SH	8.20	12.1	TOKAIDO, JAPAN	4	T	A	2,144
1927 03 07	35.6	135.0 10	7.60	11.3	SW. HONSHU ISLAND, JAPAN	4	T	A	1,100
*1933 03 03	39.2	143.0 10	8.30	28.0	SANRIKU, JAPAN	4	T	A	3,000
*1944 12 07	33.8	136.0	8.30	8.4	TOKAIDO, JAPAN	4	T	A	1,040
1946 12 21	33.0	135.6 30	8.00	6.0	NANKAIDO, JAPAN	4	T	A	1,997
1952 03 04	42.2	143.8 45	8.00	6.5	SE. HOKKAIDO ISLAND, JAPAN	4	T	A	33
1964 06 16	38.3	139.2 40	7.60	6.4	NW. HONSHU ISLAND, JAPAN	4	T	C	26
1968 04 01	32.3	132.5 32	7.75	2.3	SEIKAIDO, JAPAN	4	T	B	
1968 05 16	41.4	142.9 33	7.05	5.0	JAPAN TRENCH	4	T	B	
1973 06 17	43.2	145.8 33	6.50	3.0	KURIL, USSR-HOKKAIDO, JAPAN	4	T	C	
REGION 6	7 TOTAL; 4 CONSIDERABLE DAMAGE; 2 EXTENSIVE DAMAGE; 258 DEATHS								
1918 09 08	45.6	151.6 SH	8.30	12.1	S. KURIL ISLANDS, USSR	4	T	C	23
1923 02 04	54.0	161.0 SH	8.30	8.0	KAMCHATKA PENINSULA, USSR	4	T	B	3
1923 04 14	56.6	162.6 SH	7.20	20.0	KAMCHATKA PENINSULA, USSR	4	T	B	18
1940 08 02	44.0	139.6 10	7.00	3.5	W. HOKKAIDO ISLAND, JAPAN	4	T	A	7
*1952 11 05	52.8	159.6 45	8.30	18.0	KAMCHATKA PENINSULA, USSR	4	T	A	A
1958 11 07	44.6	148.9 1008	8.30	4.0	S. KURIL ISLANDS, USSR	4	T	B	
*1983 05 26	40.2	140.0 24	7.80	14.1	NOSHIRO, JAPAN	4	T	B	107
REGION 7	7 TOTAL; 3 EXTENSIVE DAMAGE; 371 DEATHS								
1899 09 10	60.0	140.0	8.2		GULF OF ALASKA	4	T&L	C	
1936 10 27	58.6	-137.1	----	150.0	S. ALASKA	4	L	C	
*1946 04 01	52.8	-163.5 50	7.40	32.0	E. ALEUTIAN ISLANDS	4	T	A	247
*1957 03 09	51.3	-175.8	8.30	16.0	CENTRAL ALEUTIAN ISLANDS	4	T	A	
1958 07 09+	58.0	-138.8 SH	7.50	525.0	S. ALASKA	4	T&L	C	2
*1964 03 27+	61.0	-147.7 33	8.40	32.0	GULF OF ALASKA-ALASKA PENINSULA	4	T	A	122
1965 02 03	51.2	178.6 40	8.70	10.0	W. ALEUTIAN ISLANDS	4	T	C	
REGION 8	7 TOTAL; 3 CONSIDERABLE DAMAGE; 676 DEATHS								
1887 05 03	-31.0	109.0	8.0		N. MEXICO	2	T	C	44
1902 02 26	13.5	- 89.5		5.0	GUATEMALA-NICARAGUA	4	T	B	185
1907 04 14	17.0	-100.0	8.00	1.8	S. MEXICO	4	T	C	8
1928 06 16	16.3	- 98.0 SH	7.90	2.0	S. MEXICO	4	T	C	4
1932 06 03	19.8	-104.2 SH	8.00	2.8	CENTRAL MEXICO	4	T	B	425+
1932 06 22	18.7	-104.7 SH	6.90	6.0	CENTRAL MEXICO	4	T	B	C
1934 07 17	8.0	-82.5	7.75	2.0	COSTA RICA-PANAMA	4	T	C	
REGION 9	14 TOTAL; 5 CONSIDERABLE DAMAGE; 3 EXTENSIVE DAMAGE; 2,878 DEATHS								
*1906 01 31	1.0	- 81.5 SH	8.60	5.0	COLOMBIA-ECUADOR	4		C	500+
*1906 08 16	-33.0	- 72.0 SH	8.40	3.6	S. CENTRAL CHILE	4	T	C	
1914 01 12	-12.0	- 76.6		3.0	PERU	4		B	
1918 12 04	-26.0	- 71.0 SH	7.80	5.0	N. CENTRAL CHILE	4	T	C	
*1922 11 10	-29.0	- 71.0	8.25	9.0	N. CHILE	4	T	A	A
1927 11 21	-44.6	- 73.0 SH	7.00	2.8	S. CHILE	4	T	B	
1943 04 06	-30.8	- 72.0 55	7.90		N. CENTRAL CHILE	4	T	B	C
1955 04 19	-30.0	- 72.0 30	7.00	1.0	N. CENTRAL CHILE	4	T	A	1
1958 01 19	1.5	- 79.5 40	7.50	4.0	COLOMBIA-ECUADOR	4	T	C	5
*1960 05 22+	-39.5	- 74.5	8.30	22.6	S. CHILE	4	T	A	1,590
1960 11 20	- 6.9	- 80.8 55	6.75	9.0	PERU	4	T	B	13
1966 10 17	-10.7	- 78.8 24	8.00	3.0	PERU	4	T	B	
1971 07 09	-32.5	- 71.2 58	6.80	1.2	CHILE	2	T	C	
1979 12 12	1.5	- 79.3 24	7.70	4.9	COLOMBIA-ECUADOR	4	T	A	259

DAMAGE CODE:
C = MINOR DAMAGE I.E. FEW HOUSES, BOATS, ONE LOCATION
B = CONSIDERABLE DAMAGE, I.E. 100 HOUSES, ONE LOCATION
A = EXTENSIVE DAMAGE, I.E. 1000 HOUSES, ONE LOCATION OR MANY HOUSES AT SEVERAL LOCATIONS

DEATH CODE:
C = FEW
B = MANY

CAUSE:
T = TECTONIC (EARTHQUAKE)
L = LANDSLIDE
V = VOLCANIC

VALIDITY:
4 = DEFINITE
3 = PROBABLE
2 = QUESTIONABLE

*INDICATES TSUNAMIS THAT CAUSED DESTRUCTION OR FATALITIES BEYOND SOURCE REGION
DEATHS AND DAMAGE FIGURES INCLUDE EFFECTS CAUSED OUTSIDE REGION OF ORIGIN

TABLE 3

TSUNAMIS DESTRUCTIVE BEYOND SOURCE REGION

THIS IS A LISTING OF TSUNAMIS OF THE LAST 100 YEARS INCLUDING INFORMATION ABOUT THE LOCATION AND SIZE OF THE EARTHQUAKES THAT GENERATED THEM; THE LOCATION AND HEIGHT OF THE GREATEST RUNUP PRODUCED BY EACH TSUNAMI BEYOND THE SOURCE REGION; AND THE LOCATIONS OF DAMAGE AND FATALITIES CAUSED OUTSIDE THE REGION OF THE EARTHQUAKE EPICENTER.

EVENT DATE	SOURCE REGION NAME	EQ.MAG.	REGION OF GREATEST RUNUP MEASURED IN METERS		DAMAGED AREAS (FATALITIES)	DEATHS
1906 08 16	S. CENTRAL CHILE	8.4	MAALAEA, MAUI, HI	3.6	HAWAII	
1922 11 10	N. CHILE	8.2	HILO, HI	2.1	JAPAN,PHIL.,TAIWAN,SAMOA,HAWAII	
1923 02 04	KAMCHATKA PENINSULA, USSR	8.3	HILO, HI	6.1	HAWAII(1)	1
1933 03 03	SANRIKU, JAPAN	8.3	MIDWAY IS., HI	6.5	HAWAII	
1946 04 01	E. ALEUTIAN ISLANDS	7.4	NE COAST HAWAII, HI	17.0	HAWAII(241),CHILE,CALIF.	241
1952 11 05	KAMCHATKA PENINSULA, USSR	8.3	HAENA POINT, HI	10.5	MIDWAY,HAWAII,SAMOA,PERU,CHILE,ECUADOR	
1957 03 09	CENTRAL ALEUTIAN ISLANDS	8.3	HAENA POINT, HI	16.0	CALIF.,EL SALVADOR,JAPAN,HAWAII	
1960 05 22	S. CHILE	8.3	HILO, HI	10.5	CALIF.,SAMOA,HAWAII(61),JAPAN (199)	260
1964 03 27	GULF OF ALASKA-ALASKA PENINSULA	8.4	CRESCENT CITY, CA	6.3	CANADA,W.COAST U.S.A.(15),HAWAII	15

NUMBER OF TIMES EACH REGION APPEARS IN ABOVE TABLE AS A SOURCE FOR A MAJOR TSUNAMI		NUMBER OF TIMES EACH REGION RECORDED THE MAXIMUM RUNUP HEIGHT FROM A MAJOR TSUNAMI OUTSIDE THAT REGION		NUMBER OF TIMES EACH REGION RECEIVED DAMAGE FROM A MAJOR TSUNAMI OUTSIDE THAT REGION		DEATHS IN EACH REGION FROM REMOTE TSUNAMIS
0 HAWAII	= 0	HAWAII	= 8	HAWAII	= 9	303
1 NEW ZEALAND,SOUTH PACIFIC ISLANDS	= 0	NEW ZEALAND	= 0	NEW ZEALAND,SAMOA	= 3	
2 NEW GUINEA AND SOLOMON ISLANDS	= 0	NEW GUINEA (& AUSTRALIA)	= 0	NEW GUINEA	= 0	
3 INDONESIA	= 0	INDONESIA	= 0	INDONESIA	= 0	
4 PHILIPPINES	= 0	PHILIPPINES	= 0	PHILIPPINES (TAIWAN)	= 1	
5 JAPAN	= 1	JAPAN	= 0	JAPAN	= 3	201
6 KURILE ISLANDS, KAMCHATKA	= 2	KURIL IS., KAMCHATKA	= 0	KURIL IS.,KAMCHATKA	= 0	
7 ALEUTIAN ISLANDS, ALASKA	= 3	ALASKA	= 0	ALASKA	= 0	
8 WEST COAST NORTH AND CENTRAL AMERICA	= 0	NORTH & CENTRAL AMERICA	= 1	N. & C. AMERICA	= 4	15
9 WEST COAST SOUTH AMERICA	= 3	SOUTH AMERICA	= 0	SOUTH AMERICA	= 2	

TABLE 4 - DAMAGING TSUNAMIS WITH MAGNITUDE LESS THAN 7.5 IN 20TH CENTURY - BY MAGNITUDE

EVENT DATE	EQ.MAG.	MAX. RUNUP	LOCATION OF EARTHQUAKE	LOCATION OF DAMAGE	TYPE OF DAMAGE	DEATHS
1967 04 11	5.50	3.0	MAKASSAR STRAIT, INDONESIA	MOUTH OF TINAMBUNG RIVER	BOATS DESTROYED	13
1930 12 24	5.75	2.5	MELANESIA	N. COAST NEW GUINEA	VILLAGES DAMAGED	5
1927 12 01	6.00	15.0	CELEBES SEA, INDONESIA	PALU BAY, SULAWESI IS.	HUTS, PIER DESTROYED	14
1968 08 14	6.10	10.0	BANDA SEA	DONGOLA DISTRICT, INDON.	800 HOUSES DESTROYED	200
1914 01 12	6.20	3.0	SEIKAIDO, JAPAN	KAGOSHIMA, JAPAN	BOATS DAMAGED	15
				ALL OF JAPAN		35
1921 05 14	6.25		MAKASSAR STRAIT, INDONESIA	SEKURAH, INDONESIA	SEVERE DAMAGE	
1973 06 17	6.50	3.0	KURIL, USSR-HOKKAIDO, JAPAN	HOKKAIDO, JAPAN	FISHING BOATS SUNK	
1975 07 21	6.70	2.0	SOLOMON ISLANDS	TOROKINA, SOLOMON IS.	VILLAGE DESTROYED	200
1960 11 20	6.75	9.0	PERU	PERU		11
1953 09 14	6.80	2.0	FIJI ISLANDS	BEGA, SUVA IS.	BOATS DAMAGED	SEVERAL
1971 07 09	6.80	1.2	CHILE	VALPARAISO, CHILE	SOME DAMAGE	
1969 02 23	6.88		MAKASSAR STRAIT, INDONESIA	W. COAST CELEBES IS.	4 VILLAGES DESTROYED	600
1932 06 22	6.90	6.0	CENTRAL MEXICO	CAYUTLAN, MEXICO	SEVERE DAMAGE	
1951 08 21	6.90	3.6	HAWAII	KONA COAST, HAWAII, HI	MINOR DAMAGE	
1926 09 17	7.00	2.0	SOLOMON ISLANDS	GUADALCANAL, SOLOMON IS.	PORT INUNDATED	
1927 11 21	7.00	2.8	S. CHILE	AISEN PROVINCE, CHILE	INUNDATION ALONG COAST	
1940 08 02	7.00	3.5	W. HOKKAIDO ISLAND, JAPAN	RISHIRI IS., JAPAN	1000 BOATS LOST	7
				VLADIVOSTOK, PRIMORSKIY, USSR	EXTENSIVE DAMAGE	
				SW. COAST SAKHALIN, USSR	CELLARS FLOODED, BOATS WASHED AWAY	
				E. COAST KOREA	MERCHANT VESSEL CAPSIZED	
1955 04 19	7.00	1.0	N. CENTRAL CHILE	LA SERENA, COQUIMBO	DAMAGE	1
1970 11 01	7.00	3.0	BISMARCK SEA, NEW GUINEA	N. COAST NEW GUINEA	WAVES UPSET CANOE	3
1974 02 01	7.00	4.0	SOLOMON ISLANDS	KOROVU, SHORTLAND IS.	POLICE STATION FLOODED	
1923 04 14	7.20	20.0	KAMCHATKA PENINSULA, USSR	UST' KAMCHATSK	CANNERIES, BOATS, HOUSES DESTROYED	
				E. COAST KOREA	FISHING STATION DESTROYED	
1949 12 29	7.20	2.0	E. LUZON ISLAND, PHILIPPINES	CAGAYAN RIVER, LUZON	BOATS SUNK	16
1975 11 29	7.20	8.0	HAWAII	HAWAII	$1.5 MILLION DAMAGE	2
				CATALINA IS., CA	$2,000 DAMAGE	
1907 03 30	7.25	4.0	CELEBES SEA, INDONESIA	KARAKELONG IS.	CULTIVATED AREAS DEVASTATED	
1946 04 01	7.40	32.0	E. ALEUTIAN ISLANDS	UNIMAK IS., ALEUTIAN IS.	LIGHTHOUSE DESTROYED	5
				SANTA CRUZ, CA		1
				HILO, HAWAII	$26 MILLION DAMAGE	68
				NE. COAST HAWAII	$10 MILLION DAMAGE	173
				IQUIQUE, CHILE	BOATS DAMAGED	
				ISLA JUAN FERNANDEZ,CHILE	DAMAGE	
1975 10 31	7.40		PHILIPPINE TRENCH	SAMAR IS., PHIL	30 HOUSES DESTROYED	1

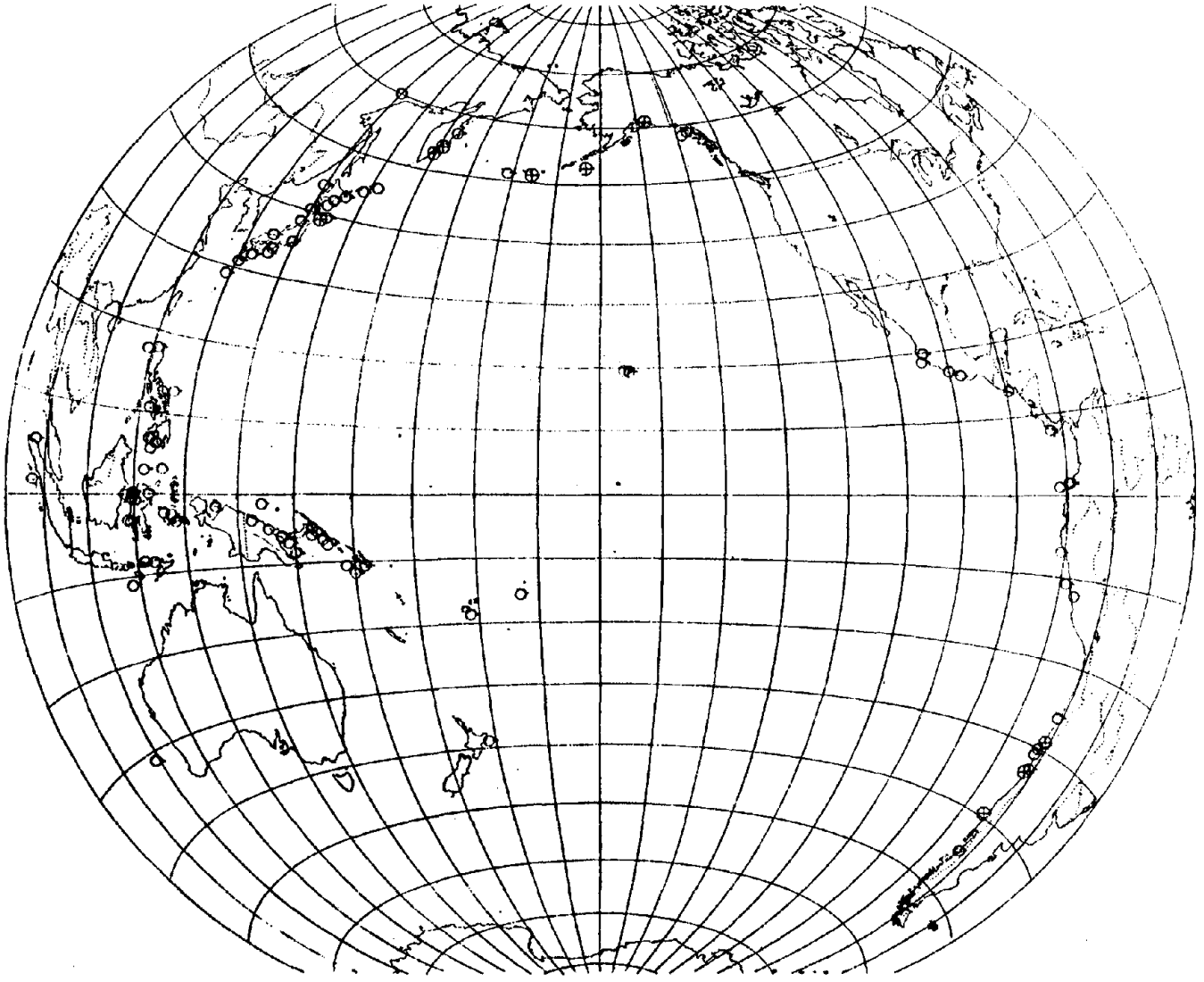

Figure 1 - Sources of destructive tsunamis - 100 years
○ = regional or local
⊛ = destructive beyond source region

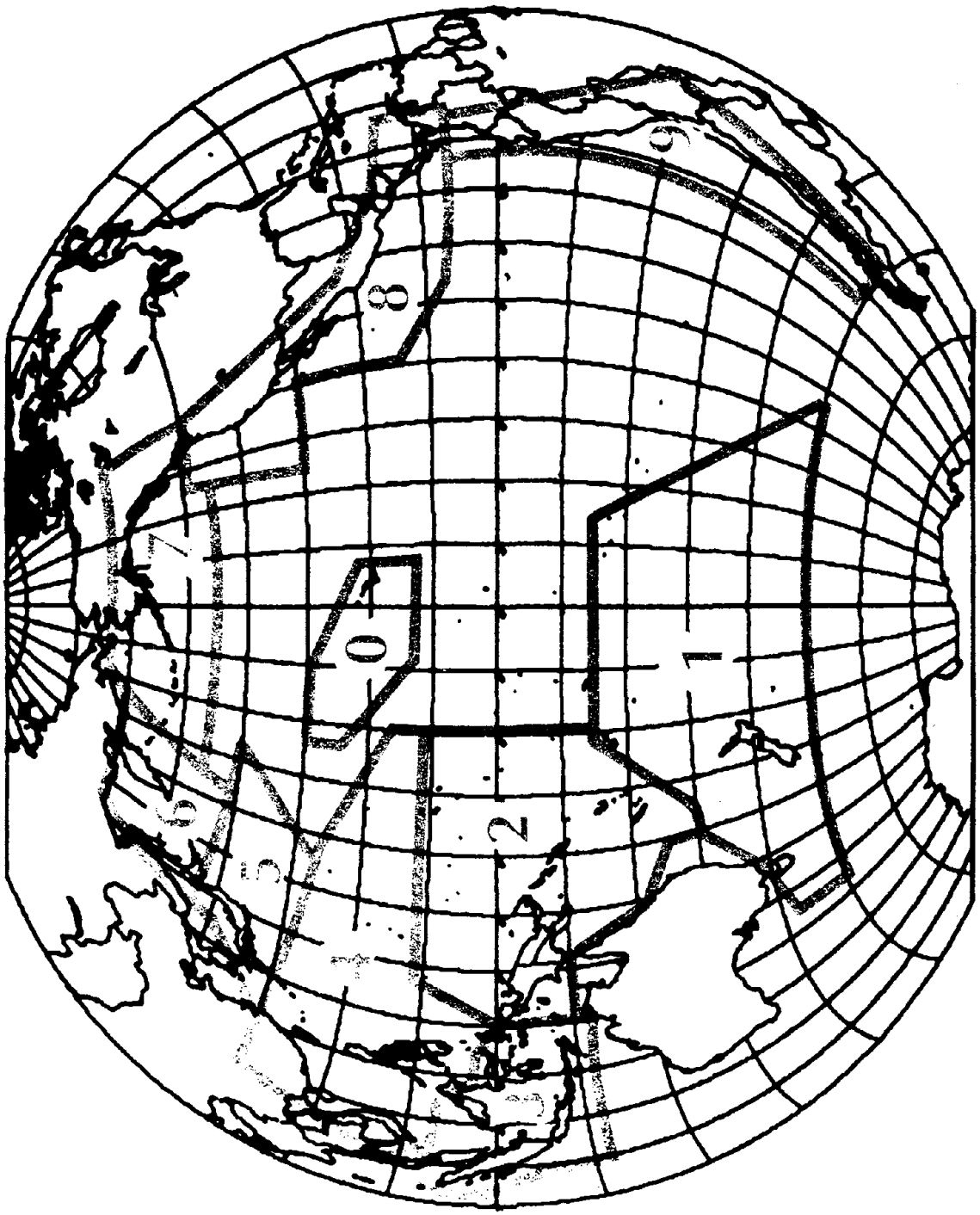

Figure 2. Tsunami source regions in the Pacific Basin

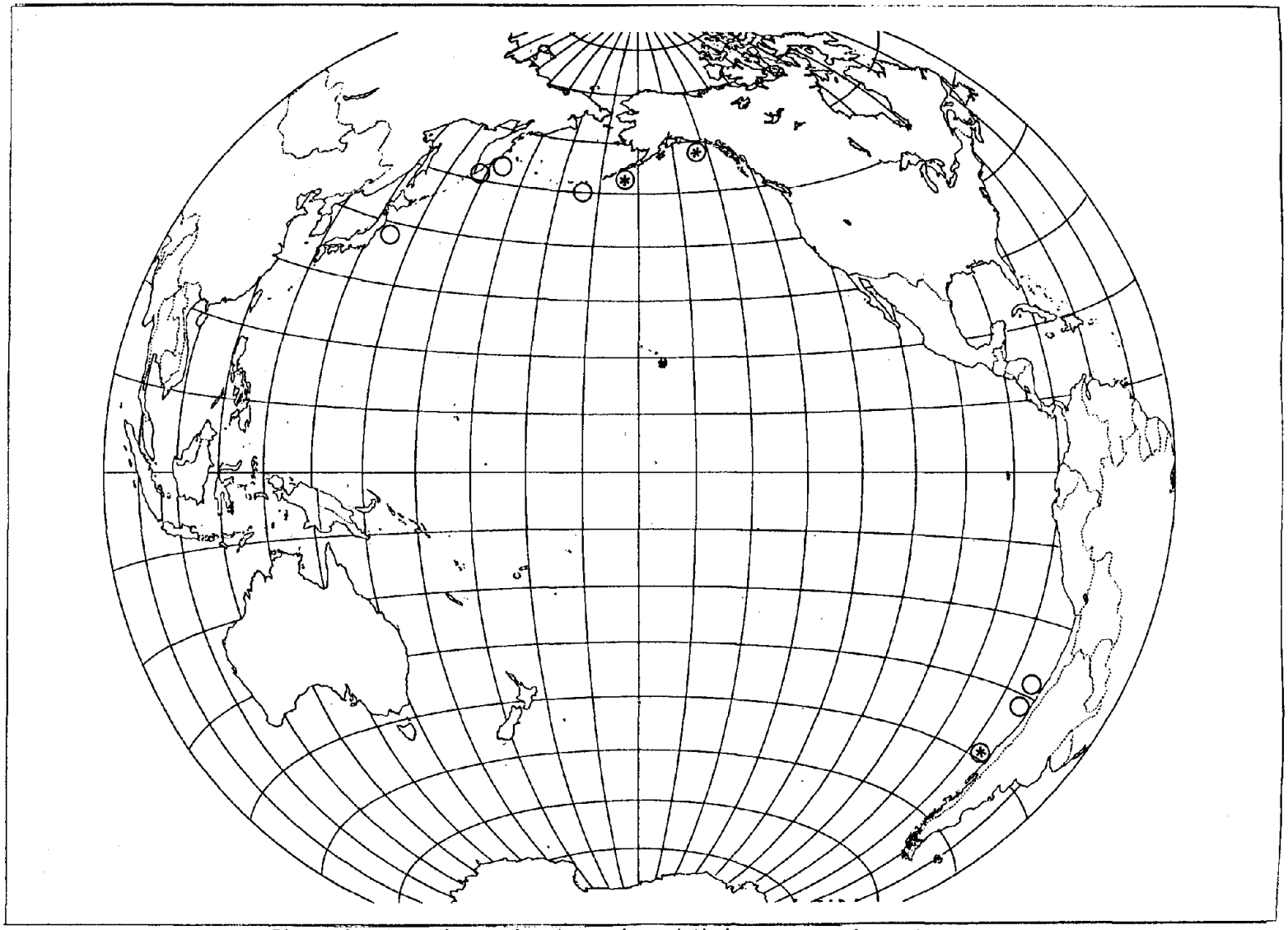

Figure 3 - Tsunamis causing damage beyond their source region - 100 years
○ = damage
⊛ = damage and fatalities

Figure 4

NUMBER OF TIMES TSUNAMIS HAVE CAUSED DAMAGE

BY REGION - 100 YEARS

SOURCE REGION

	0	1	2	3	4	5	6	7	8	9
0	3					1	2	3		3
1		3					1			2
2			15							
3				18						
4					7					1
5						13	2*	1		2
6							7*			
7								7		
8								3	7	1
9							1	1		14

* Includes Hokkaido and Noshiro tsunamis

Figure 5

DEATHS FROM TSUNAMIS

BY REGION - 100 YEARS

SOURCE REGION

	0	1	2	3	4	5	6	7	8	9
0	35						1	241		61
1		10								
2			407							
3				5,400						
4					5,000					
5						36,500				199
6							257			
7								115		
8								15	676	
9										2,618

Key:
0 - Hawaii
1 - South Pacific
2 - New Guinea/Solomon Islands
3 - Indonesia
4 - Philippines
5 - Japan
6 - Kuril-Kamchatka
7 - Alaska & Aleutian Islands
8 - West Coast, North & Central America
9 - South America

EARTHQUAKE MAGNITUDE FREQUENCY
FOR DAMAGING TSUNAMIS
1885-1984

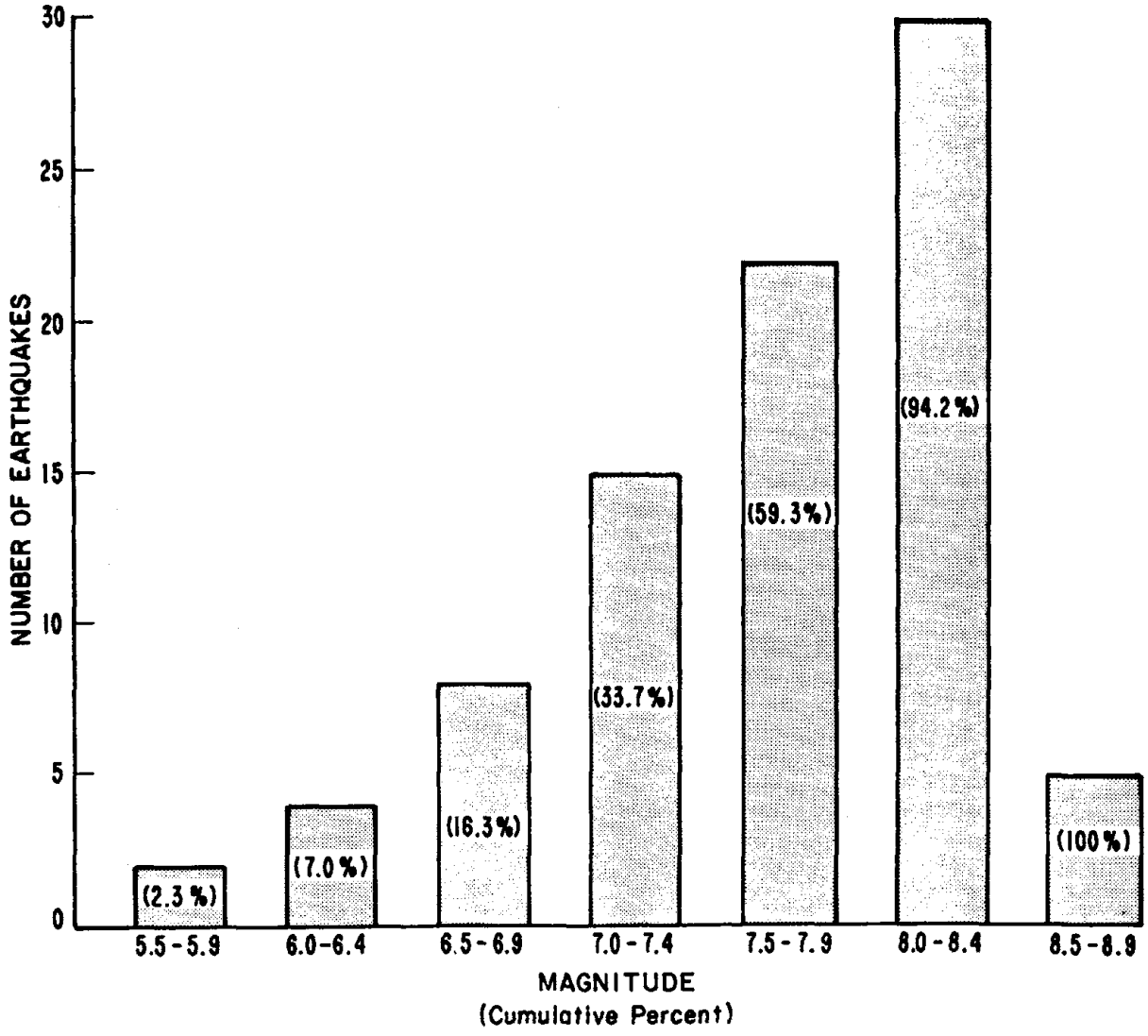

Figure 6

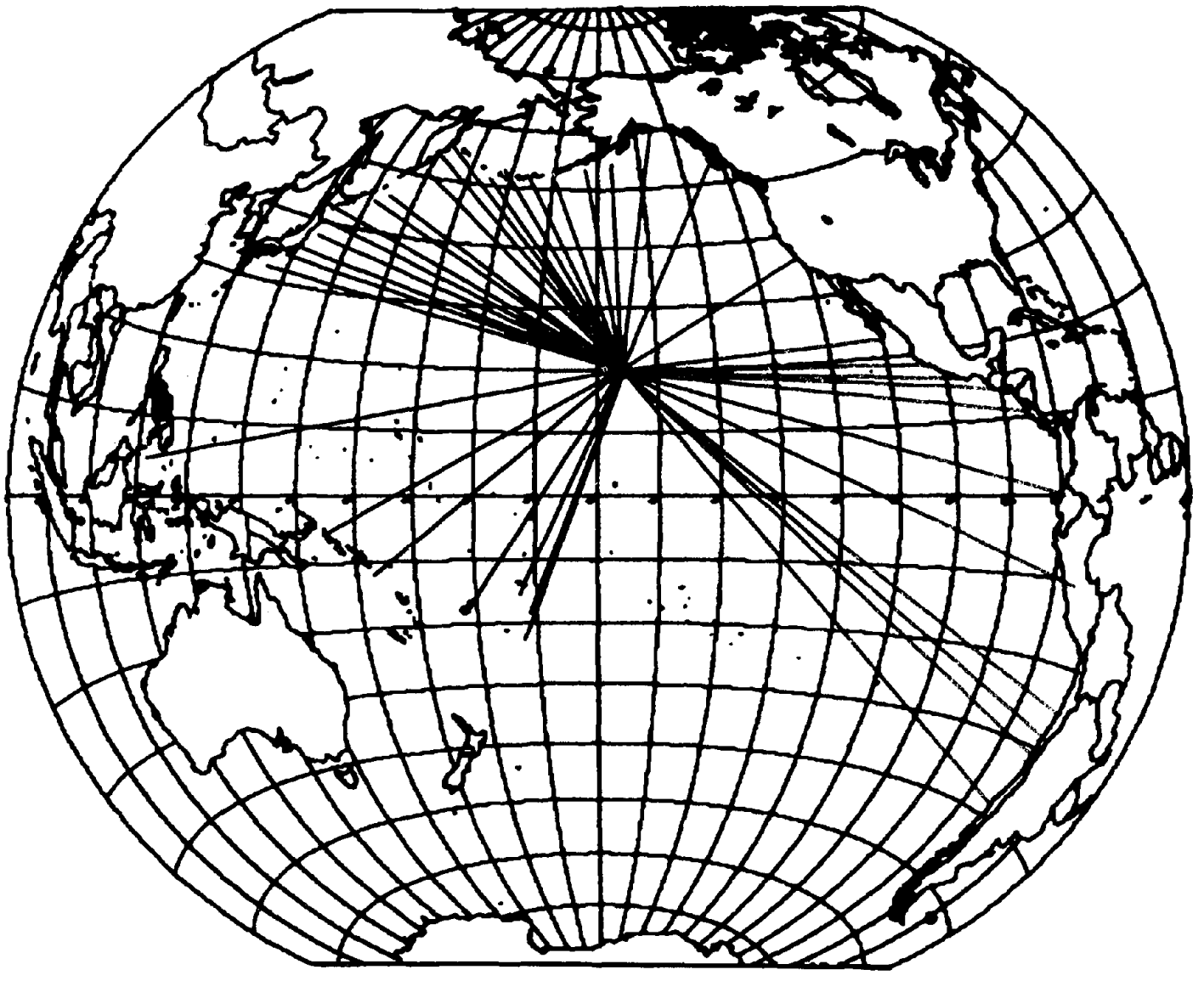

Figure 7. Tsunamis recorded in Hawaii, 1900-1983

TSUNAMIS IN THE JAPAN SEA WITH NUMERICAL CALCULATION

Yoshinobu Tsuji, National Research Center for Disaster Prevention
Tatsuo Konishi, Japan Meteorological Agency
Hiroshi Takahashi, National Research Center for Disaster Prevention

ABSTRACT

Earthquake-tsunamis frequently occur in the northeast part of the Japan Sea. Among these tsunamis, the Nihonkai-Chubu Earthquake-Tsunami of 1983 (M = 7.7, tsunami magnitude m = 2.5), the Kamuimisaki-Oki Earthquake-Tsunami of 1940 (M = 7.5, m = 2), and the Kampo Earthquake-Tsunami of 1741 (M = 7.5, m = 3) are discussed. Traces of these big tsunamis were recorded not only at the coast near the epicenters, but also on remote coasts, such as Noto Peninsula and the Korean Peninsula. A detailed survey was made of inundation height of the Nihonkai-Chubu Tsunami along the coasts of the Japanese Islands and the south part of the Korean Peninsula.

Also, a magnetic tape file of the sea bottom topography has been compiled and the numerical calculation of the propagation of the tsunamis for the whole Japan Sea has become possible.

In the present study, we discuss the distribution of the height of these tsunamis and the result of the numerical calculations for them.

1. INTRODUCTION

The dates of 21 tsunamis occurring in the Japan Sea, in the area off the west coasts of the northern part of Honshu Island and Hokkaido Island are given in Table 1. Earthquake-tsunamis have occurred only in a narrow zone in the sea which runs along the north part of the Japanese Islands. They occurred frequently during the periods of 1741 through 1834 and after 1939. No earthquake-tsunami occurred during 1614 to 1740, and 1834 to 1938. The reason for such a pattern of occurrence is not clear.

In the present paper, we discuss the distribution of tsunami inundation height of the 1983 Nihonkai-Chubu EarthquakeTsunami, which is compared with the result of a numerical calculation. We also discuss the 1741 Kampo and the 1940 Kamuimisaki-Oki Earthquake-Tsunami.

2. NIHONKAI-CHUBU EARTHQUAKE-TSUNAMI (1983-V-26, M = 7.7, m = 2.5)

Losses of life and property caused by the Nihonkai-Chubu Earthquake-Tsunami are listed in Table 2. A total of 100 people, out of 104 killed in Japan, were the victims of the tsunami. Major damage was done on the coasts of Hokkaido Island, Aomori and Akita Prefectures. The coasts of Shimane Prefecture, in the western part of the Honshu Island, and of the east coast of the Korean Peninsula were also badly damaged. Those coasts are 700 km to 1,000 km, respectively, from the tsunami source area.

Just after the occurrence of the tsunami, surveys of effects and interviews of witnesses were made by scientists and engineers, and several kinds of reports were published. Inundation heights of the tsunami were measured at about 600 points in total. The surveyed area covers almost all of the coasts facing the Japan Sea on the Japanese side.

Baek (1983) reported the distribution of tsunami height and the statistics of damages on the Korean side. One person was killed and two were lost in South Korea.

No information has come from the northern part of the Korean Peninsula, and only a few details have been gathered for the coast of the USSR.

Figure 2 shows the outline of the distribution of the tsunami height. The maximum height of 14 meters was reported at Minehama Village, Akita Prefecture. The largest peak appears in the north part of Akita Prefecture and smaller peaks appear at Shakotan Peninsula (Hokkaido Island), the northern tip of Sado Island, outside coast of Noto Peninsula, Oku-Tango Peninsula, Oki Islands (Shimane Prefecture), and at Shimane Peninsula. Prominent peaks also appear at Imweon Port, Gangweon-Do of South Korea, where heights of 3.6-4.0 meters were reported.

Figures 3 through 6 show the detailed maps of the distribution of tsunami heights.

2.1 Numerical Calculation

Numerical calculations of the tsunami propagation with grid size of 252 X 311 in the mesh intervals of 5 km X 5 km, which covers the whole area of the Japan Sea were made. The initial sea bed deformation was assumed as shown in Figure 7, which had been given by Aida (1984), who decided on the parameters for two faults on the basis of the data of release of stress, direct measurements of land, the distribution of the epicenters of aftershocks, distribution of initial motion of sea level observed at tide gauge stations, and so on. Influences of the rotation of the Earth, the surface curvature of the Earth, viscosity of sea water, non-linearity in the equations of motion, and of wave dispersion were neglected. As we cannot simulate the behavior of waves in shallow water, sea areas with depths shallower than 200 meters were replaced with seas of 200 m. depth. We assumed that there were vertical walls situated at the coastline, and that the wave was perfectly reflected there. Calculations were made using the finite difference method with time steps of 12 seconds for a total time of 2 hours 40 minutes.

Figure 8 shows the result. Short lines on the graphs show the maximum sea level at the coast. One mesh interval denotes 50 cm wave height. Tsunami heights on the coast of smaller islands are shown with lines beginning on the middle column.

We can recognize that the distribution pattern is generally well simulated, except that the absolute values do not agree.

2.2 Amplification of Tsunami Height On Continental Shelf Region

As the effect of amplification of a tsunami wave by the continental shelf region was not taken into account, the absolute value of the calculated tsunami height is as small as one-third or fifth of the actual height (Figure 9). Shuto (1972) gave the amplification formula under the condition that the depth changes linearly, deeper sea is flat, and that the incident wave is a stationary sinusoidal wave. We assume that tsunami height at the outside edge of the shelf is α and inundation height at the coast is R, then,

$$R/\alpha = 2\left\{J_0^2\left(\frac{4\pi L}{\sqrt{gD}\,T}\right) + J_1^2\left(\frac{4\pi L}{\sqrt{gD}\,T}\right)\right\}^{1/2} \quad (1)$$

where, L, T, and D are the length of slope, wave period, and depth at outside boundary of the slope (200 m). If we put L = 0, then α/R converges to 2. That is, in the case that the length of slope is zero, incident wave would be perfectly reflected, and therefore sea water climbs up to the height of twice the amplitude of incident wave, which is the case of the condition of the computer system. The actual topography of the coasts facing to the Japan Sea has a length of the shelf L of 10 to 30 km in general. We write the inundation height for the slope length being zero as R_0, and that for finite slope length as R, and the ratio R/R_0 as r, which we call the "amplification ratio." Figure 10 shows the ratio of amplification for T = 5, 7, 10, 15, and 20 minutes. It had been indicated that the predominant period of the tsunami is 7 to 10 minutes and therefore, it is reasonable that the actually observed tsunami height is three to five times the calculated height.

2.3 Effect of "Yamato Rise"

In the center of the Japan Sea, there is a remarkable table-shaped shallow sea region called the "Yamato Rise," the top of which is about 300 m depth while the depth of the surrounding sea is about 3,000 m. It has the dimensions of 300 km in the east-west direction and 150 km in the north-south direction. The prominent peak of wave heights on the coast of Korea as seen in Figure 2 or Figure 6, and the calculation result of Figure 8 is located just at the counter point of the tsunami source with the Yamato Rise at the center. We are apt to jump to the conclusion that the rise acted as a lens for the propagation of tsunami (Miyoshi, 1984, Tsuji et al., 1984). In order to test that idea, we made another numerical calculation removing the rise and replaced by the sea of 3,000 meters depth. We obtained the result as seen in Figure 11. The tsunami height on the coast of Korea becomes higher than that in Figure 8 showing that "Yamato Rise" does not act as a lens at all. We should not use the phrase "lens effect" without quantitative verification.

2.4 Calculation With Simplified Initial Sea Bed Deformation

We made a numerical calculation also under the condition that the initial sea bed deformation is simplified as shown in Figure 12, instead of Aida's model. The result is shown as Figure 13. Comparing it with Figure 8, we can recognize that on the coasts, except in the area close to the source, both tsunami height distribution patterns resemble each other, which shows that we can calculate the general pattern of the tsunami distribution for almost all coasts around the Japan Sea except that close to the source even if we assume the initial sea bed deformation to be simple as that in Figure 12.

2.5 Kamuimisaki-Oki Earthquake-Tsunami (1940-VIII-2, M = 7.5, m = 2)

Distribution of the 1940 Kamuimisaki-Oki Earthquake-Tsunami height is shown in Figure 14. We assumed the initial sea bed deformation simplified as Figure 12, and made a numerical calculation. The result is shown as Figure 15. Peaks of distribution of height at Rishiri Island, Teshio Port (northern Hokkaido), appear in both figures, and moreover the distant coasts of Oki Islands, Uljin Port on the Korean Peninsula, and Oliga Bay in USSR were hit by a rather high tsunami, which is also well simulated.

2.6 Kampo Earthquake-Tsunami (1741-VIII-29, M = 7.5, m = 3)

Tsunami source and distribution of tsunami height is shown in Figure 16. The source area was decided by Hatori (1984). On the coast of the southern district of Hokkaido, 1,467 people were killed. Recently an old record from the Korean side was discovered, and it reported that houses were washed away and vessels were destroyed in Gangweon-Do Province. The result of the numerical calculation with the simplified initial deformation of sea bed is shown as Figure 17. Higher peaks at Sado Island, Noto Peninsula, and east of the Korean Peninsula correspond well with the information of historical documents.

3. CONCLUSION

Comparing the observed tsunami height with the result of numerical calculations for three earthquake-tsunamis in the Japan Sea, we might conclude that:

i) There are several specific coasts where the tsunami height becomes higher than that of the neighboring coasts for any earthquake tsunami whose source is located in any sea region of the northeast part of the Japan Sea.

ii) Most of those "specific coasts" are coasts having the shape of a peninsula protruding in the direction of the tsunami source region.

iii) Pattern of the distribution of tsunami height can be simulated by a calculation using a grid in which the shelf region was replaced by a sea of 200 m depth, and the grid interval is set as 5 km x 5 km or so. If we consider the effect of amplification on the shelf region, we might explain the difference of absolute values between calculated and observed tsunami heights.

iv) Except for the coast near to the source, the distribution pattern of tsunami height can be simulated by simplified source deformation model like that shown as Figure 12.

v) Without quantitative examination, we should not try to explain the convergence of tsunami energy with the phrase "lens effect."

Table 1. List of earthquake-tsunamis in Japan Sea.

No	Date	Earthquake Magnitude	Epicentre lati. N	Epicentre long. E	Tsunami Magnitude	Remarks
1	850 ? ?	7.0	39.1°	140.0°	2	Yamagata Prefecture
2	887 VIII 2	6.5	37.5.	138.1	2	several thousands killed
3	1092-IX-13	-	"	"	"	uncertain
4	1341-X-31	"	"	"	"	Tsugaru Pen., Aomori Pref.
5	1614-XI-26	7.7	37.5.	138.0	2	uncertain
6	1741-VIII-29	7.5	41.5.	139.4	3	about 1,500 killed, see text
7	1762-X-31	6.6	38.1.	138.7	1	26 houses washed
8	1766 III 8	6.9	40.8.	140.6	-	in Mutsu Bay, Aomori Pref.
9	1792-VI 13	6.9	43.6.	140.3	2	near Shakotan Pen. Hokkaido
10	1793 II-8	6.9	40.7.	140.0	1	Tsugaru Pen., Aomori Pref.
11	1804-VII-10	7.1	39.0.	140.0	1	Kisakata, Yamagata Pref.
12	1810-IX-25	6.6	39.9	139.9	1?	Oga Pen., Akita Pref.
13	1833 XII 27	7.4	38.7.	139.2	2	off Yamagata Pref.
14	1834-II-9	6.4	43.3.	141.4	-	Isikari, Hokkaido
15	1939 V-1	7.0	40.0.	139.8	-1	Oga Pen., Akita Pref.
16	1940 VIII 2	7.5	44.1.	139.5	2	10 killed, see text
17	1947 XI 4	7.0	43.8.	141.0	1	off Rumoi, Hokkaido
18	1964 V 7	6.9	40.3.	139.0	-1	off Aomori Pref.
19	1964-VI-16	7.5	38.4.	139.2	2	"Niigata Earthquake"
20	1983-V 26	7.7	40.4.	139.1	2.5	"Nihonkai Chubu Earthquake"
21	1983 VI 21	7.0	41.3.	139.2	0	largest aftershock of No 20

Fig. 1 Locations of the Earthquake-Tsunamis listed in Table 1.
○...M ≥ 7.0. o...M ≤ 6.9.

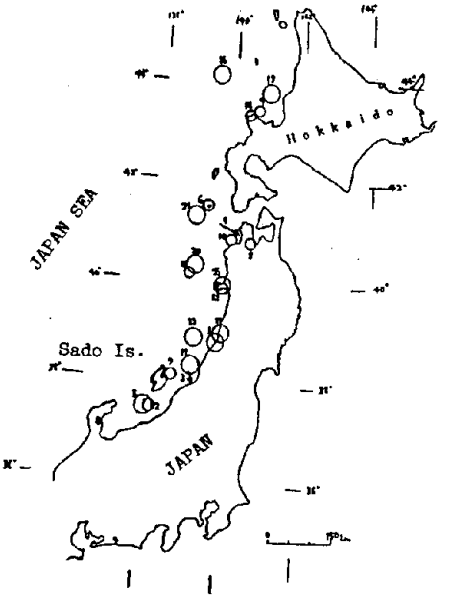

Table 2. Statistics of damages of the Nihonkai-Chubu Earthquake Tsunami After National Land Agency, Japan and Central Meteorological Observatory, Republic of Korea.

country	Japan						Korea
prefecture/ province	Hokkaido	Aomori	Akita	Shimane	other prefectures	total	Gangwoon-Do *Kyeongsanghug Do*
persons							
killed	4	17	83	0	0	104	1
lost	0	0	0	0	0	0	2
injured	24	25	265	5	5	324	2
damaged houses							
entirely & swept	5	447	1.132	0	2	1.584	1
partially	16	865	2.622	0	2	3.505	0
slightly	69	3.108	2.867	0	0	5.954	22
submerged							
above floor	27	62	65	141	3	298	
below floor	28	152	277	277	8	742	19
damaged vessels	837	853	681	319	161	2.851	81

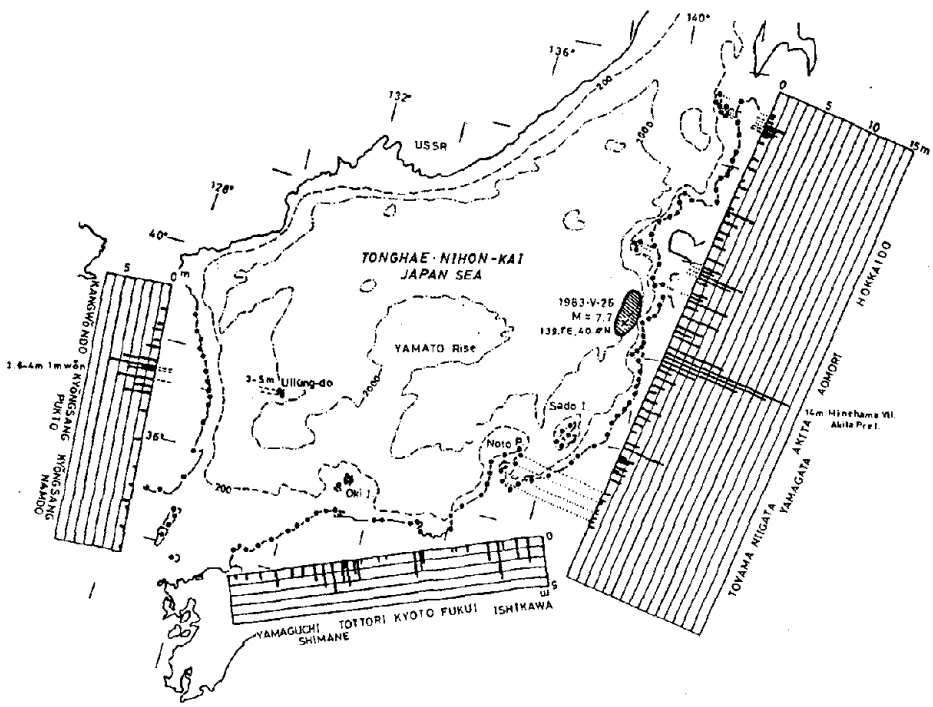

Fig. 2 Schematic distribution of inundation height of the Nihonkai-Chubu Earthquake-Tsunami of May 26th, 1983.

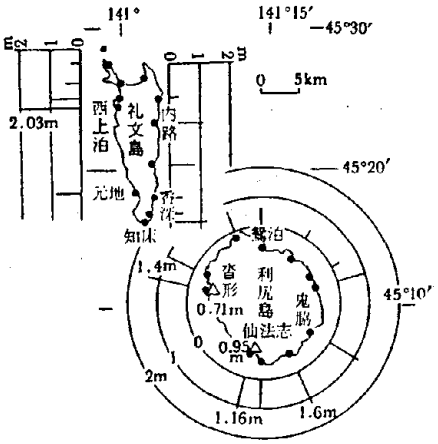

Fig. 3-a Detailed map of Rishiri and Rebun Islands.

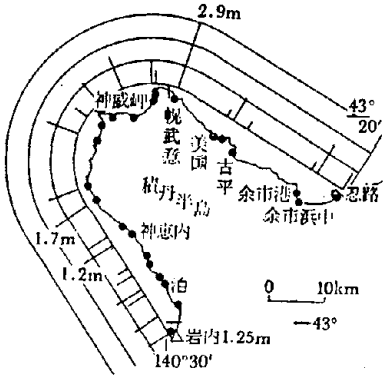

Fig. 3-b Detailed map of Shakotan Peninsula.

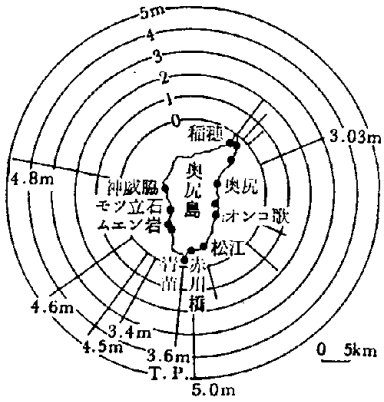

Fig. 3-c Detailed map of Okushiri Island.

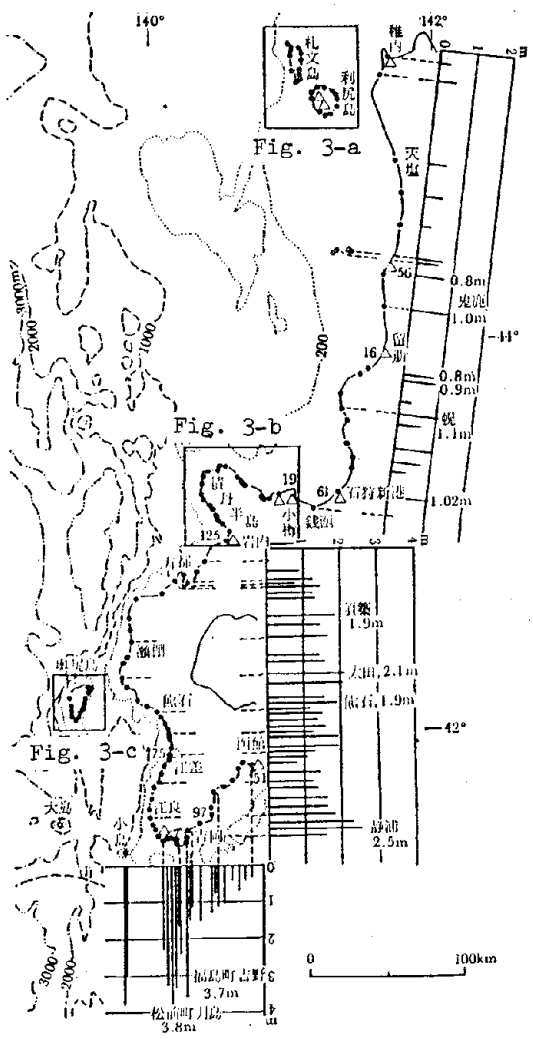

Fig. 3 Distribution of inundation height of the Nihonkai-Chubu Earthquake-Tsunami along the west coasts of Hokkaido Island.

Black circles show the locations of the measured points, and triangles show tide gauge station with tsunami height(cm).

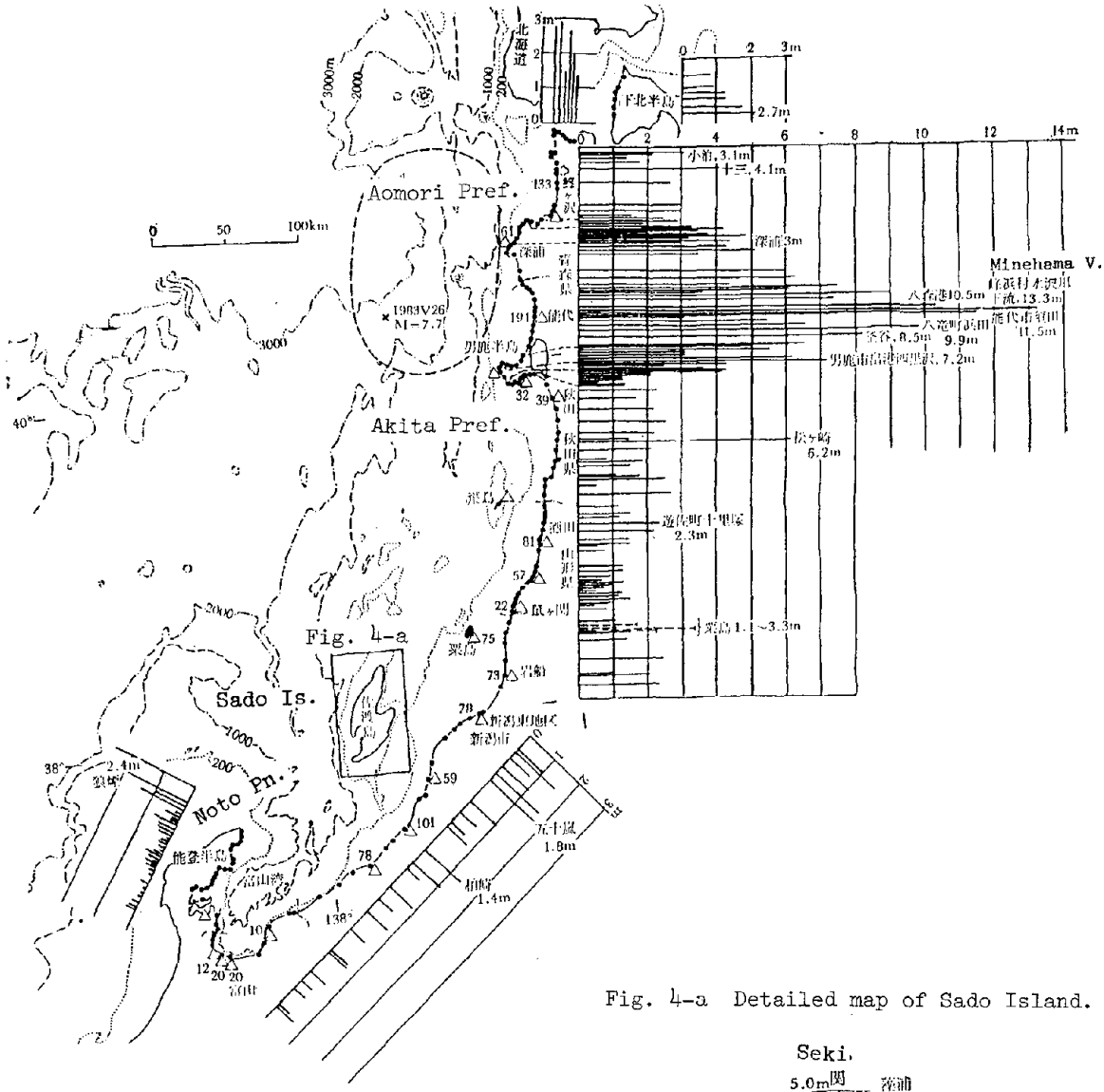

Fig. 4 Distribution of Tsunami height in the northern part of Honshu Island. Broken line shows the tsunami source area given by Hatori(1983).

Fig. 4-a Detailed map of Sado Island.

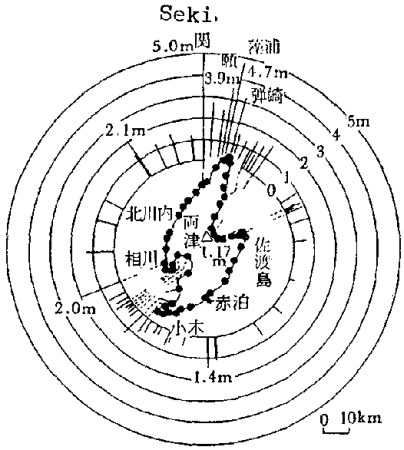

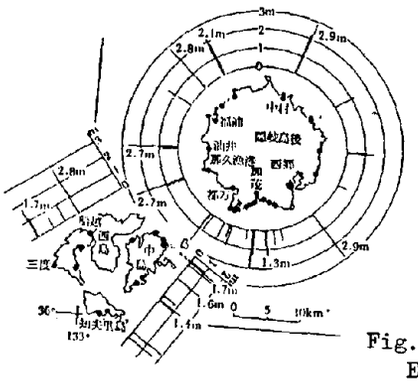

Fig. 5-a Detailed map of Oki Islands.

Fig. 5 Distribution of height of the Nihonkai-Chubu Earthquake-Tsunami in the south part of the Japanese Islands. Notice that higher tsunami was recorded on the coasts of Noto Peninsula and Shimane Prefecture.

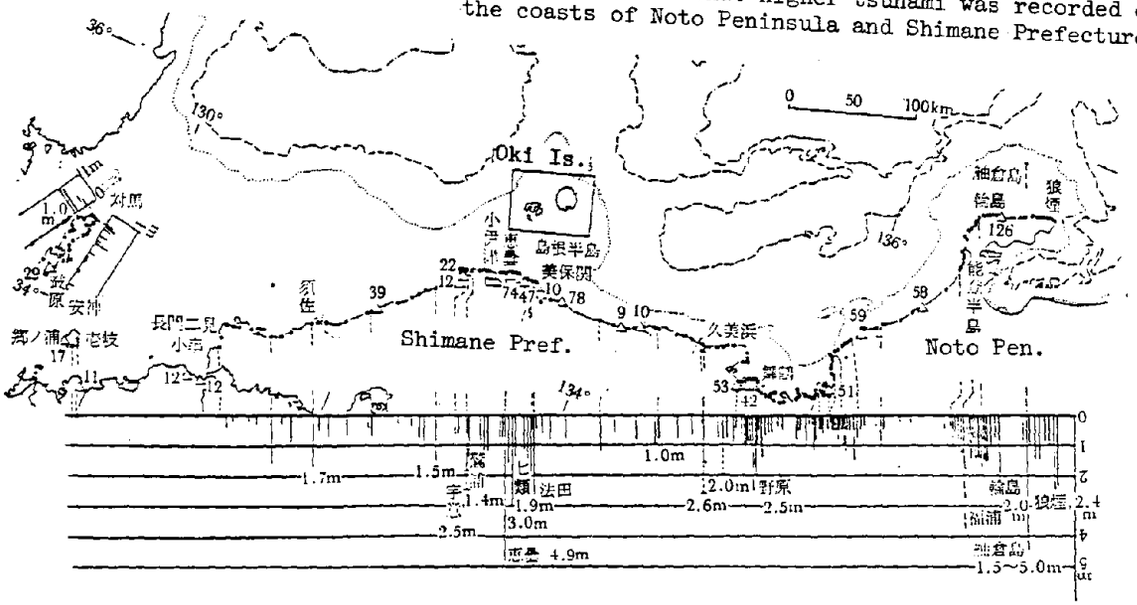

Fig. 6 Distribution of height of the Nihonkai-Chubu Earthquake-Tsunami along the east coast of Korea. No information has come from North Korea till May 1985.

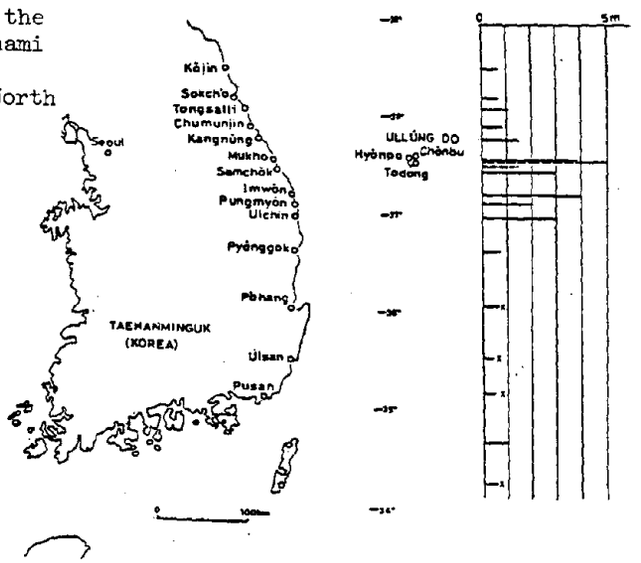

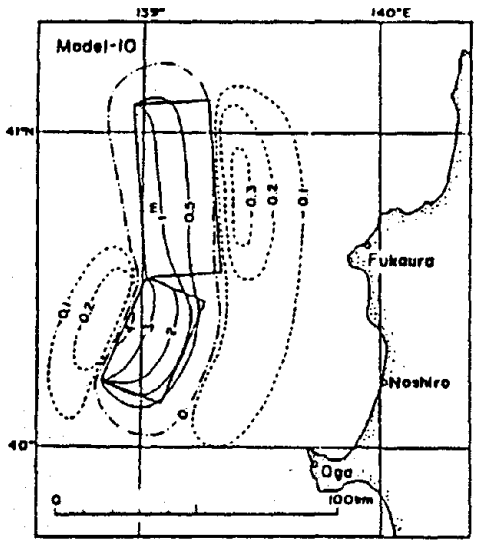

Fig. 7 Initial sea bed displacement caused by the Nihonkai-Chubu Earthquake. After Aida(1984).

Full line shows the area of upheaval and broken line shows that of subsidence.

Fig. 8 Result of numerical calculation for the Nihonkai-Chubu Earthquake-Tsunami. One mesh corresponds to 50cm of tsunami height. Notice that the depth in the shelf region is assumed uniform as 200m.

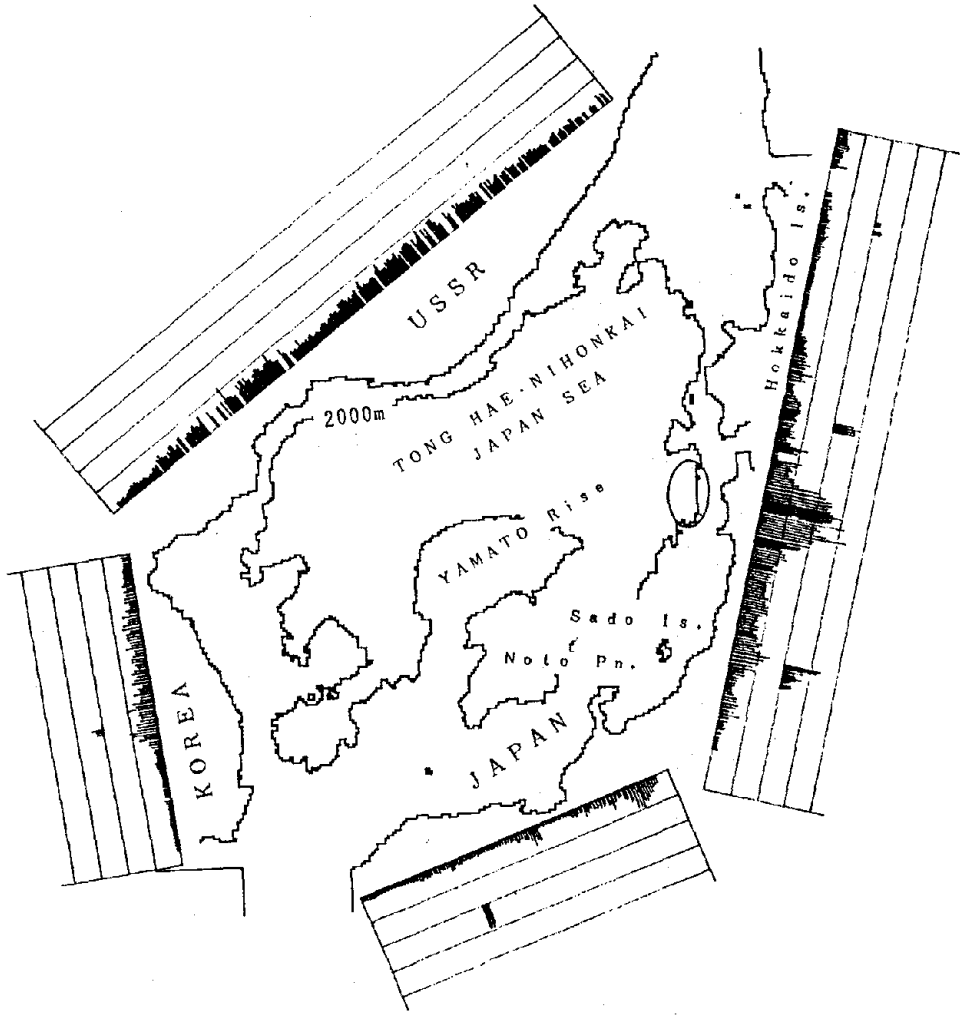

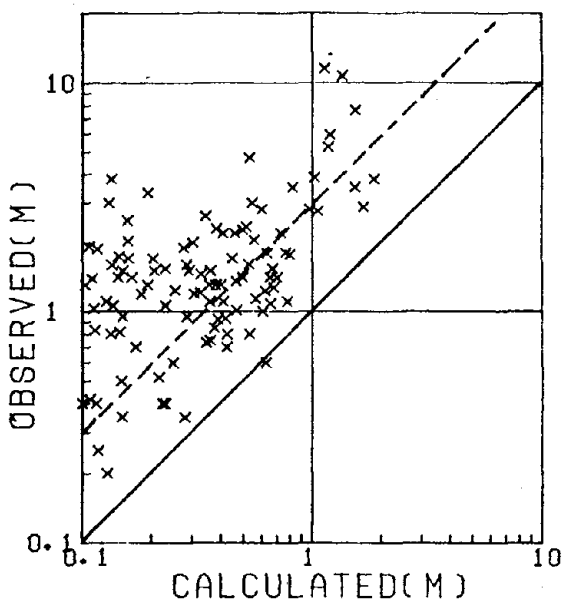

Fig. 9 Comparison of observed tsunami height(h_{obs}) with numerically calculated height(h_{cal}). Full line denotes $h_{obs} = h_{cal}$, and broken line denotes $h_{obs} = 3.0 \times h_{cal}$.

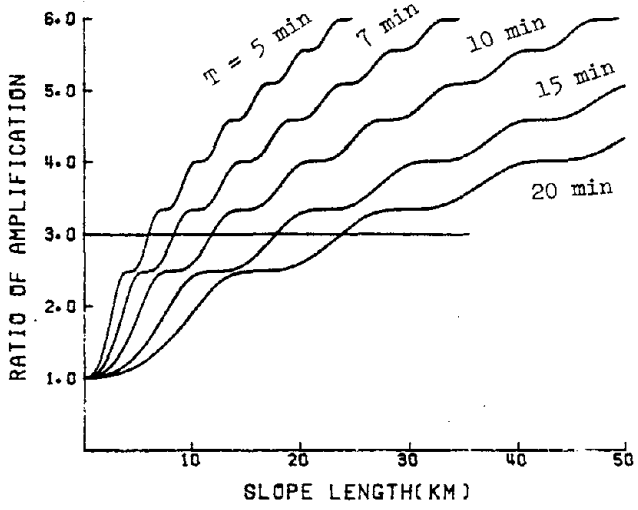

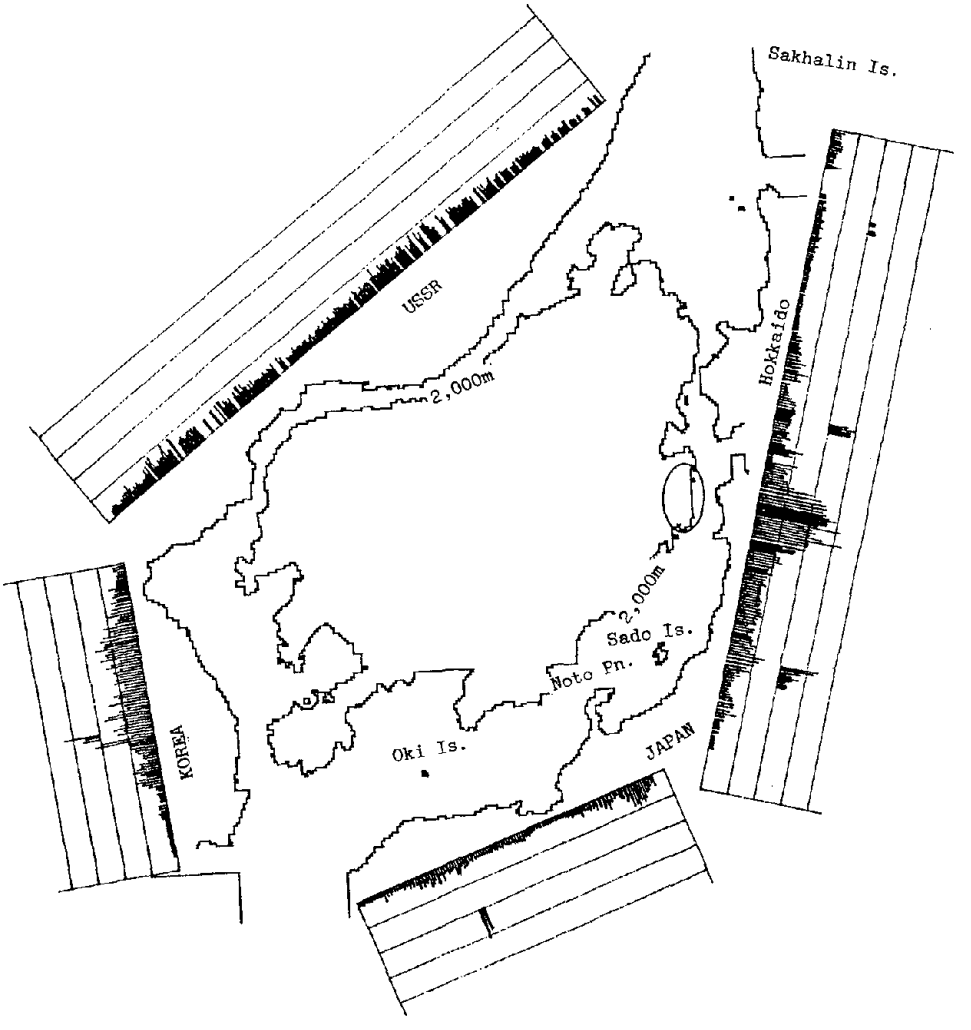

Fig. 11 Result of numerical calculation of the Nihonkai-Chubu Earthquake-Tsunami under the condition that Yamato Rise is removed.

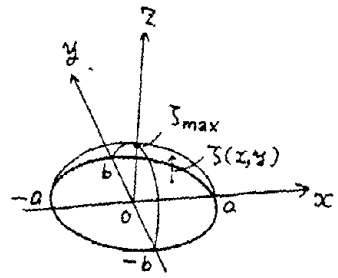

$$\zeta(x,y) = \zeta_{max}\left(1 - \frac{x^2}{a^2} - \frac{y^2}{b^2}\right)$$

Fig. 12 Simplified seabed upheaval model.

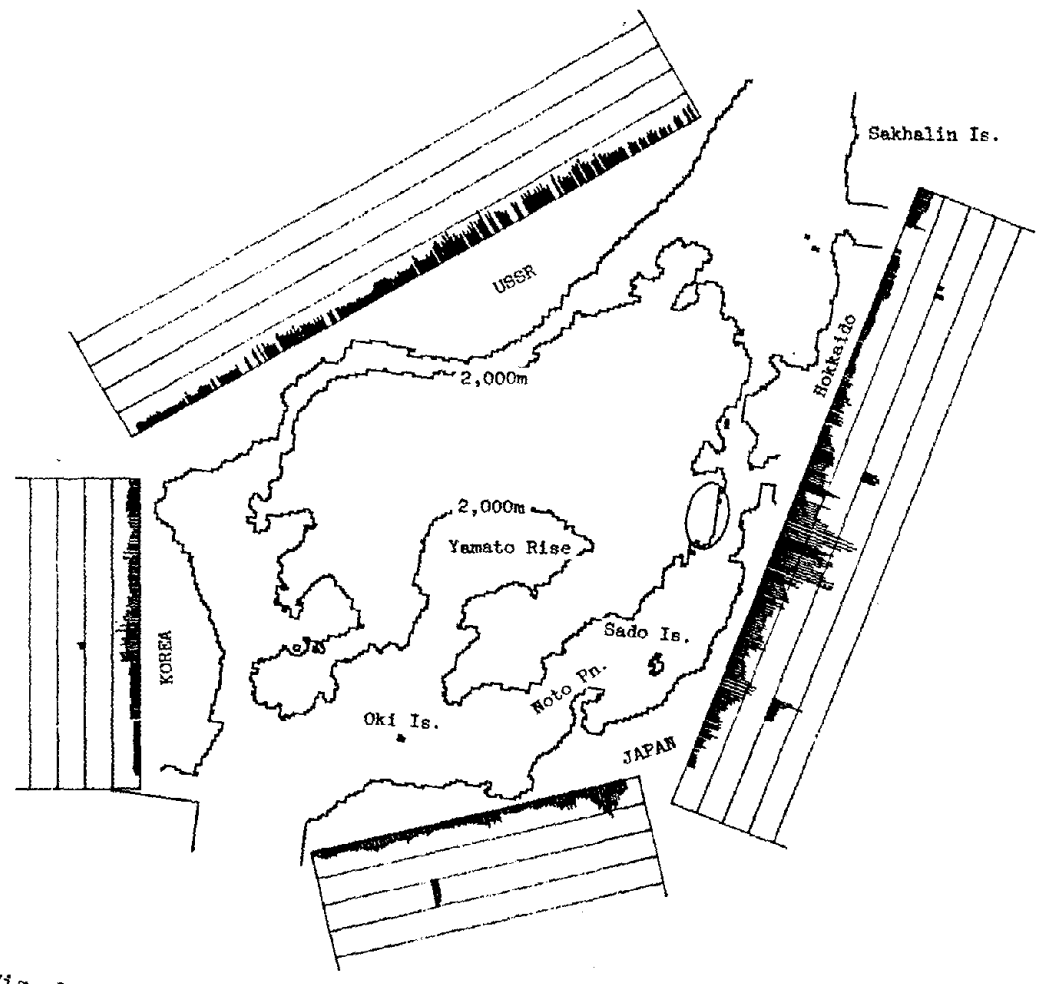

Fig. 13 Tsunami height distribution for the symplified model.

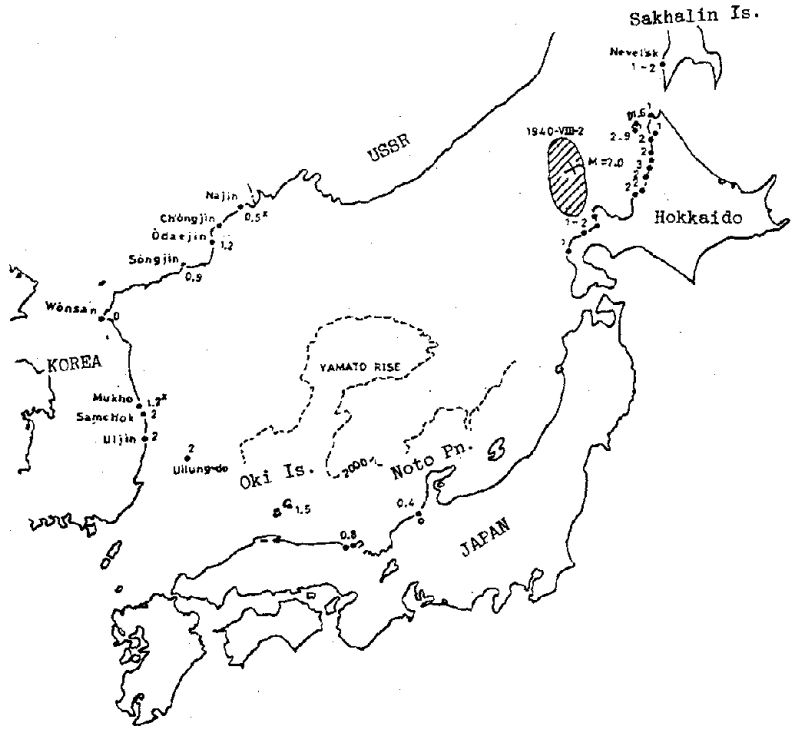

Fig. 14 Distribution of height of the Kamuimisaki-Oki Earthquake-Tsunami of 1940-VIII-2, M = 7.5, m = 2. unit:m.

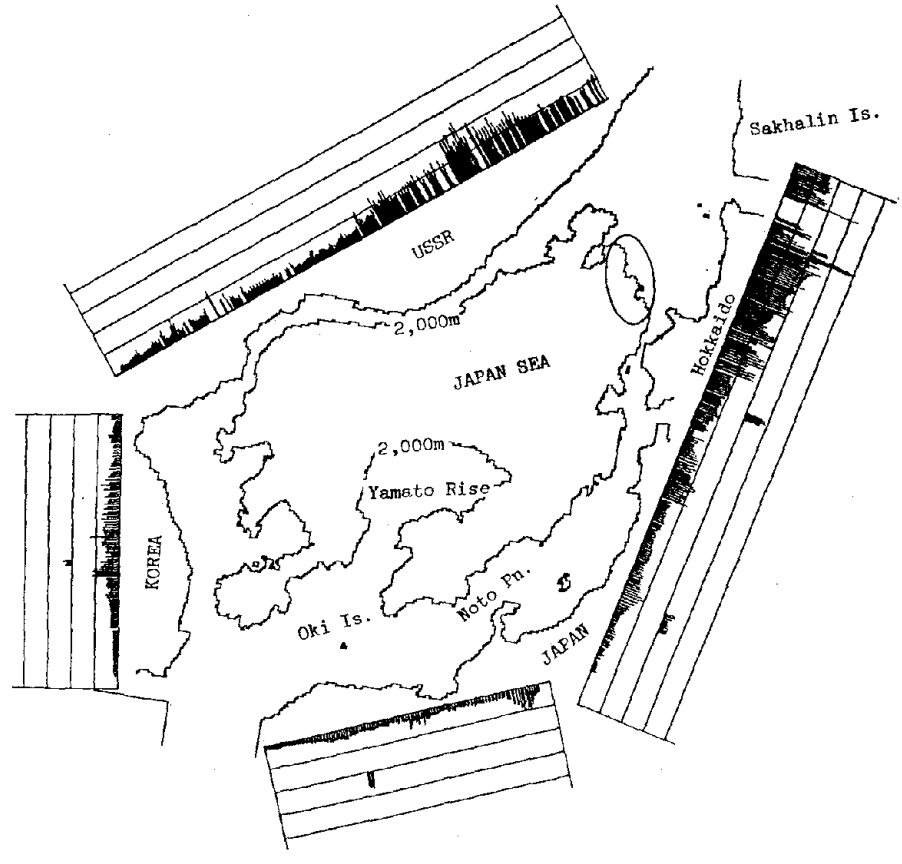

Fig. 15 Result of the numerical calculation of the Kamuimisaki-Oki Tsunami.

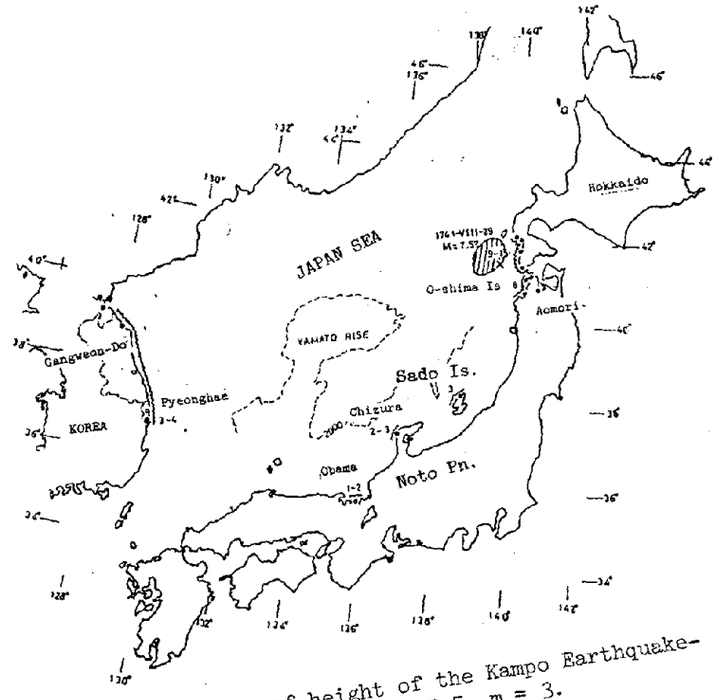

Fig. 16 Distribution of height of the Kampo Earthquake-Tsunami of 1741-VIII-29, M = 7.5, m = 3.

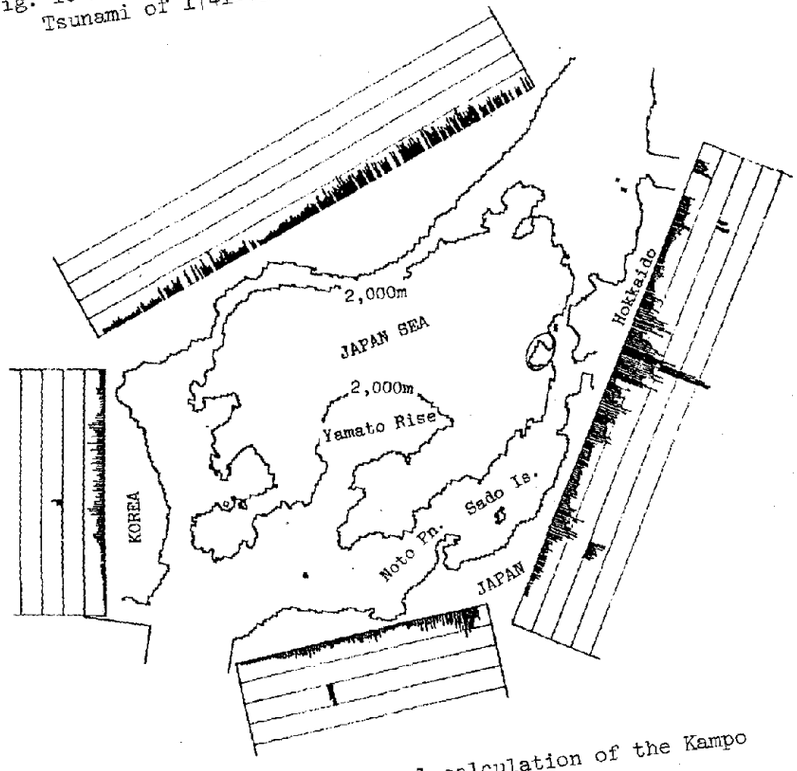

Fig. 17 Result of the numerical calculation of the Kampo Tsunami.

Theme IV

U.S.-JAPAN COOPERATIVE RESEARCH PROGRAM

RECOMMENDED U.S.-JAPAN JOINT RESEARCH ON SEISMIC BEHAVIOR OF BURIED PIPELINES AND TELECOMMUNICATIONS SYSTEMS

BY

M. SHINOZUKA

ABSTRACT

The U.S.-Japan Workshop on Seismic Behavior of Buried Pipelines and Telecommunications Systems was held under the sponsorship of the U.S. National Science Foundation with Dr. K. Thirumalai as Program Director in cooperation with Task Committee F Disaster Prevention Methods for Lifeline Systems (Co-Chairman Dr. W. W. Hakala, and Dr. T. Iwasaki, PWRI), UJNR Panel on Wind and Seismic Effects (Co-Chairmen Drs. R. N. Wright, NBS, and Dr. R. Iida, PWRI) at PWRI, Tsukuba Science City, Japan on December 5-7, 1984. Nippon Telegraph and Telephone's cooperation is also noted. The workshop reviewed the current knowledge, analytical, experimental and field observation, of seismic effects on buried pipelines and telecommunications systems, and presented technical papers by the participants on the subject matters. This paper summarizes the recommended U.S.-Japan joint research as a result of the Workshop.

Keywords: Telecommunications Systems; Buried Pipelines; Ground Motions; Seismic Analysis; Reliability Analysis

1. RECOMMENDATIONS

On the basis of the paper presentations, comprehensive discussions were conducted during the resolution session to reach a consensus on the research topics that need immediate attention and to identify the specific research areas that are most suitable for future coordinated research between the U.S. and Japan. The discussions led to the recommendation that, in the immediate future, coordinated research and information exchange between the U.S. and Japan dealing with buried pipelines and telecommunications systems place the highest priority on the following areas of research.

1.1 Definition of Ground Motions Including Ground Strain Measurements for Lifeline Engineering

Ground motion information for lifeline engineering purposes is relatively scarce. Acquisition and development of information to define a proper intensity of ground motions explicitly for lifelines should advance the state-of-the-art of lifeline engineering and reliability analysis. The deployment of dense strong motion instrument arrays, e.g., at PWRI and elsewhere in Japan, provide data to improve analytical models for predicting the relative motions and ground strains.

The proposed joint activity is to expand existing Japanese dense arrays for direct measurement of ground strains and response of representative lifeline configurations (e.g., welded steel pipelines, jointed pipelines, conduits, etc.). The cooperative program should also include the following related tasks: (a) data reduction and analysis (including spectral and correlation studies) of available and future array data to develop the power spectral density of differential motions as functions of separation distance; (b) the development of related attenuation relationships as a function of earthquake magnitude and epicentral distance; and (c) seismic hazard analysis techniques should be developed to evaluate hazard curves in terms of the pertinent intensity scale. The proposed improved definition of ground motions is of greatest significance for disaster preparedness that require reliability of lifeline systems; for this purpose,

the demand for such information is critical and urgent.

1.2 Improvement of System Serviceability of Telecommunications Field Facilities And Equipment Under Seismic Conditions By More Advanced Earthquake-Resistant Design

It appears that the current contingency plans for telephone services in the case of an earthquake emergency are largely dependent upon the routing redundancy of networks. While this is probably adequate enough in most cases, the following questions remain: (1) are such plans possible for all physical equipment and outside facilities? (2) is the common cause nature of earthquake events reflected in such plans? and (3) has a cost-benefit analysis been carefully performed? A joint research project to address these questions is proposed.

1.3 Analytical and Experimental Investigation of Continuous and Segmented Buried Pipelines in Liquefield Areas

One of the most important geotechnical hazards for buried pipelines involves those associated with liquefaction. Liquefaction induced movements include (a) lateral spreading, (b) flow failure, (c) loss of bearing, and (d) subsidence and buoyancy effects. At present in the US, little work is devoted to the behavior and failure mechanism of pipelines in liquefield regions, even though it has been recognized that there exists a great need for analytical and experimental research on this subject matter. The behavior and failure of both continuous and segmented pipelines should be determined and design procedures must be developed. In this respect, a joint project is proposed in which technical data be exchanged and coordination of analytical and experimental efforts by the US and Japanese groups established.

1.4 Seismic Performance of Water and Sewer Pipelines

Present work to correlate number of leaks per mile with peak acceleration of MMI suggests that only some damage appears immediately after the earthquake. More damage, often extensive, appears later. We propose to extend examination of leak rates in water and sewer pipes by including Japanese records and by collecting and interpreting data on post-earthquake performance. Data collection and interpretation would be performed jointly by the US and the Japanese groups. The specific objectives of the joint project are primarily information exchange on (a) collected data on leak rates in water and sewer lines before, immediately after and for a longer period after an earthquake; (b) observed correlation between post- and pre-earthquake performance to help understand how pre-earthquake condition of the pipes influences seismic performance.

1.5 Model and Prototype Testing of Soil Restraint on Buried Pipelines in Large Displacement

Algorithms for modeling soil restraint on buried pipelines subjected to large ground distortions (e.g., faulting, landslides) are based on a limited number of model tests of soil-pipeline interaction and selected anchor pull-out tests reported in the literature. Although these algorithms have been used extensively in nonlinear finite element models, the need for verification/calibration is well-recognized. A comprehensive program of model testing (possibly some centrifuge and a soil box) is recommended. In addition several well-planned field tests on prototype-size pipeline segments are needed to validate model test results. Even though no clearly defined faults exist near-field in Japan, it should be mutually beneficial for the US and Japan to pursue a joint program in this area which could involve a number of university and research organizations in both countries. Since the proposed testing requires a substantial effort and budget, our immediate goal is to exchange experimental data so that we can maximize the utility of our current resources and at the same time, begin to coordinate our experimental efforts in the US and Japan.

1.6 Study of Current Seismic Protection Methods For Telecommunications, Related Electronic, and Peripheral Equipment Supported on Raised Floors

The objective of the proposed research project is to provide better seismic protection for sensitive telecommunications, electronic and computer and other equipment supported on raised floors, possibly in a clean room environment. These types of equipment are expected to remain operational during and immediately after a strong earthquake. As a matter of fact, during the 1970s, lateral bracing of equipment frames was widely adopted as a cost-effective method of stiffening against toppling. However, the increasing reliance on computer-based telecommunications justifies considering alternative protection systems, including base isolation for raised floor systems. We propose a joint project to identify more cost-effective support systems among various alternatives. The steps we might follow in this project are: (a) identify equipment which can be advantageously supported by alternative systems; (b) develop requirements for alternative systems; (c) develop and screen analytically candidate systems for their cost-effectiveness; (d) construct and test the most promising system by a shaker table; and (e) investigate if active control concepts might be applicable.

EXPERIMENTAL INVESTIGATION ON HYSTERETIC BEHAVIOR OF REINFORCED CONCRETE BRIDGE PIER COLUMNS

BY

Toshio Iwasaki[1], Kazuhiko Kawashima[2], Ryoji Hagiwara[3], Kinji Hasegawa[3], Tatsuhiko Koyama[4], and Takeshi Yoshida[5]

ABSTRACT

Substantial damage to reinforced concrete piers were observed during recent earthquakes in Japan and these failures were most likely caused by large lateral seismic forces experienced by the bridge. It is therefore necessary to evaluate nonlinear hysteretic behavior of reinforced concrete piers. This report summarizes the experimental studies on dynamic strength and deformation characteristics of reinforced concrete piers, which were conducted between 1981 and 1984 fiscal years at the Earthquake Engineering Division, Public Works Research Institute. Tentative conclusions obtained through the past studies as well as future experimental research programs are presented.

1. INTRODUCTION

Japan is one of the most earthquake-prone countries in the world, and it is of particular importance to assure safety of highway bridges against seismic disturbances in accordance with the Earthquake Disaster Prevention Countermeasures of Highway. Although seismic resistant design by means of seismic coefficient method has been used for highway bridges, substantial damage to reinforced concrete piers were observed in recent earthquakes such as the Miyagi-ken-oki Earthquake of 1978 and the Urakawa-oki Earthquake of 1982 (refer to Photos 1, 2 and 3). Such failures were most likely caused by lateral seismic forces, experienced by the bridge during large earthquakes of a short epicentral distance to the site, which are far larger than the seismic force currently considered in the design in terms of a seismic coefficient of 0.2 to 0.3.

Because it is anticipated that substructures including piers would experience large shaking when subjected to severe ground motions, the bridge should be designed to avoid the collapse of the primary bridge system such as falling-off of

---

[1] Director, Earthquake Disaster Prevention Department, Public Works Research Institute, Ministry of Construction, Tsukuba Science City, Japan.

[2] Head, Earthquake Engineering Division, Earthquake Disaster Prevention Department, Japan.

[3] Research Engineer, Earthquake Engineering Division, Japan.

[4] Research Engineer, Earthquake Engineering Division, Japan.

[5] Assistant Research Engineer, Earthquake Engineering Division, Japan.

the superstructure from the substructure. To maintain the integrity of the bridge during severe earthquakes, it is particularly important to evaluate nonlinear hysteretic behavior of reinforced concrete piers.

Because, up to now, much of seismic resistant design has been conducted on the basis of elastic behavior, comparatively few investigations have been made on nonlinear hysteretic behavior of reinforced concrete piers. Consequently, comprehensive experimental investigation on dynamic strength and deformation characteristics of reinforced concrete piers in inelastic range was initiated at the Earthquake Engineering Division of the Earthquake Disaster Prevention Department, the Public Works Research Institute, in 1981 using the Dynamic Structural Testing Facility.

This report summarizes the experimental studies performed between 1981 and 1984 fiscal years, and tentative conclusions obtained from the studies as well as future experimental research program needs.

2. EXPERIMENTAL INVESTIGATIONS CONDUCTED BETWEEN 1981 AND 1984 FISCAL YEARS

2.1 Experimental Procedure and Specimen of Model Pier

Model specimens of reinforced concrete pier were fixed at the footing which in turn was tied down to the reaction floor as shown in Fig. 1. The footing was designed as large as possible and stirrups were densely spaced so that failure in the footing would be prevented. The pier model was subjected to static and/or dynamic loadings at the top by an electro-hydraulic servo actuator (the maximum loading capacity of ±125 tf and the maximum stroke of ±125mm). The applied load to the pier simulated the force which would occur at the pier top during an earthquake including the effects of the inertia force due to the mass of super - and substructures. Such a loading condition is appropriate for testing of bridge piers in which the inertia force associated with the superstructure is pronounced.

Reversed-cyclical lateral force was applied to the pier with a loading time history of displacement as shown in Fig. 2. Up to the yielding of the longitudinal reinforcement, the load was increased step by step to about 10 increments. The displacement developed at the top of the pier when the longitudinal reinforcement exhibited yielding is defined hereinafter as the yield displacement, δy, and is used as a reference value to specify the displacement loading subjected to the pier. After initial yielding of the longitudinal reinforcement, displacement loading with n-cycles were applied to the pier by successively increasing the displacement amplitude as δy, $2\,\delta y$, $3\,\delta y$, ----. According to such loading scheme, envelopes of the load-displacement hysteresis loops can be obtained as shown in Fig. 3. Although there are many definitions on failure of a structural element, in this study the pier is assumed to have failed when the strength becomes smaller than the yield strength after the pier had attained its maximum strength.

The scale of the specimens used in this study was approximately 1/5 of typical highway bridge piers, and the standard cross section was selected as 50cm x 50cm. Table-1 summarizes the dimensions and loading procedure of the 34 model piers tested in this study. It should be noted here that although bridge piers are subjected to nominal axial stress of 5 - 20Kgf/cm^2 associated with dead weight of superstructure, it was disregarded in this experiment, because their effects are relatively insignificant.

2.1 Effect of Loading Velocity (1981 Fiscal year)

To investigate the effects of loading velocity on the dynamic strength and deformation of reinforced concrete piers, dynamic loading tests were conducted by varying the loading velocity as 17.5cm/sec., 35cm/sec. and 70cm/sec. For this purpose, three model piers with the same dimensions as shown in Fig. 4 were used (Model P-1 P-2, P-3, refer to Table-1).

Figs. 5 and 6 show the effects of loading velocity in terms of the envelope of load-displacement hysteresis loops and the equivalent hysteretic damping ratio. Table-2 summarizes dynamic performance of the three specimens.

The conclusion derived from this series of tests is as follows:

1) The variation in loading velocity on the maximum strength and ductility factor (displacement ductility factor) is not significant in the case of flexural failure with loading velocity as high as 70cm/sec. However, hysteretic damping ratio increases with the increase in loading velocity after yielding of longitudinal reinforcement (after approximately 2 δy).

2.3 Effect of Dynamic Loading and Longitudinal Reinforcement Ratio (1982 Fiscal Year)

To investigate the effects of dynamic loading and longitudinal reinforcement ratio on flexural failure of reinforced concrete piers, both static loading test (loading velocity of 2.4cm/sec.) and dynamic loading test (loading velocity of 25cm/sec.) were conducted on model piers with longitudinal reinforcement ratio of 1.79%, 0.87% and 0.48%. Fig. 7 represents six specimens used for the experiments (Model P-4 - P-9, refer to Table-1).

Figs. 8 and 9 show the effect of dynamic loading and longitudinal reinforcement ratio as shown by the envelope of load-displacement hysteresis loops and the equivalent hysteretic damping ratio. Table 3 summarizes the dynamic performance of the six specimens.

The conclusions derived from this series of tests are as follows:

1) The yield strength, the maximum strength and yield displacement associated with flexural failure developed at the bottom of the pier increased with increase in longitudinal reinforcement ratio.

2) Although significant differences between dynamic loading and static loading are not observed, the maximum strength, ultimate displacement and ductility factor in the dynamic loading were slightly larger than those in the static loading.

3) Plastic hinge region, in which extensive spalling and cracks of concrete were developed, increased with the increase in the longitudinal reinforcement ratio.

2.4 Effect of Tie Reinforcement Ratio (1983 Fiscal Year)

To investigate the effects of tie reinforcement ratio on flexural failure of reinforced concrete piers, dynamic loading tests were conducted on four model piers (Model P-10 - P-13, refer to Table-1). The tie reinforcement ratios ranged from 0.1% to 0.3%, and the height of pier from the bottom where tie bars were placed densely was also taken as a variable as shown in Fig. 10.

Figs. 11 and 12 represent the effect of tie reinforcement ratio as shown by the envelope of load-displacement hysteresis loops and the equivalent hysteretic damping ratio. Table-4 summarizes the dynamic performance of the four specimens.

The conclusion derived from this test series is as follows:

1) Tie reinforcement ratio between 0.1% and 0.3% does not have significant effect on dynamic strength and ductility factor in case of flexural failures developed at the bottom of the pier.

2.5 Effect of Cut-off of Longitudinal Reinforcement (1983 Fiscal Year)

To investigate the effects of cut-off of longitudinal reinforcement, dynamic loading tests were conducted on three model piers (Model P-14, 15 and 16, refer to Table-1). The bars were cut-off at the height of 110cm, 135cm and 160cm from the bottom as shown in Fig. 13. Because the height from the bottom of pier from which longitudinal reinforcement can be reduced was set at 110 cm, the height of cut-off at 110cm, 135cm and 160cm corresponds, respectively, to no anchoring length (ℓ=0), anchoring length of half width of pier (ℓ=d/2, d: width of pier), and anchoring length of pier width (ℓ =d). Dimensions of the model P-14, 15 and 16 were the same with those of model P-10 (no cut-off) so that the effect of cut-off could be investigated by comparing the two results.

Figs. 14 and 15 represent the effect of cut-off as shown by the envelope of load-displacement hysteresis loops and the equivalent hysteretic damping ratio. Table 5 summarize the dynamic performance of the four specimens.

The conclusions derived from this series of tests are as follows:

1) Flexural failure occurred at the bottom of pier in model P-10 (no cut-off) and P-16 (=d). In the model P-15 (ℓ =d/2), although cracks were initiated both at the bottom of pier and at the

cut-off point, flexural failure was predominantly developed at the bottom at failure. Model P-14 (ℓ=0) failed due to progress of diagonal cracks at the cut-off point.

2) Equivalent damping ratio and ductility factor were very small in model P-14 (ℓ=0), which failed at the cut-off point, as compared with the other model piers.

3) Failure at the cut-off point could be prevented if the anchorage length of longitudinal reinforcing bars are greater than or equal to the width of the pier.

2.6 Effect of Shear-Span Ratio (1983 Fiscal Year)

To investigate the effects of shear-span ratio, dynamic loading tests were conducted on three model piers (model P-10, 17 and 18, refer to Table-1). The shear-span ratio was 5.4, 3.8 and 2.2 as shown in Fig. 16.

Figs. 17 and 18 represent the effect of shear-span ratio in terms of the envelope of load-displacement hysteresis loops and the equivalent hysteretic damping ratio. Table-6 summarizes the dynamic performance of the four specimens.

The conclusions derived from this series of tests are as follows:

1) Flexural failure was developed at the bottom for model piers with a shear-span ratio of 3.8 and 5.4 whereas shear failure occurred in the model pier with a shear-span ratio of 2.2.

2) Hysteretic damping ratio of the model pier with ductility factor of 2.2, which failed due to shear failure, is substantially smaller (50 ~ 60%) than that of the model piers with shear-span ratio of 3.8 and 5.4.

3) Ductility factor decreases in accordance with decrease in the shear-span ratio.

2.7 Effect of Number of Loading (1983 Fiscal Year)

To investigate the effects of number of loading cycle, n, dynamic loading tests were conducted on seven model piers (Model P-10, 17 ~ 22, refer to Table-1) as:

- model P-10, 19 and 22 (shear-span ratio of 5.4) n=3, 5, and 10.
- model P-17 and 20 (shear-span ratio of 3.8); n=3 and 10.
- model P-18 and 21 (shear-span ratio of 2.2); n=3 and 10.

Fig. 19 represents dimensions of the seven specimens.

Figs. 20 and 21 show the effect of number of loading in terms of the envelope of load-displacement hysteresis loops and the equivalent hysteretic damping ratio. Table-7 summarizes the dynamic performance of the seven specimens.

The conclusions derived from this series of tests are as follows:

1) In the case where flexural failure developed at the bottom of

pier , the effect of loading cycle, n, on hysteresis loops is not significant until spalling of concrete cover occured. However, after the spalling has developed, breaking of longitudinal reinforcing bars occurred at early stages as the number of loading cycle increased. This, in turn, caused substantial reduction in the resistance to lateral load. The hysteretic damping ratio is also significantly affected by the number of loading cycle after spalling of concrete cover, and it became larger for a small number of loading cycles.

2) The effect of the number of loading cycle on load-displacement hysteresis loops and equivalent hysteretic damping ratio is much more pronounced in shear failure than in flexural failure described above.

2.8 Effect of Two Directional Loading (1983 Fiscal Year)

To investigate the effects of two directional loading on flexural failure of reinforced concrete piers, dynamic loading tests were conducted for two model piers (Model P-23 and 24). The model piers were subjected to the loading condition as shown in Fig. 22, in which the number of loading cycle, n, was also taken as parameter (n=5 and 10). It should be noted here that two directional loading was not applied to the pier simultaneously, but applied alternatively due to the limitation of the experimental facility. The dimensions of Model P-23 and 24 were the same as Model P-10 and 22, which were tested under one directional loading, so that the effect of two directional loading could be investigated in comparison with the test results of Model P-10 and 22.

Fig. 23 and 24 show the effect of two directional loading in terms of the envelope of load-displacement hysteresis loops and the equivalent hysteretic damping ratio. Table-8 summarizes the dynamic performance of the four specimens.

The conclusions derived from this study are as follows:

1) Spalling of concrete cover, and breaking of longitudinal reinforcing bars as well as the reduction in strength occurred earlier in the two-directional loading than in the one-directional loading. Ductility factor under the two-directional loading was about 60 80% of that under the one-directional loading. However, the ultimate strength of pier was not significantly effected by the two directional loading.

2) Effect of the number of loading cycles under the two-directional loading is the same with that under the one directional loading as described in the preceding section.

2.9 Effect of Shear Reinforcement for Piers with Square Cross Section (1984 Fiscal Year)

The effectiveness of shear reinforcement against brittle shear failure of reinforced concrete piers with short shear-span ratio was investigated using three model piers with a shear-span ratio of 2.5 (Model P-25, 26 and 27, refer to Table-1). The

shear reinforcement was provided in three ways, i.e., placing tie bars densely at 5cm intervals (Model P-25), spiral hoops with a pitch of 2.5cm (Model P-26), and diagonal reinforcing bars with a reinforcement ratio of 25 percent of the longitudinal reinforcement ratio (Model P-27). Fig. 25 presents the dimensions of model piers studied.

The effectiveness of shear reinforcement is compared with the test result of Model P-18, which had a shear-span ratio of 2.2 and ties spaced at 25cm on centers.

Figs. 26 and 27 represent the effectiveness of shear reinforcement in terms of the envelope of load-displacement hysteresis loops and the equivalent hysteretic damping ratio. Table-9 summarizes the dynamic performance of the four specimens.

The conclusions derived from this series of tests are as follows:

1) Placing tie bars densely, spiral hoops and diagonal reinforcing bars are all effective for increasing ductility factor of piers with small shear-span ratio. However, shear reinforcement has no effect in increasing the maximum strength of the piers.

2) Among the three procedures for shear reinforcement described above, spiral hoops is most effective in increasing ductility.

The effectiveness of spiral hoops for round pier will be described in section 2.12.

2.10 Effect of Cross Sectional Shape (1984 Fiscal Year)

Dynamic tests were conducted on three model piers having a circular cross section to investigate the effect of cross sectional shape on the lateral load resistant capacity (Model P-28, 29 and 30, refer to Table-1). The shear-span of the specimens were 4.7, 3.3 and 1.9 as shown in Fig. 28. The cross sectional area, height, longitudinal and tie reinforcement ratios, and loading procedure were the same as the model P-10, 17 and 18 (square cross section) described in the preceding section. It should be noted here that because the diameter of round piers and the width of square pier are different when the cross sectional area is taken as the same, apparent shear-span ratio is not identical between the round pier and the square pier.

Figs. 29 and 30 represent the effect of cross sectional shape on the seismic behavior of piers in terms of the envelope of load-displacement hysteresis loops and the equivalent hysteretic damping ratio. Table-10 summarizes the dynamic performance of the six specimens.

The conclusions derived from this series of tests are as follows:

1) In the case where flexural failure is developed at the bottom, the effect of cross sectional shape between circular and square is not significant if cross sectional area, height, and longitudinal and tie reinforcement ratios are the same.

2) In the case where shear failure occurs, the maximum strength is substantially larger in the round pier than in the square piper.

2.11 Effect of Loading Direction (1984 Fiscal Year)

Three model piers (Model P-10, 33 and 34, refer to Table-1) were tested under dynamic loading to evaluate effect of loading direction on the seismic behavior of piers. Fig. 31 shows the three specimens in which shear-span ratio, longitudinal and tie reinforcement ratios, and cross section are the same. However, the principal axes of the cross section was rotated with respect to the footing at an angle of $\pi/6$ and $\pi/4$ in the Model P-33 and 34, respectively. Only the principal axes of the pier were related, while the position of the actuator remained parallel to the major axes of the footing.

Fig. 32 and 33 represent the effect of loading direction in terms of the envelope of load-displacement hysteresis loops and the equivalent hysteretic damping ratio. Table-11 summarizes the dynamic performance of the three specimens.

The conclusions derived from this series of tests is as follows:

1) In the case where flexural failure is developed at the bottom of pier, the effect of loading direction is less significant until spalling of concrete cover. However, after the spalling of concrete cover, reduction of the resistance to lateral load occurred significantly in the piers subjected to the loading in the direction rotated to the axis of cross section.

2.12 Effect of Spiral Hoops of Pier with Circular Cross Section (1984 Fiscal Year)

Two model piers with shear-span ratio of 4.7 and 3.3 (Model P-31 and 32, refer to Table-1) were tested to investigate the effect of spiral hoops on the seismic behavior of piers. They were reinforced by spiral hoop with a pitch of 2.5cm within the range of 50cm in height from the foot as shown in Fig. 34. Effect of such spiral hoop was investigated in comparisons with the test of Model P-28 and 29, which have the same dimensions and shear-span ratios as Model P-31 and 32, respectively, and are reinforced with ties at 25cm on centers.

Figs. 35 and 36 represent the effect of spiral hoops in terms of the envelope of load-displacement hysteresis loops and the equivalent hysteretic damping ratio. Table-12 summarizes the dynamic performance of the four specimens.

The conclusion derived from this series of tests is as follows:

1) Significant increase in ductility factor and hysteretic damping ratio can be achieved by placing spiral hoops having a pitch of 2.5cm for both shear-span ratio of 4.7 and 3.3 as compared with the reinforcement with ties. The effect of spiral hoops on the maximum strength is small.

3. FUTURE EXPERIMENTAL PROGRAM

3.1 Investigation on Structural Characteristics

(1) Effect of Cross Sectional Shape (Hollow and Rectangular)

Following the study described in section 2-10, the effect of cross sectional shape, hollow and rectangular which are frequently adopted at sites, on the seismic behavior of piers needs to be investigated.

(2) Effect of Diameter of Longitudinal Reinforcement

It is necessary to investigate the effect of diameter of longitudinal reinforcement, which affects buckling fracture of longitudinal reinforcing bars, and height of plastic hinge zone.

(3) Scale Effect

The model piers, which have been used for the experimental study, had a scale factor of about 1/5 in length to typical prototype highway bridge piers. Therefore, it is necessary to assure the scale effect on dynamic performance obtained from the model pier tests.

3.2 Investigations on Loading Characteristics

(1) Effect of Torsional Load

Bridge piers such as skewed and curved bridges are subjected to twisting load as well as lateral load in the longitudinal and transverse directions to the bridge axis. It is, therefore, necessary to investigate the effect of twisting loading on the dynamic performance of reinforced concrete piers.

(2) Effect of Loading Hysteresis

The loading time history as shown in Fig. 2 has been adopted in the experiments, i.e., reversed cyclic loading with n repetitions was applied to the pier, and amplitude of displacement is increased monotonically. Because it became apparent that the dynamic performance of reinforced concrete piers is significantly affected by the history of loading, it is necessary to investigate such effects on the dynamic performance of reinforced concrete piers.

(3) Effect of Force-controlled Loading

In the experiments presented in Chapter 2, the bridge piers were subjected to displacement-controlled loading. In this loading procedure, no matter how much the pier sustained damage, it was forced to return to the original rest position. Thus, progressive failure of the pier in one direction can be avoided. However, the actual inertia force developed in the pier during severe earthquakes is more likely to be simulated by force-controlled loading. It is, therefore, necessary to assure the difference of ultimate failure modes developed under displacement-controlled loading with those developed under force-controlled loading.

(4) Comparison with Shaking Table Tests

During an actual earthquake, the structural response of a bridge depends on deterioration of stiffness and damping characteristics of piers, which, in turn, affects the lateral loading subjected to piers. It is, therefore, necessary to take such hysteretic behavior into account in evaluating failure modes of the pier. From this point, it is necessary to conduct shaking table test and assure the test results presented in the preceding chapter in comparison with shaking table tests.

4. CONCLUDING REMARKS

This paper summarized the experimental study, conducted between 1981 and 1984 fiscal years, on dynamic strength and deformation characteristics of reinforced concrete bridge piers. It is necessary to promote the experimental study for the remaining problems from both structural and loading characteristics point of view. It is further needed to conduct precise examination on the important factors, which have pronounced effects on the dynamic behavior of piers to get rational seismic design procedure for reinforced concrete piers of highway bridges.

5. REFERENCES

1. Saeki, S., Ota, M., Kobayashi, S., Shioi, Y., Kawashima, and Nishikawa, K.: Damage of Bridges, Chapter 9 of Report on the Disaster caused by the Miyagi-ken-oki Earthquake of 1978, Report of the Public Works Research Institute, Vol. 159, 1983.

2. Narita, N., Murakami, M. and Asanuma, H.: Report of the Investigation on Earthquake Damage Shizunai Bridge, 15th Joint Meeting, U.S. - Japan Panel on Wind and Seismic Effect, U.J.N.R., Tsukuba, Japan, 1983.

3. Kuribayashi, E., Iwasaki, T., Hadate, T. and Hagiwara, R.: Experimental Studies on Seismic behavior of Structural Members Using a Dynamic Structural Testing Facility At PWRI, 14th Joint Meeting, U.S. - Japan Panel on Wind and Seismic Effects, U.J.N.R., Washington, D.C., U.S.A., 1982.

4. Iwasaki, T., Hagiwara, R., Hasegawa, K., Koyama, T. and Yoshida, T.: Model Experiments on Dynamic Behavior of Reinforced Concrete Bridge Pier Columns, 16th Joint Meeting, U.S. - Japan Panel on Wind and Seismic Effects, U.J.N.R., Washington, D. C., U.S.A., 1984.

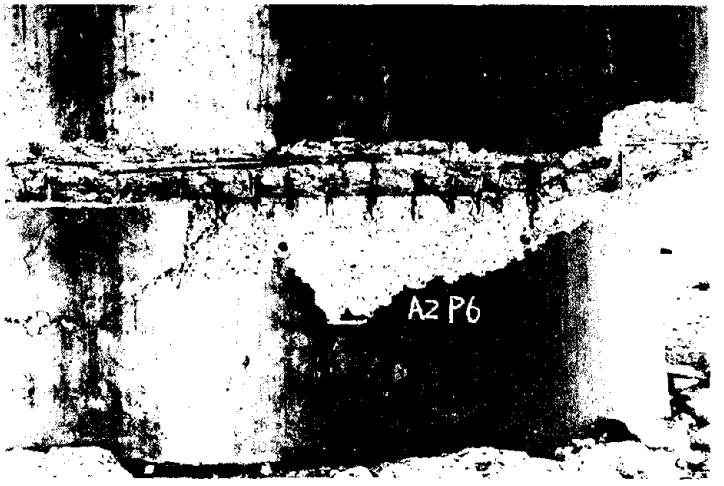

Photo 1 Damage of Pier 6 in the Sendai Bridge by Miyagi-ken-oki Earthquake of 1978

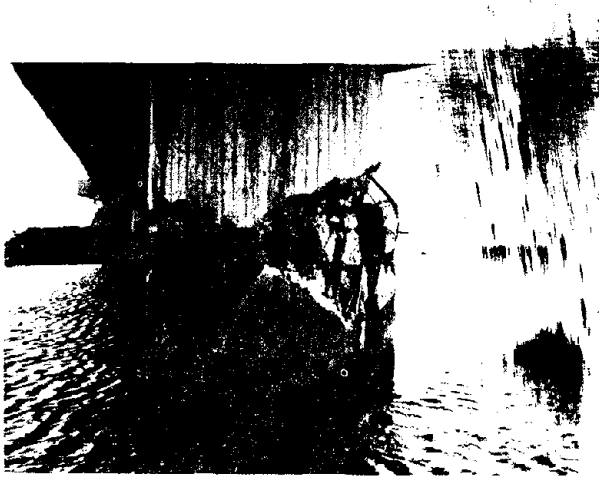

Photo 2 Damage of Pier 3 in the Shizunai Bridge by Urakawa-oki Earthquake of 1982

Photo 3 Damage of Pier 6 in the Shizunai Bridge by Urakawa-oki Earthquake of 1982

Table-1.1 Summary of Dimensions and Loading Procedures

Model No.		P-1	P-2	P-3	P-4	P-5	P-6	P-7	P-8	P-9
Cross Section [cm]		40x80	40x80	40x80	40x80	40x80	40x80	40x80	40x80	40x80
Covering Depth of Concrete [cm]		5	5	5	5	5	5	5	5	5
Effective Height [cm]		240	240	240	240	240	240	240	240	240
Shear-Span Ratio		6.9	6.9	6.9	6.9	6.9	6.9	6.9	6.9	6.9
Longitudinal Reinforcing Bar (Deformed Bar)	Material and Diameter [mm]	SD30,19	SD30,19	SD30,19	SD30,19	SD30,19	SD30,16	SD30,16	SD30,13	SD30,13
	Cut-off [cm]	-	-	-	-	-	-	-	-	-
	Ratio of Reinforcement [%]	0.82	0.82	0.82	1.79	1.79	0.87	0.87	0.48	0.48
Hoop Tie	Material and Diameter [mm]	SR24,9	SR24,9	SR24,9	SR24,9	SR24,9	SR24,9	SR24,9	SR24,9	SR24,9
	Ratio of Reinforcement [%]	0.08	0.08	0.08	0.08	0.08	0.08	0.08	0.08	0.08
Concrete	Material	Portland Cement	Portland Cement	Portland Cement	Portland Cement	Portland Cement	Portland Cement	Portland Cement	Portland Cement	Portland Cement
	Max Grain Size of Aggregate [mm]	20	20	20	20	20	20	20	20	20
	Uni-Axial Strength [Kg/cm^2]	311	310	314	290	258	290	258	290	258
Lateral Force	Direction of Loading	1 Direction	1 Direction	1 Direction	1 Direction	1 Direction	1 Direction	1 Direction	1 Direction	1 Direction
	Velocity of Loading [cm/sec.]	17.5	35.0	75.0	2.4	25.0	2.4	25.0	2.4	2.25
	Number of Loading for Each Specific Lateral Displacement	10	10	10	10	10	10	10	10	10

Table-1.2 Summary of Dimensions and Loading Procedures

Model No.		P-10	P-11	P-12	P-13	P-14	P-15	P-16	P-17	P-18
Cross Section [cm]		50x50	50x50	50x50	50x50	50x50	50x50	50x50	50x50	50x50
Covering Depth of Concrete [cm]		3.5	3.5	3.5	3.5	3.5	3.5	3.5	3.5	3.5
Effective Height [cm]		250	250	250	250	250	250	250	175	100
Shear-Span Ratio		5.4	5.4	5.4	5.4	5.4	5.4	5.4	3.8	2.2
Longitudinal Reinforcing Bar (Deformed Bar)	Material and Diameter [mm]	SD30,13	SD30,13	SD30,13	SD30,13	SD30,13	SD30,13	SD30,13	SD30,13	SD30,13
	Cut-off [cm]	-	-	-	-	110	135	160	-	-
	Ratio of Reinforcement [%]	2.03	2.03	2.03	2.03	2.03 (1.02 after Cut-off)	2.03 (1.02 after Cut-off)	2.03 (1.02 after Cut-off)	2.03	2.03
Hoop Tie	Material and Diameter [mm]	SR24,9	SR24,9	SR24,9	SR24,9	SR24,9	SR24,9	SR24,9	SR24,9	SR24,9
	Ratio of Reinforcement [%]	0.10	0.20 (Bottom ∿ 0.5m)	0.20 (Bottom ∿ 1.0m)	0.31 (Bottom ∿ 0.5m)	0.10	0.10	0.10	0.10	0.10
Concrete	Material	Portland Cement	Portland Cement	Portland Cement	Portland Cement	Portland Cement	Portland Cement	Portland Cement	Portland Cement	Portland Cement
	Max Grain Size of Aggregate [mm]	10	10	10	10	10	10	10	10	10
	Uni-Axial Strength [Kg/cm^2]	319	327	321	334	327	332	325	338	334
Lateral Force	Direction of Loading	1 Direction	1 Direction	1 Direction	1 Direction	1 Direction	1 Direction	1 Direction	1 Direction	1 Direction
	Velocity of Loading [cm/sec.]	25.0	25.0	25.0	25.0	25.0	25.0	25.0	25.0	25.0
	Number of Loading for Each Specific Lateral Displacement	10	10	10	10	10	10	10	10	10

Table-1.3 Summary of Dimensions and Loading Procedures

Model No.		P-19	P-20	P-21	P-22	P-23	P-24	P-25	P-26	P-27
Cross Section [cm]		50x50	50x50	50x50	50x50	50x50	50x50	50x50	50x50	50x50
Covering Depth of Concrete [cm]		3.5	3.5	3.5	3.5	3.5	3.5	3.5	3.5	3.5
Effective Height [cm]		250	175	100	250	250	250	116	116	116
Shear-Span Ratio		5.4	3.8	2.2	5.4	5.4	5.4	2.5	2.5	2.5
Longitudinal Reinforcing Bar (Deformed Bar)	Material and Diameter [mm]	SD30,13	SD30,13	SD30,13	SD30,13	SD30,13	SD30,13	SD30,13	SD30,13	SD30,13
	Cut-off [cm]	-	-	-	-	-	-	-	-	-
	Ratio of Reinforcement [%]	2.03	2.03	2.03	2.03	2.03	2.03	2.03	2.03	2.03
Hoop Tie	Material and Diameter [mm]	SR24,9	SR24,9	SR24,9	SR24,9	SR24,9	SR24,9	SR24,9	SR24,9	SR24,9
	Ratio of Reinforcement [%]	0.10	0.10	0.10	0.10	0.10	0.10	0.51	1.02 (Spiral)	0.10 (Diagonal Reinforcement)
Concrete	Material	Portland Cement	Portland Cement	Portland Cement	Portland Cement	Portland Cement	Portland Cement	Portland Cement	Portland Cement	Portland Cement
	Max Grain Size of Aggregate [mm]	10	10	10	10	10	10	10	10	10
	Uni-Axial Strength [Kg/cm^2]	340	324	321	320	338	337	390	390	390
Lateral Force	Direction of Loading	1 Direction	1 Direction	1 Direction	1 Direction	2 Direction	2 Direction	1 Direction	1 Direction	1 Direction
	Velocity of Loading [cm/sec.]	25.0	25.0	25.0	25.0	25.0	25.0	25.0	25.0	25.0
	Number of Loading for Each Specific Lateral Displacement	3	3	3	5	10	5	10	10	10

Table-1.4 Summary of Dimensions and Loading Procedures

Model No.		P-28	P-29	P-30	P-31	P-32	P-33	P-34
Cross Section [cm]		ϕ56.4	ϕ56.4	ϕ56.4	ϕ56.4	ϕ56.4	50x50	50x50
Covering Depth of Concrete [cm]		3.5	3.5	3.5	3.5	3.5	3.5	3.5
Effective Height [cm]		250	175	100	250	175	250	250
Shear-Span Ratio		4.7	3.3	1.9	4.7	3.3	5.4	5.4
Longitudinal Reinforcing Bar (Deformed Bar)	Material and Diameter [mm]	SD30,13	SD30,13	SD30,13	SD30,13	SD30,13	SD30,13	SD30,13
	Cut-off [cm]	-	-	-	-	-	-	-
	Ratio of Reinforcement [%]	2.03	2.03	2.03	2.03	2.03	2.03	2.03
Hoop Tie	Material and Diameter [mm]	SR24,9	SR24,9	SR24,9	SR24,9	SR24,9	SR24,9	SR24,9
	Ratio of Reinforcement [%]	0.10	0.10	0.10	1.02 (Spiral)	1.02 (Spiral)	0.10	0.10
Concrete	Material	Portland Cement	Portland Cement	Portland Cement	Portland Cement	Portland Cement	Portland Cement	Portland Cement
	Max Grain Size of Aggregate [mm]	10	10	10	10	10	10	10
	Uni-Axial Strength [Kg/cm^2]	406	406	406	406	406	406	406
	Direction of Loading	1 Direction	1 Direction	1 Direction	1 Direction	1 Direction	1 Direction (θ=30°)	1 Direction (θ=45°)
Lateral Force	Velocity of Loading [cm/sec.]	25.0	25.0	25.0	25.0	25.0	25.0	25.0
	Number of Loading for Each Specific Lateral Displacement	10	10	10	10	10	10	10

Table 2 Seismic Performance of Pier Model P-1 P-2 and P-3 (Effect of Loading Velocity)

Model No.	P-1	P-2	P-3
Loading Velocity [cm/sec.]	17.5	35	70
Yield Strength Py [t]	12.2	10.0	12.0
Maximum Strength Pu [t]	13.6	13.0	13.3
$\frac{Pu}{Py}$	1.11	1.3	1.11
Yield Dispalcement δy [mm]	22.5	22.5	22.5
Ultimate Displacement δu [mm]	84.0	90.0	84.0
$\frac{\delta u}{\delta y}$	3.73	4.0	3.73

Table 3 Seismic Performance of Pier Model P-4 ∿ P-9 (Effect of Dynamic Loading and Longitudinal Reinforcement Ratio)

Model No.	P-4	P-5	P-6	P-7	P-8	P-9
Longitudinal Reinforment Ratio Pℓ [%]	1.79		0.87		0.48	
Loading Procedure	Static Loading	Dynamic Loading	Static Loading	Dynamic Loading	Static Loading	Dynamic Loading
Yield Strength Py [t]	14.3	13.8	7.1	7.1	4.3	3.9
Maximum Strength Pu [t]	15.4	16.2	8.8	9.2	4.8	5.0
$\frac{Pu}{Py}$	1.08	1.17	1.24	1.3	1.12	1.28
Yield Displacement δy [mm]	19.0	19.0	12.2	12.2	5.4	5.4
Ultimate Displacement δu [mm]	69.0	79.0	80.0	86.0	55.0	55.0
$\frac{\delta u}{\delta y}$	3.6	4.2	6.6	7.0	10.2	10.2

Table 4 Seismic Performance of Pier Model P-10 ∿ P-13
(Effect of Tie Bar)

Model No.	P-10	P-11	P-12	P-13
Interval of Hoop	25cm (Bottom ∿ crest)	12.5cm (Bottom ∿ 0.5m) and 25cm (0.5m ∿ crest)	12.5cm (Bottom ∿ 1.0m) and 25cm (0.5m ∿ crest)	8.3cm (Bottom ∿ 0.5m) and 25cm (0.5m ∿ crest)
Yield Strength Py [t]	13.9	13.2	13.2	12.2
Maximum Strength Pu [t]	17.0	16.8	16.9	16.0
$\frac{Pu}{Py}$	1.22	1.27	1.28	1.31
Yield Displacement δy [mm]	15.4	14.8	14.7	15.0
Ultimate Displacement δy [mm]	74.1	78.4	77.6	88.3
$\frac{\delta u}{\delta y}$	4.81	5.30	5.28	5.89

Tablr 5 Seismic Performance of Pier Model P-10, P-14, P-15 and P-16
(Effect of Cut-off)

Model No.	P-10	P-14	P-15	P-16
Height of Cut-off from Bottom [cm]	No Cut-off	110	135	160
Yield Strength Py [t]	13.9	12.0	12.9	12.7
Maximum Strength Pu [t]	17.0	15.1	16.4	16.9
$\frac{Pu}{Py}$	1.22	1.26	1.27	1.33
Yield Displacement δy [mm]	15.4	16.2	17.9	15.6
Ultimate Displacement δu [mm]	74.1	70.6	83.5	80.0
$\frac{\delta u}{\delta y}$	4.81	4.36	4.66	5.13

Table 6 Seismic Performance of Pier Model P-10, P-17 and P-18 (Effect of Shear-span Ratio)

Model No.	P-10	P-17	P-18
Shear-span Ratio h/d	5.4	3.8	2.2
Yield Strength Py [t]	13.9	21.7	37.8
Maximum Strength Pu [t]	17.0	23.8	41.1
$\frac{Pu}{Py}$	1.22	1.1	1.09
Yield Displacement δy [mm]	15.4	10.1	6.0
Ultimate Displacement δu [mm]	74.1	33.1	11.2
$\frac{\delta u}{\delta y}$	4.81	3.28	1.87

Table 7 Seismic Performance of Pier Model P-10 and P-17 ∿ 22 (Effect of Number of Loading)

Model No.	P-10	P-17	P-18	P-19	P-20	P-21	P-22
Number of Loading	10			3			5
Shear-span Ratio	5.4	3.8	2.2	5.4	3.8	2.2	5.4
Yield Strength Py [t]	13.9	21.7	37.8	13.6	22.1	40.0	13.0
Maximum Strength Pu [t]	17.0	23.8	41.1	16.7	24.2	42.6	16.7
$\frac{Pu}{Py}$	1.22	1.1	1.09	1.23	1.1	1.07	1.28
Yield Displacement δy [mm]	15.4	10.1	6.0	16.4	11.1	6.7	16.4
Ultimate Displacement δu [mm]	74.1	33.1	11.2	72.3	40.4	11.1	73.0
$\frac{\delta u}{\delta y}$	4.81	3.28	1.87	4.41	3.64	1.66	4.45

Table 8 Seismic Performance of Pier Model P-10 and P-22 ∿ P-24 (Effect of Two Directional Loading)

Model No.	P-10	P-22	P-23	P-24
Loading Procedure	One Directional Excitation		Two Directional Excitation	
Number of Loading	10	5	10	5
Yield Strength Py [t]	13.9	13.0	14.0	13.1
Maximum Strength Pu [t]	17.0	16.7	16.6	17.2
$\frac{Pu}{Py}$	1.22	1.28	1.19	1.31
Yield Displacement δy [mm]	15.4	16.4	16.3	17.4
Ultimate Displacement δu [mm]	74.1	73.0	51.3	64.3
$\frac{\delta u}{\delta y}$	4.81	4.45	3.15	3.7

Table 9 Seismic Performance of Pier Model P-18 and P-25 ∿ P-27 (Effect of Reinforcement for Shear Failure)

Model No.	P-18	P-25	P-26	P-27
Reinforcement for Shear Failure	Hoop with Interval of 25cm	Hoop with Interval of 5cm	Spiral	Diagonal Reinforcement
Yield Strength Py [t]	37.8	28.8	30.7	32.0
Maximum Strength Pu [t]	41.1	37.5	38.6	42.8
$\frac{Pu}{Py}$	1.09	1.3	1.26	1.34
Yield Displacement δy [mm]	6.0	6.2	7.4	6.0
Ultimate Displacement δu [mm]	11.2	36.0	46.1	27.9
$\frac{\delta u}{\delta y}$	1.87	5.81	6.23	4.65

Table 10 Seismic Performance of Pier P-10, P-17, P-18 and P-28 ∿ P-30
(Effect of Shape of Cross Section)

Model No.	P-10	P-17	P-18	P-28	P-29	P-30
Shape of Cross Section	Square			Circle		
Pier Height [cm]	250	175	100	250	175	100
Yield Strength Py [t]	13.9	21.7	37.8	13.4	20.4	37.0
Maximum Strength Pu [t]	17.0	23.8	41.1	17.3	25.2	42.8
$\frac{Pu}{Py}$	1.22	1.1	1.09	1.29	1.24	1.16
Yield Displacement δy [mm]	15.4	10.1	6.0	15.2	10.0	4.9
Ultimate Displacement δu [mm]	74.1	33.1	11.2	63.8	43.5	17.0
$\frac{\delta u}{\delta y}$	4.81	3.28	1.87	4.2	4.4	3.5

Table 11 Seismic Performance of Pier P-10, P-33 and P-34
(Effect of Direction of Lateral Loading)

Model No.	P-10	P-33	P-34
Direction of Lateral Loading [radian]	0	$\pi/6$	$\pi/4$
Yield Strength Py [t]	13.9	16.0	16.7
Maximum Strength Pu [t]	17.0	18.6	18.7
$\frac{Pu}{Py}$	1.22	1.16	1.12
Yield Displacement δy [mm]	15.4	17.9	18.5
Ultimate Displacement δu [mm]	74.1	54.4	55.3
$\frac{\delta u}{\delta y}$	4.81	3.04	2.99

Table 12 Seismic Performance of Pier Model P-28, P-29, P-31 and P-32
(Effect of Spiral Reinforcement)

Model No.	P-28	P-29	P-31	P-32
Reinforcement at Bottom	Hoop		Spiral	
Shear-Span Ratio	4.7	3.3	4.7	3.3
Yield Strength Py [t]	13.4	20.4	15.6	24.0
Maximum Strength Pu [t]	17.3	25.2	17.0	25.4
$\frac{Pu}{Py}$	1.29	1.24	1.09	1.06
Yield Displacement δy [mm]	15.2	10.0	19.5	12.5
Ultimate Displacement δu [mm]	63.8	43.5	93.0	63.6
$\frac{\delta u}{\delta y}$	4.2	4.4	4.77	5.09

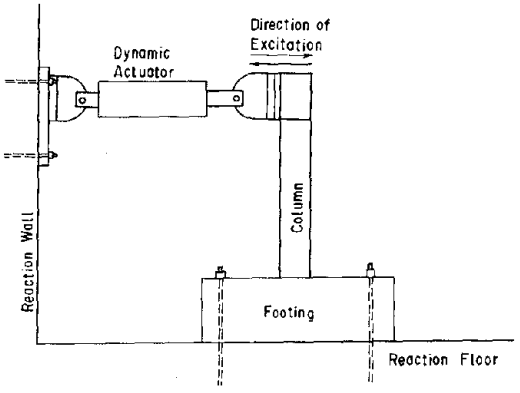

Fig. 1 Set-up of Model Reinforced Concrete Pier and Dynamic Loading Systems

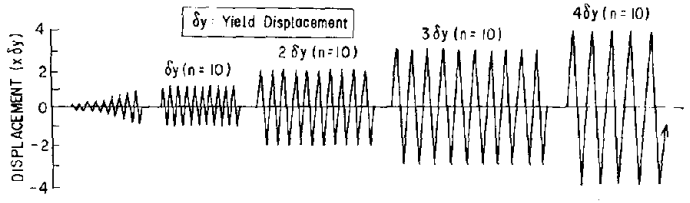

Fig. 2 Lateral Displacement Applied to Pier Crest

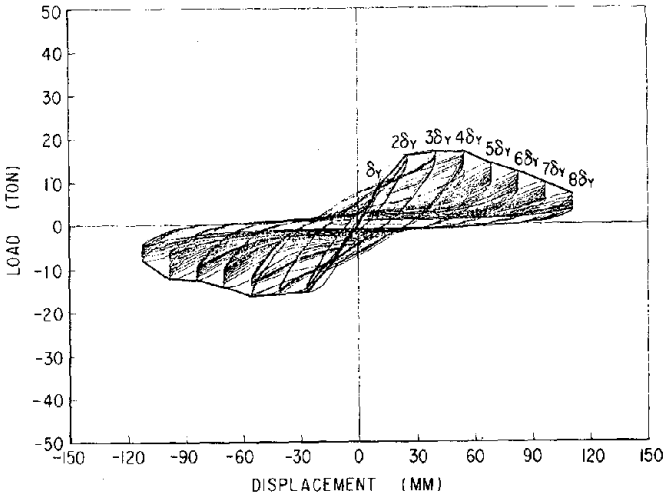

(a) Hysteresis Loop and Its Envelope

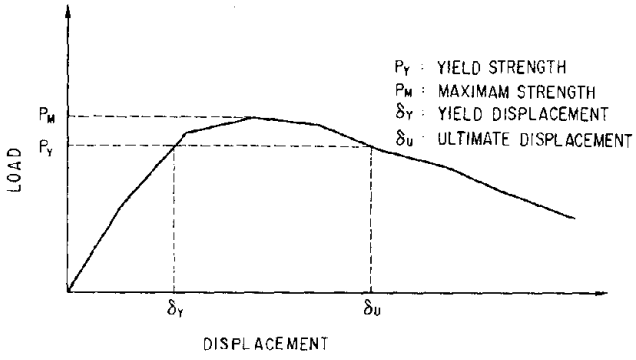

(b) Definition of Yield, Maximum and Ultimate Strength

Fig. 3 Hysteresis Loops by Reversed Cyclic Loading Tests

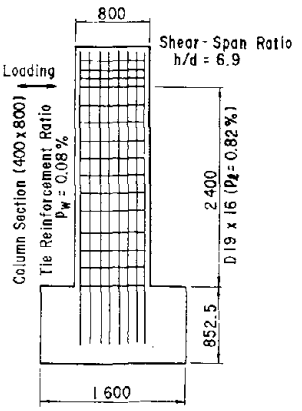

Fig. 4 Pier Models for Studying Effect of Loading Velocity (P-1, P-2 and P-3)

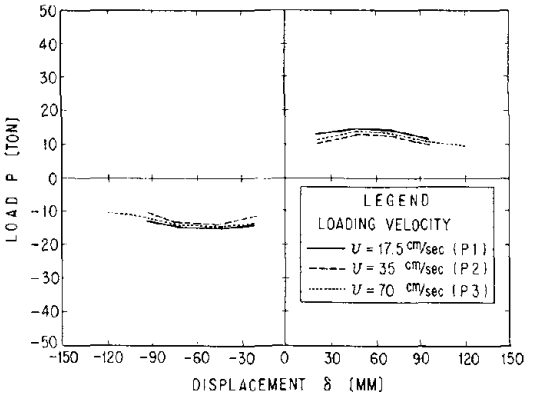

Fig. 5 Effect of Loading Velocity on Envelope of Load-Displacement Hysteresis Loops

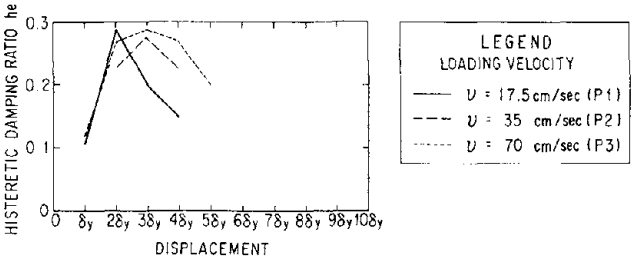

Fig. 6 Effect of Loading Velocity on Equivalent Hysteretic Damping Ratio

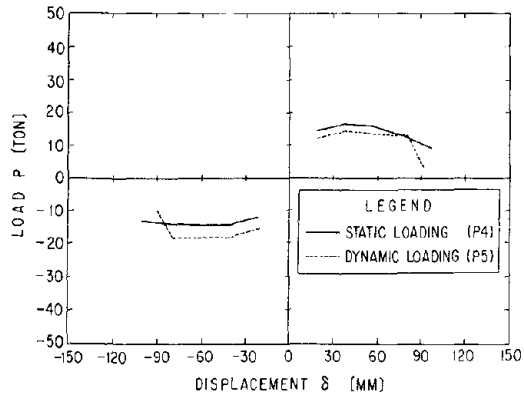

(a) Longitudinal Reinforcement Ratio of 1.79%

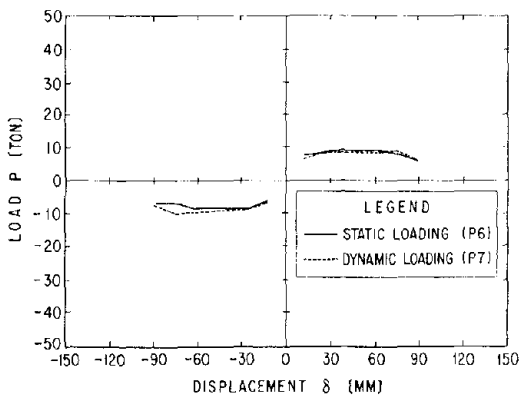

(b) Longitudinal Reinforcement Ratio of 0.87%

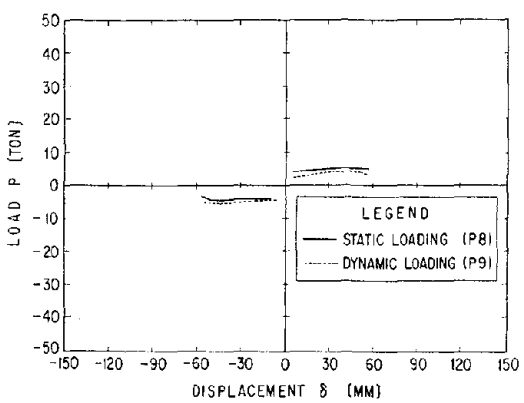

(c) Longitudinal Reinforcement Ratio of 0.48%

Fig. 8 Effect of Dynamic Loading and Longitudinal Reinforcement Ratios on Envelope of Load-Displacement Hysteresis Loops

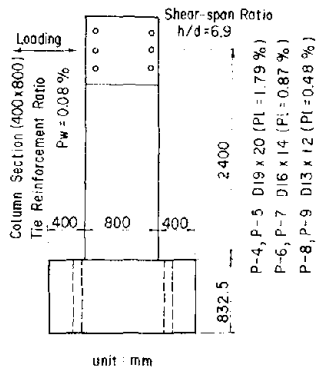

Fig. 7 Pier Models for Studying Effect of Dynamic Loading and Longitudinal Reinforcement Ratios

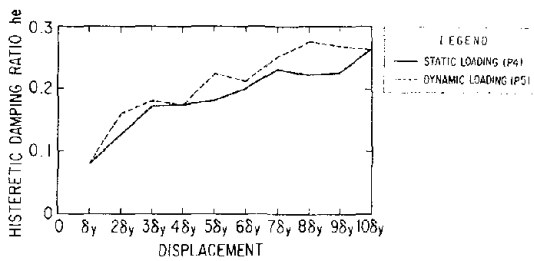

(a) Longitudinal Reinforcement Ratio of 1.79%

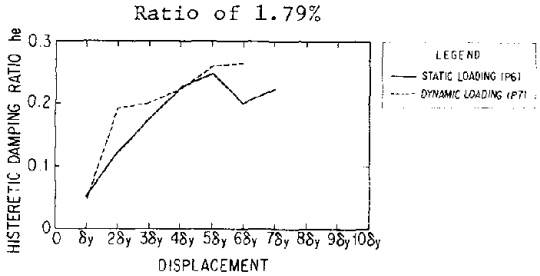

(b) Longitudinal Reinforcement Ratio of 0.87%

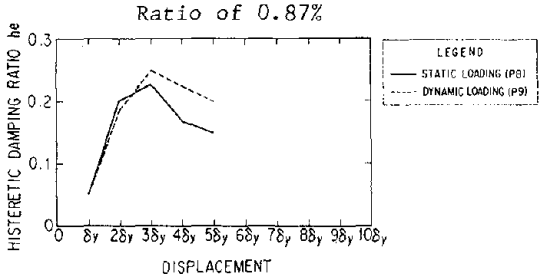

(c) Longitudinal Reinforcement Ratio of 0.48%

Fig. 9 Effect of Dynamic Loading and Longitudinal Reinforcement Ratios on Equivalent Hysteretic Damping Ratio

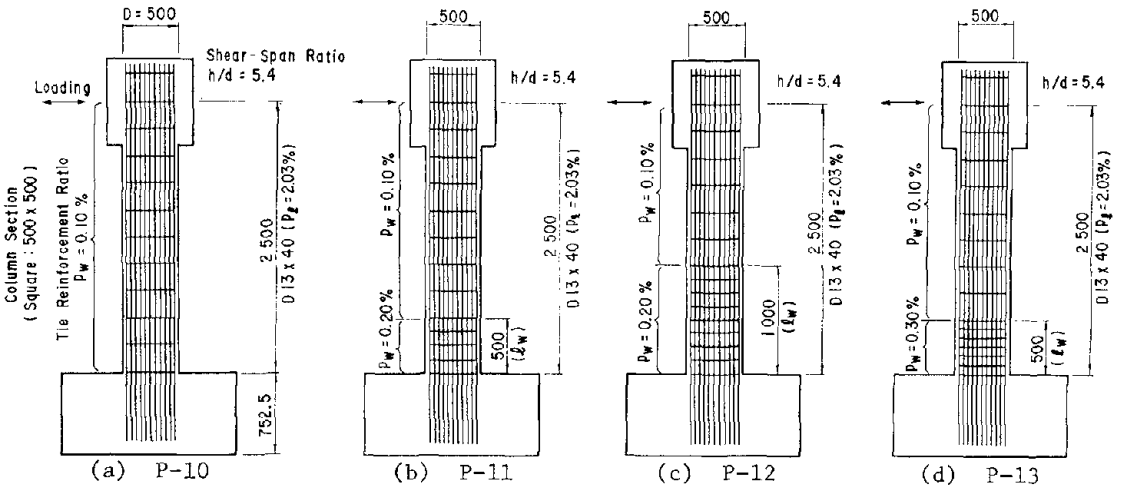

Fig. 10 Pier Models for Studying Effect of Tie Reinforcement Ratio

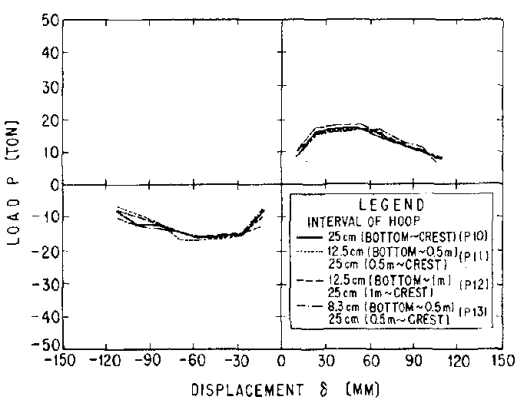

Fig. 11 Effect of Tie Reinforcement Ratio on Envelope of Loading-Displacement Hysteresis Loops

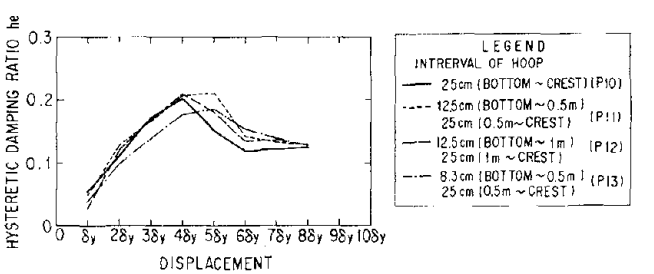

Fig. 12 Effect of Tie Reinforcement Ratio on Equivalent Hysteretic Damping Ratio

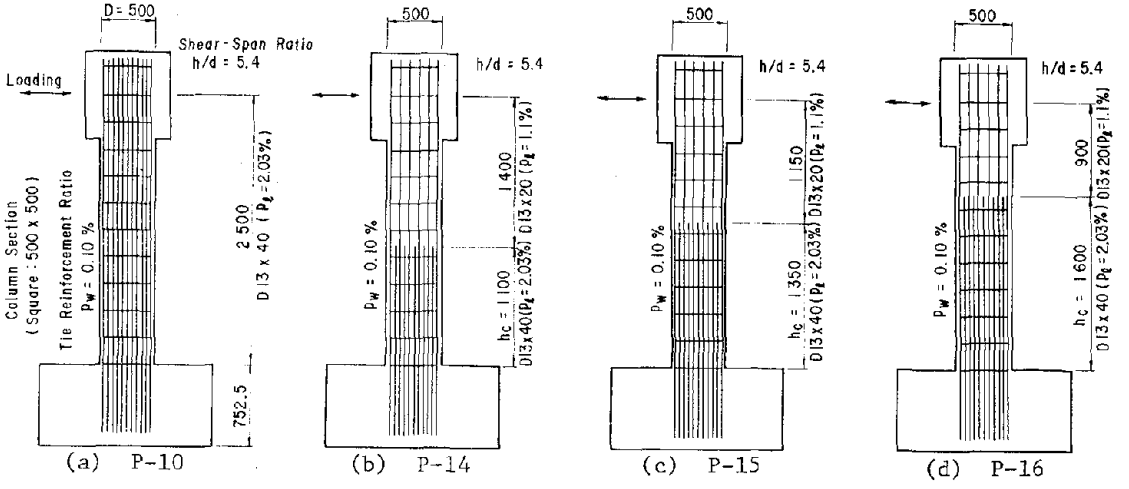

Fig. 13 Pier Models for Studying Effect of Cut-off of Longitudinal Reinforcement

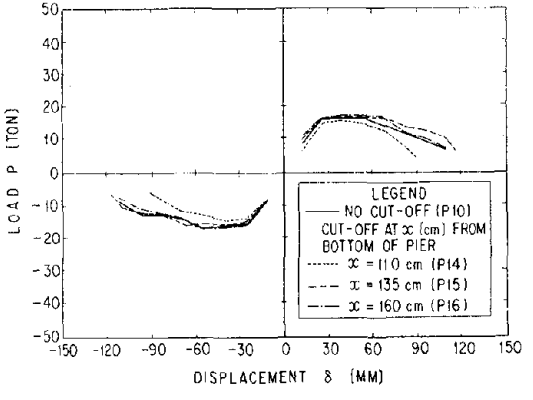

Fig. 14 Effect of Cut-off on Envelope of Loading-Displacement Hysteresis Loops

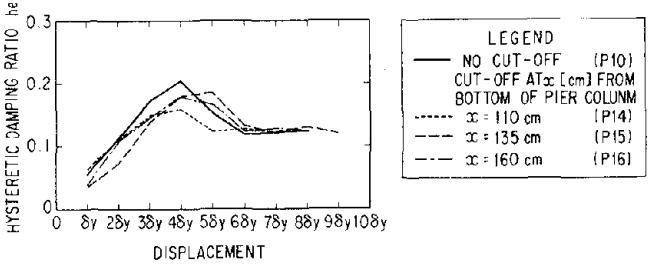

Fig. 15 Effect of Cut-off on Equivalent Hysteretic Damping Ratio

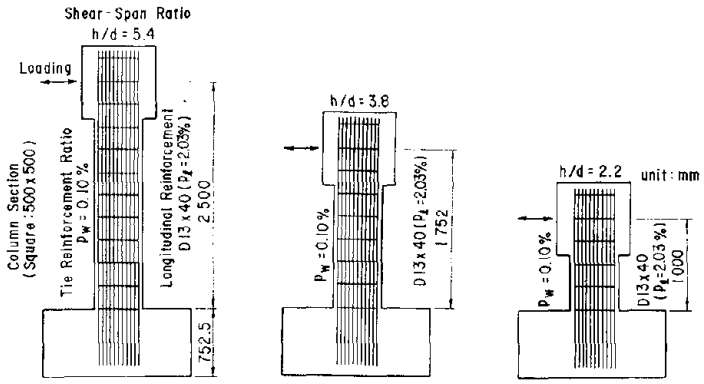

(a) P-10 (b) P-17 (c) P-18

Fig. 16 Pier Models for Studying Effect of Shear-span Ratio

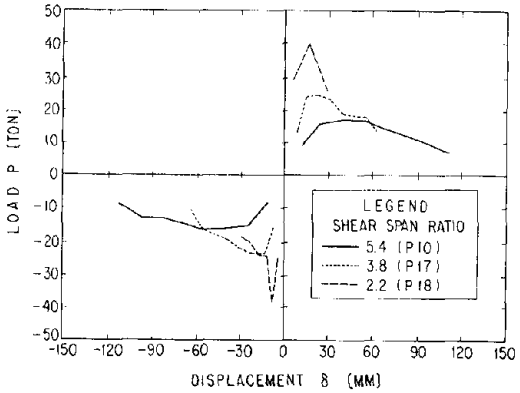

Fig. 17 Effect of Shear-span Ratio on Envelope of Loading-Displacement Hysteresis Loops

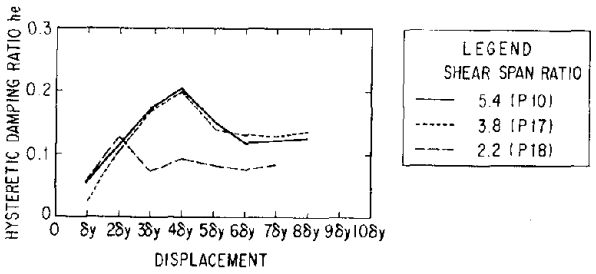

Fig. 18 Effect of Shear-span Ratio on Equivalent Hysteretic Damping Ratio

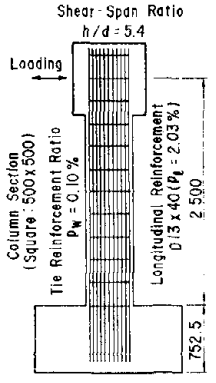

(a) P-10(n=10), P-19 (n=3) and P-22 (n=5)

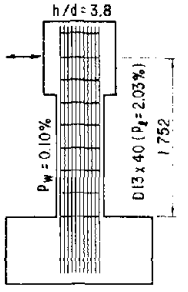

(b) P-17(n=10), P-20 (n=3)

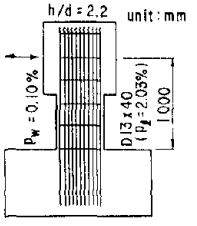

(c) P-18(n=10), P-21 (n=3)

Fig. 19 Pier Models for Studying Effect of Number of Loading

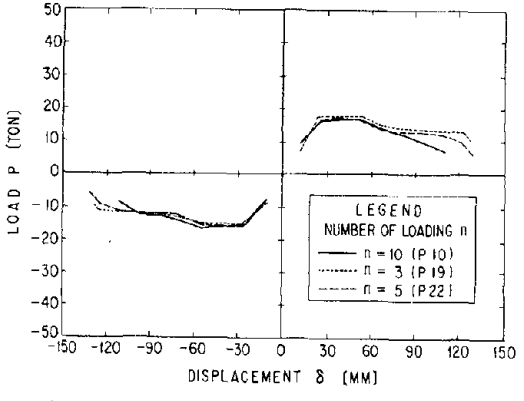

(a) Shear-span Ratio h/d of 5.4

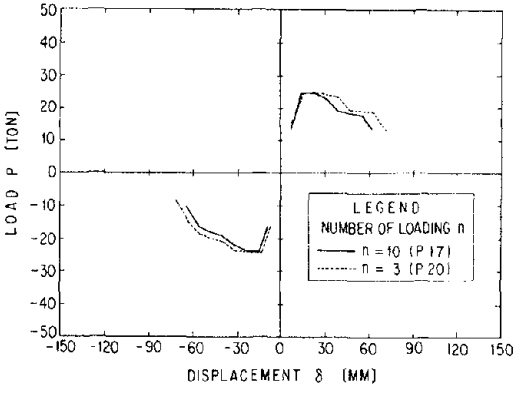

(b) Shear-span Ratio h/d of 3.8

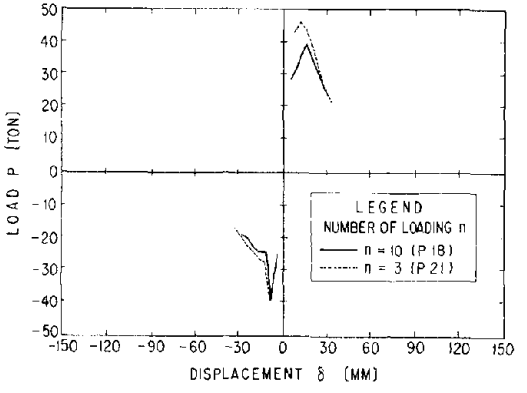

(c) Shear-span Ratio h/d of 2.2

Fig. 20 Effect of Number of Loading on Envelope of Loading-Displacement Hysteresis Loops

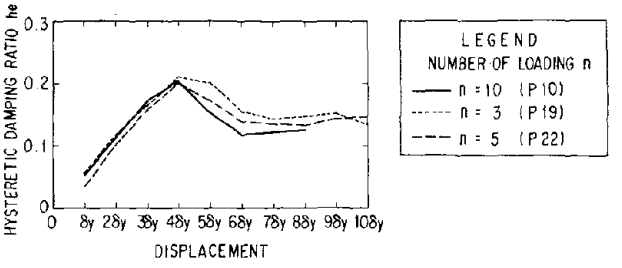

(a) Shear-span Ratio h/d of 5.4

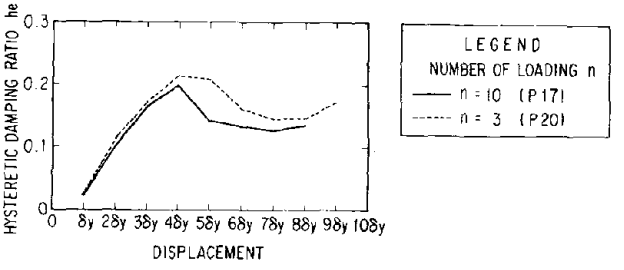

(b) Shear-span Ratio h/d of 3.8

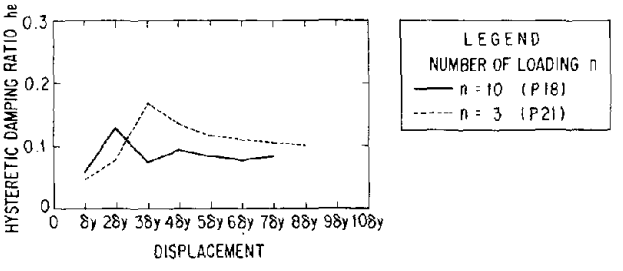

(c) Shear-span Ratio h/d of 2.2

Fig. 21 Effect of Number of Loading on Equivalent Hysteretic Damping Ratio

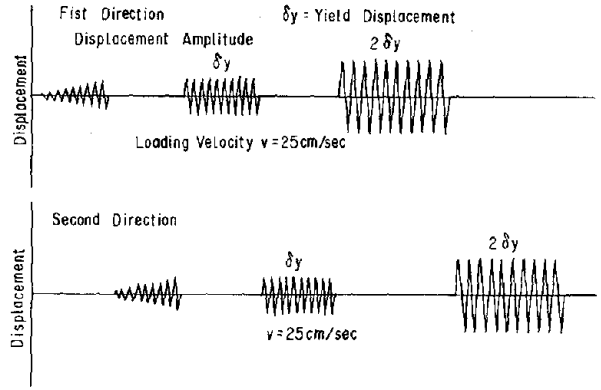

Fig. 22 Loading Time History of Displacement in Two Directional Loading

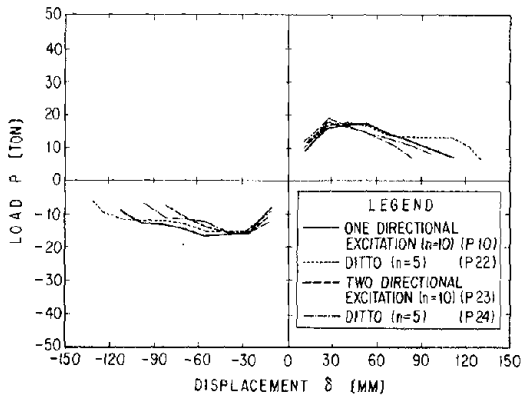

Fig. 23 Effect of Two Directional Loading on Envelope of Loading-Displacement Hysteresis Loops

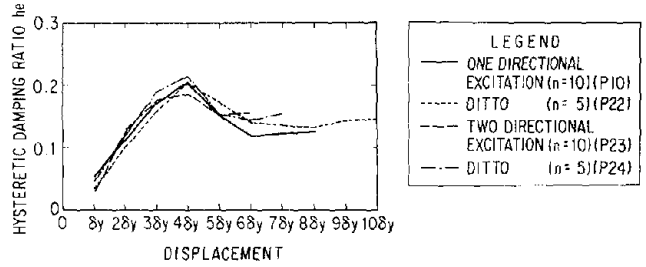

Fig. 24 Effect of Two Directional Loading on Equivalent Hysteretic Damping Ratio

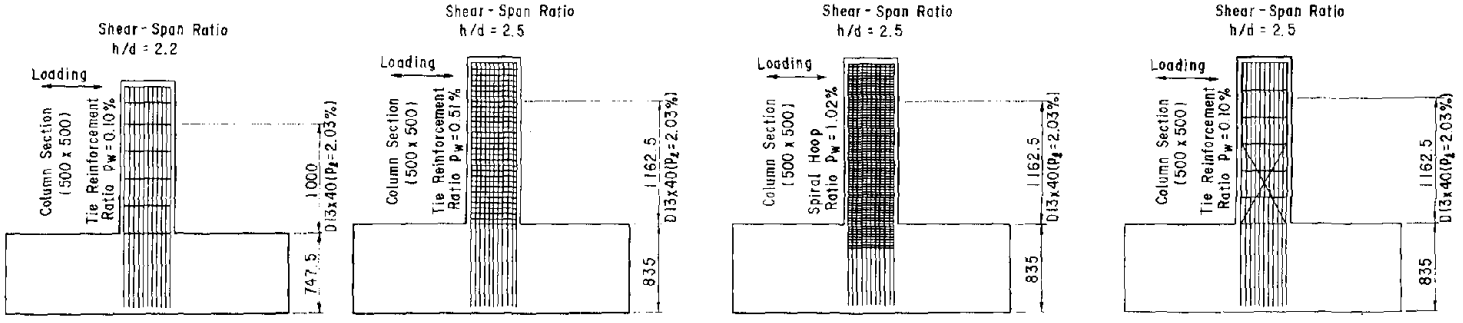

(a) P-18 (b) P-25 (c) P-26 (d) P-27

Fig. 25 Pier Models for Studying Effect of Shear Reinforcements

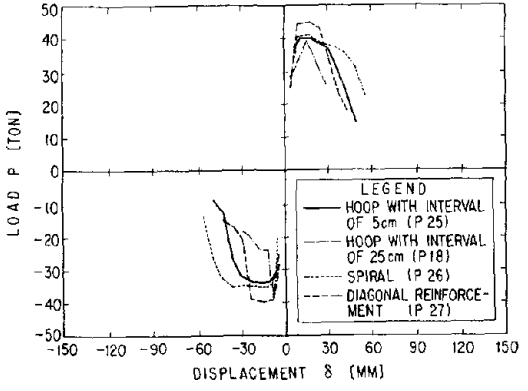

Fig. 26 Effect of Shear Reinforcements on Envelope of Loading-Displacement Hysteresis Loops

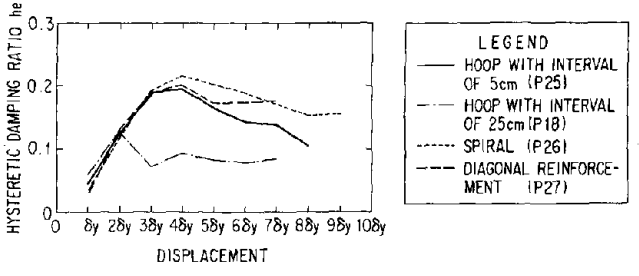

Fig. 27 Effect of Shear Reinforcement on Equivalent Hysteretic Damping Ratio

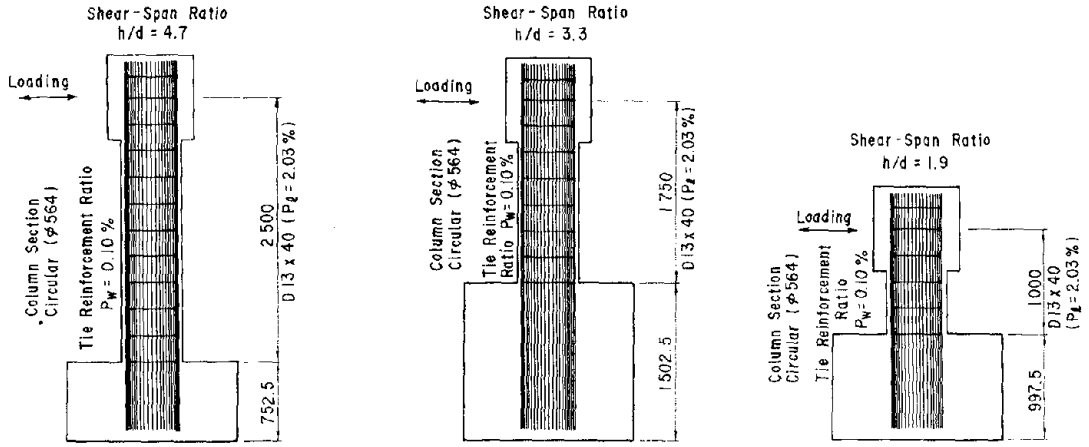

(a) P-28 (b) P-29 (c) P-30

Fig. 28 Pier Models for Studying Effect of Shape of Cross Section

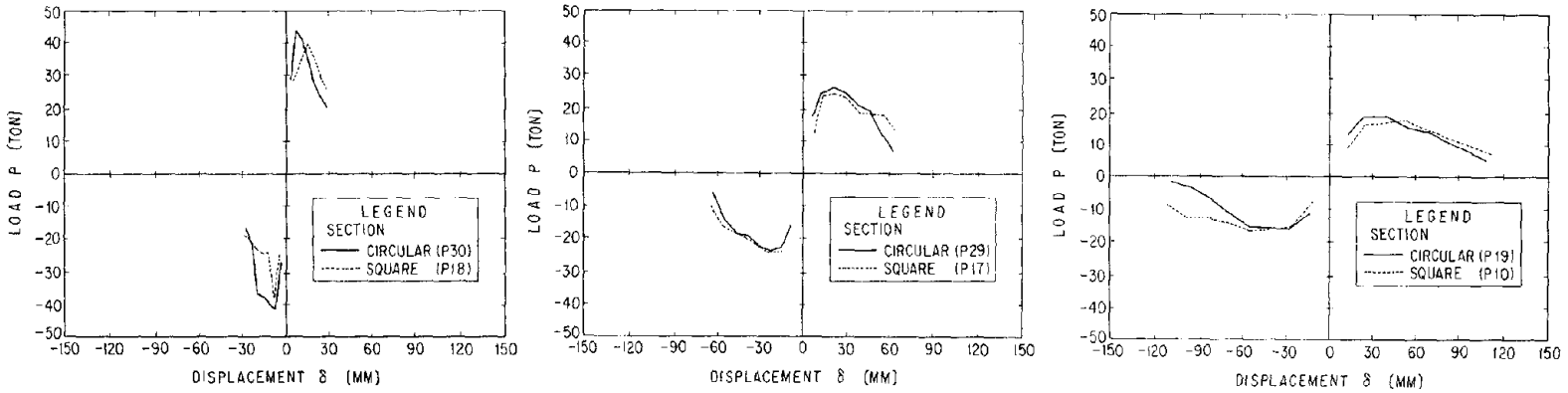

(a) Pier Height of 100 cm (b) Pier Height of 175 cm (c) Pier Height of 250 cm

Fig. 29 Effect of Shape of Cross Section of Envelope on Loading-Displacement Hysteresis Loops

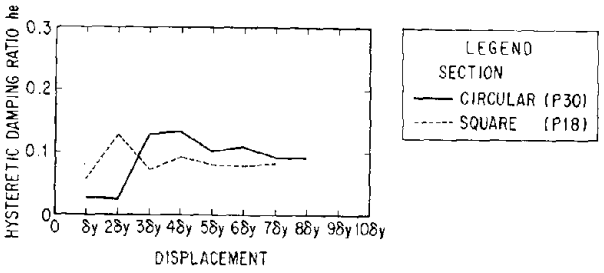

(a) Pier Height of 100 cm

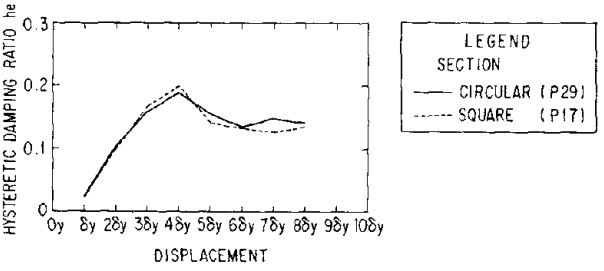

(b) Pier Height of 175 cm

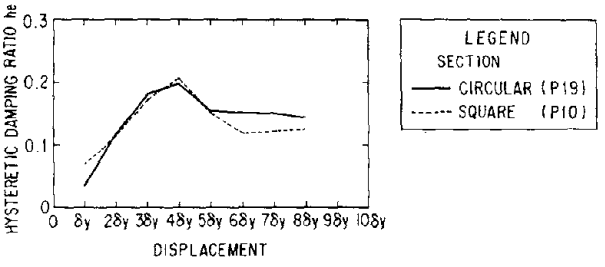

(c) Pier Height of 250 cm

Fig. 30 Effect of Shape of Cross Section on Equivalent Hysteretic Damping Ratio

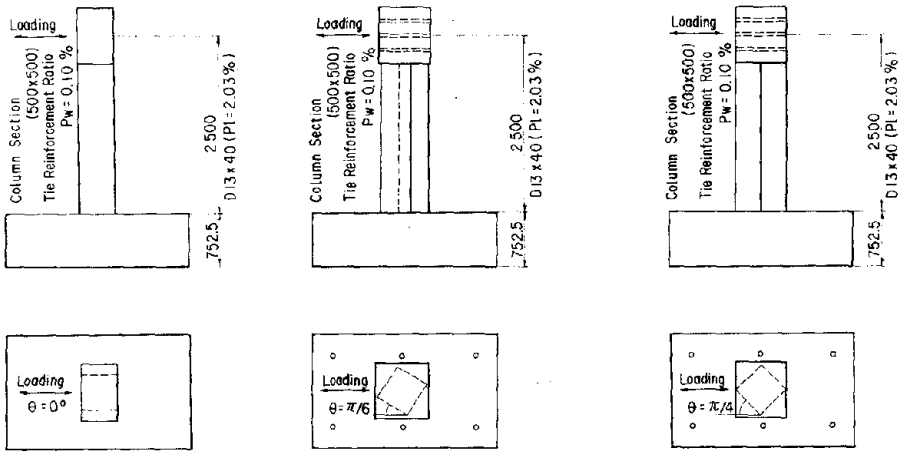

(a) P-10 (b) P-33 (c) P-34

Fig. 31 Pier Models for Studying Effect of Direction of Loading

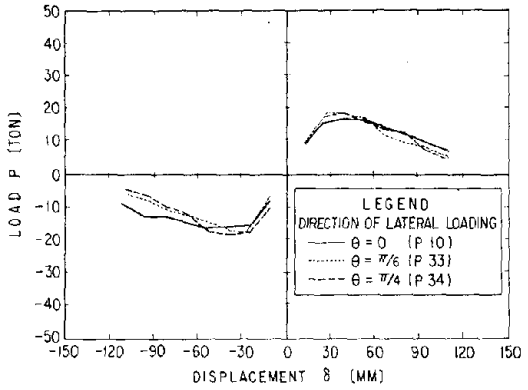

Fig. 32 Effect of Direction of Loading on Envelope of Loading-Displacement Hysteresis Loops

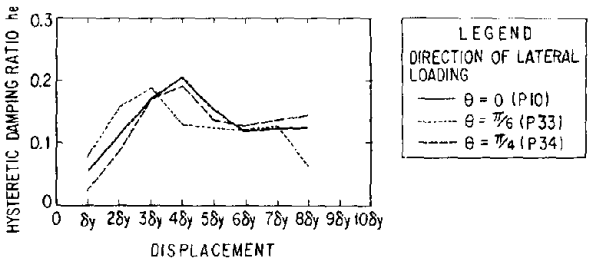

Fig. 33 Effect of Direction of Loading on Equivalent Hysteretic Damping Ratio

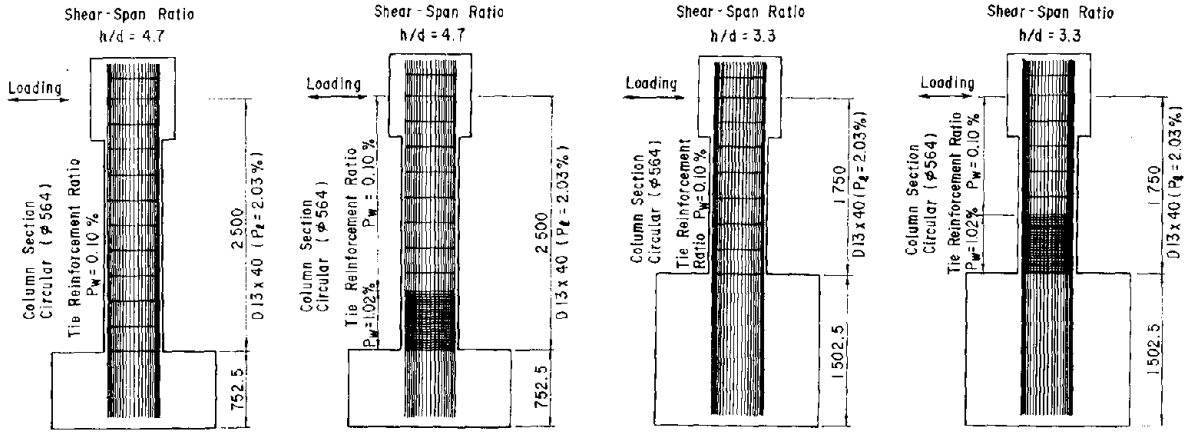

Fig. 34 Pier Models for Studying Effect of Spiral Reinforcement

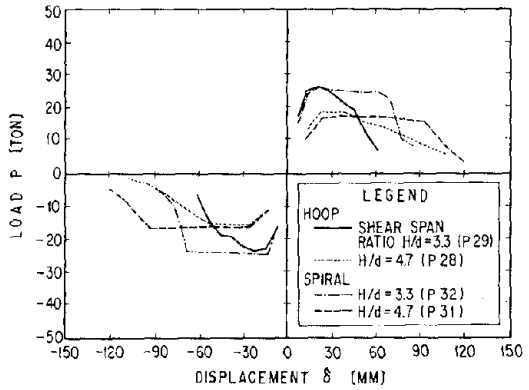

Fig. 35 Effect of Spiral Reinforcement on Envelope of Loading-Displacement Hysteresis Loops

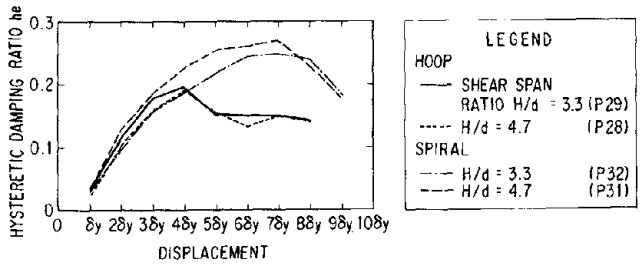

Fig. 36 Effect of Spiral Reinforcement on Equivalent Hysteretic Damping Ratio

REEVALUATION OF LIQUEFACTION RESISTANCE CURVES

by

Riley M. Chung[I]
H. Bolton Seed[II]
A. G. Franklin[III]
J. A. Farrar[IV]

ABSTRACT

This paper updates the status of the U.S.-Japan Cooperative Program in SPT testing and the correlation of SPT with liquefaction resistance of saturated soil deposits.

SPT field practice in Japan was found to result in higher energy ratios (ER_i) than those from the U.S. practice for the same rope and pulley method used (67% in Japan vs 60% for the safety hammer widely used in the U.S.). The use of an ASTM sampler without liner resulted in N-values which are about 80% of those measured using a sampler of straight barrel configuration.

From an assessment of the overall worldwide SPT practices based on the most recent available information, a standard energy ratio of 60% is recommended. The field data relating SPT to liquefaction susceptibility, accumulated from previous earthquakes throughout the world, have been reinterpreted and replotted with respect to this recommended standard energy level.

Key Words: Earthquake Engineering, Soils, Liquefaction, In Situ Tests, Standard Penetration Test

1. INTRODUCTION

Evaluation of liquefaction resistance of saturated soil deposits during earthquakes is one of the most challenging tasks that geotechnical engineers face today. Due to the unavoidable consequences of sample disturbance, design approaches using laboratory test results are now beginning to receive less emphasis as compared with methodologies developed from in situ testing techniques. The Standard Penetration Test (SPT), due to its popular use in site exploration and its very large accumulated world-wide data base, has proved to be very useful as an index of soil liquefaction resistance during earthquake shaking.

However, it has long been recognized that there are problems associated with the use of SPT and its results for engineering design in general, and for liquefaction resistance evaluation in particular, due to the large number of variables that affect the N-values obtained from SPT tests. Schmertmann in 1976 [16] and Kovacs, et al. in 1983 [8] showed that the SPT test is in fact conducted, in different parts of the world, using different kinds of hammers, different energy delivery systems with differing degrees of efficiency, different borehole fluids, and different kinds of sampling tubes, in addition to differences caused by operator idiosyncrasies. This situation certainly raises a legitimate question as to the consistency of the SPT N-values which have been used in developing the correlations between liquefaction resistance and modified penetration resistance, N_1 [21, 22, 27].

I U.S. National Bureau of Standards
II University of California, Berkeley, CA
III U.S. Army Engineer Waterways Experiment Station
IV U.S. Bureau of Reclamation

Research to measure the amount of energy delivered by a hammer to the sampling spoon through a SPT test set up has been an important program in the geotechnical engineering operation at the National Bureau of Standards (NBS). In 1981, a field measurement system and procedure which measures the energy delivered by a drill rig operation were developed and successfully used to study the factors that affect delivered energy [7]. The developed measurement system has been used by the researchers at NBS, with cooperation and support from the Nuclear Regulatory Commission, Bureau of Reclamation (BuRec), and Waterways Experiment Station (WES), to calibrate drill rigs throughout the U.S. In this energy calibration study, summarized by Kovacs, et al. in 1983 [8], the energy ratios measured for 56 drill rigs and operators in the U.S. were reported. Based on the data from this study, the mean energy ratio delivered by a safety hammer is about 61 percent, whereas the mean energy ratio for a donut hammer is about 45 percent. It should also be noted that the safety hammer is the most popularly used hammer type in the U.S.

In October, 1983, under the auspices of the UJNR Panel on Wind and Seismic Effects and through the financial support of many organizations both in Japan and in the U.S., engineers from the NBS and Bureau of Reclamation carried out a successful SPT program to a) document how the SPT is performed and used in present Japanese engineering practice; b) compare the Japanese SPT results with those found in the U.S.; and c) comment on the SPT vs. liquefaction resistance curves with respect to the Japanese data base. Preliminary findings from this study were presented to the 16th UJNR panel meetings held at NBS in May 1984. An NBS report [9] has been prepared to present in detail the conclusions with respect to the objectives of the study. The results will be summarized herein.

Additionally, this study provided the opportunity to examine in detail the suitability of the SPT vs. liquefaction resistance curves now used extensively by the profession for the liquefaction potential determination [23]. Findings from this examination will be briefly presented in this paper.

2. FIELD SPT TEST PROGRAM IN JAPAN, OCT. 1983

Standard penetration tests were conducted at Akita, Niigata, Tokyo, and Yokohama sites in Japan during the Japan trip using the SPT technique typical of the Japanese practice. In essence, three different procedures in raising and releasing the 140 lb (63.5 kg) hammer are in use [28]:

a. a mechanical trip device (the tonbi method) which is essentially a free-fall technique,

b(1). the rope and pulley technique, and

b(2). the rope and pulley technique with a special throw of the rope in which an effort is made to throw the rope at least partially off the pulley during the release.

All three methods were used; the majority of the tests were conducted using either method (b1) or (b2). The amount of energy delivered to the sampling spoon, in terms of energy ratio, ER_i, with respect to the theoretical energy delivered by a 140 lb (63.5 kg) hammer falling 30 inches (760 mm) was measured using the measurement system described in Ref. 7. Figure 1 shows a frequency diagram of the data which indicates an overall average of 68 percent with a standard deviation of 9.6 percent and a coefficient of variation of about 14 percent. When the data from tests using the tonbi method are separated from that using the rope and pulley methods, the

averages would be 80 and 67 percent, respectively. Data from the U.S. practice averages about 55 percent with a standard deviation of 12 percent and a coefficient of variation of 22 percent [8].

The standard penetration test in Japan is performed according to the Japanese Industrial Standard (JIS) A1219, which is based on the present version of the ASTM D1586. It specifies the size of the SPT sampler to a 2 in. (51 mm) O.D. and 1-3/8 in. (35 mm) I.D. throughout its length. However, in the current ASTM standard, the I.D. of the SPT sampler is specified to be 1-1/2 in. (38 mm) to allow insertion of a brass liner. With the liner in place, it would have a uniform inside diameter of 1-3/8 in. (35 mm). Even though the ASTM standard calls for a uniform 1-3/8 in. (35 mm) inside diameter split barrel, many U.S. operators do not use the liner, probably because of the greater ease with which the soil sample can be examined and removed from the sampler without the liner.

An ASTM sponsored survey conducted in July 1980 among members of the Association of Soil and Foundation Engineers (ASFE) showed that only 52 percent of the member firms who responded to the questionnaire said that they used the liner (Kovacs, 1981). Without the liner, the friction is reduced, which could account for a 10 to 30 percent reduction in N-values in sands, according to Schmertmann [19, 20].

To investigate the sampler effect on N-value, the SPT tests were conducted under similar conditions with the sampler as an only variable. In many cases, tests were conducted in a pair of borings which were about 3 to 5 m apart. The JIS sampler and the ASTM sampler without liner were used alternately in both borings so that the SPT tests could be carried out at the same depth with two different types of samplers. A typical plot is given in Figure 2 which illustrates the N-value profile with depth for borings C1 and C2 at the Niigata site. Open circles are used for data points obtained using the JIS sampler, and triangles for the data from the ASTM sampler without liner. The numbers in parentheses adjacent to the data points are the average values of the measured energy ratios in the drill rod, ER_i. A solid line connects the data points for a given boring. The dashed lines in the figure represent the profiles of the normalized N-values with respect to the averaged energy ratio of 68 percent versus depth.

Using the data from Figure 2 and other similar data obtained from the tests at other sites, it is possible to compare the N-value results at a given depth using a JIS sampler and an ASTM sampler without liner to study the effect of sampler type. Figure 3 gives the results of this comparison. The N-values in this figure have been normalized for a 68 percent energy ratio. It is apparent from this figure that at the same depth the JIS sampler produces greater N-values than the ASTM sampler without liner.

In his review of the data from this study, Schmertmann suggested that additional data points could be obtained by comparing the N-values from the JIS sampler with those from the ASTM sampler without liner by interpolation on the data sets where direct depth comparisons are lacking. Figure 4 shows the results when all the data points are plotted together and the N-value correlation between JIS and ASTM samplers without liner may be established as follows:

$$N_{us} = 0.8\ N_j, \qquad (1)$$

if a straight line relationship is assumed.

In general, it can be stated that the use of an ASTM sampler without liner leads to N-values lower than those measured with a sampler of a

constant inside diameter, by about 10 to 30 percent.

2.1 Average Energy Ratios for SPT Procedures Countries Where SPT is Most Popularly Used

The rope and pulley technique is still the most widely used method for hammer raise and release in the U.S. and other Pan-American countries. Two types of hammers are currently used: the donut hammer and the safety hammer. As stated earlier, a study by Kovacs, et al. [8] found an average energy ratio of about 45 percent delivered by the donut hammer whereas the average energy ratio for the safety hammer is about 60 percent. This difference in energy ratios means that a donut hammer could be expected to result in about 30 to 35 percent higher N-values than a safety hammer. This range of difference is also found in field comparisons between the two different hammer types [1, 4, 13, 14, 25, 30].

Major hammer release mechanisms used in the Japan SPT practice are discussed earlier in this paper. Several investigators have attempted recently to quantify the energy ratios delivered to the drill rods with the different types of releases. Their findings, including that from the 1983 Japan study described earlier, are summarized [23] in Table 1. The results show generally good agreement. Also shown in the table are the overall energy ratios considered most representative of the Japanese practice and thus adopted for the present study.

Until about 20 years ago, the Chinese were using a manual method analogous to the rope and pulley method for SPT hammer release. However, the normal method today in China in performing the SPT tests uses an automatic mechanical trip to release the hammer [24]. The automatic "free fall" hammer used in the Chinese practice is similar in configuration to "free fall" hammers such as the Borros AB drop-hammer and the Pilcon hammer. A comparative field study was conducted by Douglas and Strutznsky [3] to evaluate the difference between the Chinese free fall hammer and the Pilcon hammer and no significant difference was found between the N-values by the two types of hammers.

Thus, while we do not have direct energy ratio measurements on the free fall hammers used in the Chinese practice, it is logical to use the energy ratios measured for the Pilcon type hammer as the reference for the Chinese data. Several studies of the energy delivered by the Pilcon hammer were conducted and their results are summarized [23] in Table 2. An average of 60 percent is derived.

Shi-Ming [24] also reported that N-values measured by a mechanical trip system are about 83 percent of those measured using a manual system. Thus, the energy ratio for hammers operated with the rope and pulley method in China is likely to be about 50 percent, which is in good agreement with that determined for U.S. hammers using the same hammer releasing mechanism (55 percent).

3. RECOMMENDED STANDARD ENERGY RATIO

Several authors [5, 15, 18] have in the past recommended that an energy ratio of 55 percent be adopted as the standard for SPT data correlation since this seems to be the average energy delivered by hammers used in the U.S. This means that SPT data obtained from both safety and donut hammers can be correlated using the following equation:

$$N_{55} \cong N_m \, (ER_m/55) \qquad (2)$$

where N_m = N-value for method used in investigation

ER_m = Energy ratio for method used in investigation

It should be noted that neither the safety hammer not the donut hammer produces an average energy ratio of 55 percent. The task of correcting field SPT data would be minimized if an energy ratio of 60 percent is adopted as a standard [23]. If this were done, data obtained by safety hammers, the most commonly used hammer type in the U.S., would not need correction, nor the SPT data from the Chinese practice using an automatic trip hammer. The SPT N-value determined in this way is designated as N_{60}, and is determined by:

$$N_{60} = N_m \ (ER_m/60) \qquad (3)$$

The energy ratios for SPT tests from the countries included in this discussion have been summarized by Seed et al. [23] as shown in Table 3. Table 3 also gives the correction factors for each condition, derived using eq. 3.

Other corrections may sometimes be required to the SPT data, particularly with respect to comparison of N-values obtained from Japanese and U.S. practices. For example, the frequency of hammer drops is significantly lower in Japan than in the U.S. They range from 17 to 20 blows per minute in the Japanese rope and pulley method using a special throw, but typically about 30 to 40 blows per minute in the U.S. practice. Consideration of the effect of the hammer drop rate on the rate of dissipation or accumulation of excess pore water pressure during sampler penetration suggests the following relationships:

$(N_j)_{60} > (N_{us})_{60}$ for loose sands, $(N_1) < 20$

and

$(N_j)_{60} < (N_{us})_{60}$ for dense sands, $(N_1) > 20$

where N_1 is the blow count corrected to 1 tsf (1 kg/cm^2) overburden pressure [21, 22]

Another correction which is sometimes necessary with respect to comparison of Japanese and U.S. data is the effect of different borehole diameters. In Japan, the most commonly used borehole diameter is 2.6 in. (66 mm) whereas in the U.S. it is normally not less than 4 in. (100 mm). The use of a smaller borehole would tend to increase the penetration resistance of a deposit, thus leading to the conclusion that

$$(N_j)_{60} > (N_{us})_{60}$$

There is little data available that could be used to quantify the two effects described above. Furthermore, it should also be noted that the two effects are compensating for dense sands while for loose sands they are cumulative. Thus, it is suggested [23] that for soils with $(N_{60}) < 20$, the following relationship may be used provisionally for the combined influence of these two effects.

$$(N_{60})_{us} = 0.9 \ (N_{60})_j \qquad (4)$$

Corrections should also be given for the case where very short drill rod length (less than 10 ft) is used. In this case, studies [13, 17] have shown that there is a reflection of energy in the rods which reduces the energy available for driving the sampler, resulting in fictitiously high N-values. Seed, et al. [22] recommended that the measured N-values for tests made at depths between 0 and 10 ft be corrected by a multiplier of 0.75, which is also used in the present study.

4. REINTERPRETATION OF SPT LIQUEFACTION RESISTANCE DATA BASE

Liquefaction resistance curves such as the one shown in Figure 5 have been developed [22], comparing the earthquake-induced cyclic stress ratio in the soil at any depth to the normalized soil penetration resistance, N_1, for cases of both occurrence and nonoccurrence of

liquefaction-related ground failure phenomena during the earthquake.

The cyclic stress ratio for soil at any depth during an earthquake can be estimated using the following equation [21, 22]:

$$\frac{\tau_{av}}{\sigma_o'} = 0.65 \frac{a_{max}}{g} \frac{\sigma_o}{\sigma_o'} r_d \qquad (5)$$

where a_{max} = maximum ground surface acceleration

σ_o = total overburden pressure at depth under consideration

σ_o' = effective overburden pressure at depth under consideration

r_d = a stress reduction factor which decreases from a value of 1 at the ground surface to a value of about 0.9 at a depth of 35 ft

The value of N_1 can be obtained from the value of N measured in a standard SPT investigation by using the relation [22]:

$$N_1 = C_N \cdot N, \qquad (6)$$

where C_N is a correction factor determined as a function of overburden pressure and relative density of the soil under investigation.

All available field performance data for soil deposits which have or have not liquefied under known conditions of past earthquakes have been reviewed, reinterpreted and related to the recommended standardized values of $(N_1)_{60}$ as outlined earlier by Seed et al. [23]. Most of the available field data were collected for earthquake magnitudes close to M = 7-1/2. Resistance curves for other earthquake magnitudes can be obtained from the curve for 7-1/2 magnitude by using the correction factors given in Ref. 21.

The available body of data used in reinterpretation of the correlation between cyclic stress ratio and the normalized standard SPT value, $(N_1)_{60}$, is obtained from sites in North and South America, Japan and China. Appropriate corrections, as discussed earlier, were applied to all the field values to determine the cyclic stress ratio corresponding to M = 7-1/2 earthquake and the corresponding values of $(N_1)_{60}$. The results for clean sands with fine contents less than 5 percent are plotted as shown in Figure 6. Soil deposits known to have liquefied are plotted as solid points, those which did not show any evidence of liquefaction are shown as open points and sites of marginal liquefaction by half-solid points. The boundary line is drawn to separate conditions associated with liquefaction from conditions for which liquefaction occurrences have not been observed, which is the same principle used in developing previous resistance curves. In Figure 6, the boundary line from Figure 5 is also superimposed for comparison. It may be noted that the correlation line drawn for the case of clean sand is very close to that proposed by Seed et al. in 1983 [22] indicating that the N_1 values used in the earlier work correspond closely to $(N_1)_{60}$ values. In fact, the two boundary lines merge at $(N_1)_{60}$ = 15. Beyond this level, the original boundary line is slightly more conservative. For example, at a cyclic stress ratio of 0.3, the standardized N_1 values would have to be 25 from the revised boundary line, rather than 27 from the original boundary line.

5. CONCLUSIONS

The following conclusions can be drawn from the results of the studies presented herein:

1. The differences in SPT practice in Japan and the U.S., caused by the variations in equipment and procedure, result in differences in the actual energy passing through the drill rods, ER_i. The cooperative study in Japan indicated

that the average ER_i values are 67 and 80 percent for the rope and pulley method and the tonbi method, respectively, used as the hammer release mechanism. Both values are substantially higher than the U.S. average of 55 percent, using the rope and pulley method.

2. The Japanese energy data are found to have less scatter than those from the U.S. practice.

3. The effect of sampler type on the SPT N-Value is significant. On the average, SPT N-values obtained using an ASTM sampler without liner were found to be approximately 20 percent lower than those obtained using a sampler of a constant inside diameter. The sampler effect is smaller for loose sands, on the order of 10 percent. However, its effect may be as large as 25 to 30 percent for dense sands.

4. Examination of energies delivered to the sampler by different methods of performing SPT tests in different countries and with different equipment led to the choice of a standard energy ratio, $(N_1)_{60}$, determined in SPT tests where the driving energy in the drill rods is 60 percent of the theoretical free fall energy. The selection of $(N_1)_{60}$ will allow us to minimize the task in converting any measured N-value to this recommended standard.

5. Field performance SPT data with respect to liquefaction resistance have been reexamined, reinterpreted, and replotted with respect to $(N_1)_{60}$. Other corrections considered in the reinterpretation included the effect of hammer drop rate, the borehole diameter, the condition where very short drill rod length was used, and the sampler effect.

6. A liquefaction resistance curve, shown in Figure 6, is developed for an earthquake magnitude of M = 7-1/2. The figure also includes the boundary line from the original design curve. It can be concluded from these two boundary lines that there is no difference in the correlation for $(N_1)_{60}$ values up to 15. Above $(N_1)_{60}$ = 15, the original boundary line is slightly more conservative.

6. ACKNOWLEDGEMENT

The studies presented in this paper were sponsored by the National Science Foundation, the Naval Facilities Engineering Command, and the Japan Society for the Promotion of Science, in addition to the parent organizations of the authors. The support of these organizations is gratefully acknowledged. The authors also wish to thank Messrs. W. D. Kovacs, K. Tokimatsu, and L. F. Harder for their valuable advice provided in the course of the study.

7. REFERENCES

1. Clark, K. R. (1969), "Research on Undisturbed Sampling of Soils, Shales, Air Drilling Techniques, and Data on Penetration Resistance Testing - Third Progress Report on Soil Sampling Research," Report No. EM-770, U.S. Department of Interior, Bureau of Reclamation.

2. Decker, M. D., Holtz, R. D., and Kovacs, W. D., "Energy Transfer of SPT Hammers," In Preparation.

3. Douglas, B. J., and Strutznsky, A. (1984), "SPT Hammer Energy Measurements and Piezocone," Ertec Western, Inc., Report to U.S. Geological Survey.

4. Harder, L. F., Hammond, W. D., Ross, P. S., Kassel, J. W. and Motumah, L. K. (1983), "Thermalito Afterbay Dam Seismic Evaluation," California Department of Water Resources, Final Draft.

5. Kavazanjian, E., Jr., Roth, R. A., and Echezuria, H. (1983), "Probabilistic Evaluation of Liquefaction Potential for Downtown San Francisco," Report No. 60, Department of Civil Engineering, Stanford University, 147 pp.

6. Kovacs, W. D. (1981), "Results and Interpretation of SPT Practice Study," Geotechnical Testing Journal, American Society of Testing and Materials, September, pp. 126-129.

7. Kovacs, W. D., Salomone, L. A., and Yokel, F. Y. (1981), "Energy Measurement in the Standard Penetration Test," Building Science Series 135, National Bureau of Standards, Gaithersburg, MD, August, 99 pp.

8. Kovacs, W. D., Salomone, L. A., and Yokel, F. Y. (1983), "Comparison of Energy Measurements in the Standard Penetration Test Using the Cathead and Rope Method," National Bureau of Standards Report to the U.S. Nuclear Regulatory Commission, Report No. NUREG/CR-3545, November, 80 pp.

9. Kovacs, W. D. and Salomone, L. A. (1984), "Field Evaluation of SPT Energy, Equipment, and Methods in Japan Compared with the SPT in the U.S.," NBSIR 84-2910, National Bureau of Standards, Gaithersburg, MD, August, 72 pp.

10. Liang, Nancy (1983), "An Examination of the Standard Penetration Test with Comparison to Other In Situ Tests," Senior Thesis, University of British Columbia, Canada, April.

11. Nishizawa, Y., Fuyuki, S., and Uto, K. (1980), "In Situ Tests and Efficiency Concerning SPT," Proceedings of Sounding Symposium, JSSMFE, (in Japanese).

12. Oh-oka, H. (1984), "Comparison of SPT N-values by Cathead-and-Rope Method and Trip Monkey Method (Concerning Diluvial Sandy Deposits)," Proc. of 19th Annual Meeting, JSSMFE, (in Japanese).

13. Palacios, A. (1977), "The Theory and Measurement of Energy Transfer During Standard Penetration Test Sampling," Dissertation submitted in partial fulfillment of Doctoral of Philosophy Degree, University of Florida, Gainesville, FL.

14. Rebertson, P. K. (1983), "In situ Testing of Soil with Emphasis on its Application to Liquefaction Assessment," Dissertation submitted in partcal fulfillment of Doctoral of Philosophy Degree, University of British Columbia, December.

15. Rebertson, P. K., Campanella, R. G. and Wightman, A. (1982), "SPT-CPT Correlations," Soil Mechanics Series No. 62, University of British Columbia, Department of Civil Engineering, October, 19 pp.

16. Schmertmann, J. H. (1976), "Predicting the q_c/N Ratio-Interpreting the Dynamics of the Standard Penetration Test," University of Florida Report to the Department of Transportation, FL, October.

17. Schmertmann, J. H. (1977), "Use of the SPT to Measure Dynamic Properties? -- Yes, But...!" Proceedings, American Society for Testing and Materials Symposium on Dynamic Field and Laboratory Testing of Soil and Rock, Denver, CO, June.

18. Schmertmann, J. H. and Smith, T. V. (1977), "A Summary of SPT Energy Calibration Services Performed for the Florida Department of Transportation Under Service Contract 99700-7150-010," Final Research Report 245*D73 College of Engineering, University of Florida, Gainesville, FL, 21 pp. plus appendices.

19. Schmertmann, J. H. (1979), "Statics of SPT," Journal of the Geotechnical Engineering Division, American Society of Civil Engineers, Vol. 105, No. GT5, May.

20. Schmertmann, J. H. (1980), "Guidelines for Cone Penetration Test - Performance and Design," Report FHWA-TS-78-209, Federal Highway Administration Implementation Division, 145 pp.

21. Seed, H. B. (1979), "Soil Liquefaction and Cyclic Mobility Evaluation for Level Ground During Earthquakes," Journal of the Geotechnical Engineering Division, ASCE, Vol. 105, No. GT2, Proc. Paper 14380, February, pp. 201-255.

22. Seed, H. B., Idriss, I. M., and Arango, I. (1983), "Evaluation of Liquefaction Potential Using Field Performance Data," Journal of the Geotechnical Engineering Division, Vol. 109, No. GT3, March.

23. Seed, H. B., Tokimatsu, K., Harder, L. F., and Chung, R. M. (1984), "The Influence of SPT Procedures in Soil Liquefaction Resistance Evaluations," Report No. UCB/EERC-84/15, Earthquake Engineering Research Center, University of California, Berkeley, CA, October.

24. Shi-Ming, Huang (1982), "Experience on a Standard Penetration Test," Proceedings of the Second European Symposium on Penetration Testing, Amsterdam, May.

25. Steinberg, S. (1982), "Energy Calibration and Hammer Influence on SPT," Paper presented at the Engineering Foundation Conference on Updating Subsurface Sampling of Soils and Rocks and Their In situ Testing, Santa Barbara, CA, January.

26. Tokimatsu, K. and Yoshimi, Y. (1981), "Field Correlation of Soil Liquefaction with SPT and Grain Size," Proceedings of International Conference on Recent Advances in Geotechnical Earthquake Engineering and Soil Dynamics, St. Louis, MO, Vol. 1, pp. 203-208.

27. Tokimatsu, K. and Yoshimi, Y. (1983), "Empirical Correlation of Soil Liquefaction Based on SPT N-value and Fines Content," Soils and Foundations, Vol. 23, No. 4, December.

28. Yoshimi, Y. and Tokimatsu, K. (1983), "SPT Practice Survey and Comparative Tests," Soils and Foundations, Vol. 23, No. 3, September, pp. 105-111.

29. Yoshimi, Y., Tokimatsu, K. and Oh-oka, H. (1983), "Comparison of SPT N-values by Cathead-and-Rope Method and Trip Monkey Method," Proceedings of the 18th Annual Meeting, JSSMFE, (in Japanese).

30. Youd, T. L. and Bennett, J. J. (1983), "Liquefaction Sites, Imperial Valley, California," Journal of the Geotechnical Engineering Division, ASCE, Vol. 109, No. GT3, March.

Table 1. Summary of Rod Energy Ratios for Japanese SPT Procedures [23]

Study	Mechanical Trip System (tonbi)	Rope & Pulley
Nishizawa et al. (1980)	80 - 90	63 - 72
Decker, Holtz, and Kovacs (In press)	76	
Kovacs and Salomone (1984)	80	67
Tokimatsu and Yoshimi (1981) Yoshimi and Tokimatsu (1983), Yoshimi et al. (1983), Oh-oka (1984)	76*	
Adopted for this study	78	67

* Equivalent rod energy ratio if rope and pulley method is assumed to have an energy ratio of 67 percent and values for mechanical trip method are different from this by a factor of 1.13.

Table 2. Summary of Rod Energy Ratios for Pilcon-Type Free-Fall Hammer [23]

Study	Hammer	Energy Ratio (%)
Decker, Holtz, and Kovacs (1984)	Pilcon	55
Douglas et al. (1984)	Pilcon	62
Liang (1983)	Pilcon-type	58
Overall average		≅ 60

Table 3. Summary of Energy Ratios for SPT Procedures [23]

Country	Hammer Type	Hammer Release	Estimated Rod Energy (%)	Correction Factor for 60% Rod Energy
I.	JAPAN**			
	A. Donut	Free-Fall	78	78/60 = 1.30
*	B. Donut	Rope & Pulley with special throw release	67	67/60 = 1.12
II.	USA			
*	A. Safety	Rope & Pulley	60	60/60 = 1.00
	B. Donut	Rope & Pulley	45	45/60 = 0.75
III.	ARGENTINA			
*	A. Donut	Rope & Pulley	45	45/60 = 0.75
IV.	CHINA			
*	A. Donut	Free-Fall***	60	60/60 = 1.00
	B. Donut	Rope & Pulley	50	50/60 = 0.83

* Prevalent method in this country today

** Japanese SPT results have additional corrections for borehole diameter and frequency effects.

*** Pilcon Type hammers develop an energy ratio of about 60 percent.

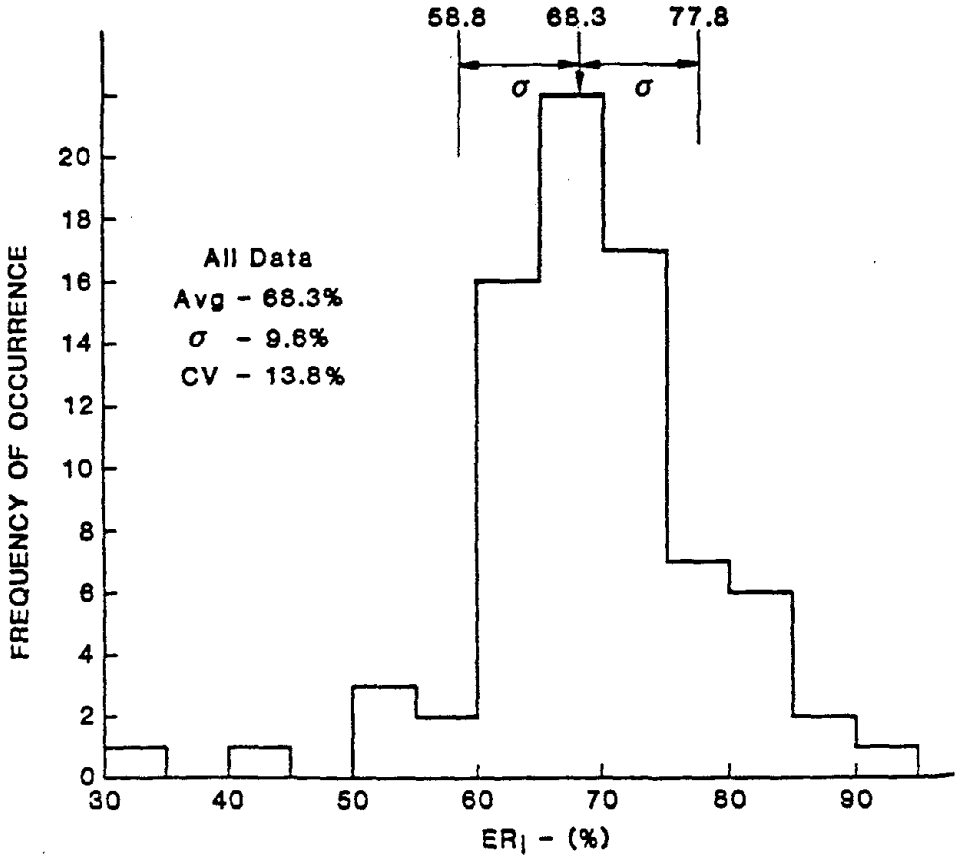

Figure 1. Frequency Diagram of ER_i Results

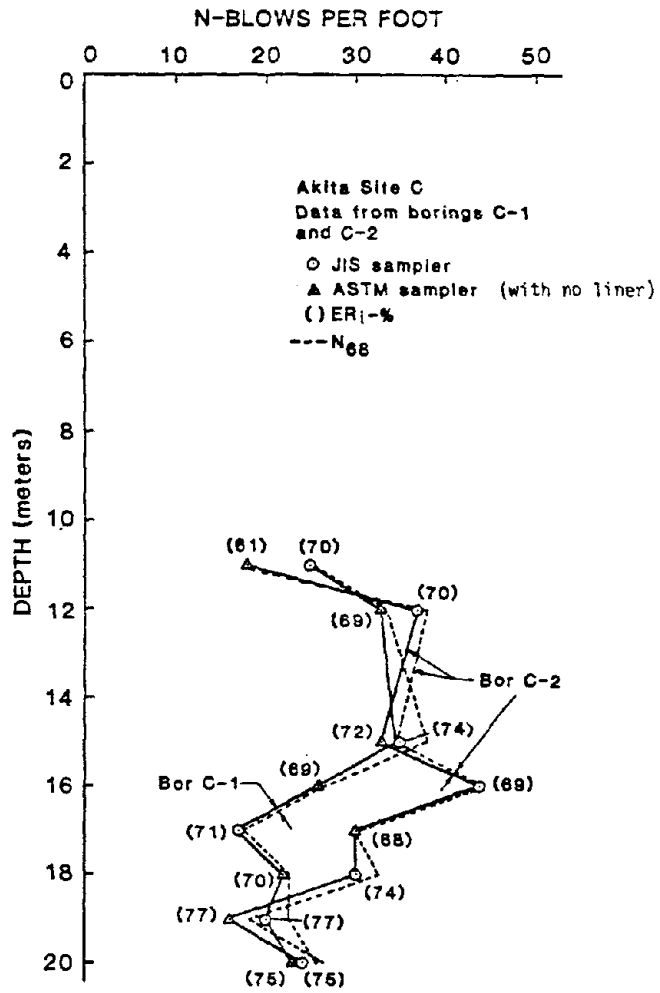

Figure 2. N-Value vs Depth Profile for Akita Area: Borings C-1 and C-2

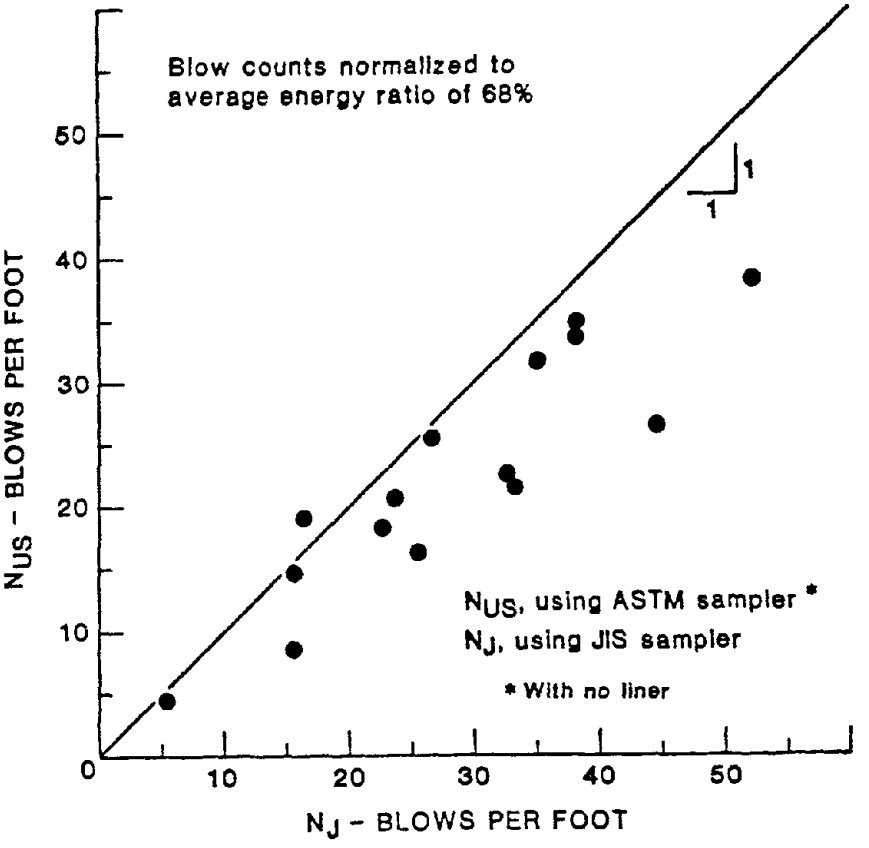

Figure 3. N-Value Correlation Between JIS Sampler and ASTM Sampler Without Liner, Normalized to Average Energy Ratio of 68 Percent, Direct Measurement Data

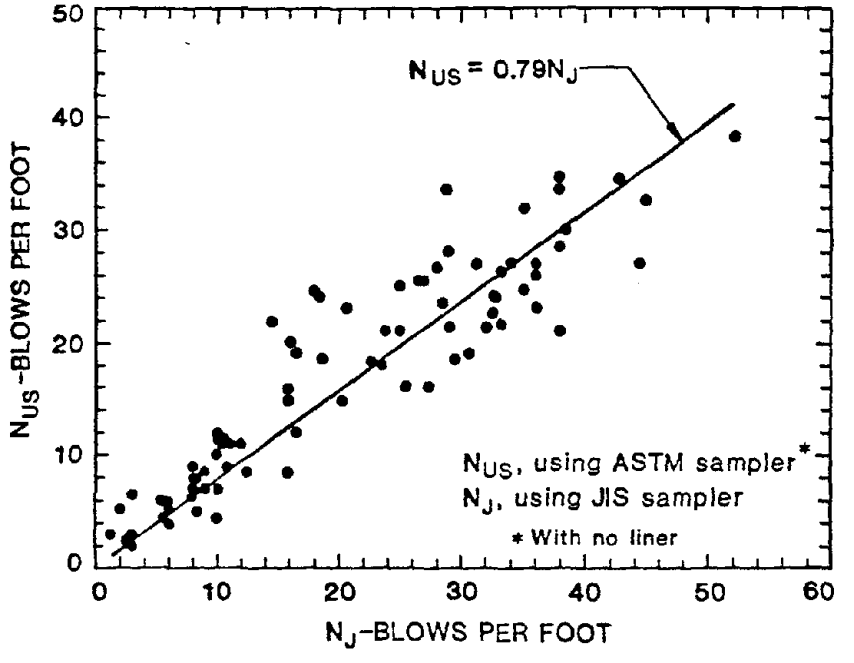

Figure 4. N-Value Correlation Between JIS Sampler and ASTM Sampler Without Liner, Direct Measurement Data and Data Obtained from Interpolation

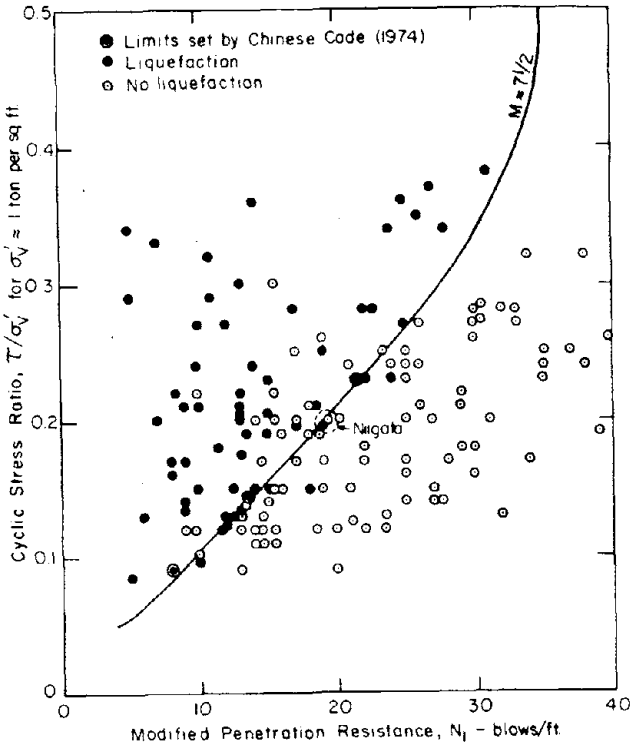

Figure 5. Correlation Between Field Liquefaction Behavior of Sands (D_{50} > 0.25 mm) under Level Ground Conditions and Standard Penetration Resistance (Ref. 22)

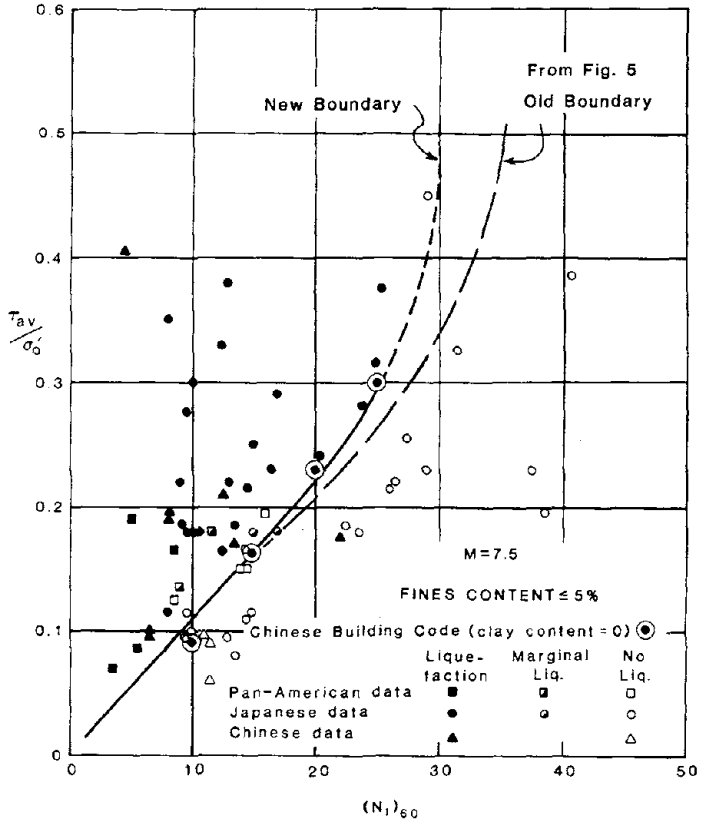

Figure 6. Relationship Between Stress Ratios Causing Liquefaction and N_1-values for Clean Sands for M = 7-1/2 Earthquakes

IN SITU TEST FOR ASSESSING LIQUEFACTION POTENTIAL USING VIBRATORY CONE PENETROMETER

Yasushi Sasaki
Yasuyuki Koga
Yoshihiro Itoh
Takao Shimazu
and
Masuo Kondo

Public Works Research Institute
Ministry of Construction

ABSTRACT

In situ tests using the newly developed vibratory cone penetrometer were carried out at sites where liquefaction of ground took place during past earthquakes.

The results obtained by these tests were compared with the cyclic triaxial test results on undisturbed samples taken from the same sites. The test results by the vibratory cone penetrometer at Akita sites were compared with the earthquake-induced settlement of Hachirogata-Dikes which were severely damaged by the Nihonkai-Chubu Earthquake of May 26, 1983.

1. INTRODUCTION

In Japan, the SPT (standard penetration test) is the most popular test used as the in situ test method for assessing liquefaction potential of soils during earthquakes. Blow counts (or N-values) from the SPT, however, are obtained discontinuously with respect to depth, generally at every one meter of depth. Therefore, the SPT is not always the best way to get continuous information of soils, especially for assessing liquefaction potential of complicated deposits which are composed of sandy and clayey layers, alternatively.

In order to solve this disadvantage, the VCPT (vibratory cone penetrometer test) has been newly developed at the PWRI (Public Works Research Institute) and field tests using this apparatus have been carried out in the laboratory and at several sites.

The development of the VCPT and some results of tests were introduced in the past UJNR Joint Meeting [1, 2]. The in situ test results by this VCPT are partially described in the U.S.-Japan joint research report submitted to the 16th Joint Meeting [2], in which a relationship between results obtained by the VCPT and liquefaction strength by triaxial tests is proposed.

In this present paper, the same relationship is reexamined; in addition, the relation between VCPT results and earthquake-induced settlements of embankments is discussed.

2. OUTLINE OF VIBRATORY CONE PENETROMETER

The vibratory cone penetrometer has been developed in order to satisfy the following objectives:

(1) To obtain liquefaction strength of soils continuously along depth,
(2) To get liquefaction strength of soils accurately, even for loose silty fine sands having much fine content,
(3) To know precise liquefaction strength of soils, in their existing state, at sites,
(4) To get liquefaction strength of soils at sites rapidly, and to get data at many sites easily,
(5) To carry out in situ tests in an inexpensive way.

The VCPT apparatus is composed of parts similar to the Dutch Cone Penetrometer. A basic difference between them, however, is that a small

vibrator is installed inside the vibratory cone, as illustrated in Fig. 1.

When the installed vibrator is turned on, the whole body of the vibratory cone vibrates around its axis. By this excitation, the pore water pressure in soils surrounding the cone may build up as in the case of a saturated sandy ground. Therefore, penetration resistances under the condition in which the vibrator works, will become smaller than those without excitation.

Although the effects of the vibrator on soils surrounding the cone might be different from those of actual earthquakes, the pore water pressure change is deemed to represent an indicator of the vulnerability of the in situ soils to liquefaction. It is considered that the difference between penetration resistances with and without cone excitation will reflect in situ liquefaction resistance of soils.

Figure 2 shows an example of in situ measurement of penetration resistances. As shown in this figure, the penetration resistances decrease when the vibrator works. This difference can be expressed by the degree of penetration resistance decrease which is defined by the following equation.

$$D = \frac{Q_c^S - Q_c^V}{Q_c^S} \qquad (1)$$

where D = degree of penetration resistance decrease

Q_c^S = penetration resistance without operation of vibrator (kgf/cm^2)

Q_c^V = penetration resistance with operation of vibrator (kgf/cm^2)

The value of D, the degree of penetration resistance decrease, is nondimensional and can have any value between zero and one. When a soil has a large value of D, close to one, the soil can be regarded vulnerable to liquefaction during earthquake. Among the vibratory cones shown in Fig. 1, Cone-II has only the vibrator and is without any sensors to measure pore water pressure or cone resistance. Table 1 summarizes the main features of the vibratory cone.

3. SOIL STRENGTH AGAINST LIQUEFACTION AND DEGREE OF PENETRATION RESISTANCE DECREASE

In Fig. 3 is shown the relation between the soil strength against liquefaction and the degree of penetration resistance decrease which was orginally proposed in the previous paper [2].

The data points shown in this figure were obtained at Hachirogata site where the river dikes were severely damaged during the Nihonkai-Chubu Earthquake of May 26, 1983, and Kawagishi-cho site and Showa-Ohashi bridge site damaged during the Niigata Earthquake of June 16, 1964.

The following equation was proposed in the previous paper, based on the data obtained from these sites. In this figure, the stress ratios to cause liquefaction, which were measured by cyclic triaxial tests for undisturbed samples taken from the sites, are plotted against the degrees of penetration resistance decrease at the same depth.

$$R_{\ell 20} = 0.26 + 0.16\ (1-D)^{1.5} \qquad (2)$$

Where, $R_{\ell 20}$ = liquefaction strength (stress ratio) obtained by triaxial tests

D = degree of penetration resistance decrease [Eq. (1)]

In situ tests were carried out at several additional sites other than the above mentioned sites. The data from these tests are plotted in Fig. 4, together with the data shown in Fig. 3. In Fig. 4 the data points are plotted with different marks according to effective overburden pressure. Table 2 summarizes the test results.

From Fig. 4, it is known that the Eq. (2) expresses fairly well the relation between stress ratio to cause liquefaction and the degree of penetration resistance decrease, as most points are distributed close to the curve obtained by Eq. (2). However, the points are scattered around the curve. Reasons for this scatter are discussed below.

The following are some assumptions on liquefaction characteristics:

Assumption 1. - Logarithm of stress versus logarithm of stress cycles has a linear relation, namely

$$\log R = a + b \log N \tag{3}$$

where R = stress ratio
N = stress cycles
a, b = constants

Assumption 2. - Pore water pressure ratio versus stress cycles ratio has a linear relation, namely

$$r_u = r_N \tag{4}$$

where r_u = pore water pressure ratio ($=u/\sigma_v'$)
u = pore water pressure generated by the cyclic stress (kgf/cm2)
σ_c' = initial confining pressure
r_N = stress cycles ratio = N/N_ℓ
N = stress cycles
N_ℓ = stress cycles to cause liquefaction

Futhermore, it is supposed that the stress ratio $R_0 = \tau_0/\sigma_v'$ acts for N_0 cycles on soils surrounding the vibratory cone that has penetrated undergound and generates the pore water pressure of $u_0 = r_u \cdot \sigma_v'$.

Then the following relations are reduced

$$R_{20} = 10^a \cdot (20)^b \tag{5}$$

$$R_0 = 10^a \cdot (N_\ell)^b \tag{6}$$

$$r_u = N_0/N_\ell \tag{7}$$

Considering Eq. (8), Eq. (9) is reduced

$$N_\ell = n_0/r_u \tag{8}$$

$$R_{20} = R_0 \cdot (1/N_\ell)^b \cdot (20)^b$$

$$= R_0 \cdot (20/N_0)^b \cdot (r_u)^b \tag{9}$$

If the relations of $R_{20} = \tau_{20}/\sigma_v'$, $R_0 = \tau_{20}/\sigma_v'$ are taken into account and the pore water pressure ratio caused by the penetration of the vibratory cone is supposed to be equal to the value of the degree of penetration resistance decrease, then the following equations are reduced:

$$r_u = D \tag{10}$$

$$\tau_{20} = \tau_0/(20/N_0)^b \cdot (D)^b \tag{11}$$

When the dynamic stress is caused by the penetrating vibratory cone acts constantly on soils surrounding the cone (τ_0 = const.), the value of R_0 ($= \tau_0/\sigma_v'$) in Eq. (9) differs by changing the depth of penetration. On the contrary, since the terms in Eq. (11) have constant values, except for $(D)^b$, τ_{20} is given by Eq. (11) by substituting the measured value of D.

Considering this fact, the results shown in Fig. 4 might be better illustrated by plotting the stress itself to cause liquefaction rather than the stress ratio. Figure 5 shows the result plotted for the stress.

Comparing with Fig. 4, the plotted points in Fig. 5 are spaced more closely if the confining pressure has the same condition. It seems, however, that the relation between τ_ℓ and D is affected by the confining pressure. This can be explained by the fact that the supposed relation expressed by Eq. (10) is different from the real relation and the assumption established might differ slightly from the actual condition. This

may imply that for estimating more precise liquefaction strength by utilizing the VCPT results, the effect of the overburden pressure should be considered. Regarding this point, further studies should be carried out in the near future.

4. DAMAGE TO HACHIROGATA DIKE AND DEGREE OF PENETRATION RESISTANCE DECREASE

In situ tests by the vibratory cone penetrometer were carried out near the toe of the Hachirogata river dikes, which were severely damaged during the Nihonkai-Chubu Earthquake of May 26, 1983. The number of test points were 32 and their locations are shown in Fig. 6.

Although the geological conditions at these 32 points differ from each other as illustrated in Fig. 7, they can be classified into four types considering ground response characteristics during the earthquake. Four ground types and their peak surface accelerations calculated by dynamic analysis of the material based on the multireflection theory are shown at the bottom of Fig. 7.

Calculated values of peak surface accelerations have a different range for each ground type. Peak surface accelerations at these points are estimated between 160 and 220 gal during the earthquake.

Due to this earthquake, the Hachirogata river dikes settled and suffered from the cracks on their slopes. Although the height of the dikes vary from place to place, front dikes are some 4 to 6 m high. The earthquake-induced settlements vary from place to place; the maximum dike settlement induced by the earthquake was about 1.5 m in this area [3].

As sand boils were observed along the toe of the dike at most of these settlement places, the settlement is considered to be caused by liquefaction of the ground. The authors intended to find out a relation between the damage to the dikes and the liquefaction degree obtained by the VCPT.

The settlements of the crest of the dikes are used as an index value of the damage to the dikes. There are recorded elevations of the crest measured in July 1976, so the differences between the elevations of the crest after the earthquake (measured in June 1983) are defined as the settlements caused by the earthquake.

Several factors, including ground conditions, height of dikes, seismic effects and so on, are generally considered to affect complex earthquake-induced settlements of dikes. In the case of the damage at Hachirogata, however, the heights of the dikes are comparatively identical and the formation of soil layers of the ground is considered to be almost the same in a fairly wide area. So, the estimated thicknesses of liquefied ground are taken as a principal factor to explain the degree of the settlements.

In estimating liquefied thickness, integrated values of the degree of penetration resistance decrease are taken as index values. Since it is considered that liquefaction of the shallow part of the ground affects the settlement more intensively than liquefaction of deeper layers, the calculation of integrated values is made considering a weighting function as shown in Fig. 8. In this calculation, however, the effects of the overburden pressure on the VCPT results mentioned in a previous section are neglected. Integrated values of the degree of penetration resistance decrease with the weight function in this manner are tentatively denoted as the thickness of liquefiable layers.

Fig. 9 shows a relation between the settlements of dikes and the thickness of liquefiable layers. The ground types mentioned in the above

are designated by different marks in this figure.

In Fig. 9 is seen a fairly good correlation between the settlements of the dikes and the thickness of the liquefiable layer for each ground type. Settlements of dikes are affected by thickness of liquefiable layers, as well as ground types. This implies that for estimating possible damages to embankments during earthquakes, it is important to know the liquefiable thickness of ground in addition to the degree of liquefaction potential. Since the VCPT can give continuous information on liquefaction potential, it is considered that the VCPT is one of the more useful in situ tests.

5. CONCLUSIONS

The following are concluded from the results of in situ tests using the vibratory cone penetrometer which was developed at PWRI:

(1) A good correlation is noticed between the degree of penetration resistance decrease and the shear stress to cause liquefaction.

(2) As the degree of penetration resistance decrease becomes larger, the soil strength against liquefaction gets smaller.

(3) The effects of the degree of penetration resistance decrease on the liquefaction strength of soils are affected by the effective overburden pressure at tested depth.

(4) A good correlation is noticed between the thickness of the liquefiable layer and the settlement of the dikes damaged by the Nihonkai-Chubu Earthquake. The larger the thickness of the liquefiable layer is, the larger the settlement is.

(5) Settlements tend to get larger for sites exposed to larger accelerations, even if the thicknesses of liquefiable layers are the same.

6. ACKNOWLEDGEMENTS

The in situ test data and the triaxial test data introduced in this paper are obtained by cooperation of several organizations. The authors express sincere acknowledgment to individuals concerned at Tohoku Regional Construction Bureau, Kanto Regional Construction Bureau, Hokuriku Regional Construction Bureau, Chubu Regional Construction Bureau, Metropolitan Highway Public Corporation, Akita Prefectural Government, and Miyagi Prefectural Government.

7. REFERENCES

1. Yasushi Sasaki and Yasuyuki Koga, "Vibratory Cone Penetrometer to Assess the Liquefaction Potential of the Ground," 14th Joint Meeting, JUNR, 1982.

2. Yasushi Sasaki, et al., U.S.-Japan Cooperative Research on In-situ Testing Procedure for Assessing Soil Liquefaction (No. 1), 16th Joint Meeting, UJNR, 1984.

3. Public Works Research Institute, Report on Damages due to the Nihonkai-Chubu Earthquake, Report of Public Works Research Institute, No. 165, March 1985.

Table 1 Vibratory Cone

(a) Comparison of Vibratory Cone

	Standard Cone	Vibratory Cone					
		I	II	III	IV	V	VI
Diameter (mm)	35.7	41	41	42	41	42	44
Length (mm)	205	789.6	789.6	760.2	333.2	1177.8	743.8
Apex Angle	60°	60°	60°	60°	60°	60°	60°
Weight (kg)	1.1	6.3	6.3	5.2	2.7	8.6	6.7
Vibrator	No	Yes	Yes	Yes	No	Yes	Yes
Sensor	No	Yes	No	Yes	Yes	Yes	Yes

(b) Specification of Vibrator

Item	Size, etc.	
	I, II	III, V, VI
Diameter	41 mm	31 mm
Length	576 mm	431.5 mm
Frequency	200 Hz	
Power Source	AC 3ϕ 48V 200 Hz	
Centrifugal Force	160, 80, 32 kgf	80 kgf

(c) Specification of Transducers

Symbol	Item	Type	Capacity	
			I, II, III, V	VI
qc	Load Transducer of Point Resistance	Strain Gauge	2tf	5tf
fc	Load Transducer of Side Friction	Strain Gauge	2tf	——
P	Pore Pressure Transducer	Strain Gauge	2kgf/cm^2	5kgf/cm^2
S	Displacement Transducer of Penetration	Potentiometer	106 cm	

Table - 2 Summary of VCPT & Cyclic Triaxial Test Result -- 1 --

Site	Depth(m)	Q_c^s	Q_c^v	D	σ_v'	$R_{\ell 20}$	τ_ℓ	FC
A-1	2.3	64.0	12.0	0.813	0.27	0.280	0.076	4.0
A-2	3.3	35.0	30.0	0.143	0.36	0.400	0.144	8.0
A-3	4.0	84.0	67.0	0.202	0.49	0.410	0.201	12.0
B-1	3.3	42.0	12.0	0.714	0.38	0.330	0.125	2.0
B-2	4.8	31.0	5.0	0.839	0.52	0.325	0.169	0.5
B-3	10.8	80.0	23.0	0.713	1.05	0.280	0.294	0.5
C-1	3.8	60.0	94.0	0.000	0.53	0.365	0.193	4.0
D-1	1.8	59.0	2.0	0.966	0.25	0.304	0.076	1.0
D-2	4.8	44.0	14.0	0.682	0.53	0.368	0.195	0.5
D-3	6.3	46.0	14.0	0.696	0.68	0.310	0.211	1.0
D-4	9.8	26.0	26.0	0.000	0.98	0.315	0.309	1.0
E-1	2.8	40.0	0.5	0.988	0.35	0.348	0.122	53.0
E-2	4.4	55.0	0.5	0.991	0.49	0.233	0.114	20.5
E-3	5.4	65.0	4.0	0.938	0.58	0.215	0.125	13.5
E-4	7.3	75.0	6.0	0.920	0.77	0.217	0.167	19.0
E-5	8.1	91.0	13.0	0.857	0.84	0.238	0.200	23.0
E-6	9.4	72.0	16.0	0.778	0.96	0.210	0.202	19.0
E-7	11.4	92.0	36.0	0.609	1.15	0.190	0.219	15.0
F-1	2.4	65.0	42.0	0.354	0.32	0.528	0.169	60.0
F-2	3.2	17.0	10.0	0.412	0.38	0.268	0.102	51.0
F-3	5.0	68.0	50.0	0.265	0.52	0.275	0.143	18.5
G-1	14.4	24.6	17.4	0.293	0.83	0.307	0.255	60.0
G-2	17.4	27.3	12.0	0.560	1.07	0.330	0.353	49.0
G-3	19.4	40.8	35.3	0.135	1.22	0.295	0.360	36.0
H-1	3.4	25.6	11.9	0.535	0.36	0.422	0.152	
H-2	5.3	70.8	52.8	0.254	0.57	0.368	0.210	
H-3	6.5	93.3	75.9	0.186	0.63	0.278	0.175	
I-1	6.9	52.4	35.1	0.330	0.65	0.373	0.242	
J-1	6.9	133.5	122.2	0.085	0.65	0.373	0.242	
K-1	5.4	48.5	43.3	0.107	0.52	0.400	0.209	
K-2	7.3	72.6	60.9	0.161	0.69	0.383	0.264	
L-1	8.3	58.3	34.2	0.413	0.78	0.345	0.269	
L-2	10.3	147.0	128.9	0.123	0.96	0.575	0.552	
L-3	12.3	122.3	96.1	0.214	1.14	0.407	0.464	
M-1	3.3	33.7	21.0	0.377	0.33	0.377	0.124	
M-2	12.5	133.9	104.9	0.161	1.16	0.483	0.560	

Table - 2 Summary of VCPT & Cyclic Triaxial Test Result -- 2 --

Site	Depth(m)	Q_c^s	Q_c^v	D	σ_v'	$R_{\ell 20}$	τ_ℓ	FC
N-1	3.4	36.7	53.7	0.000	0.35	0.501	0.175	
N-2	7.3	114.5	102.1	0.108	0.69	0.350	0.242	
N-3	9.3	150.1	143.8	0.042	0.88	0.510	0.449	
O-1	5.3	42.1	38.4	0.088	0.50	0.450	0.225	
O-2	6.1	72.2	72.1	0.001	0.58	0.442	0.256	
P-1	16.5	40.9	42.7	0.000	1.57	0.272	0.427	13.0
Q-1	2.4	15.0	3.0	0.800	0.36	0.410	0.148	83.0
Q-2	8.5	81.0	47.0	0.420	0.91	0.330	0.300	38.0
R-1	5.5	121.0	98.4	0.187	0.60	0.435	0.261	5.0
R-2	9.4	101.6	90.7	0.107	0.95	0.385	0.366	21.0
S-1	3.3	45.6	28.8	0.368	0.35	0.340	0.119	49.0
S-2	9.3	93.4	97.9	0.000	0.90	0.305	0.275	32.0
T-1	6.2	55.3	25.1	0.546	0.96	0.255	0.245	9.8
T-2	7.2	96.6	34.4	0.644	1.10	0.352	0.387	5.0
T-3	12.3	205.4	123.2	0.400	1.47	0.345	0.507	4.1
T-4	15.4	90.8	64.5	0.290	1.74	0.290	0.505	52.6
U-1	4.4	43.0	5.1	0.881	0.59	0.270	0.159	37.0
U-2	7.9	120.9	101.6	0.160	0.90	0.310	0.279	2.8
V-1	3.0	71.5	45.5	0.364	0.46	0.260	0.120	2.3
V-2	3.9	41.3	52.2	0.000	0.55	0.290	0.160	1.9
V-4	8.3	165.3	81.4	0.508	0.94	0.235	0.221	9.3
V-5	10.6	167.1	160.2	0.041	1.15	0.280	0.322	23.4
W-1	5.7	41.2	32.5	0.211	0.63	0.280	0.176	74.3
X-1	8.2	67.0	74.8	0.000	0.82	0.290	0.238	5.4
X-2	9.4	113.7	102.0	0.103	0.92	0.300	0.276	5.2
Y-1	2.5	17.1	11.4	0.333	0.41	0.315	0.129	41.2
Y-2	3.5	13.5	7.0	0.481	0.48	0.305	0.146	25.0
Y-3	5.6	72.0	24.9	0.654	0.63	0.270	0.170	3.4
Y-4	7.2	102.0	80.0	0.216	0.78	0.290	0.226	5.0
Z-1	4.9	59.0	51.0	0.136	0.80	0.200	0.160	

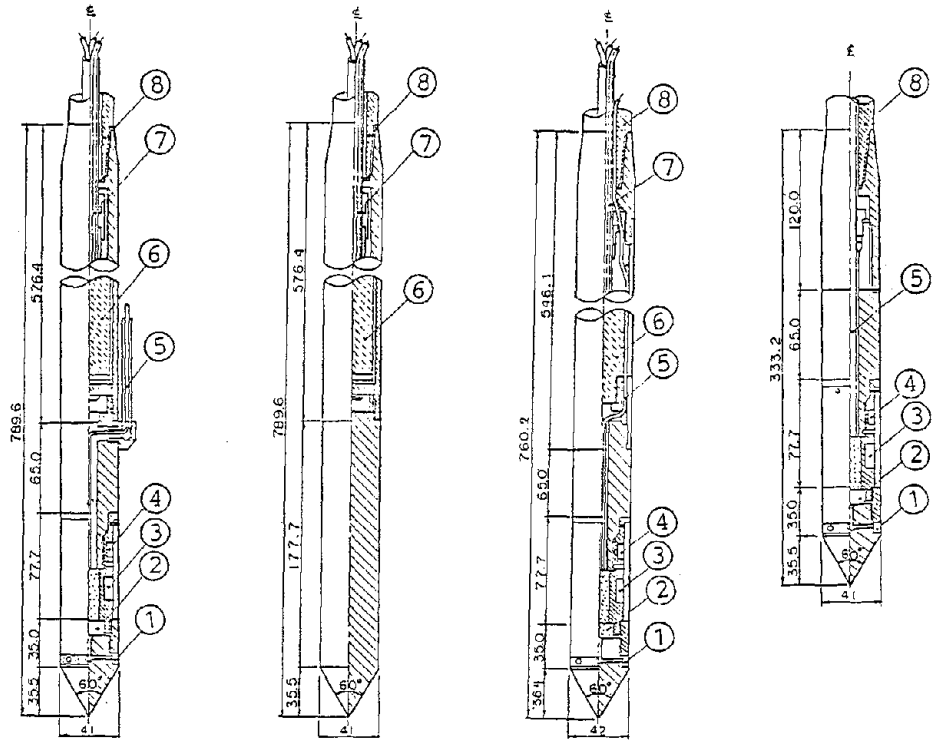

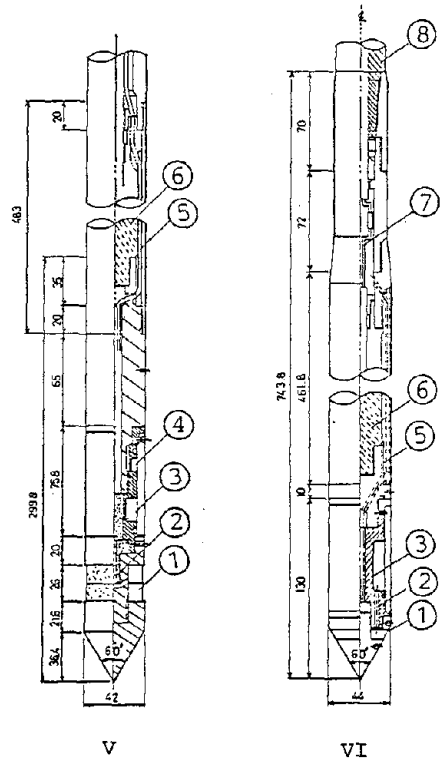

① Porous metal
② Pore pressure transducer
③ Load transducer of point resistance
④ Load transducer of side friction
⑤ Take-out cable for transducer
⑥ Vibrator
⑦ Power source cable for vibrator
⑧ Penetrating rod

Fig. 1 Vibratory Cone

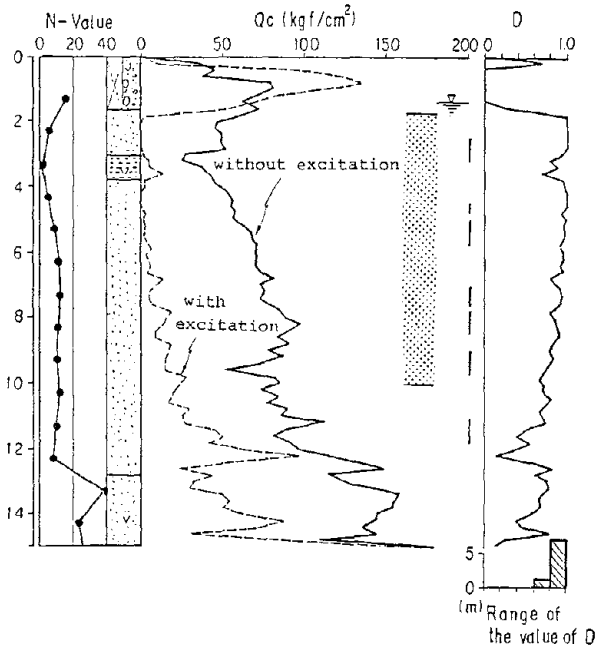

Fig. 2 Example of in-situ Measure of VCPT
— Showa-Ohashi Bridge Site —

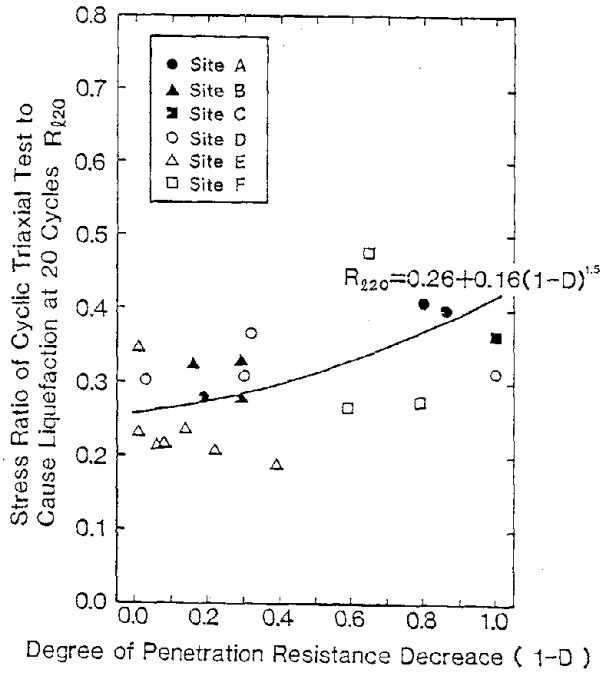

Fig. 3 Relation between Liquefaction Strength and Degree of Penetration Resistance Decrease
— U.S.-JAPAN Cooperative Research (No.1) —

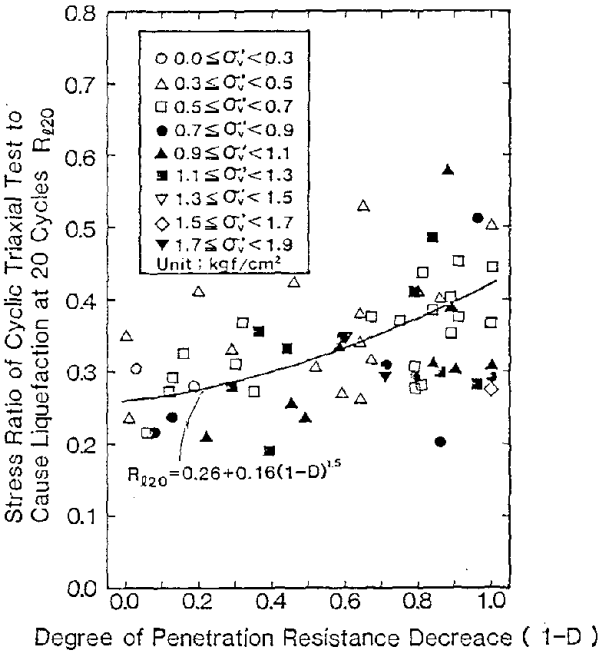

Fig. 4 Relation between Liquefaction Strength and Degree of Penetration Resistance Decrease
— R_{120} - (1-D) —

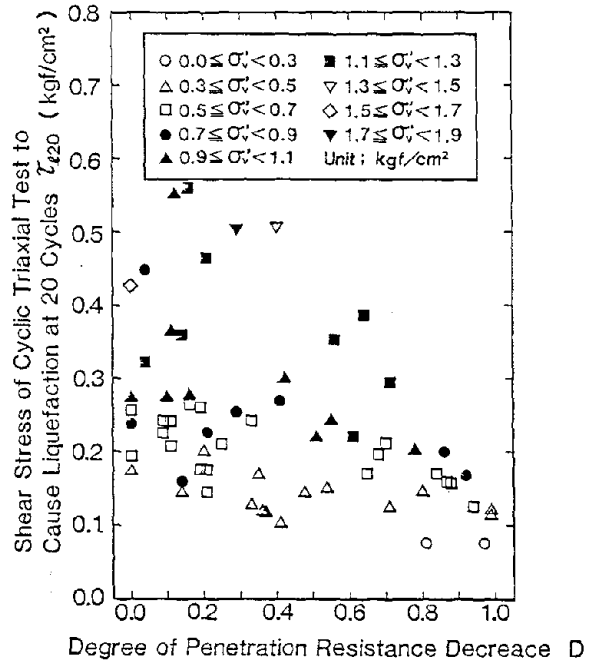

Fig. 5 Relation between Liquefaction Strength and Degree of Penetration Resistance Decrease
— τ_{120} - D —

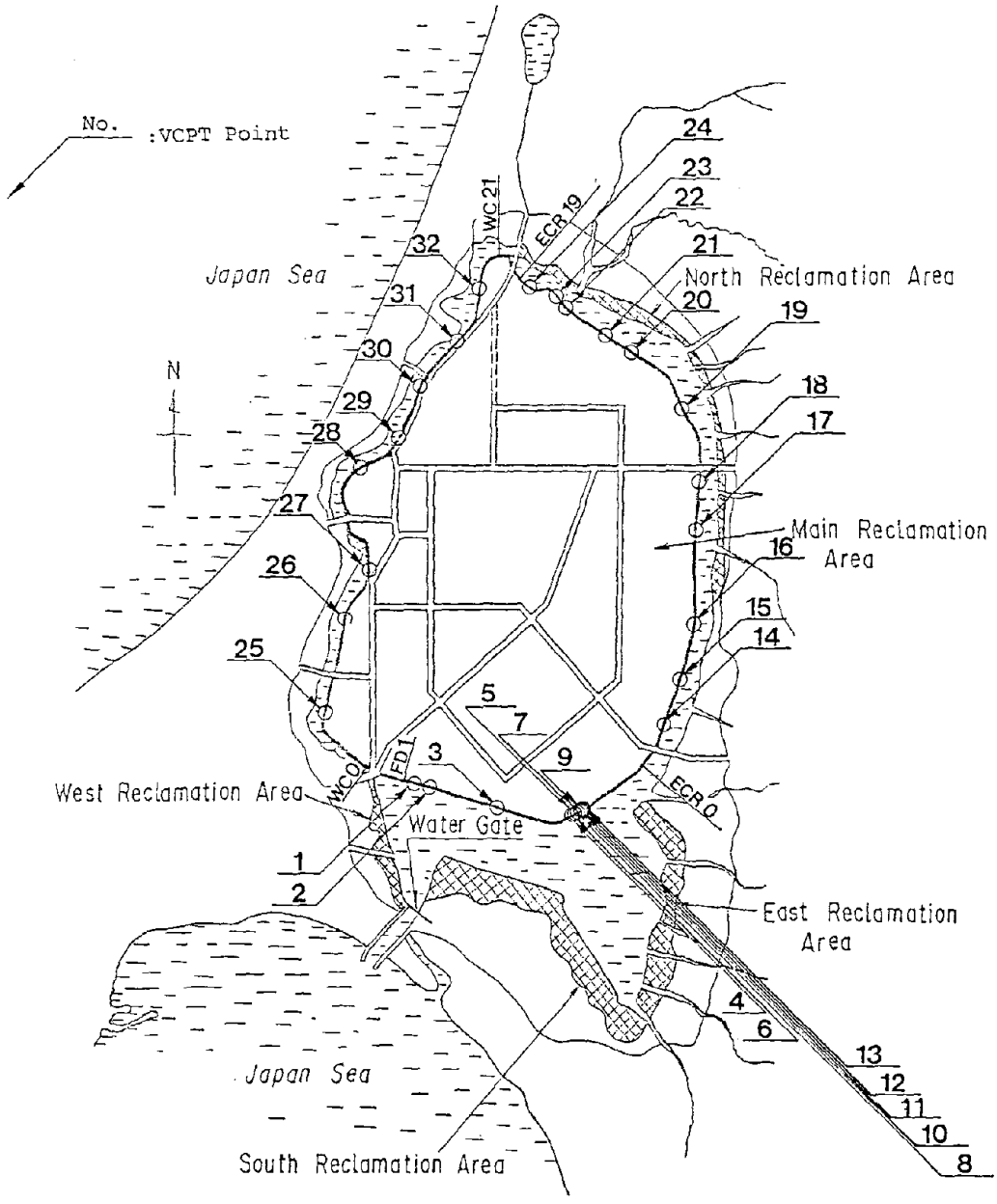

Fig. 6 Location of VCPT Points at HACHIROHGATA

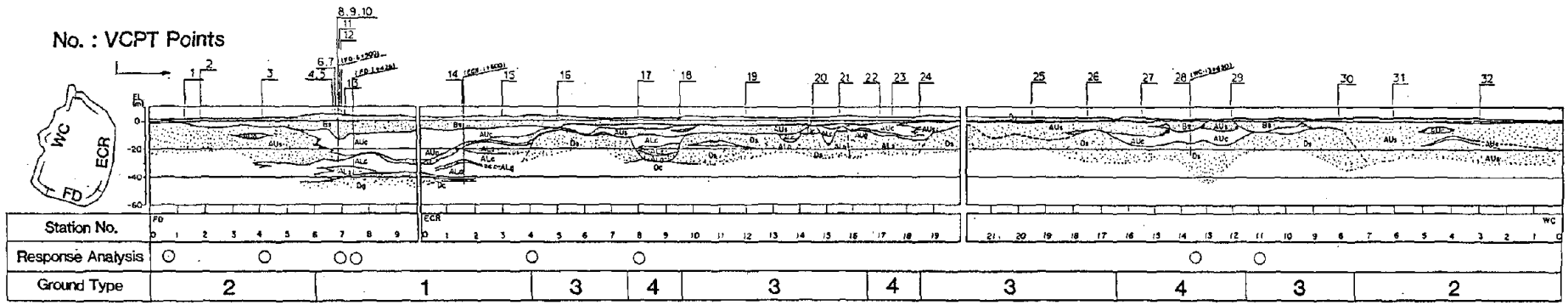

Ground Type – 1 (Thick alluvial layer with clayey deposit)

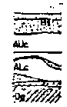

FD5+900 (165gal), FD7+426 (166gal)

Ground Type – 2 (Thick alluvial layer with sandy deposit)

FD0+660 (174gal), FD4+100 (191gal)

Ground Type – 3 (Thick alluvial layer with sandy layer)

ECR4+000 (194gal), WC11+000 (198gal)

Ground Type – 4 (Thick alluvial layer with clayey deposit)

ECR7+964 (246gal), WC13+650 (224gal)

Fig. 7 Loaction of the VCPT Points and Soil Profile

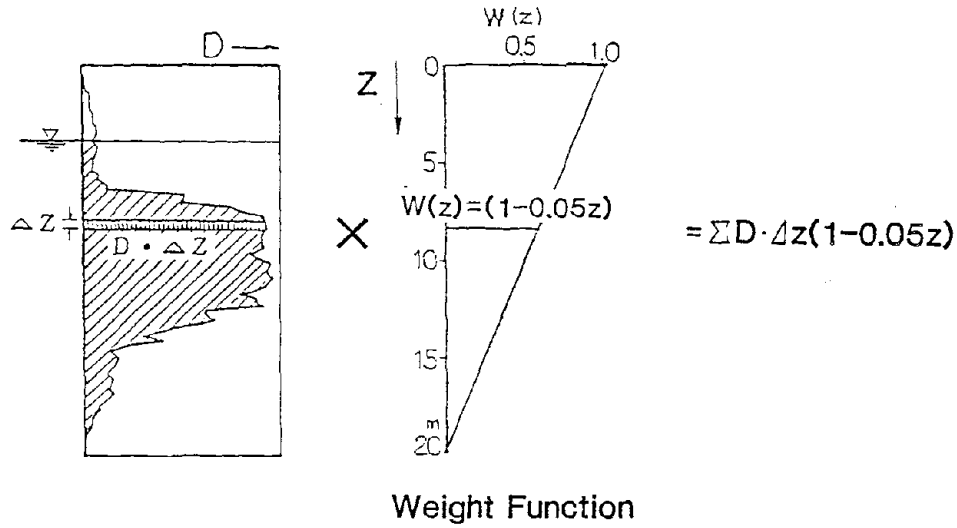

Fig. 8 Weight Function and Integration of D

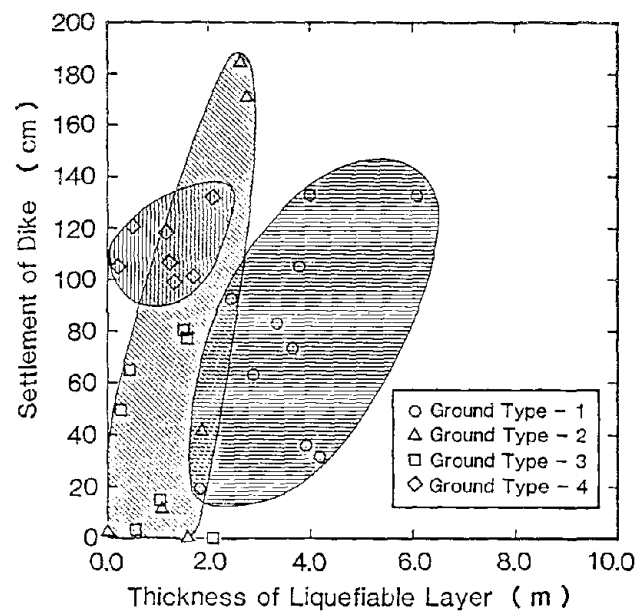

Fig. 9 Relation between Settlement of Dikes and the Thickness of Liquefiable Layer

U.S.-JAPAN JOINT EARTHQUAKE RESEARCH PROGRAM INVOLVING LARGE-SCALE EXPERIMENTS ON MASONRY BUILDING STRUCTURES-JAPANESE SIDE RESEARCH PLAN

BY

Shin Okamoto[1], Yutaka Yamazaki[2], Akio Baba[2], Masa-omi Teshigawara[3], and Hisahiro Hira-ishi[4]

ABSTRACT

A joint earthquake research program of building structures involving large-scale experiments was carried out since 1979 between Japan and the U.S. under the auspices of the Panel on Wind and Seismic Effects of the U.S.-Japan Natural Resources Development Program. During the first two years (1979-1980), earthquake response behavior of a reinforced concrete building was investigated based on experiments of a full-scale seven-story specimen. This work was carried out at the Building Research Institute, Japan. A similar experimental research program on steel building structures was held during the next three years (1981-1983). At this time, as a third phase of the joint program, masonry building structures, is being developed for the five year period 1984-1988. This paper introduces the Japanese-side research objectives and research plan for masonry building structures for the U.S.-Japan joint research program.

1. INTRODUCTION

A joint research program on earthquake engineering of building structures was performed since 1979. This research was conducted between the U.S. and Japan under the auspices of the Panel on Wind and Seismic Effects of the U.S.-Japan Natural Resources Development Program.

Testing earthquake response simulation of large-scale building structures is the objective of this program. It was carried out at the Building Research Institute of the Ministry of Construction, Japan. To perform the large scale test, a new earthquake simulation test technique, designated as the pseudo dynamic test method, was developed by the Building Research Institute and was effectively employed in this research program. In addition to the large-scale test, several other types of experimental work is included in the program. They are 1) component test of structural beam and column elements, 2) planar test of frame subassemblages, 3) shaking table test of replicas of building structures, (4) correlation study between shaking table and pseudo dynamic tests.

The research program including these experimental programs is aimed at investigating the effectiveness of a variety of procedures developed to evaluate the seismic behavior of structures such as analytical simulation procedures, design procedures, and safety evaluation procedures. Such a comprehensive effort in this joint program is believed to be the first to achieve the above objective. The expected outputs of this study are:

(1) to establish design methods to ensure higher safety;
(2) to establish more economical design methods without losing structural safety;
(3) to develop more accurate procedures to estimate the seismic safety of structures;
(4) to develop experimental and analytical procedures to simulate the earthquake response behavior of structures with a greater accuracy;
(5) to make the overseas construction by U.S. and Japanese contractors more competitive; and

[1]Director, [2]Division Heads, [3]Research Engineer, [4]Senior Research Engineer, Structural Engineering Department, Building Research Institute, Ministry of Construction, Tatehara, Oho-machi, Tsukuba, Ibaraki, 305, JAPAN

(6) to enhance information and personnel exchange. The joint program was initiated in 1979 as shown in Fig. 1. In the first phase of this program, the reinforced concrete structural system was examined; a full-scale seven-story reinforced concrete structure was tested using the pseudo dynamic test technique. In the second phase, the steel structural system was studied with a test of a full-scale six-story steel braced frame. For the third phase of this program, the masonry structural system was selected. This third phase masonry program was initiated in 1984 and is to continue for five years. The first joint workshop on the masonry program was held in March, 1984 at the Building Research Institute.

2. BACKGROUND OF MASONRY STRUCTURES AND NEEDED AREAS OF RESEARCH

The masonry structural system is known worldwide to be a traditional but efficient structural system having high capacity in durability, fire resistance, sound and heat insulation, and high flexibility in construction. The structural system was first imported to Japan from Europe, and, therefore, little attention was given to the earthquake resistance of the constructed masonry structures. Accordingly, those structures sustained great damage in the Great Kanto Earthquake. Since then, masonry structures practically disappeared in Japan, and very little effort was made for the study of seismic resistance of the masonry structural system.

Because of large demand of building construction after World War II, Japan developed various mass produced construction systems. During those periods, however, the masonry structural system was not used mainly because masonry systems require tedious labor work. Today, more value is put on quality than quantity, and versatility is more appreciated than uniformity. To comply with this new demand, it is natural to reconsider benefits of the masonry structural system. Since the late 1960s various types of new masonry construction systems have been developed to make the construction more reliable and competitive. The reinforced concrete block system, named RCB, is one example. The Building Research Institute has contributed much to the development of the masonry structural system. One current project, "Application of Small PC Unit to Urban Housing," involves developing quality masonry units to better resist earthquakes.

This is a brief review of the background of the masonry research in Japan. Considering this situation, the immediate target of this program as the third phase of the U.S.-Japan Joint Research Program will be the development of a masonry construction system fit to low- to medium-rise building structures.

3. JAPANESE RESEARCH PLAN

3.1 Organizations

Fig. 2 shows the organization for promoting U.S.-Japan cooperative research on masonry structures. The Japanese have three committees: Technical Coordinating Committee on Masonry Research (TECCMAR), Promoting Committee on Masonry Research (PROCMAR), and Building Construction Committee on Masonry Research (BLDCMAR). The first committee, TECCMAR, coordinates technical research planning on materials, components, assemblies and full-scale experiments. They are drafting a proposal of aseismic design guidelines of low/medium-rise reinforced masonry building structures in Japan. The second one, PROCMAR, was organized under domestic cooperation research agreement among the Building Research Institute, the Japan Association for Building Research Promotion and the Building Contractors Society for promoting U.S.-Japan cooperative research on masonry structures. The committee members are composed of government officials, local self-governing body's officials, and representatives from many industrial organizations. The last committee, BLDCMAR, was organized under PROCMAR. Problems concerning masonry building construction techniques, except structural matters, are dealt

with in this committee.

3.2 Research Plan

The Japanese research items of interest for the five year program are:

1) material test;
2) static test of walls;
3) static test of beams;
4) static test of wall and beam assemblies;
5) full-scale planar static test;
6) shaking table test of scale model specimen;
7) full-scale five-story structure test; and
8) establishment of aseismic design guidelines.

Research time schedule for the above items are shown in Fig. 3. During the first two years, fundamental tests on materials, wall and beam components, assemblies and full-scale planar static tests will be carried out. The program for shaking table tests of a scale model specimen and a full-scale five-story structure test will be performed in the third year of the program.

4. JAPANESE RESEARCH OBJECTIVES

The joint research program is to propose aseismic design guidelines for low/medium-rise reinforced masonry building structures in Japan. At present, only the reinforced masonry buildings with height up to 12 meters (one to three stories buildings) are permitted to be constructed in Japan. Under this program in Japan, the design guidelines for low- to medium-rise reinforced masonry buildings (up to about five stories maximum) are being proposed.

In addition to this final target, the following objectives in structural design of masonry buildings are considered:

1) to ensure sufficient aseismic performance:
   Aseismic performance which is substantially equal to the one to be required for present wall type R/C buildings in Japan is expected for newly developed reinforced masonry buildings under the program.
2) to propose decreased wall length rate:
   21-cm/m^2 at present regulation to;
   15-18cm/m^2 for five-story buildings and
   12-15cm/m^2 for three-story building in proposal
3) not to use reinforced concrete collar beams:
   Reinforced concrete collar beams are required in reinforced masonry buildings under present regulations
4) to simplify joint works of reinforcing bars:
   Effectiveness of lap joint or mechanical joint works of vertical reinforcing bars in walls is experimentally investigated.

Through Japanese research, high strength block units in which design prism strength is more than 180kg/cm^2 are now used. In the present regulations, 80kg/cm^2 design strength for full section area of a block unit and 135kg/cm^2 design strength for grout concrete are required. Standard concrete and clay block units used in Japanese research, which were newly designed and produced for the program, are shown in Figs. 4 and 5.

To allow setting relatively large amount of reinforcing bars into unit holes, large size holes are prepared for the units, and are fully grouted. R/C slab system will be applied to future full-scale five-story specimen which is to be tested under 1987 Japanese side research plan.

5. 1984 RESEARCH WORKS IN JAPAN

5.1 Test Plan on Materials and Construction Method

The following items are important to realize low/medium-rise masonry buildings in this research program.

a) The prediction of the compressive strength of prism specimens from properties of block units, grout concrete, and joint mortar:
   1) basic poperties of units;
   2) the effect of particle size distribution of aggregate on the strength of joint mortar;

3) the effect of joint mortar on the prism strength;
4) the effect of grout concrete or grout mortar strength on the prism strength.

b) Possibility of high lift grouting to execute construction works fast:
It is necessary to confirm fullness of grouting and bond between reinforcing bars and grout concrete or grout mortar. Eight specimens, six concrete block and two clay block specimens were tested. Test specimen is shown in Fig. 6.
c) Applicability of lap joints on vertical reinforcing bars:
Now, in Japan, lap joint in masonry structures is inhibited. It is necessary for easy execution of works to confirm effectiveness of lap joints. Six types of twelve specimens as listed in Table 1 were tested.
d) Anchoring strength of reinforcing bars:
Large amount of reinforcing bars would be set in a small unit hole to resist seismic horizontal loading to vertical components of buildings. Tests on the effect of face shell and the thickness of covering grout concrete were carried out using the specimens as listed in Table 2.

5.2 Test Plan on Masonry Walls and Beams

In 1984 static tests of isolated walls and beams constructed by Japanese practice were conducted to obtain basic knowledge of five-story masonry structures. The major purpose is to investigate their deformation performance and shear capacity. Therefore, the shear-span ratio, amount of cross sectional area of main reinforcing bars and amount of shear reinforcement of test specimens were mainly varied in this test program. Prism compressive strength, f'm, and ratio of vertical shear reinforcement sectional area to the gross concrete area of a horizontal section of the wall, PWV, are constant values and those are f'm = 200-250kg/cm^2 (would be 240kg/cm^2) and Pwv - 0.25%, respectively.

Test series of masonry walls and beams are summarized in Table 3. It is expected to be clarified from these test series how much effect each factor has on deformation performance and shear capacity.

5.3 Masonry Walls

Test specimens of walls are listed in Table 4 and an example, Specimen WSR1 (shear failure type) is shown in Fig. 7. Photo 1 shows the specimen WSR1 after testing. The following test series were considered.

a) Tests on shear capacity and deformation performance (WS specimens)
   - Average compressive stress σ_0 = 20kg/cm^2, and for specimens with symbol "N" σ_0 = 40 and 60kg/cm^2
   - Main reinforcing bars a_t = D16, 2-D19 and 2-D25
   - Horizontal shear reinforcement ratio Pwh = 0 to heavy (0.668%)
   - Shear span ratio M/QD = 0.45, 0.75 and 1.13
b) Test on flexural deformation performance (WF specimens)
   - M/QD = 0.75 and 1.13
   - Ratio of shear strength to bending strength Qsu/Qmu = variable
   - Average compressive stress σ_0 = 5kg/cm^2
c) Test on effect of transverse wall on strength and deformation performance (WT specimens)
   - T and + types
d) Test on effect of ladder steel on shear capacity and deformation performance (J specimens)
e) Test on effect of unit shape on shear capacity and deformation performance (B1 specimens)
f) Test on effect of open joint work on shear capacity and deformation performance (O specimens)
g) Reinforced concrete wall test to compare shear capacity and deformation performance with those of masonry walls (RC specimens).

5.4 Masonry Beams

Test specimen of beams are listed in Table 5, and the test specimen, GSR1 (shear failure type) is shown in Fig. 8. The following test series were

considered.

a) Test on shear capacity and deformation performance (GS specimens)
   - a_t = 2-D16, 2-D19 and 2-D25
   - Pw = light (0.16%) to heavy (0.67%)
   - M/QD = 0.71 and 1.18
b) Test on flexural deformation performance (GF specimens)
   - Qsu/Qmu = variable
c) Test on beams with slab (GF1, GS1 and GF2 specimens)
   - Slab thickness = 15cm
   - Slab width = 1m on both sides of a beam
   - Slab reinforcement = 2-D10@300
d) Test on effect of unit shape (B1 specimens)
e) Test on effect of Hoop shape (H specimens)

5.5 Loading System and Sequence

The loading system used in wall and beam tests is shown in Fig. 9 and in Photo 2. This loading system consists of three actuators. A and B actuators are controlled by a computer in order not to produce any angle of rotation at top and bottom of a specimen under constant axial load. C-actuator is controlled by another computer in order to apply horizontal force to a specimen under predetermined loading sequence as shown in Fig. 10.

6. CONCLUSION

The Japanese research plan for masonry building structures under the U.S.-Japan Joint Earthquake Research Program involving LargeScale Experiments was presented. There are few masonry buildings of concrete and clay block in Japan compared with the other types of structural systems such as timber houses, reinforced concrete and steel buildings. Through the five years epoch-making research program concerning low/medium-rise reinforced masonry buildings, masonry structural systems in Japan are being considered as a viable and safe construction system and are increasing in number.

7. ACKNOWLEDGMENT

The authors wish to express their sincere thanks to TECCMAR members for their coordination of Japanese technical research planning under the U.S.-Japan Joint Program on masonry building structures. The authors also express their gratitude to PROCMAR members for their contribution to promote U.S.-Japan cooperative research on masonry structures in Japan.

Table 1

Test Specimen of Lap Joint Applicability

SPECIMEN	LENGTH OF LAP JOINT	WIRE JOINT REINFORCEMENT	SPIRAL REINFORCEMENT	SECTION
1	–	–	–	
2	–	–	–	
3	40d	–	–	
4	40d	4Φ@400	–	
5	40d	–	4Φ50 PITCH	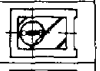
6	40d	4Φ@400	4Φ50 PITCH	

Table 2

Test Specimen of Anchoring of Reinforcing Bars

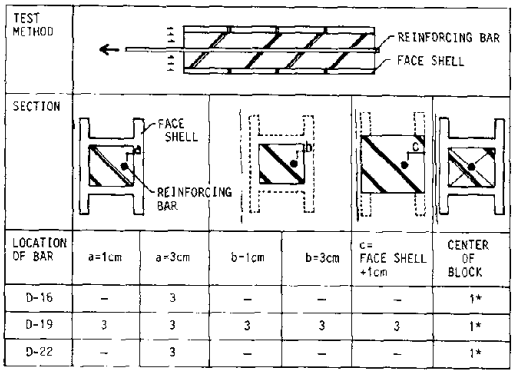

LOCATION OF BAR	a=1cm	a=3cm	b=1cm	b=3cm	c= FACE SHELL +1cm	CENTER OF BLOCK
D-16	–	3	–	–	–	1*
D-19	3	3	3	3	3	1*
D-22	–	3	–	–	–	1*

Table 3 Test Series of Wall & Beam Specimens

	SERIES	SPECIMENS				TOTAL
		STANDARD C/B	B1 C/B	CLAY BLOCK	R/C	
A)WALL	A-1)M/QD	WS1,WS4,WS7 WTT1,WTT2 (5)	–	WSR1,WSR4,WSR7 (3)	WSRC,WTRC (2)	10
	A-2)FLEXURE	WF1,WF2,WTC1 WFL1,WFLM,WFJ1 WFJ2 (7)	WFB1,WFB10 (2)	WFR1,WFR2 (2)	WFRC (1)	12
	A-3)AXIAL FORCE	WSN1,WSN2 (2)	WSB1,WSB10 (2)	–	–	4
	A-4)Pw	WS2,WS4,WS5 WS6,WS8,WS9 WS10 (7)	–	WSR2,WSR4,WSR5 WSR6 (4)	–	11
	A-5)At	WS3,WS4,WS11 WS2,WSJ1,WSJ2 (6)	–	WSR3 (1)	–	7
	SUB-TOTAL	27	4	10	3	44
B)BEAM	B-1)HOOP	GS2, GSH1,GSH2 (3)	GSB1 (1)	–	–	4
	B-2)Pw	GS2,GS3,GS4 (3)	–	GSR1,GSR2 (2)	–	5
	B-3)FLEXURE	GF3,GF4,GF5 GF6 (4)	–	GFR1,GFR2,GFR3 GFR4 (4)	–	8
	B-4)SLAB	GF1,GS1,GF2 GF3 (4)	–	–	–	4
	SUB-TOTAL	14	1	6	–	21
	TOTAL	41	5	16	3	65

Table 4 Test Specimen List of Walls

Pw / TRANSVERSE WALL		0		D13@400 (0.167%)		D13@200 (0.334%)		2D13@200 (0.668%)	
M/QD	At(cm²)	×	○	×	○	×	○	×	○
0.45	D16 (1.99)								
h/l= 180/200	2D19 (5.74)			WS1,WSR1					
	2D25 (10.1)								
0.75	D16			WS3,WSR3					
h/l= 180/120	2D19	WSR2 WSJ1 WS2×2		WS4×3,WSB1 WSR4×2,WSN1 WSN2,WF1,WFR1 WFL1,WSRC,WFJ1 WFLM,WFRC WSB10,WSJ2	WTT1 WTC1 WTRC	WS5 WSR5		WF2,WFB1 WFR2 WFJ2 WFB10 WS6 WSR6	WTT2
	2D25	WS8		WS11		WS9		WS10	
1.13	D16								
h/l= 180/80	2D19			WS7,WSR7					
	2D25								

PRISM STRENGTH fm'=250Kg/cm² VERTICAL REINFORCEMENT D16@400

WS ; SHEAR FAILURE TYPE
WF ; FLEXURAL FAILURE TYPE
WT ; TT:T-SHAPE, TC:CROSS-SHAPE SPECIMEN
R ; CLAY BLOCK
J ; EFFECT OF LADDER STEEL
B1 ; 300mm LENGTH C/B SPECIMEN
RC ; R/C SPECIMEN
O ; OPEN JOINT SPECIMEN
N ; AXIAL FORCE SERIES SPECIMEN

Table 5 Test Specimen List of Beams

Pw / R/C SLAB		D13@400 (2D10@400)*1 D13@400 *2		D13@200 D13@150*2		2D13@200 D16@150*2	
M/QD	At(cm²)	○	×	○	×	○	×
0.71	2D16 (3.98)			GF1			
l/h= 120/95	2D19 (5.74)		GF6,GFR4				
	2D25 (10.1)	GS1	GS2,GSR1 GSH1,GSB1 GSH2				GS3,GSR2
1.18	2D16						
l/h= 200/95	2D19	GF2	GF3,GFR1		GF4,GFR2		GF5,GFR3
	2D25		GS4				

PRISM STRENGTH fm'=250Kg/cm² HORIZONTAL REINFORCEMENT D16@400

*1 FOR HOOP SERIES SPECIMEN
*2 FOR 300mm LENGTH UNIT SPECIMEN

GS ; SHEAR FAILURE TYPE
GF ; FLEXURAL FAILURE TYPE
R ; CLAY BLOCK
B1 ; 300mm LENGTH C/B SPECIMEN
H ; HOOP SERIES SPECIMEN

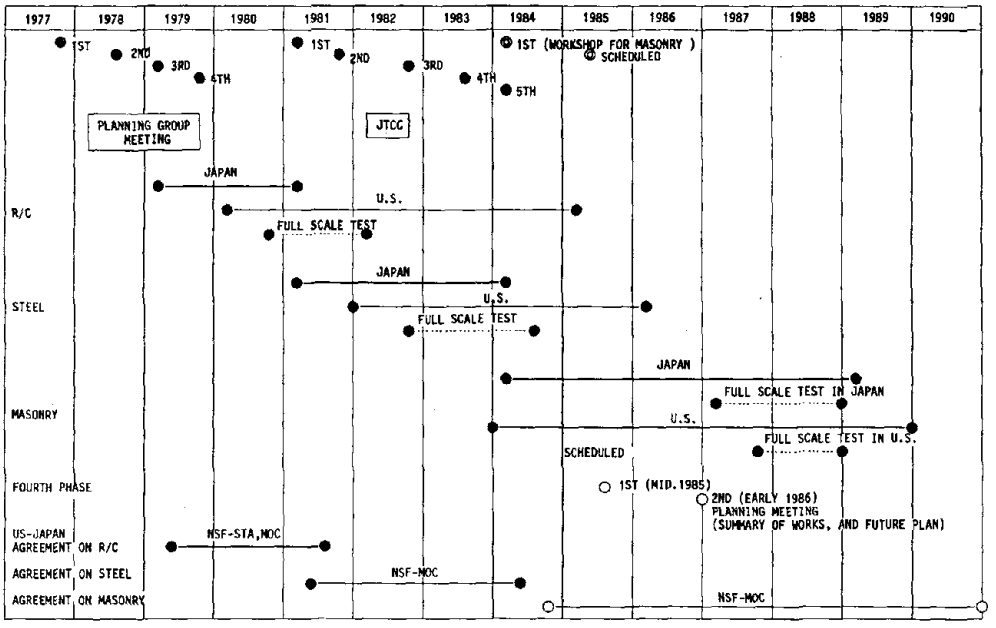

*First Workshop for masonry project was held on March 16, and 17, 1984.
*Two planning meetings, one in the middle of 1985, and the other in early 1986, are proposed. The first one will be held in Japan, and the second in USA.

NSF : National Science Foundation, STA : Science Technology Agency, MOC : Ministry of Construction

Fig.1 Schedule of U.S.-Japan Joint Research Program

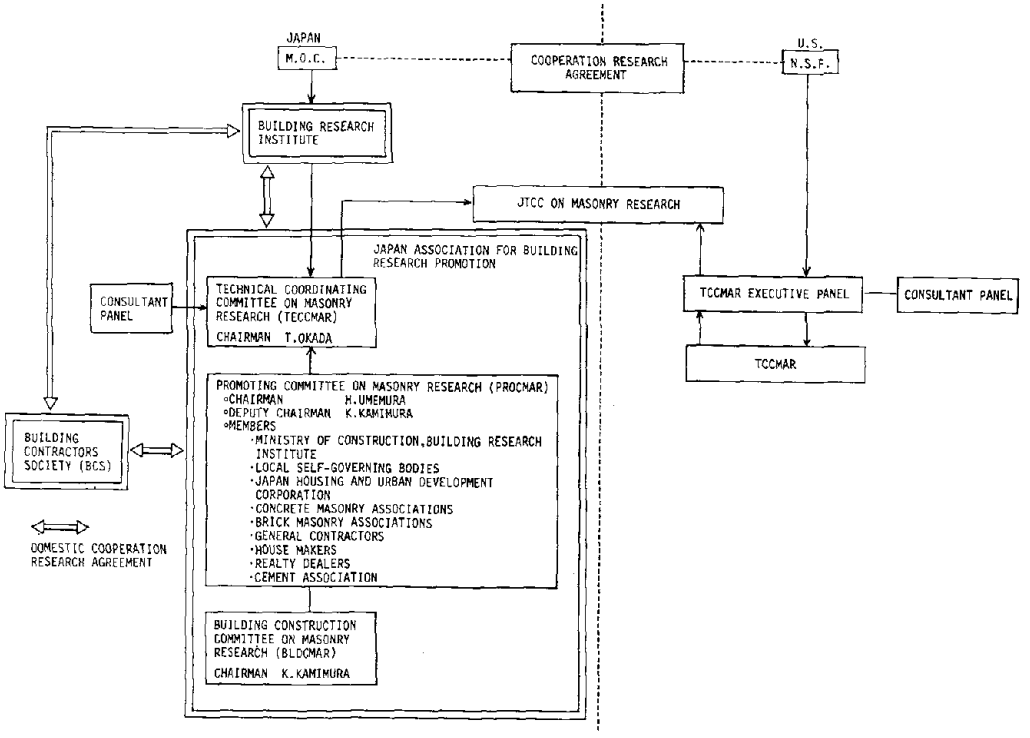

Fig.2 Organization for Promoting U.S.-Japan Joint Research on Masonry Building Structures

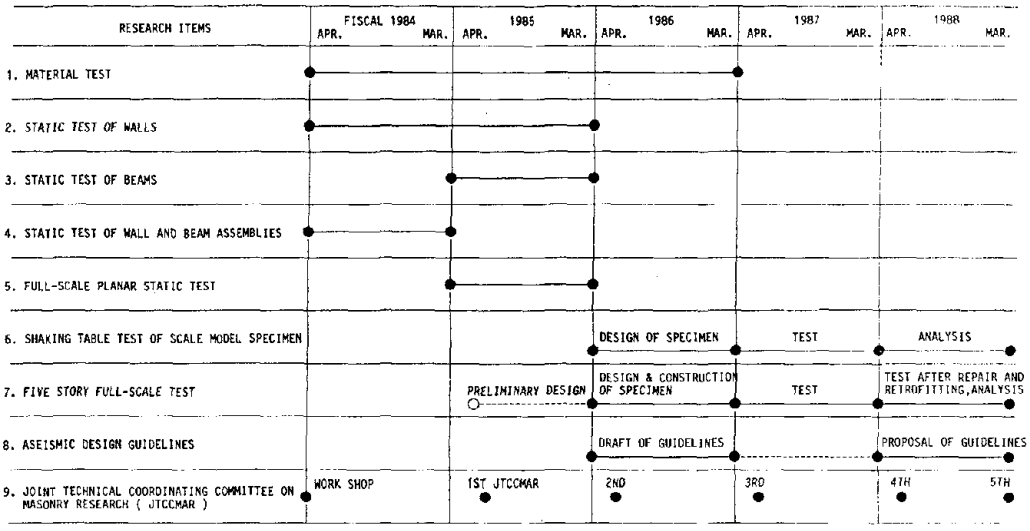

Fig.3 Japanese Research Plan on Masonry Building Structures

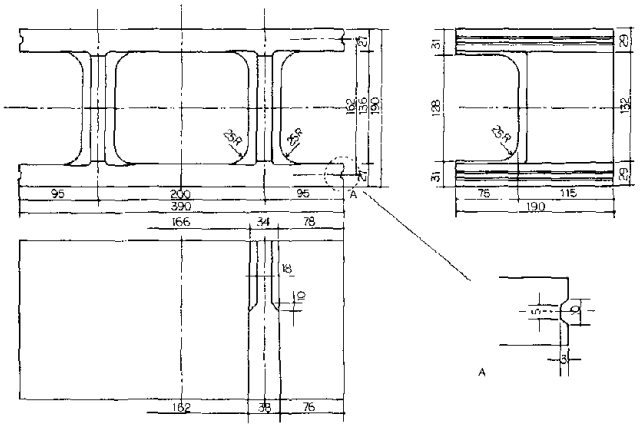

Fig.4 Standard Concrete Block Unit in Japanese Research Program

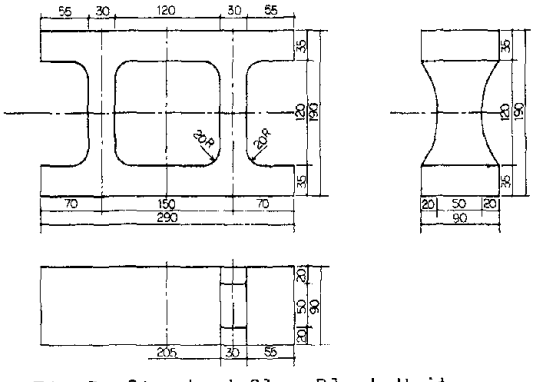

Fig.5 Standard Clay Block Unit in Japanese Research Program

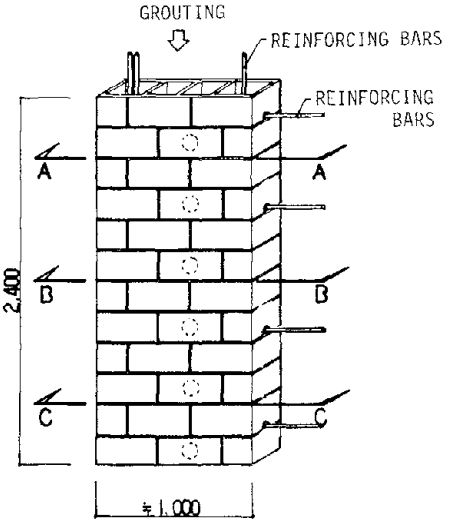

Fig.6 High-Lift Grouting Test Specimen

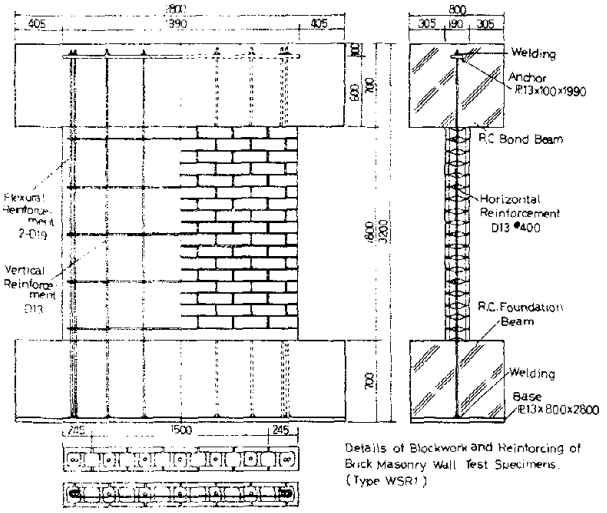

Fig.7 Test Specimen of Wall : WSR1

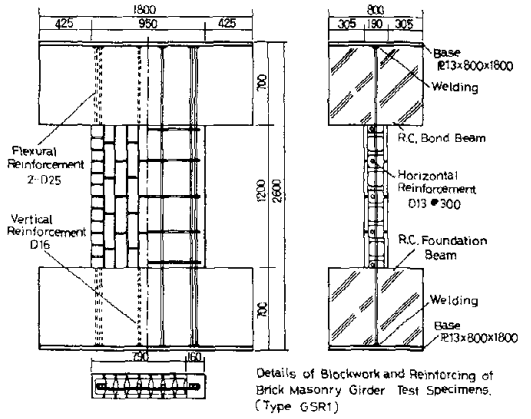

Fig.8 Test Specimen of Beam : GSR1

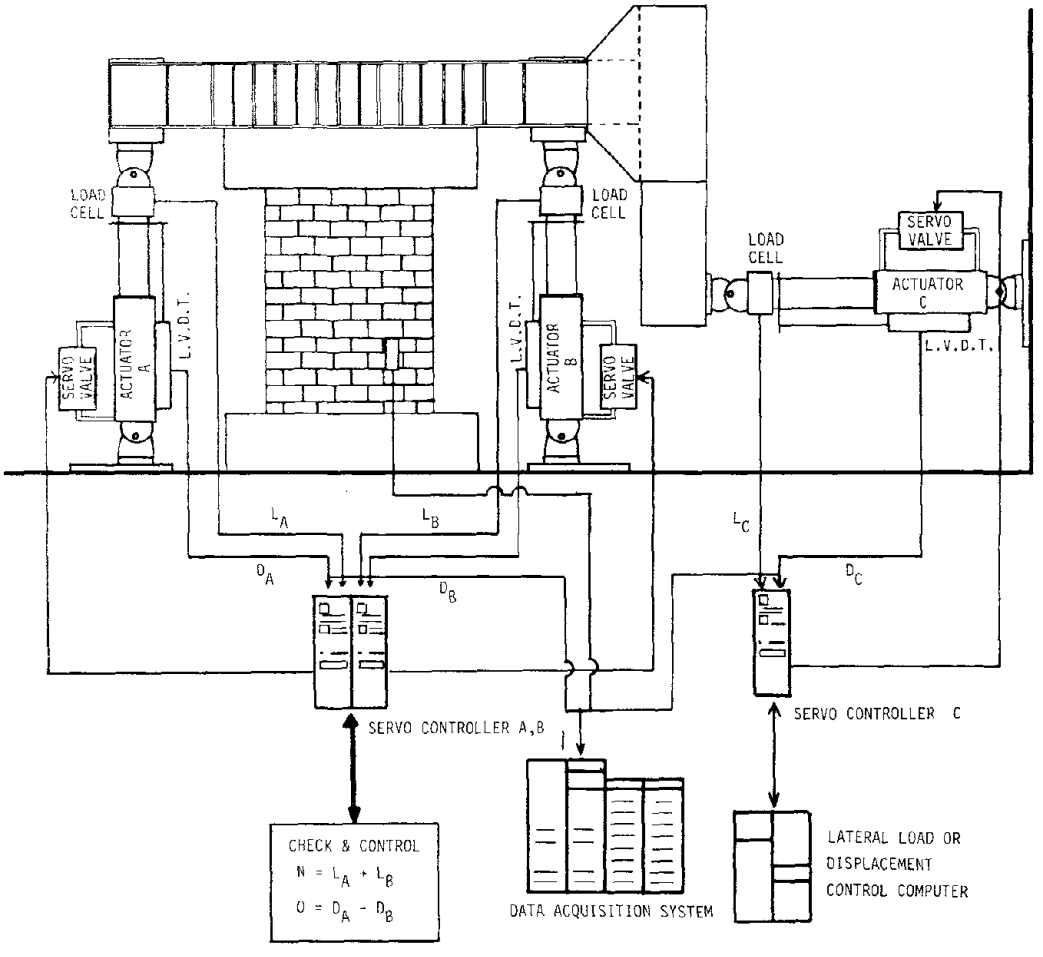

Fig.9 Loading System

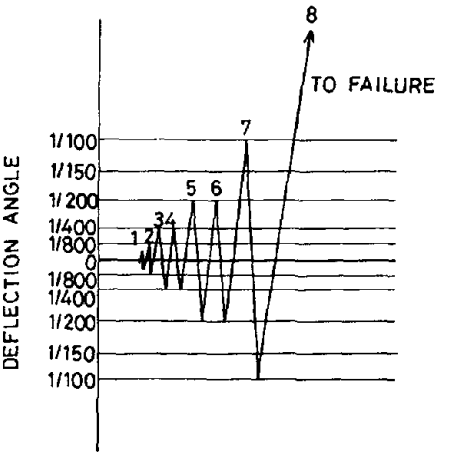

a) Shear Failure Type

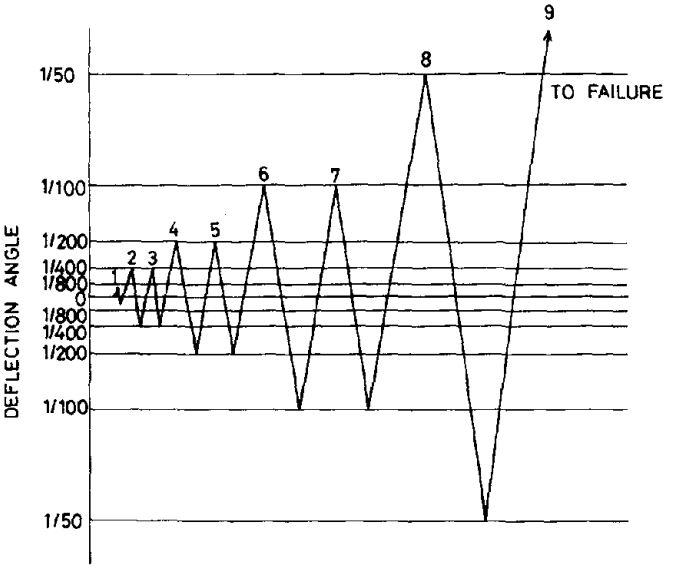

b) Bending Failure Type

Fig.10 Loading Sequence

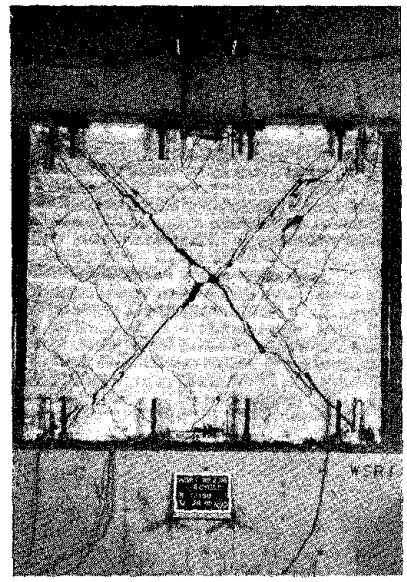

Photo 1 Specimen WSR1 after Tested

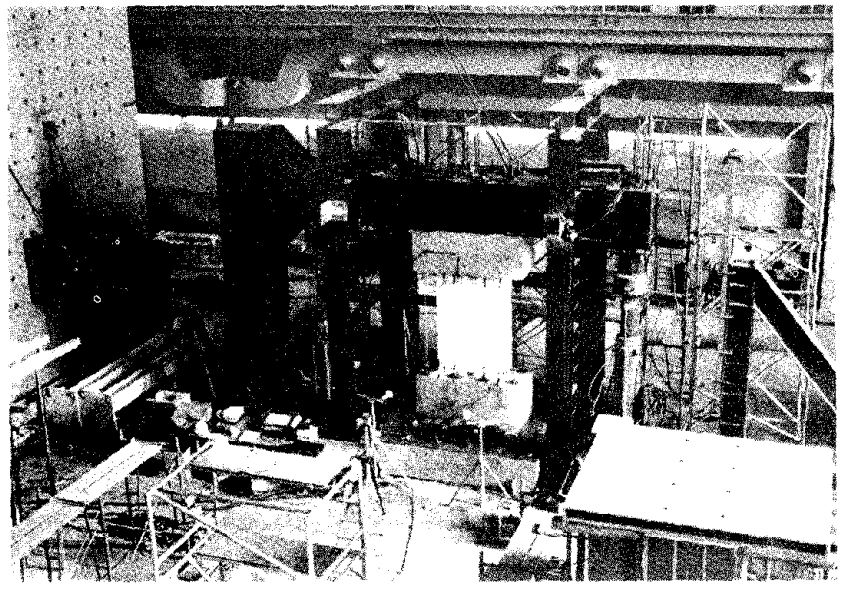

Photo 2 Loading System

INELASTIC SEISMIC TESTS ON A FULL-SCALE SIX-STORY ECCENTRIC-K BRACED STEEL BUILDING - U.S.-JAPAN COOPERATIVE EARTHQUAKE RESEARCH PROGRAM -

BY

Hiroyuki YAMANOUCHI[1], Mitsumasa MIDORIKAWA[2]
Isao NISHIYAMA[3] and Masaya HIROSAWA[4]

ABSTRACT

As part of the U.S.-Japan Cooperative Earthquake Research Program Utilizing Large-Scale Testing Facilities full-scale seismic tests on a steel building were performed as a three-year research project from 1981. This research involves comparing full-scale building behavior with scale model behavior and assesses the damage and safety levels of buildings subjected to earthquakes designed by current design practices.

Reported are results of tests on a full-scale six-story steel building with eccentric-K braces which followed the tests on a full-scale six-story steel building with concentric-K braces. The latter results were reported previously.

A six-story, 2x2 bay, steel building constructed inside the Large-Size Structure Laboratory of the Building Research Institute of the Japanese Ministry of Construction, had its buckled concentric-K braces cut off. The field welding of the new eccentric-K braces to the structure followed the repair of the cracked R/C slabs by epoxy injection.

All of the seismic tests were run as a six degree of freedom pseudo-dynamic system (computer on-line system). The input excitation was the NS component of the 1952 Taft Earthquake and the maximum intensity was set at two levels. To simulate working load conditions, the earthquake motion was scaled to 65 gal in the 1st stage test. The maximum earthquake was run at 500 gal in the 2nd stage test. Sinusoidal excitation input test followed to determine the strength, deformability and failure mechanism of the eccentric-K braced structural system in the ultimate stage.

1. INTRODUCTION

As part of the U.S.-Japan Cooperative Earthquake Research Program Utilizing Large-Scale Testing Facilities (Ref. 1), full-scale seismic tests on a six-story steel office building were carried out at the Building Research Institute of the Japanese Ministry of Construction to compare actual full-scale building behavior with scale model or member behavior and to assess the damage and safety levels of buildings subjected to earthquakes, which were designed to satisfy the requirements of current seismic design codes.

Reported are the results of the tests on a full-scale six-story steel building with eccentric-K braces which followed the tests on the building with concentric-K braces (Ref. 2). Overall tests were carried out according to the test sequence listed on Table 1.

---

[1]Head of Structure Division, Department of Structural Engineering, Building Research Institute
[2]Chief Research Structural Engineer, Department of Structural Engineering, BRI
[3]Research Structural Engineer, Department of Structural Engineering, BRI
[4]Director of Research Planning and Information Department, BRI, Tsukuba, Ibaraki 305, JAPAN

All of the concentric-K braces, some of which had buckled in PHASE I TEST (Ref. 2), had been cut off and the cracked R/C slabs were repaired by epoxy injection. The eccentric-K braces were newly installed and welded to the existing frames by field welding.

All of the seismic tests were run as a six degree of freedom pseuo-dynamic system (computer on-line system) that was applied to the concentric-K brace tests. The input excitation was the NS component of the 1952 Taft Earthquake and the maximum intensity of it was set at two levels. To determine the strength, deformability and failure mechanism of the eccentric-K braced structural system in the ultimate stage, sinusoidal excitation input test followed these seismic response tests with the test building deformed into the ultimate stage.

2. REPAIR OF FULL-SCALE TEST BUILDING

Prior to the tests on the concentric-K braced building (PHASE I TEST), discussions were held between Japanese and U.S. researchers on the allowable degree of damage of the test building in PHASE I TEST. The following agreements were made on the test conditions in PHASE I TEST and on the repair conditions before PHASE II TEST.

1) Maximum story drift angle should be less than about 1/60 radian.
2) Member change or deformation reform is not necessary if residual member rotation angle is less than about 1/300 rad. in the principle member.
3) If the residual vertical displacement at the midspan joint of each girder (girder in the braced frame between lines 1 and 2 in Fig. 1) where the concentric-K braces are connected is larger than about 3 cm, the girder should be changed by new one.
4) Large cracks in the composite R/C slabs should be repaired by epoxy injection.

Immediately after PHASE I TEST, the maximum residual vertical displacement was about 2.5 cm at the midspan of the girder where braces are connected. The residual deformations were in the allowable range, only the epoxy injuection of the principal cracks in the composite R/C slabs was conducted before PHASE II TEST. The epoxy injection was performed within 1 m width in both sides of the girder parallel to the loading direction and within 0.5 m width in both sides of the girder parallel to the loading direction and within 0.5 m width in both sides of the girder transverse to the loading direction. Other cracks wider than 0.2 mm were also repaired. Epoxy injection repairing was carried out after removing the concentric-K braces by gas.

3. DESIGN OF ECCENTRIC-K BRACES AND THEIR INSTALLATION

The plan and elevation of the eccentric-K braced building are shown in Fig. 1. The detail of the eccentric-K braced frame is shown in Fig. 2. Principal member size is tabulated in Table 2. The eccentric-K braces were installed in the braced frame between Lines 2 and 3 after the concentric-K braces between Lines 1 and 2 were removed. The sectional shapes of the braces were rectangular tubes in inch size and they were arranged so their weak axes coincided with the plane of the braced frame. The braces were selected so they would not buckle until the shear panels in the griders yield due to the shear force produced by the brace axial force. Each of the shear panels was the web plate of the girder of its length 711 mm, which was surrounded by both of the flange plates of the girder and a pair of vertical stiffeners (2-PL19) to transmit the brace axial force into the girder.

This structural system is aimed to make the shear panels yield prior to the buckling or yielding of the eccentric-K braces, to absorb the energy in these panels, and to show stable restoring force characteristics. As shown in Fig. 2, three vertical stiffeners (PL12) were welded on one side of each of the shear panels to prevent the panels

from shear buckling in the early stage of loading. Sub beams in the transverse direction were installed to restrain the distortion of the girder at both ends of the shear panel on one side of the girder (Fig. 1a). All the gusset plates, stiffeners and braces were welded to the central frame in the field.

After the repair of the R/C slabs and the installation of the eccentric-K braces, straightness along the height of the test building was measured before the Each Floor Level Loading Test (Table 4). The measured data are listed in Table 3. The residual roof horizontal displacement was 1.1 cm and the maximum residual story drift was 0.53 cm (story drift angle: 1/645 rad.) in the 6th story. These initial unstraightnesses of the test building were about the same order of magnitude as the construction accuracy. Therefore, it may be assumed that the structure before the PHASE II TEST was in almost the same condition as those of the test buildings just after construction.

5. TEST SEQUENCE

The tests on the eccentric-K braced building (PHASE II TEST) were carried out in the sequence shown in Table 4. The main tests consisted of two seismic response tests the Elastic Pseudo-Dynamic (PSD) Test and the Inelastic PSD Test. The maximum intensity of the input excitation was set at two different levels for earthquake excitation and at three levels for the Inelastic PSD Sine Wave Input Test. Other tests were performed before and after the main tests so as to get the dynamic characteristics of the test building and also the characteristics of the PSD test system as was done in the PHASE I TEST. In the PHASE II TEST, the PSD Pulse Response Test was also performed to examine the dynamic characteristics in the higher modes. Displacement and strain measurements in the PHASE II TEST were almost the same as those in the PHASE I TEST, and several measurements around the shear panel in the girder were newly added. The total number of measurements was 980.

6. NATURAL PERIODS AND DAMPING RATIOS

Table 5 shows the natural periods and damping ratios observed in the Free and Forced Vibration Tests, for Each Floor Level Loading Test, for the PSD Free Vibration Tests and for the PSD Pulse Response Tests which were compared with those calculated by frame analysis (Ref. 3).

Natural periods of each of the modes obtained by the tests conducted prior to the seismic response tests were a little smaller but coincided well with those calculated using frame analysis. Periods of the 1st mode were about 4 to 9% shorter than those of the concentric-K braced building (Ref. 2). The fundamental natural period after PHASE II TEST was almost 1.2 times longer than that before PHASE II TEST. The increase in natural period was a little smaller than those (1.3 - 1.4 times) observed in the test of the concentric-K braced building (Ref. 2).

The damping ratios of 1st and 2nd modes obtained by the Forced Vibration Test conducted just before the seismic response tests were 0.35% and 0.31% respectively. They were almost the same as those (about 0.5%) obtained in the PHASE I TEST (Ref. 2). On the basis of these results, Rayleigh type damping was used in the PSD tests; both 1st and 2nd damping ratios were set at 0.35%. However, the apparent 1st damping ratios observed in the PSD Free Vibration Test and the PSD Pulse Response Tests were 1.17-3.4% and they were larger by 0.82-3.05% than those (0.35%) assumed. This difference seems to come from the additional damping produced by the testing system as explained in the previous paper (Ref. 2). The amount of this additional damping depends on both the control conditions of the testing system and the displacement amplitude of response of the test building.

7. PSEUDO-DYNAMIC SEISMIC RESPONSE TESTS AND SINE WAVE INPUT TESTS

The pseudo-dynamic seismic response tests and the sine wave input tests were carried out by using a six degree of freedom pseudo-dynamic testing techniques the same as that used in the concentric-K brace tests. In the pseudo-dynamic seismic response tests, the input excitation was the NS component of the 1952 Taft Earthquake as shown in Fig. 3 and the maximum intensity of the excitation was set at two levels, that is, 65 gal to simulate the working load conditions (Elastic PSD Test) and 500 gal as the maximum earthquake (Inelastic PSD Final Test) (Table 4). In the sine wave input tests, the maximum acceleration was set at three levels; 92.6-100 gal, 270 gal and 320 gal. These sine wave input tests were carried out in place of the static cyclic loading tests. In these tests, the periods of the input sine waves were so selected that they coincided with those of the 1st mode of the test building in the stationary response conditions under the different excitation levels. The tests were continued for about 0.5-1.0 cycle on each of the excitation levels.

The maximum responses obtained from these tests are tabulated in Table 6. The time intervals used for the calculation in PSD tests are 1/100 sec. in the Elastic PSD Test, 1/200 sec. in the Inelastic PSD Final Test and 1/100 sec. in the Inelastic PSD Sine Wave Input Test. In the following sections, the test results and the frame analysis results (Ref. 3) are described. In the frame analysis, the damping ratio of the 1st mode was assumed 0.5% in the eleastic response and 2% in the inelastic one. The effect of the yielding of the members which occurred in the PHASE I TEST was not considered in the frame analysis.

8. ELASTIC PSEUDO-DYNAMIC TEST

The input wave was the NS component of the 1952 Taft Earthquake motion scaled to 65 gal and the test was continued up to 17.92 second. The time histories of the horizontal displacements at the 3rd, 5th and roof floor levels are shown in Fig. 4. The maximum roof horizontal displacement was 1.41 cm at 12.39 sec., the maximum story drift angle was 1/1339 rad. in the 3rd story (story drift: 0.25 cm) and the maximum shear force in the 1st story was 59.6 tonf, which corresponds to 0.114 of the base shear coefficient (ratio between the shear force in the 1st story and the total weight of the building - only the actual weight of the test building is used in this estimation). These maximum responses were about one-half of those obtained in the concentric-K brace test (PHASE I TEST - Elastic Test (3) (Ref. 2). The dotted lines in Fig. 4 show the results of the frame analysis (Ref. 3). As the damping ratios in the analysis (0.5% in the 1st mode) differed from those in the test (1.2-1.3% in the 1st mode), the maximum responses obtained in the test were about less than half of those calculated in the analysis. The relationship between story shear force versus story drift in each of the stories was almost linear.

9. INELASTIC PSD FINAL TEST

After the Elastic PSD Test, the NS component of the 1952 Taft Earthquake scaled to 500 gal was input and the test was continued for 17.10 secs. The time histories of the horizontal displacements at the 3rd, 5th and roof levels are shown in Fig. 5 and the relationships of story shear force vs. story drift in the 1st to 4th stories are shown in Fig. 6. In Fig. 7 are shown the shear force vs. shear deformation relationships in the shear panels of the web plates of the girders where the eccentric-K braces are connected. The shear force is estimated from the vertical components of the axial forces of a pair of braces. The roof horizontal displacement reached almost 8.6 cm at around 7.5 sec. and reached its maximum (8.8 cm) at 14.505 sec. As shown in Fig. 6, the relationship of story shear force vs. story drift obtained in the first story showed stable hysteresis loops without deterioration. As shown

in Table 6, the maximum responses of the story drift angle are larger in lower stories, that is, 1/150 rad. in the 1st story, 1/156 rad. in the 2nd story, and 1/225 rad. in the 3rd story. The maximum shear force in the 1st story was 312.8 tonf, which corresponds to 0.597 of the base shear coefficient. In this estimation, only the actual weight of the test building was considered as the building weight. The maximum shear force corresponds to 0.383 of the base shear coefficient if live loads for seismic design and the exterior wall weight plus actual dead weight of the test building (816 tonf) are considered. The maximum displacement responses obtained were about one-half or less than those obtained in the concentric-K brace test (PHASE I TEST - FINAL TEST, Ref. 2). The shear deformations in the shear panels, where several yieldings were observed, were relatively large in the lower three stories as shown in Fig. 7, and the shear deformation angle reached 0.047 rad., 0.029 rad. and 0.015 rad. in each of the stories from the lowest at around 14.5 sec. Although these shear panels yielded by a large amount, they retained a relatively large stiffness in the plastic range. In addition to the yielding in the shear panels, other yielding was observed in the column and in the gusset plates connecting braces and girder. However, the apparent damage is not so severe. In Fig. 5, the responses calculated by frame analysis (Ref. 3) shown by dotted lines are about 30% larger than those obtained in the test. This is because the damping ratio used in the frame analysis (2%) is small compared with that obobserved in the test (3.4%).

10. INELASTIC PSD SINE WAVE INPUT TEST

In the Inelastic PSD Final Tests, the damage of the test building was rather smaller than expected. In order to find out the strength, deformability and failure mechanism of the eccentric-K braced structural system in the ultimate stage, three levels of sine wave input tests were conducted. The time histories of the horzontal displacements at the 3rd, 6th and roof levels are shown in Fig. 8, and the relationships of story shear force vs. story drift in the lowest four stories are shown in Fig. 9. In these figures, the test results obtained in the three indedependent tests are simply combined and shown. Therefore, the figures don't represent continuous responses.

In Figs. 8 and 9, the origins of the figures coincide with the residual displacements at the beginning of the sine wave input tests; 0.423 cm, 0.426 cm, 0.383 cm, 0.337 cm, 0.303 cm and 0.185 cm from the roof level to the 2nd floor level. Therefore, the maximum displacements in these figures are smaller than those shown in Table 6 by the residual displacements after the Inelastic PSD Final Test.

As shown in Fig. 9 the story shear force vs. story drift relationships showed slight successive degradation in the last one-and-a-half cycle. This degration was due to the local deformation in the girder web and the out-of-plane deformation of the gusset plate near the joint (Fig. 2) of the braces in the 1st story and the girder of the 2nd floor level. Because of the out-of-plane deformation of the gusset plate, lateral-torsional deformation occurred in the girder and the braces in the 1st story started to buckle. Therefore, the test was stopped when the roof horizontal displacement reached its maximum 23.2 cm. The story drift angles in the lowest three stories were larger than those in the other stories as in PHASE I TEST and they finally reached 1/46.4rad. in the 1st story, 1/52.7 rad. in the 2nd story and 1/96.7 rad. in the 3rd story as shown in Table 6.

The maximum story shear force in the 1st story was 359.9 tonf which corresponds to 0.687 of the base shear coefficient, and at this stage the story drift in the 1st story was 4.4 cm (story drift angle: 1/102 rad.). In this estimation, only the actual weight of the test structure was considered as the building weight. If live loads for seismic design and exterior wall weight besides actual weight of the test structure are considered, the base shear coefficient changes to 0.441. The maximum horizontal displacements were almost the same

as those obtained in the PHASE I TEST (Final Test). With respect to the deformation of the shear panel in the girder and its surroundings, out-of-plane buckling of the gusset plates connecting 1st story braces and 2nd floor girder and the yielding of the bottom of the 1st story columns (C5-column in Fig. 1(a)), some photographs showing these effects are presented in Ref. 3.

11. CONCLUSIONS

From the results of the seismic response tests on a full-scale six-story eccentric-K braced steel building using the multi-degree of freedom pseudo-dynamic testing system at the Building Research Institute (Tsukuba-Japan), the shear panels in the web plates yielded by a large amount as was intended in the design philosophy for an eccentric-K braced structural system. It was verified that this type of structural system has a remarkable capacity for energy absorption. According to the test results obtained in the Inelastic PSD Final Test (the maximum intensity of the NS component of the 1952 Taft Earthquake was scaled to 500 gal), the maximum base shear coefficient was 0.597, the roof horizontal displacement reached its maximum 8.8 cm and the maximum story drift angle reached 1/150 rad. in the 1st story. At the same time, a large amount of shear yielding was observed in the lowest three stories and the shear deformation angle attained 0.047 rad. in the shear panel of the second floor level. In spite of a large amount of yielding in the shear panels their hysteresis loops were quite stable and the observed damage of the test building was modest.

In the PSD Sine Wave Input Test, the maximum base shear coefficient was 0.687, the maximum roof horizontal displacement was 23.2 cm and the maximum story drift angle was 1/46.4 ra. in the 1st story. The strength of the test building gradually decreased and the test building almost reached its ultimate strength stage. Finally, local deformation in the girder web next to the gusset plate at the brace-girder junction were observed. Lateral-torsional deformation of the girders occurred associated with the out-of-plane buckling of the braces.

12. ACKNOWLEDGMENTS

The authors wish to express their gratitude to the members of the J.T.C.C. (the Joint Technical Coordinating Committee of the U.S.-Japan Cooperative Research Program: Co-chairman; Profs. H. Umemura and J. Penzien) who encouraged the authors and cordially gave advice. The authors are also thankful to the visiting researchers at B.R.I. and from the general contractor companies, for their excellent help in the analysis, tests and data processing. The research staff of the Structural Engineering Department and Production Dept., of the International Institute of Seismology and Earthquake Engineering in V.R.I., and the U.S. visiting researchers are also acknowledged. This research was supported in part by the Japanese Ministry of Construction, the Kozai Club, the Building Contractors Society, and the National Science Foundation of the U.S.A.

13. REFERENCES

1. U.S.-Japan Planning Group, "Recommendations for a U.S.-Japan Cooperative Research Program Utilizing Large-Scale Testing Facilities," Report No. UCB/EERC-79/26, University of California, Berkely, Californis, Sept., 1979

2. Yamanouchi, H., Midorikawa, M., Nishiyama, I. and Hirosawa, M., " Inelastic Seismic Tests on a Full-Scale Six-Story Concentric-K Braced Steel Building - U.S.-Japan Cooperative Earthquake Research Program, Proceedings of the 16th Joint Meeting of U.S.-Japan Panel on Qind and Seismic Effects, U.J.N.R., National Bureau of Standards, Gaithersburg, Maryland, May 15-18, 1984

3. Goel, S. C., and Foutch, D.A., "Preliminary Studies and Test Results of Eccentrically Braced Full-Size Steel Structure, U.S.-Japan Cooperative Earthquake Research Program Utilizing Large Scale Test Facilities," Proceedings of the 16th Joint Meeting of U.S.-Japan Panel on Wind and Seismic Effects, U.J.N.R., National Bureau of Standards, Gaithersburg, Maryland, May 15-18, 1984

TABLE 1 WHOLE TEST PROGRAM

1. PHASE I TEST — Apr. 11 - Oct. 21 1983
   Concentrically K-Braced Frame Test
   Input Motion: 1978 Miyagi-Ken-Oki Earthquake
   Tohoku University NS
   Maximum Input Acceleration:
   Elastic Test - 65gal
   Inelastic Test - 250gal and 500gal

2. PHASE II TEST — Nov. 24 1983 - Mar. 9 1984
   Eccentrically K-Braced Frame Test
   Input Motion: 1952 Kern County Earthquake
   Taft NS(N21°E)
   and Sine Wave
   Maximum Input Acceleration:
   Elastic Test - 65gal Inelastic Test - 500gal
   Sine Wave Test - 92.6~320gal

3. PHASE III TEST — Mar. 21 - 28 1984
   Unbraced Moment-Resisting Frame Test
   Input Motion: 1940 Imperial Valley Earthquake
   El Centro NS
   Maximum Input Acceleration: Inelastic Test - 350gal

4. PHASE IV TEST — Apr. 23 - July 19 1984
   Unbraced Frame With Nonstructural Elements Test
   Loading Condition: Displacement Control
   Maximum Interstory Drift Angle: 1/40

TABLE 2 MEMBER SIZE AND PROPORTION

(A) GIRDER SCHEDULE

MARK / FLOOR	G1	G2	G3	G4
RFL-6FL	W 16 x 31 H-403.4x140.3 x6.98x11.18	W 16 x 31 H-403.4x140.3 x6.98x11.18	W 18 x 35 H-449.6x152.4 x7.62x10.80	W 21 x 50 H-529.1x165.9 x9.65x13.59
5FL	W 16 x 31	W 18 x 35	W 18 x 35	W 21 x 50
4FL	W 18 x 35	W 18 x 35	W 18 x 35	W 21 x 50
3FL	W 18 x 35	W 18 x 40 H-454.7x152.8 x8.00x13.34	W 18 x 35	W 21 x 50
2FL	W 18 x 40	W 18 x 40	W 18 x 35	W 21 x 50

Note: ASTM A36 structural steel

(C) BRACE SCHEDULE

MARK / STORY	BR1
6 - 5	Tube 8x6x0.313 Box-203.2x152.4x7.95
4 - 1	Tube 8x6x0.375 Box-203.2x152.4x9.53

Note: ASTM A500 GRADE B
structural steel

(B) COLUMN SCHEDULE

MARK / STORY	C1	C2	C3	C4	C5
6-5	W 10 x 33 H-247.1x202.2 x7.37x11.05	W 10 x 33	W 10 x 49 H-253.5x254.0 x8.64x14.22	W 10 x 33	W 12 x 40 H-303.3x203.3 x7.49x13.08
4-3	W 10 x 39 H-252.0x202.8 x8.00x13.46	W 12 x 53 H-306.3x253.9 x8.76x14.60	W 12 x 65 H-307.8x304.8 x9.91x15.37	W 10 x 60 H-259.6x256.0 x10.67x17.27	W 12 x 72 H-311.2x305.8 x10.92x17.02
2	W 12 x 50 H-309.6x205.2 x9.40x16.26	W 12 x 65	W 12 x 79 H-314.5x306.8 x11.94x18.67	W 12 x 79	W 12 x 106 H-327.4x310.4 x15.49x25.15
1	W 12 x 65	W 12 x 87 H-318.3x308.0 x13.08x20.57	W 12 x 87	W 12 x 106	W 12 x 136 H-340.6x315.0 x20.07x31.75

Note: ASTM A36 structural steel

TABLE 3 RESIDUAL HORIZONTAL DISPLACEMENTS BEFORE PHASE II TEST

FLOOR	DISPLACEMENT AT FLOOR LEVEL (cm)	STORY	INTERSTORY DISPLACEMENT (cm)	DRIFT ANGLE (radian)
RFL	1.124	6	0.527	1/645
6FL	0.597	5	0.199	1/1709
5FL	0.398	4	-0.390	1/872
4FL	0.788	3	0.090	1/3778
3FL	0.698	2	0.260	1/1308
2FL	0.438	1	0.438	1/1027

Note: Displacements in this table are a little different from those measured just after Concentrically K-Braced Frame (PHASE I) Test.

TABLE 4 TEST SEQUENCE

Gas Cutting Works of Concentric K-Braces
Repair Works of Concrete Floor Slabs by Epoxy Injection
Welding Works of Eccentric K-Braces

		1983
1.	Free and Forced Vibration (VT) Test #3	Nov. 24-25
2.	Each Floor Level Loading (FLL) Test #4	Jan. 17
3.	Elastic Pseudo-Dynamic (PSD) Test (Maximum Input Acceleration 65gal)	Jan. 18-26 1984
4.	PSD Free Vibration (F-Vt) Test #4	Jan. 30
5.	PSD Pulse Response Test #1	Jan. 31
6.	PSD Pulse Response Test #2	Feb. 1-3
7.	PSD Pulse Response Test #3	Feb. 2
8.	PSD Pulse Response Test #4	Feb. 4
9.	Inelastic PSD Final Test (Maximum Input Acceleration 500gal)	Feb. 7-27 1984
10.	Inelastic PSD Sine Weve Input Test (Maximum Input Acceleration 92.6-320gal)	Mar. 1-5 1984
11.	Free and Forced Vibration (VT) Test #4	Mar. 8-9

TABLE 5 NATURAL PERIODS AND DAMPING RATIOS

TEST	NATURAL PERIOD(sec) 1st	2nd	3rd	DAMPING RATIO(%) 1st	2nd	3rd
Analysis	0.595	0.214	0.119	——	——	——
Free VT Test #3	0.565∿0.567			0.35∿0.37(0.6∿2.2ton)*1		
Forced VT Test #3	0.568	0.201	——	0.35	0.31	
FLL Test #4	0.545	0.193	0.106	——	——	——
Elastic PSD Test - 65gal peak input						
PSD F-VT Test #4	0.553	——	——	1.25(6∿10mm)*2		
PSD Pulse Test #1	0.550	——	——	3.10(1.4∿4mm)*2		
PSD Pulse Test #2	0.554	——	——	2.68(2.5∿4.5mm)*2		
				1.17(4.5∿12mm)*2		
PSD Pulse Test #3	0.550	——	——	——		
PSD Pulse Test #4	0.553	——	——	5.90(2.3∿5mm)*2		
				3.40(5∿12mm)*2		
Inelastic PSD Final Test - 500gal peak input Inelastic PSD Sine Wave Input Test - 92.6∿320gal peak input						
Free VT Test #4	0.679∿0.686			0.50∿0.55(0.5∿1.7ton)*1		
Forced VT Test #4	0.680	0.229	——	0.48	0.34	——

Note: *1) Pulling force *2) Roof displacement amplitude

TABLE 6 MAXIMUM RESPONSES

TEST	NOMINAL DAMPING COMBINATION	DISPLACEMENT AT FLOOR LEVELS (cm)	(sec)	INTERSTORY DISPLACEMENT (cm)	(sec)	DRIFT ANGLE (radian)	BASE SHEAR (ton)
		RF -1.405	12.39	6 -0.226	12.39	1/1504	
ELASTIC	0.35 0.35	6F -1.204	12.38	5 -0.240	12.40	1/1417	+59.6
PSD TEST	2 90	5F -0.988	12.37	4 -0.239	12.36	1/1423	12.66sec
	90 90%	4F -0.749	12.37	3 -0.254	12.36	1/1339	
65gal	(1st-6th)	3F +0.512	12.65	2 -0.228	12.37	1/1491	-59.2
peak input		2F +0.305	12.66	1 +0.305	12.66	1/1475	12.93sec
		RF -8.841	14.505	6 -0.935	7.275	1/364	
INELASTIC							
PSD FINAL	0.35 0.35	6F -8.337	14.510	5 -1.236	7.285	1/275	+293.6
TEST	5 90	5F -7.560	14.515	4 -1.279	7.295	1/266	14.175sec
	90 90%	4F -6.586	14.515	3 +1.512	7.040	1/225	
500gal	(1st-6th)	3F -5.170	14.520	2 -2.173	14.525	1/156	-312.8
peak input		2F -3.004	14.520	1 -3.004	14.520	1/150	14.515sec
		RF -23.239	1.75	6 +1.090	1.32	1/312	
INELASTIC							
PSD SINE WAVE	0.35 0.35	6F -22.454	1.75	5 +1.428	1.36	1/238	+359.2
INPUT TEST	5 90	5F -21.308	1.75	4 +1.832	1.25	1/186	0.85sec
	90 90%	4F -19.671	1.75	3 -3.517	1.75	1/96.7	
92.6-320gal	(1st-6th)	3F -16.154	1.75	2 -6.457	1.75	1/52.7	-359.9
peak input		2F -9.697	1.75	1 -9.697	1.75	1/46.4	1.03sec

Note: 1) Displacement and shear force to the left in Fig. 1 are positive.
2) The origins of displacements at floor levels in Inelastic PSD Sine Wave Input Test are the same as those in Inelastic PSD Final Test.

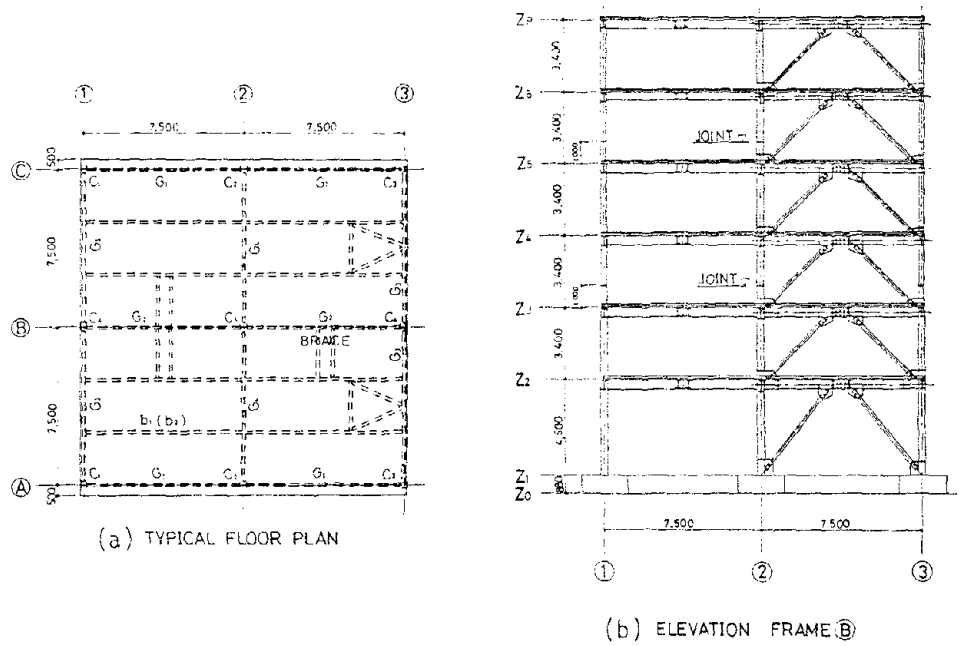

(a) TYPICAL FLOOR PLAN

(b) ELEVATION FRAME Ⓑ

FIG. 1 PLAN AND ELEVATION OF TEST STRUCTURE

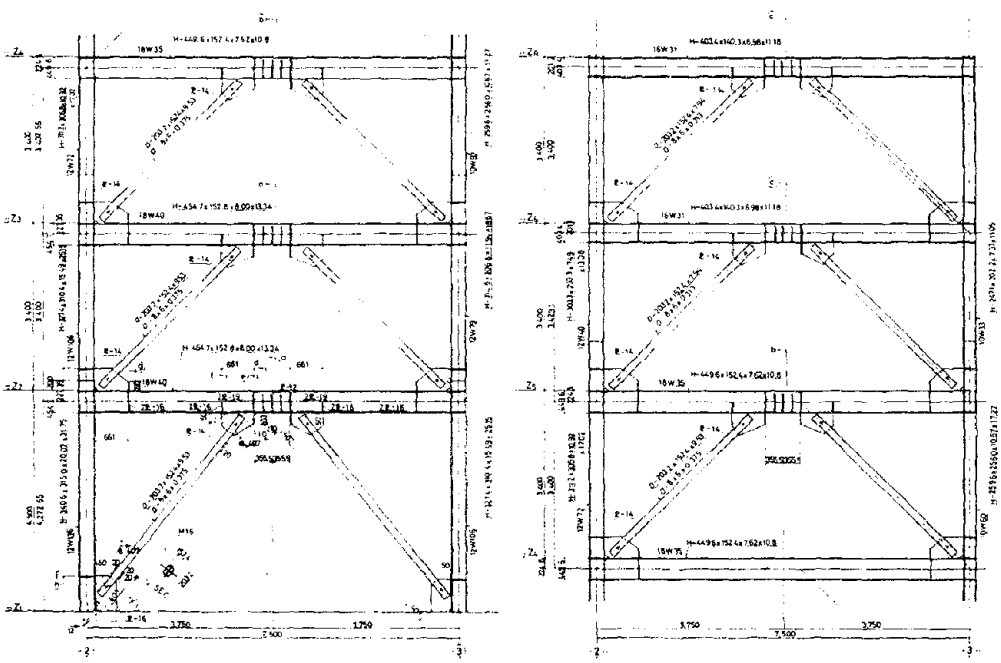

FIG. 2 DETAIL OF ECCENTRIC-K BRACED FRAME

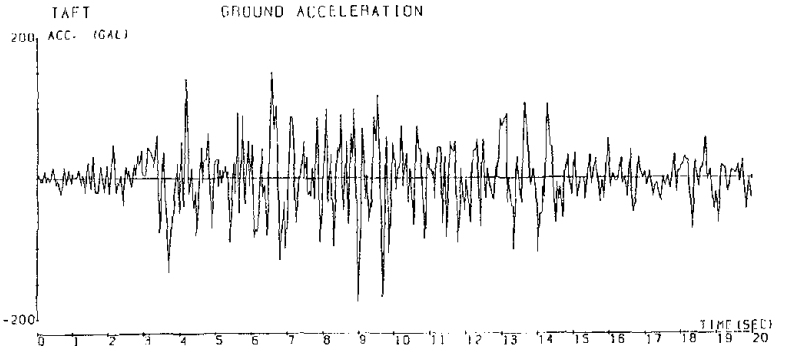

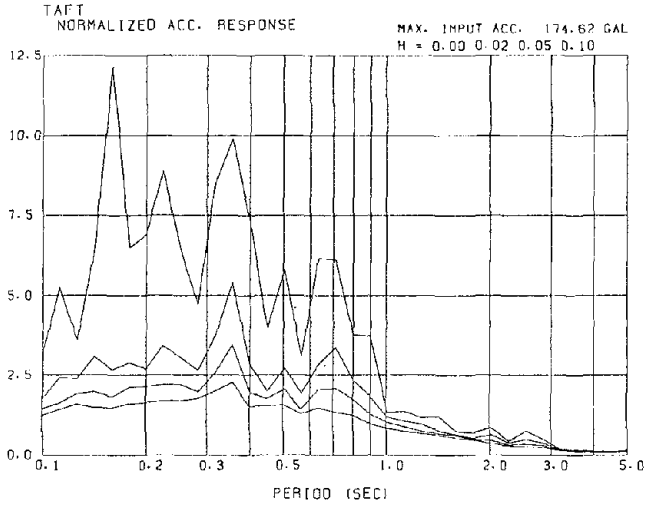

FIG. 3 INPUT MOTION AND RESPONSE SPECTRA

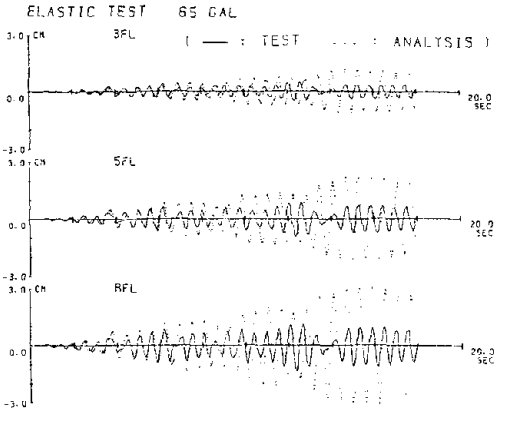

FIG. 4 TIME HISTORIES OF HORIZONTAL FLOOR DISPLACEMENTS (ELASTIC PSD TEST)

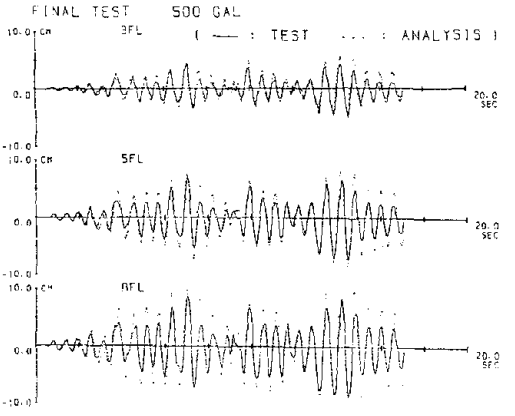

FIG. 5 TIME HISTORIES OF HORIZONTAL FLOOR DISPLACEMENTS (INELASTIC PSD TEST)

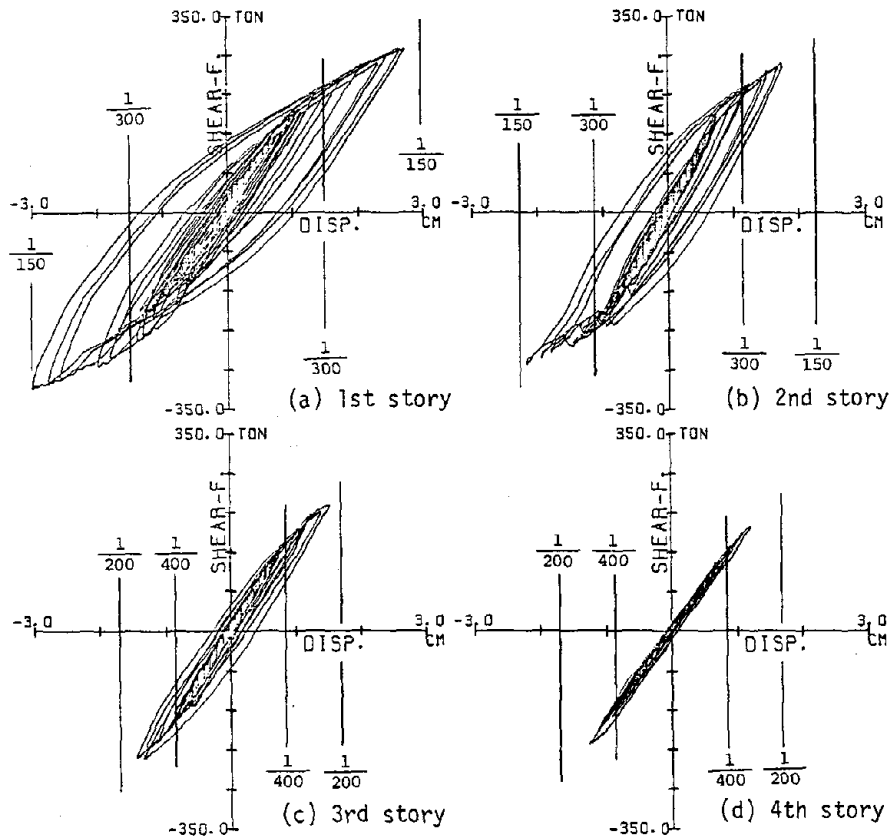

FIG. 6 STORY SHEAR FORCE VS. STORY DRIFT RELATIONSHIPS (INELASTIC PSD TEST)

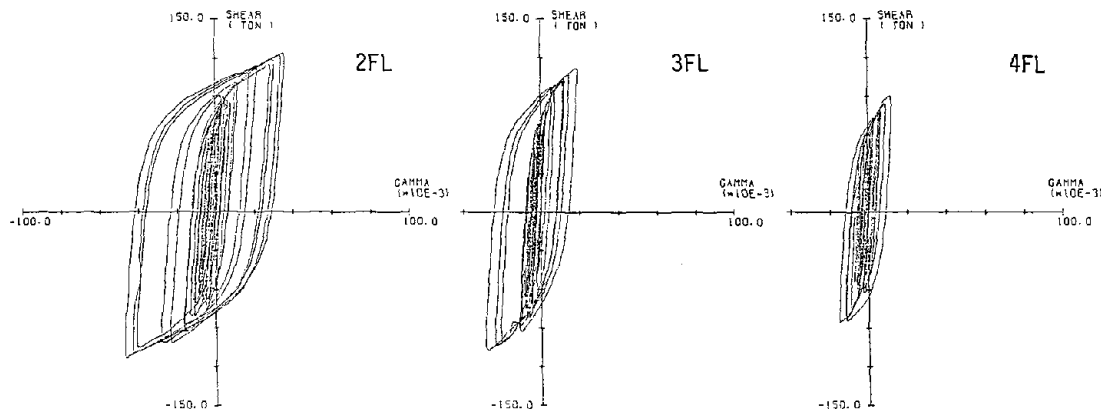

FIG. 7 SHEAR FORCE VS. SHEAR DEFORMATION RELATIONSHIPS IN SHEAR PANELS (INELASTIC PSD TEST)

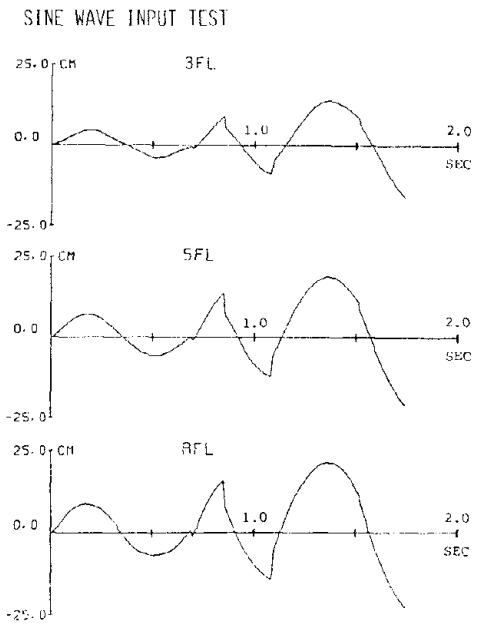

FIG. 8 TIME HISTORIES OF HORIZONTAL FLOOR DISPLACEMENTS (INELASTIC PSD SINE WAVE INPUT TEST)

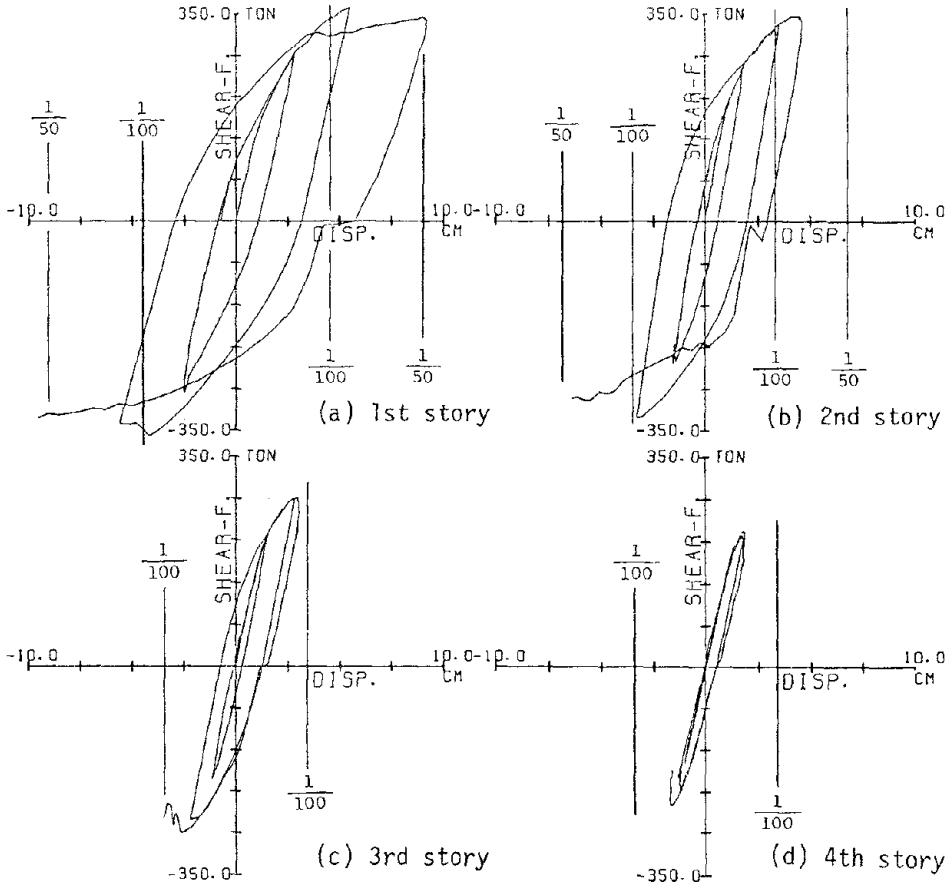

FIG. 9 SHEAR FORCE VS. STORY DRIFT RELATIONSHIPS (INELASTIC PSD SINE WAVE INPUT TEST)

SEISMIC PERFORMANCE OF EXISTING BUILDINGS
A PROGRESS REPORT

by

Richard N. White and Peter Gergely
Department of Structural Engineering
School of Civil and Environmental Engineering
Cornell University
Ithaca, N.Y. 14853

ABSTRACT

This progress report is based on two workshops held in 1983 and 1984 on "The Evaluation of the Performance of Existing Buildings for Resistance to Earthquakes." The workshops were organized through Task Committee D, Evaluation of the Performance of Structures, and were supported by the National Science Foundation (Grant CEE-8217190 to Cornell University).

The first workshop, held in Tsukuba in May 1983, had thirteen representatives from Japan and twelve from the U.S.; seventeen papers were presented in five theme areas: (I) Overview of evaluation of buildings for seismic resistance, (II) Practical methodology, (III) Computer programming, (IV) Evaluation of structural performance through full scale tests, and (V) Post-earthquake evaluations. The second workshop took place in July 1984 in Berkeley, California with twelve representatives from Japan and eighteen from the U.S.; eighteen papers were presented in three theme areas: (I) Safety evaluation methods, (II) Evaluation methods applied to benchmark structures, and (III) Damage and analysis of other structures. Names of participants and paper titles are given in Appendices A and B in this paper.

Highlights of the workshops are presented here, along with discussion and conclusions.

Keywords: Buildings, Building screening, Damage, Damaged buildings, Evaluation, Existing buildings, Full scale tests, Post-earthquake evaluation, Rapid evaluation, Safety evaluation, Seismic performance

1. INTRODUCTION

The problem of the assessment of the safety of various types of existing buildings in seismic zones has received increasing attention in recent years. Engineering design offices in areas with high seismic risk as well as appropriate government agencies devote a growing fraction of their efforts to the evaluation and strengthening of existing buildings and other structures.

The existence of a large number of unsafe buildings, or buildings with unknown safety, makes it necessary to conduct a thorough, critical evaluation of current techniques, and to plan research that will further advance the state-of-the-art of evaluation methodology. Extensive discussions of this subject within UJNR Task Committee D, "Evaluation of the Performance of Structures" led to a recommendation that a workshop be held on evaluation methods. The entire UJNR Panel, at its 14th joint in 1982, adopted the following resolution:

> "This panel agrees with the recommendation of Task Committee (d) on 'Evaluation of Performance of Structures' that workshops be held on the 'Evaluation of the Performance of Existing Buildings for Resistance to Earthquakes'. The first workshop is tentatively planned to be held in Tsukuba Science City, Japan, in May 1983, prior to the 15th Joint US-Japan Panel Meeting on Wind and Seismic Effects. Specific details and agenda of the workshops will be established by each side and coordinated by

correspondence. A final report is expected to be published in 1985 and reported to the 17th Joint Panel Meeting in Japan."

With the support of the National Science Foundation through Grant CEE-8217190 to Cornell University), two workshops have been held (May 1983 in Japan and July 1984 in Berkeley, California). The proceedings of these workshops have been published in two volumes [1] and [2]. A third workshop devoted primarily to critical comparisons of evaluation results and to planning of the final year's activities was held on May 17, 1985, in Tokyo.

2. EVALUATION METHODOLOGIES

There are many evaluation methods currently in use for assessing the seismic performance of buildings. They range from very approximate screening methods for identifying potential problem structures in large groups of buildings, to detailed analytical approaches for studying performance of structural members, components, and systems on an individual structure basis. Some of these detailed methods involve dynamic analysis and others are done on equivalent static idealizations.

Evaluation methodologies discussed at the workshops may be classified into several categories:

1. Screening methods for quick evaluation of large groups of buildings.
2. Rapid evaluation procedures for individual buildings.
3. Multi-level procedures for progressively more accurate evaluation of individual structures, including the 1977 Japanese Standard for Seismic Capacity Evaluation of Existing Reinforced Concrete Buildings, and the U.S. Navy Procedure.
4. Detailed analytical approaches, usually involving dynamic analysis, and computer-based methods such as WOODAM (for evaluation of timber structures).
5. Special approaches still under active development, including rule-based inference procedures for formal damage assessment, and the use of expert systems.

One of the difficulties in placing a given paper from the workshops into a category is that the multi-level procedures in use overlap into at least two different categories. Hence we will begin this section with a general discussion of methodologies, and then move into review of the individual contributions for the workshops.

It is convenient to divide the several levels of approximate analysis into two groups: those that require little analysis and are used mainly to classify buildings, and those that require load-deflection and limited modal analysis. These approaches are reviewed briefly here.

2.1 Rapid Evaluation Methods

The purpose of rapid classification is to be able to judge the safety of typical buildings. These methods are useful in surveying large groups of buildings at the municipal or regional level. The calculations typically require about two to four hours per building, and often much less.

The key aspect of these approaches is that various allowable stress levels are assigned to supporting elements (columns or walls) depending on their composition, length, and ductility. These stress levels were established from tests and from studies of actual damage. The great advantage of these rapid classification methods is that they can easily be modified to account for new knowledge gained about the behavior of systems. The interaction of various types of structural elements can be accounted for. Poor behavior of certain materials or elements, such as the problems with short (captive) columns

are readily included in the evaluation.

These simple classification approaches are not usable or at least are not reliable for unusual structures. For example, highly unsymmetrical structures or poor soil conditions are so variable that only much more rigorous analysis can assess safety in these cases. The rapid evaluation methods are normally quite conservative, and higher level approaches are necessary for screening structures that fail the rapid test.

2.2 Rapid Analysis Methods

The common characteristic of these approaches is that the nonlinear load-deflection relationship for the structure, or for each story, is required as shown in Fig. 1. Structures behave inelastically when subjected to a major earthquake and it is necessary to know the deflections beyond the elastic limit. This is especially important for buildings composed of several types of lateral resisting elements (frames, stairways, walls) because there is then a second line of defense.

Some engineers question whether we can establish the load-displacement curve for complex structures. In most cases only a rough estimate of the elastic limit and the stiffness is necessary in these evaluation methods. The second point is that since the structure will deform inelastically, with various post-elastic stiffnesses, a realistic estimate of the safety must rely on an approximate knowledge of the load-displacement relationships.

Three different rapid analysis methods are summarized here:

a. The substitute structure method
In this approach (developed by Sozen and his associates) the inelastic response is estimated by calculating an increased period and an increased damping to account for the energy absorption due to hysteretic response. The changes in period and damping are functions of estimated damage indices which represent a measure of the inelastic deformation level of the structure.

This method is relatively simple because only an elastic model analysis is required. However, it has been calibrated only for concrete frames and more work is needed to extend it to other types of structures. In essence, the use of inelastic response spectra is replaced by elastic spectra but with changed periods and damping. In the use of inelastic spectra the period is not changed. Of course, this approach can be used only on the high-period (descending) side of the spectrum.

b. The capacity spectrum method
In this method the inelastic load-deflection curve is first estimated; often rough calculations will suffice. This curve is best drawn as the roof displacement versus the base shear for a lateral load representing the inertia force vector (Fig. 1). For low buildings a straight line load vector is acceptable. A static linear computer program can be used as follows: the load is increased until a few hinges form and then the rotational stiffnesses are greatly reduced at these locations. The load is increased until another group of hinges form and in this manner a piece-wise linear load-displacement relation is produced. In some cases a rough estimate of the initial stiffness, the elastic limit, and the subsequent stiffness can be done without a computer.

In the next step the roof displacement is related to the corresponding spectral displacement, S_d, and the base shear is related to the spectral acceleration S_a through the well-known modal equations. These transformations are ordinarily based on the first mode only. The period corresponding to S_d and S_a values are

calculated.

The plot of S_a versus the period T is called the capacity spectrum (after Freeman). It is next superimposed on the design spectrum curve (Fig. 2). The relative position of the capacity and response spectra determines the safety of the structure. An interpolation is necessary because the damping changes as inelasticity develops.

The capacity spectrum method is a relatively simple and attractive method when the first mode dominates, although the contribution of higher modes to the roof deflection can be incorporated in an approximate manner. It is usually more satisfactory to estimate the bilinear stiffness of the structure.

c. The reserve energy technique

This approach was proposed by John Blume in the early 1960's but it has not been used widely (perhaps because its title is not descriptive). It is also based on the nonlinear load-displacement curve but instead of developing a capacity spectrum, the input kinetic energy is calculated using the velocity spectrum and modal masses $0.5\bar{m}S_v^2$. The area under the load-displacement curve represents the absorbed strain energy and by equating the two energies, one can estimate the deflection and the corresponding damage.

In both the capacity spectrum method and the reserve energy technique, the static load-displacement curve is estimated. Cyclic behavior is not accounted for directly, although it may be possible to modify the curve to do that. As with all approximate methods, it is important for the engineer to have a good feel for the real behavior of structures.

3. SUMMARIES OF PAPERS IN WORKSHOP VOLUMES

3.1 Screening Methods

Methodology for screening a group of buildings is given by Agbabian in Paper II-4, Vol. 1. His approach includes the initial preparation of a detailed seismic safety plan to specify the evaluation criteria, methods of analysis to be used, basis for damage estimates, practical methods for upgrading the earthquake resistance of the structures being studied, and a management plan for implementation of the seismic safety requirements. Important steps in the evaluation process include: (1) study of as-built drawings plus visual inspection to categorize the buildings, (2) determination of the level of refinement to be used in analyzing the buildings, (3) establishment of consistent criteria for degrees of damage, (4) estimates of damage to each building for different levels of earthquake intensity, and (5) definition of acceptable level of risk based on the evaluation of the expected damage. The end product is information on percentage of damage and associated costs for each building for differing levels of maximum ground acceleration. An example illustrating the cost of repair and replacement due to earthquakes of different severities, for six buildings, is given in Table 1.

Three screening procedures are given by Lew in Paper II-3, Vol. 1. These methods, developed by the National Bureau of Standards, the General Services Administration, and the State of California Seismic Safety Commission, can be used for a large number of buildings to identify hazardous conditions and to supply decision makers with information on the extent of hazard and the feasibility of retrofit measures.

The three methods are based on structural performance indices which are derived from past performance records of particular types of

buildings, from engineering judgement, and on seismicity considerations for particular sites. The structural performance indices are related to structural characteristics, structural configurations, and the degree of deterioration of buildings, whereas the seismicity index is obtained by considering the distance from active faults and expected magnitude and frequency of earthquakes.

3.2 Multi-Level Procedures

a. Japanese Standard, 1977

The Japanese "Standard for Seismic Capacity Evaluation of Existing Reinforced Concrete Buildings" was compiled in 1977 under the Ministry of Construction. It is described in some detail in Paper I-2, Vol. 1, by Aoyama. It is intended to be applied primarily to low rise buildings up to 6 or 7 stories.

The three-level procedure involves calculation of a Seismic Index

$$I_s = E_o G S_D T$$

where $E_o = \phi(CxF)$ is the basic seismic index. Within the term E_o, C is a strength matrix, F is a ductility matrix, and ϕ is a story index that relates single DOF system response to that of the multi-story system. Thus it is apparent that this method evaluates both strength and ductility capacities and expresses the result E_o as a product of these capacities.

The other necessary definitions are G = geological index, S_D = structural design index ranging from 0.4 to 1.2, and T = time index ranging from 0.4 to 1.0 to cover such items as previous damage, shrinkage and settlement effects, and deterioration of the structure from loadings and environmental factors.

The first level procedure is very easy to apply -- it is based on the average stress in the column and wall areas. It is well-suited for wall-dominated structures but is quite conservative for ductile frames. The second level procedure concentrates on potential problems in vertical members by identifying five types of vertical elements: extremely brittle short columns, shear-critical columns, shear walls, flexure-critical columns, and flexural walls. Simple equations are given for treating each type of element.

The third level procedure recognizes flexural hysteresis by considering the response of three additional types of vertical members: columns governed by shear beams, columns governed by flexural beams, and rotating walls with uplift effects from overturning. Equations are again provided for these calculations.

Results of the application of these procedures to damaged structures are given in Fig. 3, where the correlation between first and second level procedures applied to buildings from 1978 earthquakes in Japan is given in Fig. 3a. A comparison of damage levels and seismic index I_s values calculated for both the longitudinal (L) and transverse (T) motions of a group of school buildings is shown in Fig. 3b.

Additional examples of damage level and index values are given in Paper II-2, Vol. 1, and in some of the benchmark structure analyses to be described later in this paper.

While seismic capacity is best judged by comparing I_s to an E_t index that is tied to specific ground acceleration levels and other critical factors, general guidelines on performance may be stated. Superior performance is indicated by I_s values of 0.9, 0.7, and 0.6 for levels 1, 2, and 3 evaluation procedures, respectively. I_s values less than 0.4 at the 2nd and 3rd levels indicate questionable performance, and the borderline of damage for level 1 is often taken as 0.8 (Paper II-2, Vol. 1).

b. U.S. Navy procedure

A methodology is presented by Freeman (Paper

II-1, Vol. 1) for the preliminary evaluation of the safety of existing buildings for earthquake effects. The procedure was developed for the U.S. Navy to evaluate its existing structures throughout the naval shore establishment that are located in areas of high seismicity. The scope of the methodology includes a screening process for a large number of buildings, a rapid procedure for approximating building capacity, and a graphical procedure for estimating damage due to postulated earthquake motion and the costs of their corrections. The fundamental ideas in this approach have been described above in the discussion of the capacity spectrum method.

Freeman states that it cannot be expected that the rapid evaluation method will give an accurate prediction of building response, but it is highly useful in giving a general picture of behavior and it is also useful as an aid in determining which buildings will require a full-scale dynamic analysis.

3.3 Other Methodologies

a. General

The United States Department of Housing and Urban Development (HUD) published a three-volume manual in November 1978 titled "A Methodology for Seismic Evaluation of Existing Multistory Residential Buildings" to be used to satisfy the HUD requirement that all multistory residential buildings in Seismic Zones 3 and 4 (Uniform Building Code) shall be evaluated for earthquake hazard and seismic resistance. Since that time, HUD has published a series of additional guidelines on building rehabilitation. This HUD methodology for evaluation and structural assessment of building rehabilitation is summarized by Fuller in Paper II-5, Vol. 1.

The methodology has proven to be a valuable tool in analyzing existing buildings that have been proposed for renovation in HUD programs, and it has been used a number of times for specific buildings in the U.S. The paper gives a case study on a building constructed in 1900 and upgraded recently to meet 1979 UBC Seismic Zone 3 forces.

Tabulated cost data related to degree of compliance with the Uniform Building Code have proven to be invaluable to program administrators and building officials who must make decisions on strengthening or demolishing buildings. This data not only helps in economic and engineering planning, but it is also a major factor in determining levels of acceptable risk.

b. Computer-based approaches

The computer program WOODAM, developed for the U.S. Navy to estimate damage to wood frame buildings, is described by Hart in Paper III-2, Vol. 1. The method provides determination of expected damage for a given structural reliability over an entire range of earthquake levels, and it is implemented on a microcomputer (such as the HP 85). Thus the evaluation procedure can be done on-site.

The program modules are used to calculate the earthquake loading on critical components of the lateral force resisting system, taking into account uncertainties in the seismic loading and in the analytical model for the building. The next step is to calculate the load carrying capacity of the lateral load system of the structure, including uncertainties in material properties, geometry, and the capacity model. From these two steps, the reliability index for each possible failure mode for each critical element in the lateral force resistant system is determined.

A damage matrix is next constructed that relates the damage to the magnitude of seismic load for a determined value of reliability index. The final step is to calculate the expected damage on a probabilistic basis for given levels of

seismic load. The latter are expressed in terms of maximum response spectra for different time periods up to 50 years.

Meyer and Roufaiel (Paper I-5, Vol. 2) describe an analytical method for determining the reliability of reinforced concrete frames that may or may not have been damaged by earlier earthquakes. A model is described for simulation of reinforced concrete frame elements to large cyclic loads, and ground motion input is simulated as a non-stationary random process. Damage probability matrices are constructed using Monte Carlo simulation, accounting for the variability of the ground motion and the building strength parameters. The methodology is applied to a three-story, two-bay reinforced concrete frame building. The results indicate that it is unusual for even strong ground motions to appreciably extend damage sustained under earlier seismic loadings.

The wealth of computer programs available for analyzing structures subjected to seismic loads is illustrated by the compilation of Japanese programs by Aoyama in Paper III-1, Vol. 1, where nearly 70 programs are described by name, company or organization responsible for the program, and critical features of the program.

c. Rule-based inference procedures

The rule-based inference procedure for structural damage assessment called SPERIL-I is reviewed by Yao in Paper I-3, Vol. 1. This approach is a highly structured formal damage assessment method utilizing structural reliability, the theory of fuzzy sets, and expert systems to arrive at consistent results to imperfectly formulated problems. Fig. 4 indicates the numerous factors to be considered and the complex linking between these factors.

Yao continues his treatment of expert systems in safety evaluation in Paper I-1, Vol. 2, where he summarizes recent results since May 1983. The status of this promising area for the future is captured in the following quote:

> "The fundamental question regarding the use of inference machine evaluation methods is whether such methods can be relied upon without a careful review by a human expert. It must be recognized that subjective knowledge and experience of an expert imply a higher level of intellectural organization that is possible in data bases containing large sets of information . . . Nevertheless, the use of appropriate evaluation techniques utilizing inference machine approaches can greatly enhance the effectiveness and reliability of human expert evaluations. Furthermore, it may also contribute to improvements in human expertise through increased communication among experienced engineers."

3.4 Miscellaneous

a. Structures to be tested by actual earthquakes

Okada and Tamura report in Paper I-6, Vol. 2 on the behavior of model structures that have been constructed deliberately weak (either weak beams or weak columns) at the Chiba Experimental Field Station. The experiment has yielded more than 20 sets of acceleration and displacement records up to June 1984. The information from these 5 story model structures should be of substantial benefit in calibrating analysis methods for imperfect structures and to study the influence of repeated seismic loadings on the response of the structures.

b. Post-earthquake evaluation

Several papers were presented in Session V of the First Workshop on this important topic. Johnston (Paper V-1) reported on the post-earthquake evaluation of a large hospital in California. He summarized the major factors

involved in this type of engineering work:

"(1) A careful assessment of the physical damage caused by the earthquake. This assessment should be made by a structural engineer, (2) A knowledge of the historical background of earthquake engineering code requirements and construction practice, (3) An evaluation of the ultimate behavior of the structural system and materials, particularly its toughness, (4) A recognition of what constitutes acceptable risk, (5) Confirmation of the assessment by a peer review, (6) Consultation with medical experts to establish the operational feasibility and the ability to remain functional under repair, and (7) An honest and objective decision based on the engineering data."

Hirosawa and Murota (Paper V-2) provided a summary of many projects being conducted as part of the Japan National Project on Development of Post-Earthquake Measures for Buildings and Structures Damaged by Earthquake. Each summary includes the objectives of the study, progress made to date, and the product of the research task.

Paper V-3 by Gergely was the closing paper in the First Workshop; it dealt with the many planning and coordinating efforts needed in emergency safety evaluation and rating of structures after a major earthquake in a large urban environment. Issues needing the combined attention of city, state, and federal government agencies, as well as police and other enforcement agencies, are discussed.

c. Analysis methods and damage levels

There were a number of papers that reported on analysis methods for structures (in particular dynamic methods), and on damage analysis of other structures. Included are Papers I-2, I-4, III-1 and III-2 in Vol. 2 of the workshop proceedings.

3.5 Applications to Benchmark Structures

Six benchmark structures were selected for evaluation by the various methods; they are described in Appendix A of Ref. (2). The buildings are:

1. 7 story reinforced concrete frame tested under the U.S.-Japan Cooperative Research Program
2. Imperial County Services Building, California
3. 9 story ATC benchmark structure, reinforced concrete, 1964
4. 7 story reinforced concrete building (Holiday Inn), instrumented
5. Reinforced concrete building, Japan
6. 6 story steel frame tested under U.S.-Japan Cooperative Research Program

Inasmuch as the evaluation procedures are still being applied to these structures, and critical comparisons of all results are not yet complete, we will provide only selected results in this paper. Final conclusions will be given in a later report on this project.

a. 7 story U.S.-Japan reinforced concrete building

This combination frame-shear wall structure had three bays of 19.7, 16.4, and 19.7 ft (6, 5, and 6 m) in the longitudinal direction and two spans of 19.7 ft each (6 m) in the transverse direction. A shear wall was placed parallel to the direction of loading in the middle bay of the center frame, continuous from the first to the seventh story.

Several papers (Yoshimura, IV-2 and Kabeyasawa, IV-3, both Vol. 1), provide detailed experimental and analytical results for this structure. This wealth of data is extremely valuable for comparison with both approximate and detailed analytical techniques.

Okamoto (Paper IV-1, Vol. 1) evaluated the seven story reinforced concrete building using the

Japanese Standard described earlier. The evaluation was made only for the direction in which the seismic forces were applied during the loading in the laboratory, and the weight of each story was taken as the dead weight of the floor level plus the weight of the loading frames. The Ground Motion Index G, the Shape Index S, and the Time Deterioration Index T were all taken as unity.

Results are quoted directly from Okamoto: "The Basic Structure Performance Index, E_o, was computed as 0.36 (1st Screening), 0.68 (2nd Screening), and 0.59 (3rd Screening). The index given by the first screening is found to be significantly lower than those given by the second and third screenings. This low value of index was obtained primarily because of small areas of the columns and shearwalls. In the second and third screenings, on the other hand, E_o was much larger because the structure was estimated to exhibit flexural failure. Nevertheless, if the weight is increased to 1 ton/m^2 by taking live load into account, E_o will decrease significantly to a level at which the structure is considered to be unsafe."

b. Imperial County Services Building

The Imperial County Services Building is well-known for its unsatisfactory performance in the 1979 Imperial Valley earthquake, and has received considerable attention in various post-mortem analyses. It was designed in 1968 in accordance with the 1967 UBC and construction was completed in 1971.

The poor performance of this building under seismic loads has been attributed partially to the poor shear transfer properties at one end of the building.

Force-deformation relations for this building were obtained by Stephens and Yao (Paper I-3, Vol. 2) from structural acceleration records using a structural identification technique. The study showed that these relations are highly useful in studying the structural response both qualitatively and quantitatively; it is possible to extract such information as the range and number of cycles of inelastic response for use in damage expressions. The planned extension of this research includes identification of damage expressions to more effectively use the quantitative information from the force-deformation relations, calculation of energy dissipation and its correlation to structural damage, comparison of results with other investigators, and possible extension of the methodology to include torsional effects and overturning.

Aoyama (Paper II-8, Vol. 2) applied the Japanese Standard procedures (levels 1 and 2) to the structure, using S_D = 0.95, G = 1.0, and T = 1.0, and obtained the following results:

	Story	E-W I_s	N-S I_s
	6	0.65	1.06
	5	0.31	0.52
(First Level	4	0.23	0.37
Procedure)	3	0.18	0.31
	2	0.17	0.29
	1	0.11	0.48
(Second Level Procedure)	1	0.22	0.48

In comparison with accepted Japanese standards, it was found that the Imperial County Services Building fell in a region regarded to be dangerous under earthquake loads.

By the Japanese standard, the upper level walls would be regarded as "miscellaneous walls" with only 1/3 the effectiveness of regular shear walls. The average axial stress level in the vertical elements was about twice that of typical Japanese building designs. While there is a question on the validity of using the Japanese approach on the N-S framing, the E-W direction framing does fit within assumptions.

The analysis by Hart (Paper II-10, Vol. 2) showed that the normal assumption of fixed base

shear walls was not valid and that the soil-building system must be modeled. He also showed that the floor diaphragms were flexible, not rigid, and that using a rigid diaphragm analysis is misleading in terms of the distribution of loads at the ground floor column level.

Sozen (Paper II-9, Vol. 2) summarizes the key findings from the PhD dissertation of M. Kreger (U. Illinois, August 1983) who analyzed the Imperial County Services Building with particular emphasis on the causes of the column failures. It is shown that it is difficult to explain the failures by considering forces in only one direction at a time. Sozen provides some very interesting philosophical discussion at the end of his paper:

> "Evaluation of existing buildings is better kept simple. A simple analysis tempered by judgement will suffice in most cases. In the interest of the community, it is a better buy to invest less in reanalysis at the risk of missing a few potential disasters than to invest more with the possibility of identifying some of those few. Vulnerable buildings are in general like bad wine. Even a naive analysis can identify the vinegary taste. It is very unlikely that spending more professional resources on analysis routines will automatically identify the buildings with subtle vulnerabilities. The Imperial County Services Building is a good example. It is very unlikely that calculation alone would have identified the problem and it is very likely that a structural engineer who was informed of similar events would have avoided the conditions at the east end of the structure."

c. 9 story reinforced concrete ATC benchmark building

This structure was designed with the 1964 UBC provisions, and has been the subject of re-design in the ATC project. The building framing is concrete pan-joist on 20 by 24 ft (6.1 by 7.3 m) bays framing into girders and columns, with shear walls along both axes of the building to resist lateral loads. The plan dimensions of the main portion of the building are 141.5 by 80.67 ft (43.1 m by 24.6 m).

Lew (Paper II-7, Vol. 2) applied the rapid, Level 1 Field Evaluation Method of the NBS approach, and concluded that for an earthquake intensity of 9 MMI, the building rated fair. The unsymmetrical distribution of shear walls in the transverse direction controlled the rating of the structure.

Okamoto and Watanabe (Paper II-2, Vol. 2) applied the Japanese Standard 1st level procedures. In the longitudinal direction, I_s values ranged from 1.37 at the top floor to 0.34 at the base; the fifth floor had $I_s = 0.37$. In the transverse direction, I_s ranged from 2.30 to 0.67, with 0.68 at the 5th floor. These I_s values are low by Japanese standards.

Freeman (Paper II-3, Vol. 2) used the capacity spectrum method for the ATC building, in a very quick one page calculation. He estimated the static capacity for the uncoupled walls and the spandrel frames and plotted the capacity spectrum curve as two straight lines. The intersection with a design spectrum is at about 0.19g.

d. 7 Story Holiday Inn

The Orion Holiday Inn building in Los Angeles is a reinforced concrete flat plate structure with 8 bays (18.75 ft or 5.71 m) in the E-W direction and 3 bays (about 20 ft or 6.1 m) in the N-S direction, with spandrel beams in the periphery. The building is instrumented and measured response during the 1972 San Fernando earthquake is available.

This structure was studied by Freeman, Shimizu (Paper II-1, Vol. 2) and Moehle (Paper II-4,

Vol. 2). Shimizu applied the Japanese Standard and obtained E_o values between 0.20 and 0.36 by rapid evaluation, and 0.24 to 0.45 by detailed evaluation. By Japanese standards, E_o should be at least 0.6.

Moehle made a relatively simple analysis plus an assessment of connections and details. He concluded that (a) the structure is fairly flexible and excessive nonstructural damage could be expected in a moderate earthquake, (b) inadequate ductility may be a problem during a more intense earthquake, (c) analysis underpredicts initial stiffness by nearly two to one, and (d) the first floor column details are considered inadequate.

The Capacity Spectrum method results in spectral accelerations in the 0.15g - 0.21g range, depending on the contribution of nonstructural elements, in the transverse direction. The range is 0.20g to 0.26g in the longitudinal direction.

e. 6 story steel frame (U.S. - Japan Program)
The six story steel frame building tested in Tsukuba, Japan consisted of three two-bay frames of 24.6 ft (7.5 m) spans with a first story height of 14.8 ft (4.5 m) and upper story heights of 11.1 ft (3.4 m). The two exterior frames were rigid and the interior frame had K-bracing in one bay. The structure was designed to satisfy the requirements of both the 1976 UBC and the 1980 Japanese Aseismic Design Code, with a design base shear coefficient of 0.197.

Lew (Paper II-7, Vol. 2) rated this building using the NBS rapid FEM, and concluded that the structure rated fair for a MMI 9 earthquake. The semi-rigid nature of the steel deck with concrete topping was a critical factor in reaching this rating.

Hart (Paper II-6, Vol. 2) did a detailed structural analysis of the system, based on a perspective which recognizes the use of site dependent earthquake response spectra. The analysis required about 100 engineering labor hours. It provides a rather detailed prediction of the development of plastic hinges in the structure, the lateral displacement (nonlinear), and the variation of period with base shear. Typical U.S. steel frames have a much flatter curve for change in period with change in base shear.

Paper II-5, Vol. 2 (by Yamanouchi et al) provides detailed test results for this structure.

4. SUMMARY AND CONCLUSIONS

Methods of seismic safety evaluation of existing buildings were studied in three U.S.-Japan workshops. The methods range from rapid classification of groups of buildings to detailed dynamic analysis of individual structures.

Methods developed in Japan and in the U.S. are "tuned" to the characteristics of typical buildings in each country. Comparative analyses of benchmark structures reflect the relatively more conservative Japanese seismic design approaches.

The comparisons reveal that the various methods are suitable for the expected level of evaluation accuracy for buildings with good arrangement of lateral strength elements, and that a general idea of expected damage level can be estimated. However, additional developments are required to validate and improve the methods to make them more useful, especially for buildings of unusual geometry or with special secondary elements, and to include effects of soil-structure interaction.

5. REFERENCES

(1) Proceedings of the First Workshop on Seismic Performance of Existing Buildings, May 1983, edited by Richard N. White and Peter Gergely, Department of Structural Engineering, Cornell University, Ithaca, N.Y. 14853, April 1985, 370 pp.

(2) Proceedings of the Second Workshop on Seismic Performance of Existing Buildings, July 1984, edited by Richard N. White and Peter Gergely, Department of Structural Engineering, Cornell University, Ithaca, N.Y. 14853, April 1985, 516 pp.

6. ACKNOWLEDGEMENTS

The financial support of the National Science Foundation and the personal support and encouragement provided to the series of workshops by Dr. John B. Scalzi, NSF Program Manager, are greatly appreciated. The efforts of Dr. M. Watabe, Dr. S. Okamoto, and G. R. Fuller in helping to organize the workshops are also much appreciated, as is the enthusiastic involvement of the many individuals from Japan and the United States who participated in the workshops.

- - - - - -

- - - - - -

Building	Replacement Cost ($ Millions)	Percent Damage At			Cost (in $ Millions) of Repair or Replacement At		
		0.20 g	0.30 g	0.40 g	0.20 g	0.30 g	0.40 g
A	1.000	35	100	100	0.350	1.000	1.000
B	5.000	23	100	100	1.150	5.000	5.000
C	0.500	5	28	85	0.025	0.140	0.425
D	1.000	10	26	58	0.100	0.260	0.580
E	2.000	2	18	48	0.040	0.360	0.960
F	3.000	0	0	15	0	0	0.450
Total	12.500				1.665	6.760	8.415

TABLE 1. EXAMPLE ILLUSTRATING COST OF REPAIR AND REPLACEMENT DUE TO EARTHQUAKES OF DIFFERENT SEVERITIES

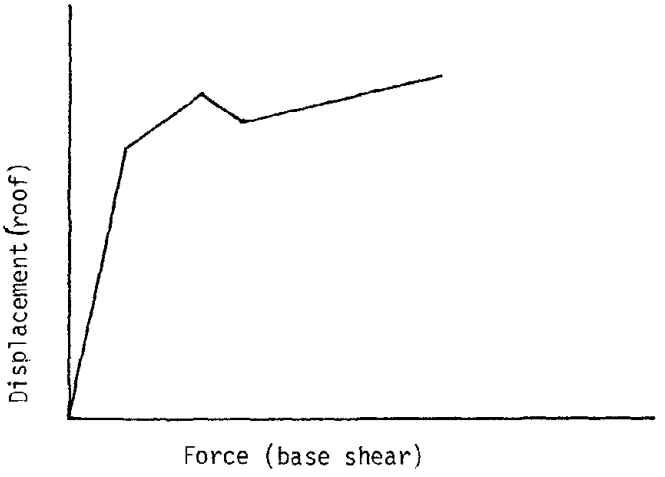

Fig. 1 Roof displacement vs. base shear for building

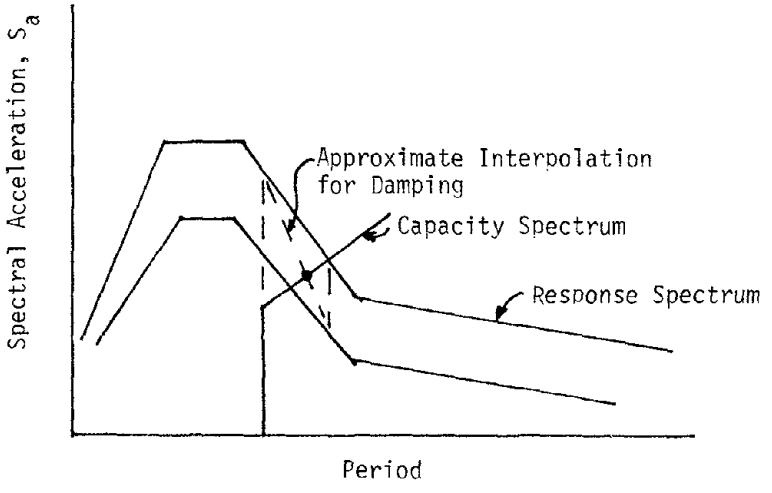

Fig. 2 Capacity spectrum method plot

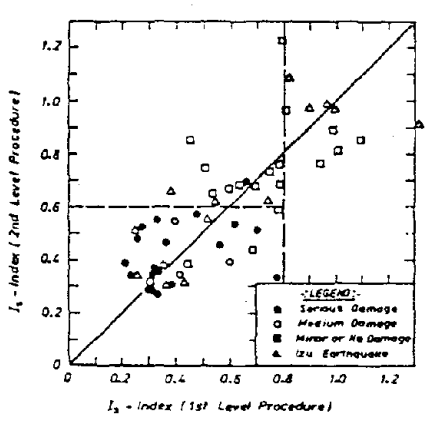

a. Seismic index and damage in 1978 earthquakes in Japan

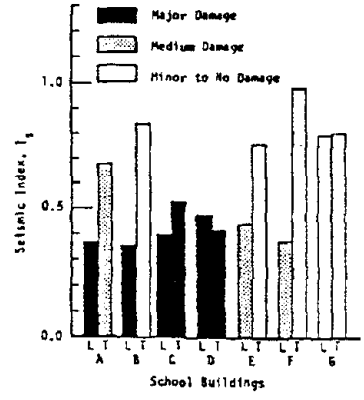

b. Seismic index and damage of school buildings in 1968 Tokachi-Oki EQ (2nd level procedure)

Fig. 3 Seismic indices and damage, Japanese Standard (1977)

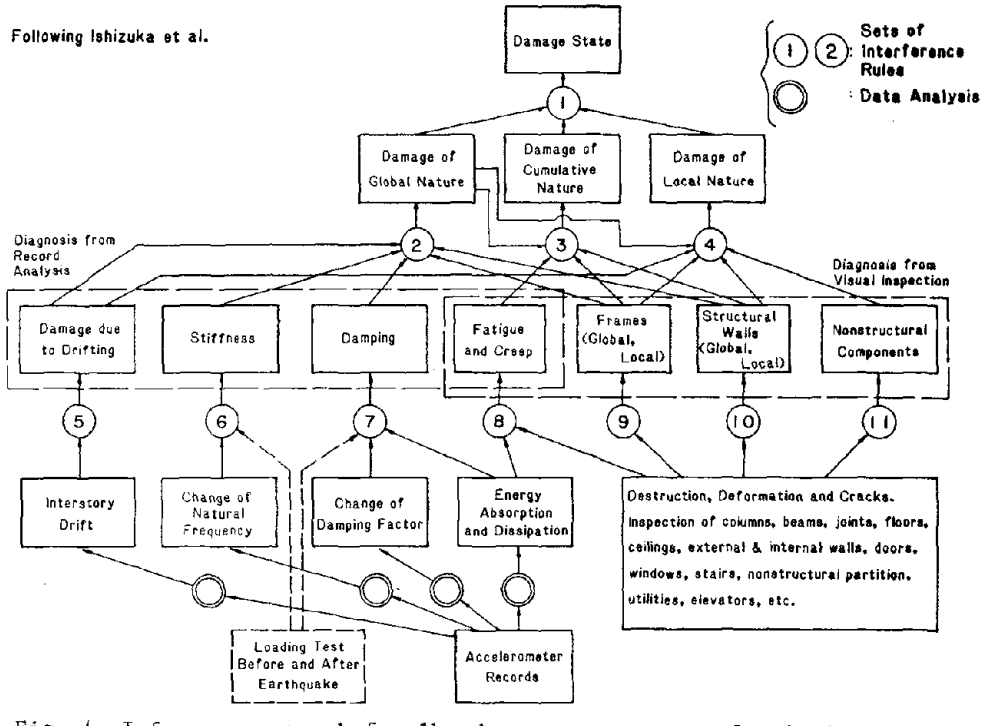

Fig. 4 Inference network for the damage assessment of existing structures

APPENDIX A — FIRST WORKSHOP, MAY 1983

List of Participants:

From Japan:

H. Aoyama	University of Tokyo
M. Hirosawa	Building Research Institute
M. Izumi	Tohoku University
T. Kabeyazawa	University of Yokohama
K. Kamimura	Building Research Institute
T. Murota	Building Research Institute
T. Okada	University of Tokyo
S. Okamoto	Building Research Institute
M. Watabe	Building Research Institute
M. Yoshimura	Building Research Institute

Observers:

M. Ishizuka	University of Tokyo
T. Kaminosono	Building Research Institute
M. Teshigawara	Building Research Institute

From the United States:

M. Agbabian	Agbabian Associates
D. Foutch	University of Illinois
S. Freeman	Wiss Janney Elstner Associates
G.R. Fuller	Department of Housing and Urban Development
P. Gergely	Cornell University
P. Gurvin	Department of State
G. Hart	University of California, Los Angeles
R. Johnston	Brandow and Johnston Associates
H.S. Lew	National Bureau of Standards
J. Scalzi	National Science Foundation
R.N. White	Cornell University
J. Yao	Purdue University

Papers Presented:

APPENDIX B — SECOND WORKSHOP, JULY 1984

List of Participants:

From Japan:

H. Aoyama	University of Tokyo
T. Fukuta	Building Research Institute
T. Kabeyazawa	University of Yokohama
T. Okada	University of Tokyo
S. Okamoto	Building Research Institute
S. Otani	University of Tokyo
H. Umemura	Shibaura Technical University
M. Watabe	Tokyo Metropolitan University
H. Yamanouchi	Building Research Institute

Observers:

T. Kaminosono	Building Research Institute
S. Nakata	Building Research Institute
M. Yoshimura	Building Research Institute, on leave

From the United States:

M. Agbabian	Agbabian Associates
G. Brandow	Brandow and Johnston Associates
S. Freeman	Wiss Janney Elstner Associates
G.R. Fuller	Department of Housing and Urban Development
P. Gergely	Cornell University
G. Hart	University of California, Los Angeles
H.S. Lew	National Bureau of Standards
J. Moehle	University of California, Berkeley
C. Meyer	Columbia University
J. Scalzi	National Science Foundation
M. Sozen	University of Illinois
R.N. White	Cornell University
J. Yao	Purdue University

Observers:

A.J. Eggenberger	National Science Foundation
J. Noland	Atkinson Noland and Associates
R. Nutt	Applied Technology Council
M. Wagner	H. J. Degenkolb & Associates
S. Wood	University of Illinois

Papers Presented:

Theme V

REPORTS ON THE NIHONKAI-CHUBU EARTHQUAKE AND THE NAGANOKEN-SEIBU EARTHQUAKE

A STUDY OF THE ECONOMICAL LOSSES CAUSED BY A CHANGE OF CARGO FLOW AT THE PORT OF AKITA DUE TO THE NIHONKAI-CHUBU EARTHQUAKE, 1983

BY

Akira Yonezawa*
Hajime Tsuchida**

ABSTRACT

Port facilities that are damaged by an earthquake result in a decreased cargo handling capacity of the port since the cargo flow is interrupted. Therefore, users of the port will experience economical losses caused by the time delays in handling cargo, i.e. reduced cargo flow.

This paper addresses the Port of Akita and the decreased cargo handling capacity of that port as a result of the major Nihonkai-Chubu Earthquake of May 26, 1983. For the first time at this port, economic losses due to the change of cargo flow were surveyed. These losses were evaluated to have amounted to 570 million yen during the period of one year after the earthquake.

The results of this study will be used for planning of restoration work at port facilities after future earthquakes, for port planning and earthquake port preparedness planning.

Keywords: Earthquakes; Port facilities; Economic losses

1. INTRODUCTION

Damage to the port facilities by an earthquake has a great impact on the community. Cargo flow through the port has to be changed because of the decrease of cargo handling capacity. This change results in economic losses to the enterprises which have been using the port. Proper port planning and earthquake preparedness planning have to be established to maximize the investment efficiency, taking social and economical losses into consideration. The restoration work also has to be planned to minimize those losses.

It was pointed out that those plannings required sufficient information on the change of cargo flow and the occurrence of the social and economical losses caused by the earthquake.[1]

Until now, earthquake damage of a port was surveyed only from the viewpoint of structural engineering, and was not surveyed from the viewpoint of reduced cargo flow and accompanied economic losses.

The reasons were as follows:

1) The cargo flow through the port is very complex.

2) The methodology for a survey had not been established.

The 1983 Nihonkai-Chubu Earthquake (magnitude 7.7) occurred offshore Akita Prefecture on May 26, 1983 (Fig. 1). As a result, the coast along the Sea of Japan (Nihonkai) experienced a strong ground shaking and Tsunami. The loss of lives exceeded 100, and the total damage to facilities amounted to 180 billion yen.

Damage which occurred in Akita Prefecture (which was the nearest to the epicenter) amounted to 110 billion yen. The damage to ports in Akita Prefecture amounted to 10 billion yen in total, and Akita Port suffered the severest damage among them.[2]

For the first time, the economic losses were surveyed at Akita Port after the Nihonkai-Chubu Earthquake. The survey was possible because of the availability of data on cargo flow from the preceding years and the cooperation of the enterprises which have been using Akita Port.

It was one year after the earthquake occurred that the cargo handling capacity was restored to the original level.

In this paper, the results of the survey will be presented on the change of cargo flow and the accompanied economic losses during the one year after the earthquake occurrence.

2. DAMAGE, RESTORATION AND USE OF PORT FACILITIES

Akita Port is located in Akita City which is the center of industry and economics in Akita Prefecture.

The volume of cargoes handled in Akita Port is 5 million tons per year, which represents 80 percent of the total cargo that is transported through all of the ports in Akita Prefecture. The goods of large amounts are oil, wood and ore. They are foreign or domestic imports (Fig. 2).[3] They support

* Researcher, Port Planning Laboratory, Port and Harbour Research Institute, Ministry of Transport
** Director, Structures Division, Port and Harbour Research Institute, Ministry of Transport

manufacturing facilities of many enterprises nearby the port.

Port facilities were seriously damaged by the earthquake. This damage amounted to 8 billion yen. On the other hand, the manufacturing facilities of the enterprises were only slightly damaged. The manufacturing activities were interrupted after the earthquake to inspect the facilites, but were restored in a short period.

2.1 Damage of Port Facilities[2]

None of the 11 private berths (steel pile-type dolphin) for oil handling were damaged, but 20 out of the 25 public berths (caisson or sheet pile-type structure) were very seriously damaged and became unserviceable (Table 1, Fig. 3).

Three ship unloaders and four warehouses became unserviceable because of the damage.

For a week after the earthquake, the arrivals of vessels were restricted due to the outflow of logs caused by the Tsunami.

2.2 Restoration

The restoration works started in August 1983. From June 1983 to March 1984, the 11 public berths were able to be used (Table 1).

In fiscal year 1983, one ship unloader and one tower-crane were set up and two warehouses were repaired. In addition, the principal facilities were restored.

After April 1984, cargo handling returned to almost the same level as that before the earthquake.

2.3 Use[3]

The number of vessels arriving at Akita Port and the volume of cargoes handled is shown in Fig. 4. From May to June 1983, they decreased due to the restrictions on the vessels arriving and on the utilization of the berths.

After July 1983, they were in the same or higher levels in comparison to those before the earthquake. This fact shows that the serviceable berths were used very excessively, and this excessive use required extra expenditures to many enterprises, and those extra expenditures are considered as an economic loss in this paper.

The volume of cargoes handled at Gaiko -13-meter-depth wharf (damaged) and O-hama -10- meter-depth No. 1 wharf (not damaged) are shown in Fig. 5. It clearly shows that the volume of cargoes handled at each berth changed before and after the earthquake.

3. ECONOMIC LOSSES CAUSED BY CHANGE OF CARGO FLOW[4]

The 43 enterprises which had been using Akita Port were interviewed concerning their economic losses caused by the change of cargo flow (Table 2). These enterprises can be divided into two groups: manufacturers/wholesalers and port service enterprises.

In this paper, the economic losses are defined as follows:

(1) The additional charge and cost of transportation caused by the damage to port facilities.

(2) Reduction of income, as income is closely related to the number of vessels arriving and the volume of cargoes handled at Akita Port.

The results of the survey are classified into the three categories according to the cargo flow:

Case 1 Change of transportation route

Case 2 Change of facilities (berth, warehouse, others)

Case 3 Others

Each case will be described in more detail as follows:

Case 1 Change of transportation route

This case occurred due to the congestion of vessels and the restriction on the vessels arriving and on the utilization of the berths. This case was observed intensively from May to July 1983, but continued to some extent for a year. The details were as follows (Fig. 6, Table 3):

1. Foreign Import

    1) Zinc ore: Zinc ore which was scheduled to be discharged at Gaiko -13-meter-depth wharf was transported to Akita Port after the transshipping to domestic small-size vessels at Hachinohe Port. The volume of the ore transported in this way was 19 thousand tons and the additional cost was 42 million yen.

2. Domestic Export

    1) Zinc ingot: 1,000 tons of zinc ingot produced in Akita City were transported to Funakawa Port by motor trucks, and loaded on a ship there. The additional cost was 1 million yen. Some other ingots were transported to Kurobe City

by rail. (The volume and the cost were unknown.)

3. Domestic Import

1) Cement: Before the earthquake, the cement had been transported to the users from Akita Port by motor trucks. After the earthquake, it was transported by motor trucks or rail from nearby ports and factories without passing through Akita Port. The volume of cement transported by the alternative means was 130 thousand tons, and the additional cost was 260 million yen.

2) Aluminum hydroxide: 1,400 tons of aluminum hydroxide were transported from Funakawa Port to the factory in Akita City. The additional cost was 2 million yen.

3) Bean cake: 600 tons of bean cake were transported by motor trucks from Funakawa Port to the factory in Akita City. The additional cost was 1 million yen.

Note: Log and flourite (foreign import) and gasoline (domestic import) were unloaded at other ports, but their volumes and additional costs were unknown.

The total additional cost amounted to 300 million yen.

Case 2 Change of facilities in Akita Port

The handling of half of the total volume of cargoes was affected by the damage to the facilities. The economical loss extended over a period of one year, until main facilities were restored.

Details to interruption of specific goods were as follows (Table 3):

1. Foreign import

1) Lauan: The additional cost caused by the change of handling berth, the decrease of handling efficiency and the congestion of vessels was 18 million yen.

2) Wood chip: The additional cost caused by the change of handling berth, the congestion of vessels and the increase of transportation distance from the berth to the factory was 8 million yen.

3) Illuminate: The handling efficiency was lowered by the change of handling berth, so that the illuminate had to be unloading even at night. The additional cost was 3 million yen.

4) Zinc ore: The additional cost caused by the changes of handling berth, warehouse used and the decrease of handling efficiency was 55 million yen.

5) Phosphorus ore: The additional cost caused by the change of warehouse used was 3 million yen.

6) Flourite: The handling efficiency was lowered by the change of handling berth, so that it had to be unloaded at night. The additional cost was 3 million yen.

2. Domestic Import:

1) Cement: Handling berth was changed. A new cement duct was constructed in a newly specified berth. Furthermore, the cement was transported by small-size ships and the transportation frequency had to be increased. The additional cost was 150 million yen.

2) Potassium chloride: The additional cost caused by the change of warehouse used was 1 million yen.

Note: The berth for handling cryptomeria and pine log (foreign import) and rice (domestic export) were changed, but the economic losses caused by this change were unknown.

The total economic loss amounted to 240 million yen.

Case 3 Others

Other economic losses were as follows:

1) Demurrage was 8 million yen, as the vessel arrivals were restricted after the Tsuanmi.

2) Pilot income decreased by 6 million yen, as numbers of entry of big-size vessels (over 10 thousand dead-weight tonnage class) arriving at Akita Port decreased.

3) Some enterprises bought their materials from adjoining enterprises because of lack of stock. The additional cost due to such unusual supply of the materials was 9 million yen.

The total economic loss covering the three cases amounted to 570 million yen. It was equivalent to 7 percent of the total cost to reconstruct the damaged facilities.

4. CONCLUSIONS

For the first time, the economic losses caused by the change of cargo flow were surveyed at Akita Port, which was seriously damaged by the

1983 Nihonkai-Chubu Earthquake. It was concluded that the total economic loss was 570 million yen.

It is considered that the economic losses at Akita Port were minimized since the damaged port facilities were restored within the short time period of one year.

5. AFTERWORD

It was not possible to evaluate the economical losses of some enterprises. In the near future this survey will be evaluated for its effectiveness.

The results of the survey presented in this paper will be helpful for evaluating several alternatives on priorities of damaged facilities for reconstruction work and on the arrangement of high earthquake-proof berths in port planning and earthquake preparedness planning.

6. ACKNOWLEDGMENT

Mr. Tomoo Ishiwata, Director of Design Standard Division, Port and Harbour Research Institute reviewed the draft of this paper and made many valuable comments. The authors wish to express their sincerest thanks to him.

7. REFERENCES

1) Port and Harbour Research Institute, et al.; The Report on the Damage to Port Structures and the Investigation of the Tsunami Caused by the Nemuro Hanto Oki Earthquake on June 17, 1973; October 1973.

2) Civil Engineering Division, Akita Prefecture; Damage Report of Civil Engineering Facilities by the 1983 Nihonkai-Chubu Earthquake; May 1984.

3) Civil Engineering Division, Akita Prefecture; Year Book of Post Statistics, 1982 through 1984.

4) Akita Yonezawa; Study on the Change of Cargo Flow and Economical Losses at Port Caused by Earthquake; Technical Note of the Port and Harbour Research Institute; No. 497; September 1984.

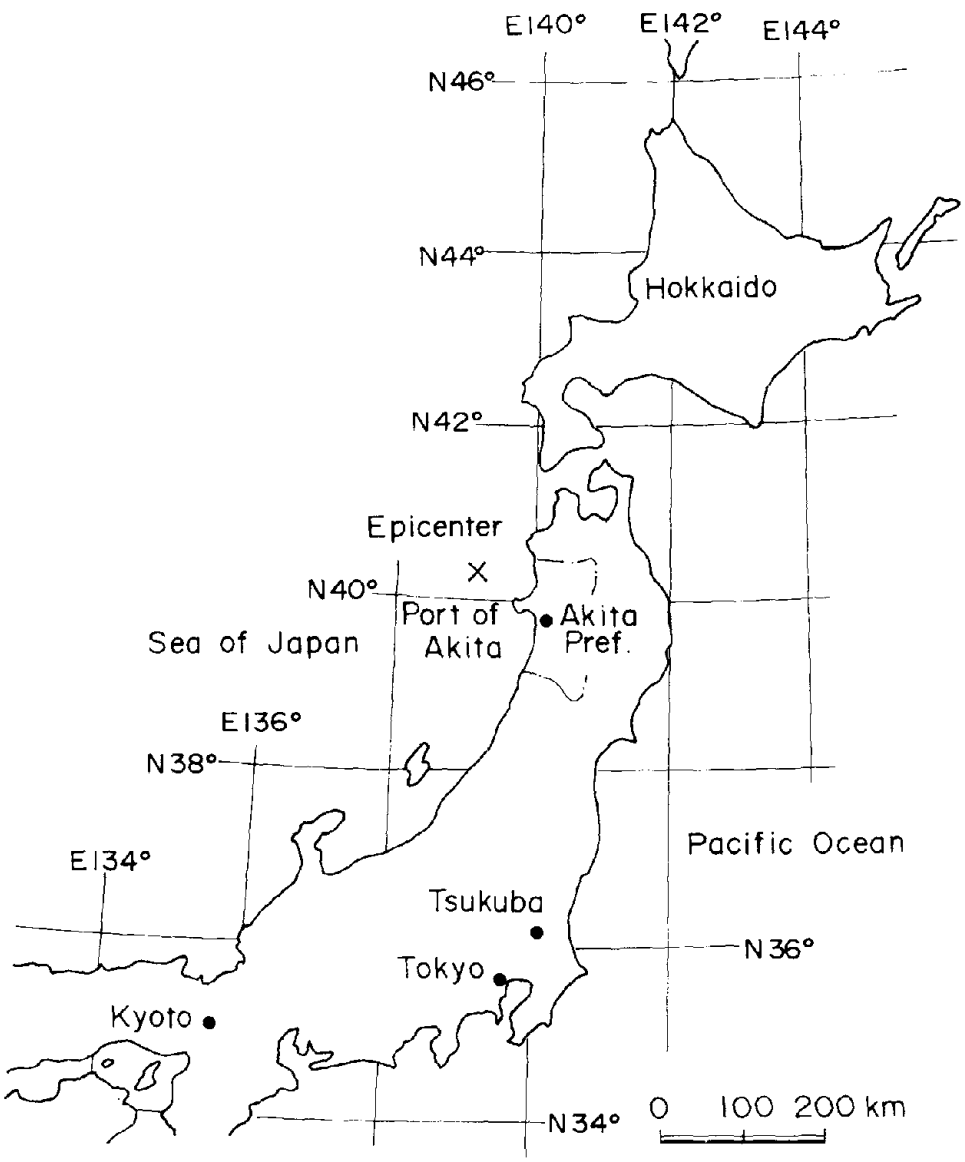

Fig. 1 Epicenter of the 1983 Nihonkai-Chubu Earthquake[2)]

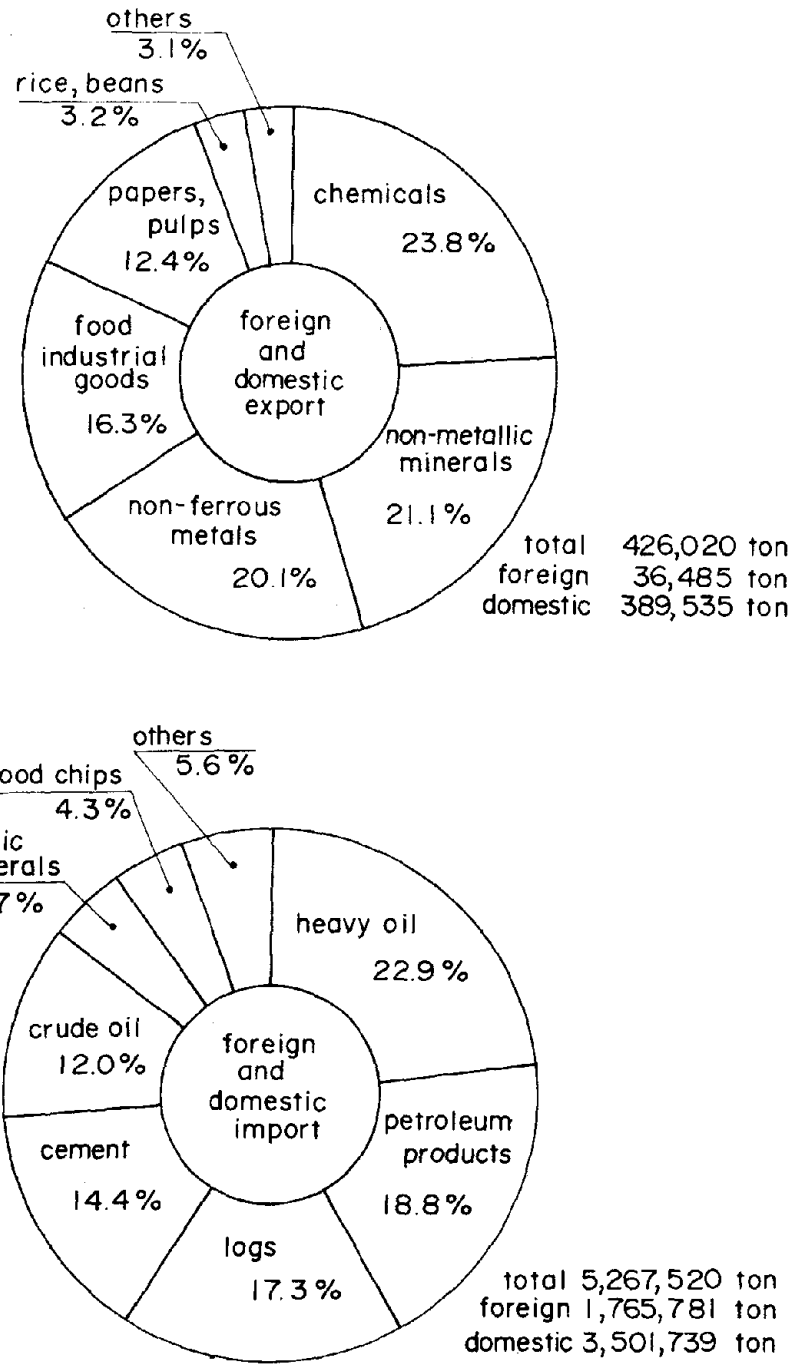

Fig. 2 Trade cargoes at Port of Akita (1982)[3)]

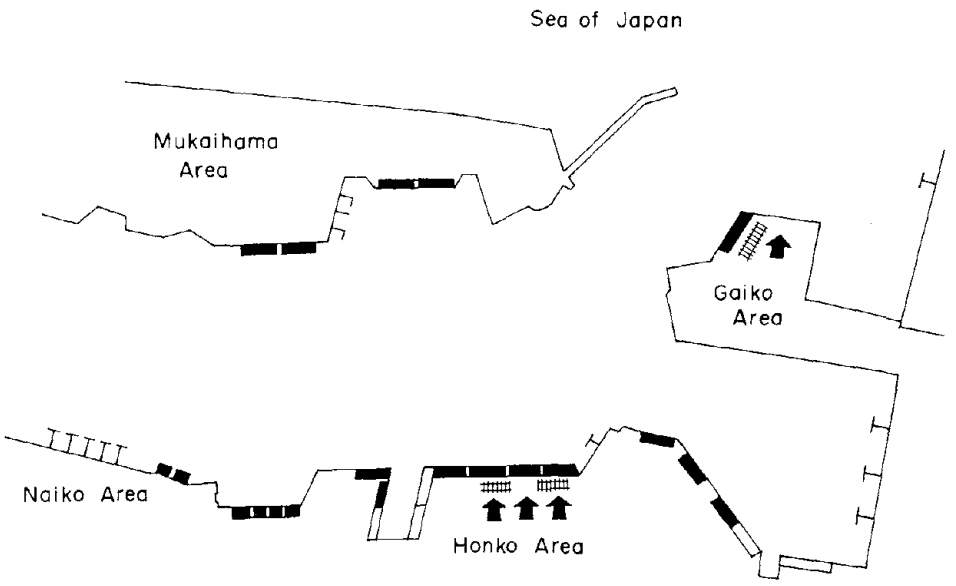

Legend

Marks	Facilities	
▬	Pubulic berth	(damaged)
▭	ditto	(not damaged)
⊣	Private berth	(not damaged)
▦	Unloader	(damaged)
⬆	Public warehouse	(damaged)

Fig. 3 Damage of main port facilities[2)]

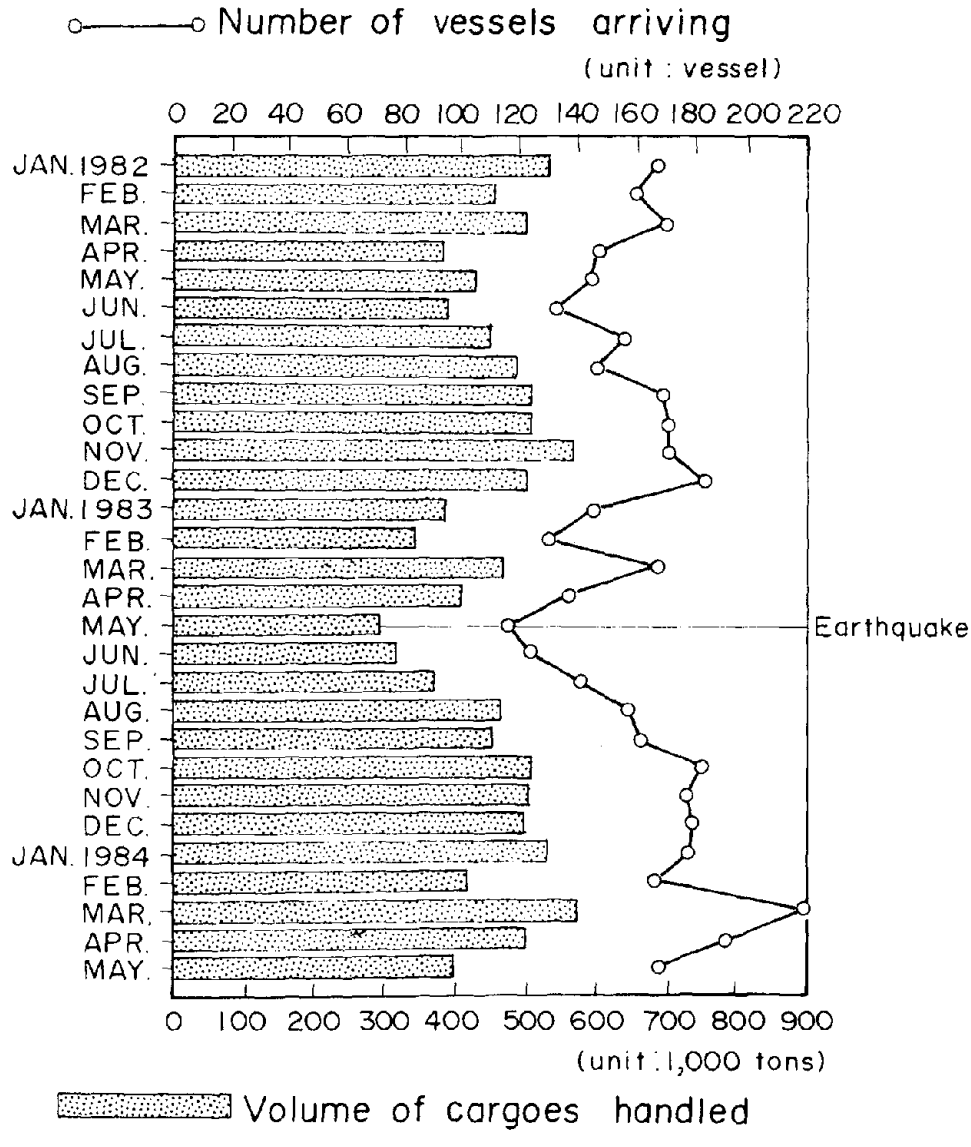

Fig. 4 Number of vessels arriving and volume of cargoes handled by month[3)]

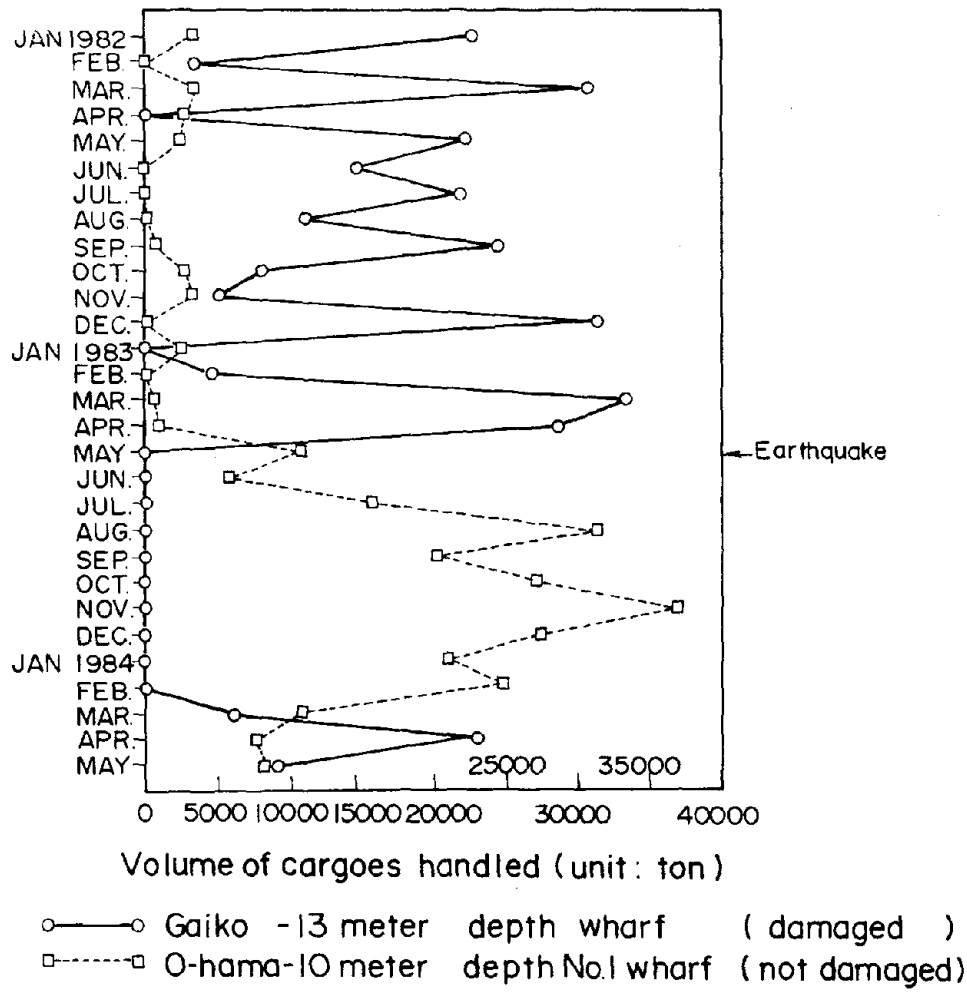

Fig. 5 Comparison of volume of cargoes handled at wharves[3)]

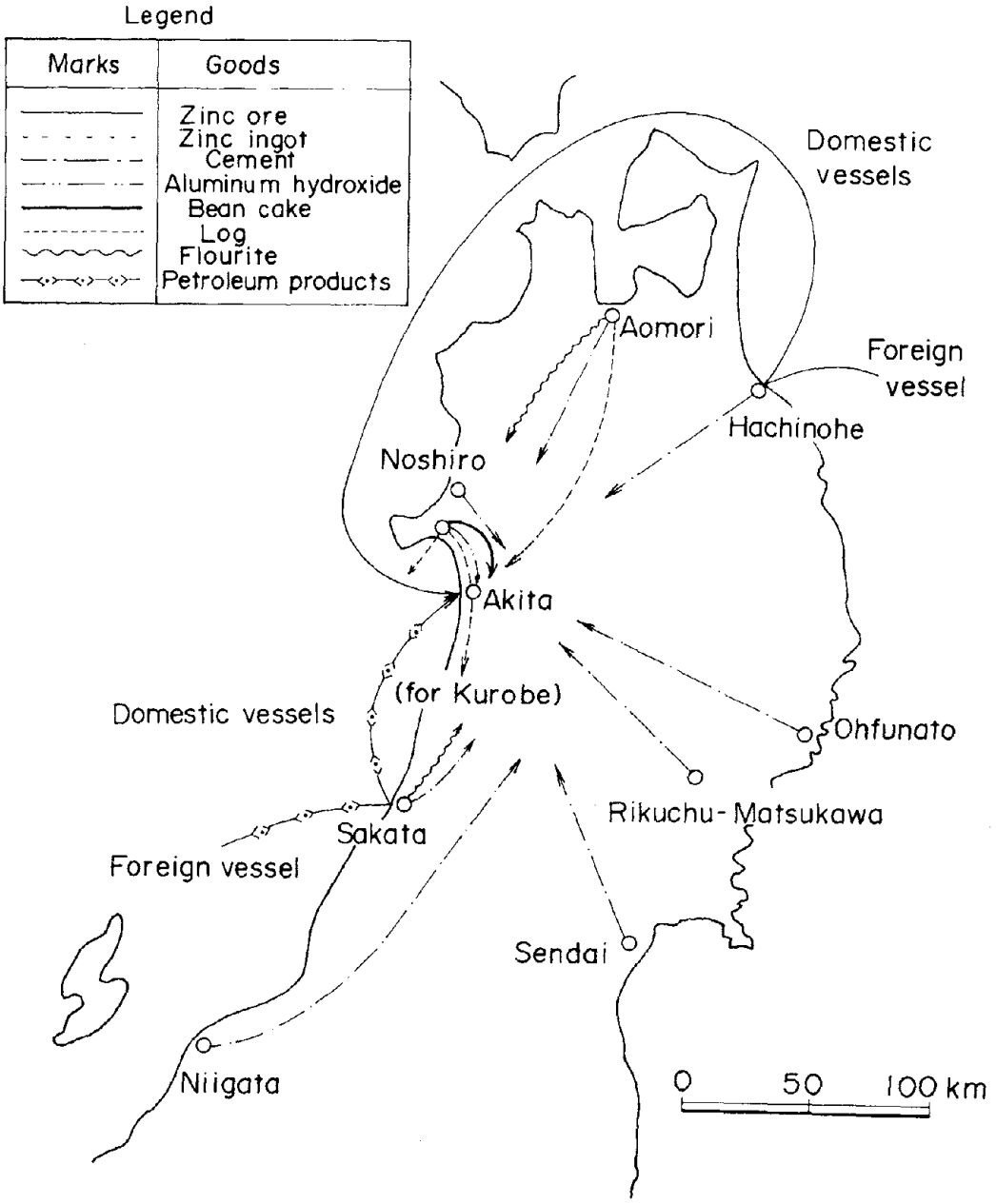

Fig. 6 Transportation map of goods after the 1983 Nihonkai-Chubu Earthquake (They were handled at Port of Akita before the earthquake)[4)]

Table 1 Number of serviceable public berths

Existing mooring facilities			Number of berths		Number of serviceable berths			
Depth (meters)	Objective scale of vessel (dead weight tonnage)	Number of berths	not damaged	damaged	From June to July, 1983	From Aug. 1983 to Mar. 1984	From April to June, 1984	From July to Dec. 1984
-4.5	700	2	1	1	1	1	2	2
-5.0	1,000	4	0	4	4	2	4	4
-5.5	2,000	3	1	2	1	1	3	3
-7.5	5,000	7	2	5	7	4	7	7
-9.0	10,000	1	0	1	1	0	0	1
-10.0	15,000	7	1	6	5	3	3	5
-13.0	50,000	1	0	1	1	0	1	1
Total	——	25	5	20	20	11	20	23

After January 1985, all the berths were able to handle cargoes.

Table 2 Number of enterprises surveyed[4)]

Item	Activities	Number
Manufacturing industry and wholesaler	Chemical industry	3
	Refining industry	3
	Paper industry	2
	Lumbering industry	3
	Cement wholesaler	7
	Petrolium wholesaler	10
	Others	2
Port servise industry	Shipping broker Stevedoor Warehousing Pilot, etc	6
	Nonlife insurance company	7
Total		43

Table 3 Economical losses at Port of Akita

Item	Goods	Economical loss (million Yen)	Period of loss (from)	(until)
(1) Change of transportation route		306		
Foreign import	Zinc ore	42	May 1983	July 1983
Domestic export	Zinc ingot	1	May	1983
Domestic import	Cement	260	May 1983	May 1984
ditto	Aluminum hidroxide	2	May	1983
ditto	Bean cake	1	May	1983
(2) Change of facilities in Akita Port		241		
Foreign import	Lauan	18	June 1983	Jan. 1984
ditto	Wood chip	8	June 1983	Nov. 1983
ditto	Illminate	3	Aug. 1983	Feb. 1984
ditto	Zinc ore	55	May 1983	Mar. 1984
ditto	Phosphrus ore	3	Aug. 1983	Mar. 1984
ditto	Flourite	3	May 1983	Nov. 1983
Domestic import	Cement	150	June 1983	May 1984
ditto	Potassium chloride	1	Aug. 1983	May 1984
(3) Others		23		
Dumurrage		8	May	1983
Decrement of income		6	May 1983	Dec. 1983
Others		9	May 1983	May 1984
Total		570		

LANDSLIDES AND DAMAGES DUE TO THE NAGANOKEN-SEIBU EARTHQUAKE OF SEPTEMBER 14, 1984

Masateru Tominaga
Yasushi Sasaki
Katsumi Senoo
Hiroyuki Yoshimatsu
Eiichi Taniguchi
Kimiaki Nakano
Naomi Obinata
Yoshifumi Hara
Tetsurou Kuwabara

Public Works Research Institute
Ministry of Construction

ABSTRACT

On September 14, 1984, a severe earthquake with a magnitude of 6.8 on the J.M.A. scale occurred in central Japan. The magnitude had been tentatively reported as 6.9 just after the earthquake but was modified to be 6.8 later.

As a result of this earthquake, a large scale landslide named Ontake-kuzure and many other landslides occurred near the epicentral area causing damage to human lives and civil engineering facilities.

In this paper the authors report the damages to civil engineering facilities and three main landslides induced by the earthquake.

1. INTRODUCTION

A severe earthquake occurred in the central part of Japan on September 14, 1984. Details of this earthquake were reported by Japan Meteorological Agency (J.M.A.) as follows:

Earthquake Name	:	The Naganoken-seibu Earthquake of September 14, 1984
Date and Time	:	8:48 a.m. September 14, 1984 (Japan Standard Time)
Epicentral Region	:	Western Nagano Prefecture
Hypocenter	:	Latitude 35°49.3'N Longitude 137°33.6'E Focal Depth 2 km
Magnitude	:	(Mj) 6.8 (Mj: J.M.A. Magnitude)

Fig 1.1. shows seismic intensities of various stations and Fig. 1.2 shows the number of aftershocks observed at Iida Station of J.M.A. The largest aftershock of magnitude 6.2 is reported to have occurred at 7:14 a.m. September 15. Fig. 1.3 shows distribution of epicenter of aftershocks observed by J.M.A.

According to the investigation carried out by the Science and Technology Agency, the seismic intensity around the Matsukoshi Area in the epicentral region had to be almost 6 in J.M.A. scale. In addition, it is reported that seismic motion around the epicenter of the main shock was motion in which the short period component was predominant, rather large vertical motion was included, and the duration time of the main shock was relatively short.[1)]

Fig. 1.4 shows maximum acceleration recorded by accelerographs installed at various structures and on the ground near these structures. At the Makio Dam near the epicenter no records of strong motion by the main shock were obtained because the earthquake shocks were beyond the scales of the electromagnetic seismograph recorders. However, the maximum acceleration is known to have exceeded

200 gal from the gain which was set at 200 gal for maximum acceleration.

Fig. 1.5 is an example of an acceleration record of an aftershock obtained by the seismograph which was installed at Makio Dam by P.W.R.I. (Public Works Research Institute, Ministry of Construction) after the main shock.

Although there is no record of ground motion near the epicenter, the maximum horizontal acceleration is estimated by Eq. (1.1).[2)]

$$A_{max} = 2.67R + 200 \qquad (1.1)$$

A_{max}: Maximum Horizontal Acceleration (gal)

R : Overturning Ratio of Gravestones (%)

As overturning ratio of gravestones at Matsukoshi Area was reported over 90% by some investigations, [1)] maximum horizontal acceleration of main shock is estimated to exceed 400 gal.

2. OUTLINE OF THE LANDSLIDES

Due to this earthquake, numerous landslides occurred in many slopes near the epicentral region. Landslides which are larger than $100m^2$ in area were caused at about 500 locations by the earthquake.

Four of them were huge landslides whose collapse volumes were larger than $100,000m^3$; others were rather small and were slides whose collapse volumes were about $800m^3$ on the average. The largest landslide, which occurred at the south-east slope of Mt. Ontake, was named "Ontake-kuzure" and the collapse volume is estimated to be $36,000,000m^3$. The debris from this landslide flowed down about 14 km along the valley and caused serious damage to people, houses, and forestry. The second largest landslide was "Matsukoshi Landslide", which occurred on the left bank of the Ohtaki River at the upper reach of Makio Dam reservoir. The volume was about $290,000m^3$. The third one, whose volume was about $150,000m^3$, was "Takigoshi Landslide". It occurred on the left bank of the Ohtaki River at the upper reach of Ohtaki Dam reservoir. The fourth largest landslide occurred in the south-east slope of Ontake Plateau and the volume was about $100,000m^3$ (Fig. 2.1). Small-scale landslides were concentrated in the area along the Ohmata River and in the upper reaches of the Nigorisawa River and the Senzawa River. The landslides along the Ohmata River and in the upper area of the Nigorisawa River occurred in the slopes of valleys incising the stratovolcano. The geology of the landslides in the upper area of the Senzawa River is a shattered Paleozoic layer.

Some rainfall had been recorded five days before and on the day of the earthquake (Table 2.1). The mountain slopes were undoubtedly wet on the days of the rainfall.

3. DAMAGE TO CIVIL ENGINEERING FACILITIES

Most damage due to this earthquake was concentrated in an area of radius not farther than 10-15 km from the epicenter, and most of the damage was related to landslides.

The damage statistics are summarized in Table 3.1. The total amount of damages was 46.3 billion yen. The cost of damages to civil engineering facilities and to forestry amount to 12.4 billion yen and 29.4 billion yen, respectively, and the sum of these two damage costs is about 90% of the total damage cost.

Roads were closed at many points because road embankments had collapsed, because the roads were covered by debris from collapsed slopes adjacent to the roads, because several bridges were swept away by debris flow and because a road tunnel was filled by a debris flow.

As shown in Photo 5.1, the main entry route to Ohtaki Village collapsed at two places due to landsliding. Photo 3.1 shows the Kohrigase Tunnel which was buried by the flow of debris from "Ontake-kuzure".

The large amount of debris from the "Ontake-kuzure" dammed up the Ohtaki River at Yanagase, causing a natural reservoir, and this made local inhabitants worry about a secondary disaster such as a flood which might occur by failure of this natural dam.

Other disasters, besides landslides, which were directly caused by seismic motion, were the cracking of road surfaces, the collapse of road shoulders, settlements at the access portions to bridges, damage to reinforced concrete bridge piers, cracking of concrete girders, buckling of the side corners of steel girders, damage to footings, and others. Photo 3.2 shows the damages to Matsubara bridge piers. The Makio Dam (rockfill dam) which is located near the epicenter, had minor damage consisting of a small crack along the crest. Water supply was interrupted by damage to pipes and muddiness of the sources.

4. SEDIMENT RUNOFF DUE TO SLOPE COLLAPSE

4.1 Ontake-kuzure

The Ontake-kuzure is the largest landslide that occurred on a ridge of the southeastern slope of Mt. Ontake (elevation: 3,063m). The elevation of the top of the landslide collapse was 2,550m, the elevation of its lower end was 1,900m, the length of collapse slope was about 1,500m, the maximum width was about 700m, the maximum depth was about 150m, its collapse area was 7,500,000 m^2 and the volume of the collapse was 36,000,000 m^2. The slope gradient of the collapsed part was originally about 25° (Fig. 4.1, Fig. 4.2, Photo 4.1). This landslide was the second largest in Japan in this century after the 150,000,000 m^3 Hiedayama landslide of 1911.

The ridge in which the landslide occurred was composed of alternate strata of andesite lava and pyroclastic material underlain by a pumice stratum. This pumice stratum is believed to have been the slip surface.

It is presumed from the testimony of those who heard the sound of the landslide that the collapse occurred almost simultaneously with the earthquake.

4.2 Outline of Sediment Runoff

The debris avalanche caused by the Ontake-kuzure reached the Ohtaki River by the route shown in Fig. 4.3. It first flowed into the Denjo River Valley. Most of the debris avalanche flowed down this river valley, passed through the Nigorisawa River Valley and reached the Ohtaki River Valley. Part of the debris avalanche passed over a ridge about 100m in height on the right bank of the Denjo River before entering the Nigorisawa River Valley, and this part flowed down to the confluence of the Denjo River where it combined with that part of the debris avalanche that had continued in the Denjo River Valley. The combined debris avalanche reached the Ohtaki River, passing over the ridge near the confluence of the Danjo and Ohtaki Rivers, passed through two narrow parts of the Ohtaki River and flowed to a stop in the Kohrigase area. Meanwhile, some of the debris avalanche from the source area passed over a ridge on the left bank of the Denjo River and flowed into the Higashimatazawa and Nakamatazawa Rivers above Suzugasawa River. The debris that flowed into the Nakamatazawa River was deposited above its confluence with Higashimatazawa River, while the debris that flowed into the Higashimatazawa River passed through the Suzugasawa River and reached the Ohtaki River.

The volumes of erosion and deposition were as indicated in Fig. 4.4. In the Denjo River, erosion was predominant and caused a riverbed scour of 10-20m downstream to the point where the debris flowed over the ridge into the Nigorisawa River. Below that point, riverbed scour was 1-10m. In the Nigorisawa River Valley there was a tendency to deposition with a riverbed rise of 0-14m. The bed of the Nigorisawagana River rose 20-30m. In the Ohtaki River, the large debris deposits caused a riverbed rise of 30-40m. These deposits caused the Ohtaki River to be blocked above its confluence with the Nigorisawa River and to form a dammed lake with a depth of about 30m (Photo 4.2).

The volumes of erosion and deposition in the Suzugasawa River were smaller than those in the Nigorisawa River; erosion was the tendency in the upper reaches of the stream and deposition was the tendency in its lower reaches.

The volumes of deposits shown in Fig. 4.4 have not been multiplied by such factors as volumetric increase rate (expansion factors). If the deposits flowing into the Makio Dam reservoir was zero, the volume of erosion was larger than the volume of deposition by 1320m^3. It is considered that, due to volcanic geology, the porosity of the material involved was smaller after the landslide than before the collapse.

4.3 Riverbed Deposits

After the debris avalanche, hardly any deposits were left on the bed of the Denjo River, debris avalanche deposits and small hummocks resulted in the Nigorisawa River bed, and debris deposits and large hummocks occurred in the Nigorisawa River bed. In the Ohtaki River, the riverbed deposits consisted of debris avalanche deposits covered by hummocks and mud-flow deposits.

The surface of the mud-flow deposits was very smooth but the surface of the debris deposits was uneven and looked like that of roughly loosened soil. The hummocks structurally retained the texture of the original natural ground and appeared to be dry. When artificially crumbled, they were very brittle. Since this structure was retained during the flow, it can be imagined that the flow wasn't mixed violently (Photo 4.3).

In the Suzugasawa River, the amount of riverbed deposits was small above elevation 1,450m. Below this elevation, there were debris avalanche deposits and mud-flow deposits. The mud-flow deposits were predominant in the downstream direction.

4.4 Flow Marks

The debris flow stripped vegetation and soil off the valley walls and left flow marks as it proceeded. Fig 4.5 is a profile of the levels of flow marks on both the right and left banks of the Nigorisawagawa River where vegetation and soil had obviously been stripped by the debris avalanche. It shows that the highest level of flow marks was about 100m above the old riverbed and that the marks were highest on the sides of the gorges of the river.

The height of flow marks in the Suzugasawa River (Fig. 4.6) was 20-40m in the upper reaches and less than 10m in the middle reaches and suddenly decreased in the vicinity of the elevation of 1,350m. This may indicate that a large amount of sediments was deposited in the vicinity of this elevation.

4.5 Movement of Debris Avalanche

The debris avalanche velocity was presumed from the observations of people watching some of the series of sediment movements that attended the Ontake-kuzure. First, two people witnessed the initial debris avalanche in the vicinity of the upper gorge (named Gakiganodo) of the Ohtaki

River; the time of their observation was estimated to be about 8:56 a.m. Assuming that the Ontake-kuzure occurred simultaneously with the earthquake, the average flow velocity for the distance from the base of the landslide to Gakiganodo was about 23 m/sec. Then, the average flow velocity for the distance from Gakiganodo to Kohrigase can be estimated to be 4 - 7 m/sec from testimony that the sediment had reached Kohrigase area on the Ohtaki River some time between 9:00 and 9:05 a.m. It can be imagined from these facts that, in the upper reaches forming the Denjo and Nigorisawa Rivers, the flow velocity exceeded the velocity of a debris flow with a normal wave height and that from Gakiganodo down the Ohtaki River the flow was rather slow.

Another important testimony is that an aqueduct crossing the gorge of Gakiganodo had not fallen in the debris avalanche at about 8:56 a.m., but fell in the first aftershock of the earthquake, causing water to pour from the pipe. The pipe fell about 15m, onto newly deposited sediments on the right bank. The debris avalanche seems to have occurred more than once since the height confirmed in a subsequent field survey was 2-3m (Fig. 4.7).

Calculated from the time 8:55 a.m., when a person saw mud-flow runoff in the lower reaches of the Suzugasawa River, the average flow velocity along this river from the toe of the Ontake-kuzure was about 20 m/sec. Later, sediment runoff was observed several times in the lower reaches.

K.J. Hsu charted the relation between collapse volumes in great landslides of the past and their equivalent friction coefficients (Fig. 4.8).[3] If the Ontake-kuzure landslide is included in this chart, it is at a position with a smaller equivalent friction coefficient than the rest. The Ontake-kuzure landslide apparently took a runoff form having fairly small friction resistance.

5. MATSUKOSHI LANDSLIDE

5.1 Outline of Landslide

The Matsukoshi landslide occurred along the right bank of the Ohmata River which flowed with the Matsukusa River. The landslide scale was 30m in maximum depth, 170m in width, 225m in length, and 290,000m^3 in volume. The collapsed area is located at the southerly-facing hillside slope of Mt. Kurakoshi (EL 1100m) and is composed of andesite layers originating from Ontake Volcano. Two clear scarps, like the shape sharply cut by a spoon, are successively observed through the terrace plain as shown in Photo 5.1 and Fig. 5.1. After the landslide pushed a concrete plant factory, which was located near the Ohmata river-bed, up the opposite riverside slope about 35m vertically, the greater part of these soils then flowed down along the Ohmata River and were deposited widely in the upper area of Ontake reservoir, about 890m in horizontal distance from the landslide collapse area. On that day much of the lake bed was seen because the water level was low (the reservoir water volume only attained 23.5% of filling).

The deposited soils consisted mainly of volcanic ash, but partially contained some hummocks about 2m in diameter. From the geotechnical characteristics of this debris, the deposited form with ripple marks along the margin of the deposit area, and also from the observations of a person who happened to watch the landslide, the soils riding over the opposite slope behaved like cement milk, and the flowing soil behavior is estimated to be the same as a mud-flow type.

5.2 Outline of Geology

The landslide scarp forms a vertical wall shaped, from above, like a horseshoe, and layered structure is clearly observed on the scarp wall. A geological profile of this structure is shown in Fig 5.2. The base rock consists of Paleozoic

layers containing slate, sandstone and chert strata striking N70°E. This outcrop was partially observed in the collapsed surface of the head zone after the landsliding. Volcanic products originating from Mt. Ontake lay on this base rock in layers. These products are classified into two parts. One part which is called new product consists of volcanic cobble, tuff breccia and andesite lava layer. The other is old product containing layers of pumice, gravel, volcanic ash and clastic deposits of mud-flows. By the boring investigation which was done around the periphery of the landslide area, the new product layers cannot be correlated with layers observed only a short distance from the landslide. Therefore, great erosional processes which created a very irregular erosional surface are estimated to have taken place before the sedimentation of new product. The landslide slip surface was observed successively in the strongly weathered pumice layer.

5.3 Causes of Landslide

Soil investigations including borings were performed at the collapsed slope of Matsukoshi, and triaxial tests were conducted by using undisturbed soil samples taken from the slope. The following three causes may be pointed out for the landslide at Matsukoshi based on the soil investigation, geographical condition and the characteristics of the earthquake motion:

(1) The weathered pumice layer which formed a slip surface had very low shear resistance.

(2) The contours of the top of the Paleozoic rock which underlies the weathered pumice layer formed a valley and water was likely to infiltrate into the slopes of this buried valley.

(3) A considerably strong earthquake motion occurred.

It is estimated that a slip surface existed in the weathered pumice layer from observations resulting from the collapsed slope and soil investigations. Triaxial tests were performed by using undisturbed soil samples taken from the weathered pumice layer. Cohesion of the soil, C_{cu}, was 0.29 - 0.76 kgf/cm^2 and angle of shear resistance, ϕ_{cu}, was 22 - 24 degrees. Those values are relatively small. The weathered pumice contains a wide range of soil particle sizes from clay to gravel; the mean particle size D_{50} is 0.02 - 0.3 mm and the uniformity coefficient U_c is over 180.

Observations of the collapsed slope and measurements of strike and dip of strata indicated that the Paleozoic rock contours under the weathered pumice layer formed a valley and water may easily have permeated into the buried valley slope. The Matsukusa River flows into contact with the slope on its north side and it is estimated that the weathered pumice contained a lot of water when the earthquake occurred.

No strong motion record was obtained near Matsukoshi during the main shock, but, as mentioned before, it is estimated from the collapse of gravestones that the horizontal maximum acceleration was over 400 gal. Therefore, considerably large accelerations must have been applied to the slope at Matsukoshi during the earthquake.

6. TAKIGOSHI LANDSLIDE

6.1 Outline of the Landslide

The escarpment of this landslide is found at the level ridge (about 1,200m elevation) on the west-facing slope behind Takigoshi hamlet on the left bank of the main stream of the Ohtaki River. This slope dipped about 50° before the landslide. The landslide collapse was 60m in maximum height, 150m in average width, 50m in average thickness, and the volume of soil involved was about

150,000 m^3. It occurred on the left bank of a gully running at a right angle to the main stream of the Ohtaki River. The plane configuration of the escarpment is rather straight and the profile is almost perpendicular (Fig. 6 1).

Some of the collapsed soil remained immediately below the escarpment and in the gully, but most flowed away. Most of the soil flow went down along the gully for about 850m to the main stream of the Ohtaki River. It then flowed into the reservoir of Ohtaki River Dam, spread out for a width of about 300m and was deposited there. Many hummocks measuring about 2.5m in height and about 10m in diameter can be seen in this area of deposition, particularly at the upstream apex of the area. These hummocks consist mainly of boulders about 30cm in diameter.

6.2 Details of the Escarpment

The upper part of the escarpment contains brown to dark brown volcanic ash soil (marked A in Fig. 6.2) with a thin layer of light grey clay near the ground surface. A brown sand layer (B) is below the ash soil. Under the sand layer is light gray to bluish gray andesite tuff (C and D) and in its center there is apparently hard rock with distinct columnar jointing (E). The lowest part of the escarpment seems to be composed of andesite tuff and volcanic effusive rock. It is presumed from outcrops around the collapsed area that a layer of lacustrine sand and a clayey layer exist underneath.

Under these geological conditions and considering that the configuration of deposition of the collapsed soil at the toe of the escarpment is flat, the slip plane of collapse is concluded to have been formed in an aquiferous sand layer of the Takigoshi lacustrine stratum distributed almost horizontally near the elevation of 1,140m.

7. REHABILITATION WORK TO REPAIR DAMAGED FACILITIES[4)]

The rehabilitation of facilities under prefectural control has cost a total of about 6,000 million yen for 90 sites, namely: about 1,940 million yen for 75 road sections, 120 million yen for 4 bridge sections, 40 million yen for an erosion control site, and 3,950 million yen for 10 river sections. The rehabilitation of facilities under municipal control has cost a total of about 2,000 million yen for 171 sites, namely: 1,880 million yen for 158 road sections, 130 million yen for 10 bridge sections, and 50 million yen for 3 river sections. Thus, the grand total is about 8,000 million yen for 261 sites.

Of these public works facilities, the first to require urgent rehabilitation was the Matsukoshi and Azuma area of Ohtaki Village, and sections of the Ontake-Ohtaki-Kurosawa prefectural road line as a road necessary for local life. This rehabilitation work was delayed for several reasons, such as the search for missing people buried in the landslide in the Matsukoshi area. However, the Matsukoshi section of the road was opened on October 14, after the Matsukoshi area temporary road construction (length: 310m, width: 6m, approximate cost: 65 million yen) including the erection of a temporary New Ohmata Bridge using a transportable built-up bridge rented from the Ministry of Construction (length: 40m, width: 6m). The Azuma section of the road was opened on October 29 after the Azuma area temporary road construction (length: 600m, width: 3 - 6m, approximate cost: 38 million yen).

From its confluence with the Nigorisawagawa River, and downstream for a section of about 3 km in length, the channel of the Ohtaki River was filled to a depth of 30 - 40m with 20,000,000 m^3 of sediments discharged from the Nigorisawagawa River. These deposits dammed the river and caused a lake of about 3,700,000 m^3 in the upper

reaches of the Ohtaki River. Since this abnormal deposition of sediments might be scoured in a future freshet and cause a washout of this new dam with subsequent flooding, channel excavation (length: 1,580m, volume: 89,500 m^3) was carried out to release water from the dammed-up lake. This work assured adequate channel capacity. A groundfill, using 349 concrete riprap blocks, was constructed in the Kohrigase area to stop movable sediments. The approximate cost was 240 million yen (Fig. 7.1).

About 10,400,000 m^3 of debris deposited in the general area of the confluence of the Nigorisawa and the Denjo Rivers and in the Nigorisawagawa River from the Ontake-kuzure may well cause damage in the lower reaches by abnormal sediment flows during future freshets. Therefore, 14 small check dams were scheduled to be constructed near the area of the confluence of the Nigorisawa River and the Denjo River. This work was planned by the Nagano Regional Forestry Office to be accomplished by the end of fiscal 1984 at a cost of 1,150 million yen as an emergency forestry conservancy and damage rehabilitation project. Further, two sabo dams with a height of 14 m (Nigorisawa Dam No. 1 and No. 2) are scheduled to be constructed at the Nigorisawa River gorge mouth by Nagano Prefecture under an emergency erosion control project and a countermeasure for landslides project.

Also scheduled is the construction of a few sabo dams each on the main Ohmata River, on the Matsukusa River, which is a branch of the Ohmata River, and in the Suzugasawa River, where hillside collapses along its upper reaches during the earthquake were remarkable (Fig. 7.2, Table 7.1).

In the Matsukoshi and Takigoshi areas, where large landslides occurred, and in the Uwajima area where large hillside collapses must be prevented, emergency landslide countermeasures including drainage, pile driving and a small check dam, were carried out by the Nagano Prefectural government (Fig. 7.2, Table 7.1).

8. CONCLUSIONS

Characteristics of the damages due to the Naganoken-seibu Earthquake of September 14, 1984 can be summarized as follows:

1) Since the epicenter was in the middle of Honsyu Island, the shaking was felt widely in all directions. This felt area was similar to those in the past due to earthquakes with the same magnitude.

2) Severe damages were caused by landslides on slopes near the epicenter. The number of slopes where the sliding area exceeds 100 m^2 was about 500.

3) The severest of all damages to civil engineering facilities was the deposition of debris in the Ohtaki River channel, where the volume was estimated to be 20,000,000 m^3. Adding to this, damage to sabo dams, slope failures adjacent to roads, and damage to bridges took place.

4) The major damages to civil engineering facilities were caused mostly by landslides and debris from landslides.

5) The big landslides were "Ontake-kuzure", landslides at Matsukoshi, at Takigoshi and at Ontake Plateau. The shape of these landslides were different from each other. Although failure mechanisms of each landslide are not yet clarified, the existence of a weathered pumice layer among the strata which constitute a slope is considered to be one of the main reasons.

6) The movement of the debris from the Ontake-kuzure was presumably affected by water, especially in the lower reaches of

the Nigorisawa River, as determined from the study of the flow marks.

7) It was learned, from the damage caused by this earthquake, that the method of estimating the stability of mountain slopes during earthquakes, the rehabilitation of river channels filled by huge amounts of debris, and the countermeasures to increase the stability of roadside slopes during earthquakes, are important engineering subjects to be investigated in the near future.

9. ACKNOWLEDGEMENT

The authors are very grateful to all concerned in the Chuubu Regional Construction Bureau, Nagano Prefectural Government and Ohtaki Village Office for their cooperation given to this earthquake survey. The authors are also very grateful to Science and Technology Agency, National Land Agency and Fill Type Dam Division of Public Works Research Institute for their supplying precious data.

10. REFERENCES

1) Investigation of Seismic Intensities Distribution: Study Progessing Data of Urgent Study on Sediment Disaster caused by Naganoken-seibu Earthquake of 1984, March, 1985 (In Japanese).

2) Ohhashi, Iwasaki, Kawashima: Strength of Earthquake Motion of the Izu-Ohshima-Kinkai Earthquake of 1978 estimated from Overturning Ratio of Gravestones, Civil Engineering Journal 20-11 (1978).

3) Hsu, K.J.: Catastrophic Debris Streams (Sturzstrons Generated by Rockfalls), Geological Society of America Bulletin, vol. 86, 1985.

4) Kiso Construction Office: Disaster of the Naganoken-seibu Earthquake, Nagano Prefecture, November 1984 (In Japanese).

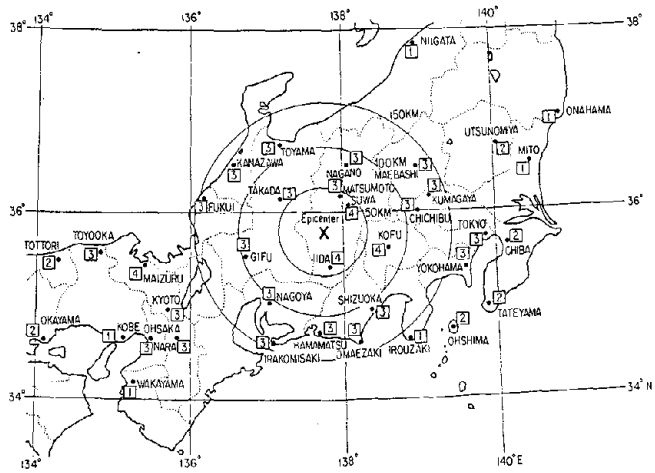

Fig. 1.1 Seismic Intensity Distribution of Various Stations (After J.M.A.)

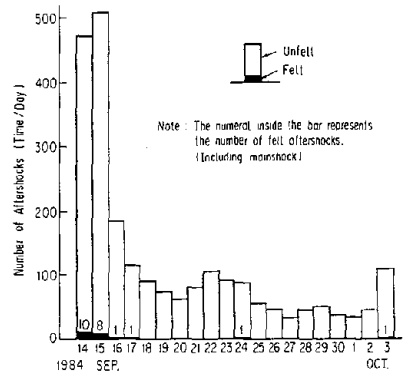

Fig. 1.2 Daily Frequency of Aftershocks observed at Iida Station (After J.M.A.)

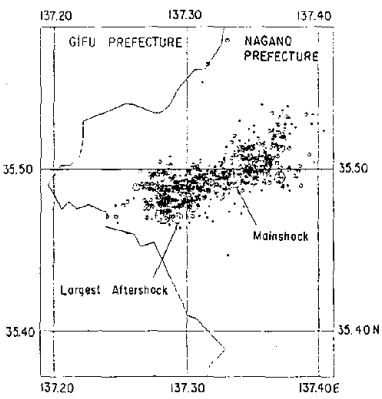

Fig. 1.3 Distribution of Aftershocks (After J.M.A.)

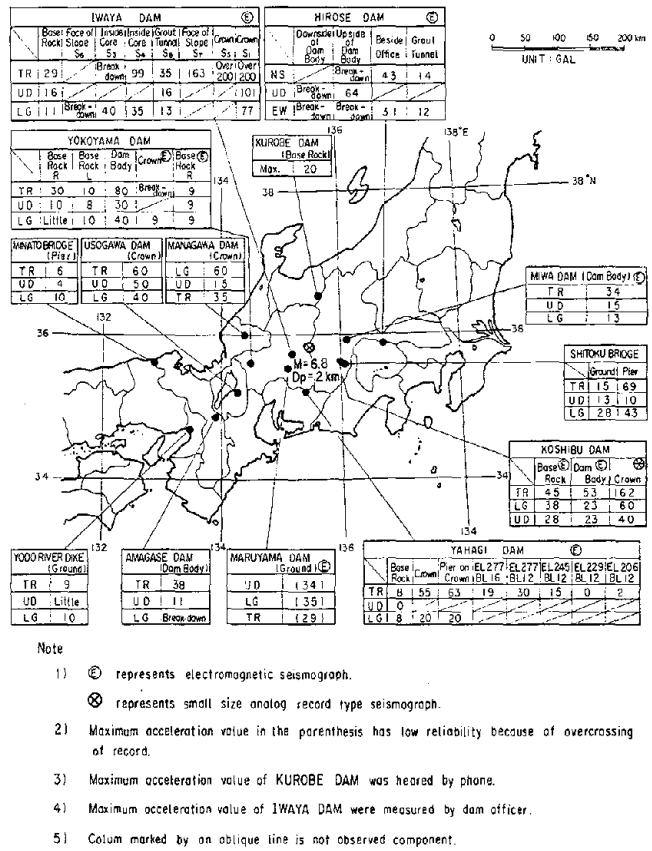

Note

1) Ⓔ represents electromagnetic seismograph.
⊗ represents small size analog record type seismograph.

2) Maximum acceleration value in the parenthesis has low reliability because of overcrossing of record.

3) Maximum acceleration value of KUROBE DAM was heared by phone.

4) Maximum acceleration value of IWAYA DAM were measured by dam officer.

5) Colum marked by an oblique line is not observed component.

Fig. 1.4 Maximum Acceleration of Various Site based on Seismogram

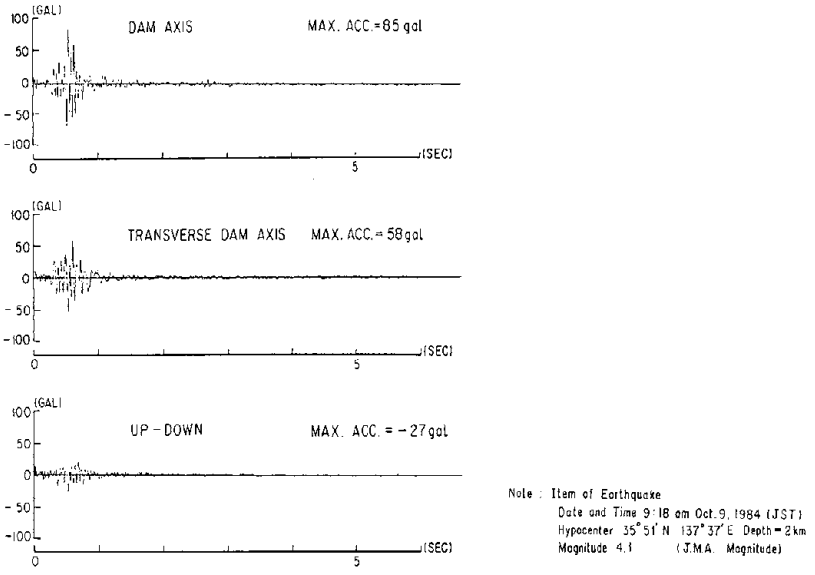

Fig. 1.5 Acceleration Record of Aftershock observed on Rock beside Makio Dam

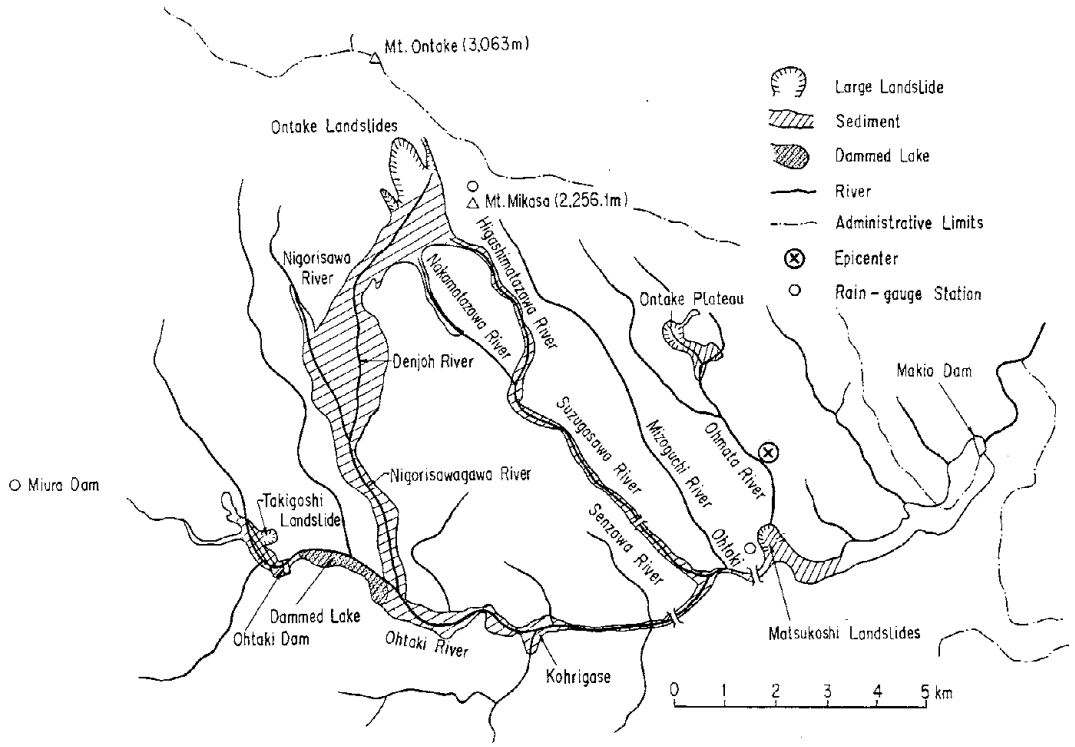

Fig. 2.1 Plane of Landslides Locations

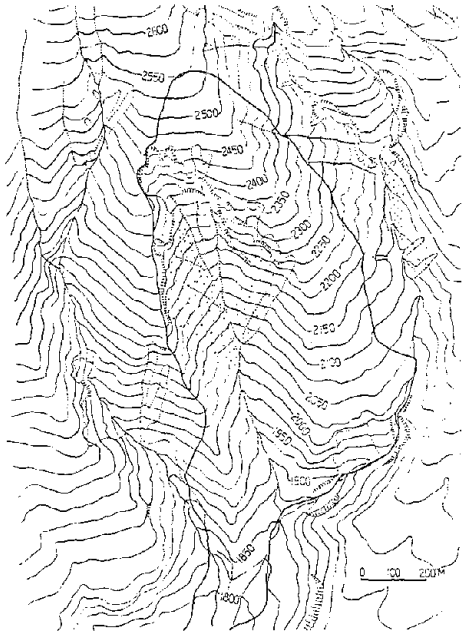

Fig. 4.1 Plane of "Ontake-kuzure"

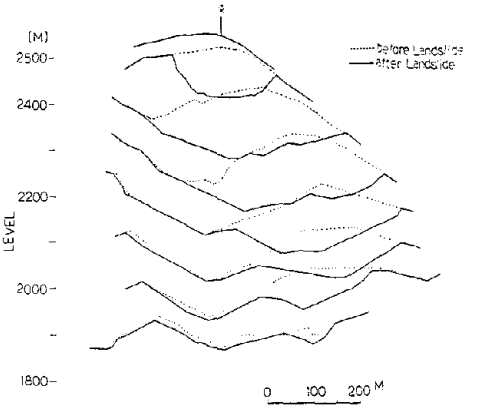

Fig. 4.2 Cross Section of "Ontake-kuzure"

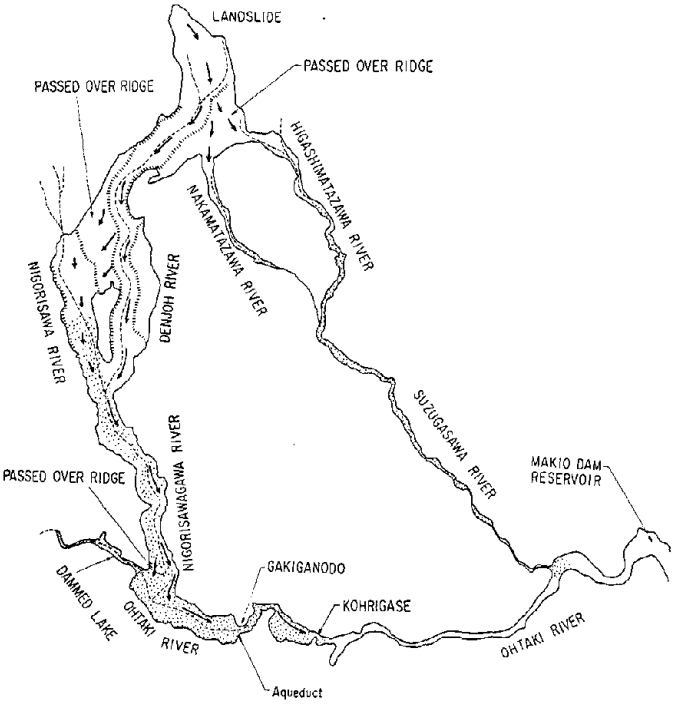

Fig. 4.3 Sediment Runoff from "Ontake-kuzure"

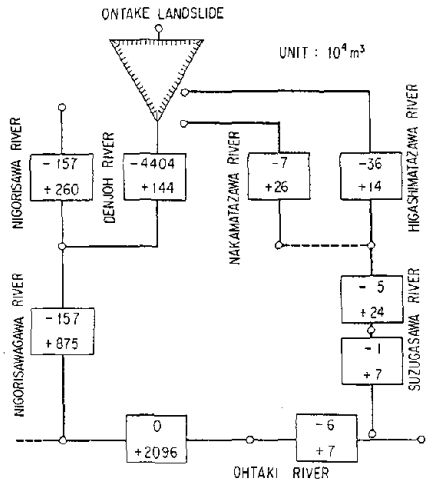

Fig. 4.4 Diposition and Erossion Volume

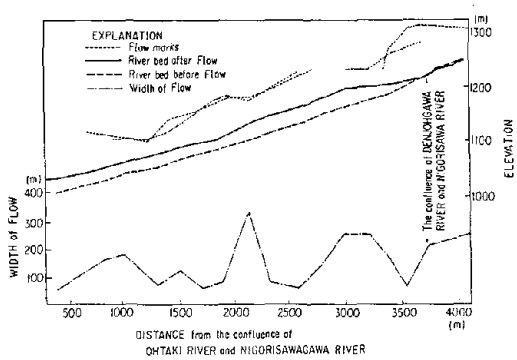

Fig. 4.5 Flow Marks Vertical Section of Nigorisawagawa River

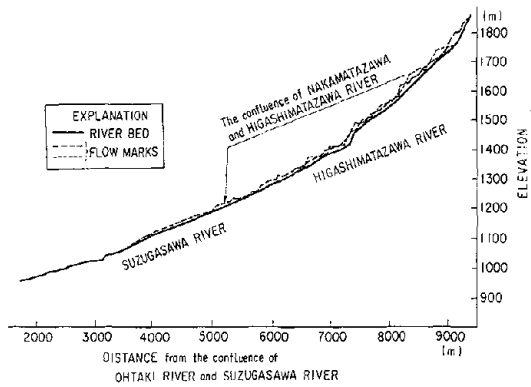

Fig. 4.6 Vertical Section of Suzugasawa River

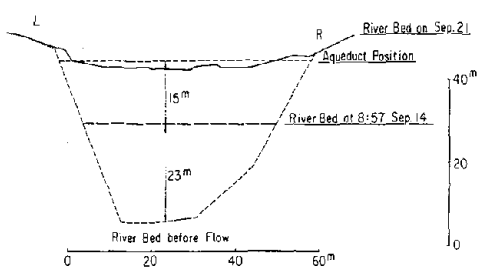

Fig. 4.7 Cross Section near Aqueduct

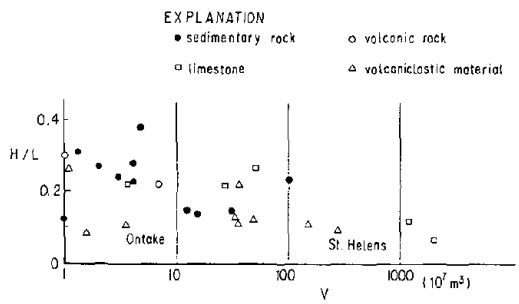

Fig. 4.8 Relationship between Equivalent Coefficient (H/L) and Rockslide Volume

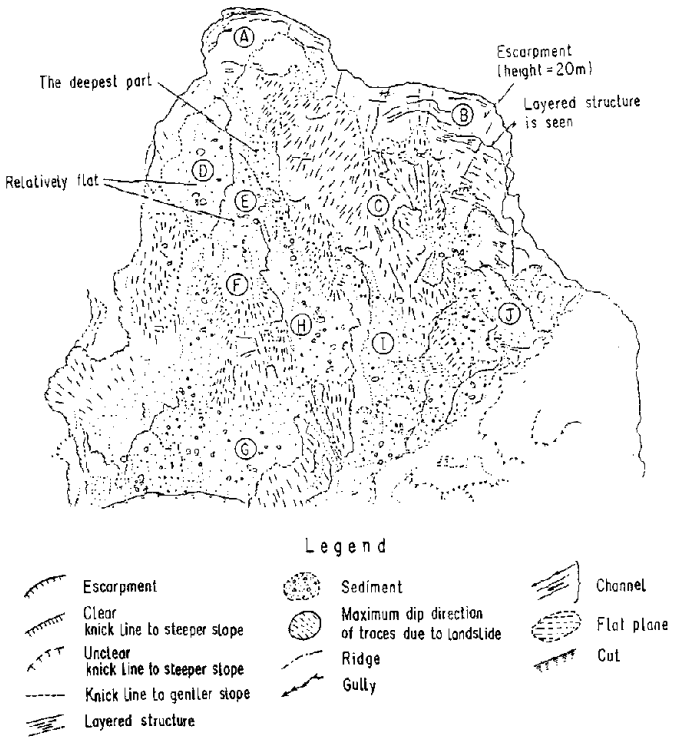

Fig. 5.1 Collapsed Area at Matsukoshi observed from Oblique Photograph

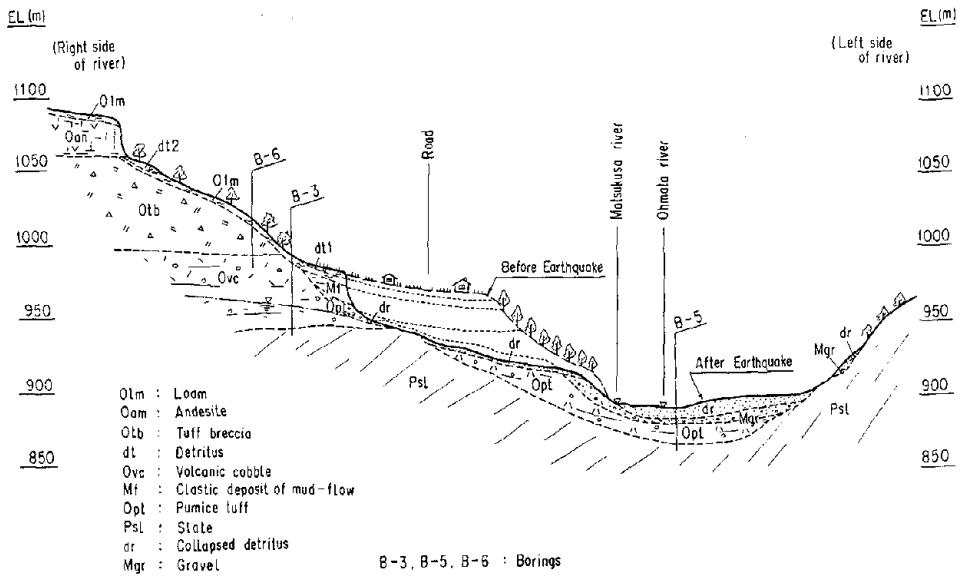

Fig. 5.2 Geological Profile at Matsukoshi

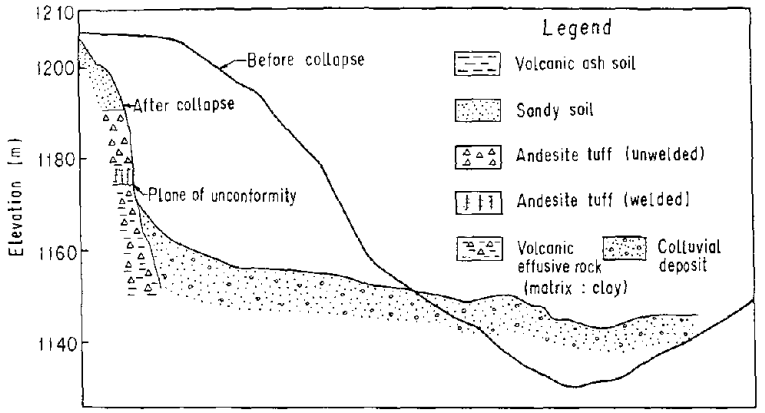

Fig. 6.1 Profile of Collapsed Area and Geological Conditions

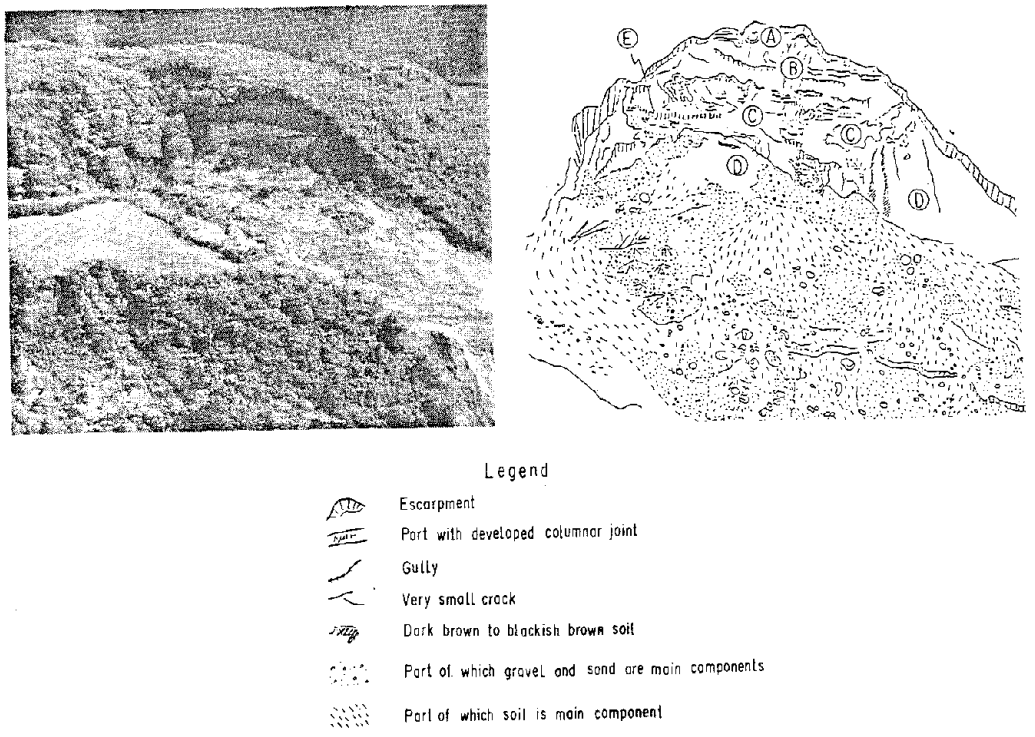

Fig. 6.2 Oblique Photograph of Collapsed Area and Its Sketch

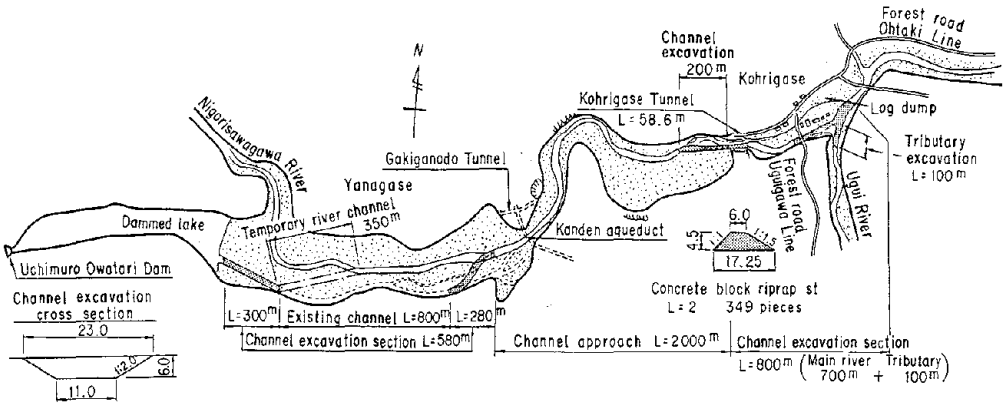

Fig. 7.1 Repair Works of Damage in Ohtaki River

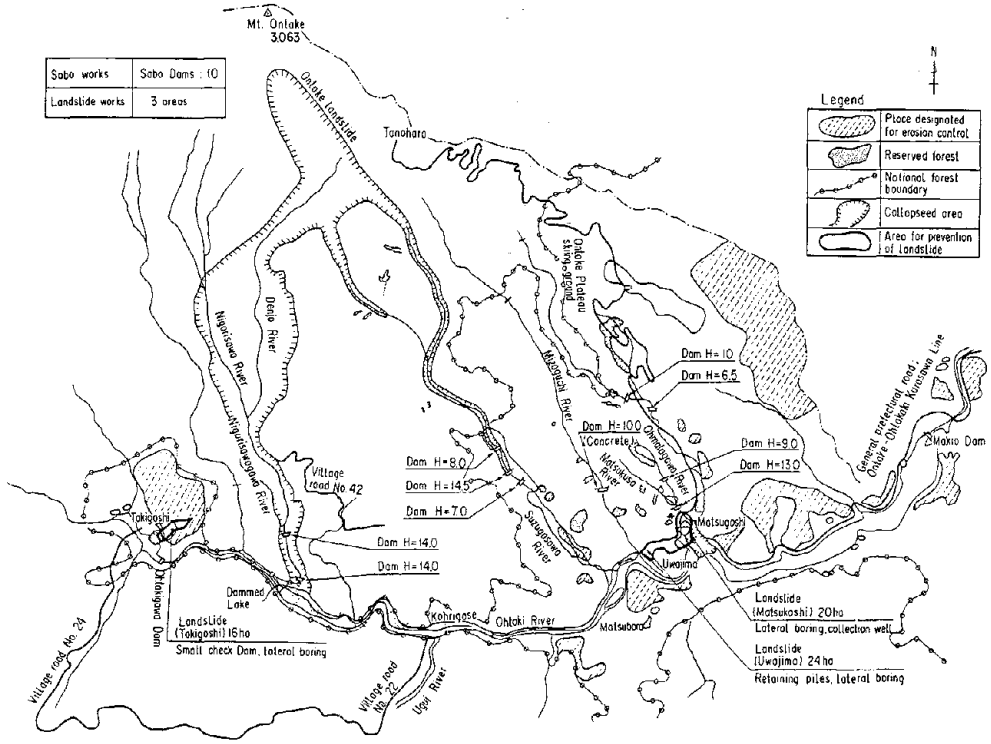

Fig. 7.2 Sabo and Landslide Repair Works Plan

Table 2.1 Rainfall during 7-14 Sep. 1984

Unit: mm

Day / Rain-gauge station	Sep. 7	8	9	10	11	12	13	14 A.M. (0:00 8:00)	Total
Mt. Ontake (Mt. Mikasa)	0	0	119	10	1	0	1	27	158
Miura Dam	0	1	80	3	3	0	0	24	110
Ohtaki	0	0	27	2	0	0	0	20	49

Table 3.1 Damage Statistics (After National Land Agency, As of December 20, 1984)

Category		Unit	Number of Damage	Damage Cost (Million Yen)
Human	Fatality	Person	14	
	Obscurity	Person	15	
	Injury	Person	10	
Damage to Residential Houses	Complete Failure	House	14	
	Half Failure	House	73	
	Part Failure	House	565	
Public Works	Highway	Site	264	6,940
	Bridge	Bridge	14	443
	River	Site	15	4,930
	Sabo	Site	1	40
	Total	Site	294	12,353
Forestry				29,419
Others				4,556
Total				46,328

Table 7.1 Statement of Item on Sabo and Landslide Works

Erosion control works						Landslide countermeasures	
Urgent rehabilitation Sabo works			Most urgent rehabilitation Sabo works			Most urgent and urgent rehabilitation Sabo works	
Name of torrent	Name of dam	Scale	Name of torrent	Name of dam	Scale	Name of area	Scale
Ohmata River	Ohmata No.1	H=6.5m H=41.0 (steel)	Ohmata River	Ohmata No.2	H=6.0m(10.0) L=124.0 (steel)	Matsukoshi	Drainage, pile driving, small check dam, etc.
Ohmata River	Ohmata No.2	H=4.0(10.0) L=96.0(124.0) (steel)	Matsukusa River	Matsukoshi	H=13.0 L=76.0 (concrete)	Uwajima	Drainage, pile driving, piling works, etc.
Matsukusa River	Kurakoshi	H=9.0 L=32.0 (steel)	Suzugasawa River	Suzugasawa No.2	H=14.5 L=99.0 (concrete)	Takigoshi	small check dam Drainage, etc.
Suzugasawa River	Suzugasawa No.1	H=7.0 L=62.0 (steel)	Suzugasawa River	Suzugasawa No.3	H=8.0 L=109.0 (concrete)		
Nigorisawa River	Nigorisawa No.1	H=4.0 L=101.6 (steel)(apron)	Mizoguchi River	Mizoguchi	H=10.0 L=112.0 (concrete)		
			Nigorisawa-gawa River	Nigorisawa No.1	H=14.0 L=101.6		
			Nigorisawa-gawa River	Nigorisawa No.2	H=14.0 L=111.6		
5 torrents Estimated total project cost: 740 million yen			7 torrents Estimated total project cost: 2,800 million yen			3 areas Estimated total project cost: 1,020 million yen (including 200 million yen for emergency works)	

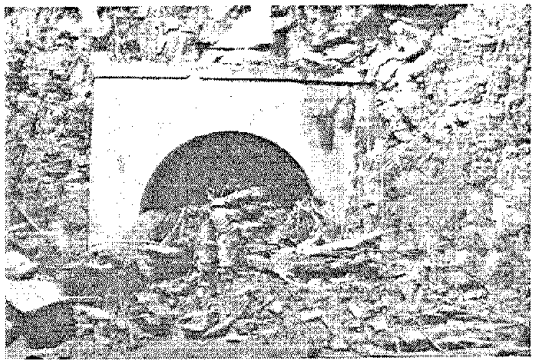

Photo. 3.1 Damage to Kohrigase Tunnel

Photo. 3.2 Damage to Matsubara Bridge

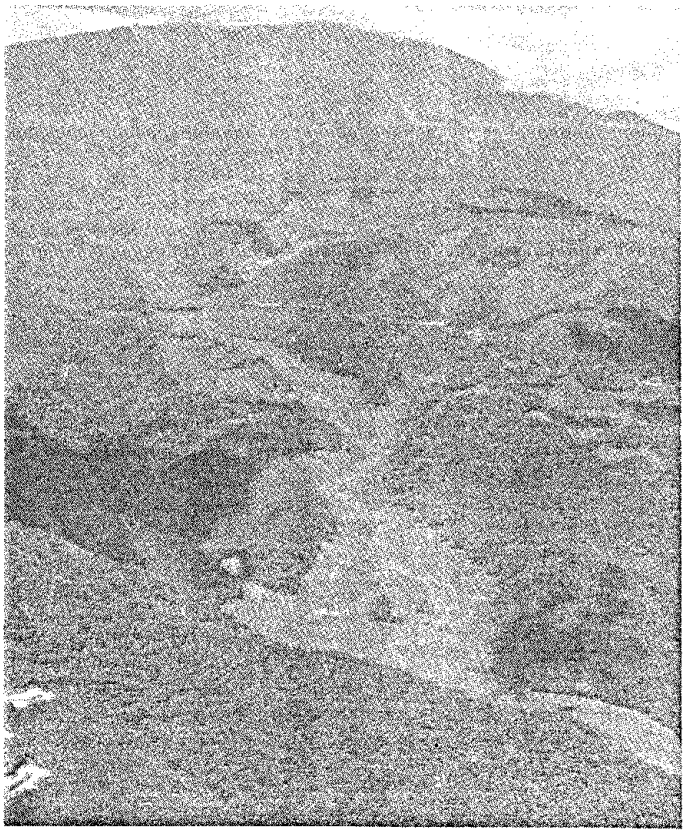

Photo. 4.1 Ontake-kuzure

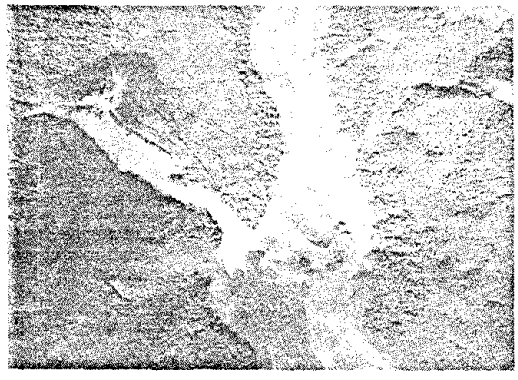

Photo. 4.2 Natural Reservoir in Ohtaki River

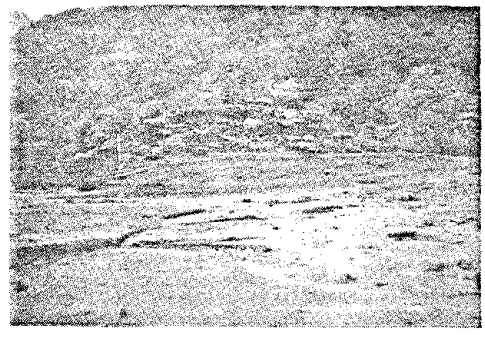

Photo. 4.3 Hummock in Ohtaki River

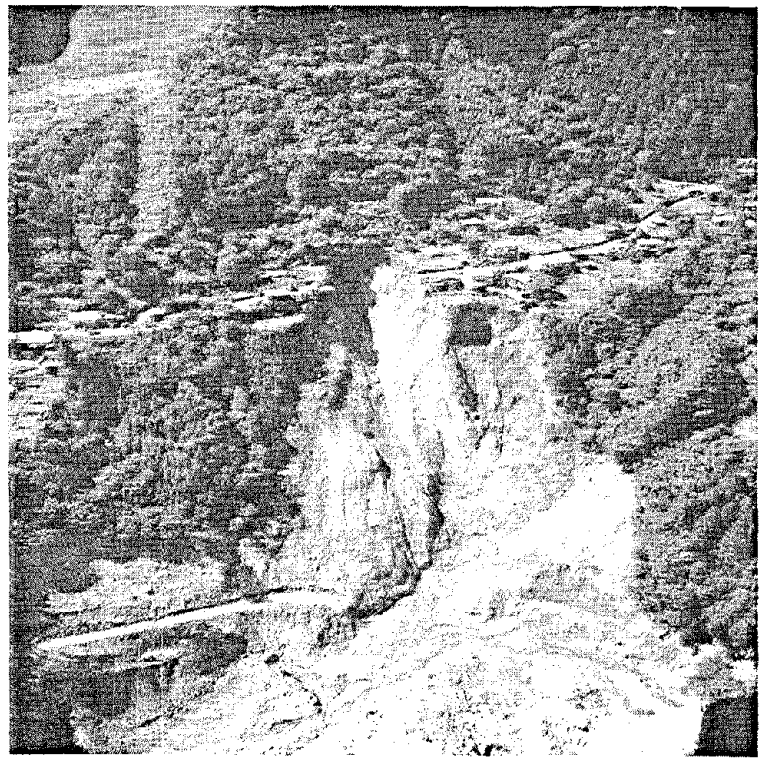

Photo. 5.1 Landslide at Matsukoshi

GEOMORPHOLOGICAL CHARACTERISTICS AND FACTORS OF THE LARGE-SCALE LANDSLIDE AND DETRITUS FLOW ON THE SOUTH SLOPE OF ONTAKE VOLCANO CAUSED BY THE NAGANOKEN-SEIBU EARTHQUAKE, 1984

Masatoshi Nagaoka
Yoshihisa Hoshino
Yoshimichi Takei
Seiji Ichikawa
Fumio Saitoh

Geographical Survey Institute

ABSTRACT

The largest landslide caused by the 1984 Naganoken-seibu earthquake was $3.4 \times 10^7 m^3$ in volume. It is the third largest in Japan in the past 100 years. This landslide consisted mostly of scoria and lava beds deposited in an old buried valley on the slope of Ontake Volcano. During the earthquake shaking, these beds collapsed and slid along the old valley surface. The characteristic microtopography of the area and its changes before the landsliding are recognized as precursors from a viewpoint of historical development of landform.

The second largest landslide of $2.3 \times 10^5 m^3$ caused by this earthquake is also ascribed to similar topographical and geological factors.

1. INTRODUCTION

The landslides caused by the 1984 earthquake are different in mechanism from those caused by heavy rainfalls. These earthquake-triggered landslides have the potential to take place repeatedly in areas where earthquakes are common.

In this paper, the processes and causes of the landslides triggered by the earthquake are discussed. Large scale maps of pre- and post-landslides have been produced by photogrammetrical methods for this purpose. The progressive topographical changes preceeding the earthquake are analysed by photo interpretation and characteristic microtopography related to the landslides is discussed.

2. GENERAL BACKGROUND

2.1 The Naganoken-seibu Earthquake

The earthquake of M 6.8 occurred in the western part of Nagano Pref. at 8:48 a.m. on September 14, 1984. The epicenter was at the southeastern foot of Mt. Ontake, very close to Otaki Mura (village). Although the magnitude of the earthquake was not very large, Otaki Mura suffered heavy damage, losing 29 lives and many houses and facilities, due to the very shallow hypocenter. According to the analysis of the earthquake mechanism by Japan Meteorological Agency, the fault or underground slip plane causing the earthquake is a normal plane of ENE-WSW strike. Widespread damage was caused by the landslides and accompanying detritus and mud flows derived from the volcanic products of Ontake Volcano and fluvial gravel beds.

2.2 Topography and Geology

The topography of the studied area is shown in Fig. 1. The landslides and the subsequent detritus flow and mud flows, excepting small scale landslides, are displayed in Fig. 1.

The studied area is in the southern foot of Ontake Volcano, which has formed in the late Quaternary. Volcanic products are widely distributed in this area. The basal rocks of Ontaki Volcano consist of two major types separated by an inferred fault extending from the central part of the volcano to the south-southeast. One rock type is the Chichibu Palaeozoic formation (to the east) and the

other is Nohi Cretaceous rhyolites, including intrusive granites, to the west.

2.3 Precise Large Scale Maps

The Geographical Survey Institute made pre- and post-landslide large scale topographic maps (1/5,000 for the largest-scale landslide, 1/2,500 for Matsukoshi and Takigoshi landslide) for the areas involving the largest landslide and two other smaller landslides. The mapping is specially noted as follows:

(1) It was taken into account to obtain sufficiently high accuracy for determining topographic changes from the pre- and post-landslide maps.

(2) For financial reasons, 1/1,000 topographic maps made by Nagano Pref. were reduced and compiled for making the post-landslide topographic maps (field surveys were not carried out since mapping had to be done urgently).

(3) Locations and altitudes on post-landslide maps were adopted as the control points in conducting aerial trianglation for pre-landslide maps.

(4) The aerial photos taken in the season of defoliation (Forestry Agency, Yama-56, taken in April 1969) contributed to the accurate indication of the topographic configuration.

For the geomorphological studies, many aerial photos taken by various organizations (1948, '59, '63, '69, '74, '75, '79, and '80) were used for the pre-landslide survey. For the post-landslide survey, many photos (scale is around 1/10,000, but some have a scale of 1/4,000) taken by survey companies soon after the landslides were used. Also, the maps mentioned above were used.

3. TOPOGRAPHIC CHARACTERISTICS AND FACTORS OF THE LARGEST LANDSLIDE

3.1 Topographical Features

Pre- and post-landslide precise large scale maps and aerial photos are shown in Fig. 2 and in Photo 1-10. The results of the field surveys and interpretations of aerial photos (1948 to the time of the landslide) in the area of the largest landslide are as follows:

(1) A ridge collapsed and became a valley with a downslope dip of 25°. A pumice layer is the slip plane, and lava-scoria layers, with a maximum thickness of 160-170 m, were deposited above the pumice layer.

(2) Comparison of several aerial photos taken since 1948 shows that a small scale landslide at the foot of the collapsed ridge had been gradually growing (Photo 10-1 to -4), i.e. the right-side wall of the valley in the upper part of Denjo Gawa (River). This is particularly apparent by comparing those photos taken in 1959 and 1963.

(3) Some lineaments (observed as small stepped cracks) striking ENE-WSW were present at elevations from 2,025 to 2,150 m in the upper part of a small scale landslide. They are interpreted stereoscopically in Photos 2 and 3.

3.2 The Process of the Largest 1984 Landslide

Based on the above-mentioned facts, the causes and processes of the largest 1984 landslide are inferred as follows:

(1) Deposits of pumice and lava scoria layers had filled up the buried valley, which was exposed after the landslide.

(2) The foot of the collapsed ridge was intersected by the upper part of the Denjo Gawa (River) valley, where a knickpoint, seen as a waterfall, was present. Assuming that the fall kept receding, the foot of the ridge was subjected to the downward erosion of the valley, giving rise to instability.

(3) Items 3-1(2) and (3) indicate that bedrock creep was progressing in the lower part of the ridge. The position of enlargement of the small scale landslide coincides with that of the downstream portion of the buried valley exposed after the landsliding. This seems to suggest that groundwater flows in the buried valley enlarged the small scale landslide.

(4) The processes mentioned gave rise to instability in the ridge, and the landslide was induced by the earthquake. The landslide's plane overlies the pumice layer on the buried valley slopes. In the process of landsliding, sliding of the lower part of the valley fill induced the major landslide above. These landslides seem to have occurred simultaneously.

(5) A similar landform of an old landslide can be observed to the west of the 1984 landslide. This landform has probably been formed following the same processes as already mentioned, i.e. the receding fall in the lower part, the unstable foot, and, finally, landsliding.

The culmination of various destabilizing conditions such as the receding waterfall, downward erosion, and increased instability of the foot of ridge gave rise to both the large 1984 landslide and the prehistoric landslide mentioned in (5).

4. OTHER LANDSLIDES

Many other landslides occurred during the 1984 Naganoken-seibu Earthquake. Matsukoshi landslide ($2.3 \times 10^5 m^3$) and Takigoshi Landslide ($1.7 \times 10^5 m^3$) are the next largest. Ontake Kogen landslides are slightly smaller in size (the largest of them is $3 \times 10^4 m^3$). There were many other smaller landslides.

The process of Matsukoshi landslide is similar to the largest landslide previously discussed. As to Takigoshi landslide, it is inferred that a lava layer slid due to liquefaction of underlying lacustrine sediments. The straight scarp of Takigoshi landslide might be of structural origin. At Onkake Kogen, landslides were mostly of tephra layers.

Precise large scale topographic maps and aerial photos of pre- and post-landslides are shown in Fig 2-4 and Photo 11-20.

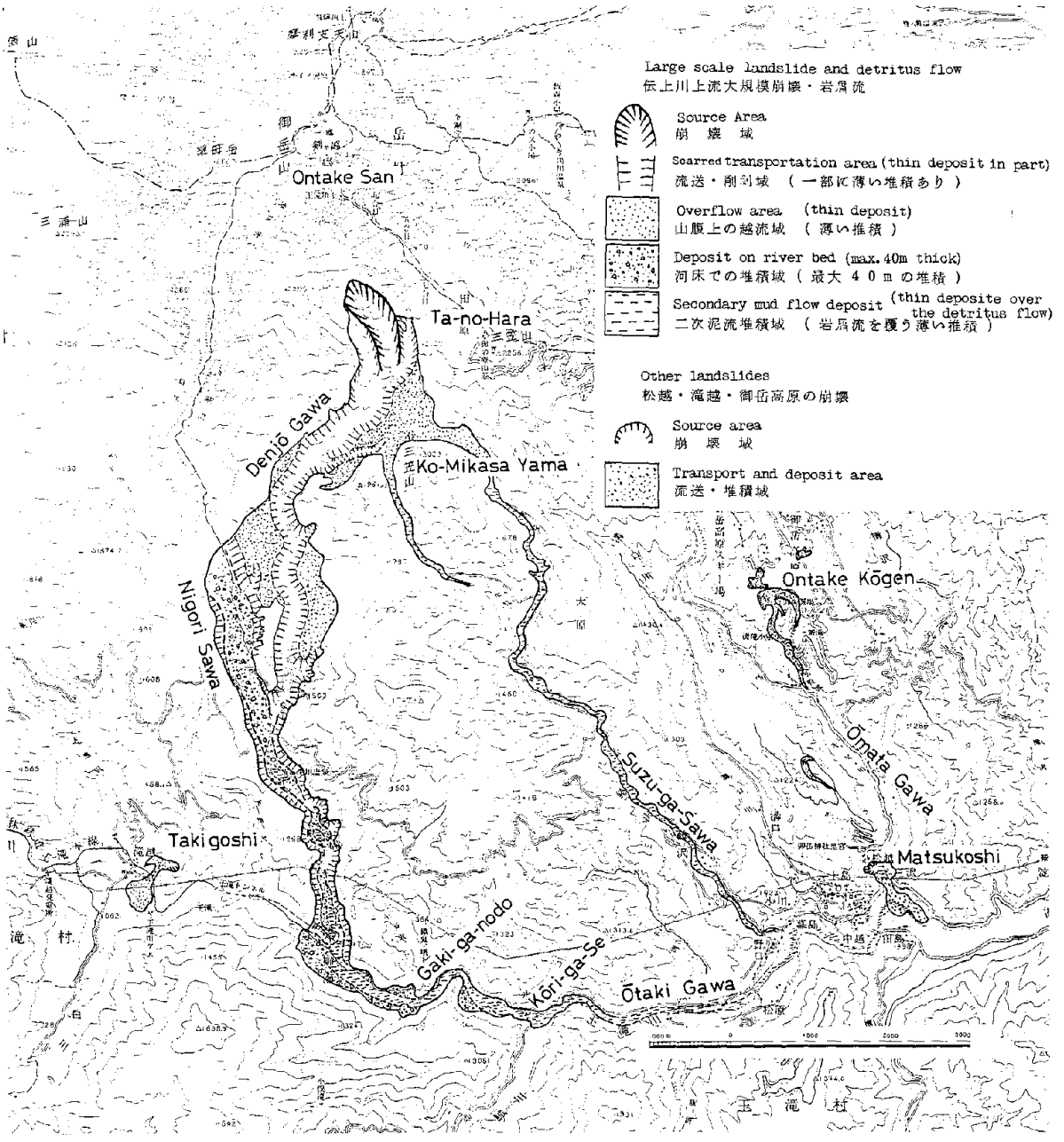

Fig. 1 Distribution of landslide and accompanying deposits
(except small landslides)

(notice San, Yama : mountain or peak
Gawa, Sawa : river or valley)

Fig. 2 Large—scale Landslide on the south slope of Ontake Volcano

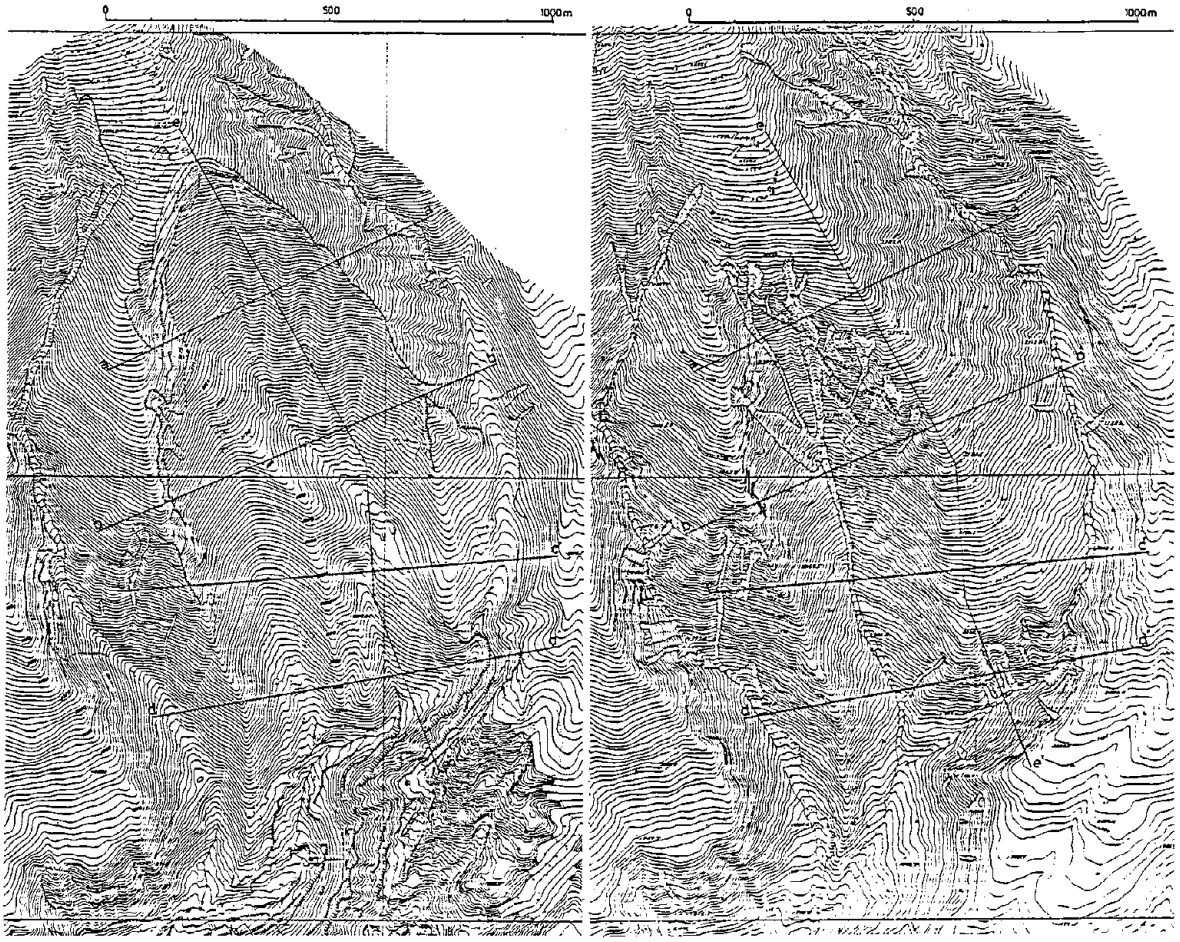

A) Post—landslide, 1/5,000 topographic map based on 1984. 9. 22 aerial photo, × 0.5

B) Pre—landslide, 1/5,000 topographic map based on 1969. 5 aerial photo, × 0.5

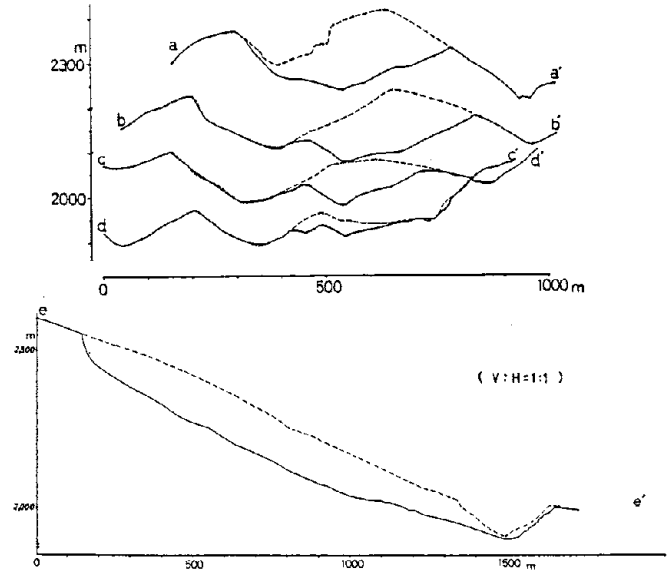

C) Profile of the landslide

Fig. 3 Matsukoshi Landslide

A) Post—landslide, 1/2,500 topographic map based on 1984. 9. 22 aerial photo, × 0.5

B) Pre—landslide, 1/2,500 topographic map based on 1969. 5 aerial photo, × 0.5

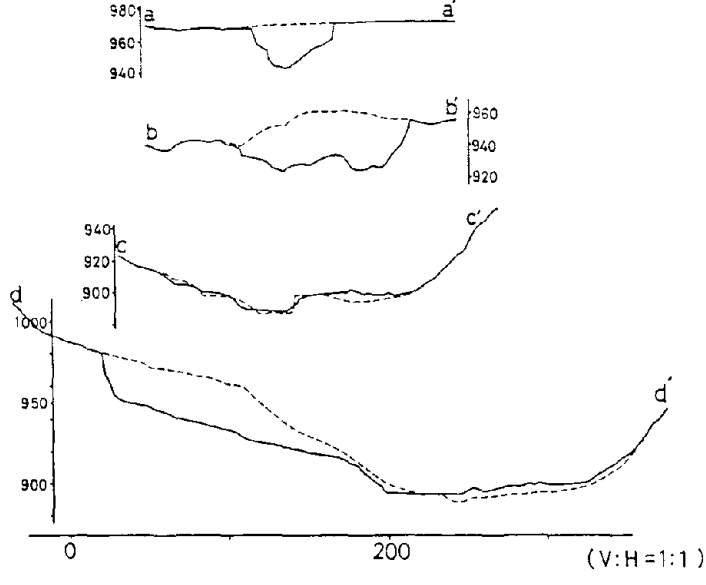

C) Profile of the landslide

Fig. 4 Takigoshi Landslide

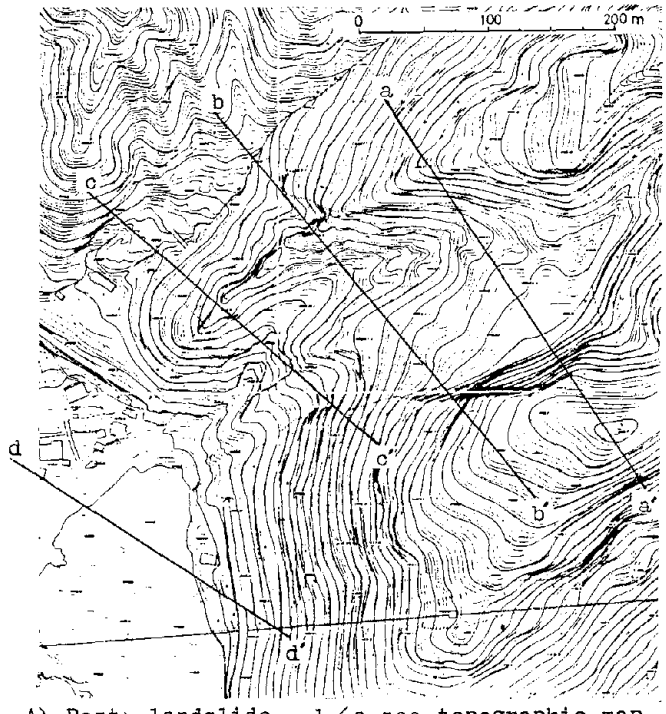

A) Post—landslide, 1/2,500 topographic map based on 1984. 9. 22 aerial photo, × 0.5

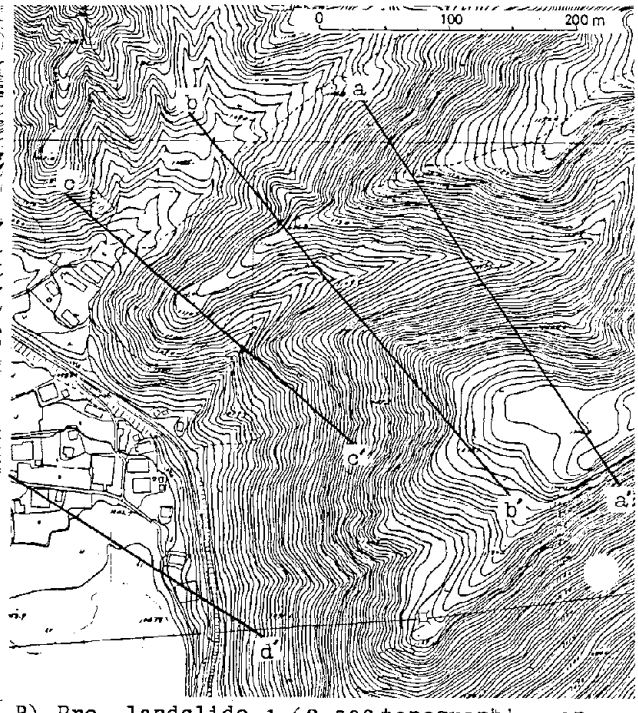

B) Pre—landslide, 1/2,500 topographic map based on 1969. 5 aerial photo, × 0.5

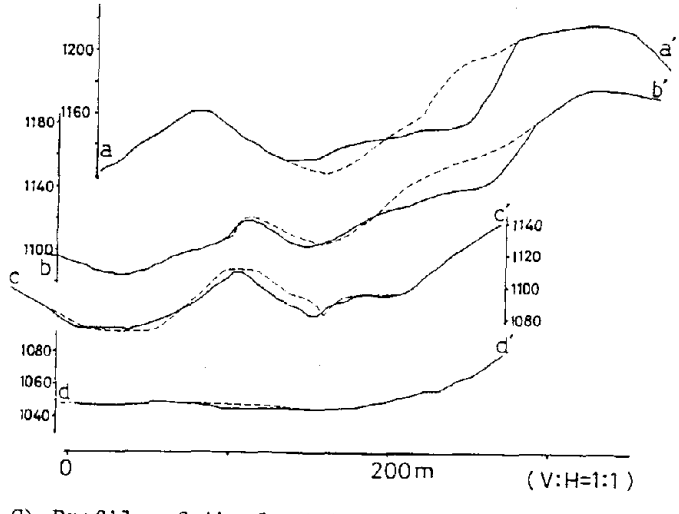

C) Profile of the landslide

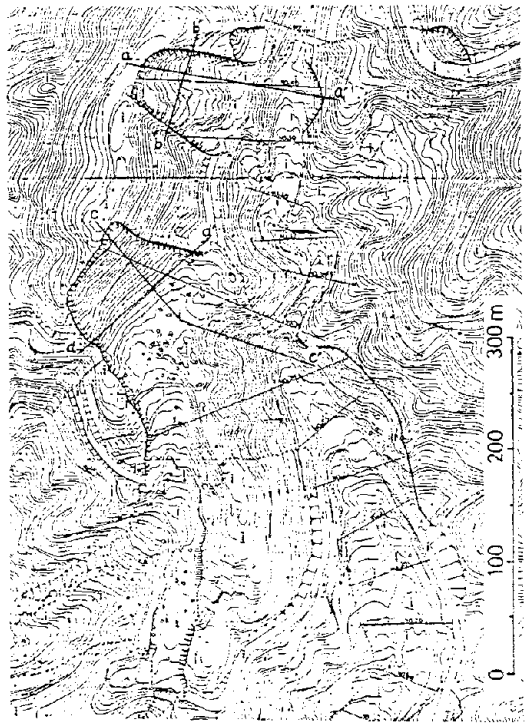

Fig. 5 Ontake Kōgen Landslides

A) Post—landslide, 1/1,000 topographic map based on 1984. 9. 22 aerial photo, × 0.18

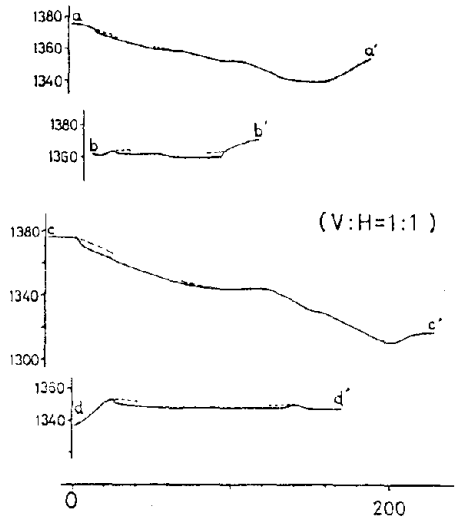

B) Profile of the landslides

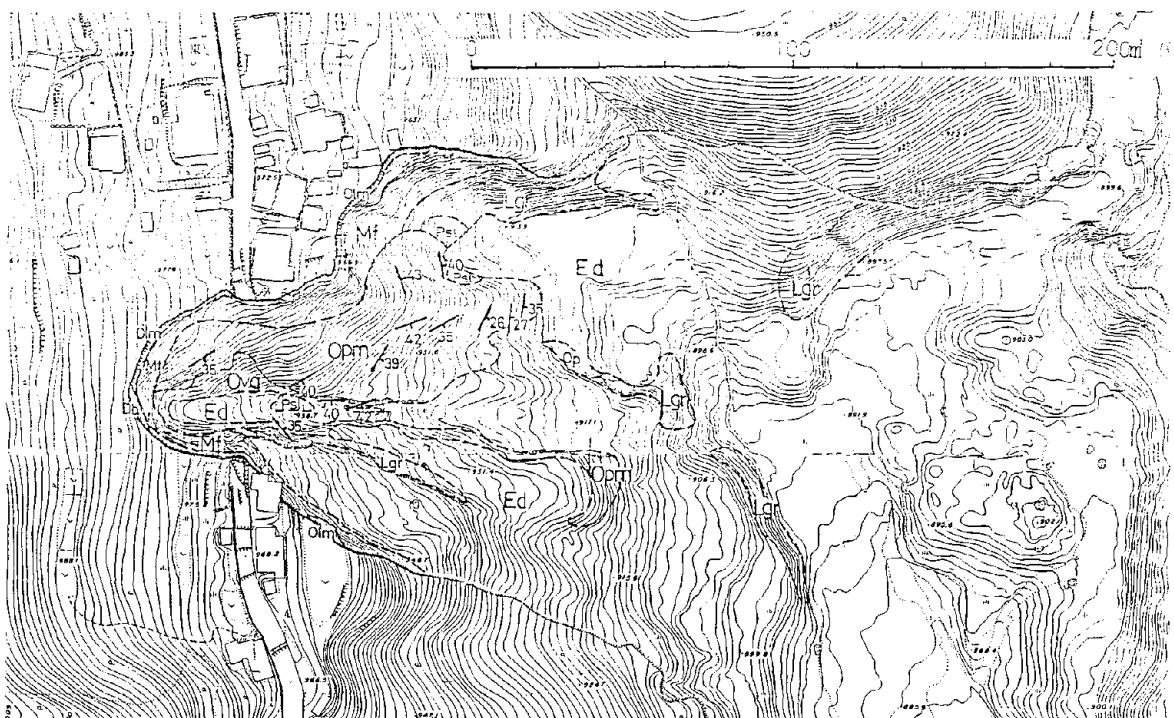

Fig. 3 · D) Surface geologic map of Matsukoshi Landslide

Legend

Quaternary	Holocene	Ed : Earth flow deposit accompanying Matsukoshi Landslide (sand and gravel)	unconsolidate
		Db : Debris (breccia)	
	Pleistocene (Volcanics of Ontake volc. and derived sed.	Olm : Loam	unconsolidate semiconsolidate
		Mf : Mud flow deposits and debris (sand and gravel, interbedded pumice layers)	
		Lgr : Lacustrine sediments (sand and gravel, interbedded pumice layers)	
		Opm : Pumice layer (thin)	
		Ovg : Mud flow deposit and lacustrine sed.(underlying) (sand and gravel)	semiconsolidate
Palaeozoic		Psl : Slate	consolidate

: Crack caused by the earthquake

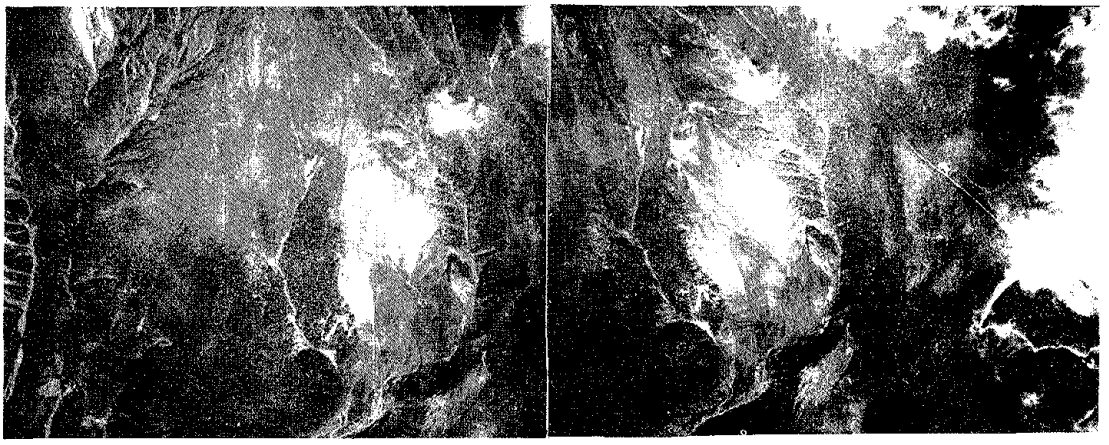

Photo. 1 Large-scale landslide on the south slope of Ontake Volcano taken on 1984. 9. 22 (8 days after the sliding)
王滝村伝上川上流大規模崩壊の崩壊部，崩壊8日後の1984．9．22 撮影，中日本航空 C2 4715～4716，約1/13,000(×0.40)

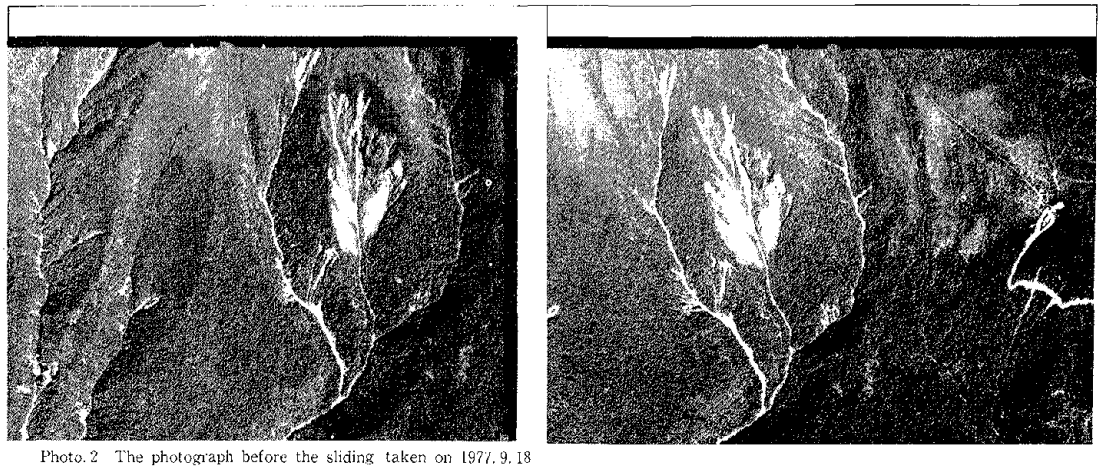

Photo. 2 The photograph before the sliding taken on 1977. 9. 18
同上地域の崩壊前の状況，1977．9．18 撮影，地理院 CCB-77-12 C6 17～18，約1/14,000(×0.43)

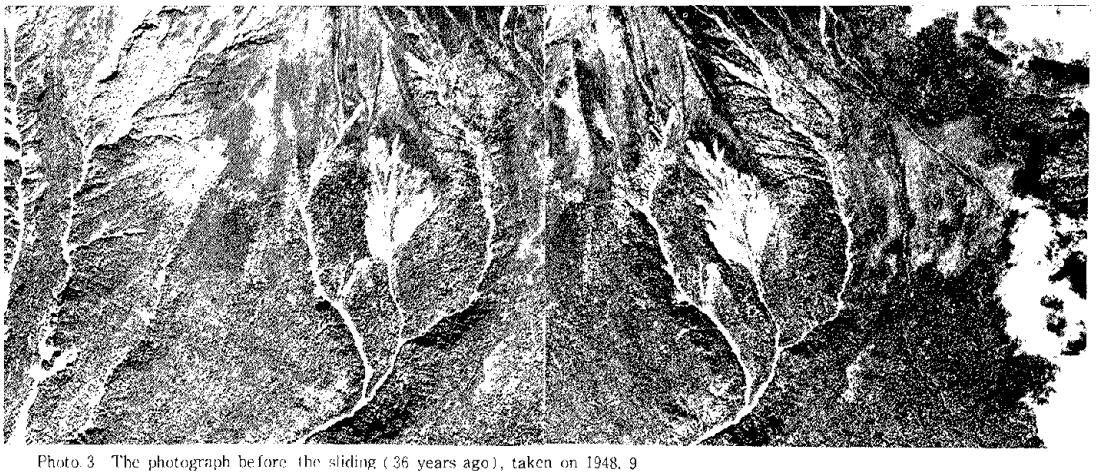

Photo. 3 The photograph before the sliding (36 years ago), taken on 1948. 9
同上地域の36年前の状況，1948．9 撮影，米軍 M1171 215～216，約1/36,000 (×1.0)

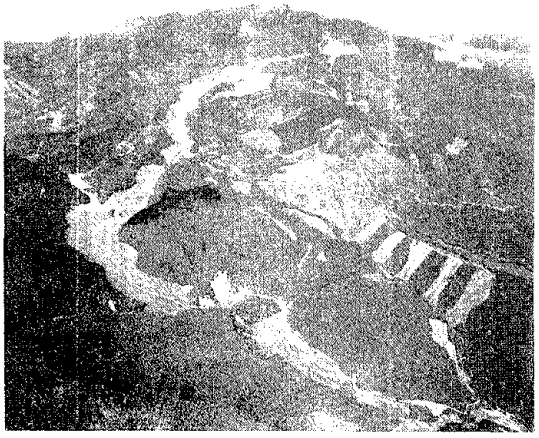

Photo. 4 Source area and accompanying detritus flow
伝上川上流大規模崩壊の全景，崩壊部(雲の直下)から濁川の流送部，王滝川本流の堆積部及び背後の湛水域，1984. 9. 17 中日本航空撮影

Photo. 5 Main scarp of the landslide
大規模崩壊最上部の滑落崖，1984. 9. 30 土木研究所撮影

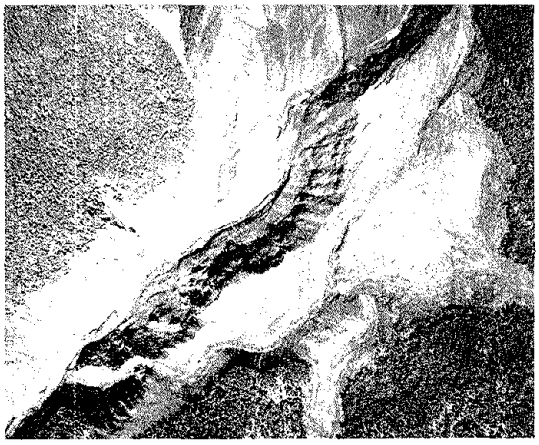

Photo. 6 Lower part of the landslide and overflow area
大崩壊直下の尾根に乗り上げた堆積物上の縞模様及び下部谷壁の削剝状況，1984. 9.22 中日本航空撮影

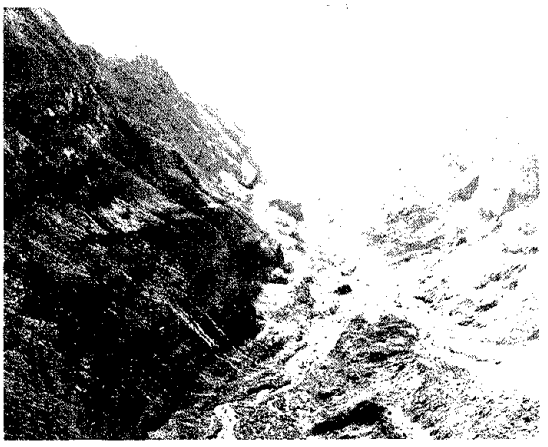

Photo. 7 Scarred transportation area of detritus flow
流送部の削剝状況，左岸谷壁は湧出した地下水による無数のガリー，1984. 11. 11 撮影

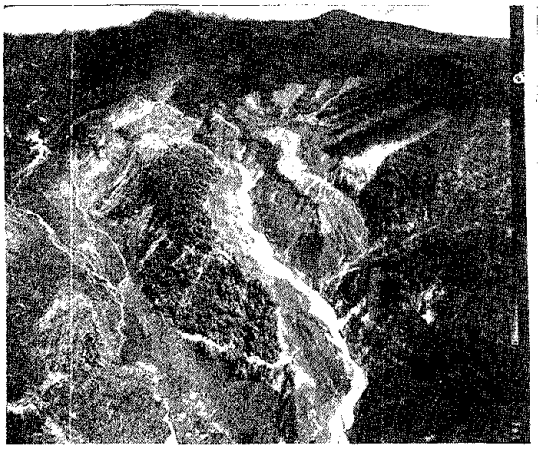

Photo. 8 Middle reaches of the detritus flow
隣りの沢（濁沢）への越流と堆積物表面の微地形（左下部），1984. 9. 17 朝日航洋撮影

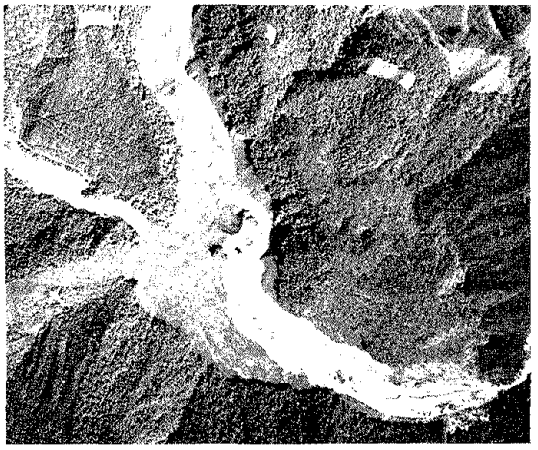

Photo. 9 Lower reaches of the detritus flow
濁沢（写真上部）・王滝川合流点付近における岩屑流及びその直後に生じた土石流の堆積状況，1984. 9. 17 朝日航洋撮影

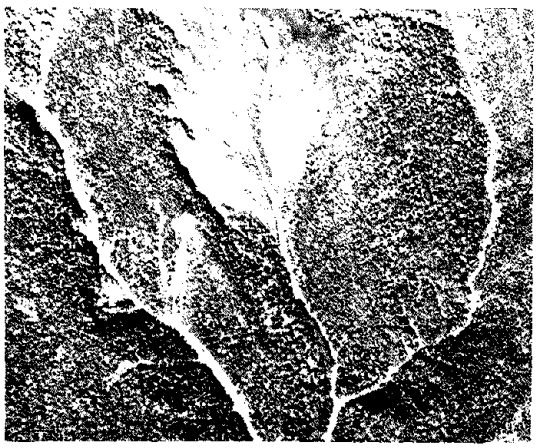

Photo. 10-1 Widening of shallow slide scar on the valley side since 36 years ago taken on 1948. 9
崩壊源下部での経年的な小崩壊の拡大状況，その①，1948. 9 撮影，米軍 M1171-215, 1/36,000 (×2.3)

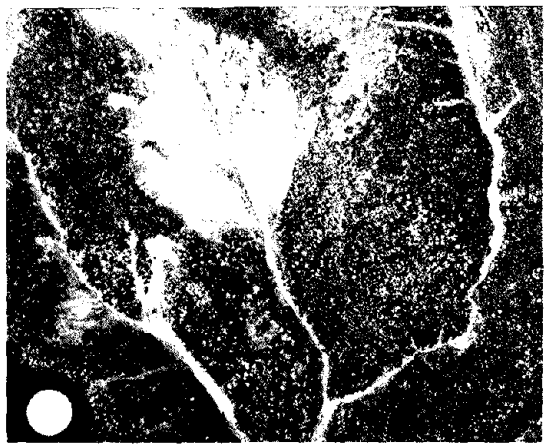

Photo. 10-2 Same place as 10-1 taken on 1959. 11.
同，その②，1959. 11 撮影，林野庁 山-148 10-C38, 1/15,000 (×1.0)

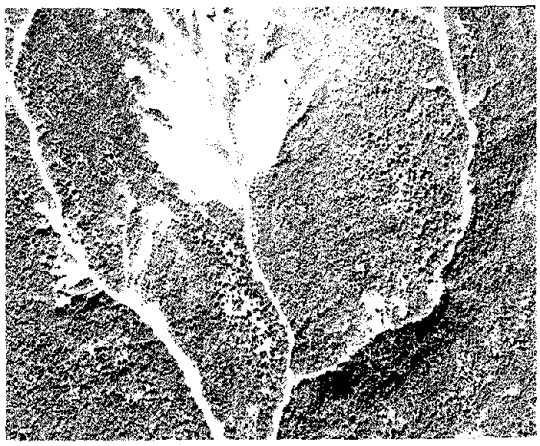

Photo. 10-3 Same place as 10-1 taken on 1969. 9.
同，その③，尾根末端部の小規模な崩壊の拡大に着目，尾根全体の微地形については Photo. 2 及び 3 参照，1969. 5 撮影，林野庁 山-560 C15-23, 1/17,000 (×1.2)

Photo. 10-4 Same place as 10-2 taken on 1979. 10
同，その④，1979. 10 撮影，林野庁 山-882 C14A-9, 1/17,000 (×1.1)

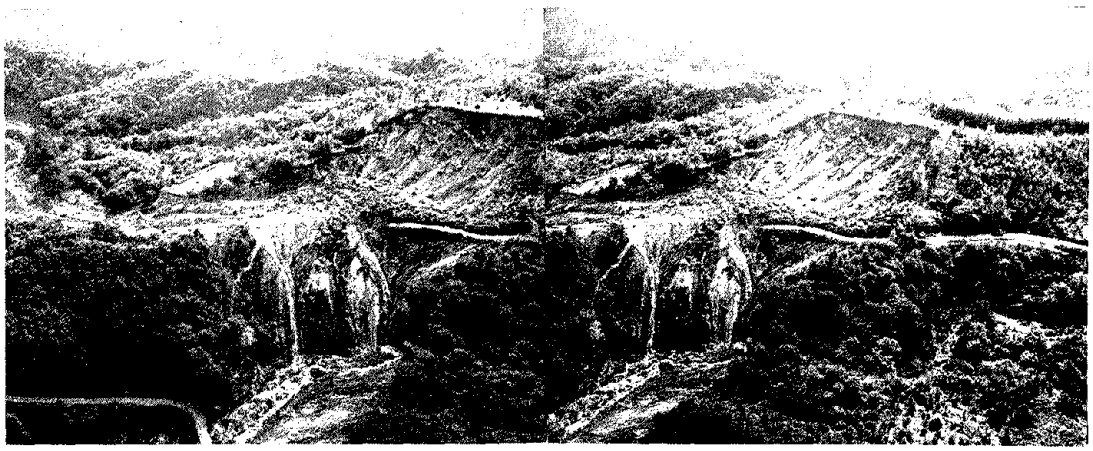

Photo. 11 Landslides of tephra layer on Ontake kōgen
御岳高原における表層崩壊，1984. 9. 30 土木研究所撮影

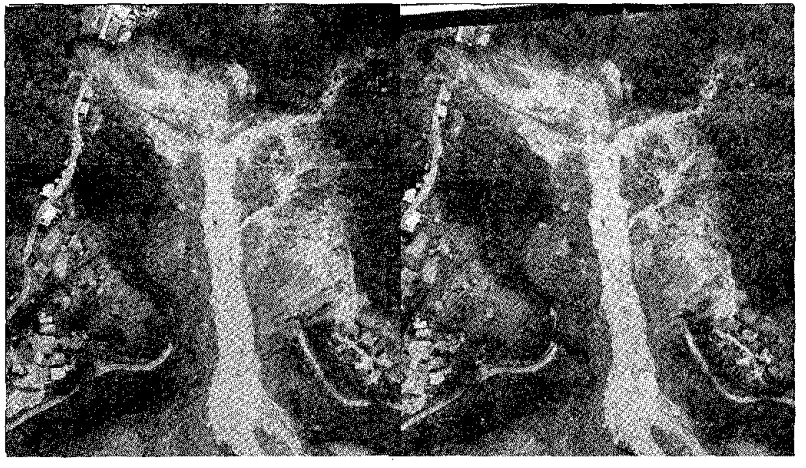

Photo. 12 Source area of Matsukoshi landslide
松越地区における崩壊，1984. 9. 15 撮影，協同測量 C9 8407~8408, 1/4,100 (×0.57)

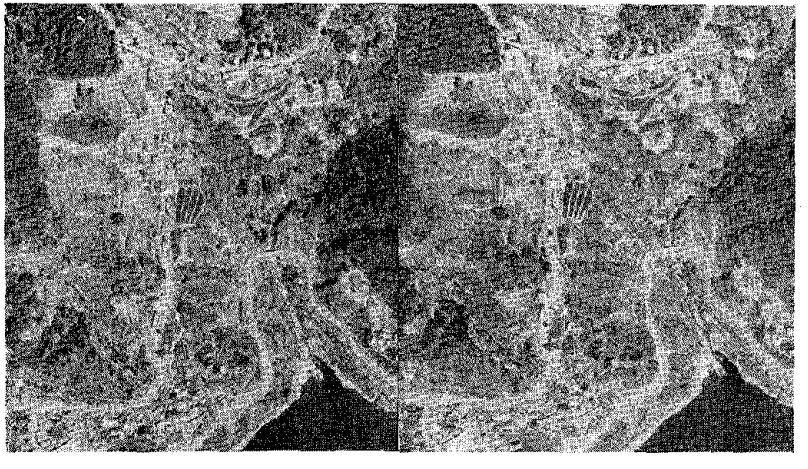

Photo. 13 Landscape before the landslide
(notice : Vertical exaggeration is less than photo. 12 because of the differences of focal lengths)
同上地域の崩壊前の状況，1969. 4 撮影，林野庁 山-560 C19 29--30 1/23,000 (×2. 2)

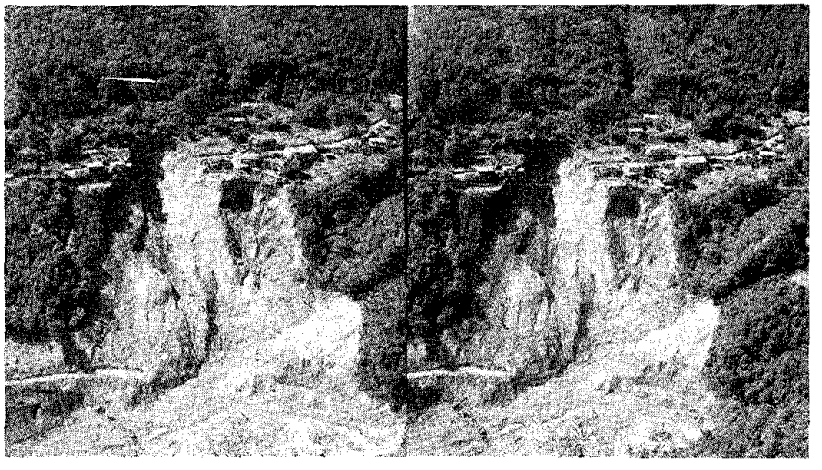

Photo. 14 Oblique view of source area of Matsukoshi landslide
松越地区における崩壊，斜め写真，1984. 9. 30 土木研究所撮影

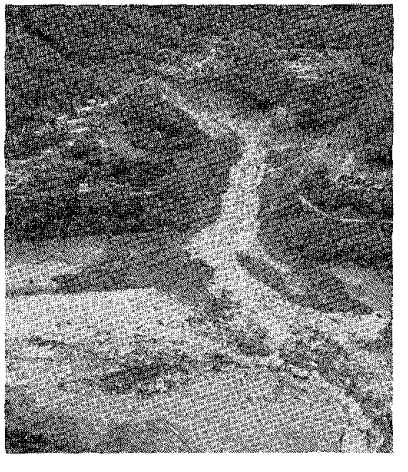

Photo. 15 Panoramic view of the landslide
崩壊の全景，1985. 9. 14 中日本航空撮影

Photo. 16 Slide plane (buried valleyslope) formed by tephra layers
崩壊によって露出した埋積谷斜面とこれを覆う急傾斜の軽石層，前方は滑落崖頂部，1985. 3. 24 撮影

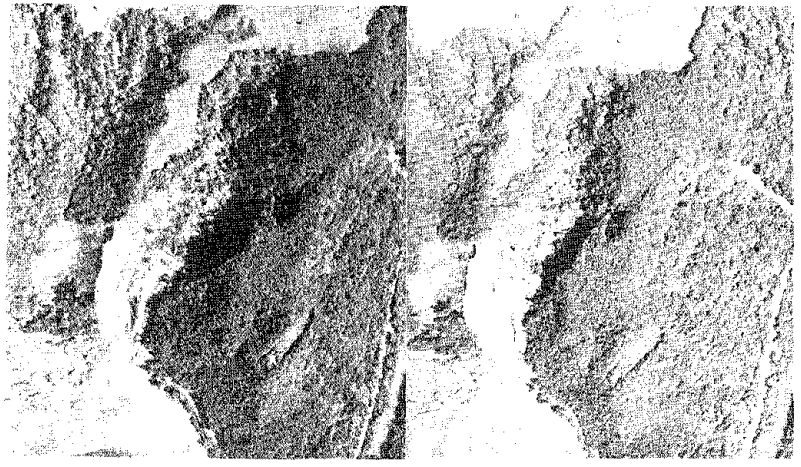

Photo. 17 Source area of Takigoshi landslide
滝越地区における崩壊，1984. 9. 22 撮影，朝日航洋 9606~9607, 1/ 7,700 (×0.65)

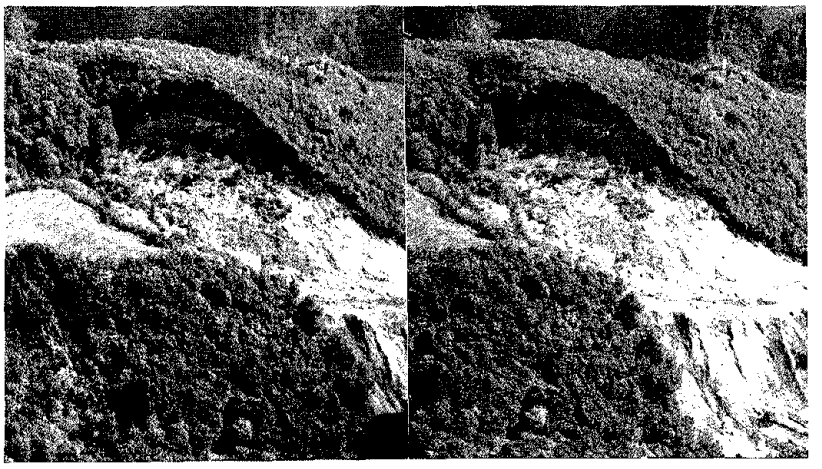

Photo. 19 Oblique view of source area of Takigoshi landslide
滝越地区における崩壊，斜め写真，1984. 9. 30 土木研究所撮影

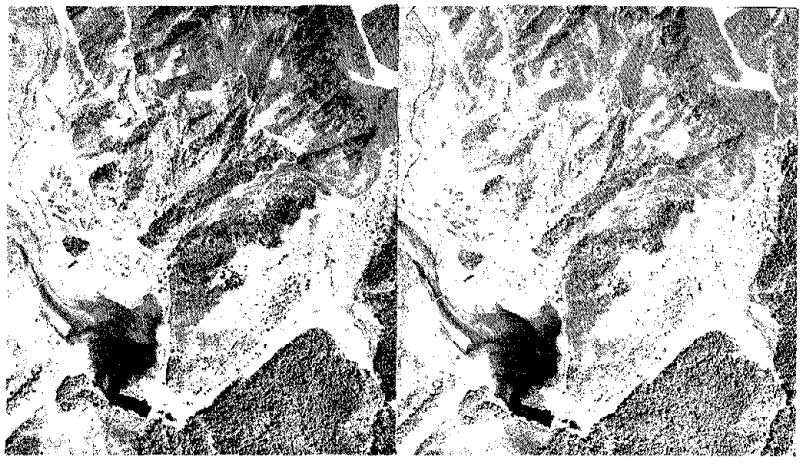

Photo. 18 Landscape before the landslide
(notice : Vertical exaggeration is less than photo. 17 because of the differences of focal lengths)
同上地域の崩壊前の状況，1969. 4 撮影，林野庁 山-560 C19 22~23 1/25,000 (×1.0)

Photo. 20 Panoramic view of the landslide
崩壊の全景，1985. 9. 14 中日本航空撮影

[Stereo view is possible for Photo. 1~3, 11~14, 17~19]

SEISMOLOGICAL STUDIES ON THE NAGANOKEN-SEIBU EARTHQUAKE, 1984 BASED ON JMA SEISMIC NETWORK

Minoru Takeo, Naoya Mikami and Masaji Ichikawa
Meteorological Research Institute, Japan Meteorological Agency (JMA)

ABSTRACT

The Naganoken-seibu Earthquake (M; 6.8) accompanied by a large-scale slope failure occurred on 14 September 1984. The source process of this earthquake was investigated in detail by using various seismic data obtained by the JMA seismic network.

Distribution of seismic intensities for the main shock suggests that the main shock was a peculiar earthquake which radiated short-period waves strongly. By using strong motion seismograms which were recorded at stations within one hundred kilometers of the epicenter, the distribution of dislocations and the character of the rupture propagation on the fault were investigated. Results from this analysis indicate that large dislocations ranging from 1.5 m to 2 m occurred at the shallower part on the fault plane. Such a localized large dislocation might have caused the strong radiation of short-period waves.

The size of the fault plane is 12 km X 6 km, and the seismic moment of the main shock is 3 X 10^{25} dyne*cm.

Ground motions at the summit of Mt. Ontake and at Kisofukushima were estimated by using the source process models obtained in this study. The results obtained are as follows:

	maximum displacement	maximum velocity
Summit of Mt. Ontake	15 (cm)	12 (cm/s)
Kisofukushima	18 (cm)	37 (cm/s)

1. INTRODUCTION

On 14 September 1984 at 0848 JST (Japan Standard Time) an earthquake accompanied by a large-scale slope failure, called "Ontake-kuzure," occurred at the western part of Nagano-Prefecture, Honshu, Japan. Focal parameters determined by the Japan Meteorological Agency (JMA) are as follows:

Epicenter:	35°49.3'N, 137°33.6'E
Focal depth:	2 km
Magnitude:	6.8

This earthquake was named "the Naganoken-seibu Earthquake, 1984" by JMA.

In the past, two earthquakes (Zenkoji Earthquake 1847 and Hida Earthquake 1858) with large landslides have occurred near the present epicenter. Detailed focal processes for these two earthquakes, however, were not obtained because of lack of instrumental observations. On the other hand, for the present earthquake there are many data observed at stations around the source region which belong to JMA, universities and other research institutes. In this study, we investigate the distribution of seismic intensities, focal mechanisms and the aftershock distribution of the main shock and of the largest aftershock, based on the data of JMA seismic network. Furthermore, by the use of strong motion seismograms obtained by JMA stations near the epicenter ($\Delta < 100$ km), we estimate the source process of main shock in detail. From this result, ground motions, which had periods longer than 1 second for the nearby source region are calculated. The results of this study provide useful fundamental data about the mechanism of the landslide.

2. DISTRIBUTION OF SEISMIC INTENSITIES

The distributions of seismic intensities for the main shock and the largest aftershock are shown in Figure 1. Radii of felt area (R) of these two earthquakes are both about 400 km. According to the relation between R and JMA magnitude (M) for shallow earthquakes in Japan [Ichikawa (1960)]:

$$M = -1.0 + 2.7*\log(R),$$

magnitudes of the main shock and the largest aftershock are both about 6.0. Though this value is consistent with the magnitude of the largest aftershock (M = 6.2), it is too small for the main shock magnitude (M = 6.8).

The maximum intensity reported by JMA was 4 (JMA scale) for the main shock and 3 for largest aftershock, respectively. It is reported that in the source region the acceleration of the ground motion of the main shock exceeded gravitational acceleration [Kuroiso et al. (1985), Ito et al. (1985)]. These facts suggest that the main shock is characterized by high-frequency seismic waves radiated rather strongly compared with the ordinary inland shallow earthquakes in Japan.

3. AFTERSHOCK DISTRIBUTION

Figure 2 shows the spatial distribution of aftershocks that occurred from September 14 to October 20. Their hypocenters were routinely determined by JMA. Most of the aftershocks are distributed on an almost vertical plane striking in the N70°E direction. In order to see the aftershock distribution in detail, the aftershocks are plotted in Figure 3 by dividing the period of time. The main shock is located at the center of the aftershock area (region A) that occurred in 3 hours immediately after the main shock. Assuming that region A is the source area of the main shock, the fault length is about 12 km. The largest aftershock occurred in the western edge of region A. Judging from the aftershock area (region B) following the largest aftershock in 3 hours, its fault is conjugate to the main shock fault. After September 27, the number of aftershocks increased in the eastern part of region A, and many events occurred in regions C and D. The aftershock distribution is deeper eastward and the activity is lower near the main shock hypocenter.

4. FOCAL MECHANISM

Records obtained by JMA 59-type seismographs (T_0 = 5 sec, h = 0.7, V - 100) indicated that the main shock consisted of two events and that a small pre-event preceded the large fracture (main event) about 1.5 seconds [Ishikawa et al. (1985)]. The starting point of the main fracture was determined to be about 3.7 km west of the main shock epicenter (pre-event epicenter) by Ishikawa et al. (1985). We determined the mechanism solutions of the main shock (main event) and the largest aftershock by using the P-wave first motion data of JMA and of WWSSN long-period records. In Figure 4 are shown the lower hemisphere equal-area projection of the fault plane solutions. Both earthquakes have strike-slip faulting with NW-SE maximum pressure axis. The nodal plane of the main event striking in N70°E direction agrees well with the strike of the aftershock distribution. For this reason, we consider this nodal plane to be the fault plane. The fault plane of the largest aftershock is considered to be the nodal plane striking in N-S direction.

5. ANALYSIS OF THE SOURCE PROCESS

The source process of the main shock was analyzed by using the records obtained by the JMA strong motion seismographs at Iida (IID), Takayama (TKY), Matsumoto (MTM) and Gifu (GIF), and by the long-period seismographs at Matsushiro Seismological Observatory (MAT) of JMA. The strong motion seismograms are shown in Figure 5. As exhibited in Figure 6, the above four stations are distributed around the epicenter of the main shock, and the distances from the epicenter to the stations are 43 km, 46 km, 60 km and 86 km, respectively.

In order to carry out the analysis of the source process, the seismograms were digitized at a rate of 0.1 mm on each record. The distortion of the original records due to a mechanical recording system were corrected after the digitization, except for large traces just after the direct S wave arrival on the records at IID and MTM. After these corrections, the digitized records were also interpolated at a rate of 4 samples per second.

The digitized records for the vertical component at each station were not used in the analysis of the source process, because the records were too small to use.

In addition to these strong motion seismograms, records obtained by long-period velocity type seismographs (natural period; about 30 seconds) installed at Matsushiro Seismological Observatory were used in the analysis of the source process, in order to cover the eastern side of the epicenter.

The records were transformed to those equivalent to the JMA strong motion seismograms. Arrows in Figure 7 indicate times when the records were off scale.

In order to investigate the distribution of the dislocation and the character of rupture propagation, a nonlinear inversion method [Takeo (1985)] was used. In the present study, the fault of the main shock was divided into twelve sections at 3 km intervals, and double couple point sources were arranged in the center of the sections. The source process of the earthquake was assumed to be expressed by an integration of the double couple point sources having the same source time functions. The source mechanism, obtained by the distribution of compressions and dilatations of P waves of the main event, was used for that of each source on the fault. Horizontally stratified velocity structures were assumed for the calculation of Green's functions, too.

t_j^s and m_j denote the starting time of fracture and the seismic moment at j-th point source, respectively. f_{ij} denotes Green's function which formulates the i-th seismogram due to the j-th point source. Then, the synthetic seismogram ($F_i(t)$) corresponding to the i-th observed seismogram ($O_i(t)$) can be expressed as:

$$F_i(t) = \sum_j m_j * f_{ij}(t-t_j^s).$$

We determine t_j^s and m_j by minimizing the least-square error ($S(P)$) defined by

$$S(P) = \sum_i w_i * [O_i - F_i(p)]^2$$

where w_i is the weight for the i-th seismogram and p is the column vector of parameters. $S(p)$ is a nonlinear function for t_j^s, so that this inverse problem is nonlinear. We employ the modified Marqurdt method in order to solve this nonlinear inverse problem.

In this study, we also investigated the difference of final solution due to the difference in velocity structures used in the calculation of Green's functions. Green's functions were calculated by the use of two velocity structures as shown in Figure 8. In order to calculate Green's functions, DWFE method [Olson (1982)] was used for the broken-line structure (structure-A). Furthermore, taking into account the effect of unelastic attenuation of the crust, Green's functions were calculated for the solid line structures (structure-B) [Takeo (1984)]. The assumed Q structure of the crust is shown in the right side of Figure 8. A fairly low velocity in the surface layer is assumed, and the effect of unelastic attenuation is not taken into account in the structure-A. Therefore, the seismic moments investigated by using the structure-A may be nearly minimum values. On the other hand, the effect of unelastic attenuation in the surface layer of the structure-B is fairly low-Q and the seismic moments investigated by using the structure-B may be nearly maximum values.

The resolution of frequency for the analysis data was about 1 Hz, because the records were digitized at a rate of 4 samples per second. In this study, we divided the fault plane into twelve sections at intervals of 3 km. Judging from the average value of rupture velocity and rise time of shallow earthquakes, and from the distances and the solid angles from the fault to the stations, this division may be enough to analyze the waves over the frequency range from zero to one Hertz. The distribution of aftershocks occurring before the largest aftershock and the point sources are shown in Figure 9. The parameters m_j and t_j^s represent the source process in the three square kilometers region round about the j-th point source. The rise time of each point source represents the duration of the source process in each region.

Twenty four parameters of m_j, t_j^s (j=1-12) were investigated by the use of the two different velocity structures, independently. The rise time of double couple sources was assumed to be 1.5 seconds. These final solutions are shown in Figure 10. Instead of the distribution of seismic moments, the average dislocations at each region are shown in Figure 10.

The solutions are influenced by the initial values of parameters because of the nonlinearity in this problem. There were several solutions which showed much small residuals in comparison. Large minus seismic moments were given in some solutions. The minus moment may be caused by the difference of velocity structure for the real and assumed crust, irregularity in the rise time function of dislocation, variation in the source mechanisms on the fault plane, and the inverse dislocation. In view

of the evidence that the shortest epicentral distance used in the present study was about 40 km, further discussion on this matter is meaningless. Particularly, source processes with large minus seismic moments in the middle part of the fault plane may require one to suppose there were very complicated distributions of the initial stress and fracture strength in and around the fault. Such a complicated dynamics situation seems to be unnatural, so that the solution having smaller residual and no large minus moments was adopted as a final one.

The synthetic seismograms calculated by using the final solution are compared with the observed seismograms. As shown in Figure 11, the synthetic and observed seismograms agree very well. The structure-B was slightly revised, as shown in Figure 8 with the thin solid lines, in order to fit the S-P time in the Green's function to the observed S-P time at MTM and MAT.

In spite of the difference of the velocity structures used in the calculation, the overall characteristics of the final solutions are similar to each other. More concrete, the fracture starts at the shallower point in the central part of the fault and spreads over the whole source region within about 3 seconds. The large dislocation occurs in the near surface region. The field investigation suggests that the acceleration may be larger than the gravitational acceleration in the region ranging from 1 km to 4 km westward of the epicenter [Kuroiso et al. (1985), Ito et al. (1985)]. This evidence is consistent with the dislocation estimated in this study.

The dislocation at the deeper part of the fault seems to be small. In particular, the final solutions obtained by the two different velocity structures suggest that no dislocation may occur at the deeper part of the western edge on the fault where the largest aftershock occurred.

The total seismic moments estimated from the final solutions for the structure-A and the structure-B, which are named model-A and model-B, are 2×10^{25} dyne*cm. The maximum dislocations on the fault estimated from the model-A and the model-B are about 1.5 m and about 2 m, respectively. The consistence between the two models suggests that the final solutions are highly reliable.

The seismograms at TKY, IID, and GIF, calculated from the final solutions, are shown in Figure 12. High frequency waves in the later part of the seismograms of the mode-A are caused by the calculation without the unelastic attenuation in the crust. However, these synthetic and observed seismograms agree very well. In particular, the seismograms of the vertical components are fairly consistent with the observed seismograms which were excluded from the analysis data.

6. ESTIMATION OF GROUND MOTION IN SOURCE REGION

Using the source process models obtained in the former section, the ground displacement and velocity whose period is longer than 1 second at the summit of Mt. Ontake (Δ = 16.3 km) and at Kisofukushima (Δ = 13.0 km) were estimated. Since the divided sections at intervals of 3 km used in the former section were too large to calculate the ground motion of these short epicentral distances, we divided the fault plane into forty sections at intervals of 1.5 km. Moments and fracture starting times of each source were interpolated from the model-A and -B. Figure 13 shows the calculated ground displacement and velocity. At the summit of Mt. Ontake the estimated maximum displacement and velocity are 8.3 cm (model-A), 15 cm (model-B), and 11 cm/sec (model-A), 12 cm/sec (model-B), respectively. The location of Kisofukushima is in the direction of strong SH radiation, so that the N-S component of ground motion is predominant. The maximum displacement and velocity are estimated to be 14 cm (model-A), 18 cm (model-B) and 33 cm/sec (model-A), 37 cm/sec (model-B), respectively.

7. CONCLUSION

The Naganoken-seibu Earthquake, 1984 was analyzed on the basis of the data obtained by the JMA seismic network.

Distributions of seismic intensities for the main shock and the largest aftershock suggested that the main shock is a peculiar earthquake which radiated short-period seismic waves strongly. Results from the analysis of strong motion seismograms indicate that dislocation is inhomogeneously distributed on the fault plane and has a maximum of about 1.5-2 m.

Such a localized large dislocation might cause the strong radiation of short-period waves.

From the distribution of dislocation on the fault, the size of the source area is approximately 12 km X 6 km. The total seismic moment of the main shock is estimated to be $3(\pm 1) \times 10^{25}$ dyne*cm.

Using Aki's formula:

$$\log(M_0) = 1.5*M_S + 16.0 \qquad \text{[Aki (1972)]},$$

surface wave magnitude (M_S) is calculated to be $6.3(\pm 0.1)$.

Ground motion, with periods longer than 1 second, accompanying the main shock were estimated by using the final solutions. The results obtained as follows:

	maximum displacement	maximum velocity
Summit of Mt. Ontake	15 (cm)	12 (cm/s)
Kisofukushima	18 (cm)	37 (cm/s)

8. REFERENCES

Aki, K., (1972), Scaling Law of Earthquake Source Time-Function, Geophys. J.R., 31, 3-25.

Public Works Research Institute (1982), Analysis of Long-period Seismic Motion on the Basis of JMA Strong Motion Seismograms.

Ichikawa, M., (1960), On the Relation between Earthquake Magnitude and Maximum Value of Epicentral Distance at Limit of Perceptibility. Quarterly Journal of Seismology, 25, No. 3, 13-17.

Ishikawa, Y., N. Mikami, N. Hamada and S. Kashiwabara (1985), Naganoken-seibu Earthquake and Its Preceding Seismic Activity, Abstr. Seismo. Soc. Japan, No. 1, 1.

Ito, K., A. Kuroiso and Y. Umeda (1985), Region of Large Acceleration Accompanied with Naganoken-seibu Earthquake, 1984, Abstr. Seismo. Soc. Japan, No. 1, 18.

Kuroiso, A., K. Ito, Y. Iio, Y. Umeda and I. Muramatsu (1985), Stones and Bogwoods Jumped due to Seismic Waves, Abstr. Seismo. Soc. Japan, No. 1, 17.

Olson, A. H., (1982), Forward Simulation and Linear Inversion of Earthquake Ground Motion, Ph.D thesis, University of California, San Diego.

Takeo, M., (1984), Synthetic Seismograms near Source Region Taking into Account Unelastic Attenuation of Crust, Abstr. Seismo. Soc. Japan, No. 2, 255.

Takeo, M., (1985), Inversion of Source Process by Using Near-Field Seismograms, Abstr. Seismo. Soc. Japan, No. 1, 168.

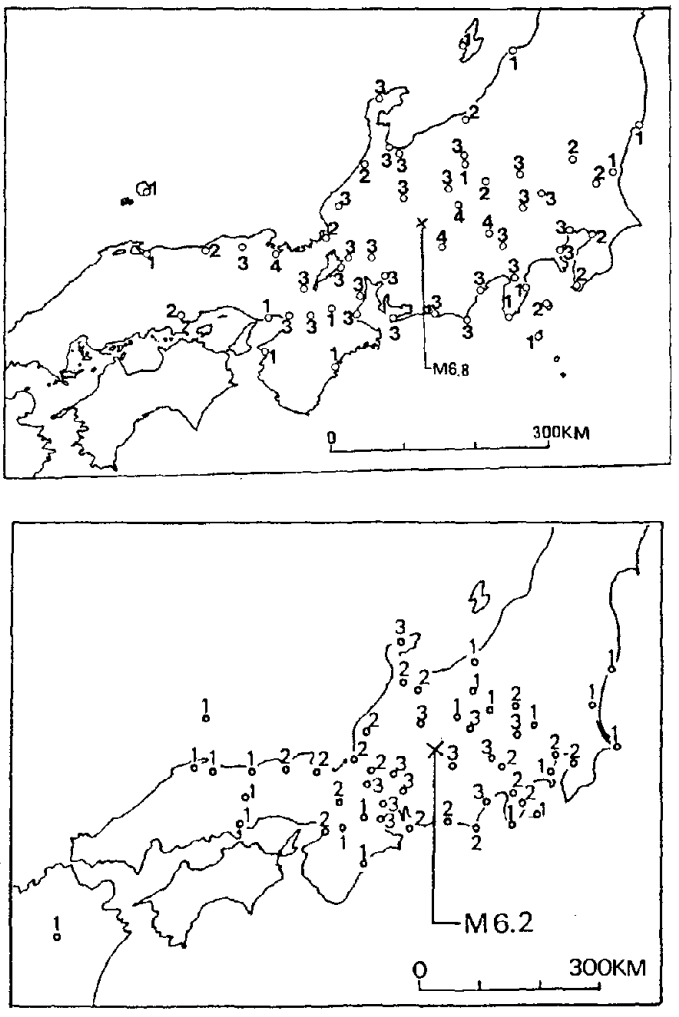

Fig. 1. Distributions of seismic intensities (JMA scale) for the main shock (M = 6.8, Sep. 14) and the largest aftershock (M = 6.2, Sep. 15).

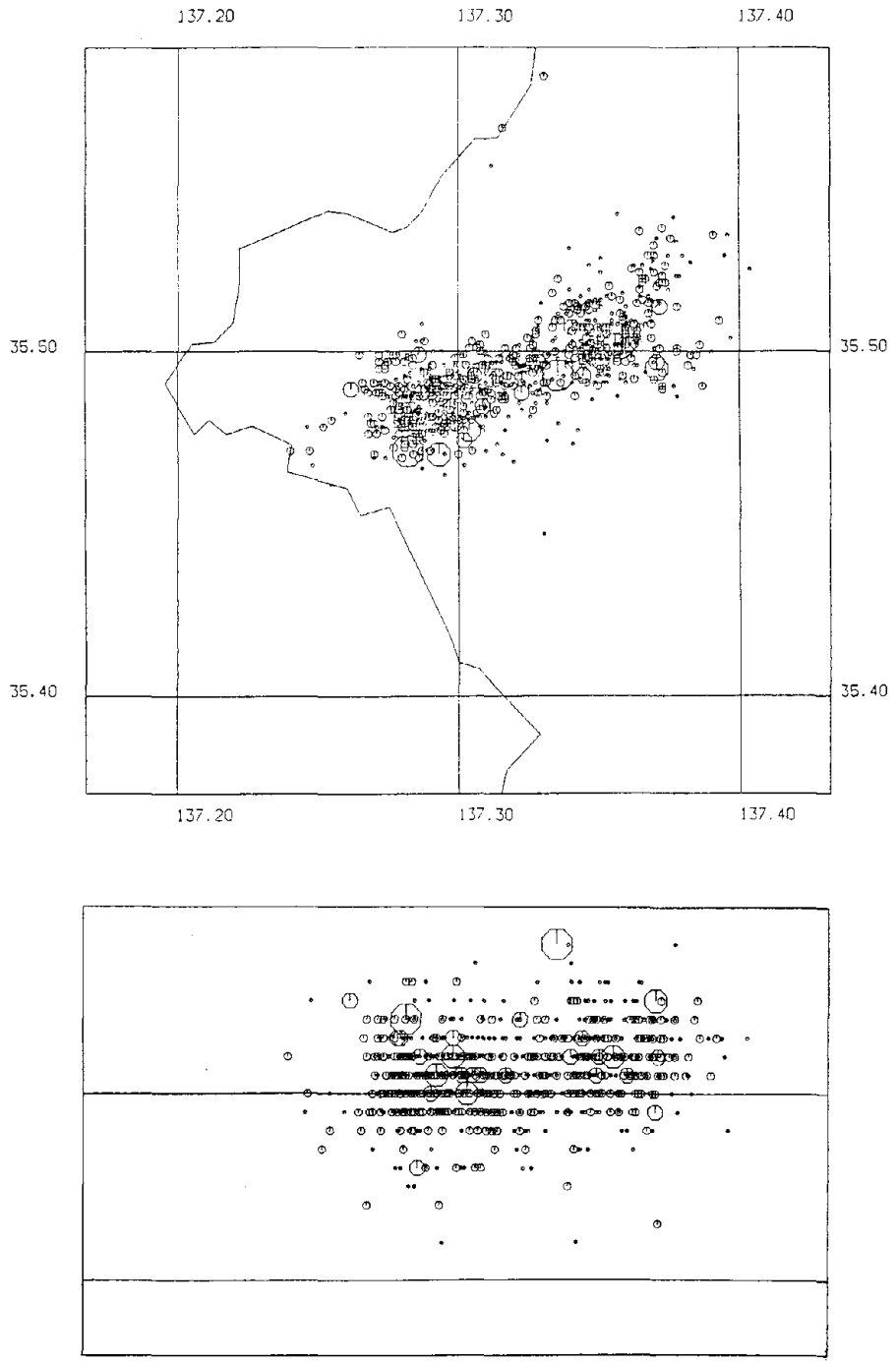

Fig. 2. Spatial distribution of aftershocks that occurred from Sep. 14 to Oct. 20.

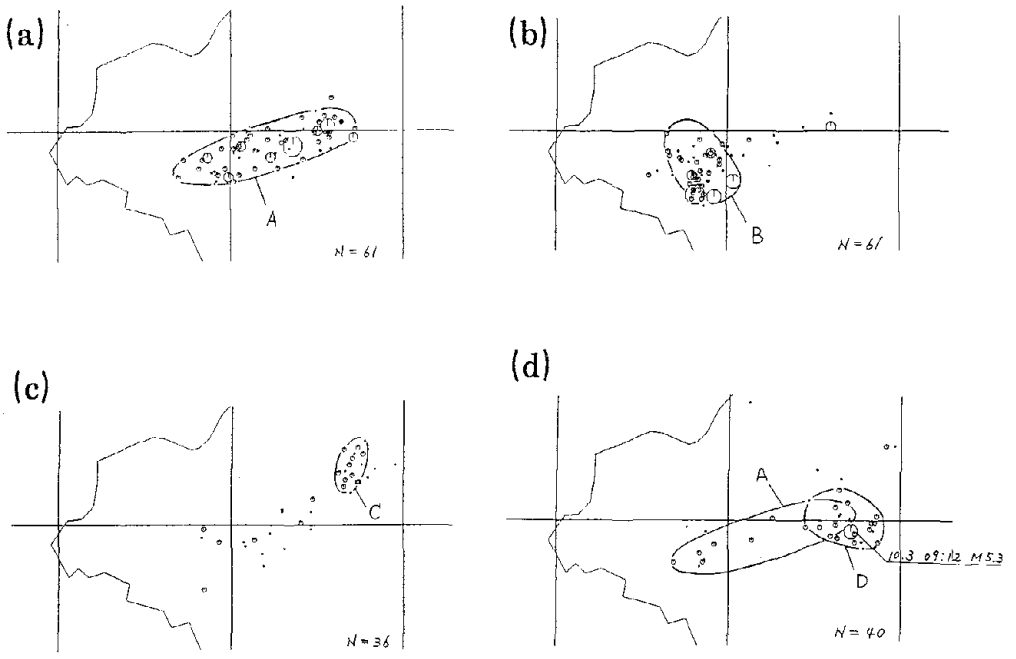

Fig. 3. Epicenter distribution for four periods: (a) 3 hours period immediately after the main shock. (b) 3 hours period immediately after the largest aftershock. (c) Sep. 27 to Sep. 29. (d) Oct. 3 to Oct. 4.

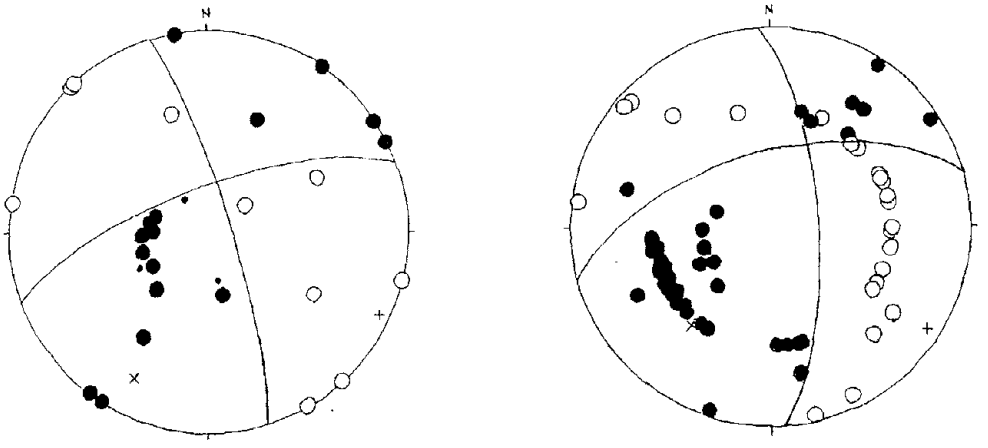

Fig. 4. The focal mechanisms of the main shock (main event) and the largest aftershock plotted onto the lower hemisphere by equal-area projection. Solid and open circles indicate compression and dilatation.

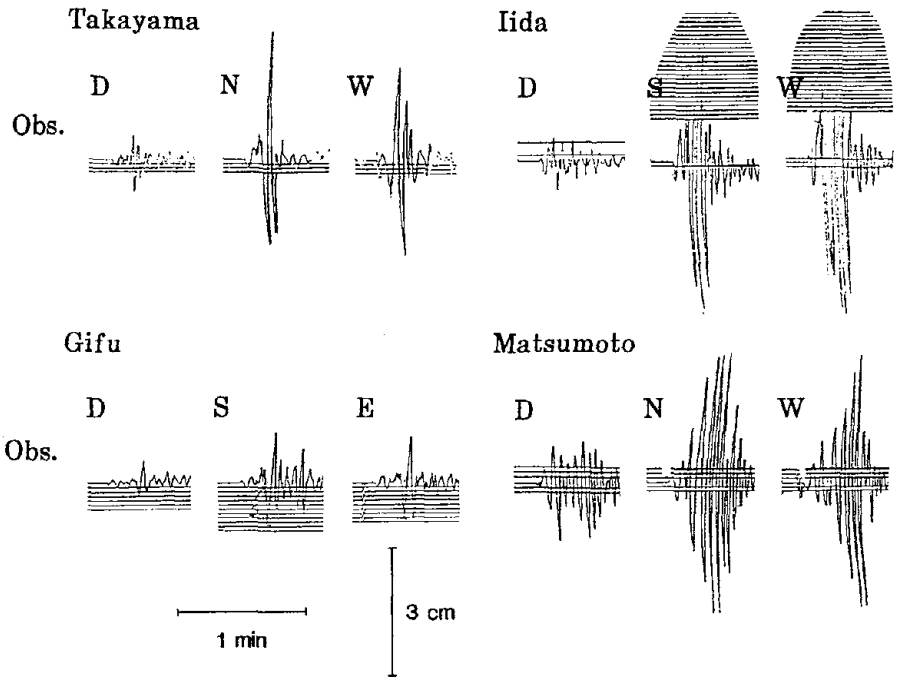

Fig. 5. Strong-motion records used in this analysis.

Fig. 6. Location of the main shock epicenter (Star) and the JMA stations used in the analysis of the source process.

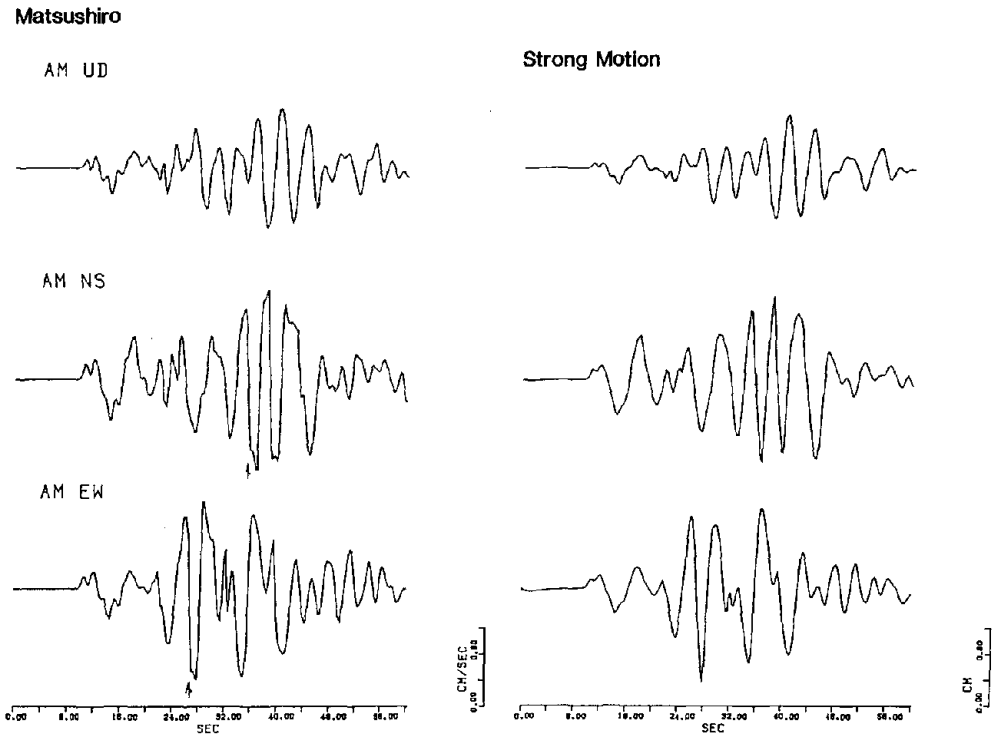

Fig. 7. The long-period velocity type seismograms at Matsushiro (left) and the corresponding strong motion seismograms (right).

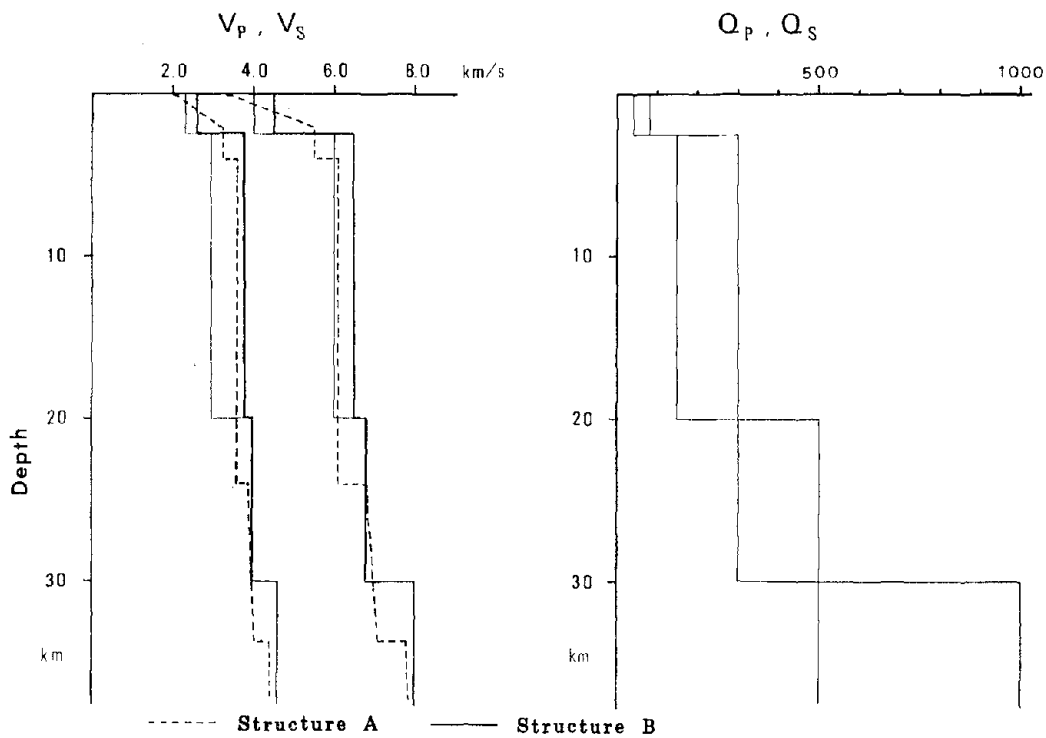

Fig. 8. Models of velocity and Q structure used for calculation of Green functions. Dashed and solid lines indicate structure A and B, respectively. Thin solid lines indicate structure B revised for MTM and MAT.

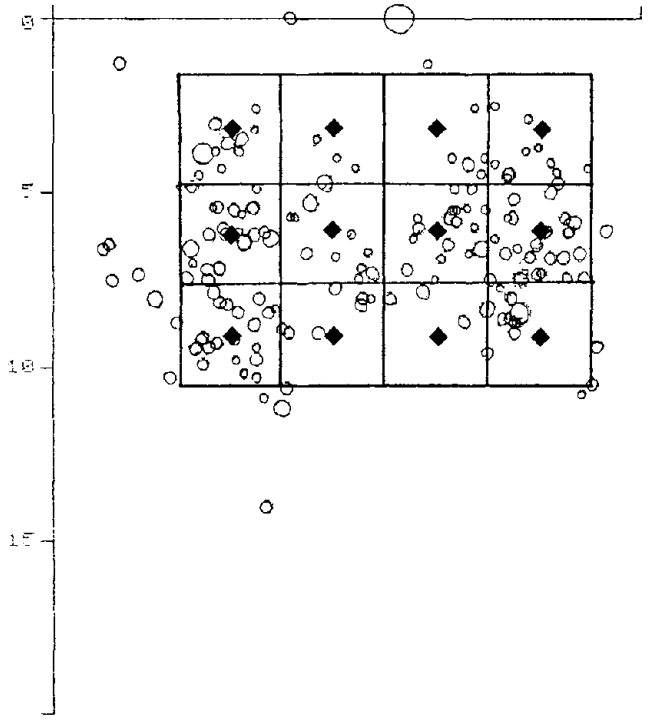

Fig. 9. Arrangement of the point sources plotted on cross-section with aftershocks that occurred before the largest aftershock.

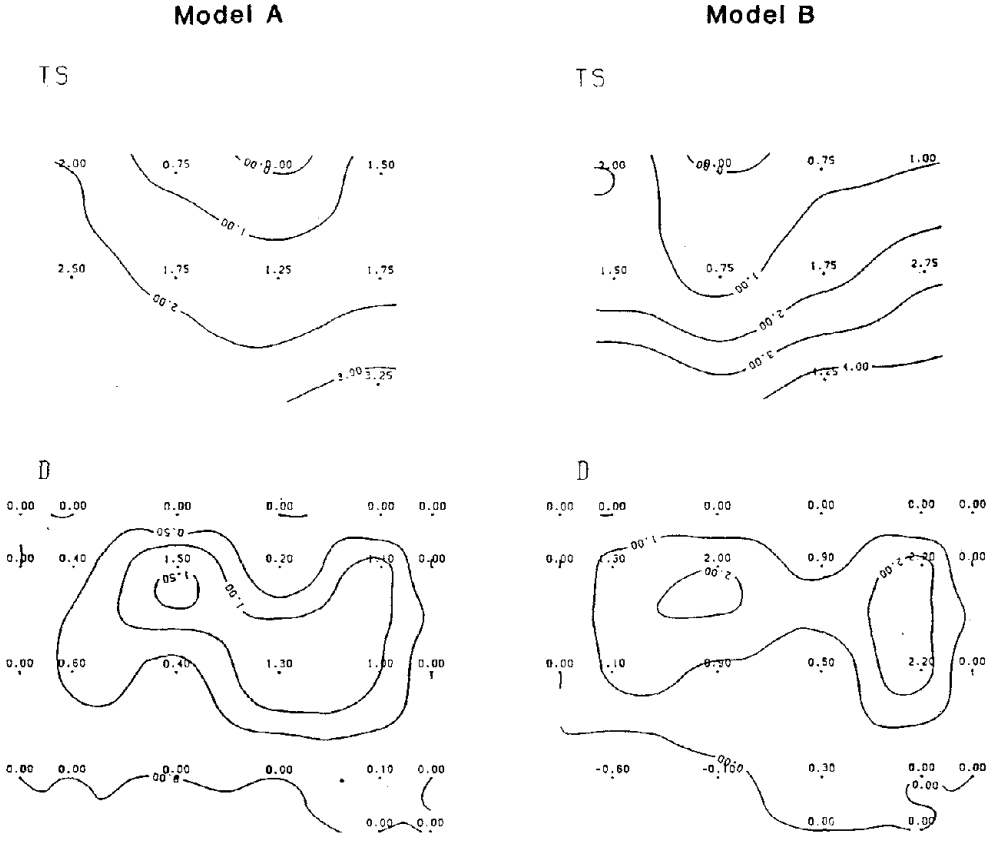

Fig. 10. The starting time of fracture of each point (top) and the average dislocation at each region (bottom).

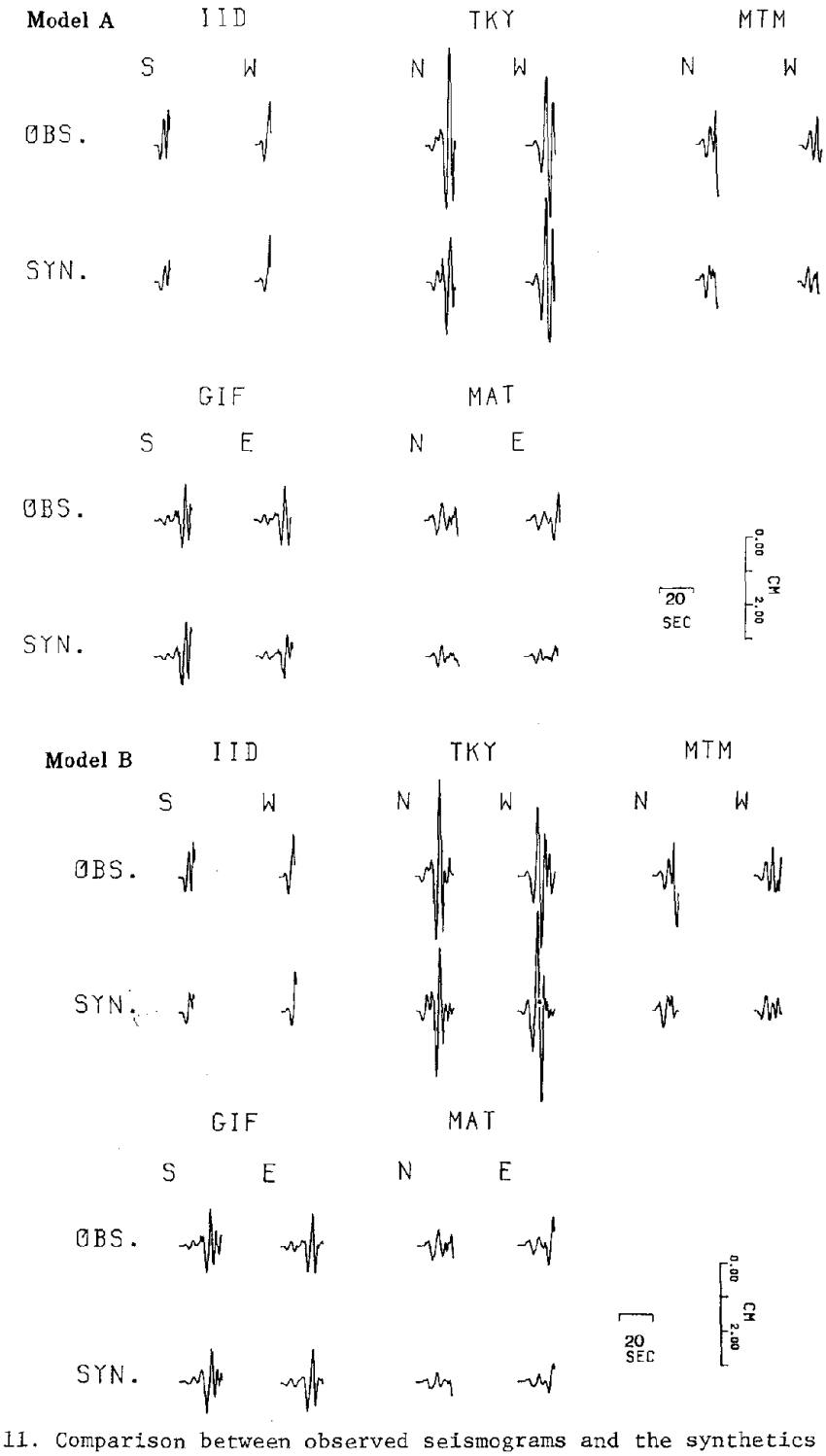

Fig. 11. Comparison between observed seismograms and the synthetics from the final solutions.

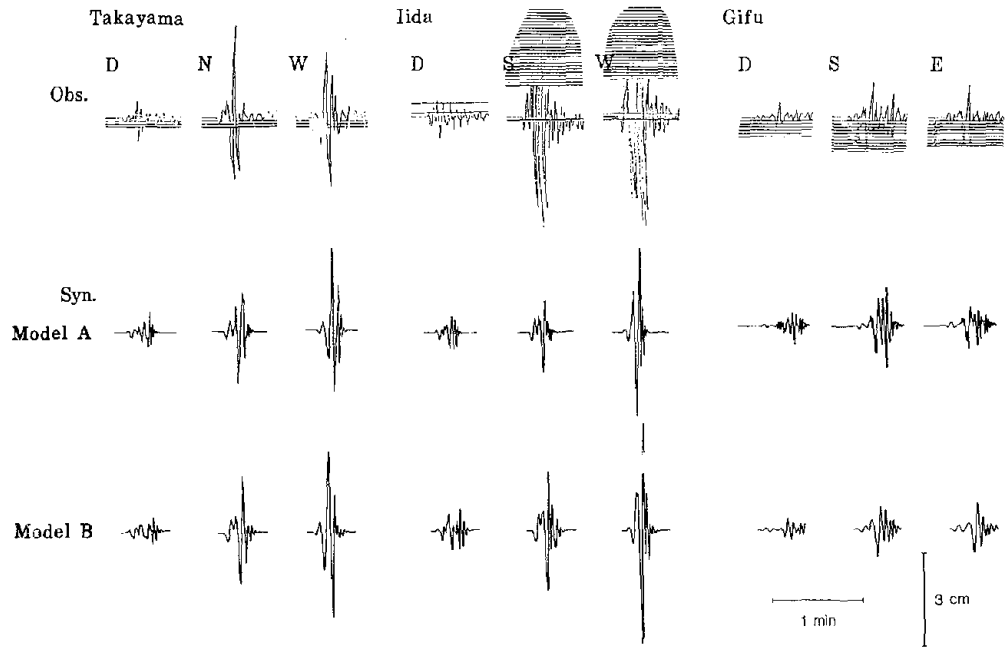

Fig. 12. The whole strong motion records and synthetic seismograms calculated from the final solutions.

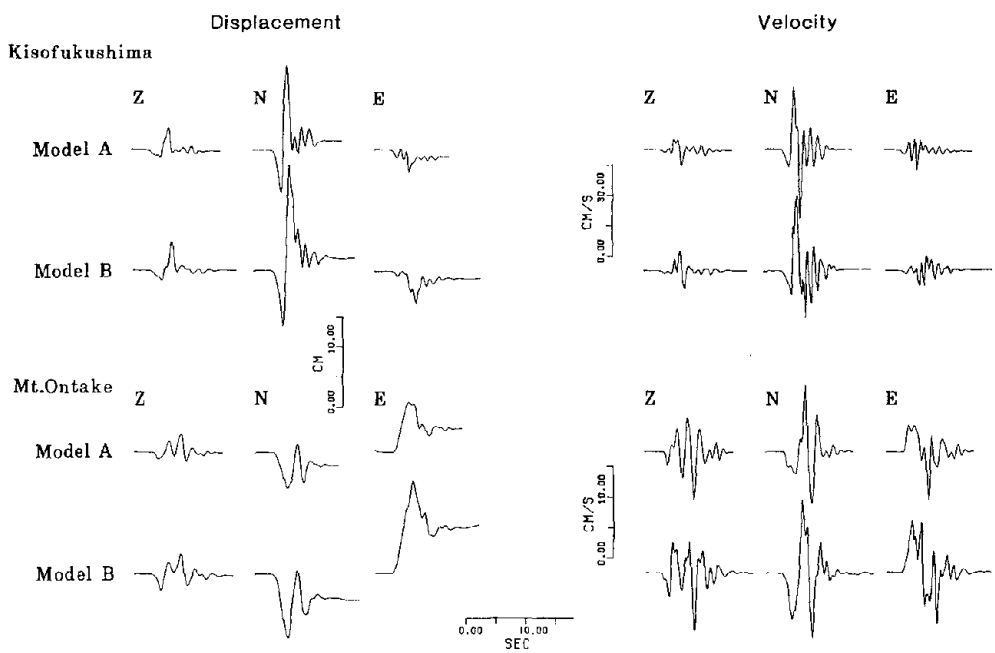

Fig. 13. The estimated ground displacement and velocity at the summit of Mt. Ontake and at Kisofukushima for model A and B.

PAPERS
NOT PRESENTED ORALLY
BUT INCLUDED
IN THE PROCEEDINGS

FEATURES OF OCEAN WIND FLUCTUATIONS DURING TYPHOON PASSAGES

BY

Gen'ichi Naito* and Hiroshi Takahashi**

ABSTRACT

Characteristics of atmospheric fluctuations have been investigated concerning two typhoons which made passage around the Japan Islands. The wind observation were made on the off-shore tower in Sagami Bay, and the waves were also simultaneously observe.

Features of the ocean surface wind are considered to be that behaviours of the large scale disturbance are added to ordinary turbulent characteristics of the atmospheric boundary layer under high winds. Furthermore, when the high waves interfere with the air flow of the surface layer, this interference should be taken into account.

Under typhoon conditions, the abnormally large gust factor is often shown, and the turbulent intensities are very large. The surface drag co-coefficient is also large, and depends strongly on the mean wind speed.

Spectra of the wind vectors and of the vertical momentum flux are analyzed under strong winds, and those behaviours are discussed in the frequency field. Additionally, the wave spectrum is shown for the storm.

* Head of Second Coastal Disaster Laboratory, Hiratuska Branch, National Research Center for Disaster Prevention.
**Director-General, National Research Center for Disaster Prevention.

1. INTRODUCTION

Observations of sea winds under typhoons passages have been made at an observation tower in Sagami Bay. The tower is situated about 1 km off the Hiratsuka Coast, and is founded on the seabed in approximately 20 m of water. Sagami Bay is about 50 km wide in the east-west direction, and is open toward the south. Therefore, an infinite fetch can be expected for southerly winds.

The observation tower is about 20 m high above the sea surface, and various sensors for the measurements of the atmospheric phenomena are attached around it. Winds have been measured by a sonic anemometer and by a vane and anemometer. The former was fixed at 685 cm high above the mean sea level, and the latter at 23 m high (see Fig. 1). The tower proper is fairly large, and so a sonic anemometer at the lower level is subject to blockage effects for certain directions. Therefore, winds can be observed only for the upward direction in order to exclude the disturbances induced by the tower. In the present observation, a sensor of the sonic anemometer was positioned for the measurement of southerly winds.

Features of the air flow over the sea are strongly influenced by waves. Therefore, to

clarify the structure of the atmospheric boundary layer, it is very important not only to observe wind fluctuations but also to observe wave heights. Wave heights have been measured by a capacitance-type wave gauge whose sensor responds rapidly to wave variations.

Three-dimensional wind components by the sonic anemometer and a wave component are digitized in the tower and transmitted to the data processing system on land by a cable buried in the seabed. Finally, the gathered data are processed by various statistical techniques. Other data are recorded on an analogue recorder.

Wind fluctuations and wave heights are usually sampled every 0.06 sec. A duration of one run is 30 min, and the FFT method is used for spectral analysis of the turbulent eddies.

Under the condition of high winds, a wind sensor is covered with a lot of water spray and, occasionally, is destroyed by high waves. Thus, the very long observation is difficult, and the feature of the air flow over a long time can be rarely investigated.

The main purpose of the present report is to estimate characteristics of the atmospheric fluctuations above the sea during typhoon passages near the observation site, and to compare these characteristics with characteristics observed under ordinarily wind conditions.

2. TYPHOON TRACK AND SEA WIND

We have presently analyzed data from Typhoons 8305 and 8410. Both typhoons moved northward off Hiratsuka, in which the observatory was located. Therefore, the strong sea winds could be observed at the observational tower. Each typhoon had the following development and history.

2.1 Typhoons 8305 (Abby)

The typhoon began to form in the sea near the Mariana Islands, on August 5, 1983, and developed to extremely strong and large disturbances. The minimum central pressure was temporarily below 900 mb. The track of the typhoon near the Japan Islands is shown in Fig. 2(a). The central intensity decreased with movement toward the southern coast of the islands and remained large in size. The typhoon made landfall near Hamamatsu city on the afternoon of August 17. Her forward speed was slow and she passed through the northern region of the Kanto district. She decayed off the Sanriku coast. Fig. 2(a) shows the weather map for 0300 JST of August 18. The central pressure was 970 mb before 24 hours.

Fig. 3 shows the time history of the mean wind direction W·D, the mean wind speed $\bar{U}$, and the maximum wave height ζ_{max} during 10 min periods. The wind data were obtained by a sonic anemometer at a height of about 7 m above the mean sea level after 0000 JST of August 17. The wind speed gradually increased after 0200 JST.

The wind direction changed to the southeast at about 0300 JST, and simultaneously the speed came up to the high value beyond 10 m/s. Since the typhoon developed vigorously in the southern sea and approached the entrance to Sagami Bay, severe high waves were generated. As shown in the figure, before high winds arrived, there existed wave heights of about 4 m. Waves developed with time and destroyed the sensor of the anemometer of 0530 JST. After that time, wind fluctuations near the sea surface could not be observed. The high waves resulted from wind-generated waves being superimposed on large swells. We find also a beat of the ocean waves with a relatively long period. The mean wind speed was 1,449 cm/s at 0500 JST, and then it became much higher. But we could not quantitatively observe the wind because of the above mentioned occurrence.

2.2 Typhoon 8401 (Holly)

No typhoons made landfall in the Japan Islands on 1984. Typhoon 8410 is the typhoon which passed nearest to the Japan Islands. She was of average size, and brought southern high winds for a long time. The typhoon began to form into the sea around the Minamidaito Island, and passed through the Tsushima Strait after approaching Japan. Then she moved northeastward in the central area of the Japan Sea and turned into a extratropical cyclone on 2100 JST of August 22 (see Fig. 2(b)). The minimum central pressure was 965 mb in the south of the Korea Peninsula before moving into the Japan Sea.

As the typhoon passed to the north of the islands, the southern wind direction was observed much earlier in Hiratsuka, and then the large change of the mean wind direction did not occur. Fig. 4 shows the history of the 10 min wind direction and wind speed as the typhoons moved near the islands. As shown in the figure, the wind speed at Hiratsuka increased after the typhoon passage through the Tsushima Strait. The mean wind direction was southward over 24 hours, and showed considerably large variations with a short period. Moreover, the wind speed also varied abruptly, corresponding to the variation of the direction. When a well-developed extratropical cyclone passes in the Japan Sea, its track resembles that of the present typhoon. In this case, high winds also blow for a long time. But we can scarcely find the abrupt variation of the wind direction and speed (Naito, 1984). Characteristics of the atmospheric disturbance induded by a typhoon are considered to differ from those associated with an extratropical cyclone. When the typhoon moved nearer to the observatory from 0200 to 0900 JST, the wind direction and speed varied must abruptly. The maximum mean wind speed of 10 min was recorded at 0600 JST, and had the value of $\bar{U}$ = 1,426 cm/s. The corresponding gust factor was G = 2.4 and the maximum instantaneous wind speed was 3,434 cm/s. The center of the typhoon moved

over the sea and was about 460 km from Hiratsuka.

As the typhoon did not approach Sagami Bay directly, there existed only wind waves generated by southern winds and there was no swell in the bay. Accordingly, the maximum wave height during 10 min was not large, that is, from 130 to 220 cm.

3. STATISTICAL FEATURES OF ATMOSPHERIC TURBULENCE

Turbulent characteristics of the air flow near the ground surface are dominated by the surface roughness. But we cannot ignore the long variation of winds as regards the structure of the surface boundary layer. In other words, it should be considered that atmospheric disturbances having a scale much larger than the surface layer affect behaviour of the turbulent eddies above the ground surface. Therefore, atmospheric fluctuations associated with a typhoon may add special properties to the turbulence in the boundary layer.

3.1 Gust Factor

The gust factor G of the ocean wind is small in comparison with that of the land wind. Moreover, the factor varies as waves develope, because the surface roughness increases with wave height. The observed gust factor also depends upon the response of the anemometer. An aerovane-type anemometer is not sensitive to short gusts because the distance constant is usually about 8 m and the anemometer cannot respond to wind variations shorter than about 0.5 sec, even in high winds. A sonic anemometer can be sensitive to much faster variations, and so presently the sampling has been done every 0.06 sec. Therefore, the present gust factor is somewhat larger than would be obtained using an aerovant-type anemometer.

Fig. 5 shows the gust factor G during 10 min against the mean wind speed. Each symbol corresponds to a different typhoon. Usually, G is small over the sea surface covered with wind waves only, and slightly increases with U. We have reported that the averaged value is G = 1.33 for moderate winds in the previous observations (Naito, 1984). A group of the data plotted in the part of the figure corresponds to the above described value, and agrees with it very well. But the atmospheric disturbance by typhoon gives gusts which do not relate to the surface roughness. In the present observation, its gust factor is in the neighborhood of G = 2.8, and has the maximum value of G = 3.0. This air flow essentially differs from the forced convection near the sea surface.

In the case of Typhoons 8305, the gust factor has the special feature in high winds, and is larger than the gust factor associated with wind-generated waves. The fluctuations induced by high waves form the greatest part of wind fluctuations. The maximum instantaneous wind speed during the observational time shown in the figure is almost constant and is from 24.5 to

25.0 m/s. Therefore, G decreases with increasing mean wind speed $\bar{U}$.

3.2 Turbulent Intensity

The standard deviation of wind vector (u,v,w) is denoted by $(\sigma_u, \sigma_v, \sigma_w)$, and the turbulent intensity can be expressed by $(\sigma_u/\bar{U}, \sigma_v/\bar{U}, \sigma_w/\bar{U})$. Fig. 6 shows the turbulent intensity of 30 min against the mean wind speed. The values observed in Typhoon 8410 are divided into two groups in the figure. One group was measured before 1000 JST of August 22, at which the center of the typhoon approached nearest, and the other group was measured after that time. The lines in the figure represent the approximate expression of the turbulent intensity in the previous observations (Naito, 1983). As the values observed in Typhoon 8305 are few, we cannot compare them with values obtained under ordinary wind conditions. However, we find that the intensity of the w component does not behave as well as the characteristics of the turbulent eddies in the surface boundary layer. The fluctuations induced by waves determine the feature of the w component in this case. The present plotted values are obviously larger than the previous ones. As shown in Fig. 5, it is the case that the air flow contains very strong gusts under the typhoon. We scarcely indicate the difference before and after the nearest approach of Typhoon 8410, although the intensity under the later condition is a little small. Approximately, the averaged intensity is

$$\sigma_u/\bar{U} = 0.122,\ \sigma_v/\bar{U} = 0.096,\ \sigma_w/\bar{U} = 0.053$$

for $\bar{U}$ = 11 m/s. We can find for the u component that the large fluctuations beyond the scale of the surface boundary layer greatly contribute to the turbulent intensity.

3.3 Friction Velocity and Surface Drag Coefficient

When the momentum of the atmospheric fluctuations transfers toward the sea surface, the scale of the flux is represented by the friction velocity:

$$u_* = \sqrt{-\overline{uw}}.$$

In the boundary layer near the surface, u_* is constant with respect to the height. As the atmospheric stability is neutral under the condition of high winds, the vertical profile of the mean wind speed U can be described by using u_* in the following expression:

$$\bar{U} = \frac{u_*}{\kappa} \ln \frac{z}{z_0}, \quad \kappa = 0.39$$

where κ is Vou Karman's constant, z the height above the mean sea level, and z_0 the aerodynamic roughness. z_0 gradually increases with the wave development, and is very small in comparison with that on land. The coefficient of the sea surface drag, which produces the shear stress of the air flow, is defined by

$$C_D = (u_*/\bar{U})^2.$$

Therefore, we deduce the expression for the surface roughness by wind waves to have the form

$$z_0 = z \exp(-\frac{\kappa}{\sqrt{C_D}}) ,$$

and then we can obtain z_0 if the drag coefficient C_D at the height of z is known. Usually, the reported C_D is the value at 10 m high, and z_0 is of the order of 0.1 mm from the above equation. We are not aware that the roughness under a severe storm such as a typhoon has been directly measured because of very difficult observation.

Fig. 7 shows C_D of 30 min as a function of mean wind speed U. The wind fluctuations in Typhoon 8305 were strongly influenced by ocean waves, as described in the section on wind gusts. Therefore, the covariance of the u and w components has a very large positive value. In other words, the height of the anemometer was too low to obtain the atmospheric momentum flux which is transferred to the sea surface. Consequently, C_D could not be obtained in this case.

The curve in the figure expresses the dependency of the average C_D in the previous observations (Naito, 1978). Also shown is the drag coefficient reported by Davies and Flather (1978) who expect to derive the surface wind from the geostrophic wind over the ocean. C_D observed in Typhoon 8410 is larger than those of the two examples. Moreover, the different feature is that C_D increases with the wind speed and resembles the wind dependency of C_D by Davies, et al.

From the figure, the average C_D can be expressed as

$$C_D = 0.00019\bar{U} \text{ for } 7<\bar{U}<14 \text{ m/s},$$

where $\bar{U}$ is expressed in m/s. We can obtain from the above formula $C_D = 2.28 \times 10^{-3}$ for $\bar{U} = 12$ m/s, and then the friction velocity is $u_* = 57$ cm/s. Under the same condition, the sea surface roughness is $z_0 = 2.0$ mm from those values.

Various statistical quantities of wind vectors and waves in Typhoon 8410 are shown in Table 1. Those were obtained by processing the data for 10 min every one hour. We can point out the characteristics from 1440 to 1700 JST of August 21. In the table, S_u/S_w and K_u/K_w are the third and fourth moments of the u/w component, and are called the skewness and kurtosis factors respectively. ζ_{max} and T_{max} are the maximum wave height and its corresponding period. σ_ζ denotes the standard deviation of the wave height and indicates the intensity of the wave energy. We find from the table that the w fluctuation deviates from the Gaussian distribution. When K_u becomes very large, G is large. But when G is large, K_u is not always abnormal. This fact indicates that the strong gust has various types. The waves are not large, and those periods are from 4 to 6 sec. Consequently, the wind field is typically in the circumstance of wind waves.

4. SPECTRAL BEHAVIOUR OF WIND FLUCTUATIONS AND WAVES

4.1 Spectra of Wind Vectors

As is well known, the power spectrum of wind fluctuations in the surface layer is represented as a function of the frequency normalized by the height and the mean wind speed, and of the atmospheric stability. In other words, the geometric similarity of the air flow is suggested to exist (Lumley and Panofsky, 1964). But the similarity cannot be obviously applied to the air flow such that the large scale fluctuations are superimposed on the turbulence of the surface boundary layer.

In high winds, the atmospheric stability is near neutral. Additionally, except for summer, it is unstable in the ocean region close to the Kuroshio such as Sagami Bay. Fig. 8 shows the frequency power spectrum P(n) of the wind fluctuations (u,v,w) in Typhoon 8305. The analyzed example is obtained under high wind where the 30-min averaged speed is 1,380 cm/s. In this case, as the atmospheric disturbance induced by high waves is superimposed on the essential wind fluctuations, the spectrum is extraordinary in form. For the w component, with which the waves interfere strongly, the spectrum resembles the form produced by white noise, although it decay at high frequencies show a little turbulent behaviour. For the u and v components, the spectra behave almost the same except in the high frequency region. Consequently, it is noted in severe storms that the fluctuating component along the wind direction is not strongest, and the horizontal wind field becomes almost uniform. The decay corresponding to the -5/3 power law cannot be found in the inertial subrange of high frequencies, and the spectrum decays slowly with increasing frequency. This dependency is considered to be caused by the interference of high waves. The power spectra in Typhoon 8305, including the example of Fig. 7, are the special cases in which the interference of waves superimposes large scale disturbance.

Fig. 9 shows the power spectrum of the u component in Typhoon 8410. In the figure, the case of A-28 is under high winds before the nearest typhoon approach, and the cases of B-3 and B-20 are after that time. Those spectra are of 30 min. In the figure, the spectrum extending over the lower frequencies is analyzed for the wind fluctuations during 720 min (equal to 12 hours), including B-3 and B-20. Its behaviour corresponds to the wind variation of the latter duration of Fig. 4. While the observation was made, the wave condition scarcely varied, but the deviation of the tide was about 60 cm. As the level of the anemometer is about 7 m, the variation of 60 cm is large. But its influence could not be made clear as a result of analysis. We find from the figure that the spectra at high frequencies decay according to the -5/3 powers law. In the inertial subrange, the spectrum is described as follows,

$$nP(n) = \frac{\alpha}{2} \varepsilon^{2/3} \left(\frac{\bar{U}}{2\pi n}\right)^{2/3}$$

where $\alpha = 0.48$ and ε is the viscous dissipation rate. The above formula assumes Taylor's frozen turbulence. Hence, we indicate that the three spectra in the figure do not satisfy the above formula according to the mean wind speed $\bar{U}$ and have deviations larger than the values given by the formula. This tendency can be seen in the other examples. Therefore, considering the turbulent structure of the surface layer, we note that the relation of the reduction of the wave number (or the wave length) to the frequency has not been sufficiently established yet.

One of the spectral characteristics during the long period is that there exists a minimum in the neighborhood of $n = 10^{-3}$ Hz. Now, the wind disturbances weaken about every 17 min. A smoothed curve with the observed values is given by the empirical formula of the spectrum under neutral atmospheric conditions from Naito (1978). The long-period case and B-3 are connected to apply the formula in the figure.

Since the spectrum is non-dimensionalized using the standard deviation $\sigma_u = 109$ cm/s the case B-3, the appropriate curve of the figure represents

$$\frac{nP_u(n)}{\sigma_u^2} = \frac{74f}{(1+84f)^{5/3}}, \quad f = \frac{nz}{\bar{U}}$$

where f is the non-dimensional frequency, and z the level above the mean sea surface. Many empirical formulas have been proposed for the u component. However, most of them are based on the wind observation over land. The present example shows that the sea surface wind has a large spectral density deviated toward the longer period side in comparison with the land surface wind.

Fig. 10 shows the power spectrum $nP_w(n)$ of the w component and the co-spectrum $nC_{uw}(n)$ of the momentum flux by the turbulence. Each smoothed curve with the observed values is given by the following formulas. The power spectrum of the w component can be approximated by the formula of Naito (1978):

$$\frac{nP_w(n)}{\sigma_w^2} = \frac{1.2f}{1+11f^{5/3}}.$$

The above formula does not agree well with the observed data around the frequency $n = 0.5$ Hz, but is in good agreement elsewhere.

The spectral scales λ_u and λ_w are given by the peak frequency of the spectrum, and can be obtained from Figs. 9 and 10. As the measured height is $z = 685$ cm, these scales are

$\lambda_u = 380$ m for the u component;

$\lambda_w = 23$ m for the w component.

In a severe storm, such as seen in Fig. 8, the spectral peak cannot be determined and so the spectral scale cannot be reduced.

In general, there exists a large scatter of the covariance $\overline{uw}$ which determines the vertical transport of the atmospheric momentum. Then, the co-spectrum $C_{uw}(n)$ abruptly varies about the frequency n. Fig. 10 shows a example of the smaller variation. The $\overline{uw}$ co-spectrum decays more rapidly at high frequencies. Moreover, as the spectrum is wide and flat around its peak frequency, its form resembles a trapezoid. Therefore, it is very difficult to obtain a suitable approximate expression. The curve in the figure has the form

$$\frac{nC_{uw}(n)}{u_*^2} = \frac{14f}{(1+11f)^{7/3}} .$$

The observed form decays more rapidly than the above formula, a high frequencies, and the u and w components correlate effectively at frequencies of less than about n = 6 Hz. This cut-off frequency corresponds to the eddy scale of about 2 m. Eddies smaller than this case usually do not contribute significantly to the shear stress.

4.2 Interference of Waves with Air Flow

The layer in which waves interfere with the air flow is close to the sea surface and is thin (Kondo, et al., 1972). Therefore, the atmospheric fluctuations induced by waves are usually ignored as regards to discussions of the characteristics of the wind turbulence. But we can never find examples observed under the condition of severe high waves which are considered to influence the behaviour of the air flow.

Fig. 11 shows a power spectrum of the waves in Typhoon 8305. The maximum wave height during 30 min is ζ_{max} = 352 cm, and its corresponding period is T_{max} = 11 sec. As the wave has been recorded ζ_{max} = 455 cm before this run, the sea circumstance is not severest, but is under the ordinary condition of high waves. We indicate from the figure that the spectral peak corresponds to the period of the maximum wave height. The spectrum in the high frequency region decays with the -5 power of the frequency. Accordingly, although the sea surface is not covered with only wind waves, the -5 powers law can be applied in the equilibrium range.

In order to clarify the degree of interference of the waves with the wind fluctuations, the coherences between the wave height ζ and the u/w components were computed (see Fig. 12). The coherence represents the correlation with frequency. The sensor of the wave gauge was not just below the anemometer, but about 6 m off. Therefore, we cannot obtain a more accurate correlation. However, we notice the relatively high correlation in the range from 0.07 to 0.15 Hz. From Fig. 11, these frequencies correspond to the strongest energy range of the wave height.

5. CONCLUSIONS

Features of the sea surface wind in Typhoons 8305 and 8410 have been investigated from the measured values at the off-shore tower. The former storm is high winds with high waves, and

the latter is long lasting high winds moderate wind waves. Remarkable results are shown as:

(1) The gust factor above the sea surface with high waves is much larger than the ord inary one due to turbulence alone. The factor under typhoon conditions is irregular and abnormally large.

(2) The turbulent intensity under the condition of typhoon is large, and has the average value that $\sigma_u/\overline{U} = 0.122$ and $\sigma_w/\overline{U} = 0.053$.

(3) The sea surface drag coefficient is large and increases with increasing wind speed. We obtain that $C_D = 2.28 \times 10^{-3}$ for $\overline{U} = 12$ m/s.

(4) The previously reported formulas can be applied to the power spectra of the three wind components and the co-spectrum of the momentum flux, except for the condition of strong interference of the waves. The power spectrum of high waves is shown.

The study of sea winds under typhoon conditions continues to clarify the more detailed feature of gusty winds. Many observations will contribute to obtain the basic data of the atmospheric disturbance for the disaster prevention of winds and waves in coastal regions.

6. REFERENCES

1) Davies, A. M. and R. A. Flather, 1978: Application of numerical models of the North-west European Continental Shelf and the North Sea to the computation of the storm surges of November-December 1973. Dtsch. Hydrogr. Z.Eng.-H. A. 14, 1-72.

2) Kondo, J., Y. Fujinawa, and G. Naito, 1972: Wave-induced wind fluctuation over the sea. J. Fluid Mech., 51, 751-711.

3) Lumley, J. L. and H. A. Panosky, 1964: The structure of atmospheric turbulence. Mono graphs and Texts in Physics and Astronomy. Interscience, New York.

4) Naito, G., 1978: Direct measurement of momentum and sensible heat fluxes at the tower in the open sea. J. Meteorol. Soc. JPN, 56, 25-34.

5) Naito, G., 1983: Spatial structure of surface wind over the ocean. J. Wind Eng. Industr. Aerodyn., 13, 67-76.

6) Naito, G., 1984: Characteristics of long lasting winds over the ocean. Proc. 8th Natl. Symp. Wind Eng., Tokyo, 1984, 1-6.

Table 1. Statistical quantities of wind vectors and waves in Typhoon 8410.

RUN	$\bar{U}$ (cm/s)	σ_u (cm/s)	σ_v (cm/s)	σ_w (cm/s)	S_u	S_w	K_u	K_w	u_* (cm/s)	C_D x1000	G	ξ_{max} (cm)	T_{max} (s)	σ_ξ (cm)
A- 25	894	89	79	45	-0.26	0.24	2.99	3.43	41	2.11	1.28	151	4.5	21
A- 37	1060	118	78	56	-0.22	0.21	2.81	3.63	47	2.00	1.39	115	7.7	22
A- 49	808	148	178	49	0.12	0.07	4.95	3.78	33	1.72	1.82	149	5.9	27
A- 61	1068	125	77	57	0.37	0.28	9.67	3.74	47	2.01	2.90	189	6.7	30
A- 73	1162	134	91	63	-0.04	0.14	2.65	3.71	50	1.91	1.33	194	6.5	31
A- 85	1289	145	101	77	-0.15	0.14	2.69	3.53	60	2.19	1.33	170	5.0	29
A- 97	1397	169	119	82	-0.08	0.18	2.91	3.46	65	2.20	1.40	178	6.2	31
A-109	1055	208	145	71	-0.09	-0.30	2.78	5.58	52	2.44	3.03	137	5.2	27
A-121	1195	122	89	69	-0.14	-0.12	2.57	3.48	54	2.06	1.31	172	6.4	33
A-133	1066	133	77	57	0.04	0.12	2.76	3.88	46	1.86	1.39	153	5.9	30
B- 4	1078	157	89	56	0.17	0.28	7.85	3.78	43	1.58	2.79	135	4.4	30
B- 16	975	102	70	52	0.00	0.16	2.64	3.87	40	1.65	1.35	207	6.0	30
B- 28	1097	134	86	64	0.08	0.24	3.06	3.55	56	2.61	1.44	165	5.7	28
B- 40	1179	137	82	67	0.01	0.13	2.41	3.28	55	2.16	1.33	164	5.1	27
B- 52	908	102	83	49	0.12	0.04	2.94	3.73	40	1.91	1.41	174	5.8	29
B- 64	1122	113	92	61	0.08	0.26	2.91	3.60	44	1.57	1.39	190	5.8	29
B- 76	1046	104	75	56	-0.12	0.04	2.78	3.64	44	1.77	1.33	132	6.2	27

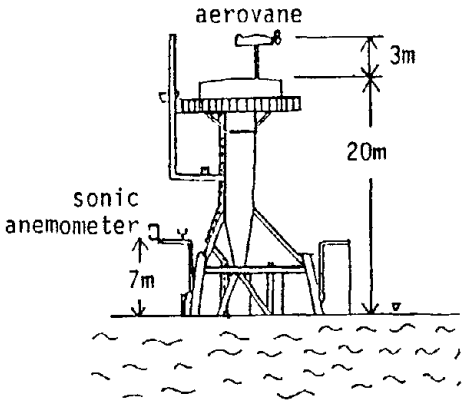

Fig. 1 Schematic diagram showin the spacing of anemometers

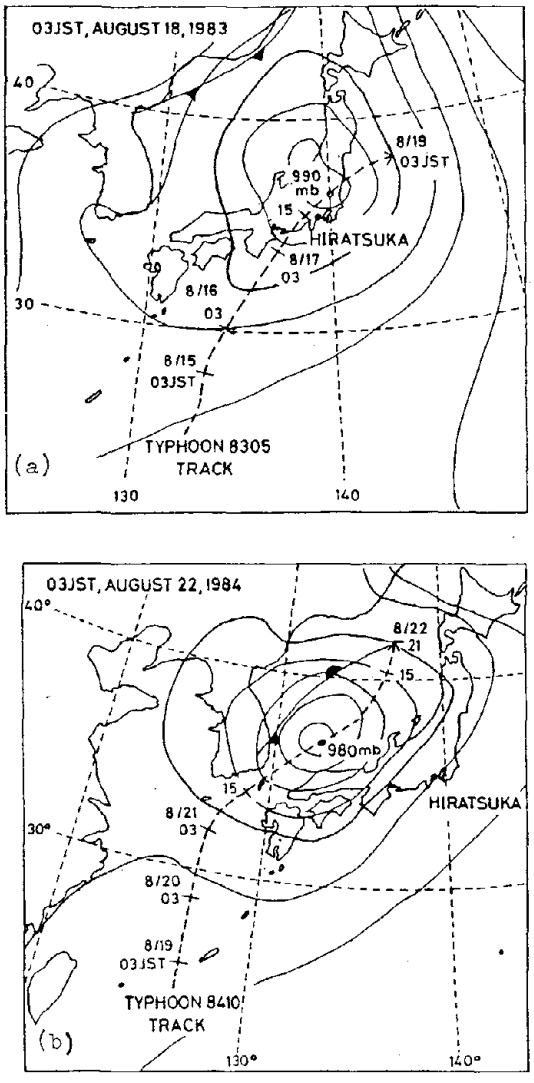

Fig. 2 Track of the typhoon: (a) Typhoon 8305, (b) Typhoon 8410

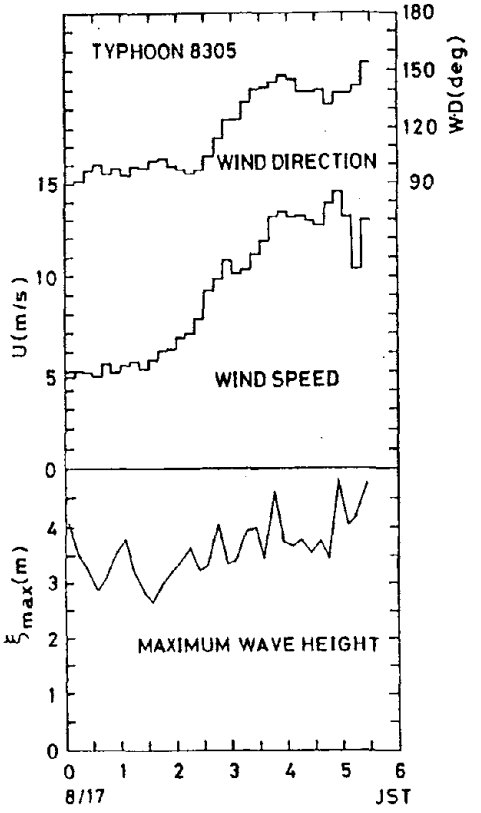

Fig. 3 History of mean wind direction and speed, and maximum wave height during 10 min in Typhoon 8305

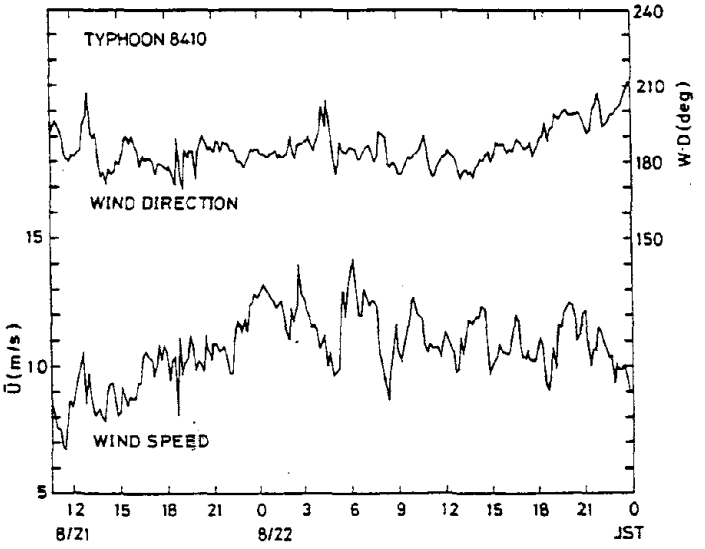

Fig. 4 History of mean wind direction and speed in Typhoon 8410

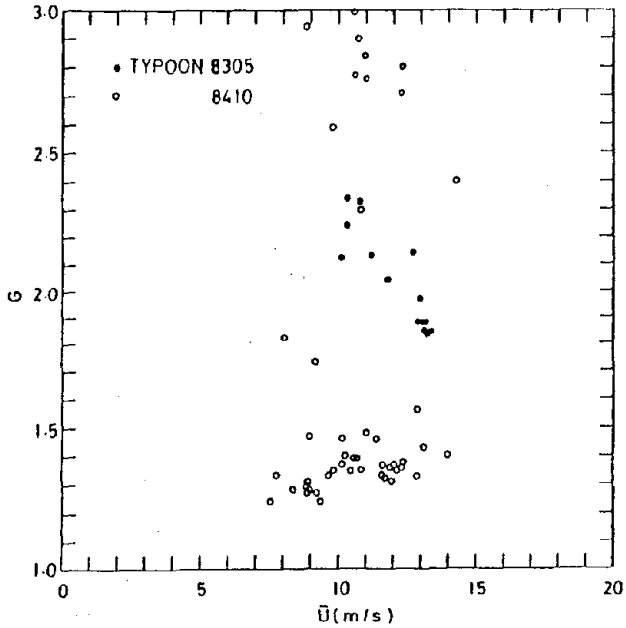

Fig. 5 Gust factor against mean wind speed

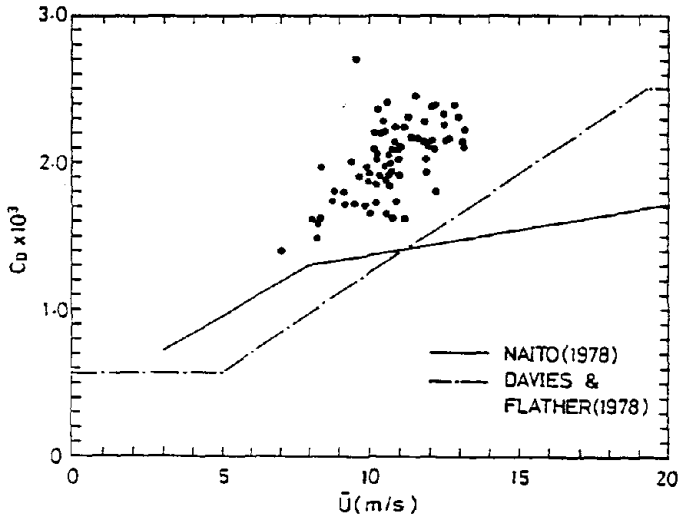

Fig. 7 Surface drag coefficient as a function of mean wind speed at 685 cm high

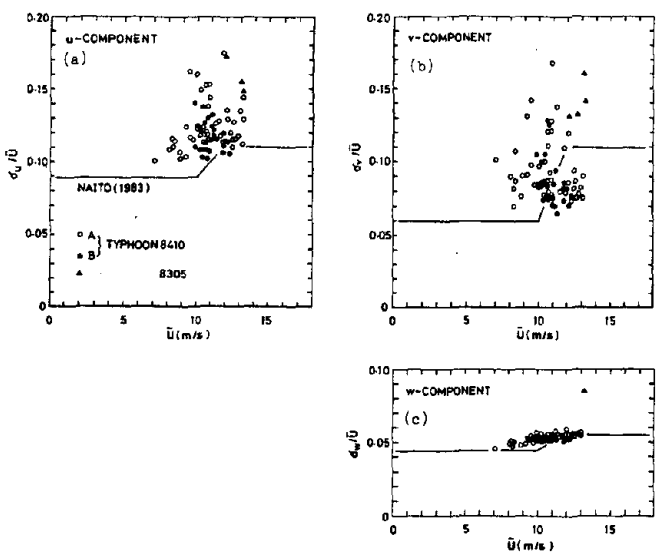

Fig. 6 Turbulent intensity of wind fluctuations: (a) u component, (b) v component, (c) v component. Solid lines are from Naito (1983).

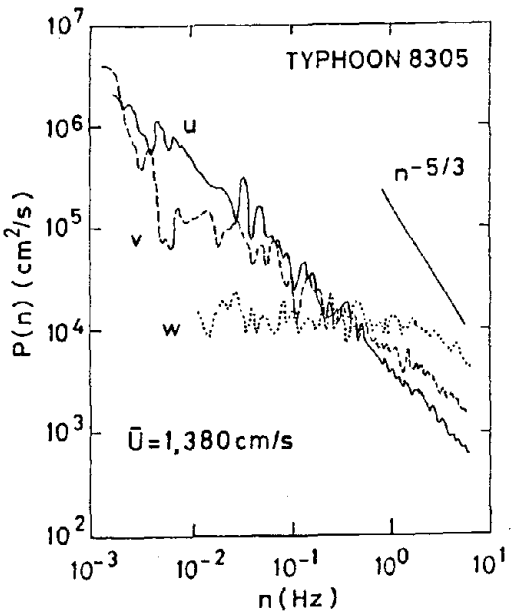

Fig. 8 Frequency power spectra of wind vectors in Typhoon 8305.

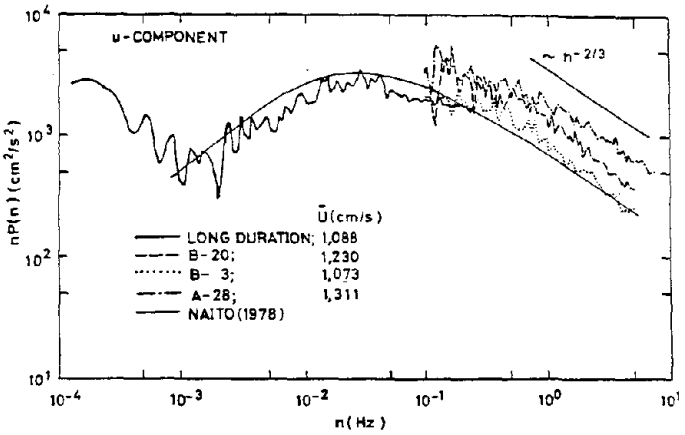

Fig. 9 Power spectra of longitudinal wind component in Typhoon 8410. Smoothed solid curve is from Naito (1978).

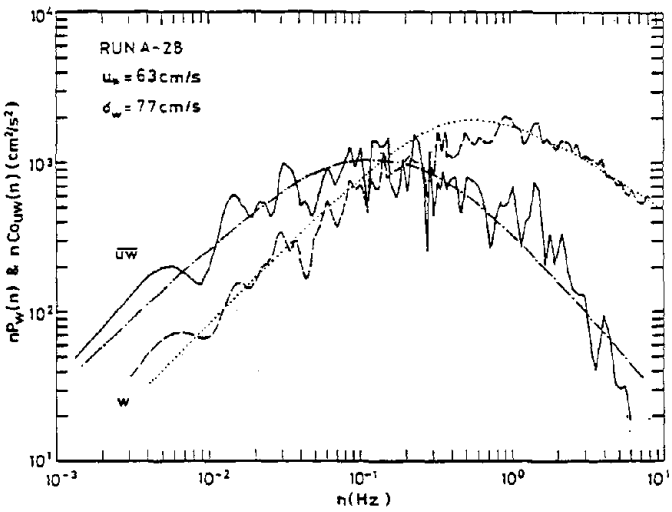

Fig. 10 Power spectrum of vertical wind component, and co-spectrum of momentum flux in Typhoon 8410. Smoothed curves correspond to empirical formulas.

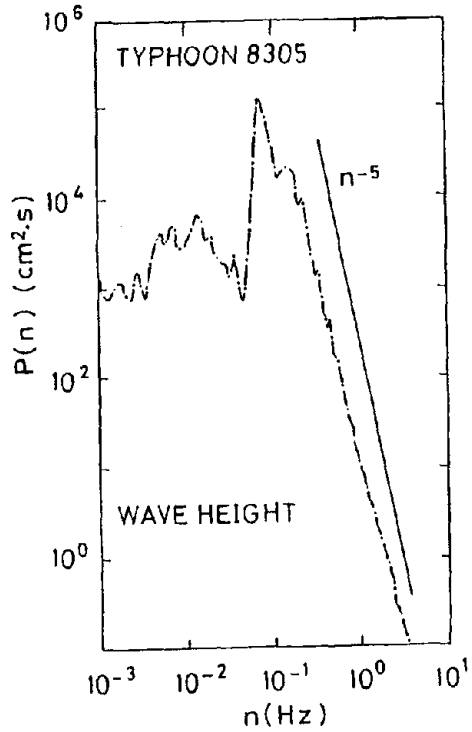

Fig. 11 Same as Fig. 8 except for wave height

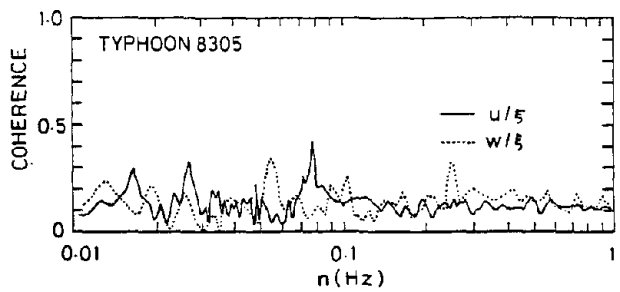

Fig. 12 Frequency coherence of wave height with longitudinal wind component (solid line), and with vertical wind component (dotted line)

THE VARIATION OF GUST STRUCTURE WITH HEIGHT UP TO 200 M

BY

K. Naito*, T. Hanafusa**, and T. Fujitani***

ABSTRACT

The variation of gust structure with height up to 200 m was investigated by using the data from a meteorological observation tower equipped with sonic anemometer-thermometers at six levels.

The vertical and horizontal scales of turbulence for three wind components were discussed with the integral scales obtained by the integration of the auto-correlation coefficient of wind fluctuations and the cross-correlation coefficients at two different levels.

The variation of the spectral scales with height was obtained by the spectral analysis of wind fluctuations.

All terms in the energy balance equation except the pressure transport term were estimated directly and the energy balance was discussed.

1. INTRODUCTION

Earthquake forces have been more important for planning the most structures in Japan than have wind forces. But recently, the reduction of tall buildings' weight, the utilization of outer walls to achieve strength and stiffness in buildings, and the construction of long space suspension bridges have made the consideration of the wind forces and earthquake equally important.

Accordingly, the study of the characteristics of high wind at only one point is not sufficient and spatial and time variations of high wind's characteristics are required.

This paper will concentrate on the variation of gust sturcture with height by using wind data from a meteorological observation tower with 213 m height.

2. INSTRUMENTATIONS AND DATA REDUCTION METHOD

The principal source of the data for this study is wind fluctuations measured by three dimensional sonic anemometer-thermometers located at 10, 25, 50, 100, 150, and 200 m on a meteorological tower. The signals from the sonic anemometer-thermometers were digitalized at every 0.1 sec and recorded on magnetic tapes. The data analysis was carried out on the MRI large electric computer (HITAC-M-200H). The data discussed in this paper were the same ones presented in the previous UJNR session (Naito, et al. (1983))[1]). The tower and the observation system were presented in detail in another paper (Hanafusa, et al. (1981))[2]).

* Head of the Meteorological Satellite Research Division

** Physical Meteorological Research Division, Chief of the Second Research Laboratory.

3. RESULTS AND DISCUSSIONS

3.1 Frequency Distribution of Wind Fluctuation Maximum Instantaneous Wind Speed

Frequency distribution of wind fluctuation is considered to be almost normally distributed, regardless of the atmospheric stability and of the roughness length. Examples of the frequency distributions of wind component are shown in Fig. 1 and the values of skewness and kurtosis are plotted in Fig. 2. Though the observed points vary a little widely, the values of skewness are central to zero and the values of the kurtosis are close to 3. Accordingly, the frequency distribution of each component is considered to be adequately described by the normal distribution.

In the case of studying wind load, it is preferable to adopt the maximum instantaneous wind speed rather than the mean wind speed. As the response of the anemometer has a limit, even the maximum instantaneous wind speed indicates the mean wind speed which is averaged for a certain degree of time. Accordingly, as the value of maximum instantaneous wind speed will depend on the averaging time, it is very important to make a description of the averaging time when the maximum instantaneous wind speed is measured. The gust factor is defined as the ratio of the maximum wind speed to the mean wind speed for some long period. Then the maximum wind speed can be estimated from the mean wind speed by a gust factor. On the other hand, the maximum wind speed can be infered from the fact that the frequency distribution of the wind fluctuation is normal. As mentioned previously, the frequency distribution of the u component is found to be normal. Accordingly, the probability of a maximum 5 sec wind speed for 10 min sampling duration is indicated by the shaded region as shown in Fig. 3. From the normal distribution table, it is about 2.4 and the value of the 5 sec maximum wind speed for 10 min sampling duration, U_{max} can be expressed as follows,

$$U_{max} = M + t\sigma = M(1+2.4\ \sigma/M)$$

where M is mean wind speed and σ/M, intensity of turbulence. The calculated values obtained by using observed mean wind speed and intensity of turbulence are compared with observed maximum wind speeds. The results are shown in Table 1 and Fig. 4. From these results there is no remarkable difference between them. It is very easy to estimate the maximum wind speed if the intensity of turbulence can be estimated.

The power index of the vertical distribution of the maximum wind speed is usually smaller than that of the mean wind speed. It will depend on the averaging time that the index in this experiment is relatively smaller than the root of that for mean wind speed a shown in Fig. 5.

3.2 Correlation and Scale of Turbulence

The spatial scale of turbulence can be determined by the integration of the auto-correlation function for wind fluctuations. An example of the auto-correlation coefficient for u, v and w components vs time lag is shown in Fig. 6. The values for v and w components become smaller compared with that of u component at same time lag and the higher the measurement height is, the larger the lag time at which R(t) becomes zero. The values of R(t) plotted against the height are shown in Fig. 7 for each wind component. For the u component, the values of R(t) increase linearly with height up to 100 m and are nearly constant at higher levels. On the other hand, the value for the v component are almost constant for the entire 200 m layer while the values of w component increase linearly with height. This tendency can be found in the previous paper (Naito, et al. (1983))[1]) for the case of τ_o where $R(\tau_o)$ is 0.6. For each component, $\int R(t)dt$ can be expressed as follows,

u component	$\int R_u(t)dt \sim z^{0.5}$ (except the higher two levels)
v component	$\int R_v(t)dt$ - const
w component	$\int R_w(t)dt \sim z^{0.4}$

If the Taylor's hypothesis can be assumed to be applied for every component, the integral scale of the turbulence of each component can be expressed as follows, as the vertical mean wind profile can be approximated as $z^{0.3}$, (Naito, et al. (1983))[1])

$$L_u \sim z^{0.8}$$

$$L_v \sim z^{0.3}$$

$$L_w \sim z^{0.7}$$

In order to examine the spatial characteristics of wind fluctuations, we must measure wind fluctuations by the sme type of instruments at the same time and at several points.

The cross correlation coefficient between two different heights can be estimated by the sonic anemometer's data at six levels. Its value is considered to be a function of the averaging time. The dependence of this coefficient on the averaging time is shown in Fig. 8 and Table 2. The longer the averaging time becomes, the larger the coefficient is and the tendency of the increase becomes large abruptly at more than 3 sec. This indicates that there are phase differences between wind fluctuations at two levels.

Table 3 indicates the time lag when the cross correlation coefficient has a maximum value. From this table, the maximum value can be found at plus time lag (the gust wind at higher levels is faster than that at lower levels) for u and v components, though there is no remarkable difference for w component. The time lag between 100 m and 50 m is largest when the wind shear is largest.

As shown in Fig. 9, the cross correlation coefficients among three wind fluctuations at three different levels are approximately expressed as follows,

$$r_{1,3} = r_{1,2} \cdot r_{2,3}$$

$r_{i,j}$ = cross correlation coefficient between height z_i and z_j

This suggests that it should be possible to express the cross correlation coefficient by the following formula,

$$r_{1,2} = \exp\{-k(\phi(z_2)-\phi(z_1))\}$$

As there has been no definite function for $\phi(z)$, the relation between the correlation and $\phi(z)$ can be examined by changing the value of n from 0.2 to 0.7, assuming $\phi(z)$ is z^n. Results are shown in Fig. 10. As observed values fairly scattered, the function of $\phi(z)$ can not be determined uniformly. For w component, $\phi(z)$ is almost $z^{1/3}$ as mentioned by Panofsky and Singer (1965). For u and v components, the power index larger than 1/3 is seen to be fitted for the entire range. From the figure, the cross correlation coefficient can be expressed as follows,

$$R_u = \exp\{-0.5(z_2^{0.4} - z_1^{0.4})\}$$

$$R_v = \exp\{-0.3(z_2^{0.6} - z_1^{0.6})\}$$

$$R_w = \exp\{-1.2(z_2^{0.3} - z_1^{0.3})\}$$

As mentioned before, the correlation will vary according to the averaging time, and the values of n and k will change. Accordingly, the averaging time is a very important factor in determining the correlation and scale of turbulence.

Finally, the scale of turbulence by the above formula can be expressed as follows,

$$L_z^u(z) \sim z^{0.6}$$

$$L_z^v(z) \sim z^{0.4}$$

$$L_z^w(z) \sim z^{0.7}$$

The dependency of the vertical scale of turbulence on height is similar quantitatively with that of the horizontal scale of turbulence.

3.3 Spectral Characteristics of Wind Fluctuations

In turbulent flow, various scale eddies mix in confusion and the distribution of their energy is not homogeneous. It is a very important problem to examine how the energy is distributed over the frequency range in order to consider the dynamic characteristics of the structures. One of the methods used to examine the distribution of wind energy is spectral analysis of wind fluctuations. Spectral analysis was carried out by the Blackman and Turkey method and the sampling duration was 10 min for all components.

The averaging time is 2 sec for u and 0.2 sec for v and w components. Example of spectra for each component are shown in Fig. 11. The dotted line in the figure for u and v components indicates the experimental formula proposed by Davenport[4] and for w, by Busch and Panofsky[5]. The spectra were shifted in order to match the peak frequency. For the u component, the experimental formula was in agreement with the spectra obtained in the lower levels (50, 25, and 10 m) in this experiment. But for higher levels there are remarkable spectral peaks with frequency about 0.006 Hz at which the experimental formula can not be fitted.

On the other hand, Davenport's spectra coincide with observed v spectra and the -2/3 power law

can be observed in the higher frequency range. For w spectra, the experimental spectra proposed by Busch and Panofsky well fitted the observed one. It is found that the peak frequency, n_m, in which nF(n) has a peak shifts to a higher frequency range as the height decreases. The spectral scales, $\lambda_m(=u/n_m)$, are shown in Fig. 12. For up to 50 m layer, it is shown that $\lambda_u \sim z^{0.5}$ and λ_v, $\lambda_w \sim z^{0.3}$ and at higher levels than 50 m, the spectral scale of each component is proportional to height, ~z.

The relative magnitudes of the spectral scale hardly change with respect to height and it is found that $\lambda_u : \lambda_v : \lambda_w = 6 : 2 : 1$.

3.4 Energy Balance Equation

The energy balance equation can be written as follows, assuming homogeneity of turbulence and zero mean vertical velocity,

$$\frac{\partial}{\partial t}(\bar{E}) = \underbrace{-\overline{u'w'}\frac{\partial u}{\partial z}}_{M} + \underbrace{\frac{g}{T}\overline{w'T'}}_{B} - \underbrace{\frac{\partial}{\partial z}\overline{\frac{1}{\rho}(w'p')}}_{P} + \underbrace{\frac{\partial}{\partial z}\overline{(w'E)}}_{T} - \varepsilon$$

where $E = 1/2(u'^2+v'^2+w'^2)$

- M: mechanical product term
- B: Buoyant production term
- P: Pressure transport term
- T: Divergence of the flux of turbulent kinetic energy term

All terms except the pressure term can be estimated and the values of ε can be obtained indirectly from the spectra of wind fluctuations.

The pressure transport term is estimated as the residual. An example of the height variation for each term is shown in Fig. 13 and results are shown in Table 4. The height variation of ε are shown in Fig. 14 indicates that $\varepsilon \sim z^{-1}$ for heights less than 50 m and $\varepsilon \sim z^{-2}$ for height greater than 50 m. It may indicate that the height of the constant flux layer is at most 50 m.

The distribution of w'E has a maximum at 100 m for all runs and then the direction of the turbulent energy flow will change at 100 m height (Fig. 15). The balance proposed by Busch and Panosfky (1968)[5], namely that $\varepsilon = M+B$, seems appropriate in this case as is shown in Fig. 16. Accordingly, insofar as the residual represents the pressure term, P, the results then indicate that $-P=T$, i.e., that the divergence of pressure transfer and divergence of the turbulent energy flux sum to about zero. This conclusion is in agreement with that by McBean and Elliott (1975) in which these two terms were estimated at a height of 5.77 m above dry prairie grassland.

4. CONCLUSION

The variation of gust structure with height up to 200 m was investigated by using the data from the meteorological observation tower with sonic anemometer-thermometers at six levels and the major levels results obtained in this experiment were as follows,

(1) It is found that the wind fluctuations for each component, u, v, and w are normally distributed and there is good agreement between observed and calculated maximum instantaneous wind speed.

(2) The height dependency of the integral scales obtained in this experiment is shown to be approximately as follows,

$$L_x^u \sim z^{0.8},\ L_x^v \sim z^{0.3}\quad L_x^w \sim z^{0.7}$$

(3) The height dependency of the vertical scale obtained from the cross correlation coefficient at two different points is expressed approximately as follows,

$$L_z^u \sim z^{0.6},\ L_z^v \sim z^{0.4}\quad L_z^w \sim z^{0.7}$$

(4) The spectral scale obtained by using the spectral peak and the mean wind speed can be expressed by the following equations,

$\lambda_u \sim z^{0.5}$

$\lambda_v,\ \lambda_w \sim z^{0.3}$ $(z \leq 50\ \text{m})$, $\lambda_u,\ \lambda_v,\ \lambda_w \sim z$ $(z > 50\ \text{m})$

(5) In the energy balance equation, it is found that the sum of the mechanical production and buoyant production is nearly equal to the rate of dissipation and that the divergence of pressure transport and the divergence of turbulent energy flux sum to about zero.

6. REFERENCES

1) Naito, K., T. Hanafusa, and T. Fujitani, 1983: On spatial structures of high winds. 15th Joint Meeting, U.S. Japan Panel on Wind and Seismic Effects, UJNR, Tsukuba.

2) Hanafusa, T., T. Fujitani, 1981: Characteristics of high winds observed from a 200 m meteorological tower at Tsukuba Science City. Papers in Meteorology and Geophysics, Vol. 32, No. 1, pp. 19-35.

3) Panofsky, H.A. and I.A. Singer, 1965: Vertical structure of turbulence. Quart. J. Roy. Met. Soc., Vol. 91, pp. 339-344.

4) Davenport, A.G., 1961: The spectrum of horizontal gustiness near the ground in high winds. quart. J. Roy. Meteor. Soc., 87, 194-211.

5) Busch, N.E. and H.A. Panofsky, 1968: Recent Spectra of Atmospheric Turbulence. Quart. J. Roy. Meteor. Soc., Vol. 94.

6) McBean, G.A. and J.A. Elliott, 1975: The Vertical Transports of Kinetic Energy by Turbulence and Pressure in the Boundary Layer. J. Atmos. Sci., 32, 753-766.

Table 1. Comparison the observed maximum wind speeds with calculated ones

Term \ Height	200m	150m	100m	50m	25m	10m
$\bar{U}$	16.39	14.39	12.82	10.39	9.44	7.26
σ_u	1.95	2.14	2.08	2.18	1.83	1.78
$\sigma_u/\bar{U}$	0.119	0.149	0.162	0.210	0.194	0.245
MW_{obs}	21.70	19.26	17.59	15.15	15.43	11.75
MW_{cal}	21.07	19.54	17.80	15.63	13.84	11.53
$\bar{U}$	16.92	15.67	14.62	11.61	10.44	7.99
σ_u	2.10	2.00	2.33	2.53	2.41	2.08
$\sigma_u/\bar{U}$	0.124	0.128	0.159	0.218	0.231	0.260
MW_{obs}	22.30	21.07	21.22	18.21	16.53	13.43
MW_{cal}	21.96	20.48	20.20	17.68	16.23	12.98
$\bar{U}$	16.85	15.26	14.32	10.73	8.85	6.59
σ_u	1.99	2.23	2.59	2.60	2.28	2.07
$\sigma_u/\bar{U}$	0.118	0.146	0.181	0.242	0.258	0.305
MW_{obs}	20.58	19.25	18.54	17.28	16.39	13.19
MW_{cal}	21.62	20.61	20.54	16.96	14.33	11.41

Table 2. Dependency of the cross correlation coefficients on the averaging time

A.T. \ C.C.	$u_{200} \sim u_{150}$	$u_{150} \sim u_{100}$	$u_{100} \sim u_{50}$	$u_{50} \sim u_{25}$	$u_{25} \sim u_{10}$
0.2 sec	0.62	0.54	0.38	0.42	0.50
0.4 sec	0.63	0.55	0.37	0.43	0.52
0.8 sec	0.65	0.56	0.40	0.45	0.55
1.6 sec	0.67	0.58	0.42	0.47	0.59
3.0 sec	0.69	0.61	0.45	0.50	0.62
5.0 sec	0.73	0.63	0.47	0.54	0.66
10.0 sec	0.78	0.68	0.54	0.62	0.73
20.0 sec	0.84	0.72	0.59	0.68	0.82
60.0 sec	0.90	0.77	0.64	0.79	0.88

A.T. \ C.C.	$v_{200} \sim v_{150}$	$v_{150} \sim v_{100}$	$v_{100} \sim v_{50}$	$v_{50} \sim v_{25}$	$v_{25} \sim v_{10}$
0.2 sec	0.40	0.37	0.20	0.24	0.32
0.4 sec	0.41	0.38	0.21	0.25	0.33
0.8 sec	0.42	0.40	0.22	0.26	0.36
1.6 sec	0.45	0.42	0.24	0.29	0.40
3.0 sec	0.49	0.46	0.27	0.33	0.47
5.0 sec	0.51	0.50	0.31	0.38	0.55
10.0 sec	0.60	0.57	0.38	0.43	0.67
20.0 sec	0.66	0.60	0.49	0.44	0.73
60.0 sec	0.74	0.68	0.68	0.48	0.84

A.T. \ C.C.	$w_{200} \sim w_{150}$	$w_{150} \sim w_{100}$	$w_{100} \sim w_{50}$	$w_{50} \sim w_{25}$	$w_{25} \sim w_{10}$
0.2 sec	0.44	0.37	0.23	0.31	0.31
0.4 sec	0.46	0.39	0.25	0.33	0.34
0.8 sec	0.49	0.42	0.27	0.36	0.39
1.6 sec	0.54	0.46	0.31	0.41	0.46
3.0 sec	0.60	0.54	0.36	0.46	0.52
5.0 sec	0.64	0.59	0.43	0.51	0.58
10.0 sec	0.70	0.64	0.48	0.61	0.65
20.0 sec	0.76	0.67	0.65	0.62	0.70
60.0 sec	0.83	0.78	0.82	0.69	0.78

C.C.: Cross correlation coefficient
A.T.: Averaging Time

Table 3. Lag time when the cross correlation coefficient is maximum

Height diff.		200-150	150-100	100-50	50-25	25-10	Mean wind speed at 10m
Run 1	u*	0.4	8.0	8.0	0.4	2.6	
	v	4.0	4.8	6.4	2.8	1.8	7.26
	w	-0.4	0.2	-1.2	0.2	0.4	
Δu(m/s)		2.01	1.57	2.43	0.95	2.18	7.26
Run 2	u	2.2	2.2	4.0	0.0	0.8	
	v	4.0	2.0	4.0	2.2	2.6	8.00
	w	0.6	0.8	0.0	0.2	0.0	
Δu(m/s)		1.23	1.04	3.02	1.17	2.44	8.00
Run 3	u	2.0	4.8	8.0	4.0	0.6	
	v	2.4	3.2	4.0	2.4	2.4	6.59
	w	0.2	0.0	-0.6	0.2	0.0	
Δu(m/s)		1.59	0.93	3.60	1.88	2.26	6.59

Unit; wind speed: m/sec

time: sec

Table 4. Observed values of each term in the energy balance equation

Run No.	Height (m) / Term	173	122	71	35	16
1	M	0.032	0.025	0.089	0.089	0.232
	B	0.003	0.004	0.006	0.006	0.005
	T	-0.023	-0.020	0.026	0.054	0.125
	ε	0.011	0.016	0.046	0.109	0.206
	(P)	0.047	0.033	0.023	-0.068	-0.094
2	M	0.050	0.038	0.156	0.204	0.368
	B	0.007	0.008	0.008	0.006	0.007
	T	-0.015	-0.004	0.022	0.168	0.154
	ε	0.010	0.017	0.054	0.154	0.276
	(P)	0.072	0.033	0.088	-0.112	-0.055
3	M	0.027	0.018	0.069	0.070	0.150
	B	0.004	0.004	0.006	0.006	0.006
	T	0.001	-0.020	0.042	0.032	0.035
	ε	0.014	0.021	0.063	0.103	0.158
	(P)	0.016	0.021	-0.009	-0.059	-0.037
4	M	0.023	0.012	0.065	0.072	0.175
	B	0.004	0.005	0.006	0.007	0.006
	T	-0.007	-0.024	0.028	0.030	0.136
	ε	0.012	0.019	0.050	0.103	0.241
	(P)	0.022	0.044	-0.007	-0.054	-0.194
5	M	0.025	0.019	0.096	0.146	0.274
	B	0.002	0.003	0.004	0.005	0.003
	T	0.003	-0.016	0.024	0.129	0.059
	ε	0.010	0.018	0.056	0.135	0.220
	(P)	0.014	0.020	0.020	-0.113	-0.002
6	M	0.023	0.016	0.048	0.062	0.116
	B	0.000	0.000	0.001	0.001	-0.001
	T	0.013	-0.008	-0.002	0.034	0.029
	ε	0.009	0.016	0.050	0.115	0.193
	(P)	0.001	0.008	0.001	-0.086	-0.107

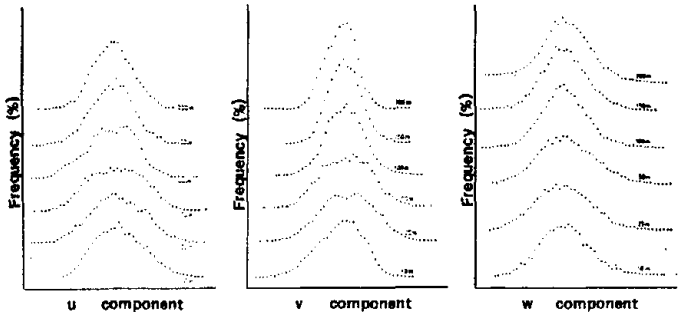

Fig. 1 An example of the frequency of wind fluctuations

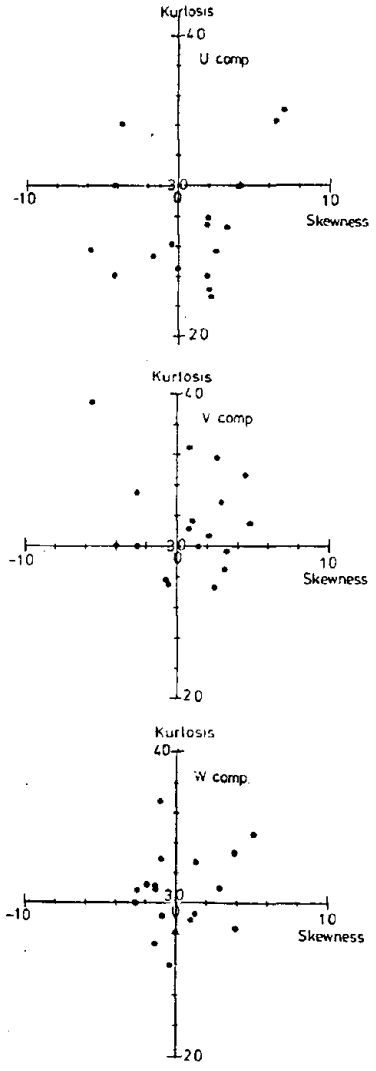

Fig. 2 An example of the frequency of skewness and kurtosis

Fig. 3 Normal frequency distribution (the shadow part indicates 1/120 (5=/600))

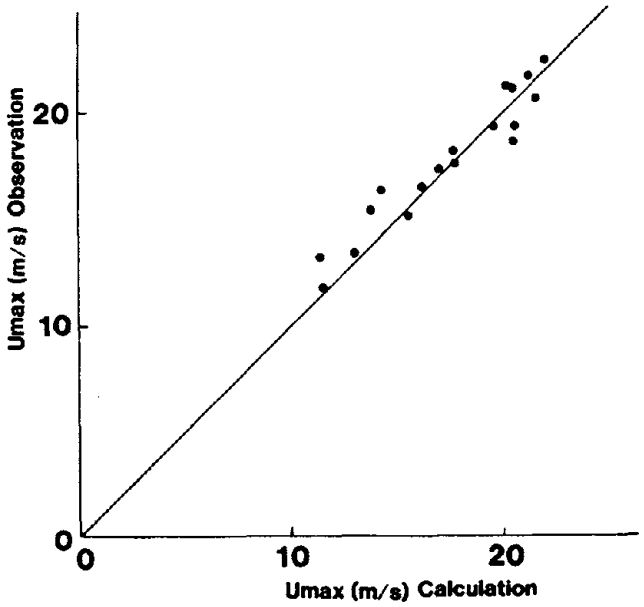

Fig. 4 Comparison of observed maximum wind speeds with calculated ones

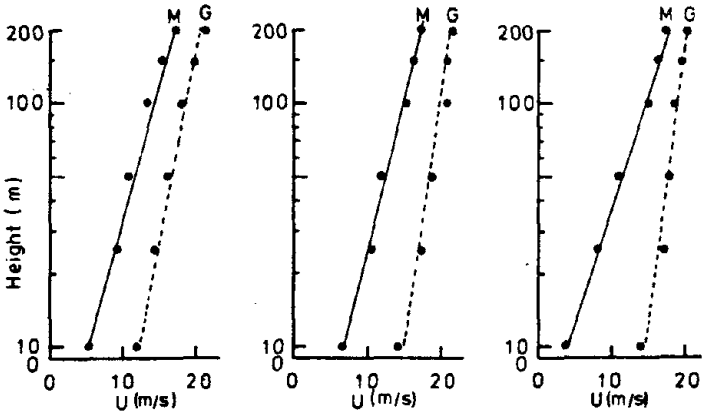

Fig. 5 Height distribution of mean wind speed (M) and maximum wind speed (G)

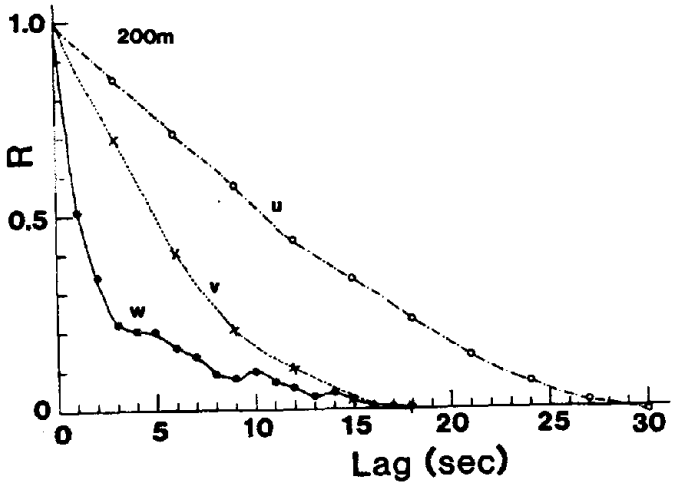

Fig. 6 Auto correlation of wind fluctuation

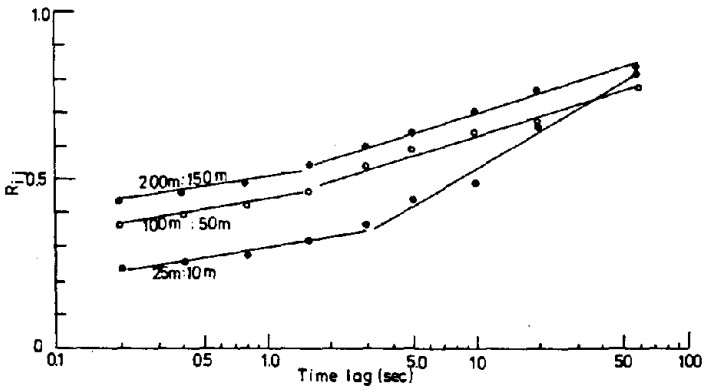

Fig. 8 Dependency of the cross correlation coefficient on the averaging time

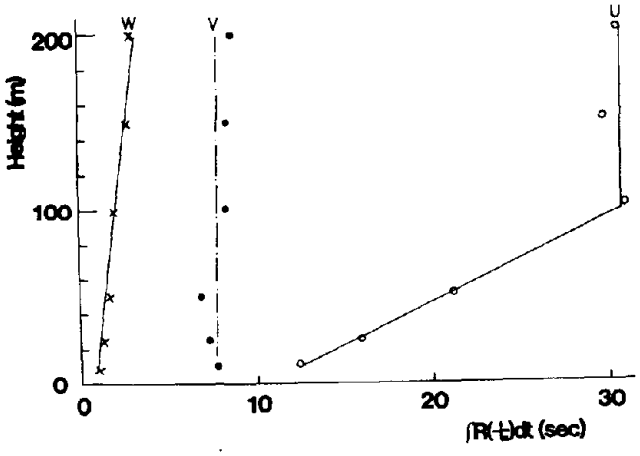

Fig. 7 Height distribution of $\int R(t)dt$

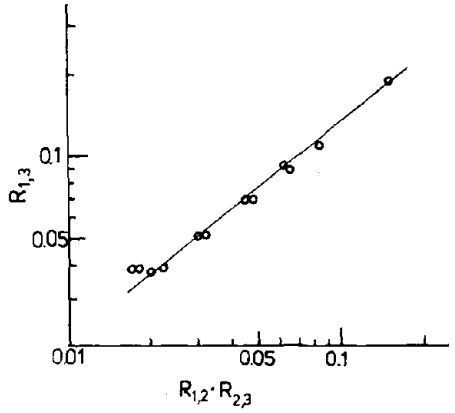

Fig. 9 The relation among the cross correlation coefficients at different levels

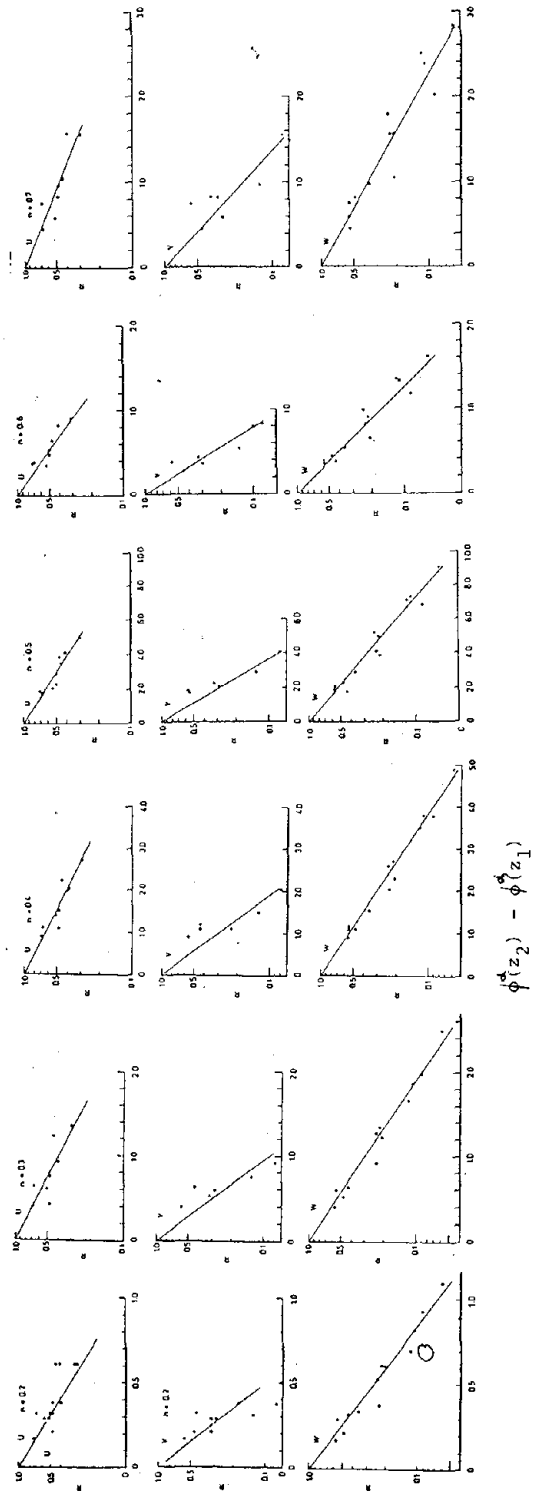

Fig. 10 Relation between the cross correlation coefficient and $\phi(z)$

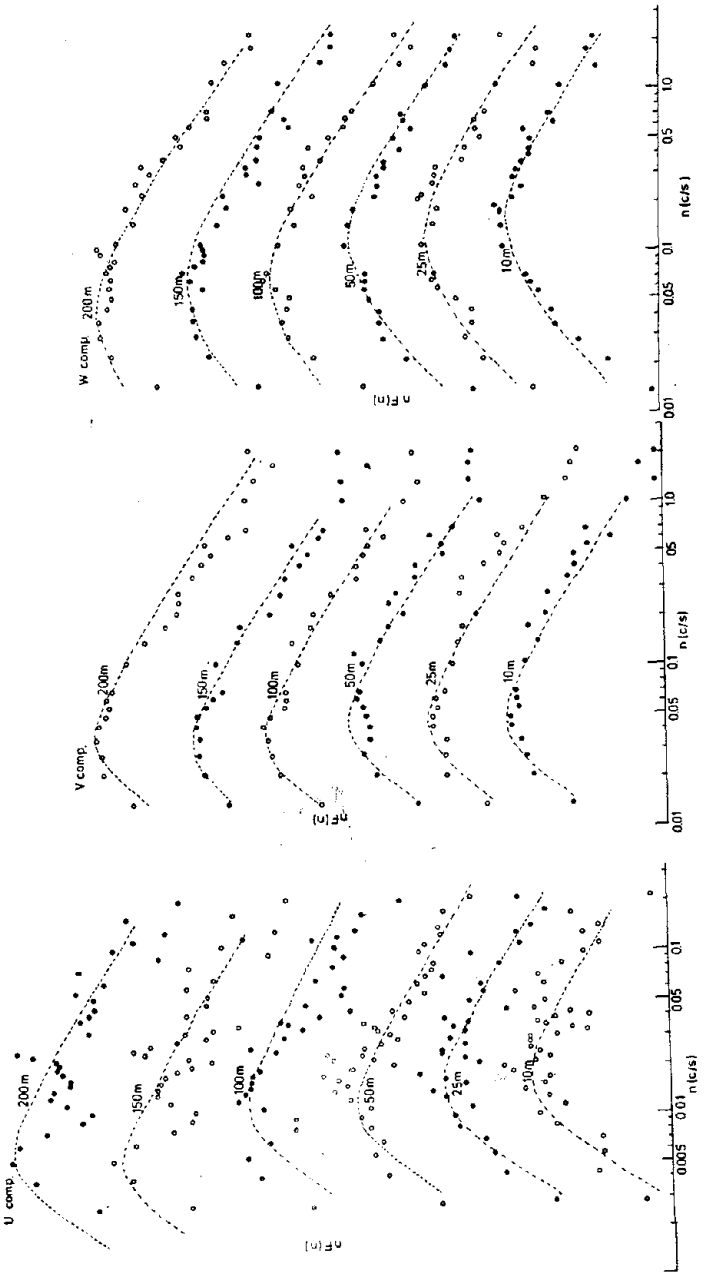

Fig. 11 Examples of spectra of wind fluctuations

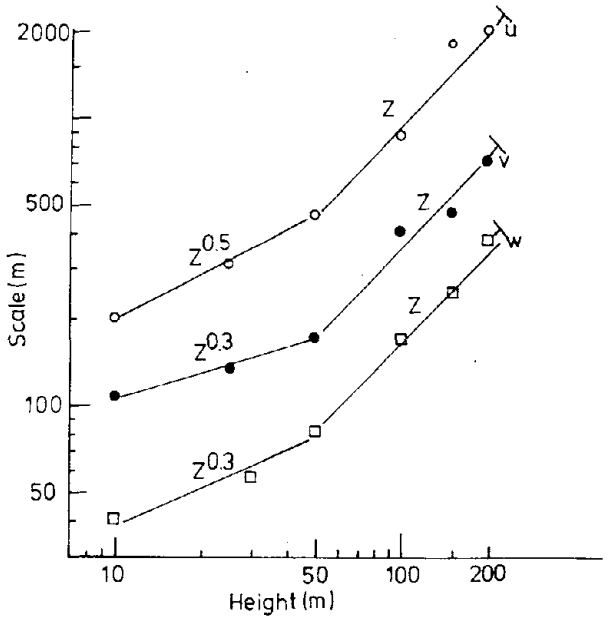

Fig. 12 Height variation of the spectral scale, λ_m

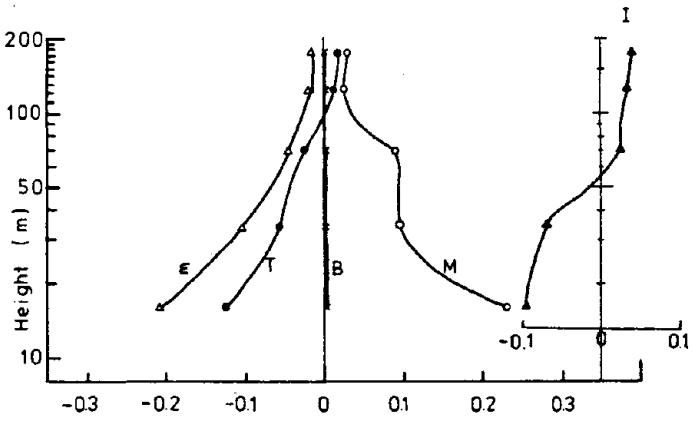

Fig. 13 Height variation of turbulent energy

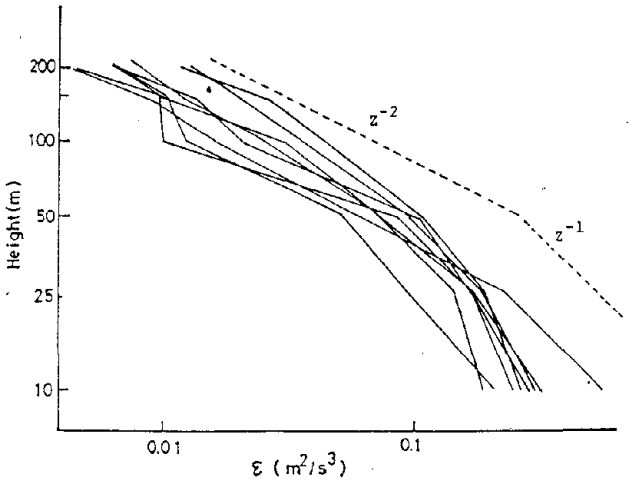

Fig. 14 Height variation of the dissipation rate

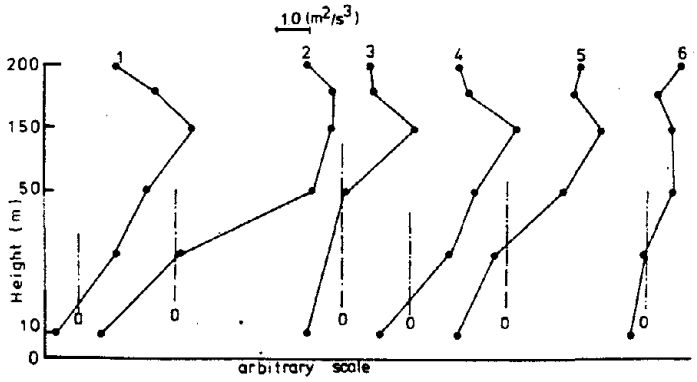

Fig. 15 Height variation of W'E

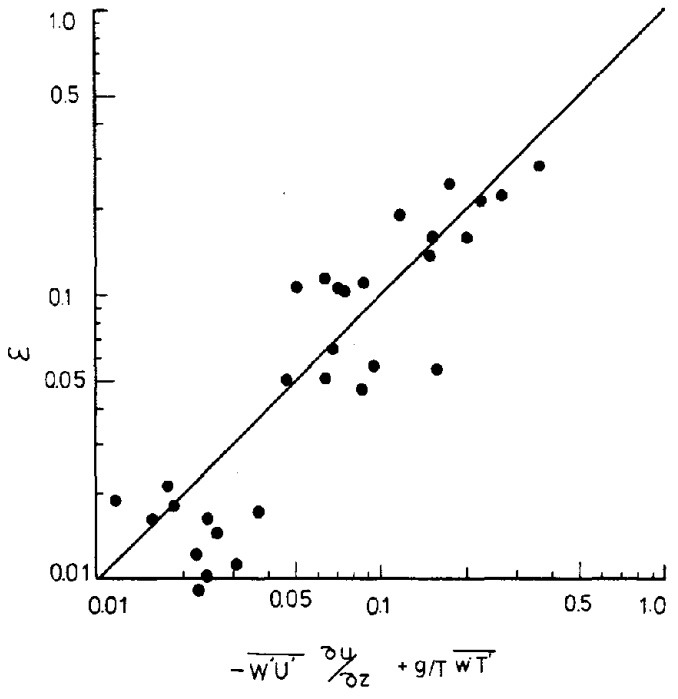

Fig. 16 Comparison ε with $\overline{-u'w'}\ \frac{\partial u}{\partial z} + g/T\ \overline{w'T'}$

SEISMIC VULNERABILITY OF LIFELINE SYSTEM USING COMPUTERVISION CADDS COLOR GRAPHICS SOFTWARE

by
C. V. Chelapati*
Stanley K. Takahashi**

ABSTRACT

Seismic vulnerability of lifeline utility systems are highly 'graphics' intensive. Several maps involving the layouts of utility systems, site plans, soil parameters, fault zones and buildings are involved in the study. The efforts involved in the analysis part is relatively simple when compared to the management of extensive 'graphics' data and reporting.

In this pilot study, the color graphics software, "CADDS", developed by "Computervision" Company is used to develop the Seismic Vulnerability Model (SVM) of a lifeline utility system at a typical Navy facility. This model displays in color the land base map, including site outline, roads, runways, buildings, utility system layout, fault break, liquefaction and acceleration zones. Pertinent information regarding each utility segment is encoded onto the SVM as "Intelligent" data on each pipe.

An earthquake is simulated on an assumed fault break, and the strain levels in each pipe is computed using "NEWVAR"; a programming language for Computervision applications. A damage criteria is established for failure/ breakage of the pipes as a function of strain in the pipes, acceleration due to shaking and the susceptibility of the liquefaction zone. Using the 'Boolean' operations, a damage state for each segment of the wastewater system is estimated. This information is displayed in various ways using color and the Area Information Management (AIM) software.

Each building is encoded with the designation of pipeline segments that serve its functions. A comparison of these with the damaged pipeline segments, will identify the buildings that will not be served due to the occurrence of an earthquake. This information is presented using a color display monitor and by generating a report using the Data Extract/Data Merge software of Computervision.

Color graphics are an excellent way of visually inspecting the status of each utility line and the consequences of damage to utility lines in the event of an earthquake. This pilot study shows that it is efficient in studying the problem associated with seismic vulnerability of lifeline systems.

Keywords: Seismic, Lifelines, Computer graphics, Computervision, CADDS, Damage criteria, Strains, Pipes, Faults

1. INTRODUCTION

1.1 Background

The United States Navy has several installations throughout the world on the CircumPacific belt where the facilities could be subjected to potentially strong earthquake motions. The need for basic operations at any installation to proceed with minimal disruptions after an earthquake is obvious. The operations of a base depend not only on the safety of the buildings but also on the lifeline utilities serving the building and its functions in the building. Most lifeline utilities should remain operational or be repaired with minimum delays.

Most utilities have a source, distribution network, collection and disposal points. They serve various buildings on a Naval base, and the physical characteristics of components in a utility line frequently changes. They may pass through different soil zones. Thus, it is very difficult either to describe or process the utility system information without appropriate maps. The recent advances in computer graphics and Computer Aided Design and Drafting System (CADDS) software make it more convenient now to investigate and study the seismic vulnerability of lifeline utilities.

This report utilizes the North Island Naval Air Station (NINAS) as a pilot project to study the seismic vulnerability of lifeline systems. The seismic vulnerability of buildings at NINAS was presented in Reference 1. The soil studies and the liquefaction potential at the NINAS site was

*California State University Long Beach
**Now with L. I. Dimmick Corp., Oxnard, CA

presented in Reference 2. The Seismic Vulnerability Model (SVM) will eventually include all buildings, roads, airfields, wharfs, piers, soil conditions, liquefaction zones, fault traces, groundwater profile, zones that might be subjected to flooding in case of tsunami, all lifeline systems that serve the facility, location of emergency supply measures such as water storage tanks, power generators, portable gas and all other items necessary for functioning of the base. The SVM can also capture the data on the damage potential to buildings in case of potential earthquakes. At NINAS, the site selected for this study, the following lifeline utility systems are identified:

a) Fresh Water
b) Sanitary Sewer
c) Industrial Waste
d) Potable Water between NINAS and City of Coronado
e) Salt Water
f) Steam/Condensate Distribution
g) Compressed Air Distribution
h) Oily Waste - Recovered Oil
i) Natural Gas Distribution System
j) Telephone System
k) Electrical Power System

Utility systems a) through i) have pipes with either gravity flow or are under pressure in their distribution system. In the telephone or electrical system, the distribution system is cable and/or circuits with equipment at various nodes. Thus, the main features and the vulnerability analysis of these two utilities are quite different from other utility systems.

A graphic database for the SVM containing most of the above information is to be established using the Computervision CADDS System. A seismic vulnerability criteria for lifelines should be based on the site characteristics which might have an adverse effect on the utility pipes, the physical characteristics of the pipes and the potential for earthquake hazard at the site. Vulnerabilty analysis on this SVM will be performed using the established criteria to locate the pipes that might break or be damaged during an earthquake. The resulting data will be merged into the graphics database. The buildings that will be denied utility services due to potential failure will be identified; information will then be merged into the graphic database and displayed.

1.2 Objective

The objective of this study is to develop seismic vulnerability lifeline system model using computer color graphics and the Computervision CADDS software.

1.3 Scope of Work

In Phase I of this study, the methodology to analyze the lifeline systems will be developed and applied to the sanitary system. The methodology developed will be applied to other utilities during the next phase.

2. SITE DESCRIPTION

2.1 North Island Naval Air Station (NINAS)

NINAS occupies about 2,580 acres of land and constitutes a major portion of Coronado Island, which is situated between San Diego Bay and the Pacific Ocean. Portions of the Naval Air Station are hydraulically filled, reclaimed areas. Two areas called Spanish Bight (Region I) and Whalers Bight (Region II) are prone to liquefaction (Figure 1).

This region is affected by four major fault systems (Figure 2). These are offshore the San Clemente, Elsinore, San Jacinto and San Andreas faults. There is a 25 year, 90% probability of not exceeding peak ground acceleration levels of 0.05g, 0.13g, 0.06g and 0.07g due to earthquake magnitudes of 5.9, 6.9, 6.6 and 7.3 occurring respectively from the four fault systems (Ref. 1). From past experience with earthquakes, these acceleration levels are too low to cause any disruptions in the utility systems; however, the Spanish Bight Fault is assumed to run through the NINAS (Reference 3), and the length of the fault is estimated to be 10 miles. There

is no recorded history of earthquakes occurring on this fault. Since this assumed fault passes through the site, a sharp high acceleration jolt confined to a small area could occur and rupture utility lines. Further, the assumed Spanish Bight Fault runs through the Spanish Bight area which has a potential for liquefaction. Utility lines which serve many buildings traverse this area.

In this pilot study to develop a methodology for the analysis of Seismic Vulnerability Model, the Spanish Rose Fault break, high acceleration levels and liquefaction are assumed and this is a very unlikely event.

3. UTILITY INFORMATION

Information on all utilities was gathered by visiting the Public Works Office and other appropriate administrative offices at the NINAS site. The information is in the form of several sheets of detailed drawings for each utility. Site visits were also made to observe the utility locations.

From the site plan and other available information, the outline of the island, roads, aircraft runways, liquefaction zones, fault rupture due to a hypothetical event on the Spanish Bight Fault, estimated acceleration zones and "footprints" of most important buildings are extracted and a graphic database for the SVM is established using the Computervision CADDS software. From the detailed utility maps, the needed information on the sanitary pipe elements is extracted and transferred to a key map on a Size E (34"x44") drawing. For this study, the key map for sanitary system provides the diameter of the pipe, pump stations, lift stations, type of material and direction of flow from collection of sewage from various buildings to a main collection point to be treated by the City of Coronado Sewage System. Then, from the key map of the sanitary sewer utility system, the layout of the pipes and other elements are entered manually into the graphics database. In addition, the "intelligent" information on each pipe is coded into graphic database separately.

4. USE OF COMPUTERGRAPHICS FOR ANALYSIS

For their analysis and design, engineers extensively use computations, figures, drawings and reports. Therefore, the ability to access information from a graphic database and to display the results in graphic form provides tremendous advantage. In addition, with the aid of color, visualization is very effective. The current trend of practice is to capture graphic information in the form of drawings. Storing the drawings on paper for retrieval and updating purposes is very cumbersome and time consuming. However, when this information is captured on a graphic database, it is extremely versatile and efficient for many engineering uses. Computergraphics is extensively used in aerospace applications and this segment of computer industry is destined to be a multi-billion dollar industry. The US Navy has acquired several Computervision "CV" workstations and has begun to capture much information on Computergraphics. One of the areas which has extensive application is Automated Mapping and Facility Management (AM/FM). Aerial photography and stereo mapping is used to capture the "footprint" of an installation. This information is then converted using Automated Mapping procedures into a "Computervision" graphics database and is used for facility management and updates (Ref. 4). Computergraphics are widely used in many other areas of application including mechanical design, finite element analysis, numerical control, architecture/engineering/construction, piping design, printed circuit and wiring diagrams to name a few. Since this field is new, several applications are constantly emerging and better software packages are being written. For this study, extensive use of Computervision CADDS Color Graphics System is made to study the Seismic Vulnerability of a lifeline utility system at a Naval installation.

5. COMPUTERVISION WORKSTATION DESCRIPTION

The Computervision "CV" graphics computer system consists of hardware and software. The hardware consists of Computervision Graphics Processor

Unit (GPU) with several microprocessors (to do graphic functions), a tape drive, disk drive and a workstation (Figure 3). A workstation consists of display monitor, digitizing tablet, tablet menu, digitizing pen, image control unit and hard copy graphics printer. Computervision has developed its own graphics language. There are several thousand commands; each command is structured with a verb, noun and modifiers as necessary (Fig. 4). The input needed is supplied via the keyboard or digitizer. The Computervision workstation has two levels; one is an Operating System (OS) level and the other is Computer Aided Design Drafting System (CADDS) level. Different functions are performed at different levels.

The Computervision supports several programming languages which are used for different environments. Some of the languages are FORTRAN, NEWVAR and VARPRO2.

Although Computervision is extensively used for graphics intensive applications, the use of CADDS for Computer Aided Engineering (CAE) is relatively new. The present application of CADDS software for the Seismic Vulnerability Analysis of Lifeline Systems is a new development (Figure 5).

6. SEISMIC VULNERABILITY MODEL (SVM)

6.1 Database Management (DBM) Schema

Figure 6 shows the overall Database Management configuration. Central to this schema is a "virtual map". This virtual map is a computer generated image of the NINAS "physical map". The physical map is a conventional two-dimensional "Paper Map" limited to displaying lines, surface textures, symbols and graphics text. The virtual map is enhanced with geo-coded nongraphic attribute data (feature codes) associated with individual graphic elements.

6.2 Graphic/Nongraphic Interface

Nongraphic attribute data resides in the virtual map as "property values" -- Alpha/Numeric (A/N) data inserted into various graphic entities making up the map image (lines, strings, nodal lines, symbols and polygon nodes). Each of these coded entities serves as a "hook" for posting or reporting geographically distributed A/N data "through" the map. Pertinent feature codes can be added manually at a graphic workstation. More important, however, A/N data records resident on any computer can be merged into the map. This can greatly expedite the coding of utility systems if there are already pertinent computer data files. If an Automated Mapping/Facilty Management (AM/FM) system is already in place or is being established for a Naval facility, the SVM can be included by adding additional feature codes and map layers to those essential to a full AM/FM system.

6.3 Database Management (DBM) Components

The following is a description of the system's individual components of SVM.

- Land Base
- Area Information Management Applications
- Utility System Network
- Report Extraction and Merge

Each of these components are discussed in general detail.

6.4 Land Base Map

The graphic map for NINAS was prepared by calibrating the E size "paper" base map to a Computervision Instaview Digitizing Tablet. Control points were defined at the four corners of the map based on a local grid. The base map elements include:

- Runway Edges
- Road Center Lines
- Building Footprints
- Property Boundary
- Approximate Location of Earthquake Fault
- Liquefaction Zones
- Approximate Earthquake Acceleration Zones

Each of these elements reside on different layers; there are 256 separate layers available for use.

The land base map is a fair representation of the physical features of the NINAS. However, the precision of this automated map is limited by the precision of the originally drafted lines that make up the "paper" map. A far more precise and practical approach to "capture" this data is the direct conversion of digital photogrammetrical data to a Computervision Graphic Database. This technique has recently been proven to be practical in a pilot project being conducted by the Mare Island Naval Shipyard (Ref. 4). It is not only possible to directly derive highly precise representations of building "footprints," pavement edges and other visual physical features, but the graphic data can be converted to "polygon" entities without any human intervention. "Polygon" entities are used to create, categorize, manipulate and report map properties. However, all utility lines and other associated components have to be manually inserted. The photogrammetrical data has far more information than is needed for the SVM. Thus, special editing has to be done to create the base map.

6.5 Area Information Management (AIM)

The AIM software makes it possible to convert boundaries of area information critical to earthquake impact assessment into "intelligent" polygon entities. Each polygon has a node that contains feature codes describing conditions pertinent to the SVM. Area information so converted to polygons included:

- Building "Footprints"
- Known Liquefaction Zones
- Estimated Limits of Earthquake Acceleration in Various Zones

Polygon manipulations performed with these data enhanced areas include:

1) Polygon Overlays. Acceleration zones were spatially correlated (intersected) with liquefaction zones to derive a mosaic of subareas representing varied combinations of earthquake impact conditions. Each subpolygon carries automatically generated sets of feature codes describing the combination of conditions present.

2) Polygon CrossHatching. Polygons were crosshatched in various colors according to the findings of Boolean operations searching out specific conditions or combination of conditions present. These include:

- Presence of liquefaction conditions
- Intensity of earthquake acceleration potential
- Varied combinations of acceleration and liquefaction
- Building subject to interruption of service due to failure of specific utility line segment(s)

3) Polygon Projections. Edges of polygons were projected in 3D spaces to display relative conditions. Any "real" property value placed on the polygon can be used as a basis. Areas so projected included:

- Actual estimated height of buildings
- Relative intensity of earthquake impact potential. In this instance, the projected distance was accentuated by a scaling factor; i.e., the horizontal acceleration values were multiplied by a factor of 1,000 so that they appeared projected 300 to 2,000 feet vertically to visually dramatize the relative potential impact.

4) Data Extraction/Data Merge. Feature codes automatically placed on polygon nodes (area, perimeter, unique database number designator) or manually added (building heights, liquefaction conditions, etc.) can be extracted by using the "Extract Definition File" (EDF) and by generating User Defined reports. Most important, information that may already reside in a main frame data set (i.e., real property record files) may be automatically merged into polygons adding (potentially vast) arrays of data to the Virtual Map without human intervention. This capability will be described later.

This work to date has shown that the Computervision AIM software is an appropriate tool for performing spatial analysis, displaying and reporting extraction essential to the SMV's DBM needs. A capability proven possible, but not employed at this time, is the overlay of the building "footprint" polygons with the earthquake impact polygons to determine varied impact potential on a single building. This is important when large buildings straddle liquefaction zones. Reference 1 gives the amount of damage to each building as a function of ground acceleration at the site. It is also possible, using AIM software, to display the amount of potential damage to each building for each level of earthquake.

6.6 Utility System Networks

Nodal lines were used to represent piping networks to utilize their "rubberbanding" capabilities. Line ends are connected to "Connect Nodes" (CNODES). It is possible to manipulate the locations of the CNODES, and regardless of CNODE displacements, the nodal line(s) will "snap" to their new end position. Since the length of nodal lines can be extracted to a thousandth of a foot, strain in pipes induced by earthquake generated ground movement can be computed.

To best represent the before and after conditions of these pipes, their length was broken by a CNODE at each vertex represented in the utility map from which they were digitized. Significant distribution collection system facilities were also defined with nodal symbols (pump stations, lift stations, etc.). Feature codes pertinent to the SVM were added to the pipes including:

- Unique network segment designation
- Sequence of pipe in network segment starting at furthest distance from central plant (sewage treatment, central supply point, water, gas, electrical) or point of generation (compressed air, steam, other)
- Type of pipe material
- Year pipe was installed
- Acceleration level at midpoint of pipe
- Liquefaction condition at midpoint of pipe
- Length of pipe before earthquake
- Length of pipe after earthquake
- "Dummy Value" regarding damage potential of pipe due to earthquake

The first two features, segment designator and sequence number provide a unique address of each pipe segment critical to report generation and data merge/analysis operations. The sequence number (an interger property value) makes it possible to determine which buildings along the same network segment experience service interruption due to a pipe breaking at the beginning, middle or end of the segment (Figure 7).

Accelerations of pipe elements were added using Entity Classification software which automatically adds feature codes associated with polygon to any components origin present inside the polygon's edges.

The before and after lengths were automatically added as feature codes using a macro (NEWVAR language) written specially for the SVM study effort.

Pipe condition data (type, year installed, diameter) is manually encoded. However, this data, if already available in A/N form on a mainframe, can automatically be merged into the pipes.

Data capture cost in digitization of data, is not prohibitive but will require substantial amount of work hours to digitize and code each utility line. This study proved that nodal lines can be used to successfully measure precise before and after conditions of utility networks.

A key management consideration is that the SVM could very well be another dimension of a full AM/FM system. The graphic and nongraphic DBM requirements of both are similar. Based on the lessons learned from the Mare Island Naval Shipyard AM/FM system prototypical concept model (Ref. 4), it is reasonable to say that a complete SVM represents costs which could have been

reduced if a full AM/FM system were already available. As such, the SVM cost would be less expensive if performed in conjunction with a full AM/FM system. This would save time in capturing the raw data of Land Base Map from drawings.

6.7 Report Extraction and Merge

As previously discussed, the virtual map is designed with an array of graphic hooks for extracting and merging A/N data from and to the map. This capability is supported by existing CADDS 4/4x Data Extract/Data Merge software. These "instruments" set the property values (feature codes) to be included in and the formatting parameters of the desired reports. Report extract/merge operations can be performed for local use (within the CV system exclusively) or be used as a mainframe (via modem) and other computers in the communication network. Likewise, the "merge" capabilities of the data extract software makes it possible to automatically (and regularly) update the "virtual map" with information encoded exclusively at the mainframe.

The data extract form prepared for the SVM is designed to:

- Extract all information in a utility network pertinent to the impact assessment.
- This data is used as a source file by the NEWVAR program that processes this information to determine the estimated pipe strain (deformation), strain level and the damage rating.
- Once these findings are generated, these pertinent fields in the EDF are overwritten.
- The data extract file is "merged" into the pipe nodes in the virtual map.
- The pipes meeting a user defined damaged rating are then identified with a "Mark Ent Cond" Command.
- The extract is then run again. The list of pipe addresses are the unique addresses of the damaged pipes.
- The buildings that have interrupted services due to a damaged pipe(s) are then marked (or cross hatched).

7. RESULTS

Using the Computervision "CADDS" workstation, all the needed information for the seismic analysis from the key is entered into the graphics database. Figure 8 shows a reproduction of some of the features of the SVM. Different types of information is on different layers so that the needed information can be displayed in a variety of ways.

The seismic vulnerability criteria for the lifeline utility system is developed as follows. In many cases of actual earthquakes, the damage to underground utilities is mostly limited to areas near the fault break zone.

There are three basic parameters associated with the rupture of pipes: excessive strains caused by the rupture of potential fault, liquefaction and the level of acceleration due to shaking. A potential fault rupture scenario was created on the assumed Spanish Bight Fault. Using the coordinates of each node point which resides in the graphics database, the length of each pipe before the earthquake was computed using a "Macro" written in "NEWVAR" language. The deformed length after the fault rupture is computed and the resulting strain in each pipe is determined. From this explicit strain, a rating of 1 to 5 is given (5 being the most severe to 1 being a very low strain). The explicit acceleration levels are converted to Zone 1 being the lowest level of acceleration and Zone 5 being the highest. The graphics database also contains liquefaction zones. Table 1 shows a utility damage level interaction matrix as a function of liquefaction and acceleration zones. If a pipe is located in the liquefaction zone and subjected to high and long duration acceleration, then it is assumed that the soil support for pipes is weakened, and high damage to pipes occur. Table 2 shows the utility damage level interaction matrix as a function of the acceleration zone and strain level. A subjective judgement criteria is shown where the damage level will be highest with increasing strains and increasing levels of acceleration.

From the three variables, a damage level to each pipe is determined. This information can be displayed in various forms and in color to aid visualization. Thus, one could easily identify the "damaged" or "ruptured" pipes.

Each building is coded with all the pipes in the utility that are necessary for performing the designated functions. For this report, this is a network/branch of pipes that carry the sanitary sewage from a building to the main trunks that lead to the City of Coronado Sewage System.

By comparing this information with the list of damaged pipes, the buildings that will not be served by the damaged lifelines can be displayed visually. Figure 9 shows an assumed earthquake fault, partial area where the sanitary sewer pipes are damaged and the buildings that will not be serviced by the damaged utility.

Since all the information is in computer graphics format, it is very convenient to study the situation in case of emergency and to devise alternate plans expeditiously. Since time is of essence, in case of a potential earthquake, the graphical information will be extremely useful as an aid in bringing up the facilities to a normal functioning level.

Table 3 summarizes a typical output of the information stored by Computervision. Additional information on the SVM may be obtained from Reference 5.

8. SUMMARY AND CONCLUSIONS

This pilot study shows that the emerging computer graphics and Computervisions CADDS software can be used with great advantage in conducting the Seismic Vulnerability of Lifeline Utility Systems. The development of the Seismic Vulnerability Model (SVM) will provide tools to predict damage in case of an earthquake. By studying several scenarios, intelligent decisions can be made to reduce or to mitigate potential damage. In case of an earthquake, the SVM will provide instant visualization of damaged conditions to utility networks and can be used as a tool to make decisions to alleviate the damaged state.

9. RECOMMENDATIONS

It is highly recommend that the remaining utility lines be included in the Seismic Vulnerability Model study so that a complete system can be studied for the vulnerability of lifeline facilities at NINAS.

It is also recommended that the complete AM/FM system be created for NINAS so that the management can study other functions (such as maintenance and facilties management) in addition to the lifeline vulnerability of utility system. When the complete AM/FM/SVM is created, it would be very easy to update this system on a regulr basis. The computer management of facilties would not only be highly accurate but it will also provide the capabilty of fast information retrieval and manipulation.

10. ACKNOWLEDGMENTS

The authors wish to thank Mr. J. V. Tyrrell (NAVFAC, Code 04BA) for his continual financial and technical support and Mr. Dennis H. Klein and Mr. Hugh Williams (AM/FM consultants) for their participation in the development of the Seismic Vulnerability Model. Appreciation is also extended to Mr. Jerome H. Hopkins of NCEL for providing Computervision system assistance during very crucial times.

11. REFERENCES

1. Naval Civil Engineering Laboratory, Technical Report M51-78-08: "Earthquake Hazard Reduction Program, North Island Naval Air Station, San Diego, Calif." by C. V. Chelapati, S. K. Takahashi and T. K. Lew, Port Hueneme, Calif., April, 1978.

2. Naval Civil Engineering Laboratory, Technical Report R847: "An Earthquake Analysis of the Liquefaction Potential at the Naval Air Station, North Island," by J. Forrest and J. Ferritto, Port Hueneme, Calif., Sept., 1976.

3. "Report of Geotechnical Studies Investigation/Evaluation of Seismic Vulnerability of Structures, Naval Ocean Systems Center and Naval Communications Station, San Diego, CA for the United States," By Leroy Crandall & Associates. Contract No. 247483C2466, Dec., 1984

4. "Mare Island Naval Shipyard Automated Mapping/Facility Management System Prototypical Concept Model," by Dennis Klein & Associates, Mill Valley, Calif., March, 1985.
5. "Seismic Vulnerabilty of Lifeline Systems Using Computervision CADDS Color Graphics Software - Phase I" (In preparation), by C.V. Chelapati, Huntington Beach, Calif., 1985.

12. DEFINITIONS

AIM	Area Information Management
AM/FM	Automated Mapping and Facility Management
A/N	Alpha/Numeric
CAD/CAM	Computer Aided (Design)/Computer Aided Manufacturing
CADDS	Computer Aided Design and Drafting System
CAE	Computer Aided Engineering
CV	Computervision
EDF	Extract Definition File
FORTRAN	Formula Translation Programming Language used mostly for scientific and engineering applications
GPU	Graphical Processer Unit
Macro	A series of CADDS commands grouped together to perform a certain function
NEWVAR	An interactive programming language to generate CADDS commands
NINAS	North Island Naval Air Station
OS	Operating System
Polygon	Entity used to create categories, manipulate and report map properties
SVM	Seismic Vulnerability Model
VARPRO2	A Computervision CAD/CAM Language
Virtual map	Computer generated image of a physical map

Table 1. Utility Damage Level Interaction Matrix, Acceleration Zone/Liquefaction

Liquefaction	Acceleration Zone				
	1	2	3	4	5
No 0	0	0	0	0	0
Yes 1	0	0	5	5	5

Table 2. Utility Damage Level Interaction Matrix, Acceleration/Strain

Strain Level	Acceleration Zone				
	1	2	3	4	5
1	0	0	0	0	0
2	0	0	0	1	2
3	0	0	1	2	3
4	0	1	2	3	4
5	1	2	3	4	5

Table 3. Typical Report Output from Computervision

North Island Naval Air Station Automated Earthquake Assessment Model
Using Computergraphics-Computervision CADDS System
Siesmic Hazard Evaluation of Utility Systems

MM-DD-YY 5- 1-85 Page ## 1

A B System Segm.	C Matl Type	D Strain	E Strain Level	F Quake Accel	G Accel Ratg	H Liq Ratg	I Length Before	J Length After	K Damage Rating
A1 1	TC	0.773	5	0.20	3	Y	129.2250	129.2250	
A2 1	TC	-0.658	5	0.20	3	Y	108.7710	108.7700	
A3 1	VC	-0.274	5	0.20	3	Y	66.5170	66.5150	
A3 2	VC	0.842	5	0.20	3	Y	122.5180	122.5180	
A3 3	VC	-0.428	5	0.20	3	Y	70.0410	70.0410	
A3 4	VC	0.149	5	0.20	3	Y	50.8090	50.8100	
A352	CI	-0.244	5	0.20	3	'	153.9990	154.0000	
A353	TC	9.258	5	0.20	3	'	203.7180	201.4730	
A4 1	VC	-0.884	5	0.20	3	Y	45.9670	27.6560	
A4 2	VC	1.934	5	0.20	3	Y	144.8800	134.8700	
A4 3	VC	-0.731	5	0.20	3	Y	79.3960	79.3940	
A4 4	VC	2.001	5	0.20	3	Y	238.2710	238.2710	
A8 2	TC	-0.330	5	0.20	3	Y	72.8900	72.8890	
A8 3	TC	-0.776	5	0.20	3	Y	91.6050	91.6040	
A8 4	TC	-0.809	5	0.20	3	Y	114.8830	114.8830	
A9 1	TC	1.769	5	0.20	3	Y	318.1410	318.1390	
B1 1	TC	-0.388	5	0.20	3	Y	108.0490	108.0480	
B1 1	TC	3.910	5	0.20	3	Y	249.4510	249.4510	
B1 2	TC	0.366	5	0.20	3	Y	176.5270	176.5270	
B1 3	VC	0.185	5	0.20	3	Y	295.5350	295.5340	
B1 4	TC	2.711	5	0.20	3	Y	408.4520	401.0180	
E2 1	TC	1.053	5	0.20	3	'	19.6410	297.5090	
1>									

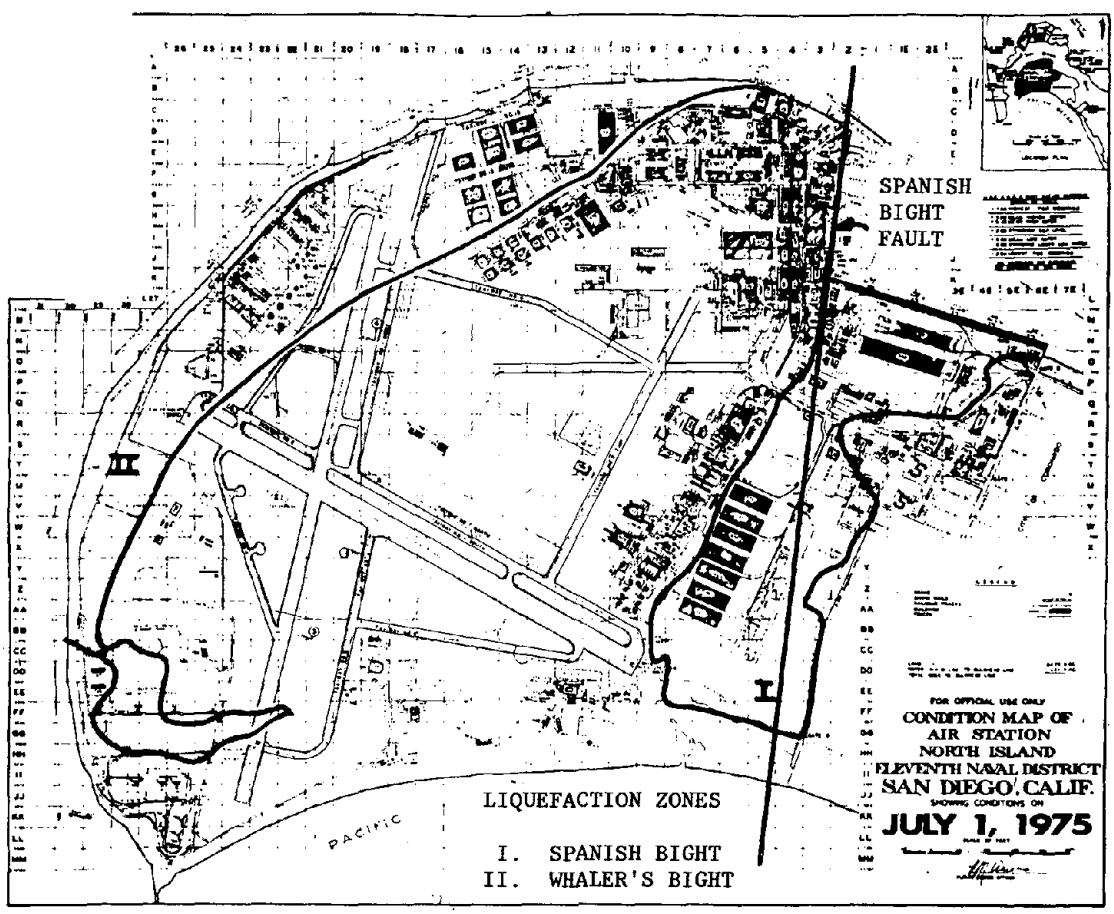

Figure 1. Condition map of NAS North Island.

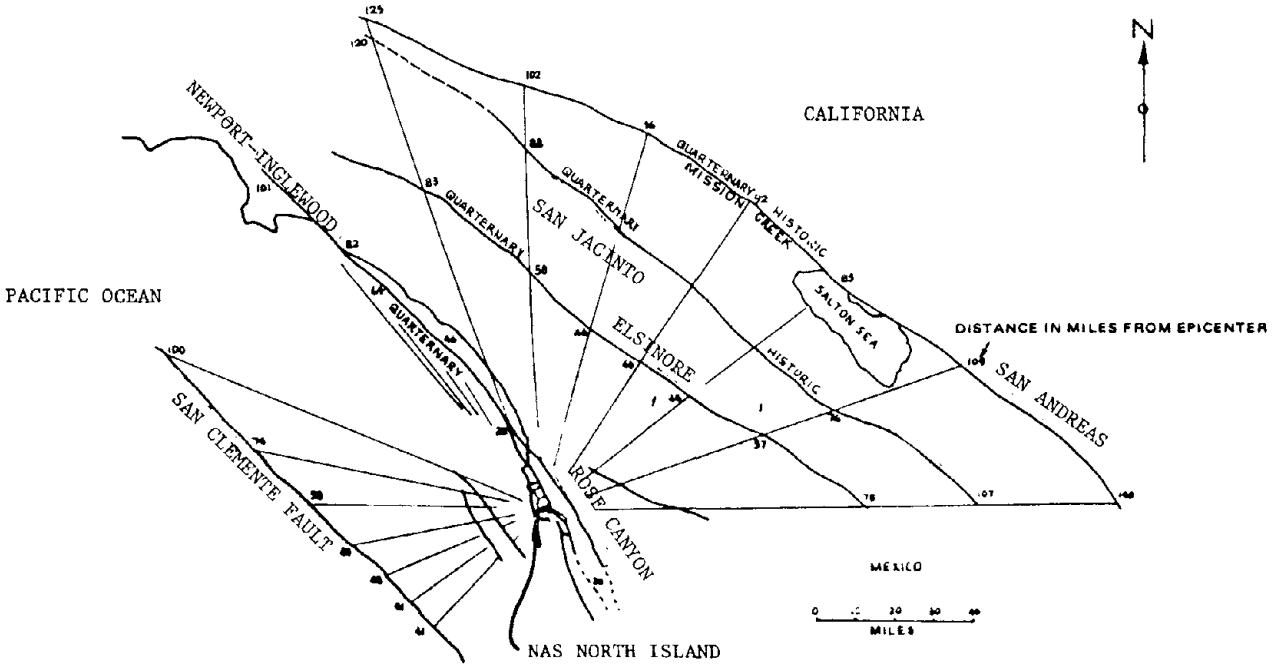

Figure 2. Faults used for estimating ground accelerations at site of NAS, North Island.

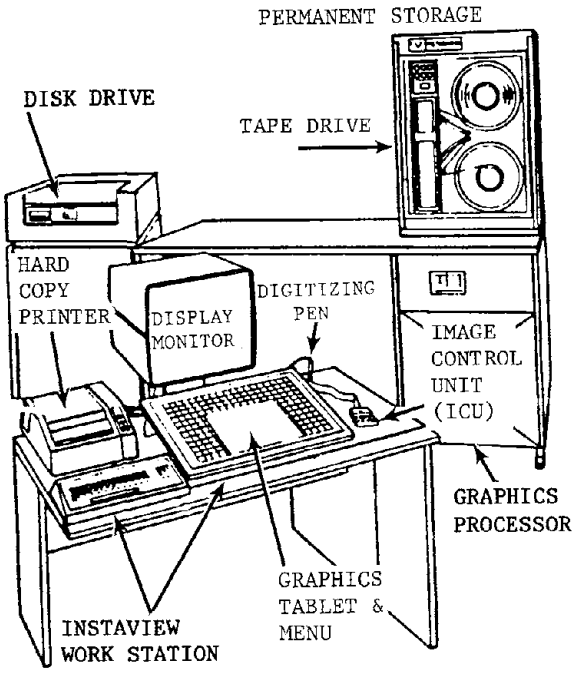

Figure 3. Computervision graphics CADDS work station.

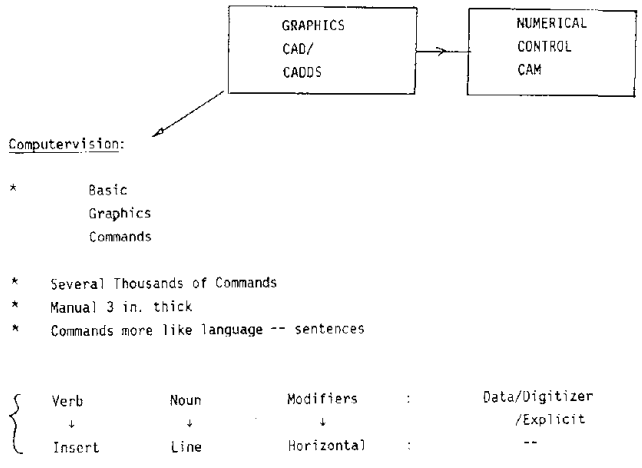

Figure 4. Computer graphics command language structure.

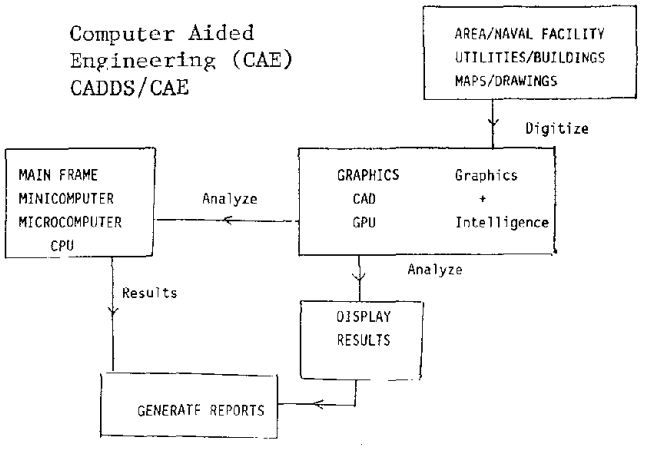

Figure 5. Computer aided design and drafting systems (CADDS).

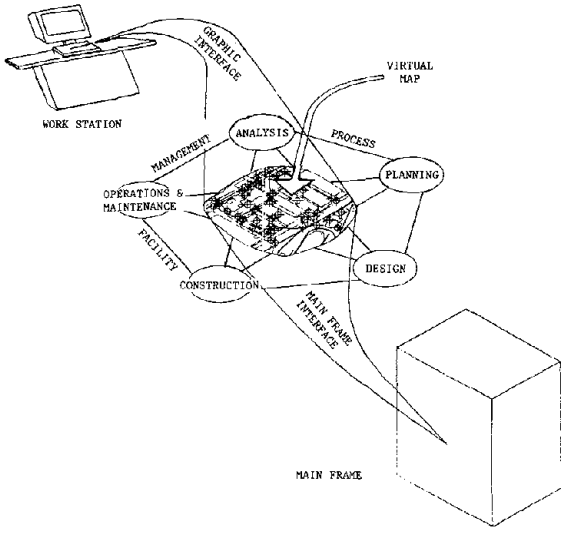

Figure 6. Data base management schema.

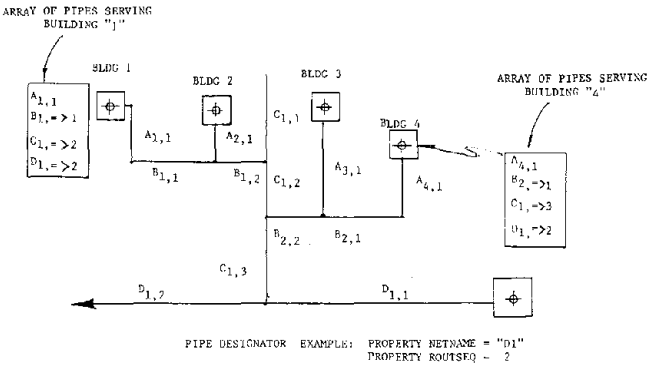

Figure 7. Coding of utility line and building schema.

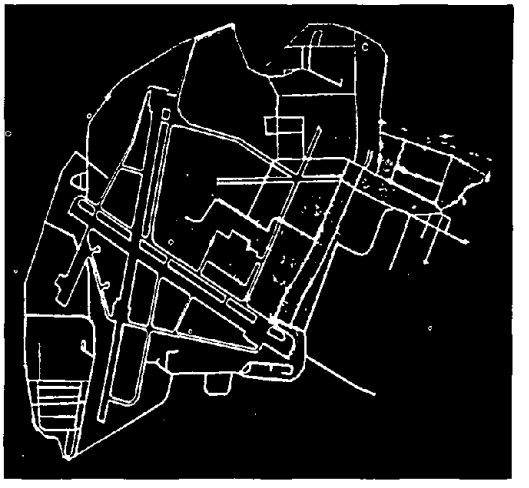

Figure 8. Snapshot of Computervision monitor screen showing NAS, North Island and portion of sanitary sewer.

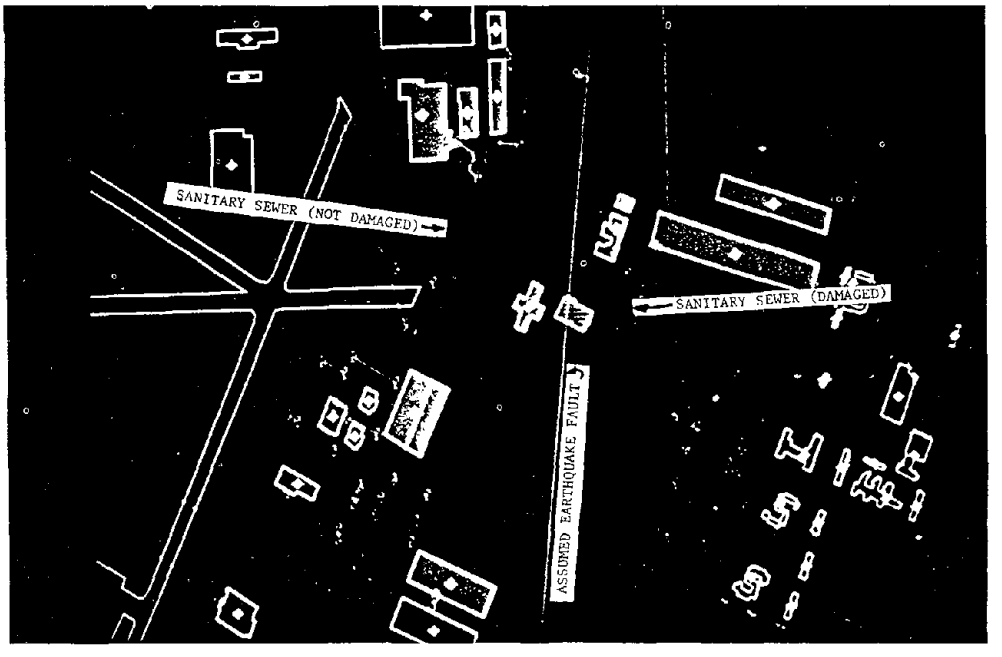

Figure 9. Snapshot of Computervision monitor screen showing zoomed view of earthquake fault and damaged and undamaged sewer lines.

VERTICAL DISTRIBUTION OF SUBSURFACE HORIZONTAL EARTHQUAKE ACCELERATIONS

P. C. Chen
Interpacific Technology, Inc.
180 Grand Avenue, Suite 900
Oakland, California 94612
(415) 444-7081

Abstract A total of 192 sets of peak horizontal accelerations of subsurface earthquake motions recorded at 20 sites in Japan were studied to determine the vertical distribution with depth of peak subsurface horizontal accelerations. The 20 sites are classified as either soft or medium sites depending on the blow count number, N, near the ground surface and the average blow count number, $\bar{N}$, of the soil layers between the ground surface and the depth at which N first reaches a value of 50. The 192 sets of peak accelerations were separated into five groups according to different peak ground-surface accelerations. The mean values of peak accelerations at various depths for each acceleration group were computed for each site classification. The amplification factors of the mean peak accelerations between the ground surface and the depth at which N first reaches a value of 50 were studied. These amplification factors were compared with the calculated site amplifications using the average normalized acceleration response spectra for soft and medium sites.

1. Introduction

With the recent trend of constructing more deeply embedded and buried structures, there is increasing need for better knowledge of the engineering characteristics of subsurface earthquake motions such as accelerations and response spectra. Many sites have been instrumented to record subsurface earthquake motions, either to develop seismic design criteria for structural facilities at these sites or to observe the patterns of these motions. Some observed earthquake motions at individual sites have been reported; however, no study has been performed using recorded subsurface earthquake motions at various sites to investigate their engineering characteristics. A comprehensive and systematic study was therefore initiated using as many recorded subsurface earthquake motions as possible at various sites to investigate the vertical distributions of accelerations and response spectra of subsurface earthquake motions and the effects of site geological conditions and earthquake parameters on these distributions. This paper presents some of the results with regard to the vertical distribution of subsurface horizontal earthquake accelerations.

2. Data Base

The subsurface horizontal acceleration data of earthquakes with peak horizontal accelerations at or near the ground surface equal to or larger than 10 gals (as reported in References 1 to 16) were studied. All the data were recorded at 20 Japanese sites. No U.S. data were used in the study, as their recorded peak accelerations were less than 10 gals.

References 1 to 16 contain information on the site locations; site geological information; instruments used to record the subsurface earthquake motion data; earthquake information such as date of occurrence, magnitude, etc.; and the peak horizontal accelerations at different depths of each site caused by different earthquakes. The site classification, instrument locations (depths), and the number of earthquake data sets used in the study are summarized in Table 1. The earthquake data sets are divided into five groups according to the peak acceleration values at or near the ground surface. One set of data contains all horizontal peak accelerations recorded for an earthquake event at

different instrument depths of the site. For example, for Site 1, there are 11 data sets in Group (a) and 5 data sets in Group (b) recorded at depths of 3m, 21m, 50m, and 90m below the ground surface.

3. Analysis Approaches

3.1. Site Classification

All the 20 sites are classified as either soft or medium sites depending on the blow count number, N, near the ground surface and the average blow count number, $\bar{N}$, of the soil layers between the ground surface and the depth at which N first reaches a value of 50. If the N value near the ground surface is less than or equal to 5, and $\bar{N}$ is equal to or less than 10, the site is considered soft. A site is classified as medium when its N value near the ground surface is less than 50 but larger than 5, and $\bar{N}$ is larger than 10. Because the depth at which N first reaches 50 varies from site to site, each site is further classified as either shallow or deep. If this depth is less than 15m, the site is considered shallow; otherwise, the site is considered deep. In Japan, the depth at which N first reaches a value of 50 is generally considered the base rock for design purposes. The other factor that suggests the selection of N is that Japanese bole-hole data normally stop at a depth when N reaches a value of 50.

3.2. Data Analysis

The mean values of the peak horizontal accelerations (peak accelerations) at different depths for each acceleration group of each site were computed. In order to have a common base, the mean peak accelerations of some sites were extrapolated to the ground surface (0m); because not all sites have instruments located at the ground surface. For example, one of the instruments for Site 1 is at -3m. The extrapolation is achieved by assuming a linear relation between 0m and -3m. Also, for many sites, the instruments are not located at a depth when N first reaches 50; the mean peak acceleration at this depth is computed from the mean peak accelerations at the neighboring instrument locations, again by assuming a linear relation.

The ratios of the mean peak accelerations at different depths of the same site are the peak acceleration amplification factors (amplifications factors) calculated for this site. Because these amplification factors were obtained from recorded data, they are called observed amplification factors to differentiate them from calculated site amplifications. The amplification factors were studied for three cases: (1) amplification factors between the ground surface and the depth at which N first reaches a value of 50; (2) amplification factors between the ground surface and depths at which N is less than 50; and (3) amplification factors below the depth at which N first reaches a value of 50. Once the amplification factors for each site were examined, they were grouped according to the three cases listed above. Of the three types of amplification factors discussed above, only the amplification factors between the ground surface and the depth at which N first reaches 50 are presented herein.

4. Amplification Factors Between Ground Surface and the Depth at Which N First Reaches 50

The amplification factors of the mean peak accelerations between the ground surface and the depth at which N first reaches 50 for both the soft and medium sites are shown in Figure 1 and 2, respectively. They are the ratios of the mean peak accelerations at the ground surface to that at which N first reaches a value of 50. For each site, various acceleration groups are identified, together with the site's average blow count number, $\bar{N}$. For example, the amplification factors of various acceleration groups of Site 6 are identified with different symbols and site numbers. The average blow count number $\bar{N}$ for the site is given in parentheses.

The amplification factors for soft and medium sites are discussed below.

4.1. Soft Sites

4.1.1. Observation of Amplification Factors

- o Amplification factors are not necessarily larger for acceleration groups with larger mean peak accelerations at the ground surface (Sites 1, 6, 14, 16 and 17). This is because when the peak accelerations at the ground surface are larger, the peak accelerations at depths also are larger. The resulting amplification factors between the ground surface and the depth at which N first reaches 50 can therefore be smaller compared with cases where the peak accelerations at the ground surface are smaller.
- o In Figure 1, a weighted solid line that takes into account the number of data sets in each acceleration group is drawn through the amplification factors of various sites. This line is extended by a dash line to the ground surface, because at ground surface, the amplification factor is 1.0. It can be seen from the solid line that the amplification factors for all soft sites fluctuate about a value of 2.5.
- o The average blow count number, $\overline{N}$, of all soft sites except for Site 11 are less than or equal to 10. The top 25m of Site 11 has a N value less than 5, a N value of 10 between the depths of 25m and 37m, and an average N value of 30 between 37m and 56m, at which N first reaches a value of 50. Although the overall average N is larger than 10 for Site 11, it is classified as a deep soft site because the N value of the top 25m is less than 5.

4.1.2. Comparison of Observed Amplification Factors and Calculated Site Amplifications

The average normalized acceleration response spectra at given sites can be considered as site amplifications that are largely affected earthquake parameters and by the depths and the material properties of soil layers between the ground surface and base rock of these sites. The observed amplification factors are the amplifications of the mean peak accelerations between the ground surface and a depth at which N first reaches 50. Because these two amplifications have similarities, a comparison was made of their amplification values. Ideally, site acceleration response spectra and site geological data would be used to determine site amplifications. However, except for Sites 1 and 9, site acceleration response spectra were not available. The average normalized site acceleration response spectra for soft sites (Reference 17) were therefore used for calculating site amplifications.

The period of each site was calculated using site geological properties between the ground surface and the depth at which N first reaches 50, and assuming that earthquake waves propagate vertically. The calculated periods of all the soft sites are shown in Figure 1. They range from 0.268 second for Site 6 to 1.17 second for Site 11. In general, the period increases as the depth increases; but there are exceptions where the site period decreases when the depth increases and the $\overline{N}$ is larger (Sites 1 and 11).

Once the site periods were calculated, the site amplifications were obtained from the average normalized acceleration response spectrum with a 5% damping for soft sites (Figure 3). They are marked by small circles in Figure 1, and are connected by a dash-dot line. The portion of the dash-dot line from the site amplification of Site 6 to that of 1.0 (ground surface) was extended.

The calculated site amplifications (dash-dot line) fluctuate about a value of 2.5. The observed amplification factors (solid line) and the calculated site amplifications are seen to be very close. The calculated site amplifica-

tions fluctuate about 2.5 for two reasons: The average normalized acceleration response spectrum with a 5% damping for soft sites (Figure 3) has an amplification factor of 2.5 in the period range of 0.25 to 1.0 second, and the periods of the sites studied also are mostly in this range.

It should be noted that the data base for developing the average normalized acceleration response spectra for soft sites is different from that used to obtain the observed amplification factors of mean peak accelerations. The values of $\bar{N}$ are unknown for the sites used to develop the average normalized acceleration response spectra. In spite of the different data base, the comparison between the two amplifications is good. This suggests that the average normalized site acceleration response spectra with a 5% damping for soft sites may be used to estimate the amplification factors of the mean peak accelerations between the ground surface and the depth at which N first reaches 50.

4.2. Medium Sites

4.2.1. Observation of Amplification Factors

- Amplification factors are not necessarily larger for acceleration groups with larger mean peak accelerations at the ground surface.
- A weighted solid line that takes into account the number of data sets in each acceleration group is drawn through the amplification factors of various sites. This line is extended by a dash line to the ground surface. The amplification factors start with 1.0, gradually increase to about 2.5, and then fluctuate about 2.5.

4.2.2. Comparison of Observed Amplification Factors and Calculated Site Amplifications

An effort was made to compare the observed amplification factors with the calculated site amplifications, using the same approaches taken for soft sites. The calculated periods of medium sites are shown in Figure 2. The site amplifications obtained from the average normalized acceleration response spectrum with a 5% damping for medium sites (Figure 4), using the calculated site periods are marked by small circles in Figure 2. These small circles are connected by a dash-dot line. The portion of the dash-dot line from the site amplification of Site 15 to that of 1.0 (ground surface) was extended.

An examination of the observed amplification factors (solid line) and the calculated site amplifications (dash-dot line) indicate that for deep medium sites, the observed and calculated amplifications are close. However, there exist larger differences between observed amplification factors and calculated site amplifications for shallow medium sites.

The calculated site amplifications were obtained using the thickness and soil properties of the soil layer, measured from the ground surface to the depth at which N first reaches 50, and the average normalized horizontal response spectra, assuming that earthquake waves propagate vertically. The above soil layer thickness for shallow medium Sites 15, 10, 13, and 4 is less than 15m. The periods of these sites are 0.175 second, 0.179 second, 0.269 second, and 0.295 second, respectively. Because these periods fall in the range at which large site amplifications occur (Figure 4), the calculated site amplifications are therefore large.

However, the average blow count number, $\bar{N}$, for Sites 15, 10, 13, and 4 varies from 30 to 35 (Figure 2). These large $\bar{N}$, together with the small thickness of the soil layer (less than 15m for these four sites), would suggest that the site amplification factors for these sites would be small when the earthquake waves are assumed to propagate vertically. The differences between the observed amplification factors and the calculated site amplifications for shallow

medium sites are probably due to the different data base used to obtain the observed amplification factors and that used to develop the average normalized horizontal acceleration response spectra for medium sites. Further investigation of the data base, including the N values of sites used to develop the average normalized horizontal response spectra, will clarify the above differences.

5. Conclusions

Observed amplification factors were obtained for both soft and medium sites of the mean peak accelerations between the ground surface and the depth at which N first reaches a value of 50. For soft sites, the amplification factors fluctuate about a value of 2.5. For deep medium sites, the amplification factors are also about 2.5. For shallow medium sites, the amplification factors are less than 1.5.

The observed amplification factors for both the soft and medium sites were compared with the site amplifications calculated using previously published average normalized acceleration response spectra with a 5% damping for soft and medium sites. Although different data bases were used to obtain amplification factors and site amplifications, the comparisons are good for soft sites and deep medium sites.

Because of the above observations, it appears that the average normalized acceleration response spectrum with a 5% damping may be used for soft sites to estimate the amplification factors of the mean peak accelerations between the ground surface and the depth at which N first reaches a value of 50. The average normalized acceleration response spectrum with a 5% damping for medium sites can also be used for this estimate, provided the differences between the observed amplification factors and the calculated site amplifications for shallow medium sites are accounted for.

6. Acknowledgment

This study was supported by the U.S. National Science Foundation under Grant No. CCE-8304066 and an in-house research and development program of Interpacific Technology, Inc. The author is indebted to Dr. Y. Ohsaki for his inspiration; Drs. Y. Osawa, Y. Sakai, T. Okubo, T. Tanaka, T. Iwasaki, K. Ishida, Y. Kitagawa, S. Kawamura, K. Kawashima, T. Ohta, J. Jido, T. Tsunoda, T. Suzuki, M. Nakamura, and Messrs. Y. Saito and I. Katayama for their assistance and discussions; and to Drs. H. Tsuchida and T. Morioka, J. Litehiser, Y. K. Lin, and B. Schmidt for their assistance, discussions, and review of the study results.

7. References

1. Aria, H., and Saito, S., "Observation of Earthquake Motions in Foundation Soil Layers of Shore Protection Facilities," Technical Note No. 251, December 1977, Port and Harbour Research Institute, Ministry of Transport, Japan.

2. Yokota, H., "Observation of Underground Earthquake Motions at Shibaura, Minato-ku, Tokyo," Proc. 7th Symposium on Ground Vibrations, A.I.J., March 1979.

3. Yokota, H. and Watanabe, H., "Results of Earthquake Observation at Hibiya in Tokyo," Proc. 3rd Symposium on Ground Vibrations, A.I.J., Nov. 1974.

4. Nasu, N. et al., "An Interim Report on the Results from Underground Earthquake Observation at the Site of Grand Heights, Narimasu, Tokyo." June 1975. Published by Tokyo Soil Research Co.

5. Saito, T. et al. "Underground Observation of Earthquake Motion in the Uptown Sections of Tokyo," Taisei Technical Report, No. 6.

6. Iwasaki, T. et al., "Observation of Underground Earthquake Motions Around Tokyo Bay," Report No. 1, Public Works Research Institute, Ministry of Construction, March, 1981.

7. Private Communication, Earthquake Research Institute, Tokyo University, 1981.

8. Sugimoto, M. and Abe, Y., "Underground Observation of Earthquake Motion in Soft Ground," Proc. Annual Meeting, A.I.J., Sept., 1979.

9. Private Communication, Hokkaido University, 1981.

10. Tsunoda, T. and Seo, K., "An Approach to Input Seismic Waves for Structural Design (Part 2. Observation of Ground Motion)," Proc. Annual Meeting, A.I.J., Oct. 1973.

11. Matsushima, Y. and Iwashita, M., "Results from Earthquake Observation in Kawaguchi City," Proc. 3rd Symposium on Ground Vibrations, A.I.J., Nov., 1974.

12. Report on Digitized Earthquake Accelerograms in a Soil-Structure System," Kenchiku Kenkyu Shiryo, No. 12, March, 1976, Building Research Institute, Ministry of Construction.

13. Science & Engineering Research Lab., Waseda University, "Results from Earthquake Observation at Tatemachi, Hachioji City," Proc. 3rd Symposium on Ground Vibrations, A.I.J., Nov., 1974.

14. Yokota, H., "Observation of Underground Earthquake Motions at Toyosu," Proc. 3rd Symposium on Ground Vibration, A.I.J., Nov., 1974.

15. Private Communication, Science & Engineering Research Laboratory, Waseda University, 1982.

16. Private Communication, Kajima Corporation, 1981.

17. Hayashi, S., Tsuchida, H., and Kurata, E., "Average Response Spectra for Various Subsoil Conditions," Third Joint Meeting, U.S.-Japan Panel on Wind and Seismic Effects, UJNR, Tokyo, May 10-12, 1971.

Table 1. Site and Subsurface Earthquake Data Information

Site	Layer thickness		Site Classification				Subsurface Instrument Locations (m)	No. of EQ Data Set Used in Analysis				
			Soft[x]		Medium[xx]							
	h^{+}(m)	hh^{++}(m)	Shallow[x+]	Deep[ox]	Shallow[x+]	Deep[ox]		(a)	(b)	(c)	(d)	(e)
1	56			X			-3,-21,-50,-90	11	5			
2		34				X	-3,-20,-50,-91	9	3	1		
3		20			X		-3,-20,-50,-90	5				
4		13			X		0,-20,-60	2	2			
5	22			X			-1,-25,-50	10				
6	7		X				-1,-5,-8, -22,-55	2	4			2
7		25				X	-2,-33,-85	6	2	2		
9	53			X			0,-27,-67, -127	24				2
10		10			X		0,-70,-110	25	7	4	1	
11	57			X			-5,-15,-38, -160	3		2		
13		12			X		0,-41	8	3	1		
14	45			X			-3.5,-11.2, -44.4	1	1			
15		7			X		0,-30,-50				1	1
16	13		X				0,-18,-26.5	4	4	3	2	
17	30			X			-7,-14,-21, -30,-43,-60	1	1			
18	50			X			0,-20,-30,-60	2				
19		25				X	-1,-14,-25	2				
20	38			X			-2,-18,-38, -71	1				
21		15			X		-1,-17,-67 -123	10	8			2
22	25			X			-2,-5.5,-9, -13,-30,-100				2	

+ - layer thickness to N first equals 50 for soft site. x = for $N \leq 5$. xx - for $5 \leq N \leq 50$.
++ - layer thickness to N first equals 50 for medium site. x+ - for depth up to 15m, ox for depth larger than 15m.
(a) 10-20 gals*, (b) 20-40 gals*, (c) 40-60 gals*, (d) 60-80 gals*, (e) 80-130 gals*
*Peak ground surface acceleration.

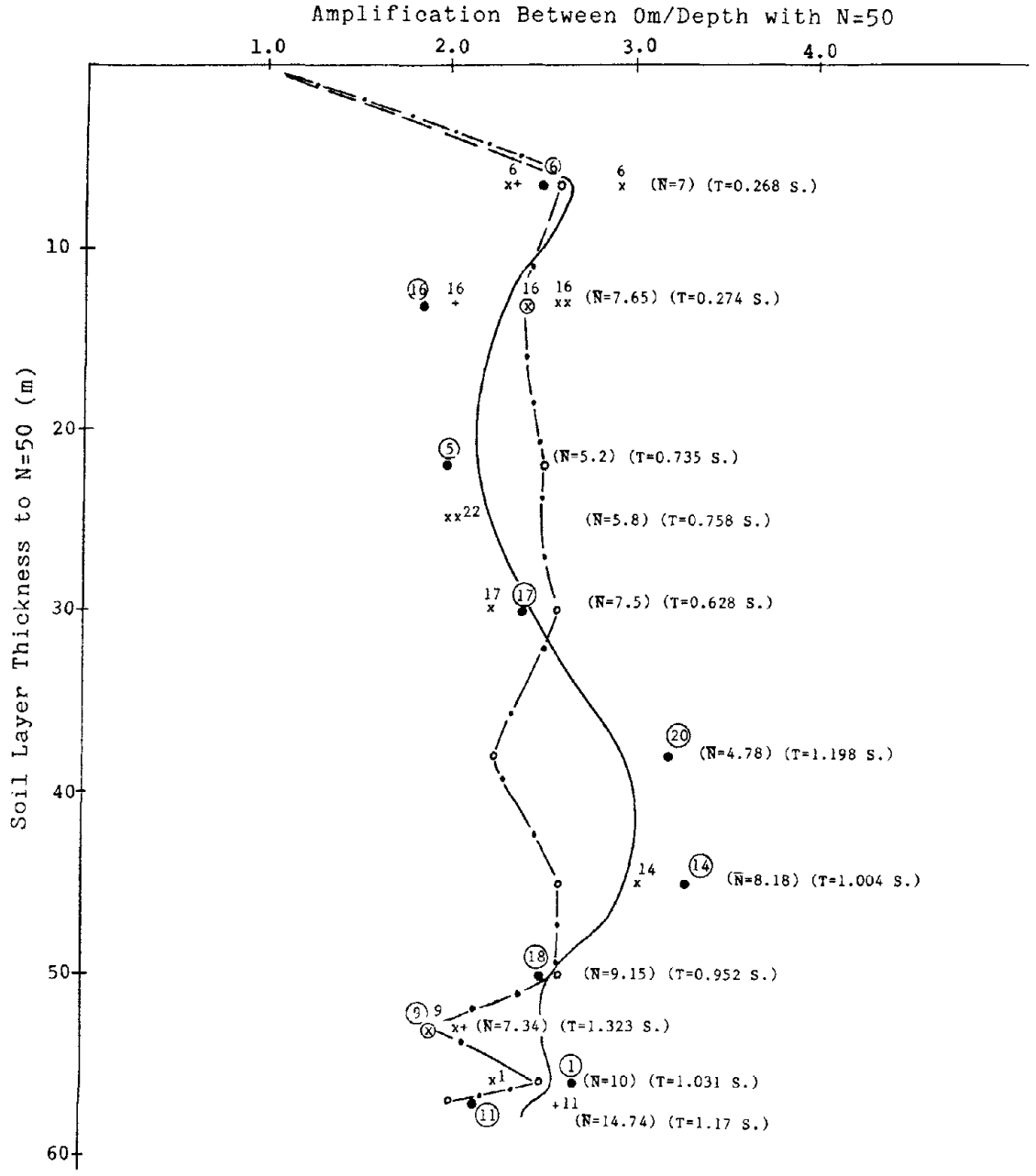

Figure 1. Amplification Factors for Soft Sites

Legend:
• - 10-20, x - 20-40, + - 40-60, xx - 60-80, x+ - 80-130 gals peak ground surface acceleration of various groups

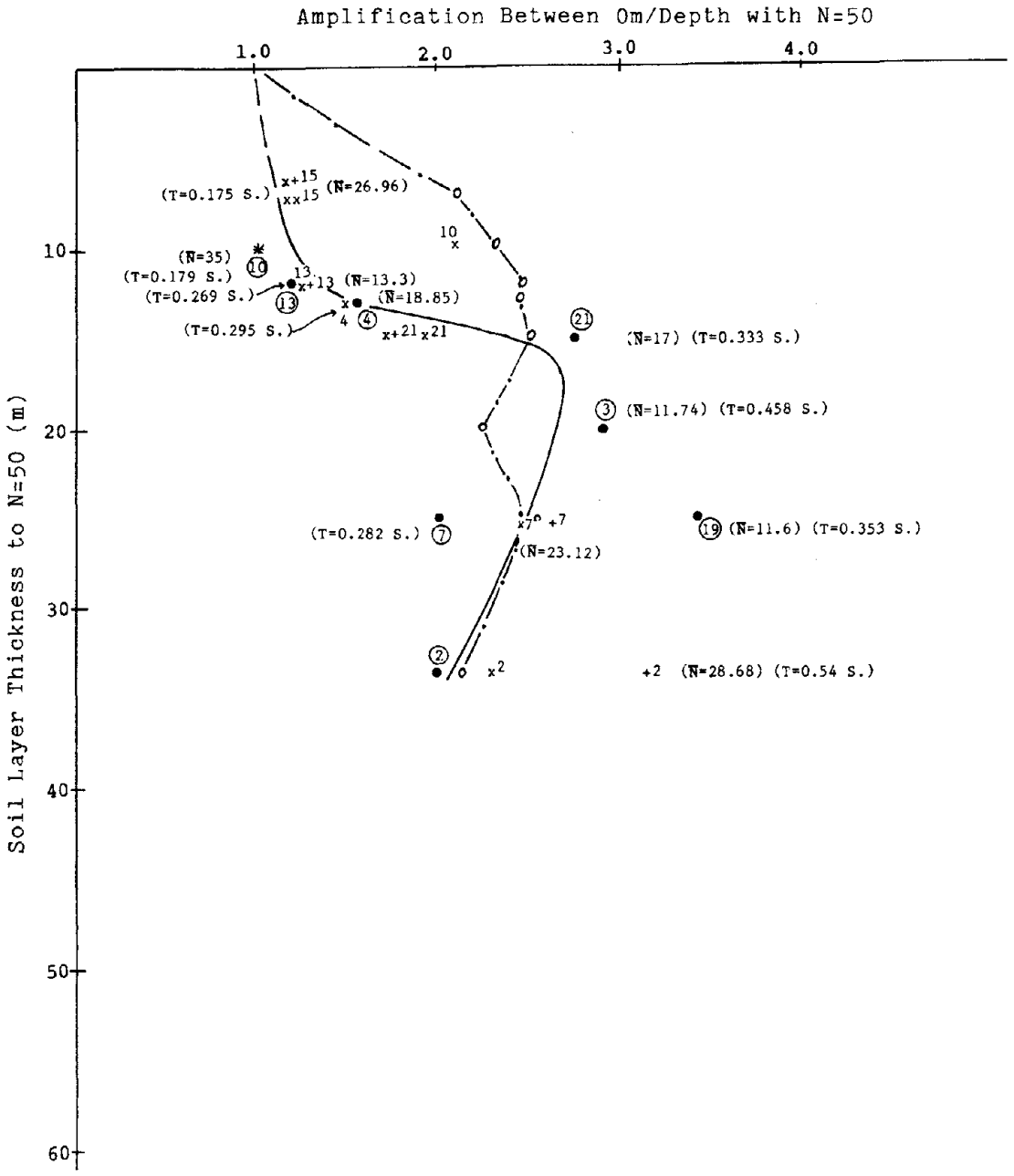

Figure 2. Amplification Factors for Medium Sites

Legend:
• - 10-20, x - 20-40, + - 40-60, xx - 60-80, x+ - 80-130 gals peak ground surface acceleration of various groups

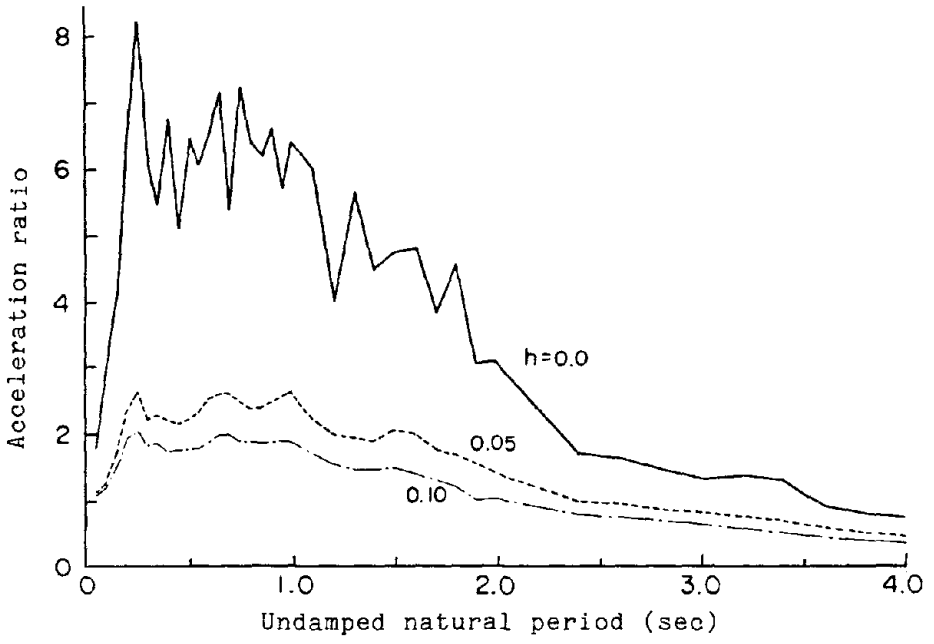

Figure 3. Average Response Spectra for Soft Sites

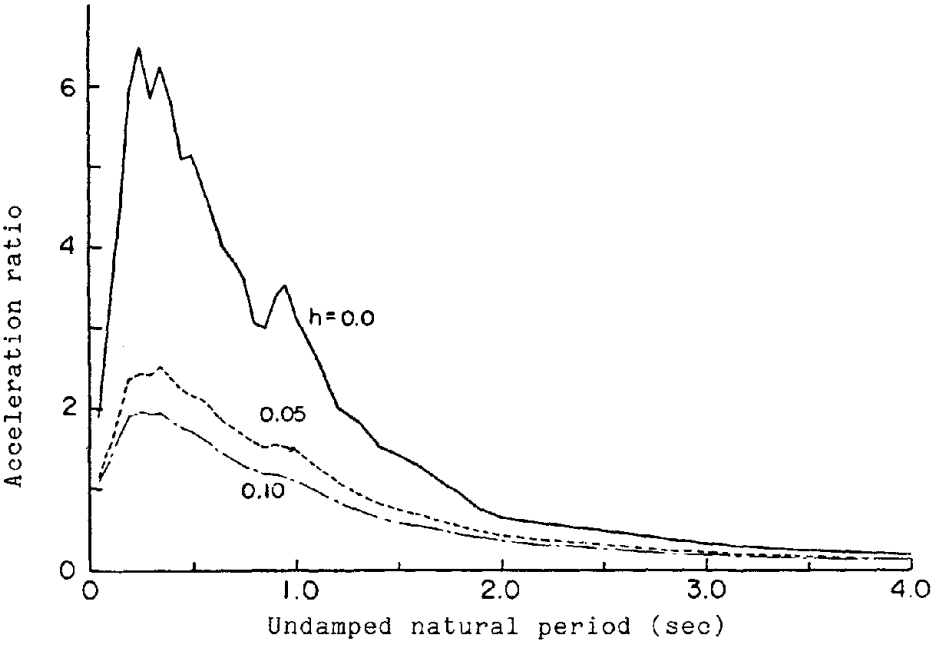

Figure 4. Average Response Spectra for Medium Sites

SHAKING TABLE TEST ON THE EFFECTS OF THICKNESS OF LIQUEFIED LAYER ON DEFORMATION OF EMBANKMENTS

BY

Toshio IWASAKI,* Yasushi SASAKI,**

Hideo MATSUMOTO*** and Masuo KONDO****

ABSTRACT

Earthquakes have caused tremendous damages to earth structures such as road embankments and river dikes. Typical damages of earth structures are settlements, openings and crackings of embankments. Many of these damages to embankments occurred in areas where ground layers are liable to liquefaction, namely in old river beds and lowlands between sand dunes.

The amount of seismic deformation of embankments on liquefied ground layer depends, largely, on several factors such as the intensity of earthquake motion, the degree of liquefaction and the thickness of the liquefied layer. The authors of this paper have conducted a series of shaking table tests to observe how the thickness of the liquefied layer affects the amount of seismic deformation of the embankment. The following describes the results of these tests.

Keywords: Earthquakes, Embankments, Ground Motion, Liquefied Layers, Seismic Deformation, Shaking Table

1. INTRODUCTION

Earth structures, such as road embankments and river dikes, were frequently damaged in the Niigata Earthquake of 1964 (magnitude=7.5), the Tokachi-oki Earthquake of 1968 (M=7.9), the Miyagiken-oki Earthquake of 1978 (M=7.4) and the Nihonkai-chubu Earthquake of 1983 (M=7.7). In the plains, these earthquakes have caused heavy damages to embankments constructed on loose alluvial sandy grounds or soft clayey grounds; while in the mountainous areas, high embankments on steep slopes were greatly damaged.

One remarkable damage in the plains is the collapse of embankments which occurred extensively in the suburbs of Niigata City during the Niigata Earthquake. Even for low embankments openings and large longitudinal cracks developed as the embankments settled. Embankments thus damaged were mostly resting on old river beds or lowlands between sand dunes where the ground layers are liable to liquefaction. This was also the case for the Nihonkaichubu Earthquake of 1983. Thus, it is considered essentially important to assure earthquake resistance of earth structures standing on easily liquefied grounds.

The amount of seismic deformation of embankments on liquefied grounds is known to depend largely on the intensity of earthquake motion, the degree of liquefaction and the thickness of the liquefied layer. Yet, there are many other factors that remain to be clarified in this connection.

Under these circumstances, the authors conducted a series of shaking table tests to see how the amount of seismic deformation of an embankment is affected by the thickness of the liquefied layer. This paper briefly describes the method and the results of the experiments.

2. METHOD OF EXPERIMENTS

Vibration tests were carried out, using models consisting of a lower subground layer of loam which is not liable to liquefaction, an upper subground layer of mountain sand which is likely to liquefy during vibration, and an embankment. Those models were set up in a container (1.8 m long, 0.6 m wide and 1.1 m high) placed on a

*Director, Earthquake Disaster Prevention Dept., Public Works Research Institute, Ibaraki-Ken, Japan

, *, and **** Ground Vibration Division, do.

shaking table.

Six models with different thicknesses of liquefiable ground layers were used for the experiments.

2.1 Ground Models and Embankment Models

As shown in Fig. 1, each of models had a ground thickness of 80 cm, an embankment top width of 20 cm and an embankment height of 15 cm and the side section was symmetrical along the central vertical line.

As for the model ground, a loam layer which is not liable to liquefy was first prepared in a container, a certain amount of water was poured and then a liquefiable sand layer was prepared by means of the underwater drop method, using mountain sand taken from Mt. Sengen in Chiba Prefecture. Upon completion of the model ground, the model embankment was prepared, using air-dried mountain sand and making the water level equal to the surface of the ground. The characteristics of materials used for the experiments are indicated in Table 1.

Regarding model conditions, the same compaction condition was maintained for the embankment and the ground. Thickness of the liquefiable mountain sand layers ranged from 15 to 60 cm. Also the relative density of the actual embankment models ranged 25-40% and that of the ground 61-80% (see Table 2).

2.2 Shaking Table Tests

In each test, a low-amplitude resonance test was first made to obtain frequency characteristics of the model, and then large-amplitude excitation tests intending to identify failure characteristics of the models. In the resonance test sinusoidal exceitation with a constant shaking table acceleration of 10 gal was used and the excitation frequencies ranged 5 to 40 Hz.

In the excitation tests for getting failure characteristics, several levels of accelerations were applied. In each of them constant sinusoidal acceleration with a frequency of 5 Hz was employed for 8 seconds (40 cycles). After vanishment of the pore water pressure was confirmed, a test with higher acceleration was done. Successive tests were conducted until the embankment completely failed. The relation between the stage of excitation and the measured maximum acceleration of the shaking table was indicated in Table 3 for 6 models. Values at the bottom excitation step for the models, indicate accelerations when failure occurred.

Accelerometers and pore water pressure meters were installed in the ground and the embankment (as illustrated in Fig. 1) to measure vibration amplitudes and pore water pressure changes. Meshes of white-color sand at intervals of 10 cm were prepared on the side of the model to watch the deformation of the model during and after the shaking test. Also displacement gauges and bench mark points were seen on the surfaces of the ground and the embankment to measure the movement of the surface.

3. RESULTS OF EXPERIMENTS

3.1 Resonance Test

Fig. 2 shows the resonance curve for the crest of the embankment. The ordinate indicates response amplification factor representing the ratio of acceleration amplitude at the crest of the embankment to that of the shaking table.

It can be seen from this that the resonance frequency of the model embankment is about 17-18 Hz and has almost identical vibration characteristics regardless of thickness of liquefiable layers (varying from 15 to 60 cm).

3.2 Failure Test

(1) Relation Between Acceleration and Deformation

Fig. 3 shows the relation between the acceleration of the shaking table and the accumulative settlement of the embankment crest. From this it can be seen that the accumulative settlement increases as table acceleration increases. It is

observed that the accumulative settlement of the embankment models with layer thickness of 30 cm or less tends to increase in proportion to the thickness of the liquefiable layer, when subjected to the same table acceleration. For models with layer thickness larger than 30 cm, however, accumulative settlement nearly equals regardless of layer thickness. Fig. 4 shows the relationship between the response acceleration of the ground just below the embankment and the accumulative settlement of the embankment crest. Similarly to the fact seen in Fig. 3, accumulative settlement tends to increase in proportion to the thickness of the liquefiable layer. For these experiments where accumulative settlements are only about 7 cm, characteristics of accumulative settlement may be divided into two categories, namely the case of shallow liquefiable layer with thickness of 15-20 cm and the case of deep liquefiable layer with thickness of 30cm or more. In the case of shallow liquefiable layer, the rate of increase of settlement tends to become small when accumulative settlement is large, however, in the case of deep layer, accumulative settlement tends to increase in proportion to the response acceleration in the ground just below the embankment. This is presumably because of the difference of liquefiable layer thickness which may affect the deformation characteristics of the embankments and grounds.

Fig. 5 shows successive changes in the mesh lines at each end of excitation stages 3 (shaking table acceleration of about 100 gal), 4 (about 130 gal) and 5 (about 160 gal). Those figures were drawn from photographs taken through the observation glass window on the side of the container. The glass window is equipped for watching the deformation of the ground and the embankment. In the case of A-1 with a shallow liquefiable layer with thickness of only 15 cm, horizontal displacement in the ground was observed for the entire depth of the liquefied layer, with the maximum displacement at the ground surface. In the case of A-5 with a deep liquefiable layer with thickness of 50 cm, horizontal displacement was observed up to a depth of 30-40 cm from the ground surface. The maximum horizontal displacement in the ground was observed not on the ground surface but at a depth of 20-30 cm from the surface. Also, in the case of A-1, embankment settlement was caused by the movement of embankment slope toward the toe of slope. In the case of A-5, however, the entire embankment settled uniformly into the ground. Photographs of failure patterns of each model after the final stage when the excitation were finished, are shown in Photos 1-6.

(2) Relation Between Excessive Pore Water Pressure and Embankment Deformation

Fig. 6 shows settlements of the embankment crest for each model at the excitation stage 5 (shaking table acceleration of 159-171 gal). From this, it can be seen that embankment settlements increase with increases in the thickness of the liquefiable layer.

Figure 7 shows the settlement speed at the embankment crest for each model at the excitation stage 5. In the case of A-1 with a shallow liquefiable layer with thickness of only 15 cm, settlement speed takes its maximum at about one second after the start of excitation. Characteristics of settlement speed can be generally divided into these two types.

Similarly, Fig. 8 shows time histories of excessive pore water pressure in the ground just below the embankment, at excitation stage 5. Excessive pore water pressure becomes the maximum at about 2.5 seconds after the start of excitation in the case of A-1. For the liquefiable layer thickness of 20 cm or more, however, excessive pore water pressure takes its maximum at about 0.5 to 1 second after the start of excitation. It is seen that excessive pore water pressure well corresponds to the settlement speed of the embankment. Also, it can be seen from Fig. 8 that the settlement speed of the embankment crest monotonously increases until the excessive pore water pressure ratio in the ground just below the embankment reaches 0.5-0.6, but after that it becomes nearly constant or decreases. This decrease in set-

tlement speed occurs for the case of A-2 and subsequent models where the settlement of the embankment crest is large. This probably indicates that the decrease in settlement speed can attribute, largely, to the decrease in embankment load resulting from the decrease in embankment height.

4. CONCLUSIONS

The following can be concluded from shaking table tests on embankment models with various liquefiable layer thicknesses:

(1) The amount of embankment settlement for the same input acceleration gets large as the thickness of liquefiable ground layer increases.

(2) In case where the thickness of the liquefiable layer exceeds a certain level, the effects of the thickness on embankment settlement become minor.

(3) This threshold thickness generally agrees with the depth at which the horizontal displacement of the ground can be observed for the case of deep liquefiable layer.

(4) Generation of excessive pore water pressure in the ground just below the embankment well corresponds with the settlement speed of the embankment crest. The settlement speed monotonously increases as long as the excessive pore water pressure ratio remains up to about 0.5-0.6. But for the pore water pressure exceeding this level settlement speed decreases with the decrease in embankment height.

The test results point out that for an embankment with a height of 15 cm, the range of layer thicknesses that affect settlement is 30-40 cm (approximately double the embankment height). Since the above is the results from the shaking table tests on model embankment with a certain section shape made in a container, the results cannot be directly applicable to actual embankments. Yet, it is considered that the above tendencies may apply to actual embankments. The above conclusions may be helpful when determining the depth of soil improvement of liquefiable ground layers which are likely to cause embankment deformation.

5. REFERENCES

1) P.W.R.I., "Report on the Damage during the Niigata Earthquake of 1964," Public Works Research Institute Report, Vol. 125, 1965.

2) P.W.R.I., "Report on the Damage During The Tokachi-oki Earthquake of 1968," Public Works Research Institute Report, Vol. 141, 1970

3) Sasaki, Y., et al, "Seismic Damage Examples of Earth Structures," Technical Memorandum of Public Works Research Institute, Vol. 1756, 1970

4) Iwasaki, T., Tokida, K., Kimata, T., "Studies on Liquefaction of Sands during Earthquakes," 13th Joint Meeting, UJNR, 1981

5) Iwasaki, T., et al., "Estimation Procedure of Liquefaction Potential and Its Application to Earthquake Resistant Design," 14th Joint Meeting, UJNR, 1982

6) Osterberg, J.O., "Influence Values for Vertical Stresses in a Semi-infinite Mass due to an Embankment Loading," Proc. 4th ICSMFE, Vol. 1, 1957

7) Arakawa, T., Kimata, T., Kondo, M., "Experimental Study on Failure Pattern of Embankment Supported by Sandy Layers During Earthquakes" 15th Joint Meeting, UJNR, 1983

8) Arakawa, T., Kawashima, K., Matsumoto, H., Kondo, M., "Experimental Study of Embankment on Sandy Layers During Earthquakes - Characteristics of Reconstructed Embankment on Liquefied Layers," 16th Joint Meeting, UJNR, 1984

Table 1 Characteristics of materials used for the Experiments

Items	Sign	Unit	Sand	Loam
Specific Gravity of Soil Particle	G_s	——	2.641	2.556
Optimum Moisture Content	W_{opt}	%	18.0	——
Maximum Dry Density	γ_{dmax}	tf/m³	1.574	——
Maximum Void Ratio	e_{max}	——	1.007	2.543
Minimum Void Ratio	e_{min}	——	0.647	1.665
60% Grain Size	D_{60}	mm	0.301	0.225
10% Grain Size	D_{10}	mm	0.217	0.042
Mean Grain Size	D_{50}	mm	0.290	0.165
Coefficient of Uniformity	U_c	——	1.387	5.36

Table 2 Characteristics of Models of Embankments and Grounds

Model No.		A－1	A－2	A－3	A－4	A－5	A－6
Thickness of the Liquefiabl Layer [cm]		15	20	30	40	50	60
Dry Unit Weight γ_d [tf/m³]	Embankment	1.39	1.38	1.41	1.41	1.42	1.38
	Ground	1.49	1.50	1.54	1.48	1.49	1.49
Void Ratio e	Embankment	0.905	0.915	0.877	0.878	0.861	0.917
	Ground	0.769	0.762	0.718	0.786	0.778	0.768
Relative Density D_r [%]	Embankment	28.2	25.4	36.0	35.7	40.4	24.9
	Ground	66.0	67.8	80.2	61.3	63.5	66.3

Table 3 Measured Maximum Acceleration of the Shaking Table

Model No.		A－1	A－2	A－3	A－4	A－5	A－6
Thickness of the Liquefiabl Layer [cm]		15	20	30	40	50	60
Mesured Maximum Acceleration [gal]	Excitation Stage 1	36	37	36	32	38	36
	Excitation Stage 2	71	74	68	60	68	68
	Excitation Stage 3	103	103	103	100	100	100
	Excitation Stage 4	139	133	134	132	132	128
	Excitation Stage 5	171	164	163	159	161	167
	Excitation Stage 6	204	197	—	—	—	195

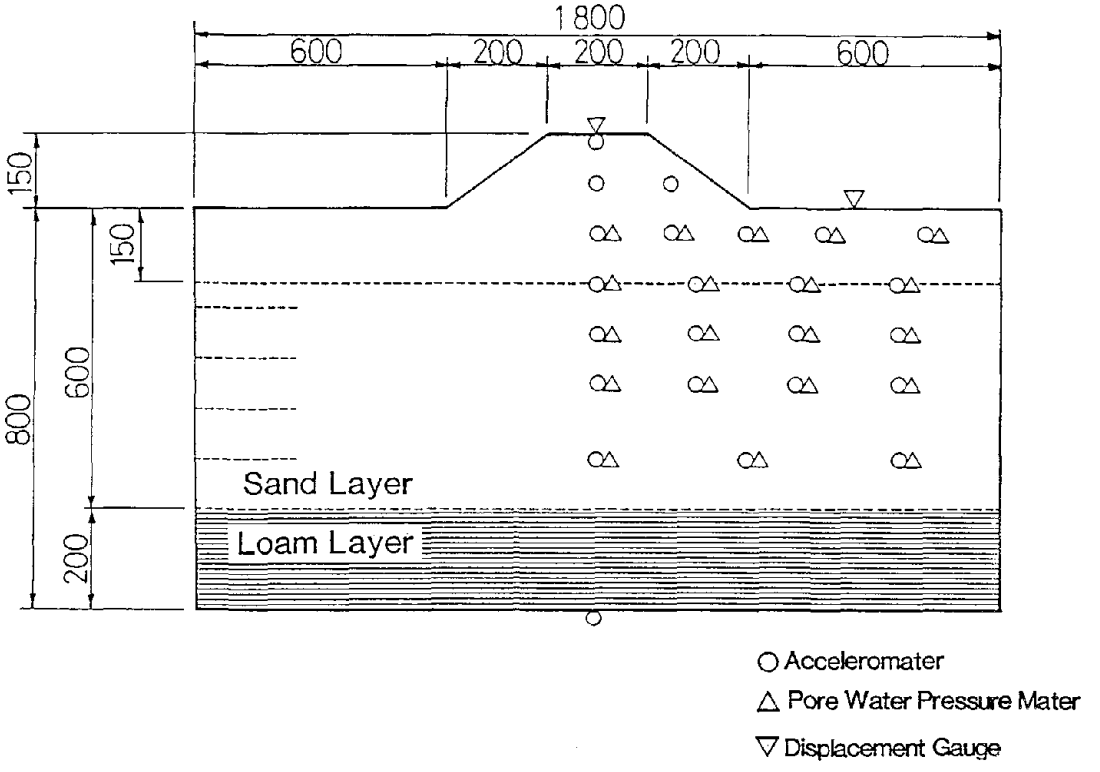

Fig. 1 Ground and Embankment Model

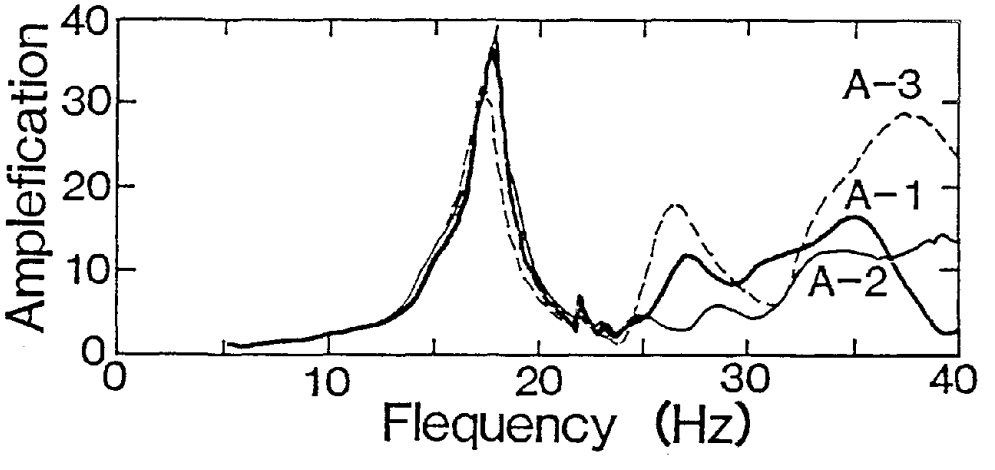

Fig. 2 Examples of Resonance Curve (at the crest of the embankment)

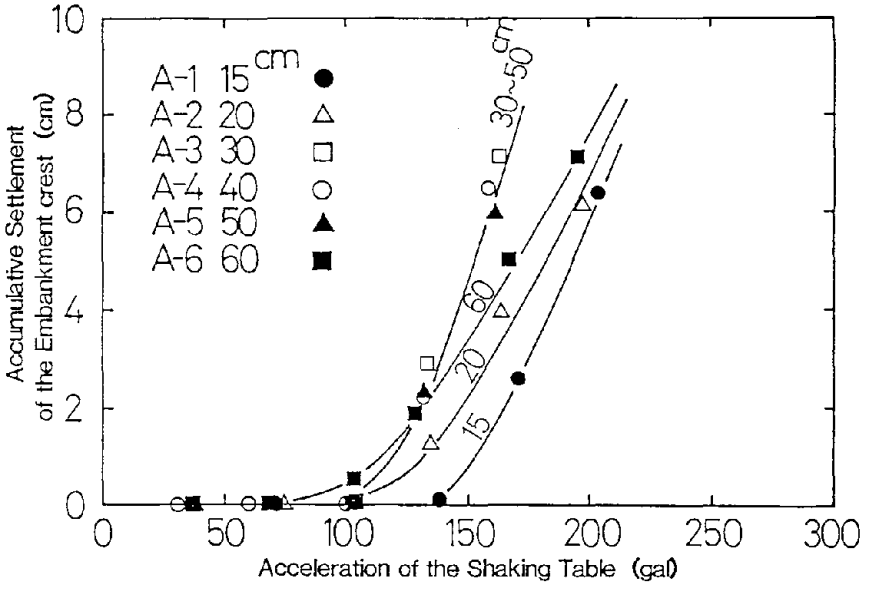

Fig. 3 Relation between the Acceleration of the Shaking Table and the accumulative Settlement of the Embankment crest

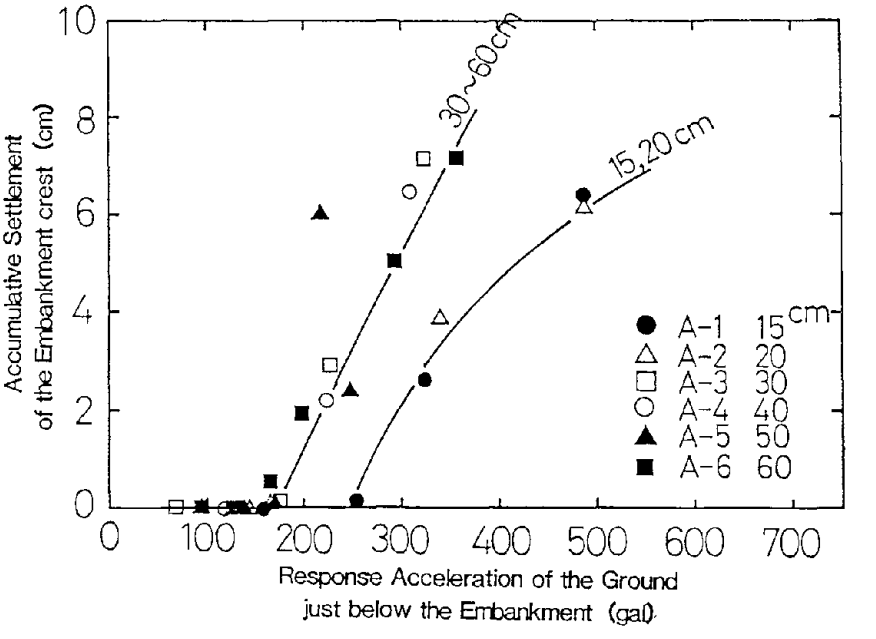

Fig. 4 Relation between the Response Acceleration of the Ground just below the Embankment and accumulative Settlement of the Embankment crest

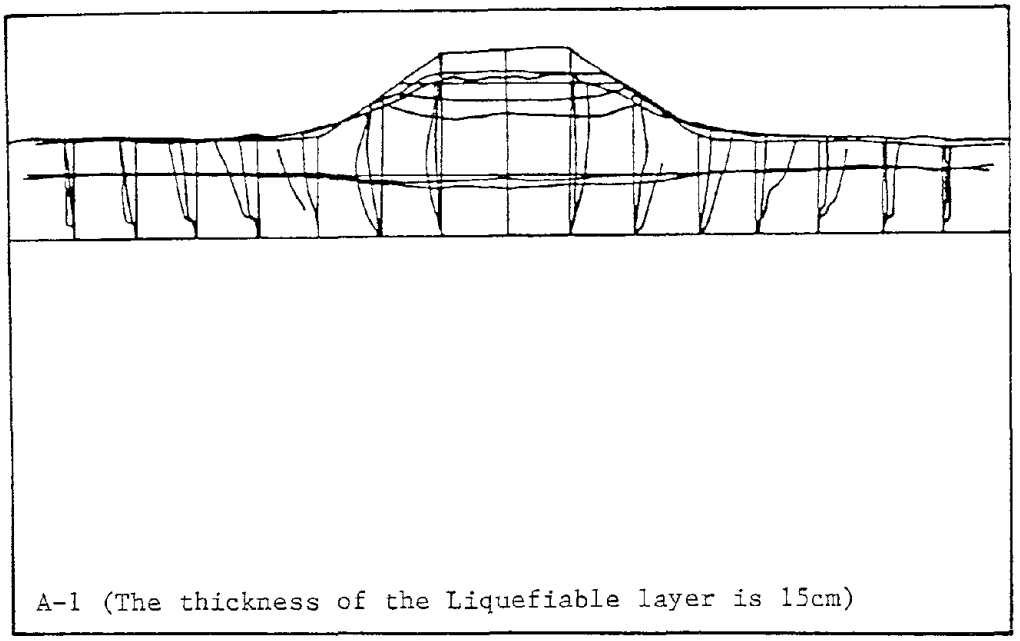

A-1 (The thickness of the Liquefiable layer is 15cm)

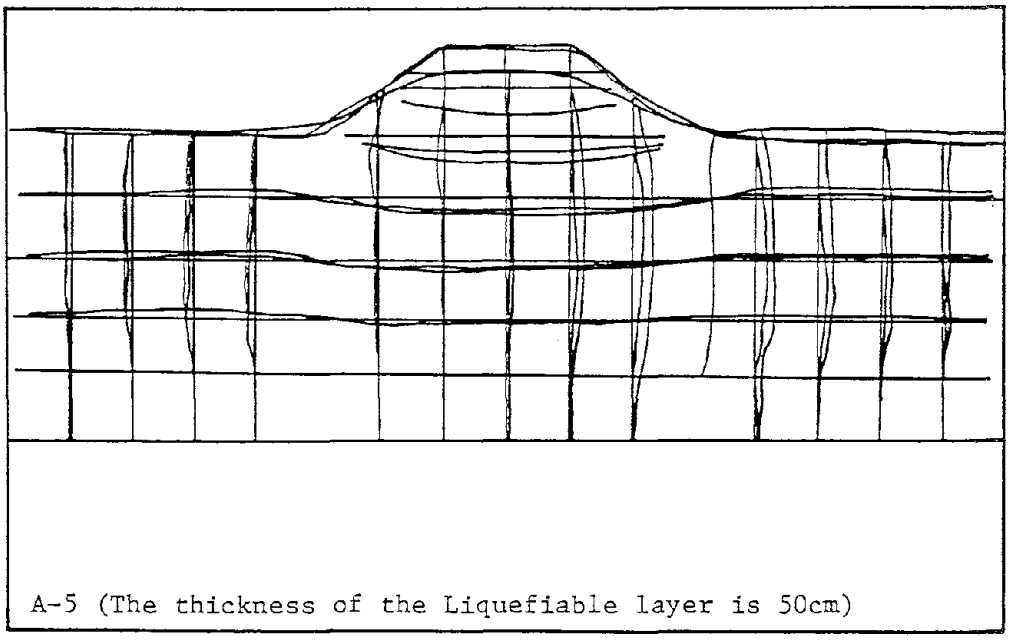

A-5 (The thickness of the Liquefiable layer is 50cm)

Fig. 5 Successive changes in the mesh lines at each end of excitation stages 3,4 and 5

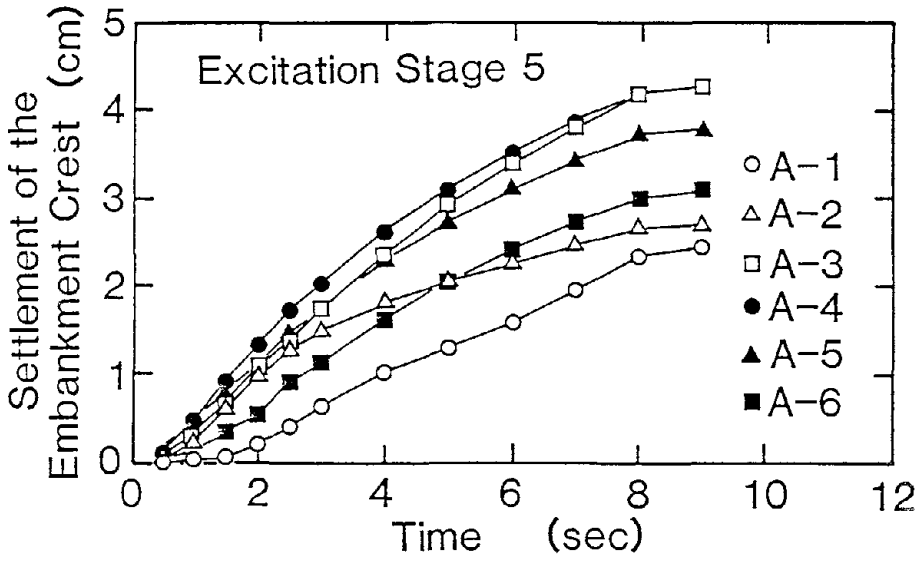

Fig. 6 Relation between Time and Settlement of the Embankment crest

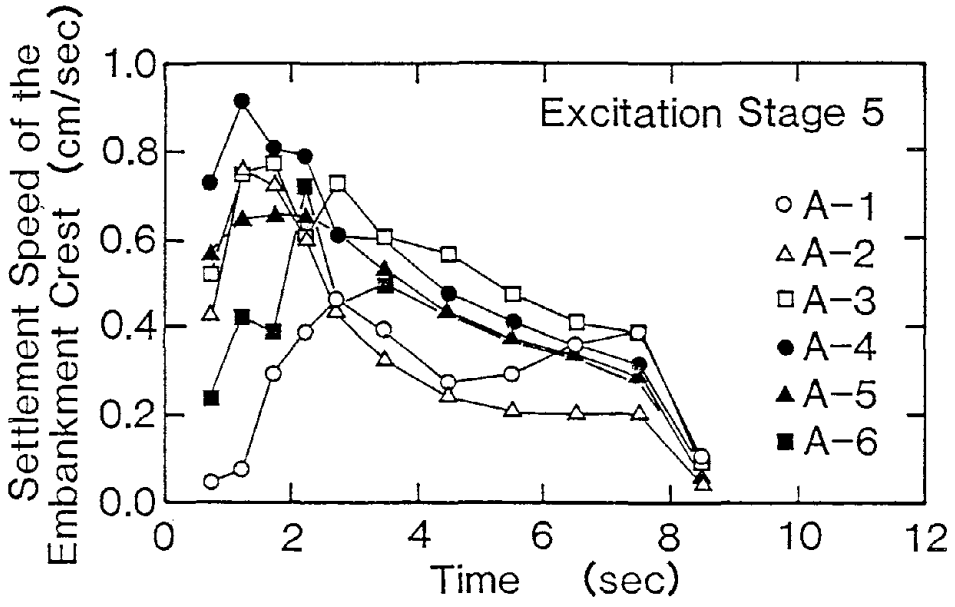

Fig. 7 Relation between Time and Settlement Speed of the Embankment crest

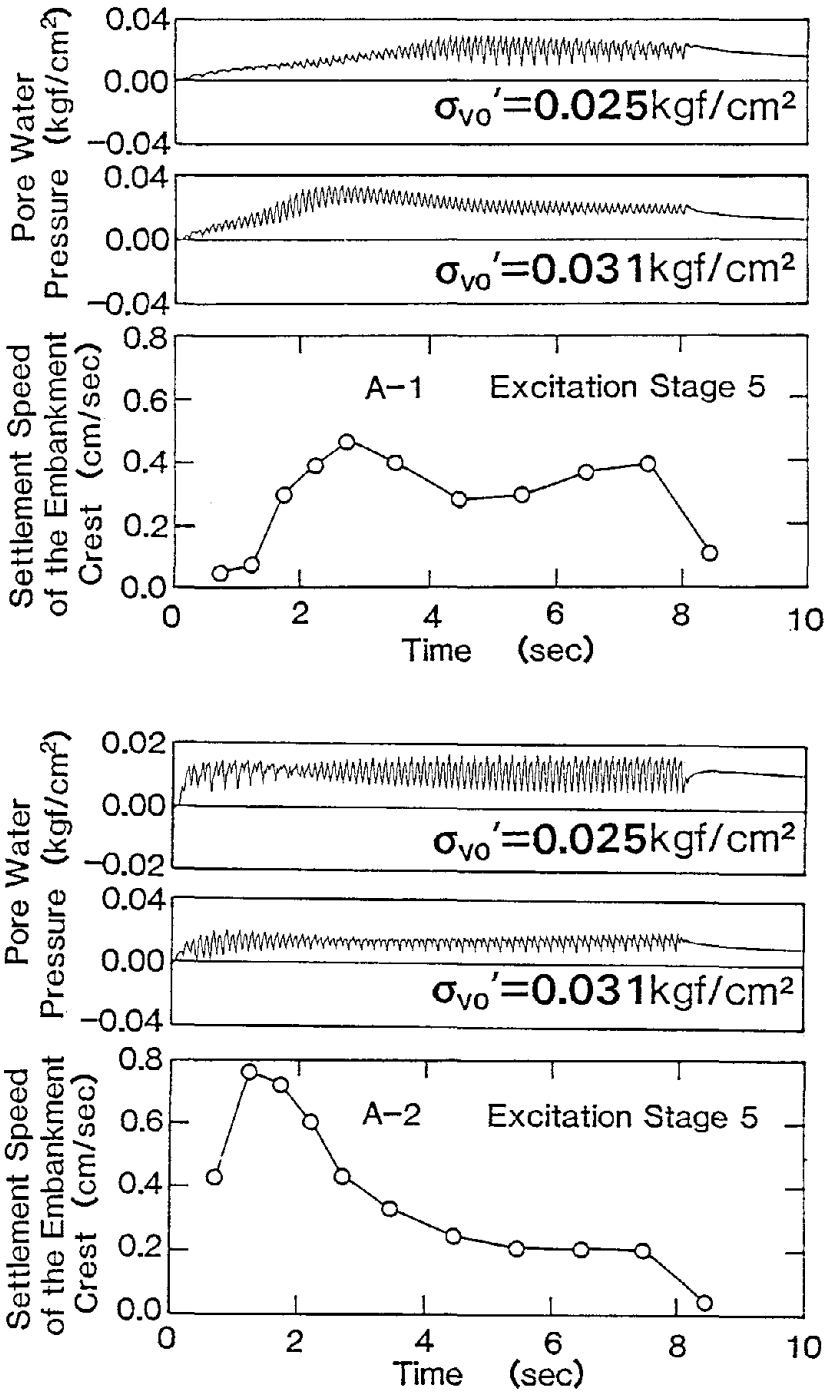

Fig. 8 Example of Records of Pore Water Pressure

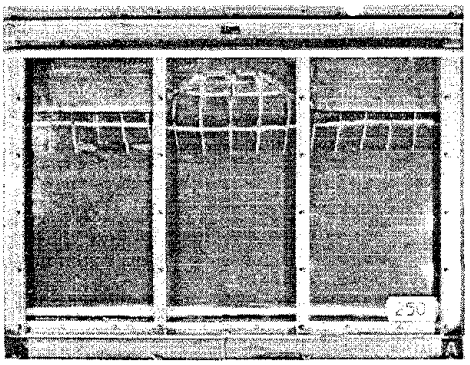

Photo. 1 Failure pattern of Case A-1 (excitation stage 5)

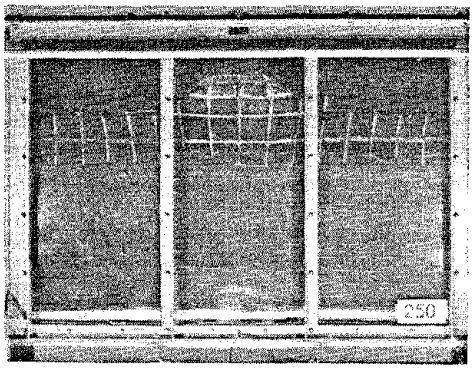

Photo. 2 Failure pattern of Case A-2 (excitation stage 5)

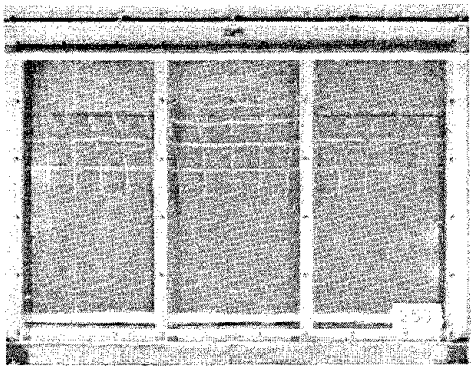

Photo. 3 Failure pattern of Case A-3 (excitation stage 5)

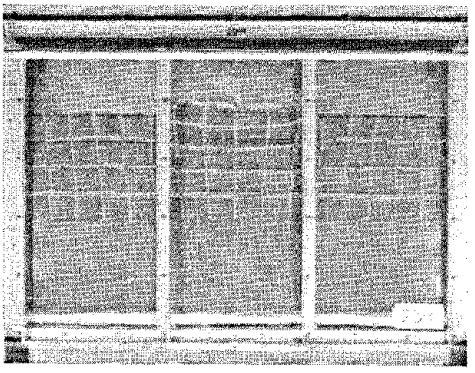

Photo. 4 Failure pattern of Case A-4 (excitation stage 5)

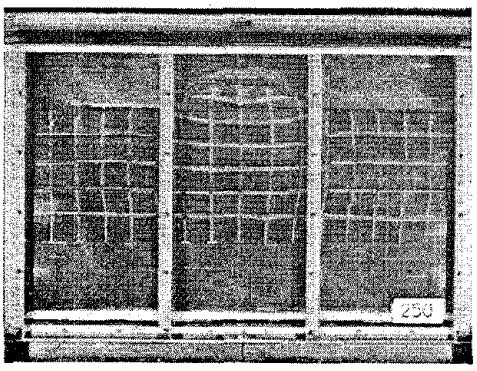

Photo. 5 Failure pattern of Case A-5 (excitation stage 5)

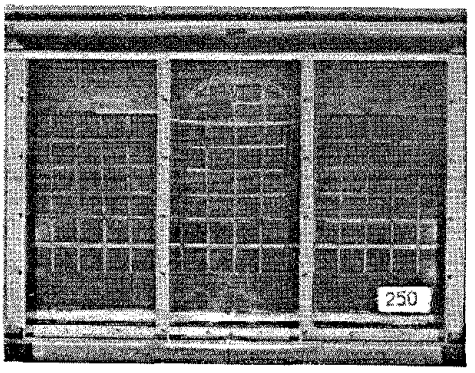

Photo. 6 Failure pattern of Case A-6 (excitation stage 5)

STUDY ON ASEISMIC MEASURES TO EMBANKMENTS ON SOFT CLAY GROUND

by
Yasuyuki Koga (1) and Osamu Matsuo (2)

ABSTRACT

The effects of four types of aseismic measures to embankments constructed on soft clay ground were studied by model shaking table tests and finite element analysis. Aseismic measures investigated in this study were "Counterweight fill method", "Sheet pile method", "Soil improvement method", and "Reinforced earth method". Shaking table tests were performed on a model embankment on soft clay ground prepared in a 2.5m x0.6m x 0.7m steel box. Analyses to obtain earthquake-induced deformation were also conducted. Settlements of the various measures were compared with unmodified embankments. The experimental and analytical results are summarized as follows:

1. Shake table tests and analyses showed that all the measures reduced the settlement of embankment on soft clay ground.
2. Calculated settlements were in a range from a half to twice the observed settlements. The "earthquake induced permanent deformation analysis method" was considered applicable.
3. Application of the "earthquake induced permanent deformation analysis method" revealed the following:
   i) Counterweight fill method: As the width and height of the counterweight fill are increased the earthquake-induced settlement is reduced.
   ii) Sheet pile method: As the length of piles is increased, the effect becomes larger. The effect of this method was not confirmed in shake table tests.
   iii) Soil improvement method: Improving the ground outside of the toe of the embankment showed comparatively larger effect than improving the portion inside the toe.
   iv.) Reinforced earth method: Even a very high modulus geotextile showed little effect on the settlement, though lateral spreading of the ground was reduced.

1. INTRODUCTION

The Nihonkai-Chubu Earthquake (1983) caused damage to many earth structures such as road and river embankments. Most of this damage was caused by liquefaction of loose saturated sandy deposits.

For the last decade, liquefaction-induced damages have attracted the attention of researchers because of their numerous and catastrophic examples. But there sometimes occur similar heavy damages to embankments on soft clay ground, such as the failure at the Yoshida-River embankment caused by the Miyagi-ken-Oki Earthquake (1978). Therefore, aseismic stability and earthquake-resistant measures to embankments on soft clay ground should also be studied. This paper describes the results of both experimental and analytical studies on the effects of several types of aseismic measures to embankments on soft clay ground.

2. OUTLINE OF STUDY PROGRAM

The objective of the study described herein is to estimate the effects of several types of aseismic measures to embankments on soft clay ground in a qualitative and quantitative manner. For this purpose, a series of shaking table tests and finite element analyses were undertaken. Aseismic measures considered in this study, numbers of shaking table tests and parameters considered in the analysis are shown in Table 1. Fig. 1 shows the flow of this study. Firstly, a series of shaking table tests on clay ground-embankment models with and without aseismic measure were performed to estimate the qualitative effects of the measures. Secondly, finite element analyses were applied to the test models, and by comparing calculated and observed results the applicability of the analysis method to predict the earthquake-induced deformation was investigated. Lastly, applying this analysis method to the hypothetical proto-scale ground-embankment model with and without several types of aseismic measures, these effects were estimated. The procedure shown in Fig. 1 seems to be generally used to study such geotechnical problems, and in this case the followings are pointed out as the advantage.

1. The scale model need not necessarily satisfy the similarity conditions of the prototype.
2. Even if the physical and mechanical conditions of the models are not the same, the effect of the difference can be corrected by analysis, so we can indirectly know the effect of the remedial measures.
3. Because FEM simulation is far more convenient than model tests, we can easily examine many different cases by using simulation analysis.

However, as the analysis is applied to the cases other than those verified by experimental results, the simulation is essentially an "extrapolative method", therefore the applicability of the analysis method should always be considered.

(1) Head, Soil Dynamics Div. P.W.R.I., Ministry of Construction, Tsukuba, Japan
(2) Researcher, Soil Dynamics Div. P.W.R.I., Ministry of Construction, Tsukuba, Japan

3. EXPERIMENTAL STUDY

3.1 Test Procedure

Shaking table tests were carried out on 4 models as shown in Fig. 2. Each model consisted of a clay ground, embankment with or without a remedial measure. The ground was prepared by consolidating the slurry clay in a steel box with the length of 2.5 m, a height of 0.6 m and width of 0.68 m. The material was an alluvial clay, of which physical properties are as follows:

Soil classification: CH
Natural water content: Wn approx. 60%
Liquid limit: LL = 51%
Plasticity index: PI = 24
Specific gravity: Gs = 2.686

The consolidation was performed for three months under both sides drainage condition, however, the primary consolidation was not completed. The embankment was constructed on the clay ground by compacting the material with a wooden plate, just after the consolidation weight was removed. The embankment material was prepared by mixing lead shots (Gs - 11.6, 2.0 mm dia) and clay (w approx. 50%) with weight proportions of 25 : 3. The sheet piles and tie rods in case-4, waveform steel plates (EI = 500000. kgf.sq cm/m) and 2 mm diameter steel wires were used respectively, considering the similarity of stiffness. Main sheet piles and anchor sheet piles are 35 cm and 10 cm in length respectively. They were connected with 4 tie rods on each side. The sheet piles and tie rods were installed into the ground prior to embankment construction, and tie rods were pretensioned to 1.0 kgf respectively. For the model ground, prior to embankment construction, a set of vane shear tests (with 4 cm height by 2 cm diameter vane), cone penetration tests (with shape angle of 30 degrees and section area of 1.0 sq cm cone), shear wave loggings and water content tests were performed. The shaking table test consisted of a resonance test and strong vibration test. Sinusoidal horizontal vibration was applied. Firstly, a resonance test was performed at a constant acceleration amplitude of 10 gal. Fundamental frequency obtained was in the range of 15 - 18 hz in all cases. The strong-vibration test was subsequently performed. In this test , input acceleration was a sinusoidal wave with a frequency of 5 hz and duration time of 5 sec. Acceleration amplitude was changed intermittently from 50 gal to 350 or 400 gal with a pitch of 50 gal and pauses of 20 - 30 minutes. During the test, displacement, acceleration, pore water pressure and tensile stress of tie rods (only in Case 4) of the model were recorded.

3.2 Test Results

3.2.1 Properties of Models

Fig. 3 shows some properties of the model grounds. It is shown that in the middle part of the ground the water content ratio was high and shear strength was low compared with the other part. This indicates that a primary consolidation was not completed in this part. The degree of consolidation in terms of strain, U , was 80-90% in all cases. It is also shown that the shear strength was relatively low in the upper part in Case 4 compared with that in other cases. This fact seemed to influence the test results that the Case 4 model was not so stable seismically.

3.2.2 Results of Strong Vibration Tests

It was found that in all cases the amplitude and the distribution of response acceleration was relatively stable and the amplification factor of the embankment was 1.5 - 2.0, up to the input acceleration level of about 100 gal where a significant deformation did not occur in the models. However, at the acceleration level where a plastic deformation began to occur in the model, the amplification of response acceleration increased rapidly during vibration. On the contrary, at a greater input acceleration level, it decreased. It would be because the weaker portion of the ground yielded by the shear stress induced by the vibration. Fig. 4 illustrates the deformed shape of all models after final vibration (350 - 400 gal). The vertical lines in the ground shown in Fig. 4 are the deformation of the line markers which were inserted after the consolidation of the ground ended. This figure indicates that the embankment settles as the ground is compressed vertically and spreads laterally. In Case 1 of no measure, the horizontal deformation and internal tension crack at the center portion can be seen in the embankment. In Case 2 and 3 of counteweight-fill method, it can be seen that lateral spreading of the ground at the filled side were comparatively restrained and this tendency is more evident in Case 3 with wider fill. Moreover, because the tension crack of the main embankment was restrained, large cracks appeared at the approaching portion of the fill. This phenomenon seems to be supported by the deformation pattern of the ground surface. In Case 4 of the sheet-pile method, the outside ground was rather uniformly deformed, whereas in Case 1 the lateral spreading was concentrated in the upper part of the ground, due to the existence of sheet piles. Further, the tensile stress amplitude of the tie rods during vibration were not large and after the vibration ended. Therefore, it is concluded that the supporting sheet piles were not effective for Case 4. In addition, the test results described herein are considered to appear qualitatively as the deformation pattern of an embankment which is subjected to earthquake just after construction (i.e., the consolidation has hardly progressed.) Fig. 5 shows the relationship between the input acceleration and the settlement at the top of the embankment. It should be noted that the settlement shown in Figure 5 is accumulated and includes settlements induced by previous vibration stages, therefore the settlement shown should be reduced to some extent to obtain the settlement from the vibration stage. Although there were some

differences in shear strength of each model ground as shown in Fig. 3, it can be seen in Fig. 5 that in the case of the counter-weight fill method, the settlement of the main embankment was decreased as the width of the fill was increased. But in the case of the sheet pile method the settlement was larger than that in the case with no measure (Case 1). The following two reasons can explain this result. One is the fact that the shear strength of the upper part of the ground was lower in Case 4 than that in other cases. Another is that the response acceleration at large input shaking was also larger in Case 4, which might indicate the possibility that the shear force during shaking was transmitted to the upper portion on the model through the main sheet piles and this accelerated the deformation. Finally, it should be noted that the test results described herein were derived under the test condition and all the models were prepared in a constant size test box whereas the size and location of embankment and fill are different among models, which would have influenced each test result differently as a boundary condition. This kind of problem peculiar to model testing will be solved by the analysis described in the following chapters.

4. ANALYSIS FOR THE MODEL TESTS

Finite element analysis was applied to the test models described previously. This analysis was intended to confirm the applicability of the analysis method. "Earthquaked-induced permanent deformation analysis method" was used in the analysis, which can calculate the permanent deformation of the earth structure induced by earthquakes and was developed and improved by the authors for these years.

4.1 Method of Analysis

This method is described in detail in Ref. 1. Parameters of the analysis were provided as follows. Most physical and mechanical properties were determined from the results of physical property tests, cone penetration tests, vane shear tests and triaxial compression tests. Moreover, the cyclic stress-permanent strain relationship of the clay material, which is one of the most important parts of the analysis method, was given by performing some 20 cyclic triaxial compression tests and compiling these test results. Poisson's ratio of 0.499 was used in the deformation analysis considering that the deformation of the models during shaking would be occurring in substantially in an undrained condition. Using the parameters described above, permanent deformation was calculated under the condition of input acceleration of 100 and 200 gal, for all the cases. A computer program SADAP was used in the analysis, which was developed by the first author and can conduct static and dynamic analysis of earth structures considering non-linear stress-strain characteristics of the soil(2).

4.2 Results of Analysis

Fig. 6 shows the amplification factor of acceleration in the middle section of the model obtained by the dynamic response analysis of Case 1, being compared with observed one. This figure shows that the analysis provides fairly good agreement between calculated and observed response accelerations at 10 gal shaking but the calculated value is greater than observed at 20 gal shaking. This would be because of yielding of the ground at from middle to upper portion, subjected to large shear stress caused by large shaking. On the other side, the calculated response acceleration is slightly increasing at 200 gal shaking compared with 100 gal shaking. This is because the non-linear characteristics influenced the response of the model and a larger strength parameter for the material was used in the non-linear dynamic analysis to obtain a stable solution. Overall, it was concluded that the dynamic response analysis gave satisfactory and practical results. Fig. 7 shows the deformed finite element mesh after 200 gal shaking obtained from the permanent deformation analysis. Such deformation can be compared with the test results in Fig. 4 qualitatively, although the shaking acceleration level is different from each other. In all cases, the settlement of the embankment occurs accompanied by lateral spreading of the underlying ground, at the same time a heaving occurs beyond the toe of the embankment. Comparing the deformation of Case 2, 3 with Case 1, lateral spreading is relatively reduced in the ground side where counterweight fill is constructed, and it is more effective when a larger fill is constructed. In Case 4, the sheet piles are restraining the local lateral spreading of the ground. These analytical results correspond well to those of the model tests.

In addition, in Case 4, as the stresses of tie rods were calculated as compression, re-analysis was done using the model without the tie rods because the tie rods do not resist compression stress. This also corresponds very well to the test result that the stresses of tie rods were minimally increased by shaking. A comparison between observed and calculated settlement at the top of the embankment in all cases is shown in Fig. 8. But it should be noted that the observed settlement shown in this figure is accumulated and includes that having already occurred at the end of previous shaking stage, so the settlement will be underestimated to some extent. It is found in this figure that the both settlements appear to be in good agreement with each other except that in Case 4. It is likely that effect of sheet piles would be over estimated because a slippage between the sheet pile and the ground was not considered in the analysis. Further study will be needed in this area.

5. ANALYSIS FOR COMPARISON OF EFFECTS OF COUNTERMEASURES

5.1 Models of Analysis

Analytical investigation was performed on the effects of several types of aseismic measures assuming that they were applied to a hypothetical prototype embankment. Fig. 9 shows analytical models used in the analysis. The fundamental model is the embankment with dimensions of 5 m in both height and top width and with side slopes of 1:2 constructed on the clay ground (thickness = 10 m) underlain by a sand layer (thickness = 5 m). In other models counter-measured were added to be the fundamental model. The sand layer was assumed to be good enough to resist liquefaction during shaking and normally consolidated so that the strength distribution increased with depth. The Cu/p ratio was assumed to be 0.34. All the other properties were given realistic values that can be observed in the field. A safety factor of the fundamental model in a static condition is calculated as 1.2 by the circular sliding surface method. Sheet piles were used at both sides. As a soil-improvement method, a wall-shaped-type "Deep Mixing Method" was taken which consists of a row of three walls with a thickness of 1.0 m and a pitch of 1.6 m. Two cases were assumed in the analysis where the walls are driven into the ground inside and outside of the toe of the embankment. The walls are not perfectly supported in the sand layer, and the clay between the walls were not improved.

5.2 Conditions of Analysis

The clay layer was considered to be fully consolidated by the embankment load and therefore the shear strength increased to the depth according to the ratio of strength increase, Cu/p of 0.34. Counterweight fill was considered to be made of the same material as that of main embankment. The improved walls were considered elastic (G = 400kgf/cm2) without yield strength. In case of the reinforced-earth model, joint elements were arranged at both sides of the geotextile to permit slip deformation between geotextile and soil, where the interface shear strength parameter was given as the normal stress times the tangent of 20 degrees, whereas joint elements were never used in other models. An acceleration record obtained at the ground surface near Tsugaru-Ohashi Bridge at the Nihonkai-Chubu Earthquake, 1983, was used as an input acceleration, with the maximum acceleration of 200 gal in most cases. In each case, parameters presented in Table 1 were considered in the analysis.

5.3 Results of Analysis

It was found as a result of the dynamic response analyses that the differences of maximum response accelerations among all the cases were not significant for a constant input acceleration level.

Fig. 10 illustrates the deformed finite element mesh due to 200 gal shaking. The followings are found from Fig. 10. Deformation patterns of (a), (b) and (c) in Figs. 4 and 7. It can be seen from figure (d) that the improved walls tilt outwards, at the same time resisting the local spreading of the ground. The effect of the improved walls seems to look like that of sheet piles. In figure (e), a slippage occurs between the ground surface and the geotextile, whereas it does not occur between the geotextile and the embankment, and the amount of lateral spreading of the ground is slightly reduced by the geotextile compared with that in figure (a). But the effect of reducing the settlement is insignificant. Fig. 22 summarizes the results of the analyses which show the relationship between the settlements and maximum input acceleration in all cases. The result indicates that most types of countermeasures are more or less effective for reducing the earthquake induced permanent deformation of the embankment by comparing the deformation with that in the fundamental model without measure. Fig. 12 shows how the calculated settlement varies by changing the dimensions of the counterweight fill. This indicates that the counter-weight fill method is more effective when its dimension is larger. In Fig. 11 again, it is found that the soil improvement method is slightly more effective in Case A than in Case B of Fig. 9(d). This might be due to the ground condition, that is, shear strength of the ground is gradually weaker depending on the distance from the center because of the absence of consolidation stresses by the embankment load. Moreover, the weaker portion of the ground is improved in Case A than in Case-B. This might explain why the soil improvement is more effective in Case A. Next, the sheet-pile method appears most effective among all the cases shown in Fig. 11, however, it should be noted that the analysis in this case has the problem mentioned previously. Therefore further study will be needed in the analysis of the sheet-pile method. Fig. 13 shows the settlement and Young's modulus of geotextile obtained from the analysis of the reinforced-earth method. When a value of EA is smaller than 100 tf/m, there is no effect, but when it is 1,000 tf/m, the settlement is reduced by about 20%.

6. CONCLUSIONS

Effects of four types of aseismic measures to embankments constructed on soft clay ground have been studied experimentally and analytically. Countermeasures investigated herein were as follows: counterweight fill method, sheet-pile method, soil improvement method, and reinforced earth method. The latter two methods were studied only analytically. The main conclusions obtained from this study are as follows:

1. Each countermeasure showed the effect more or less to reduce the earthquake induced settlement of embankment.
2. The method of analysis adopted in this paper provided satisfactory agreement between calculated and observed settlement of the embankment due to earthquake motion.
3. The counterweight fill method was more effective, as the dimension of the fill becomes large.
4. The sheet-pile method was effective in restraining the ground to make local lateral spreading, but the effect to reduce the embankment settlement was not confirmed in the experiment.
5. The soil improvement method, of which the Deep Mixing Method was adopted in this study, showed the effects that are similar to that of the sheet-pile method.
6. The reinforced earth method which uses the geotextile under the embankment showed little effect to reduce the embankment settlement.

7. ACKNOWLEDGEMENTS

The study described in this paper was sponsored by the Arakawa-Karyu Construction Office, Kanto District Bureau of Construction, Ministry of Construction. The authors wish to acknowledge their financial support. Acknowledgement is also given to Mr. Yasuaki Karasawa for his participation in this study.

8. REFERENCES

1. Sasaki, Y., Matsuo, O. and Karasawa, Y.: Analysis method of earthquake-induced deformations of earth structures and its application, Civil Engineering Journal, Vol. 27, No. 3, pp. 46- 51, 1985. (in Japanese)

2. Koga, Y., Tateyama, S. and Karasawa, Y. : SADAP-1, A computer program for the static and dynamic analysis of earth structures considering nonlinear stress-strain relationship of soils, Memorandum of the Public Works Research Institute, No. 1688, 1981. (in Japanese)

Table 1. Aseismic measures considered in the study

Aseismic measure	Case number of model test	Parameters considered in analysis
No measure	Case-1	———
Counterweight-fill method	Case-2, 3	width, height of counterweight-fill
Sheet-pile method	Case-4	length of sheet piles
Soil improvement method	———	location of improved zone
Reinforced earth method	———	modulus of geotextile

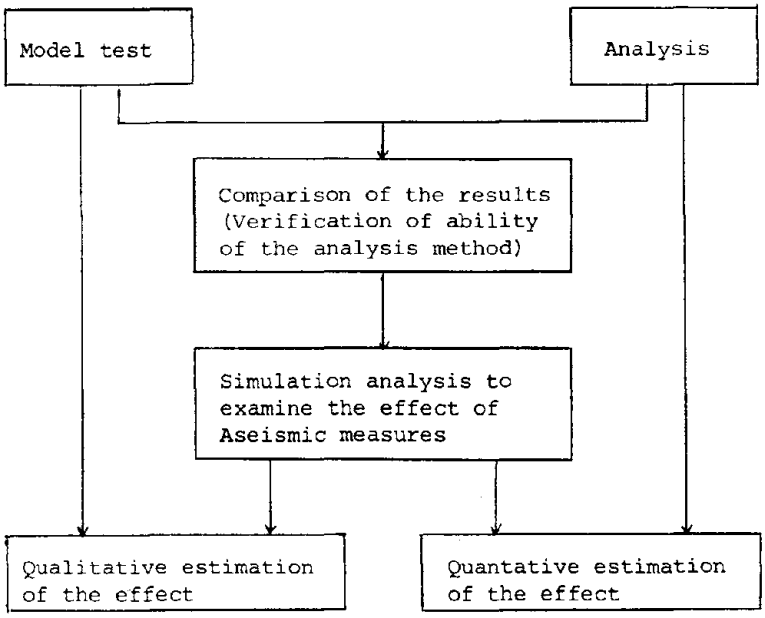

Fig. 1. Study flow

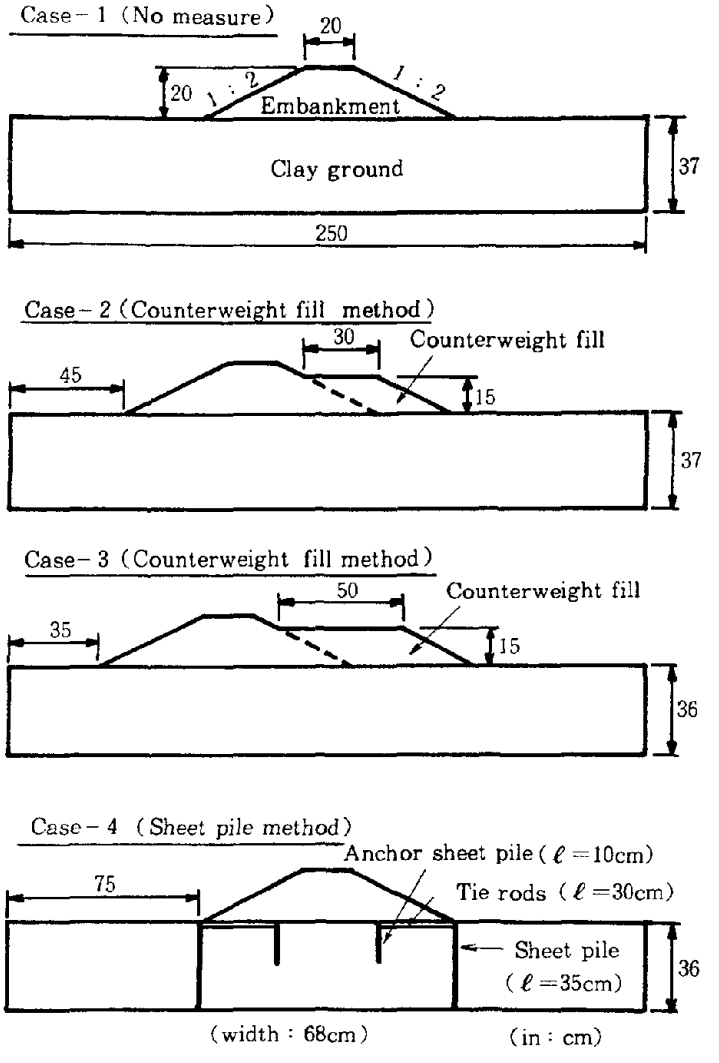

Fig. 2. Schematic diagram of test models

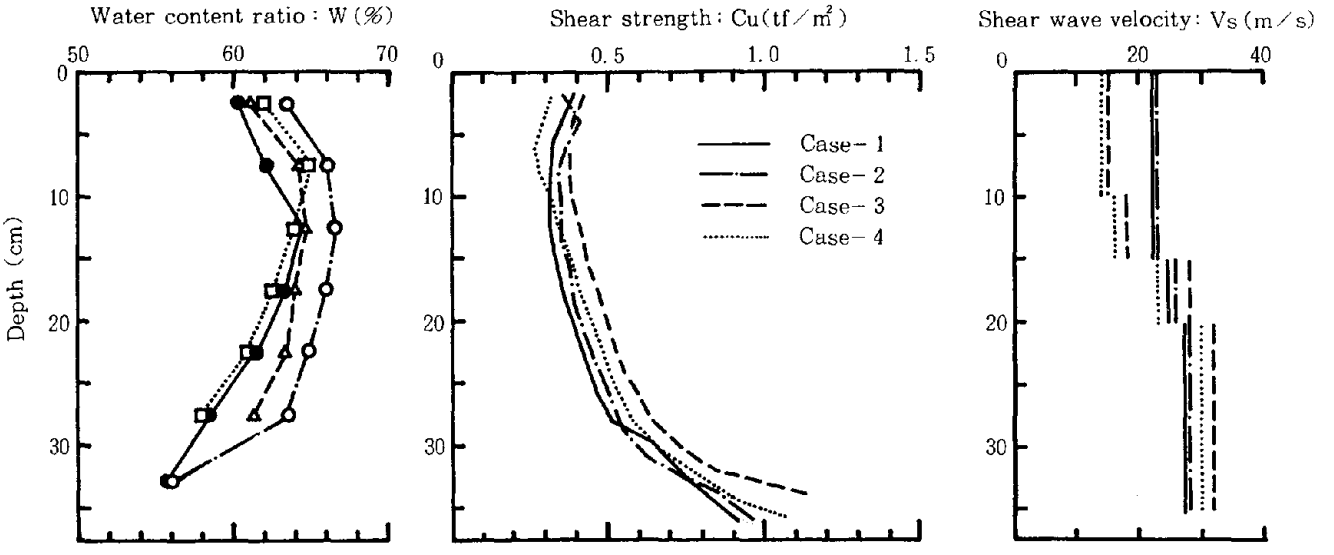

Fig. 3. Properties of model ground

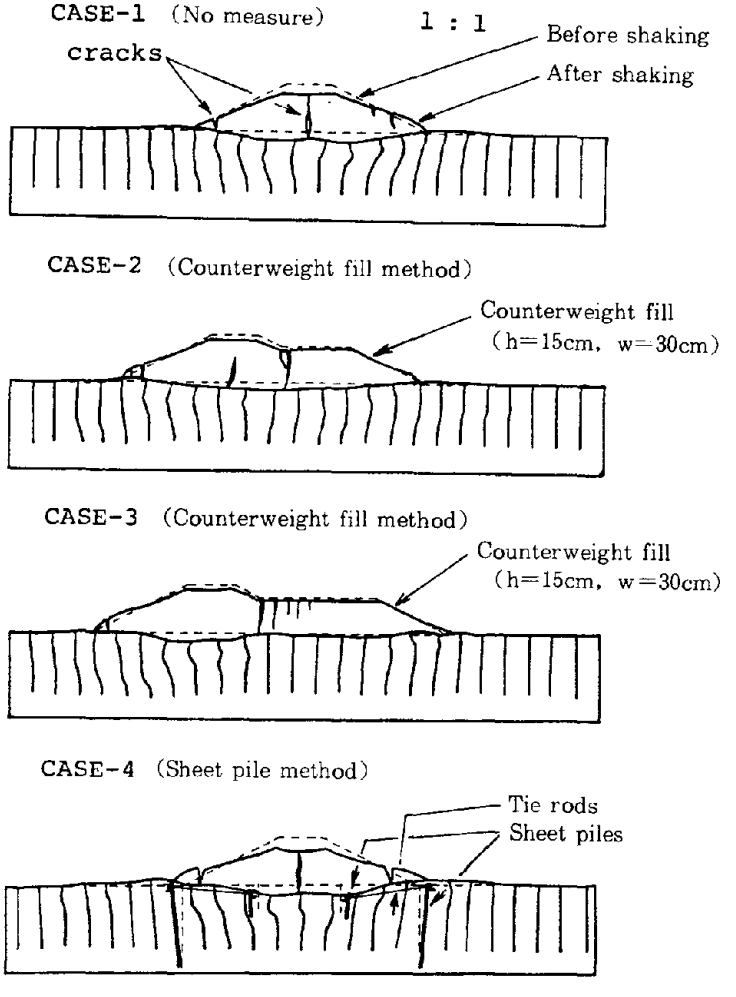

Fig. 4. Observed deformations of the test models (after 350-400gal shaking)

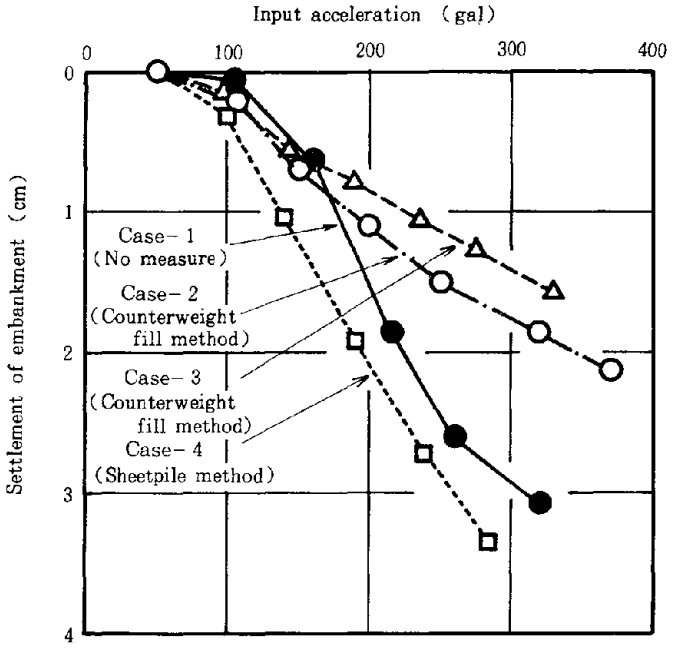

Fig. 5. Relationship between input acceleration and settlement of embankment in the experiment

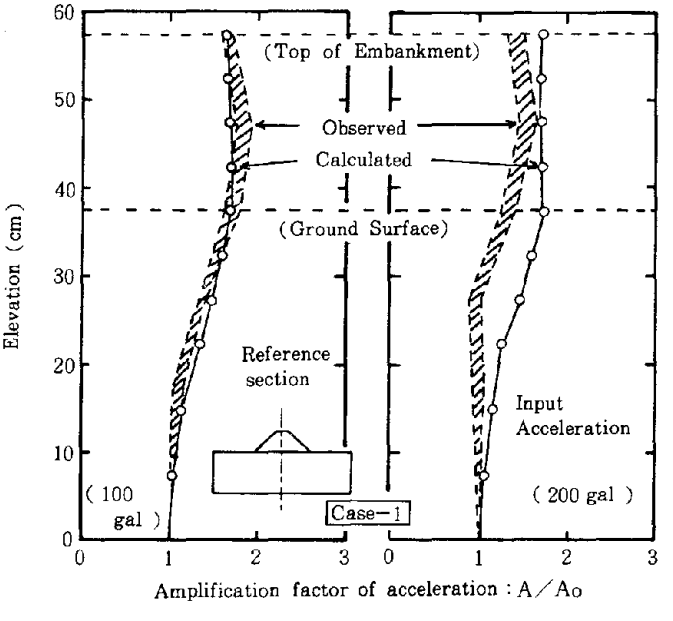

Fig. 6. Comparison of calculated and observed amplification factor of acceleration

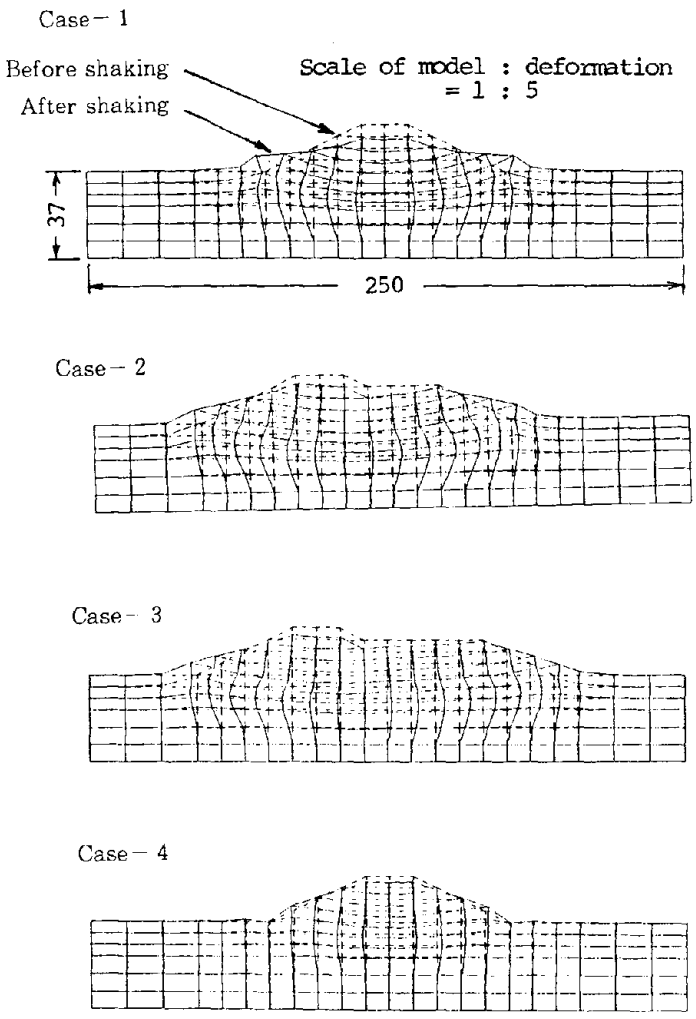

Fig. 7. Calculated deformations of the test models (after 200gal shaking)

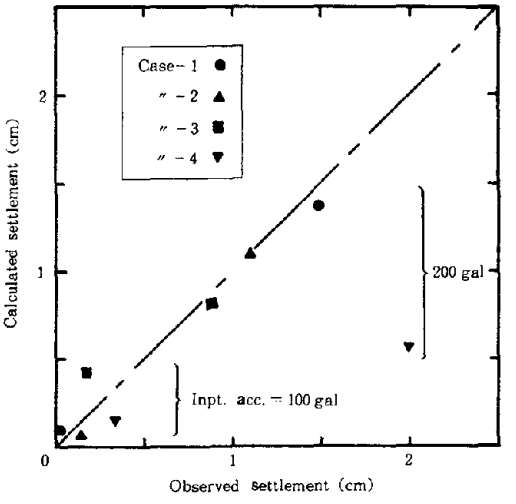

Fig. 8 Comparison of calculated and observed settlements of embankments

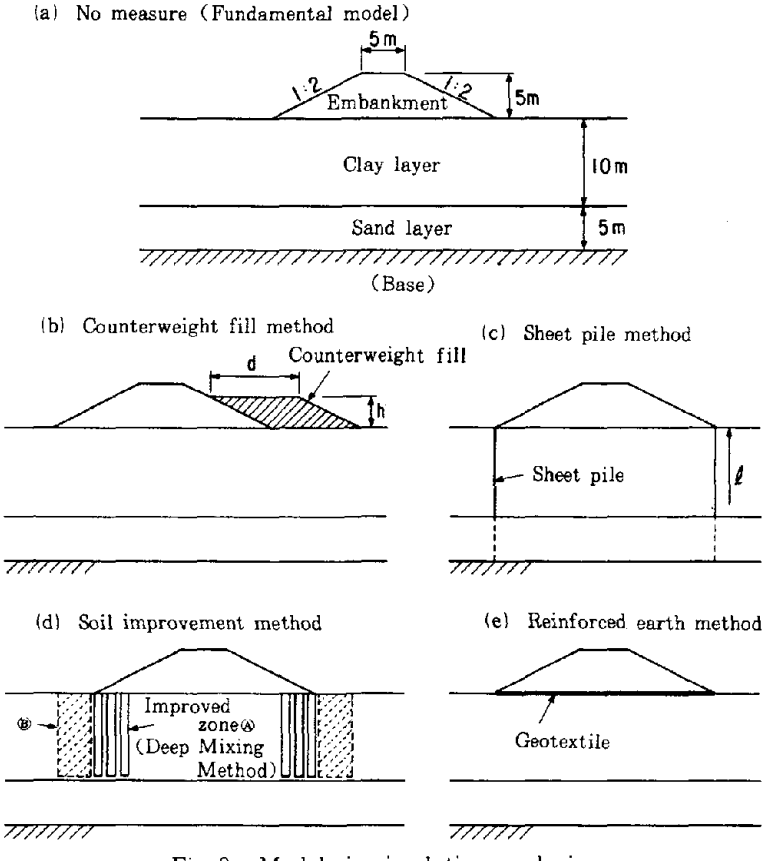

Fig. 9 Models in simulation analysis

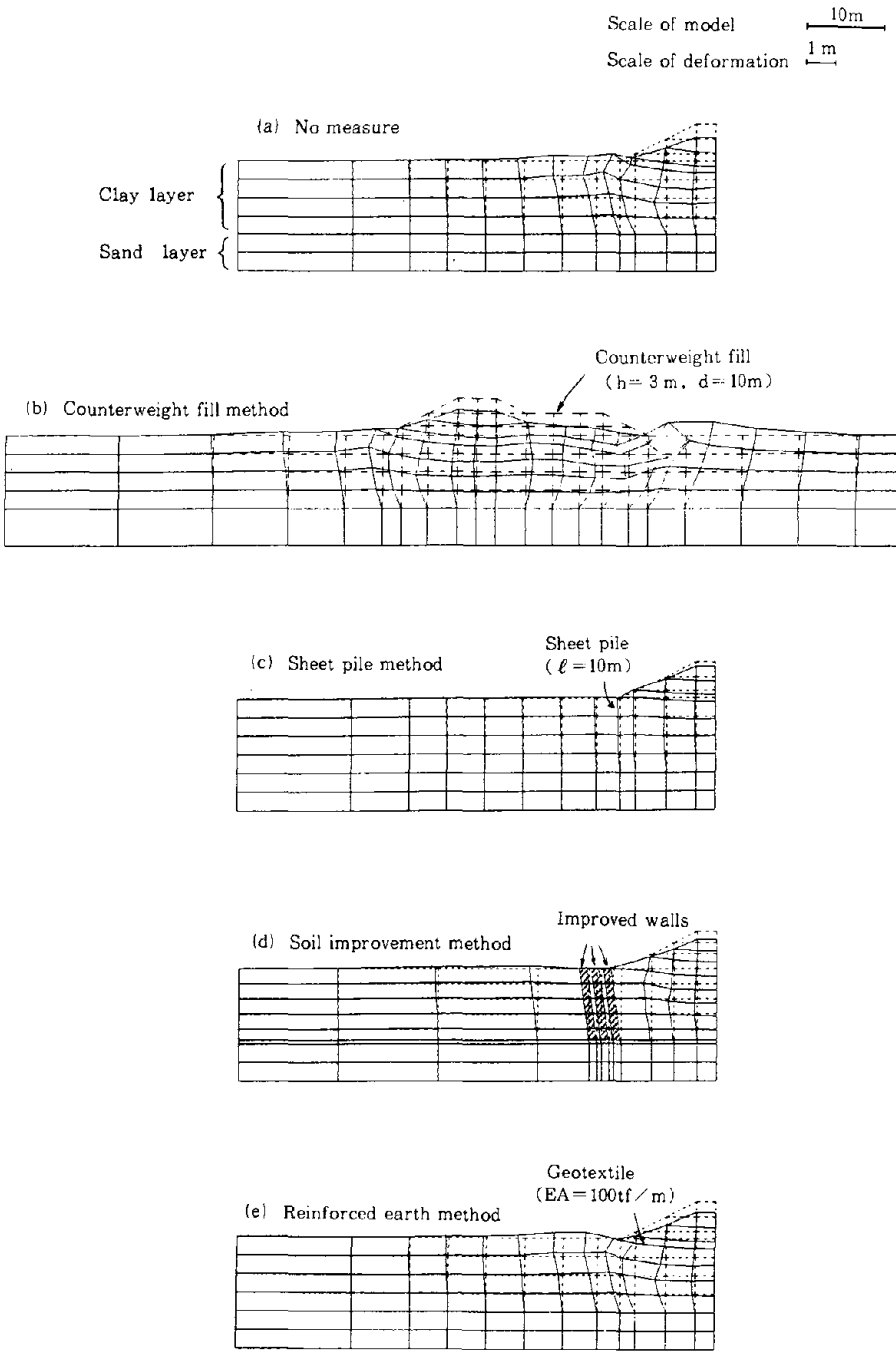

Fig.10 Deformed finite element mesh

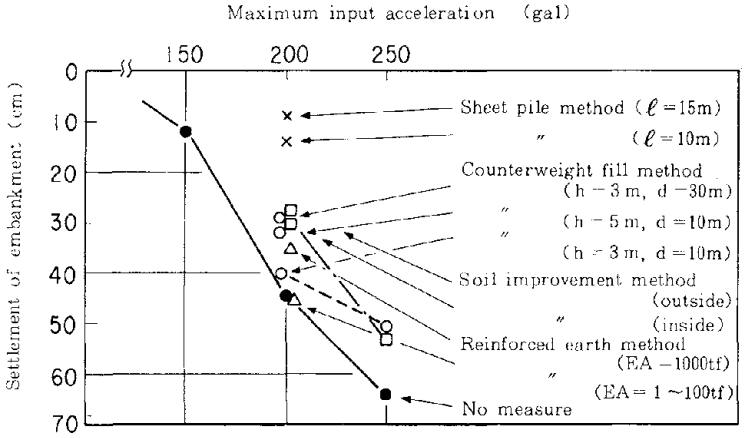

Fig.11 Calculated settlement v.s. maximum input acceleration

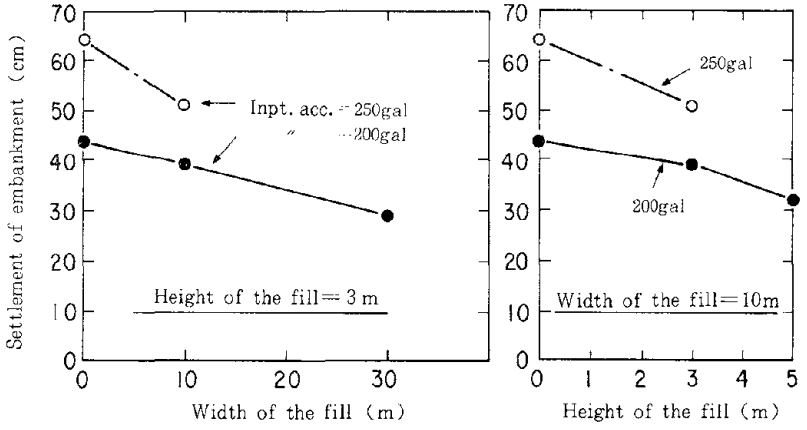

Fig.12 Relationship between the dimensions of the fill and the settlement of embankment

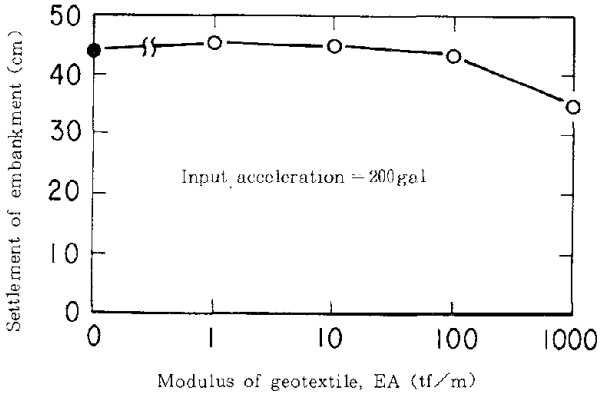

Fig.13 Relationship between modulus of geotextile and settlement of embankment (calculated)

DRAFT GUIDELINES FOR POST-EARTHQUAKE INSPECTION AND EVALUATION OF EARTHQUAKE DAMAGE IN REINFORCED CONCRETE BUILDINGS AND ITS APPLICATION TO THE NAMIOKA TOWN HOSPITAL BUILDING

BY

Tsuneo Okada,[1] Masaya Hirosawa,[2] Hisahiro Hiraishi,[3] and Manabu Yoshimura[4]

ABSTRACT

The Ministry of Construction, Japanese Government has been promoting a five-year project which is called "Development of Repair and Strengthening Techniques for Buildings and Structures Damaged by Earthquakes" since 1981.

The guidelines for post-earthquake inspection and evaluation of earthquake damage in buildings, which is one of the objects of the project, was established in 1985.

They are applied for wooden structures, steel structures, reinforced concrete structures and artificially field ground. This paper describes the summary of the guideline which is applied to reinforced concrete buildings, and also describes the results when the guidelines were applied to the inspection and evaluation of the earthquake damage of the Namioka Town Hospital Building in Aomori Prefecture which was severely damaged during the 1983 Nihonkai-Chubu Earthquake.

The guidelines consist of 1) the guideline for emergency inspection and evaluation for risks of damaged buildings to aftershocks, 2) the guideline for the first level inspection and evaluation identifying damaged buildings and treatment for continued occupancy, and 3) the guideline for the second level inspection and evaluation for necessity of structural strengthening. The judgement for these is based on foundation settlement and listing of buildings and degree of damage to columns and walls.

As a result of application of the above three guidelines for inspection and evaluation of damage to the Namioka Town Hospital, the following decisions were drawn.

a. Entry prohibition (based on the emergency inspection and evaluation).

b. Severe damage (based on the first level inspection and evaluation).

c. Structural strengthening needed (based on the second level inspection and evaluation).

---

[1] Professor, Institute of Industrial Science, University of Toyko.

[2] Director, Research Planning and Information Department, Building Research Institute, Ministry of Construction (B.R.I.).

[3] Senior Research Engineer, Structural Engineering Department, B.R.I.

[4] Special Assistant of Director for International Corporation, B.R.I.

These results are the same as the ones which had been reached by the authority based on detailed inspection and evaluation. This paper finally describes newly recognized several matters of concern.

1. THE GUIDELINE FOR INSPECTION AND EVALUATION OF EARTHQUAKE DAMAGE OF REINFORCED CONCRETE BUILDINGS

1.1 The Objective of This Guideline

The objective is to make possible the prevention of incidents of deaths and injuries to occupants from aftershocks immediately after a major earthquake and the selection of methods for restoration.

1.2 The Outline of This Guideline

There are three types of guidelines to be established for identification of earthquake damages. They are called 1) Guideline for Emergency Inspection and Evaluation, 2) Guideline for the First Level Inspection and Evaluation, and 3) Guideline for the Second Level Inspection and Evaluation. Each guideline is made based on the consideration of emergency degree.

a. Guideline for Emergency Inspection and Evaluation

This is to judge safe entry to a building by investigating potential risk of occupancy of buildings from aftershocks immediately after a major earthquake.

b. Guideline for the First Level Inspection and Evaluation

This is to judge the degree and location of damage of a building and the required strengthening for continued occupancy.

c. Guideline for the Second Level Inspection and Evaluation

This is to judge the necessity for strengthening the damaged buildings which is unclear to be judged only by the guideline for the first level inspection and evaluation.

Figure 1.1 shows the general flow to be applied for each guideline. Each guideline was prepared by the subcommittee on reinforced concrete structures and the working group affiliated with the subcommittee under the Committee on the Development of Post-Earthquake Measures of National Project based on the draft written by Prof. Shunsuke Otani of the University of Tokyo, Prof. Katsumi Takiguchi of The Tokyo Institute of Technology, and Prof. Masamichi Ohkubu of the Kyushu Institute of Design. The chairman of the subcommittee on reinforced concrete structures is Prof. Tsueno Okada of the University of Tokyo, the chairman of the working group is Prof. Masaya Murakami of the Chiba University, and the chairman of committee of the National Project is Prof. Hajime Umemura of the Shibaura Institute of Technology. In the following chapters, the detail of each guideline is mentioned.

1.3 Guideline for Emergency Inspection and Evaluation

This is to make the urgent judgement

of the entry prohibition and the limited entry to reinforced concrete frame structures and wall structures in damaged areas of a major earthquake, with considering hazards produced by dropping of fixtures and the falling of debris, risk to lives of people due to collapse of buildings caused by aftershocks. This guideline is also applied to public buildings to judge the safety of the building. The investigation should be executed immediately after a major earthquake by building and civil engineers from governmental organizations in concern, mainly through visual observation of exterior appearance of damaged buildings, in accordance with Emergency Earthquake Damage Inspection Form: the outline of a building, damage condition of a superstructure, foundation settlement, inclination, appendage dropping hazard, debris falling hazard, etc. The investigation takes about half an hour per building. At public buildings, the following items are also to be investigated: the damage condition of interior columns and walls, the falling hazard, the dropping hazard in the building and the adequacy of accommodating the sufferers from a major earthquake. The degree of danger is determined according to each hazard identification rank of each investigation item. The rank is stated like rank A, rank B, and rank C. An identification of damage of superstructure is defined based on damage ranks of exterior columns of the frame structures and exterior walls of the wall structures, of most severely damaged floor, whose damage rank are equal to or higher than moderate. The damage ranks III (moderate), IV (severe) and V (collapse) are classified based on (1) crack of concrete, (2) spalling of concrete of columns, and (3) bending or fracture of reinforcing bars.

Table 1.1 shows the investigation items of foundation settlement, inclination of buildings and of superstructures, and corresponding hazard rank.

The classification of judgement for danger, caution and safety is decided as follows, and each decision is accompanied by the posting of "entry prohibited", "entry limited" or "safety".

DANGER

1. If there is one "rank C" in the investigation items of superstructure of a building, and/or there are two or more than two "rank B" in the same investigation items, the whole building is judged to be in danger.

2. If there is found damage degree V in the interior of exterior columns and walls, the area of "danger" is from the damaged columns and walls to the undamaged columns and walls less than damage degree III nearest to the damaged ones, and the upper floor of the overhead of the damaged columns and walls.

3. Every floor which support damaged stairways.

4. If there is any rank C in the investigation items of

the dropping hazard, the area which is estimated to have the hazard is decided as "danger".

5. If there is any rank C in the investigation items of the falling hazard, the area which is estimated to have the hazard is decided as "danger".

CAUTION

The building with one or more than one rank B in each investigation item of supersturcture of a building, the dropping hazard of appendage and the falling hazard of debris.

SAFETY

This judgement is applied only for public buildings. Its determination is made only for the buildings without any rank B and C in the investigation items of the dropping hazard and the falling hazard, and with a very slight damage which is less than damage degree III in columns of frame structures and walls of wall structures.

1.4 Guideline for the First Level Inspection and Evaluation

This guideline is used to investigate the outline of damaged buildings suffered from a major earthquake, to identify the degree of damage of the building, to determine the safety against further earthquakes through the investigation of the intensity of the earthquake ground motion which has caused the damage, and to decide the treatment of the damaged buildings for continuous occupancy. If necessary, this guideline is applied to revise the results of the emergency inspection and evaluation. If the judgement of repair for restoration or strengthening is difficult, the guideline for the second level inspection and evaluation is applied. The treatment for continuous occupancy has the following four types.

1. REUSE WITHOUT ANY STRUCTURAL REPAIR

Only cosmetic repair is done. Repair such as injecting epoxy resin, for example, is not necessary.

2. REPAIR FOR RESTORATION

The goal of this repair is to make the seismic performance of damaged structures the same level as the condition before damage.

3. STRENGTHENING

The goal of this strengthening is to improve the seismic performance of damaged structures better than the condition before damage.

4. DEMOLITION OR WITHOUT REUSE

The investigation is made by building and civil engineers from governmental organizations in concern, by persons admitted as an investigator by governmental organizations and by persons whom the organizations required the investigation. They make measurements of the inclination of buildings and of foundation settlements, and investigate damage conditions of superstructures (as to frame structures, every columns and beams, and as to wall structures exterior walls should

be inspected as much as possible). If earthquake damage of a structure is obviously identified, inspection is stopped at that stage. The inspection may take, at most one day for two inspectors per building.

Identification of damage of the building is defined as the worst of inclination, foundation settlement and damage of superstructure. The damage of beams of frame structures is assessed by replacing that by damage of columns. Identification of the damage of the superstructure is judged based on damage rate (shown in Table 1.2) defined by damage rank of columns, beams and walls of the most severely damaged floor.

Table 13 through 1.5 show the each relationship between inclination, maximum foundation settlement and maximum damage rate, and identification of damage. Table 1.6 shows relationships between the identification of damage of the building and the treatment of continuous occupancy.

1.5 Guideline for the Second Level Inspection and Evaluation

This guideline is used to judge the necessity for strengthening the damaged buildings, which are unclear to be judged according to the guideline for the first level inspection and evaluation, or requires detailed analysis for seismic capacity of a building to resist anticipated earthquakes before restoration for continuous occupancy, and to obtain basic information about strengthening of the building for restoration.

The inspection is conducted on damage of columns and walls, tilitng and foundation settlement of the building, and damage to piles, etc. The necessity for strengthening is evaluated based on the tilting of the building, soil condition and intensity of earthquake ground motion etc., if the foundation or pile is damaged. This is done based on earthquake damage index being function of the potential of the seismic capacity of the building to resist further earthquakes, if the superstructure is damaged. Table 1.7 (omitted) shows relationship between the tilting of building caused by damage of foundation and pile and the need for strengthening of foundation and pile.

Table 1.8 shows upper limit values of earthquake damage index requiring strengthening. The earthquake damage index is calculated according to the following procedures.

1. Seismic index I_s before damage is calculated by "Guideline for evaluation of Seismic Capacity of Existing R/C Building," issued by Japan Association for Building Disaster Prevention, April 1977.

2. In the same manner, seismic index Is' after damage is calculated by the following equation.

$$I_S' = E_O' \times G \times S_D' \times T$$

where,

E_O' = basic seismic index after damage given by the evaluation of seismic capacity of existing

R/C building in which reduction coefficient of seismic capacity shown in Tables 1.9 and 1.10, depending on damage level of columns and walls, is multiplied to the basic seismic index before damage,

G, T = geological index and time index, respectively, which are the same as those before damage,

S_D' = Structural design index after damage which is the same value for the first level evaluation of seismic capacity and for S_D' for the second level evaluation of seismic capacity the effect of damage is considered in items of the eccentricity between center of gravity and center of stiffness in plan and irregularity of the stiffness along the height of the building. Here the stiffness of columns and walls after damage is given by multiplying that before damage by .

3. Earthquake damage index Φ is given by the following equation.

$$\Phi = \{1-(I_S'/I_S)\} \times 100 \ (\%)$$

Earthquake damage index Φ should be calculated in both X and Y directions of each story. However, damage to a certain story should be focused if damage to that story is obviously severe compared to other stories.

1.6 Other Contents and Application of the Guideline

This draft of guideline was prepared as one of the intermediary research products of the national project. Although, here in this report, inspection and evaluation methods of structural damages are mainly described, the following data should be obtained with the report.

a. hazard inspection for falling of exterior cladding of buildings.
b. hazard inspection for overturning of stairways for escape and equipment.
c. inspection for buildings for places of refuge.
d. many photographs of damaged buildings and portions as references to evaluating damage, and
e. application examples of inspection and evaluation of actually damaged buildings.

However, as this guideline was compiled as one of the first drafts for each structural kind, the following problems should be sufficiently discussed until the guideline is actually applied widely to damaged buildings. Up to that time, this guideline will be used as an available reference in case by case.

a. To consolidate data related to several numerical constants without sufficient back data.
b. To adjust the evaluation standard for safety among the guidelines for each kind of structure.

c. How to qualify persons to inspect and evaluate earthquake damages.
d. How to treat the guidelines administratively.

2. OUTLINE OF THE DAMAGES OBSERVED IN THE NAMIOKA TOWN HOSPITAL BUILDING

2.1 Outline of the Hospital Building

The observed damage, analyses and restoration of the hospital were already reported at the 16th Joint Meeting[2)3)4)]. Therefore, the data necessary to apply the guideline to the hospital building are presented here.

The hospital, as shown in Fig. 2.1, is a 5-story reinforced concrete structure with one story basement. The first floor is wider than the other floors. The structural system of the 5-story portion of this building comprised of frames with few shear walls in the longitudinal direction. The external two frames, out of the four frames, are distinguished by uniformly existing spandrel walls. Those in the transverse direction are mainly consisted of multi-storied frame shear walls. This building was constructed from 1968 to 1970 and had not suffered from other earthquakes until the May 1983 Nihonkai-Chubu Earthquake.

2.2 Outline of Damages and Restoration

(1) Outline of Damage

The damage of this building is summarized as follows.
a. On the whole, damage in the longitudinal direction are pronounced and those in the transverse direction are fairly slight. The 3rd and 4th stories were damaged severely; the 5th story was damaged moderately; the 2nd story was damaged slightly as well as the 1st and basement. Damage of each story did not cause a total collapse to the story as a whole.
b. In the longitudinal direction, pronounced shear failures and bond splitting failures were observed in many columns with spandrel walls at the 3rd, 4th and 5th floors. In the same ways, shear failures or shear cracks appeared in the reinforced concrete walls at the 2nd, 3rd, 4th and 5th floors.
c. Additionally, a reinforced concrete chimney and parapets on the roof tilted and many window glasses were broken and fallen down. Out of the above-mentioned damage, crack patterns of the exterior frame in the longitudinal direction are shown in Fig. 2.2 and examples of the detailed crack patterns of columns are shown in Fig. 2.3.

(2) Outline of Restoration

This building had been functioning normally until the earthquake occurred. After the earthquake, use of the building was stopped partially and the overall reuse was started from August, 1984. Outlines of limited occupancy of the building during this period are as follows.
a. The patients in the sick rooms on

the 3rd, 4th and 5th floors were evacuated to outdoor by nurses immediately after the earthquake and these floors were sealed off except authorized persons until reuse of the entire building.

b. The function of operation rooms was stopped during the period of strengthening construction work from Feb. 1984 to June 1984.

c. The use of the other portions at the first and basement floors were stopped for about one through three months because of the repair and strengthening work. However, even in this period, function as a hospital except the above-mentioned sick rooms and operation rooms was continued by using temporally other portions of the building.

In Fig. 2.4, main strengthening construction methods adopted and their location are shown.

2.3 Observed Damage of Columns and walls

As shown in Fig. 2.2, several kinds of damage, classified into several damage ranks, were observed in columns and walls. Concerning these damages, classification to several damage ranks were carried out based on Table 1.2 and Table 1.11 and the results are shown in Fig. 2.5.

As shown in the figure, damages ranks are as follows:

a. In the portions higher than the 3rd floor, many members are ranked higher degree than those in the lower portion.

b. Although damage ranks of the interior columns in the exterior frames are generally high, those columns of the interior frames are ranked low except columns in the 3rd and 4th stories.

c. Although damage ranks of the interior columns in the exterior frames at the 3rd and 4th floors are classified to the rank IV, their damage of the several columns are very close to the rank V as the bucking of longitudinal bars and cracking of the floor slab were partially observed.

3. EVALUATION OF THE EARTHQUAKE DAMAGE OF THE HOSPITAL BUILDING

3.1 Outline

The guideline described in the first chapter is applied to evaluate the earthquake damage observed in the hospital building. That is, the guideline for emergency inspection and evaluation is applied to determine safe for entry to the building etc.; the first level inspection and evaluation is applied to classify the damage of the building; and the second level inspection and evaluation is applied to judge whether the building should be strengthened or not.

3.2 Emergency and First Level Inspection and Evaluation

(1) Emergency inspection and evaluation

In absence of any tilting and settlement of a building, safety of the building is judged as a whole based on the degree of damage exterior

columns in most severely damaged stories using Table 1.1. In case of this hospital building, the 3rd story was most severely damaged and 8 columns out of 12 exterior columns in the 3rd story is rated as V. Accordingly, as the hazard rank of the superstructure is rated as rank C by Table 1.1. Thus, this building is judged to be dangerous and the entry was prohibited.

(2) The first level inspection and evaluation

After identifying the most severely damaged story, and rating each column in the story, repair of the structure for occupancy was decided by the resultant identification and the seismic intensity of the earthquake.

The result obtained by applying the first level evaluation is shown in Table 3.1. In this table, the results are shown of all stories from the first to the fifth where damage of all columns were inspected. Furthermore, the results judged only from rating of all exterior columns, assuming all interior columns are not accessible for inspection, are also shown in the table. As shown in the table, identification of the damage at each story is generally reasonable but when there are many damaged columns unable to be investigated, a different identification may be obtained because of significant difference in the sum of damage rates. That is, although the result of the 4th story was judged to be "severe" based only from the inspection of the exterior columns, the result from the all columns was rated as "moderate".

3.3 The Second Level Inspection and Evaluation

(1) Calculation of residual seismic capacity

The objective of this level of evaluation is to further refine the residual seismic capacity of a damaged building for strengthening. In the case where foundation piles suffered no damage, the residual seismic capacity is decided by the damage ranks of all vertical load carrying members at all floors. That is, after deciding damage rank of each member and coefficient to reduce seismic capacity of the member by the damage rank, residual seismic capacity using the coefficients of each member by the damage rank, residual seismic capacity of the building is calculated by the first or second level evaluation of seismic capacity using the coefficients η of each members.

In Table 3.2, shear coefficients, C, of all vertical members in the 2~5th stories are listed with the shear coefficients, C', of those after earthquake. And as the basic seismic index, Eo, of each story is shown in the following expression in the case without any extremely short column, the value of $Cc(C_w + 0.7C_c)$, ΣC and the ratio of $\Sigma C'/\Sigma C$ are also shown in the table.

$$E_o = \frac{n+1}{n+1} (C_w + 0.7C_c) \qquad (1)$$

where,

C_w, C_c = sum of shear coefficient of each wall and of each column,

respectively, and

n, i = number of stories above ground and location of the story under investigation counting from the first floor, respectively.

As understood from the values of $\Sigma C'/\Sigma C$ in Table 3.2, deterioration ratios of seismic capacity of this building are 0.97, 0.54, 0.67 and 0.89 at the 2nd, 3rd, 4th and 5th story, respectively, and this means that damages of 3rd floor was most severe.

(2) Determination for strengthening

Necessity to strengthen a damaged building is judged from Table 1.8 based on the earthquake damage index Φ shown in the following expression and the intensity of earthquake.

$$\Phi = \{1 - (I_S'/I_S)\} \times 100 \ (\%) \qquad (2)$$

where,

$I_S = E_O' \times G \times S_D' \times T$ = Seismic Index after earthquake

G = geological index

S_D' = structural design index after earthquake

T = time index

As shear reinforcement was not adequate both in columns and walls in the case of this building, the value of ductility index, F, of each member is less than 1.27. Therefore, the basic seismic index, E_O, in the second level evaluation of seismic capacity is also shown in Eq. (1). However, in this case, the strength of each member should be based on calculated ultimate flexural strength and shear strength.

S_D' index of this building after the earthquake is almost same as the before plan the earthquake so far as the eccentricity of the building is concerned. But stiffness distribution along the height became lower after the earthquake became lower due to severe damage in the third story. However, neglecting this change of S_D', Φ values are calculated assuming $I_S'/I_S = \Sigma C'/\Sigma C$.

The results are listed in Table 3.3 with strengthening requirements according to Table 1.8. Also listed are the results obtained from the first and second level evaluations of seismic capacity. As shown in the table, the two results by the first and second level evaluations agree with each other and it is concluded from the investigation on the 3rd and 4th floors that this building should be strengthened.

3.4 Comparison Between Results of Judgement and Actual Treatment, and Discussions

(1) Entry prohibition

Whole building is prohibited for entry as a result of seismic evaluation according to this guideline. However, entry prohibition for the floors above 2nd floor was actually recommended for individuals who conducted investigations. Entry to the floors below the 2nd floor was permitted because this was the only hospital in the town. This was also the reason for strengthening.

(2) Identification of damage of the building

The building was classified as "severe damage" to the whole structure (but, "moderate damage" is concluded if all columns is inspected and evaluated). On the contrary, experts actually classified 5th, 4th, 3rd and 2nd floors as moderate, severe, severe and small damages, respectively. Although both results agree with each other if they are investigated in detail, in the former classification - severe damage it is necessary to distinguish whether damage is partial or total.

(3) Necessity or unnecessity of strengthening of the building for restoration

Strengthening of the building for the restoration is necessary only for the 3rd and 4th stories as a result of the application of this guideline to the building. However, other floors were also repaired and strengthened while the repair was mainly concentrated on the 3rd, 4th, and 5th floors. The degree of repair depended largely on the difference in the expected intensity of earthquake motion considered for the seismic structural analysis. A careful consideration should be paid in carrying out strengthening work in areas other than damaged floors, particularly strengthening continuously from lower floors to upper floors.

4. CONCLUSIONS

This paper described the outline of the guidelines for inspection and evaluation of damaged reinforced concrete building developed by the National Project promoted by the Ministry of Construction, and described the results when this guideline was applied to the Namioka Town Hospital which was damaged during the Nihonkai-Chubu Earthquake in May 1983.

The result of the judgement agreed reasonably well with the actual strengthening work which was actually carried out. However, the following subjects are decided to be investigated as to the guideline.

(1) General Comments

a. The treatment for the judgement on structural members whose damage is likely to be unclear because of existence such as wooden finishing should be explained.

b. Judgement whether the treatment of entry prohibition, identification of the damage and necessity of strengthening of the building for restoration, etc. is applied or not for whole building should be explained in detail.

c. Selection of a most severely damaged floor from the damage of exterior columns should be explained (the emergency and first level inspection and evaluation).

(2) The guideline for emergency inspection and evaluation

a. Execeptional cases, where identification of the damage is not classified by the damage of only exterior columns, should be explained as example.

b. There should be more examples about dropping hazards and falling hazards, and definite examples of the area of these hazards should be added.

c. It should be explained that there are exceptional cases of partially entry prohibition, etc.

(3) The guideline for first level inspection and evaluation

a. Judgement for continuous occupancy in such a case wherein building suffers moderate damage, moderate earthquake ground motion should be discussed further (see Table 1.6).

b. It should be explained that there is a difference in the treatment among floors (see Table 1.6).

c. The method of identification of the flexural failure column and shear failure column should be explained.

(4) The guideline for second level inspection and evaluation

a. Quantitatively values for the earthquake damage index representing a potential of seismic capacity to resist to further earthquakes Φ should be prepared.

b. The relationship between the limit value of for strengthening for restoration and intensity of suffered earthquake ground motion should be discussed further from the viewpoint of the target of strengthening.

c. It should be explained that it is not rare that strengthening might be conducted for even slightly damaged floor.

5. ACKNOWLEDGEMENTS

The authors would like to extend their heartily gratitude to many experts of universities and of Building Research Institutes, for giving much cooperation in the investigation of earthquake damage of the Namioka Town Hospital and on the preparation of the draft of the guidelines for inspection and evaluation which were quoted in this paper.

6. REFERENCES

1. "Guideline for Post-Earthquake Inspection and Evaluation of Earthquake Damage in Buildings," Report of Development of Repair and Strengthening Techniques

for Buildings and Structures Damaged by Earthquakes, Building Research Institute, 1984.

2. Masaya Hirosawa, et.al., "Damage and Repair of Namioka Town Hospital Damaged by the Nihonkai-Chubu Earthquake, 1983 - Part 1: OUtline of Damage and Screening of Structural Safety," Sixteenth Joint Meeting, UJNR, May 1984.

3. Yoshikazu kitagawa, et.al., The same as the above -Part 2: Analysis of Damage by Elasto-Plastic, Static and Dynamic Analyses," ditto.

4. Masaya Hirosawa, et.al., "The same as the above -Part 3: Retrofit Design and Estimation of the Effect," ditto.

5. "A Seismic Diagnosis Standards for Existing RC Building Structures," Japan Building Disaster Prevention Association.

Table 1.1 Items of Inspection and Hazard Rank of Foundation Settlement Inclination and Superstructure

(Damage Condition Inspected from Outside of the Buildings)

Kind of Damage	Hazard Rank		
	Rank A	Rank B	Rank C
A. Inclination of Building Caused by Foundation Settlement	Less than 1°	1° ∿ 2°	More than 2°
B. Foundation Settlement of Building	Less than 0.2m	0.2 ∿1.0m	More than 1.0m
C. Damage Degree of Superstructure			
(a) Frame Structure			
◦Ratio of Exterior Columns with the Damage Rank IV	Less than 10%	10 ∿ 20%	More than 20%
◦Ratio of Exterior Columns with the Damage Rank V	Less than 1%	1 ∿ 10%	More than 10%
(b) Wall Structure			
◦Ratio of Exterior Wall Length with the Damage Rank IV	Less than 10%	10 ∿ 20%	More than 20%
◦Ratio of Exterior Wall Length with the Damage Rank V	Less than 1%	1 ∿ 10%	More than 10%

(Damage Condition Inspected from Inside of Superstructure ; Shall be Carried out about Public Building)

(a) Frame Structure			
◦Ratio of Interior Columns with the Damage Rank IV	Less than 10%	10 ∿ 20%	More than 20%
◦Ratio of Interior Columns with the Damage Rank V	Less than 1%	1 ∿ 10%	More than 10%
(b) Wall Structure			
◦Ratio of Interior Wall Length with the Damage Rank IV	Less than 10%	10 ∿ 20%	More than 20%
◦Ratio of Interior Wall Length with the Damage Rank V	Less than 1%	1 ∿ 10%	More than 10%

Table I.2 Damage Rank of Column, Beam and Exterior Wall by Observed Damage Pattern and Damage Rate by Observed Damage Ratio

Damage Rank of Column, Beam and Exterior Wall	Damage Pattern	Observed Damage Ratio*1	Damage Rate (di : %)
I	Visible Narrow Crack of Conc. (Crack Width; less than 0.2mm)	Less than 10%	0.5
		10 ∿ 20	1
		20 ∿ 30	2
		30 ∿ 40	3
		40 ∿ 50	4
		More than 50%	5
II	Visible Clear Crack of Conc. (about 0.2 ∿ 1.0mm)	Less than 5%	0.5
		5 ∿ 10	1
		10 ∿ 15	2
		15 ∿ 20	4
		20 ∿ 25	5
		25 ∿ 30	6
		30 ∿ 35	8
		35 ∿ 40	9
		40 ∿ 45	10
		45 ∿ 50	11
		More than 50%	13
III	Clear Crumbling of Conc. or Remarkable Wide Crack of Conc. (about 1.0 ∿ 5.0mm)	Less than 3%	2
		3 ∿ 5	3
		5 ∿ 10	5
		10 ∿ 15	8
		15 ∿ 20	10
		20 ∿ 25	13
		25 ∿ 30	15
		30 ∿ 35	18
		35 ∿ 40	20
		40 ∿ 45	23
		45 ∿ 50	25
		More than 50%	30
IV	Remarkable Crumbling of Conc. with Exposure of Reinforcing Bar	Less than 3%	3
		3 ∿ 5	5
		5 ∿ 10	9
		10 ∿ 15	14
		15 ∿ 20	18
		20 ∿ 25	23
		25 ∿ 30	27
		30 ∿ 35	32
		35 ∿ 40	36
		40 ∿ 45	41
		45 ∿ 50	45
		More than 50%	50
V	Bending of Reinforcing Bars, Crumbling of Core Conc. and Visible Vertical Level Down (Distinguished by settlement and / or Inclination)	Less than 3%	4
		3 ∿ 5	7
		5 ∿ 10	14
		10 ∿ 15	21
		15 ∿ 20	27
		20 ∿ 25	34
		25 ∿ 30	40
		30 ∿ 35	48
		More than 35%	50

Note *1 Observed Damage Ratio D.R.

(Frame Structure)

$$D.R. = \frac{\text{Number of Columns of the Same Damage Rank}}{\text{Number of Columns inspected}}$$

(Wall Structure)

$$D.R. = \frac{\text{Total Length of Exterior Wall of the Same Damage Rank in Same Direction}}{\text{Total Length of Exterior Wall inspected in Same Direction}}$$

Table 1.3 Identification of Damage due to Total Inclination

Inclination Angle (θ)	$\theta < \frac{1}{100}$	$\frac{1}{100} \leq \theta \leq \frac{3}{100}$	$\frac{3}{100} \leq \theta \leq \frac{6}{100}$	$\frac{6}{100} < \theta$
Identification of Damage	Small or Slight	Moderate	Severe	Collapse (Overturned)

Table 1.4 Identification of Damage due to Total Settlement

Maximum Settlement (S:m)	S < 0.2	0.2 ≦ S ≦ 1.0	1.0 < S
Identification of Damage	Small or Slight	Moderate	Severe

Table 1.5 Identification of Damage due to Maximum Damage Rate out of Ones of each Story

Maximum Damage Rate Σdi(%)	$\Sigma di \leq 5$	$5 < \Sigma di \leq 10$	$10 < \Sigma di \leq 50$	$50 < \Sigma di$
Identification of Damage	Slight	Small	Moderate	Severe

Note) Building with a story where members with damage rank V occupy more than 50% of all members shall be judged as collapsed.

Table 1.6 Permanent Treatments of Damaged Buildings Based on the Identified Result and Intensity of Suffered Earthquake Ground Motion

Intensity of Earthquake Ground Motion (JMA Degree of Seismic Intensity)	Indentification of Damage of Building				
	Slight	Small	Moderate	Severe	Collapse
Less than or Equal to V			Repair Strengthening Second Level Check	Strengthening Demolition	Strengthening Demolition
Greater than or Equal to VI	Reuse	Reuse	Repair	Repair Strengthening Second Level Check	Strengthening Demolition

Table 1.8 Upper Limit Value of Earthquake Damage Index Φ (%) Requiring Strengthening for Restoration

Construction year[1]	Intensity of Earthquake Ground Motion (JMA Degree)[2]			
	Less than IV	Lower V	Upper V	Greater than VI
Before 1971	20	30	40	50
After 1971	30	40	50	

Note) 1. Φ-values corresponding to ones after 1971 may be applied to building of which hoop spacing is less than 10cm, even if it was constructed before 1971.

2. In order to divide the intensity V into Lower V and Upper V, 150gal of ground acceleration may be used as boundary.

Table 1.9 Coefficient to Reduce Seismic Performance of Members, η (For First Level Evaluation)

Damage Rank of Column or Wall[1]	Kind of Member		
	Column-M[2]	Column-S[3]	Wall[4]
I	1.0	1.0	1.0
II	1.0	0.8	0.9
III	0.6	0.4	0.6
IV	0.3	0	0.3
V	0	0	0

Note) 1. These damage ranks are classified according to Table 1.11

2. Column-M : flexure failure column

3. Column-S : column failing in other modes than flexure mode

4. All kinds of reinforced concrete wall, i.e., wing wall with column and wall out of frame line etc.

Table 1.10 Coefficient to Reduce Seismic Performance of Members, η (For Second Level Evaluation)

Damage Rank of Column or Wall[1]	Kind of Member				
	Flexure Failure Column[2]	Shear Failure Column[2]	Column with wing Wall[2]	Shear Failure Wall[2]	Flexure Failure Wall[2]
I	1.0	1.0	1.0	1.0	1.0
II	1.0	0.8	0.8	0.9	1.0
III	$0.4(1+\frac{F}{3.2})$	0.4	0.4	0.6	$0.4(1+F/2)$
IV	0.3	0	0	0.3	0.3
V	0	0	0	0	0

Note) 1. These damage ranks are classified according to Table 1.11

2. Classification of members with damage is fundamentally same as that in the second level diagnosis before damage. However, in case that observed failure mode is obviously different from those before damage, obserbed one has priority.

Table 1.11 Standard for Classification of Damage Rank of Members[1)]

Damage Rank	Column[2)]		Wall[3)]	
	Flexure Failure[4)]	Shear Failure[5)]	Flexure Failure[4)]	Shear Failure[6)]
I	Visible narrow cracks of concrete (crack width less than 0.2mm)			
II	* Clear cracks of conc. of which width is about 2mm. * Partial clumbling of conc. without exposure of bars * Falling down of mortal finishing is admissible.	* Clear cracks of conc. of which width is about 2mm. * Falling down of mortal finishing but no clumbling of conc.	(Similar damage as in flexure failure of column)	(Similar damage as in shear failure of column)
III	* Clumbling of cover conc. and partially buckling of bars	* Fairly wide shear cracks of 2∿5m wide * Several virtical splitting cracks of 2∿5mm wide along longitudinal bar		* Several inclined cracks of 2∿5mm and partially clumbling of conc. in wall without exposure of bars Small cracks in sorounding columns but without deterioration in capacity
IV	* Distinguished clumbling of conc. and residual horizontal deformation larger than 1/100 of story drift angle	* Large slippage by shear * Buckling of bars, fracture of hoops and failure of core conc.		* Severe failure of conc. making holes in wall, but damage rank of surrounding columns are smaller than that of rank IV of columns.
V	* Significant buckling of longitudinal bars and fracture of column hoop and complete deterioration of horizontal and vertical load carrying capacity, vertical shortening of column, buckling of window sashes and settlement of floor slab			

Note 1) Classification of failure mode, flexure failure or shear failure, should be made based on actual failure mode observed in site.

2) Column with wing walls whose length of one-side is more than three times wide of column, should be treated as wall.

3) Classification of wall includes columns with wing wall stated in ferm of 2).

4) This category includes Column (m) in Table 1.9, and Flexure Failure Column and Flexure Failure Wall in Table 1.10.

5) This category includes Column (S) in Table 1.9, and Shear Failure Column and Column with Wing Wall in Table 1.10.

6) This category includes Wall in Table 1.9 and Shear Failure Wall in Table 1.10.

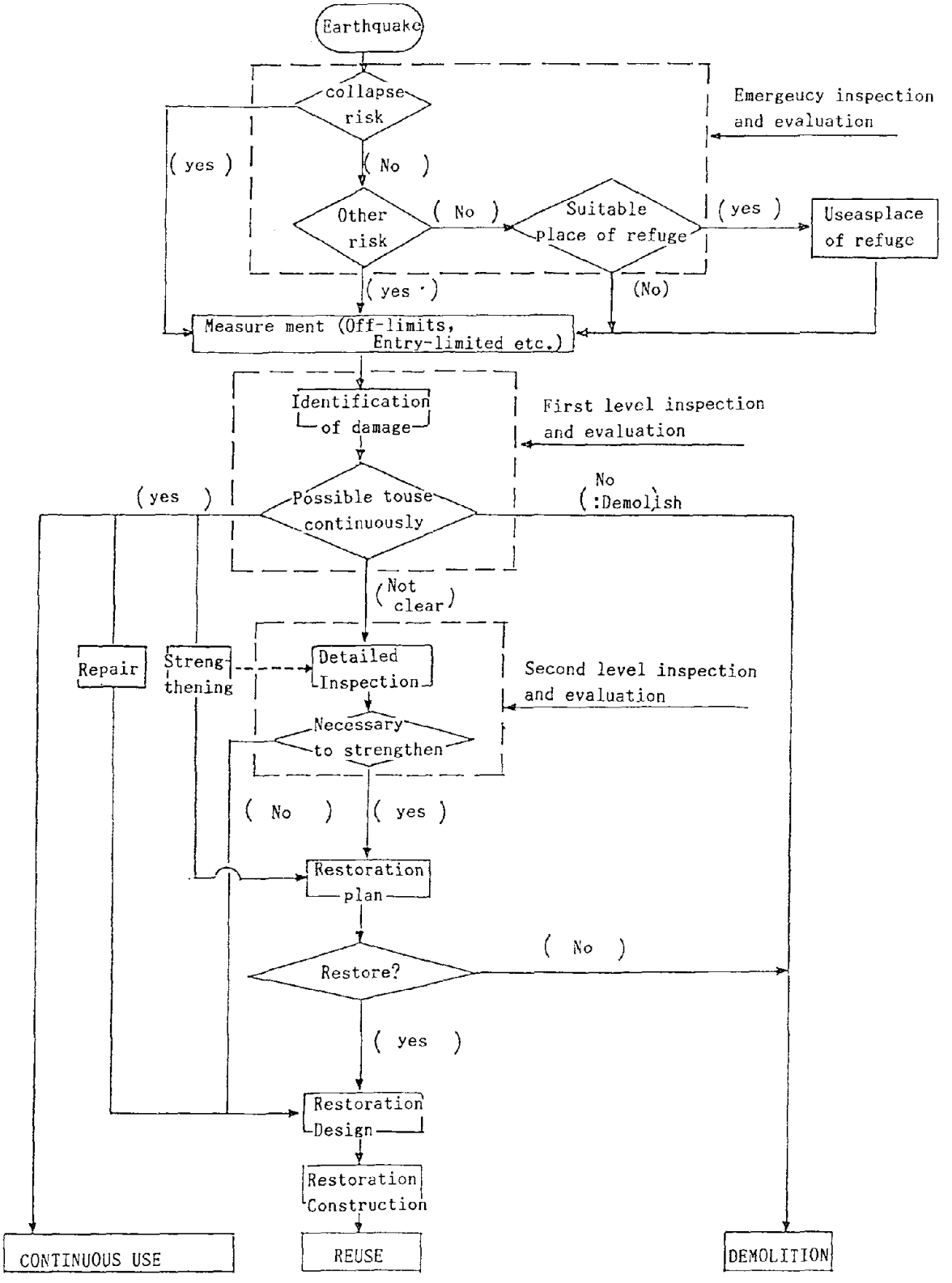

Fig.1.1 General Flowchart of Post Earthquake Inspection and Evaluation

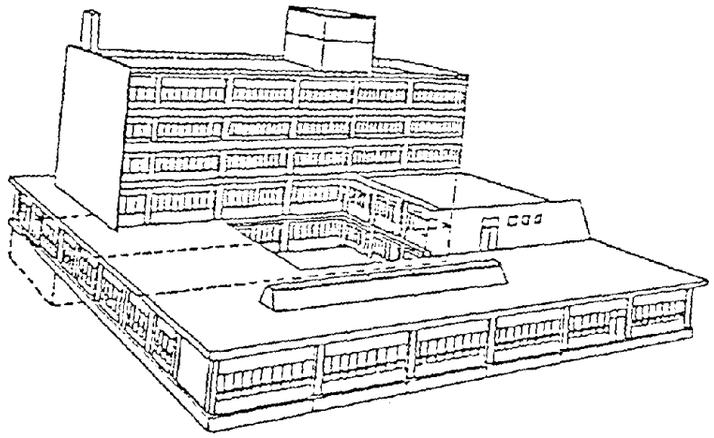

Fig.2.1 Perspective View of the Namioka Town Hospital Building

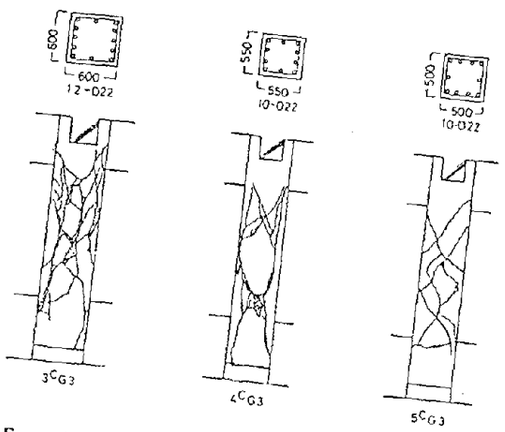

Fig.2.3 Examples of Detailed Crack Patterns of Columns

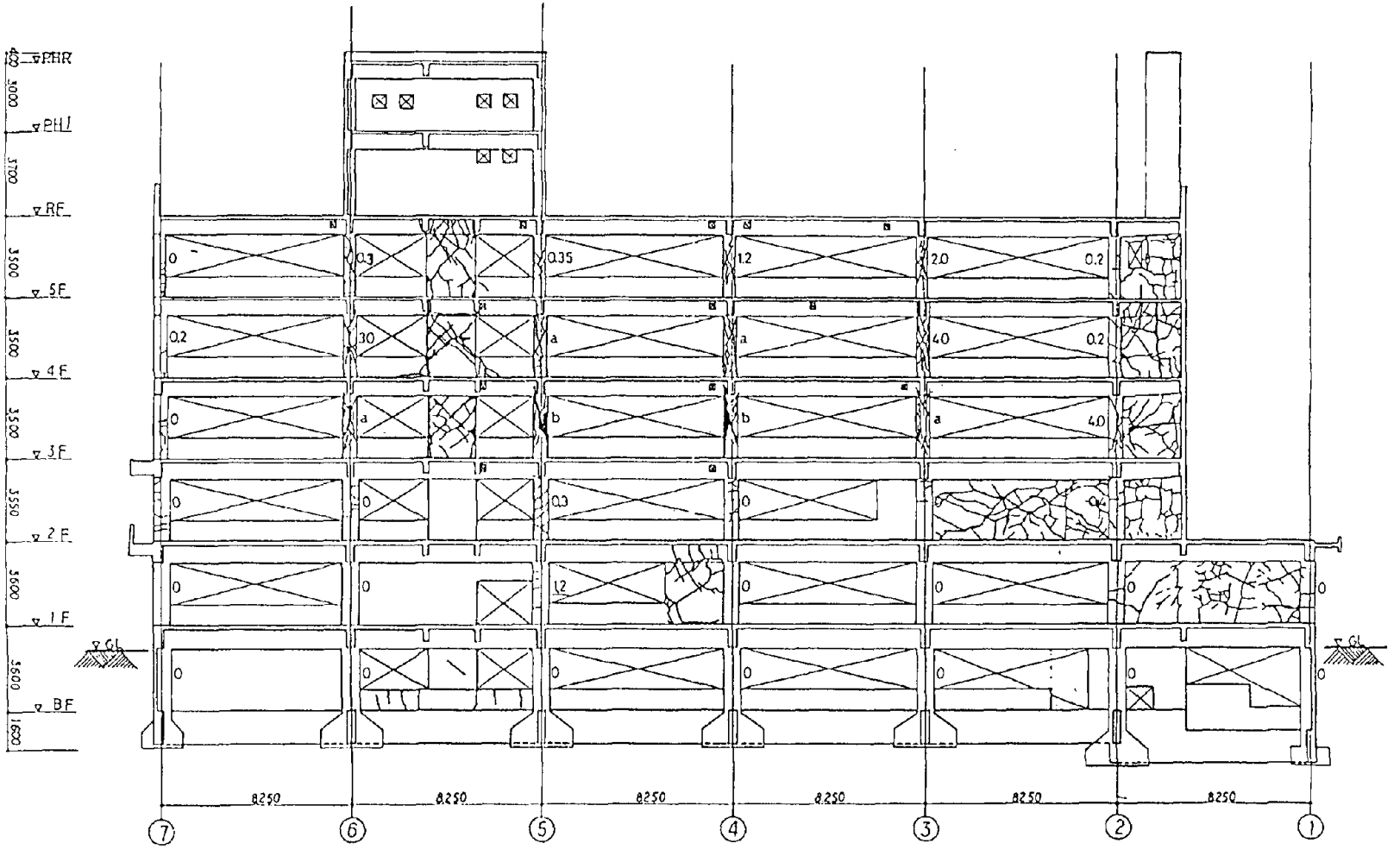

Fig.2.2 Crack Pattern of Exterior(J)-Frame
(Note:Crack Pattern of walls between ⑤and⑥ line at the floors below the second and that of the wall between ②and③ line at basement floor could not be inspected)

	Position	Streugthening Method and Number of Members Streugthened
Column	·Interior Columns of Exterior Frames (3~5th floor) ·Exterior Columns of Exterior Frames (3~5th floor) ·All Columns of Interior Frames (3~5th floor) ·Isolated Columns at 1st and 2nd floor	Replacing Canc 24 Wire-Mesh Reinforceng 48 Wrapping by steel angles and plate 10
Wall	·Hand I frames (B~5th floor) ·J frame (B~5th floor) ·2 through 7 frames(B~5th floor)	New Walls or Increase of Thickness 29 Replacing Walls Conc 12 New Walls or Increase of Thickness 32

*12 Boundary beams between new walls were reinforced by many stirrups

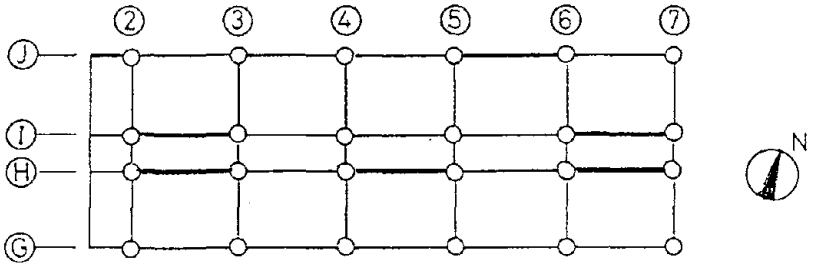

Fig.2.4 List of Adopted Strengthening ConstructionMethod and Key Plan Showing Location of Shear Walls newly Constructed

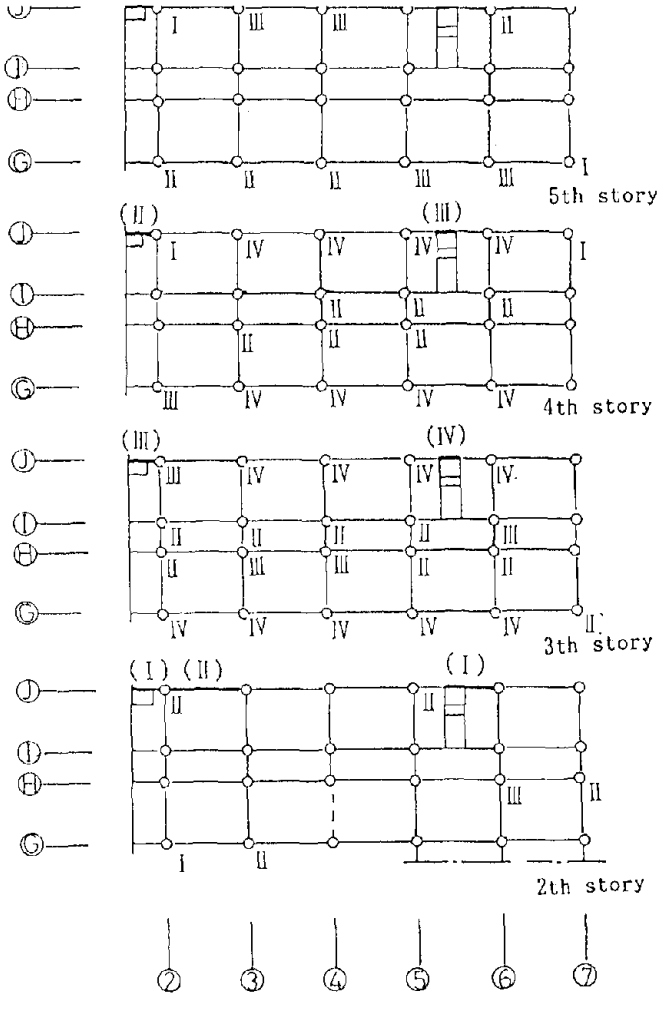

·Symboleo I through IV means damage rank of column.
·Symboleo(I)through(IV)means damage rank of wall.
·Damage of member without symbol is less than I (I).

Fig.2.5 Damage rank of columns and walls of each story

Table3.1 Identification of Damage of Each Story
by First Level Evaluation

Story		Damage Rank of Column												Identification of Damage
		0		I		II		III		IV		V		Total		
5	n *1	1	(13)	2	(2)	5	(5)	4	(4)	0	(0)	0	(0)	12	(24)	
	R *2	8	(53)	17	(8)	42	(21)	33	(17)					100		Moderate
	di *3	0	(0)	1	(0.5)	10	(5)	18	(10)	0	(0)	0	(0)	29	(15.5)	(Do)
4	n	1	(7)	2	(2)	0	(6)	1	(1)	8	(8)	0	(0)	12	(24)	
	R	8	(29)	17	(9)		(25)	8	(4)	66	(33)			100		Severe
	di	0	(9)	1	(0.5)	0	(5)	5	(3)	50	(32)	0	(0)	56	(40.5)	(Moderate)
3	n	1	(3)	0	(0)	1	(8)	1	(4)	9	(9)	0	(0)	12	(24)	
	R	8	(13)			8	(33)	8	(17)	75	(38)					Severe
	di	0	(0)	0	(0)	1	(8)	5	(10)	50	(36)	0	(0)	56	(54.0)	(Do)
2	n	0	(0)	1	(1)	3	(4)	0	(1)	0	(0)	0	(0)	12	(24)	
	R		(75)	8	(4)	25	(17)		(4)							Small
	di	0	(0)	0.5	(0.5)	5	(4)	0	(3)	0	(0)	0	(0)	5.5	(7.5)	(Do)
1	n	12	(25)	1	(1)	1	(2)	0	(0)	0	(0)	0	(0)	14	(28)	
	R	86	(81)	7	(4)	7	(7)							100		Slight
	di	0	(0)	0.5	(0.5)	1	(1)	0	(0)	0	(0)	0	(0)	1.5	(1.5)	(Do)

Note)*1 n:Number of columns classified into same rank

*2 $R = n/\Sigma n \times 100(\%)$

*3 di:Damage Rate(%)of column classified into same damage rank

*4 Values out of parenthesis show the result by exterior columns only and those with parenthesis show the result by all columns

Table3.3 Judgement for Necessity of Streugthening using the First and Secoud Level Seismic DiagnosisMethod (By Second Level Evaluation)

Story	Evaluation Level	Is	Is	Is/Is	ϕ (%)	Strengthening
5	1	0.183	0.163	0.89	11	Unnecessary
	2	0.265	0.233	0.88	12	do
4	1	0.140	0.094	0.67	33	Necessary
	2	0.231	0.145	0.63	37	do
3	1	0.145	0.078	0.54	46	Necessary
	2	0.243	0.112	0.46	54	do
2	1	0.243	0.234	0.97	3	Unnecessary
	2	0.273	0.262	0.96	4	do

Table3.2 Sahear coefficient (C) of Each Member and Those after Damage Calculated by the First Level Seismic Diagnosis Method

Story (W) *1	Damage Rank	Type of Member					ΣC, ΣC′
		C_B ($\tau=10$) *2	C_S ($\tau=10$)	W_1 (30) *2	W_2 (20) *2	W_3 (10) *2	
5 (1246)	0. I	12×50^2 (1.0. 0.241)	2×50^2 (1.0. 0.040)	—	3900 (1.0. 0.062)	—	ΣC= 0.062+0.039+ 0.7 (0.241+ 0.221) =0.424
	II	—	5×50^2 (0.8. 0.080)	—	—	4900 (0.9. 0.035)	
	III	—	4×50^2 (0.4. 0.032)	—	—	—	ΣC′=0.376
	Total (C. C′)	12×50^2 (0.241. 0.241)	11×50^2 (0.221. 0.152)	—	3900 (0.062. 0.062)	4900 (0.039. 0.039)	ΣC′/ΣC=0.89
4 (2100)	0. I	6×55^2 (1.0. 0.086)	2×55^2 (1.0. 0.029)	—	—	—	ΣC=0.291
	II	6×55 (1.0. 0.086)	—	—	3900 (0.9. 0.034)	—	ΣC′=0.195
	III	—	1×55^2 (0.4. 0.006)	—	—	4900 (0.6. 0.016)	
	IV	—	8×55^2 (0. 0)	—	—	—	ΣC′/ΣC=0.67
	Total (C. C′)	12×55^2 (0.172×0.172)	11×55^2 (0.158. 0.035)	—	3900 (0.039. 0.034)	4900 (0.023. 0.016)	
3 (2974)	0. I	2×60^2 (1.0. 0.024)	1×60^2 (1.0. 0.012)	—	—	—	ΣC=0.258
	II	7×60^2 (1.0. 0.085)	1×60^2 (0.8. 0.010)	—	—	—	ΣC′=0.144
	III	3×60^2 (0.6. 0.022)	—	—	7148 (0.5. 0.029)	—	
	IV	—	9×60^2 (0. 0)	—	—	7463 (0.3. 0.008)	ΣC′/ΣC=0.538
	Total (C. C′)	12×60^2 (0.145. 0.131)	11×60^2 (0.133. 0.022)	—	7148 (0.048. 0.029)	7463 (0.025. 0.008)	
2 (4258)	0. I	$9\times65^2-\pi\times(65/2)^2$ $+6\times50^2$ (1.0. 0.132)	7×65^2 (1.0. 0.070)	—	24960 (1.0. 0.117)	12720 (1.0. 0.030)	ΣC=0.393
	II	1×65^2 (1.0. 0.010)	3×65^2 (0.8. 0.024)	9900 (0.9. 0.063)	—	—	ΣC′=0.379
	III	1×65^2 (0.5. 0.006)	—	—	—	—	
	Total	$11\times65^2-\pi\times(65/2)^2$ $+6\times50^2$	10×65^2	9900	24960	12720	ΣC′/ΣC=0.965
	(C. C′)	(0.152. 0.148)	(0.099. 0.094)	(0.070. 0.063)	(0.117. 0.117)	(0.030. 0.030)	

Note)*1 W:Total weight inton from top floor to thefloor concerned.

*2 τ :Ultimate average shear stress in kg/cm² assumed for simplified calculationhere,W1,W2 and W3 mean Wall with sur rounding columns at both eud,wall with column at one eud and wall without sur rounding column,respectively.

*3 Total cross sectional area of columns (Acin cm²);or of walls(Aw in cm²)

*4 Two values within parenthesis mean coefficient to reduce seismic capa city, η ,and sheav coefficent,c,of each member

DENSE STRONG-MOTION EARTHQUAKE SEISMOMETER ARRAY AT SITES WITH DIFFERENT TOPOGRAPHIC AND GEOLOGIC CONDITIONS IN SERDAI

BY

Yoshikazu KITAGAWA, Toshihide KASHIMA

and Masaya HIROSAWA

ABSTRACT

Strong ground motions induced by an earthquake occurrence are known to be affected not only by the earthquake process itself, but by the propagating path of seismic topographies and properties of ground surface layers as well. These factors apparently influence the type of structural damages. In order to have reasonable aseismic standards, therefore, it is necessary to examine how each of those factors would contribute to the actual ground motions. Based on these circumstances, the dense seismometer array at various sites with difference topographic and geologic conditions was started in the 1983 fiscal year and has been constructed on a five-year plan in the Sendai area, the Northeastern part of Japan.

The array network is composed of eleven stations with spacing of approximately 3 to 4 km on the E-W line passing through the center of Sendai City. At each station, three observation points are arranged vertically, respectively, on the surface, at about 20 to 30 m underground, and in the structural base rock lying at a depth of about 50 m. A control and monitoring center is set up in the Building Research Institute (BRI) at Tsukuba via public telephone lines.

1. INTRODUCTION

Strong ground motion induced by an earthquake occurrence are known to be affected not only by the earthquake process itself, but by the propagating pass of seismic topographies and properties of ground surface layers as well. These factors apparently influece the type of structural damages. Therefore, many efforts, both theoretical and experimental, have been directed in clarifying the complex effects of surface soil-layers during earthquake ground motion. The advent of large-scale structures and important facilities since the 1960s has led to a remarkable increase in research with special reference to the underground earthquake observation. At the present time, more than 200 vertical arrays for earthquake engineering purposes exist in various places in Japan.

With rapid progress in the field of seismology and earthquake engineering, demand for observations of more highly qualified strong motion earthquake records is keenly requested on an international scale. Under these circumstances, the International Workshop on Strong Motion Earthquake Instrument Array was heldin Honolulu, Hawaii in 1978, sponsored by the International Association for Earthquake Engineering. As a goal of the workshop, the delegates approved a resolution on the immediate establishment of arrays which would be capable of resolving the nature of earthquake source mechanisms, wave propagations, and local site effects.

Around the same time, a national workshop for the deployment and observation of strong-motion seismometer arrays was organized, and the first ten-year plan was made. In May 1980, the Science Council of Japan adopted this plan and recommended the Prime Minister implement it immediately. National and private research projects on earthquake observation using seismometer arrays were put into practice in the 1981 fiscal year. Then the purposes of conducting observation were determined according to the interest of organizations carrying out those individual projects. Considering this circumstance, BRI began a project on earthquake observation by seismometer arrays, as a five-year plan, in the 1983 fiscal year.

The Sendai area has a wide variety of topography and geology, and many types and scales of structures exist. The Sendai area suffered severe damage from the 1978 Miyagi-Ken-Oki Earthquake (M=7.4), and various studies were performed to examine them.

In this report, the dense seismometer array, placed at various sites with different topographic and geologic conditions in the Sendai area, is briefly introduced. Particular attention is paid to the geological conditions in the Sendai area, the plan configuration, and system of seismometer array.

2. Outline of Geological Condition

2.1 Topographical Aspects-As for the geological conditions of surface soil, the Sendai district is generally classified into three areas as shown in Fig. 1: (1) the hilly tertiary terrane; (2) the terrace area; and (3) the alluvial plain. The oblique NE-SW line passing near the center of the map is called the Rifu-Nagamachi tectonic line.

The area west of the tectonic line is characterized by hilly tertiary terrain and several levels of terraces. The surface deposit of this terrace is loam, which is underlain by hard clay, gravels, pelite, and shale. The hilly terrain is either of very hard andesite or shale, but the surface is covered with loam at several places.

The alluvial plain develops east of the tectonic line and is composed mostly of sand, silt, and gravels. The depth of the tertiary base rock varies abruptly near this line. There are several areas in the plain which are covered by very soft peat or mud.

The values of shear-wave velocity at intervals of 0.5' in both latitude and longitude in the Sendai area are estimated from the soil profile, results of the penetration tests, and the geological conditions. The profile of shear-wave velocity on each section from line of N38°13'30" to N38°17' are shown in Fig. 3.

2.2 Microtremor Measurements - The microtremors are measured at several sites shown in Fig. 1, with the electromagnetic seismometer having the natural period of 1.0 sec in obtaining dynamic properties of soil layers. The area where the measurements were performed belongs to the two types of geological conditions, (2)

terrace area, and (3) alluvial plain, mentioned above.

The representative Fourier spectra of microtremors in the E-W and N-S directions are shown in Fig. 3, where sites G-06 through G-08, and sites G-17 and G-18 are on the outcrop of the terrace and on the alluvial plain, respectively. The peaks at long periods more than 1.0 sec reflect the deep ground characteristics, whereas the peaks at short periods less than 1.0 sec reflect the shallow ground ones.

2.3 Distribution of Dynamic Characteristics for Underground Structure - The structural base rock with shear-wave velocity of 700 m/s was set up to obtain the ground characteristics in the range of short periods less than 1.0 sec. The predominant period and magnification factor of the elastic media were calculated at an interval of 0.5 in both latitude and longitude by Haskell's Method.

The distribution maps for the predominant period and magnification factor of the underground structure above the structural base rock are shown in Figs. 4 and 5, respectively. As shown in these figures, the predominant period is around 0.2-0.3 sec in the terrace area and 0.3-0.8 sec in the alluvial plain. Similarly, the magnification factor is about 2-3 in the former and 3-5 in the latter.

3. ARRAY CONFIGURATION AND OBSERVATION SYSTEM

The Sendai area is designated as one of the ten high-priority sites in Japan for the deployment of strong motion seismometer arrays. The array network is composed of eleven stations with spacing of approximately 3 to 4 km on the E-W line passing through the center of Sendai City, and the N-S line passing through Nigatake and Oroshimachi, which suffered severe damages of structures in the 1978 Miyagi-Ken-Oki Earthquake. The layout of array configuration is shown in Fig. 6.

At each station, three observation points are arranged vertically; one on the surface, one at about 20-30 m underground with the shear-wave velocity of 300-400 m/s, and one in the structural base rock having the shear-wave velocity of 700 m/s and lying at a depth of 50-60 m. A control and monitoring center is set up in the BRI. The center is connected to a sub-center at Sendai, and the sub-center is further connected to each observation station via public and exclusive telephone lines. Figure 7 shows a block diagram of the dense strong motion seismometer array system. Figure 8 shows a plan and a section of the standard observatory.

The array observation system consists essentially of an accelerometer sensor, an amplifier, an A-D converter, a pre-event memory, a digital magnetic tape recorder, and a time-code generator. In order to obtain large dynamic range and high resolution in recording, a digital system is used. Specifications of the array observation system are as follows:

3.1 Accelerometer-Triaxial force-balance type is used. Recording and overall frequency ranges are ± 1G and 0.05 to 30 Hz.

3.2 Amplifier and A-D Converter (ADC)-16 bit ADC is used. The final dynamic range is 96 dB. The signals from the accelerometer are digitized AD and a sampling rate of 1/100 or 1/200 sec.

3.3 Pre-Event Memory-Delay device utilizing IC memory with 5 sec delay time is adopted.

3.4 Time-Code Generator-Quartz with an accuracy of 10^{-7} to 10^{-8} is used for tracking time. The absolute time is corrected automatically to the Japanese standard time within an error of ±5 m sec by receiving the time signal broadcasted by NHK (the Japanese Broadcasting Corporation).

3.5 Digital Date Recorder-Digital magnetic tape with 9 tracks, half-inch in width and 1600 BPI in recording density is used for the accelerograph of a signal set.

A telemetric monitoring device is used. The device transmits data, such as peak acceleration, triggered time, duration of recording, and the operating condition of the observation system. The control system enables one to calibrate the recording sensitivity and to adjust remotely the triggering level of the recording device at each station.

4. OBSERVATION STATION

The dense strong-motion earthquake seismometer array project was started in fiscal year 1983, for the purposes of studying the effect of geological and topological conditions of earthquake ground motions and establishing the standard earthquake motions for dynamic design criteria. Two observation stations have been installed respectively at Miyagino (MIYA station) and Nakano (NAKA station) primary schools. In addition to these stations, another station is scheduled to be installed in fiscal year 1985 at the Tamagawa secondary school (TAMA station).

4.1 MIYA Station-The station is located near the eastern part of the Rifu-Nagamachi tectonic line shown in Fig. 6. Locations of the seismometers and observatory are shown in Fig. 9. Photo 1 shows overviews of the observatory. The soil profile and the result of seismic prospecting tests are shown in Fig. 10. As seen in this figure, the underground structure is classified into eight soil layers in P- and S-wave velocities. Three seismometers are placed along the vertical line at depths of 1 m, 22 m, and 55 m below the ground level.

The transfer function (U_O/U_{IN}), defined as the ratio of the wave on the ground surface, U_O, to the incident wave, U_{IN}, for the underground structure at the observation site is shown in Fig. 16.

4.2 NAKA Station-As shown in Fig. 6, the station is located at the far eastern part of the Rifu-Nagamachi tectonic line, which is the alluvial plain near the lower reaches of the Nanakitada River and the Sendai Bay. The locations of the seismometers and observatory are shown in Fig. 12. Photo 3 shows overviews of the observatory. The soil profile and the resulting seismic prospecting test are shown in Fig. 13. As seen in this figure, the un-

derground structure is classified into 6 and 9 soil layers in P- and S-wave velocity, respectively. Three seismometers were placed along the vertical line at depths of 1 m, 29.5 m, and 61 m below the ground level. The transfer function (U_O/U_{IN}) is shown in Fig. 14.

5. EXAMPLE OF EARTHQUAKE RECORD

Operation of the MIYA station was initiated in March 1984. A total of four earthquakes have been observed. As an example, the E-W and N-S components of the acceleration records, during the Southeast--Off Boso Peninsula Earthquake of September 1984 (Date and Time: 02.03 a.m., September 19, 1984, Magnitude=6.8, Epicenter: Lat. 33°56'N, long. 141°51'E, Focal depth: 46 km) are shown in Fig. 15. As seen in this figure, the maximum values of accelerations at the ground level are 7.7 gal and 7.2 gal in the E-W and N-S directions, respectively. The magnification factors of the surface maximum acceleration relative to that observed 54 m below the ground level are 1.7 times in the E-W and N-S directions.

The Fourier spectra of the accelerograms are shown in Fig. 16. Figs. 16 and 17 show the spectral ratio and the phase lag between the surface and underground layer 54 m below the ground level. Judging from these figures, the predominant frequency of the soil layers is around 2 Hz and 7 Hz. These values correspond to the values in the transfer function shown in Fig. 11.

6. CONCLUSIONS

The dense seismometer array at various sites with different topographic and geological conditions is briefly introduced in this paper. The numer of observation sites has increased year by year, and high-quality array data will be accummulated in the near future. In relation to the increase of data, dissemination of the data is necessary for cooperation and coordination between the earthquake observations under individual projects. Because of this, establishment of a national data bank system to aid in exchange is hoped for in the near future.

7. ACKNOWLEDGMENTS

The dense strong-motion earthquake seismometer array observation is implemented by a work group in the Subcommittee of Earthquake Observation in and around buildings organized in BRI. Members of the working group for the array observation are Y. Kitagawa, Head of Structural Dynamics Div.; Y. Yamazaki, Head of Large-Scale Structural Testing Div.; H. Mizuno, Senior Research Staff of IISEE; T. Okawa, Research Staff of IISEE; and T. Kashima, Assistant Research Staff of Structural Dyanmics Div. In order to discuss the array observation plan, the committee of dense strong-motion earthquake seismometer array (Chairman: Y. Osawa, Professor of Toyko University) is organized in KKSK. The authors wish to express their sincere thanks to members of the committee, working group, and persons concerned.

8. REFERENCES

(1) Kitagawa, Y., and Tanaka, T., Observation of Underground Earthquake Motions in Japan, Some Recent Earthquake Engineering and Practice in Japan: Japanese Nat. Comm. of IAEE, pp. 14-26, 1980

(2) Tanaka, T., and Kitagawa, Y., Strong Motion Earthquake Seismometer Arrays in Japan, Some Recent Earthquake Engineering and Practice in Japan: Japanese Nat. Comm. of IAEE, pp. 17-31, 1984

(3) Report on the Damage by 1978 Off-Miyagi Prefecture Earthquake (in Japanese): Report of BRI, No. 86, pp. 75-81, 1979

(4) Kitagawa, Y., and Matsushima, Y., Evaluation of Dynamic Ground Characteristics and Seismic Microzoning: Proc. of Third South Pacific Regional Conference on Earthquake Engineering, New Zealand, pp. 73-84, 1983

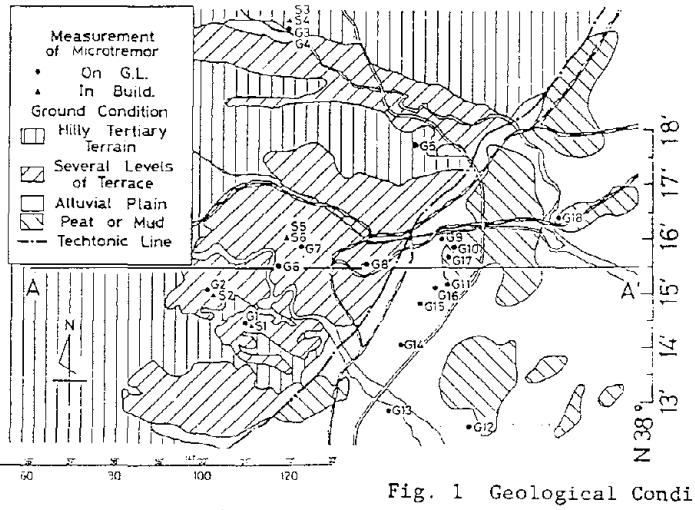

Fig. 1 Geological Condition

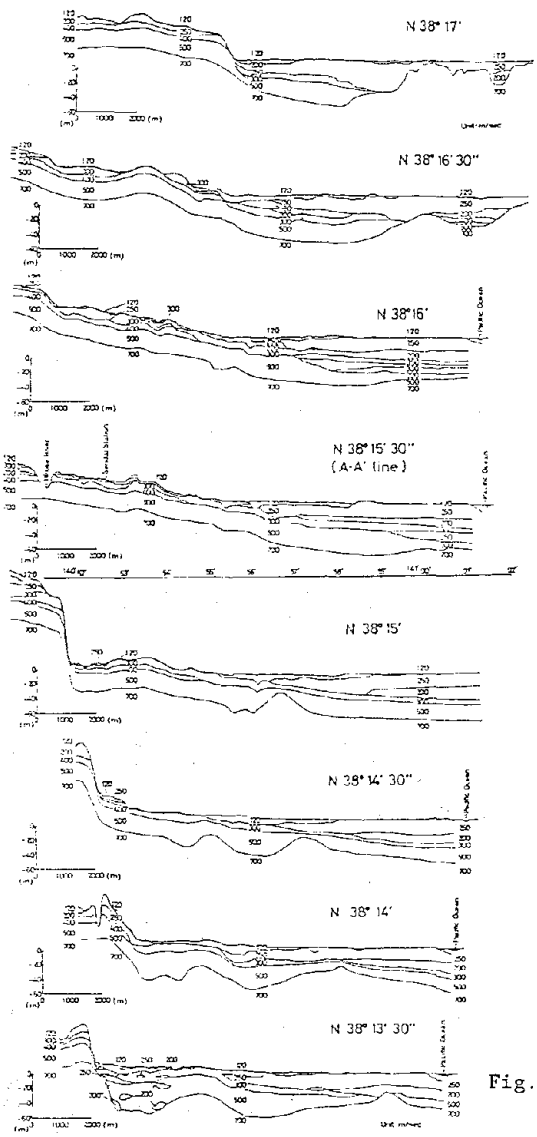

Fig. 2 Profile of Shear Wave Velocity

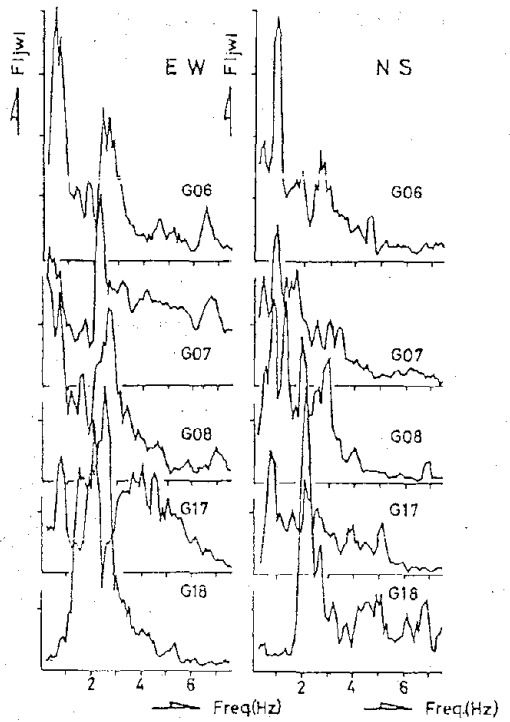

Fig. 3 Fourier Spectra of Microtremors

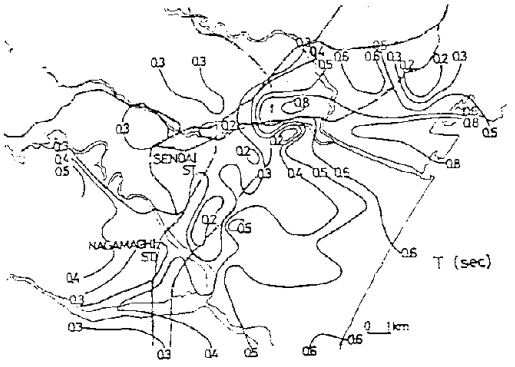

Fig. 4 Distribution Map of Predominant Period

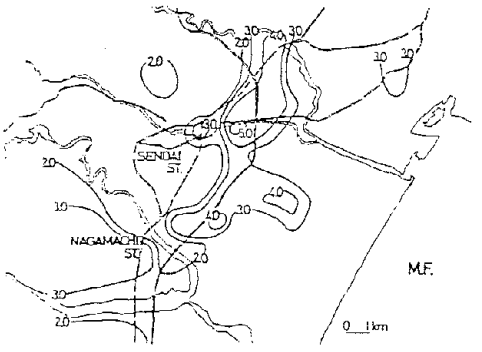

Fig. 5 Distribution Map of Magnification Factor

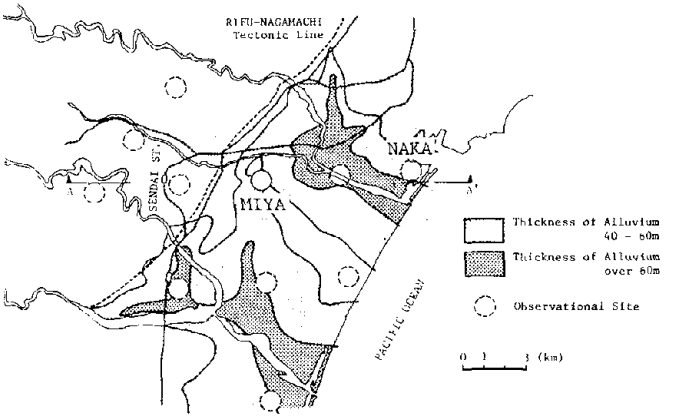

Fig. 6 Layout of Array Configuration in Sendai Area

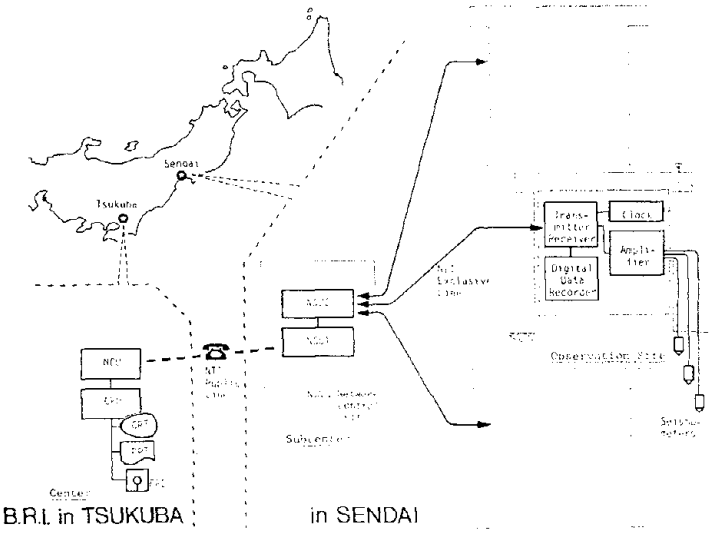

Fig. 7 Block Diagram of Dense Array Observation System

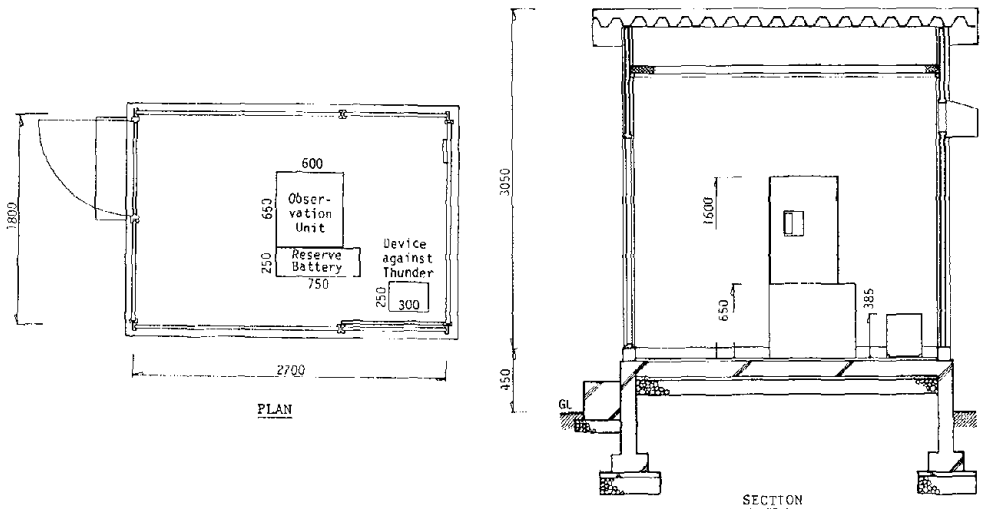

Fig. 8 Plan and Section of Standard Observatory

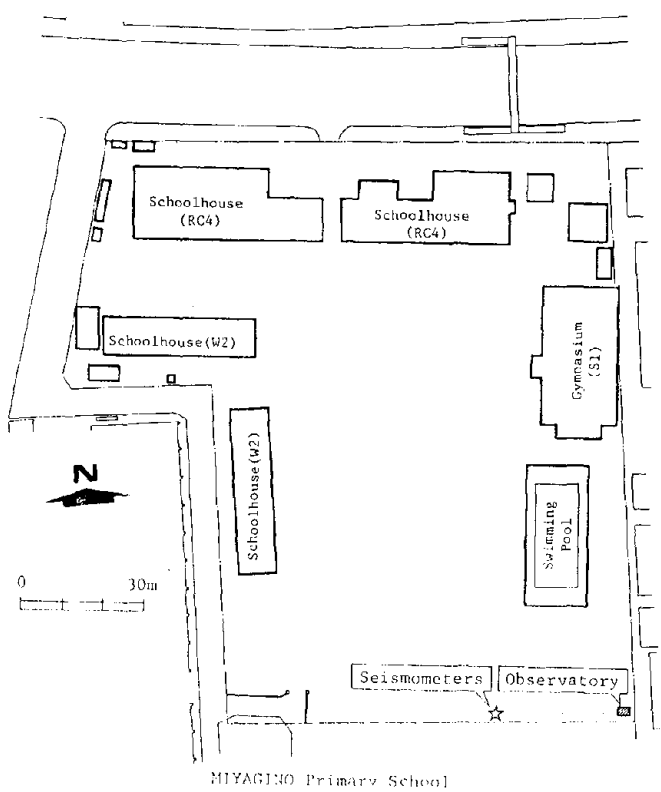

Fig. 9 Location of Seismometers and Observatory at MIYA Station

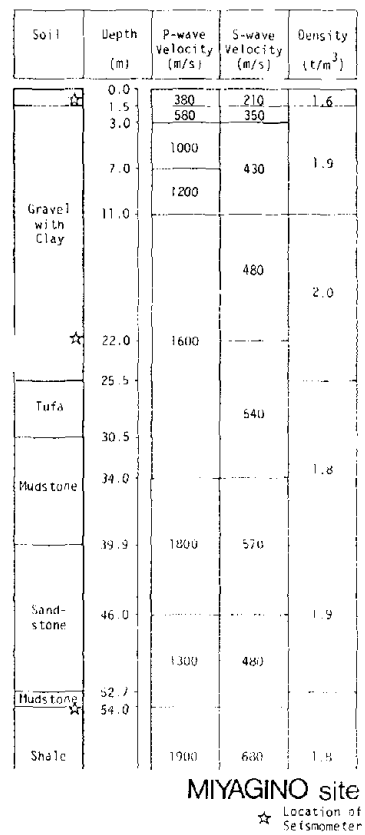

Fig. 10 Soil Profile at MIYA Station

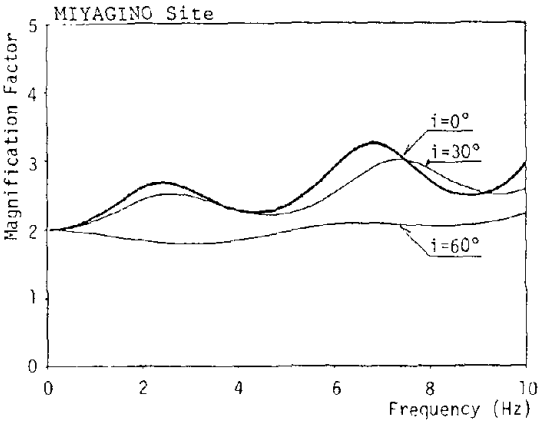

Fig. 11 Transfer Function of Soil-layers at MIYA Station

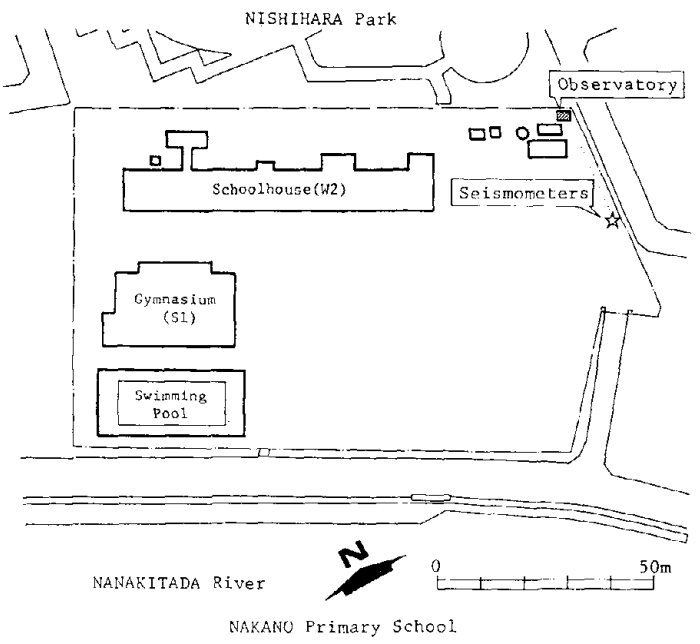

Fig. 12 Location of Seismometers and Observatory at NAKA Station

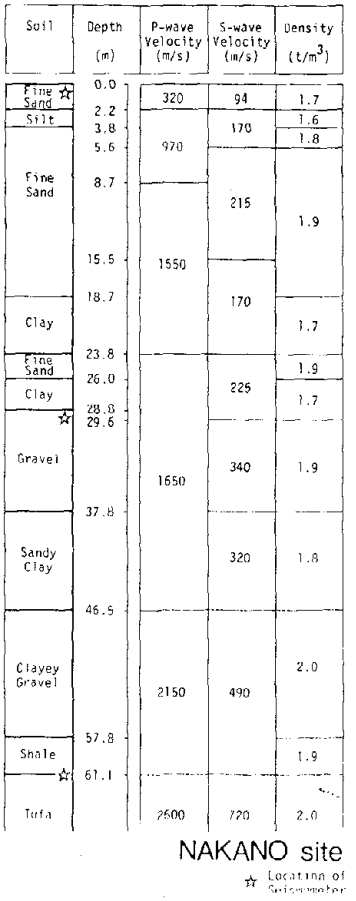

Fig. 13 Soil Profile at NAKA Station

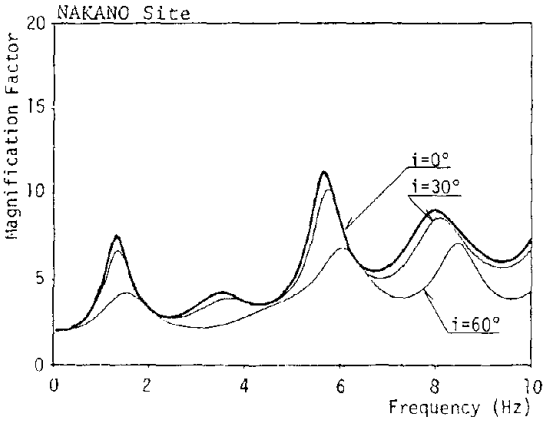

Fig. 14 Transfer Function of Soil-layers at NAKA Station

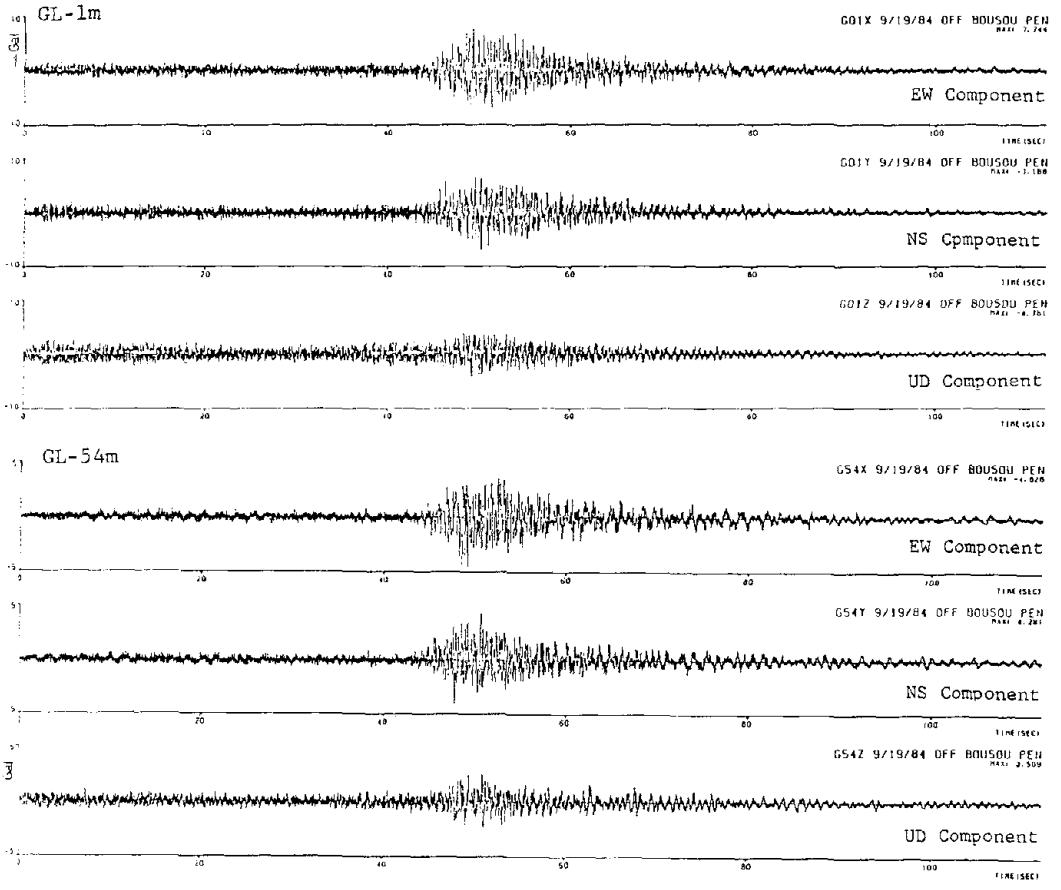

Fig. 15 Accelerograms at GL and GL-54m

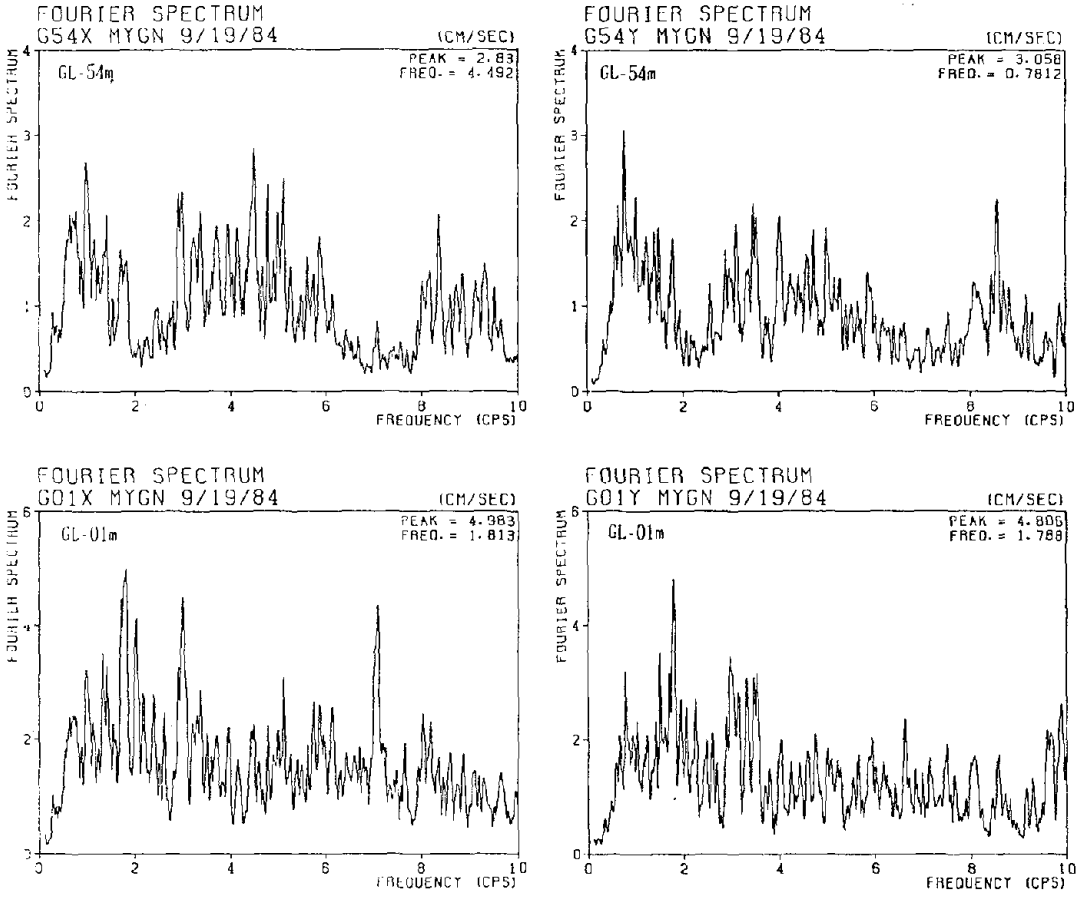

(a) EW Component (b) NS Component

Fig. 16 Fourier Spectra of Accelerograms

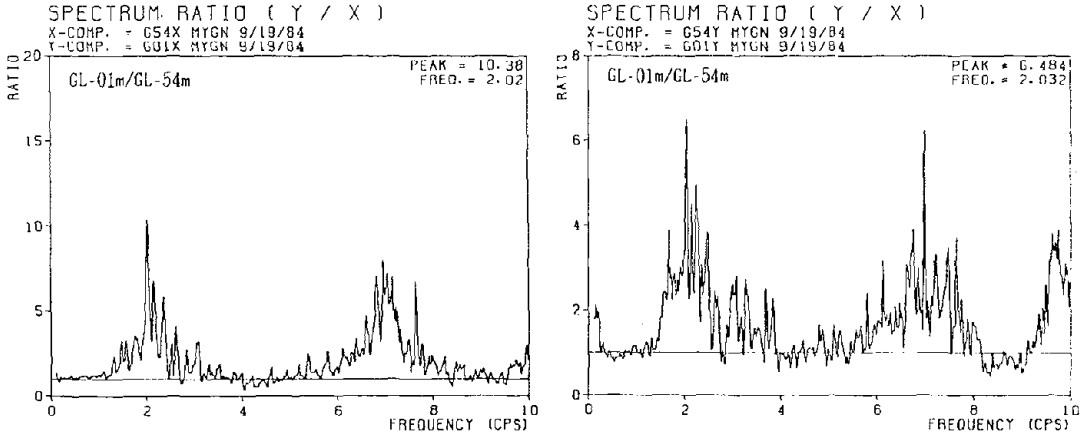

(a) EW Component (b) NS Component

Fig. 17 Fourier Spectral Ratio between GL and GL-54m

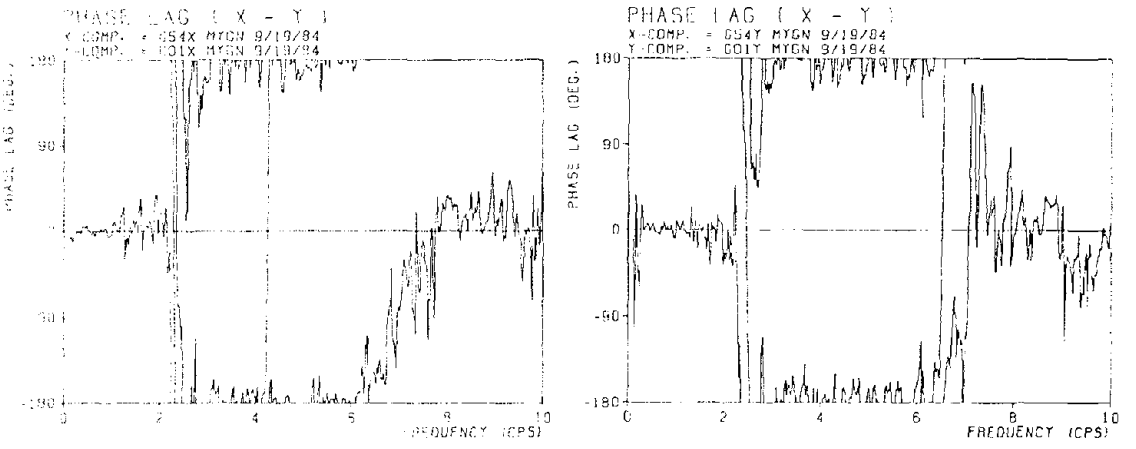

(a) EW Component (b) NS Component

Fig. 18 Phase Lag between GL and GL-54m

Photo 1 Overviews of Observatory at MIYA Station

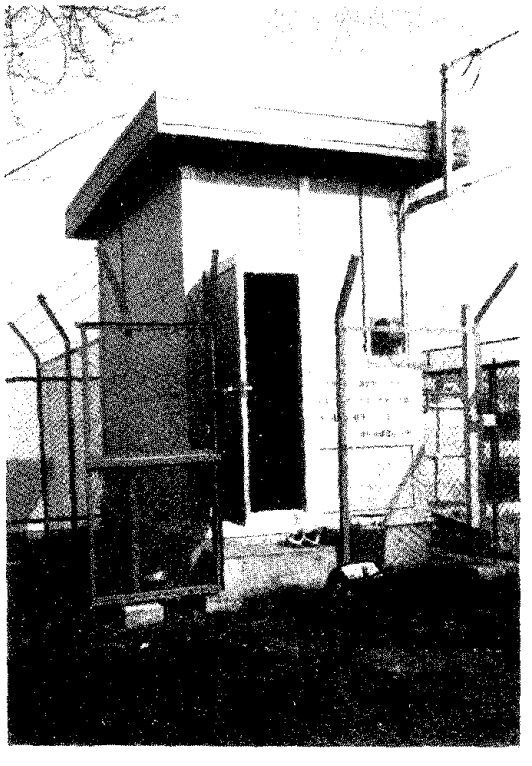

Photo 2 Overviews of Observatory at NAKA Station

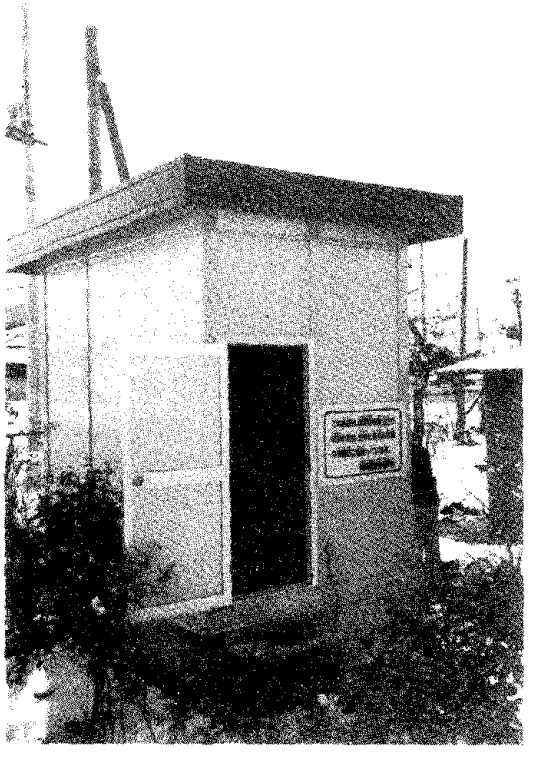

INFLUENCE OF SOIL CONDITIONS UPON RESPONSE SPECTRUM OF STRONG GROUND MOTION

BY

Izuru OHKAWA*

Yuji ISHIYAMA*

ABSTRACT

The intensity of the earthquake ground motion is often expressed in terms of some parameters such as maximum acceleration, maximum velocity and response spectra. These characteristic values are generally a function of eathquake magnitude, epicentral distance, hypocentral distance, and the soil conditions of the sites where the earthquake ground motions are observed.

In this paper, the response spectra are related with especially the soil conditions, i.e., stiffness of soil deposits etc., and the magnitude and the distance from the fault.

Keywords: Earthquakes; Response spectrum; Soil conditions; Strong ground motion

1. INTRODUCTION

The maximum amplitudes and the response spectra have been related with eathquake magnitude and the distance from the fault. These relationships ever presented are originated from the definition of the earthquake magnitude. In Japan, Kanai (1968) presented the following semi-empirical relationship to provide the maximum acceleration and maximum velocity amplitudes at so-called seismic base layer as,

$$A_{max}=\frac{1}{T}\,10^{0.61M-(0.66=3.60/X)\log(X)+(0.167-1.83/X)}$$

$$V_{max}=10^{0.61M-(0.66=3.60?X)\log(X)-(0.631+1.83/X)}$$

where,

A_{max} : maximum acceleration in cm/sec^2

A_{max} : maximum velocity in cm/sec

T : fundamental period of the ground in second

M : earthquake magnitude

X : hypocentral distance in kilometer

Ohsaki and Watabe(1977) performed the regression analysis by using the accelerograms recorded on hard ground and presented the following equation.

$$A_{max}=10^{0.472M-(1.97+1.80/X)\log(X)+(2.20-11.1/X)}$$

Many other researchers proposed so-called attenation formulae of maximum amplitudes of strong earthquake motions, Ohsaki et al (1980), at first, classified the records according to the shear wave velocities at observation site into the regression analysis for records of each group. They presented the formulae to obtain the maximum velocity.

$V_{max} = 10^{0.54M-1.31\log(X)-0.95}$ for soft rock

$V_{max} = 10^{0.65M-1.36\log(X)-2.00}$ for hard rock

Watabe and Tohdo (1981) obtained the formulae for maximum acceleration and maximum velocity, using the records observed on hard rock with shear wave velocity greater than 0.6 km/sec.

$$A_{max} = 10^{0.44M-1.38\log(X)+1.04}$$

$$V_{max} = 10^{0.607M-1.19\log(X)-1.40}$$

P.W.R.I. (1983) presented the equations to give the maximum amplitudes by analyzing with many cases of mathematical models involving the soil conditions. For example,

$A_{max}=1073\ 10^{0.221M}$

$(\Delta+30)^{-1.251}$ for stiffer soil

$A_{max}=227.3\ 10^{0.308M}(\Delta+30)^{-1.201}$ for med. soil

$A_{max}=403.1\ 10^{0.262M}(\Delta+30)^{-1.208}$ for soft soil

where, Δ : epicentral distance in kilometer

As for response spectra, the equations with

*International Institute of Seismology and Earthquake Engineering, Building Research Institute, Ibaraki Prefecture, 305, JAPAN

the coefficients of same types except being functions of period T are assumed are obtained by the regression analyses.

Kobayashi and Nagahashi (1976) presented the average response spectra at the seismic base layer the shear wave velocity of which is larger than 3.0 km/sec by using the accelrograms observed at the ground surface. They adopted the equation of the following type.

$$Sv_o(T) = 10^{a(T)M - b(T)\log(X) - c(T)}$$

Hisada et al.(1978) presented the design spectra for stiff structures such as nuclear power reactor buildings. The shear wave velocities of the ground to which this spectra can be applied are greater than 0.7 km/sec.

Thereafter, many researchers are concerned about the influence of soil (rock) conditions upon the response spectra of earthquake ground motion.

Ohsaki et al.(1980) reported the results that the velocity response spectra of the records on hard rock sites (Vs greater than 1.0 km/sec) are about half of those on soft rock sites (Vs less than 1.0 km/sec).

Ohta et al.(1982) presented the similar results that the response spectra for hard rock are similar than those for soft rock, from the regression analyses considering the site effects.

P.W.R.I.(1983) presented the equations to give the acceleration response spectra with many cases of mathematical models involving the soil conditions of observation site.

2. COMPARISON OF RESPONSE SPECTRA OF DIFFERENT SOIL CONDITIONS

Two types of analyses are performed in this part. One is based on the analyses of the accelerograms which are classified into three groups according to the soil conditions in advance. The other is based on the analyses with dealing those data in the gross applying the model involving the effect of soil conditions in the equation.

2.1 Analysis I

The earthquake records are classified into three groups according to the shear wave velocity Vs of the soil layer of the observation sites. The classifications are made as (1) Soft: Vs less than 0.75 km/sec, (2) Hard: Vs greater than 1.5 km/sec. The numbers of available accelerograms classified into these groups are 30, 18 and 60 for Soft, Hard and HH, respectively.

Then, the following equation is used to express the average response spectra for each group at each natural period.

$$pSv(T) = 10^{a(T)M - b(T)\log(X) - c(T)}$$

where,

pSv : pseudo velocity response spectrum in cm/sec

M : earthquake magnitude (JMA)

X : hypocentral distance in kilometer

a,b,c: coefficients determined by regression analyses

T : natural period of SDOF system in second

The accelerograms are classified as summarized in Table 1. In that table, magnitude, epicentral distance, focal depth and shear wave velocity are also described. In Fig. 1 the distribution of the data with respect to earthquake magnitude and epicentral distance is shown. It should be noted here again that number of data of each classification and the distribution of magnitude and distance are different.

Fig. 2 shows the coefficients a(T), and b(T) and c(T) in the above equation derived from the Soft data using the least square method. Fig. 3 and Fig. 4 also show those coefficients derived from the Hard and HH rock data, respectively. From those figures, the coefficient a(T) the multiplier of magnitude takes a value from 0.4 to 0.8 and is larger at the longer period. The coefficients b(T) and c(T), the multiplier of the hypocentral distance and the constant, respectively, have the maximum and minimum. Using these coefficients

we plotted the response spectra corresponding to the magnitudes 6 and 7, the hypocentral distance 100 and 200 km in Fig. 5(a) - 5(d). In each figure, the calculated spectra for Soft, Hard and HH soils are plotted for the quantitative comparison.

From these figures, it is seen that the spectral values are smaller, when the soil becomes stiffer.

When we compute the ratio of the spectra to those for Soft rock and plot the ratio in Fig. 6, the ratio of the Hard rock to the Soft rock varies from 0.5 to 1.0, whereas the ratio of the HH rock to the Soft rock varies from 0.2 to 0.6.

2.2 Analysis II

The shear wave velocity of each observation site is known, then we can make the shear wave velocity represent the soil condition. In this case of analysis, the accelerograms are not classified. The mathematical model of the empirical formula we adopted herein is as follows:

$$pSv(T) = 10^{a(T)M-b(T)\log(X)-c(T)\log(Vs)-d(T)}$$

where,

A,b,c,d: coefficients determined by the regression analyses. It should be noted that c(T) has different meaning from the obprevious analysis.

Vs: shear wave velocity at the observation site in km/sec, other parameters are same as used in the Analysis I.

The regression analyses are applied to the model by using whole data in Table 1. The coefficients a(T), b(T), c(T) and d(T) thus obtained are shown in Fig. 7. The coefficient a(T) shows a similar feature with that obtained in Analysis I. However, coefficients b(T) and constant term d(T) are changing, because of the introduction of the Vs term.

Using these coefficients, we plotted the average response spectra of magnitudes 6 and 7, hypocentral distances 100 and 200 km, in Fig. 8(a) - 8 (d). It is apparent from the above equation that the ratio of the spectral values between the different shear wave velocities depends on the coefficient c(T), when the magnitude and distance are same. Fig. 9 shows the ratios of the spectra of those for Vs-1.0 km/sec and 1.5 km/sec to that for Vs-0.7 km/sec. From this figure, when the shear wave velocity of the ground is 1.5 km/sec Vs, the spectral ratio becomes 0.3 to 0.5

3. DISCUSSIONS AND CONCLUSIONS

From the Analysis I and Analysis II, it can be generally said that the spectral values are reduced when the shear wave velocity of the ground becomes higher. Though the spectral value for Hard rock partly exceeds that for Soft rock, this may be due to the shortcomings of the records to be used, as is mentioned before. The feature of the Analysis II is the introduction of Vs term into the equation. The ambiguous expression such as "soft" or "hard" which is frequently used in the past research works is inconvenient for the practical applications. But the authors are not fully convinced of the results. There are many problems to be solved, i.e., the analyses by using more number of data, and the theoretical explanation of the property, etc.

4. REFERENCES

1. Kanai,K.,Suzuki,T.(1968),"Expectancy of the maximum velocity amplitude of earthquake motions at bed rock," B.E.R.I., Vol. 46

2. Ohsaki,Y.,Watabe,M.(1977),"On the peak values of earthquake ground motions," Proc. of Annual Meeting of A.I.J.

3. Ohsaki,Y.,Sawada,Y. et al.(1980), "Spectral Characteristics of Hard Rock Motions," Proc. of 7th W.C.E.E., Istanbul, Turkey

4. Watabe,M.,Tohdo, M.(1981), "Research on the design earthquake ground motions," Transactions of A.I.J., Vol. 303

5. P.W.R.I. (1983), "Estimation of peak ground motions and response spectra," Research Material, P.W.R.I., Vol. 1993

6. Kobayashi,H.,Nagahashi,S.(1976),"Amplification characteristics of the ground and spectral characteristics of earthquake motions on

the seismic bedrock inferred from spectral characteristics of earthquake motions observed on the ground surface," Traus. of A.I.J., Vol. 240

7. Hisada,T. et al.(1978),"Design spectra for stiff structures on rock," Proc. of 2nd Micro zonation Conference, Vol. 3

8. Ohta,T. et al.(1982),"Characteristics of peak acceleration and response spectra for observed records at hard and soft rock sites," Proc. of 6th J.E.E.S.

Table 1 Earthquake Records Used in This Study

Soft Rock

NO.	NAME	M	DEP. (km)	DIS. (km)	Vs (km/sec)
1	C1-1-2	4.9	0	145	0.60
2	C1-2-2	4.7	20	170	0.60
3	C1-3-2	4.4	60	100	0.60
4	C1-4-2	4.4	40	120	0.60
5	C1-5-2	4.2	40	85	0.60
6	C1-6-1	5.8	80	270	0.60
7	C1-7-1	4.7	50	50	0.60
8	C1-8-1	6.2	40	180	0.60
9	C1-9-1	6.0	50	145	0.60
10	C1-10-1	7.0	60	475	0.60
11	C1-11-1	7.0	70	460	0.60
12	C1-12-1	5.3	50	50	0.60
13	C1-13-1	7.2	50	460	0.60
14	C1-14-1	5.3	50	60	0.60
15	C1-15-1	6.3	40	110	0.60
16	C1-16-1	5.9	30	80	0.60
17	C2-1-1	5.4	10	90	0.60
18	C2-2-1	5.5	40	155	0.60
19	C2-3-1	6.0	50	150	0.60
20	C2-4-1	4.1	50	35	0.60
21	C2-5-1	5.5	40	55	0.60
22	C2-6-1	6.3	50	320	0.60
23	C2-7-1	5.3	50	50	0.60
24	C2-8-1	6.3	40	100	0.60
25	C2-9-1	5.9	30	85	0.60
26	C4-1-1	7.2	50	245	0.75
27	C4-1-2	7.2	50	245	0.75
28	C4-2-1	6.9	10	110	0.75
29	C4-2-2	6.9	10	110	0.75
30	C5-1-1	6.9	10	120	0.55

Hard Rock

NO.	NAME	M	DEP. (km)	DIS. (km)	Vs (km/sec)
1	D1-1-2	6.6	0	160	1.00
2	D1-2-1	5.5	30	40	1.00
3	D1-2-2	5.5	30	40	1.00
4	D1-3-1	6.9	10	60	1.00
5	D1-3-2	6.9	10	60	1.00
6	A1-2-2	7.0	60	330	1.30
7	A1-3-1	6.4	80	270	1.30
8	A1-3-2	6.4	80	270	1.30
9	A1-4-1	5.4	60	240	1.30
10	A1-4-2	5.4	60	240	1.30
11	A1-5-1	7.4	40	440	1.30
12	A1-5-2	7.4	40	440	1.30
13	A1-6-1	7.1	40	505	1.30
14	A1-6-2	7.1	40	505	1.30
15	A1-7-1	6.6	30	500	1.30
16	A1-7-2	6.6	30	500	1.30
17	A1-8-1	6.5	100	120	1.30
18	A1-8-2	6.5	100	120	1.30

HH (Hard-Hard) Rock

NO.	NAME	M	DEP. (km)	DIS. (km)	Vs (km/sec)
1	G2-2-2	5.3	10	51	1.50
2	G2-3-1	4.6	20	220	1.50
3	G2-3-2	4.6	20	220	1.50
4	G2-4-1	4.3	10	80	1.50
5	G2-4-2	4.3	10	80	1.50
6	G2-5-2	6.1	10	52	1.50
7	G2-6-2	5.5	10	55	1.50
8	G2-9-1	4.0	0	56	1.50
9	G2-9-2	4.0	0	56	1.50
10	T1-2-1	3.9	10	28	1.50
11	T1-2-2	3.9	10	28	1.50
12	T1-4-1	5.1	10	51	1.50
13	T1-5-1	5.1	10	94	1.50
14	T1-6-1	4.7	0	112	1.50
15	T1-7-1	6.1	10	137	1.50
16	T1-7-2	6.1	10	137	1.50
17	N1-1-1	6.1	10	67	2.00
18	N1-1-2	6.1	10	67	2.00
19	C6-1-1	4.7	10	8	2.00
20	C6-2-1	4.4	0	6	2.00
21	C6-2-2	4.4	0	6	2.00
22	C6-3-1	5.0	0	8	2.00
23	C6-3-2	5.0	0	8	2.00
24	C6-4-1	6.6	0	70	2.00
25	C6-4-2	6.6	0	70	2.00
26	C6-5-1	4.0	0	8	2.00
27	C6-6-1	6.0	10	90	2.00
28	C6-6-2	6.0	10	90	2.00
29	E1-1-1	5.1	0	85	1.50
30	E1-1-2	5.1	0	85	1.50
31	E1-2-1	4.5	20	90	1.50
32	E1-2-2	4.5	20	90	1.50
33	E1-3-1	5.5	0	145	1.50
34	E1-3-2	5.5	0	145	1.50
35	E1-4-1	4.0	0	56	1.50
36	E1-4-2	4.0	0	56	1.50
37	F1-1-1	6.6	0	145	2.20
38	G1-1-1	4.2	0	50	1.80
39	G1-2-2	5.1	10	45	1.80
40	K1-1-2	6.6	0	95	1.60
41	P1-2-1	5.1	5.8	24.5	1.50
42	P1-2-2	5.1	5.8	24.5	1.50
43	P1-3-1	4.3	18.3	21.5	1.50
44	P1-3-2	4.3	18.3	21.5	1.50
45	P1-4-1	5.8	8.0	26	1.50
46	P1-4-2	5.8	8.0	26	1.50
47	P1-5-1	5.4	8.3	27.2	1.50
48	P1-5-2	5.4	8.3	27.2	1.50
49	P1-6-1	4.7	9.4	24.7	1.50
50	P1-6-2	4.7	9.4	24.7	1.50
51	Q1-1-1	4.9	13.9	33.2	1.50
52	Q1-1-2	4.9	13.9	33.2	1.50
53	Q1-5-1	4.0	10.6	15.6	1.50
54	Q1-5-2	4.0	10.6	15.6	1.50
55	Q1-8-1	4.3	9.0	10.2	1.50
56	Q1-8-2	4.3	9.0	10.2	1.50
57	Q1-9-1	4.1	8.7	3.5	1.50
58	Q1-9-2	4.1	8.7	3.5	1.50
59	Q1-10-1	4.2	5.0	33.3	1.50
60	Q1-10-2	4.2	5.0	33.3	1.50

M : magnitude, DEP. : focal depth, DIS. : epicentral distance, Vs : shear wave velocity

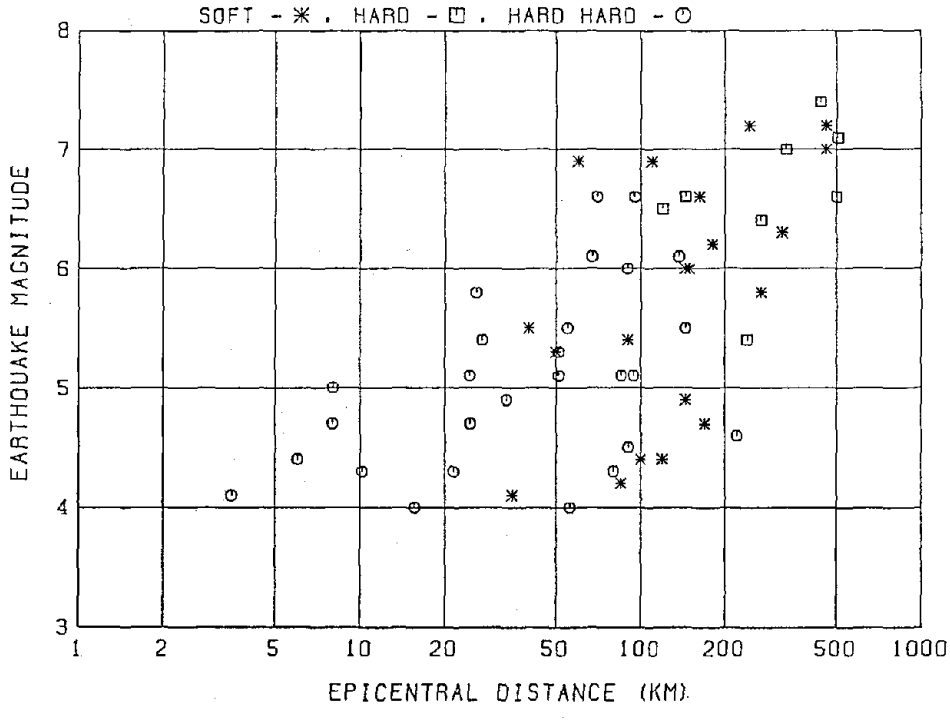

Fig. 1 Distribution of Earthquake Records

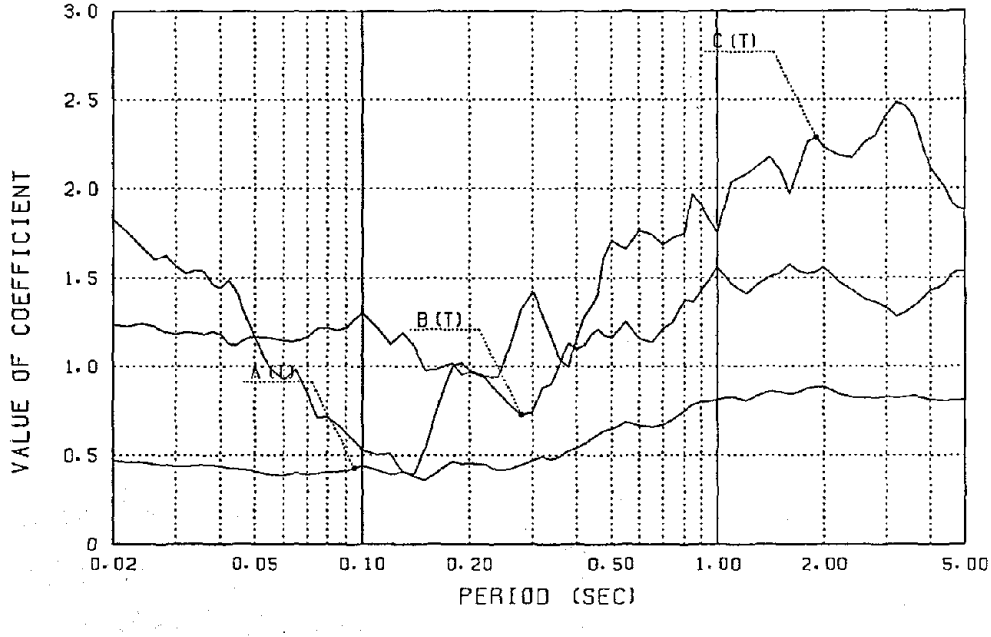

Fig. 2 Coefficients a(T), b(T), c(T) in Analysis I (Soft Rock)

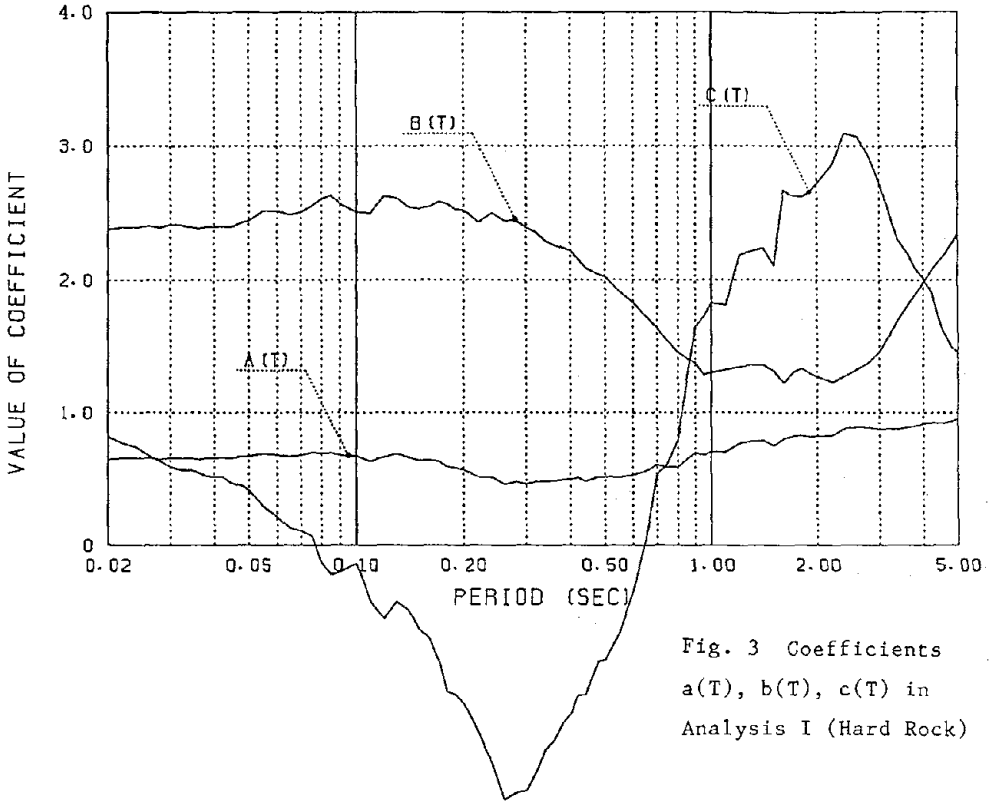

Fig. 3 Coefficients a(T), b(T), c(T) in Analysis I (Hard Rock)

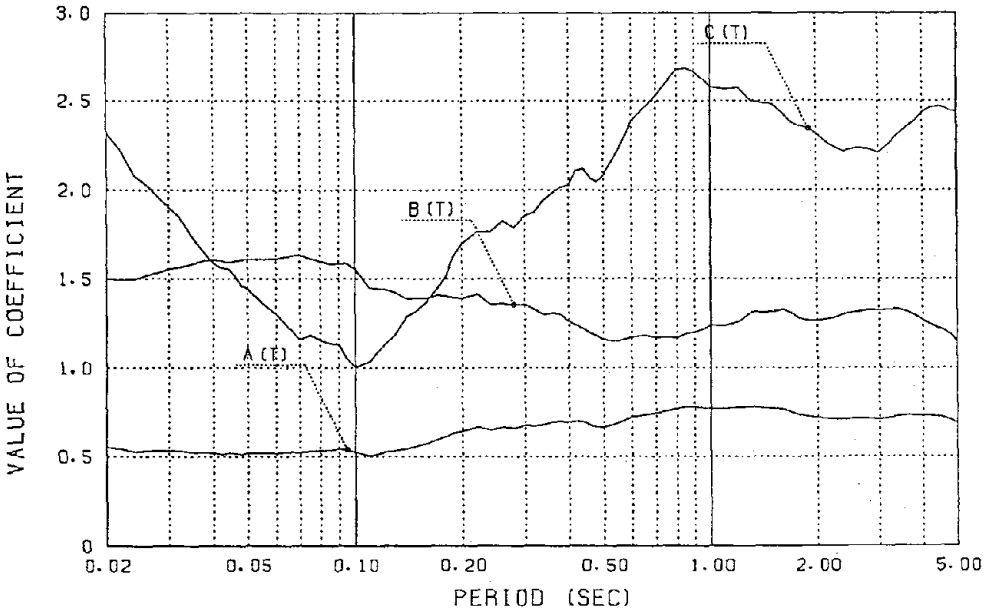

Fig. 4 Coefficients a(T), b(T), c(T) in Analysis I (HH Rock)

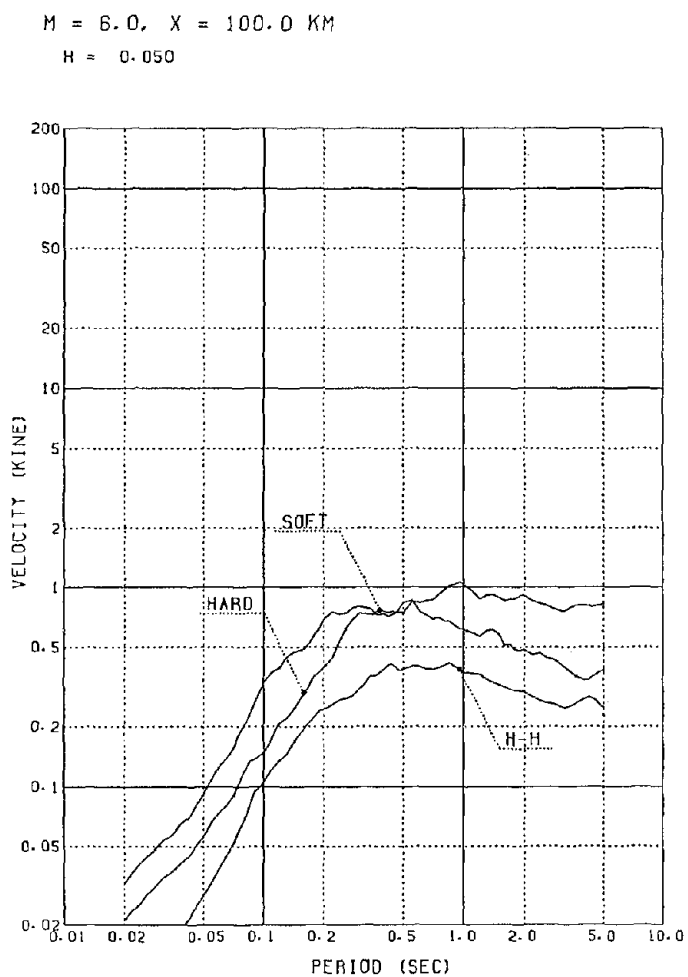

Fig. 5(a) Computed Spectra in Analysis I
(M=6.0,X=100km)

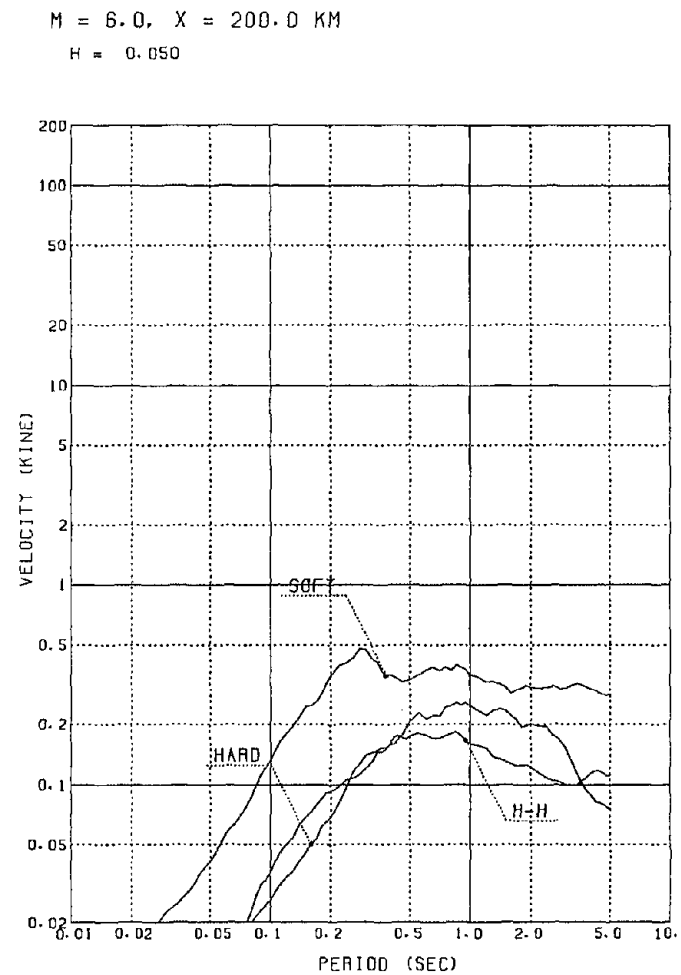

Fig. 5(b) Computed Spectra in Analysis I
(M=6.0,X=200km)

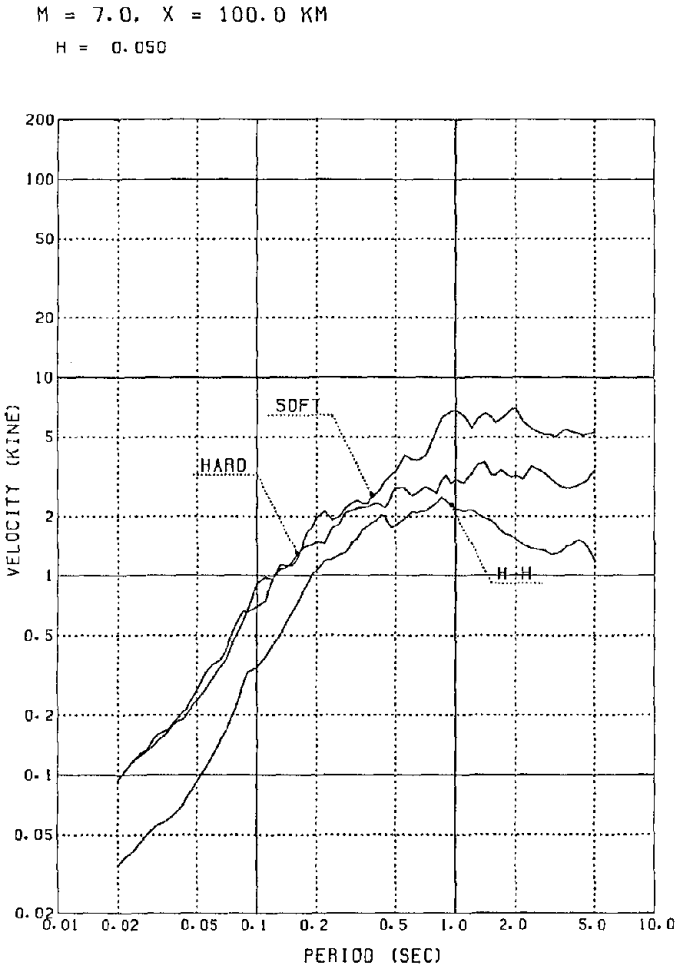

Fig. 5(c) Computed Spectra in Analysis I
(M=7.0,X=100km)

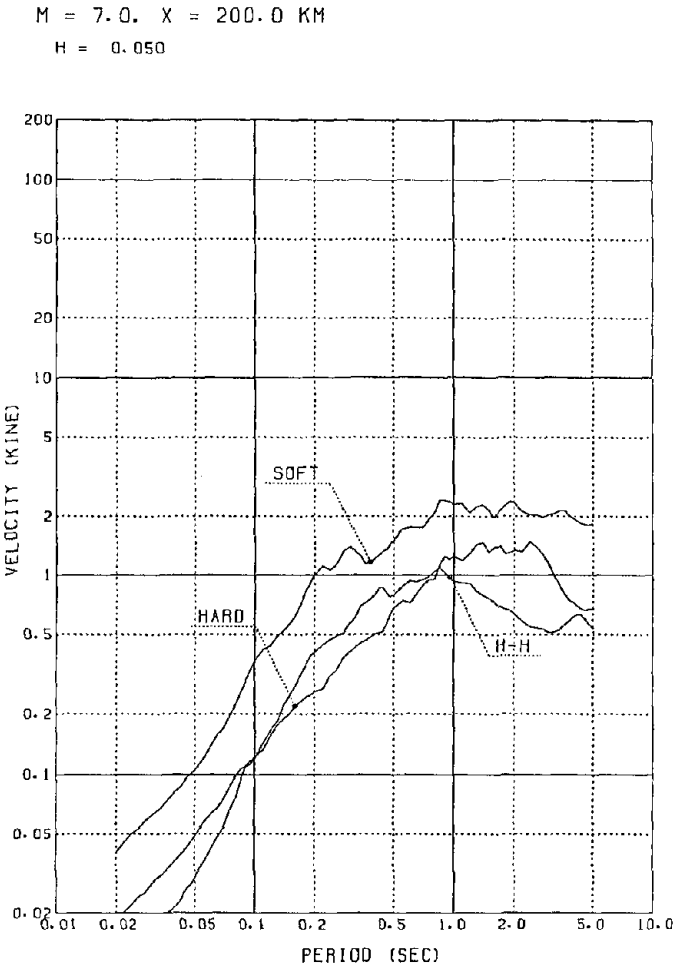

Fig. 5(d) Computed Spectra in Analysis I
(M=7.0,X=200km)

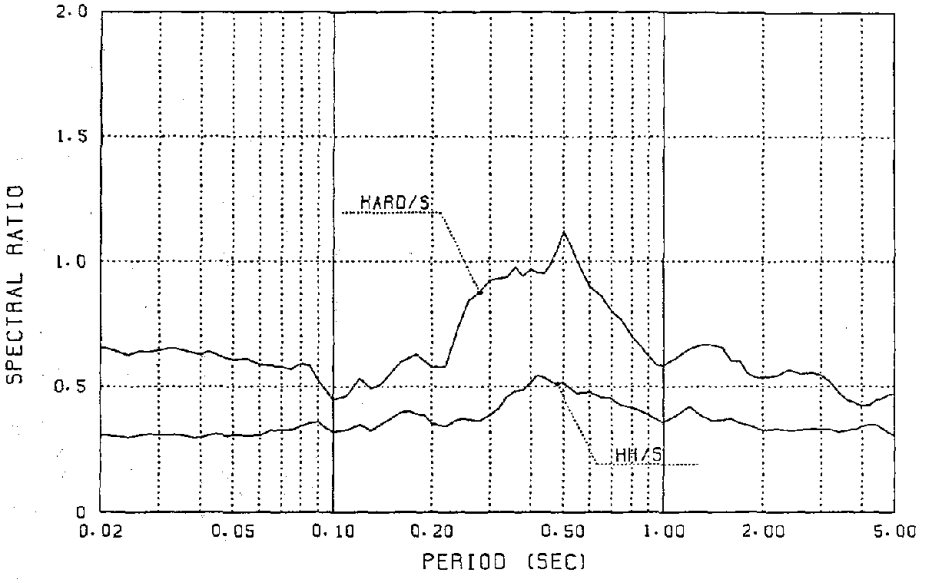

Fig. 6(a) Spectral Ratio to the Soft-Rock Spectra
(M=6.0,X=100km)

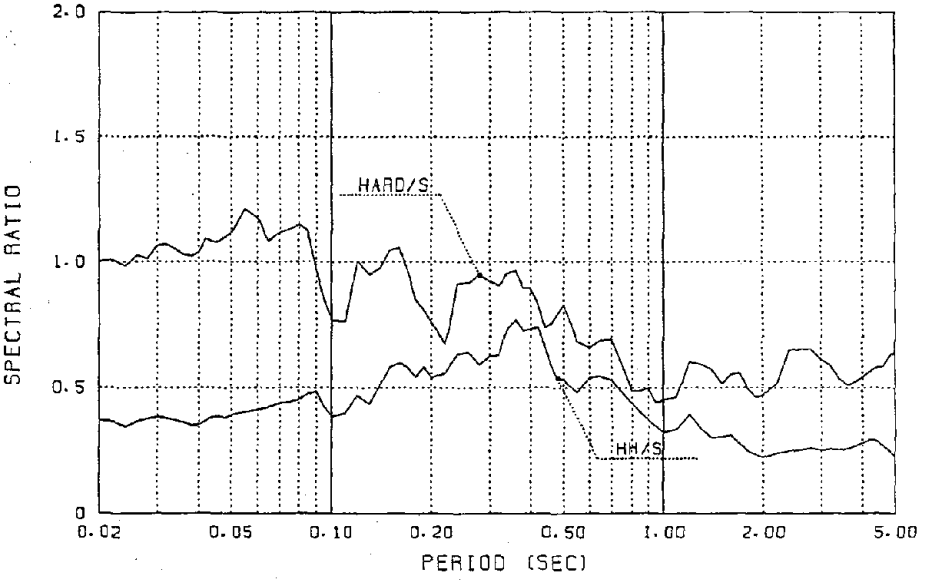

Fig. 6(b) Spectral Ratio to the Soft-Rock Spectra
(M=7.0,X=200km)

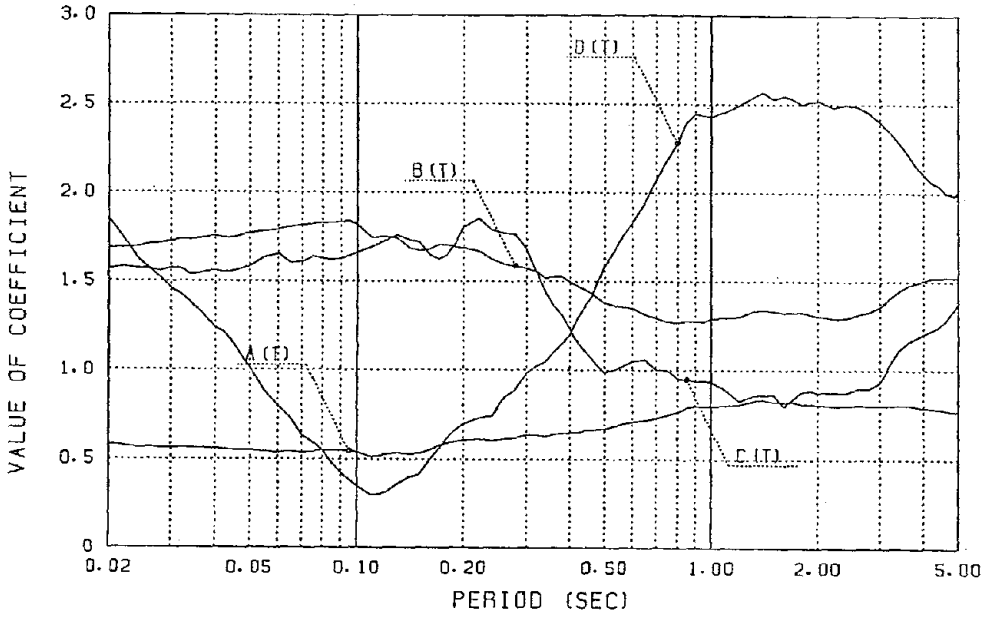

Fig. 7 Coefficients a(T), b(T), c(T) and d(T) in Analysis II

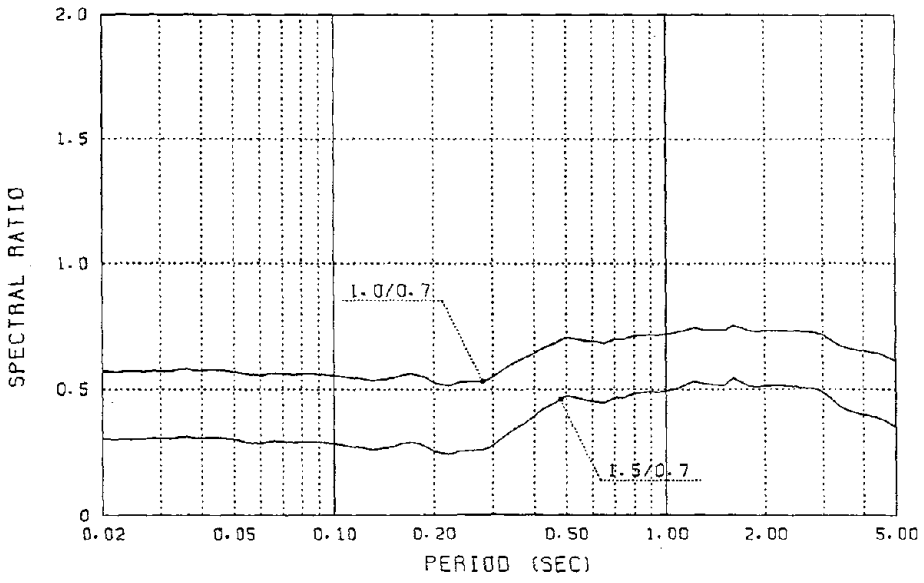

Fig. 9 Ratios to the Vs=0.7km/sec-Spectra (numeral indicates shear wave velocity in km/sec)

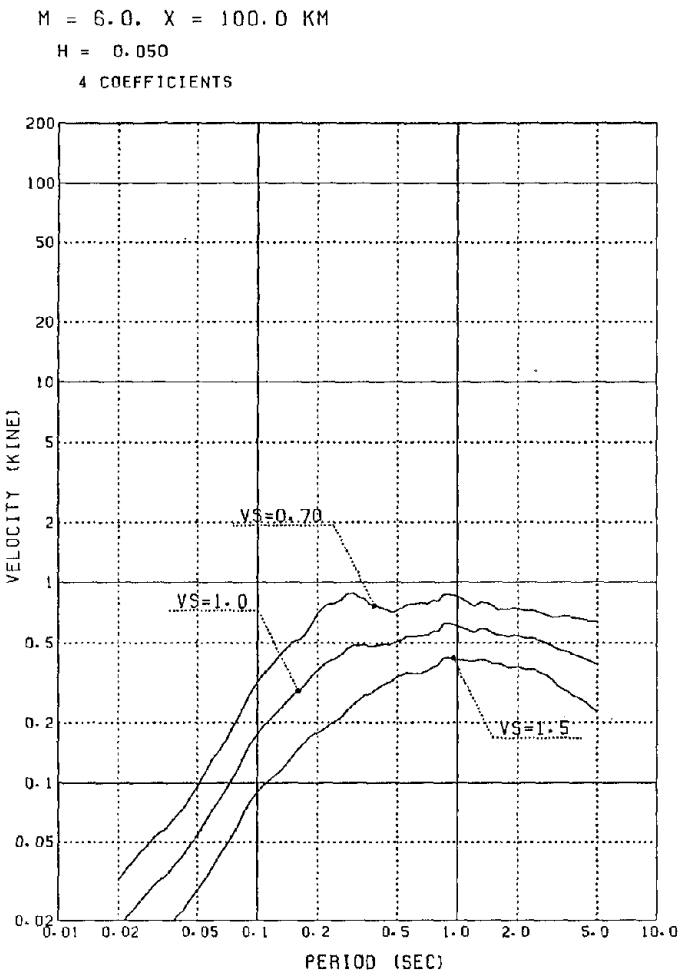

Fig. 8(a) Computed Spectra in Analysis II
(M=6.0,X=100km)

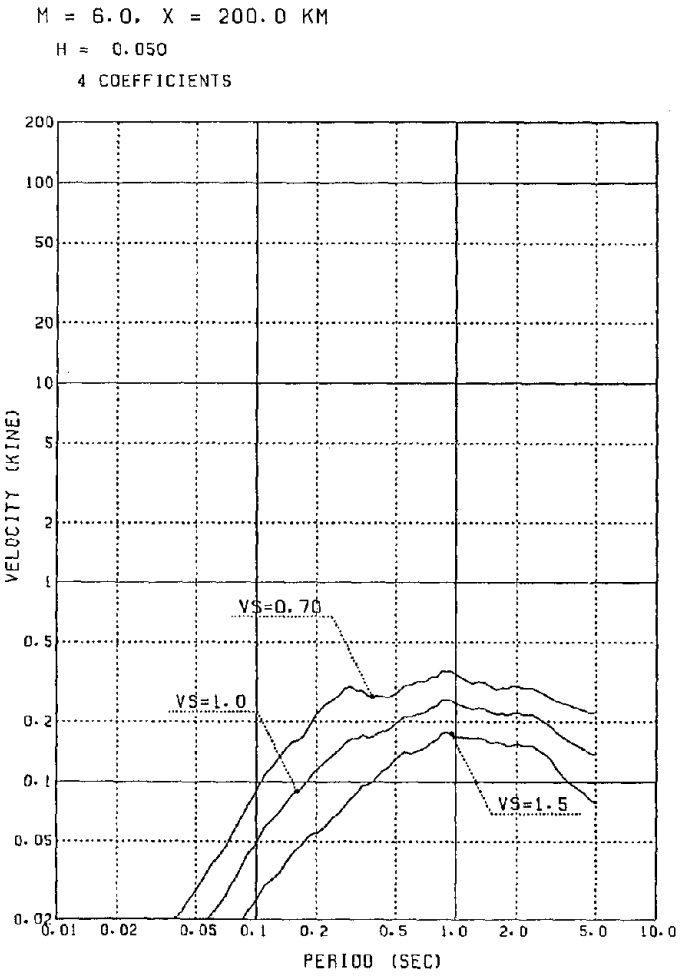

Fig. 8(b) Computed Spectra in Analysis II
(M=6.0,X=200km)

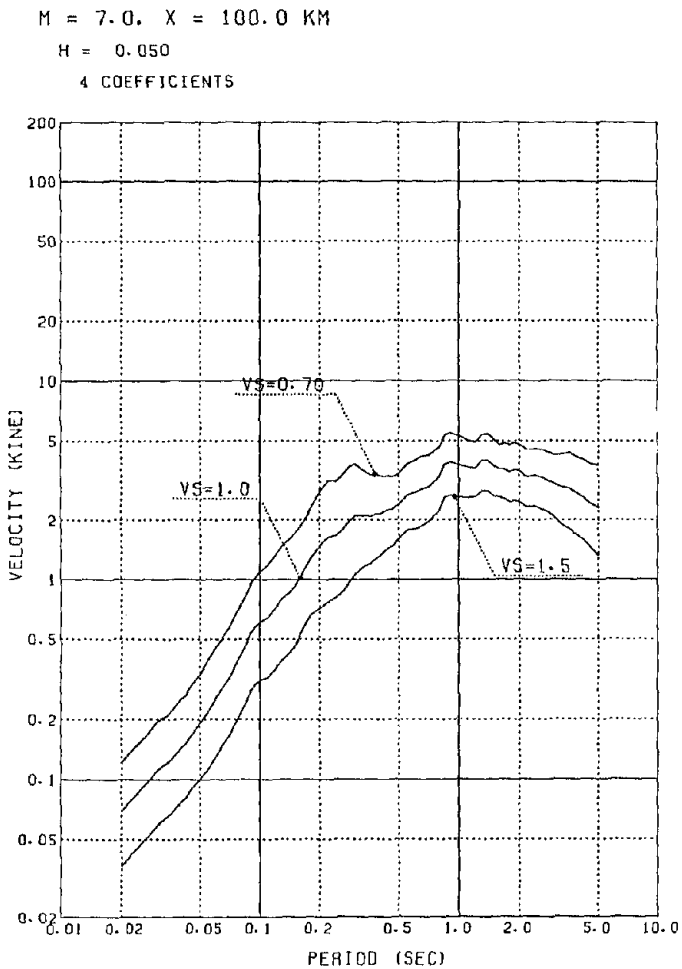

Fig. 8(c) Computed Spectra in Analysis II
(M=7.0,X=100km)

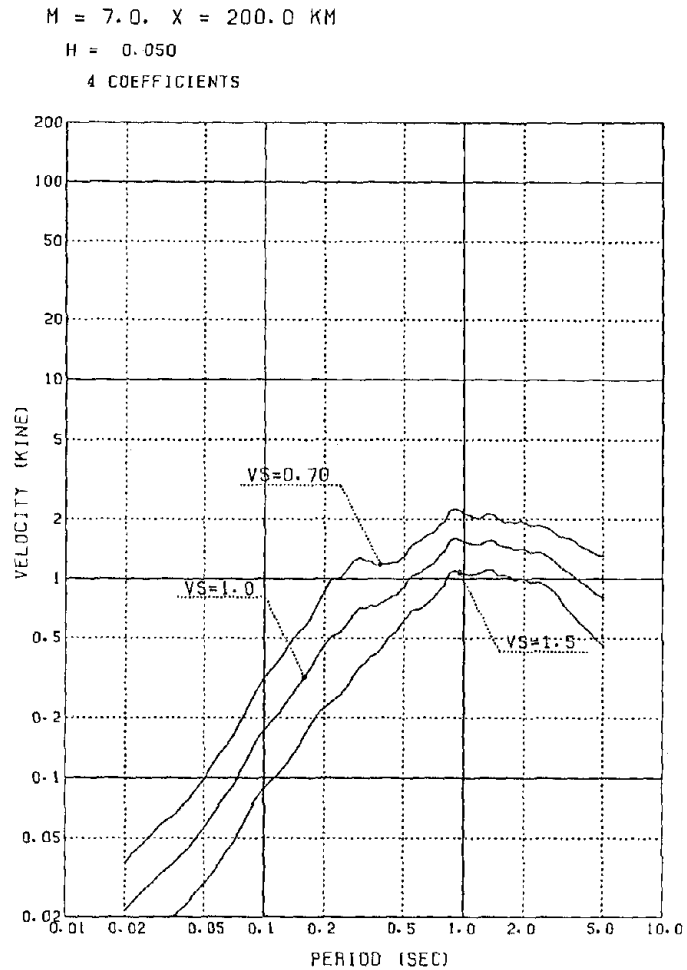

Fig. 8(d) Computed Spectra in Analysis II
(M=7.0,X=200km)

REGIONAL TSUNAMI WARNING SYSTEM (THRUST)

BY

Eddie N. Bernard and Richard R. Behn*

ABSTRACT

The National Oceanic and Atmospheric Administration (NOAA) has embarked on a 3-year project, Tsunami Hazard Reduction Using System Technology (THRUST), to create a pilot regional tsunami warning system. THRUST, which is being funded by the Agency for International Development (AID) and developed by the Pacific Marine Environmental Laboratory (PMEL) for the country of Chile, is utilizing existing instrumentation connected to satellite communication to establish an early warning system. All pre-event work has been completed including hazard map, numerical modeling simulations, and the creation of an emergency operating plan. Instrumentation design has been completed and bench testing is expected to begin in summer of 1985.

1. INTRODUCTION

One of the most destructive natural hazards within the Pacific Basin is the seismic sea wave, or tsunami. More than two million people support themselves or reside in the tsunami prone areas of the Pacific Basin. Since the early 1850's, more than 70,000 of these people have lost their lives due to the devastation of tsunamis (Iida *et al.*, 1967).

Developing countries within the Pacific Basin, with minimal or no regional warning system, cannot be alerted of tsunamis originating close to their shores. The present operating limitations of the existing Pacific-wide tsunami warning network (the Pacific Tsunami Warning Center (PTWC) near Honolulu, Hawaii, USA) allows a warning to be issued ½ to one hour after the generation of a tsunami. A gap, the ½ to one hour after tsunami generation, exists in the present warning structure.

The purpose of the THRUST (Tsunami Hazard Reduction Using Satellite Technology) project has been to examine existing technology and to ascertain if an early warning system can be designed that would fill the "gap" in nations with minimal or no regional warning system. Specifically, the objective is to design, assemble, test, install and evaluate a system that can deliver early warnings to a developing country (Bernard *et al.*, 1982).

The Valparaiso, Chile area was selected as the site in which the THRUST project will take place because of its great tsunami threat and its existing warning infrastructure.

2. THRUST SYSTEM

Warning systems can be divided into two time frames, the pre-event stage--the period (days, weeks, months, years, etc.) prior to the event (tsunami); and the real-time stage--the first hours after the event (tsunami generation). The pre-event time frame of this warning system determines the potential danger the event presents to that area and the solutions to these dangers. The real-time time frame's efforts are focused on the collection and analysis of seismic and water level data and the dissemination of the warning information.

*Pacific Marine Environmental Laboratory
National Oceanic and Atmospheric Administration
Seattle, WA 98115 USA

The technologies that are being examined in THRUST can be categorized into three areas: data collection, data analysis, and information dissemination.

The THRUST system, being an early warning system, can be conceptually described as combining the time frames of a warning system with the areas of technology to form a working matrix. Utilizing Table 1, we can describe the system in the following fashion (Bernard *et al.*, 1983).

3. PRE-EVENT

3.1 Data Collection

This task consisted of compiling, cataloging and synthesizing all available data relating to tsunami effects in the Pacific Basin, concentrating on the country of Chile.

To date, three files utilizing this data have been assembled. The first file is a pre-twentieth century file that include 382 events (categorized into run-up heights, magnitudes, origin, etc.) of which 178 have caused death or destruction. The second file is a twentieth century file which includes 405 events (categorized as mentioned above). The third file is a file of all Chilean tsunamis since the 16th century. This file contains 249 events of which 34 have caused death or destruction.

Utilizing the above data files, a "Tsunami in the Pacific Basin" map has been assembled and published. This map details earthquake origin and magnitude, tsunami run-up height, related deaths, dollar damage, etc. of all tsunamigenic earthquakes in the Pacific Basin from 1900 to 1983. The data files have also been utilized for validating the numerical models and assisting in the development of the Standard Operating Plan.

3.2 Data Analysis

This task has produced computer simulations which have provided estimates of potential inundation levels, flood hazard areas, and worst case effects of observed and potential tsunamis.

The SURGE II model was applied to all modeling efforts (Reid *et al.*, 1977). A ½ km grid was utilized with a seafloor uplift (within the grid) being the source of the tsunami. These simulations provided information that the threat to Valparaiso from local tsunamis approaching from the west and/or northwest is quite great. Data obtained from the Chilean Navy Hydrographic Institute (IHA) in Valparaiso, Chile on the May 22, 1960 tsunami in Corral, Chile was utilized to verify the model (Hebenstreit, 1984a).

THRUST SCHEMATIC PILOT STUDY

FUNCTIONAL AREA / TIME FRAME	DATA COLLECTION	DATA ANALYSIS	DISSEMINATION
PRE-EVENT	DEVELOP TSUNAMI DATA BASE	EVALUATION OF HAZARD USING SIMULATIONS	DEVELOPMENT OF EMERGENCY OPERATIONS, PROCEDURES
REAL-TIME	SENSOR DEVELOPMENT INSTRUMENT + PROCESSING + TRANSMISSION	OPERATIONAL "PREDICTIVE" MODEL	INTEGRATION OF EARLY WARNING DEVICE INTO EMERGENCY SYSTEM

Table 1.

Results of these numerical simulations will be used to formulate the evacuation plan in the Standard Operating Plan (SOP) and for the development of the Real Time Processor (RTP).

3.3 Information Dissemination

This task includes the development of the Standard Operating Plan (SOP) for the city of Valparaiso, Chile. The purpose of the SOP is to achieve effective preparedness and to organize a coordinated program of tsunami warning dissemination which will ensure a prompt and flexible response by the local population, thus minimizing loss of life and property. Mr. Emilio Lorca, IHA, has assisted THRUST in formulating the SOP. Information obtained from the data files and numerical simulation were utilized to formulate an effective SOP.

4. REAL TIME

4.1 Data Collection

This task will coordinate the collection and dissemination of all data. The instruments for THRUST will utilize a satellite-based communications system, in the form of the Geostationary Operational Environmental Satellite (GOES) system. Utilizing the GOES system will allow the lag time between the event and the receipt of initial data to be reduced to the order of minutes--enough time to provide regional early warnings (see Figure 1).

After reviewing the requirements of the seismic system needed for THRUST, it was decided that strong motion triggers would be well suited for our needs. Two seismic triggers, made by Kinemetrics, will initiate the system when a seismic event occurs. One of the triggers will be in Valparaiso and the other will be in Santiago (see Figure 2).

Pressure digital water level sensors are best suited for this project because of their large dynamic range. Paroscientific Digiquartz pressure transducers will be used as the water level gauges. Both water level sensors will be placed on the concrete pier located in the Valparaiso harbor (see Figure 2).

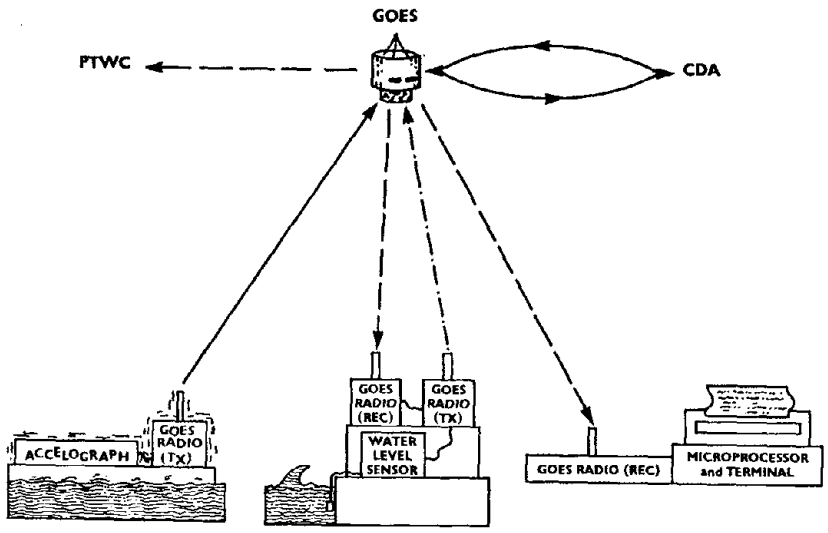

Figure 1.
THRUST instrumentation design.
CDA refers to Command Data and Acquisition.

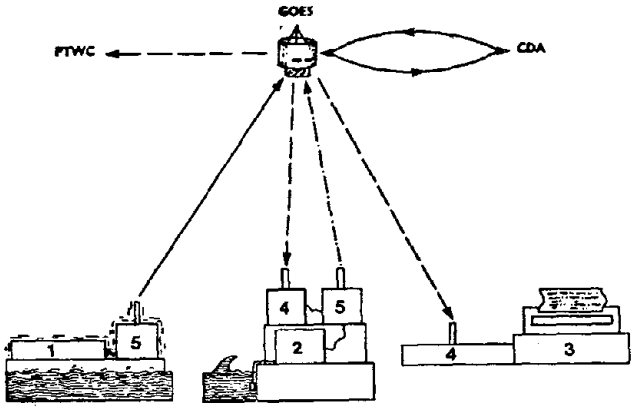

INSTRUMENTATION:

1. Accelograph: Kinemetrics Vertical Seismic Trigger (VS-1)
2. Water Level Gauge: Paroscientific Digitiquartz Pressure Transducer (2100AS-002)
3. Microprocessor/Terminal: Commodor 64 with Dot Matrix Printer
4. GOES Radio Receiver: Kinemetrics True Time Receiver (468-DC)
5. GOES Radio Transmitters: Synergetics (3401A)

Figure 2.
THRUST instrumentation.
CDA refers to Command Data and Acquisition.

The GOES radio sets that will be utilized by the THRUST system will be manufactured by Synergetics. These radio sets will be transmitters (TX) only. The radio sets will be connected to the seismic triggers and water level sensors. Kinemetrics True Time Receivers will be utilized as the Commodore 64 with a dot matrix printer (see Figure 2). The RTP will be located at IHA in Valparaiso, Chile.

Procurement of the above mentioned items has been initiated. After PMEL receives all the equipment (Summer 1985) it will be assembled and tested for approximately 6 months. After a successful test, all equipment will be installed in Chile (May 1986) for one year of testing and evaluation.

4.2 Data Analysis

This task deals with the development of the Real Time Processor (RTP). The RTP is the first link between the THRUST instrumentation and the Chilean Tsunami Warning Center personnel. The RTP will consist of a microprocessor and a printer that will print a stored message (see Figure 3) when it receives an event alert signal through GOES from the seismic trigger. The RTP will:

1) Alert Warning Center personnel that the seismic trigger was turned on by an event;
2) provide some level of assessment of the tsunami threat;
3) remind Warning Center personnel of the procedures to follow (Hebenstreit, 1984b).

4.3 Information Dissemination

This final task deals with the transmission of warning information to threatened population areas. In this final step of the warning process, the incoming data and the accompanying analysis are used to determine which areas to warn, in what order to warn them, and what instructions to issue (SOP).

The THRUST project has received eight satellite addresses for the GOES System. Four of these

VALPARAISO EARTHQUAKE ALERT

A STRONG EARTHQUAKE OCCURRED AT z ON IN THE VICINITY OF VALPARAISO. CONTACT THE FOLLOWING AUTHORITIES:

- OFICINA NACIONAL DE EMERGENCIA TELEPHONE No 718333
- DEPARTMENT OF GEOPHYSICS TELEPHONE No 6968586

AND AVISE THEM OF THIS EARTHQUAKE ALERT AND DISSEMINATE THE ATTACHED TSUNAMI WATCH MESSAGE.

TSUNAMI WATCH

ESTABLISH A TSUNAMI WATCH. A TSUNAMI MAY ACCOMPANY THIS EARTHQUAKE. IF A TSUNAMI OCCURRED, THE WAVE WILL RETARD IN REACHING THE COAST AT THE COAST AT THE SHOWN LOCALITIES THE NEXT SPECIFIED TIMES:

VALPARAISO	minutes
COQUIMBO	minutes
CALDERA	minutes
TALCAHUANO	minutes
CHANARAL	minutes
CORRAL	minutes
ANTOFAGASTA	minutes
ISLA DE CHILOE (ANCUD)	minutes
TOCOPILLA	minutes
IQUIQUE	minutes
ARICA	minutes

REMEMBER, THIS IS ONLY A TSUNAMI WATCH. NO TSUNAMI HAS BEEN OBSERVED BUT ONE MAY OCCUR.

Figure 3.
RTP message format.

addresses will be for the daily test made of the system. The remaining four will be for the standard operation of the system. NOAA, manager of the GOES system, has assigned THRUST a random report channel with very little usage for the demonstration of the THRUST system to ensure successful transmissions of messages.

Every seismic trigger (uplink) message, whether test mode or standard operation, will be sent through the GOES system four times to ensure the receipt of the message. Each message will be sent within a 15 second window with a 60 second delay after each window. Thus, a message could be received by GOES in as little as 15 seconds or as much as 7 minutes after the occurrence of the event. Upon receipt of this event triggered message, the GOES-CDA (Command Data and Acquisition) would be alerted that this is an emergency message and immediate action is to be initiated. This action (to be initiated within 1 minute) is a message sent back through GOES to turn on the water level sensors and the RTP (see Figure 1) (THRUST Pilot Study, 1984).

5. THRUST SCENARIO

Once the THRUST study has been installed and operating, a typical event scenario should occur in the following manner (see Figure 1).

An earthquake will activate the seismic trigger. This instrument then transmits four messages through the GOES system which responds by initiating an alert code back through the GOES system to the RTP located at the Hydrographic Institute in Valparaiso. The RTP instantly responds by initiating a prerecorded message based on the Standard Operating Plan and procedures established prior to the tsunami. The message format THRUST will use is similar to that used in Figure 3.

In addition, The GOES alert code will initiate the water level sensors in the Valparaiso harbor to begin sending data via satellite to CDA. This information can then be accessed via telephone line.

Note that this process is entirely automatic and should take no more than 10 minutes to complete. But no real decisions have been made, except possibly a predetermined one to sound a general alert. Final authority to make decisions, to issue further alerts or sound the evacuation alarm, must rest with human officials. This task should be made simpler because of several factors. The decision makers will now be familiar with the historical and potential hazard analyses performed during the pre-event phase and will now be aware of the general type of threat the coast of Chile faces. Also, because of the Standard Operating Plan implemented during the project, IHA will have a set of procedures to follow and should not find it necessary to improvise. In addition, because of the public awareness program established during the project, the Chileans should be confident that the threatened population know how to respond to ensure their own safety. And lastly, the Chileans can be sure that the sensors and the real-time analysis package are providing them with the most up-to-date information available.

6. CONCLUSIONS

The goals of THRUST are to show that such a system can be built, to work with the Chilean government to integrate the technical system into its disaster control structure, and to train the Chilean personnel in the operation and maintenance of the system. Each phase of THRUST, then, will be conducted in conjunction with personnel from Chile. In this way the technology behind THRUST can be demonstrated to other tsunami-prone (and geophysical hazard-prone, in general) nations, while concurrently enhancing the technological capabilities of Chile. Successful completion of the THRUST project will not only enhance the tsunami protection of Chile but will, by adding addi-

tional input to PTWC, improve the protection of the entire Pacific community.

7. REFERENCES

Bernard, E.N., G.T. Hebenstreit, J.F. Lander and P.F. Krumpe, Regional Tsunami Warnings Using Satellites. Proceedings of 1983 Tsunami Symposium, U.S. Dept. of Commerce, PMEL, Seattle, WA, 1983.

Bernard, E.N., J.F. Lander, G.T. Hebenstreit, Feasibility Study on Mitigating Tsunami Hazards in the Pacific. NOAA Technical Memorandum ERL PMEL-37, 1982.

Hebenstreit, G.T., THRUST Model Results for Valparaiso, Chile. Science Application International Corporation, McLean, Virginia, 1984a.

Hebenstreit, G.T., Basic Criteria for the THRUST Real-Time Processor. Science Application International Corporation, McLean, Virginia, 1984b.

Iida, K., D. Cox and G. Pararas-Carayannis, Preliminary Catalog of Tsunamis Occurring in the Pacific Ocean. H.I.G. University of Hawaii, 1967.

Reid, R.O., A.C. Vastano and T.J. Reid, Development of SURGE II program with application to the Sabine-Calcasiev area for hurricane Carla and design hurricanes. Coastal Studies Inc., College Station, TX, Report TP77-13, 1977.

THRUST Pilot Study for Pacific Marine Environmental Laboratory, Task I - Final Report, CyberLink Corp, Boulder, CO, 1983.

THRUST Pilot Study Prototype System Work Plan, Task II - First Quarter Report, CyberLink Corp., Boulder, CO, 1984.

Keywords:

1. Tsunami
2. GOES
3. Hazard Reduction
4. Numerical Model
5. Seismology
6. Oceanographic Instruments

STUDIES ON STORM SURGES IN TIDAL ESTUARIES

BY

Tatsuo Konishi
Takeo Kinosita
Hiroshi Takahashi

National Research Center for Disaster Prevention
Science and Technology Agency, Japan

ABSTRACT

Characteristics of storm surges in rivers and estuaries in connection with the discharge of rivers are studied in this report.

The time difference between storm surges and a flood is dependent upon the drainage area of the river if it has not rained before the onset of the typhoon. Three types are categorized by means of drainage areas, as follows.

In a river whose drainage area is over 3000 km^2 (for example, the Kiso river), the flood is delayed from the storm surges. The characteristics of storm surges during the non-flood period are clarified in this type. The storm surges occur simultaneously with the flood in a river whose drainage area is smaller than 1000 km^2 (for example, the Tsurumi river). The analysis of this type explains combined effects of storm surges with floods. A river whose drainage area is from 1000 to 3000 km^2 (for example, the Arakawa river) shows the intermediate effect of storm surges taking place in the rivers mentioned above where the storm surge meets the flood in the middle reach.

Finally, other effects not obtained from the observed data are discussed in light of numerical experiments.

Keywords: Seismology, storm surge

1. INTRODUCTION

Research on storm surges is not active because a serious storm surge has not occurred recently. This does not imply that there are no problems in storm surges. For example, the cause of the big storm surge that occurred in Tosa Bay in 1970 has not yet been determined. Storm surge modification in a river reach as well as an estuary and a port and harbor has not been solved hydraulically. On the other hand, it has been noticed that the flood characteristics change remarkably due to urbanization. Completion of an urban drainage system, such as a sewerage, makes the time of concentration short and induces a big runoff coefficient. Considering these changes in the relation to storm surges, the time difference between storm surges and a flood, occurring late, becomes shorter. The probability of their superposition becomes greater. From the view point of disaster prevention, it is necessary to determine the risks due to superposition. This paper describes the effects of superposition. In addition, though the storm surges in embayments were well studied, the behavior of the storm surges in rivers and estuaries, even in the non-flood period, are not well known.

The first purpose of this paper is to clarify the nature of storm surges in rivers during the non-flood period. The second is to make clear the combined effects of floods and storm surges in rivers. These problems are discussed using the observed data, water levels and discharges. From the analyses, the nature of storm surges in rivers may be understood as a whole.

2. STORM SURGES IN THE NON-FLOOD PERIOD (FROM CASES OF THE KISO RIVER)

The Kiso river system is composed of the Kiso (drainage area, 5275 km^2), the Nagara (1985 km^2) and the Ibi (1840 km^2) rivers. As the Kiso

river has a large river basin, the flood peak will be delayed from the peak of storm surges, if it has not rained heavily before the typhoon onset. Therefore the characteristics of storm surges can be discussed in the non-flood period from the results obtained in the Kiso river. The location of the Kiso river is shown at point "a" in Fig. 1 and the water level stations and weather stations are shown in Fig. 1a. Typhoons 7220 and 7916 are chosen for analysis. The tidal anomalies at the tide gauge station of Nagoya are observed at 2 m and 1.4 m respectively. Fig. 2 shows the hydrographs of the water level stations along the Kiso river during the period of typhoon 7220. The peak, which is observed at 24:00 on 16 September at Yokomakura, is produced by the storm surges, and the peak at 15:00 on the 17th at Naruto is produced by the flood. The case of typhoon 7916 is shown in Fig. 3. The peak of the storm surge is observed at 24:00 on 30 September at Yokomakura and the flood peak is observed at 17:00 on 1 October at Naruto. It is understood that the water levels are varying as the sum of the astronomical tide, the storm surges and the flood. The details about meteorological conditions and hydrographs of the Ibi and the Nagara rivers are explained by Konishi and Kinosita (1983).

The most important data for disaster prevention concerning storm surges are maximum heights in rivers and estuaries. Figs. 4 and 5 show these heights along the Kiso river system. These graphs include the high water levels of astronomical tide and the 25-hour average of the water level before the onset of the storm surges. Mean levels and high water levels are almost horizontal on the lower reaches and increase upstream according to the rise of the river bed. These trends are already mentioned by Unoki (1968). On the other hand, the maximum heights of the storm surges increase with the distance from the river mouths. A difference of 1 m of water level was observed between the river mouth and the station 18 km from the mouth. Surge peaks on upper reaches occur at the rising stage of the floods in the Ibi and the Nagara rivers, especially in the Ibi, whose drainage area is smaller than other rivers'. Therefore the maximum height is partly composed of the flood. But the peaks of storm surges in the Kiso river are separated from the peaks of floods, as seen in Figs. 2 and 3. The maximum water level at the downstream of the Kiso river is mainly caused by the storm surges. The amplitude of storm surges is defined as the difference between the maximum water level of the storm surge and the mean water level at a certain station as shown in Figs. 4 and 5. The amplitude at a distance of about 13 km from the mouth is 20 or 40 percent higher than the amplitude at the mouth. It decreases to 0.9 percent of the amplitude at the mouth at 20 km. The results show that storm surges are amplified in rivers and estuaries.

Why are storm surges amplified in the lower reach? Two kinds of phenomena are considered as causes, such as run-up of the storm surge wave and wind stress. In order to evaluate the effectiveness of these causes, numerical simulations are applied. The following equations of motion and continuity in one dimension,

$$\frac{\partial U}{\partial t} + U \frac{\partial U}{\partial X} = -g \frac{\partial D}{\partial X} - \frac{\tau b}{\rho w R} + \frac{\tau a}{\rho w R} \qquad (1)$$

$$\frac{\partial D}{\partial t} = -\frac{1}{B} \frac{\partial Q}{\partial X} \qquad (2)$$

are used for the basic equations, where U is the mean flow velocity over the vertical cross section of the river, D is the water level measured from the reference level, R is the hydraulic radius, Q is the flow flux, τb is the bottom friction, τa is the wind stress, B is the width of the river, g is the gravitational acceleration and ρw is the density of the water. They are transformed into the difference equations. A is the area of the cross section and the following relation,

$$Q = U \cdot A \qquad (3)$$

is introduced. By the survey of the river channel, the width of the river, A and R are determined as functions of the water level for each cross section. The simple shape of the river channel is actually used in this computation. The part of the river channel higher than "H" and the part lower than -2 m T.P. are supposed to be constant in width. "H" means the water level above which the channel width is practically constant. The bottom friction, τb is expressed by the Manning formula,

$$\tau b = \rho w \frac{g n^2 U|U|}{R^{\frac{1}{3}}}$$

where n is the roughness coefficient. Normally, τa is proportional to the square of wind speed, W, as follows,

$$\tau a = \rho a \, Cd \, W^2$$

where ρa is the air density and Cd is the drag coefficient. The boundary conditions are assigned for the inflow flux at the upper boundary and the tide level at the river mouth. The arrangement of temporal and spatial grid points is similar to Unoki's (Unoki, 1968). Main terms of differential equations are approximated by centered differences.

The water level in the Kiso river is simulated. The storm surges appear separately from a flood in the river. Therefore the inflow hydrographs from the upper reach need not be considered. The inflow at the upper boundary for the case of typhoon 7220 is 242 m^3/s, which is the daily mean discharge on 15 September at Okoshi, 34 km from the river mouth. The inflow for typhoon 7916 is 646 m^3/s, which is observed at the Umakai weir on 30 September. The water level at the lower boundary is chosen to be the water level hydrograph at Yokomakura, 2 km upstream from the mouth. The river channel form used in the computation is obtained by the survey. The spatial grid is 1 km and the temporal grid is 100 seconds. The upper boundary is located at 50 km from the river mouth.

Two roughness coefficients, n = 0.02 and n = 0.025, are used in the computation. The drag coefficient of wind is varying within the range of $(0,2,4,6) \times 10^{-3}$. 2.6×10^{-3} has often been used in numerical simulations for similar phenomena, but it does not agree with the observation in the cases described below. The wind observed at Kuwana is applied over the entire model, but only the component parallel to the river channel is used. More detailed information is found in Konishi and Kinosita (1983).

The longitudinal profile of the maximum storm surge height from the river mouth is shown in Figs. 6b, 7a and 7b for different drag coefficients. Figs. 6 and 7 are the profiles produced by typhoons 7220 and 7916, respectively. The zero drag coefficient means that wind stress plays no role in the river and the result shows horizontal water level. This is quite different from the real profile of maximum height of the storm surges. The wind stress in the river is important in such a river as the Kiso. The drag coefficient adequate to explain the observed profile may be $4\text{-}6 \times 10^{-3}$. These values are somewhat larger than usually reported. The reason for the large difference is not well understood. The simulated hydrographs are shown in Figs. 2 and 3 by circles and dots. Cd and n are equal to 4×10^{-3} and 0.025, respectively. Good agreement may be seen in the figures.

3. CASES OF COMBINED STORM SURGES WITH A FLOOD: 1 (FROM CASES OF THE TAURUMI RIVER)

Small rivers which pour into the vulnerable bay of storm surges always have the combined effects of storm surges and floods, because their basins are small and therefore the time of concentration is short. Such a case is the flood in the Tsurumi river, whose drainage area is 235 km^2. In this section, the water levels during the storm surge period in a small-scale river, the Tsurumi river, are considered. The location of the Tsurumi river is shown at point

"b" in Fig. 1 and the water level stations are shown in Fig. 1b.

Fig. 8 shows hydrographs observed along the Tsurumi river during the period of typhoon 8218 in September 1982. In Fig. 9 tidal anomalies observed at Kawasaki, Yokohama and the river mouth of the Tsurumi river are shown. A flood peak is found at 15:00 at Tsunashima station and at 18:00 at Ashiho in Fig. 8. On the other hand, the tidal anomaly at 18:00 is about 50 cm, which is 80 percent of the maximum tidal anomaly, as shown in Fig. 9. Thus, these figures indicate the superposition of storm surges and a flood in the Tsurumi River.

At Tsunashima, which is 11 km upstream from the river mouth, the relation of observed water level and discharge is shown in Fig. 10. Two cases are mixed in the figure. One is the case of superposition of storm surges and a flood, and another is the case of a flood only. A single relationship is found on the figure. Consequently, it may be expected that the tidal oscillation has no influence on the water level at Tsunashima. The relation can be reproduced by the numerical simulation. The curve in the figure is drawn by the numerical solution of Eqs. (1) and (2) with the assumption of stationary state. The upper boundary is Kamenoko-Bashi which is 16 km upstream from the mouth. The lower boundary is the river mouth, where the water level is supposed to be constantly T.P. 0 m. The spatial grid is 400 m. The river bed form is based on the survey in 1982. The curve obtained by the solution of Eqs. (1) and (2) with n = 0.025 agrees well with the observed values. It is concluded that the water level at Tsunashima is simply determined by the discharge from the upper reach.

The water levels at Ashiho-Bashi, which is 4 km upstream from the mouth, and Sueyoshi-Bashi, 8 km from the mouth, are analyzed. There are two kinds of flood discharge variations at these stations, a large variation along the river and a small variation. The variation comes from water of the tributaries.

The water levels of Ashiho-Bashi and Sueyoshi-Bashi, in the case of a small variation, are mostly determined by the assumption of stationary state. The boundary conditions are given as the discharge from the upper reach at Tsunashima and as the tidal level at the mouth. The difference between the observed water level and the computed one is about 20 or 30 cm. In the case of a large variation, the water levels at the stations can be reproduced by the assumption of stationary state. But the upper boundary condition, the water level at Tsunashima, is not available, because the discharge from the tributary, the Yagami river, is important. Two discharges, Qa and Qs, are introduced. Qa is given by the surface gradient between the Ashiho and the river mouth with the assumption of stationary state. Qs is given by the surface gradient between the Sueyoshi and the river mouth with the same assumption. If Qa equals Qs, the assumption can be acceptable in the reach. The comparison is shown in Fig. 11. Fig. 12 compares the calculated result with the observed value at Sueyoshi-Bashi. Data include both cases of superposition and a flood only. Fairly good agreement is found in these figures. The water levels at Ashiho-Bashi and Sueyoshi-Bashi can be calculated by the assumption of stationary state. In this scale of the river, the past conditions have no influence on the water level, where the water level can be computed by tide level at the mouth and the discharge from the upper reach at the same time.

4. CASES OF COMBINED STORM SURGES WITH A FLOOD: 2 (FROM CASES OF THE ARAKAWA RIVER)

The combined characteristics of storm surges in both the Kiso and the Tsurumi are studied in medium scale rivers. Wind stress amplifies storm surges in the river and the amplified storm surges meet a flood in the middle reach. Such cases are found in the Ibi river and the

Arakawa river whose drainage areas are 1840 km^2 and 2940 km^2 respectively. Attention is directed to the Arakawa river during the period of typhoon 7920, because sufficient data were acquired. The location of the Arakawa river is shown as "c" in Fig. 1 and the water level stations are shown in Fig. 1c. The maximum tidal anomaly is 116 cm at the Tokyo tide gauge station. Detailed information on the typhoon, tides at the various stations and disasters are collected in Tsuji (1981) and Konishi and Kinosita (1985).

Fig. 13 shows the hydrographs observed at the stations along the Arakawa river during the typhoon period. At Minamisuna, the peak at 15:00 on the 19th is produced by the storm surges and the peak of Chisuibashi at 24:00 on the 19th is by the flood. There is a weir at Akigase. The water level at the upstream side ("Akigase-kami") is different from that at the downstream side ("Akigase-shimo") before a flood. But the difference disappears during the flood period because the gate is opened during the period.

In order to know whether the storm surges are amplified or not, the separation of the storm surge component from the flood is required. The following steps lead to it. First, observed water level and discharge variations are simulated numerically by Eqs. (1), (2) and (3). In the process the roughness coefficient, which is the most appropriate to the observed data, is determined. Using the roughness coefficient, the expected water level (hereinafter called E.L.) is computed under the condition of no storm surges, including a flood and an astronomical tide. The difference between observed water level and E.L. may be caused by storm surges only and is defined as surge component. The river bed form is determined by the survey of 1979. The discharge hydrography is given at the upper boundary, Chisuibashi, and the variation of tidal level is given at the mouth, Minamisuna. The wind measured by the AMEDAS station, Shinsuna, is applied over the Arakawa river model. The spatial grid is 1 km and the drag coefficient of 4×10^{-3} is used, based on the calculation of the Kiso river. The appropriate roughness coefficient used to reconcile the numerical results with observed data is 0.015 at the lower reach of 22 km and 0.02 at the upper reach of 22 km. The results are shown in Fig. 13. The agreements are good. At Akigase, the weir is not considered in this run and the difference may be fairly large. The surge component is calculated by the method mentioned above. The ratio of the maximum surge component at each station to that at the mouth is shown in Fig. 14. In the middle of the figure, the white circles indicate the ratio mentioned above, while the black circles are the ratio of the simulated water level minus E.L. at each station to that at the river mouth. Crosses are the storm surge amplitude, defined in section 2, by the difference between the peak of the storm surges and the mean water level before the storm surges and therefore the amplitude includes the flood effect. In Fig. 14, the surge component increases 40 percent at about 22 km upstream from the river mouth. The longitudinal profile of the river bed is also shown in the figure. Comparing the ratio with the profile, maximum storm surges may occur near the place where the profile bends. Similar relationships between the ratios and the profile are seen in other rivers. The surge components are calculated in the Edo river during the period of typhoon 7920 and in the Kiso river during the periods of typhoons 7220 and 7916. As both rivers have large basins, it takes a long time for a flood to arrive at the estuary. The water level during the period of storm surges is mainly influenced by both surge component and astronomical tide. Harmonic analysis is performed for the water levels before the storm surge to determine the contribution of astronomical tide and to separate the surge component from the observed data. The period of analysis is 25 hours, about a lunar day. The differences between the observed storm surge heights and the

tidal levels obtained from the harmonic analysis give the surge components. They are shown in Fig. 15 for the Kiso river and Fig. 16 for the Edo river, as the ratio of the maximum surge component to the value at the river mouth. In the Kiso river, the ratio is 1.4 at 12-18 km upstream from the river mouth, while the ratio is 1.2 at 14 km upstream from the river mouth in the Edo river. The position where the maximum ratio appears is near the place where the longitudinal profile bends. This trend is also found in the Arakawa river. It is therefore concluded that the storm surge is 20 or 40 percent larger at the place where the longitudinal profile bends than at the mouth. The flood superposes over the storm surges, and consequently the water level must be expected high at that point.

5. DISCUSSIONS

From the above analysis, if it has not rained before the onset of the typhoon, the characteristics of the storm surges in rivers may be classified by drainage areas, as follows.

(1) River with a large drainage area (over 3000 km^2)

A peak of storm surges is normally separated from a flood. The surge component increases by 20 or 40 percent over that at the river mouth. The maximum amplification occurs near the place where the longitudinal profile of the river bed bends. It is mainly caused by wind stress in the river. The drag coefficient obtained from the observed data is 4-6 $\times$ 10^{-3}.

(2) River with a medium drainage area (from 1000 to 3000 km^2)

A flood meets storm surges in the middle reach. In the moderate flood, the surge component has the same characteristics as in the case of the large drainage area, (1). The astronomical tide and flood components are superimposed on the storm surges and the high water level is expected around the place where the longitudinal profile bends.

(3) River with a small drainage area (below 1000 km^2)

A flood occurs simultaneously with storm surges in the lower reach. The water level in the river is determined by the calculation with the assumption of stationary state. The boundary conditions are the flood discharge at the upstream and the tidal level at the river mouth at the same time.

Several other effects are discussed by Konishi and Kinosita (1985) using the numerical experiments in an ideal river. Two important results are pointed out. (1) The water level calculated by the assumption of the stationary discharge is sometimes underestimated at the back water region. (2) Supposing that storm surges and a flood occur separately, T_1 is defined as the time when storm surges only attain to the maximum at the place where the longitudinal profile of the river bed bends, while T_2 is the time when a flood only attains to the maximum at the place where the river bed height is the mean sea level. If T_1 is T_2, the combined water level attains to the maximum.

6. ACKNOWLEGEMENTS

The authors would like to express hearty thanks to the Kanto Regional Construction Bureau, the Kisogawa Work Office, the Mie Work Office, the Keihin Work Office, the Arakawa Work Office, the Edogawa Work Office of the Ministry of Construction and the Oceanographical Division of the Japan Meteorological Agency for providing us with valuable data and support.

7. REFERENCES

Konishi, T. and T. Kinosita (1983): Studies on the river invasion of the storm surge (I). *Report of the National Research Center for Disaster Prevention, 31*, 67-87.

Konishi, T. and T. Kinosita (1985): Studies on the river invasion of the storm surge (II). *Report of the National Research Center for Disaster Prevention, 34*, 13-42.

Tsuji, Y. (1981): On the high tide and wind waves caused by typhoon 7920. *Report of the National Research Center for Disaster Prevention, 25*, 155-168.

Unoki, S. (1968): Studies on the tide in rivers. *Report of the 15th Coastal Engineering in Japan*, 228-235.

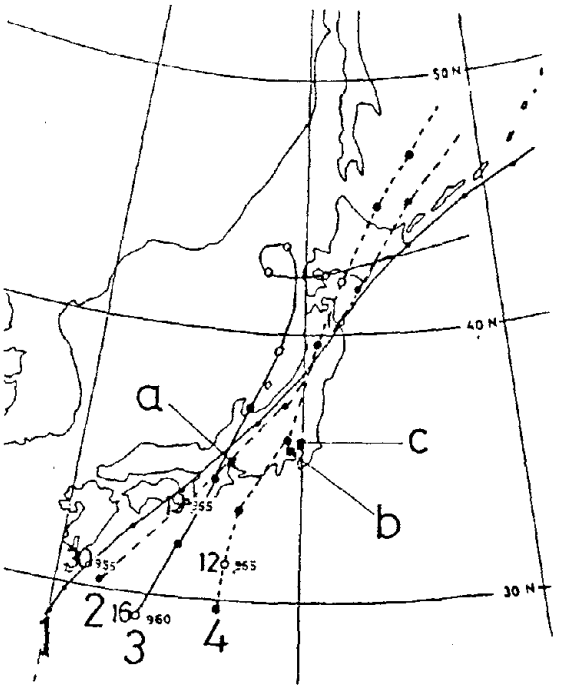

Fig. 1 Storm surges occurred at (a) the Kiso river, (b) the Tsurumi river, and (c) the Arakawa river. The tracks of the typhoons: 1 indicates typhoon 20 in 1979 (7920), 2 = 7916, 3 = 7220, 4 = 8218.

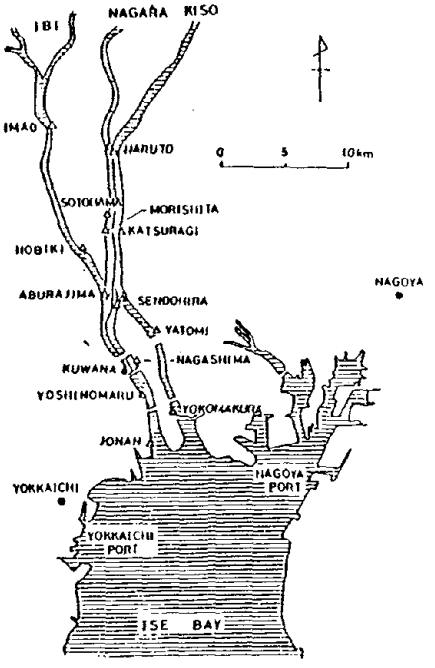

Fig. 1a Water level stations (Δ) and weather stations (●) around the Kiso river system.

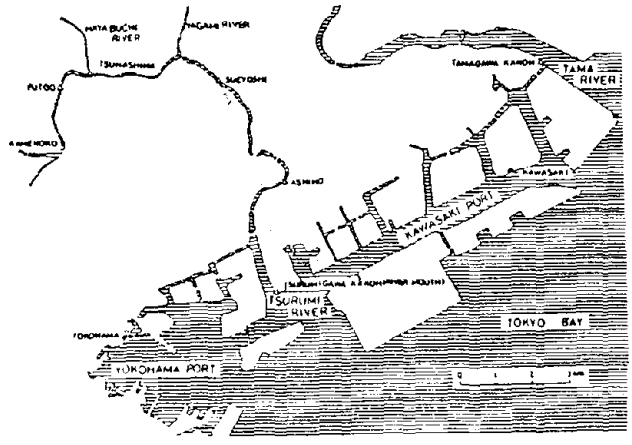

Fig. 1b Water level stations (△) and tidal stations (●) around the Tsurumi river.

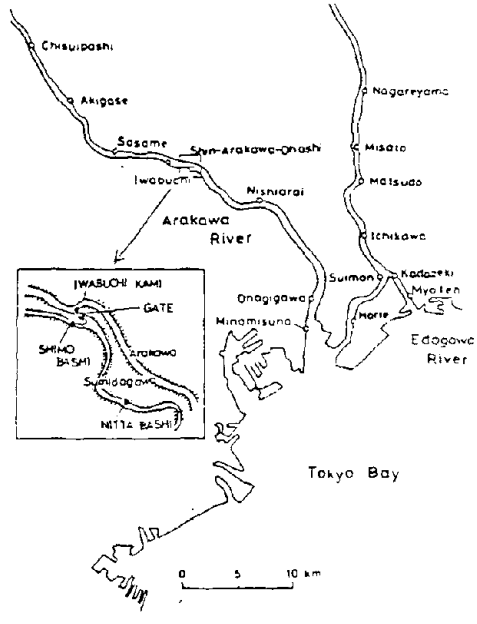

Fig. 1c Water level stations (○) around the Arakawa (or Ara) river.

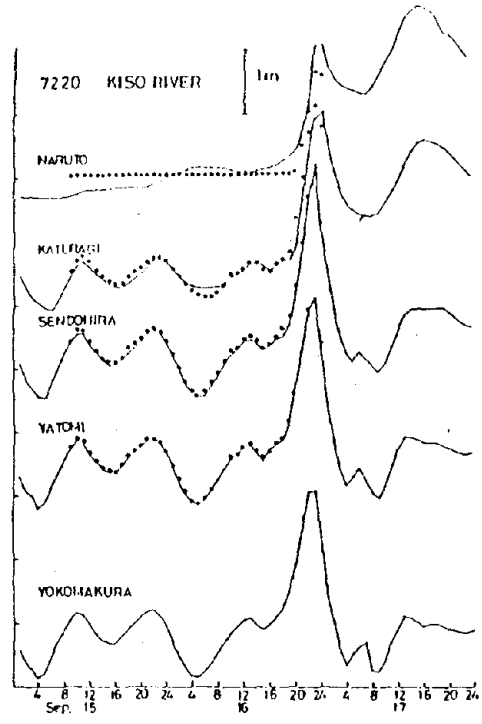

Fig. 2 Solid lines show observed water levels along the Kiso river, typhoon 7220. 0's show the computed water levels for $Cd = 4 \times 10^{-3}$ and $n = 0.025$.

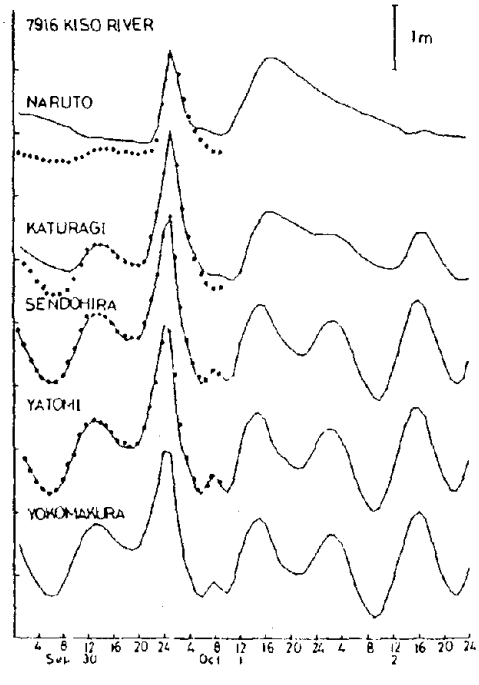

Fig. 3 Same as Fig. 2, except for typhoon 7916.

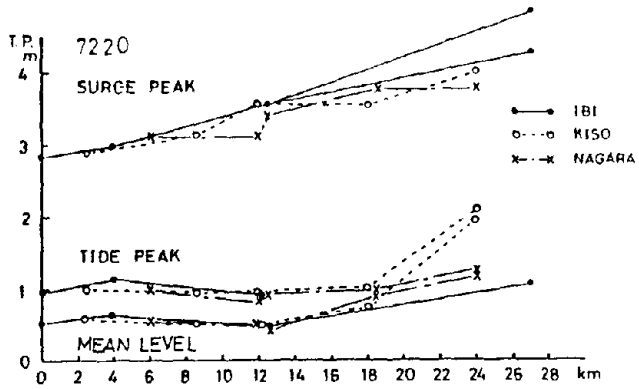

Fig. 4 Storm surge peaks, astronomical tide peaks and mean water levels with the distance from the river mouths, typhoon 7220.

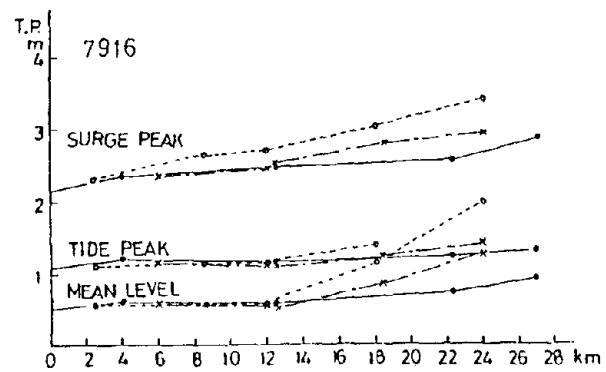

Fig. 5 Same as Fig. 4, except for typhoon 7916.

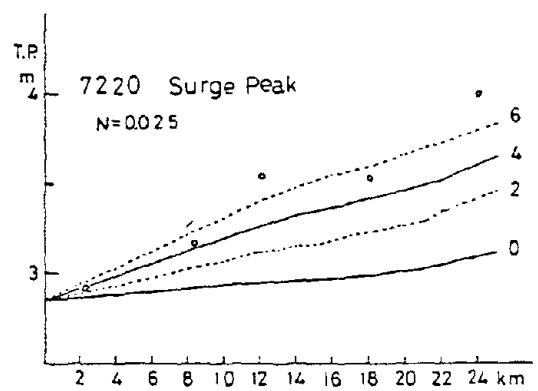

Fig. 6a Computed results of the surge peaks, typhoon 7220. 0's are observed values. n is equal to 0.025. The numerals in the figure correspond to the drag coefficients with the unit 10^{-3}.

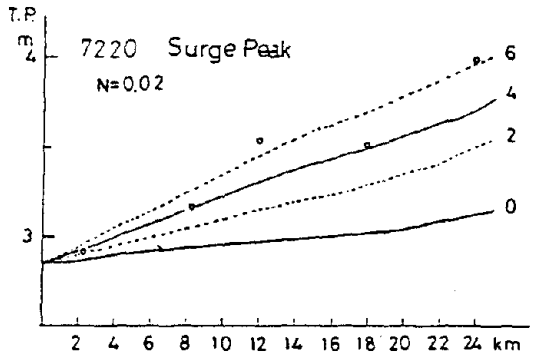

Fig. 6b Same as Fig. 6a, n is equal to 0.02.

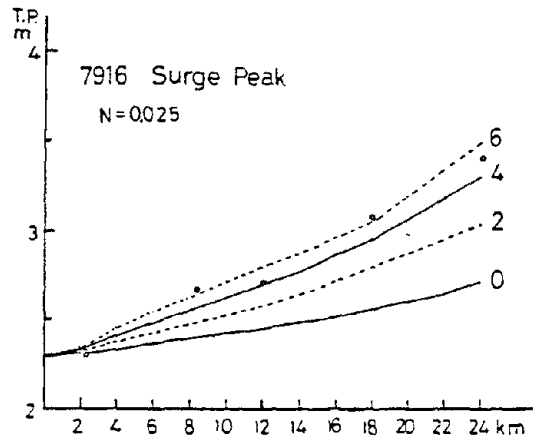

Fig. 7a Same as Fig. 6a, except for typhoon 7916.

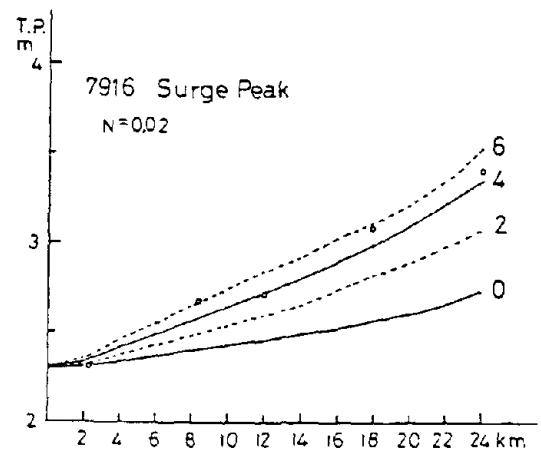

Fig. 7b Same as Fig. 7a, n is equal to 0.02.

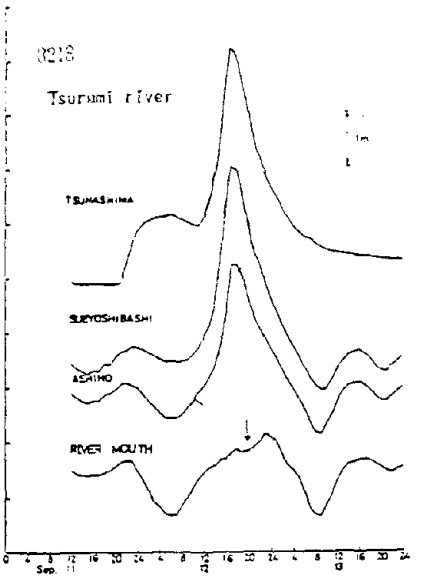

Fig. 8 Observed water levels along the Tsurumi river, typhoon 8218. An arrow indicates the time of the nearest passing of the typhoon.

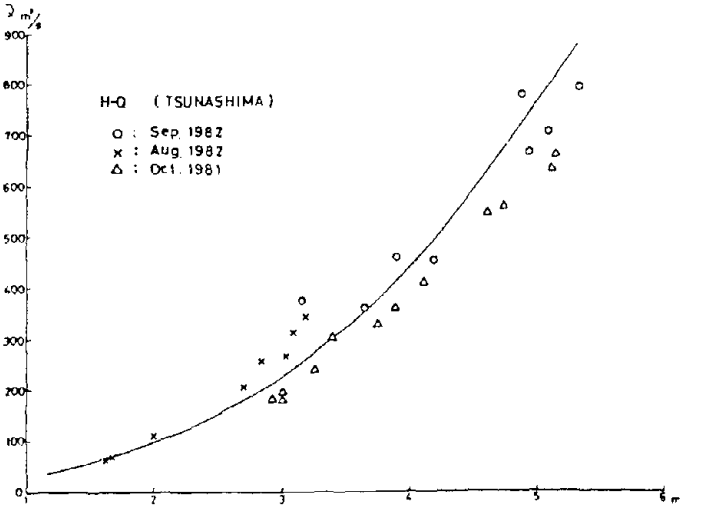

Fig. 10 Relation between water level and discharge at Tsunashima. The curve is obtained by the calculation with Eqs. (1) and (2) under the assumption of stationary state.

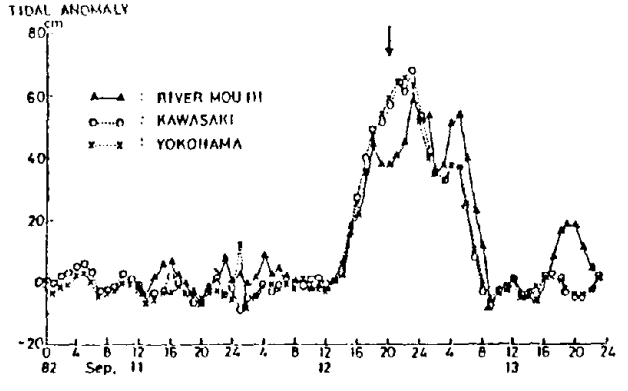

Fig. 9 Tidal anomalies observed at the river mouth, Kawasaki and Yokohama, typhoon 8218.

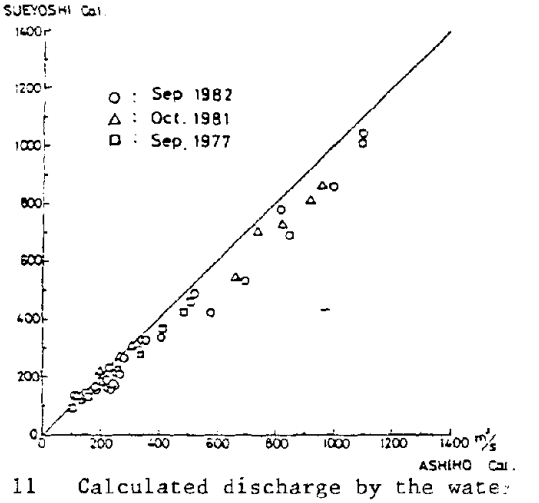

Fig. 11 Calculated discharge by the water level gradient, Ashiho-the mouth vs. that of Sueyoshi-the mouth.

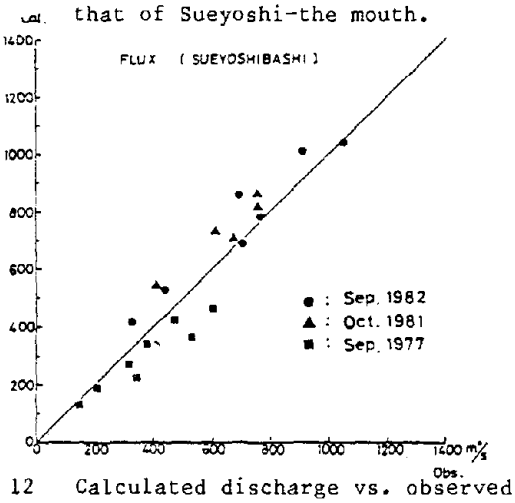

Fig. 12 Calculated discharge vs. observed discharge.

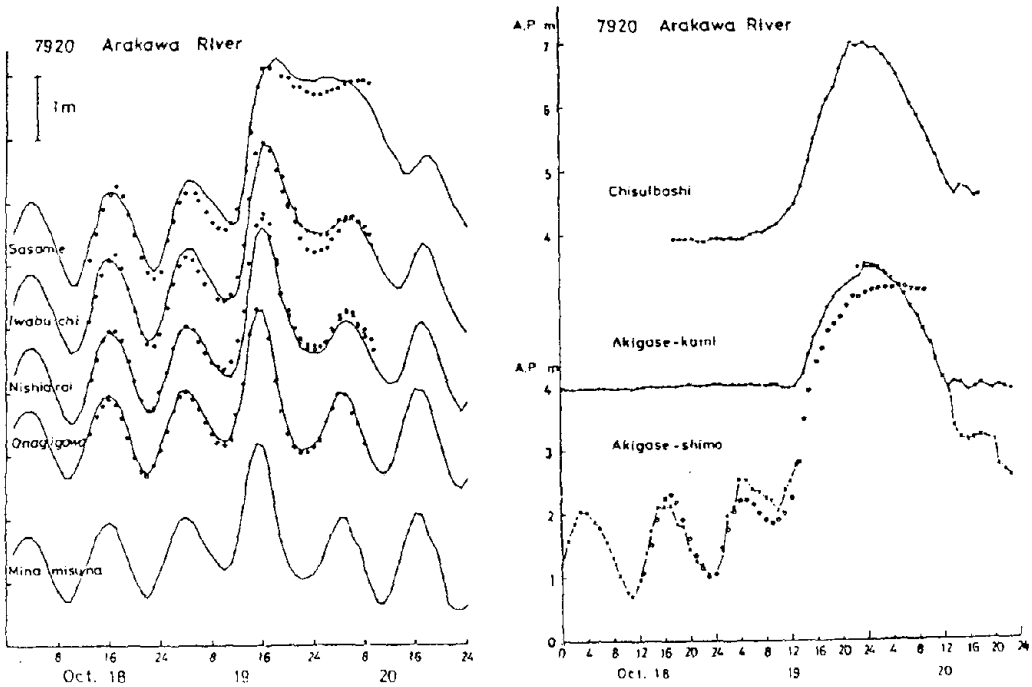

Fig. 13 Water level hydrographs along the Arakawa river. 0's are calculated and ●'s are observed at the time of the discharge observation.

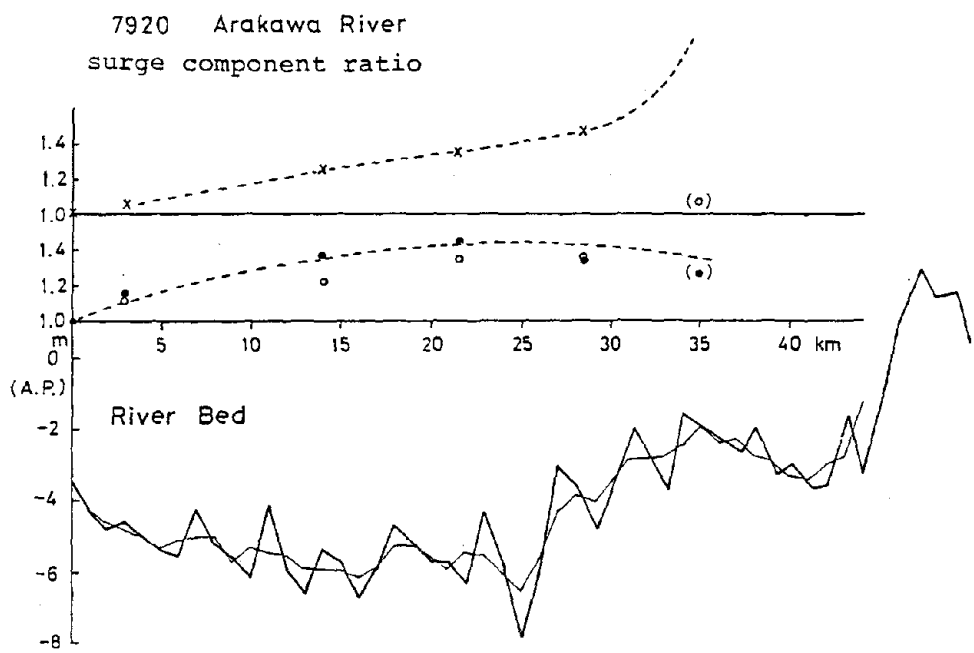

Fig.14 Amplitude ratio(✕), the surge component(O is refered to the observation and ● to the calculation) and the river bed and its running mean with the distance from the river mouth.

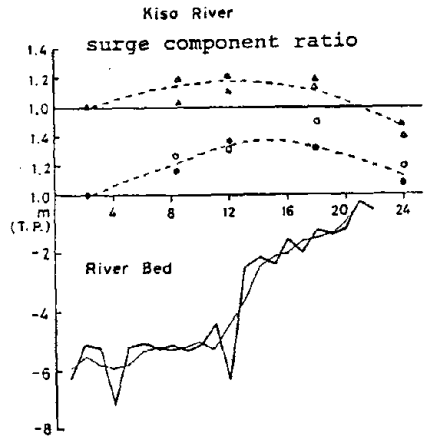

Fig.15 Same as Fig.14 for the Kiso river, the typhoon 7220(○, △) and the typhoon 7916(●, ▲)

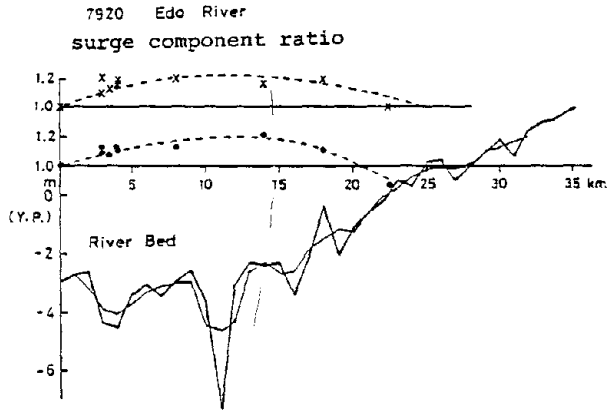

Fig.16 Same as Fig.14 for the Edo river, the typhoon 7920.

A SDOF MODEL TO ANALYZE EARTHQUAKE RESPONSE OF A FULL-SCALE SEVEN-STORY REINFORCED CONCRETE STRUCTURE

BY

Manabu Yoshimura*
Shin Okamoto**
Vladimir Sigmund†

ABSTRACT

If initial assumptions about the single-degree-of-freedom (SDOF) modeling of a multi-story reinforced concrete (RC) structure are reasonable, and the hysteretic model used is capable to reasonably simulate inelastic behavior of the structure under earthquake excitation, it is believed that earthquake responses of the structure, such as time history of displacements and maximum displacements, base shear and base moment can be reasonably well simulated by the use of a SDOF system of the structure.

In order to verify this, a SDOF model of a full-scale seven story RC structure built and tested at BRI, Tsukuba, Japan, was studied. In the study, input acceleration was used, which was the same as the one used during the test, and initial skeleton curve characteristics of the structure were also derived from the test. Feasibility of common hysteresis models for force-displacement relationship of reinforced concrete was studied by comparing the calculated response to the measured.

In the second phase of the study, results from the chosen SDOF model of the structure subjected to different base motions with different intensities, were used to predict the general response behavior of the structure.

Keywords: Earthquakes; Hysteretic model; SDOF

1. INTRODUCTION

The response of a structure to the excitation caused by an earthquake are fundamental to earthquake resistant design. If a variety of parametric studies can be easily and economically performed using a simple SDOF model and the results obtained adequately reproduce the behavior of the real structure, then the practical importance of such a model is verified. However, there are many practical problems in reducing a MDOF structure to a SDOF model and in evaluating its hysteretic properties. In most pratical cases, we can only make reasonable estimates of the deflection mode shape, properties of the initial skeleton curve and the hysteretic behavior of a structure.

This paper studies the possibility to simulate earthquake responses of the SDOF system of a full-scale seven-story RC structure by using common-type hysteretic models. It is also attempted in this paper to predict the response of the structure for different base motions with different intensities.

2. DESCRIPTION OF THE STRUCTURE

The full-scale seven-story RC structure was built and tested as part of the US-Japan Cooperative Research Program utilizing Large-Scale Testing Facilities at the Building Research Institute, Ministry of Construction, Tsukuba, Japan.[1,2] The building was designed and constructed in accordance with normal construction specifications and practices (Fig. 1). It had three longitudinal bays and two transverse spans. Cross sections of columns are 500 by 500 mm, and cross sections of beams are 300 by 500 mm and 300 by 450 mm, respectively, in longitudinal and transverse directions. The structure has a shear wall thickness of 200 mm in the middle frame. It was placed parallel to the loading direction. The building was tested by performing the "SDOF Pseudo Dynamic" (SPD) earthquake response test procedure.[1,2,3] Load was applied by use of eight actuators which were controlled to keep inverted triangular lateral load distribution during the test. The details of the structure and test can be found in Reference 1.

3. INPUT GROUND MOTION

The intensity of earthquake motions was varied in four test runs of the SPD test to yield expected roof level displacements (Fig. 2). The earthquake record used in the test was modified from the original record, and free vibration tests were performed between pseudo dynamic test runs to study the change in period and damping. In this way, by combining the consecutive pseudo dynamic tests, in which the next test stage is started immediately after the previous free vibration test is finished, the behavior of the structure from its initial intact stage to the

* Building Research Institute, Planning Department.
** Building Research Institute, Production Department.
† Building Research Institute, Visiting Scholar, on leave from University of Zagreb, Yugoslavia.

last damaged stage, was simulated. The second, third and fourth pseudo dynamic tests, together with free vibration tests, were considered in this paper.

4. MEASURED STRUCTURAL BEHAVIOR

Observed behavior of the test structure is presented in the form of the roof level displacement waveform and hysteretic behavior of the roof level displacement and base shear during the test sequences of SPD-2, 3 and 4. Measured time history of the displacement response is given in Fig. 3 and hysteretic behavior, together with interpolated initial curve, is shown in Fig 4.[1,5]

5. DERIVATION OF EQUIVALENT SDOF MODEL

The differential equation of motion for an undamped equivalent SDOF model representing MDOF system, as derived in Reference 1, is:

$$Me * \ddot{X}e + Pe = -Me * \ddot{X}o$$

where:

$Me = \Sigma MrUr$ (equivalent mass)

$\beta = Me/\Sigma MrUr^2$ (mode participation factor)

$Xe = (1/\beta)X$ (equivalent displacement)

$Pe = \Sigma PrUr$ (equivalent force)

(Ur) (mode displacement vector)

(Mr) (story mass vector)

(Pr) (external force vector)

$\ddot{X}o$ (ground acceleration)

X (time-varying function)

Numerical integration of the differential equation of motion is performed by Newmark's β method with the value of β equal to 0.167. Mode displacement vector, story mass vector and external force distribution vector, taken from Reference 1, are as follows:

(Ur) = (1.00; 0.85; 0.696; 0.540; 0.384; 0.234; 0.102)

(Mr) = (0.156; 0.173; 0.173; 0.173; 0.173; 0.173; 0.187) ($t * sec^2/cm$)

(Pr) = (21.75; 18.75; 15.75; 12.75; 9.75; 6.75; 3.75) (ton)

β , Me and coefficients which correlate Pe and Xe to the base shear Q1 and roof level displacement X7 of the structure are:

$\beta = 1.422$

$Me = 0.643$ ($t * sec^2/cm$)

$Q1 = 1.457\ Pe$

$X7 = 1.422\ Xe$

Initial equivalent stiffness Ke of the SDOF system was derived from the first mode period T of the structure:[1,4]

$$Ke = Me * (2\pi/T)^2$$

By substituting T = 0.448 sec, it becomes:

$$Ke = 126\ t/cm$$

6. HYSTERETIC MODELS

In this paper, three different common hysteretic models were used to simulate hysteretic behavior of the structure. They dominantly represent flexural behavior of the RC. The primary curve is symmetric about its origin and is represented either by bilinear or trilinear lines. The models are extensively described in the literature and just their main characteristics are outlined herein.

a) Degrading Trilinear (D-tri) Hysteretic Model (Fukada, 1969)

It is presented in Fig. 5 and its main characteristics are: 1) the envelope curve is trilinear, 2) stiffness continuously degrades with increasing maximum displacement amplitudes after yielding and the cracking point controls fatness of a hysteretic loop (hysteretic energy dissipation).*

b) Modified Clough Degrading Stiffness Model (Clough, Johnston, 1966)

It is described in Fig. 6. Its main characteristics are: 1) the envelope curve is bilinear, 2) stiffness degrades with the increase of a maximum displacement and unloading stiffness degrades in a form of $Kr = Ky * (2Dy/(Dmax - Dmin))^A$ (meaning of the symbols used in obvious from the figure, and when the value of A = 0 , then Kr is equal to Ky).

---

* Using the symbols shown in Fig. 5, unloading stiffness Kr is expressed as:

$$Kr = Kc * ALF$$

where:

$$ALF = (Fmax - Fmin) * Dy/Fy/(Dmax - Dmin)$$

c) Takeda Hysteretic Model (Takeda, Sozen, Nielsen, 1970)

Its main characteristics are shown in Fig. 7 and are summarized as follows: 1) the envelope curve is trilinear, 2) stiffness degrades with increasing maximum displacement, and unloading stiffness degrades in a form of:

$$Kr = (Fc + Fy)/(Dc + Dy) * ABS(Dy/Dm)^{A}$$

where Dm defines Dmax or Dmin with respect to the direction.

7. RESULTS OF ANALYSIS

A primary curve for different hysteretic models was chosen so that stiffness properties and hysteretic energy dissipation capacity are as similar as possible to the measured values (Figs. 8, 9 and 10). The effect of different hysteretic models on the response is investigated through comparisons of the measured and calculated responses, such as:

a) roof level displacement time histories,

b) maximum displacements and base shear,

c) maximum displacements at two phases of the test (SPD-3 and 4),

d) free vibration periods, and

e) roof level displacement and base shear relationship.

7.1 Behavior of SDOF Model with D-tri Hysteresis Rule

Fitting of the initial curve to the measured is shown in Fig. 8, and properties of the models selected are presented in Table 1. Comparisons on the above terms are described below.

a) The calculated roof level displacement time histories are shown in Fig. 11. For all three models shown in the figure, the response waveforms were similar, but they poorly matched the measured waveforms, in other words, response amplitudes were much underestimated especially in medium- and low-level amplitude oscillations. The calculated response was usually shifted due to residual deformations remaining at the end of SPD-3.

b) A comparison is presented in Table 2. Calculated displacement maxima were very sensitive upon the assumption of cracking level and yielding level (D1 and D3). Base shear was less sensitive to the assumed force level.

c) A comparison is presented in Table 3. Maximum calculated displacements were much underestimated during the SPD-3 phase of the test, while somewhat more reasonable results were obtained for the SPD-4 phase.

d) As shown in Table 4, the free vibration period after the SPD-3 phase of the test was calculated much shorter than the measured value. Such shorter periods calculated after SPD-3 are closely related to the fact that the maximum calculated displacement during SPD-3 are much smaller than the measured value. Stiffness degradation of the SDOF model was considerably different (smaller) even in SPD-4 than the observed behavior of the structure.

e) Calculated roof level displacement and base shear relations are shown in Fig. 12. It bears not much resemblance to the measured behavior; the calculated hysteresis show considerably smaller stiffness degradation properties and larger hysteretic energy dissipation properties than the measured one.

Through the above discussion, it is made clear that behavior of the analytical SDOF model using the D-tri hysteresis rule poorly represents behavior of the RC structure even when the skeleton curve properties are precisely known.

7.2 Behavior of the SDOF Model with Modified Clough Hysteresis Rule

Assumed initial curve is shown in Fig. 9, and properties of the models are presented in Table 5. Comparisons on the previously mentioned terms (a) through (e) are described below.

a) The calculated roof level displacement time histories of the selected three models are presented in Fig. 13. High-amplitude oscillations were favorably represented in all models. When the initial stiffness was low (model C1), the SPD-2 phase was poorly represented; in other words, the calculated displacements were much larger than the measured ones. This is because the structure remained dominantly in the elastic range in this test run. When the initial stiffness was equal to stiffness of the intact structure derived from free vibration tests (model C2), SPD-2 phase oscillations were well represented but the model failed to represent medium-level oscillations (SPD-3) after pronounced excursions in the inelastic domain. For the initial stiffness value set equal to 0.6 of the intact stage (model C3), the model favorably represented measured waveforms throughout the entire period of the test.

b) Maximum displacements and base shears were favorably represented for all five models with different initial stiffness values, see Table 6. The bigger unloading stiffness value (A) considerably increased displacements and base shear in both directions (comparison of models C1 and C4). Note that a smaller unloading stiffness (bigger coefficient) means smaller hysteretic energy dissipation properties, hence, leading to larger response values. Lower yield level decreased base shear but did not have much effect on displacement (comparison of models C1 and C5).

c) As shown in Table 7, all models except C4 failed to represent maximum displacements during the SPD-3 phase of the test, and especially underestimated negative displacements considerably.

d) Calculated amd measured free vibration periods are presented in Table 8. Observation of the stiffness degradation through comparison of those periods at the end of each test phase shows favorable representation of the stiffness degradation of all models.

e) Calculated roof level displacement and base shear relationship are shown in Fig. 14. Observed and calculated behavior compare favorably.

Based on this analysis using the Clough hysteresis rule, it was found that: 1) the overall response of the structure can be favorably represented except for low-level amplitude oscillations, and 2) response is not very sensitive to the estimation of the yield level or unloading stiffness.

7.3 Behavior of SDOF Model with Takeda Hysteresis Rule

Fitting the initial skeleton curve to the measured one is shown in Fig. 10. As this hysteresis rule was deemed as representing the observed behavior most favorably among the three hysteresis rules, more extensive studies were made for this rule than the others. Characteristics of selected models are presented in Table 9 in which main parameters are yield level, post-yield stiffness and unloading stiffness, etc. Comparisons on the previously mentioned terms (a) through (e) are described below.

a) Calculated waveforms of different models are presented in Fig. 15. They represented the measured one favorably during all stages, except for low-level oscillations, say, 11 to 13 sec. in some models (T1 and T9). The best results were obtained for model T2 when the stiffness characteristics of the model fitted in the best way with the measured one. Observed and calculated response waveforms showed no appreciable sensitivity of the shape when the parameters of the initial curve were changed within 20 percent in area. The study included the effect of changes in the following parameters: yield level, yield displacement, post-yield stiffness, unloading stiffness degradation parameter and mass of the model, which could be different if a different assumption about the displaced mode shape was used. Within this area (+-10 percent of the ideally fitted initial curve), the calculated response waveform is a favorable representation of the observed one.

b) Comparison of the calculated and measured maxima is presented in Table 10. For all models whose initial skeleton curve was different with ±10 percent range of the ideally fitted one, calculated maximum values of the displacement and base shear were within ±10 percent of the measured values with few exceptions. Variation of maxima, owing to the specific changes in the initial curve, is presented in Fig. 16. The ratio of the calculated and measured maximum values is plotted against the assumptions of the initial curve. Those figures show us only a trend of the influence of certain parameters, and general characteristics cannot be derived as this trend is changing with the changes in the input motion characteristics. Note that this ratio tends to increase as the unloading stiffness coefficient increases. This trend can be explained by the fact that assumption of a larger coefficient results in smaller hysteretic energy dissipation properties.

c) Comparison of the calculated and measured values of displacements is presented in Table 11. Calculated negative maximum displacement values for the SPD-3 phase of the test showed greater sensitivity of input parameters. This was especially pronounced for changes in yield displacement (T2 and T8) and unloading stiffness degradation parameters (T2, T9 and T10). Variations of the ratio of calculated and measured maximum displacements for two phases of test (SPD-3 and 4) are plotted in Fig. 17 against the change in the initial skeleton curve parameters. This also verifies the previously stated conclusion under b). This behavior can be explained on the basis of the sensitivity of the response upon the frequency content of the input motion. Stiffness behavior of the model sometimes failed to represent the change of the structural stiffness, in other words, stiffness of the analytical model degrades only when the response point exceeds the previously obtained maximum displacement, while the structure degrades continuously in

stiffness. If in this case the response displacement spectra for a certain ground motion has drastic changes within the area of interest, slight changes in the effective stiffness of a model can have perceptible influence on calculated waveforms. The sensitivity of the response to the unloading stiffness coefficient, stated under b), is also observed in this table.

d) Comparison of the calculated and measured free vibration periods is presented in Table 12. From that, it can be concluded that the models represented change of stiffness properties favorably. It is also obvious, however, that those models which failed to represent maximum values of the SPD-3 test phase (T4, T9 and T13), showed rather poorer representation of the change of stiffness.

e) Calculated roof level displacement and base shear relation are presented in Fig. 18. As can be seen by comparing it to the measured one in Fig. 4, the overall hysteretic shape calculated for the SDOF model has favorable similarities with the measured one.

Through the above discussion, it can be concluded that the SDOF model of the full-scale structure using the Takeda hysteresis rule with initial stiffness properties and hysteretic energy dissipation capacity as similar as possible to the measured one with allowable tolerance of $\pm$10 percent, gave favorable representation of the earthquake response of the structure.

8. EARTHQUAKE RESPONSE OF THE FULL-SCALE STRUCTURE AGAINST DIFFERENT BASE MOTIONS

In the preceding part, it was proven that by reasonably estimating the initial curve, and using a reasonable hysteretic model, we could favorably simulate the earthquake response of a full-scale seven-story structure. In this part, model T2 was used which fitted initial stiffness properties and the hysteretic behavior of the structure in the best manner to study the response of the full-scale test structure under different base motions with different intensities.

Input base motions were modified in terms of the peak acceleration from the following earthquake records:

El Centro 1940 N-S with intensities of 300, 400 and 500 gals.

Tokachi Oki 1968 E-W with intensities of 300, 400 and 500 gals.

Miyagi Oki 1978 N-S with intesnities of 300, 400 and 500 gals.

Obtained maximum values of displacements and base shear are shown in Table 13. Calculated values of the response of Miyagi Oki and Tokachi Oki Earthquakes were larger than that of the El Centro record, although the acceleration was of the same intensity. This result is believed to be correlated to different energy contents of those earthquakes. Behavior of the structure would be satisfactory if it was exposed to those base motions with the intensities of 300 and 400 gals, considering maximum obtained displacement and base shear. Furthermore, it is believed that this structure can withstand with sufficient safety even the base motions with 500 gal intensity.

9. CONCLUSIONS

By using a reasonable hysteretic model and assuming an appropriate initial skeleton curve of the structure, we favorably simulated the behavior of a full-scale seven-story structure using a SDOF response analysis. Common flexural-type hysteretic models of RC were used, namely: D-tri, Clough and Takeda models. The Takeda model showed the most favorable results, and calculated response with this model was less sensitive to changes in the input parameters.

In the second part of the study, the response of the tested structure was predicted using the SDOF model under different base motions with different acceleration amplitudes. From the study, the tested structure was found to withstand safely based motions with a 400 gal intensity and even with a 500 gal intensity.

10. REFERENCES

1) S. Okamoto, et al.; A Progress Report on The Full-Scale Seismic Experiment of a Seven-Story Reinforced Concrete Building;" BRI Research Paper No. 94.

2) T. Kaminosono, et al.; SDOF Pseudo Dynamic Test;" US-Japan Cooperative Research; VIII WCEE; San Francisco, CA; 1984.

3) S. Okamoto, et al.; Techniques for Large-Scale Testing at BRI Large Structure Test Laboratory;" BRI Research Paper No. 101.

4) Y. Kitagawa, et al.; Dynamic Characteristics of a Full-Scale Seven-Story Reinforced Concrete Building;" BRI Research Paper No. 108.

5) M. Yoshimura; Ultimate Moment Resisting Capacity; US-Japan Cooperative Research; VIII WCEE; San Francisco, CA; 1984.

Table 1. Model Characteristics (D-tri Model)

Model	Kc t/cm	Me ton	Dc cm	Dy cm	Fy ton	γ
D1	126	630.8	0.85	3.83	201	0.045
D2	126	630.8	0.59	3.83	201	0.045
D3	126	630.8	0.59	3.83	188	0.045

Note γ : stiffness reduction coef. after yielding (relative to Kc)

Table 2. Comparison of Response Maxima (D-tri Model)

Model	Calc. shear ton	Meas. shear ton	Error %	Calc. disp. cm	Meas. disp. cm	Error %
D1	371.0	432.5	-14.3	18.9	34.2	-44.7
	-411.3	-439.0	-6.3	-25.8	-32.1	-10.0
D2	440.2		1.8	30.8		-10.0
	-433.3		-1.3	-29.6		-7.8
D3	389.6		-9.9	25.4		-25.7
	-402.7		-8.3	-27.6		-14.0

Table 3. Comparison of Displacement Maxima at Two Phases of the Test (D-tri Model)

Model	Calc. disp. cm	Meas. disp. cm	Error %	Calc. disp. cm	Meas. disp. cm	Error %
	SPD-3			SPD-4		
D1	12.0	23.8	-49.6	18.9	34.2	-44.7
	-4.1	-22.3	-81.6	-25.8	-32.1	-19.5
D2	18.7		-21.4	30.8		-10.0
	-7.3		-67.3	-29.6		-7.8
D3	17.6		-26.1	25.4		-25.7
	-5.3		-76.2	-27.6		-14.0

Table 4. Comparison of Free Vibration Periods
(D-tri Model)

Model	Calc. sec.	Meas. sec.	Error %	Calc. sec.	Meas. sec.	Error %
	SPD-3			SPD-4		
D1	0.53	1.16	-54.3	1.13	1.36	-16.9
D2	0.66		-43.2	1.23		-9.6
D3	0.61		-47.5	1.15		-15.4

Table 5. Model Characteristics
(Modified Clough Model)

Model	Ky t/cm	Me ton	Fy ton	γ	A
C1	52.5	630.8	201	0.11	0.40
C2	126.0	630.8	201	0.05	0.60
C3	74.5	630.8	201	0.05	0.60
C4	52.5	630.8	201	0.11	0.60
C5	52.5	630.8	188	0.11	0.40

Note γ : stiffness reduction coef. after yielding
(relative to Ky)
A : coef. defining unloading stiffness

Table 6. Comparison of Response Maxima
(Modified Clough Model)

Model	Calc. shear ton	Meas. shear ton	Error %	Calc. disp. cm	Meas. disp. cm	Error %
C1	437.8	432.5	1.2	29.9	34.2	-12.6
	-434.0	-439.0	-1.1	-29.3	-32.1	-8.7
C2	459.8		6.3	28.1		-17.8
	-467.5		6.5	-29.3		-8.7
C3	406.1		-6.2	33.5		-2.1
	-388.6		-12.5	-28.9		-10.0
C4	505.2		16.8	41.3		20.8
	-449.8		2.5	-32.0		-0.3
C5	419.8		-2.9	29.8		-12.9
	-414.5		-5.6	-27.3		-15.1

Table 7. Comparison of Displacement Maxima at Two Phases of the Test (Modified Clough Model)

Model	Calc. disp. cm	Meas. disp. cm	Error %	Calc. disp. cm	Meas. disp. cm	Error %
	SPD-3			SPD-4		
C1	21.3	23.8	-10.5	29.9	34.2	-12.6
	-16.7	-22.3	-25.1	-29.3	-32.1	-8.7
C2	14.9		-37.4	28.1		-17.8
	-10.4		-53.4	-29.3		-8.7
C3	22.7		-4.6	33.5		-2.1
	-14.7		-34.1	-28.9		-10.0
C4	24.0		0.8	41.3		20.8
	-24.0		7.6	-32.0		-0.3
C5	22.4		-5.9	29.8		-12.9
	-17.8		-20.2	-27.3		-15.0

Table 8. Comparison of Free Vibration Periods (Modified Clough Model)

Model	Calc. sec.	Meas. sec.	Error %	Calc. sec.	Meas. sec.	Error %
	SPD-3			SPD-4		
C1	1.00	1.16	-13.8	1.20	1.36	-11.8
C2	1.00		-13.8	1.13		-16.9
C3	1.07		-7.8	1.33		-2.0
C4	1.04		-10.3	1.33		-2.0
C5	1.09		-6.0	1.23		-9.6

Table 9. Model Characteristics (Takeda Model)

Model	Kc t/cm	Me ton	Dc cm	Dy cm	Fy ton	γ	A
T1	126	630.8	0.85	3.83	201	0.045	0.60
T2	126	630.8	0.85	3.83	188	0.045	0.60
T3	126	630.8	0.85	3.83	188	0.040	0.60
T4	126	630.8	0.85	3.83	188	0.040	0.50
T5	126	630.8	0.85	3.83	188	0.050	0.55
T6	126	630.8	0.85	3.83	188	0.050	0.60
T7	126	630.8	0.85	3.83	176	0.045	0.60
T8	126	630.8	0.85	4.36	188	0.045	0.60
T9	126	630.8	0.85	3.83	188	0.045	0.50
T10	126	630.8	0.85	3.83	188	0.045	0.70
T11	126	655.0	0.85	3.83	188	0.045	0.60
T12	126	655.0	0.85	3.83	201	0.045	0.60
T13	126	610.2	0.85	3.83	188	0.045	0.60

Note γ : stiffness reduction coef. after yielding (relative to Kc)
A : coef. defining unloading stiffness

Table 12. Comparison of Free Vibration Periods (Takeda Model)

Model	Calc. sec.	Meas. sec.	Error %	Calc. sec.	Meas. sec.	Error %
	SPD-3			SPD-4		
T1	1.07	1.16	-7.8	1.27	1.36	-6.6
T2	1.09		-6.0	1.29		-5.1
T3	1.07		-7.8	1.29		-5.1
T4	1.00		-13.8	1.29		-5.1
T5	1.04		-10.3	1.20		-11.8
T6	1.08		-6.9	1.28		-5.9
T7	1.08		-6.9	1.31		-3.7
T8	1.11		-4.3	1.32		-2.9
T9	1.04		-10.3	1.21		-10.1
T10	1.11		-4.3	1.37		0.7
T11	1.09		-6.0	1.31		-3.7
T12	1.04		-10.3	1.31		-3.7
T13	1.04		-10.3	1.28		-5.9

Table 13. Maximum Response Values against Different Base Motions

Earthquake rec.	300 gal		400 gal		500 gal	
	disp. cm	shear ton	disp. cm	shear ton	disp cm	shear ton
El Centro 1940 NS	10.9	305.4	16.5	337.9	18.4	349.0
	-9.7	-298.9	-17.8	-345.5	-25.7	-391.5
Tokachi Oki 1968 EW	29.5	413.8	43.2	493.2	48.3	522.7
	-29.6	-414.5	-37.9	-462.7	-45.5	-506.5
Miyagi Oki 1978 NS	20.2	359.5	35.3	447.6	47.0	515.4
	-25.0	-387.6	-35.4	-447.7	-48.0	-521.6

Table 10. Comparison of Response Maxima (Takeda Model)

Model	Calc. shear ton	Meas. shear ton	Errpr %	Calc. disp. cm	Meas. disp. cm	Error %
T1	461.6	432.5	6.7	34.5	34.2	0.9
	-447.8	-439.0	2.0	-32.1	-32.1	0.0
T2	445.5		3.0	35.0		2.3
	-416.3		-5.2	-30.0		-6.5
T3	423.0		-2.2	34.3		0.3
	-394.6		-10.1	-28.8		-10.3
T4	399.4		-7.7	29.7		-13.2
	-389.4		-11.3	-27.8		-13.4
T5	455.7		5.4	33.6		-1.8
	-433.1		-1.3	-30.1		-6.2
T6	472.8		9.3	36.3		6.0
	-437.2		0.5	-30.7		-4.3
T7	427.5		-1.2	34.8		1.8
	-390.6		-11.1	-28.5		-11.1
T8	443.8		2.6	35.4		3.5
	-408.1		-7.0	-29.3		-8.7
T9	415.4		-4.0	29.8		-12.9
	-410.3		-6.5	-28.9		-10.0
T10	483.4		11.8	41.5		21.3
	-423.4		-3.5	-31.2		-2.8
T11	445.8		3.1	35.0		2.3
	-407.3		-7.2	-28.4		-11.5
T12	467.7		8.1	35.5		3.8
	-438.2		-0.2	-30.5		-5.0
T13	445.8		3.1	35.2		2.9
	-407.3		-7.2	-31.2		-2.8

Table 11. Comparison of Displacement Maxima at Two Phases of the Test (Takeda Model)

Model	Calc. disp. cm	Meas. disp. cm	Error %	Calc. disp. cm	Meas. disp. cm	Error %
	SPD-3			SPD-4		
T1	20.4	23.8	-14.0	34.5	34.2	0.9
	-17.6	-22.3	-21.1	-32.1	-32.1	0.0
T2	22.0		-7.6	35.0		2.3
	-19.9		-10.8	-28.8		-6.5
T3	21.7		-8.9	34.3		0.3
	-19.5		-12.6	-28.8		-10.3
T4	21.2		-10.9	29.7		-13.2
	-16.0		-28.3	-27.8		-13.4
T5	21.3		-10.5	33.6		-1.8
	-17.5		-21.5	-30.1		-6.2
T6	21.7		-8.8	36.3		6.0
	-19.6		-12.1	-30.7		-4.3
T7	23.7		0.4	34.8		1.8
	-21.3		-4.5	-28.5		-11.1
T8	22.9		-3.8	35.4		3.5
	-16.3		-27.0	-29.3		-8.7
T9	21.3		-10.5	29.8		-12.9
	-16.0		-28.3	-28.9		-10.0
T10	23.1		-3.0	41.5		21.3
	-24.0		7.6	-31.2		-2.8
T11	22.8		-4.2	35.0		2.3
	-21.1		-5.4	-28.4		-11.5
T12	21.3		-10.5	35.0		3.8
	-18.1		-18.8	-30.5		-5.0
T13	20.1		-15.5	35.2		2.9
	-16.4		-26.5	-31.2		-2.8

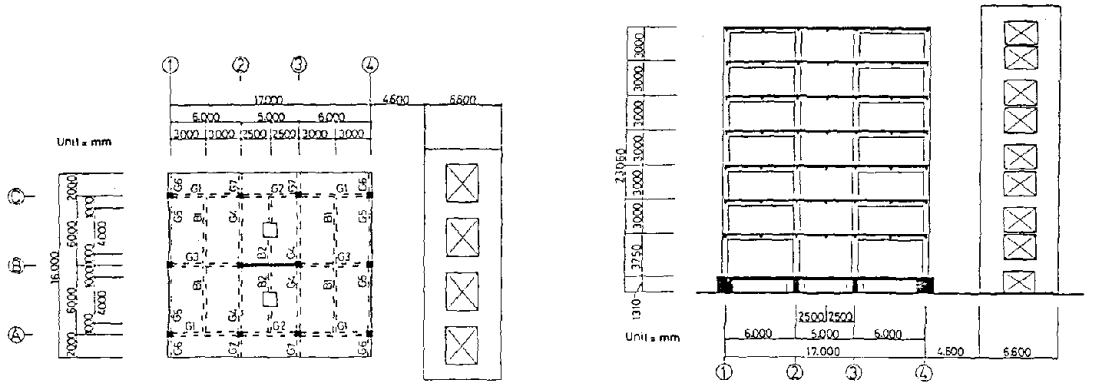

a) Plan b) Elevetion

Fig.1 Outline of the Test Building

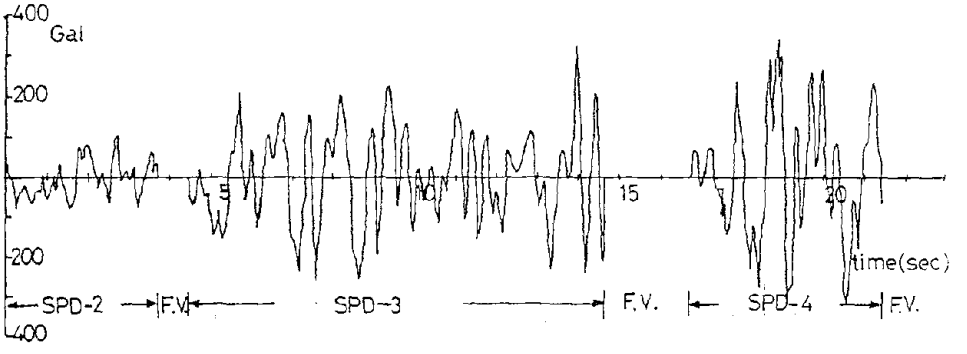

Fig.2 Input Acceleration Data

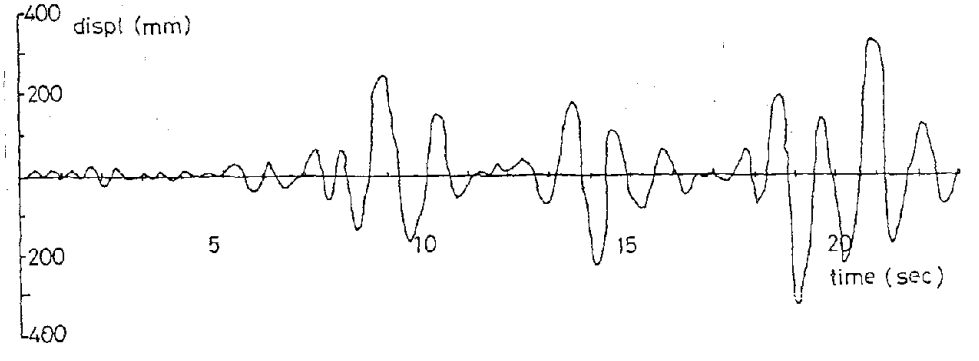

Fig.3 Measured Time History of Roof Level Displacement

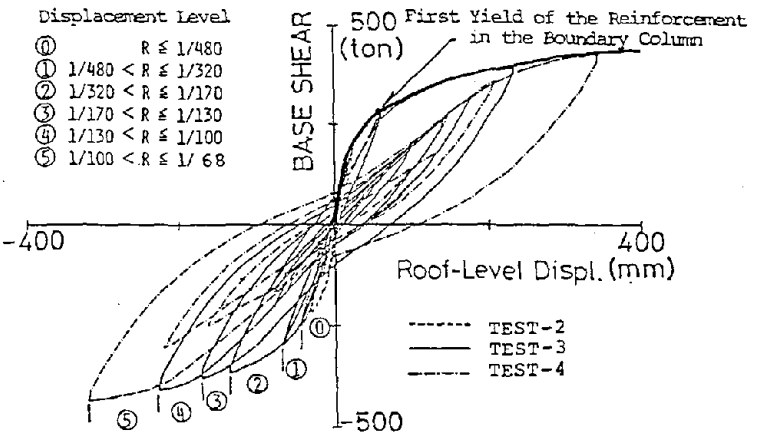

Fig.4 Measured Roof Level Displacement and Base Shear Relationship

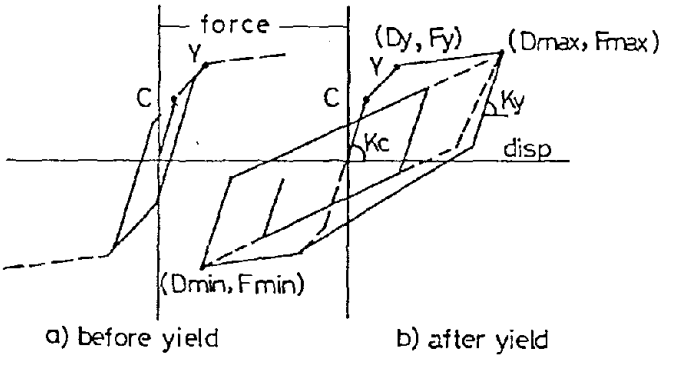

Fig.5 Hysteresis Rule of Degrading Trilinear Model

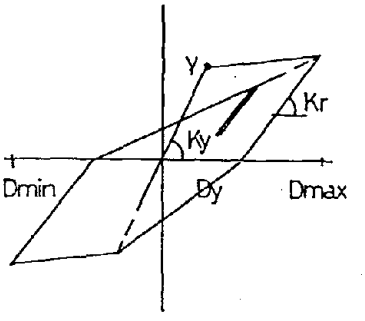

Fig.6 Hysteresis Rule of Modified Clough Model

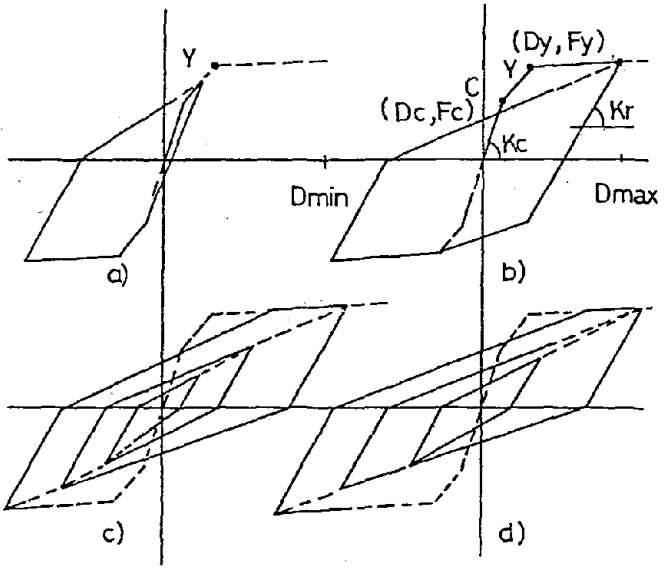

a) unloading after cracking
b) unloading after yielding
c) small amplitude reversals
d) small amplitude reversals

Fig.7 Hysteresis Rule Takeda Model

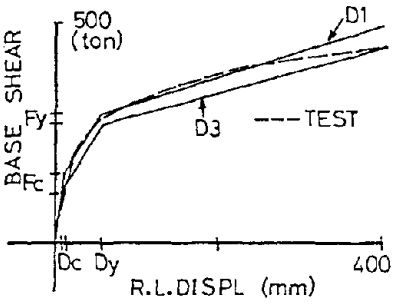

Fig.8 Initial Curve of D-tri Model

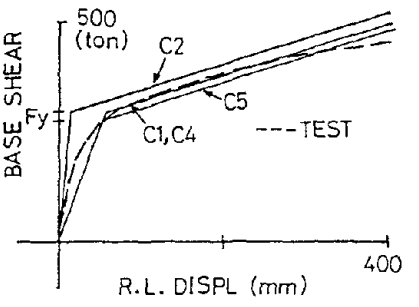

Fig.9 Initial Curve of Modified Clugh Model

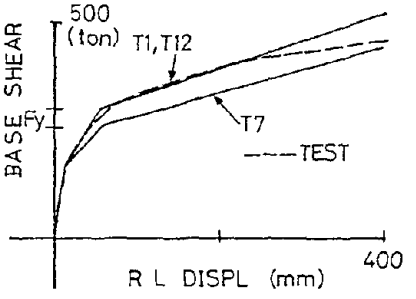

Fig.10 Initial Curve of Takeda Model

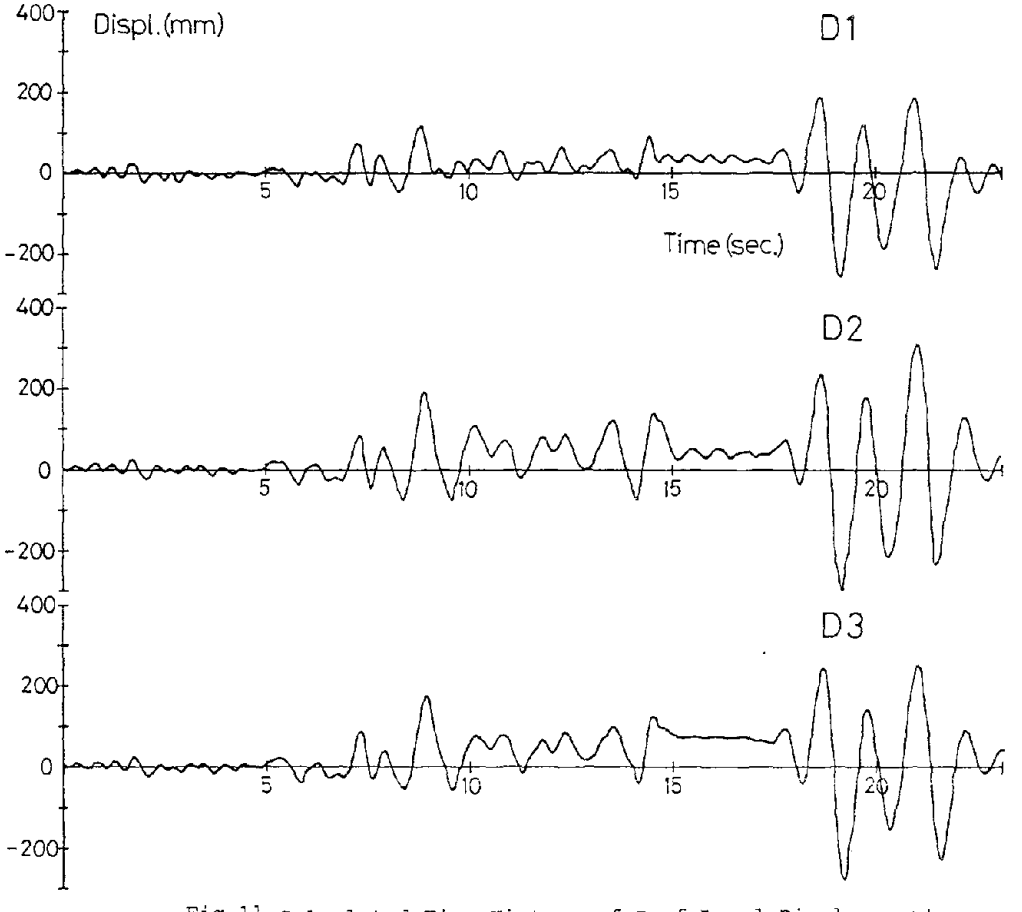

Fig.11 Calculated Time History of Roof Level Displacement (D-tri Models)

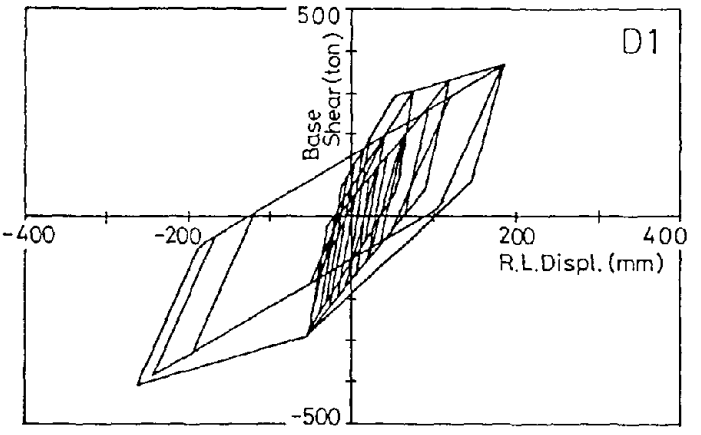

Fig.12 Calculated Roof Level Displacement - Base Shear Relationship
(D-tri Model)

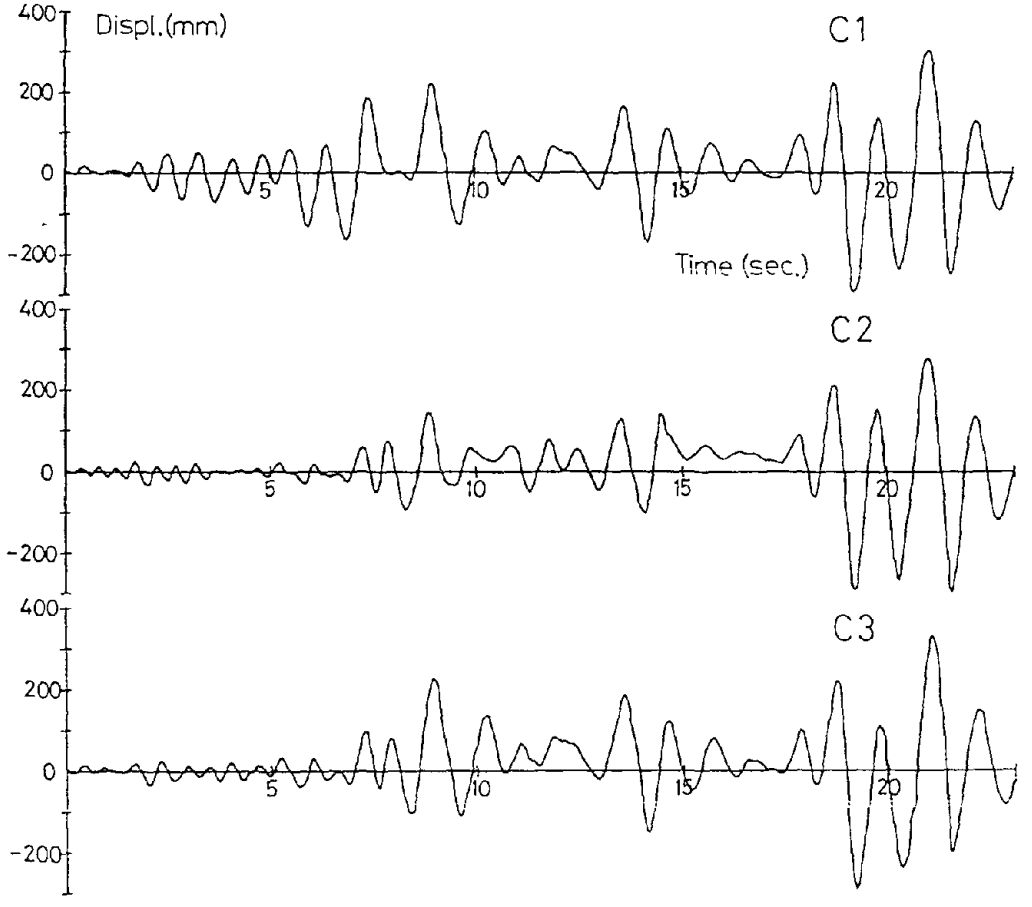

Fig.13 Calculated Time History of Roof Level Displacement
(Modified Clough Model)

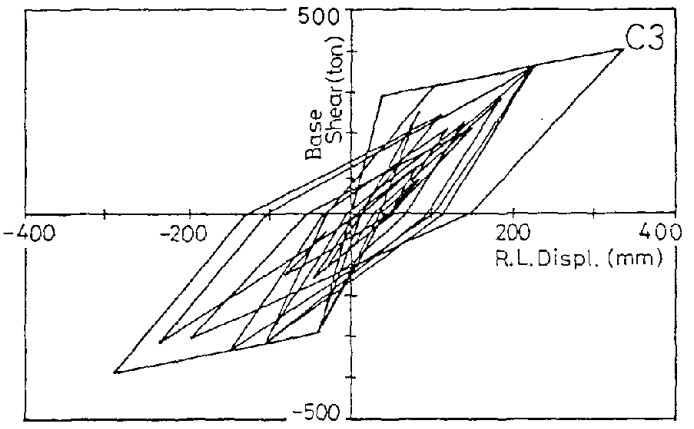

Fig.14 Calculated Roof Level Displacement - Base Shear Relationship
(Modified Clough Model)

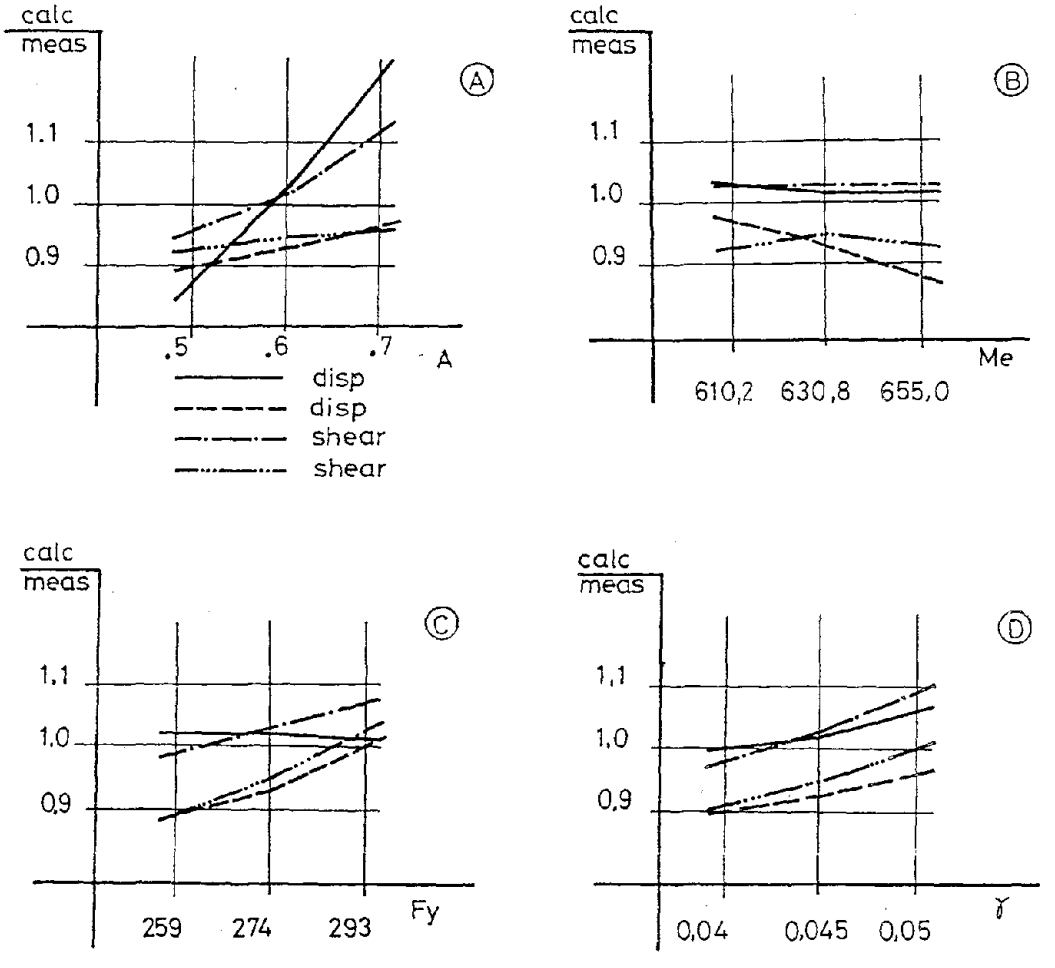

Fig.16 Sensitivity of Maxima to Different Parameters
(Takeda Model)

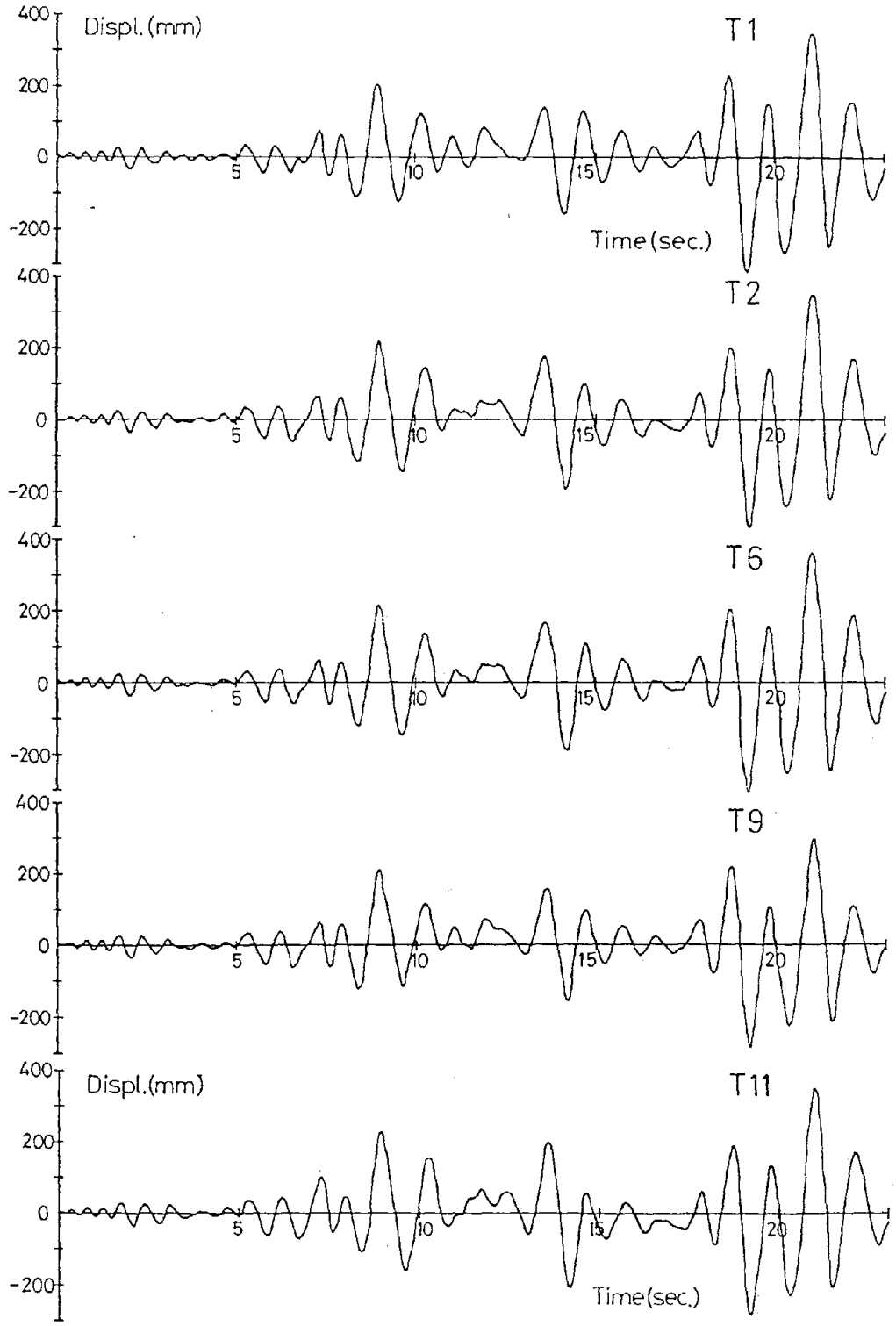

Fig.15 Calculated Time History of Roof Level Displacement
(Takeda Model)

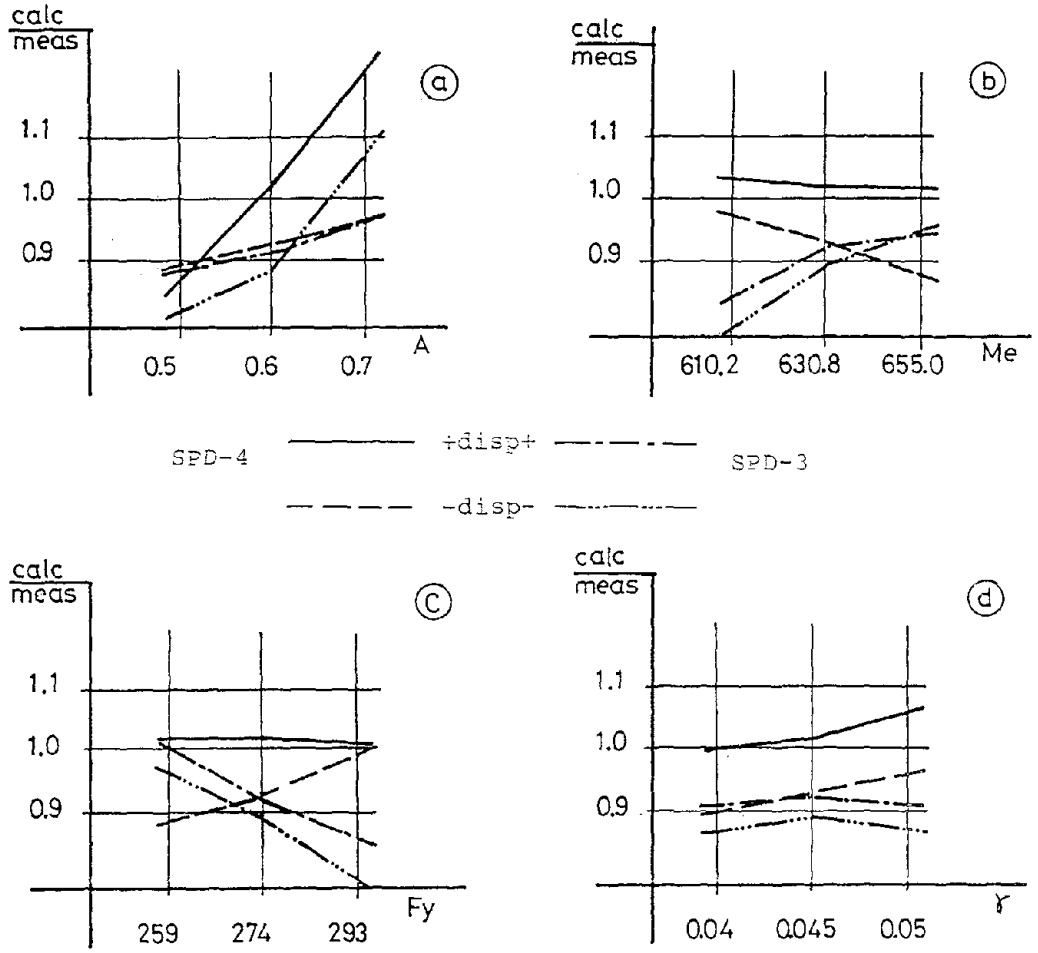

Fig.17 Sensitivity of Maximum Displacements to Different Parameters during Two Phases of the Test (Takeda Model)

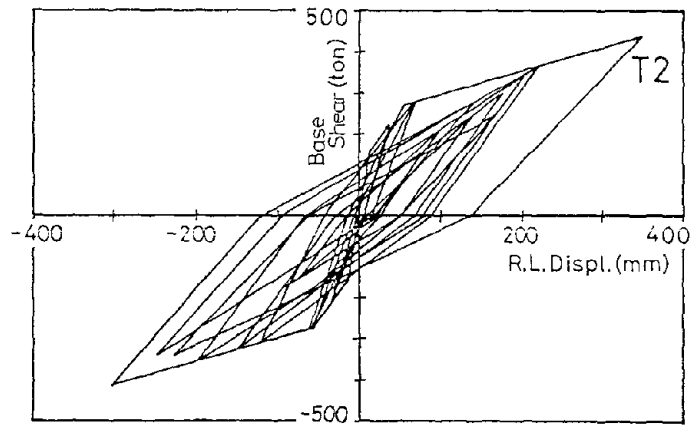

Fig.18 Calculated Roof Level Displacement Base Shear Relationship (Takeda Model)

SETTLEMENT OF APPROACHING EMBANKMENTS TO BRIDGES CAUSED BY THE NIHONKAI CHUBU EARTHQUAKE

by
Yasuyuki Koga (1) and Eiichi Taniguchi (2)

ABSTRACT

The Nihonkai Chubu Earthquake, May 26, 1983 caused settlements of approaching embankments to bridges. This paper evaluates the relationship between the damage rate of approaching embankments and various factors based on the results of an investigation on actual damage to approaching embankments. Factors influencing the damage to approaching embankments are: epicentral distance, soil condition of embankment, soil condition of ground and micro-relief. It is concluded that an approaching concrete slab is very effective to maintain a smooth road surface after earthquakes.

Keywords: Earthquakes, embankments, settlements

1. INTRODUCTION

The Nihonkai Chubu Earthquake, May 26, 1985, caused severe damage to roads, especially to approaching embankments to bridges as shown in Photo 1. Investigations were performed on the actual damage to all the approaching embankments to bridges of national roads, main local roads and prefectural roads in Aomori and Akita Prefecture by means of questionnaires. The results of investigations are described.

2. PURPOSE

The purpose of the investigation was to find factors which affect earthquake-induced damage to approaching embankments and to obtain basic data for developing countermeasures to prevent settlement of approaching embankments by analyzing those factors.

3. METHOD

The investigation was performed on all the approaching embankments to bridges, with a height of over 1 m and a length of over 15 m, on national roads, main local roads and prefectural roads in Aomori and Akita Prefecture. All the approaching embankments under above mentioned conditions were investigated regardless of the occurrence of damage. If a bridge had two approaching embankments at both sides, it is counted as two sites If an approaching part to bridge was in a cut slope, it is was not investigated.

A questionnaire form was sent to Aomori, Noshiro and Akita Local Construction Office of Ministry of Construction and Aomori and Akita Prefecture. These questionnaires were filled out by staff members of such organizations and were collected and analyzed.

A questionnaire form also included figures of the investigation location, plan, longitudinal and transverse sections and photographs of the damaged embankments.

Items of investigation included the characteristics of the embankment (height, soil name of embankment, etc.), subsoil conditions (micro-relief, depth of water table, etc.), and the characteristics of the abutments and failure patterns.

4. RESULTS AND DISCUSSIONS

Table 1 shows the number of investigation locations. A location is judged damaged if one of the following three conditions are satisfied:

1) The maximum settlement of the crest of embankment is over 5 cm, or cracks with the width of over 5 cm developed at the crest of embankment.
2) The slope of the embankment collapsed, or cracks with the width of over 5 cm developed at the slope.
3) The retaining wall tilted or collapsed or cracks with the width of over 1 cm developed at the retaining wall.

Table 1 shows that the number of all the investigation locations is 1673 and 97 locations were damaged, therefore the damage rate is 5.8%. The damage rate of approaching embankments (which will be called merely "the damage rate" in this paper) is defined as follows:

$$\text{Damage Rate of Approaching Embankments} = \frac{\text{Number of Damaged Locations}}{\text{Total Number of Approach Embankments}} \quad (1)$$

Fig. 1 shows the relationship between the epicentral distance and the damage rate. The epicentral distance of the investigation locations is between 80km and 240 km and the maximum epicentral distance of damaged locations is 219 km. Fig. 1 indicates that the damage rate is less than 5% at locations where the epicentral distance is over 170 km, and that the damage to approaching embankments mainly occurred in the region with the epicentral distance less than 170 km. In Fig. 1 the damage rate in the region with an epicentral distance less than 100 km is relatively low. This is because the region is located in Oga Penninsula

(1) Head, Soil Dynamics Div. P.W.R.I., Ministry of Construction, Tsukuba, Japan
(2) Senior Research Engineer,
Soil Dynamics Div. P.W.R.I., Ministry of Construction, Tsukuba, Japan

which consists of mountainous and hill sites with good subsoil conditions.

Fig. 2 shows the relationship between the soil condition of embankments and the damage rate. This figure indicates that the damage rate is low in the case for embankments made up of gravelly material. The gravelly material is defined as material whose content of gravel (grain size = 2 - 75 mm) is over 50% in weight. The Earth Work - Construction Manual (Japan Road Association, 1977) describes good material for backfill of retaining structures or buried structures as shown in Table 2. Although this regulation was determined with consideration of settlement of embankments during earthquakes, it is effective in preventing seismically induced settlements of embankments by requiring soil with a lot of gravel for backfill material.

Fig. 3 shows the relationship between the thickness of soft soil layer and the damage rate for gravelly and sandy ground and clayey ground. The thickness of soft soil layer is defined as follows:

Thickness of Soft Soil Layer (m) =

Sum of Thickness of Layers with N value < 10 at the depth of less than 10 m.

Fig. 3 indicates that the damage rate is higher at locations with soft layers over 4 m thick in gravelly and sandy ground and at locations over 8 m thick in clayey ground. It may be said that the damage rate increases for the softer ground.

The relationship between the micro-relief and the damage rate is shown in Fig. 4. The micro-relief classification was carried out by using "micro-relief classification map for flood control". When this map was not available at certain locations, the "land classification map" by the Economic Planning Agency was used. Figure 4 shows that reclaimed land, swamp or former swamp has higher damage rate and that the damage rate is as high as 9.4% in flood plains where most damaged locations were. The damage rate in sand dune is high because of liquefaction of sandy ground during earthquake.

Table 3 shows the relationship between abutment foundation type and the damage rate. In this figure the damage rate is high for spread foundation and it is low for pie and caisson foundation. This is because a rock layer is located near the ground surface which has a large resistance against earthquake loadings at locations where the spread foundation is used, and the ground has small resistance at locations where pile and caisson foundation is used.

Fig. 5 shows the relationship between the maximum settlement of embankment and the height of embankment. The maximum settlement of approaching embankment obtained in this investigation was 80 cm. Fig 5 indicates that about 90% of damaged approaching embankments had earthquake-induced settlements which is less than 10% of the height of embankment, and that the settlement at only one location exceeds 20% of the height of embankment

Table 4 shows the installation rate and damage rate of the approaching concrete slab. The approaching concrete slab is a reinforced concrete slab which is installed to prevent the gap between abutment and embankment as shown in Fig. 6. Table 4 shows that there were two locations where approaching concrete slab were installed and earthquake-induced settlement was observed. Actually at these two locations nonuniform settlement occurred for a long distance along the road, but a car could negotiate the roadway after earthquake. It can be concluded from Table 4 that the approaching concrete slab is very effective to keep the road open to traffic after an earthquake, because it is able to prevent an earthquake-induced gap between abutment and embankment. However attention should be paid to the fact that caving was observed under the approaching concrete slab as shown in Photo 2.

Therefore it is necessary to inspect if there is caving under the approaching concrete slab after a big earthquake and to fill the hollow with soil or mortar if it is found.

5. CONCLUSIONS

(1) The damage rate of approaching embankments to bridges was 5.8% in the Nihonkai Chubu Earthquake.
(2) The damage to approaching embankments to bridges mainly occurred in the region with an epicentral distance of less than 170 km.
(3) The damage rate of approaching embankments to bridges is low in the case that embankment consists of gravelly soil and high in the case when the embankment is located in reclaimed land, swamp or former swamp and sand dune in micro-relief.
(4) The settlement of 90% of all the damage approaching embankments to bridges is less than 10% of the height of embankment.
(5) The approaching concrete slab is very effective to keep the smoothness of road surface after earthquakes.

6. ACKNOWLEDGEMENTS

The authors express their appreciation to staff members of the Disaster Prevention Section of Road Bureau, Ministry of Construction, Planning Division and Road Division of Tohoku Local Construction Bureau, Aomori, Noshiro and Akita Local Construction Office, Aomori and Akita Prefecture for their cooperation on the investigation. The authors also thank Mr. Y. Sasaki, Head of Ground Vibration Division of PWRI for his advice.

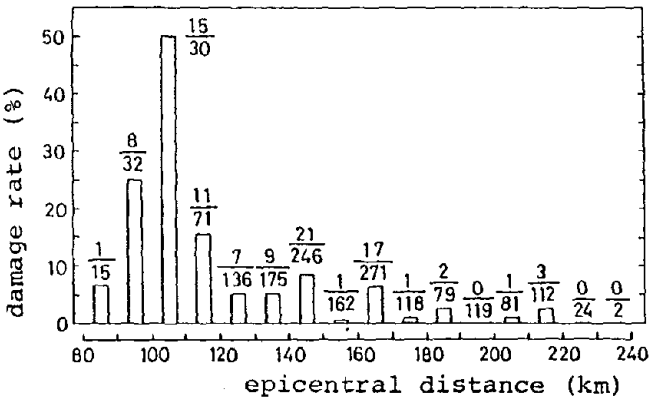

Fig.1 Epicentral distance and damage rate of approaching embankments to bridges

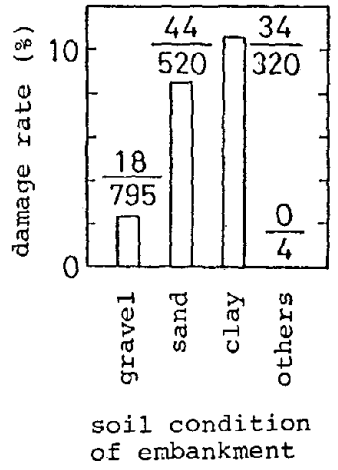

Fig.2 Soil condition of embankment and damage rate of approaching embankments to bridges

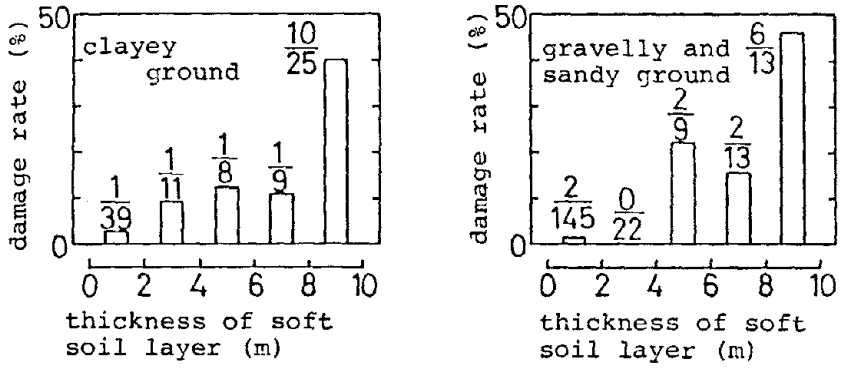

Fig.3 Thickness of soft soil layer and damage rate of approaching embankments to bridges

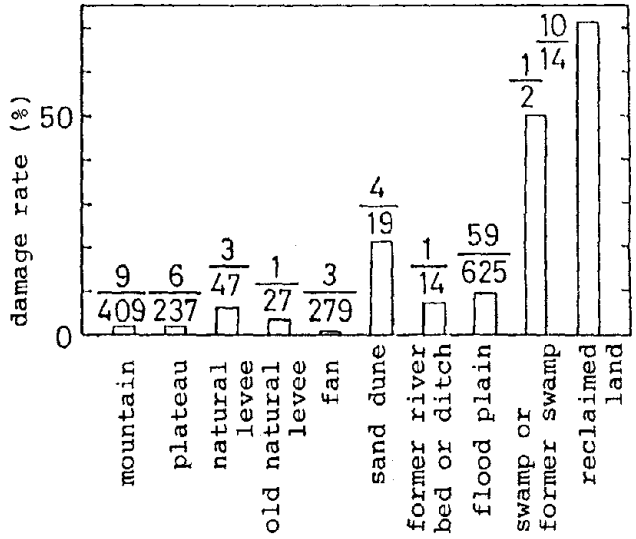

Fig. 4 micro-relief classification and damage rate of approaching embankments to bridges

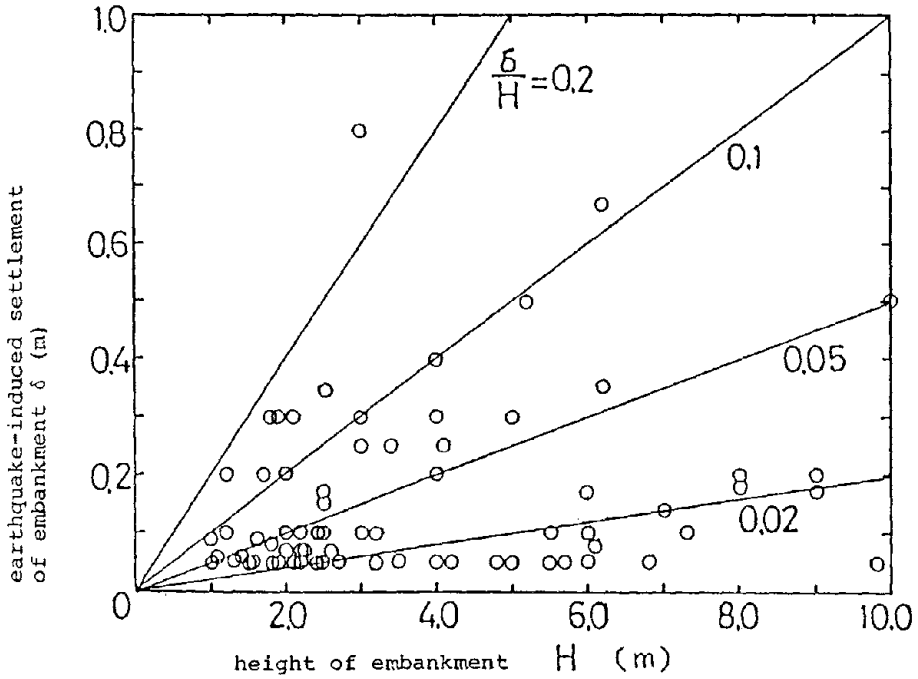

Fig.5 Earthquake-induced settlement of approaching embankments to bridges and the height of embankments

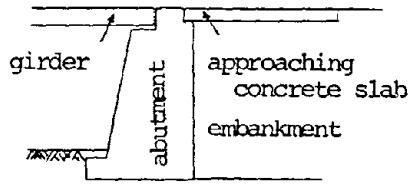

Fig. 6 Schematic view of approaching concrete slab

Table 1 Number of investigation points

organization		A not damaged	B damaged	A + B	B/(A + B) damage rate (%)
Ministry of Construction	Aomori Local Construction Office	120	0	120	0.0
	Akita Local Construction Office	100	3	103	2.9
	Noshiro Local Construction Office	56	4	60	6.7
total of Ministry of Construction		276	7	283	2.5
Akita Prefecture		991	35	1026	3.4
Aomori Prefecture		309	55	364	15.1
total		1576	97	1673	5.8

Table 2 Characteristics of good material for back fill (Earth Work-Construction Manual)

maximum grain size	100mm
percent finer (4.76mm sieve)	25 - 100%
percent finer (0.074mm sieve)	0 - 25%
plasticity index	less than 10

Table 3 Kind of foundation of abutment and damage rate of approaching embankment to bridges

kind of foundation	total	number of damaged points	damage rate (%)
direct	907	19	2.1
pile	522	51	9.8
caisson	10	1	10.0
unknown	234	26	11.1

Table 4 Effect of approaching concrete slab to prevent settlement of road surface

organization	number of approaching embankments to bridges A	number of points where approaching concrete slab was installed B	installation rate $\frac{B}{A}$ (%)	number of points where approaching concrete slab was installed and no settlement of road surface was observed C	$\frac{C}{B}$ (%)	number of points where approaching concrete slab was installed and settlement of road surface was observed D	$\frac{D}{B}$ (%)
Ministry of Construction	283	40	14.8	40	100	0	0
Akita Prefecture	1026	9	0.7	9	100	0	0
Aomori Prefecture	364	6	1.6	4	66.7	2	33.3
total	1673	55	3.3	53	96.4	2	3.6

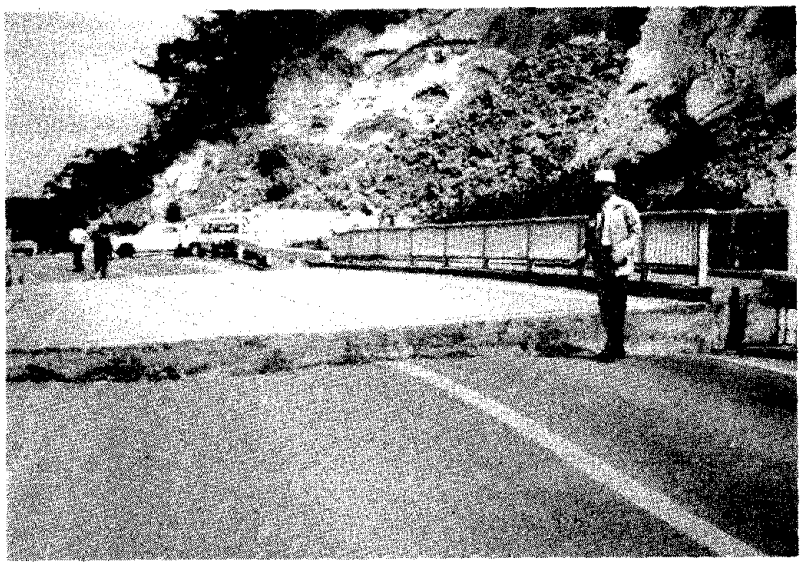

Photo. 1 Example of settlement of approaching embankment to bridge (settlement = 50 cm, height of embankment = 10 m)

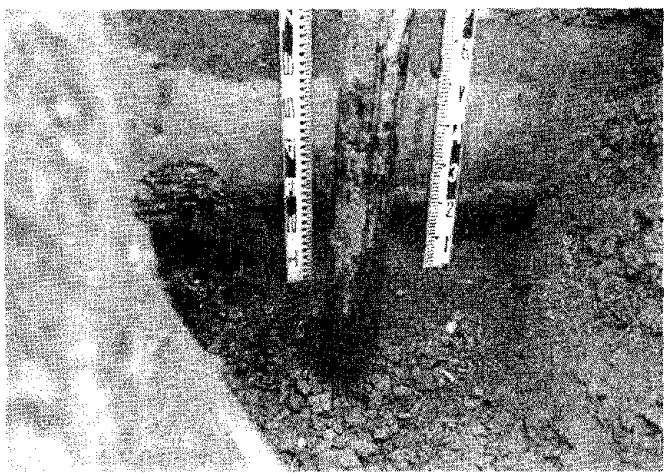

Photo. 2 Cave under the approaching concrete slab (this photograph was taken after the earthquake)

ROCK AVALANCHES AND SLOPE FAILURES INDUCED BY THE NAGANOKEN-SEIBU EARTHQUAKE, 1984

BY

Kohei Tanaka*, Norio Oyagi*, Takashi Inokuchi*, Shigetsugu Uehara*, and Hiroshi Takahashi*

ABSTRACT

A strong earthquake occurred at the southern foothills area of Mt. Ontake on September 14, 1984. A ridge, near the top of Mt. Ontake, collapsed and an immense amount of debris fell 13 km. This was one of the largest rock avalanches in history. Several large slope failures also occurred at Matsukoshi, Ontakekogen, and Takikoshi. In the majority of the failures, rupture surfaces were situated in layers of pumice from the Ontake volcano. These pumice layers contained halloysite which has less cohesion and a smaller friction angle than pumice layers containing allophane.

Key words: Avalanches, earthquake, landslides, slope failure.

1. INTRODUCTION

The Naganoken-Seibu earthquake in Japan on September 14, 1984, triggered several hundred landslides. One landslide was particularly large, with debris forming one of the largest rock avalanches in history. Other relatively large slope failures occurred in Matsukoshi, Ontakekogen, and Takikoshi. A total of 29 people were killed. This paper is a report of a survey conducted by the National Research Center for Disaster Prevention.

*National Research Center for Disaster Prevention.

2. THE NAGANOKEN-SEIBU EARTHQUAKE, 1984

The earthquake occurred at 8:48 in the morning on September 14, 1984, at a latitude of 35.807 N, longitude of 137.554 E, 1.1 km depth (data from the National Research Center for Disaster Prevention), and magnitude of 6.8. The epicenter was situated in an active area which has suffered many small earthquakes since 1976. Judging from the analysis of the earthquake vibration, this earthquake was caused by the lateral fault whose main stress direction is northwest to southeast, but the fault could not be located on the ground surface. The aftershock area had a width of 10 km from ENE to WSW and a depth of about 5km. The seismic intensity of the main shock was 4^{o} at the Japan Meteorological Agency at Iida, Suwa, and Kofu. However, at the mountainfoot area of Mt. Ontake it was though to be 6^{o} or more, because the maximum acceleration was estimated as about 370-390 gal, based on the condition of grave stones. Most slope failures were caused by this main shock (Fig. 1, 2, and 3, Uehara, et al. 1985).

3. THE GEOLOGY OF MT. ONTAKE

The earthquake occurred at the foothills area Mt. Ontake which is 3063 m high. The mountain is supported by Paleozoic formations and rhyolite in Cretaceous formations. The activity of Mt.

Ontake is divided into four stages (Kobayashi, 1975). In the first period, andesitic material formed a large stratovolcano. Then it was dormant for a long period, and the mountain body became heavily eroded. About eighty thousand years ago the second period began. Activity of rhyolitic magma characterized this new stage. At first, an enormous volume of pumice (Pm-I layer) erupted and simultaneously the caldera was formed at the center of the mountain body. An eruption of rhyolitic lava and pyroclastic rocks buried the caldera and formed a new mountain body during the third period. This was a period of active andesitic magma. Almost all the mountain body which we see now was then formed in the fourth period. As mentioned later, the pumice layers from the second period are related to large slope failures.

4. SLOPE FAILURES AND ROCK AVALANCHES

4.1 Ontake Kuzure - Failure at the Head of the Denjo River and - Rock Avalanche

4.1.1 The Situation of the Disaster

The severest damage caused by this earthquake is that which occurred near the top of Mt. Ontake and brought a rock avalanche from the Denjo River to the Otaki River through the Nigorigawa River. This rock avalanche killed at least fifteen persons. This failure was the biggest one induced by this earthquake. The scale of this failure was approximately 1300 m long, 450 m wide, and 180 m in maximum depth; an estimated 3.6×10^7 m^3 of material was removed (The Japan Geographical Survey Institute, 1984).

4.1.2 Topography

The source area is situated on a ridge which stretches in a southeasternly direction from the central cone of the volcano. Its elevation is from 2550 m to 1850 m. The topography of this failure follows the valley, so that it looks as if a steep valley which borders the main scrap begins from the ridge. Its form is a long strip and at the lower part it curves to the west.

4.1.3 Geology

This failure occurred in the area which is covered by the material from the third active period of Mt. Ontake. The order of rock layers is: volcanic breccia, tuff including pumice, scoria and then lava from the lower part. The source area of the failure is broadly covered by the tuff layer including the pumice as mentioned above. This tuff layer is very soft and wet, and striations are carved on the surface of it (Photo 1). This layer was formed by deposits falling on the eroded valley and then scoria and lava layers covering it. Erosion then produced a ridge there. The cause of the failure is thought to be that the earthquake caused a fracture in the tuff layer, which worked as the rupture surface so that the rock body above it fell down as one large block. Judging from a longitudinal section of the source area, if the initial velocity had been great, almost all the debris would have jumped over the front valley and then flowed toward the Suzugasawa River. Yet, actually almost all the debris flowed down

the Denjo River. Therefore, the initial velocity could not have been great (Fig. 5).

4.1.4 Flow and Sedimentation of Debris

4.1.4.1. Rock Avalanche. The debris flow which was caused by this great failure flowed down along the Denjo River - Nigorigawa River - Ontake River and finally arrived at Korigase 13 km down the river. This debris flow was thought to have been a "mud flow", "pulverulent body flow" or "rock avalanche" by many researchers right after the disaster. There is a strong possibility judging by the observed data, that the main body of debris contained very little water. And it was observed from the inside structure of the debris that big blocks with cracks had flowed so that it cannot be thought that all the debris was in a powdery condition. Thus the debris flow is described as a rock avalanche. In this paper, the area of the flow means from the lower part of source area to the Denjo River and the Nigorigawa River. And the area of sedimentation means along the Otaki River. But actually debris sedimentation was observed along the Nigorigawa River, too (Fig. 4).

4.1.4.2 Denudation of the Valley-Wall. The denudation of the valley-wall was observed in the whole of the flow area. Especially, it reached a point 100 m from the bottom of the valley in the Denjo River. This shows that a huge debris aggregation, baring the valley as high as that place, flowed down at high velocity. Because the top level of denudation is undulating, it is thought that the rock avalanche flowed down irregularly. As there is little sedimentation of debris in the flow area, most of the debris flowed down to the sedimentation area with the aggregation (Photo 2).

4.1.4.3. Banded Sedimentation Structure. One of the characteristic features of the flow area is found on flat places where the rock avalanche overtopped the ravine wall. That is the banded sedimental structure in which different colored rocks are disposed in a striped structure. It is observed on the opposite flat ridge of the source area putting into the Denjo River, on the flat ridge 2 km downstream from the source area and on a flat part of the valley wall 3 km downstream. This structure has patterns like geological banded folding. The cause is thought to be a part of the rock aggregates kept their geological structure and overtopped the bend of the valley without becoming mixed. The difference of the color in the banded structure must have come from difference of original rock faces (Photo 3).

4.1.4.4. Double Layer Structure Sediment of Rock Avalanche. The sedimentation of rock avalanche appears as a double layer structure. The upper thin layer contains much water and appears as a muddy layer, but the lower layer consists of debris aggregation with little water. The upper muddy layer has fragments of wood and little

roots, but these are not observed in the lower layer. The upper layer is generally thin (under 1 m), but the thickness of the lower layer is thought to be 30-40 m, by comparison with the original topography. The material in the lower layer must have come from the source area of the failure, but the origin of the upper layer is not clear. However, judging from the many sticks in the upper layer and its tendency to become thicker and clearer near the valley-wall, the origin of the upper layer may be related to the denudation of the valley wall. The time gap in the sedimentation of these two layers may not be great, because the form of the upper layer is thought to be closely related to the movement of the lower layer (Photo 4).

4.1.4.5. Hummock. There are hummocks which form small prominences on the sediment in the flow and sedimental areas. The hummocks mainly consist of rock aggregate and area covered with thin mud. They appear at the places where the velocity of the rock avalanche was decreased by the topography or other factors. The velocity of the downward flow was approximately 80 km per hour according to eyewitness reports (Geological Survey of Japan, 1984).

4.2 Landslide Failure of Matsukoshi

4.2.1 The Situation of the Disaster

A large failure, approximately 150 m wide and 200 m long, happened on the right bank of a conjection of the Omata River and Matsukusa River. This failure killed 13 persons. A cement-mixing plant was damaged, and several houses were destroyed (Fig. 6).

4.2.2 Topography and Geology

The Matsukoshi area is situated on the river terrace of the Otaki River near the junction of the Omata River. The basement of this area is paleozoic formation and debris deposits with volcanic ash from Mt. Ontake forms the river terrace. There is terrace gravel between the basement and debris deposits too. Almost all areas near the source area covered with a layer of volcanic ash, included pumice. This layer of volcanic ash does not appear as a horizontal layer but is distributed along undulations of the source area. the volcanic ash layer was deposited to cover an original valley and then debris sediments were deposited thickly horizontally. It was a buried valley before the failure occurred. But in this earthquake the volcanic ash layer was sheared and then sediments above it flowed down along it. This valley structure must also have gathered ground water (Fig. 7, Photos 5 and 6).

4.2.3 Flow and Sedimentation of Debris

The debris, which failed on the right river terrace flowed across the conjunction of the Omata River and the Matsukusa River, ran against a wall of the left river terrace, then changed direction to the right and climbed up the right terrace wall about 200 m downstream from the source area. Finally, the debris flowed into the Otaki River along the Omata River.

4.3 Landslide Failure at Ontake Kogen

4.3.1 The Situation of the Disaster

Five rather large scale failures occurred at Ontake Kogen; identified as A, B, C, D, and E in Fig. 8. No one was killed but the road was badly damaged by these failures.

4.3.2 Topography and Geology

Judging by the topography at Ontake-Kogen the failure did not occur easily, because it is gentle slope (about 15°) covered by new tephra. But many traces of slope failure were found in this area, which suggests that this area had suffered slope failures of same type in this time. The geology of Ontake Kogen is a pumice and ash sequence. The geologic column made in failure A is shown in Fig. 9.

These five failures appear characteristic of translational slides, of which rupture surfaces are flat, and the depth of failures is shallow and constant. It means that the failures were caused by a rupture in a specific layer which was formed parallel to the slope. This specific layer was a white pumice layer which is Pm-I layer of Mt. Ontake volcano (Photo 7).

4.3.3 Flow and Sedimentation of Debris

The debris from Failure A flowed about 1 km down two streams, respectively. The debris from Failure B did not move much, remaining in the source area; a white pumice layer was observed in it. Failures of C, D, and F were small and there was little debris flow.

4.4 Landslide

4.4.1 The Situation of the Disaster

This failure occurred on the north-western wall of one ridge extending north-east from Otaki River Dam. The failure is 150 m wide and 50 m long. The debris attacked the east edge of Takikoshi village, destroying four houses and killing one person (Photo 8).

4.4.2 Topography and Geology

The main scrap is straight, which suggests that there is a fault along the main scarp. The rupture surface is situated between a layer of impermeable volcanic ash and a layer of volcanic sand composed of lacustrine sediments. Antecedent precipitation was thought to have had an effect in this case too. Ground water had collected on the impermeable volcanic ash layer at the time when earthquake happened. In this situation liquefaction occurred in the sand layer above the layer of volcanic ash. Therefore, the rupture surface was in an almost horizontal plane (Fig. 10).

4.4.3 Flow and Sedimentation of Debris

The main body of debris was deposited fanwise on the reservior, which contained no water. Debris cones are concentrated at the front of the fan shape and the thickness of debris decreases at the center of sedimentation. On the whole, the shape is very similar to that of the Oike landslide induced by the Izu-Oshima Kinkai earthquake, 1978. This sedimental situations suggests that the majority of debris moved in a

mass and has deposited at the front leaving a very thin layer on the flow area.

4.5 Other Smaller Failures

4.5.1 The Situation of the Disaster

Many small failures were recognized along the swamp near the tollgate of the road, along the upper stream of Nigorizawa River or along the trail to Nigorigawa hot spring. These failures were small scale but numerous. Nobody was killed (Fig. 3).

4.5.2 Topography and Geology

These failures occurred on the steep slopes cut by the river erosion or the road. They were concentrated in the thick lava layer with joints or at the fracture zone in the Palaeozoic formation.

4.5.3 Flow and Sedimentation of Debris

The debris was deposited directly under the source area and moved a very short distance. Most of the sedimentation is talus.

5. MINERAL ANALYSES AND SHEARING TESTS ON THE PUMICE LAYER

At the large scale failures of Ontake Kuzure, Matsukoshi and Ontake Kogen, the rupture surfaces were situated in layers of pumice or volcanic ash from the Ontake volcano. Therefore, these pumice layers were examined by x-ray diffraction analysis, observation under an electron microscope, and the shearing tests.

5.1 X-ray Diffraction Analysis

A sample was picked up at each rupture surface, but samples at Takikoshi were also taken from the volcanic ash below the rupture surface. Each sample was about 150 g, material under 2μ was separated by hydraulic elutration and analyzed. The diffraction pattern of hallyosite was recognized in each sample. In particular, strong peaks of halloysite were detected in samples from Matsukoshi and Ontake Kogen (Fig. 11).

5.2 Observation Under an Electron Microscope

Samples analyzed by the x-ray diffraction method were observed under an electron microscope with an acceleration voltage of 200 kv and magnification of 50,000. That data coincides with the data of x-ray diffraction analysis. Ball type halloysites were common in samples of Matsukoski and Ontake Kogen and there were few in the sample from Ontake Kuzure. But it was not detected in the sample from Takikoshi (Photo 9 and 10).

5.3 Shearing Tests

The shearing test was formed against Pm-I pumice layer's sample from Ontake Kogen and another pumice layer (M-Pm) from Ontake Kogen which was not connected with the failure. The Pm-I layer contained halloysite and the M-Pm layer contained allophane. The cohesion and the friction angle of the Pm-I layer was

$$C = 1.9\,tf/m^2,\ \phi = 7°$$

and the M-Pm layer was

$$C = 8.7^{tf}/m^2, \quad \phi = 29^\circ$$

6. DISCUSSION

6.1 Classification of Slope Failures

All the failures which occurred in the Naganoken-seibu earthquake, 1984 are classified into two groups according to the topographical and the geological features of the source area. Failures in the first group were on a large scale but not numerous, whereas failures in the second group are the reverse. The first ones were related to the geological structure, especially pumice layers, and the second ones were affected by high slope angles.

6.2 Pumice Layers

Pumice layers tend to be very sensitive to vibrations from earthquakes. We have several examples of this problem: the white clay layer in the Imaichi area in the Imaichi earthquake, 1949 (Morimoto, et al. 1957); Shirasu, which is a kind of pumice layer, in the Ebino-Yoshimatsu earthquake, 1968 (Ando, 1971); and Hachinohe pumice layer in the Tokachi-oki earthquake, 1968 (Hotta, et al. 1968). As in the case under discussion, halloysite was detected in them except Hachinohe pumice layer which has not yet been examined. It is possible that the presence of halloysite affects the physical property of pumice layer.

6.3 Failures of Steep Slopes

Contrasted with big failures, small failures or rock falls are caused by weathered surface soil or weathered rocks with developed joints. These failures are surface phenomena; topographical factors are the main cause.

6.4 Precipitation

The nature of failures in the Tokachi-oki earthquake, 1968, is thought to be the same as that of huge failures in the Naganoken-seibu earthquake, 1984. That case had precipitation of about 200 mm and then the earthquake occurred. Many failures occurred on gentle slopes and 49 persons were killed. There was precipitation of 165 mm at the observation point of Mt. Ontake, and it is thought that ground water was concentrated by the geological structure at the head of the Denjo River, Matsukoshi and Takikoshi. Judging from these observations, it is necessary to check the existence of pumice layer, effect of precipitation, and concentration of ground water, in order to predict large slope failures occurring as a result of earthquakes.

7. REFERENCES

1) Ando, T. (1971), Landslides in "Shirasu" area caused by Ebino-Yoshimatsu Earthquake, Reports Cooperative Research Disaster Prevention, No. 26, pp 147-156, National Reseach Center for Disaster Prevention (In Japanese).

2) Geographcial Survey Institute (1984), Disaster Caused by the Naganoken-Seibu Earthquake, 1984, Bull. Geographical Survey Institute, No. 60, pp 48-52 (In Japanese).

3) Geological Survey of Japan (1985), Two debris-avalanches associated with the Naganoken-seibu Earthquake, in 1984, Report of Coordinating Committee for Prediction of Volcanic Eruption, No. 32, pp 48-51 (In Japanese).

4) Hotta, H., Miura, O., and Tamura, T. (1968), Slope Failures Caused by the Tokachi-oki Earthquake in the Southeastern part of Aomori Prefecture, Annals of the Tohoku Geographical Association, Vol. 20, No. 4, pp 195-201 (In Japanese).

5) Kobayashi, T. Ohmori, E., and Ohmori, T. (1975), Petrochemistry of Ontake Volcano, Bull. Geological Survey Japan, Vol. 26, No. 10, pp 7-22 (In Japanese).

6) Morimoto, R., Ossaka, J., and Fukuda, T. (1957), Geology of Imaichi District with Special Reference to the Earthquake of Dec. 26, 1949 (III), Bull. Earthquake Res. Institute, Vol. 35, Part 2, pp 359-375.

7) Uehara, S., Tanaka, K., Inokuchi, T., Kinoshita, S., Imoto, S., Kishi, S., and Iwasaki, M. (1985), Report on the Survey of the Naganoken-seibu Earthquake, 1984, Report of the Investgation of Principal Natural Disaster, Vol. 25 (In Japanese).

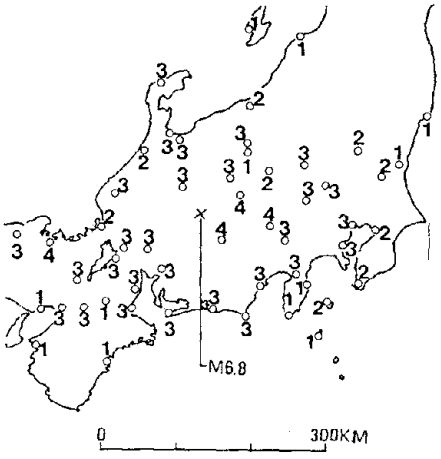

Fig. 1 Seismic intensity (Meteorological Agency).

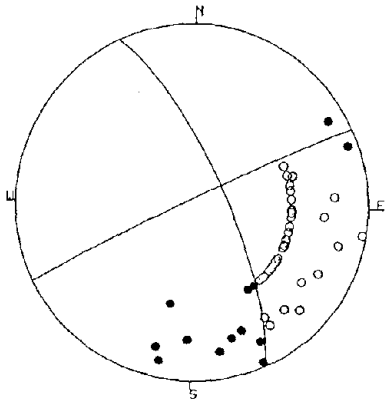

(Lower hemisphere projection)

Fig. 2 Earthquake mechanism of main shock. (Uchara et al. 1985)

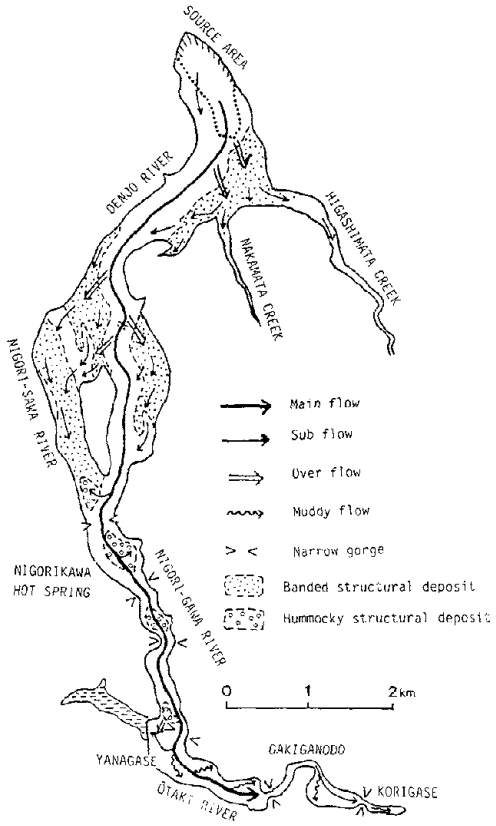

Fig. 4 Rock avalauche.

Photo. 1 Striation on rupture surface (Ontake Kuzure)

Photo. 2 Denudation of the valley-wall (Ontake Kuzure)

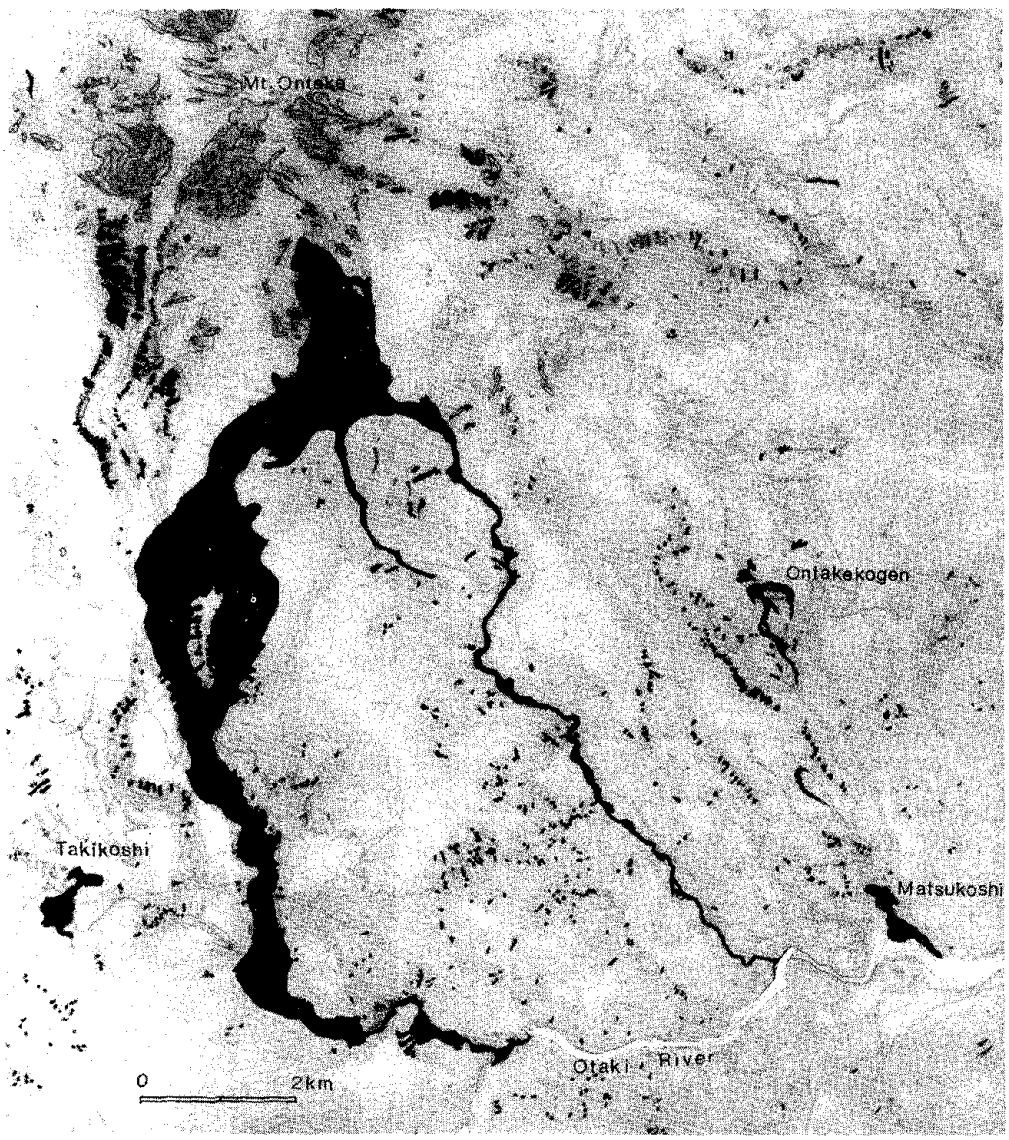

Fig. 3 Distribution map of slope failures.

Old slope failures
Slope failures induced by the Naganoken-seibu Earthqueake, 1984

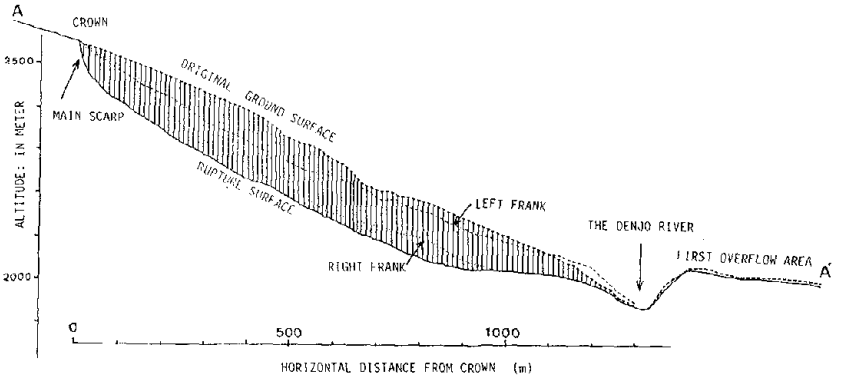

Fig. 5 Longitudinal section (Ontake Kuzure)

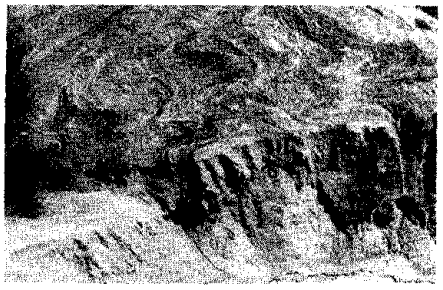

Photo. 3 Banded Structure (Photo. Asahikoyo)

Photo. 4 Double layer structure of sediment of rock avalanche.

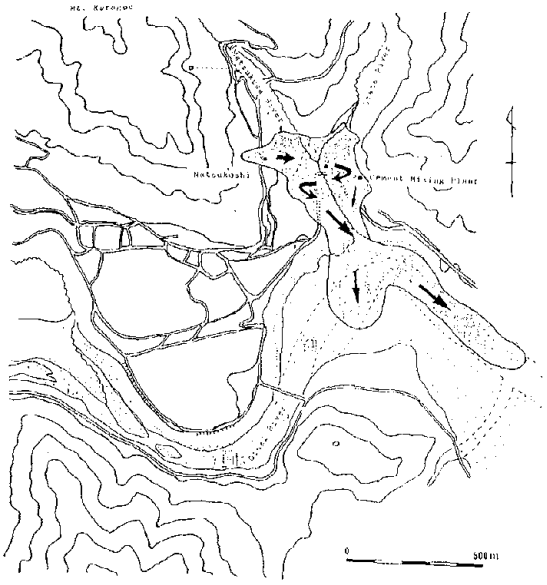

Fig. 6 Slope failure at Matsukoshi.

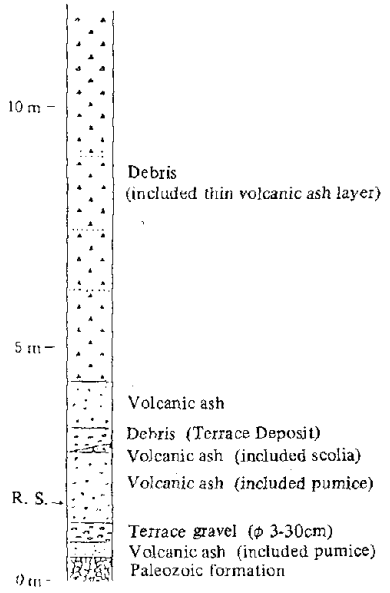

Fig. 7 Geologic column of Matsukoshi.

Photo. 5 Source area (Matsukoshi)
(photo. Shinano-mainichi).

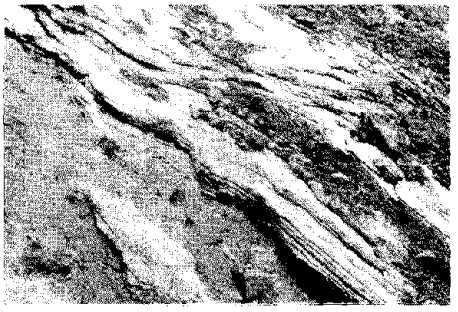

Photo. 6 Rupture Surface (Matsukoshi)

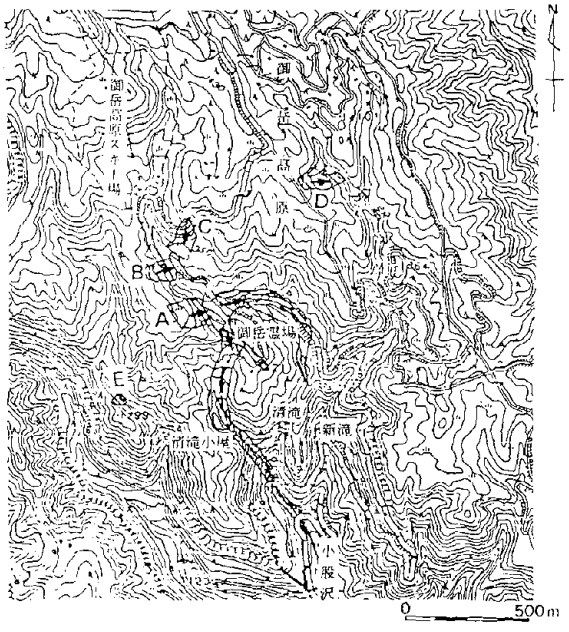

Fig. 8 Slope failure at Ontake Kogen

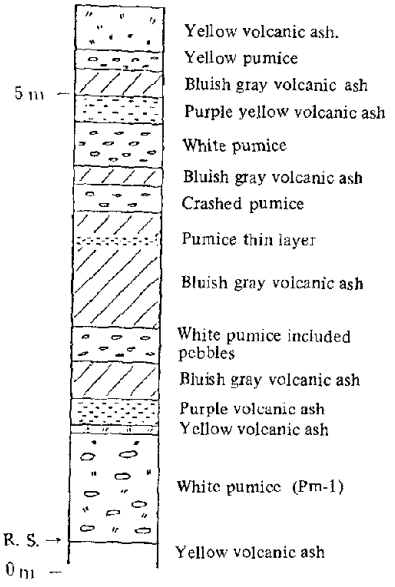

Fig. 9 Geologic column of Ontake Kogen

Photo. 7 Slope failures at Ontake Kogen.
Failure A (right) and Failure B (left)

Photo. 8 Slope failure at Takikoshi
(Photo. Nakanihon-koku)

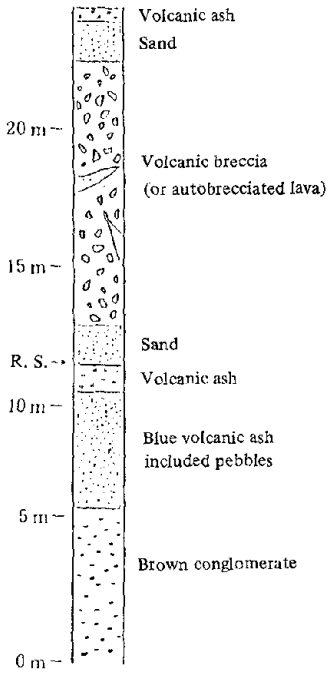

Fig. 10 Geologic columan of Takikoshi

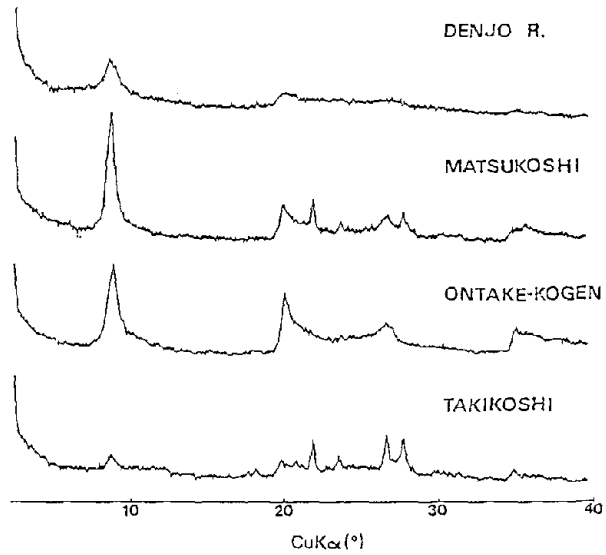

Fig. 11 X-ray diffraction patterns of clay minerals on rupture surfaces

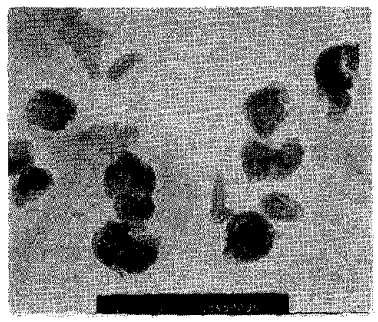

Photo. 9 Electron microscope image of clay minerals (Ontake Kogen)

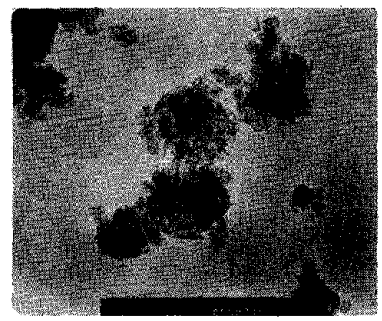

Photo. 10 Electron microscope image of clay minerals (Ontake Kuzure)

TASK COMMITTEE REPORTS

Report of Task Committee on

(A) STRONG-MOTION INSTRUMENT ARRAYS AND DATA

Date : May 23, 1985

Place : Public Works Research Institute, Ministry of Construction
Tsukuba Science City, Ibaraki, Japan

Attendees : Japan Side- H. Tsuchida (Chairman)(PHRI)
S. Hattori (BRI)
M. Ichikawa (MRI)
S. Noda (PHRI)
K. Ohtani (NRCDP)
Y. Sasaki (PWRI)
K. Tamura (PWRI)
T. Kuwabara (PWRI)

U.S. Side- R.B. Borcherdt (Temporary Chairman)(USGS)
A.G.Franklin (WES)
J,F. Lander (NOAA)
R.B. Mac Donald (USBR)
A.M. Abdel-Ghaffar (Princeton Univ.)

I. Activities and Principal Accomplishments to Date

Catalogs of strong-motion earthquake records observed both in the United States and Japan are being exchanged. U.S. data are published in the "Seismic Engineering Program Report," and the Japanese data are published in the "Strong-Motion Earthquake Records in Japan."
Dr. Krinitzky of WES visited PWRI, NRCDP and PHRI, exchanged the reports, and discussed strong motion records and their analysis.

II. Future Programs

Both sides of the Task Committee plan to continue their respective efforts in the following nine points 1) to 9) and to initiate two points 10) and 11).

1) After an earthquake which has caused damage to structures or an earthquake during which maximum acceleration exceeding about 0.1G has been recorded, the task committee of the country where the earthquake has taken place will provide a list of the strong-motion earthquake records for the counterpart of the task committee. The list contains maximum component acceleration of each record. If there is such a list compiled by any organization, the list mentioned above may be replaced by it.

2) Every year the task committee will exchange catalogs of the strong-motion earthquake records during the previous year. The catalog contains maximum component accelerations and wave forms of major records. If there is such a catalog compiled by any organization, the catalog mentioned above may be replaced by it.

3) The Task Committee makes appropriate arrangements to provide digitizable copies of records when they are requested. In addition, arrangements will be made to provide information on the characteristics of the site and structures at the locations where such records are obtained.

4) When the organizations taking part in the panel publish reports on the strong-motion earthquake records, the organizations will distribute copies of the reports to the organizations of the panel interested in them. The Task Committee exchanges lists of the organizations which wish to receive the reports.

5) The Task Committee will continue to exchange digitized data on all the major strong-motion earthquake records recovered in both countries, under the condition mutually acceptable to the agencies involved in aquisition of the data.

6) The Task Committee will exchange technical information concerning seismometers to be developed, and deploying and installing instruments with emphasis on the instal-lation of bore-hole instruments and the design of seismic arrays.

7) The Task Committee plans to assist and cooperate, where possible, in the following areas:

   a. Assistance and cooperation with governmental organiza tions in other seismic areas, in order to promote high quality strong earthquake motion observations in all seismically active areas of the world.

   b. Assistance and cooperation with any international effort to record strong ground motion close to the source of a large magnitude shock.

8) The Task Committee feels the UJNR Panel on Wind and Seismic Effects should play a major cooperative role in the implementation or relevant parts of the Resolution of the International Workshop on Strong-Motion Earthquake Instrument Arrays held May 1978, in Honolulu, Hawaii. The exchange of complete information on all aspects of the program, as it develops particularly in Japan and the United States, will be carried out in the manner of our standard exchange when appropriate. Particularly with unique data from arrays, or deep bore-hole instruments in the U.S. and Japan, Task Committee Chairmen will retain the responsibility of relaying information on their existence and subsequently of transferring the digital data from such institutions as in the U.S., the USGS, CDMG, USC; and in Japan, PWRI, BRI, PHRI, MRI, and NRCDP.

9) The Task Committee will make a preliminary study on comparison of digitizing and computer processing techniques of member organizations on strong-motion earthquake records. The Task Committee chairmen will exchange their ideas on a proposed plan for this study to possibly include digitizing specific records, and computer processing of all such digitizings; followed by a workshop to discuss the results.

10) The Task Committee recommends collaborative studies involving strong-motion instrumentation and interpretation of resulting strong-motion data sets for purposes of earthquake hazard reduction.

11) The Task Committee will study the possibility of exchange of scientists, engineers, and appropriate equipment in a timely fashion for the observations following large earthquakes in either country. As the largest and most interesting aftershocks occur immediately following the main earthquake, recovery of the most useful aftershock data requires that the response to major earthquakes be initiated as rapidly as logistics permit.

Report of Task Committee on

(B) LARGE-SCALE TESTING PROGRAM

Date : May 22, 1985

Place : Public Works Research Institute, Ministry of Construction, Tsukuba Science City, Ibaraki, Japan

Attendees : Japan Side- K. Ohtani (Chairman) (NRCDP)
S. Noda (PHRI)
S. Okamoto (BRI)
K. Yokoyama (PWRI)

U.S. Side - H.S. Lew (Temporary Chairman) (NBS)
J.H. Gates (Cal. Tran.)
R.N. White (Cornell Univ.)

I. Activities and Principal Accomplishments to Date

The main activities related to this task committee during the past year are as follows:

1) All of the experimental and analytical studies related to the reinforced concrete structure have been completed. The results have been published in Special Publication 84 by the American Concrete Institute.

2) Testing of the full-scale steel structure and other suport tests have been completed in Japan. Support tests in the U.S. is in progress. Analytical studies are currently in progress.

3) Active exchanges of U.S. and Japanese researchers have occurred under the reinforced concrete, steel and masonry programs and have been very useful.

4) The Joint Planning Committee on the masonry program met in the U.S. in July, 1984. Researches on the coordinated masonry structures were discussed.

5) Ministory of Construction and National Science Foundation signed on December, 1984, the Implementing Arrangement for Cooperation in the U.S.-Japan Earthquake Research Program Involving Large-Scale Experiments of Masonry Structures.

II. Future Programs

The status of the U.S.-Japan Joint Program of reinforced concrete and steel structures and the results of the masonry planning committee were reviewed. The Task Committee adopted the following resolutions as a result of discussion.

1) Each country should collect copies of reports for all coordinated research conducted in that country in a single set. Each country should exchange a set of these reports.

2) The major aspects and conclusions of the reinforced concrete and steel test programs in each country should be synthesized into two separate reports. Since it is critical to disseminate the program results to engineering profession in both countries, the Joint Technical Coordinating Committee is strongly encouraged to expedite this effort.

3) To assure effective exchange of information on masonry structures, immediate and expanded personnel exchange is encouraged under the Large-Scale Testing Program.

4) The Task Committee will review progress of the Joint Research Program and continue to reassess the need for testing of other structures and report its findings and recommendations to the Panel.

5) The Task Committee recommends that the Panel endores the Implementing Arrangement on the coordinated masonry program between the Ministry of Construction and the National Science Foundation.

6) Task Committees on (B), Large-Scale Testing Program and Task Committee on (D), Evaluation of Performance of Structures should maintain closer liaison to facilitate the planning of instrumentation and analysis for full-scale test structures.

7) Technical exchange of information on masonry structures should be continued through this Task Committee. The following information will be exchanged;

   a. bibliography of research reports, and
   b. copies of existing reports.

8) Exchange of information on large-scale testing facilities and large-scale testing programs should be encouraged.

Report of Task Committee

(C) TASK COMMITTEE ON REPAIR AND RETROFIT OF EXISTING STRUCTURES

Date : May 22, 1985

Place : Public Works Research Institue, Ministry of Construction, Tsukuba Science City, Ibaraki, Japan

Attendees : Japan Side- M. Hirosawa (Chairman)(BRI)
T. Iwasaki (PWRI)
H. Tada (PWRI)

U.S. Side - M. P. Gaus (Temporary Chairman)(NSF)
S. K. Takahashi (NCEL)
R. N. Wright (NBS)

I. Activities and Accomplishments to Date

In Japan the following activities have been carried out:

1) The Japan National Project - Post - Earthquake Measures of Buildings and Structures Damaged by Earthquake is now carried out as a five-year plan from 1981 to 1985.

Research products in 1984 are

a. Inspection Method of Damaged Structure
b. Investigation Results of Repairing Methods

2) Following handbook was compiled and published by the Japan Concrete Institute in October, 1984.
"Hand book of Seismic Retrofitting of Existing Reinforced Concrete Structures"

3) "Total System for Aseismic Design, Inspection and Repair and Retrofit of New or Existing Building, Equipment and Non-Structural Element for Official Use" was compiled by Government Buildings Department, Ministry of Construction in March, 1985 and was under trial use.

In the U.S. the following activities have been carried out:

1) Initial studies on behavior of unreinforced masonry structures were concluded. A conference on this subject was held in Charleston, South Carolina.

2) Studies on base isolation devices have been in progress which may be of benefit in repair and retrofit of existing structures.

3) Research has been initiated on techniques to assess current material and structural properties in structures which are aging or showing the effects of weathering or heavy use. Such information is essential in developing retrofit measures.

4) Research on methods to assess the structural capabilities of existing and damaged structures is continuing along with research on methods to repair and retrofit such structures.

II. Future Programs

The task committee recommends the following items for future activities:

1) Continue and expand the exchange of reports, books and special publications related to repair and retrofit of existing structures.

2) A cooperative workshop on repair and retrofit should be held in the near future. Possible dates might be in August 1986 in conjunction with the National earthquake meeting to be held in Charleston, South Carolina or in conjunction with the May 1987 UJNR meeting to be held in Japan. The Charleston, SC meeting was considered to be particularly appropriate because of the very strong interest in assessment and retrofit in the eastern U.S. at the present time.

3) Exchange information and give consideration to possible cooperative efforts to study methods to quickly and economically assess the characteristics and residual structural capabilities of material which may have suffered degradation due to weathering, aging, misuse or change of use and on methods to upgrade the capabilities of such materials where required. Develop methods of analysis for predicting the structural capacities of structures containing such materials.

4) Share information such as handbooks and on specific completed projects such as evaluations of particular designs for which retrofit studies have been carried out and which may provide specific validation of retrofit design methods.

5) Arrange for the evaluation of the reports and manuals on seismic retrofit of concrete structures and of museum building and contents and of historical structures which were prepared under the UNIDO Balkans Project.

6) Carry out research to evaluate the potential structural benefits and relative economics of using base isolation devices for retrofit of existing structures. Such devices may be of particular interest for historical or monumental structures.

7) Give increased attention to developing methods to assess nonstructural items in existing structures which could pose severe hazards and/or cause loss of service. Develop methods for retrofit or repair of important non-structural elements.

8) Coordinate with Committee D "Evaluation of Performance of Structures" to identify and possibly encourage a joint U.S.-Japan paper on computer programs which are usefull for evaluation of existing structures and which could be used to guide repair and retrofit decisions.

Report of Task Committee on

(D) EVALUATION OF STRUCTURAL PERFORMANCE

Date : May 23, 1985

Place : Public Works Research Institute, Ministry of Construction, Tsukuba Sience City, Ibaraki, Japan

Attendees : Japan Side- S. Okamoto (Chairman)(BRI)

U.S. Side - G. R. Fuller (Chairman)(HUD)

I. Activities and Principal Accomplishments to Date

1) Second Workshop: July 1984, Berkeley Marina Marriott Hotel, California. Analysis and evaluation case studies of six benchmark structures were presented by U.S. and Japanese representatives. Three types of analysis were conducted by each side : 1) Rapid Evaluation Method, 2) Detailed Structural Analysis, and 3) Research Computer Analysis Method. Participants included 12 Japanese and 18 Americans.

2) Third Workshop: May 17, 1985, Housing and Urban Development Corp., Tokyo, Japan.
Papers were presented on the following subjects:

a. Progress Report on Seismic Performance of Existing Buildings (R.N. White),
b. Rapid Evaluation Methods (S.A. Freeman),
c. Comparison of U.S. Spectrum Capacity Method and Japan Standard Evaluation Method (S. Okamoto),
d. Summary and Recommendations for Improvement of Building Seismic Design and Construction (M. Ozaki),
e. Seismic Capacity Evaluation of Existing SRC Buildings (H. Aoyama),
f. Status Report on U.S. Activities of Interagency Committee on Seismic Safety in Construction (ICSSC), Applied Technology Council (ATC-14), and Federal Emergency Management Agency (FEMA) program for Abating Seismically Hazardous Non-Federal Buildings (ATC, BSSC, EERI)(G.R. Fuller),
g. Guideline for Post-Earthquake Evaluation of Earthquake Damaged R/C Buildings (H. Hiraishi),
h. Emergency Standard for Classification of Risk Levels of Earthquake Damaged R/C Buildings (S. Otani),
i. Standard for Evaluation of Seismic Performance of R/C Block Masonry School Building (T. Okada),
j. Instrumentation of Building No.5, Ministry of Public Welfare (Y. Yamazaki),
k. Insrumentation of Buildings (M. Agbabian).

3) Workshop Proceedings: A two-volume publication containing the proceedings of the First and Second Workshops was completed by Cornell University under a research contract with National Science Foundation. Copies were furnished to Task Committee (D) members at the Third Workshop on May 17, 1985.

4) UJNR Panel Meeting: A "Summary Report on the U.S.-Japan Workshops on Evaluation of Structural Performance" was presented by Dr. R.N. White in Session 4 of the 17th UJNR Panel Meeting on Wind and Seismic Effects.

5) Coordination of U.S. and Japan Activities: Discussions were held by Task Committee Members on the coordination of several activities in each country concerning evaluation of existing buildings for earthquake resistance. A closer liaison with Task Committee (B), Large Scale Testing Program will be maintained to coordinate the testing, instrumentation and analysis of the full-scale masonry structure.

II. Future Programs

1) The Task Committee reconfirmed the objectives and recommendations of May 17, 1984 concerning analysis, instrumentation, and post-earthquake evaluation of benchmark structures.

2) Encourage the continued exchange of literature, analyses, and research reports relative to assessment of seismic resistance of buildings.

3) Expand the inventory of existing buildings in each country that have been evaluated and instrumented, and then observed after any future seismic activity. Continue to evaluate other buildings in each country using Japanese and American methods of analysis.

4) Continue to evaluate differences and similarities in various analysis methods used in each country.

5) Develop recommended evaluation and screening methods for determination of seismic resistance of existing buildings and identify research needs to improve evaluation technology.

6) Consider planning for a final workshop to be held in the U.S. in conjunction with the 18th Joint Meeting, and arrange for publication of a Final Report for distribution at the 18th Joint Meeting.

Report of Task Committee on

(E) LAND USE PROGRAMS FOR CONTROLLING NATURAL HAZARD EFFECTS

Date : May 22, 1985

Place : Public Works Research Institute, Ministry of Construction, Tsukuba Science City, Ibaraki, Japan

Attendees : Japan Side- K. Kawashima (Chairman)(PWRI)
S. Hattori (BRI)
T. Iwasaki (PWRI)
M. Nagaoka (GSI)
Y. Sugimura (BRI)

U.S. Side- G. R. Fuller (Temporary chairman)(HUD)
R. D. Borcherdt (USGS)

I. Activities and Principal Accomplishments to Date

1) The US-Japan Workshop on "Urban Earthquake Hazards Reduction," sponsored by the U.S. Earthquake Engineering Research Institute (EERI) was held at Stanford Univ. in July 1984. Attendees included UJNR members Dr. Kazuhiko Kawashima and Dr. John B. Scalzi, and representatives of the Government of Shizuoka Prefecture: Messrs. Toshiroh Sugiyama and Katsunori Imado. The final report from EERI is to be published in July 1985 and will be furnished to Task Committee (E) members.

2) EERI Report on "The Anticipated Tokai Earthquake" was published in June 1984 and was distributed to Task Committee (E) members. Copies will be obtained from EERI for new Task Committee (E) members.

3) Several papers pertaining to Task Committee (E) were presented at the 17th Joint Panel Meeting:

a. Session 3, Theme IV, "Liquefaction."
b. Session 9, "Survey of Recent Chilean Earthquake."
c. Session 10, Theme III, "Storm surge and Tsunamis."
d. Session 11, Theme V, "Nihonkai-Chubu and Naganoken-Seibu Earthquakes."

II. Future Programs

Following the discussion, the Task Committee recommends the following coordinated works between the U.S. and Japan.

1) Both sides will continue to exchange technical information on the following subjects:

a. Seismic risk maps, socio-economic programs, and studies of recent earthquakes.
b. Planning methodologies for earthquake disaster mitigation in large populated cities.
c. Geological conditions, soil liquefaction potential, seismic risk, and tsunami risk maps.

2) Both sides will continue to promote coordinated research and exchange of specialists in land use programs for earthquake hazard mitigation.

3) The U.S. Chairman will furnish to Task Committee members future reports on land use programs being coordinated or sponsored by the Federal Emergency Management Agency (FEMA), the Interagency Coordinating Committee of the National Earthquake Hazards Reduction Program (ICC/NEHRP), the U.S. Geological Survey (USGS), the National Science Foundation (NSF), or the National Academies of Science and Engineering.

Report of Task Committee on

(F) DISASTER PREVENTION METHODS FOR LIFELINE SYSTEMS

Date : May 23, 1985

Place : Public Works Research Institute, Ministry of Construction, Tsukuba Science City, Ibaraki, Japan

Attendees : Japan Side- T. Iwasaki (Chairman) (PWRI)
K. Kawashima (PWRI)
T. Murota (BRI)
S. Noda (PWRI)
K. Ohtani (NRCDP)
Y. Sasaki (PWRI)

U.S. Side - M.P. Gaus (Temporary Chairman) (NSF)
S.K. Takahashi (NCEL)

I. Activities and Principal Accomplishments to Date

A US-Japan Workshop on Seismic Behavior of Buried Pipelines and Telecommunications Systems was held on December 5-7, 1984, at the Public Works Research Institute, Tsukuba Science City, Japan, with the participation of more than 40 experts on lifeline earthquake engineering from both countries. The workshop reviewed the current knowledge, analytical, experimental and field observations of seismic effects on buried pipelines and telecommunications systems, and had presentations of 17 technical papers on current reserach in the area of buried pipelines and telecommunications systems. On the basis of these reviews and paper presentations, comprehensive discussions were conducted, and specific research areas that are most suitable for future coordinated research between the US and Japan were identified. The proceedings of this workshop including the 17 technical papers and the resolutions was published by Columbia University, and will be distributed to appropriate members of the UJNR Panel on Wind and Seismic Effects, participants of the Workshop, and other interested parties. Also an outline of the workshop was presented at the 17th Joint Meeting of the UJNR Panel on Wind and Seismic Effects.

In Japan, the Public Works Research Institute is conducting a 5-year (1981-1985) research project on the development of repairing technology of seismically damaged structures which includes assessment of damage degree and proposal of appropriate repair methods for buried sewer pipelines. PWRI is also conducting a dense instrument array measurement program to identify ground motions applicable to seismic design of buried pipeline structures. An evaluation of the economic losses due to minimal cargo movements because of structural damages to port and harbor facilities following the Nihonkai-Chubu Earthquake of 1983 was conducted by the Port and Harbour Research Institute.

In the U.S., the National Science Foundation has continued to sponsor research on risk analysis of lifeline systems and effects of ground deformation waves on underground pipelines. Papers submitted at the 17th UJNR meetings by the U.S. were on dynamic stresses and displacement in a buried tunnel and seismic vulnerability of lifeline facilities using CADDS-CAE system. A study on gas and liquid lifelines has been completed by a special committee of the American Society of Civil Engineers. The committee report on a manual of recommended practice for seismic design of gas and liquid lifelines has been published by the American Society of Civil Engineers.

II. Future Programs

1) The members of the Task Committee will facilitate the continued exchange for technical information and cooperation in research on specialized problems listed as follows:

   a. Seismic damages to lifeline systems
   b. Seismic design procedures for lifeline systems
   c. Procedures to detect and inspect damages to buried pipelines
   d. Repair and retrofit methodology for lifeline systems
   e. Estimation of reliability of lifelines
   f. Management and public education on importance of lifeline systems
   g. Investigation of needs for large-scale testing of lifeline systems

2) It was agreed that the knowledge derived from the US-Japan Workshop of December 1984 was significant. Therefore, it is recommended to hold another US-Japan Workshop on lifeline earthquake engineering in conjunction with the 18th UJNR Joint Meeting in Washington, D.C. in May 1986. It is also proposed that Task Committee (F) members be encouraged to participate in the lifeline earthquake engineering session at the Third U.S. National Conference on Earthquake Engineering in Charleston, South Carolina in August 1986.

Report of Task Committee on

(G) WIND CHARACTERISTICS AND STRUCTURAL RESPONSE

Date : May 23, 1985

Place : Public Works Research Institute, Ministry of Construction, Tsukuba Science City, Ibaraki, Japan

Attendees : Japan Side- K. Naito (Chairman)(MRI)
K. Masamura (MRI)
T. Murota (BRI)
N. Narita (PWRI)
K. Yokoyama (PWRI)

U.S. Side- M.P. Gaus (Temporary Chairman)(NSF)

I. Activities and Principal Accomplishments to Date

Noting that:

a. High winds frequently cause loss of life and extensive property damage,
b. The knowledge derived from the exchange of high wind data and information on wind effects can be useful inreducing loss of life and property damage,
c. Insufficient knowledge exists on the effects of high windson structurres and methods for modeling these effects, and
d. The needs for wind data for various applications and new projects are increasing.

The Task Committee carried out the following activities;

1) The following documents were exchanged:

a. Report entitled "Building Damage in South Carolina Caused by the Tornadoes of March 28, 1984", published by Committee on Natural Disasters Commission on Engineering and Technical Systems, National Research Council, U.S.A.
b. Paper entitled "Features of Ocean Wind Fluctuations during Typhoon Passages" by G. Naito and H. Takahashi,
c. Paper entitled "The Variation of Gust Structure with Height up to 200m" by K. Naito, T. Hanabusa and T. Fujitani.

2) Some qualified instruments to measure high winds at coastal or sea regions were installed or prepared in Japan: Kashima coast observation with several masts 20 to 30 m high, an off-shore tower 20 m high at Hiratsuka, wind measurements at long span bridges in the Setonaikai Sea, et al.

3) Coastal wind measurements were considered in the U.S.A. with the use of portable equipment. Concerning high wind effects, particular investigations were started in the U.S.A. on various projects, such as
wind loading and strength prediction of glass cladding, wind loading and response of transmission towers and wind pressure difference between the interior and exterior of buildings.

II. Future Programs

The Task Committee hereby proposes to carry out the following programs:

1) Exchange observation reports of high winds.

2) Encourage interaction between meteorologists and engineers to identify the types of wind data required for future use in establishing extreme wind distributions; in determining wind loadings on buildings and structures; in understanding the urban wind climate; and in considering design issues involved with the wind generation of energy.

3) Encourage the establishment of minimum requirements for the simulation of atmospheric boundary layers in wind tunnels and the exchange of boundary layer wind tunnel test results, including comparisons with corresponding full-scale situations.

4) Exchange information on critria, techniques and instrumentation for structural modeling in boundary layer wind tunnels. Also encourage the exchange of information of measurements made on actual structures and on comparisons with predictions from wind tunnel studies of these structures.

5) Continue the exchange of engineers and meteorologists, and make available research facilities for mutual use.

Report of Task Committee on

(H) SOIL BEHAVIOR AND STABILITY DURING EARTHQUAKES

Date : May 22, 1985

Place : Public Works Research Institute, Ministry of Construction, Tsukuba Science City, Ibaraki, Japan

Attendees : Japan Side - Y. Sasaki (Chairman)(PWRI)
T. Iwasaki (PWRI)
Y. Koga (PWRI)
N. Matsumoto (PWRI)
K. Oshima (PWRI)
Y. Sugimura (BRI)
S. Iai (PHRI)
T. Kuwabara (PWRI)
M. Matsumoto (PWRI)

U.S. Side - A.G. Franklin (Chairman)(WES)
A.M. Abdel-Ghaffar (Princeton Univ.)

I. Activities and Accomplishments to Date

1) Exchange of relevant documents on soil behavior during earthquakes was made. Eight papers were submitted to the Joint Meeting from the Japanese side and three papers were submitted from the U.S. side.

2) Under the auspices of the UJNR, Dr. E. L. Harp and Dr. D. K. Keefer of the USGS, inspected damaged areas in Nagano Prefecture with Japanese Panel members from the PWRI immediately following the Naganoken-Seibu Earthquake of September 14, 1984.

3) Members from both sides of the Task Committee exchanged information for preparing the workshop on in-situ testing for soil liquefaction susceptibility.

4) The PHRI provided to representatives of the U.S. side information on Japanese practice in seismic design of breakwaters and jetties.

II. Future Programs

1) The Task Committee will hold the workshop on in-situ testing methods for evalution of soil liquefaction potential from 17 through 20 August, 1985, in Berkeley, California.

2) Information on U.S. practice in seismic design of breakwaters and jetties will be provided to the Japanese side.

3) When requested, the Task Committee will assist in arrangements for visits to earth embankments including fill dams and foundations which have been subjected to significant ground motions.

4) The Task Committee encourages the maximum exchange of information on the following areas of earthquake engineering which are currently of intense interest to both U.S. and Japanese engineers.

   a. Liquefaction potential of soils
   b. In-situ testing methods for evaluation of soil liquefaction potential
   c. Seismic stability of embankment structures and natural slopes
   d. Remedial treatment of embankments and foundations to improve seismic stability
   e. Seismically induced permanent displacements in earth structures
   f. Seismically induced settlements of soils and foundations
   g. Earthquake effects on semi-buried concrete structures
   h. Earthquake effects on retaining walls
   i. Centrifuge testing facilities and methods
   j. Field performance data showing full-scale seismic response of earth dam

5) The Task Committee requests that the Panel encourage visits and exchanges of engineers and scientists between U.S. and Japanese goverment research organizations, and that the Panel assist such exchanges by providing the channels of communication for arrangements to be made.

Report of Task Committee on

(I) STORM SURGE AND TSUNAMI

Date : May 22, 1985

Place : Public Works Research Institute, Ministry of Construction, Tsukuba Science City, Ibaraki, Japan

Attendees : Japan Side- Y. Goda (Chairman) (PHWR)
M. Ichikawa (MRI)
K. Masamura (MRI)
T. Uda (PWRI)

U.S. Side - J.F. Lander (Temporary Chairman) (NOAA)

I. Activities and Principal Accomplishments to Date

1) In July, 1984, Dr. Goto from Tohoku University completed a six-weeks visit to Texas A & M University under an exchange program between the universities funded by the National Science Foundation (U.S.).

2) A copy of the Proceedings of the Tsunami Symposium of the Hamburg IUGG General Assembly published by NOAA (U.S.) was sent to the Japan side.

3) The U.S. side received a copy of "Survey of the Nihonkai-Chubu Earthquake", Ministry of Education, Pub. No.58022002 from Prof. Kajiura.

4) NOAA(U.S.) published multi-color wall map "Tsunamis of the pacific 1900-1983" and sent copies to the Japan side.

5) Technical information of data basis and studies on tsunamis produced by the Nihonkai-Chubu Earthquake were presented during the 17th Joint Meeting.

II. Future Programs

1) The Task Committee recommends that the program of exchange tsunami-related information will be continued and to do the same for storm surge. The U.S. side will specifically supply the Japan side with a copy of its digital history of tsunami occurrence which the Japan side will review particularly for accuracy and completeness of data on Japanese tsunamis. This may include a working visit to the National Geophysical Data Center (NGDC) by a Japanese expert upon the request of the U.S. side.

2) The Japan side (PWRI) is planning to send copies of photographs or slides taken right after the Nihonkai-Chubu Earthquake Tsunami to NGDC. This will improve the understanding on tsunami effects in the U.S. side.

3) The Task Committee proposes that investigators in the U.S. and Japan explore the possibility of undertaking specific joint projects by the two countries, results of which may benefit disaster-prone countries worldwide. The U.S. side, in particular, will try to organize a workshop composed of experts of the both sides on computational and experimental methods in tsunami and storm surge.

Report of Task Committee on

(J) WIND AND EARTHQUAKE ENGINEERING FOR TRANSPORTATION SYSTEMS

Date : May 23, 1985

Place : Public Works Research Institute, Ministry of Construction, Tsukuba Science City, Ibaraki, Japan

Attendees : Japan Side- H. Tada (Chairman)(PWRI)
T. Iwasaki (PWRI)
K. Kawashima (PWRI)
N. Narita (PWRI)
K. Oshima (PWRI)
Y. Sasaki (PWRI)
H. Shinohara (PWRI)
K. Yokoyama (PWRI)

U.S. Side - H.S. Lew (Temporary Chairman)(NBS)
J.H. Gates (Cal. Tran.)
A.M. Abdel-Ghaffar (Princeton Univ.)

I. Activities and Principal Accomplishments to Data

The major accomplishments of Task Committee (J) during the past year were as follows;

1) Summaries of wind and earthquake research on bridges conducted by both countries were presented to the 17th Joint Meeting, and exchange of information was made.

2) The coordinated research study on the seismic performance of bridge piers and columns was commenced in 1983, and the following experiments were made.

a. the performance of reinforced concrete piers and columns subjected to dynamic cyclic loading
b. model tests on the failure of reinforced concrete piers
c. testing full-scale concrete columns and associated small-scale model tests
d. the behavior of concrete filled steel tubes

3) The report of the U.S. group on the U.S. National Plan to improve the seismic performance of highway bridges has been published and sent to the Japanese Task Committee.

II. Future Programs

As a result of comprehensive discussions, the Task Committee (J) hereby resolves to carry forth with the following programs:

1) Continue with the coordinated experimental research study on the seismic performance of bridge piers and columns.

2) Initiate a coordinated research study both theoretical and experimental on the seismic, aeroelastic and aerodynamic response of cable-supported bridges.

3) The Second U.S. - Japan Bridge Workshop is going to be held in Berkeley, California, in August 19-22, 1985 with the cooperataion from organizations concerned in both countries in order to exchange the technical information on bridge engineering and discuss the future cooperative programs. Some of the subjects to be discussed include;

   a. Research on aerodynamic stability of suspension bridges and cable-stayed bridges
   b. Laboratory experiments on the seismic behavior of reinforced concrete piers and columns including concrete-filled steel tubes
   c. Repair procedure for seismically damaged bridge structures
   d. Experimental field testing of bridges including forced and ambient vibration measurements
   e. Experimental and analytical studies on the effects of soils on the behavior of bridge structures
   f. Strengthening procedures for existing bridges
   g. Strong motion instrumentation of bridges, corresponding data processing and parameter identification
   h. Seismic design and construction procedures of highway bridges

4) Encourage the continued exchange of information and research personnel through the Panel on Wind and Seismic Effects of UJNR.

5) Dr. H. Tada, Chairman of Task Committee (J), will stay in the U.S. for one month beginning in August 9, 1985 and visit laboratories and organizations related to the Panel on the basis of personnel exchange program of the UJNR Panel.

NBS Technical Publications

Periodical

Journal of Research—The Journal of Research of the National Bureau of Standards reports NBS research and development in those disciplines of the physical and engineering sciences in which the Bureau is active. These include physics, chemistry, engineering, mathematics, and computer sciences. Papers cover a broad range of subjects, with major emphasis on measurement methodology and the basic technology underlying standardization. Also included from time to time are survey articles on topics closely related to the Bureau's technical and scientific programs. Issued six times a year.

Nonperiodicals

Monographs—Major contributions to the technical literature on various subjects related to the Bureau's scientific and technical activities.

Handbooks—Recommended codes of engineering and industrial practice (including safety codes) developed in cooperation with interested industries, professional organizations, and regulatory bodies.

Special Publications—Include proceedings of conferences sponsored by NBS, NBS annual reports, and other special publications appropriate to this grouping such as wall charts, pocket cards, and bibliographies.

Applied Mathematics Series—Mathematical tables, manuals, and studies of special interest to physicists, engineers, chemists, biologists, mathematicians, computer programmers, and others engaged in scientific and technical work.

National Standard Reference Data Series—Provides quantitative data on the physical and chemical properties of materials, compiled from the world's literature and critically evaluated. Developed under a worldwide program coordinated by NBS under the authority of the National Standard Data Act (Public Law 90-396). NOTE: The Journal of Physical and Chemical Reference Data (JPCRD) is published quarterly for NBS by the American Chemical Society (ACS) and the American Institute of Physics (AIP). Subscriptions, reprints, and supplements are available from ACS, 1155 Sixteenth St., NW, Washington, DC 20056.

Building Science Series—Disseminates technical information developed at the Bureau on building materials, components, systems, and whole structures. The series presents research results, test methods, and performance criteria related to the structural and environmental functions and the durability and safety characteristics of building elements and systems.

Technical Notes—Studies or reports which are complete in themselves but restrictive in their treatment of a subject. Analogous to monographs but not so comprehensive in scope or definitive in treatment of the subject area. Often serve as a vehicle for final reports of work performed at NBS under the sponsorship of other government agencies.

Voluntary Product Standards—Developed under procedures published by the Department of Commerce in Part 10, Title 15, of the Code of Federal Regulations. The standards establish nationally recognized requirements for products, and provide all concerned interests with a basis for common understanding of the characteristics of the products. NBS administers this program as a supplement to the activities of the private sector standardizing organizations.

Consumer Information Series—Practical information, based on NBS research and experience, covering areas of interest to the consumer. Easily understandable language and illustrations provide useful background knowledge for shopping in today's technological marketplace.

Order the **above** *NBS publications from: Superintendent of Documents, Government Printing Office, Washington, DC 20402.*

Order the **following** *NBS publications—FIPS and NBSIR's—from the National Technical Information Service, Springfield, VA 22161.*

Federal Information Processing Standards Publications (FIPS PUB)—Publications in this series collectively constitute the Federal Information Processing Standards Register. The Register serves as the official source of information in the Federal Government regarding standards issued by NBS pursuant to the Federal Property and Administrative Services Act of 1949 as amended, Public Law 89-306 (79 Stat. 1127), and as implemented by Executive Order 11717 (38 FR 12315, dated May 11, 1973) and Part 6 of Title 15 CFR (Code of Federal Regulations).

NBS Interagency Reports (NBSIR)—A special series of interim or final reports on work performed by NBS for outside sponsors (both government and non-government). In general, initial distribution is handled by the sponsor; public distribution is by the National Technical Information Service, Springfield, VA 22161, in paper copy or microfiche form.